High Temperature Corrosion due to Biomass Firing: A Study on the Reactivity between Potassium Chloride and Oxides

Kiamehr, Saeed; Dahl, Kristian Vinter; Lomholt, Trine Nybo; Christiansen, Thomas Lundin; Somers, Marcel A. J.

Published in:
ISHOC 2014. International Symposium of High-temperature Oxidation and Corrosion 2014. Abstracts

Publication date:
2014

Document Version
Publisher's PDF, also known as Version of record

ISHOC 2014

International Symposium on High-temperature Oxidation and Corrosion 2014

Abstracts

23-27 June 2014
Hakodate, Hokkaido Japan

Organiser
The Iron and Steel Institute of Japan

Co-Organiser
Japan Society of Corrosion Engineering

ISHOC 2014

International Symposium on High-temperature Oxidation and Corrosion 2014

Abstracts

June 23-27

Hakodate, Hokkaido
Japan

Organiser
The Iron and Steel Institute of Japan
Co-Organiser
Japan Society of Corrosion Engineering

Abstracts: International Symposium on High-temperature Oxidation and Corrosion 2014, June 23-27, 2014/ Hakodate, Hokkaido, Japan
Published by The Iron and Steel Institute of Japan,
Niikura Building (2F), 2 Kanda-Tsukasacho 2-chome, Chiyodaku, Tokyo 101-0048, Japan

Preface

The International Symposium on High-temperature Corrosion was held at the Lake Yamanaka near the Mt Fuji, which was organized by Prof. Ryohei Tanaka in 1982. The “Mt. Fuji” symposium was the first meeting on high-temperature corrosion in Japan. Following the first symposium, the workshop was organized by Prof. Yasutoshi Saito at Tokyo Institute of Technology in 1990.

After these meeting, the Japanese community of high-temperature corrosion decided to arrange the symposium every 5 years. The first one was organized by Prof. Toshio Narita at Hokkaido in 2000, the second one was by Prof. Shigeji Taniguchi at Nara in 2005, and the third one was by Prof. Toshio Maruyama at Zushi in 2010. The symposium in 2014 is the fourth one held at Hakodate city, Hokkaido, named as ISHOC-2014 (International Symposium on High-temperature Oxidation and Corrosion 2014).

The global interests on energy and environmental issues increase remarkably in these days, in particular, because of the Fukushima nuclear accident and the global warming issue. The improvement of the efficiency in energy conversion requires structural materials to be exposed to higher temperatures and higher pressure in aggressive environments. Science and technology on high-temperature oxidation and corrosion of materials are being important more and more. In this symposium, more than 120 papers are presented. The discussions among participants in this symposium will find the future prospective to solve materials issues at high temperatures in aggressive environments.

On the behalf of the organizing committee, I would like to express the great appreciation to your important contribution to ISHOC-2014.

Sincerely yours,

June, 2014

Kazuya Kurokawa
Chair of Organizing Committee

Organizing Committee

Chairpersons

Kazuya KUROKAWA (Hokkaido University)

Head of Local Organizing Committee

Masayuki YOSHIBA (Tokyo Metropolitan University)

Vice Chairpersons

Isao SAEKI (Muroran Institute of Technology)
Hideyuki MURAKAMI (National Institute for Materials Science)
Kiyoshi IMAI (Toshiba Corporation)

Symposium Secretariats

Shigenari HAYASHI (Hokkaido University)
Makoto NANKO(Nagaoka University of Technology)

International Advisory Boards

S. Chevalier (France)
H. E. Evans (UK)
A. Galerie (France)
W. Gao (New Zealand)
B. Gleeson (USA)
M. J. Graham (Canada)
Y. Harada (Japan)
L. Heikinheimo (Finland)
S. Ito (Japan)
J. Jedlinsky (Poland)
S. Kihara (Japan)
T. Maruyama (Japan)
G. H. Meier (USA)
D. Monceau (France)
T. Narita (Japan)
R. Nemoto (Japan)
J. Nicholls (UK)
Y. Nii, (Japan)
E. Opila (USA)
F. J. Perez Trujillo (Spain)
J. H. Perepezko (USA)
B. A. Pint (USA)
K. Przybylski (Poland)
J. W. Quadakkers (Germany)
F. Rizzo (Brazil)
Y. Saito (Japan)
M. Schutze (Germany)
J. E. Svensson (Sweden)
R. Tanaka (Japan)
S. Taniguchi (Japan)
P. F. Tortorelli (USA)
F. Wang (China)
D. J. Young (Australia)
G. Tatolock (UK)

Local Executive Committee

S. Hayashi (Hokkaido Univ.)
H. Takahashi（Hokkaido Res. Org.）
M. Fukumoto（Akita Univ.）
Y. Nishiyama（NSSMC）
Y. Hidaka（NSSMC）
S. Takahashi（Tokyo Metro. Univ.）
M. Nanko（Nagaoka Univ. Tech.）
K. Kusabiraki(Toyama Univ.)
Y. Shibata（Tomakomai Tech. Ctr.）
K. Yanagihara（NSSMC）
Y. Kondo（NSSMC）
T. Nishimoto（NSSMC）
S. Ishikawa（JFE）
S. Ide（JFE）
Y. Matsunaga（IHI）
K. Kawamura（Tokyo Inst. Tech.）
S. Ono（MEP）
M. Ueda（Tokyo Inst. Tech.）
M. Takeda（KOBELCO）
M. Noguchi（Ebara）
T. Teratani（TOCALO）
M. Segawa（NGK）
S. Kyo (KEPCO)

Local Organizing Committee

M. Yoshiba (Tokyo metropolitan Univ.)
T. Goto (Tohoku Univ.)
S. Suzuki (Tohoku Univ.)
M. Hara (Akita University)
S. Kuroda (NIMS)
A. Motoi (Tokyo)
A. Nishikata (Tokyo Inst. Tech.)
A. Murata (Nagoya Univ.)
A. Nitta (CEPRI)
T. Amano (Shonan Inst. Tech.)
F. Ono（NMC）
Y. Isomoto（Hiroshima Univ.）
M. Sakamoto（AIST）
F. Masuyama（Kyushu Inst. Tech.）
T. Ishitsuka（NSSMC）
S. Sato（JFE）
T. Onishi（KOBELCO）
N. Hiramatsu（Nisshin Steel）
Y. Kadoya（MHI）
K. Nakagawa（IHI）
Y. Kamei（KHI）
Y. Fukuda（BHK）
M. Miyasaka（EBARA）
Y. Kojima (Hitachi)
S. Hirata (Nippon Yakin)
Y. Tanaka (Mitsui Chemicals)
Y. Kawahara (DHF)
M. Nakamori（High Temp. Res.）
N. Otsuka (NSSMC)
T. Ujiro (JFE Tech.)、
T. Anraku (NSST)
M. Yoshihara (Yokohama Natl. Univ.)
Y. Watanabe (Tohoku Univ.)
T. Suidzu（TOCALO）
T. Tanaka (NGK)
H. Habazaki (Hokkaido Univ.)

Sponsors

The Iron and Steel Institute of Japan

Hyuga Memorial Grant for International Conference

JSCE
JAPAN SOCIETY OF CORROSION ENGINEERING

SWTF
SUGA WEATHERING TECHNOLOGY FOUNDATION

Suga Co., Ltd.

Sumitomo Heavy Industries, Ltd.

HIGH TEMPERATURE CORROSION
& PROTECTION TECHNOSEARCH Co. LTD

Hitachi Metals, Ltd.

Daido Steel Co., Ltd.

Pacific Steel Manufacturing Co., Ltd.

K&I Tubular Corporation

International Symposium on High-temperature Oxidation and Corrosion (ISHOC 2014)
23 JUN 2014 – 27 JUN 2014, Hakodate, Hokkaido Japan

Plenary 50 min, Keynote 30 min, Oral 20 min (including discussion)

---------- 23 Monday ----------

Registration (13:00-17:00)
Welcome Party (18:00-)

---------- 24 Tuesday ----------

Opening (8:30)
K. Kurokawa

Plenary Lecture (8:40-9:30)
Chairperson: S. Hayashi
(PL01) Environmental and Compositional Effects on Deposit-Induced Hot Corrosion: Improving Testing and Extending Component Performance, B. Gleeson, University of Pittsburgh, USA

Coffee / Tea (9:30-10:00)

Session 1, Coating 1 (10:00-11:40)
Chairperson: F. Wang and Y. Isomoto
(K01, Keynote) Oxidation resistance of thermal barrier coatings based on hollow alumina particles, F. Pedraza, B. Bouchaud, B. Rannou, M. Mollard, Pôle Sciences et Technology, FRANCE
(**O01) Development of ultra thick TBCs used in steam turbine components**, K. Wada, Toshiba Corporation, JAPAN
(**O02) Evolution of Oxide Scale on Aluminide and Pt-Aluminide Coatings Exposed To Type I Hot Corrosion Condition**, K. Shirvani[(1)], A. Rashidghamat[(1)], M. Mohammadi[(2)], [(1)]Iranian Research Organization for Science and Technology, [(2)]Shiraz University, Shiraz, IRAN
(**O03) Effects of Plasma Gas Compositions on the Microstructure of Suspension Plasma Sprayed Thermal Barrier Coatings**, X. Chen[(1)], S. Kuroda[(1)], T. Ohnuki[(1)], M. Coudert[(2)], H. Araki[(1)], Y. Sakka[(1)], K. Sato[(1)], [(1)]National Institute for Materials Science, JAPAN, [(2)]University of Limoges, FRANCE

Lunch (11:50-13:00)

Session 2, Coating 2 (13:00-14:40)
Chairperson: D. Monceau, T. Nishimoto
(**K02, Keynote) High Temperature Oxidation of Mo-Si-B Alloys and Coatings**, J.H. Perepezko, T. Sossaman, P. Ritt, University of Wisconsin-Madison, USA
(**O04) Observation and modeling of α-NiPt(Al) and void formations after interdiffusion of Pt Coating with a γ-Ni(Al) alloy at high temperature**, P. Audigié [(1)], A. R. Put[(1)], A. Malié[(2)], P. Bilhé[(2)], S. Hamadi[(2)], D. Monceau[(1)], [(1)]CIRIMAT, [(2)]SNECMA, FRANCE
(O05) Long term operational behavior of Re alloy diffusion barrier coated micro turbine combustor in digester gas combustion, H. Yakuwa[(1)], S. Hayashi[(2)], T. Narita[(3)], R. Yamamoto[(1)], T. Nakagawa[(1)], T. Kishikawa[(1)], [(1)]Ebara Corporation, [(2)]Hokkaido University, [(3)]DBC System R&D Co., Ltd., JAPAN
(**O06) Coatings for Oxycombustion - Supercritical Steam Boilers Components**, A. Agüero[(1)], I. Baraibar [(1)], V. González[(1)], M. Gutiérrez[(1)], R. Muelas[(2)], D. Plana[(1)], [(1)]Instituto Nacional de Técnica Aeroespacial, [(2)]Ingenieria de Sistemas para la Defensa de España SA, SPAIN

Poster Session 1 (14:40-16:30)

Session 3, Chromia Former (16:30-18:10)

Chairperson: A. Galerie, K. Kawamura,

(**K03, Keynote) Corrosion of Chromia Formers by Hot CO_2 Gas: a Review**, D.J. Young, T. D. Nguyen, J. Zhang, University of New South Wales, AUSTRALIA

(**O07) The Effect of Temperature on the Protective Oxide Layers in Cr-containing Steels**, J. Lehmusto, P. Yrjas, M. Hupa, Abo Akademi University, FINLAND

(**O08) Employing the effect of specimen thickness to study chromia scaling on Ni25Cr and its interactions with water vapour in N_2-O_2-H_2O test gases at 1000°C**, M. Hänsel, E. Turan and V. Shemet, Forschungszentrum Jülich, GERMANY

(**O09) Effect of Spinodal Decomposition on Oxidation of Fe-Cr Alloys**, J. Shen, E. Monazami, J. B. McClimon, P. Reinke, W. A. Soffa , E. J. Opila, University of Virginia, USA

---------- **25 Wednesday** ----------

Plenary Lecture (8:40-9:30)

Chairperson: E. J. Opila

(PL02) High-Temperature Oxidation Mechanism of Chemical Vapor Deposited Silicon Carbide, T. Goto, H. Katsui, and M. Oguma, Tohoku University, JAPAN

Coffee / Tea (9:30-10:00)

Session 4, High-temperature Corrosion of Ceramics (10:00-11:40)

Chairperson: J. Sumner, T. Akashi

(**K04, Keynote) Roles of high temperature oxidation in fiber reinforced self-healing ceramics**, W. Nakao, Yokohama National University, JAPAN

(O10) Raman study on the reaction behavior of AlN powder in wet air between 1000-1500℃, X. Hou, Y.Liu, E. Wang, J. Zhang, K.-Chih Chou, University of Science and Technology Beijing, CHINA

(**O11) Oxidation Behavior in Crack-healing of Metal/Al_2O_3 Nanocomposites**, M. Nanko[(1)], D. Maruoka[(1,2)], [(1)]Nagaoka University of Technology, [(2)]Yokohama National University, JAPAN

(**O12) Oxidation resistance of SiC-based composite materials against high temperature in air and steam environments**, K. Shimoda[(1)], T. Hinoki[(2)], Hideyuki Murakami[(1)], [(1)]National Institute for Material Science, [(2)]Kyoto University, JAPAN

Lunch (11:50-13:00)

Session 5, Alumina Former (13:00-14:40)

Chairperson: B. Gleeson, S. Kitaoka

(**K05, Keynote) Mass-transfer in Polycrystalline α-Alumina under Oxygen Potential Gradients at High Temperatures: An Experimental Approach**, S. Kitaoka[(1,3)], T. Matsudaira[(1)], T. Ogawa[(1)], T. Nakagaw[(2)], Y. Kagawa[(3)], [(1)]Japan Fine Ceramics Center, [(2)]Kyoto University, [(3)]The University of Tokyo, JAPAN

(**O13) Oxidation Resistance and Lifetime of ODS FeCrAl Alloys**, S. Dryepondt, B. Pint, Oak Ridge National Laboratory, USA

(**O14) The effect of Cr on formation and growth of Al_2O_3 scale on Fe-Cr-Al alloys at 1000°C**, S. Yoneda, S. Hayashi, S. Ukai, Hokkaido University, JAPAN

(**O15) Exposures in a waste-fired CFB boiler vs. laboratory exposures of a FeCrAl alloy at 600 °C - the influence of alkali salt**, N. Israelsson[(1)], K.A Unocic[(2)], J-E. Svensson[(1)], L-G. Johansson[(1)], [(1)]Chalmers University of Technology, SWEDEN, [(2)]Oak Ridge National Laboratory, USA

Poster Session 2 (14:40-16:30)

Session 6, Non-ferrous Alloys (16:30-18:10)

Chairperson: D. Naumenko, M. Nanko

(**K06, Keynote) Investigation of the initial stages of the halogen effect in TiAl oxidation**, H. -E. Zschau, S. Friedle, M.Schütze, DECHEMA-Forschungsinstitut, GERMANY

(**O16) Comparison between the oxidation kinetics of two high temperature titanium alloys Ti-6Al-2Sn-4Zr-2Mo (Ti-6-2-4-2) and Ti-15Mo-3Nb-3Al-0.4Si (beta-21S) in relation with their microstructure and ductility**, A. R. Put[(1)], C. Thouron[(1)], P. Emile[(2)], R. Peraldi[(2)], D. Monceau[(1)], [(1)]CIRIMAT, [(2)]AIRBUS, FRANCE

(**O17) Effect of minor boron addition in Ni-base superalloys on oxide scale formation, in high pO_2, SO_2-containing environments**, D. Naumenko, A. Jalowicka, W. Nowak, L. Singheiser, W.J. Quadakkers, Forschungszentrum Jülich GmbH, GERMANY

(**O18) Study of Microstructure Phenomena Occurring in the Sub-surface of Cast Carbides-strengthened Refractory Alloys during High Temperature Oxidation**, P. Berthod, E. Conrath, University of Lorraine, FRANCE

---------- 26 Thursday ----------

Plenary Lecture (8:40-9:30)

Chairperson: Y. Nishiyama

(**PL03) Current Status of Japan Advanced Ultra-Supercritical (A-USC) Technology Development**, Y. Fukuda, Babcock-Hitachi K.K., JAPAN

Coffee / Tea (9:30-10:00)

Session 7, A-USC (10:00-11:40)

Chairperson: M. Schütze, Y. Matsunaga

(**K07, Keynote) Corrosion of superheater materials – full scale test loops**, L. Intiso, O. Tassa, Centro Sviluppo Materiali S.p.A via di Castel Romano, ITALY

(**O19) Fireside Corrosion of Steels and Ni-based Alloys in Simulated Superheater / Reheater Environments for Advanced Air- and Oxy-fired Coal-Biomass Combustion Power Plants**, N. J Simms, T. Hussain, A. Syed, J. E. Oakey, Cranfield University, UK

(**O20) Effects of Cr and Mo on Coal Ash Corrosion Resistance of Ni-based Alloy for 700 ºC class A-USC boilers,** M. Shimizu[(1)], T. Sato[(1)], T. Uehara[(2)], [(1)]Babcock-Hitachi.K.K., [(2)]Hitachi Metals, Ltd., JAPAN

(**O21) High Temperature Corrosion of Top Rank Fuel Cladding Candidate Materials for Canadian Generation IV Supercritical Water-Cooled Reactor**, Y. Zeng, J. Li, B. S. Amirkhiz, M. Matchim, P. Liu, W. Zheng, CanmetMATERIALS, Natural Resources Canada, CANADA

Lunch (11:50-13:00)

Session 8, High-Temperature Application (13:00-14:40)

Chairperson: S. Chevalier, H. Yakuwa

(K08, Keynote) Enhancing the Oxidation Behavior of Ferritic-Martensitic Steels for Water Vapor Containing Power Conversion Environments, D. Schmidt, M. C. Galetz, X. Montero, M. Schütze, DECHEMA-Forschungsinstitut, GERMANY

(O22) Self-fluxing coating protection against fireside corrosion in WtE, J.M. Brossard[(1)], F. Maad[(1)], Y. Kawahara[(2)], [(1)]Veolia Environnement Recherche et Innovation, FRANCE [(2)]DAI-ICHI HIGH FREQUENCY, JAPAN

(O23) Sputtered Mn-Cu Coating for Solid Oxide Fuel Cell Interconnect Application, S. Geng[(1,2)], Y. Li[(1)], S. Zhu[(2)], F. Wang[(2)], (1)Northeastern University, [(2)]Institute of Metal Research, CHINA

(O24) Nano RE coatings on ferritic steels in high steam content hydrogen atmospheres – A material study for SOFC and SOEC applications, P. Alnegren, J. G. Grolig, J-E. Svensson, J. Froitzheim, Chalmers University of Technology, SWEDEN

Poster Session 3 (14:40-16:30)

Session 9, High-temperature Corrosion (16:30-18:10)

Chairperson: M. C. Galetz, N. Otsuka

(K09, Keynote) Electrochemical corrosion behavior of Fe, Cr with a solid NaCl deposit in wet oxygen at medium temperature, L. Liu, Y. Li, F. Wang, Institute of Metal Research, Chinese Academy of Sciences, CHINA

(O25) Vanadium Attack of Tube Materials in Boilers Firing Crude-Residues, N. Otsuka, Nippon Steel & Sumitomo Metal Corporation, JAPAN

(O26) Hot Corrosion Modeling of Gas Turbine Materials in Novel Combusted Syngas Environments, J. Sumner, A. Potter, N. J. Simms, John E. Oakey, J. R. Nicholls, Cranfield University, UK

(O27) Electrochemical Characterization of the Behavior of Chromia and Alumina Passivation Layers on Nickel Base Superalloys in Contact with Molten Silicate Glass, T. K. Abdullah[(1,2)], C. Petitjean[(1)], P. -Jean Panteix[(1)], C.Rapin[(1)], M. Vilasi[(1)], Z. Hussein[(2)], A. A. Rahim[(2)], [(1)]IJL-UMR, FRANCE, [(2)]Universiti Sains Malaysia, MALAYSIA

Banquet (19:00-21:00)

---------- 27 Friday ----------

Plenary Lecture (8:40-9:30)

Chairperson: D. J. Young

(PL04) High Temperature Oxidation from a Viewpoint of Solid State Chemistry, T. Maruyama, Tokyo Institute of Technology, JAPAN

Coffee / Tea (9:30-10:00)

Session 10, Fundamentals (10:00-11:40)

Chairperson: N. Simms, Y. Kondo

(K10, Keynote) Cation Distribution in Oxide and Sulfide Scales, Toshio Narita, Hokkaido University / DBC systems, JAPAN

(O28) Nucleation and Growth of ZnO Particles by Internal Oxidation in Pd, N. Sakaguchi, K. Watanabe, Hokkaido University, JAPAN

(O29) Experimental study and numerical simulations of high temperature (1100 – 1250°C) oxidation of pre-oxidized zirconium alloy, C. Desgranges[(1)], B. Mazères[(1,2)], C. Toffolon[(1)], D. Monceau[(2)], [(1)]CEA, DEN. [(2)]CIRIMAT, Université de Toulouse, ENSIACET, FRANCE

(O30) The Development of Tensile Test to Asses the Adhesion of Thermal Oxide Scales Grown on Low Carbon Steels Oxidised in Water Vapour, S. Chandra-ambhorn, N. Klubvihok, King Mongkut's University of Technology, THAILAND

Closing Remarks (11:40)

POSTER Presentation

(* student poster)

POSTER 1, Fundamentals / Coatings (24 Tuesday, 14:40-16:30)

*** (P01s) Solid state reaction of Fe and Cr_2O_3 in the H_2/H_2O gas mixture at 1073 K**, K. Watanabe, M. Ueda, T. Maruyama, M. Takeyama, Tokyo Institute of Technology, JAPAN

*** (P02s) Influences of the Base Element, the Oxide Scale Thickness and the Cooling Start Temperature on the Oxide Spallation of Cast Alloys during the Post-Isothermal Oxidation Cooling**, E. Conrath, P. Berthod, University of Lorraine, FRANCE

*** (P03s) High Temperature Corrosion due to Biomass Firing: A Study on the Reactivity between Potassium Chloride and Oxides**, S. Kiamehr, K. V. Dahl, T. N. Lomholt, T. L. Christiansen, M. A.J. Somers, Technical University of Denmark, DENMARK

*** (P04s) Oxide growth characterization of four commercially available high temperature alloys (RA 602CA; Inconel 693; Manaurite 40XO; Sumitomo 696) in air and Ar-H_2O at 950°C**, L. Aranda, L. Portebois, S.Mathieu, Y. Bouizi, P. Panteix, S. Mathieu, M. Vilasi, Université de Lorraine, FRANCE

*** (P05s) Applicability of Thermodynamic Simulation in the Environmental Predication of the High-Efficiency Waste-to-Energy Plant Boiler**, Y. Sudo[(1)], K. Takemura[(1)], M. Yoshiba[(1)], Toshiro Anraku[(2)], S. Tokura[(2)], [(1)]Tokyo Metropolitan University, [(2)]Nippon Steel & Sumikin Technology, JAPAN

(P06) Near Ambient Pressure XPS studies on the oxide formation on Fe-2Mn during thermal treatment, S. Borodin, D. Vogel, S. Merzlikin, P. Keil, M. Rohwerder, [(1)]Max-Planck-Institut für Eisenforschung GmbH, GERMANY

(P07) Adhesion of scales on carbon steels containing boron or phosphorus, E. Ahtoy[(1,2,3)], G. Leprince[(1)], M. Picard [(1)], Y Wouters[(2)], A. Galerie[(2)], X. Wang[(3)], A. Atkinson[(3)], [(1)]Arcelor Mittal Research, FRANCE, [(2)]Université de Grenoble, FRANCE, [(3)]Imperial College, London, UK

(P08) Effect of Scale layer Structure on Blister Generation during High Temperature Oxidation of Steel, Y. Kondo, H. Tanei, K. Ushioda, M. Maeda, Nippon Steel & Sumitomo Metal Corporation, JAPAN

(P09) Adhesive Strength Measurement of Oxide Scale Formed on Low-Carbon Steel, H. Tanei, Y. Kondo, Nippon Steel & Sumitomo Metal Corporation, JAPAN

(P10) Oxidation behavior of silicon containing steel due to heating processes, S. Nakakubo[(1)], A. Kitahara[(2)], R. Kamata[(2)], M. Takeda[(1)], [(1)]Kobe Steel Ltd., [(2)]Kobelco Research Institute, Inc., JAPAN

(P11) Study of the High Temperature Oxidation in Vapor-rich Air of Cast Chromia-forming Nickel-based and Cobalt-based Alloys, P. Berthod[(1)], L. Aranda[(1)], T. Schweitzer[(1)], A. Navet[(2)] , A. Leroy [(2)], [(1)]University of Lorraine, [(2)]Lycée Henri Loritz, FRANCE

(P12) Fracture and Erosion Characteristics of Self-Fluxing Alloy Coatings in High Temperature Environment, Y. Isomoto Oka[(1)], Y. Kawahara[(2)], Michiko Yoshihara[(3)], [(1)]Hiroshima University, [(2)]Dai-ichi High Frequency Co., Ltd., [(3)]Yokohama National University, JAPAN

(P13) Origin of the ω-Zr Phase formed during High Temperature Oxidation of Zirconium Alloys, J. Favergeon[(1)], S. Chevalier[(2)], T. Montesin[(2)], G. Bertrand[(2)], [(1)]University of Technology of Compiegne, [(2)]Université de Bourgogne, FRANCE

(P14) High temperature oxidation of austenitic stainless steels: effect of sulfur content on scale adhesion, V. Parry[(1)], E. Fedorova[(2)], C. Pascal[(1)], M.Braccini[(1)], M. Mantel[(1,3)], D.Oquab[(4)], D. Monceau[(4)], Y. Wouters[(1)], [(1)]University of Grenoble, FRANCE, [(2)]Polytechnic Institute of Siberian Federal University, RUSSIA, [(3)]UGITECH SA, Ugine, [(4)]University of Toulouse, FRANCE

(P15) Mechanisms of Localized Corrosion in Boiler Combustion Gas Environment, Y. Kawahara, Dai-Ichi High Frequency Co., Ltd., JAPAN

(P16) How stress and temperature effect the high temperature corrosion mechanisms in Waspaloy in various gas/catalysts environments, P. Dowson[(1,*)], D. Dowson[(1)], H. Yakuwa[(2)], S. Sawada[(3)], [(1)]Elliott Group Ebara

Corporation, USA, [(2)]Ebara Corporation, [(3)]Elliott Ebara Turbomachinery Corporation, JAPAN

(P17) Structural Stability of Diffusion Barrier Coating at High Temperatures based on Experimental Phase Diagrams, S. Saito[(1)], T. Takashima[(1)], K. Miyama[(1)], K. Kurokawa[(2)], T. Narita[(3)], [(1)]Hokkaido University of Science, [(2)] Hokkaido University, [(3)]DBC System R&D Co., Ltd, JAPAN

(P18) Effects of Cu Content on the Oxidation and Dissolution Behavior of Fe-Cu Alloys, T. Nishimoto, H. Tanei, Y. Kondo, K. Uemura, Nippon Steel & Smitomo Metal Corporation, JAPAN

(P19) Inhibition of chromium volatilization on a 22 wt. % Cr austenitic alloy in wet environment containing traces of SO_2 and Na_2SO_4, L. Intiso[(1)], N. Mortazavi[(2)], L-G. Johansson[(2)], M. Halvarsson[(2)], [(1)]Centro Sviluppo Materiali S.p.A via di Castel Romano, ITALY, [(2)]Chalmers University of Technology, SWEDEN

(P20) Initial Corrosion Behavior of Low Carbon Steel in Molten Lead-free Solder, A. Yamauchi, K. Uesugi, Gunma National College of Technology, JAPAN

(P21) High temperature oxidation behavior of CrMoV steel in carbon dioxide gas
T. Hino, K. Imai, D. Saito, Takeo Takahashi, Toshiba Corporation, JAPAN

(P22) Effect of CaO addition on the Oxidation of Magnesium Alloys, D. B. Lee, S. Y. Park, P. Yadav, M. A. Abro, M. J. Kim, Sungkyunkwan University, SOUTH KOREA

* **(P24s) Effects of Si Addition on Fabrication of Ti-Al Intermetallic Coatings by Hot Pressing of Warm Sprayed Precursors**, J. Sienkiewicz[(1,2)], S. Kuroda[(1)], K. Minagawa[(1)], H. Murakami[(1)], H. Araki[(1)], K.J. Kurzydłowski[(2)], [(1)]National Institute for Materials Science, JAPAN, [(2)]Warsaw University of Technology, POLAND

*** (P25s) Oxidation of Type 430 Stainless Steel Covered with Aluminosilicate Thin Coating at Elevated Temperatures**, T. Kimura[(1)], T. Yano[(2)], E. Tsuji[(1)], Y. Aoki[(1)], H. Habazaki[(1)], [(1)]Hokkaido University, [(2)]JFE Steel Corporation, JAPAN

(P26) Preparation and high temperature performance of a dual-phase PtAl coating on K38G superalloy, Y. Yang, Q. Liu, Z. Bao, S. Zhu, and F. Wang, Institute of Metal Research, CHINA

(P27) Development of Self-Mending Coating System on Nb and Nb-based Alloys, M. Ohtsuka[(1)], D. Hotta[(1)], T. Yoshioka[(1)], T. Narita[(1)] T. Nagata[(2)], I. Masuda[(2)], T. Masuoka[(2)], [(1)]DBC System R&D Co., Ltd., [(2)]Japan Aerospace Exploration Agency, JAPAN

POSTER 2, Corrosion / Coatings / Material Production (25 Wednesday, 14:40-16:30)

*** (P28s) The effect of co-firing of sewage sludge with waste wood on furnace wall corrosion**, Y. Alipour[(1)], P. Henderson[(1, 2)], [(1)]KTH Royal Institute of Technology, [(2)]Vattenfall Research and Development AB, SWEDEN

*** (P29s) Behavior in Oxidation at 1200°C of Cast Co-based, Ni-based and Fe-based Alloys Containing HfC Carbides**, E. Conrath, P. Berthod, University of Lorraine, FRANCE

*** (P30s) Corrosion behavior of Ti60 with a solid NaCl deposit in wet oxygen at 600°C**, L. Fan, L. Liu, Y. Li, F. Wang, Institute of Metal Research, CHINA

*** (P31s) Behavior in High Temperature Oxidation of Cast Chromium-rich Co-based, Ni-based and Fe-based Alloys containing Very High Fractions in Tantalum Carbides**, L. Corona, T. Schweitzer, L. Aranda, P. Berthod, University of Lorraine, FRANCE

*** (P32s) High Temperature Oxidation of Sintered β-$FeSi_2$ from Cast Iron Scrap Chips in Air**, A. Laila, M. Nanko, Nagaoka University of Technology, JAPAN

*** (P33s) Effects of third elements on oxidation resistance of $NbSi_2$**, T. Kanaya[(1)],K. Kimura[(2)], M. Ukegawa[(3)], L. Zhang[(1)], K. Kurokawa[(1)], [(1)]Hokkaido University, [(2)]Ebara Elliott, [(3)]Mitsubishi Heavy Industry, JAPAN

(P34) Corrosion of 316L steel in liquid Te at 550°C, L. Martinelli, K. Ginestar, CEA, DEN, DPC, SCCME, Laboratoire d'Etude de la Corrosion Non Aqueuse, FRANCE

(P35) High-Temperature Oxidation of Zircaloy-4 in oxygen-nitrogen mixtures, M. Steinbrück[*], S. Schaffer**,** Karlsruhe Institute of Technology, GERMANY

(P36) Process investigation of corrosion experiments at low oxygen activity environment containing H_2/H_2O, H. Hooshyar, J. Liske, J-E. Svensson, Chalmers University of Technology, SWEDEN

(P37) Characterization of Spark Plasma Sintered $FeSi_2$-Al Alloys Oxidized in Air at 1073 K, T. Sudiro[(1)], K. A. Zaini Thosin[(1)], K. Kurokawa[(2)], [(1)]Indonesian Institute of Sciences, INDONESIA, [(2)] Hokkaido University, JAPAN

*** (P38s) High temperature cyclic oxidation with water cooling: The study of alumina-forming coatings**, M. Brossard[(1)], F. Pedraza[(1)], M. Craig[(2)], J.R. Nicholls[(2)], [(1)]Université de La Rochelle, FRANCE, [(2)]Cranfield University, UK

*** (P39s) Effect of Pre-oxidation on Metal Dusting of Nano-crystalline Sputtering Coated Ni-Cr Alloys**, Z. Xiang[(1)], J. Zhang[(1)], C. Kong[(1)], X. Peng[(2)], and D. J. Young[(1)], [(1)]University of New South Wales, AUSTRALIA, [(2)]Institute of Metal Research, CHINA

*** (P40s) Nano-Micro Structural Investigation of the Oxide Scale on Carbon Steel Substrate**, E. Sugiarti[(1)], K. A. Zaini[(1)], Y. Wang[(2)], N. Hashimoto[(2)], S. Hayashi[(2)] and S. Ohnuki[(2)], [(1)]Indonesian Institute of Sciences, INDONESIA, [(2)]Hokkaido University, JAPAN

*** (P41s) Temperature Dependence of Oxidation Behaviors in Thermal Sprayed Bond Coatings by HVOF and Warm Spray**, T. Ohnuki[(1)],S. Kuroda[(2)], H. Murakami[(2)],H. Araki[(2)],Y. Sakamoto[(1)], [(1)]Chiba Institute of Technology, JAPAN, [(2)]National Institute for Materials Science, JAPAN

*** (P42s) Microstructure and Oxidation Resitance of Aluminized Ni-based superalloys**, K. Kasai[(1,2)], H. Murakami[(1)], and Y. Noda[(2)], [(1)]National Institute for Materials Science, [(2)]Shibaura Institute of Technology, JAPAN

(P43) Selection Oxidation in Fe-Ga alloys Annealed under Low Partial Pressure of Oxygen, S. Suzuki, S. Fujieda, R. Ukai, Tohoku University, JAPAN

(P44) Formation of the NiAl containing Hf by the Simultaneous Electrodeposition of Al and Hf using a Molten-Salt and Cyclic Oxidation, M. Fukumoto, A. Yokobori, M. Hara, Akita University, JAPAN

(P45) Preparation of Ni Aluminide / Ni Bilayer Coating on Nb –W Alloys by Molten Salt Electrodeposition and Oxidation Resistance, N. Sato, M. Fuji, N. Kohiruimaki, M. Fukumoto, M. Hara, Akita University, JAPAN

(P46) Study on oxidation behavior of pure Cr at high temperature in water vapor, Z. Wang[(1)], T. Song[(2)], Wuhan University, [(2)]WISCO, CHINA

(P47) Influences of several coatings on oxidation behavior of single crystal superalloy DD98M, L. Shi[(1,2)], L. Xin[(1)], X. Wang[(1)], S. Zhu[(1)], F. Wang[(1)], H. Wei[(1)], [(1)]Institute of Metal Research, [(2)]Northeastern University, CHINA

(P49) Microstructure and Oxidation Resistance of Ti and Ir Based Alloys Aluminized with NiAl Alloy Powders, H. Murakami[(1)], D. Ohtsubo[(1,2)], R. Zempo[(1,2)], K. Kasai[(1,2)], Y. Noda[(2)], [(1)]National Institute for Materials Science, [(2)]Shibaura Institute of Technology, JAPAN

*** (P50s) Mechanical and Physical Properties of Iron Oxides**, T. Aiza, Y. Kurashige, L. T. Dung, M. Nanko, Nagaoka University of Technology, JAPAN

(P51) Suppressing the selective oxidation during the recrystallization annealing of steel band for improved hot dip galvanizing: laboratory study, S. V. Merzlikin, A. Vogel, M. Auinger, D. Vogel, M. Rohwerder, Max- Planck Institute for Iron Research, GERMANY

(P52) Reduction of iron oxide scale formed on steel surface by containing elements, K. Ikeda, H. Okada, Nippon Steel & Sumitomo Metal Corporation, JAPAN

(P53) Spallation behavior of oxide scale on stainless steels, A. Hayashi[(1)], N. Hiraide[(1)], and Y. Inoue[(2)], [(1)]Nippon Steel & Sumikin Stainless Steel Corporation, [(2)]Nippon Steel & Sumitomo Metal Corporation, JAPAN

POSTER 3, Corrosion / A-USC / SOFC / Alumina former (26 Thursday, 14:40-16:30)

*** (P54s) Effect of Ni addition on the Formation of SiC-$ZrSiO_4$ Porous Composites and Thermal Cyclic Oxidation Behavior**, K. Kobiyama, T. Akashi, Hosei University, JAPAN

*** (P55s) Preparation of Carbon Composite Bricks and its Interfacial Reaction Behavior with Hot Metal and Slag**, Jiao Ke-xin[(1)], Zhang Jian-liang[(1)], Liu Zheng-jian[(1)], Hou Xin-mei[(1)], Liu Yan-xiang[(1)], Zhao Yong-an[(2)], [(1)]University of Science and Technology Beijing, [(2)]Henan Winna Industrial group Co. Ltd, CHINA

*** (P56s) Contribution of high-temperature oxidation of self-healing agent for strength recovery behavior of self-healing ceramics**, S. Yoshioka, W. Nakao, Yokohama National University, JAPAN

*** (P57s) Influence of Al_2O_3 matrix on crack-healing function and high temperature oxidation of nano-Ni/Al_2O_3**

composites, H. Vu Pham[(1)], D. Maruoka[(2)], M. Nanko[(1)], [(1)]Nagaoka University of Technology, [(2)]Yokohama National University, JAPAN

*** (P58s) Evaporation of Gallium Suboxide from Mixture by Carbothermal Reduction and Deposition of Gallium Trioxide on Different Substrates by Oxidation**, Y. Ando, T. Akashi, Hosei University, Tokyo, 184-8584, JAPAN

(P59) Simulation of SiC Passive Oxidation and oxidation transitions, T. Yoshinaka[(1)], Y. Kubota[(2)], H. Hatta[(1)], [(1)]Japan Aerospace Exploration Agency, [(2)]The Graduate University for Advanced Studies, JAPAN

(P60) Interface Reaction Between Different Refractory and Hot Metal, L. Zheng-jian, Z. Jian-liang, J. Ke-xin, H. Xin-mei, L. Yan-xiang, University of Science and Technology Beijing, CHINA

(P61) Effect of SiC Addition on the Oxidation Behavior of ZrB_2 at 1273 K and 1473 K, L. Zhang, K. Kurokawa, Hokkaido University, JAPAN

(P62) $TiSi_2$ assisted SiC oxidation for self-healing function in fiber reinforced self-healing ceramics at high-temperature, D. Maruoka, H. Yo, W. Nakao, Yokohama National University, JAPAN

*** (P63s) New approach for identifying areas of sulfidation on water wall tubes in coal-fired boilers**, S. Najima[(1)], M. Morinaga[(1)], S. Hayashi[(2)], [(1)]Central Research Institute of Electric Power Industry, [(2)]Hokkaido University, JAPAN

*** (P64s) Oxidation Behavior of Cladding Tube-Shaped 15Cr-20Ni Austenitic Stainless Steels in Supercritical Water at 700°C**, R. Suzuki, H. Abe, Y. Watanabe, Tohoku University, JAPAN

*** (P65s) Failure Mechanism by Hot Corrosion of Alloy 625 Superheater Tubein High-Efficiency Waste-to-Power Plant Boiler**, N. Kamiyama[(1)], K. Takemura[(1)], H. Morita[(1)], M. Yoshiba[(1)], M. Takakura[(2)], [(1)]Tokyo Metropolitan University, [(2)]JEOL Ltd., JAPAN

(P66) Enhanced Formation of Chromia Scale on Fe-20Cr-30Ni Alloys by Addition of Nb, Mo and W in Steam Environments, N. Kochi, S. Ishikawa, Y. Nishiyama, Nippon Steel & Sumitomo Metal Corporation, JAPAN

(P67) Water Vapor Oxidation Behavior of Precipitation-Strengthened 15Cr Ferritic Steels with Ni Addition, M. Auchi. Y. Toda, K. Sawada, H. Kushima, K. Kimura, National Institute for Materials Science, JAPAN

(P68) Microstructure development of oxide scales in the early stage of steam oxidation of the Fe-20Cr-30Ni-2Nb (at.%) steel at 1073 K, M. Ueda, A. Okubo, M. Takeyama, T. Maruyama, Tokyo Institute of Technology, JAPAN

(P69) The Long Term Coal Ash Corrosion Behavior of the Superheater Tube Materials in Oxy-fuel Gas Conditions, Y. Matsunaga[(1)], K. Nakagawa[(1)], T. Goto[(1)], T. Yamada[(1)], N. Fujiwara[(1)], T. Kiga[(1)], K. Kurokawa[(2)], [(1)]IHI Corporation, [(2)]Hokkaido University, JAPAN

*** (P70s) Effect of Electrical Current on Growth of Oxide Scale in Interface between Electrode and Fe-22mass% Cr SOFC Interconnect at 1073 K,** M. Febry, M. Ueda, K. Kawamura, T. Maruyama, Tokyo Institute of Technology, JAPAN

(P71) The influence of La_2O_3 nanoparticles on the oxidation resistance of Crofer 22 APU steel, A. Gil, J. Wyrwa, T. Brylewski, AGH-University of Science and Technology, POLAND

(P72) Fabrication of Cobalt Oxide Coating for SOFC Interconnector by Electrodeposition and Thermal Oxidation, I. Saeki, T. Yoshida, Y. Watanabe, Muroran Institute of Technology, JAPAN

*** (P73s) Effect of Nano Metal Coatings on Growth Kinetics of α-Al_2O_3 Formed on Ni-50Al Alloy**, A. Shaaban[(1, 2)], K. Azumi[(1)], and S. Hayashi[(1)], [(1)]Hokkaido University, JAPAN, [(2)]Central Metallurgical Research and Development Institute (CMRDI), EGYPT

(P74) Factors Affecting the Development Mechanism of the Protective Oxide Scale on Alumina-Forming High Temperature Materials: A Brief Survey, Jerzy Jedliński, AGH University of Science and Technology, POLAND

(P75) Reducing effect of a slight amount of NaCl vapor to pest oxidation of Ta-75at%Al at high temperature, Y. Sato, M. Hara, Akita University, JAPAN

(P76) Oxidation Behavior of Cu-modified Alumina Forming Austenitic Fe-Ni-Cr-Al Alloys, S. Hayashi, T. Kudo, S. Yoneda, S. Ukai, Hokkaido University, JAPAN

(P77) Influence of Mo on High Temperature Oxidation Behavior of La added 20 mass%Cr-6 mass%Al Ferritic Stainless Steel, A. Mizutani[(1)], M. Fujisawa[(1)], C. Kami[(1)], S. Hayashi[(2)], [(1)]JFE Steel Corporation, [(2)]Hokkaido

University, JAPAN

(P78) Case study for boiler tube failure of welded austenitic stainless steel, H.-sang Lee, S.-hee Na, J.-sung Jung, D.-soo Kim, K.-bong Yoo, Research Institute of Korea Electric Power Corporation, SOUTH KOREA

(P79) Early stage oxidation behaviour of single-crystal nickel-base superalloy during heating in various environments ,J.-sung Jung[(1)], B. A. Shollock[(2)], K.-bong Yoo[(1)], [(1)]Korea Electric Power Corporation, SOUTH KOREA, [(2)]University of Warwick, U.K.

Oral Presentations

Environmental and Compositional Effects on Deposit-Induced Hot Corrosion: *Improving Testing and Extending Component Performance*

Brian Gleeson

Department of Mechanical Engineering and Materials Science, University of Pittsburgh, 815D Benedum Hall, Pittsburgh, PA, 15261, USA

e-mail: bgleeson@pitt.edu

1. Overview

Hot corrosion is an accelerated degradation process that is generally considered to involve deposition of corrosive species (*e.g.*, sulfates) from the surrounding environment (*e.g.*, combustion gas) to the surface of hot components, followed by destruction of the protective oxide scale. Gas turbine engine components, particularly high-pressure turbine blades and rotors, exposed to marine environments are apt to encounter two modes of hot corrosion [1,2]: high temperature hot corrosion (Type I) in the temperature range 850-1000°C and low temperature hot corrosion (Type II) in the range 600-800°C.

Typically, hot corrosion testing is conducted using Na_2SO_4 (with a melting temperature of 881˚C) in an SO_2-containing environment. However, it is known that the deposit chemistry is much more complex (see, for example, Bornstein [3, 4]), consisting of multiple sulfates and silicates. Moreover, reports on atmospheric particulate matter (PM) show that the relative amounts of sulfate constituents contained in PM can vary significantly, depending on geographic region. This is shown in Fig. 1, which maps the variation in atmospheric PM throughout the world [5]. The designation $PM_{2.5}$ is for particles less than 2.5μm in size. In agreement with what is shown in Fig. 1, components operating in certain regions of the world, such as China and India, are found to be at an increased risk of deposit-induced hot corrosion due to atmospheric pollutants rather than the combustion process (*i.e.*, sulfur impurity in the fuel), which is usually the concern. Indeed, the combination of increased operating temperatures of turbine engines and activities within regions of the world that have relatively high pollutant (PM, SO_2, etc) levels are contriving to cause previously unobserved forms of high-temperature corrosion.

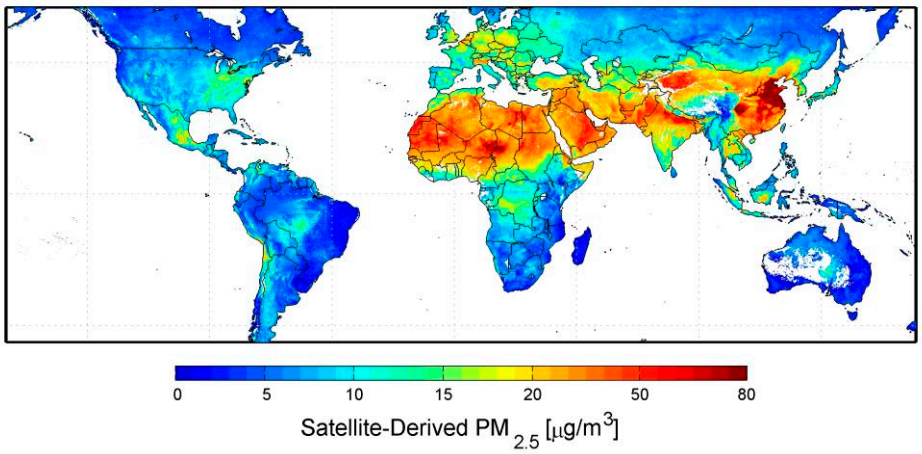

Fig. 1 Global satellite-derived map of $PM_{2.5}$ averaged over 2001-2006 [5].

This presentation will overview recent research conducted at the University of Pittsburgh to advance understanding of sulfate-based deposit-induced hot corrosion. It will be shown that (1) an effective laboratory-scale testing procedure has been developed that better simulates the form and extent of degradation found in service, and (2) that new insights on alloy/coating composition-structure relations for enhanced corrosion resistance have been established.

As an example of composition-structure relations, Fig. 2 summarizes recently obtained 700°C (Type II) hot-corrosion results for NiCoCrAl alloys containing various Cr and Al contents, but a fixed Co content in the range 18-20 at.%. The alloy microstructures were primarily γ-Ni + β-NiAl, with the amount of β varying with change in the Cr and Al contents. The sulfate deposit was ~2 mg/cm^2 Na_2SO_4 and the total exposure time was 100 h. The alloy indicated by "35Cr" in this figure is Ni-20Co-12Al-35Cr (at.%) and is seen to have exceptional hot-corrosion resistance (*i.e.*, low weight change) for

exposures to both O_2-2.5ppm SO_2 and O_2-1000ppm SO_2. Moreover, it is seen in Fig. 2 that the extent of corrosion increases with increasing β-NiAl volume fraction in the NiCoCrAl microstructure. Such a result may seem counterintuitive, since the Al-rich β phase is generally considered to be the more protective constituent; however, it is the low Cr solubility in β that makes it particularly susceptible to hot-corrosion attack.

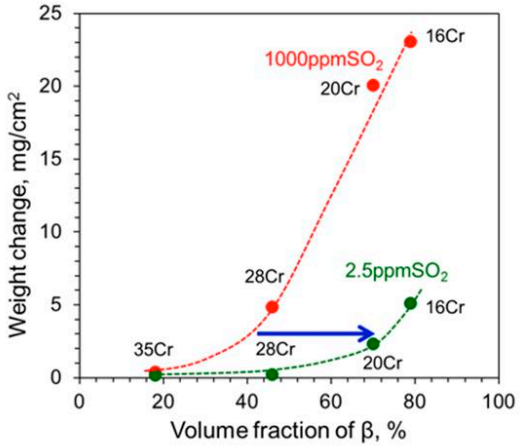

Fig. 2 Weight change as a function of β-NiAl volume fraction in NiCoCrAl alloys after Na_2SO_4-induced hot corrosion exposure for 100 h at 700°C in flowing O_2-2.5ppm SO_2 and O_2-1000ppm SO_2 atmospheres. All alloys contained 18-20 at.% Co and "xCr" corresponds to x at.% Cr in a given alloy.

As a further example, superalloys used in turbine disks have relatively high Co contents, and low Cr contents to insure adequate strength for these components. The effects of Co and Cr in on the 700°C hot corrosion resistance of Ni-based superalloys are indicated in Fig. 3. It is seen that Co-containing alloys having more than about 25 wt.% Cr undergo minimal corrosion; although, the higher the Co content the greater is the susceptibility to extensive attack. It is also seen that the amount of Cr needed for excellent corrosion resistance in significantly reduced to ~16 wt.% if the Co is reduced to nominally zero (*i.e.*, Haynes 214). However, the presence of cobalt in Ni-based superalloys leads to a number of advantages, including reducing the amount of phase transitions at elevated temperatures, reducing the coefficient of thermal expansion at higher temperatures, significantly improving the oxidation resistance at 1100°C by forming a stable alumina scale, and improving the hot corrosion resistance at 900°C [1]. As a result, and as will be discussed, a balance in alloying additions must be achieved in order to optimize overall performance.

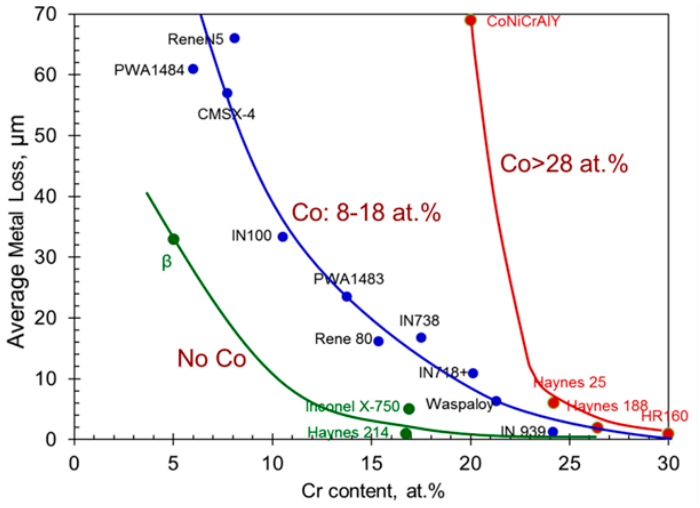

Fig. 3 Graphs of amount of metal loss for different Ni-based superalloys after 700 °C hot corrosion testing for 100 hours.

2. ACKNOWLEDGMENT

The research presented is primarily of support received over the years from the US Office of Naval Research, with Dr. David Shifler being the Program Manager.

3. REFERENCES

[1] F.S. Pettit, "Hot Corrosion of Metals and Alloys," *Oxidation of Metals*, 76 (2011) pp. 1-21.
[2] R.A. Rapp and Y-S. Zhang, "Hot Corrosion of Materials: Fundamental Studies," *JOM*, 46, No. 12 (1994) pp. 47-55
[3] N.S. Bornstein and W.P. Allen, "The Chemistry of Sulfidation Corrosion - Revisited," *Materials Science Forum*, Vols. 251-254 (1997) pp. 127-134.
[4] N.S. Bornstein, "Reviewing Sulfidation Corrosion – Yesterday and Today," *JOM*, 48, No. 11 (1996) pp. 37-39.
[5] http://www.nasa.gov/topics/earth/features/health-sapping.html.

Oxidation resistance of thermal barrier coatings based on hollow alumina particles

F. Pedraza [(1,*)], B. Bouchaud[(1)], B. Rannou[(1)] and M. Mollard [(1)]

[(1)] LaSIE FRE-3474 CNRS-Université de La Rochelle, Pôle Sciences et Technology, 17042 La Rochelle, FRANCE

e-mail: fpedraza@univ-lr.fr.fr

Abstract

Thermal barrier coatings were synthesized in a single step process from a slurry containing Al microspheres onto different Ni-based superalloys. Upon growth of the coating a top coat of hollow alumina spheres linked to an aluminium diffused coating through an alumina TGO formed. The isothermal and cyclic oxidation tests at different temperatures (900 till 1100°C) up to 1000h revealed progressive growth of different thermal oxides depending on the substrate composition. Faster degradation of the coatings occurred in the titanium-rich substrates (e.g. IN-738LC and PWA1483) compared to the titanium-poor ones (CM-247LC and René N5). By comparing with conventional low activity aluminide coatings, it appeared that the incorporation of alloying elements (notably Ti and Ta) to the diffused layers upon the high activity slurry coating process is responsible for such fastest degradation.

1. INTRODUCTION

The use of thermal barrier coatings in the high pressure turbine components of aeroengines made of nickel based superalloys is compulsory nowadays to withstand the very high surface temperatures of the corrosive gas released from the combustion chamber. This system is based on a top ceramic coat of YSZ made by EB-PVD with columnar structure to comply with cycling, an intermediate α-Al_2O_3 thermally grown oxide to attach the YSZ and to provide oxidation protection and an underlying β-NiPtAl diffusion coating that acts as an aluminium reservoir [1]. New low-cost and environmentally friendly coatings were recently proposed in the European project "Particoat" [2] in which a water-based slurry containing Al microparticles was sprayed and annealed [3] onto pure nickel [4] and different nickel-based superalloys [5] or steels [6]. The isothermal oxidation behavior of these coatings onto a pure Ni [7] and a René N5 superalloy [8] indicated faster oxidation kinetics and faster β-NiAl$\rightarrow\gamma$'-Ni_3Al transformation than in conventional low activity β-NiAl although both systems grew duplex $NiAl_2O_4/Al_2O_3$ scales. In contrast, the presence of the hollow alumina top coat and the precipitates segregated at the thermally grown oxide limited the appearance of rumpling compared to the conventional coatings. Nevertheless, the incorporation of alloying elements from the substrate to the coating (e.g. titanium, tantalum, chromium…) may affect the corrosion/oxidation resistance of such coatings. Indeed, as pointed out by Evans et al. the bond coat is the most crucial component of the TBC system as its chemistry and microstructure influence durability through the structure and morphology of the TGO upon oxidation [9]. For instance, titanium grows non protective TiO_2 on nanocrystalline IN-738 superalloy [10] whereas tantalum develops interspersed tantalum rich oxide particles ($CrTaO_4/NiTa_2O_6$) in the top spinel ($(Ni(Cr,Al,Co)_2O_4$) scale onto PWA-1484 superalloy [11]. It therefore appears that further understanding in this field is required for these new single step thermal barrier coatings. For such purpose, the increasing amounts of Ti and of Cr in the superalloys and their incorporation to the coatings, hence into the oxide layers were investigated in this work. The evolution of the diffusion coatings in terms of β-NiAl$\rightarrow\gamma$'-Ni_3Al and growth of TCPs will be also considered to shed light on the durability of these new slurry coatings.

2. EXPERIMENTAL

The thermal barrier coatings shown in Figure 1 were obtained from a 1/10 PVA/H_2O solution to which 45wt% 5µm-sized Al microparticles were added [3]. After spray and dry in air, the slurries were annealed at 700°C/2h and additional 1100°C/2h in Ar(g). The traces of O_2 (2 vpm) and H_2O (5 vpm) in Ar were shown to be sufficient to grow the top coat and the TGO composed of hollow α-Al_2O_3 [4]. Differences in the microstructure layer appeared as a result of the different composition and crystal structure of the Ni-based superalloys investigated (Table 1). Short (100h) isothermal tests were

Table 1. Nominal composition (wt%) of the nickel-based superalloys investigated.

	Ni	Cr	Co	Mo	W	Ta	Al	Ti	Other
René N5	61.6	7	8	2	5	7	6.2		0.2 Hf, 3.0 Re
CM-247LC	61.7	8.1	9.2	0.5	9.5	3.2	5.6	0.7	1.4 Hf
PWA-1483	61.2	12.2	9	1	3.8	5	3.6	4.1	
IN-738LC	61	16	8.5	1.7	2.6	1.7	3.4	3.4	0.9Fe, 0.3 Si

performed in a Setaram TGA92 thermobalance while for the long term (500 and 1000h) tests a Pyrox furnace was employed. In both cases, purging with Ar was let in the chamber till the 1100°C were reached and synthetic air replaced Ar. For the cyclic oxidation tests at 1100°C ambient air was employed in a Delta Thermique furnace upon the cycle of 1100°C/45 min + 40(±10)°C/15min. X-ray diffraction (Bruker AXS D8, $K\alpha_{Cu}$=0.15406 nm), Raman spectroscopy (Jobin Yvon Horiba LabRam HR, λ=632.817 nm), SEM/EDS (FEI-Quanta 200F/EDAX and JEOL5410/Oxford) and Electron probe microanalysis (EPMA, JEOL JXA-1800) allowed to characterize the degradation of the coatings upon oxidation.

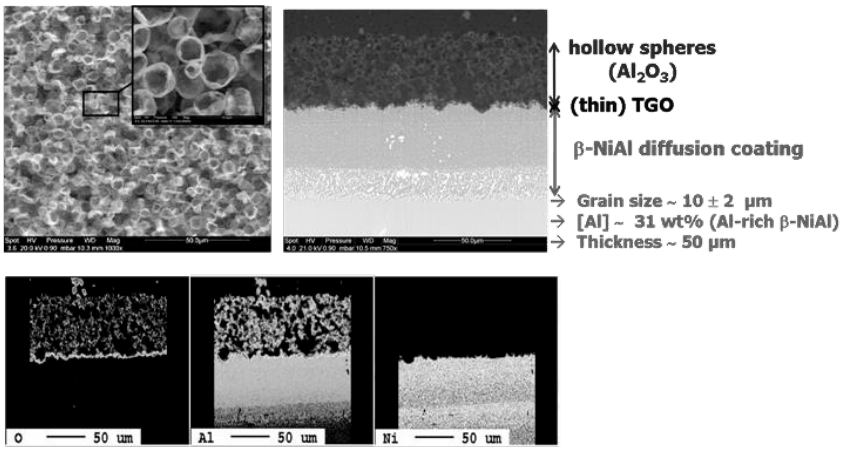

Figure1.- Slurry TBC coatings grown on nickel based superalloys showing a top coat of hollow alumina spheres, a TGO of alumina and a β-NiAl diffusion layer over the substrate (here for René N5).

3. RESULTS AND DISCUSSION

3.1.- Isothermal oxidation

The parabolic rate constants calculated using the complete law approach [12] were plotted in the Arrhenius diagram derived from a bulk β-NiAl by Brumm and Grabke [13] in Figure 2. It appeared that the slurry coatings onto pure nickel grew transition θ-Al_2O_3 for the first 100h regardless of the oxidation temperature. In contrast, the coated superalloys exhibited an evolution from θ to α-Al_2O_3 with increasing temperature. However one must bear in mind that the greatest kinetics of the slurry coatings can be related to further oxidation of remnants of metallic Al in the spheres after the coating elaboration process [7]. Further extension to 500 and 1000h of oxidation displayed less differences in terms of specific mass gain compared to a low activity β-NiAl. It shall be noted however that the top coat partially detached depending on the substrate (coating) composition.

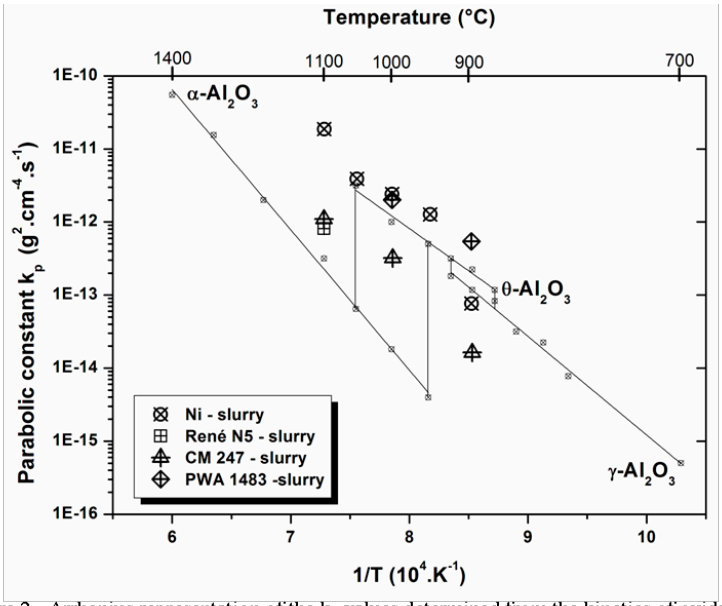

Figure 2.- Arrhenius representation of the k_p values determined from the kinetics of oxidation and comparison with the kp values from a pure β-NiAl [Brumm & Grabke, 1992].

This hypothesis was confirmed from the X-ray patterns (Table 2), where the incorporation of titanium and tantalum oxides became more relevant with oxidation time in all the systems. Additional tungsten, hafnium and spinel oxides appeared on N5, CM and PWA substrates. The EDS elemental maps in the cross sections confirmed the XRD results. Cr mainly partitioned to the interdiffusion zone (IDZ) [14] and therefore could not contribute to the formation of Cr_2O_3. In contrast, Ta and Ti were found in both at the bond coat/TGO interface and within the IDZ. This behaviour has been previously quoted for both Ta [15] and Ti [16] and can be related to the relatively high diffusion coefficient of both refractory elements in these systems [17]. It was also noted that upon transformation of the β-NiAl→γ'-Ni_3Al, dissolution of the precipitates of refractory elements occurred with temperature and time because of their limited solubilities in the β-NiAl phase [e.g. 18].

This is clearly demonstrated in Figure 3, where the low activity (CVD) bond coat transformed less β-NiAl phase than the high activity slurry one and therefore refractory-rich oxides precipitated in the duplex oxide scale with $NiAl_2O_4$ on top of a α-Al_2O_3 grown in both systems. However, and in spite of further transformation into the $L1_2$ (or martensitic $L1_0$) γ'-Ni_3Al quoted to induce rumpling [18,19] in the slurry coatings than in the conventional CVD ones, the latter displayed a more rumpled surface. It therefore appeared that the presence of the refractory oxide precipitates within the scale and the top coat of hollow alumina particles to pin the TGO and the underlying bond.

Table 2.- Oxide phases identified by XRD and Raman spectroscopy after isothermal oxidation in air of the slurry coated substrates.

Oxidation time (h)	Substrate			
	René N5	CM 247	PWA 1483	INCO 738
Oxidation at 900°C				
100h	X	α-Al_2O_3 / Ta_xO_y / TiO_2 / HfO_2	α-Al_2O_3 / TiO_2	
500h	X	α-Al_2O_3 / Ta_xO_y / TiO_2	α-Al_2O_3 / TiO_2	α-Al_2O_3 / TiO_2
1000h	X	α-Al_2O_3 / Ta_xO_y / TiO_2 / HfO_2	α-Al_2O_3 / $NiAl_2O_4$ / TiO_2	α-Al_2O_3 / TiO_2
Oxidation at 1000°C				
100h	X	α-Al_2O_3 / Ta_xO_y / TiO_2 / HfO_2	α-Al_2O_3 / $NiAl_2O_4$ / TiO_2	X
500h	X	α-Al_2O_3 / Ta_xO_y / TiO_2 / HfO_2	α-Al_2O_3 / $NiAl_2O_4$ / TiO_2	X
1000h	X	α-Al_2O_3 / Ta_xO_y / TiO_2 / HfO_2	α-Al_2O_3 / $NiAl_2O_4$ / TiO_2 / Ta_4O	X
Oxidation at 1100°C				
100h	α-Al_2O_3 / Ta_xO_y / WO_2	α-Al_2O_3 / $NiAl_2O_4$ / Ta_xO_y / TiO_2 / HfO_2	X	X
500h	α-Al_2O_3 / Ta_xO_y / $AlTaO_4$ / WO_2	α-Al_2O_3 / $NiAl_2O_4$ / Ta_xO_y / TiO_2 / HfO_2	X	X
1000h	α-Al_2O_3 / Ta_xO_y / $AlTaO_4$ / WO_2	α-Al_2O_3 / $NiAl_2O_4$ / Mo_xO_y / TiO_2 / HfO_2	X	X

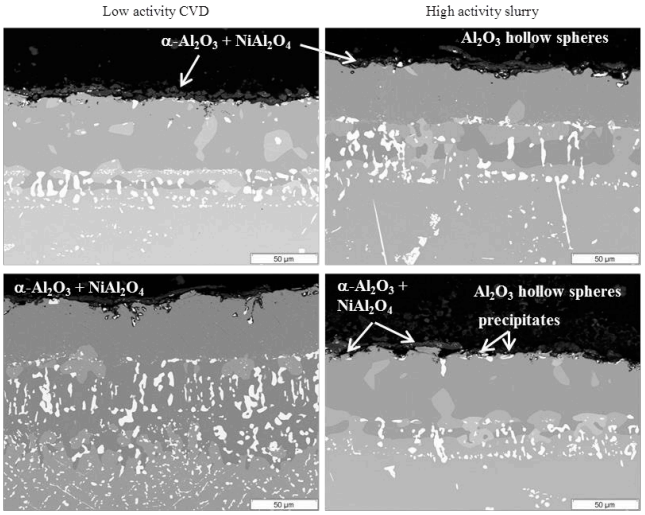

Figure 3.- Evolution of the microstructures in CM-247LC aluminized by (a) and (c) conventional low activity and by (b) and (d) high activity slurry after oxidation at 1100°C in air for 500h (a) and (b) and 1000 h (c) and (d).

3.1.- Cyclic oxidation

Figure 4 displays the mass gains per surface unit of René N5 and PWA 1483 aluminized using the conventional low activity and the slurry methods upon cyclic oxidation at 1100°C in air. Compared to the low activity aluminide, some spallation compensated by further mass gains occurred in the slurry René N5. In contrast, the slurry PWA 1483 underwent significant mass losses in less than 100 cycles. Since the major mass loss can be attributed to the top coat of hollow spheres, it appears that quite extended areas became naked (see inset in Fig. 4). The naked surface displayed a dark yellow colour indicative of TiO_2 and the presence of this oxide was confirmed by Raman spectroscopy and XRD. Therefore, it can be considered TiO_2 as the cause of such spallation. Indeed, by decreasing the oxidation temperature to 1000°C, the top coat remained adherent until 1500 cycles of oxidation although some low intensity peaks of TiO_2 were detected together with those of the major α-Al_2O_3 and $NiAl_2O_4$ spinel oxide phases.

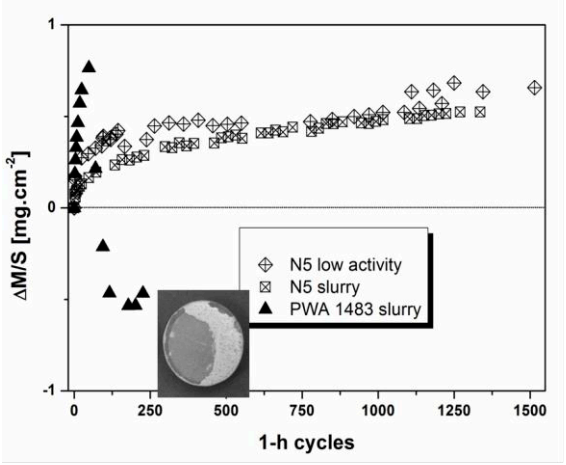

Figure 4.- Evolution of the mass gains per surface unit of the aluminized René N5 and PWA1483. Note the great spallation of the slurry aluminized PWA1483 compared to René N5.

4. CONCLUSION

The slurry coatings grown through a high activity process underwent relatively faster oxidation kinetics than bulk β-NiAl materials at the different temperatures investigated (900, 1000 and 1100°C). Although remnants of metallic Al may contribute to the overall mass gain, the formation of titanium and tantalum oxides very likely enhanced growth of the oxide scales that were mainly based on a top $NiAl_2O_4$ and a bottom α-Al_2O_3. These detrimental oxides grew with increasing oxidation temperature in particular in the Ti and Ta-rich alloys. However, Cr remained trapped in the TCP

phases and did not influence the oxidation kinetics. Although the oxidation kinetics and the β-NiAl→γ'-Ni_3Al transformation were enhanced in the high activity slurry coatings, the refractory-rich precipitates at the hollow spheres top coat/diffusion layer interface and the presence of the top coat seemed to limit rumpling compared to the conventional low activity β-NiAl ones. Nevertheless, extensive growth of TiO_2 appears to be the major cause of spallation as demonstrated in the cyclic oxidation tests and therefore the operating temperature for the high activity coatings rich in Ti shall not surpass 1000°C.

Acknowledgements
The DECHEMA Forschung Insitut is gratefully acknowledged for the EPMA analyses. This study was performed under the programme PARTICOAT FP7-NMP-2007-LARGE-1-CP-IP-211329-2 (2008-2012) funded by the European Union.

References

[1] Nicholls, J. R. "Advances in coating design for high-performance gas turbines" MRS Bull. Vol. 28 (2003), pp.659-670
[2] www.particoat.eu
[3] Rannou, B. *et al.* "Aging and thermal behavior of a PVA/Al microspheres slurry for aluminizing purposes", Mater. Chem. Phys. Vol.134 (2012) pp. 360– 365.
[4] Pedraza, F. *et al.* "Potential thermal barrier coating systems from Al microparticles. Mechanisms of coating formation on pure nickel", Mater. Chem. Phys. Vol. 134 (2012) 700-705.
[5] Montero, X. *et al*. "A single step process to form in-situ an alumina foam/aluminide TBC system for alloys in extreme environments at high temperatures", Surf. Coat. Technol. Vol. 206, No.7 (2011), pp. 1586-1594.
[6] Juez-Lorenzo, M. J. *et al.* "Diffusion aluminide coatings using spherical micro-sized aluminium particles", Defect Diff Forum Vols. 289-292 (2009), pp. 261-267.
[7] Mollard, M. *et al.* "Comparative degradation of nickel aluminized by slurry and by pack cementation under isothermal conditions", Corros. Sci. Vol. 66 (2013) pp. 118–124.
[8] Rannou, B. et al. "Comparative isothermal oxidation behaviour of new aluminide coatings from slurries containing Al particles and conventional out-of-pack aluminide coatings", Oxid. Met. DOI 10.1007/s11085-013-9427-6.
[9] Evans, A. G. *et al.* « Mechanisms controlling the durability of thermal barrier coatings", Progress in Materials Science Vol. 46, No. 5 (2001) pp. 505-553.
[10] Geng, G. *et al.* "High-temperature oxidation behavior of sputtered IN 738 nanocrystalline coating", Oxidation of Metals, Vol. 57, Nos. 3/4 (2002), pp. 231-243.
[11] J.A. Nychka et al. "Spallation and transient oxide growth on PWA 1484 superalloy", Mater. Sci. Eng. A, Vol. 490, Nos. 1-2 (2008), pp. 359–368.
[12] Pieraggi, B., "Calculations of parabolic reaction rate constants" Oxid. Met. Vol. 27, Nos. 3-4 (1987), pp. 177–185.
[13] Brumm, M.W. *et al.* « The oxidation behaviour of NiAl-I. Phase transformations in the alumina scale during oxidation of NiAl and NiAl-Cr alloys", Corros. Sci. Vol. 33, No.11 (1992), pp. 1677-1690.
[14] Rae, C.M.F. *et al.*, "The effect of TCP morphology on the development of aluminide coated superalloys" Mater. Sci. Eng. A Vol. 396, Nos. 1-2 (2005), pp. 231-239.
[15] Bouchaud, B. *et al.*, "Cyclic and isothermal oxidation at 1,100 °C of a CVD aluminised directionally solidified Ni superalloy", Oxidation of Metals Vol. 69, Nos. 3-4 (2008), pp. 193-210.
[16] Pfennig, A. *et al.*, « Oxidation of single crystal PWA 1483 at 950 °C in flowing air ", Corros. Sci. Vol. 50, No. 9 (2008), pp. 2484-2492.
[17] Pedraza, F., "Implications of diffusion on the composition and microstructures of platinum modified aluminide coatings on CMSX-4 single crystal superalloy" Defect Diff. Forum Vols. 289-292 (2009), pp. 277-284.
[18] Pennefather, R. C. *et al.*, "Mechanical degradation of coating systems in high temperature cyclic oxidation, Surf. Coat. Technol. Vols. 76-77, Nos. 1-3 (1995), pp. 47-52.
[19] Bouchaud, B. *et al.*, "Evolution of oxide scales on aluminide coatings under isothermal and cyclic conditions », Mater. Sci. Forum Vols. 595-598, Part. I (2008) pp. 11-16.

Development of Ultra thick TBCs used in steam turbine components

Kunihiko Wada [(1,*)], Satoru Kuboya [(1)], Tsuguhisa Tashima[(2)] and Tekeo Takahashi[(3)]

[(1)] Power and Industrial Systems R&D Center, Toshiba Corporation, 2-4, Suehiro-cho, Tsurumi-ku, Yokohama 230-0045, JAPAN
[(2)] Turbine Design & Assembling Dept., Toshiba Corporation, 1-9, Suehiro-cho, Tsurumi-ku, Yokohama 230-0045, JAPAN
[(3)] Thermal & Hydro Power Systems & Services Div., Toshiba Corporation, 1-1-1, Shibaura, Minato-ku, Tokyo 105-8001, JAPAN

e-mail: kunihiko.wada@toshiba.co.jp

1. INTRODUCTION

Thermal barrier coating systems (TBCs) are widely applied to hot gas path components in gas turbines so far. The steam temperatures of coal-fired steam turbine systems also increase. Over 700˚C-class advanced-ultra supercritical steam turbine system (A-USC) has been developed in Toshiba corporation since 1980 [1,2]. Ni-based or Co-based superalloys with superior high temperature strength will be used as the structural material of high temperature components in the A-USC system instead of high chromium steels. However, the thermal stress of the hot components induced by the temperature difference between steam side and cooling side is high. Nozzle box is the component which is located at the steam inlet part of the steam turbine and guides the steam flow into 1st nozzle and blade section. In order to reduce the thermal stress generated in the nozzle box, we consider the use of TBCs [3,4]. Since the superalloy substrate has enough high temperature strength at steam temperature, the role of this TBCs is to reduce the temperature difference between the steam side and the cooling side of the component. Therefore, TBCs can be applied to the cooling side of the nozzle box. As the result of the heat conduction analysis, this TBCs requires high thermal resistivity compared with usual TBCs for gas turbines. When we assume that the thermal conductivity of the ceramics layer is about 1.3 W/mK, its thickness requires over 3 mm. In this paper, the mechanical and thermal properties of the ultra thick TBCs will be explained. Moreover, the performance of the TBCs tested in our steam turbine test facility will be shown.

2. EXPERIMENTAL

2.1 Coating Process and Microstructure

The ultra thick TBCs is composed of a MCrAlY alloy as the bondcoat and an yttria-stabilized zirconia (YSZ) as the topcoat. These layers are coated by the use of atmospheric plasma spray (APS) equipment. In order to reduce the thermal stress during deposition process, the porosity of the topcoat was carefully controlled by means of spray parameters and powder.

Consequently, we have succeeded in producing the ultra thick TBCs. The cross-sectional images of a conventional and an ultra thick TBCs are shown in Fig.1. As seen in this figure, the thickness of the topcoat exceeds 3 mm which we require. We do not observe any spallation and cracks in the as-deposited topcoat layer. This is the result of thermal stress relaxation effect of high porosity topcoat.

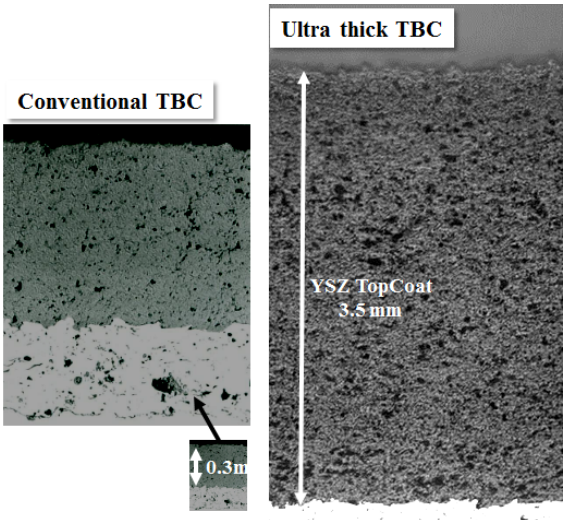

Fig.1 Cross-sectional SEM micrographs of conventional and ultra thick TBCs.

2.2 Evaluation of Properties

The TBCs requires a wide variety of thermal, chemical and mechanical properties. Before the durability test using steam turbine test facility, we investigated many properties as follows: (1)steam oxidation resistance of bondcoat, (2)thermal conductivity of the topcoat by laser flash method, (3)coefficient of thermal expansion (C.T.E.) of the topcoat by push-rod dilatometer and (4)Young's modulus of the topcoat by vibration method. These

properties are obtained up to 750˚C. In addition, thermal cycle tests between R.T. and 750˚C and thermal shock tests which are heated at 750˚C and quenched in water were carried out.
After these property measurements, the developed ultra thick TBCs are applied to actual steam turbine components in our steam turbine test facility. The TBCs was coated on the inner casing with about 1m diameter to evaluate the producibility. The coating was also deposited on the side part of the 1st nozzle diaphragm. This part is directly exposed to the inlet steam with the highest temperature. Therefore, the environmental condition of this part is very severe on the TBCs.

3. RESULTS AND DISCUSSION

3.1 Steam Oxidation Resistance of Bondcoat

The comparisons of the steam oxidation resistance among several plasma-sprayed bondcoat alloys are shown in Fig.2. Ni-Cr binary alloy shows the lowest oxidation resistance at the both temperatures. It is suggested that aluminum is effective element to prevent steam oxidation even at low temperature (550˚C). High-Cr MCrAlY shows the lowest weight gain at 550˚C. In contrast, high-Al MCrAlY shows the superior resistance against steam oxidation at 750˚C. These results of the temperature dependencies of the effects of Al and Cr on the oxidation resistance have a good agreement with the previous reports [5]. We should select the bondcoat alloy of the TBCs for steam turbines depending on its service temperature.

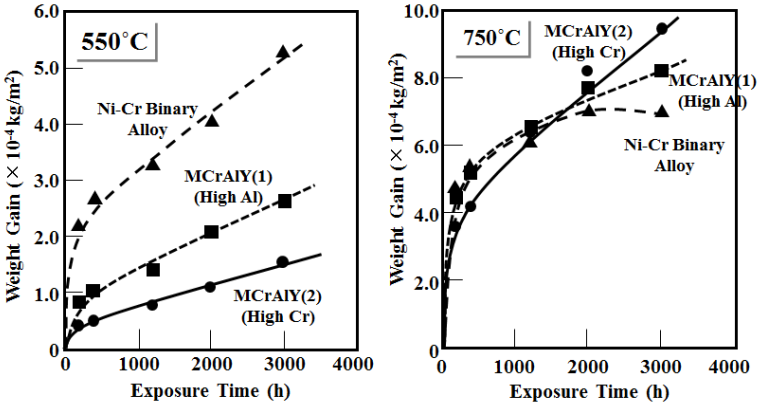

Fig.2 Weight change of bondcoat alloys under saturated steam environment at atmospheric pressure.

3.2 Thermal and Mechanical Properties of Topcoat

Some important thermal and mechanical properties of the conventional and the ultra thick TBCs are shown in Table I. The thermal conductivity of the ultra thick TBC is lower at the both temperatures due to its high porosity. The thermal conductivities of these TBCs gradually increase at 750˚C. The coefficient of thermal expansion (C.T.E.) and Young's modulus of the ultra thick TBC are slightly lower than those of the conventional one as well. These tendencies are also caused by the high volume content of the pore in the topcoat. These properties of the ultra thick TBC are suitable as the coatings for thermal barrier use. The remaining problem of this TBCs is the resistance against crack initiation and propagation due to low adhesion strength between lamellar layers.
Thermal cycling tests were carried out to evaluate the resistance against heat cycles. We did not observe any cracks and spallation in the ultra thick TBCs after 200 thermal cycles. Moreover, water-quenched thermal shock tests were done up to 50 cycles. The developed TBCs shows the excellent durability to severe thermal shocks. It can be concluded that the fundamental properties of the ultra thick TBCs are sufficient as the results of the laboratory tests.

Table I. Comparison of the thermal and mechanical properties between conventional and ultra thick TBCs.

	Thermal Conductivity (W/mK)		C.T.E.(×10⁻⁶/K)		Young's Modulus (GPa)	
	R.T.	750°C	R.T.	750°C	R.T.	750°C
Conventionl TBC	1.2	1.4	9.2	10.3	21	20
Ultra Thick TBC	1.0	1.2	9.0	10.1	18	18

3.3 Durability Test under Steam Environment

The performance of the ultra thick TBCs under actual steam turbine environment was investigated by Toshiba's high pressure steam turbine test facility in Mikawa power station. The appearances of the TBCs coated on the nozzle diaphragm and on the inner casing after 450h operation are shown in Fig.3 respectively. We cannot observe any significant damage as the results of the visual

Fig.3 Apperances of the ultra thick TBCs coated on the nozzle diaphragm and the inner casing of the steam turbine test facility after 450h operation.

inspection. In addition, there is no reduction in thickness via the inspection of a thickness meter. We can conclude that this TBCs shows the good performance at the early stage of the operation. The durability test of the TBCs is going on to evaluate the longterm performance under actual steam environment.

4. CONCLUSION

Toshiba has developed the advanced ultra super critical steam turbine system (A-USC). In order to reduce the thermal stress in the high temperature component such as nozzle box, TBCs with high thermal resistivity is required. The ultra thick TBCs produced by APS process was developed for the A-USC use. TBCs shows good thermal and mechanical properties. The durability of the ultra thick TBCs under actual steam environment was evaluated in high pressure steam turbine test facility. We did not observed any damage of the TBCs up to 450h operation. This test is still going on to evaluate its longterm durability.

References

[1] N. Okita, T. Sasaki, T. Suga and S. Iwai: Proc. of ASME 2011 Turbo Expo, GT2011-45549, pp.2321-2325(2011).
[2] T. Takahashi, Y. Murakami, S. Iwai, S. Miyashita and K. Nemoto: Proc. of International as Turbine Congress 2011 Osaka, IGTC2011-ABS-0210, pp.1-4(2011).
[3] K. Wada and S. Kuboya: Proc. Turbine Forum 2012, Session-III-2, pp.1-3(2012).
[4] K. Wada, S. Kuboya, T. Tashima, S. Iwai and T. Takahashi: Proc. The 5th Asian Thermal Spray Conference, pp.13-14(2012).
[5] A. S. Khanna: High Temperature Oxidation and Corrosion, Ed. by ASM International, pp.119-125(2002).

Evolution of Oxide Scale on Aluminide and Pt-Aluminide Coatings Exposed To Type I Hot Corrosion Condition

K.shirvani [1,*], A.Rashidghamat [1], M.Mohammadi [2]

[1] High-Temperature Corrosion & Coating Laboratory, Department of advanced Materials and Renewal Energies, Iranian Research Organization for Science and Technology, Tehran, Iran
[2] Department of Materials Engineering, Shiraz University, Shiraz, Iran

E-mail: koush1@yahoo.com, arash.rashidghamat@gmail.com

1. INTRODUCTION

Aluminide diffusion coatings are widely used for hot corrosion protection of Ni-based superalloy components in gas turbines. The conventional aluminide coatings have an ability to form a protective and slow-growing oxide (Al_2O_3) scale at elevated temperatures, but in general they do not possess adequate adhesion characteristics to maintain this oxide over long periods of time in their extreme working conditions [1]. This fact has forced further improvements in these coatings. As a part of this improvements enacted to date, the aluminide coatings are modified by the addition of elements such as Cr, Si and Pt to increase their performance in the hostile turbine chamber environment [2]. Although coating modification by platinum has been known to improve the adherence of alumina scales [3,4], however, evolution of oxide scales formed on pt-modified aluminide coatings exposed to hot corrosion conditions has not been investigated.

This paper is dedicated to evaluate the oxide scale during long exposures of samples to high temperature hot corrosion conditions and a comparative study of Pt-Al coating scales versus Al coating scales. The hot corrosion test was performed using a tube furnace and application of Na_2SO_4 + %30NaCl salt on both Al and Pt-Al coatings. The oxide scale characterization was carried out using both XRD and low angle XRD to better detection of scales. Scanning electron microscope coupled with EDS analyzer and EPMA device were used to detect element traces on the surface of samples.

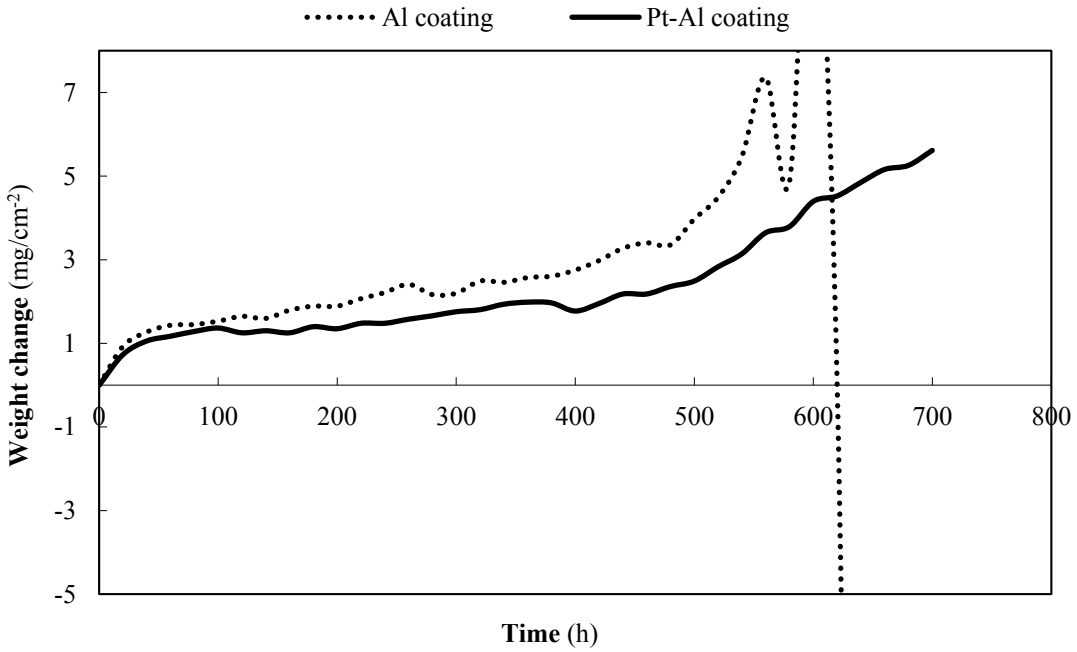

Figure 1: Weight change vs. hot corrosion time for Al and Pt-Al coatings after 700 hours exposure to high temperature hot corrosion.

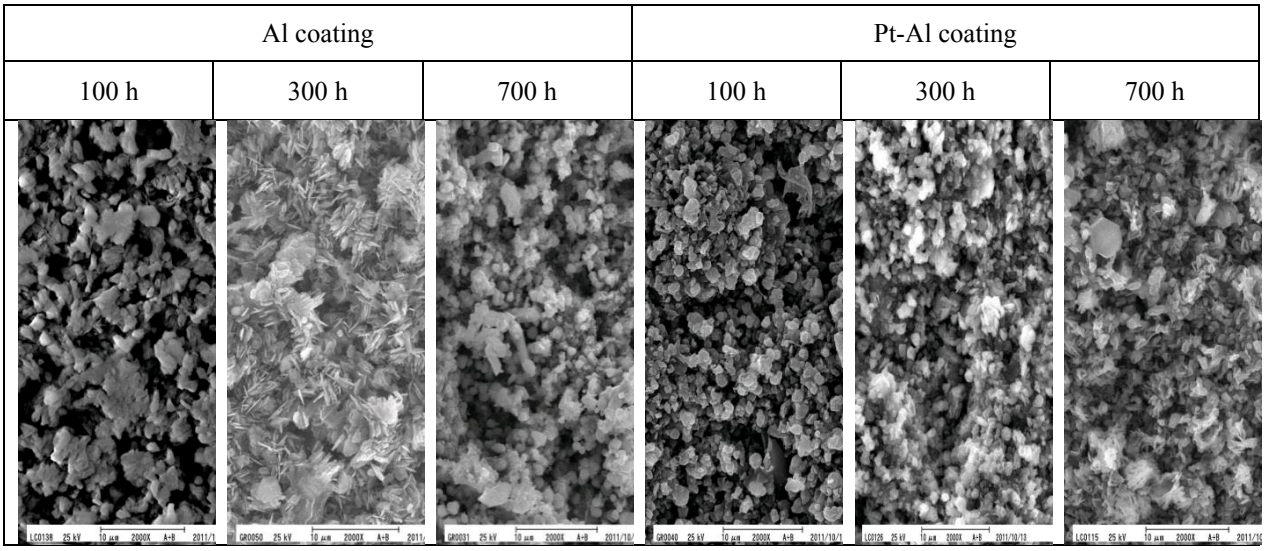

Figure 2: SEM surface morphology images of Al and Pt-Al coatings after 100, 300 and 700 hours exposure to high temperature hot corrosion.

Figure 1 shows the weight change versus time plot of hot corrosion test at 870°C. As it can be seen Pt-aluminide coating shows a better resistance under test conditions and reveals a steady oxide growth as compared to Al coating which shows massive weight gain as a result of corrosion products build up before its catastrophic failure at about 620 h. Figure 2 shows the SEM images of surface topography. The surface microstructure of the hot corrosion products along with XRD analysis showed that the harmful transition reaction of α-$Al_2O_3 \rightarrow \theta$-$Al_2O_3$, which can be considered as the starting point of deterioration of aluminide coatings under high temperature corrosion, was prolonged from 300 h for Al coating to 700 h for Pt-Al coating. Extensive formation of Al_2O_3 whiskers on the Al coating is evident in the corresponding SEM image after surpassing 300 h of the hot corrosion test.

References

[1] E.J. Felten, F.S. Pettit, "Development, growth, and adhesion of. Al_2O_3 on platinum-aluminum alloys", *Oxid. Met.,* Vol. 10, (1976), P.189.

[2] J. Angenete, K. Stiller, V. Langer, "Oxidation of Simple and Pt-Modified Aluminide Diffusion Coatings on Ni-Base Superalloys—I. Oxide Scale Microstructure", *Oxid. Met.*, Vol. 60, (2003), P. 47.

[3] J.G. Fountain, F.A. Golightly, F.H. Stott, G.C. Wood, "The influence of platinum on the maintenance of α-Al_2O_3 as a protective scale", *Oxid. Met.,* Vol. 10, (1976), P.341.

[4] H. Svensson, J. Angenete, K. Stiller, "Microstructure of oxide scales on aluminide diffusion coatings after short time oxidation at 1050°C", *Surf Coat Technol*, Vol. 177–178, (2004), P.152-157.

Effects of Plasma Gas Compositions on the Microstructure of Suspension Plasma Sprayed Thermal Barrier Coatings

Xiaolong Chen[(1,*)], Seiji Kuroda[(1)] , Takuma Ohnuki[(1)], Marina Coudert[(2)], Hiroshi Araki[(1)], Yoshio Sakka[(1)], Kimitoshi Sato[(1)]

[(1)] National Institute for Materials Science, 1-2-1 Sengen, Tsukuba, Ibaraki 305-0047, JAPAN
[(2)] Ecole Nationale Suprieure d'Ingnieurs de Limoges, University of Limoges, 16 rue Atlantis, 87068, Limoges, FRANCE

E-mail: KURODA.Seiji@nims.go.jp

1. INTRODUCTION

Thermal barrier coatings (TBCs) are widely used to provide thermal and corrosion protections for the hot-section components of gas turbine engines. TBCs are usually fabricated either by atmospheric plasma spraying (APS) or electron beam physical vapor deposition (EB-PVD). EB-PVD TBCs are characterized by disconnected quasi-single crystal columnar grains which are growing primarily perpendicular to the substrate surface leading to high strain tolerance and long service durability. The mean diameter of separated columnar grains is about 10 μm. An APS TBC is commonly built by stacked lamellae resulting in a layered structure with interlamellar pores and microcracks, such a coating has a lower thermal conductivity and reduced strain tolerance than EB-PVD coating. [1-3] In the case of conventional plasma spray, the feedstock particles are usually well flowable powders with the particle size distribution of 10-100 μm which are introduced to the plasma torch by carrier gas such as argon etc. However, for powders whose particle size less than 5 μm, the required carry gas velocity which could impart the fine powders enough momentum to go to the center of plasma plume would significantly perturb the plasma flow. As a result, suspension plasma spray (SPS) is an emerging process for TBC preparations, by which YSZ suspensions consisting of nanometer and submicron powders can be directly used for plasma spray to impart the final TBCs with fine microstructures and better performances. In SPS, suspensions are gas-pressurized injected directly into the plasma plume through a nozzle at a certain velocity. Due to the drag force of plasma jet, the initial suspension droplet may fragment into smaller droplet, which will be decreased further as the solvent vaporizes. Ethanol as a volatile solvent is commonly used for YSZ suspension preparation in order to reduce the enthalpy required for vaporization. As nanometer and submicron powders have large surface tension to agglomerate, which will block the nozzle for suspension injection, so, a proper dispersant usually has to be chosen to make a good dispersion of YSZ fine powder in ethanol-based solvent.[4-6] As SPS is a much different process from conventional APS, and the microstructure and quality of the final TBC are significantly process parameter dependent, in this study, the effects of plasma gas composition on the microstructure of SPS TBCs has been investigated.

2. EXPERIMENTAL

Commercially available fusion and crushed 8 wt.% yttria stabilized zirconia powders (YSZ, UCM advanced ceramics GmbH) with the particle size of D50 = 650 nm were used for YSZ suspension preparation. Reagent grade ethanol (99.5%) was used as the solvent. YSZ suspension with a powder loading of 25 wt.% were prepared by combining starting available YSZ powders, and ethanol (99.5%) . Wet milling was used to break apart the fine powder aggregates by using 5 mm zirconia balls media, 1.5 wt.% polyethyleneimine (PEI) with a mean molecular weight of 10,000 was added as the dispersant. The ball-milled YSZ suspension was ultrasonicated followed by sieving to remove aggregates larger than 90 μm prior to SPS. The obtained YSZ suspension had a viscosity of 1.2 mPa S. Coatings were fabricated by using a Sulzer Metco Multicoat plasma spray unit with a Triplex Pro 210 gun. The spray parameters are listed in **Table I**, two different plasma gas compositions were selected. Suspension was pressurized by argon and injected through a plastic tube connected to a 200-μm diameter orifice. One pass SPS experiment was carried out by spraying coating on the polished stainless steel substrate with the dimension of 60 mm × 20 mm × 5 mm for splat observation. In-flight particles were collected by using a metal container with water.

Table I. Parameters (P1 and P2) for SPS coating deposition, only the plasma gases ratio of Ar/He was changed for comparison.

	Voltage (V)	Current (A)	Ar/He (SLPM)	Suspension flow rate(g/min)	Spray distance (mm)
P1	92.2	466	**44/6**	32	50
P2	93.8	466	**15/50**	32	50

TBCs were fabricated on the 30 mesh alumina grit-blasted stainless substrates and the substrates with 80 μm thick HVOF bond coats. The collected in-flight particles were characterized by dynamic laser scattering particle analyzer. Surface and cross-section microstructures of the as-sprayed coatings were characterized by SEM (JEOL, JSM-6010LA). For cross-section analysis, samples were sectioned and mounted in epoxy resin, and prepared by standard metallographic methods to produce a polished cross section.

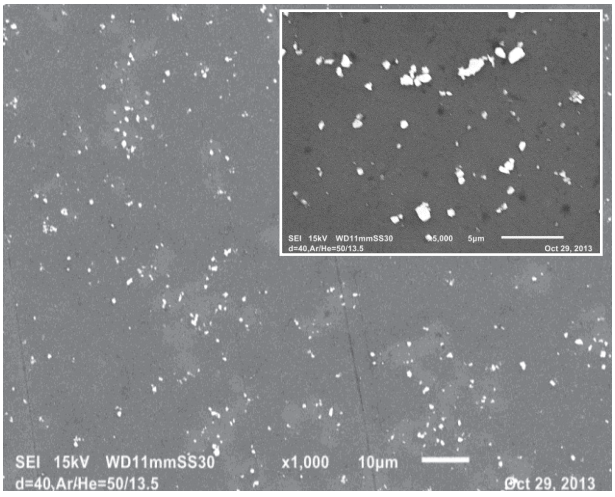

Fig. 1. SEM micrograph of as-prepared YSZ suspension for SPS.

3. RESULTS AND DISCUSSION

Fig.1 shows SEM micrographs of the as-prepared YSZ suspension after drying ethanol. It can be seen that YSZ powders almost exhibit monodispersity in ethanol solvent with the aid of 1.5 wt.% PEI. The suspension demonstrated a good stability, and no blocking was encountered during SPS process. **Fig. 2** shows the particle size distributions of the as-prepared YSZ suspension and those of collected in-flight particles sprayed by P1 and P2 parameters as listed in **Table I.** It can be seen that YSZ suspension has a small particle size with the D_{50} of ~ 426 nm, collected in-flight particles sprayed with a plasma gas composition of Ar/He= 44/6 SLPM are much larger with the D_{50} of ~1.53 μm, while collected in-flight particles sprayed with a plasma gas composition of Ar/He=15/50 SLPM has a median particle size distribution with the D_{50} of ~ 1.27 μm. From the SEM examinations on one pass SPS coatings, **Fig. 3(a)** demonstrates that by using the P1 parameter with a plasma gas compositions of Ar/He=44/6 SLPM, the coating exhibits much better melting conditions and a higher thickness indicating a good deposition efficiency. **Fig. 3 (b)** shows that by using the P2 parameter with a plasma gas composition of Ar/He=15/50 SLPM, the obtained coating has a poor melting condition, unmelted powders are even present, such a coating is much thinner indicating a much lower deposition efficiency in this case.

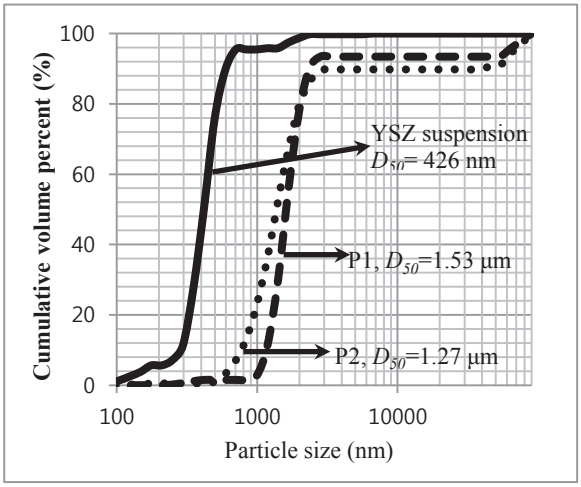

Fig. 2. Particle size distribution of as-prepared YSZ suspension (D_{50}=426 nm) and collected in-flight particles sprayed by P1 (D_{50}=1,534 nm) and P2 (D_{50}=1,267 nm) parameters as listed in **Table I** .

Fig. 4 shows typical cross section SEM micrographs of suspension plasma sprayed thick YSZ coatings fabricated by using P1 and P2 parameters as listed in **Table I.** As can be seen in **Fig. 4(a)** and **(b),** there are feathery columnar microstructures which are similar to EB-PVD coatings, present at the cross section of the as-sprayed coating by using P1 parameters. The obvious difference between the present coating and EB-PVD coating is that SPS columnar grains are about 50-100 μm in diameter, while conventional EB-PVD columnar grains are around 10 μm in diameter. However, though the coatings were prepared by using the same parameters, the shape of columnar grains and the gaps among them are much more clear as can be seen in **Fig. 4(a)** compared to that seen in **Fig. 4(b).** In this case, it

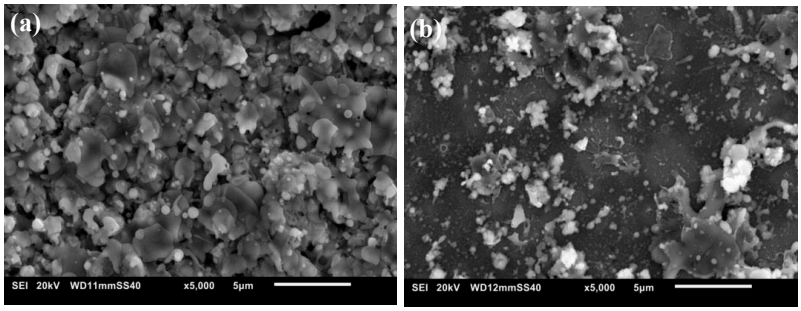

Fig. 3. SEM micrographs of one pass SPS coating by using parameters as listed in **Table I** : P1-(a) and P2-(b).

seems that the substrate roughness plays the major role, since the substrate roughness of the sample shown in **Fig. 4(a)** and **(b)** are about 8.8 μm and 2.5 μm, respectively. While, in the case of thick coating deposited by SPS using the P2 parameters, a similar dense vertically-cracked microstructure as shown in **Fig. 4(c)** can be observed, and the different substrate roughness seems to make no contribution to their microstructures.

Particle distribution analysis indicates that suspension was fragmented to different extents when it was injected into plasma jet by using P1 and P2 parameters. Actually, in case of one pass experiment, the obtained coating was symmetrically distributed on the substrate by using P1 parameters. While, by using P2 parameters, most of the obtained coating was distributed below the center scanning line of plasma jet, and lots of un-melted YSZ powders could be found. In such two deposition parameters, the injection condition of suspension was fixed, and the injecting velocity was 16.9 m/s. So, the probable reason is that plasma jet had a much smaller drag force in the case of using P2 parameters compared to that of using P1 parameters, leading to the suspension passing through the plasma jet, and very limited powders were well heated and melted by plasma jet. This may be another reason responsible for the collected in-flight particles using P2 parameters had a smaller particle size distribution due to the presence of fine YSZ powders. For the feathery columnar and similar dense vertical crack formations, the in-flight particle's velocity at the time when they impact the substrate, the temperature of the plasma jet as well as the roughness condition of the substrate etc. are tightly related. Further studies are needed to get a better understanding of their formation mechanisms.

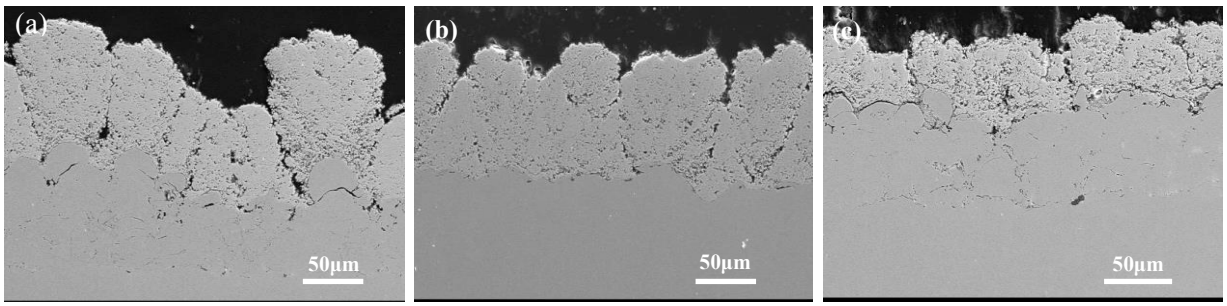

Fig. 4. Cross-section SEM micrographs of SPS YSZ coating fabricated by using parameters: P1-(a) with HVOF bond coat having a roughness of Ra=8.8 μm and P2-(b) with grit-blasted substrate having a roughness of Ra=2.5 μm, as well as P2-(c) with a HVOF bond coat having a roughness of Ra = 8.6 μm.

4. CONCLUSION

In this study, we investigated the effects of different plasma gas compositions on the microstructure of SPS TBCs. The results indicate that plasma gas composition had strong influences on the properties such as the specific enthalpy of plasma plume and plasma jet velocity etc. which should contribute to coating's microstructure formations, though they could not accurately be detected due to the present technique limitation. Substrate roughness also made large contributions to the final TBC microstructure. Further deposition parameter optimizations shall be made in the near future in order to make TBCs with good quality and reproducibility.

Acknowledgements

The authors thank Mr. Hiraoka for his help for the preparations of TBC samples. Thanks also to Prof. A.Vardelle and Prof. M.Vardelle for their valuable discussions.

References:

[1] Padture, N. et al, "Thermal Barrier Coatings for Gas-Turbine Engine Applications," Science, Vol.296, (2002), pp. 280-284.
[2] Vassen, R. et al, "Overview on Advanced Thermal Barrier Coatings," Surf. Coat. Technol., Vol. 205, No.4 (2010), pp. 938-942.
[3] Guignard, A. et al, "Deposition and Characteristics of Submicrometer-Structured Thermal Barrier Coatings by Suspension Plasma Spraying," J. Therm. Spray Technol., Vol. 17, No.3 (2008), pp.31-59.
[4]Fauchais, P. et al, "Parameters Controlling Liquid Plasma Spraying: Solutions, Sols, or Suspensions," J. Therm. Spray Technol., Vol. 21, No.3-4 (2012), pp.416-424.
[5] VanEvery, K. et al, "Column Formation in Suspension Plasma-Sprayed Coatings and Resultant Thermal Properties," J. Therm. Spray Technol., Vol.20, No.4(2011), pp. 817-828.
[6] Oberste Berghaus, J. et al, "Mechanical and Thermal Transport Properties of Suspension Thermal-Sprayed Alumina-Zirconia Composite Coatings," J. Therm. Spray Technol., Vol.17, No.1(2008), pp. 91-104.

High Temperature Oxidation of Mo-Si-B Alloys and Coatings

J.H. Perepezko [(1,*)], T. Sossaman [(1)], and P. Ritt [(1)]

[(1)] University of Wisconsin-Madison, Department of Materials Science and Engineering, 1509 University Ave., Madison, WI 53706, USA

e-mail: perepezk@engr.wisc.edu

1. INTRODUCTION

The challenges of a high temperature environment (T>1400°C) impose severe material performance constraints in terms of melting point, oxidation resistance and structural functionality. In metallic systems there are several high melting temperature intermetallics, but there is a much smaller number of intermetallic phases that offer a level of inherent environmental resistance. Moreover, above about 1300°C, SiO_2 films are preferred since the parabolic rate constant is lower for SiO_2 than for Al_2O_3. In fact, this selection is supported by the superior oxidation resistance of $MoSi_2$, but this intermetallic is brittle. At the same time, the multiphase microstructures that can be developed in the Mo-Si-B system offer useful options for high temperature applications [1]. Alloys based upon the coexistence of the high melting temperature (>2100°C) ternary intermetallic Mo_5SiB_2 (T_2) phase with Mo and the Mo_3Si phase allow for in-situ toughening and offer some oxidation resistance that can be enhanced by coatings. The systematic investigation of reaction kinetics involving the T_2 phase has a direct application to the analysis of oxidation behavior and to the design of effective coating systems. From this basis protective coatings are being developed with self-healing and gradient characteristics. At the current stage of development, alloys have been identified that serve as a benchmark for advanced turbine systems and as a basis for further advances.

In terms of oxidation performance, the Mo-Si-B ternary system offers an attractive option since boron additions enhance significantly the oxidation resistance of metal-rich binary silicides and the Mo phase together with the equilibrium ternary phase (Mo_5SiB_2) have demonstrated a ductile phase toughening. At the same time, at high temperature the Mo-Si-B system tends to produce favorable SiO_2 layers which exhibit useful oxidation resistance, comparable to other silicides. However, from the experience on the oxidation behavior of Mo-Si-B alloys that has been reported it is evident that the kinetics are sensitive to composition and the addition of higher order components [2]. For example, single phase T_2 compositions exhibit a high metal recession rate of over 3000μm/100 hr at 1100 °C. However, the doping of three phase alloys based upon Mo+ T_2+ Mo_3Si with small amounts of Fe, Ni or Co was reported to reduce the recession rate to about 1 μm/ hr at 1370 °C that is well below the design goal of 10 mil/100hr (i.e. 250μm/100 hr) [3]. The addition of about 1 at% Zr to Mo+ T_2+ Mo_3Si alloys was reported to improve the oxidation resistance below 1200°C, but was not beneficial at higher temperature [4]. In addition, the substitution of Ti for Mo in single phase T_1 or in Mo+ T_2+ Mo_3Si alloys [5] was found to offer useful options for improved oxidation resistance. Clearly, the understanding of the large sensitivity of the oxidation rate to alloy composition is a critical issue.

While there are several factors influencing the oxidation resistance that have been identified, it is clear that the B to Si ratio of the alloy is the dominant factor that controls the constitution, the viscosity and oxygen diffusivity as well [6] of the in-situ SiO_2-B_2O_3 passive layer upon oxidation. It is generally understood that lowering the B to Si ratio in the scale yields an increase in the high temperature oxidation resistance due to the formation of the passive SiO_2 rich layer. However, this response must be balanced by the result that excessive Si content will impact the oxidation resistant at low temperatures (i.e. 650 - 750°C) since the formation of a protective SiO_2 layer at this temperature region is slow compared to the loss of Mo by the formation and volatilization of MoO_3 [6] During initial contact with oxygen at elevated temperatures, Mo-Si-B alloys experience a transient oxidation stage characterized by rapid mass loss due to volatilization of MoO_3. After some time, the borosilica originating from the Mo_5SiB_2 and Mo_3Si extends to cover the surface sample, thereby reducing the inward oxygen diffusion. Further, it was also found that none of the alloys were passivated at lower temperatures, and all suffered from catastrophic oxidation between 700°C and 800°C. In addition, there is an issue with the high volatility of B_2O_3 at temperatures above 1200°C, which consequently impacts the metal recession rate even though a continuous borosilica glass can be retained . Moreover, since the alloy compositions that exhibit the lowest oxidation rate will most likely not yield optimum mechanical properties performance, it is important to develop robust and compatible oxidation resistant coatings. Thus, coating designs are necessary to provide enhanced oxidation protection. An effective strategy to address this challenge is based upon in-situ reaction processing to develop coating systems that are thermodynamically compatible with the base alloy and also incorporate an inherent capability for repair.

2. EXPERIMENTAL

Ingots of Mo-rich Mo-Si-B alloys with compositions of Mo-3Si-1B (wt.%) [Mo-8.9Si-7.1B (at.%)] and Mo-14.2Si-9.6B (at%) were prepared by repeated arc-melting in a Ti – gettered Ar atmosphere. Each ingot was sliced to a typical 3mm thickness, polished through a 0.05 μm Al_2O_3 slurry and cleaned with ethanol in an ultrasonic cleaner. Briefly, the pack cementation process involves the elevated temperature deposition of Si or Si+B, carried by a volatile metal-halide vapor species to the substrate embedded in a mixed powder pack containing powder of the deposition element, a halide salt activator, and an inert filler [7]. The powder mixture composed of 70 wt% Al_2O_3, 25 wt% total of Si and B powders, and 5 wt% NaF was loaded in an alumina crucible together with the clean alloy pieces followed by sealing with Al_2O_3 slurry bond. The prepared crucible was annealed at 900 ºC for 48 hours in an Ar atmosphere. In the pack cementation, silicon fluoride (SiF_4) vapor synthesized from the reaction between NaF and silicon powders at elevated temperature reacts with the substrate to enrich the surface with Si. After high temperature annealing, the samples were removed from the alumina crucible and ultrasonically cleaned. For oxidation testing, the alloys were annealed in air between 700 and 1700 °C. Microstructural evaluation was performed by both optical and scanning electron microscopy (SEM) using either secondary or back scattered electron (BSE) imaging modes. Thermogravimetric analysis (TGA) was conducted in a Netzsch 409 instrument.

3. RESULTS AND DISCUSSION

In order to control the B/Si ratio a pack cementation process was adapted for coating synthesis. During the silicon pack cementation process coating process, a steep chemical potential gradient of B and Si across the vapor-substrate interface produces a flux into the substrate that uniformly enriches the local B and Si concentration and results in the synthesis of a $MoSi_2$ coating layer [2,7]. For example, with a single Si source, As Si diffuses into the Mo-Si-B alloy, the composition trajectory should follow the line connecting the Si source to the composition of the substrate (Mo-3Si-1B wt%, Mo-8.9Si-7.1B at.%). From the tie line between MoB and $MoSi_2$ in the Fig. 1b, it is clear that only a limited amount of MoB (as the boron source can be created as the $MoSi_2$ layer starts to develop on the surface.

Enrichment of silicon via pack cementation does not provide the amount of boron needed to stabilize a continuous layer of borosilicide and/or boride phases. Therefore, it is important to pursue a simultaneous or co-deposition of B and Si onto the Mo-rich Mo-Si-B alloys followed by annealing treatments at 1200 – 1400°C [2]. Indeed, as exemplified in figure 1a, by partly substituting Si with B in the pack powder mixture, a continuous layer of MoB can be stabilized underneath the silicide layer coating onto the Mo-3Si-1B wt% substrate. As illustrated in Fig. 1b, the nominal composition path for the co-deposition processes can be represented by rotation about the substrate nominal composition whereby the initial vapor source moves from the pure Si to a mixed Si/B source.

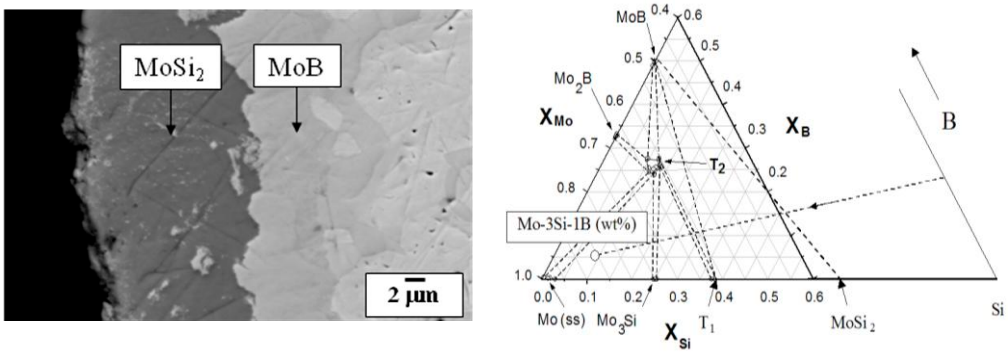

Figure 1:. a) Pack-cementated Mo-3Si-1B (wt %) with a partial substitution of Si with B (1:20 B to Si weight ratio) b) Composition trajectory of Si+B pack cementation process on Mo-3Si-1B (wt %) alloys depicted in the Mo-Si-B phase diagram. A full development of the boride phase underneath the silicide phase is observed with the partial substitution

During oxidation tests of the (B+Si)-pack alloys, the initial $MoSi_2$ outer layer is consumed by formation of the T_1 phase as one consequence of the transient composition trajectory. With continued elevated temperature exposure during oxidation, the outer T_1 phase layer would eventually be consumed by dissolution into the substrate. However, part of the initial transient stage of reaction that yields the T_1 phase from the inward flux of Si and B also leads to the development of the T_2 borosilicide and/or boride phase layer. The relative amounts of the T_2 and MoB phases below the T_1 phase region depend on the B/Si ratio of the powder sources as illustrated in the diffusion path trajectory in Fig. 1b. The T_1 phase is always in contact with the MoB or T_2 borosilicide phase, which guarantees B saturation in the T_1 phase. Furthermore, since the T_1 phase that is saturated with B has excellent oxidation resistance and the loss of Si is blocked by the underlying diffusion barrier (i.e. the borosilicide and boride phases), the T_1 layer thickness change can be arrested [8]. Further, any damage to the outer T_1 layer can be recovered from the underlying T_2 + MoB layer. In effect, the in-situ reaction that yields the T_2 + MoB layer also provides a kinetic bias that allows for the continued existence of the outer T_1 layer and also yields a self-healing characteristic of the coating.

The coating is also effective in providing an oxidation protection at low temperature. Without the coating, the exposure leads to oxidation failure with characteristics corner cracks due to the rapid growth kinetics of MoO_3 layer in addition to the high Pilling-Bedworth ratio of 3.3 of the Mo oxide (the molar volume of MoO_3 = 30.7 cm^3 and the molar volume of

Mo =9.3 cm^3). In contrast, the coating produces an effective protection due to the formation of continuous coverage of borosilica glass [2].

The environmental resistance can be enhanced up to at least 1700°C and also extended against attack by water vapor and CMAS by multilayer coatings developed through a kinetic biasing by either external pack cementation or by internal doping to provide an in-situ diffusion barrier with self-healing and gradient character resistance for oxidation resistance and potential thermal barrier applications.. With these advances the multiphase microstructures in the Mo-Si-B ternary system offer useful options for ultrahigh temperature applications. Moreover, the coating strategy can be adapted to apply to other refractory metal systems and ZrB_2 and SiC composites to provide excellent high temperature environmental resistance.

4. CONCLUSIONS

The synthesis of robust coatings that provide protection against environmental attack at ultrahigh temperatures is a difficult challenge. However, the experience with the oxidation response of alloys in the Mo-Si-B system highlights the important role of the B/Si ratio as a key element in coating design strategies for Mo-base alloys. In order to achieve compatibility, a multilayer coating structure is an effective approach. In this way, compatibility can be assured as well as to provide a diffusion barrier to limit transport. The use of kinetic biasing has been demonstrated to be effective to alter the B/Si ratio and control the coating diffusion pathway. Silica biasing effectively limits oxygen transport through the coating while silicide biasing alters the phase sequencing to incorporate an oxidation resistant T_1 layer in the diffusion path and silicide and boride biasing shifts the pathway to include a diffusion barrier underlying the T_1 phase. The high temperature protection originates from the formation of continuous borosilica on the surface and the stability and integrity of the coating is assured by incorporation of an underlying diffusion barrier. The coating performance confirms the utility of the diffusion path trajectory and kinetic bias analysis to design the layer formation and to enhance the oxidation resistance. The general applicability of the kinetic biasing strategy provides a useful flexibility so that the approach can be adapted to enhance the high temperature environmental resistance of other metallic and ceramic materials.

Acknowledgements: The support from the Office of Naval Research (N00014-10-1-0913, Dr. David A. Shifler, program manager) for research on oxidation resistant coatings is most gratefully acknowledged.

References

[1] J.H. Perepezko, *Science*, **326**, 1068 (2009)
[2] J.H. Perepezko and R. Sakidja, *JOM*, **65**(2) 307 (2013)
[3] D.M. Shah, D.M. Berczik, D.L. Anton and R. Hecht, *Mat. Sci. & Engr. A*, **155**, 45 (1992)
[4] S. Burk, B. Gorr, V.B. Trindade and H.-J. Christ, *Oxid. Met*., **73**, 163 (2010)
[5] R. Sakidja and J.H. Perepezko, *J. Nuclear Mater.,* **366** 407 (2007)
[6] J.H. Perepezko, K. Hildal, F. Rioult and R. Sakidja, *Proceedings 17th International CorrosionCongress, (NACE International)*, 275 (2008)
[7] R. Sakidja, J.S. Park, J. Hamann and J.H. Perepezko, *Scripta Mater*., **52**, 723 (2005)
[8] F.A. Rioult, S.D. Imhoff, R. Sakidja and J.H. Perepezko, *Acta Mater*, **57**, 4600 (2009)

Observation and modeling of α-NiPt(Al) and void formations after interdiffusion of Pt Coating with a γ-Ni(Al) alloy at high temperature

Pauline Audigié [1,*], Aurélie Rouaix-Vande Put [1], André Malié [2], Pascal Bilhé [3], Sarah Hamadi [3], and Daniel Monceau [1]

[1] CIRIMAT, University of Toulouse, ENSIACET, 4 Allée Emile Monso, BP 44362, 31030 Toulouse Cedex 4, FRANCE
[2] SNECMA, SAFRAN-Group, 99 rue Maryse Bastié, BP 129, 86101 Châtellerault Cedex, FRANCE
[3] SNECMA, SAFRAN-Group, rue Henry-Auguste Desbruères, 91003 Evry Cedex, FRANCE

e-mail: pauline.audigie@ensiacet.fr, aurelie.rouaix@ensiacet.fr, andre.malie@snecma.fr, pascal.bilhe@snecma.fr, sarah.hamadi@snecma.fr, daniel.monceau@ensiacet.fr

1. INTRODUCTION

Thermal barrier coating systems (TBCs) are widely used to decrease the operating temperature of the underlying Ni-based superalloy in gas turbines [1]. Ni-based superalloys are used because of their mechanical properties at high temperature. To protect them against high-temperature oxidation and hot corrosion, they are coated with an α-alumina-forming protective coating. Among several possibilities, β-(Ni,Pt)Al and MCrAlYs are the most commonly used bond-coatings. However, in the last 15 years, the Pt-rich γ-γ' bond-coatings have been studied for their corrosion and oxidation resistance, and as a lower cost alternative to β-(Ni,Pt)Al bond-coatings in TBC systems [2-5]. Despite a lower initial Al reservoir and a higher sensitivity to the substrate composition [6, 7] when compared with β-(Ni,Pt)Al, Pt-rich γ-γ' bond-coatings decrease rumpling [8-10] and suppress the precipitation of brittle Topologically Closed Packed (TCP) phases [8, 11] resulting from the interdiffusion between the bond-coating and the substrate. Similarly to β-(Ni,Pt)Al, Pt additions improve the oxide scale adherence by reducing the sulfur detrimental effect [12, 13] and void formation at metal/oxide interface [14]. Another study has shown that Pt increases Al diffusion [15], then reduces the vacancies flux from the metal to the surface and inhibits vacancy coalescence and interfacial void formation. Many voids have also been observed at the bond-coating / substrate interface [16-19]. Vialas and Monceau [17] and ORNL [20] attributed it to a Kirkendall effect without proving it and Yamaguchi et al. [18] suggested that cyclic oxidation is an additional source for vacancy sursaturation.

This study was focused on the investigation of bond-coatings behavior. It consists in modeling interdiffusion between the main chemical elements of the bond-coat and the substrate (nickel, platinum, aluminum) at high temperature. In order to improve the TBC lifetime, it is thus interesting to investigate these diffusion and oxidation phenomena. In that respect, the interdiffusion between a γ-Ni(Al) model alloy and a pure Pt coating has been studied. A computer model based on a previous one developed in 90's for kinetic demixing in oxides under a vacancy flux [21] has been used and simulations have been run to predict the occurrence of phase transformations, system lifetime and void formation.

2. EXPERIMENTAL

A polycrystalline alloy rod of Ni-13Al (at.%) was prepared by argon arc melting from high-purity Ni and Al pieces at Institut Jean Lamour, Nancy (France) and annealed for 1h at 1100°C in air. After this latter heat treatment, the alloy grain size was on average 250 µm. As-cast alloy mean composition was Ni-13.1Al (at.%). Coupons of 17 mm in diameter and 1.5-2mm thick were cut and polished with SiC paper down to P600 and cleaned with ethanol in an ultrasonic bath. Then, a grit-blasting with α-Al_2O_3 particles was performed. A pure Pt coating of 5 µm thick was deposited on one side of the substrate by electroplating with an industrial facility of SNECMA-SAFRAN Group. Then, heat treatments from 15 minutes to 10h at 1100°C were performed in-situ in the high temperature X-ray diffraction apparatus (BRUKER D8) under primary vacuum to follow phase transformations. The resulting interdiffusion zones were cross-sectionally prepared and analyzed by scanning electronic microscopy (SEM) and energy dispersive spectroscopy (EDS). Electron microprobe analysis (EPMA) was also performed to determine Ni, Al and Pt concentration profiles. A computer program using an explicit finite differences scheme was performed to calculate the fluxes and the concentration profiles in the γ-system by considering the chemical potential gradients. Calculation results were compared with experimental concentration profiles. For the calculations, many hypotheses were as follows: a single-phase system with three species

(Ni,Al,Pt), a 1D-geometry, a finite domain and oxidation can be considered as a boundary condition with the formation of an α-alumina scale.

3. RESULTS and DISCUSSION

Fig. 1. compares X-ray diffraction patterns for Ni-13Al + Pt after 15 minutes and 1h at 1100°C under primary vacuum. Both show the γ-Ni matrix peaks. The primary vacuum did not prevent oxidation and α-Al_2O_3 formed on the surface. After 15 minutes, XRD analyses revealed that all the platinum from the coating did not react with the matrix and also that the α-NiPt(Al) phase with the L_{10} crystal structure formed. This α-NiPt(Al) was already observed after a fast heating (40°C/min) and a 100 sec dwell at 1100°C. This implies the very fast Al diffusion to the surface. The α-phase vanished after 45 min or 1h at 1100°C and the γ'-$(Ni,Pt)_3Al$ phase then appeared. A two-phase γ-γ' microstructure was obtained and no significant evolution was observed from 2h30 to 10h.

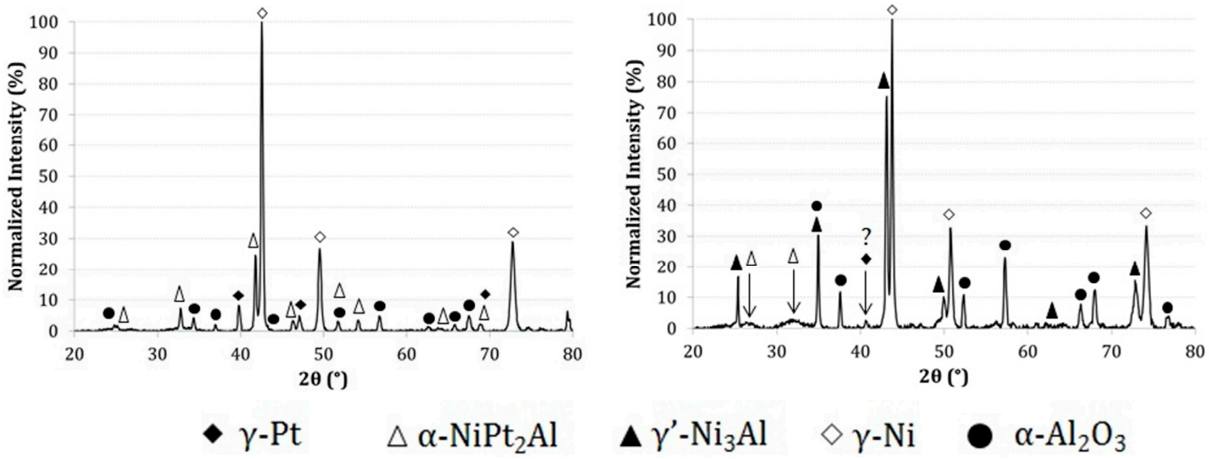

Fig. 1. X-ray diffraction patterns of Ni-13Al + Pt after a. 15 minutes and b. 1h at 1100°C

Cross-sections of annealed samples were analyzed by SEM, EDS and EPMA. The microstructures of the systems after 15min, 1h, 2h30 and 10h at 1100°C are shown in **Fig. 2**. The surface undulations correspond to the cauliflower Pt grains after deposition. α-Al2O3 particles mark the initial interface between the Pt coating and the γ-alloy. **Fig. 2.a.** is a cross-section of the interdiffused sample after 15 minutes at 1100°C. The microstructure can be divided into three zones: the Pt-enriched zone above the initial surface, the interdiffusion zone and the base material. In the Pt-enriched zone of ~6 µm thick after 15 minutes, small α-NiPt(Al) precipitates formed and appear as the brighter phase. This was due to the platinum effect on the Al activity which promotes the Al uphill diffusion from the alloy to the surface [3, 22]. The interdiffusion zone thickness was about 10 µm. The Pt diffusion in the substrate was homogeneous with a planar diffusion front. After 1h at 1100°C (**Fig. 2.b.**), α-NiPt(Al) phase vanished as confirmed by the XRD analyses and the brightest phase was γ'-(Ni,Pt)3Al. A two-phase γ-γ' microstructure was then obtained. The interdiffusion zone thickness increased with annealing time at 1100°C up to ~25 µm after 10h à 1100°C (**Fig. 2.d.**). No phase transformation and no significant microstructural evolution were observed from 2h30 to 10h. Most importantly, from 1h to 10h, voids were observed at the interdiffusion / base material interface. Their proportions seem to increase with time. Concentration profiles and EDS maps confirmed that voids were located at the Pt diffusion front and in the Al depletion zone. This may be attributed to a Kirkendall effect.

To explain void formation, calculations with a computer program in finite differences were performed to simulate the concentration profiles evolution. Experimental and calculated profiles were found to be in good agreement for the γ-phase systems (**Fig. 3.**). The fitted interdiffusion coefficients were in the range of those found in the literature. The diffusion paths were determined and compared with theoretical results. Simulations in the γ-phase were performed to predict the possible nucleation and location of the α-phase. The diffusion of vacancies was also considered in order to test its ability to predict the occurrence of Kirkendall voids. In TBC systems, voids formed at the bond-coating / superalloy interface either after fabrication or after oxidation or interdiffusion tests. Comparisons with those voids found in TBC systems in the literature are in progress.

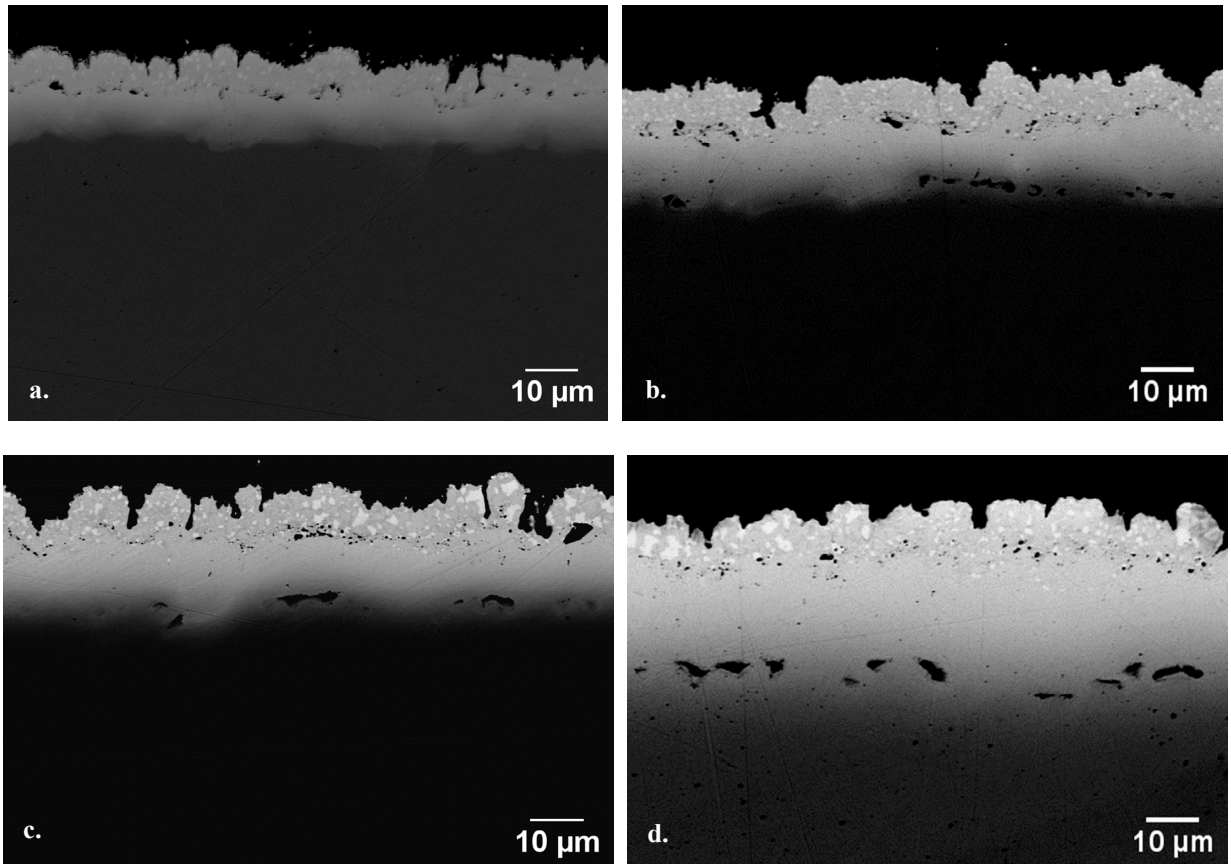

Fig. 2. Backscattered electron images of Ni-13Al + Pt after a. 15minutes, b. 1h, c. 2h30 and d. 10h at 1100°C

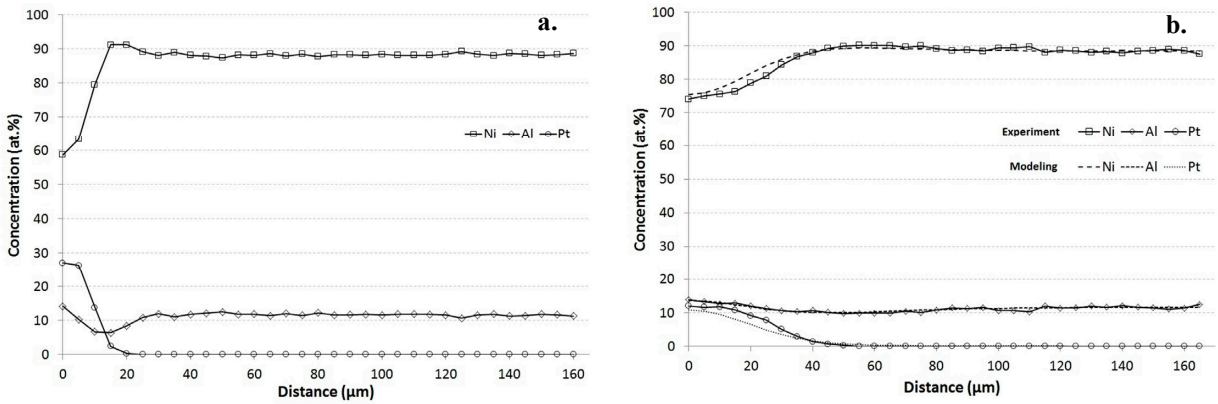

Fig. 3. a. Initial state used for modeling after 15 minutes at 1100°C and b. comparison of calculated (solid lines) and experimental (open symbols) profiles after 10h at 1100°C

4. CONCLUSION

Pt coating was synthesized by electroplating a 5 µm thick film on γ-Ni-13Al model alloy. This was followed by an interdiffusion treatment from 15 minutes to 10h at 1100°C in-situ in the high temperature X-ray diffraction apparatus under primary vacuum. The results can be summarized as follows:

1. The α-NiPt(Al) phase with the L10 crystal structure formed very quickly and was already observed after a fast heating (40°C/min) and a 100 sec dwell at 1100°C.
2. This α phase vanished after 45 min – 1h at 1100°C and the γ'-$(Ni,Pt)_3Al$ phase then appeared.
3. A two-phase γ-γ' microstructure was obtained and no significant evolution was observed from 2h30 to 10h.
4. Voids formed and were located at the Pt diffusion front and in the Al depletion zone after 1h at 1100°C.
5. First calculated concentration profiles in the γ-phase are promising and in good agreement with those obtained experimentally.

Acknowledgements,
A part of this study was performed with the financial support of SNECMA-SAFRAN Group. The authors would like to acknowledge Stéphane Mathieu and Michel Vilasi at Institut Jean Lamour, Nancy (France) for preparing the alloy rod and André Malié at SNECMA-SAFRAN Group for electroplating the platinum.

References

[1] Bose, S. and J. DeMasi-Marcin, "Thermal Barrier Coating Experience in Gas Turbine Engines at Pratt & Whitney," *Journal of Thermal Spray Technology*, Vol. 6, No. 1 (1997), pp. 99-104.

[2] Bouhanek, K., O.A. Adesanya, F.H. Stott, P. Skeldon, D.G. Lees, and G.C. Wood, *High temperature oxidation of thermal barrier coating systems on RR3000 substrates: Pt Aluminide bond coats*, in *Materials Science Forum*. 2001. p. 369.

[3] Gleeson, B., W. Wang, S. Hayashi, and D. Sordelet, "Effects of Platinum on the Interdiffusion and oxidation Behavior of Ni-Al-Based Alloys," *Materials Science Forum*, Vol. 461-464, No. (2004), pp. 213-222.

[4] Haynes, J.A., B.A. Pint, Y. Zhang, and I.G. Wright, "Comparison of the cyclic oxidation behavior of β-NiAl, β-NiPtAl and γ-γ' NiPtAl coatings on various superalloys," *Surface & Coatings Technology*, Vol. 202, No. (2007), pp. 730.

[5] Wu, R.T., K. Kawagishi, H. Harada, and R.C. Reed, "The retention of thermal barrier coating systems on single-crystal superalloys: Effects of substrate composition," *Acta Materialia*, Vol. 56, No. (2008), pp. 3622-3629.

[6] Tawancy, H.M., A.I. Mohamed, N.M. Abbas, R.E. Jones, and D.S. Rickerby, "Effect of superalloy substrate composition on the performance of a thermal barrier coating system," *Journal of Materials Science*, Vol. 38, No. (2003), pp. 3797-3807.

[7] Pint, B.A., J.A. Haynes, and Y. Zhang, "Effect of superalloy substrate and bond coating on TBC lifetime," *Surface and Coatings Technology*, Vol. 205, No. 5 (2010), pp. 1236-1240.

[8] Izumi, T., N. Mu, L. Zhang, and B. Gleeson, "Effects of targeted gamma-Ni plus gamma '-Ni3Al-based coating compositions on oxidation behavior," *Surface & Coatings Technology*, Vol. 202, No. 4-7 (2007), pp. 628-631.

[9] Wu, R.T., X. Wang, and A. Atkinson, "On the interfacial degradation mechanisms of thermal barrier coating systems: Effects of bond coat composition," *Acta Materialia*, Vol. 58, No. 17 (2010), pp. 5578-5585.

[10] Selezneff, S., M. Boidot, J. Hugot, D. Oquab, C. Estournès, and D. Monceau, "Thermal cycling behavior of EBPVD TBC systems deposited on doped Pt-rich gamma-gamma prime bond coatings made by Spark Plasma Sintering (SPS)," *Surface and Coatings Technology*, Vol. 206, No. (2011), pp. 1558-1565.

[11] Divya, V.D., U. Ramamurty, and A. Paul, "Effect of Pt on interdiffusion and mechanical properties of the γ and γ' phases in the Ni-Al-Pt system," *Philosophical Magazine*, Vol. 92, No. 17 (2012), pp. 2187-2214.

[12] Haynes, J.A., Y. Zhang, W.Y. Lee, B.A. Pint, I.G. Wright, and K.M. Cooley. *Effects of Platinum additions and sulfur impurities on the microstructure and scale adhesion behavior of single-phase CVD aluminide bond coat*. in *Elevated Temperature Coatings : Science and Technology III*. 1999: The Minerals, Metals and Materials Society.

[13] Cadoret, Y., D. Monceau, M. Bacos, P. Josso, V. Maurice, and P. Marcus, "Effect of platinum on the growth rate of the oxide scale formed on cast nickel aluminide intermetallic alloys," *Oxidation of Metals*, Vol. 64, No. 3-4 (2005), pp. 185-205.

[14] Cadoret, Y., M.P. Bacos, P. Josso, V. Maurice, P. Marcus, and S. Zanna, *Effect of Pt additions on the sulfur segregation, void formation and oxide scale growth of cast nickel aluminides*, in *High Temperature Corrosion and Protection of Materials 6, Prt 1 and 2, Proceedings*. 2004, Trans Tech Publications Ltd: Zurich-Uetikon. p. 247-254.

[15] Bouchet, R. and R. Mevrel, "Calculating the composition-dependent diffusivity matrix along a diffusion path in ternary systems. Application to beta-(Ni,Pt)Al," *Calphad*, Vol. 27, No. (2003), pp. 295-303.

[16] Zhang, Y., B.A. Pint, J.A. Haynes, and I.G. Wright, "A platinum-enriched γ+γ' two-phase bond coat on Ni-based superalloys," *Surface and Coatings Technology*, Vol. 200, No. (2005), pp. 1259-1263.

[17] Vialas, N. and D. Monceau, "Effect of Pt and Al content on the long-term, high temperature oxidation behavior and interdiffusion of a Pt-modified aluminide coating deposited on Ni-base superalloys," *Surface & Coatings Technology*, Vol. 201, No. 7 (2006), pp. 3846-3851.

[18] Yamaguchi, A., H. Murakami, S. Kuroda, and H. Imai, "Effect of Hf addition on oxidation properties of Pt-Ir modified aluminide coating," *Materials Transactions*, Vol. 48, No. 9 (2007), pp. 2422-2426.

[19] Zhang, Y., J.P. Stacy, B.A. Pint, J.A. Haynes, B.T. Hazel, and B.A. Nagaraj, "Interdiffusion behavior of Pt-diffused [gamma] + [gamma]' coatings on Ni-based superalloys," *Surface and Coatings Technology*, Vol. 203, No. 5-7 (2008), pp. 417-421.

[20] Haynes, J.A., B.A. Pint, Y. Zhang, and I.G. Wright, "Comparison of the Oxidation Behavior of [beta] and [gamma]-[gamma]' NiPtAl Coatings," *Surface and Coatings Technology*, Vol. 204, No. (2009), pp. 816-819.

[21] Monceau, D., C. Petot, and G. Petotervas, "Kinetic Demixing Profile Calculation in Oxide Solid-Solutions under a Chemical-Potential Gradient," *Solid State Ionics*, Vol. 45, No. 3-4 (1991), pp. 231-237.

[22] Hayashi, S., W. Wang, D.J. Sordelet, and B. Gleeson, "Interdiffusion behavior of Pt-modified gamma-Ni+gamma '-Ni3Al alloys coupled to Ni-Al-based alloys," *Metallurgical and Materials Transactions a-Physical Metallurgy and Materials Science*, Vol. 36A, No. 7 (2005), pp. 1769-1775.

Long term operational behavior of Re alloy diffusion barrier coated micro turbine combustor in digester gas combustion

Hiroshi Yakuwa [1,*], Shigenari Hayashi [2], Toshio Narita [3], Ryotaro Yamamoto [1], Takahiro Nakagawa [1], and Tadahiko Kishikawa [1]

[1] Ebara Corporation, 2-1, Honfujisawa-4, Fujisawa 251-8502, JAPAN
[2] Graduate School of Engineering, Hokkaido University, Kita13 Nishi8, Sapporo 060-8628, JAPAN
[3] Professor Emeritus of Hokkaido University, at present DBC System R&D Co., Ltd., 515-1, Zenibako-3, Otaru 047-0261, JAPAN

e-mail: yakuwa.hiroshi@ebara.com

1. INTRODUCTION

Distributed power generation has recently attracted attention for reducing greenhouse gas emissions and securing the supply of electricity in Japan. Distributed power generation technology includes micro gas turbines. Since micro gas turbines have many components with complicated shapes and must be manufactured at low cost, the use of ceramic coatings or high-grade materials in large gas turbines for power generation is constrained. Material life extension is especially required for combustor liners exposed to severe high-temperature corrosive conditions [1]. A Re-based alloy diffusion barrier coating developed jointly with Narita et al. [2, 3] was applied with the aim of extending micro gas turbine combustor life. This paper reports the results from the actual operation of a combustor liner with the diffusion barrier coating during sewage digester gas combustion for 11,977 hours.

2. FORMATION OF A Re ALLOY DIFFUSION BARRIER COATING

A W-Ni alloy, a Re-Ni alloy, and Ni were applied, each to a thickness of about 5 μm, to the surface of a substrate (Alloy X: Ni-22Cr-18Fe-9Mo-0.1C (mass %)) through electro-less plating processes. The plated combustor was heat-treated at 1200 ºC for 9 hours in the presence of Cr/Al_2O_3 composite powder to form an σ-(Re-W-Cr-Ni) phase. Figure 1 shows a cross-sectional view of the Alloy X specimen with a diffusion barrier layer formed under the same conditions as those for the combustor. As seen in the figure, the diffusion barrier layer has a thickness of about 7 μm and contains 30 at.% of Re, 33 at.% of Cr, 17 at.% of Ni, and 5 to 7 at.% of W, Fe, and Mo. After diffusion barrier layer formation, electro-less Ni plating was carried out until a thickness of about 10 μm was reached. Then, the material was treated with Al diffusion coating at 900 ºC for 1 hour in the presence of $Al/Al_2O_3/NH_4Cl$ composite powder to form a β-NiAl layer on the surface of the diffusion barrier layer.

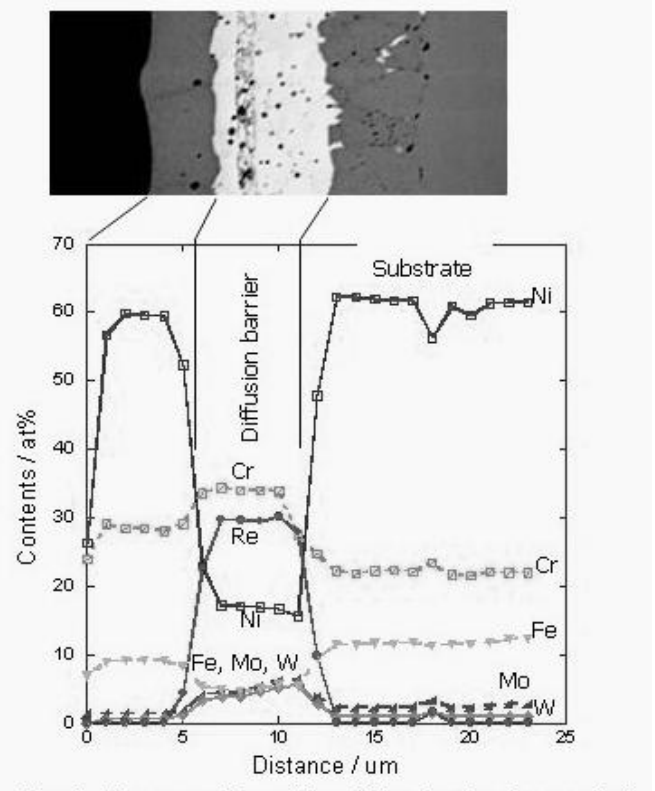

Fig.1 Cross section of the diffusion barrier coated sample by an electroless plating process.

3. DIGESTER GAS COMBUSTION

Digester gas is produced from anaerobic fermentation of sewage sludge. It contains about 60 vol.% of CH_4 and about 40 vol.% of CO_2, as well as saturated vapor and trace amounts of hydrogen sulfide and siloxane. In Japan, about 280 million m^3 of digester gas is produced from sewage treatment plants per year. However, only large-sized sewage treatment plants are equipped with power generation systems using digester gas; the installation of such systems at small and medium-sized sewage treatment plants has lagged. Micro gas turbine cogeneration systems with a capacity of around 100 kW consume about 500 thousand m^3 of digester gas per year and are suitable for power generation using digester gas at small and medium-sized sewage treatment plants [4].

4. RESULTS FROM THE ACTUAL OPERATION OF THE COMBUSTOR LINER

A combustor liner with the diffusion barrier coating was installed in a micro gas turbine and actually operated in Japan. The inside of the combustor was observed using a borescope at intervals of several months to determine

the degree of damage. After operation for 11,977 hours, the combustor was removed for cross-sectional micro structural observation.

Figure 2 shows photos of the primary tube taken with the borescope during the operation. The surface of the material appeared to be gray at 1,881 hours after the start of the operation and then changed partially to green as the operation continued. However, no traces of degradation of or damage to the coating layer (e.g. changes in the shape of corners) were found at 11,977 hours after the start of the operation.

Fig.2 Appearance of the mixing tubes after the actual operation in a digester gas

Figure 3 shows a cross section of the primary tube at 11,977 hours after the start of the operation. The diffusion barrier layer and the Al reservoir layer was still present and no remarkable degradation of or damage to the coating layer was observed.

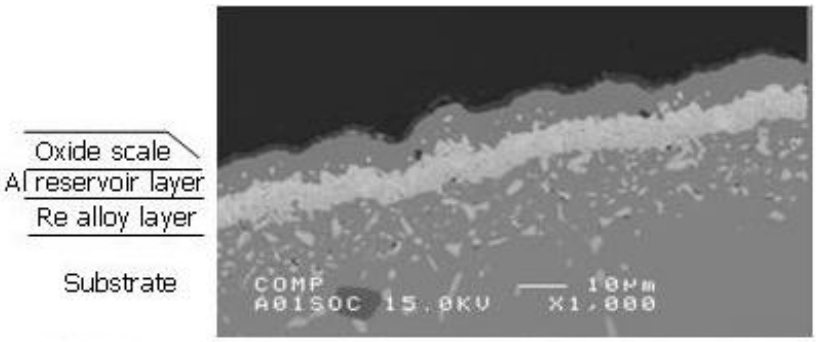

Fig.3 Cross-sectional observation of the mixing tube after 11977 hour operation in a digester gas.

5. CONCLUSIONS

A micro gas turbine combustor with a Re alloy coating for diffusion barrier was actually operated for 11,977 hours. No remarkable degradation of or damage to the coating layer was observed. These results suggest that the Re alloy coating for diffusion barrier is effective in extending the corrosion life time of the combustor.

This study has been partially funded by the Grant for the Matching Fund from the New Energy and Industrial Technology Development Organization (NEDO).

.

References

[1] Yakuwa, H and Kataoka, T, *Proc. JSCE Materials and Environments 2006*, Tsukuba, 2006, Paper D-113.
[2] Narita, T, Hayashi, S, Yoshioka, T and Yakuwa, H, JP Patent No.3,857,690.
[3] Yakuwa, H, Ford, S, Hayashi, S, Narita, T, Nakagawa, T, Yamamoto, R and Kishikawa, T, *Proc. 57th JSCE Jpn. Conf. Materials and Environments*, Okinawa, 2010, Paper E-105.
[4] Kataoka, T, Nakajima, T, Nakagawa, T and Yuasa, S, *Ebara Engineering Review*, No. 218(2008), pp.8-15.

Coatings for Oxycombustion - Supercritical Steam Boilers Components

Alina Agüero [(1,*)], Ignacio Baraibar [(1)], Vanessa González [(1)], Marcos Gutiérrez[(1)], Raúl Muelas [(2)] and Daniel Plana [(1)]

[(1)] Instituto Nacional de Técnica Aeroespacial, Ctra. Ajalvir Km 4, Torrejón de Ardoz 28850, SPAIN

[(2)] Ingenieria de Sistemas para la Defensa de España SA, Calle Beatriz de Bobadilla No. 3, Madrid 28040, SPAIN

e-mail: agueroba@inta.es

1. INTRODUCTION

The need to produce energy more efficiently and with a reduced environmental impact, has become evident. This leads to increasingly extreme conditions imposing more demanding performances on materials, such as higher temperatures and pressures, and more corrosive atmospheres. An alternative to facilitate CO_2 capture is the use of oxygen instead of air for combustion (oxycombustion) of any fuel in the boiler of steam power plants. As the nitrogen presence on the combustion atmosphere is almost zero, the NO_x emissions are drastically reduced and it is then possible to separate and capture practically 100 % of the produced CO_2 [1]. However, oxycombustion atmospheres are much higher in CO_2, SO_2 and water vapor and under this atmosphere corrosion rates are expected to be higher, moreover when supercritical steam conditions are required, and the components are exposed to temperatures higher than 600º C. In fact, some boiler components, such as the superheater tubes, are exposed to both steam and fireside corrosion at these high temperatures, and ferritic steels corrode at very fast rates under both atmospheres. Unless materials with lower thermal conductivity and higher cost are used (austenitic steels and Ni base alloys), protective coatings will be needed. A number of new coatings, applied by techniques capable of depositing said coatings both on the inner and outer surfaces of heat exchanger tubes, such as slurry application and HVOF, are being studied within the EC project POEMA [2].

Aluminide slurry coatings are already known to be very stable both under steam and fire-side corrosion at 650º C [3]. However degradation occurs by Al interdiffusion which may have two negative effects: 1) it causes Al depletion at the surface, resulting in an Al content lower than the critical value required to maintain a stable protective alumina layer and 2) it causes the precipitation of AlN, depleting the steel from N and possibly affecting the mechanical properties of the material after long term. Moreover, these coatings exhibit through-thickness cracks due to thermal expansion coefficient mistmatch between the iron aluminide phases, in particular Fe_2Al_5, and the substrate (Figure 1). In order to reduce diffusion and to avoid the presence of cracks, new Ni and Cr modified aluminide coatings have been produced on P92 by non-line-of-sight hybrid processes. In addition, an Al modified stainless steel coating has been deposited by HVOF. It is a hard, alumina former coating to be used on the external surfaces of the tubes on which erosion by ashes is an issue.

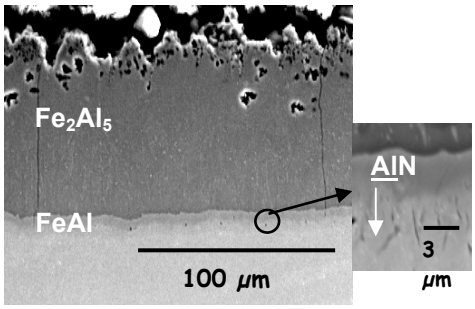

Fig. 1: Slurry aluminide coating on P92

The microstructure of the new coatings will be shown. In addition, extensive laboratory testing of these coatings is on-going, both under oxycombustion model atmospheres with and without ash erosion, as well as under pure steam at 650º C and the preliminary results will be presented. Finally, results obtained with selected coatings in a pilot oxycombustion boiler operated by CIUDEN in Leon, Spain will also be shown. Results indicate that some of the tested coatings exhibit very stable behavior under both atmospheres at 650º C.

2. EXPERIMENTAL

2.1 Substrate

Samples coupons (20x10x3 mm) were machined from tubular sections of P92 (C: 0.1, Mn: 0.5, Si: 0.03, Cr: 8.8, Ni: 0.06, Mo: 0.4, W: 1.8, V: 0.20, S: 0.006, N: 0.046 Fe: bal., wt. %,) obtained from Vallourec Mannesmann

2.2 Coatings

Slurry aluminide: The Al slurry is a CrVI free water base proprietary composition containing only inorganic compounds. Prior to coating, the samples surface was ground (Struers 120) and solvent degreased. The Al slurry was applied by

spraying and the coated samples were subjected to a diffusion heat treatment performed under argon flow at 700º C for 10 h.

Ni Aluminide: this coating was applied in two steps: 1) Ni was initially deposited by electroless deposition from a $NiSO_4$, $(NH_4)_3C_6H_5O_7$ and $NaH_2PO_2{\cdot}H_2O$ solution at 50 ºC followed by a heat treatment at 600ºC for 10 hours and 2) the sample was subsequently aluminized by means of applying an Al slurry followed by a diffusion heat treatment at 700º C for 10 h.

Cr Aluminide**:** this coating was also applied in two steps: 1) Cr was initially deposited by a chromium based proprietary slurry followed by a diffusion heat treatment at 1050 ºC for 5 h and 2) the sample was later aluminized by means of applying an Al slurry followed by a diffusion heat treatment at 1035º C for 35 min.

Table I: Composition of the HS Alloy Powder.

	Fe	Cr	Mo	W	C	Mn	Si	B
wt %.	balance	< 20	< 5	< 10	< 2	< 5	< 2	< 5

Al modified stainless steel: a nano scale hard steel (HS) alloy powder (Table I) was mixed with Al (8 wt. %) and sprayed by means of a Sulzer Metco Diamond Jet Hybrid HVOF unit (A-3120) mounted on a 6 axes robot (ABB) and fed by a twin rotation powder feeder. Before coating, the specimens were grit blasted and degreased.

2.2 Laboratory Testing

2.2.1 Steam oxidation: uncoated substrates were ground (Struers 120) prior to testing. The schematics of the closed loop laboratory rig employed at INTA are shown elsewhere [4]. Prior to testing, laboratory air is displaced from the specimen chamber by means of N_2 which is kept flowing while heating up to the test temperature (approximately at a rate of 600º C/h). Once the test temperature has been reached, the N_2 flow is stopped and pure steam is introduced at a linear velocity of 7 cm/s. To carry out weight measurements or to remove samples, the furnace is cooled to about 300º C under N_2 atmosphere and the specimens are subsequently removed. The reheat cycle is also carried out under N_2 atmosphere.

2.2.2 Fire-Side Corrosion: the test was performed using an experimental especially designed rig with four independent lines for H_2O, SO_2, O_2, N_2 and CO_2 feeding a tubular reactor placed in a furnace. The gas composition is shown in Table II. The samples were placed in alumina crucibles and exposed to the flowing gaseous atmosphere at atmospheric pressure and 650ºC. The exhaust gas was neutralized by bubbling it through alkaline solutions. The test begins by flowing nitrogen for 1 h while the furnace is heating up to the test temperature. Once the test temperature is reached, the nitrogen is closed and the corrosive gases and water are introduced at a linear velocity of 7 cm/s. Every 7 days the test is stopped to weight the specimens by cutting the corrosive gas mixture and turning the furnace off. Cooling to room temperature takes 2 h.

Table II: Composition of the oxyfuel atmospheer for the Fire-Side Corrosion Test

	CO_2	H_2O	N_2	O_2	SO_2
Vol.%	70	30	7	2	1

2.2.3 Pilot Plant Testing: the test was carried out in a fluidized bed combustion boiler burning coal and operating in oxycombustion conditions in CIUDEN´s pilot plant (Leon, Spain). Reheat tubes were coated and tested at plant conditions. The tubes were exposed to 20 days at 650º C. Special attention was focused into corrosion due to gases and fly ash.

2.3 Characterization.

The oxidized specimens were characterized by light optical microscopy (Leica MEF 4) and field emission scanning electron microscopy (FESEM) employing a JEOL JSM 840 system equipped with an energy dispersive X-ray spectrometer (EDS) KEVEX MICROANALYST 8000 with a RÖNTEC signal processor.

3. RESULTS AND DISCUSSION

New Coatings

Two new modified diffusion aluminide coatings have been deposited employing combinations of different processes, in all cases capable of being applied to both internal and external surfaces of heat exchanger tubes.

The first coating was obtained in four steps: 1) first applying 25 μm de Ni(P) by means of electroless deposition from a P containing precursor, 2) a diffusion heat treatment at 600º C, 3) application of an Al slurry and 4) a final heat

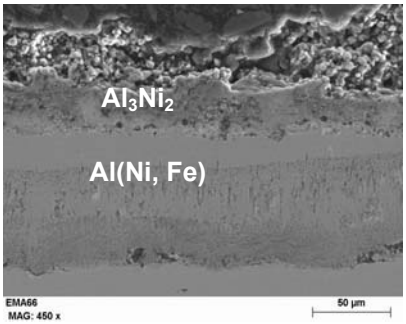

Fig. 2. Ni aluminide coating on P92

treatment at 700º C. As a result, a coating comprising distinct zones was obtained as shownin Fig. 2. According to the XRD pattern as well as EDS analysis, the other layer is composed of Ni_2Al_3 and AlP, whereas the internal zone corresponds to Al (Ni,Fe). Ni aluminides are less brittle than Fe aluminides and accordingly, no cracks are observed in this coating which exhibits an Al content of 65-70 wt. % near the surface.

A Cr enriched aluminide was also deposited by first enriching P92 with Cr by slurry application, followed by aluminization also by means of a slurry at 1000º C. Cr was added as the surface Al content was expected to be lower than that of the original aluminide coating showed in Fig. 1 due to higher diffusion degree caused by the higher heat treatment temperature. It is known than the critical amount of Al required to maintaining a protective alumina scale is related to the Cr content, the higher the Cr the lower the critical Al content. The microstructure of the coating shown in Fig. 3 is, as expected, different as only FeAl was observed by XRD instead of Fe_2Al_5. At the surface the content of Al is 15 wt. % and that of Cr 10 wt. %. Two zones are observed separated by Kirkendall porosity, below which, the Al content slowly decreases to 2 wt. %, at about 200 µm from the surface at the interface with the substrate. A heat treatment at 1000º C will cause a change in the microstructure of the P92 affecting its mechanical properties. However in the case of the heat exchanger tubes, these can be re-heat treated to obtain the required ferritic-martensitic microstructure or alternatively, the coating process may be undertaken prior to the final tempering-annealing alloy treatment [5].

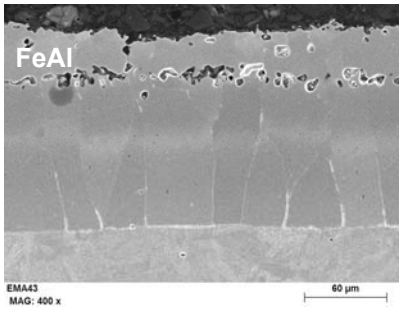

Fig. 3. Cr enriched aluminide coating on P92

The third coating was deposited by HVOF from a powder obtained by mixing a commercial HS powder with 8 wt. % Al. Although the commercial powder ir rich in Cr (18 wt. %), prior testing under steam at 650º C [6] had shown that a protective Cr rich scale did not form, and for this reason Al was added. The as deposited microstructure exhibits a non-uniform dispersion of Al particles within the coating as shown in Fig. 4 and a global Al content of 5 wt. %. The Vickers microhardness of this coating was reduced from 1000 to 750 when Al was added, but the modified coating was still considered as hard enough.

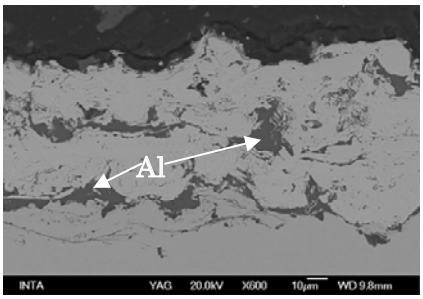

Fig. 4. Al enriched HS coating on P92

Steam Oxidation Testing

Testing of the three new coatings together with uncoated P92 and the reference pure aluminide coating has begun under 100 % atmospheric, flowing steam. The preliminary results indicate that all coatings are protective in comparison with uncoated P92 after 1000 h as shown in Fig. 5. In particular, the Cr aluminide coating has exhibited an excellent behavior confirmed by the microstructure of the sample taken after 1000 h which is exactly the same as the initial coating. In contrast with the behavior of the pure aluminide coating which as mentioned earlier exhibits a high degree of Al inwards diffusion. Both the NiAl and Al modified HS coatings shown higher weigh gains but tending to stabilized. The microstructure of the NiAl after 1000 h shown some degree of oxidation in the internal layers of the coating, likely due to defects present in the original coating microstructure. The HVOF deposited Al modified HS is very rough formed a protective Al oxide and the higher increase in weight may be simply due to the higher specific surface.

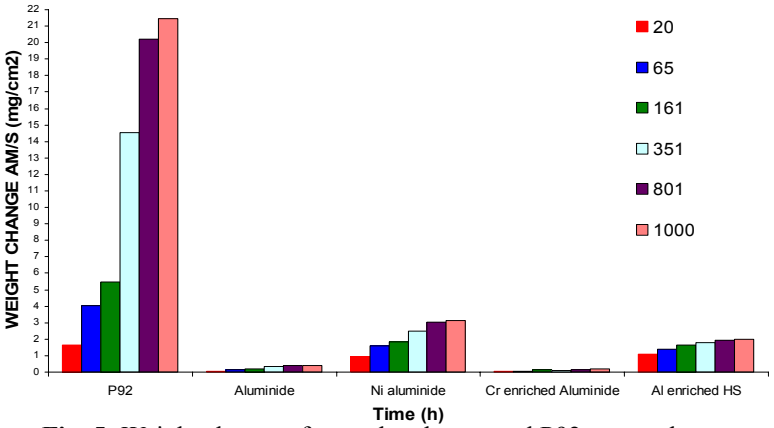

Fig. 5: Weight change of coated and uncoated P92 exposed to flowing steam at 650º

Fire-Side Oxycombustion Testing

Similar results have been obtained for up to 300 h at 650ºC under this atmosphere with very low weight gains of the

coated specimens as compared to uncoated P92 as shown in figure 6. The test will be completed after 1500 h of exposure.

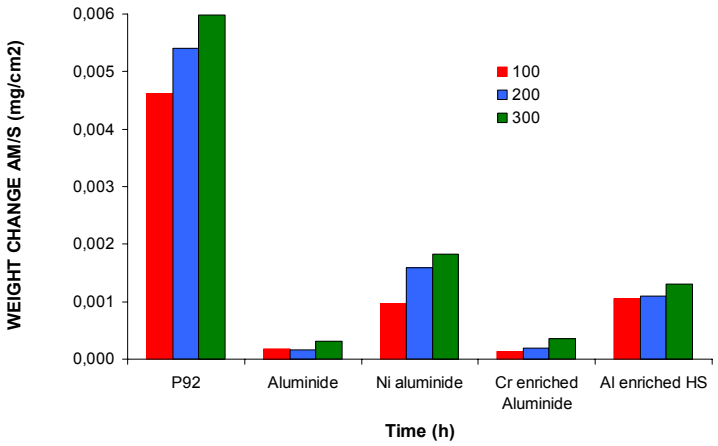

Fig. 6: Weight change of coated and uncoated P92 exposed to an oxycombustion atmosphere at 650º

Pilot Plant Testing

Although still for a short duration (480 h) both the reference aluminide coating as well as the Al modified HS were applied to the external surfaces of reheater P92 tubes and exposed to a real coal oxycombustion atmosphere in a pilot boiler at 650º C. Both coatings appeared unaffected as shown in figure 7a and b respectively. Ashes deposited on these coatings do not appear to significantly react with both materials as shown for instance in figure 7a in the case of the aluminide coating.

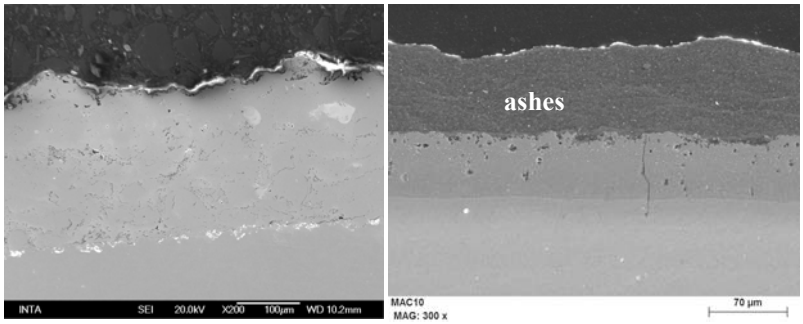

a) **b)**

Fig. 7. Coatings applied on reheater P92 tubes and exposed to a coal oxycombustion atmosphere at 650º C for 480 h: a) Al enriched HS HVOF deposited coating and b) slurry aluminide

4. CONCLUSION

New coatings have been developed for superheater tubes. Both Cr and Ni aluminides can be applied in the internal as well as external surfaces of the tubes. The preliminary test results indicate that in particular the Cr aluminide coating may represent an improvement over the pure aluminide coating as it does not exhibit cracks and degradation by diffusion is significantly slow. Both the pure aluminide and the Al modified HS coating were tested in a pilot oxycombustion boiler for 480 h at 650 º C and no degradation was observed even after deposition of ashes on the surface of the coatings. The HVOF deposited AL modified hard steel is a candidate to be used in erosion prone zones.

Acknowledgements

The authors are grateful for the support by the Spanish Ministry of Economy and Competitiveness for financial support (ENE2011-29203-C02-01) as well as the EC (POEMA, G.A. No.: 310436). We also acknowledge ENDESA for supporting the pilot plant tests at CIUDEN and all members of the Metallic Materials Area at INTA for technical support.

References

[1] CO_2 Capture Technologies: Oxi Combustion with CO_2 Capture, Global CCS Institute, Palo Alto, CA, January 2012 http://www.globalccsinstitute.com/publications/co2-capture-technologies-oxy-combustion-co2-capture
[2] Production of Coatings for New Efficient and Clean Coal Power Plant Materials (POEMA), FP7 Program, G.A. No.: 310436, 2013-2016.
[3] Agüero A., González V., Gutiérrez M., Knödler R., Muelas R. and Straub S., "Comparison between Field and Laboratory Steam Oxidation Testing of Aluminide Coatings on P92", Materials and Corrosion, Vol. 62 (2011), pp. 561-568
[4] Agüero A., González V., Gutiérrez M. and Muelas R., "Oxidation under pure steam: Cr based protective oxides and coatings", Surface and Coatings Technology, 237 (2013) 30–38
[5] Agüero A., "Progress in the Development of Coatings for Protection of New Generation Steam Plant Components", Energy Materials, 3 (2008) 35-44
[6] R. Muelas and A. Agüero, INTA, unpublished results.

Corrosion of Chromia Formers by Hot CO_2 Gas: a Review

D.J. Young (*) Thuan Dinh Nguyen and Jianqiang Zhang

School of Materials Science and Engineering, University of New South Wales, Sydney, Australia

e-mail: d.young@unsw.edu.au

1. INTRODUCTION

Early work on high temperature corrosion in CO_2 was related to gas-cooled nuclear reactor technology or fundamental studies of "mixed gas" corrosion. Fujii and Meussner [1] reported simultaneous oxidation and carburisation of Fe-Cr alloys containing 1 to 15 wt. % Cr in pure CO_2 at temperatures of 700, 900 and 1100 °C. Similar observations have been reported for carbon steel [2], 304 stainless [3] and a high alloy austenitic heat resisting steel [4] exposed to CO_2.

More recently, the topic of CO_2 corrosion has attracted renewed interest with the development of new technologies for reduced greenhouse gas emissions, such as oxyfuel combustion of coal and solar thermal power generation. Again, the observation of alloy carburisation beneath an external oxide scale has been widely reported.

The aggressive corrosion brought about by CO_2 is at first sight surprising, as carbon activities required to form the observed $(Cr,Fe)_7C_3$ or $(Cr,Fe)_{23}C_6$ precipitates are much higher than those of gaseous CO_2. Recent work directed at understanding how such high carbon activities are realized, how carbon can penetrate otherwise protective chromia scales and how these processes are associated with breakaway corrosion of the alloys is now reviewed.

2. COMPARISON OF ALLOY REACTIONS WITH CO_2 AND OXYGEN

The essential features of the reaction products are seen in Fig. 1, where the example of a model Fe-20Cr-0.1Ce (weight %) alloy is shown after reaction at 818°C. When the corrodent is oxygen, the reaction product is a protective scale of Cr_2O_3, whereas reaction with CO_2 leads to internal carburization and the nucleation and growth of iron-rich oxide nodules.

The precise nature of the reaction products depends on both alloy composition and temperature. In oxidation reactions, the level of alloy chromium required to form a protective chromia scale increases as the temperature is decreased [5]. However, more alloy chromium is required to resist corrosion by CO_2. Ferritic and martensitic steels containing 9 wt % Cr passivate in dry air or oxygen at 550 and 650°C, but develop fast-growing Fe-rich oxide scales and simultaneously carburise in CO_2 at these temperatures [5-6].

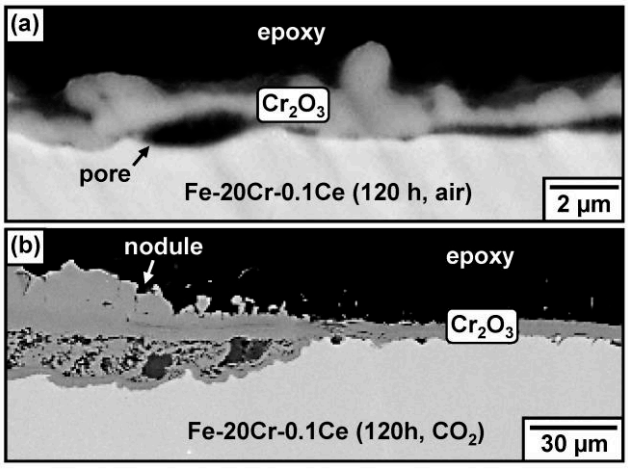

Fig. 1. BSE-SEM cross-sections of Fe-20Cr-0.1Ce after reaction for 120 h at 818 °C in (a) Ar-20% air and (b) Ar-20CO_2.

At these temperatures, a level of 20 wt % Cr is marginal in CO_2, but 25 wt % confers protection. Austenitic alloys are more resistant to carburization because their chromium carbide solubility products are higher than the corresponding ferritic alloys [7]. Small additions of cerium increase carburization rates in Fe-Cr alloys [8]. Manganese additions lead to formation of a spinel layer overlying the chromia scale [9], and Si additions can lead to a sublayer of glassy silica at the scale-alloy interface [10]. Both are barriers to carbon entry [10].

CARBON ACTIVITIES

Alloy carburization requires relatively high carbon activities. For example, an Fe-9Cr alloy carburises at 650°C in Ar-20CO_2 at 1 atm, where the carbon activity $a_C = 1.6 \times 10^{-15}$, although a value of $a_C \geq 8.5 \times 10^{-4}$ is required to stabilise the carbide [6, 11]. This is explained by scale-alloy interfacial equilibrium, where the oxygen potential is controlled at a low value by the reaction $M + \nu/2O_2 = MO_\nu$. If carbon is present, the equilibria

$$CO_2 = CO + \tfrac{1}{2}O_2 \qquad 2CO = CO_2 + C$$

are also in effect. For a given total pressure, a_C is inversely related to $p(O_2)$, and can be quite high. This model quantitatively accounts for the carbide volume fraction produced in Fe-9Cr at 650 °C beneath a scale of $FeO + FeCr_2O_4$ [6]. It also correctly predicts the carburisation rate on the basis of Wagner's internal oxidation theory.

The amount of carbide produced in Fe-20Cr beneath a Cr_2O_3 scale under the same conditions is much less than in the Fe-9Cr, and far less than predicted by the equilibrium analysis. Evidently chromia is a better barrier to carbon ingress than are the iron-rich oxide scales.

MECHANISM OF CARBON ENTRY

Carbon has been shown [12] to be essentially insoluble in Cr_2O_3 and a number of other oxides. An atom probe tomography investigation [13] of a chromia scale grown on Fe-20Cr exposed to Ar-20CO_2 at 650°C has confirmed that negligible carbon levels are to be found within the oxide lattice. However, strong enrichment of carbon at oxide grain boundaries was found, as shown in Fig. 2.

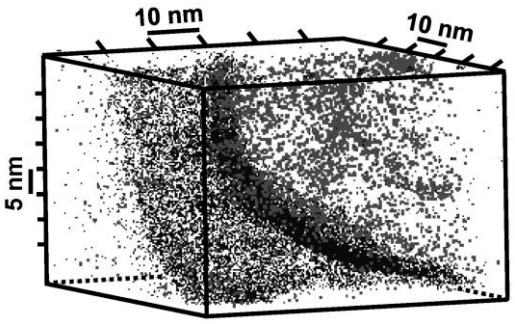

Fig. 2. Three-dimensional view of carbon atoms distribution at oxide grain boundaries with 99 % of atoms in bulk alloy and oxide removed from image.

Transmission electron microscopy showed that scales on Fe-20Cr grown in both Ar-20CO_2 and Ar-20O_2 were single-phase Cr_2O_3. It also revealed that the oxide grain size developed in CO_2 was considerably finer than that grown in O_2. As diffusion in chromia scales occurs predominantly via grain boundaries, this difference accounts for the faster scaling rate observed in CO_2. This, in turn, is relevant to the earlier onset of breakaway corrosion in the CO_2 reaction.

MECHANISM OF BREAKAWAY ACCELERATION

Breakaway occurs when an alloy is depleted in Cr, and can no longer maintain the exclusive growth of an external chromia scale. It has been shown [14] that precipitation of small amounts of Cr-rich carbide in Fe-20Cr has no effect on alloy Cr depletion beneath the chromia scale. What can change, however, is the local rate of scale thickening. This leads to more rapid Cr consumption and an increase in the a_{Fe}/a_{Cr} ratio at the alloy-scale interface. Eventually, the chromia is destabilised with respect to $FeCr_2O_4$ spinel. As shown by laser Raman microscopy [14], spinel forms locally, and allows outward diffusion of iron to form Fe-rich oxides. These local nodules of iron oxide spread laterally, coalesce and develop into a uniform, fast growing scale. The original Cr_2O_3 layer is dissolved into the scale, where it remains as a thin spinel layer.

Classical nucleation and growth theory has been shown [15] to account approximately for the form of the overall weight uptake kinetics. Once Fe-rich oxides develop, their transmission of carbon is faster, leading to more extensive internal carburisation. The resulting immobilisation of chromium within the alloy means that repassivation of its surface becomes impossible, and breakaway is irreversible.

CONCLUSIONS

Carbon dioxide is a much more aggressive corrodent of chromia-forming alloys than is oxygen. Chromia scales grown in CO_2 are finer-grained than those developed in oxygen. As a result, they grow faster, because grain boundary diffusion is rate controlling.

More rapid chromia growth causes greater depletion of alloy chromium, and eventually destabilises the chromia with

respect to spinel. Fast diffusion of iron through the spinel leads to nucleation of Fe-rich nodules which spread and cover the surface.

Carbon penetrates chromia scales via their grain boundaries. This leads to internal carburisation of the alloys. It appears likely that the presence of carbon species on the grain boundaries is an important factor in limiting grain growth.

Acknowledgement
Financial support from the Australian Research Council's Discovery program is gratefully acknowledged.

References
[1] C.T. Fujii, R.A. Meussner, "Carburisation of Fe-Cr alloys during oxidation in dry carbon dioxide", *J. Electrochem. Soc*. Vol. 114 (1967) pp. 435-442.
[2] G.B. Gibbs, M.R. Wootton, W.R. Price, K.E. Hodgson, "Scale stresses during protective and breakaway corrosion of iron and rimming steel in CO_2", *Oxidation of Metals*, Vol. 7 (1973) pp. 185-200.
[3] H.E. McCoy, "Type 304 stainless steels vs flowing CO_2 at atmospheric pressure and 1100-1800F", *Corrosion*, Vol. 21 (1965) pp. 84-94.
[4] R.A. Holm, H.E. Evans, "The resistance of 20Cr/25Ni steels to carbon deposition. I. The role of surface grain size", *Werkst. Korros.*, Vol. 38 (1987) pp. 115-124.
[5] D.J. Young, J. Zurek, L. Singheiser, W.J. Quadakkers, "Temperature dependence of oxide scale formation on high-Cr ferritic steels in Ar-H_2-H_2O", *Corros. Sci.*, Vol. 53 (2011) pp. 2131-2141.
[6] T. Gheno, D. Monceau, J. Zhang, D.J. Young, "Carburisation of ferritic Fe–Cr alloys by low carbon activity gases", *Corros. Sci.*, Vol. 53 (2011) pp. 2767–2777.
[7]] D.J. Young, High temperature oxidation and corrosion of metals, first ed., Elsevier (UK, 2008).
[8] T.D. Nguyen, J. Zhang, D.J. Young, "Martensite formation in Fe-9Cr alloys exposed to low carbon activity gas", *Scripta Mater.*, Vol. 69 (2013) pp. 9-12.
[9] T.D. Nguyen, J. Zhang, D.J. Young, "Effects of cerium and manganese on corrosion of Fe-Cr and Fe-Cr-Ni alloys in Ar-20CO_2 gas at 818 ^oC", *Corros. Sci.*, Vol. 76 (2013) pp. 231-242.
[10] T.D. Nguyen, J. Zhang, D.J. Young, "Effects of silicon on high temperature corrosion of Fe-Cr and Fe-Cr-Ni alloys in carbon dioxide", *Oxidation of Metals*, (2013) in press.
[11] Thermo-Calc Windows TCW2, version 2.2.1.1, (2003).
[12] I. Wolf, H.J. Grabke, "A study of the solubility and distribution of carbon in oxides", *Solid State Commun.*, Vol. 54 (1985) pp. 5-10.
[13] D. J. Young, T.D. Nguyen, P. Felfer, J. Zhang, J.M. Cairney, "Penetration of Protective Chromia Scales by Carbon", *Scripta Mater.,* (2013) submitted.
[14] T. Gheno, D. Monceau, D.J. Young, "Mechanism of breakaway oxidation of Fe–Cr and Fe–Cr–Ni alloys in dry and wet carbon dioxide", *Corros. Sci.*, Vol. 64 (2012) pp. 222-233.
[15] T. Gheno, D. Monceau, D.J. Young, "Kinetics of breakaway oxidation of Fe–Cr and Fe–Cr–Ni alloys in dry and wet carbon dioxide", *Corros. Sci.*, Vol. 77 (2013) pp. 246-256.

The Effect of Temperature on the Protective Oxide Layers in Cr-containing Steels

Juho Lehmusto*, Patrik Yrjas, and Mikko Hupa

Laboratory of Inorganic Chemistry, Abo Akademi University, Piispankatu 8, 20500 Turku, FINLAND

*e-mail: juho.lehmusto@abo.fi

1. INTRODUCTION

Inhibition or at least deceleration of global warming has become one of the major goals for the coming decades. A key strategy will be to replace fossil fuels with more sustainable fuels, which has generated growing interest in the use of waste-derived fuels and of renewable fuels such as biomass. More efficient ways to prevent corrosion are needed so that power plants using biomass and waste-derived fuels can operate at higher steam temperatures. From the materials point of view, this has been achieved by modifying the chemical composition of superheater steels to enhance their resistance to corrosion. To take this step further, one possibility could be controlled manipulation of the protective oxide layer thickness through pre-oxidation.

The choice of an appropriate material for superheater tubes depends on two main factors: the conditions to which the tubes are exposed (temperature, composition of flue gases and deposits, fly ash quality, and particle velocity), and the cost of the material. At moderate temperatures and in non-corrosive environments, low alloy steels are often preferred due to their reasonable cost. These iron-based steels contain up to 4-5 wt% of alloying elements, including chromium, nickel, and molybdenum, whose role is to improve the mechanical properties rather than the corrosion resistance of the material [1, 2].

To enhance the corrosion resistance of a material, chromium can be added to create iron-based stainless steels with either a ferritic or an austenitic structure. Chromium is known to form a protective layer consisting of pure chromium oxide (Cr_2O_3), corundum-type $(Fe,Cr)_2O_3$ binary oxide, or spinel-type containing iron and chromium [3]. The formation of a protective surface oxide has been reported to start at chromium concentrations above 11-12 wt% [1]. Above this threshold, the corrosion resistance increases with increasing chromium content. The most common group of stainless steels is the austenitic steels, which contain more than 16 wt% chromium and enough nickel to ensure the stability of the austenitic structure.

The focus of this study was to shed more light on the positive effect of pre-oxidation, in terms of corrosion resistance, on various commercial steels at elevated temperatures. The aim was to emphasize the effect of both time and temperature on oxide thickness, composition, and morphology.

2. EXPERIMENTAL

The commercial steels of interest were the low alloy ferritic 10CrMo9-10, the Nb-stabilized austenitic AISI347, and the high alloy austenitic Sanicro 28 (Table 1). In power plants, all three steels are used and the choice of steel depends, among other factors, on the corrosivity of the environment and the temperature.

Table 3. Chemical composition of steels in wt%

Steel	Cr	Fe	Mn	Mo	Ni	Si	Others	n_{Cr}/n_{Fe}
10CrMo9–10	2.3	93.4	0.8	1.0	--	0.3		0.02
AISI347	17.7	68.2	2.1	--	8.5	0.4	Nb 1.5	0.26
Sanicro 28	25.9	35.9	2.0	3.4	29.2	0.5	Cu 1.2	0.72

Prior to high temperature exposure, the steel samples were polished in water with a 280 grit SiC grinding paper, followed by polishing in ethanol with a 500 grit SiC grinding paper. The samples were further cleaned in ethanol using an ultrasonic bath. High temperature exposures were carried out in temperature controlled horizontal tube furnaces, and the temperature was measured with thermocouples installed between adjacent samples and at both ends of the sample holder.

The sample temperatures were within ±5°C of the target temperature, and the heating rate was 5°Cmin^{-1}. In order to minimize the effect of ambient humidity, the samples were positioned inside a sealed quartz reactor, through which synthetic air (21% O_2, 79% N_2) was passed. The samples were positioned horizontally, parallel to the direction of the flow. The warm-up and cool-down periods were carried out in the same atmosphere as the exposures. All the experiments were run at 200°, 500°, and 700°C, with two different exposure times: 5 and 24 hours. A reference sample of each steel was treated as described above, but the reference samples were oxidized at room temperature.

After exposure, the samples were allowed to cool to room temperature in synthetic air inside the quartz reactor, and then they were analyzed. The sample surfaces, especially their morphologies and chemical compositions, were studied with a scanning electron microscope (LEO 1530 Gemini) coupled to an X-ray detector (Thermo Scientific UltraDry Silicon Drift Detector) and an energy dispersive X-ray analysis system (Thermo Scientific ThermoNORAN Vantage X-ray). The thicknesses and the depth profiles of the formed oxides were measured with X-ray Photoelectron Spectroscope (Physical Electronics Inc. Quantum 2000).

3. RESULTS AND DISCUSSION

The oxidation of the ferritic 10CrMo9-10 steel initiated already at 200°C. White, pearl necklace-like structures formed along the grain boundaries (Fig. 1, left). These structures were formed during both exposure times, but unfortunately they were so thin, that their chemical compositions could not be analyzed with SEM-EDXA. However, the XPS analyses verified that a thin iron oxide layer formed on both samples. The sputtering time needed to penetrate the oxide formed in 5 and 24 hours was 70 and 90 seconds, respectively. The sample surface was homogeneously oxidized at 500°C after both exposure times and no distinguishable structures could be detected, apart from pores in the oxide and iron oxide whiskers pointing out of it (Fig. 1, middle). The sputtering time needed to penetrate the oxide formed in 5 and 24 hours was 520 and 2250 seconds, respectively. At 200°C, the oxide layers were virtually equally thick after both exposure times, but the oxide formed at 500°C in 24 hours had a sputtering time roughly four times as long as what was needed to penetrate the oxide formed in 5 hours. This suggested that the steel had started to oxidize in an uncontrolled manner. The oxides formed at 700°C after both exposure times consisted of bigger iron oxide particles, containing larger pores and bigger whiskers (Fig. 1, right). Although the surface morphology differed from the morphologies at lower temperatures, the composition remained unchanged. The formed oxides were too thick to be analyzed with XPS, so the oxide layer thicknesses were measured from cross-sectional samples with SEM, giving the layer thicknesses of over 15 and 23 microns after 5 and 24 hours, respectively.

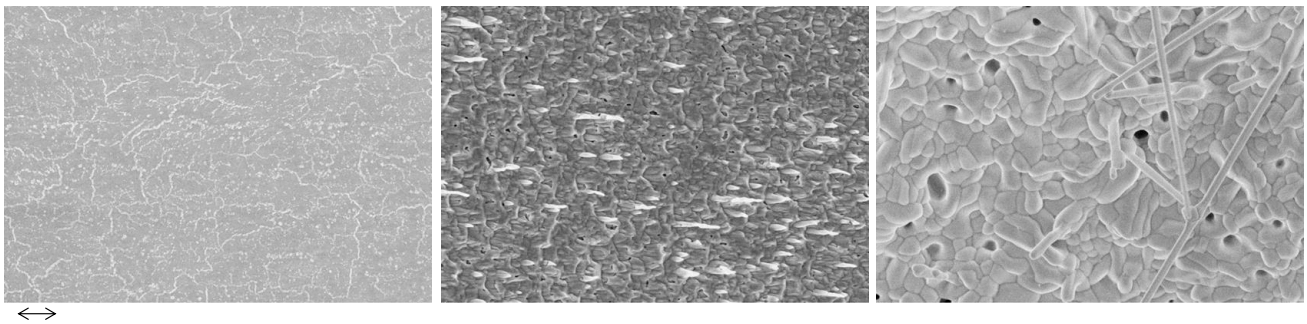

Figure 1. The surfaces of 10CrMo9-10 samples exposed for 24 hours at 200°C (left), 500°C (middle), and 700°C (right).

The oxidation of the Nb-stabilized austenitic AISI347 steel initiated already at 200°C. In contrast to the distinguishable oxide crystals at the grain boundaries of the ferritic 10CrMo9-10 steel, the surface of AISI347 appeared to be homogeneously covered with an oxide (Fig. 2, left), which could not be observed at the surface of the reference sample. The oxides formed at 200°C were too thin to be reliably analyzed in terms of chemical composition. However, the sputtering times for the oxides formed at 200°C after 5 and 24 hours were 30 and 36 seconds, respectively. A clear difference in surface structure was observed in the samples exposed at 500°C. The surface has been locally destroyed by bean-like features bursting from beneath (Fig. 2, middle). These structures contained high amounts of niobium, which suggests that alloyed niobium plays a role in local degradation of AISI347. However, Nb seems not to have diffused to the surface, because no Nb enrichment was observed, apart from the Nb-rich structures. Between these structures, more

homogeneous oxidation occurred, forming an oxide, whose outermost layers consisted of iron-rich oxide, followed by a Cr-rich oxide. The sputtering times for the oxides formed at 500°C after 5 and 24 hours were 12 and 18 seconds, respectively. Reason for thinning of the oxide, compared to 200°C, needs to be studied further. One possible explanation could be anomalous temperature dependence of oxidation kinetics, as described in the case of steam oxidation of ferritic steels in [4]. As the temperature rose to 700°C, the Nb-rich structures were slowly covered by Cr_2O_3 crystals formed in further oxidation (Fig. 3, right), and were completely coated after 24 hours. After both exposures times, the oxide consisted of almost solely chromium, with a clear manganese enrichment after 5 hours in the outermost layers of the oxide. However, manganese could not be detected in the oxide after 24 hour-exposure. The sputtering times for the oxides formed at 700°C after 5 and 24 hours were 72 and 370 seconds, respectively. Although the formed oxide consisted of Cr_2O_3, the quality of its protective properties could not be verified at this stage.

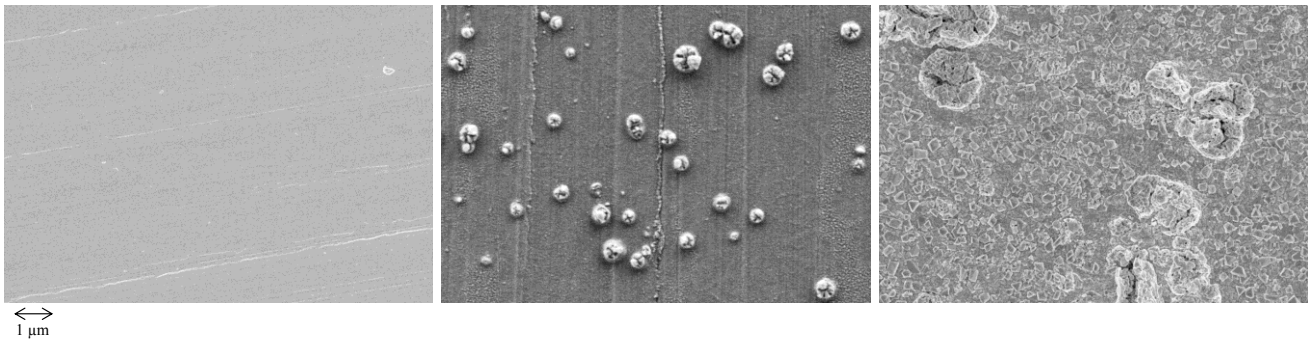

Figure 2. The surfaces of AISI347 samples exposed for 5 hours at 200°C (left), 500°C (middle), and 700°C (right).

Unlike the two steels mentioned above, no oxide formation could be detected on high alloy Sanicro 28 steel at 200°C (Fig. 3, left). The surface appeared the same as that of the reference sample. Small oxide particles have homogeneously covered the surface after 5 hours at 500°C (Fig. 3, middle), and some local structural differences could be observed after 24 hours. However, these structures were so thin, that no information could be obtained with the SEM. The sputtering times for the oxides formed at 500°C after 5 and 24 hours were 18 and 12 seconds, respectively. The similar layer thicknesses after both exposure times suggested for slow oxidation, resulting in a thin oxide consisting of some iron and mostly nickel. At the highest exposure temperature of 700°C, a continuous Cr_2O_3 layer has formed on the surface (Fig. 3, right). The sputtering times for the oxides formed at 700°C after 5 and 24 hours were 90 and 150 seconds, respectively. Both the average crystal size and the size distribution of the crystals are smaller in the case with Sanicro 28 compared to AISI347. This suggested that the oxide formed on Sanicro 28 has preserved its protective properties, at least better than the oxide on AISI347.

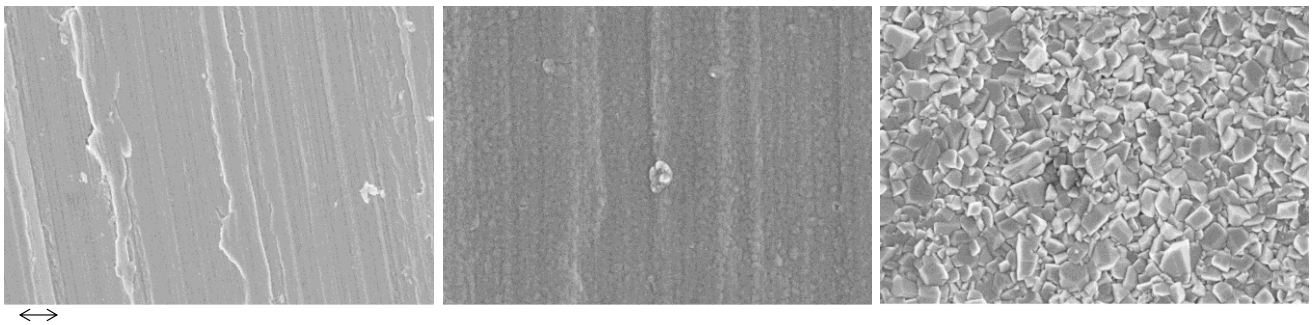

Figure 3. The surface of Sanicro 28 samples exposed for 5 hours at 200°C (left), 500°C (middle), and 700°C (right).

4. CONCLUSIONS

The oxidation behavior of three commercial steels with different grades was studied by varying the oxidation temperature and time. The aim was to shed more light on to the oxidation mechanisms of various steels. Additionally, the protective properties of the formed oxide layers will be addressed in a subsequent study, where corrosive model ash is applied onto the steel surfaces. The oxidation reaction was observed to initiate differently depending on the said steel. With all three

steels the oxide layer thickness increased as a function of temperature and time. In addition, exposure time and temperature was observed to have an effect on the oxide morphology and/or on the chemical composition of the oxide.

ACKNOWLEDGEMENTS

This work was carried out within FUSEC (2011-2014) project, as part of the activities of the Åbo Akademi Process Chemistry Centre. Other research partners are VTT, Lappeenranta University of Technology, Aalto University, and Tampere University of Technology. The authors also gratefully acknowledge the support provided by the National Technology Agency of Finland (TEKES), Andritz Oy, Metso Power Oy, Oy Metsä-Botnia Ab, Foster Wheeler Energia Oy, UPM-Kymmene OYj, Clyde Bergemann GmbH, International Paper Inc., and Top Analytica Oy Ab.

REFERENCES

[1] Aromaa, J., Klarin, A. (Eds.), Materials, Corrosion Prevention and Maintenance (in series: Papermaking Science and Technology no. 15), Fapet (Jyväskylä, 1999).
[2] Rollason, E.C., Metallurgy for engineers 4th edition, Edward Arnold Ltd (Norwich, 1973).
[3] Kofstad, P., High temperature corrosion, Elsevier applied science, (London and New York, 1988).
[4] Žurek, J., Wessel, E., Niewolak, L., Schmitz, F., Kern, T.-U., Singheiser, L., Quadakkers, W.J., "Anomalous temperature dependence of oxidation kinetics during steam oxidation of ferritic steels in the temperature range 550–650°C", *Corrosion Science*, Vol. 46, No. 9 (2004), pp. 2301-2317.

Employing the effect of specimen thickness to study chromia scaling on Ni25Cr and its interactions with water vapour in N_2-O_2-H_2O test gases at 1000°C

M. Hänsel*, E. Turan and V. Shemet

Forschungszentrum Jülich GmbH, Institute for Energy and Climate Research /IEK-2),
Leo-Brandt-Str. 1, 52425 Jülich, Germany

e-mail: m.haensel@fz-juelich.de

1. INTRODUCTION

Most modern metallic structural materials for high temperature applications depend for their protection against corrosive environments on the formation of protective alumina or chromia surface scales [1, 2]. Water vapour is invariably present in combustion gas, and is a common constituent of many industrial process streams. Its ability to alter chromia scaling rates has long been recognised, but is poorly understood because of the diversity of scale-water vapour interactions possible [3]. One obstacle is the complex defect structure of thermally growing chromia scales, which strongly depends on the atmosphere with which they are in equilibrium with [4]. For technological reasons a protective oxide scale needs to be essentially gas-tight to ensure that its growth is governed by diffusion. A gas-tight thermally growing chromia scale is commonly assumed to be in equilibrium with the atmosphere the scale is growing in, as well as the metal the scale is formed on. Consequently the type of defects, i.e. Cr vacancies or interstitials, may change throughout a thermally growing chromia scale. From this it follows that a high pO_2, Cr vacancies are the major defects determining the transport properties in thermally growing chromia scales and at very low pO_2 Cr interstitials. Because of this, the exact nature of the chromia-water vapour interaction may depend on a number of factors such as Cr activity and its mobility in the alloy as well as pO_2 and pH_2O in the test gas under consideration. To shed more light on the matter, the effect of specimen thickness on chromia scaling [5, 6] can be employed. Pilling and Bedworth [7] investigated the volume changes in the course of oxide scale formation and growth on metal surfaces. Chromia scales are under pressure during scale growth and thermally growing chromia scales are compressed oxides. For thermodynamic reasons the concentration [8] and diffusivity [5] of the intrinsic, native defects in oxides under hydro-static pressure varies with the amount of pressure applied. Quadakkers et. al. [6] studied the effect of specimen thickness on the oxidation rate of High Chromium ferritic steels. The authors conducted discontinuous air oxidation experiments with the Laves phase strengthened ferritic steel Crofer 22H at 800°C. They compared the data for solution annealed and pre-aged materials and showed that intrinsic creep strength of the alloy substantially affects oxidation rates. The authors explained their observations by assuming the relaxation of oxide growth stresses by plastic deformation of the metallic substrate and concluded that alloy creep strength might be a significant factor affecting the kinetics of oxide scale growth. Meier et.al. [5] investigated the effect of specimen thickness on the growth rate of chromia scales on NiCr model alloys, among them Ni-25%Cr. The authors used thermo-gravimetric measurements at 1000°C in synthetic air and isothermal exposures for up to 100 h at 1000°C in laboratory air and in Ar-4%H_2-2%H_2O. It was found out the growth rates of the chromia scales decreased with increasing specimen thickness in the air and Ar-4%H_2-2%H_2O. The authors concluded that the decrease in rate is the result of compressive growth stresses in the scales which can be relaxed by plastic deformation of the substrate for thin specimens but are maintained at significant levels for thick specimens. Furthermore Meier et.al. [5] compared the change in Cr vacancy diffusivity in a chromia scale formed on a thin specimen, which is apparently relaxed and is under a lot less oxide growth stress compared to a thicker specimen, which cannot relax by plastic deformation. The authors used estimates for the growth stress in chromia scales and the free volume for Cr vacancy diffusion found from the available literature. Because of their calculations the authors concluded that the change in Cr diffusivity is too small and does not account for the observed differences in chromia growth rates. The current work focuses on the question of how water vapour affects the oxidation behaviour of chromia forming alloys in dry and wet high $p(O_2)$ environments. This is attempted by using a set of different thick specimens for each experimental condition. Hereby varying the concentration of the intrinsic, native defects in a qualitative manner and observing the resulting chromia scaling rate and microstructure of the scales formed under the various conditions.

2. EXPERIMENTAL

The studied material was supplied by Thyssen Krupp VDM. Specimens of dimensions, 20x10 mm^2 and 1.0, 0.5 and 0.25mm thick, were cut from the delivered plates, ground to a 1200 grit surface finish and ultrasonically cleaned in acetone immediately before use. The alloy composition is listed in Table 1. Thermogravimetric measurements for up to 24 hours exposure at 1000°C were carried out in N_2–O_2–H_2O gas mixtures using a Setaram Thermobalance (TG92). The total gas flow rates were 2 L/h, corresponding to a linear flow in the tubular reactor of 0.2 cm/s, at a total pressure of 1 bar. The water vapour was added to the gas by flowing N_2 –O_2 through distilled water which was kept at the appropriate temperature [9]. The individual samples were suspended on an alumina hook and gravimetric data were recorded continuously during every single experiment including the cooling of the sample after the isothermal exposure. The TGA results were corrected to account for buoyancy effects, using data measured for inert alumina samples of the same geometry as the specimens used in the oxidation experiments. The reacted samples have been prepared by ion beam

cross-section polishing and were subsequently analysed using scanning electron microscopy with energy dispersive X-ray analysis to measure the Cr depletion profiles and acquire the oxide microstructure.

Table 1: The alloy composition analysed by Inductively Coupled Plasma-Optical Emission Spectroscopy (ICP-OES) and Infrared (IR) Analysis

	Composition in wt.-%					
Alloy	Ni	Cr	C	N	O	S
Ni25Cr	Bal.	25	0.004	0.0023	0.017	0.001

3. RESULTS AND DISCUSSION

Sets of different thick Ni25Cr specimen were exposed under isothermal conditions at 1000°C for 24 hours in dry and wet high p(O_2) with1%O_2.and up to 7% H_2O. Figure 1 presents the data in form of weight change after 24 hours exposure of all samples reacted under the various conditions. No scale spallation was obvious by visual inspection from any specimen exposed in the present study. The chromia growth kinetics was found to be depending on the thickness of the specimens used for the oxidation experiments. In dry N_2-O_2 gas the effect was very clear with the 0.25 mm thick specimen producing a twice as thick chromia scale compared to the 1.0mm thick specimen. The progressive addition of water vapour into the test gas levelled the differences in chromia scaling kinetics and the chromia scale thickness decreased with increasing water vapour content in the gas. The last result was in excellent agreement with the established Cr depletion profiles, which are a measure of the total Cr consumption during oxidation.

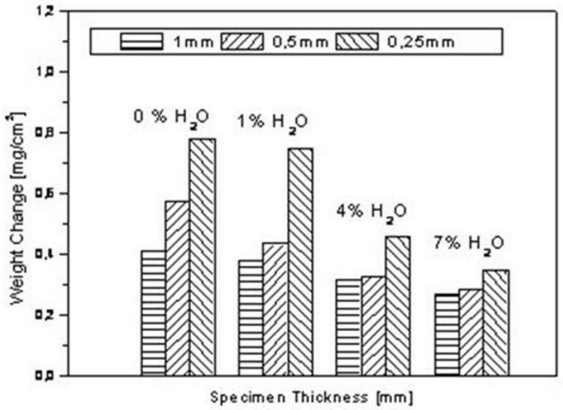

Figure 1: Weight change after 24 hours isothermal oxidation of Ni25Cr at 1000°C in N_2-1%O_2-X%H_2O

From this it can be concluded that Cr vaporisation did not play a significant role under the conditions investigated. Further assessment of the thermo gravimetric data showed, after an initial period of transient oxidation, that all specimens reacted according to approximately parabolic kinetics. It is, therefore, concluded that scale growth was always controlled by solid-state diffusion. Differences in the scaling rate constant, therefore, reflected different oxide properties and boundary conditions. Because of thermodynamic reasons the presence of a transient nitride [10] can be excluded. Now the question will be discussed how H-species originating from H_2O in the test gas affects the oxide properties, the concentration of the intrinsic, native defects, and changes the boundary condition at the oxide-gas interface.

To address this question, two sets of the exposed specimens have been cross-sectioned and prepared by ion beam polishing to reveal the microstructural changes of the oxide scales under the effect of specimen thickness and their "off-set" by H_2O addition. Figure 2 presents the oxide scale microstructures after 24 hours of exposure in dry and wet N_2-1%O_2 test gas. In the left (Fig. 2 a, c, e) are the cross-section after exposure in dry gas and at the right the set after exposure to the wet gas containing 7%H_2O (Fig. 2b, d, f). The thickness of the employed oxidation specimen decreases from top to bottom. Examining the dry set, it can be observed that the oxide scale formed on the 1.0mm thick sample (Fig. 2 a) consists of globular shaped grains, with some smaller grains at the metal-oxide interface and slightly larger ones at the oxide gas interface. The shape and size change with decreasing specimen thickness and larger columnar shaped grains have been formed on the 0.5mm specimen (Fig. 2 c). The oxide scale formed on the thinnest specimen (0.25 mm) exhibits also large, columnar grains (Fig. 2 e). But there is still a very small zone of fine, globular grains observable in the oxide scale formed on the 0.5 and 0.25mm thick specimen. Examining the wet set, where the oxide scales have been formed in N_2-1%O_2-7%H_2O, it can be observed that the size and shape of the oxide grains is almost the same for all three specimens in the set. All oxide scales are made up of globular grains, which are slightly increasing towards the oxide-gas interface. Comparing the oxide scales formed in dry and wet gas on specimen with identical thickness, it is found that the number of oxide grains formed in the scale under wet condition is considerably larger than in those formed under dry conditions, except for the 1.0mm thick specimen (Fig. 2 a, b). For the 1.0mm specimen there is no significant difference in oxide microstructure for scales formed in dry and wet conditions. The addition of 7%H_2O to the test gas "off-sets" the effect of specimen thickness.

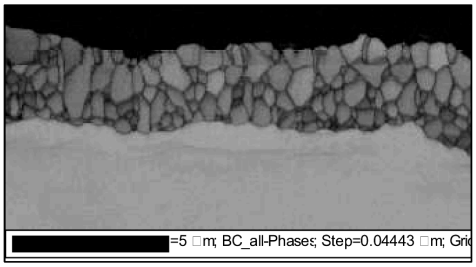

a) 1.0mm thick specimen in dry gas

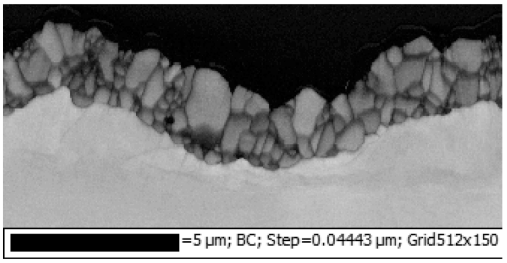

b) 1.0mm thick s pecimen in wet gas

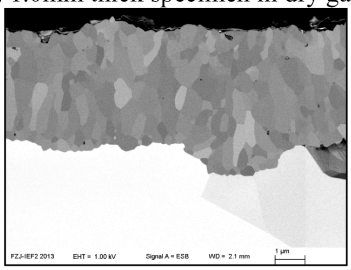

c) 0.5mm thick specimen in dry gas

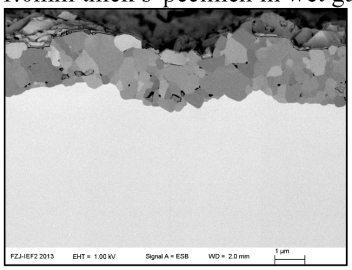

d) 0.5mm thick s pecimen in wet gas

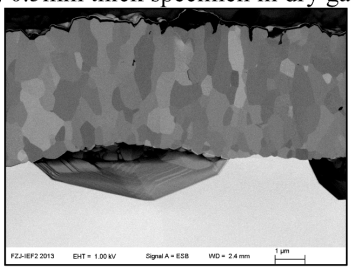

e) 0.25mm thick specimen in dry gas

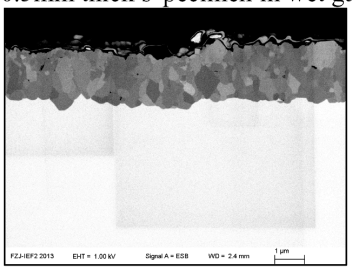

f) 0.25mm thick specimen in wet gas

Figure 2.: Oxide scale microstructures after 24 hou rs exposure at 1000 C in dry (0% H_2O) and wet (7% H_2O) $N_2$1%O_2

Following the classical theory the change of microstructure in the dry set is a clear sign for increasing Cr outward transport with decreasing specimen thickness and an increasing ability to relax the growth stress [5,6,8] during the course of oxidation. Time, temperature and test gas, were fixed for each set of different thick specimens. From this it is clear that the boundary conditions were the same for each set of different specimens at least at the oxide-gas interface. The boundary conditions at the metal-oxide interface are varying as the Cr-depletion profiles indicate after 24 hours of exposure. But this might be a consequence of the Cr transport rather than a reason for the observed differences. To facilitate the observed differences in diffusion controlled Cr outward transport the oxide properties, i.e. the concentration of the intrinsic, native defects and their mobilities, need to vary and be dependent on the stress state of the growing oxide. Because of their calculations Meier et.al. [5] concluded that the change in Cr diffusivity is too small and does not account for the observed differences in chromia growth rates on Ni25Cr model alloys. This leaves as decisive factor the change of the concentration of the intrinsic, native defects depending on the stress state in the growing oxide scales as was intended for the present investigation.

There are three factors affecting the concentrations of the intrinsic, native defects under the prevailing test conditions, for each individual set of specimens. Firstly Ni^{2+} stemming from the transient stage of oxidation and is substituted on regular Cr^{3+} sites, lowers the Cr vacancy and/or raises the Cr interstitial concentration. Considering the same set of specimen it can be regarded as equal for each specimen in the set, because their surface area is almost equal. Secondly, the effect of specimen thickness, which is a measure for the ability to relax oxide growth stress by plastic deformation. Thin specimens allow almost all oxide growth stress to be relaxed by plastic deformation and raise Cr vacancy and lower Cr interstitial concentration in the oxide scale. The opposite is in effect for thick specimen, compare with Equ. 2. in Ref. [8]. Thirdly the effect of H-defects in form of (OH^-) on regular oxygen sites or interstitial protons (H^+) raises the Cr vacancy and lowers the Cr interstitial concentration. This is directly related to the amount of water vapour in the test gases. It increases with increasing water vapour content and exceeds its maximum effect at 7%H_2O. It has to be kept in mind that for oxide growth, the concentration of both types of defects needs to be sufficiently high to facilitate and establish a Cr flux throughout the scale. Now the observed chromia scaling kinetics for each set of the various thick specimen can be rationalised. Under dry conditions the Cr vacancy concentration in the growing oxide increases with decreasing specimen thickness and the Cr interstitial concentration decreases with decreasing specimen thickness. The addition of H_2O raises the H-defect concentration in the oxide scales, which are being compensated either by increasing the Cr vacancy concentration or further decreasing the Cr interstitial concentration. Under the prevailing boundary conditions, the observed scaling kinetics in Figure 1 indicates that the latter might be in effect. The matter of the presence of H-Defects

and if they are compensated with Cr vacancies or interstitials depends on the prevailing boundary conditions, i.e. the Cr activity in the metal substrate and the $p(O_2)$ and pH_2O of the test gas. The Cr content was kept constant at 25 wt.-% and there are not enough data to discuss its effect in detail. Considering the delivery of molecular species to the oxide surface, one can write adsorption equilibria:

$$H_2O(g) + S = H_2O/S \qquad (1)$$

$$O_2(g) + S = O_2/S \qquad (2)$$

where S represents a vacant surface site, and H_2O/S, O_2/S represent adsorbed species. Assuming that at any instant during scale development, surface sites are conserved, then

$$M = [S] + [O_2/S] + [H_2O/S] \qquad (3)$$

here, M is a constant and square brackets denote area concentrations. Eliminating [S] between Eqns. (1), (2) and (3), one finds

$$\frac{[H_2O/S]}{[O_2/S]} = \frac{K_1\ pH_2O}{K_2\ pO_2} \qquad (4)$$

Because the polar H_2O molecule adsorbs much more strongly than O_2, it follows that $K_1 > K_2$. As seen from Eqns (4) and (5), the competitive adsorption process is predicted to lead to a decrease in $[O_2/S]$ at higher values, and provides an explanation for the increased extent up-take of H-defects as water vapour is progressively added to N_2-1%O_2. Generally this depends on the ratio of $p(O_2)$:pH_2O in the test gas as suggested before [12] and it can be concluded that the presence of H-defects in the oxide not only depends on the pH_2O, but also depends on the $p(O_2)$ of the test gas.

4. CONCLUSION

The addition of larger amounts of H_2O in relation to the O_2 content of the test gas "off-sets" the effect of specimen thickness. Under the prevailing boundary conditions, a(Cr)=0.25 in the metal substrate, H-defects are assumed to decrease the Cr interstitial concentration far enough to decrease oxidation rates with increasing H_2O content of the test gas. The interplay between $p(O_2)$ and pH_2O is the decisive factor for the availability of H-defects, which is a question of competitive adsorption between O_2 and H_2O.

Acknowledgements

Support for this work by the Deutsche Forschungsgemeinschaft (DFG) is gratefully acknowledged. The authors are grateful to Mr. H. Cosler for assistance in carrying out the TG experiments, and to Dr. E. Wessel, who performed the ion beam polishing of the samples and carried out the SEM analyses.

References

[1] Young, D.J., High Temperature Oxidation and Corrosion of Metals, Elsevier, (Oxford, 2008).

[2] Birks, N., Meier, G.H. and Pettit F.S., Introduction to the High Temperature Oxidation of Metals, Cambridge University Press, (Cambridge, 2006).

[3] Young, D.J., "Effects of Water Vapour on the Oxidation of Chromia Formers" *Mater. Sci. Forum*, 593-598 (2008), pp. 1189-1197.

[4] Kofstad, P., High Temperature Corrosion, Elsevier Applied Science, (London, 1988).

[5] Zurek, J. Meier, G.H., Essuman, E., Hänsel M., Singheiser, L., Quadakkers, W.J., "Effect of specimen thickness on the growth rate of chromia scales on Ni-base alloys in high- and low-pO_2 gases", *Journal of Alloys and Compounds*. 467 (2009), pp. 450–458.

[6] Asensio-Jimenez, C., Niewolak, L., Hattendorf, H., Kuhn, B., Huczkowski, P., Singheiser, L., Quadakkers, W.J. "Effect of Specimen Thickness on the Oxidation Rate of High Chromium Ferritic Steels: The Significance of Intrinsic Alloy Creep Strength", *Oxidation of Metals* 79 (2013), pp. 15–28.

[7] Pilling, N.B., Bedworth, R.E., "The Oxidation of Metals at High Temperatures". *J. Inst. Met.,* 29 (1923), pp. 529-536.

[8] Pieraggi, B., "Defects and Transport in Oxides and Oxide Scales" in Shreir's Corrosion, ed. J.A. Richardson, Vol. I, Elsevier, (Amsterdam, 2010) pp. 102-132.

[9] Haynes, W.M., CRC Handbook of Chemistry and Physics, Taylor&Francis Group (2012-2013).

[10] Grabke, H. J. "Surface and interface segregation in the oxidation of metals" *Surf. Interface Anal*. 30 (2000), pp. 112–119.

[11]Michalik, M., Tobing, S.L., Hänsel, M., Shemet, V., Quadakkers, W.J., Young, D.J. "Effects of Water Vapour on the High Temperature Nitridation of Chromium" in *Materials and Corrosion* 2013, XXX, No. XXX, in press.

[12] Michalik, M., Hänsel, M., Zurek, J., Singheiser, L., Quadakkers, W.J., "Effect of water vapour on growth and adherence of chromia scales in high and low $p(O_2)$-environments at 1000 and 1050°C", *Materials at High Temperatures* 22 (2005), pp. 39 – 47.

Effect of Spinodal Decomposition on Oxidation of Fe-Cr Alloys

J. Shen, E. Monazami, J. B. McClimon, P. Reinke, W. A. Soffa , E. J. Opila(*)

Department of Materials Science, University of Virginia, 395 McCormick Rd. Charlottesville, VA, 22902, USA

e-mail: opila@virginia.edu

1. INTRODUCTION

Iron-chromium (Fe-Cr) alloys are important engineering materials, but they suffer from the notorious "475°C embrittlement" which prevents their long-term application at intermediate temperatures. The embrittlement is due to the Spinodal Decomposition (SD) which occurs in some Fe-Cr alloys at intermediate temperatures and results in Fe-rich and Cr-rich regions. Recently the oxidation of Fe-Cr alloys has been widely studied in conditions of interest for interconnect materials in Solid Oxide Fuel Cells (SOFCs). There has also been a trend to lower the SOFC working temperatures to intermediate temperatures of 500-700°C to improve system durability, however, Fe-Cr SD might pose a problem for oxidation resistance of interconnect materials due to the resultant Fe-rich areas. In this paper we present preliminary work on the effect of SD on the oxidation mechanism of the Fe-40 wt.%Cr alloys.

2. EXPERIMENTAL

Bulk alloys of Fe-40wt.% Cr were prepared using vacuum arc melting under an argon atmosphere. The homogeneity of the as-cast alloys was examined and confirmed with X-Ray Diffraction (XRD). Homogeneous coupons were prepared from the arc-melted ingots by rolling and subsequent annealing at 950°C for 24hrs repetitively until a desired thickness (≈1mm) was achieved and then cut into coupons (≈ 25x13mm). The coupons were polished to a 15 micron surface finish. Some Fe-40wt.% Cr alloy coupons were aged at 500°C for 100hrs in low-pressure Ar atmosphere to promote phase separation via spinodal decomposition. Phase separation was confirmed by Vickers hardness testing using a load of 0.5kgf and an indentation time of 15s. Both single phase and phase separated alloy coupons were oxidized in a Thermo Gravimetric Apparatus (TGA) in 1 atm dry O_2 and wet O_2 flowing at 100mL/min at 600 and 700°C for 100hrs. Weight change was also recorded before and after oxidation using a bench top balance. Scanning Tunneling Microscopy (STM) and Scanning Tunneling Spectroscopy (STS) were used to study the initial stage of the oxidation with thin film alloys of nominal composition of Fe-40wt.% Cr deposited on (001) MgO substrate in ultra-high vacuum. The STM was used to explore the topography of the sample surface while STS was used to determine the Local Density of States (LDOS) of the surfaces.

3. RESULTS AND DISCUSSION

Hardness test results for the aged alloys are compared to the homogeneous alloys as shown in Table 1. The significant hardness increase after aging is consistent with spinodal decomposition. Spinodal decomposition of the aged coupons will be confirmed via electron microscopy. As expected, minimal weight gain is observed for the alloy coupons oxidized under most conditions examined at 600 and 700°C, rendering uncertainty in the oxidation kinetics as determined by TGA. However, weight change measurements before and after oxidation are shown in Table 2. Two results are of note. First, the phase separated coupons oxidized at 700°C show greater weight change than the single phase alloys oxidized under identical conditions. Second, overall weight loss was observed in some wet oxygen environments consistent with expected volatility of Cr_2O_3 as $CrO_2(OH)_2(g)$. Characterization of the resulting oxide phase distribution and oxide thickness is in progress.

Table 1. Hardness Results

Vickers HV unit (HV0.5/15)	Homogeneous alloy	Aged alloy
Test 1	188	367
Test 2	187	369
Test 3	188	367

Table 2. Weight change results

	Specific weight change (mg/cm^2)	Wet O_2	Dry O_2	
600°C	Single phase	0.010	0.017	0.021
	Phase separated	0.011	0.011	0.034
700°C	Single phase	-0.047	0.086	0.065
	Phase separated	0.040	0.162	n/a

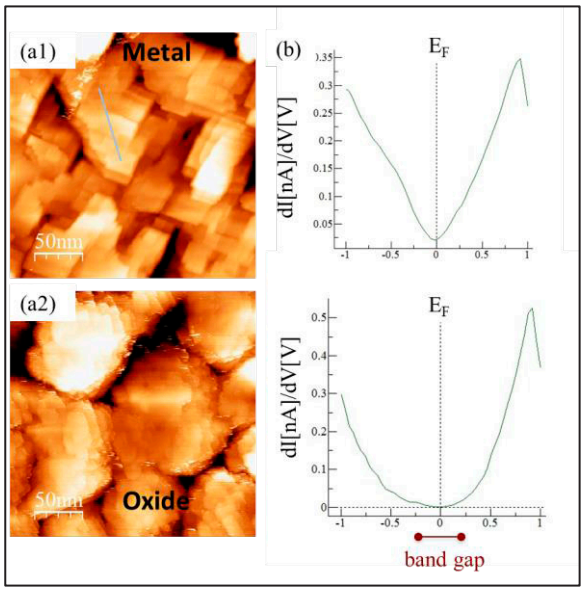

Initial stages of thin film oxidation were characterized by STM/STS demonstrating the usefulness of this technique. These results are shown in Figure 1. Changes in surface morphology as well as density of states are observed indicating formation of a semiconducting oxide with a measurable band gap. This technique will be used to distinguish between Fe-, Cr-, and mixed oxide phases forming on both thin film alloys and model Fe-Cr films patterned at different length scales.

Figure 1. (a1) STM images for the Fe-40at.% Cr alloy deposited on MgO(001) at 477°C to a thickness of about 20 nm; (a2) same surface after oxidation in $p(O_2)$ of 10^{-7} mbar at 300°C for 20mins; (b) Corresponding spectra (STS) for the metal (top) and oxidized surface (bottom).

4. CONCLUSIONS

Preliminary results indicate the small length scales of phase separation occurring during spinodal decomposition of Fe 40wt.%Cr may affect the oxidation behavior at temperatures of 700°C. Electron microscopy will be used to further characterize the phase separation, the resulting oxide phase distribution, and thereby confirm the weight change results. In addition, it has been shown that STM/STS characterization of alloy surfaces oxidized for short times provides useful information about the early stages of oxidation. Both techniques will be used to further characterize the effects of spinodal decomposition on oxidation behavior of FeCr alloys.

High-Temperature Oxidation Mechanism of Chemical Vapor Deposited Silicon Carbide

Takashi Goto, Hirokazu Katsui, and Miyuki Oguma
Institute for Materials Research, Tohoku University, 2-1-1, Katahira, Aoba-ku, Sendai 980-8577, Japan
e-mail: goto@imr.tohoku.ac.jp

1. INTRODUCTION

Silicon carbide (SiC) has high thermal conductivity, high oxidation resistance and low activation under neutron irradiation, and thus SiC provides applications to structural materials in severe operating conditions such as thermal protection tiles for space vehicles, diesel particulate filters (DPF), and fusion reactors [1]. At high temperature and high oxygen partial pressure, passive oxidation takes place forming protective oxide (SiO_2) layer. On the other hand, at low oxygen pressure, active oxidation occurs followed by gaseous SiO and CO formation. The oxidation behavior of SiC has been studied using sintered and pure single crystal and chemical vapor deposited (CVD) materials in a wide temperature range and in various atmospheres. Since the oxidation kinetics strongly depends on impurity and microstructure, pure and dense SiC bodies should be used to understand the intrinsic oxidation mechanism. The passive oxidation mechanism of Si-based ceramics, i.e., Si, Si_3N_4, and SiC, would be similar if the rate-controlling process is solely determined by inward diffusion of oxygen in the oxide (SiO_2) layer. However, the activation energies for the oxidation of SiC in the literature are lower than those of Si_3N_4 [2], and the oxidation rates of silicon-terminated faces are different from those of their opposite carbon-terminated faces of CVD and single crystalline SiC. It is generally recognized that the oxidation of Si-based ceramics is limited by oxygen inward diffusion, while a few studies have discussed CO outward diffusion -limited process to explain the oxidation of SiC at high temperatures [3]. No experimental studies so far have confirmed the occurrence of the CO outward diffusion-limited kinetics for the oxidation of SiC.

In the present study, we examined the interface between SiO_2 and CVD SiC after oxidation, and revealed the formation of carbon interlayer at the interface implying the CO outward limited process.

2. EXPERIMENTAL PROCEDURE

Translucent yellow-colored CVD SiC plates (13 mm 13 mm 0.5 mm, β-type, Admap, Japan) were used for the oxidation experiments. The mass change in the specimens during oxidation was continuously measured using an electrobalance (Chan R-101, USA) with a sensitivity of 1 μg. The oxidation temperature ranged from 1534 to 1902 K. The microstructure of the oxidized SiC was examined by transmission electron microscopy (TEM; JEM-2100, JEOL) and Raman spectroscopy (NRS-5100, JASCO) using 532 nm Nd-YAG laser excitation. The chemical composition after the oxidation was analyzed by an energy dispersive X-ray spectrometry (EDX; JED-2300T) equipped with TEM.

3. RESULTS AND DISCUSSION

Figure 1 shows the mass change of SiC oxidized at 1738 and 1873 K in O_2 plotted as a function of time in logarithmic scale. The mass of SiC increased with time. At the initial stage up to 2 and 0.2 ks at 1738 and 1873 K, respectively, the kinetics of mass change was linear, where the rate was controlled by chemical reaction. Thereafter, the gradient changed to half indicating parabolic kinetics. Fig. 2 represents the Arrhenius plot of the parabolic rate constants (kp) compared with those of single-crystal and CVD SiC in O_2 [4]. In this study, the activation energy of k_p was estimated to be 85 kJ mol^{-1}. The reported activation energies tended to increase at temperatures higher than 1600-1700 K. Costello and Tressler suggested that the rate-controlling process changed from the permeation of molecular oxygen through the SiO_2 scale to lattice diffusion of oxygen, resulting in the increase in activation energy [5].

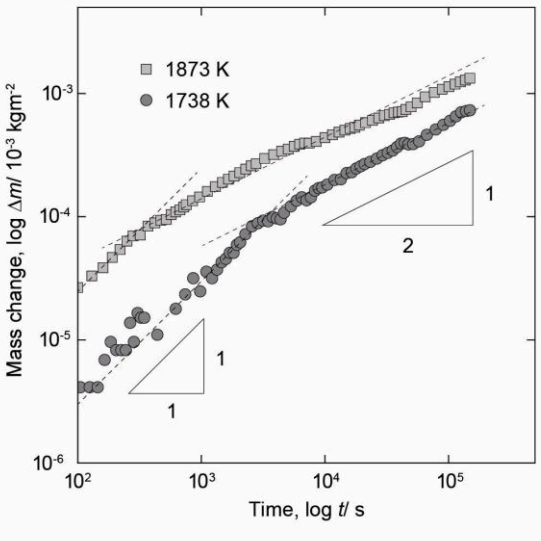

Fig. 1 Mass evolutions of CVD SiC oxidized at 1738 and 1873 K in O_2 atmosphere (P_{O2} = 0.1 MPa)

Ogbuji and Opila reported only an activation energy of 118 kJ mol^{-1} for CVD SiC in the temperature range of 1473-1773 K [2]. Since the activation energy of the CVD SiC coincided with that for pure Si by Deal and Grove (119 kJ mol^{-1}) [6], they concluded that the oxidation rate of SiC was limited by permeation of oxygen through the SiO_2 scale. The activation energy in the present study was independent of temperature up to 1902 K and rather lower compared with the values previously reported (Fig. 2).

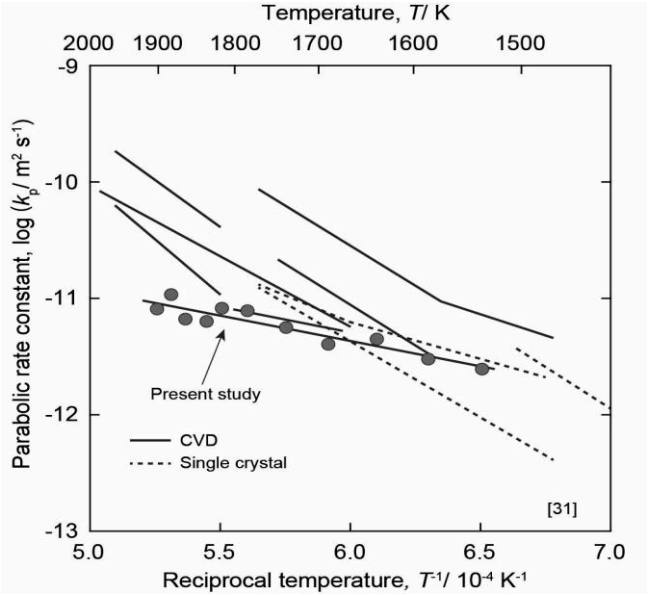

Fig. 2 Comparison of parabolic rate constants (k_p) of CVD and single crystal SiC in O_2 atmosphere

Raman spectra of the SiC oxidized at 1690 and 1873 K are shown in Fig. 3. The Raman spectrum of the SiC oxidized at 1690 K showed peaks at around 1530 and 1720 cm^{-1}, which could be attributed to the second order Raman phonon mode of SiC (Fig. 3(a)). The un-oxidized SiC also had these two peaks. In the case of SiC oxidized at 1873 K (Fig. 3(b)), the two additional Raman peaks related to carbon were observed in the spectrum; D-band at 1350 cm^{-1} and G-band at 1600 cm^{-1}. The peak position of the G-band was reported at 1500-1600 cm^{-1} and I(D)/I(G) was zero in a highly crystalline graphite, while amorphous carbon showed an increase in I(D)/I(G) and a broadening of the G and D peak shapes. The Raman spectrum of the SiC oxidized at 1873 K showed broadening of the D and G peaks, with I(D)/I(G) of 0.6. This indicated that the SiC oxidized forming amorphous-like carbon even at a high O_2 atmosphere (0.1MPa). The color of the SiC changed from translucent yellow to partially black after oxidation. These carbon-related Raman peaks could also be observed in the SiC oxidized above 1784 K, whereas no carbon-related Raman peaks were identified below 1650K.

Figure 4 depicts the TEM bright field image of the SiC oxidized at 1873 K for 154.8 ks at the interface between SiC and SiO_2 layer. An interlayer of 40 nm in thickness with a bright contrast was observed between the SiC (dark) and SiO_2 layer (gray). Fig. 5 shows the high-resolution TEM image of the interlayer in the SiC oxidized at 1873 K for 77.4 ks. A layer-by-layer structure was partially identified in the carbon layer. The distance between the layers estimated by the TEM image was almost the same as that of the c-plane spacing of 0.335 nm in graphite although the spacing changed depending on the degree of disorder.

Figure 6 depicts the stability diagram of the Si-C-O system at 1873 K as functions of carbon activity (a_C) and oxygen partial pressure (P_{O2}). The intersectional points, A and B, are coexistence points of the three phases, SiC-SiO_2-C and SiC-SiO_2-Si, respectively. The line AB is the coexistence region for the two phases of SiC and SiO_2. The slanted dashed lines in Fig. 6 depict CO pressures. The TEM and Raman results revealed the formation of a carbon layer between SiC and SiO_2 at 1873 K. This is consistent with that a carbon phase (C(s)) can exist with SiC(s) and SiO_2(s) at $a_C = 1$ in Fig. 6, where $P_{CO} = 2.3 \times 10^5$ Pa and $P_{O2} = 2.3 \times 10^{-10}$ Pa (point A). The formation of carbon suggests that carbon activity (a_C)

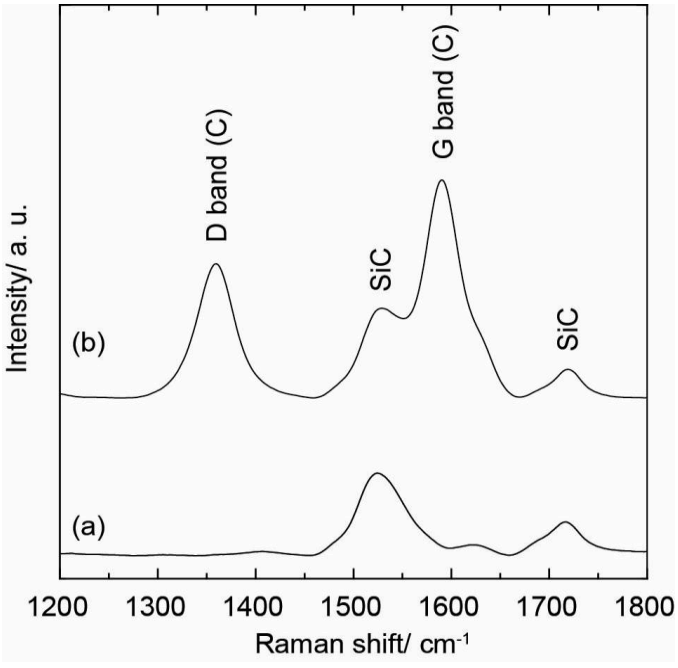

Fig. 3 Raman spectra of CVD SiC oxidized at 1690 (a) and 1873 K (b)

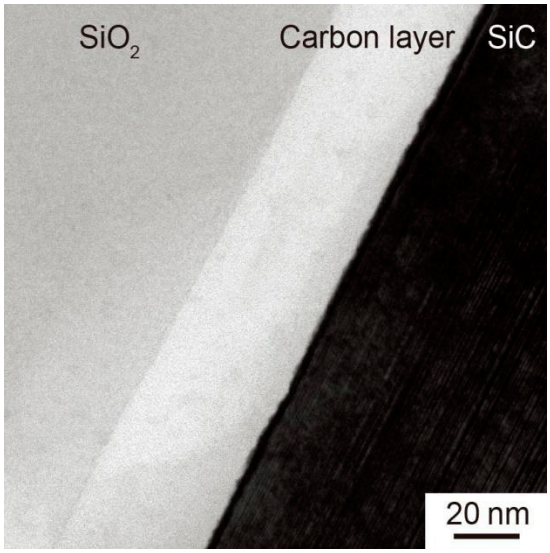

Fig. 4 TEM image of the interface between SiC and a SiO_2 layer at 1873 K for 154.8 ks

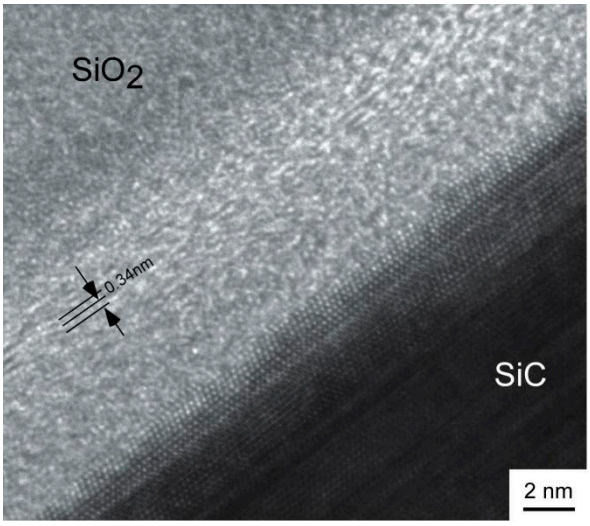

Fig. 5 TEM image of the interface between SiC and a SiO_2 layer at 1873K for 77.4 ks

is unity at the SiC/SiO_2 interface and the outward diffusion of CO could be the rate-limiting process of the oxidation of SiC. The carbon layer formed at the interface at temperatures higher than 1784 K, whereas no carbon formation was identified at lower temperatures by Raman spectroscopy and TEM. The rate-limiting process of the passive oxidation of SiC could be inward oxygen diffusion at the temperature below 1784 K, and could change to the CO outward diffusion in the higher temperature range. However, no significant change in the activation energy of k_p was identified in Fig. 2.

Bubbles may form at the SiC/SiO_2 interface if SiO and/or CO gases accumulate at the interface and the pressure inside the bubble exceeds an atmospheric pressure. Fig. 7 shows the TEM observation of the cross section of SiC oxidized at 1873 K for 154.8 ks. The bubbles of about 100 nm in diameter were identified at the SiC/ SiO_2 interface. We have studied the oxidation behavior of CVD SiC in O_2 and CO_2 atmospheres at various O_2 pressures (10^2-10^5 Pa) and reported that the transition temperature from parabolic oxidation to bubble formation was higher than 1940 K [7]. The mass change vs. time curves showed characteristic zigzag-shapes due to the sequence of bubble-formation and rupture. In the present study, the mass gain shown in Fig. 1 did not exhibit the zigzag-shaped behavior, because the size of the bubbles was small and did not rupture. Bubble formation was identified even at 1873 K, which is lower than the oxidation temperature of 1940 K reported in our previous study [7]. Given the three typical situations, i.e., carbon-saturated A (a_C=1), silicon-saturated B (a_{Si} = 1), and a stoichiometric condition (SiO_2 (s) + SiC(s) = 3SiO(g) + CO(g)), the total vapor pressure of SiO and CO gases is depicted as a function of temperature in Fig. 8 [7, 8]. Mieskowski et al. observed bubbles in α- and β-SiC sintered bodies oxidized at 1473-1673 K in air. However, no bubbles were detected in α-SiC single crystals [9]. Excess carbon and sintering additives, such as Al_2O_3 and MgO, in the SiC body would yield bubbles because of the formation of CO gas and low-melting point of the silicate scale. Schiroky et al. reported the bubble formation in CVD SiC at 1973-2073 K in air [10]. The total pressure of the CO and SiO gases would not exceed 10^5 Pa at 2000 K under silicon-saturated (a_{Si}=1) and the stoichiometric conditions. On the other hand, the total pressure at the

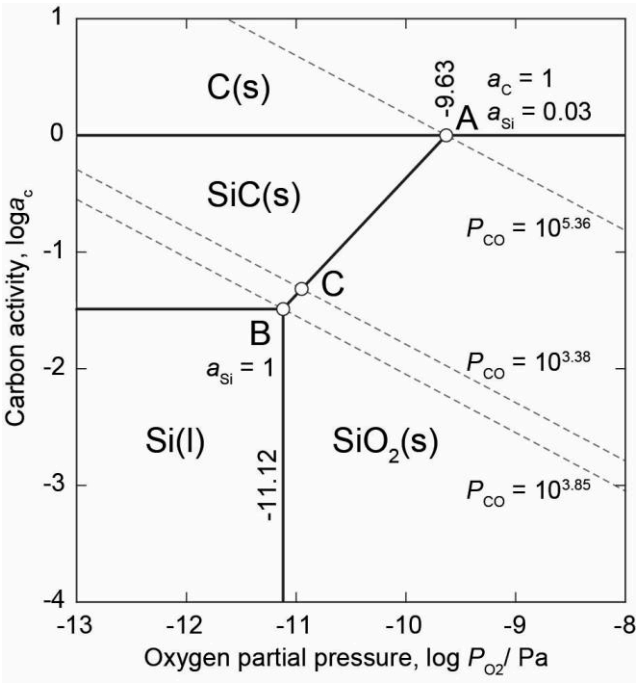

Fig. 6 Stability diagram of the Si-C-O system at 1873 K

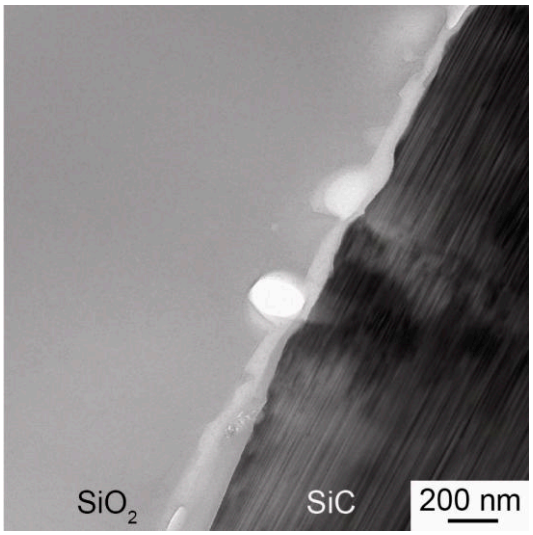

Fig. 7 TEM image of the bubbles at the SiO_2 /SiC interface at 1873 K for 154.8 ks

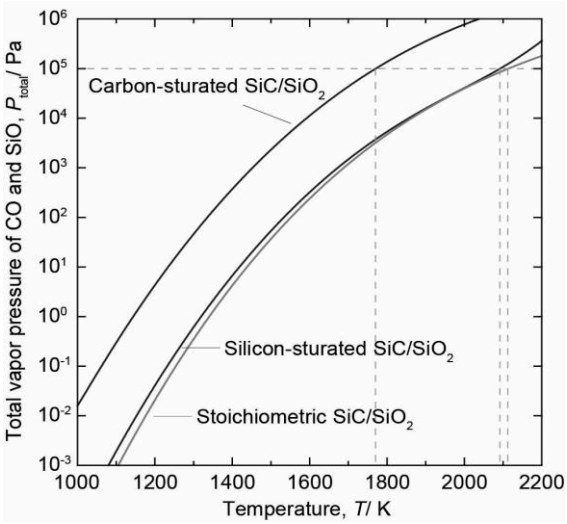

Fig. 8 The total pressures of SiO and CO at interface between SiC and SiO_2

SiC/SiO_2 interface at 1873 K under the carbon-saturated conditions suggests thatCO gas would accumulate at the SiC/SiO_2 interface and caused an increase in carbon activity to unity forming bubbles. These suggest that the passive oxidation rate of CVD-SiC would be limited by the outward diffusion of CO gas in the SiO_2 layer at high temperatures whereas the inward oxygen diffusion could be rate-limiting process at lower temperatures.

4. CONCLUSIONS

The passive oxidation kinetics of CVD SiC in the temperature range 1534-1902 K was examined by thermogravimetry, TEM, and Raman spectroscopy. Raman peaks corresponding to D- and G-bands of carbon were observed in the SiC oxidized above 1784 K. TEM observations revealed the formation of a carbon layer between SiC and the SiO_2 scale. Bubbles were formed at the SiC/SO_2 interface at 1873 K. These suggest that the oxidation rate of CVD SiC at high temperatures over 1784 K is limited by CO outward diffusion in the SiO_2 layer.

References

[1] Jacobson N. S., "Corrosion of silicon-based ceramics in combustion environments," *J. Am. Ceram. Soc.,* Vol. 76, No. 1 (1993), pp.3-28.

[2] Ogbuji L. U. J. T. and Opila E. J., "A comparison of the oxidation kinetics of SiC and Si_3N_4," *J. Electrochem. Soc.,* Vol. 142, No.3, (1995), pp. 925-30.

[3] Luthra K. L., "Some new perspectives on oxidation of silicon carbide and silicon nitride," *J. Am. Ceram. Soc.,* Vol. 74, No.5, (1991), pp.1095-103.

[4] Katsui H, Oguma M and Goto T, "Carbon interlayer between CVD SiC and SiO_2 in high-temperature passive oxidation," *J. Am. Ceram. Soc.,* in press.

[5] Costello J. A and Tressler R. E., "Oxidation kinetics of silicon carbide crystals and ceramics: I, in dry oxygen," *J. Am. Ceram. Soc.*, Vol.69, No.9, (1986), pp. 674-81.

[6] Deal D. E. and Grove A. S., "General relationship for the thermal oxidation of silicon," *J. Appl. Phys.,* Vol. 36, No. 12, (1965), pp. 3770-3778.

[7] Goto T. and Homma H., "High-temperature active/passive oxidation and bubble formation of CVD SiC in O_2 and CO_2 atmospheres," *J. Eur. Ceram. Soc*., Vol. 22, No. 14-15, (2002), pp. 2749–56.

[8] Jacobson N. S., Lee K. N. and Fox D. S., "Reactions of silicon carbide and silicon (IV) oxide at elevated temperatures," *J. Am. Ceram. Soc*., Vol. 75, No. 6, (1992), pp. 1603-11.

[9] Mieskowski D. M., Mitchell T. E. and Heuer A. H., "Bubble formation in oxide scales on SiC," *J. Am. Ceram. Soc.*, Vol. 67, No.1, C-1(1984), pp.7-8.

[10] Schiroky G. H., Price R. J. and Sheehan J. E., "Oxidation characteristics of CVD silicon carbide and silicon nitride," *GA Technologies Inc,* Vol. 2, No.2, (1987), pp.137-41.

Roles of high temperature oxidation in fiber reinforced self-healing ceramics

*Wataru Nakao[(1)]

[(1)] Faculty of Engineering, Yokohama National University,
79-5, Tokiwadai, Hodogaya, Yokohama, Kanagawa, 240-8501, JAPAN

e-mail: wnakao@ynu.ac.jp

1. INTRODUCTION

Self-healing ceramic is anticipated as one candidate of the next generation refractory materials for turbine blades. R&Ds of the Ni based superalloys [1] have been contributing the enhancement of fuel efficiency of the gas turbine generator and jet engine for air craft. Because the temperature at the metal surface will reach its melting point, further large improvement due to development of Ni based superalloys is no longer anticipated, even if the thermal barrier coating and air cooling system are applied. Thus, new technologies or advanced materials are required to break through this situation.

Due to its high refractoriness and chemical stability, the attempts to develop ceramic gas turbine blade [2] was made. However, all the projects have been failed because the ceramic turbine blade could not overcome the fracture induced by the foreign objective damage (FOD). It is difficult to prevent the occurrence of the FOD for the turbine blade, and FOD often leads to the critical fracture. Self-healing ceramic is one of the ceramic materials having high FOD resistance, because it is autonomically enable to recovery the strength decreased by FOD during service. Therefore, self-healing ceramics has enough high refractoriness and mechanical reliability to apply to the turbine blade of the next generation power plant and jet engine.

The two following attempts are needed to apply the self-healing ceramics to turbine blades. One is to discover the advanced healing argents for structural ceramics. The original self-healing ceramic has firstly reported by Chu et al. [3] and the self-healing function was induced by the high temperature oxidation of the dispersed SiC particles. However, it is noted that the ceramics requires more than 10 h to heal completely the surface cracks below 1200 ^{o}C so that the self-healing of the original self-healing ceramics is not available below 1200 ^{o}C. Moreover, the present authors [4] succeeded that the lower bound of the available temperature region is decreased by the nanometer-sizing of the dispersed SiC particles. However, further decreasing of the lower bound is necessary. The other is to combine the self-healing with the continuous fiber reinforcement. As the self-healing ceramics that are developed up to now has too low fracture toughness, the final fracture is possible to occur by one FOD. Thus, it is important that the crack propagation is arrested before the final fracture by the continuous fiber reinforcement. Subsequently the arrested cracks are completely recovered by the self-healing.

The present study aims to develop an advanced fiber reinforced self-healing ceramics (shFRC) and discuss the role of the high temperature oxidation for the shFRC. In the paper, the materials construction will be introduced and the role of the high temperature oxidation on the enhancement to self-healing ability will be discussed. After that, the fracture manner and the self-healing behavior of the prototype shFRC will be shown.

2. MATERIALS DESIGN AND FUDAMENTAL FEATURES

In the present study, endowment of the functions combing the self-healing and continuous fiber reinforcement was attempted by the arrangement of the healing agents at the interface between fiber and matrix, as shown in Fig. 1. In the continuous fiber reinforced ceramics (FRC) design, the interlayer between fiber and matrix was often used to obtain the large fiber pull-out effect. The fiber pull-out in FRC is caused by the slip of the interface between fiber and matrix during crack propagation. If interlayer or the interfaces between interlayer and fiber or matrix fractured easily, the fiber pull-out is enhanced. However, the delimitations of the interfaces and the interlayer damage act as the critical defect at the next crack propagations. If the healing agent is used to the interlayer, the delimitation and the interlayer damage was healed by the high temperature oxidation of the healing agent after crack propagation, because the crack propagation allows the healing agent react with the oxygen in the surrounded atmosphere. Consequently, the FRC containing the interlayer of the healing agent can survive the repeated crack propagation or initiation due to the FOD.

The minimum thickness of the interlayer was evaluated as shown in Fig. 2(a). The minimum thickness was determined in order that the volume of the oxide formed by the oxidation of the healing agent is filled with the free space between crack

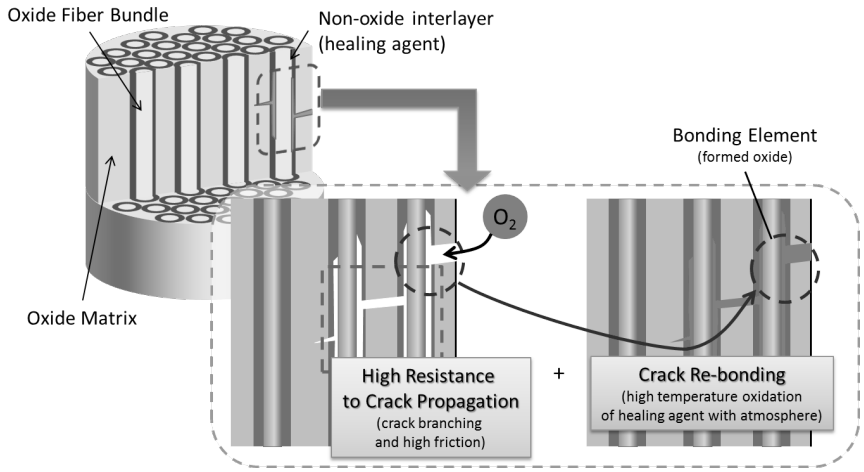

Figure 1 Schematic of self-healing function and fiber reinforcement in shFRC.

walls. A simply model of the fiber and crack geometry was constructed as shown in Fig. 2(b). In this model, it is assumed that the crack geometry is a rectangular groove, width X, length Y, depth Z, and the fibers whose diameter is D_f, align along X direction with the space of l. The volume of the interlayer, which has the thickness of d_i, in the groove was evaluated as follows;

$$X\{(D_f/2+d_i)^2 - (D_f/2)^2\}\cdot Y/l\cdot Z/l \quad (1)$$

If SiC particles are used to the healing agent, the volume expansion of its oxidation is ~80 vol%. Thus, 1.8 times value of the interlayer volume is more than the free space between cracks, $XYZ(1-V_f)$, where V_f is the volume fraction of the fibers and corresponds to $\pi D_f^2/4l^2$. Consequently, the minimum thickness of the interlayer can be expressed as,

$$d_i = 0.5D_f[\{(1+0.8V_f)/1.8V_f\}l/2 - l] \quad (2).$$

Unfortunately the evaluated value is only guideline of the interlayer thickness, because the actual crack width significantly decreases beyond the fiber pull-out. Therefore, the required interlayer thickness must be less than the evaluated value.

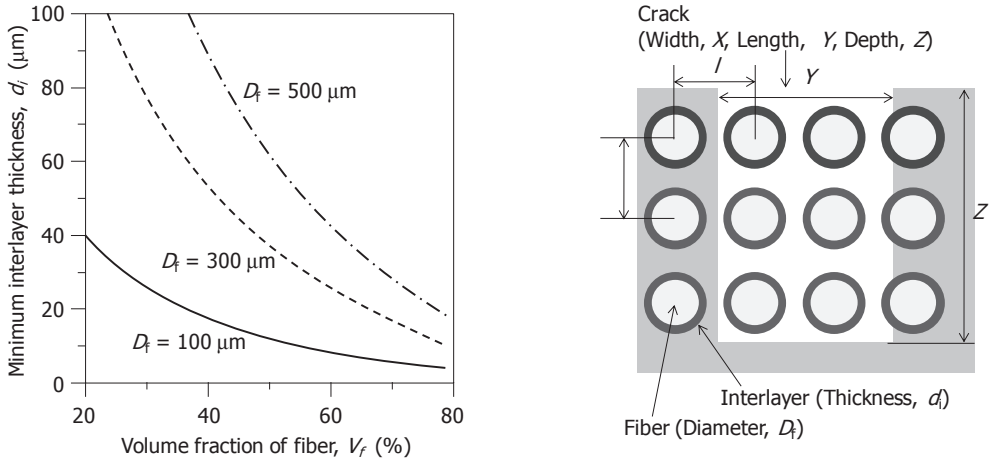

Figure 2 (a) Evaluated minimum interlayer thicknesses as a function of the volume fraction of fiber and (b) Simple model for the evaluation of (a)

Moreover, the optimal self-healing agent should be selected to be suitable for its application. For example, if the advanced shFRC is used to the the turbine blades of jet engine, the self-healing must be occur at the temperature regions 1000 -1200 ^{o}C and 600 – 1000 ^{o}C, for middle pressure turbine and low pressure turbine, respectively. Figure 3 shows the oxidation behavior of the candidates of the self-healing agents. The horizontal dash lines indicate the requisite oxidation rate for 1 h and 10 h healing. Thus, the intersection of these line and data implies the lowest temperature to occur the self-healing due to the arbitrary self-healing agents. From this figure, $TiSi_2$ was found to be a candidate of the self-healing agents for the shFRC used as the low pressure turbine blade.

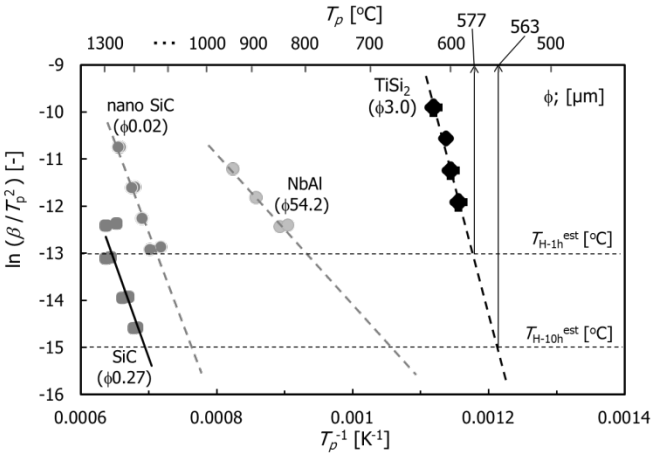

Figure 3 Oxidation behaviors of the candidates for the advanced self-healing agents

3. EXPERIMENTAL

For prototype shFRC, alumina fiber/ alumina composite with SiC interlayer was prepared in this study. The used alumina fiber (Nitivy Co. Ltd., S-640D) is 3000 filaments bundle with diameter of 0.3 mm. Fine alumina (Sumitomo Chemical Co. Ltd., AKP-50, ϕ0.23 μm) and SiC (Ibiden Co. Ltd., Ultrafine, ϕ0.35 μm) powders were used as matrix and interlayer, which plays role in healing agent.

The whole of the coating and figuration were subjected by using the fiber winding apparatus. Prior to the interlayer coating, the alumina fine particles were filled with the voids of alumina fiber bundle by letting the fiber bundle pass through alumina slurry. By using similar slurry coating, the SiC interlayer was formed on the alumina fiber bundle. After letting the SiC coated fiber bundle pass through alumina slurry, the fiber bundle was figurated by winding on 50 mm x 50 mm x 6 mm stainless plate. The figurated fiber bundle lamination was sintered at 1300 °C for 1h in Ar.

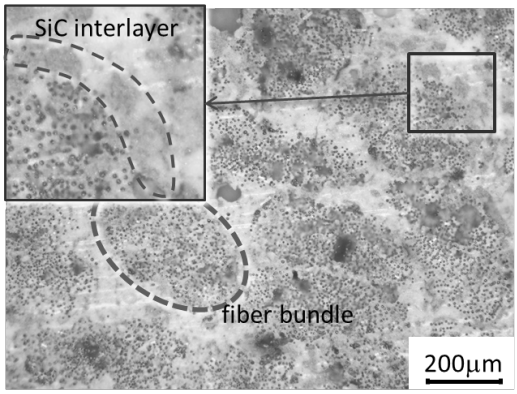

Figure 4 Microstructure of shFRC

Figure 4 shows cross-sectional microscopy of the prepared shFRC. It is found that the shFRC had the SiC interlayer thickness of ~60 μm and the means fiber distance of 60 μm. Thus, the fiber content was evaluated to be 58 %. Furthermore, the relative density of the shFRC was found to have 78 % from the Archimedes measurement.

Mechanical properties and self-healing ability of shFRC were investigated form three-point bending using 3 mm x 4 mm x 50 mm rectangular specimen with a V-shaped notch whose depth is 1 mm. Stress-strain curves were obtained from the three point bending with cross-head speed of 0.5 mm/min.

4. RESULT AND DISCUSSION

Figure 5 shows stress-strain curves of ”virgin” V-notched shFRC and the V-notched shFRC healed at 1000 °C for several time in the air after pre-loading. Black solid line indicates the stress-strain curve of “virgin” shFRC. The bending stress increases linearly as the bending strain increases below the strain which the stress shows a maximum. Above that, the stress drops but the shFRC did not fracture. This behavior implies that the crack introduced and propagated from the tip of the V-shaped notch and then branching along the interlayer when the crack reached to fiber bundle. Therefore, the whole self-healed shFRCs had the branching crack before self-healing. Although the shFRC healed for 1 h had lower maximum stress and gradient of primary part of stress-strain curve than those of “virgin” shFRC, the shFRCs healed above 5 h had same or more than maximum stress, and the gradient for the shFRC healed for 50 h reached the same value of “virgin” specimen. In other words, the self-healing of the shFRC can recover the degraded strength and stuffiness for 5 h and 50 h, respectively. From the observation of the fracture surface, the fracture initiation change from the pre-introduced branching crack, the self-healing was found to enable to re-bond the crack surface completely. Moreover, all stress-stain curves revealed that the shFRC had large deformation ability after self-healing.

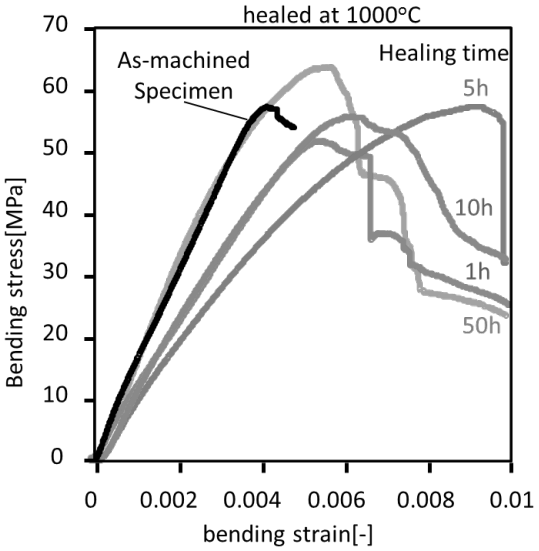

Figure 5 Stress-strain curves of the shFRC applied by three-point bending with span of 30 mm

Similar self-healing behavior was investigated for 1200 °C healing. In 1200 °C healing, the complete strength and stuffiness recoveries can be attained within only 1 h.

From the obtained self-healing behaviors, it was found that the shFRC has superior self-healing ability to the ordinary SiC particles dispersed self-healing ceramic. From the previous research [5], SiC dispersed alumina composite was reported to enable to heal semi-elliptical surface crack having surface length of 100 μm for 100 h @ 1000 °C and for 10h @1200 °C. Therefore, it is confirmed that the shFRC can effectually heal the crack, because the shFRC entices cracks into propagating to the interlayer constituting of the healing agent.

5. CONCLUSION

Advanced fiber reinforced ceramic composite (FRC) having self-healing function has been developed to be suitable for the turbine blades of jet engine. The composite includes the silicon carbide interlayer as healing agent at the interface between alumina fiber and alumina matrix. The healing agent interlayer caused the preferential fracture of the fiber/matrix interface and the interface fracture gave rise to the slip of the interface during crack propagation. Thereby the FRC could exhibit a large deformation at the fracture and large fracture energy. Moreover, the high temperature oxidation of the healing agent at 1000 °C made the interface delimitation rebounded by the formed oxide and the reaction heat for 50 h.

Acknowledgements

This work has been funded through Advanced Low Carbon Technology and Development organized by Japan Science and Technology Agency (JST-ALCA).

References

[1] Suzuki, T., Yokokawa, T., Kobayashi, T., Koizumi, Y., Harada, H., and Imai, H, *J. Jpn. Inst. Metals*, Vol. 72, (2008), pp.8-11.
[2] Makino, K., Mizuno, K., and Shimamori, T., *ASME Paper*, Vol. 97 (1997), GT-67.
[3] Chu, M.C., Sato, S., Kobayashi, Y., and Ando, K., *Fatigue Fract. Engng. Mater. Struct.*, Vol. 18, (1995), pp.1019-1029.
[4] Nakao, W., Tsutagawa, Y., and Ando, K., *J. Intelligent Mater. Sys. Struct.*, Vol. 19, (2008), pp.407-410.
[5] Ando, K., Kim, B.S., Kodama, S., Takahashi, K., and Saito, S., *Materials and processing conference*, Vol. 115, (2003), pp. 75-76.

Raman study on the reaction behavior of AlN powder in wet air between 1000-1500℃

Xinmei Hou [(1*)], Yanxiang Liu [(1)], Enhui Wang [(1)], Jianliang Zhang[(1)] and Kuo-Chih Chou [(1)]

School of Metallurgical and Ecological Engineering, University of Science and Technology Beijing, Beijing 100083, China
e-mail: houxinmei@ustb.edu.cn

1. INTRODUCTION

Because of the high thermal conductivity (3.2 W/cm K), low coefficient of thermal expansion ($4.03–6.0\times10^{-6}$/K) and high electrical resistivity (>4×10^{8}Ωcm), AlN is an attractive material used as electronic substrates or packaging, high temperature structural and refractory material [1-3]. For instance, AlN ceramics is widely applied at the belly of the blast furnace. However, AlN is sensitive to air and water resulting in the degradation of property such as the thermal conductivity [4]. Therefore investigation of the reaction behavior of AlN with O_2 or H_2O is of great interest for both fundamental science and practical application. However up to now, the work on the experiments of AlN exposed to wet air at high temperature is not enough [5-13]. In addition, the reports on this aspect are very limited. To identify the specific fields and working temperature range of the application, it is important to understand the reaction behavior and the related mechanism of AlN recession in water vapor at high temperature.

In this work, the reaction behavior of AlN powder at 1000 to 1500℃ under the condition of high-temperature water vapor was investigated. The effects of temperature and water content on both macrostructure and microstructure of AlN powder were investigated. Based on these, the reaction mechanism and kinetics were discussed.

2. EXPERIMENTAL,

In this experiment, the raw material was commercial grade AlN powder (≥99.99 mass%, Advanced Technology & Materials Co., Ltd, Beijing, China). The particle size distribution of AlN powder was determined by laser interferometer (SEISHIN LMS-30) and the average particle size was 4.733μm. The non-isothermal and isothermal reaction experiments were carried out in a vertical alumina tube furnace. The water vapor was generated by a water vapor generating device composing of a peristaltic pump and heating system. The evolution of crystalline phases before and after the reaction was accomplished through XRD, micro-Raman spectroscopy and SEM.

3. RESULTS AND DISCUSSION,

The reaction behavior depended on temperature and the water content. At lower temperature range, i.e. 1000-1150℃, oxidation reaction predominately occurred and it was diffusion controlled (Fig.1). Compared with the reaction of AlN powder in dry air, the mass change of AlN in wet air was much lower. Raman peak shift indicated water led to the formation of dense oxide layer and delayed the oxidation in wet air.

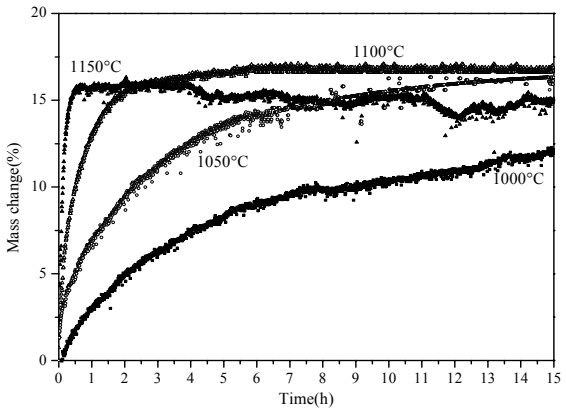

Fig.1 TG curves of AlN powder at 1000-1150℃

With temperature increasing, it can be seen that at initial stage the reaction rate increased so quickly that the mass change curves at this stage were overlapped with each other. With time prolonging, weight began to decrease and the decreasing rate increased with increasing temperature as shown in Fig.2, indicating the reaction caused by Al_2O_3 and H_2O occurred at high temperature. Raman analysis confirmed the formation of $Al(OH)_3$ caused by Al_2O_3 with H_2O (Fig.3).

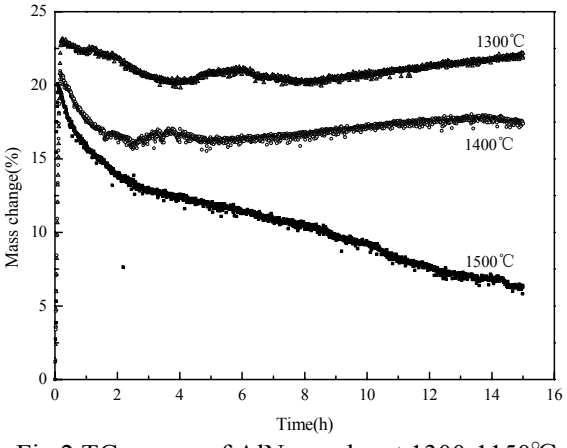

Fig.2 TG curves of AlN powder at 1300-1150℃

Based on the experimental result, the reaction kinetics was investigated with Chou's model. In view of the reaction behavior at 1000-1150℃, the reaction was mainly diffusion controlled and the reaction can be described as follows:

$$\frac{\Delta m}{\Delta m_{max}} = 16.7\left(1-\left(1-\sqrt{\frac{exp\left(-\frac{435500}{8.314\,T}\right)t}{1.85\times10^{-16}}}\right)^{3}\right)$$

From the above equation, a good agreement was obtained between the predicted curves and the experimental data with the activation energy to be 435.5kJ/mol (Fig.4).

With temperature increasing, the oxidation took place easier due to the phase transformation of oxide. It can be described by Chou's model with the activatin energy to be 195 kJ/mol. With time increasing the reaction behavior was mixed controlled by oxidation and volatile reaction because of the phase transformation.

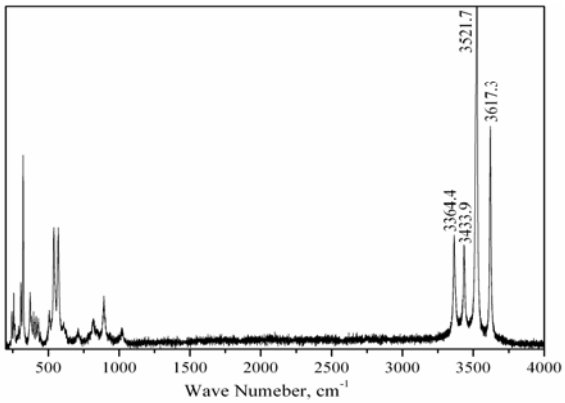

Fig.3 Raman peak shift of the volatile product

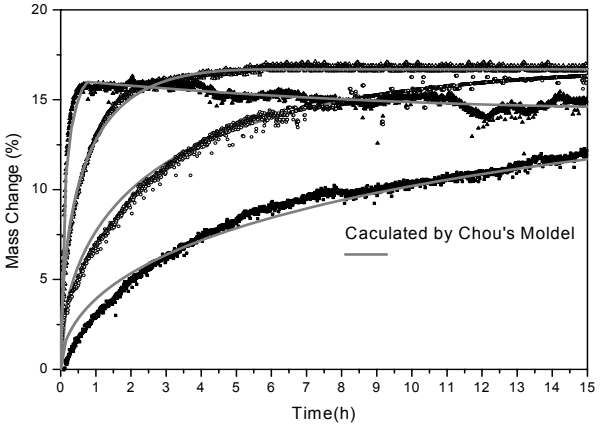

Fig.4 The comparison of Chou's model with the experimental data of AlN powder in wet air at 1000-1150℃

4. CONCLUSION,

AlN powder with average particle size of 4.733μm was exposed to wet air between 1000 to 1500℃ for 15h. The reaction behavior of AlN powder in wet air depended on temperature and the water content. At 1000 to 1150℃, oixdaiton reaction mainly took place and the reaction rate was delayed in wet air because of the formation of dense oxide layer. At higher temperature, the volatile reaction caused by Al_2O_3 and H_2O occurred simultaneously and the rate increased with temperature. Based on the experimental data, Chou's model was adopted to treat the reaction behavior.

Acknowledgements,

The authors express their appreciation to National Nature Science Foundation of China of no. 51104012, the Fundamental Research Funds for the Central Universities of no. FRF-TP-12-024A and Program for Changjiang Scholars and Innovative Research Team in University (IRT1207) for financial support.

References

[1] B. Luo, J.W. Johnson, O. Kryliouk, F. Ren, S.J. Pearton, S.N.G. Chu, A.E. Nikolaev, Y.V. Melnik, V.A. Dmitriev and T.J. Anderson, "High breakdown M–I–M structures on bulk AlN," *Solid-State Electron.*, Vol.46, (2002), pp.573-576.

[2] J.H. Edgar, L. Du, L. Nyakiti and J. Chaudhuri, "Native oxide and hydroxides and their implications for bulk AlN crystal growth," *J. Cryst. Growth*, Vol.310, (2008), pp.4002-4006.

[3] G.H. Zhang, X.M. Hou and K.C. Chou, "Kinetics and initial stages of oxidation of aluminum nitride: thermogravimetric analysis and X-ray photoelectron spectroscopy study," *J. Eur. Ceram. Soc.*, Vol.30, (2010), pp.629-633.

[4] K. Watari, K. Ishizaki and F. Tsuchiya, "Oxidation Kinetics of aluminum nitride," *J. Mater. Sci.*, Vol. 28, (1993), pp. 3709-3714.

[5] A. L. Brown and M.G. Norton, "Oxidation behavior of aluminum nitride," *J. Mater. Sci. Lett.*, Vol.17, (1998), pp.1519-1522.

[6] X.M. Hou, K.C. Chou, X.C. Zhong and S. Seetharaman, "Oxidation kinetics of aluminum nitride at different oxidizing atmosphere," *J. Alloy. Compd.*, Vol. 465, (2008), pp.90-96.

[7] P. Li, L.D. Teng, M. Guo, M. Zhang and S. Seetharaman, "Effect of the fluoride additives on the oxidation of AlN," *Metall. Mater. Trans. B*, Vol.43, (2012), pp. 406-412.

[8] A. Bellosi, E. Landi and A. Tampieri, “SIMS study on the initial oxidation process of AlN ceramic substrate in the air,”*J. Mater. Res.*, Vol.8, (1993), pp. 565-572.
[9] E.W. Osborne and M.G. Norton, “X-ray photoelectron spectroscopy characterization of aluminum nitride surface oxides: thermal and hydrothermal evolution,” *J. Mater. Sci.*, Vol.33, (1998), pp.3859-3865.
[10] H.P. Zhou, L. Qiao and R.L. Fu, “Mechanism and kinetics of aluminum nitride powder degradation in moist air,” *Mater. Res. Bull.*, Vol.37, (2002), pp. 2427-2435.
[11] C.Y. Lin and F.H. Lu, “Aluminum Nitride, a Refractory for Aluminum to 2000°C,” *J. Eur. Ceram. Soc.*, Vol.28, (2008), pp.691-698.
[12] X.M. Hou and K.C. Chou, “High temperature oxidation of hot-pressed aluminum nitride by water vapor,” *Corros. Sci.*, Vol. 51, (2009), pp.556-561.
[13] V.A. Lavrenko, A.D. Panasyuk and I.P. Neshpor, “Transformation of yttria-doped tetragonal ZrO_2 polycrystals by annealing under controlled humidity conditions,” *Powder Metall. Met.* C+., Vol. 49, (2010), pp.238-244.

O11

Oxidation Behavior in Crack-healing of Metal/Al_2O_3 Nanocomposites

Makoto Nanko[(1,*)], and Daisuke Maruoka [(2,3)]

[(1)] Department of Mechanical Engineering, Nagaoka University of Technology, 1603-1, Kamitomioka, Nagaoka, Niigata, 940-2188, JAPAN

[(2)] Graduate School of Engineering, Nagaoka University of Technology, 1603-1, Kamitomioka, Nagaoka, Niigata, 940-2188, JAPAN

[(3)] Current Address: epartment Material Science and Chemical Engineering, Yokohama National University, Yokohama, Kanagawa 240-8501, Japan

e-mail: nanko@mech.nagaokaut.ac.jp

1. INTRODUCTION

Al_2O_3 Ceramics has been known as one of the most popular structural ceramics because of excellent mechanical properties and chemical stability. This oxide ceramics has been used for chemical barrier coating on heat-resistant alloys and high-temperature filters. However, brittleness of the ceramics is still a significant disadvantage. Nanocomposites consisting of ceramics matrix dispersed with nano-particles is one of the useful approaches to improve their brittleness. Introduction of self-healing function to ceramics is one of the promising idea for overcoming the brittleness. In some ceramics with non-oxide dispersoids, crack-healing function via high-temperature oxidation has been discovered [1]. Filling-up in cracks with oxidation product can reduce the stress concentration at crack tips, resulting mechanical recovery of fracture strength up to as-polished samples.

Our research group has discovered crack healing of Ni/Al_2O_3 nanocomposites [2, 3]. In the present composite system, Ni dispersoids are oxidized with Al_2O_3 matrix into $NiAl_2O_4$, which is filled up in surface cracks. The formation of $NiAl_2O_4$ is caused with outward diffusion of Ni ions along Al_2O_3 grain boundaries. On the other hand, Ni dispersoids are oxidized with O diffusing from the sample surface to the inside [4].

In this study, diffusion in high-temperature oxidation of Ni/Al_2O_3 nanocomposites is discussed. In particular, diffusion behavior for crack-healing process was studied.

2. EXPERIMENTS

A commercial α-Al_2O_3 powder (Sumitomo Chemicals, AA-04, 0.4 μm) was used for a starting material. A slurry consisting of the Al_2O_3 powder and nickel nitrate with distilled water was prepared as being 5 vol% in Ni volume concentration. The shurry was dried by dropping into a hot glass container at 400°C in air. Powder mixture consisting of nano-Ni and Al_2O_3 was prepared after reduction at 600°C for 12 h in a stream of Ar-1%H_2 gas mixture. The powder mixture was consolidated with pulsed electric current sintering technique at 1400°C for 5 min under 40 MPa in vacuum. The samples with at least over 99% in relative density were used in the present study. Sample surface is polished with diamond slurry.

The sample was annealed in air at 1300°C for 1 h in air. The cross-sectional views were observed with scanning electron microscopy (SEM).

3. RESULTS AND DISCUSSION

Fig.1 shows cross-sectional views of Ni/Al_2O_3 nanocomposites oxidized at 1300°C for 1 d in air. In the region with 95 μm in depth, nano-Ni nickel dispersoids disappear and $NiAl_2O_4$ grains are formed. Nano-Ni dispersoids were oxidized with Al_2O_3 matrix into $NiAl_2O_4$. In Ni-Al-O ternary phase diagram, $NiAl_2O_4$ can co-exists with Al_2O_3 but NiO cannot. As shown in Fig. 1 (b), a continuous $NiAl_2O_4$ top layer is formed on the top surface and 3 μm in thickness. The ratio of thickness of surface $NiAl_2O_4$ layer with the oxidized zone was approximately 3 %.

Surface $NiAl_2O_4$ was developed by Ni outward diffusion. The volume ratio of surface $NiAl_2O_4$ layer in all $NiAl_2O_4$ developed by high temperature oxidation is regarded as the contribution of outward diffusion of Ni in total oxidation of Ni/Al_2O_3 nanocomposites. The value of the ratio is approximately 10% because volume

ratio of $NiAl_2O_4$ in the oxidized zone is calculated to be approximately 30 % in 5 vol% Ni dispersion. This argument means that major diffusion to develop the oxidized region is inward diffusion of O^{2-} passing through oxidized zone. Outward diffusion of Ni for a continuous $NiAl_2O_4$ layer is a minor diffusion in Al_2O_3 matrix for the formation of oxidized zone.

With increasing thickness of oxidized zone, the driving force for outward diffusion of Ni is decreased. Decreasing oxidation rate of Ni/Al_2O_3 nanocomposites can improve diffusion flux of Ni. Not only enhancement of outward diffusion, suppression of inward diffusion of O can improve crack-healing performance at high temperatures.

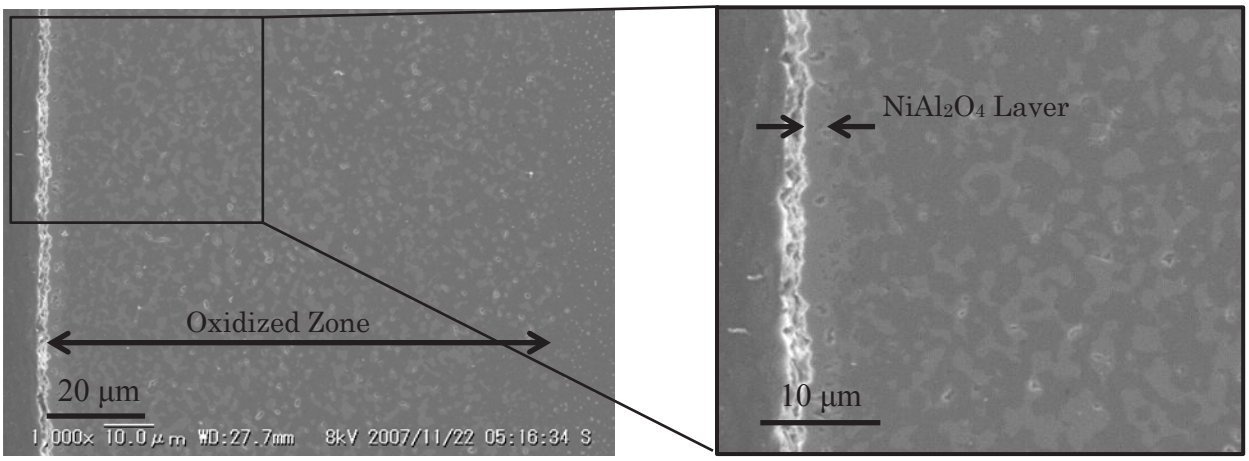

Fig. 1 SEM images of cross-sectional views Ni/Al_2O_3 nanocomposite oxidized at 1300°C for 1 d in air

4. CONCLUSIONS

Diffusion in high-temperature oxidation of Ni/Al_2O_3 nanocomposites is discussed. In particular, diffusion behavior for crack-healing process was studied. Oxidation of Ni/Al_2O_3 nanocomposites occurs for inward diffusion of oxygen from the surface to the inside. Additionally minor outward diffusion of Ni occurs simultaneously and leads to form $NiAl_2O_4$, which fills up in cracks.

Acknowledgments

The authors express our deep appropriation to Japan Society for the Promotion of Science (JSPS) and Japan Science and Technology Agency (JST) on financial support for the present studies.

References

[1] Ando K et al *Fatigue Fract. Engng. Mater. Struct.* Vol. 27 (2004) pp.533.
[2] Nanko M., "High-Temperature Oxidation and Crack Healing of Nano-Ni Dispersed Al_2O_3 Hybrid Materials", *J. Ceram. Proc. Res.*, Vol. **10** (2009) s68-s71.
[3] Maruoka, D., and Nanko, M., "Recovery of Mechanical Strength by Surface Crack Disappearance via Thermal Oxidation for Nano-Ni/Al_2O_3 Hybrid Materials", *Ceram. Intl.*, Vol. **39** (2013) pp.3221–3229.
[4] Nanko M. et al., "Role of Cation Diffusion on High-Temperature Oxidation of Metal-Dispersed Ceramic Matrix Composites", *Adv. Tech. Mater. Mater Proc. J,* .Vol. **7** No.1 (2005) pp.5-8.

O12

Oxidation resistance of SiC-based composite materials against high temperature in air and steam environments

Kazuya Shimoda [1,*], Tatsuya Hinoki[2], and Hideyuki Murakami [1]

[1] High Temperature Materials Unit, National Institute for Material Science, 1-2-1, Sengen, Tsukuba 300-0047, JAPAN
[2] Institute Advanced Energy, Kyoto University, Gokasho, Uji 600-0011, JAPAN

e-mail: SHIMODA.Kazuya@nims.go.jp

1. INTRODUCTION,

In recent years, there has been an increasing demand for high-performance continuous fiber-reinforced ceramic composites (CFCCs) for high-temperature applications. CFCCs are most promising for high-temperature structural materials/components of gas turbines, aircraft engines, rockets, and flight vehicles. Typical components include combustors, nozzles, and thermal insulation for aerospace applications. The properties of CFCCs are highly dependent on the properties of the reinforcement used in the composite. A reinforcing fiber should have high environmental stability and sufficient mechanical properties, even at high temperature. Use of bare carbon fibers as reinforcement for high-temperature applications involves environmental limits in air or steam condition due to its tendency to oxidize. SiC fibers that have high tensile strength, high elastic modulus, good thermal stability, and excellent oxidation and corrosion resistance are one of the best candidates for reinforcement. Polymer-derived SiC fibers fabricated by a precursor process in particular have the advantage of a flexible, fine diameter form over those from chemical vapor deposition (CVD) or sintering processes. Over the past two decades, the vast majority of CFCC research has focused on the SiC/SiC system. Processing of SiC/SiC composites consists of the building up of a SiC matrix around the SiC fibers. There are four common ways to create this matrix: through chemical vapor infiltration (CVI), molten silicon infiltration [MI, or reaction sintering (RS)], polymer impregnation and pyrolysis (PIP), and hot pressing via liquid-phase sintering like nano-infiltration and transient eutectic phase (NITE) process [1-9]. Generally, SiC/SiC composites exhibit pseudo-ductile fracture behavior by fiber debonding and sliding at the fiber/matrix interface like pyrocarbon (PyC). However, the PyC interface is the critical issue because it is susceptible to oxidation in air or steam condition, even under low oxygen partial pressure [10-15]. In addition, precise control of the PyC interface is an expensive process that results in low product yield. The objective of this study is to develop a pseudo-ductile SiC/SiC composite using a porous SiC matrix structure without a PyC interface and to investigate its resistance against high temperature oxidation in air or steam environments.

2. EXPERIMENTAL

A conventional SiC fiber with crystalline structure and nonstoichiometric composition (Tyrrano^{TM}-SA grade-3 (TySA3), Ube Industry, Japan) was employed as reinforcement for the fabrication of porous SiC/SiC composites in this study [16]. The unidirectional (UD) SiC fiber bundles without de-sizing treatment were impregnated into the SiC-based slurry containing SiC nanopowder (Nanomakers, France, mean diameter of 35 nm, 99% purity) and carbon powder with Al_2O_3 and Y_2O_3 powders as sintering additives for the fabrication of UD prepreg sheets. The fiber volume fraction was arranged to be approximately 60%. The SiC matrix with carbon source was formed by liquid phase sintering (LPS) method. The porous SiC matrix was formed following decarburization process in air at 700 ^{o}C. The bulk density and open porosity were measured by Archimedes's method using water. The mechanical properties were characterized by three-point bending tests in an INSTRON 5581 test machine using specimens 25 mm long, 3 mm wide, and 1.5 mm thick. The outer support span was 18 mm and the crosshead speed was 0.1 mm/min. The microstructure and fracture surface after the bending test were observed by field emission scanning electron microscope (FE-SEM, Ultra55, ZEISS, Germany). In order to evaluate the oxidation resistance, the porous SiC/SiC composite was oxidized in air and steam environments up to 1200 °C. For the thermogravimetric and differential thermal analysis (TG-DTA) using Thermo plus EVO II (Rigaku, Japan), alumina tube was used with dry air or dry air-85%H_2O (it was not possible to achieve 100% steam in this TGA system). CVI and NITE SiC/SiC composites were used for the comparison of the conventional SiC/SiC composites with a PyC interface using TySA3 SiC fibers as reinforcement.

3. RESULTS AND DISCUSSION

Table 1 lists the bulk density and open porosity of the porous SiC/SiC composite developed and conventional SiC/SiC composites fabricated by CVI and NITE process. The porous SiC/SiC composite had a bulk density of 2.5 g/cm^3 and open porosity of ~20 %.

Table 1 bulk densities, open porosities and mechanical properties of SiC/SiC composites used in this study.

ID	Bulk density (g/cm3)	Open porosity (%)	Bending strength (MPa)	Apparent modulus (GPa)
Porous	2.5	~20	282	182
CVI	2.4	18	498	174
NITE	3.1	~3	496	152

Figure 1 FE-SEM images of the porous SiC/SiC composite; (a) low magnification, (b) high magnification at the fiber bundle region and (c) high magnification among fiber bundle region. It was confirmed that most of the pores in the sample were of an open type and arranged in a chain like manner. The mechanical properties of all SiC/SiC composites using the three-point bending test are also summarized in Table 1. The average bending strength and the apparent bending modulus of the porous SiC/SiC composite were approximately 282 MPa and 182 GPa, respectively. Fracture behavior of the porous SiC/SiC composite showed a pseudo-ductile behavior, which were quite different from that of brittle ceramics without fibers.

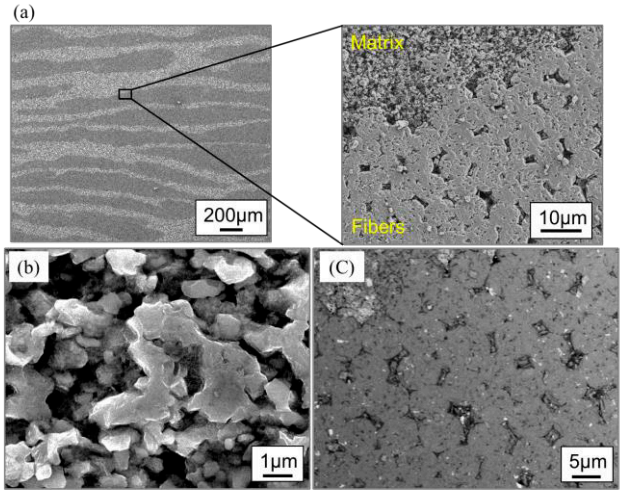

Figure 1 FE-SEM images of the porous SiC/SiC composites; (a) low magnification, (b) High magnification at the fiber bundle region and (c) high magnification among fiber bundle region

Figure 2 shows the crack propagation of the porous SiC/SiC composite after the three-point bending test. Of interest was that the porous SiC/SiC composite mainly ractured by transverse crack propagation at the edge of the fiber bundles and complicated crack propagation was generated in the porous SiC matrix among the fiber bundle regions. This was probably due to crack propagation occurring immediately through the specimen prior to breaking the fiber pull-out in order to release the bending stress between the SiC matrix and the SiC fiber bundles where the initial matrix cracking occurred.

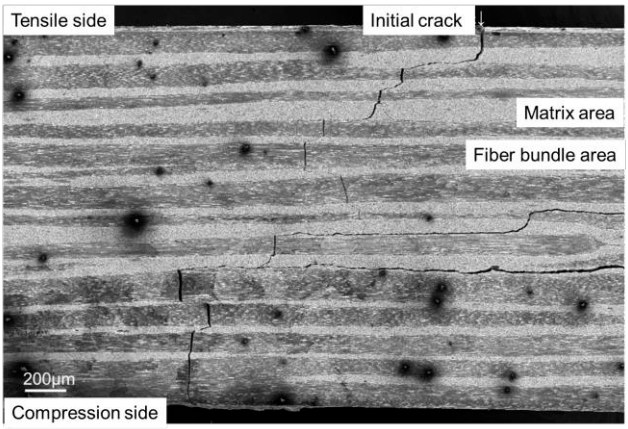

Figure 2 Crack propagation of the porous SiC/SiC composite after the three-point bending test

Figure 3 represents the TGA results in air of the porous SiC/SiC composite and TySA3 SiC fiber as reinforcement at a temperature range of 25–1200 °C. In addition, TGA results of conventional SiC/SiC composites with a PyC interface fabricated by CVI and NITE process are represented in Figure 3. The weight loss of the porous SiC/SiC began at around 700 °C, which was similar trend to TySA3 SiC fiber as reinforcement. The value of weight change was depending on the fiber volume fraction (approximately 60%) below 1000 °C. On the other hand, the weight loss of conventional SiC/SiC composites with PyC interface began at around 300 °C and the value of weight loss was depending on the total carbon content in the composites calculated from the PyC interface thickness and the carbon content including reinforced TySA3 SiC fiber.

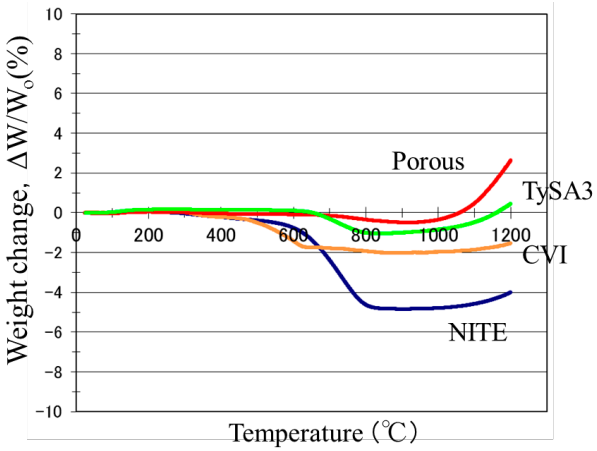

Figure 3 TGA results of SiC/SiC composites used in this study and TySA3 SiC fiber

Figure 4 represents typical bending stress-deflection curves of the porous SiC/SiC composite at room temperature (RT), after exposure at 800 °C for 10 h and 1100 °C for 10 h in air. For the porous SiC/SiC composite, significant changes in the original bending strength and fracture behavior was not observed following exposure at 1100 °C for 10 h in air. During the process of thermal oxidation at intermediate temperatures of 500–1200 °C for conventional SiC/SiC

composites with a PyC interface, the consumption of the PyC interface and the formation of silica should degrade the mechanical properties due to strong bonding with the fibers and the matrix, a phenomenon that has been recognized by various researchers [10-13,17,18]. In fact, conventional SiC/SiC composites with a PyC interface used in this study underwent sever strength degradations (43 % loss for CVI and 75 % loss for NITE) after exposure at 800 °C for 10 h and approached to a brittle fracture behavior after exposure at 1100 °C for 10 h.

Figure 5 represents the TG-DTA data of the porous SiC/SiC composite in (a) dry air or (b) dry air-85%H_2O environments at a temperature range of 25–1200 °C. The porous SiC/SiC composite showed the very small weight gain up to 1200 °C and endothermic reaction under the steam condition. There was no big difference between under dry air and dry air-80% H_2O environments. The mechanical property changes of the porous SiC/SiC composite are not probably occurred even under the steam condition, although mechanical tests after exposure are not performed in the present study. For the porous SiC/SiC without a PyC interface developed in this study, the porous SiC matrix can effectively protect the SiC fibers against oxidation and the formation of silica can fill the pores and cracks in the SiC matrix, which might maintain or strengthen the mechanical properties. Therefore, the oxidation resistance of porous SiC/SiC composites without a PyC fiber/matrix interface is much better than that of conventional SiC/SiC composites with a PyC fiber/matrix interface. The materials consist only of SiC, and thus the excellent resistance to high temperature oxygen and chemical corrosion is expected.

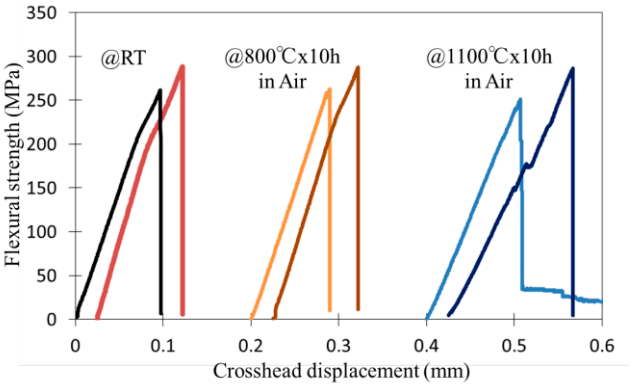

Figure 4 Fracture behavior of the porous SiC/SiC composite at room temperature, after exposure at 800 °C for 10 h and 1100 °C for 10 h.

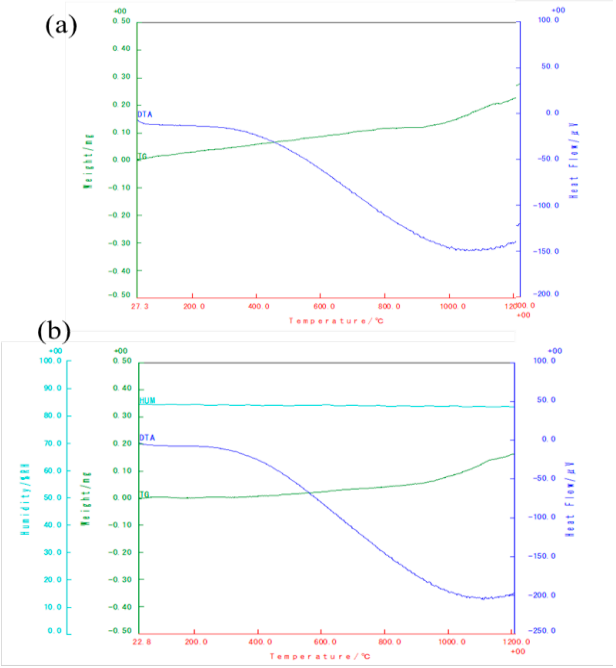

Figure 5TG-DTA results of the porous SiC/SiC composite; (a) in dry air and (b) in dry air-85%H_2O conditions.

4. CONCLUSION

A new type SiC/SiC composite was successfully developed applying a porous SiC matrix. The porous SiC/SiC composite consist with just SiC fiber and crystalline porous SiC matrix without fiber/matrix interphase like pyrocarbon. The porous SiC/SiC composite showed a pseud-ductile behavior and complicated fracture behavior due to enhanced debonding at fiber/matrix interface and frictional stress at the debonded fiber/matrix interface. The porous SiC/SiC composite was exposed at elevated temperature up to 1200 °C in air and steam environments. No apparent degradation in strength after exposure in air up to 1100 °C for 10 h was observed compared to that of the as-received material. This is because the SiC composites could form protective silica layer, which showed minimal attack against air and steam below 1200 °C.

Acknowledgements

This work was partly supported by Grant-in-Aid for Young Scientists (B): 24760560.

References

[1] Naslain RR., "The design of the fibre-matrix interfacial zone in ceramic matrix composites," *Composites Part A*, 1998;29:1145–55.

[2] Araki H, Yang W, Suzuki H, Hu Q, Busabok C, Noda T., "Fabrication and flexural properties of Tyranno-SA/SiC composites with carbon interlayer by CVI," *J Nucl Mater*, 2004;329–333:567–71.

[3] Corman G, Luthra K., "Silicon Melt Infiltrated Ceramic Composites (HiPerComp™). In: Bansal NP, editor. Handbook of Ceramic Composites," New York: Springer; 2005, pp. 99–115.

[4] Lee SP, Katoh Y, Park JS, Dong S, Kohyama A, Suyama S, Yoon HK., "Microstructural and mechanical characteristics of SiC/SiC composites with modified-RS process," *J Nucl Mater*, 2001;289:30–6.
[5] Kotani M, Inoue T, Kohyama A, Okamura K, Katoh Y., "Consolidation of polymer-derived SiC matrix composites: Processing and microstructure," *Comp Sci Technol*, 2002;62:2179–88.
[6] Yoshida K, Imai M, Yano T., "Improvement of the mechanical properties of hot-pressed silicon-carbide-fiber-reinforced silicon carbide composites by polycarbosilane impregnation," *Comp Sci Technol*, 2001;61:1323–29.
[7] Dong S, Katoh Y, Kohyama A., "Preparation of SiC/SiC composites by hot pressing, using tyranno-SA fiber as reinforcement," *J Am Ceram Soc*, 2003;86:26–32.
[8] Shimoda K, Hinoki T, Kohyama A., "Effect of additive content on transient liquid phase sintering in SiC nanopowder infiltrated SiC_f/SiC composites," *Comp Sci Technol*, 2011;71:609–15.
[9] Shimoda K, Kohyama A, Hinoki T., "High mechanical performance SiC/SiC composites by NITE process with tailoring of appropriate fabrication temperature to fiber volume fraction," *Comp Sci Technol*, 2009;69:1623–28.
[10] Ding D, Zhou W, Luo F, Chen M, Zhu D., "Mechanical properties and oxidation resistance of SiC_f/CVI-SiC composites with PIP-SiC interphase," *Ceram Inter*, 2012;38:3929–34.
[11] Morscher GN, Cawley JD., "Intermediate temperature strength degradation in SiC/SiC composites," *J Eur Ceram Soc*, 2002;22:2777–87.
[12] Ochiai S, Kimura S, Tanaka H, Tanaka M, Hojob M, Morishitam K., "Degradation of SiC/SiC composite due to exposure at high temperatures in vacuum in comparison with that in air," *Composites Part A*, 2004;35:33–44.
[13] Filipuzzi L, Camus G, Naslain R., "Oxidation mechanisms and kinetics of 1 D-SiC/C/SiC composite materials: I. An experimental approach," *J Am Ceram Soc* ,1994;77:459–466.
[14] Shimoda K, Hinoki T, Kishimoto H, Kohyama A., "Enhanced high-temperature performances of SiC/SiC composites by high densification and crystalline structure," *Comp Sci Technol*, 2011;71:326–332.
[15] Naslain R, Guette A, Rebillat F, Legallet S, Lamouroux F, Filipuzzi L, Louchet C., "Oxidation mechanisms and kinetics of SiC-matrix composites and their constituents," *J Mater Sci*, 2004;39:7303–16.
[16] http://northamerica.ube.com/content.php?pageid=54.
[17] Naslain R, Pailler Rene J-F, Lamon JL., "Single- and multilayered interphases in SiC/SiC composites exposed to severe environmental conditions: An overview," *Int J Appl Ceram Technol*, 2010;7:263–75.
[18] Wu SJ, Cheng LF. Zhang LT, Xu YD, Zhang Q., "Comparison of oxidation behaviors of 3D C/PyC/SiC and SiC/PyC/SiC composites in an O_2–Ar atmosphere," *Mater Sci Eng B*, 2006;130:215–9.

Mass-transfer in Polycrystalline α-Alumina under Oxygen Potential Gradients at High Temperatures: An Experimental Approach

Satoshi KITAOKA[(1,3,*)], Tsuneaki MATSUDAIRA[(1)], Takafumi OGAWA[(1)], Tsubasa NAKAGAWA[(2)], Yutaka KAGAWA[(3)]

[(1)] Japan Fine Ceramics Center, 2-4-1 Mutsuno, Atsuta-ku, Nagoya 456-8587, JAPAN

[(2)] Kyoto University, Yoshida-honmachi, Sakyo-ku, Kyoto 606-8501, JAPAN

[(3)] The University of Tokyo, 4-6-1 Komaba, Meguro-ku, Tokyo 153-8904, JAPAN

e-mail: kitaoka@jfcc.or.jp

1. INTRODUCTION

The oxygen permeability of polycrystalline α-alumina wafers, which serves as a model for alumina scale on alumina-forming alloys, was evaluated at temperatures above 1773 K under steep oxygen potential gradients (ΔP_{O2}). [1] Oxygen permeation occurred by the grain boundary (GB) diffusion of oxygen from the surface at higher oxygen partial pressure (P_{O2}) to that at lower P_{O2}, along with simultaneous GB diffusion of aluminum in the opposite direction. The main diffusing species was dependent not only on ΔP_{O2}, but also on the absolute magnitude of P_{O2} in the two atmospheres. The GB diffusion coefficients for oxygen and aluminum could be estimated from the oxygen permeability constant measured under certain limited values of ΔP_{O2}, where oxygen permeation occurred mainly by either oxygen or aluminum diffusion along GBs. The diffusion coefficients can be expressed in terms of P_{O2} and the mobilities, which are determined from Arrhenius equations. [1]

Oxygen GB diffusion coefficient:

$$D_O\delta = -\frac{1}{6C_{Ob}} \cdot P_{O_2}^{-1/6} \cdot \frac{A_O}{S_{gb}}, \qquad -\frac{A_O}{S_{gb}} = \frac{A_O^*}{S_{gb}} exp\left(\frac{-\Delta E_O}{RT}\right) \tag{1}$$

Aluminum GB diffusion coefficient:

$$D_{Al}\delta = \frac{1}{12C_{Alb}} \cdot P_{O_2}^{3/16} \cdot \frac{A_{Al}}{S_{gb}}, \qquad \frac{A_{Al}}{S_{gb}} = \frac{A_{Al}^*}{S_{gb}} exp\left(\frac{-\Delta E_{Al}}{RT}\right), \tag{2}$$

where δ is the GB width, C_{Ob} and C_{Alb} are the molar concentrations of oxygen and aluminum per unit volume in the alumina, respectively, and S_{gb} is the GB density. A_O/S_{gb}, A_O^*/S_{gb}, and ΔE_O are the mobility, frequency factor and activation energy for the GB diffusion of oxygen, respectively, while A_{Al}/S_{gb}, A_{Al}^*/S_{gb}, and ΔE_{Al} are those for aluminum GB diffusion. R is the gas constant and T is the absolute temperature. The ΔE_O values for oxygen diffusion obtained from the oxygen permeation experiments were similar to those determined from secondary ion mass spectroscopy depth profiles of alumina scales after double oxidation of the alloys at temperatures below 1473 K, [2,3] regardless of whether or not oxygen-reactive elements (REs) were segregated at the GBs. This suggests that the oxygen GB diffusion mechanism in the wafer is the same as that in the scale. It should be noted for the oxygen permeation experiments that REs such as Y and Lu were found to selectively reduce the frequency factor of oxygen, but did not significantly affect the aluminum diffusivity. [1] In this study, we propose a method to compare the $D_O\delta$ values determined experimentally and discuss the effect of RE doping on oxygen GB diffusion.

2. CALCULATION OF P_{O2} AND FREQUENCY FACTOR FOR OXYGEN DIFFUSION IN SCALE

The relationship between the normalized depth (x/L) in the wafer and the corresponding $P_{O2}(x)$ in equilibrium with the oxygen chemical potential at x/L is given by: [1]

$$\frac{x}{L} = \frac{\frac{A_{Al}}{S_{gb}}\left(P_{O_2}(x)^{3/16} - P_{O_2}(lo)^{3/16}\right) + \frac{A_O}{S_{gb}}\left(P_{O_2}(x)^{-1/6} - P_{O_2}(lo)^{-1/6}\right)}{\frac{A_{Al}}{S_{gb}}\left(P_{O_2}(hi)^{3/16} - P_{O_2}(lo)^{3/16}\right) + \frac{A_O}{S_{gb}}\left(P_{O_2}(hi)^{-1/6} - P_{O_2}(lo)^{-1/6}\right)} \tag{3}$$

It is postulated that Eqs. (1)-(3) are also applicable to alumina scale. ΔE_O for oxygen mobility, and $A_{Al}{}^*/S_{gb}$ and ΔE_{Al} for aluminum mobility in the scale are also assumed to be the same as those obtained from the high-temperature oxygen permeation experiments. Thus, P_{O2} and $A_O{}^*/S_{gb}$ in Eq. (1) for the scale are obtained by solving the simultaneous equations using $D_O\delta$ at x/L=0.92 reported for the scales, as listed Table I. [2,3]

Table I. GB diffusion coefficients of oxygen in alumina scales.

Scales	Alloys	T (K)	Normalized depth (x/L)	$D_O\delta$ (m^3s^{-1})	Ref.
Undoped	Fe-20Cr-5Al	1373	0.92	2.2×10^{-24}	[2]
Y-doped	ODS-MA956	1373	0.92	5.8×10^{-28}	[3]

3. RESULTS AND DISCUSSION

Figure 1 shows the temperature dependence of $D_O\delta$ for undoped and Y-doped alumina. The broken and dashed-dotted lines indicate the $D_O\delta$ corrected for the permeation experiments using P_{O2} calculated at x/L=0.92 in the scales. For undoped alumina, $A_O{}^*/S_{gb}$ determined from the permeation experiments corresponded to that calculated for the scale. The broken line, extrapolated to lower temperature, is consistent with that for the scale. Thus, the oxygen GB diffusion mechanism for undoped alumina was independent of temperature.

$A_O{}^*/S_{gb}$ values calculated at x/L=0.92 in the Y-doped scales are markedly smaller than that in the undoped scale, and with an inverse relationship to the calculated P_{O2}. The significant changes of these parameters are responsible for the considerable decrease of $D_O\delta$ due to Y-doping for the scale, according to Eq.(1). However, for Y-doped alumina, the calculated $A_O{}^*/S_{gb}$ and $D_O\delta$ for the scale were significantly smaller than that determined from the permeation experiments and the corresponding dashed-dotted line, despite the almost identical ΔE values. The magnitude of the reduction in oxygen diffusivity due to the presence of Y may decrease discontinuously with increasing temperature, namely the discontinuous increase of the nominal fast diffusion path area in the GB faces for oxygen.

Acknowledgements

This work was partially supported by the Japan Science and Technology Agency (Advanced Low Carbon Technology Research and Development Program) and by a Grant-in-Aid for Scientific Research on Innovative Areas "Nano Informatics" (25106008) from JSPS.

References

[1] T. Matsudaira, M. Wada, and S. Kitaoka, "Effect of Dopants on the Distribution of Aluminum and Oxygen Fluxes in Polycrystalline Alumina under Oxygen Potential Gradients and High Temperatures", *J. Am. Ceram. Soc.*, Vol.96, No.10 (2013), pp.3243-3251.

[2] S. Chevalier, B. Lesage, C. Legoros, G. Borchadt, G. Strehl, and M. Kilo, "Oxygen Diffusion in Alumina. Application to Synthetic and Thermally Grown Al_2O_3", *Defect and Diffusion Forum*, Vol. 237-240, (2005), pp.899-910.

[3] K. Messaoudi, A. M. Huntz, and B. Lesage, "Diffusion and Growth Mechanism of Al_2O_3 Scales on Ferritic Fe-Cr-Al Alloys", *Mater. Sci. Eng.*, Vol. A247, (1998), pp.248-262.

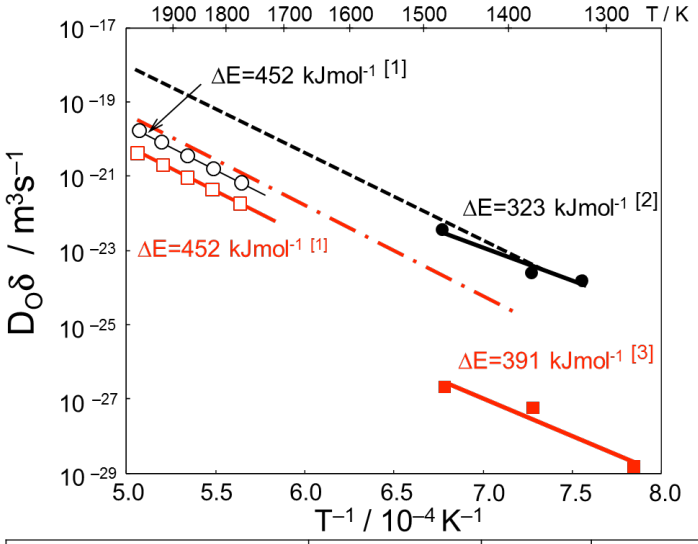

Experiments		Samples	P_{O2} (Pa)	$A_O{}^*/S_{gb}$ ($mols^{-1}Pa^{-1/6}$)
Oxygen Permeation	[1]	Undoped wafer	10^{-8}	1.5×10^{-3}
	[1]	Undoped wafer	1.6×10^{-17}	1.5×10^{-3}
	[1]	Y-doped wafer	10^{-8}	4.5×10^{-4}
	[1]	Y-doped wafer	6.7×10^{-13}	4.5×10^{-4}
Oxidation (1373K)	[2]	Undoped scale	1.6×10^{-17}	1.4×10^{-3}
	[3]	Y-doped scale	6.7×10^{-13}	2.2×10^{-6}

Fig.1. Temperature dependence of $D_O\delta$ for undoped and Y-doped alumina. Each ΔE in the figure is the reported value.

Oxidation resistance and lifetime of ODS FeCrAl alloys

Sebastien Dryepondt [1,*] and Bruce Pint [1],

[1] Oak Ridge National Laboratory, Materials Science and Technology division, Oak Ridge, USA

e-mail: dryepondtsn@ornl.gov

1. INTRODUCTION,

Oxide Dispersion Strengthened (ODS) FeCrAl alloys exhibit excellent creep and oxidation properties at high temperature and are therefore of great interest for fossil energy applications [1]. Below a load threshold that depends on the temperature, creep deformation is expected to be extremely low, and the lifetime of a well-designed component will depend on its oxidation performance. Recent results have shown that H_2O and CO_2, present in most combustion environments, can have a significant impact on the oxidation behavior of ODS FeCrAl alloys [2-3]. This paper will present long-term cyclic oxidation data for three different ODS FeCrAls obtained at 1100ºC in laboratory air and air +10%H_2O, and at 1200ºC in O_2, air+10%H_2O and a mixture of ~50%H_2O-50%CO_2. A method to estimate specimen lifetime based on the consumption of Al to form alumina will also be proposed.

2. EXPERIMENTAL,

The chemical compositions of alloy MA956 provided by Special Metals Corp. (Huntington, West Virginia), and the two different batches of alloy PM2000, provided by Metalwerk Plansee (Reutte, Austria), are shown in Table 1. The main differences are the higher level of Al for the PM2000 alloys, and the very low level of impurities for alloy PM2000_2, especially C and S. Rectangular coupons, 20x10X1.5mm were machined from plates or rods and polished down to 0.3µm for alloy MA956 and PM2000_1, and 600 grit finish for alloy PM2000_2. The alloys were all fully recrystallized leading to oxidation coupons with only 3 grains for alloys MA956 and PM2000_1, and 1 grain for alloy PM2000_2.

Cyclic oxidation testing was conducted at 1200ºC with a 1h dwell time and 10 min cooling in O_2, air +10%H_2O, and a mixture of 49.25%CO_2+50%H_2O+0.75%O_2 (CO_2/H_2O). O_2 was added as a buffer because in most fossil energy applications, the combustion reaction is not expected to be complete and the presence of O_2 could affect the alloy oxidation process. These aggressive conditions were selected to accelerate alloy degradation and reach the breakaway oxidation stage with the fast formation of Fe-rich oxides instead of alumina. Specimens were also cycled at 1100ºC in air and air + 10%H_2O with a 100h cycle time, conditions more realistic for fossil applications. For the test in laboratory air, the specimens were placed in alumina crucibles and both the specimens and the crucibles were weighted every 100h, allowing the measurement of the specimen and total (specimen + spalled oxides) mass changes. Details of the experimental procedure can be found elsewhere [3].

Table 1: Chemical alloy composition in at%, measured by inductively coupled plasma analysis (ICP) and combustion analysis

Alloys		Fe	Cr	Al	Si	Ti	Y	C (ppm)	N (ppm)	O (ppm)	S (ppm)
MA956	3 grains	69.45	20.07	8.78	0.13	0.4	0.24	640	608	6490	41
PM2000_1	3 grains	69.4	18.91	9.82	0.07	0.49	0.22	430	104	8050	34
PM2000_2	1 grain	68.7	19.13	10.48	0.04	0.52	0.23	60	318	8028	13

3. RESULTS AND DISCUSSION,

The mass changes versus exposure time for the specimens cycled every hour at 1200ºC in O_2, air+10%H_2O and CO_2/H_2O are shown in Figure 1a. The specimens were stopped once a significant increase of the mass change was observed due to the formation of Fe-rich oxides. The onset of breakaway oxidation with Fe oxide formation can be considered as the

specimen end of life. The three alloys exhibit different oxidation behaviors, with the lifetime for the PM2000-2 alloy in O_2 being more than four times longer than the lifetime of alloy MA956 and 2 times longer than the lifetime of alloy PM2000-1. The excellent oxidation behavior of alloy PM2000-2 is related to the higher level of Al and the very low S and C contents, resulting in significantly lower spallation rates. In addition, exposure to air+10%H_2O or CO_2/H_2O resulted in significantly lower lifetimes for alloy MA956 and alloy PM2000-1. Test in CO_2/H_2O for alloy PM-2000-2 is still on going, but after 4000 cycles, the specimen mass change curves look quite similar in O_2 and CO_2/H_2O.

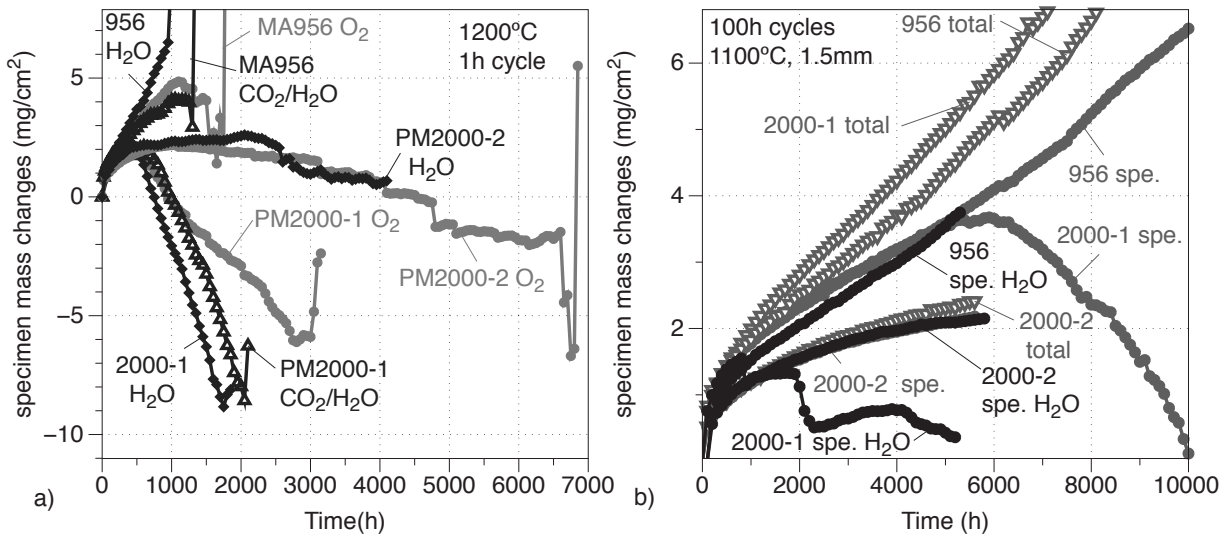

The mass changes for the specimens exposed to 100h cycles at 1100ºC in air and air+10%H_2O are presented in Figure 1b. Again, the specimen mass change curves are quite different for the three alloys, linear increase for alloy MA956 up to 10000h, increase for the first 5000h and then decrease for alloy PM2000-1, and slow parabolic increase for alloy PM2000-2. However, the total mass changes, i.e. specimens plus spalled oxides captured in the alumina crucible, are quite similar for alloy MA956 and PM2000-1. This result indicates that for alloy MA956 cracking and debonding of the alumina scale does not lead to the total separation of the oxide from the specimen. For alloy PM2000-2, the total mass change curve is nearly identical to the specimen mass change curve after 5700h, meaning that scale spallation has not yet started. Exposure to H_2O did not change the specimen mass change for alloy PM2000-2, but resulted in significant spallation for alloy PM2000-1. For alloy MA956, the specimen mass change curve in H_2O was also similar to the curve generated in air, but it does not mean that the total mass changes are the same. Longer exposure times are needed to assess clearly the effect of H_2O at 1100ºC. Overall, these oxidation results demonstrate that lowering the S and C levels in ODS FeCrAl can have a drastic effect on the scale spallation, and the presence of H_2O and CO_2 can increase the spallation rate for alloys already prone to spallation.

The lifetime of FeCrAl components will depend on the Al consumption rate to form a protective alumina scale, the initial Al reservoir, and the critical Al concentration below which alumina cannot form anymore [4]. The Al consumption rate is directly related to the total mass change, but in complex environments, only the specimen mass change is usually measured. Cyclic oxidation models such as COSP, pKp or DICOSM have been developed based on two main parameters, one related to the growth of the scale (kp) and one related to the scale spallation (for example p in the pkp model) [5-6]. These models were used successfully to fit specimen mass change curves generated during thermal cycling of NiAl and NiPtAl alloys and could therefore be used to predict the total mass gain curves and the Al consumption rate. The same models were used to fit the specimen mass change curves for ODS FeCrAl alloys generated at 1200ºC, but in many cases the resulting spallation coefficients were far too low to capture the actual spallation rate. This is again due to the fact that cracking and debonding of the alumina scale does not always lead to the detachment of the oxide from the specimen. A different approach was therefore used to determine the spallation parameter. Some specimens were cross-sectioned after cyclic exposure at 1200ºC, and the remaining Al contents were measured by microprobe analysis to determine how much Al has been consumed. The spallation parameter was then adjusted so that the Al consumption calculated by the model would match the measured Al consumption. As shown in reference [7], this approach using the COSP model led to

a good estimate of the MA956 alloy lifetime at 1200ºC.

4. CONCLUSION,

Long term cyclic oxidation testing was conducting on three ODS FeCrAl at 1100ºC and 1200ºC in O_2, air+10%H_2O and a mixture of H_2O and CO_2. The specimen mass change curves show that the low level of impurities such as C and S in alloy PM2000-2 resulted in a significantly better adhesion of the alumina scale and drastic improvement of specimen lifetime. 1h cyclic oxidation in H_2O and H_2O/CO_2 atmospheres at 1200ºC led an increase of the spallation rate and a decrease of specimen lifetime for alloy MA956 and PM2000-1 compared with cyclic oxidation in O_2. In addition, cracking and debonding of the alumina scale without detachment of the oxide from the specimen can lead to specimen mass change curves that cannot be predicted by conventional cyclic oxidation models. A new approach was therefore proposed relying on the experimental measurement of the Al remaining in the specimen after exposure to determine the cyclic oxidation kinetics and estimate specimen lifetime.

Acknowledgements,

The author wish to acknowledge G. Garner, T. Lowe, M. Stephens and for assistance with the experimental work, as well as D. N. Leonard for EPMA analysis and Elodie Martin for the modeling work. They also thank A. Rouaix-Vande Put and P. Tortorelli for exciting scientific conversations. This research was sponsored by the U.S. Department of Energy, Fossil Energy Advanced Materials Research Program.

References

[1] J.C. Healy, M. Rees, J.D. Parker, R.C. Hurst, in the proc. of the Seventh International Conference on the Creep and Fracture of Engineering Materials and Structures, Aug. 10-15, 1997, Irvine, CA, 719 (1997).
[2] A. Vande Put, S. Dryepondt, and B.A. Pint, NACE Paper 19608, Houston, TX, presented at NACE Corrosion 2010, Houston, TX, March 2011.
[3] S. Dryepondt, A. Rouaix-Vande Put, B. Pint, *Oxidation of Metals*, 79, 5-6, 627-638 (2013).
[4] W.J. Quadakkers, K. Bongartz, *Materials and Corrosion*, 45, 232 (1994).
[5] D. Poquillon and D. Monceau, *Oxidation of Metals*, 59, 3/4, 409 (2003).
[6] J. L. Smialek, *Acta Materialia*, 52, 8, 2111 (2004).
[7] S. Dryepondt, and B.A. Pint, NACE Paper 02646, Orlando, FL, presented at NACE Corrosion 2013, Orlando, FL, March 2011.

The effect of Cr on formation and growth of Al_2O_3 scale on Fe-Cr-Al alloys at 1000°C

Suzue Yoneda [(1*)], Shigenari Hayashi [(1)], and Shigeharu Ukai [(1)]

(1) Division of Materials Science and Engineering, Graduate School of Engineering, Hokkaido University, Kita13 Nishi8, Sapporo 060-8628, JAPAN

e-mail: s.yoneda@eng.hokudai.ac.jp

1. INTRODUCTION

Al_2O_3 scale can provide excellent oxidation and corrosion resistance at higher temperatures in various aggressive environments, since Al_2O_3 is thermodynamically stable and grows with a slower rate than Cr_2O_3 [1]. Higher Al additions in alloys are often required to form an external Al_2O_3 scale, but this higher Al content can result in poor mechanical properties due to formation of brittle intermetallic compounds such as γ' and β phases[2,3]. Cr addition to binary M-Al alloys (M=Fe, Ni, Co) is known to decrease the critical Al content for Al_2O_3 scale formation [5-10]. This beneficial effect of Cr is known as the Third Element Effect, where Cr acts as an oxygen getter in the alloy subsurface and/or forms Cr_2O_3 scale, decreasing oxygen partial pressure at the surface and inward oxygen flux, and favoring Al_2O_3 scale formation [11]. From our previous study on Ni-Cr-Al alloys, it was found that the initially formed Cr_2O_3 scale contained Al_2O_3 and this $(Cr,Al)_2O_3$ scale further decreases the oxygen potential at the metal-scale interface, promoting Al_2O_3 scale formation. Since Al_2O_3 content in the initially formed Cr_2O_3 scale is expected to depend on alloy Cr and Al contents, development and growth of an Al_2O_3 scale may also depend on the alloy Cr and Al content. In this study, the effect of both Cr and Al content on Al_2O_3 scale formation and growth rate was investigated. In order to avoid effects from second or third phase formation, single phase Fe-Cr-Al alloys with different Al and Cr contents were used in this study.

2. EXPERIMENTAL

Fe-xCr-yAl (x = 0, 4, 8, 12, 16, 20, 24), (y = 0, 3, 6, 10) alloys (in at.%) were prepared by argon arc melting high purity metals (99.99at.%). The alloy ingots were homogenized in vacuum at 1200°C for 48h. Approximately 1.5mm thick samples were cut from the homogenized ingots and ground to a 4000-grit finish using SiC abrasive paper. Samples were then polished using 3μm diamond paste, followed by ultrasonic cleaning in acetone. Oxidation tests were conducted at 1000°C for up to 49h in air. The weight of samples during oxidation was continuously recorded by a thermobalance. Short-term oxidation tests were performed using an electric furnace at 1000°C for up to 16h. After oxidation, samples were characterized by TEM, EDS and XRD.

3. RESULTS & DISCUSSION

Figure 1 shows oxidation weight gains of Fe-Cr-6Al alloys with different Cr contents at 1000°C up to 49h in air. All alloys showed good oxidation resistance with formation of a protective Al_2O_3 scale. The weight gain of these alloys decreased with increasing Cr content up to 16at.% , however further increase in Cr content resulted in increasing weight gain. The parabolic rate constants of alloys also showed the same dependence on Cr content. Figure 2 shows X-ray diffraction patterns of alloys after oxidation for different oxidation times at 1000°C in air. A weak peak at around 2θ=33.5° was initially detected on all alloys. The d-spacing calculated from this peak was found to decrease with increasing alloy Cr content. Since the d-spacing of Cr_2O_3 (d = 2.665Å at R.T.) is smaller than that of Fe_2O_3 (d = 2.703Å at R.T.) but higher than that of Al_2O_3 (d = 2.551Å at R.T.), the decrease in d-spacing was mainly due to different levels of solid solution of the initially formed Cr_2O_3 scale with Fe_2O_3 and Al_2O_3.

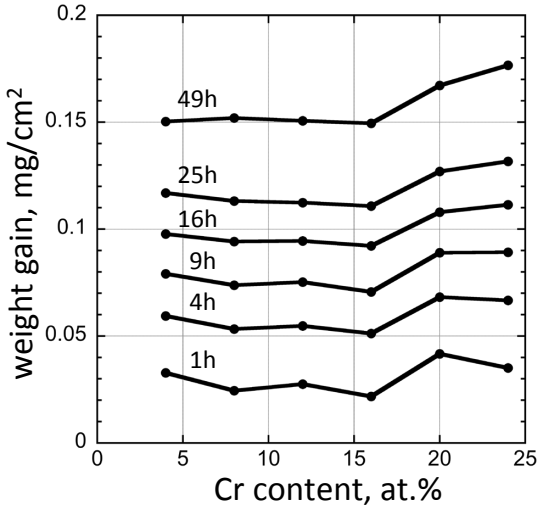

Fig.1 Change in weight gain with alloy Cr content at different oxidation times

The peak from α-Al_2O_3 at around 2θ=35° was observed on all alloys after formation of the $(Cr,Fe,Al)_2O_3$ scale, which corresponds to the reflection at around 33.5°. The time required for α-Al_2O_3 formation decreased for alloys with higher Cr content. The peak from α-Al_2O_3 formed on alloys with high Cr content consisted of double peaks, whereas those formed on low Cr alloys (~8at.%) were single peaks, indicating that formation behavior of the protective Al_2O_3 scale was different depending on the alloy Cr content.

The intensity of diffracted signals from the initially formed $(Cr,Fe,Al)_2O_3$ scale on high Cr content alloys was higher

than that formed on low Cr content alloys. A larger amount of Cr_2O_3 scale formation on alloys with higher Cr content may increase the Cr content in Al_2O_3 and increase the parabolic rate constant for Al_2O_3 scale growth. The results obtained indicate that higher Cr addition in alloys is favorable for development of an Al_2O_3 scale, but it is detrimental for the growth kinetics of Al_2O_3 scale at longer oxidation times.

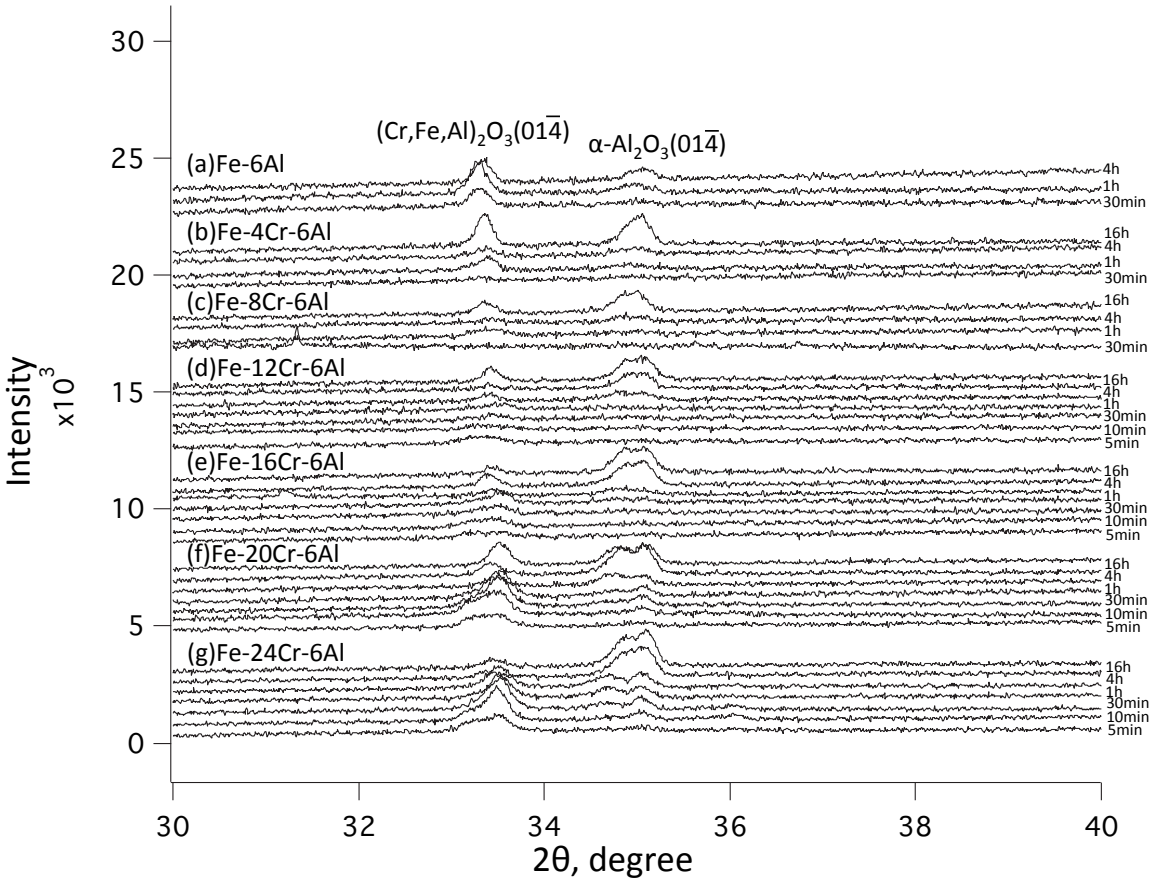

Fig.2 X-ray diffraction patterns of (a)Fe-6Al, (b)Fe-4Cr-6Al, (c)Fe-8Cr-6Al, (d) Fe-12Cr-6Al, (e) Fe-16Cr-6Al, (f) Fe-20Cr-6Al, (g) Fe-24Cr-6Al after oxidation for each time at 1000°C in air

4. CONCLUSION

The properties of initially formed oxide scales were found to have strong dependence on alloy Cr content due to formation of different $(Cr,Fe,Al)_2O_3$ oxide solid solutions. Formation and growth of Al_2O_3 scale was found to depend on this $(Cr,Fe,Al)_2O_3$ scale. Higher Cr content in alloys promoted the formation of Al_2O_3 scale because of decreasing Fe_2O_3 content in $(Cr,Fe,Al)_2O_3$, but the Al_2O_3 parabolic rate constant increased due to the higher Cr content in Al_2O_3.

References

[1] H.Hindam and D.P.Whittle, Oxid. Met., **18** (1982), 245.
[2] X.J. Zhang, S.Y.Wang, F.Gesmundo and Y.Niu, Oxid. Met., **65** (2006), 151.
[3] Y.Niu, S.Wang, F.Gao, Z.G. Zhang, F.Gesmundo, Corros.Sci., **50** (2008), 345.
[4] C.S. Giggins and F.S. Pettit, J.Electrochem. Soc., **118** (1971), 1782.
[5] Y. Niu, X.J. Zhang, Y. Wu and F. Gesmondo, Corros.Sci., **48** (2006), 4020.
[6] P. Tomaszewicz and G.R. Wallwork, Oxid. Met., **20** (1983), 75.
[7] F.H.Stott, G.C. Wood and J. Stringer, Oxid. Met., **44** (1995), 113.
[8] Z.G. Zhang, F. Gesmondo, P.Y. Hou and Y. Niu, Corros.Sci., **48** (2006), 741.
[9] E.Airiskallio, E.Nurmi, M.H.Heinonen, I.J.Väyrynen, K.Kokko, M.Ropo, M.P.J.Punkkinen, H. Pitkänen, M.Alatalo, J.Kollár, B.Johansson and L.Vitos, Corros.Sci., **52** (2010), 3394.
[10] M.P.Brady, P.F.Tortorelli and K.L.More, Oxid. Met., **74** (2010), 1.
[11] C. Wagner, Corros.Sci., **5** (1965), 751.

Exposures in a waste-fired CFB boiler vs. laboratory exposures of a FeCrAl alloy at 600 °C - the influence of alkali salt

N. Israelsson [(1,*)], K.A Unocic [(2)], J-E. Svensson [(1)] and L-G. Johansson [(1)]

[(1)] The Swedish Competence Centre for High Temperature Corrosion, Department of Environmental Inorganic Chemistry, Chalmers University of Technology, SE-412 96 Göteborg, Sweden

[(2)] Materials Science & Technology Division, Oak Ridge National Laboratory, P.O. Box 2008, Oak Ridge, TN 37831-6156, USA

e-mail: niklas.israelsson@chalmers.se & niklas.israelsson@gmail.com

1. INTRODUCTION

The corrosive environment in biomass- and waste-fired boilers has been known for several years. The traditionally used FeCr and FeNiCr steels show limited performance in the aggressive environment that contains more water vapor and alkali salts than traditional fuel [1-4]. A more sustainable material is needed to satisfy the constant strive for higher operating temperatures and increased component life time. FeCrAl alloys are well-known for their good oxidation resistance at elevated temperatures and might be a suitable candidate. When exposed to higher temperatures FeCrAl alloys form an alumina scale on the alloy surface which has better protective properties compared to chromia. This study investigates a simplified combustion environment in well controlled laboratory exposures which is compared to exposures in a real waste-fired CFB boiler. The main focus has been the influence of alkali salt and water vapor on an as delivered FeCrAl alloy at 600 °C in an oxidizing environment. The effect of pre-oxidizing the material prior to exposure was also investigated.

2. EXPERIMENTAL

The rapidly solidified powder material Kanthal® APMT with nominal composition given in Table 1 was investigated in this study. Polished samples was exposed isothermally in a tube furnace in 5% O_2 + 40% H_2O + 55% N_2 in the presence of KCl at 600 °C for up to 168 hours. 0.1-0.2 mg/cm^2 KCl was added to the sample surface prior to exposure.

Table 1. Chemical composition of Kanthal® APMT

Element	Cr	Al	Mo	Mn	Si	C	Fe	RE
wt. %	21.0	5.0	3.0	≤0.4	≤0.7	≤0.08	bal.	Y, Zr, Hf, Ti

The alloy was also pre-oxidized at 1100 °C for 24 hours in 5% O_2 + 95% N_2 prior to the salt containing exposures. The pre-oxidation resulted in a 1.5 µm dense α-alumina scale (Fig. 1). These samples were exposed several 24 hour cycles with KCl at 600 °C in order to investigate the protective nature of the formed alumina scale. The samples were investigated using gravimetry, IC, XRD, SEM/EDX, TEM/EDS.

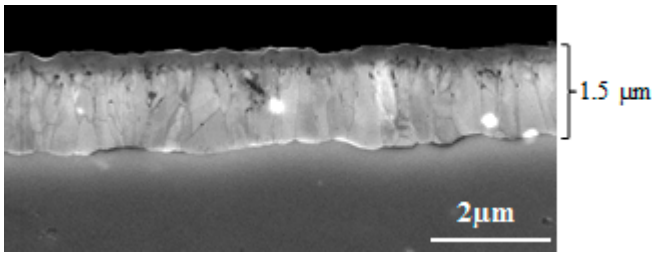

Figure 1. SE-SEM image of a cross-section of the alumina scale formed during the pre-oxidation.

Exposures were also performed in a 75 MW waste fired CFB boiler in order to validate the laboratory results. Air cooled corrosion probes were used and the temperature was set to 600 °C. The FeCrAl alloy was exposed as delivered and pre-oxidized for 1100 °C for 24 hours similar as in the laboratory experiments. The corrosion probe was exposed in the boiler for 24, 400 and 1000 hours. The samples from the probe tests were investigated by measuring the thickness before and after exposure, XRD of the deposit, SEM/EDX of sample cross sections.

3. RESULTS AND DISCUSSION

The laboratory exposures show that KCl accelerates the corrosion on the as delivered FeCrAl alloy (without pre-oxidation) and that a rapidly growing iron-rich oxide forms inward and outward relative to the initial surface. With time a chromium rich oxide forms at the metal/oxide interface. Chromate formation is believed to initiate the rapid formation of the non-protective iron oxide scale.

The alumina scale formed during the pre-oxidation greatly reduces the corrosion attack. The alumina scale fails after a three 24 hour cycles at 600 °C in the presence of KCl. The attack starts locally, often at edges and corners and then spreads over the surface (Figs. 2 and 3).

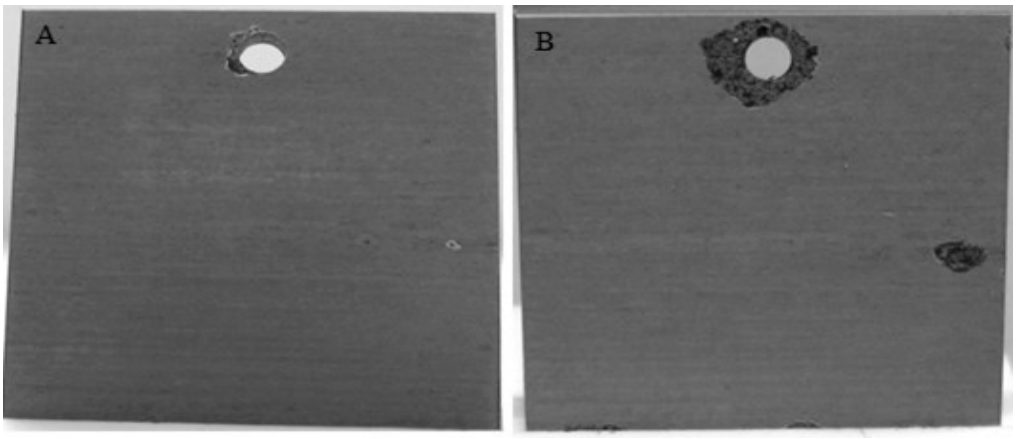

Figure 2. Pre-oxidized sample exposed for 3 cycles (A) and 4 cycles (B) at 600 °C in the presence of KCl.

The alumina scale in the vicinity of the cracks and spalled areas in Figure 3 are still considered protective at this stage.

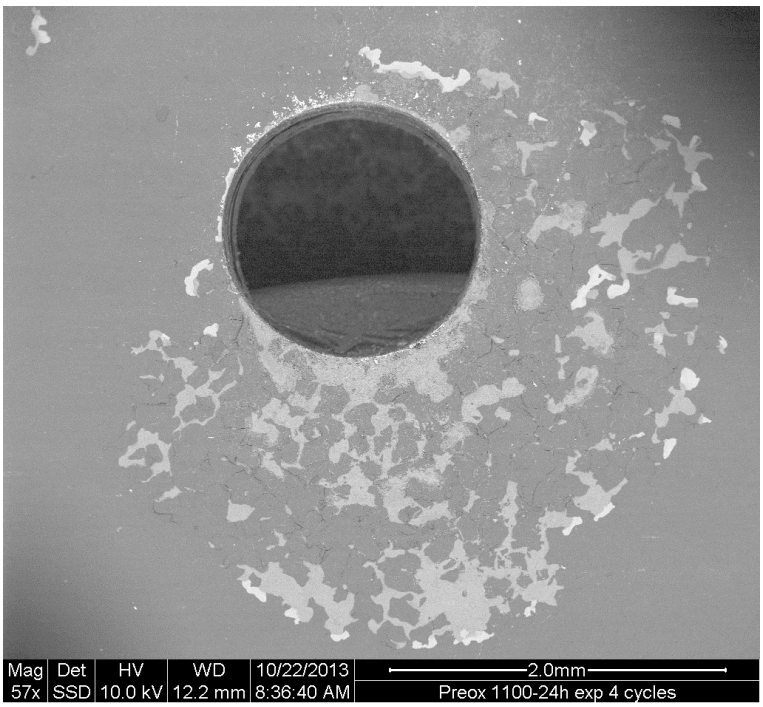

Figure 3. BSE-SEM top view image of pre-oxidized sample exposed for 4 cycles at 600 °C in the presence of KCl. A spalled area which originates from the hole.

The exposures from the CFB boiler shows similar results as the laboratory results, that the protective alumina scale fails with time (see Fig. 4). The alumina scale has detached from the alloy surface and an iron chromium rich oxide has formed due to the cracks in the alumina scale.

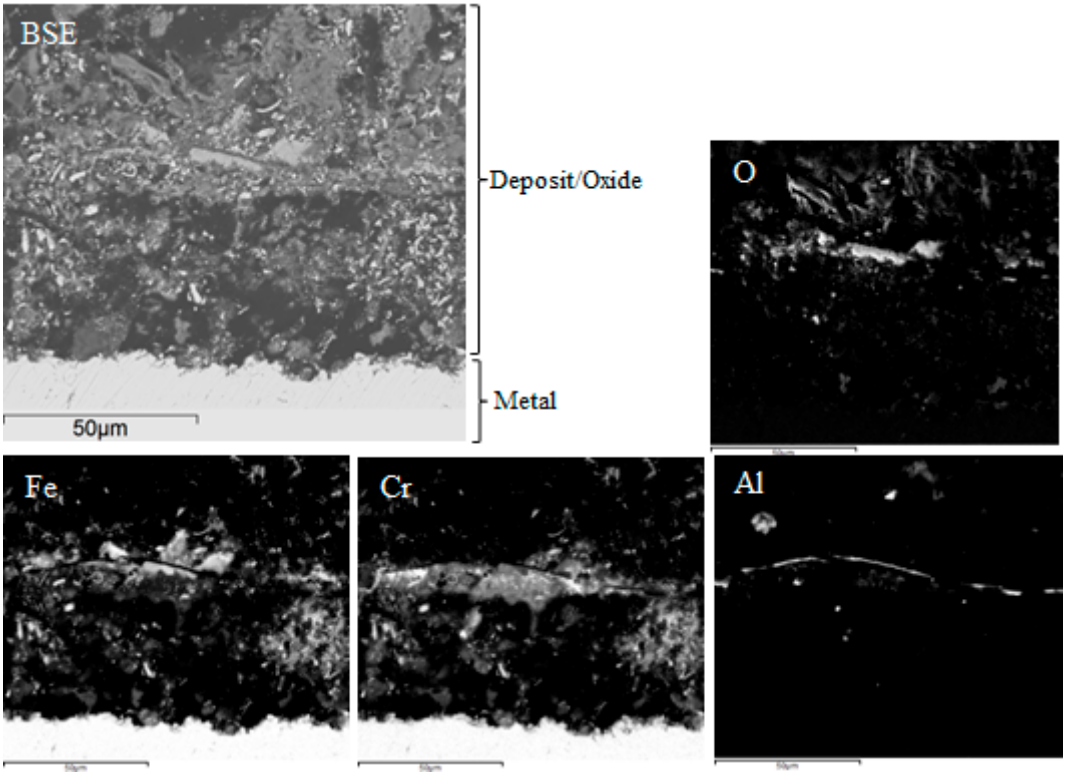

Figure 4. BSE-SEM image and elemental maps of pre-oxidized sample exposed in a waste fired boiler at 600 °C for 24 hours.

4. CONCLUSION

- KCl strongly accelerates the corrosion of the as delivered FeCrAl alloy in $O_2 + H_2O$ at 600 °C. Chromia in the scale reacts rapidly with $O_2 + H_2O$ forming K_2CrO_4 and gaseous HCl. Chromate formation depletes the protective scale in Cr, triggering the formation of a fast-growing iron-rich scale.
- The alumina scale from the pre-oxidation is considered protective as long as no defects are present in the scale and no cracks are formed during/between the exposures e.g. due to the mismatch in thermal expansion coefficients between scale and alloy that occurred during cooling between the exposure cycles.
- Both the laboratory and boiler exposures show that it is problematic to form a perfectly protective alumina scale that withstands the aggressive environment.
- If the alumina scale fails iron chromium rich oxide is formed similar to the one formed without pre-oxidation.

Acknowledgements

Microscopy Research was supported by the Center for Nanophase Materials Sciences (CNMS), which is sponsored by the Scientific User Facilities Division, Office of Basic Energy Sciences, U.S. Department of Energy.

References

[1] Michelsen, H.P., “Deposition and high temperature corrosion in a 10 MW straw fired boiler,” Fuel Processing Technology, Vol. 54 (1998), pp. 95-108.
[2] Sander, B., “Properties of danish biofuels and the requirements for power production,” Biomass and Bioenergy, Vol.12, No. 3 (1997), pp. 177-183.
[3] Bain, R. L., “Biomass-fired power generation,” Fuel Processing Technology, Vol. 54, No. 1-3 (1998), pp. 1-16.
[4] Viklund, P., “Corrosion of superheater materials in a waste-to-energy plant,” Fuel Processing Technology, Vol. 105, No. 0 (2013), pp. 106-112.

Investigation of the initial stages of the halogen effect in TiAl oxidation

H.-E. Zschau, S. Friedle, M.Schütze*

DECHEMA-Forschungsinstitut, Theodor-Heuss-Allee 25, 60486 Frankfurt am Main, GERMANY

e-mail: schuetze@dechema.de

1. INTRODUCTION

Nearly two decades ago, the beneficial effect of small concentrations of halogens on the oxidation behavior of γ-titanium aluminide (TiAl) alloys was discovered [1,2]. Of all the halogen elements, fluorine provides the most reliable protection [3]. Therefore, several fluorination methods to increase the oxidation protection of technical TiAl alloys up to temperatures of 1050°C have been developed by our laboratory [4]. Since its discovery, the mechanism of this so-called "halogen effect" has been subject of intense research. Until today, however, the mechanistic details are not completely understood for the initial oxidation stages and during heating-up. In order to gain further understanding, short-term oxidation experiments were conducted at different temperatures.

2. EXPERIMENTAL

Samples of cast γ-TiAl (Ti-50 at.% Al) were prepared in the form of coupons (10x10x1 mm^3) and polished with SiC paper down to 4000 grit. Fluorine ion implantation with a fluence of 2 x 10^{17} F cm^{-2}/20 keV was performed on one side of the sample using a 60 keV ion implanter at the Goethe-University of Frankfurt. The corresponding F-depth profiles displayed in Fig. 1 (plot c), calculated with the Monte Carlo simulation software T-DYN [5], showed a maximum F-concentration of 42 at.% for the projected range of 35 nm before oxidation. These samples were then heated under lab air up to 500, 700, 800 and 900°C, respectively, followed by an isothermal oxidation step of 1 h. Additional samples denoted by 0h/900°C were instantly removed from the furnace after reaching a temperature of 900°C. The element depth profiles of F, O, Ti, and Al were determined by non-destructive ion beam analysis methods [6]. Fluorine was measured by proton-induced gamma-ray emission (PIGE) and Ti, Al, and O by Rutherford-backscattering spectrometry (RBS) at the 7 MV and 2 MV Van de Graff – accelerators of the Goethe-University in Frankfurt. The RBS-spectra were deconvoluted by using the software codes RUMP [7] and SIMNRA [8]. He-ions of 2.03 and 3.53 MeV served as incidence particles for RBS, whereby the PIGE measurements were performed by using the nuclear reaction $^{19}F(p, \alpha\gamma)^{16}O$ at proton resonances of 430 keV and 484 keV.

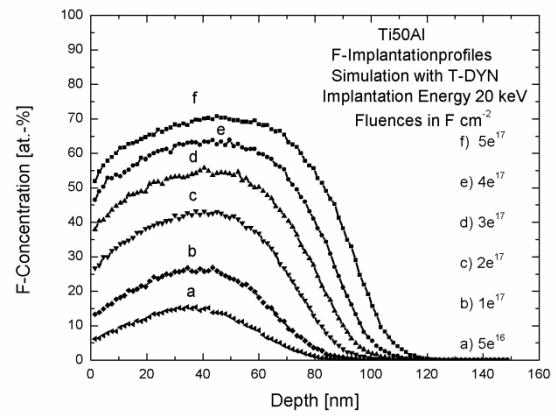

Fig. 1. F-implantation profiles in γ-TiAl calculated with the Monte Carlo simulation software T-DYN [5].

3. RESULTS AND DISCUSSION

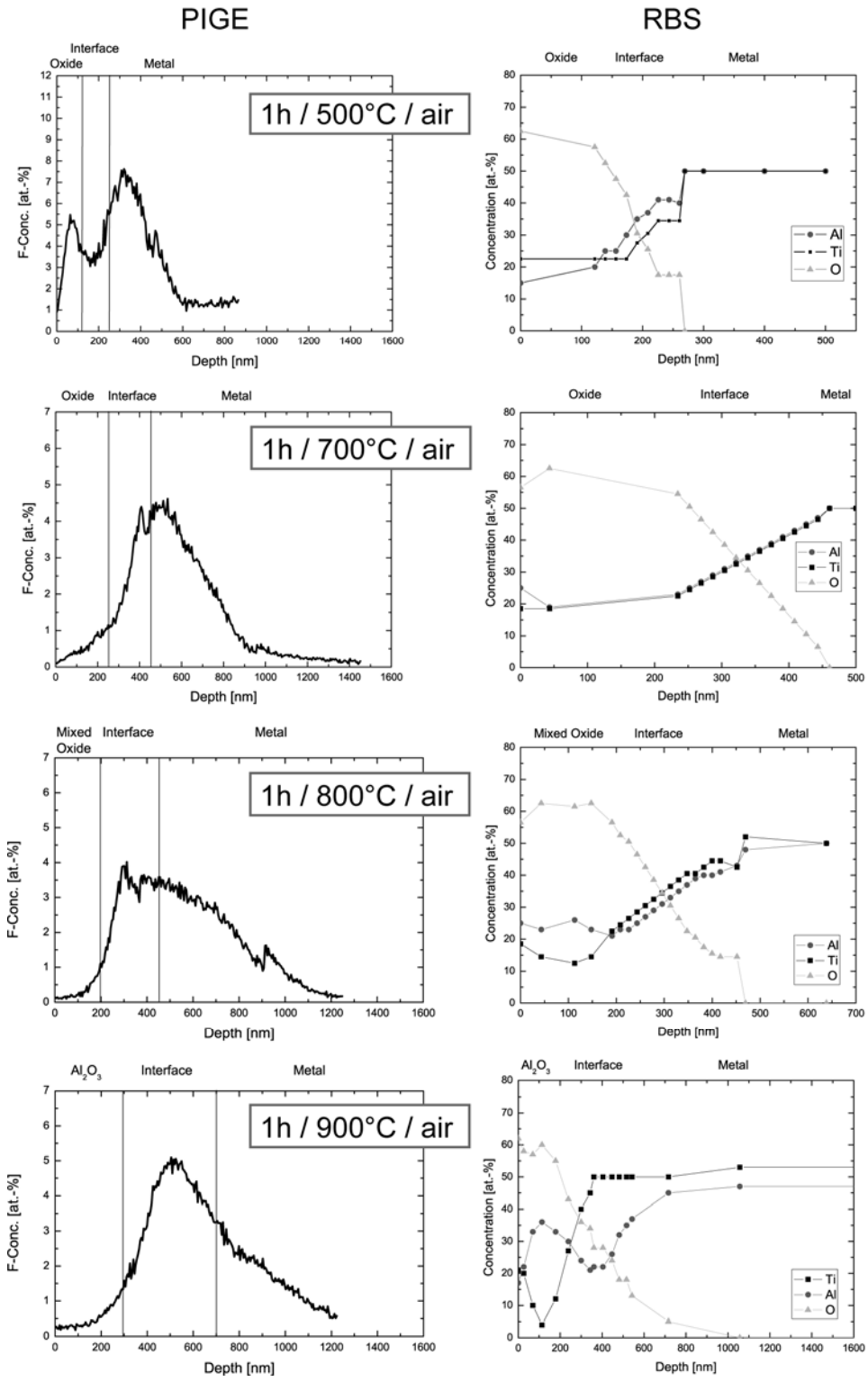

Fig. 2. Fluorine profiles (left) determined by PIGE and Ti, Al, and O-profiles (right) determined by RBS of fluorinated γ-TiAl samples, which were heated for 1h in lab air at different temperatures (as indicated). The fluence was $2*10^{-17}$ F cm^{-2}/20 keV for each sample.

The depth profiles of F, O, Al and Ti after heating to 500, 700, 800, and 900°C for 1 hour are illustrated in Fig. 2. All samples reveal a similar fluorine dose, determined by PIGE, of about 4–7.5 at.%. Except for the sample heated at 500 °C the maximum fluorine concentration lies in the region of the oxide/metal interface, as indicated by vertical lines. The

oxide thickness and composition was determined by RBS-measurements, which differ significantly after oxidation at these different temperatures. At lower temperatures of 500 and 700°C, thin mixed oxide scales of alumina and titania were detected by RBS measurements, revealing thicknesses of about 120 and 250 nm, respectively. The metal/oxide-interface reaches a width of about 250 and 450 nm, respectively. At 800°C, the Al-concentration profile within the oxide scale of 200 nm thickness reveals the beginning of selective alumina formation in this first hour of oxidation. The formation of a distinct alumina scale can be observed only at 900°C, including an Al-depleted zone beneath the oxide layer. In contrast to the other samples, in the 500°C sample, there is still a significant fluorine concentration profile located within the oxide together with fluorine in the metal subsurface zone from implantation, while at the higher temperatures fluorine is only present at the oxide/metal interface and inside the metal subsurface zone. From this observation and the fact that, with the exception of the 900 °C specimen, all other oxide scales consisted of a mixture of titanium oxide and aluminum oxide, it can be concluded that the halogen effect does not yet become fully effective during heating up but rather after a certain time at temperature. Only at 800 °C a first tendency of the formation of an oxide scale containing a higher amount of aluminum oxide can be observed, indicating that the time and temperature history of the heating phase has reached a point where the beginning of an active beneficial fluorine effect seems to become possible.

The conclusion that the beneficial halogen effect does not become effective from the very beginning of oxidation is confirmed by first results covering only the heating period as shown in Figs. 3 and 4. Here the surface scale is still largely dominated by a fluoride species (most probably a titanium fluoride species as only this one would be stable at higher oxygen partial pressures like in air). The O-profile could not be reliably determined in this measurement as the energy was too low, but it can be expected that besides the metal fluoride also aluminum oxide and titanium oxide nuclei are present in this very initial phase of oxidation. This would correspond to the common understanding that all thermodynamically stable phases exist side by side in this initial phase of the oxidation process. Further clarification of this mechanism is a subject of current investigations at our laboratory.

As the results of this work indicate, the beneficial fluorine effect only becomes active once a situation as described in the existing model for oxide growth of an existing scale has been established [9]. This situation requires a closed oxide scale and an enrichment of the halogen in the area of the oxide/metal interface. Both requirements are only fulfilled after a certain exposure time at temperature. As other results show, the temperature does not necessarily have to be as high as 900°C (ref), but it can be expected that this situation is reached the earlier, the higher the final oxidation temperature is.

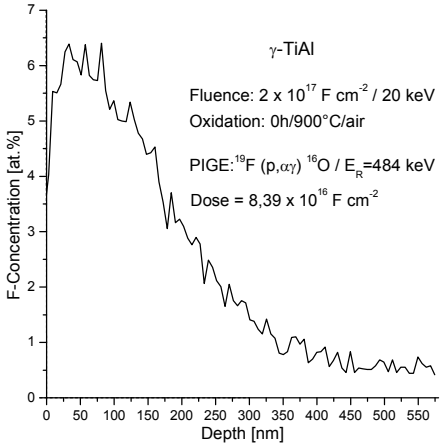

Fig. 3. Fluorine profile after 0h/900°C**.**

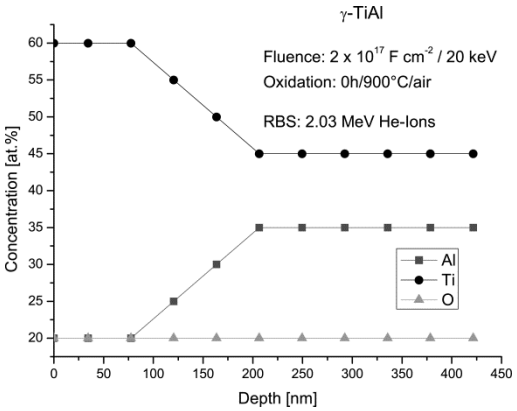

Fig. 4. O, Al, Ti-profiles after 0h/900°C.

4. CONCLUSIONS

From the present investigations it is concluded that the beneficial halogen effect in the oxidation of intermetallic titanium aluminide alloys does not yet become effective in the initial stages of oxidation, e.g. during heating up or in the very first moments at temperature. Rather a situation as described in the model for the “maintenance phase” of this effect (i.e. for an already existing oxide scale) has to be established by the initial oxidation process leading to a closed oxide scale and an enrichment of the halogen at the metal/oxide interface [9]. In the present paper this observation was made for the example of fluorine, but it is expected that a similar behavior would be found also for other halogens.

Acknowledgements
The work has been funded to a large extent by the Deutsche Forschungsgemeinschaft (DFG), which is gratefully acknowledged by the authors.

References
[1] M. Kumagai, K. Shibue, M.-S. Kim and M. Yonemitsu, "Influence of chlorine on the oxidation behavior of TiAl-Mn intermetallic compound" *Intermetallics*, Vol.4 (1996), p.557-566.
[2] M. Schütze, M. Hald, "Improvement of the oxidation resistance of TiAl alloys by using the chlorine effect" *Mater. Sci. Eng. A* Vol. 239-240 (1997), pp. 847-858.
[3] A. Donchev, M. Schütze, "Cyclic oxidation behaviour of halogen implanted Ti-46.5Al-4(Cr, Nb, Ta, B)" *Mat. Sci. Forum*, Vol. 461-464 (2004), pp. 447-454.
[4] A. Donchev, M. Schütze, W. Möller, M. Schütze, R. Yankov, "The Fluorine Effect for High Temperature Oxidation Protection of TiAl-Alloys for Automotive and Aero-Engine Applications" *Structural Aluminides for Elevated Temperatures: Proceedings of the TMS Annual Meeting*, Y. W. Kim, D. Morris, R. Yang, C. Leyens (Eds.) TMS-Warrendale (2008), pp. 323-332.
[5] J. Biersack (1999) "TRIM-DYNAMIC applied to marker broadening and SIMS dept profiling" *Nucl. Instr. & Meth. Phyics. Research*, Vol. B 153 (1999), pp. 398-409.
[6] J. R. Tesmer, M. Nastasi, *Handbook of Modern Ion Beam Materials Analysis, Materials Research Society*, Pittsburgh (1995), PA, USA.
[7] L. R. Doolittle, *Nucl. Instr. & Meth. In Phys. Res. B9* (1985) p. 334.
[8] M. Mayer, MPI f. Plasmaphysik, Garching.
[9] A. Donchev, B. Gleeson, M. Schütze, "Thermodynamic considerations of the beneficial effect of halogens on the oxidation resistance of TiAl-based alloys" *Intermetallics*, Vol. 11, No. 5 (2003), pp. 387-398.

Comparison between the oxidation kinetics of two high temperature titanium alloys Ti-6Al-2Sn-4Zr-2Mo (**Ti-6-2-4-2) and** Ti-15Mo-3Nb-3Al-0.4Si **(beta-21S) in relation with their microstructure and ductility**

Aurélie Rouaix-Vande Put [(1)], Carole Thouron [(1)], Philippe Emile [(2)], Raphaëlle Peraldi [(2)] and Daniel Monceau [(1)]

[(1)] CIRIMAT, University of Toulouse, ENSIACET, 4 Allée Emile Monso, BP 44362, 31030 Toulouse Cedex 4, FRANCE
[(2)] AIRBUS, Toulouse, FRANCE

e-mail: daniel.monceau@ensiacet.fr, aurelie.rouaix@ensiacet.fr, carole.thouron@ensiacet.fr; philippe.emile@airbus.com; raphaelle.peraldi@airbus.com

1. INTRODUCTION

With the constant increase in operating temperatures of aircraft engines, materials have to resist to more severe oxidizing conditions while maintaining good mechanical properties. Keeping suitable mechanical properties after a long time spent at high temperature in an oxidizing environment is an issue for Ti-base alloys. Large oxygen content under the oxide scale with oxygen diffusion into the alloy leads to the formation of an oxygen-rich, hard and brittle layer, which is detrimental to the mechanical behavior. Two "high temperature" commercial Ti-base alloys were selected as potential materials to build aircraft parts located next to the engines. The oxidation kinetics of these Ti6242 and β21s alloys were studied by carrying out isothermal and cyclic oxidation tests in air at 500-625°C for up to 10 kh. The oxide layer and the depth of the oxygen enriched layer under the oxide scale were characterized and samples aged in similar conditions were mechanically tested at room temperature. This was done in order to determine the kinetics of degradation of the alloys, and also to understand the effects of alloy composition and microstructure on this phenomenon.

2. EXPERIMENTAL

The oxidation of two commercial high temperature Ti-base alloys -Ti6242 and β21S- were studied by carrying out isothermal oxidation tests in laboratory air at 500, 560 and 625°C for up to resp. 10kh, 10kh and 6472h. Composition of the studied materials was determined by EDS, GDMS and IGA and is given in table 1. Shorter term isothermal (TGA) and cyclic thermogravimetry (CTGA) tests were also performed in flowing synthetic air. TGA was run at 500, 560, 590, 600 and 625°C for Ti6242 and at 560 and 600°C for β21S, all during 50h. CTGA was run using 15 min dwell times at 600°C, with heating rates of about 300°C/min and initial cooling rates of 70°C/min. The samples were submitted to 1596 thermal cycles in flowing synthetic air. The effect of surface finish was studied for the Ti6242 alloy during the long term oxidation in laboratory air and short term TGA using grit blasting with corundum, P80, P240, P320 grinding and mirror finish. But most experiments including the results presented in all the figures of this abstract were done with a P240 grit finish. In addition, tensile tests were performed at room temperature on specimens aged in similar conditions than the oxidation tests. Oxidized samples were characterized to determine the chemical composition and nature of phases in the oxide scale and in the alloy using metallography, X-Ray diffraction, scanning electron microscope (SEM), energy dispersive spectroscopy (EDS) and Raman spectroscopy. Microhardness analysis (Vickers, Hv) and electron microprobe (EPMA) were used to determine the thickness of the oxygen-rich layer in the alloy. SEM was used to determine the thickness of the oxide scale which was used to evaluate the mass of oxygen present in the oxide scale. The overall oxygen uptake was determined by mass variation measurements using a table top balance or thermobalances with 1 microgram precision. Ti6242 specimens were 4.0mm thick and the β21s were 1.8mm thick, except CTGA samples which were both 1.8 mm thick.

Table 1: composition of alloys (wt% and wt ppm)

	Al %	Si %	Fe %	Zr %	Nb %	Mo %	Sn %	C ppm	N ppm	O ppm	H ppm	S ppm
Ti6242	**6.3**	0.075	0.027	**3.7**	-	**1.6**	**2.0**	19	13	**850**	30	3.7
β21S	**3.2**	**0.4**	0.27	0.002	**2.6**	**14.5**	0.004	160	140	**1300**	33	1.6

3. RESULTS and DISCUSSION

Both alloys formed a TiO_2 oxide scale but with varying microstructures and varying proportion of rutile and anatase phases as shown by Raman spectroscopy. At 625°C, some alpha-alumina was also detected by fluorescence in the Raman microscope. The proportion of anatase and rutile was studied as a function of the alloy, and of the oxidation temperature and duration. It was shown that the increase in temperature favored the rutile phase and that more anatase was observed on the β21S alloy than on the Ti6242 alloy. This observation was correlated with the density of oxide whiskers which also increased with time and temperature, and which was larger on the Ti6242 alloy (Fig.1). After thousands of hours at 625°C, it was also observed that the oxide scale formed on the β21S alloy was "leaf shaped", i.e. was fractured parallel to the sample surface, as often observed for pure titanium oxidation [1]. Ti6242 did not show this feature (Fig.1).

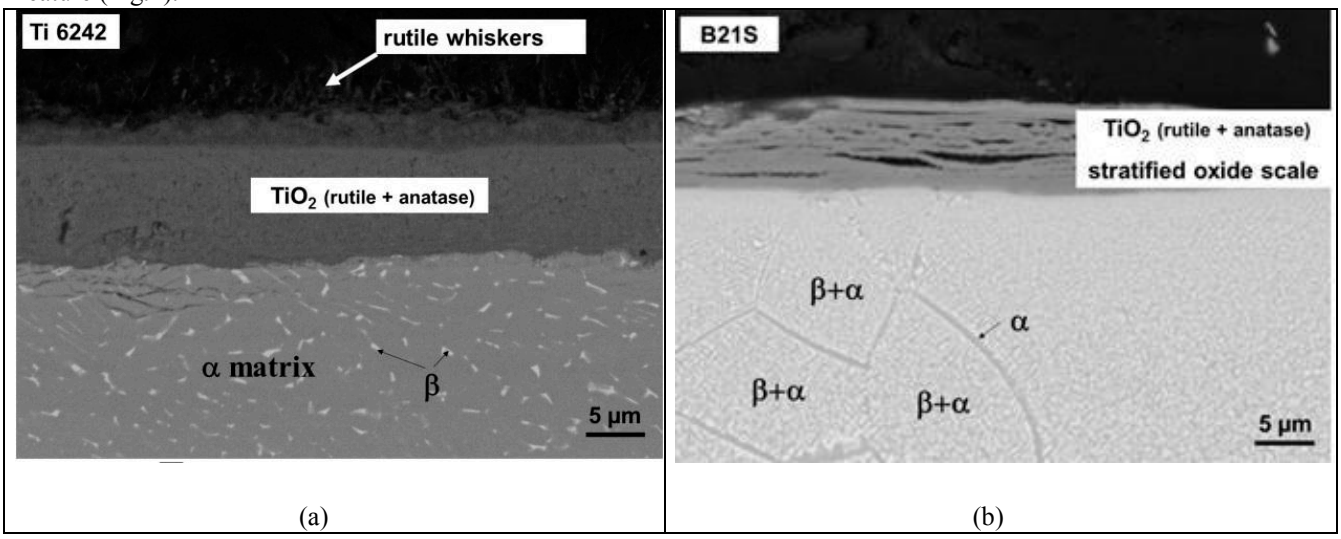

Figure 1: Microstructure of alloys Ti6242 (Fig1a) and β21s (Fig1b) after oxidation in lab air during 5951h at 625°C

The kinetics of mass gain of the two alloys were different for the two alloys (Fig.2). These differences varied with temperature and were discussed considering both the external scale formation and the oxygen diffusion in the alloy. For example, for durations longer than 1000h at 625°C, the mass gain of Ti6242 was larger than for β21S despite a thinner oxide scale. This was explained by the large proportion of the oxygen uptake which was due to dissolution in the metal and which was larger in the alpha+beta Ti6242 alloy than in the beta β21S alloy, because of the higher oxygen solubility in the alpha phase than in the beta phase [1]. As a consequence, the mass gain alone was not sufficient to characterize the depth of the oxygen-enriched layer which is a major concern for the alloy final user because of embrittlement.

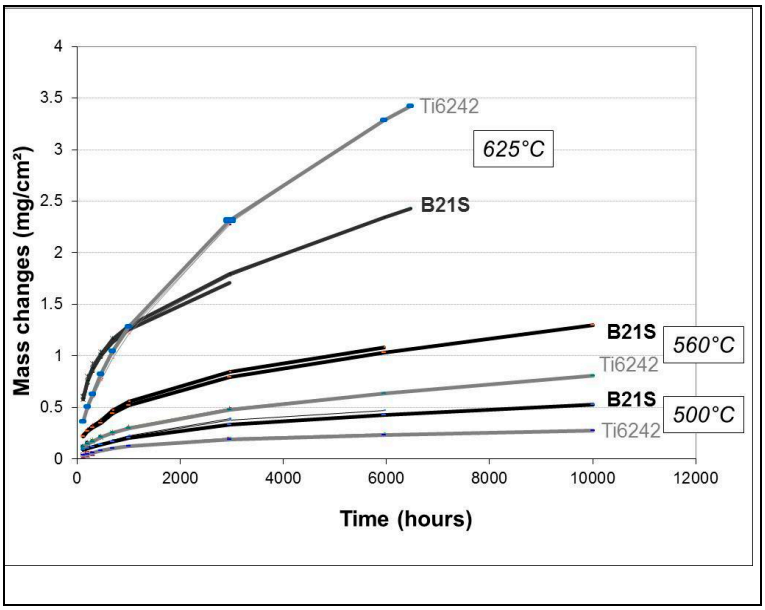

Figure 2: Oxidation kinetics at 500, 560 and 625°C in laboratory air for Ti6242 and β21s alloys

It was then necessary to perform micro-hardness profiles measurements and some microprobe analyses (EPMA) as a function of time and temperature for both alloys (Fig.3). The kinetics of growth of the "high hardness layer" was consistent with recent work from McReynolds and Tamirisakandala [2] for Ti6242 alloy.

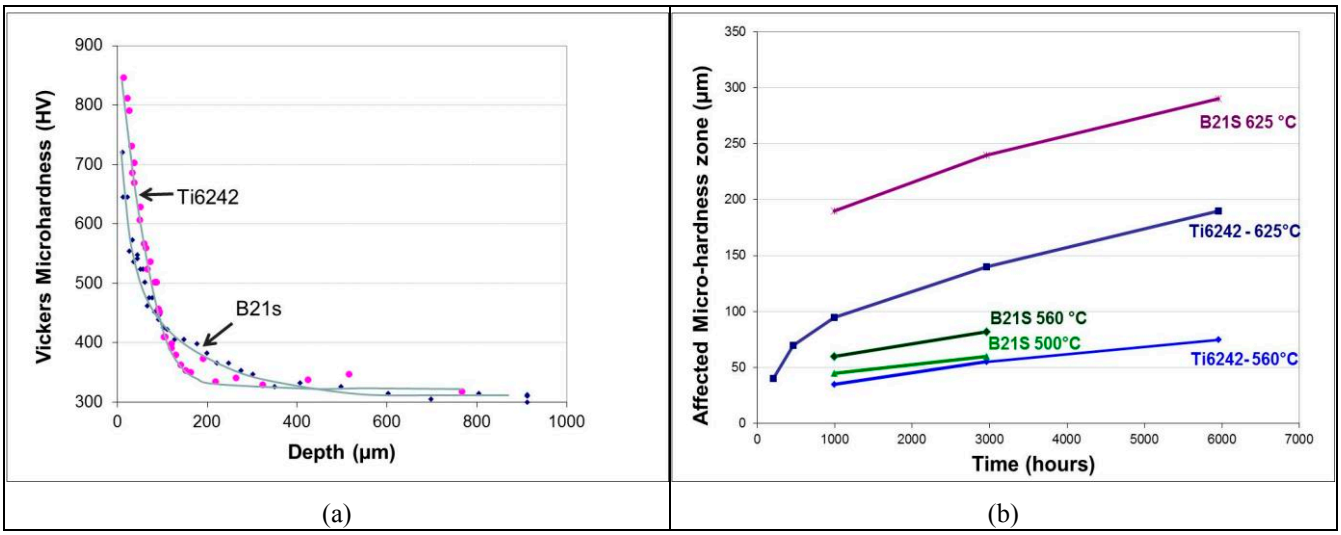

(a) (b)

Figure 3: (a) Microhardeness profiles (Hv using a 50g weight) for Ti6242 and β21S alloys after 5951h at 625°C in laboratory air, (b) kinetics of growth of the affected hardness zone for both alloys at 500-625°C.

The combination of microhardness profiles and oxygen concentration profiles allowed quantifying the kinetics of oxygen diffusion in the alloys. It was shown than at 560°C and 625°C, the microhardness affected zones were thicker for the β21S (Fig.3) despite a smaller proportion of alpha phase in this alloy. The microstructural evolution of both alloys was then characterized for several ageing times. It was seen that Ti6242 was made of a continuous matrix of alpha phase with a fraction of beta-phase precipitates decreasing with time. The β21S alloy was composed of larger grains of beta phase. But alpha phase nucleated at grain boundaries and formed a continuous path for oxygen diffusion (Fig.1) with a section increasing with time. Alpha phase also grew inside the grains. Both microstructures allowed a fast ingress of oxygen because of the percolation of the alpha phase. For some reason, the kinetics of growth of the microhardness affected layer is even faster in the β21S alloy than in the Ti6242 despite its original fully beta-phase microstructure.

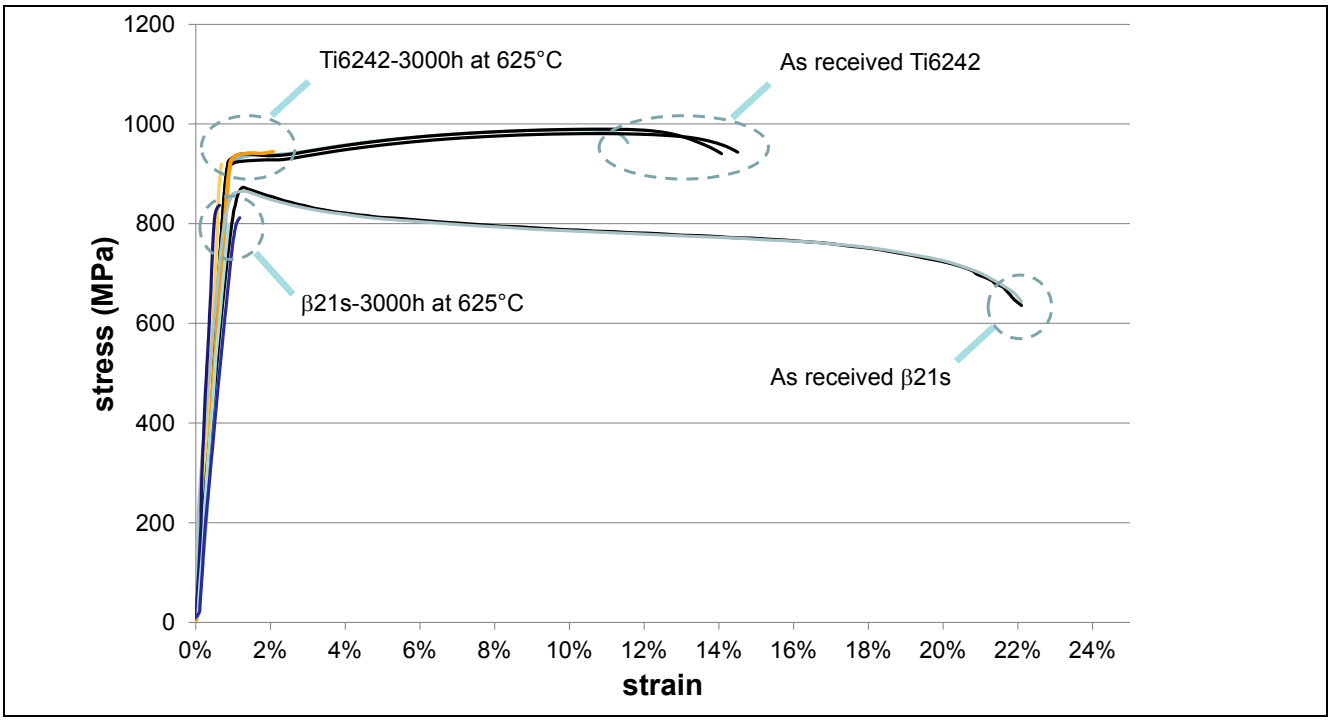

Figure 4: Mechanical testing of Ti6242 and β21s oxidized 2958h at 625°C in laboratory air.

Cyclic oxidation (CTGA) experiments showed only minor effect of thermal cycling with sparse spallation events at 600°C.
These oxidation results were compared with room temperature mechanical tests performed on pre-oxidized samples (Fig.4). The embrittlement due to oxygen was clearly evidenced for both alloys and was in good correlation with the micro-hardness affected zones. The loss of ductility was significant, e.g. from 13% (elongation at rupture) to 2% after 2958h at 625°C for the Ti6242 alloy.

Fractographies (Fig.5) revealed that the thickness of the brittle layer was well correlated with the micro hardness profiles. It was interesting to note than this thickness was about two times larger than the thickness of the "alpha-case" layer revealed after etching the Ti6242 alloy.

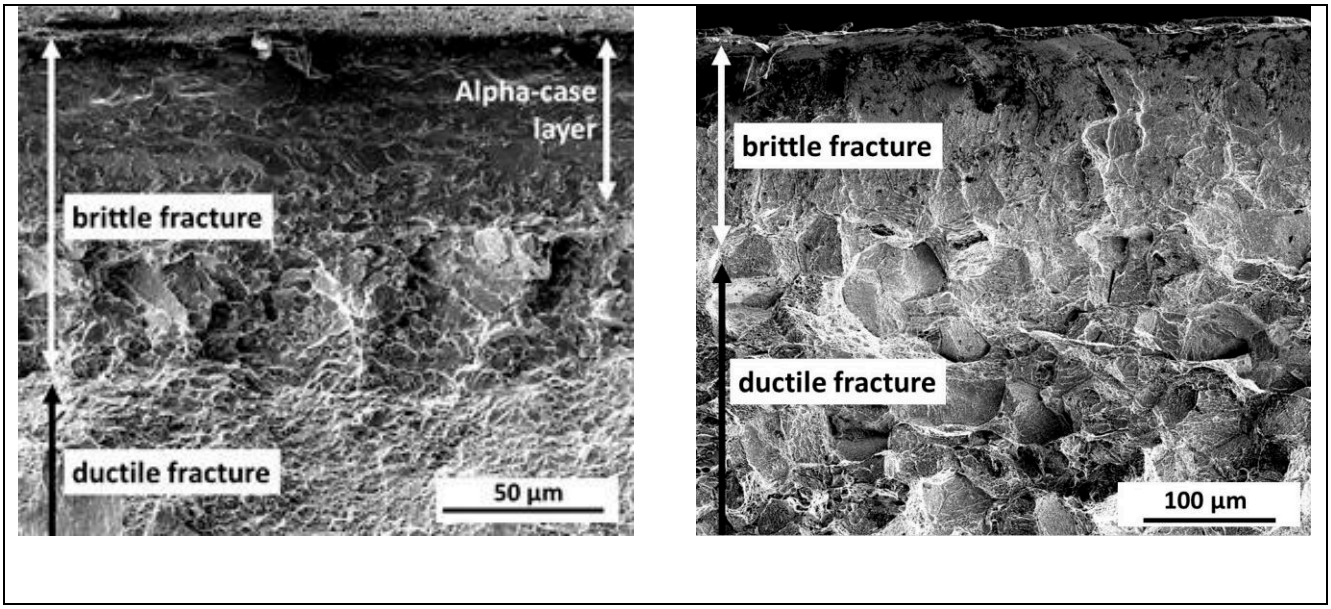

Figure 5: Fractographies of Ti6242 and β21s oxidized 2958h at 625°C in laboratory air.

4. CONCLUSION

It was shown that alloys Ti6242 and β21s experience some external oxide scale formation which should not be a problem for most structural applications up to 625°C. Nevertheless, this study confirms that they suffer from oxygen diffusion in the alloy which causes embrittlement and this could induce premature fracture in fatigue conditions. The affected zone can be a problem for millimeters thick parts used at temperatures higher than 600°C. As the beta phase dissolves much less oxygen than the alpha phase, it was expected that β21s should have a much better resistance to oxygen embrittlement, and the lowest mass gain kinetics. Nevertheless, the opposite was found in this study, the behavior of Ti6242 being superior to β21s at 625°C. The research of an explanation is under progress, but it is already clear that the morphologies of the microstructures allow oxygen to diffuse through a continuous path of the alpha phase for both alloys. This is due to the structure of the alpha/beta in the Ti6242 alloy (i.e. the continuous matrix of alpha phase) and to the alpha phase nucleation and growth at grain boundaries of the β21s alloy.

Acknowledgements,
A part of this study was performed with the financial support of AIRBUS. A special thanks to the Airbus metallic material lab in Toulouse (especially to T.Mancier for lab air oxidation experiments and A.Lepied for mechanical testing).

References

[1] Kofstad P., High temperature corrosion. London and New York, 1988.
[2] McReynolds KS, Tamirisakandala S., A Study on Alpha-Case Depth in Ti-6Al-2Sn-4Zr-2Mo. Met. Mat. Trans.A 2011;42A:1732.

Effect of minor boron addition in Ni-base superalloys on oxide scale formation in high pO_2, SO_2-containing environments

D. Naumenko [1,*], A. Jalowicka [1], W. Nowak [1], L. Singheiser [1] and W.J. Quadakkers [1]

[1] Institute for Energy and Climate Research (IEK-2), Forschungszentrum Jülich GmbH, 52425 Jülich, Germany

e-mail: d.naumenko@fz-juelich.de

1. INTRODUCTION

In order to increase the efficiency and decrease the costs of power generation, gas turbines should be able to operate using a wide range of fuels. In the future the use of alternative fuels, such as crude oil, biogas or unclean syngas will significantly increase. Many of the alternative fuels contain substantial amounts of contaminants, especially sulfur. This means that gas turbine components will be exposed to environments in which not only oxidation but also sulfidation will be an issue.

The compositions of the Ni-base superalloys have been modified significantly in recent years in order to increase creep rupture strength. Specifically, the content of Cr was decreased and the Al content increased. The latter modifications of the materials chemistry and microstructure are expected to have a significant effect on the alloy oxidation and corrosion resistance. Unfortunately there is little information on the resistance of Ni-base superalloys with 6-8 % Cr and 5-6 %Al in oxidizing-sulphidizing atmospheres without deposits. The latter conditions cannot be excluded in the case of cracking or spallation of protective coatings in the hot stages of the power generating gas-turbines. In the present work the oxidation behavior of the commercial polycrystalline Ni-base superalloy CM247 and several cast model alloys in high pO_2 SO_2-containing environment were studied.

2. EXPERIMENTAL

Commercial Ni-base alloy CM247 with nominally 9Co, 8Cr, 5.6 Al, 0.7Ti, 0.5Mo, 10 W, 3.2Ta, 1.4 Hf, 0.07C, 0.02B, 0.01Zr (wt.%) was studied. Based on preliminary studies with CM247 to study specifically the effect of boron addition on the oxidation behavior cast Ni-base model alloys were produced with the Co, Cr, Al contents similar to CM247 and B-additions varying between 0 and 0.04 wt%. The materials were exposed at 1050°C in flowing synthetic air with and without 2 vol.% SO_2 additions for between 1 and 500 hours. The oxidized materials were characterized using GD-OES, XRD and (in polished cross-sections) SEM/EDX.

3. RESULTS AND DISCUSSION

CM247 shows very low mass changes corresponding to protective oxidation when exposed up to 500 h at 1050°C in synthetic air, whereas when exposed in synthetic air with 2%SO_2 rapid breakaway failure was observed within first 200 hours (Figure 1). The failure in the SO_2-containing environment was related to the rapid sulfidation of the material beneath the oxide scale. SEM-studies of the oxide scale composition after 1-20 hours exposure times revealed that the oxide scale on CM247 contains a number of defects including nodules of oxidized primary Hf/W-carbides and HfO_2-precipitates, which apparently allowed SO_2-penetration and alloy sulfidation during transient oxidation period. The resulting Cr-sulfide formation rapidly depleted the relatively small alloy Cr-content in the near surface regions leading to breakaway oxidation. In addition GD-

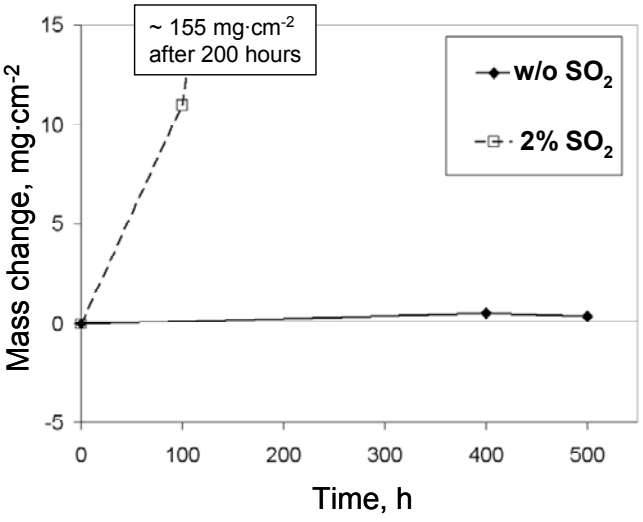

Figure 1. Mass changes of CM247 after discontinuous oxidation at 1050°C in synthetic air with and without 2vol.% SO_2 addition.

OES depth profiles on CM247 after short time exposure indicated substantial boron enrichment within the scale and in the sub-scale alloy regions (Figure 2).

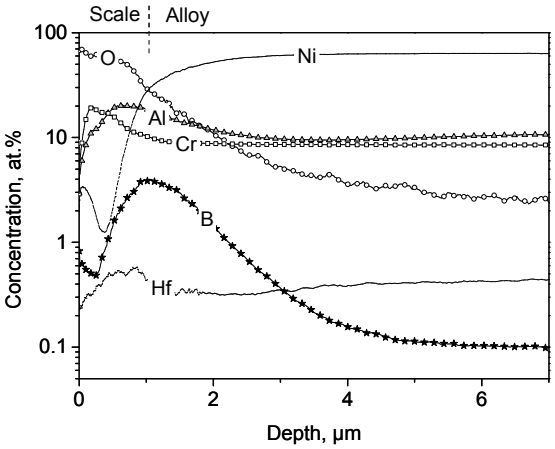

Figure 2. GD-OES elemental depth profile from CM247 after 1 h oxidation in synthetic air

In order to verify whether the boron enrichment has an effect on the oxide scale formation and/or SO_2-penetration model Ni-9Co-8Cr-5.6Al alloys with specific boron additions of 0.02 and 0.04 wt.% as well as the alloy without boron were exposed to the above mentioned atmospheres. In synthetic air the boron addition was found to locally disturb formation of the alumina rich oxide scale during transient oxidation period (1-20 hours). However, after longer exposure times (≥100 hours) the effect of boron diminished and all three model alloys formed dense alumina scales. In contrast in synthetic air with 2%SO_2 the effect of minor boron additions on the oxidation was more pronounced, namely in that the boron containing alloys did not form alumina rich surface scales at all (Figure 3). Rather Cr and B rich oxide scales prevailed and extensive internal oxidation of Al occurred in the SO_2-containing atmosphere, whereas the needle like morphology of the internal precipitates was similar to those typically observed in the Ni-Cr-Al alloys with much lower Al-contents.

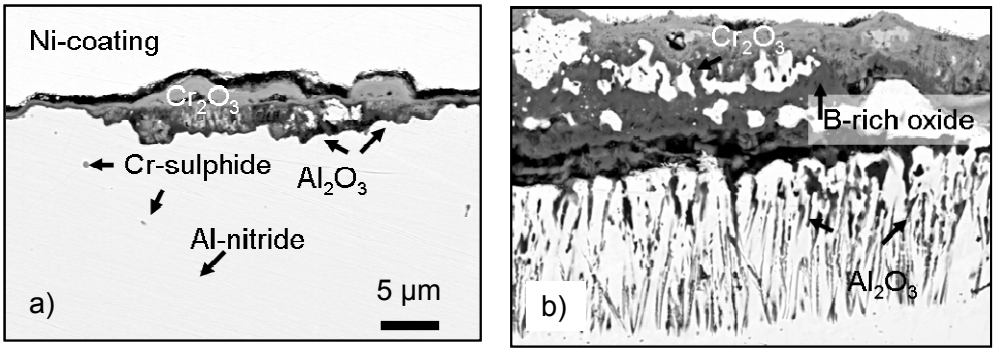

Figure 3. SEM backscattered electron images of model alloys based on Ni-9Co-8Cr-5.6Al: a) without B and b) with 400 ppm B after 1 h isothermal oxidation at 1050°C in synthetic air with 2% SO_2.

4. CONCLUSIONS

Oxidation resistance of the Ni-base superalloy CM247 at 1050°C was good in synthetic air, but catastrophic in synthetic air with 2 vol.% SO_2. This was correlated with the oxide scale composition featuring Hf-rich oxide precipitates and boron containing oxides, which allowed rapid ingress of SO_2 into the sub-scale alloy. Using model alloys the minor boron additions alone were shown to have a detrimental effect on the oxidation resistance of the Ni-base alloys, which was more pronounced in the SO_2-containing test gas.

Study of Microstructure Phenomena Occurring in the Sub-surface of Cast Carbides-strengthened Refractory Alloys during High Temperature Oxidation

Patrice Berthod [(1,*)] and Elodie Conrath [(1)]

[(1)] Institut Jean Lamour, University of Lorraine, Vandoeuvre-lès-Nancy 54506, FRANCE

e-mail: patrice.berthod@univ-lorraine.fr, elodie.conrath@univ-lorraine.fr

1. INTRODUCTION

Cast alloys and superalloys strengthened by carbides represent an important family of refractory alloys for high temperature applications [1]. The metallic elements involved in these carbides are often very sensitive to oxidation [2]. When such alloys are used in hot conditions in aggressive environments, high temperature oxidation occurring on surface may induce changes for the carbides initially present in the sub-surface [3,4]. These microstructure changes possibly modify the local refractoriness [5] and the mechanical properties in sub-surface: development (or not) of a carbide-free zone, local coarsening or nature change of the carbides initially present, precipitation of new carbides... phenomena which are different from what happens for the bulk carbides in the same time. This study focuses on the oxidation−induced phenomena encountered in their sub-surfaces by ternary Co-Cr-C, Ni-Cr-C and Fe-Cr-C alloys, as well as by more complex alloys containing also great quantities in Ta, Hf... The effect of the temperature and duration of oxidation are also studied and the phenomena interpreted using thermodynamic calculations.

2. EXPERIMENTAL

The alloys involved in this study are based on cobalt (for some of them with addition of 8 to 10wt.% Ni), on nickel or on iron. They contain 25 to 30 wt.% of chromium and carbon with various contents (between 0.2 to 2 wt.%). The carbide-former metallic elements are chromium (already present), tantalum or hafnium. The alloys were all elaborated by melting pure elements (Alfa Aesar, purity higher than 99.9%) by high induction melting (furnace CELES 300kHz) under an argon atmosphere (300millibars). Fusion, high temperature stage in the liquid state and solidification were achieved in the water-cooled copper crucible of the furnace. The obtained ingots, all of about 40g, were cut to obtain several parallelepipeds (about 10 × 10 × 3 mm^3). These ones were ground (from 240-grit SiC paper to 1200-grit final paper) with smoothing of edges and corners. These samples were isothermally exposed to synthetic dry air (80%N_2-20%O_2) in the furnace equipping a Setaram TGA92 thermobalance, at temperatures belonging to the [1000°C, 1200°C] range and for various durations [from 46-50 hours to four times these values, e.g. 184-200 hours].

After these oxidation runs, the oxidized samples were coated by gold cathodic pulverization then by electrolytic nickel deposition, to prevent oxide loss during cutting. The oxidized and coated samples were thereafter cut in two parts before cross-sections preparation: embedding in a cold resin mixture (ESCIL), grinding with SiC papers from 240 to 1200-grit, ultrasonic washing, and polishing using textile enriched with 1µm hard particles. The initial and {post-oxidation test}−microstructures of the alloys were examined using either a Philips XL30 Scanning Electrons Microscope (SEM) or a JEOL JSM 2010-LA SEM, both in Back Scattered Electrons mode (BSE). The chemical compositions were controlled by Energy Dispersion Spectrometry (EDS) apparatus equipping the SEM. Scanning electron microscopy was also used to characterize the microstructure changes in the sub-surfaces of the alloys. EDS measurements on {×250 to 1000}-magnified areas and pinpoint EDS analyses were realized respectively to specify the local chemical composition of the alloy in sub-surface and to clearly identify the carbides present in the same location.

Image analysis was performed on {×250 to 1000}-magnified SEM/BSE micrographs, using the {surface fraction}−measuring tool of the Photoshop CS software of Adobe. These data – carbides surface fractions and local alloy's chemical composition – allowed indirectly determining the local carbon content in the sub-surface of the oxidized samples by using the Thermo-Calc software [6] and an adequate database [7].

3. RESULTS AND DISCUSSION

The metallographic characterization of the sub-surfaces of the oxidized samples showed very various phenomena. This depends on the initial chemical composition and microstructure of the concerned alloy, of the temperature of the

oxidation exposure and of its duration. To expose briefly the observations done:

1°) at temperatures high enough (e.g. 1200°C) the single noticeable sub-surface phenomenon occurring during oxidation is the disappearance of the interdendritic (primary) carbides (as well as of the secondary carbides which have previously precipitated during a specific precipitation heat-treatment, if any); however, this phenomenon happens in Co-based, Ni-based and Fe-based alloys only if the initial carbides are chromium carbides or tantalum carbides for example: if they are hafnium carbides there is no disappearance of carbides (they are eventually oxidized *in situ*) and no real carbide-free zone develops; when a carbide-free zone appears and develops inwards, its progress rate decreases when the initial carbides volume fraction carbides increases (illustration in Figure 1) and this rate is higher when the oxidation temperature is higher; besides the disappearing carbides other ones more stable may remain not concerned by such disappearance, as the HfC carbides staying in the carbide-free zone when the chromium carbides are disappearing, as illustrated by Figure 2 in the case of an iron-based alloy containing initially hafnium carbides and chromium carbides;

2°) at temperatures between 1100 and 1000°C, a carbide-free zone also develops (if the carbides are not too stable as the HfC ones for example) but slower; as at 1200°C the metallic atoms released by the carbides decomposition diffuse towards the oxidation front (to form Cr_2O_3 if there are chromium atoms, Ta_2O_5 or $CrTaO_4$ if they are TaC carbides). It appears that it is, in contrast, not necessarily the case of the carbon atoms: if these ones diffuse towards the oxidation front at very high temperature, at temperatures around 1050°C they tend to diffuse inwards, partly or totally, and the carbon enrichment resulting locally in an intermediate region separating the developing carbide-free zone and the bulk, leads either to the transformation of the local chromium carbides into carbon-richer ones (e.g. $Cr_{23}C_6$ becoming Cr_7C_3, Figure 3) or to the precipitation of new carbides (of chromium and/or of tantalum if Ta is present in solid solution, as illustrated in Figure 4).

When an intermediate zone in which there is either an obvious change of the stoichiometry of the present chromium carbides for a carbon-richer one, or a coarsening of the present carbides resulting in an increase in their fraction at constant stoichiometry (without or with a precipitation of additional carbides), image analysis allow determining the new local surface (and then volume fraction) of carbides. Knowing their natures by SEM/EDS or Microprobe/Wavelength Dispersion Spectrometry (EPMA/WDS) pinpoint measurement and then their volume masses, their volume fraction may be converted in mass fraction. Multiple thermodynamic calculations performed successively for the measured local alloy chemical composition (determined by EDS for example) and for the oxidation temperature, by varying the carbon content until the calculated mass fraction reaches the one issued from the volume fraction measured by image analysis, allow deducing what is the local carbon content. It appears then that the whole additional carbon, or only a part, came from the carbide-free zone in which the carbon content has necessarily become extremely low (maximal possible contents allowing the absence of carbides, determined by thermodynamic calculations too).

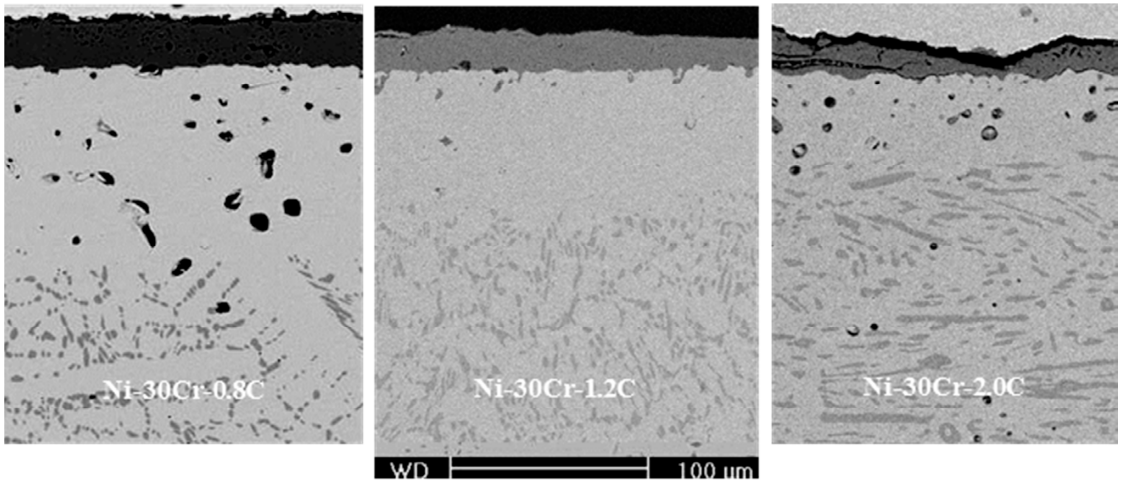

Fig. 1. Disappearance, during 50 hours of oxidation at very high temperature (1200°C), of the chromium carbides initially present in the sub-surface; decrease of the depth of this carbide-free zone when the initial carbides density increases (for carbon contents increasing from 0.8 to 2 wt.%C in these {Ni, 30wt.%Cr}−based ternary alloys)

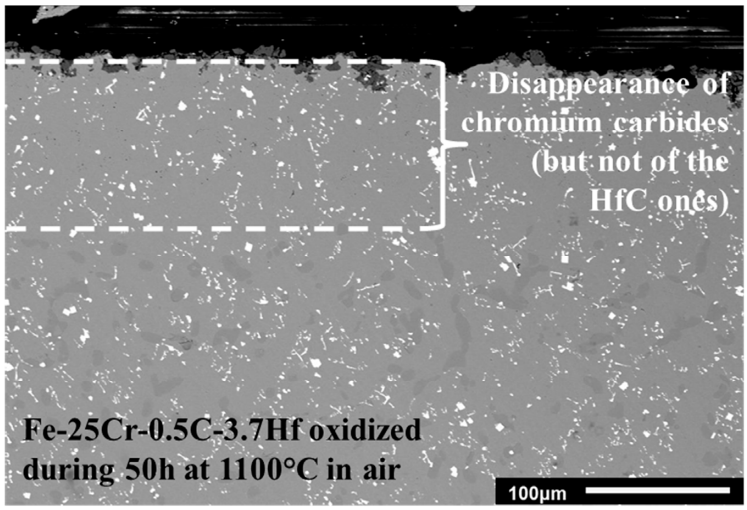

Fig. 2. SEM/BSE micrograph (Fe-25Cr-0.5C-3.7Hf alloy, 50h at 1100°C) illustrating the development of a carbide-free zone in which only one type of carbides out of the two present ones disappeared (the dark chromium carbides): the too stable HfC carbides (white) are not subjected to disappearance

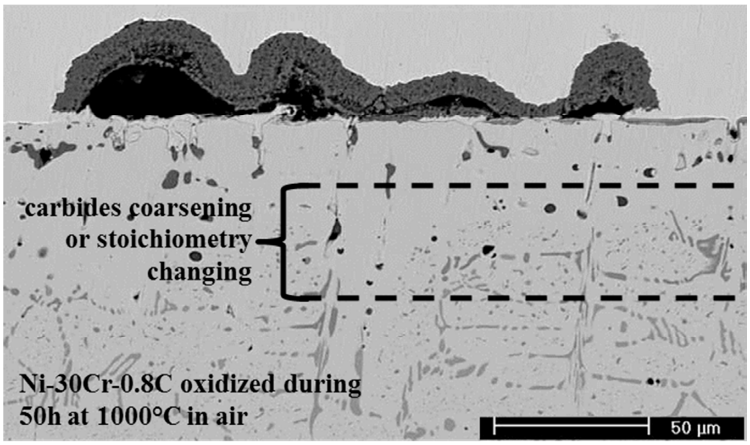

Fig. 3. SEM/BSE micrograph (Ni-30Cr-0.8C alloy, 50h at 1000°C): coarsening (or stoichiometry change), during oxidation at medium temperature (1000°C) in an intermediate region separating the carbide-free zone and the bulk

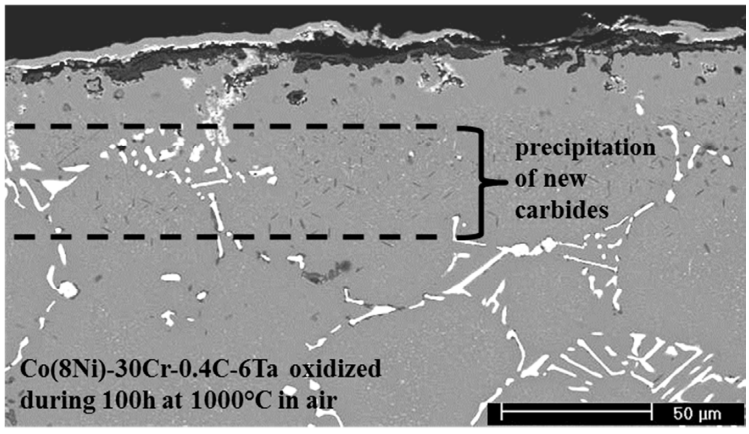

Fig. 4. SEM/BSE micrograph (Co-30Cr-0.4C-6Ta alloy, 100h at 1000°C): precipitation of new fine acicular chromium carbides (black) and fine compact TaC carbides (white) in an intermediate region separating the carbide-free zone and the bulk

Furthermore, oxidation tests performed on an alloy containing chromium carbides, at temperatures included in the [1000, 1100°C] range and during different times, show that the carbide-free zone is more extended and the intermediate zone is deeper in the alloy and richer in carbon when the duration is longer.
The inwards migration of all the carbon atoms released by the carbides dissolving in the extending carbide-free zone (rather outwards to be oxidized as observed for higher temperatures), occurring only at less than 1100°C remains to be clearly explained. But this carbon enrichment between the carbide-free zone and the bulk induces a local decrease in refractoriness (and a change in local mechanical properties, notably hardness) while, on the contrary, the loss in the carbide-free zone of almost all the carbon initially present improves the refractoriness of the most external part of the alloys, with a new local solidus temperature which can be determined also by thermodynamic calculations from the local chemical composition.

4. CONCLUSION

The possible consequences of high temperature oxidation on the microstructures of the sub-surfaces of carbides-strengthened alloys and superalloys are numerous. They vary versus the general chemical composition of the alloy and versus the temperature of exposure to oxidation. The progress with time of the microstructure changes during exposure at temperatures between 1000 and 1100°C (carbide-free depth but also the position of the carbon-enriched zone and its local carbon content) are also interesting to observe. The probable consequences on the local refractoriness or mechanical properties are certainly rather limited but it is possible that, in service, they may indirectly influence the lifetime of components in real applications, notably in situation of sudden increase in temperature or in thermal cycling.

References

[1] Donachie, M. J., Donachie, S. J., Superalloys: A Technical Guide (2nd Edition), ASM International (Materials Park, 2002).
[2] Young, D., High Temperature Oxidation and Corrosion of Metals, Elsevier Corrosion Series (Amsterdam, 2008).
[3] Berthod, P., Michon, S. *et al*, "Thermodynamic calculations for studying high temperature oxidation of superalloys", C*alphad,* Vol. 27 (2003), pp. 279-288.
[4] Berthod, P., Vébert, C. *et al*, "Study of carbide transformations during high-temperature oxidation of nickel-base superalloys", *Oxidation of Metals,* Vol. 63, No. 1/2 (2005), pp. 57-72.
[5] Berthod, P., "Experimental and thermodynamic study of nickel-based alloys containing chromium carbides. Part II: Study of the sub-surface characteristics of Ni-30 wt.%Cr-xC alloys oxidized at high temperature using thermodynamic calculations", C*alphad,* Vol. 32 (2008), pp. 492-499.
[6] Thermo-Calc version N, "Foundation for Computational Thermodynamics", Stockholm (Sweden), Copyright (1993, 2000), www.thermocalc.com
[7] SGTE: Scientific Group Thermodata Europe Database, Update 1992.

Current Status of Japan Advanced Ultra-Supercritical (A-USC) Technology Development

Yuji Fukuda

(1) Kure Research Laboratory, Babcock-Hitachi K.K., Takaramachi 3-6 , Kure , Hiroshima 737-2516, Japan

e-mail: yuji1.fukuda@mhps.com

ABSTRACT

Japan's current installed power generating capacity is about 250GW, of which about 25% is coal based. Coal is likely to remain the predominant source of power generating in Japan because of its lower cost and availability. After 2012 high efficiency coal fired plants are needed in Japan because almost all nuclear plants were shut down and the import cost of natural gas and oil has become a critical problem, today. Therefore, METI (Ministry of Economy, Trade and Industry) project of A-USC, which target is 700deg-C steam condition with 46-48% (net, HHV) is drawing greater attention. The project began in 2008 and successfully finished boiler and turbine material basic tests and two year boiler components and turbine casing test will be started in 2014 using actual plant. The paper gives details of Japan's A-USC program and the progress achieved. Furthermore, the paper focuses the hot corrosion and steam oxidation properties of candidate materials.

1. INTRODUCTION

Use of coal for thermal power generation allows large quantities of electric power to be reliably supplied. As a result, coal-fire thermal power plants provide more than 40% of the world's electric power and 25% of the Japan's electric power. The demand is growing steadily around the world, particularly in emerging economies. The demand for coal-fired electric plant is also growing in post-earthquake Japan as a substitute for nuclear power shown in Figure 1[1]. Unfortunately, coal–fired power generation is also accompanied by considerable greenhouse gas emissions. So, improving its efficiency contributes directly to a reduction in CO2 emission. High expectations are being placed on the development of technologies that improve the efficiency of coal fired power generation in environmentally conscious ways. The improvement in the efficiency of the coal fired power plants has been mainly achieved by raising steam conditions as shown in Figure 2. Steam power plants that have been built recently usually have a steam temperature of around 600deg-C and a steam pressure of 25MPa. Isogo #2, the newest power plant in Japan, was built in 2009. The temperatures of the main steam and reheat steam are 600 and 620deg-C. Realization of 600deg-C class USC plants were based on Electric Power Development Company (J-Power) USC R&D program, which started in 1981 to develop the USC technology, subsidized by the Japanese government. Following EPDC program, NIMS and METI/NEDO program were carried to develop newly ferritic steels and austenitic stainless steels for A-USC plants. Following these programs, METI A-USC development project started in 2008, which features 700deg-C steam temperature and net efficiency 46-48% (HHV).

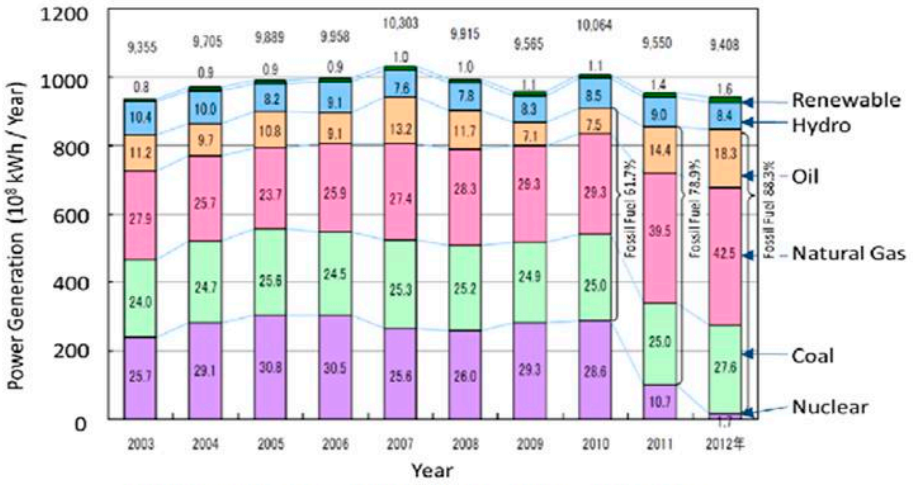

Figure1 Power Generation and fuel share Japan [1]

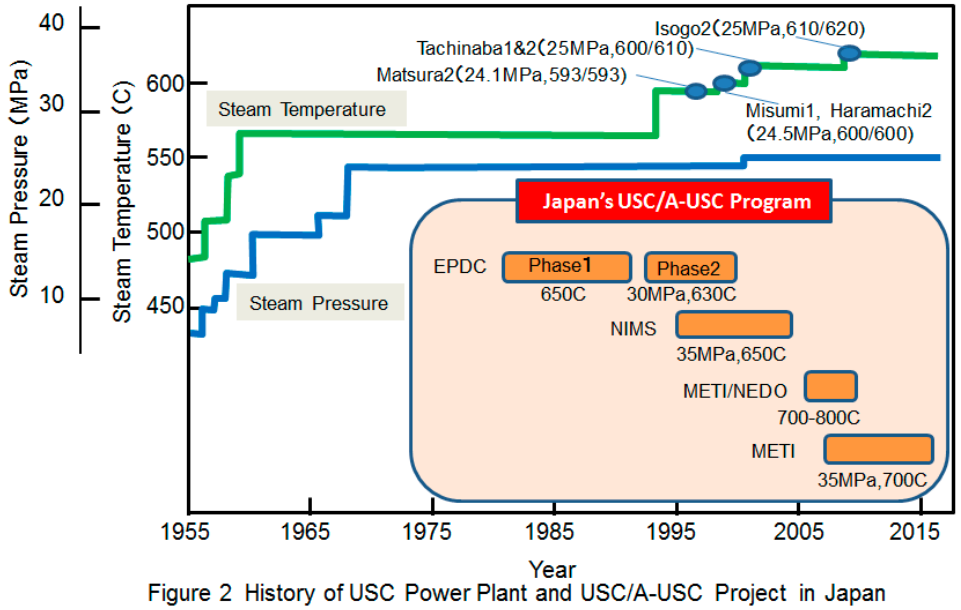

Figure 2 History of USC Power Plant and USC/A-USC Project in Japan

2. OVERVIEW OF METI A-USC PROJECT

Master schedule of METI A-USC program is shown in Figure 3. Outlines of the project are as follows,

- Japanese major turbine, boiler and material manufactures join the project. – started in 2008
- The 700deg-C class A-USC technology will be developed based on today's latest 600deg-C class USC technology by raising the steam temperature 100deg-C
- The target net thermal efficiency for the higher heating value base is 46 to 48%. This is more than 10% higher than that of the 600deg-C class USC. That means more than a 10% drop in CO2 emissions.
- In the first half of the project, boiler, turbine and valve materials are being developed and verified.
- In the second half, boiler components and small turbine tests will be done to verify the reliability.
- Throughout the project, long term creep rupture tests will be done on each candidate material and welded joint.

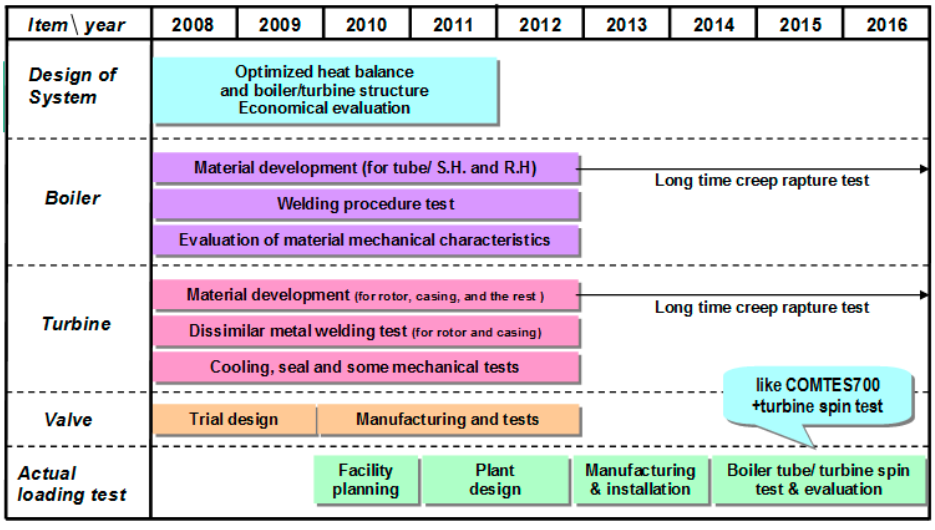

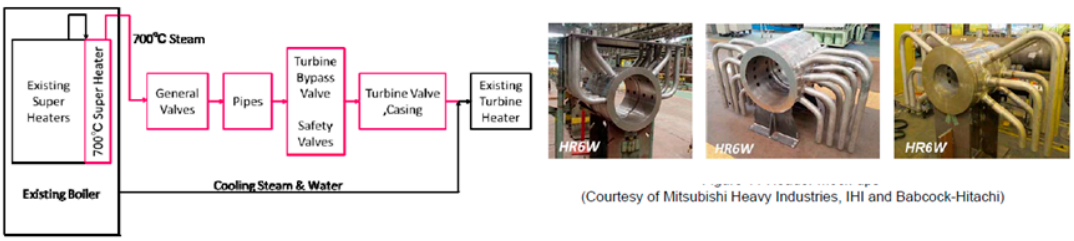

(Courtesy of Mitsubishi Heavy Industries, IHI and Babcock-Hitachi)

Figure 3 Master Schedule of METI A-USC Project [3]

3. CANDIATE MATERIALS USED FOR A-USC PLANT AND ISSUES

The materials newly selected for A-USC are mainly Ni-based alloys and advanced 9Cr steels (Figure 4). In the lower temperature components such as water-wall, primary SH, LPT etc., conventional ferrite steels and austenitic stainless steels will be used. Among material issues, coal ash corrosion and long term steam oxidation tests were carried in this project. Figure 5 shows the test results. The average metal loss decreased with higher chromium content in the alloy and these results are similar to previous study (Figure 6). Figure 7 shows the 10,000 hours steam oxidation results. Except minor intergranular attacks were observed in Alloy 617, steam oxidation property of candidate alloys are good. Two year long term tests will be carried out in actual plant from 2015.

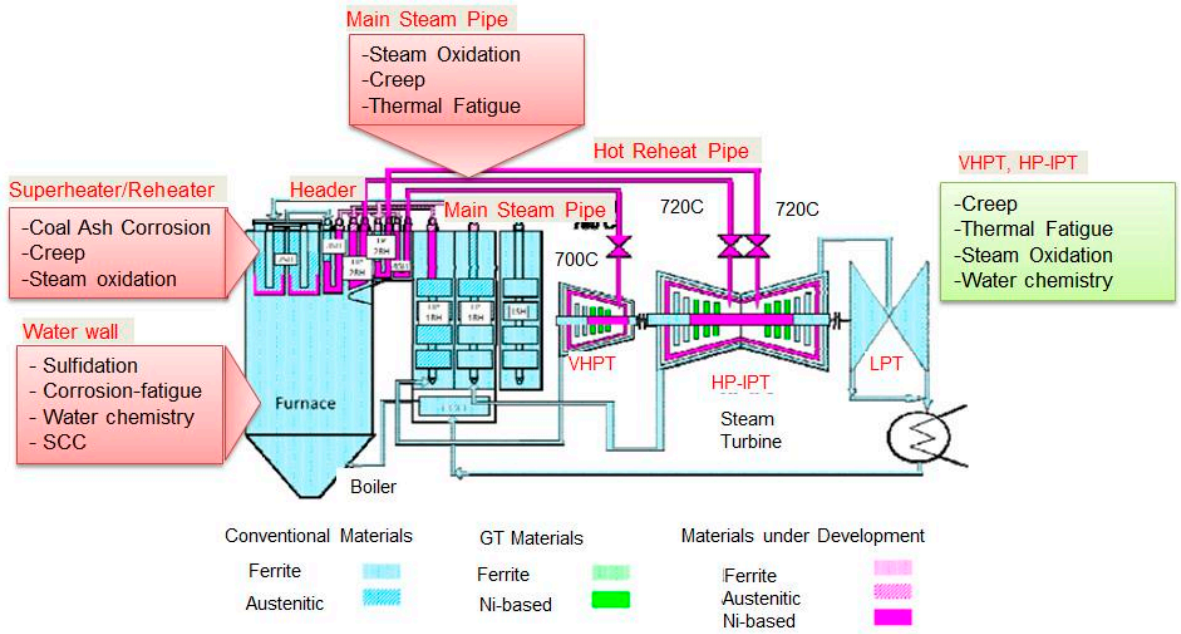

Figure 4 Selected Materials for A-USC Power plant (35MPa, 700/720/720) and Material Issus

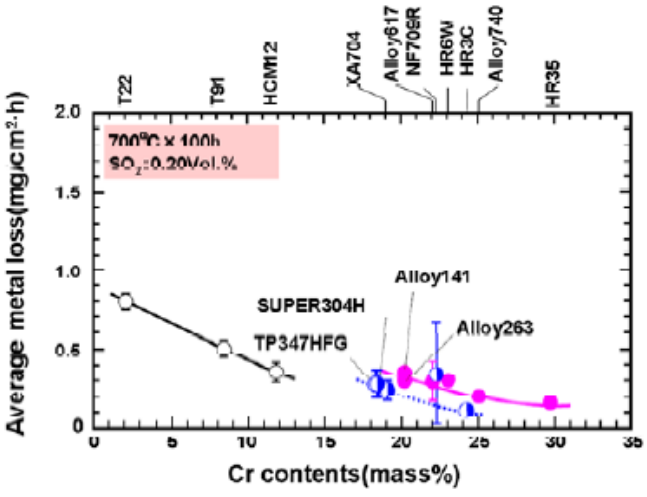

Figure 5 Hot Corrosion Test Result
(Courtesy of Mitsubishi Heavy Industries)

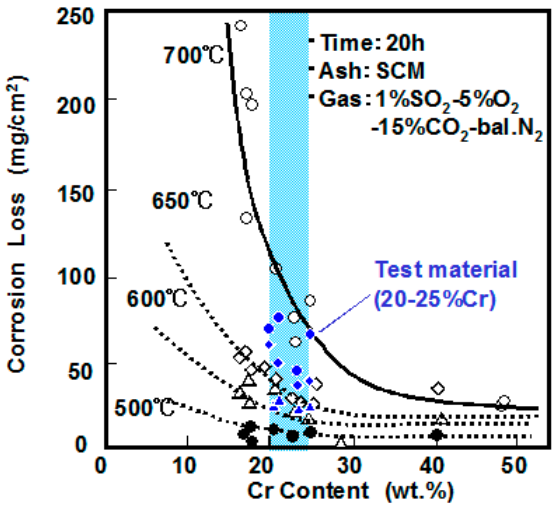

Figure 6 Effect of Cr Content on Hot Corrosion [4]

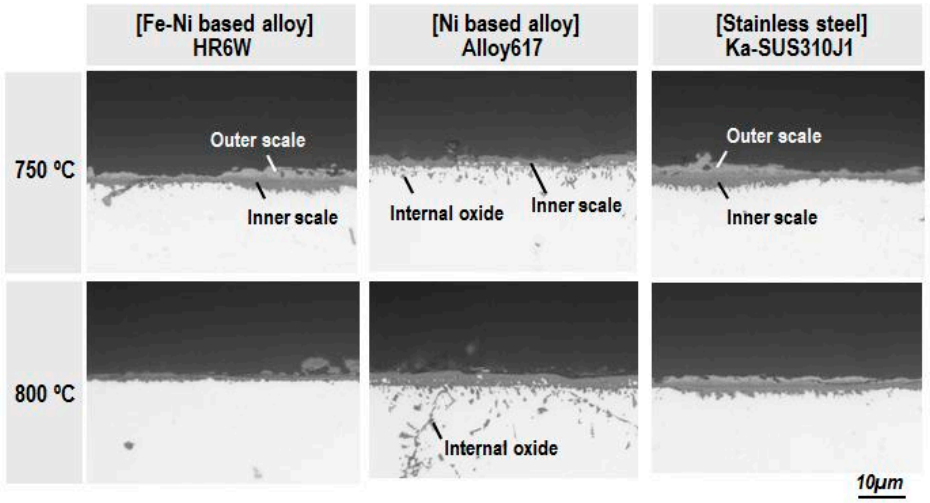

Figure7 Steam Oxidation Test Results
(Courtesy of Babcock-Hitachi)

4. SUMMARY

This paper has described how Japan's development of technology for improving the efficiency of coal-fired power generation has evolved over time. The key technologies are developing the new heat resistance alloys and their application to actual power plants. For METI A-USC project, candidate material and manufacturing technologies were developed during the first half of the project. Following actual plant tests will be carried out to verify developed technologies. In the future, the A-USC plants will be realized and contribute to reduce CO2 emissions from coal fired power plants in the world.

REFERENCES

[1] http://www.fec.or.jp/about us/pr/sonota/icsFiles/afieldfile/2013/5/17/kouseihi 2012.pdf

[2] F. Masuyama, " Materials R&D Proogram and Issues for A-USC Power Plants", 38th MPA-Seminar, October 8 and 9, 2013 in Stuttgart

[3] M. Fukuda, " The Ongoing and Planned Activities of the A-USC Project in Japan", 38th MPA-Seminar, October 8 and 9, 2013 in Stuttgart

[4] Y. Fukuda and M. Shimizu, "Hot Corrosion and Steam Oxidation Properties of New Heat Resistant Steels for Ultra Super Critical Boilers", *Proceedings of the International Symposium on High-Temperature Oxidation and Corrosion 2005* , Nara, Japan, 30th November - 2nd December 2005,p189-197.

Corrosion of superheater materials – full scale test loops

Luciana Intiso(*), Oriana Tassa

Centro Sviluppo Materiali S.p.A via di Castel Romano, 100 – 00128 Rome, Italy

e-mail: l.intiso@c-s-m.it

1. INTRODUCTION

The reduction of CO_2 emissions from coal-fired power plants is a strong function of the power generation efficiency. Increasing of power generation efficiency can be realized by moving towards higher operating steam temperatures. However, higher operating temperatures represents challenging conditions for materials now used in the conventional power plants, both in terms of creep and fatigue as well as corrosion issues. Indeed, the material degradation, due to general metal loss or to localized defect formation, can lead to failure of boiler tubes. Thus, the new operating conditions at 700/720°C require the use of new generation materials, with improved mechanical and corrosion resistance properties. Promising classes of material for this purpose are higher strength austenitic steels and Ni-based super alloys. However, the corrosion behaviour of the different materials needs to be better understood.
The flue gas of a coal–fired power plant in air combustion mainly consists of CO_2 and H_2O vapour along with some O_2 and trace gases like SO_2. In addition, deposits can accumulate on the metal surfaces. In coal power plant a common deposit are sulphates ($CaSO_4$) where the calcium and sulphur may exists as impurities in the fuel. Both H_2O and CO_2 can reduce the ability of chromia-forming alloys to form or maintain protective chromium-rich oxide scales. It has been observed that the oxidation of most technical alloys is faster in presence of water vapour [1,2] and carbon dioxide [3,4,5] than in air or dry oxygen. Furthermore, the sulphurous corrosive components, such as SO_2 and sulphate-based salt components present in many commercial atmospheres, can contribute to severely degrade corrosion properties of alloys and accelerated corrosion can occur [6]. This process of deposit-induced accelerated oxidation is called hot corrosion. Most cases of sulphate-deposit induced accelerated attack occur when the deposit is liquid.

The paper reports the main degradation phenomena occurred on different materials and compare their corrosion behaviour. HR3C, DMV310N, Sanicro 25, IN617 and IN740 were tested in a full scale test loop (Schölven-Germany) up to 20.000 hours operated in air-fired combustion gases at temperatures between 586 and 688 °C. The research was performed within MACPLUS project.

2. EXPERIMENTAL

Materials were exposed in a full scale test loop, Schölven-Germany, within two campaigns. The testing conditions, including times and temperatures are reported in Table 1. The flue gas composition is representative of a flue gas resulting by air-combustion of coal (e.g. CO_2 about 15%, H_2O about 30%, O_2 about 5%, N_2 as balance, and traces of SO_x). The materials included in the testing program were both austenitic stainless steels (HR3C, DMV310N, Sanicro 25) and Ni-based alloys (alloy 617 and 740). The materials were tested both at the fire and the steam sides. The chemical compositions of the tested materials, including the Cr/Fe ratio are reported in Table 2.

Material	Time [hours]	Temperature [°C]
HR3C	20000	606°C
Sanicro 25	20000	612°C
	15389	586-593°C
DMV310 N	20000	612°C
	18954	586-612°C
Alloy 617	20000	612°C
	20000	656°C
	15389	623-650°C
Alloy 740	20000	688°C

Table 1 Testing conditions, time and temperature

	Fe	Ni	Cr	Si	Mn	Al	Mo	W	Cu	Co	Ti	Nb	C	N	Cr/Fe
HR3C	Bal.	20	25	0.4	1.2	-	-	-	-	-	-	0.45	0.08	0.2	0.47
DMV310N	Bal.	21.5	25	0.75	2	-	-	-	-	-	-	0.4	0.07	0.25	0.50
Sanicro 25	Bal.	25.5	22.6	0.25	0.51	-	-	3.45	2.99	1.57	-	0.44	0.08		0.53
Alloy 617	1.5	Bal.	22	0.5	0.5	1.1	6	-	0.25	12.5	0.3	-	0.1		
Alloy 740	0.7	Bal.	25	0.5	0.3	0.9	0.5	-	-	20	1.8	2	0.03		

Table 2. Chemical composition of materials used within the testing program

3. RESULTS AND DISCUSSION

Fire-side corrosion

By a first observation of the tubes it is evident that one side (named Side A) appeared to be covered by deposits more than the opposite (named Side B). An example is reported in Figure 1. This suggests that the tubes were hit by the gas flow directly on side A. Deeper investigations showed that the side more covered by deposits is also the side on which the material exhibited deeper corrosion. Samples appear generally more corroded at side A, compared to side B, this evidence suggests that the corrosion attack is higher when deposits are present on the surface. A schematic view of the appearance of the tube related with the gas flow direction is shown in Figure 2. The deposits mainly consist of Al, Si, Fe - oxides, and calcium sulphates.

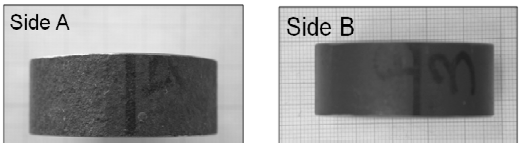

Figure 1. Appearance of Side A and side B

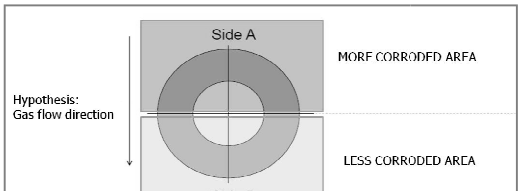

Figure 2. Schematic view of the appearance of the tube

SEM overview of the firesides of the cross sections of different samples shows that all the tested materials are able to form a Cr-rich protective oxide (oxide always present at side B – not shown here). However, when the deposits are present, at side A, almost all materials exhibited features connected to scale breakdown phenomena, suggesting that the breakdown occurs principally when the deposits are present, see Figure 3. EDX analyses revealed that a significant content of sulphur is present at the bottom of the scale (metal-scale interface), suggesting that the corrosion phenomena occurred as a result of interaction of metal with sulphur containing environment, i.e. gas and/or deposits, through the formation of metals sulphides as suggested in the literature [6]. It is argued that, under deposits, alloys initially form a Cr-rich protective oxide, which is gradually degraded by the gas-deposit-metal interactions, leading to a formation of a non protective fast growing scale.

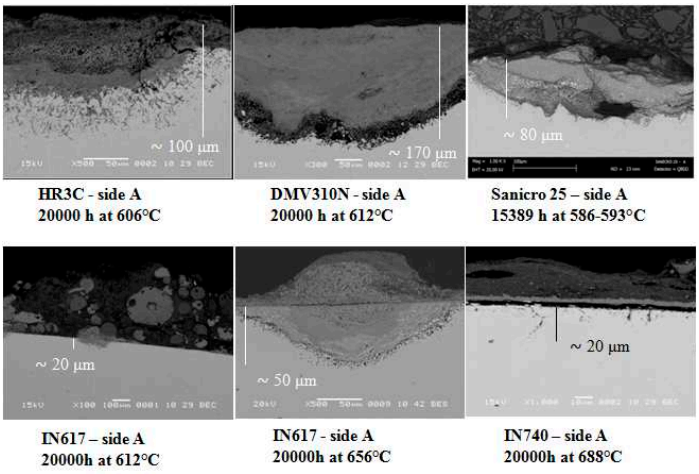

Figure 3. SEM/BSE of different tested materials – fireside A

In particular, the SEM investigation of the cross sections of specimens, shows that Alloy 740 tested at 688°C is the alloy that seems to suffer lower attack (internal corrosion 20 microns deep), compared to all other alloys, also when covered by deposits (at side A). Indeed, Alloy 740 does not show any morphology connected to the breakdown of the oxide resulting from the loss of the protection of the base oxide. At 612°C, austenitic steels (HR3C, DMV310N and Sanicro 25) appear more corroded then Alloy 617, while at higher temperature (656°C) Alloy 617 suffers higher corrosion attack, compared to the Alloy 740 at 688°C. The higher corrosion attack produced on Alloy 617 is probably due to the presence of Mo in the alloy. Indeed, following the literature Mo enhance the acidic fluxing resulting in higher corrosion rates, [7]. Furthermore, Sanicro 25 and Alloy 617 tested in the second campaign showed the presence of a kind of localized erosive phenomenon (i.e. spallation) and erosion corrosion, respectively, see Figure 4. Under erosion-corrosion conditions, the erosive flue prevents the formation of a continuous layer of chromia by removing the oxide faster than it can spread laterally [8], [9].

Figure 4. Tube cross sections.

Steam-side oxidation

SEM analyses of the steam exposed side are shown in Figure 5. HR3C and DMV310N exhibited a thicker oxide scale (50 microns) compared to the Sanicro 25 (15 microns). However, all the austenitic alloys, HR3C, DMV310N and Sanicro 25, tended to form a protective Cr-rich oxide scale. This slight different behaviour among the austenitic alloys might reflect

the different Cr/Fe ratio (Sanicro 25>DMV310N>HR3C). Ni-alloys 617 and 740 form a very thin chromia (3-5 microns). Ni-alloys (617 and 740) exhibited also some internal oxidation, alumina oxide. The precipitation of aluminium oxide is not unexpected. Indeed when the Cr_2O_3 scale is formed, the oxygen activity decreased at the scale/metal interface and aluminium, which has high affinity with oxygen, can be selectively oxidized, even though it is present at low concentration. The oxidation occurring at the steam side of Alloy 740 resulted in internal attack, enhanced if compared to Alloy 617 and can be explained by the different structure of the alloys. According to the literature [6], precipitation-hardening alloys are suffering for a preferential internal attack at the precipitation particles sites compared to solid-solution hardening alloys, which results in a more uniform oxidation and contained internal attack.

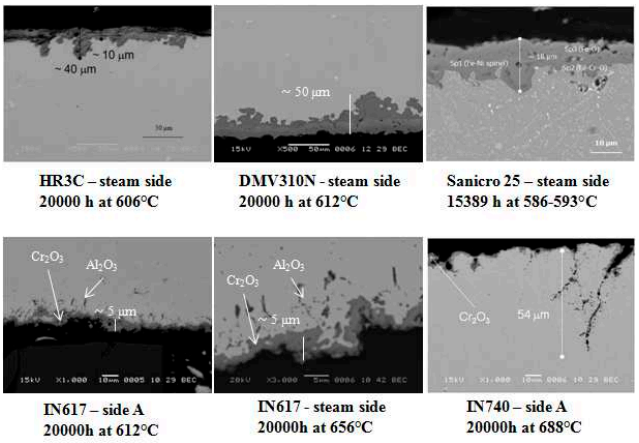

Figure 5. SEM/BSE of different tested materials – steamside

An estimation of the corrosion rate starting from the scale thickness measurements is given in Figure 6. It represents only an indicative value referred to the specific corrosion attack measured, thus it can be taken as a summary of the observation. All corrosion rates are of the same order of magnitude, 10^{-2} mm/y, except for alloy 740 that shows one lower order of magnitude, 10^{-3} mm/y. These corrosion rates are in a low corrosion range. The scale thickness of Alloy 617 when exposed at 656°C appears a bit higher compared to the other alloys, probably due to the higher tendency to suffer sulphidation and/or hot corrosion, due to the presence of Mo. Also the steam side oxidation rate is very low (about 10^{-2} mm/y): in this case the penetration of the oxidation attack is higher for alloy 740 compared to alloy 617. This phenomenon has been attributed to the different alloy structure.

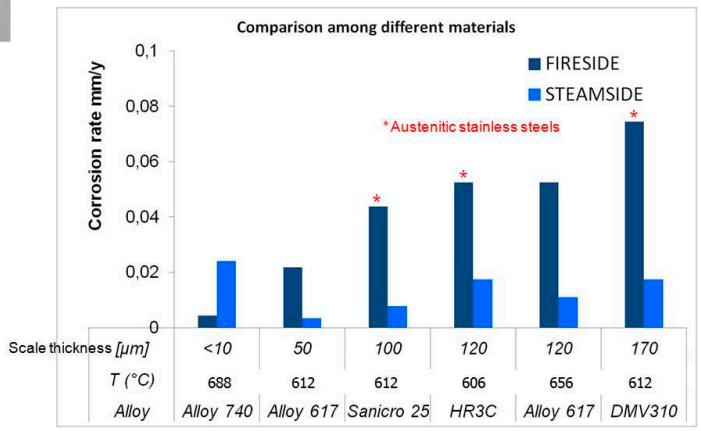

Figure 6. Estimation of corrosion rate from scale thickness measurements on tubes after exposure in power plant test loops

4. CONCLUSION

The oxidation/corrosion behaviour of the candidate materials for the highest temperature heat exchanging components in the MACPLUS project was evaluated. HR3C, DMV310N, Sanicro 25, IN617 and IN740 were tested in a full scale test loop (Schölven-Germany) up to 20.000 hours operated in air-fired combustion gases at temperatures between 586 and 688 °C.

Low steam oxidation rates of the Ni alloys were found after long term exposure in a full scale plant test loop. Both tested Ni-alloys forms a Cr_2O_3 oxide scale. The steam oxidation behaviour of the nickel base alloys mainly differs in respect to the extent of internal oxidation, being most pronounced in case of Alloy 740, because of the relatively high aluminum content (approx. 1 mass.-%) of this alloy. Slight higher values were found for the high chromium austenitic steels 310, HR3C and Sanicro 25. All the austenitic alloys tend to form a protective Cr-rich oxide scale.

The behaviour in flue gas strongly depends on the actually prevailing conditions. If no deposits are present, the corrosion rates of the mentioned candidate materials are not substantially different from those during steam exposure: all alloys tend to form chromium rich oxide oxides which tend to prevent rapid attack of the materials by corrosive species in the gas.

In contrast, the corrosion attack is much more pronounced under deposit. Sulphur enrichment is present at the bottom of the scale (metal-scale interface), suggesting that the corrosion phenomena occurred as a result of interaction of metal with sulphur containing environment, i.e. gas and/or deposits, through the formation of metals sulphides.

Ni-based alloys generally suffered lower corrosion attack compared to the high chromium austenitic steels. However, Alloy 617 (656°C) suffers higher corrosion attack, compared to the Alloy 740 (688°C). The higher corrosion attack produced on Alloy 617 is probably due to the presence of Mo in the alloy. Indeed, following the literature Mo enhance the acidic fluxing resulting in higher corrosion rates.

Acknowledgements

The research leading to these results has received funding from the European Community's Research Fund for Coal and Steel (7FP) under MACPLUS project *grant agreement* n° ENER/FP7EN/249809/MACPLUS.

1 P. Kofstad, High Temperature Corrosion, Elsevier Applied Science Publishers Ltd, (London and New York, 1988)
2. J. Ehlers *et al;* "Enhanced oxidation of the 9%Cr steel P91 in water containing environments," *Corrosion Science,* Vol. 48, No 11 (2006), pp. 3428-3454
3 C.S. Giggins, F.S. Pettit; "Corrosion of metals and alloys in mixed gas environments at elevated temperatures," *Oxidation of Metals*, Vol. 14, No 5 (1980), 363-413.
4 G.H. Meier et al., Effect of alloy composition and exposure conditions on the selective oxidation behavior of ferritic Fe-Cr and Fe-Cr-X alloys, *Oxidation of Metals*, Vol. 74, No 5-6 (2010), 319-340.
5 T. Gheno, D.Monceau, D.J.Young, "Mechanism of breakaway oxidation of Fe-Cr and Fe-Cr-Ni aloys in dry and wet carbon dioxide", *Corrosion Science*, Vol. 64, (2012), pp 222-233.
6 F. Pettit, "Hot corrosion of Metals and Alloys", *Oxidation of Metals,* Vol. 76, No 1-2 (2011), pp 1-21
7 N.Birks, G.H. Meier, F.S.Pettit, Introduction to the High Temperature oxidation of metals, 2nd ed., University press, Cambridge UK, 006
8 R.J. Link *et al.* "The response of Alloys to erosion-corrosion at high temperatures", *Oxidation of Metals*, Vol. 49, No 3-4 (1997), pp 213-236
9 S.L. Chang, F.S. Pettit, N. Birks, "Effect of angle of incidence on the combined erosion-oxidation attack of nickel and cobalt", *Oxidation of Metals*, Vol. 34, No 1-2 (1990),pp 47-70

Fireside Corrosion of Steels and Ni-based Alloys in Simulated Superheater / Reheater Environments for Advanced Air- and Oxy-fired Coal-Biomass Combustion Power Plants

Nigel J Simms [(1,*)], Tanvir Hussain [(1)], Adnan Syed [(1)] and John E Oakey [(1)]

[(1)] Cranfield University, Cranfield, Bedfordshire, MK43 0AL, United Kingdom

[*]e-mail: n.j.simms@cranfield.ac.uk

1. INTRODUCTION

Advanced solid fuel fired power generation systems are being developed within the context of multiple competing pressures, including: environmental, operational, regulatory and economic factors. Environmental emissions (e.g., SO_X, NO_X, particles and CO_2) have to be reduced to meet legislation and policy targets [1]. Such power plants need to be operated more flexibly to enable renewable energy sources, such as wind turbines, to be integrated into the electricity supply system. In addition, plants need to have increased fuel flexibility to enable a more diverse range of fuels to be fired to allow operators a choice of fuels, to minimise costs and to increase security of supply. Increases in plant efficiencies are needed to reduce both CO_2 and fuel costs, and in future plants to balance the penalties associated with CO_2 capture and transport systems. For combustion plants, increases in efficiencies require steam systems that operate with higher maximum inlet temperatures and pressures. For the EU NEXTGENPOWER project [2], the steam system targets set have been 760 °C and 300 bar, which are a significant increase over current systems and would give fireside temperatures of the final superheater as high as ~800 °C. One route to enable the introduction of CO_2 capture systems is to burn the fuel in oxygen mixed with re-cycled flue gases (or oxy-firing), as this produces a very high CO_2-steam environment, with only low levels (<~5%) of N_2, O_2 and other contaminants to separate (it should be noted that there are several possible configuration of such plants [3]).

This paper summarises research carried out in a series of laboratory studies [4-7] to evaluate the potential fireside corrosion performances of a range of steels (T92, 347HFG and HR3C) and Ni-based alloys (263, 617 and 740). These studies have been investigating different factors that can influence the fireside corrosion of superheaters / reheaters in combustion plant when using: (a) different coal-biomass mixtures; (b) air or oxy-firing; and, (c) progressively higher steam temperatures. For the purposes of this paper, common accelerated fireside corrosion exposure conditions have been extracted from these studies to enable trends in materials performance to be identified.

2. EXPERIMENTAL

The fireside corrosion tests were carried out in alumina-lined vertical controlled-atmosphere furnaces. The corrosion furnace setup to simulate oxy-firing conditions is shown in Figure 1; this is a development of the system used for air-fired conditions, with a direct water injection system required to obtain the higher steam contents of oxy-combusted gases and a higher temperature cooling water system needed to avoid the formation of acidic condensates at the top of the furnace. Each furnace could accommodate 24 samples at a time in individual alumina crucibles. Each test was run for 1000 hours using the well-established 'deposit recoat' test method, which is described in detail elsewhere [5-7,9]. Tests were carried out at 600, 650, 700, 750 and 800 °C, with the Ni-based alloys being exposed especially at the high temperatures; deposit re-coats were carried out every 200 hours. For this paper, data from two deposit conditions have been selected: an aggressive deposit (D1) that is often used as a screening deposit in

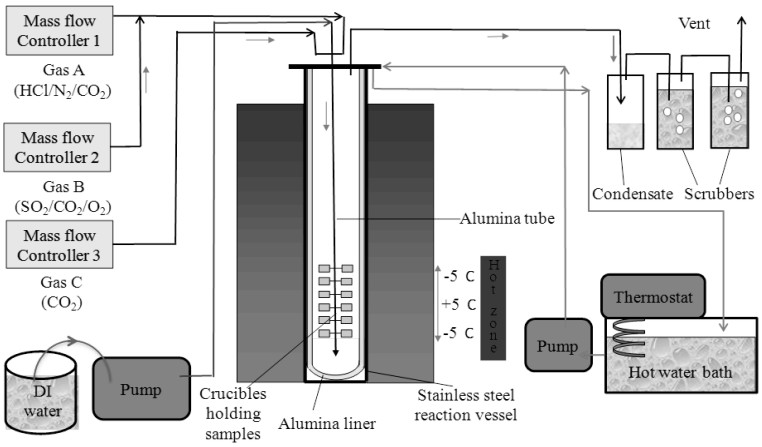

Figure 1 Schematic diagram of a controlled atmosphere furnace for fireside corrosion in simulated oxy-firing combustion gases [5].

UK / EU fireside corrosion research programmes (with a composition of 37.5 mole % Na_2SO_4 - 37.5 % K_2SO_4 – 25 % Fe_2O_3); and, bare samples, or no deposit (D0), for comparison. Two gases were selected for different exposure series (Table 1); these were calculated for a fuel mix of UK coal fired with 20 weight % cereal co-product [5] and with the air/fuel ratio selected to give 4 volume % O_2 in the combustion products. Of the many potential oxy-fired systems [3], the one selected for these tests involved hot flue gas re-cycle after the particle removal system, but upstream of the de-sulfurization system; this gives the highest SO_X, HCl and H_2O gas compositions of any of the oxy-firing variants.

Table 1 Nominal gas compositions used in fireside corrosion exposures

	N_2 (vol. %)	O_2 (vol. %)	CO_2 (vol. %)	H_2O (vol. %)	SO_2 (vppm)	HCl (vppm)
Air-firing	73.8	4	14	8	1300	400
Oxy-firing	5.2	4	59	31	6260	1700

During their exposures, the performances of the samples were tracked using mass change data that was generated on each recoating cycle. However, dimensional metrology was the method used for determining alloy performance. Pre-exposure metrology was carried out using a micrometer (with a resolution of ±1 µm and an accuracy of ±2 µm). Post-exposure metrology was carried out on carefully prepared polished cross-sections using an optical microscope / image analysis system with an automated and accurately calibrated x-y stage. By collecting data on the position of the metal surface and depth of internal damage (Figure 2), datasets could be calculated for each sample giving the 'change in metal' (or 'change in sound metal' when including internal damage); in turn metal loss (or sound metal loss) datasets could be calculated.

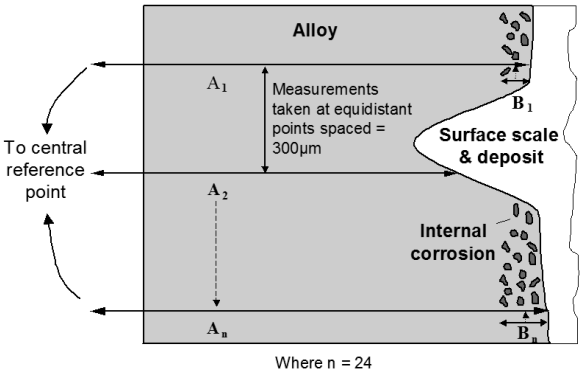

Figure 2 Features measured on sample cross-sections as part of the post-exposure dimensional metrology

3. RESULTS AND DISCUSSION,

The type of data generated from the dimensional metrology process is illustrated in Figure 3; which shows the distributions of sound metal damage measured for alloy 347HFG when exposed at 600, 650, 700 and 750 °C for 1000 hours covered in the aggressive screening deposit (D1) and in the simulated oxy-fired combustion gas stream). These data show that the highest level of damage for this alloy/deposit/gas combination was found at 700 °C (with lower damage levels at both 650 and 750 °C). Thus, under these exposure conditions, the peak in the characteristic 'bell-shaped' damage trend for fireside corrosion is somewhat above 700 °C (but less than 750 °C). The fairly uniform slopes of the datasets indicated that the damage distributions are normal; a more detailed analysis indicates that their standard deviations are ~5% of the median damage at each temperature.

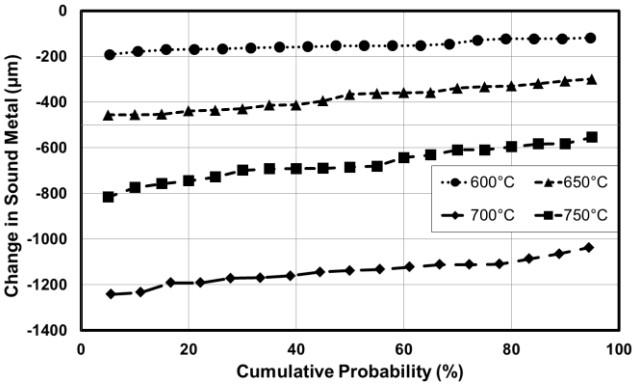

Figure 3 Alloy 347HFG covered with deposit D1 exposed to 59% CO_2 / 31%H_2O / 4%O_2 / 6260vppm SO_2 / 1700vppm HCl for 1000h

By extracting the median damage data from such distributions, it is possible to compare alloy performances more easily, as illustrated in Figure 4 for T92, 347HFG and HR3C all exposed under the same conditions. The similar damage found for both T92 and 347HFG indicates

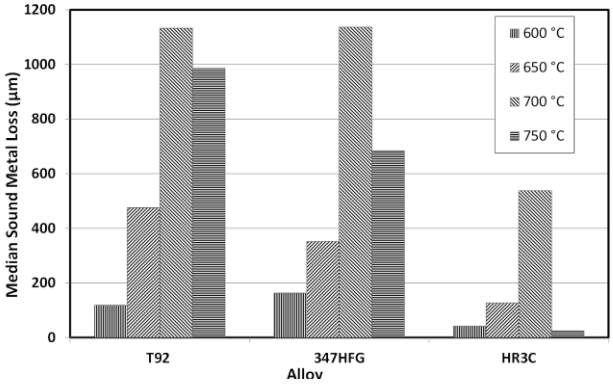

Figure 4 Alloys T92, 347HFG and HR3C covered with deposit D1 exposed to 59% CO_2 / 31%H_2O / 4%O_2 / 6260vppm SO_2 / 1700vppm HCl for 1000h

that neither of these alloys had sufficient Cr contents (at ~9 and ~18 weight %, respectively) to provide protection against such aggressive corrosion conditions. HR3C, with ~25 % Cr, performed significantly better at all temperatures. The effect of not having a surface deposit (but having the same gas, metal temperature and exposure cycle) is shown in Figure 5 (note change in scale compared to Figure 4). The much lower damage levels measured indicate the significance of the presence of the deposit in generating rapid fireside corrosion attack.

In contrast, the performance of these alloys in simulated air-fired combustion gases is shown in Figure 6 (note change in scale compared to both Figures 4 and 5). The only difference in the exposure condition used to generate the data in Figures 4 and 6 was the gas composition. The data in Figure 6 shows that under these conditions, the corrosion peaks for 347HFG and HR3C are between 650 and 700 °C, and so lower than in the oxy-fired gases. In addition, the damage levels for 347HFG and HR3C are similar to those for oxy-firing when exposed at temperatures below the peak corrosion temperature.

Figure 7 summarizes the key factors that influence the alkali iron tri-sulfate fireside corrosion peak for the steels: from the melting point of such compounds, which starts the deviation from oxidation behavior on the bottom left of the diagram to the decrease in SO_3 levels with increase in temperature (a result of the SO_2/SO_3 equilibrium with O_2) that causes the deposit to become unstable (as there is no longer enough SO_3 present to stabilize it). The particular oxy-fired combustion gas chosen for this work, with its higher SO_X level would stabilize the deposit to higher temperatures and so permit higher peak damage temperatures (and levels). The same deposit fluxes and compositions were used in all the tests reported in this paper, so the upward trend in the fireside corrosion peak was the same in both gases.

For the Ni-based alloys, a slightly different behavior was observed under these exposure conditions. Figure 8 illustrates the median damage sound metal loss found for alloy 263, 617 and 740 in the temperature range 650 – 800 °C, when using the aggressive screening deposit (D1) and the simulated air-fired combustion gas. This appears to show a double peak in corrosion damage with increasing temperature. However, detailed examination of the dimensional metrology data (confirmed by backscattered SEM examinations) showed that at the lower two temperatures there was broad front fireside corrosion attack on all the alloys, whereas at the higher

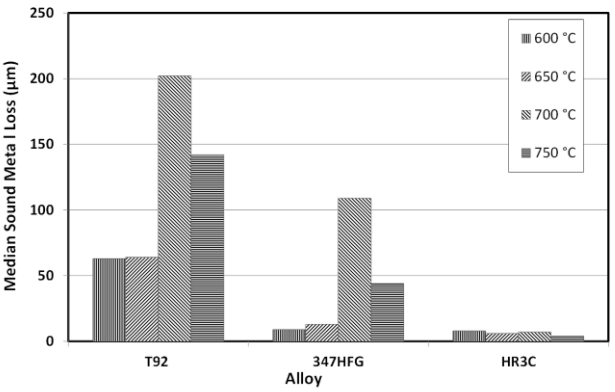

Figure 5 Alloys T92, 347HFG and HR3C exposed bare (D0) to 59% CO_2 / 31%H_2O / 4%O_2 / 6260vppm SO_2 / 1700vppm HCl for 1000h

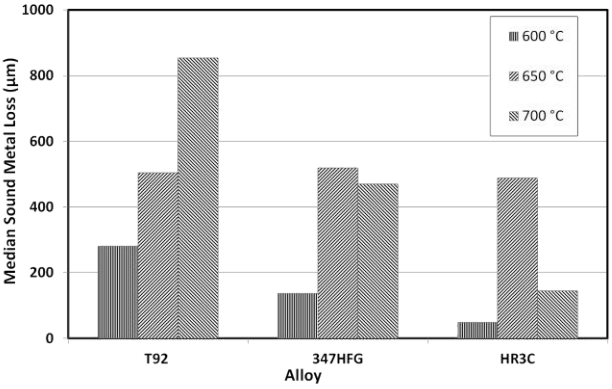

Figure 6 Alloys T92, 347HFG and HR3C covered with deposit D1 exposed to 14% CO_2 / 8%H_2O / 4%O_2 / 1300vppm SO_2 / 400vppm HCl for 1000h

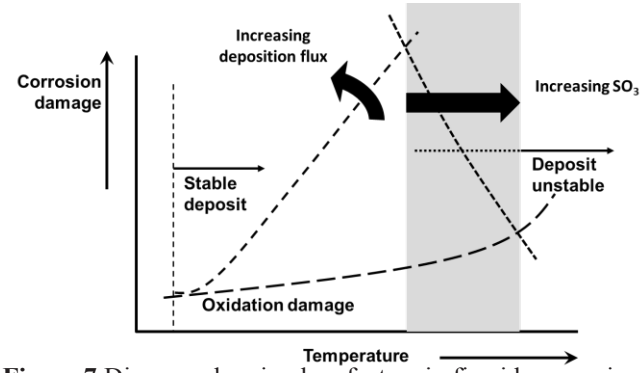

Figure 7 Diagram showing key factors in fireside corrosion peaks and the effect of changes in exposure conditions

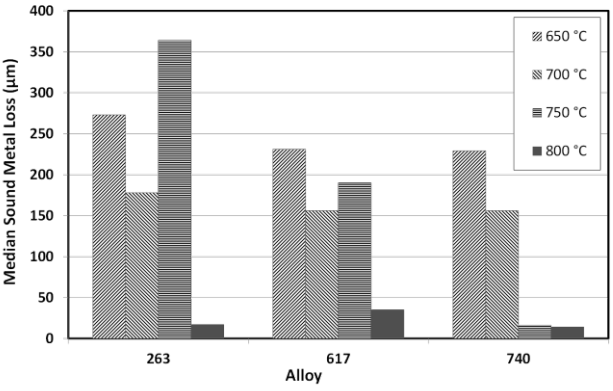

Figure 8 Alloys 263, 617 and 740 covered with deposit D1 exposed to 14% CO_2 / 8%H_2O / 4%O_2 / 1300vppm SO_2 / 400vppm HCl for 1000h

two temperatures there was significant levels of internal attack as well. This internal attacked reduced with increasing temperature. The damage morphologies were different for the three Ni-based alloys [7]. It is notable that the internal damage found on alloy 740 was much lower than for the other Ni-based alloys and was also only found in localized areas. For alloy 263 at 750 °C the internal attack was evenly distributed, finer and much more extensive, but reduced to thinner localized areas at 800 °C. In contrast, for alloy 617 the internal attack was coarser and often associated with grain boundaries.

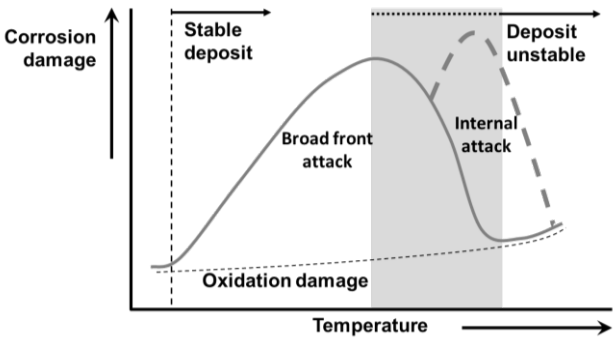

Figure 9 Change to conventional alkali iron tri-sulfate fireside corrosion damage peak for steels; extra higher temperature internal attack peak for Ni-based alloys

Figure 9 illustrates the change to the conventional alkali iron tri-sulfate fireside corrosion damage peak for stainless steels (as was shown in Figure 7), that is needed on moving to Ni-based alloys, with the addition of an extra peak at higher temperatures to accommodate the extensive internal damage observed on these materials. The exposure conditions used for the alloys in Figures 6 and 8 were the same (simulated air-fired gases combined with the aggressive screening deposit D1, but note the difference in scales). As for the steels in air-fired gases, the peak in the broad front corrosion attack on the Ni-based alloys was between 650 and 700 °C, but with generally lower damage levels.

4. CONCLUSION

A series of laboratory studies have been used to evaluate the potential fireside corrosion performances of a range of steels (T92, 347HFG and HR3C) and Ni-based alloys (263, 617 and 740). These separate studies have investigated factors that influence the fireside corrosion of superheaters / reheaters in combustion plant, including: (a) different coal-biomass mixtures; (b) air or oxy-firing; and, (c) progressively higher steam temperatures. For this paper, common accelerated fireside corrosion exposure conditions have been extracted from these studies to enable trends in materials performance to be identified. Quantitative materials performance data have been generated in terms of sound metal loss distributions to enable the development of improved fireside corrosion models.

Acknowledgements

Financial support for different groups of tests included in this paper from: (a) the European Union's Framework 7 NEXTGENPOWER project; (b) the United Kingdom (UK) Technology Strategy Board project on 'Modelling Fireside Corrosion of Heat Exchanger Materials In Advanced Energy Systems' (TP/5/MAT/6/I/H0639C); and (c) the UK Research Council's Energy Programme Supergen 2 project on 'Conventional Power Plant Lifetime Extension' (EP/F029748/1).

References

[1] "Renewable Energy Technology Roadmap: 20% by 2020", *European Renewable Energy Council* (Brussels, 2008).
[2] Stam, A.F., et al, "NEXTGENPOWER – Demonstration and Component Fabrication of Nickel Alloys and Protective Coatings for Steam Temperatures of 750°C", *Proc. 7th Int. Conf. on Advances in Material Technology for Fossil Power Plants (EPRI)*. Hilton Waikoloa Village, Hawaii, USA, October 2013
[3] Simms, N.J., Sumner, J., Hussain, T., Oakey, J.E. (2013), "Fireside Issues in Advanced Power Generation Systems", *Materials Science and Technology*, Vol. 29, No. 7 (2013), pp. 804-812
[4] Lant, T., et al, "Modeling Fireside Corrosion of Heat Exchanger Materials in Advanced Energy Systems", *Proc. 6th Int. Conf. on Advances in Material Technology for Fossil Power Plants (EPRI)*. Santa Fe, New Mexico, USA, Aug/Sept 2011 (ASM International, 2011) pp. 255-267
[5] Syed, A.U., Simms, N.J., Oakey, J.E., "Fireside corrosion of superheaters: Effects of air and oxy-firing of coal and biomass", *Fuel*, Vol. 101 (2012), pp. 62-73
[6] Hussain, T., Syed, A.U., Simms, N.J., Oakey, J.E., "Trends in fireside corrosion damage of superheaters in air and oxy-firing of coal/biomass", *Fuel,* Vol. 113 (2013), pp. 787–79
[7] Hussain, T., Simms, N.J. and Oakey, J.E., "Fireside corrosion of Ni-based alloys in simulated co-firing combustion environment", *Baltica IX - International Conference on Life Management and Maintenance for Power Plants.* Helsinki, Finland, June 2013. (VTT Technology 106, ISBN 978-951-38-8026-2, 2013), pp. 218-232
[8] Simms, N.J., et al, "Fireside Corrosion and Steamside Oxidation in Advanced Solid Fuel-Fired Power Plants", *Proc. 10th Liege Conference on Materials for Advanced Power Engineering.* Liege, Belgium. September 2013.
[9] "Draft Code of Practice for Discontinuous Corrosion Testing in High Temperature Gaseous Atmospheres". EU project SMT3-CT95-2001 (TESTCORR). (ERA Technology, UK, 2001).

Effects of Cr and Mo on Coal Ash Corrosion Resistance of Ni-based Alloy for 700 ℃ class A-USC boilers

Masaru Shimizu [1,*], Takashi Sato [1], and Toshihiro Uehara [2]

[1] Kure Research Laboratory, Babcock-Hitachi.K.K.Takaramachi6-9, Kure, Hiroshima 737-8508, Japan
[2] Metallurgical Research Laboratory, Hitachi Metals, Ltd., Hashimacho1240-2, Yasugi, Shimane 692-8601, Japan

e-mail: masaru1_shimizu@mhps.com

ABSTRACT

In 700 °C class advanced ultrasupercritical (A-USC) boilers, Ni-based alloys are required for superheater and reheater (SH/RH) tubes. One of key requirements for Ni-based alloys is coal ash corrosion resistance which is normally caused due to a molten salt corrosion by deposit ash. The coal ash corrosion resistance of Ni-based alloys depends on Cr and Mo in material. In this paper, the coal ash corrosion resistance of Ni-based alloys containing 21-24% Cr and 6-10% Mo was investigated by laboratory tests, and effects of Cr and Mo on the corrosion resistance were discussed.

1. INTRODUCTION

Research and development of advanced ultrasupercritical (A-USC) boilers with steam conditions of 700 °C or higher have been made worldwide [1-4]. To achieve such advanced steam conditions, the application of Ni based alloys with high creep rupture strength becomes essential. Creep rupture strength of Ni-based alloys is enhanced by γ 'phase precipitation strengthening due to Al and Ti and by solution strengthening due to Mo and Co. To apply Ni-based alloys to superheater and reheater (SH/RH) tubes in A-USC boilers, high coal ash corrosion resistance is also required. The coal ash corrosion of SH/RH tubes in coal-fired boilers burning higher sulfur coals (>1% S) is normally caused or accelerated by molten salts consisting of sodium-potassium-iron tri-sulfates $(Na,K)_3Fe(SO_4)_3$ in deposit ash [5]. According to previous studies, coal ash corrosion depends on metal temperature, SO_2 in gas and material component (Cr, Mo) [6-8]. The coal ash corrosion occurs at from 550 to 750 °C in combustion gas containing more than 0.1%SO_2 since $(Na,K)_3Fe(SO_4)_3$ stability exists as molten salts in this condition. As to material component, Cr has a particularly significant effect to enhance coal ash corrosion resistance due to formation of protective Cr rich oxides. In contrast, Mo is detrimental to the coal ash corrosion resistance because Mo oxides promote a molten salt corrosion by alkali sulfate such as Na_2SO_4. Most candidate Ni-based alloys for A-USC boilers contain Cr and Mo, but effects of Cr and Mo on coal ash corrosion resistance is not yet evaluated quantitatively.

In this study, coal ash corrosion resistance of Ni-based alloys containing different amounts of Cr and Mo was investigated, and effects of Cr and Mo on coal ash corrosion resistance were evaluated by comparing corrosion resistance of the materials.

2. EXPERIMENTAL

Table 1 lists chemical compositions of test materials used in this study. Eight kinds of Ni-based alloys (No.1-8) were laboratory-melted materials and contained different amounts of Cr and Mo which ranged from 21 to 24% and from 6 and 10%, respectively. Effects of Cr and Mo on coal ash corrosion property were evaluated by comparing corrosion resistance of the materials. Alloy 617 (No.9) was a candidate Ni-based alloy for large diameter pipe, SH/RH tube in the A-USC R&D project in Europe and Japan. Cr and Mo content in Alloy617 were 22% and 9%, respectively. The specimens of 10 x 10 x 3mm dimensions were cut from laboratory-melted materials and a tube for corrosion test. Two specimens for each material were prepared to evaluate coal ash corrosion resistance. The surfaces of specimens were polished with SiC paper of 320 grits and cleaned in an acetone using an ultrasonic cleaner.

Teble 1. Chemical composition of test materials

No.	Material	Nominal composition (%)
1	21Cr-1	21Cr-10Mo-2Ti-Al-bal.Ni
2	22Cr-1	22Cr-10Mo-2Ti-Al-bal.Ni
3	23Cr-1	23Cr-10Mo-2Ti-Al-bal.Ni
4	24Cr-1	24Cr-10Mo-2Ti-Al-bal.Ni
5	21Cr-2	21Cr-9Mo-2Ti-Al-bal.Ni
6	22Cr-2	22Cr-8Mo-2Ti-Al-bal.Ni
7	23Cr-2	23Cr-7Mo-2Ti-Al-bal.Ni
8	24Cr-2	24Cr-6Mo-2Ti-Al-bal.Ni
9	Alloy 617	22Cr-9Mo-12Co-Ti-Al-bal.Ni

A schematic illustration of coal ash corrosion test apparatus and test condition are shown in Figure 1 and Table 2, respectively. At first, top surfaces of the specimens were covered with synthetic ash, and placed on a tray in a test furnace equipped with a quartz chamber. Next, simulated coal combustion gas was supplied at a rate of 200ml/minute into the chamber. The gas composition was simulated combustion gas of high sulfur coal containing approximately 3% S. Subsequently, the gas was heated up to test temperature in the furnace. The gas temperature was monitored and controlled by a thermo-couple installed above the specimen. The specimens were exposed to the gas at 700 ℃ for 300 hours. The synthetic ashes on top surfaces of the specimens were removed and new synthetic ashes were recoated on the specimens once per 100 hours.

After coal ash corrosion tests, corrosion weight losses were evaluated and corrosion scale analyses were conducted. The corrosion weight losses were calculated based on weight losses per top surface area of the specimens after removing the corrosion scales using a de-scaling solution. The corrosion scale analyses were performed using a scanning electron microscopy with an energy dispersive X-ray spectrometer (SEM/EDX).

Table 2. Test condition

Temperature	700℃
Test duration	300h
Gas composition	0.25%SO_2-4%O_2-15%CO_2-N_2
Gas flow rate	200 ml/min.
Ash composition	5%Na_2SO_4-5%K_2SO_4-10%$CaSO_4$ -30%Fe_2O_3-10%Al_2O_3-40%SiO_2
Amount of coating ash	50mg/cm^2
Recoating of ash	Every 100h

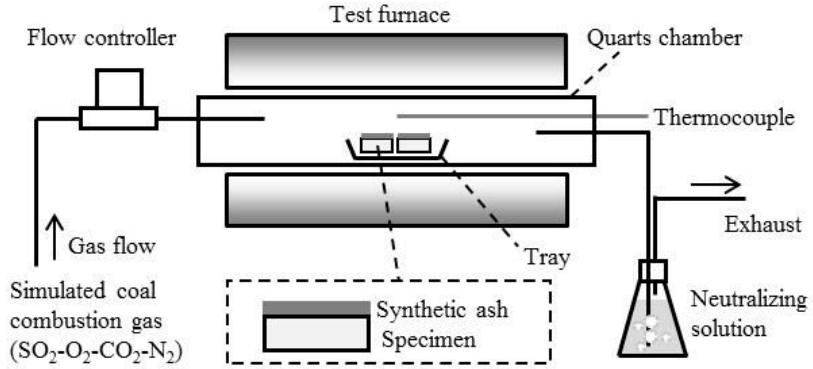

Figure 1. Coal ash corrosion test apparatus

3. RESULTS AND DISCUSSION

Figure 2 shows corrosion weight loss of the Ni-based alloys tested at 700 °C for 300 hours. Among the Ni-based alloys containing 10% Mo, Corrosion weight losses did not decrease with increase of Cr content. In contrast, corrosion weight losses decreased with decrease of Mo. Among the Ni-based alloys containing 22% Cr, Alloy617 (22Cr-9Mo) exhibited higher corrosion resistance than 22Cr-1 (22Cr-10Mo) and lower corrosion resistance than 22Cr-1 (22Cr-8Mo). The materials of 23Cr-2 (23Cr-7Mo) and 24Cr-2 (24Cr-6Mo) which contain not less than 23% Cr and not more than 7% Mo showed higher corrosion resistance compared to the other Ni-based alloys.

Figure 3 shows SEM and EDX analysis results of corrosion scales formed on 21Cr-1 (21Cr-10Mo), Alloy617 (22Cr-9Mo) and 24Cr-2 (24Cr-6Mo) after coal ash corrosion test. Scale thicknesses of 21Cr-1 and Alloy617 were thicker than that of

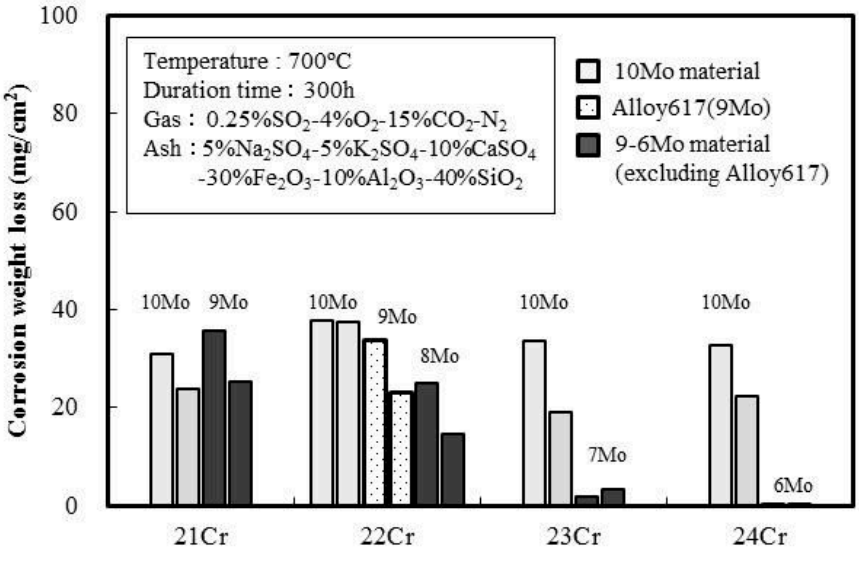

Figure 2. Corrosion weight loss of test materials

24Cr-2, and this result coincided with the result of corrosion weight loss as above. The material of 24Cr-2 containing 6% Mo exhibited double layer scale and both layers mainly consisted of Cr oxides. The inner layer contained higher S or Mo than the outer scale. It was expected that Mo oxides and Cr/Ni sulfides existed in inner scale. Alloy617 and 21Cr-1 also exhibited double layer scale, but the outer layer and inner layer mainly consisted of Ni oxides and Cr oxides, respectively. Ni oxides were also observed in other materials containing not less than 8% Mo which had low corrosion resistance. Formation of Ni oxides layer was probably due to degradation protective Cr oxides. That is, it was possible that incorporation of Mo into the sodium-potassium-iron tri-sulfates or Cr oxides promoted degradation of protective Cr oxides, and Ni diffusion rate in Cr oxides with higher Mo increases compared to that in Cr oxides with lower Mo. That meant that Ni oxides tended to be formed in Ni-based alloys containing with higher Mo. It seemed that Cr in material played an important role to decrease corrosion rate since corrosion scale mainly consisted of protective Cr oxides. From these results, it was necessary to apply Ni-base alloy containing not less than 23% Cr and not more than 7% Mo to SH/RH tubes in A-USC boilers burning higher sulfur coals (>1% S).

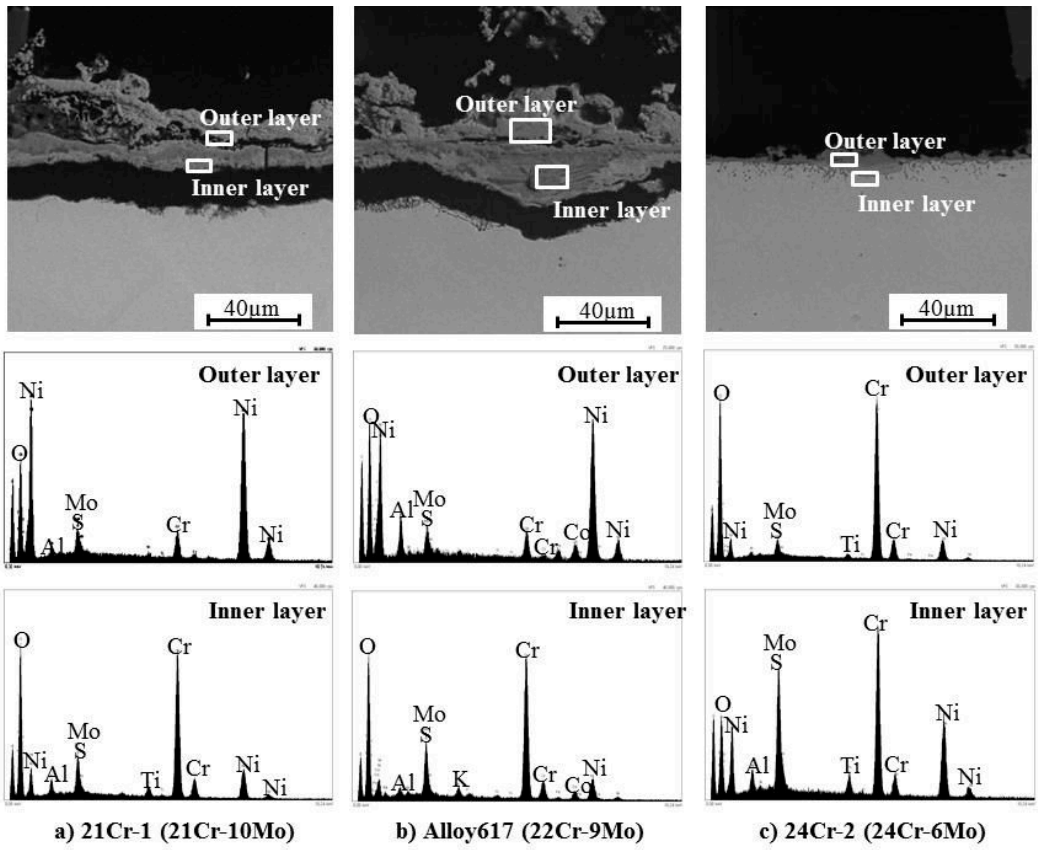

a) 21Cr-1 (21Cr-10Mo) b) Alloy617 (22Cr-9Mo) c) 24Cr-2 (24Cr-6Mo)

Figure 3. SEM and EDX analysis of corrosion scales formed on a) 21Cr-1, b)Alloy617 and c)24Cr-2 after corrosion test

4. CONCLUSION

To clarify the effects of Cr and Mo on coal ash corrosion resistance of Ni-based alloys containing 21-24% Cr and 6-10% Mo for 700 ºC class A-USC boiler tubes, laboratory coal ash corrosion tests were conducted. The obtained results are as follows.

1. The corrosion resistance of Ni-based alloy was improved with decrease of Mo. The Ni-based alloys which contain not less than 23% Cr and not more than 7% Mo showed higher corrosion resistance compared to the other Ni-based alloys.

2. Ni oxides as outer layer were observed in the Ni-based alloys which contained not less than 8% Mo. Formation of Ni oxides layer was probably due to degradation of protective Cr oxides.

3. It was necessary to apply Ni-base alloy containing not less than 23% Cr and not more than 7% Mo to SH/RH tubes in A-USC boilers burning higher sulfur coals (>1% S).

References

[1] J. Shingledecker, H. Hendrix, J. Philips, J. Siefert, R. Purgert and P. Rawls, "U.S. Program on Advanced UltraSupercritical Power Plant Materials – The Economy of Using Advanced Alloys", *Proc IEA Clean Coal Centre Workshop: Advanced Ultrasupercritical Coal-fired Power Plants*, Vienna, Austria, September. 2012, Paper No. SESSION 4-4.

[2] J.L. Marion, O. Drenik, C. Frappart, F. Kluger, M. Sell, A. Skea, V. Rod and P. Walker, "Advanced Ultra-Supercritical Steam Power Plants", *Proc IEA Clean Coal Centre Workshop: Advanced Ultrasupercritical Coal-fired Power Plants*, Vienna, Austria, September. 2012, Paper No. SESSION 4-2.

[3] M.Fukuda, "Advanced USC Technology Development in Japan", *Proc IEA Clean Coal Centre Workshop: Advanced Ultrasupercritical Coal-fired Power Plants*, Vienna, Austria, September. 2012, Paper No. SESSION 6-2.

[4] R. Sun Z.Z. Cui and Y. Tao, "Development of 700°C USC Coal-Fired Power Generation Technology in China", *Proc IEA Clean Coal Centre Workshop: Advanced Ultrasupercritical Coal-fired Power Plants*, Vienna, Austria, September. 2012, Paper No. SESSION 1-4.

[5] W. Nelson and C. Chain, Jr, *Trans. ASME J. Eng. Power 82*, Series A .1961

[6] Y. Fukuda and M. Shimizu, "Hot Corrosion and Steam Oxidation Properties of New Heat Resistant Steels for Ultra Super Critical Boilers", *Proceedings of the International Symposium on High-Temperature Oxidation and Corrosion 2005* , Nara, Japan, 30th November - 2nd December 2005,p189-197.

[7] M. Shimizu, G. Bao and Y. Fukuda, "High Temperature Corrosion Properties of Candidate Materials for 700°C Ultra Super Critical Boilers", *NACE International Corrosion2009 Conference & Expo.* Atlanta, GA, USA, 23-26th March, 2009, Paper No.09250

[8] B. A. Baker and G.D. Smith, "Nickel Base Material Options for Fabrication of Advanced Coal Fired Boiler Components", *NACE International Corrosion2009 Conference & Expo.* Atlanta, GA,USA, 23-26th March, 2009, Paper No.09250

High Temperature Corrosion of Top Rank Fuel Cladding Candidate Materials for Canadian Generation IV Supercritical Water-Cooled Reactor

Yimin Zeng (*), Jian Li, Babak Shalchi Amirkhiz, Magdalene Matchim,
Pei Liu and Wenyue Zheng

CanmetMATERIALS, Natural Resources Canada
183 Longwood Road South, Hamilton, Ontario, Canada L8P 0A5

E-mail: Yimin.Zeng@NRCan-RNCan.gc.ca

Abstract

The supercritical water-cooled reactor (SCWR) is one of six innovative Generation IV reactor concepts and merits further research and development with the intent of being pursued for implementation in the next 30 years. Canada, European Union and Japan have signed the GIF project arrangements on SCWR R&D programs, including thermal-hydraulics, materials selection/development, and operating chemistry. Canadian SCWR development is a national program funded by the Office of Energy Research and Development (OERD). This multi-years program involves Canadian Atomic Energy Canada Limited (AECL), CanmetMATERIALS and a number of Canadian universities.

Based on established knowledge and experience from ultra-supercritical coal power plants (SCFP), supercritical water oxidation systems (SCWO) for hazard waste management, and advanced materials development programs for existing nuclear reactor systems, the materials that will be used for fabricating SCWR structural components, such as calandria, pressure tube and hot/cold let piping etc., can be reasonably identified and selected. To achieve optimum thermal efficiency, however, the Canadian SCWR concept requires a fuel core outlet temperature of 650 °C at 25 MPa with fuel cladding operating temperature possibly up to 850 °C, therefore leading to the most challenging aspect of this novel reactor concept. During SCWR operation, fuel cladding candidate materials must have very strong mechanical strength, microstructure stability, and excellent resistance to general oxidation/corrosion, stress corrosion cracking (SCC), creep and radiation damage. For example, excessive general oxidation/corrosion of a fuel cladding tube can result in its thickness loss, causing the degradation of structural integrity and a noticeable decrease in thermal transfer efficiency. Moreover, the dissolved metal ions could deposit on downstream components (e.g. turbine blades and tubing), introducing other integrity problems to the whole reactor system. A number of studies and investigations have been performed in the past years and several top-ranking candidate materials, including austenitic stainless steels (310S, 800H and SS347) and nickel-based alloys (Alloy 625 and Haynes 214), have been pre-selected based on available information. To determine which alloy is suitable for the SCWR applications, there are still a number of questions needed to be clarified. Firstly, the corrosion mechanisms of theses alloys under real SCWR conditions and suitable corrosion measurement methods have not yet been well understood and documented. Secondly, most of former SCW corrosion studies were conducted at temperature < 600 °C only after short-term exposure. But the fuel cladding tubes are required to be continuously operated with coolant outlet temperature of 650°C and 25 MPa for at least one year. Thus, it is necessary to know long-term corrosion resistance of the alloys and identify the possible influence of thermal cycles. Thirdly, it is well known that the high temperature corrosion resistance of an alloy is coherently related to the properties of its surface oxide. The micrograph (including composition and microstructure) of grown oxides on these alloys at temperature > 600 °C and the variation of the oxide microstructures with exposure time are still unclear. Beside the surface oxides, the microstructure of sub-layers just under the oxides, which is critical to assess the stress cracking corrosion (SCC) and general corrosion of the alloys, has not been well investigated. Finally, according to available results, the SCC susceptibility of the alloys cannot be well predicted under the designed SCWR conditions because most of the

SCC tests were conducted under either understated or exaggerated conditions. Due to the very thin thickness (~ 0.6mm) of the fuel tubes, it is very important to know whether or not micro-cracks could be formed on the alloys under the designed operating conditions.

In this paper, the chemistry of supercritical water, possible corrosion mechanisms (chemical and/or electrochemical attacks) at high temperature, and the advantages and limitations of corrosion rate measurement techniques (such as weight gain, weight loss and electron microscopy) are reviewed and discussed. Most recent corrosion and SCC experimental results obtained at CanmetMATERIALS are present. In an autoclave made of alloy 625 alloy, a number of the alloys coupons were prepared and subsequently exposed to SCW condition (625 °C and 25 MPa) for about 1200 hours. Their corrosion rates are statistically measured using different methods and compared to those obtained at temperature < 600 °C. The effects of thermal cycles on the surface oxide formation and breakdown are also investigated and assessed. The micrograph of the grown oxides, the variation of oxide microstructures with exposure time, and the formed sub-layer under the oxides are characterized using advanced SEM and TEM methods. For example, the grown oxide on 310S stainless steel is mainly composed of Cr_2O_3 compound. Meanwhile, a Cr-depletion sub-layer is also generated only after 300 hours exposure. The SCC susceptibility of these alloys is investigated using a high temperature and pressure loop with well controlled water chemistry under the designed operating conditions. The stress-stain curves of these alloys under SCW conditions are obtained and analyzed. The micrographs (including grown oxide and formed micro-cracks) of these SCC samples before and after SCW exposure are characterized and the possible SCC mechanisms are discussed.

Enhancing the Oxidation Behavior of Ferritic-Martensitic Steels for Water Vapor Containing Power Conversion Environments

Diana Schmidt [(1)], Mathias C. Galetz [(1,*)], Xabier Montero [(1)] and Michael Schütze [(1)]

DECHEMA-Forschungsinstitut, Theodor-Heuss-Allee 25, 60486 Frankfurt, GERMANY

e-mail: galetz@dechema.de

1. INTRODUCTION

Modern heat-resistant ferritic-martensitic steels are of great interest as superheater materials in fossil fuel power plants or as material for interconnects in SOFCs. Environments of such applications often contain high amounts of H_2O, which promotes the formation of volatile chromium species $CrO_2(OH)_2$ leading to insufficient oxidation resistance due to an accelerated breakdown of the protective chromia layer, the so-called breakaway oxidation. New protection systems have been developed in order to make these steels applicable at temperatures above 600°C. Two approaches for superheater materials were followed: 1) an enrichment of Mn and Cr, which could form a spinel layer during oxidation; 2) a chromium carbide layer, which provides a high Cr reservoir in the metal subsurface region. Additionally, pure reference samples of chromium oxide, chromium carbide, and Cr-Mn-spinel as single phases were investigated in a fundamental approach in order to investigate the oxidation kinetics in high temperature water vapor containing environments.

2. EXPERIMENTAL

Reference samples for this investigation were made from pure metal powder. Different powder compositions were used: metallic chromium, chromium carbide ($Cr_{23}C_6$), and a mixture of chromium and manganese powder. Apart from the chromium carbide sample, which was not oxidized, the powders were sintered and oxidized in synthetic air at 1000°C for 50 h in order to obtain compact and homogenous samples. The samples were investigated in two different atmospheres, 3.5% oxygen and 10% water vapor in nitrogen and synthetic air with 10% water vapor, at three different temperatures, 650°C, 800°C, and 950°C. Ferritic-martensitic steel P91 (Table 1) was used as substrate material for diffusion coatings. The material was machined into coupons of dimension 20 x 10 x 3 mm³, sandblasted to remove oxides and other contaminations and ultrasonically cleaned with ethanol according to ISO 21608 [1].

Table 1: Chemical composition of the investigated steel

	composition wt%							
alloy	Fe	Cr	Mn	Mo	Si	V	Nb	C
P91	bal.	7.9-9.6	0.25-0.6	0.8-1.1	0.2-0.5	0.18-0.25	0.06-0.10	0.06-0.15

The diffusion coatings were manufactured using powder pack cementation as described in detail in previous work [2,3]. Two different diffusion treatments were applied: pure chromium diffusion and a co-diffusion process of chromium and manganese. In all cases, the activator was manganese chloride with a concentration of 5%, and alumina was used as inert filler. A time of 2 h, temperature of 1050°C, and Ar/ 5% H_2 atmosphere were used as coating parameters.

In order to investigate the oxidation behavior of the coated in comparison to the uncoated samples high temperature exposure was performed in a gas containing 3.5% oxygen and 10% water vapor in nitrogen.

The coated as well as the reference samples were removed after different high temperature exposure times for gravimetric analysis by a microbalance. Afterwards the surfaces were investigated with X-ray diffraction using Cu-Kα radiation (Bruker D8 Advance) and a detector which can discriminate fluorescence deriving from Fe and Mn. The diffractograms were measured over an angular range of 10–90° (2θ) in 0.010° steps and 2 s per step.

After exposure, cross-sections of the samples were prepared and inspected using metallographic and micro-analytical methods.

3. RESULTS AND DISCUSSION

Pure reference samples

When the reference powder samples were prepared, it was found that, although Cr and Mn had been weighed in according to the stoichiometric composition of the spinel, the formation of chromium manganese spinel from metal powders in synthetic air starts only at exposure temperatures of above 750°C as illustrated in the oxidation temperature dependent X-ray diffraction plot in Figure 1. At lower temperatures only mixed manganese oxide and chromia were observed.

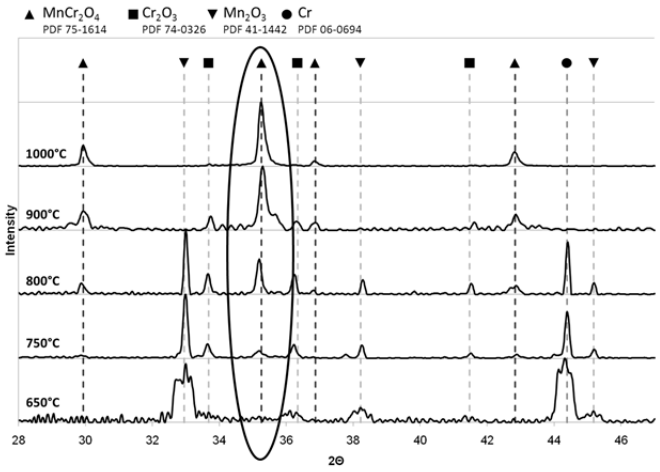

Table 2: Phase analysis of reference samples (both atmospheres)

	950°C	800°C	650°C
c-$MnCr_2O_4$ (after pre-oxidation synthetic air at 1000°C for 50 h)			
100 h	c-$MnCr_2O_4$	c-$MnCr_2O_4$, t-Mn(CrMn)O_4 (t only in 3.5% O_2)	c-$MnCr_2O_4$, c-$CrMn_{1.5}O_4$
1000 h	c-$MnCr_2O_4$	c-$MnCr_2O_4$, t-Mn(CrMn)O_4	c-$MnCr_2O_4$, c-$CrMn_{1.5}O_4$, t-Mn(CrMn)O_4
$Cr_{23}C_6$ (no pre-oxidation)			
100 h	Cr_2O_3	Cr_2O_3, Cr_7C_3, $Cr_{23}C_6$	Cr_2O_3, Cr_7C_3, $Cr_{23}C_6$
1000 h	Cr_2O_3	Cr_2O_3	Cr_2O_3, Cr_7C_3, $Cr_{23}C_6$

Figure 1: X-ray diffraction pattern of powder samples after oxidation for 12 h in synthetic air at different temperatures [4]

In Figure 2 the weight change of the pure chromia and chromium manganese spinel samples is shown. A similar porosity and surface area was found in both samples, therefore results are directly comparable. Interestingly, under all conditions investigated, the chromium manganese spinel shows higher weight loss due to evaporation than chromium oxide. Additionally the accelerating effect of temperature and oxygen partial pressure on the evaporation rate of $CrO_2(OH)_2$ is obvious. XRD measurement proves that the composition of the pure chromium manganese spinel shifts towards higher manganese contents. This can only be observed at lower temperatures, where the spinel becomes easily unstable, if chromium is extracted (Table 1). However, in contrast to thermodynamic databases [5], which do not predict volatile Manganese species, Manganese seems to get removed from the sample surface too. Manganese evaporates to a lower extent than chromium, but Mn evaporation had also been observed under other water vapor containing conditions [6].

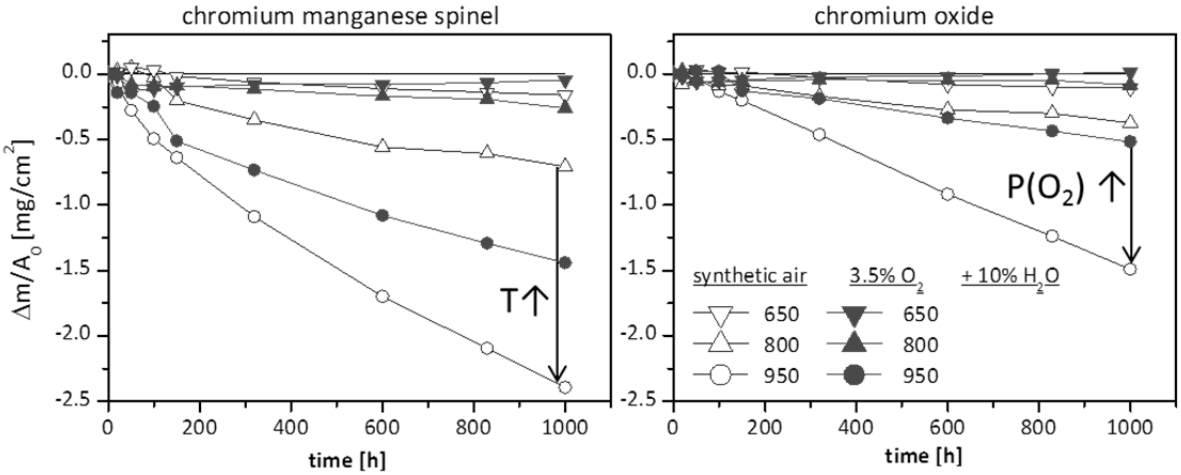

Figure 2: Weight change of chromia and chromium manganese spinel in synthetic air plus 10% water vapor, and nitrogen plus 3.5% oxygen and 10% water vapor at different temperatures

The weight change of the pure chromium carbide sample is not shown, since the simultaneous oxidation and evaporation process does not allow direct comparison to the other samples. Nevertheless in table 1 the results from the XRD measurements are included. Interestingly, Chromium from the initial $Cr_{23}C_6$ transforms into oxide and partly evaporates

during the oxidation process (at 950°C after 100 h the sample is already fully oxidized). Carbon remains in the sample and enriches to form C_7C_3 (compare Table 2). At 950°C the sample is already oxidized after 100 h.

Coatings

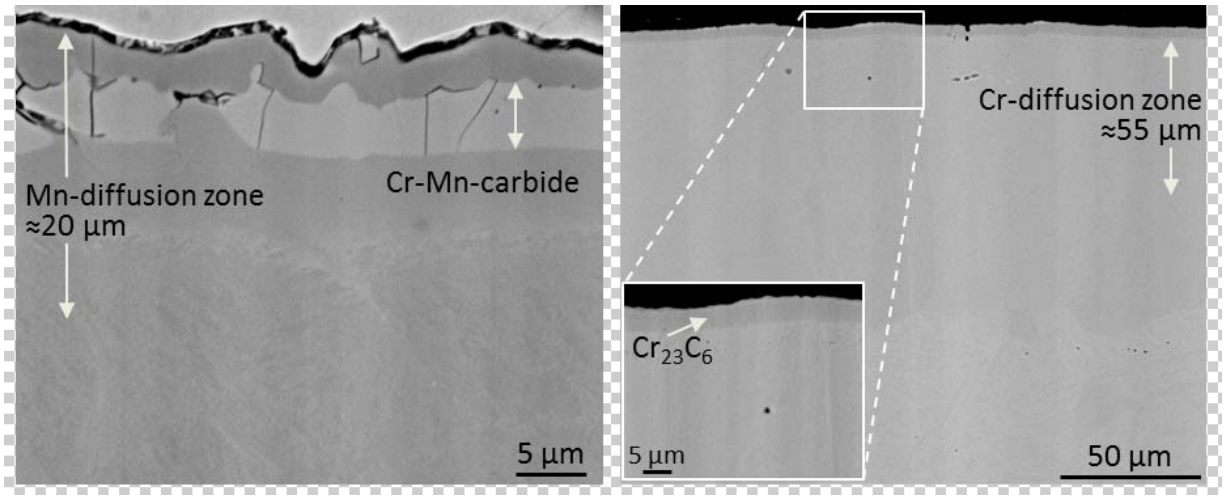

Figure 3: As coated samples of P91 enriched with Cr-Mn (left) or Cr by pack cementation

Figure 3 shows the cross-section of the as coated P91 after the pack cementation process, which enriches the surface with chromium or chromium and manganese by co-diffusion. The Cr diffusion coating consists of the chromium carbide layer and a chromium-enriched metal subsurface region, which in combination form a high-chromium reservoir. The Cr-Mn co-diffusion coating consists of a deep Mn diffusion zone and a mixed Mn-Cr carbide layer beneath the surface. Such samples were exposed for 3000 h at 650°C in N_2-3.5% O_2-10% H_2O atmosphere. Figure 3 shows the weight change of the coated samples in comparison with uncoated P91. It was found that both coatings lower the mass change. In the case of the Cr-Mn coating Manganese oxide was found on top of a mixed chromia-iron oxide scale, which in combination lowered the oxidation rate compared to uncoated P91. However, the chromium coating has a much stronger effect. The formed chromium carbide layer produces a pure chromia scale and provides a huge chromium reservoir underneath. During oxidation in steam, a protective chromium oxide initially forms on this carbide layer, indicated by a slight increase in mass due to the uptake of oxygen. In water vapor containing environments, such as steam exposure, the chromium oxide reacts with water and oxygen to form the volatile chromium oxyhydroxide, which results in an accelerated loss of chromium from the carbide layer. This is the same oxidation mechanism as in the case of the uncoated P91 sample. However, the slow chromium evaporation is compensated by the Cr reservoir underneath. Therefore after longer exposure times the sample mass does not change any further, and the mass loss by evaporation and the mass gain by oxidation seem to be in equilibrium.

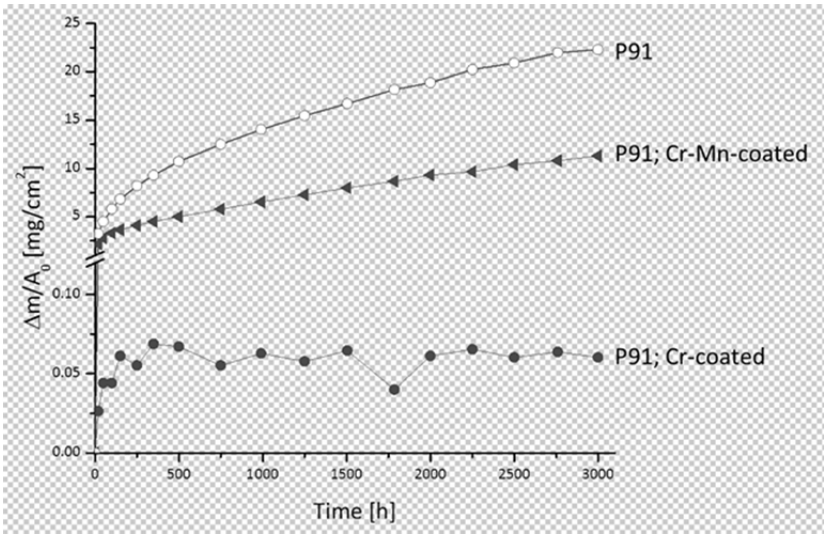

Figure 4: Mass gain of uncoated and coated samples (atmosphere: N_2-3.5% O_2-10% H_2O, 650°C)

Due to the oxidation of chromium carbide carbon is released, which diffuses through the stable oxide scale into the metal subsurface zone, where it forms chromium-molybdenum mixed carbides. These carbides are also found at the grain boundaries in the Cr-enriched zone. Figure 4 gives a schematic illustration of the phenomena occurring at the surface of the chromium-coated ferritic-martensitic steel in water vapor containing environments. The fact that carbon is trapped in the material and not released via CO or CO_2 is in good agreement with the findings

from analysis of the pure reference sample. Due to the formation of a pure chromia scale, evaporation of the chromium oxyhydroxide cannot be suppressed by this coating, but the Cr depletion from the carbide layer is very slow. Since there is no significant chromium depletion after 3000 h, the chromium reservoir phase can compensate the loss of chromium for long exposure times far beyond the reported testing time. The chromium reservoir zone and the carbide layer on the surface, which were formed during the coating process, have the potential to suppress the breakaway oxidation of ferritic-martensitic steels in water vapor containing environments even for very long exposure times.

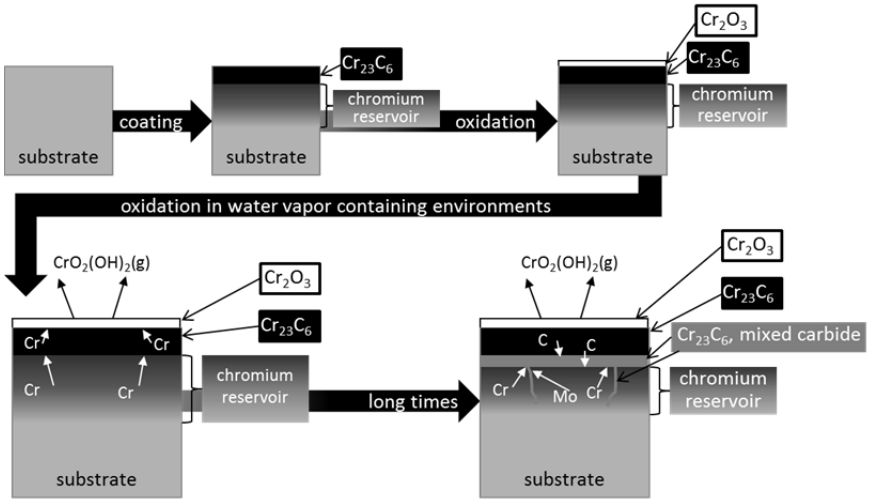

Figure 5: Schematic illustration of the oxidation behavior of chromium-coated ferritic-martensitic steel in water vapor containing environments [3]

4. CONCLUSION

Chromium-manganese spinel forms only above 750°C when synthesized from metal powder mixtures, which is in good agreement with the observation of Cr-Mn-coated samples exposed at 650°C. Such samples show lower weight gain than uncoated P91, but are covered with a mixed oxide and no spinel. Additionally, the reference samples showed a higher evaporation rate of manganese spinel compared with pure chromia under all atmospheres investigated. Following these observations, a chromium coating consisting of chromium carbide and a chromium-enriched zone underneath was developed. This coating provided very good protection for more than 3000 h. Interestingly, although chromium is lost during the oxidation process, the thickness of the chromium carbide layer under the pure chromia oxide scale remains almost stable. During the oxidation of the carbide, carbon is not oxidized. It remains in the material and reacts with chromium from the enriched zone underneath, which is then transformed into carbide.

Acknowledgements: This work was financially supported by the German Ministry of Economics via IGF no. 17205N, which is gratefully acknowledged. The authors would like to thank all colleagues from the working group High Temperature Materials of DECHEMA-Forschungsinstitut for their support.

References

[1] International Organization for Standardization, Corrosion of metals and alloys - Test method for isothermal-exposure oxidation testing under high-temperature corrosion conditions for metallic materials. **ISO 21608** (20121).

[2] Schmidt, D., Galetz, M.C. and Schütze, M., Deposition of Manganese and Cobalt on Ferritic-Martensitic Steels via Pack Cementation Process. *Oxidation of Metals*, **79** (5-6), 589-599 (2012).

[3] Schmidt, D., Galetz, M.C. and Schütze, M., Ferritic-martensitic steels: Improvement of the oxidation behavior in steam environments via diffusion coatings. *Surface and Coatings Technology*, **237**, 23-29 (2013).

[4] Schmidt, D., Galetz, M. and Schütze, M., Improved oxidation resistance of ferritic-martensitic steels in water vapour containing environments via diffusion coatings. *Materials at High Temperatures*, **29** (3), 159-165 (2012).

[5] Bale, C.W., Chartrand, P., Degterov, S.A., Eriksson, G., Hack, K., Mahfoud, R.B., Melan, J., Pelton, A.D. and Petersen, S., FactSage Thermochemical Software and Databases. *Calphad*, **26** (2), 189-228 (2002).

[6] Stanislowski, M., Wessel, E., Hilpert, K., Markus, T. and Singheiser, L., Chromium Vaporization from High-Temperature Alloys I. Chrornia-Forming Steels and the Influence of Outer Oxide Layers. *Journal of The Electrochemical Society*, **154** (4), A295-A306 (2007).

Self-fluxing coating protection against fireside corrosion in WtE

J.M. BROSSARD [1,*], F. MAAD [1], and Y. KAWAHARA [2]

[1] Veolia Environnement Recherche et Innovation, 291 Avenue Dreyfous Ducas, Limay 78520, FRANCE
[2] DAI-ICHI HIGH FREQUENCY, Mizuecho Kawasaki-Ku 1-45, Kawasaki-City 210-0821, JAPAN

e-mail: jean-michel.brossard@veolia.com, fares.maad@veolia.com, y-kawahara@dhf.co.jp

Increase of the energy recovery efficiency facilities is one of the challenges fixed by UE to municipal solid waste incineration (MSWI) operators. To achieve this target one option consists to optimize the water/steam process to increase electrical efficiency. Nevertheless, higher steam temperature into heat exchanger tube is expected to increase the risks of fireside corrosion, particularly on superheater tubes, along with important loss of materials, frequent shutdowns for repairs and high operational costs. In this study, fireside corrosion test had been performed using a laboratory-scale corrosion pilot. Self-fluxing coating performances were tested in comparison with Inconel 625 bulk alloy. These tests conditions allows to evaluate the effect of coating composition and microstructure, and the effect of increase of metal temperature from 400°C to 450°C. Mechanisms and corrosion rates are discussed in regards with lifetime reported for both materials after 1 year in service in the same plant.

1. INTRODUCTION

In the recent revision of the European Waste Framework Directive, high energy efficiency thresholds have been fixed to classify MSWI plants as energy recovery facilities (Directive 2008/98/EC). In MSWI facilities, one option for increasing the energy recovery efficiency consists to optimize the water/steam process to increase electrical efficiency. An increase of steam temperature, entering into a condensing turbine, from 400°C to 500°C leads to an increase of 20% of power generated. Nevertheless, higher steam temperature into heat exchanger tube is expected to increase the risks of fireside corrosion, particularly on superheater tubes [1], along with important loss of materials, frequent shutdowns for repairs and high operational costs. For superheater tube at 400°C/60bar currently, Inconel 625 applied by welding is currently the main solution but iron dilution is assumed to reduce lifetime of the coating. Thus self-fluxing coatings had been considered as they have a microstructure better than thermal spraying [2] and avoids iron dilution.

2. EXPERIMENTAL

The initial thickness of coating delivery by DHF for lab test is estimated to 1 mm for a great part of samples tests.
The corrosion tests carried out on corrosion lab-scale unit describe elsewhere [3]. Tests conditions during these trials are presented in the table 1: $T_{flue\text{-}gas}$ = 850°C, T_{metal} = 400 and 450°C, O_2 = 6±2%vol., H_2O = 19±2%vol., [HCl]gaz = 1100 ppm, [SO_2]gaz = 110 ppm. Synthetic ash is used contain with 10%wt of alkali chlorine and 10% of alkali sulphates in weight ash1 (table 2). The duration of tests is range between 63 and 72 hours.

Table 1. Test conditions

	Duration (h)	Metal T°	Flue-gas T°	Flue-gas T° measured	HCl (ppm)	SO2 (ppm)	O2 (%)	H2O (%)	Vgas (m/s)
Inconel625	65	450	850		1123	116	5.35	19.36	2.69
C2	63	450	850	829	1201	115	4.89	19.93	2.33
C1	72	450	850	821	880	113	5.67	19.17	2.6
Inconel625	69	400	850	782	970	111	5.82	19.29	2.89
C1	72	400	850	850	1018	110	5.77	19.6	2.9
C2	72	400	850	857	1012	113	5.39	19.87	2.79

Table 2. Chemical composition of synthetic ash

%Wt	K_2SO_4	Na_2SO_4	KCl	NaCl	SiO_2-Al_2O_3	Fe_2O_3	$CaSO_4$. $2H_2O$
Ash	5	5	5	5	25	5	50

Two self-fluxing heat treated Ni-Cr-Mo-Si-B base alloys C1 and C2 containing respectively 15.6 and 16.4 wt% Cr, were provided as coating on a pin. Additionally an Inconel 625 bulk alloy has been tested to have a reference alloy (Table 3).

Table 3. Chemical composition of tested material

Wt%	Ni	Cr	Mo	Fe	Nb	C	Cu	Si	B	Co	Σ%Ni+%Cr+%Mo
C1	Bal.	15.6									91.2
C2	Bal.	16.4									92.45
Inconel 625	Bal.	21.5	9	5	3.5	<0.3	<0.5	0		<1	93.2

After each corrosion test, deposited sample are embedded in a resin and prepared for metallographic analysis. Tube thickness loss is measured to estimate corrosion rates, following the procedure described elsewhere using a microprobe SX50. SEM observations and EDX analysis are performed to identify and localize the element in the corrosion layers.

3. RESULTS AND DISCUSSION

In previous work on carbon steel test, metal loss profiles reveal that corrosion is not uniform around the tube. Higher corrosion rates are localized perpendicularly to flue-gas flow [3]. Thus, average corrosion rate (CRAve.) is estimated from the average metal loss measured on the whole circumference of the tube. Then, perpendicular corrosion rate (CR90°) is determined using metal loss measured between ±45° and ±135°. Corrosion rates are expressed in µm/h on the basis of a linear extrapolation of the average metal loss measured after 72 hours.
Corrosion rates obtained on C1, C2 and Inconel 625 alloys after corrosion test at Tmetal = 400°C and 450°C are presented Fig. 1.

- Metal loss results

The test results are presented on the Fig 1 for ash 1 (10% Cl) and for two different metal temperatures (450 and 450°C). Corrosion rate reduction is correlated with Σ%Ni+%Cr+%Mo in the alloy. The maximal thickness loss is usually located on the side (+/-) 45-135° relative to flue-gas direction. It is not the case for Inconel 625 where thickness is lower and more uniform. It is also important to consider that Inconel 625 is a bulk alloy and the microstructure is denser than coating.
Increasing metal temperature from 400°C to 450°C causes an acceleration of thickness loss for all materials. Corrosion rates of C2 and Inconel 625 at 450°C are twice the ones observed at 400°C. C1 metal loss is around 30% higher. Nevertheless the performance ranking stay the same compared with the ranking of alloys elements effect.

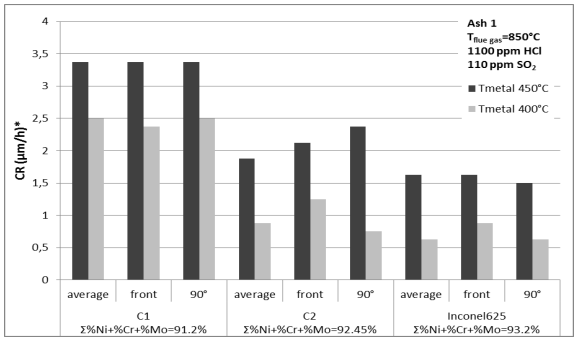

Fig. 1. Corrosion rates of tested materials

- Metallographic analysis

Table 4 shows a melting phase (K, Si, Al, S) created above C1coating surface which contains alloying elements such Ni and Cr. A silicon oxide rich scale SiO_2 is formed on external side in contact with ash. Underneath, an inner adherent mixed oxide scale Cr(Ni)xOy grows at coating interface and in depth as internal oxidation along grain boundary. Cr depletation around 20 µm related to this internal corrosion is also observed.
On C2 coating surface (Table 4) a melting phase is created which contains alloying elements such Ni and Cr. Underneath an external oxide scale (Ni,Cr)xOy is formed on the coating surface that explains the low Cr depletation and

the low internal oxide (5 µm in depth) vs C1. The oxide scale is protective, continuous and uniformed.
Inconel 625 form a Cr-rich scale oxide on surface but no homogeneous. This oxide is in contact with melted phases which prevent the formation of a uniform and adherent scale of Cr_2O_3.

Table 4. Corrosion product of metal test at 450°C.

<table>
<tr><th>Temperature 450°C</th><th>SEM picture</th><th>EDX Analysis</th></tr>
<tr><td>C1</td><td> 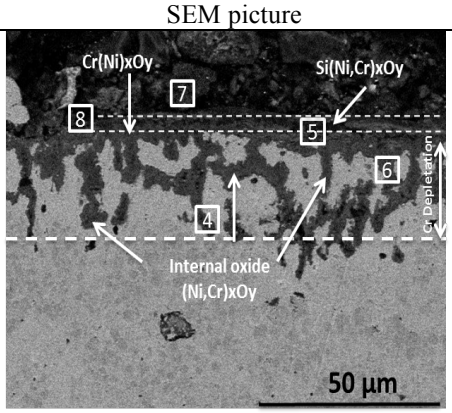
</td><td>
<table>
<tr><th>%wt</th><th>EDS 4</th><th>EDS 5</th><th>EDS 6</th><th>EDS 7</th><th>EDS 8</th></tr>
<tr><td>Ni</td><td>20</td><td>12,1</td><td>13,9</td><td>28,3</td><td>54,2</td></tr>
<tr><td>Cr</td><td>72,5</td><td>21,2</td><td>66,7</td><td>45,1</td><td>20,1</td></tr>
<tr><td>Fe</td><td>3,7</td><td>5,2</td><td>6,3</td><td>16,1</td><td>5,6</td></tr>
<tr><td>Si</td><td>3,1</td><td>54,4</td><td>11,3</td><td>3,7</td><td>14,7</td></tr>
<tr><td>Ca</td><td>0,7</td><td>-</td><td>-</td><td>3,4</td><td>2,4</td></tr>
<tr><td>K</td><td>-</td><td>7,3</td><td>1,9</td><td>3,3</td><td>1,5</td></tr>
<tr><td>S</td><td>-</td><td>-</td><td>-</td><td>-</td><td>1,5</td></tr>
</table>
</td></tr>
<tr><td>C2</td><td> 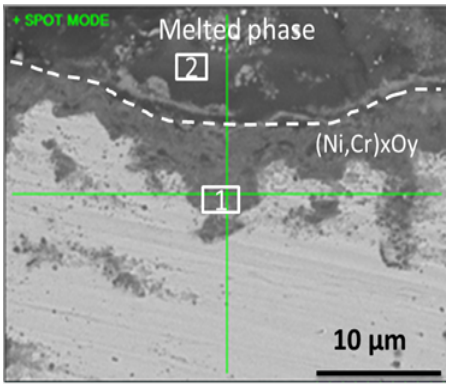
</td><td>
<table>
<tr><th>%wt</th><th>EDS 1</th><th>EDS 2</th></tr>
<tr><td>Ni</td><td>42,3</td><td>48</td></tr>
<tr><td>Cr</td><td>44,8</td><td>13,6</td></tr>
<tr><td>Fe</td><td>4,7</td><td>8,2</td></tr>
<tr><td>Si</td><td>3,6</td><td>18,8</td></tr>
<tr><td>Ca</td><td>1,8</td><td>1</td></tr>
<tr><td>Mo</td><td>2,8</td><td>2,3</td></tr>
<tr><td>Na</td><td>-</td><td>1,1</td></tr>
<tr><td>K</td><td>-</td><td>4,4</td></tr>
<tr><td>Al</td><td>-</td><td>2,5</td></tr>
</table>
</td></tr>
<tr><td>Inconel 625</td><td> 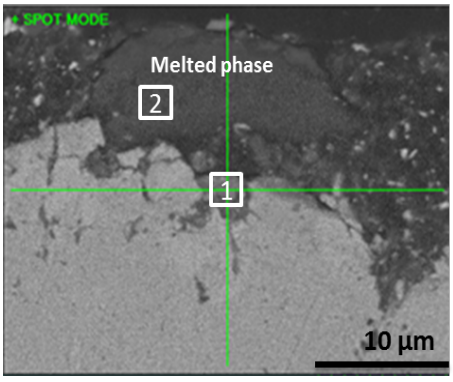
</td><td>
<table>
<tr><th>%wt</th><th>EDS 1</th><th>EDS 2</th></tr>
<tr><td>Ni</td><td>25,2</td><td>47,9</td></tr>
<tr><td>Cr</td><td>68,6</td><td>13,1</td></tr>
<tr><td>Fe</td><td>-</td><td>5,1</td></tr>
<tr><td>Si</td><td>5,1</td><td>28,9</td></tr>
<tr><td>Ca</td><td>1,1</td><td>2,4</td></tr>
<tr><td>S</td><td>-</td><td>2,6</td></tr>
</table>
</td></tr>
</table>

4. CONCLUSION

The results of the corrosion lab-scale VERI about self-fluxing coating have shown a good behavior of C1 and C2 compared to bulk Inconel 625 (reference for these tests). These short time tests were carried out for different operating conditions to evaluate the performance of alloys:

- the influence of alloying elements (Σ%Ni+%Cr+%Mo)
- the influence of metal temperature (400°C to 450°C)

The ranking of alloys performances is following: BM625>C2>C1. It follows the trend of Σ%Ni+%Cr+%Mo reducing corrosion rates already observed by Kawahara [4]. Inconel625 bulk alloy, corrosion products are difficult to detect after short term corrosion test. It point out the good corrosion resistance of this alloy.

The characterisation and analysis of corrosion product reveals that C2 (16.4%Cr) form on its surface a mixed oxide (Ni,Cr)xOy more homogenous and protector than C1 alloys (15.6% Cr). Otherwise internal oxidation is thinner on C2 coating.

The massive microstructure of Inconel 625 tested looks better than a coating applied by thermal spraying with remelting (C1 and C2). Nevertheless considering cost, application method, self-fluxing coating looks competitive with Inconel 625 cladding and further long term test on site (in progress) are needed to validate operational lifetime.

References

[1] A. Miltner G. Beckmann and A. Fried, Applied Thermal Engineering, 26 (2006), p.2005-2011

[2] M.Galetz, J.Bauer, M.Schutze, M.Noguchi a,d H.Cho, Journal of thermal Spray Technology 2013, Resistance of coatings for boiler components of WtE plants to salt melts containing copper compounds.

[3] J.-M. Brossard, I; Diop, X. Chaucherie, F; Nicol, C. Rapin and M. Vilasi, Matrerials and Corrosion, Volume 62, issue 6, 2011, p. 543-548. Superheater fireside corrosion mechanisms in MSWI plants: Lab-scale study and on-site results.

[4] Y. Kawahara et al., Development in high temperature corrosion and protection of materials, Woodhead Publishing ISBN 978-1-84569-219-3, 2008, p.557-598.

Sputtered Mn-Cu Coating for Solid Oxide Fuel Cell Interconnect Application

Shujiang Geng [1,2*], Yaohua Li [1], Shenglong Zhu [2], and Fuhui Wang [2]

[1] School of Materials and Metallurgy, Box 119, Northeastern University, 3-11 Wenhua Road, Shenyang 110819, CHINA
[2] State Key Laboratory for Corrosion and Protection, Institute of Metal Research, Chinese Academy of Sciences, 62 Wencui Road, Shenyang 110016, CHINA

e-mail: gengsj@smm.neu.edu.cn

ABSTRACT：Mn-Cu coating was deposited on ferritic stainless steel (SUS 430) by magnetron sputtering method. The coated steels were evaluated in air at 800°C corresponding to the cathode environment of solid oxide fuel cell (SOFC). It was found that the coated steel initially experienced a large mass gain, followed by slight increase with time. The Mn-Cu coating was mainly converted into $(Mn,Cu,Fe)_3O_4$ spinel layer beneath which a Cr-rich layer is grown from the steel substrate upon thermal exposure. The Cr-free outer layer not only suppressed Cr migration outward but also reduced the surface oxide scale area specific resistance (ASR) of the coated steel.

1. INTRODUCTION

Ferritic stainless steels have been extensively used as solid oxide fuel cell(SOFC) interconnects [1-4] due to their low cost, coefficient of thermal expansion match with other SOFC components, and good oxidation resistance and acceptable electrical conductivity of Cr_2O_3. However, the evaporation of Cr_2O_3 results in cathode Cr-poisoning and subsequent degradation of cell performance [5,6]. Thus, it is necessary to develop electrically conductive coating on them in order to block Cr_2O_3 evaporation. So far, $(Mn,Cu)_3O_4$ spinel [7-9] is a promising coating to improve the electrical conductivity of the surface oxide scale thermally formed on the interconnects. In this paper, Mn-Cu coating has been deposited on ferritic stainless steel (SUS 430) by magnetron sputtering method. The oxidation behavior and surface scale area specific resistance of the coated steel was investigated in air at 800°C.

2. EXPERIMENTAL

The Mn-Cu alloy used in this work was prepared in a vacuum-induction furnace. Its chemical composition (atom percent) is 50%Mn and 50%Cu. The steel samples (15×10×1.5 mm) used as the substrate for coating deposition were cut from a SUS 430 steel sheet and ground using silicon carbide papers down to 600 grit. They were sandblasted and then degreased by an ultrasonic cleaner in acetone before sputtering. The target was the cast Mn-Cu alloy sheet of 248 × 124 mm^2. The deposition was carried out at sputtering target power of 400 V and 3.0 A under chamber pressure of 0.12 Pa of argon for 2 h. The temperature of substrate samples for coating was 180°C. The samples were rotating in front of the target during sputtering to ensure better uniformity.

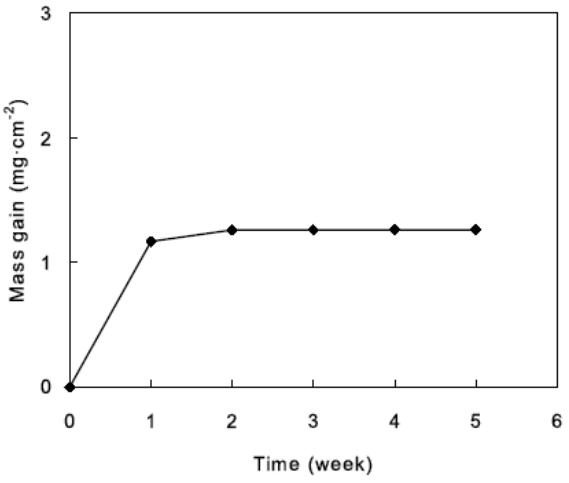

Fig.1. Oxidation kinetics of the coated steel in air at 800°C

Oxidation testing of the coated steels was conducted in a box furnace. The samples were hung in alumina crucibles. The coated steels were oxidized for total 5 weeks. The weight of each sample was measured after furnace cooling to room temperature following each 1-week thermal exposure.

Electrical resistance of oxidized samples was measured in air at 800 °C using 4-point method. The measurement setup was described in our previous work [10].

3. RESULTS AND DISCUSSION

Fig.1 shows the oxidation kinetics of the coated steel in air at 800°C. The coated steel experienced an initially large mass

gain, followed by a transition to slower oxidation kinetics after the first-week thermal exposure, implying a protective oxide scale formation between the substrate and the surface oxides developed during the initial rapid oxidation stage.

The cross-section and elements line scan of the oxide scale formed on the coated steel after 1-week oxidation in air at 800°C are shown in Fig.2. It thermally formed a double-layer oxide structure with an outer layer rich in Fe, Mn and Cu atop an inner layer rich in Cr, In case of the outer layer, in detail, it was rich in Cu near the outmost surface, followed by rich in Fe, Mn and Cu. The Fe in the outer oxide layer should be from the outward diffusion of Fe in the steel. The formation of the Cr-rich inner layer reduced the oxidation rate of the coated steel, which is consistent with the oxidation kinetics as shown in Fig.1.

Fig.3 presents X-ray diffraction patterns of the coated steel after 1- and 5-week oxidation in air at 800°C. Combined with elements line scan analyses above, the oxide scale formed on the coated steel after 1-week oxidation contained CuO and $(Mn,Cu,Fe)_3O_4$, i.e. the outer layer consisted mainly of the $(Mn,Cu,Fe)_3O_4$ spinel phase underneath the outmost surface of CuO phase. After 5-week thermal exposure, the peak intensity of CuO decreased obviously. The XRD patterns did not show the diffraction peaks of the inner Cr-rich layer due to the thick outer layer that blocked the X-ray penetration.

According to the SEM cross-section and elements line scan analyses (Figs.2 and 3) of the oxide scale formed on the coated steel, evidently, it was the formation of the Cr-free oxide outer layer that could significantly suppress the evaporation of the inner Cr-rich layer. Moreover, after 5-week oxidation of the coated steel, the area specific resistance of the scale was 45.14mΩ•cm^2 which was much lower than that of the bare steel after 4-week oxidation [11].

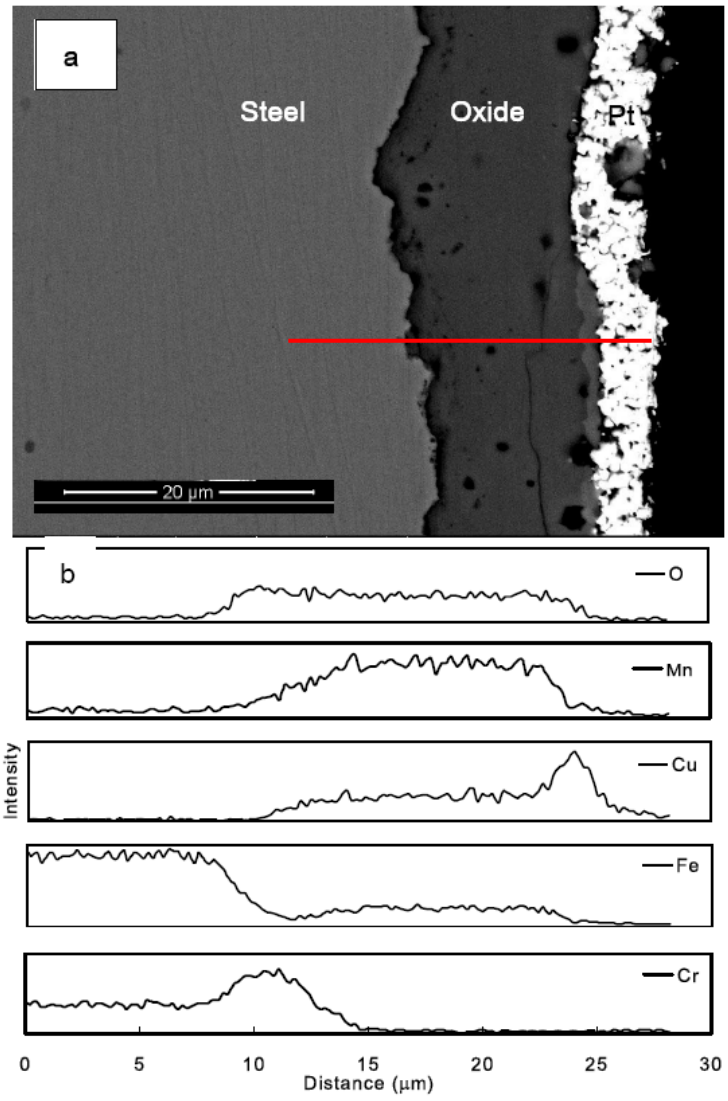

Fig.2. Cross-sectional morphologies (a) with elements line scan (b) of the coated steel after oxidation in air at 800°C for 1 week

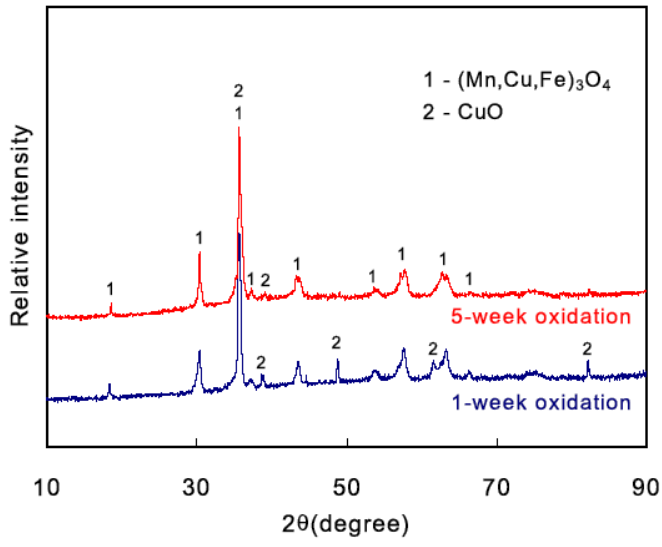

Fig.3. XRD patterns of the coated steel after oxidation in air at 800°C

4. CONCLUSION

From the results above, the following conclusions can be drawn:

After oxidation in air at 800°C, the coated steel thermally developed a double-layer oxide structure with an outer layer of $(Mn,Cu,Fe)_3O_4$ spinel containing small amount of CuO near the outmost surface atop a continuous inner Cr-rich layer. The Cr-free outer layer did suppress Cr migration outward. In addition, the surface scale exhibited

good electrical conductivity.

Acknowledgements

This work was sponsored by the National Natural Science Foundation of China (NSFC) under Grant No. 51371048 and the National Key Basic Research Program of China (973 Program, No. 2012CB625100).

References

[1] Pu J., Li J., Hua B. and Xie G., "Oxidation kinetics and phase evolution of a Fee16Cr alloy in simulated SOFC cathode atmosphere," *Journal of Power Sources,* Vol. 158(2006), pp.354-360.

[2] Han M., Peng S., Wang Z., Yang Z. and Chen X., "Properties of FeeCr based alloys as interconnects in a solid oxide fuel cell," *Journal of Power Sources,* Vol. 164(2007), pp.278-283.

[3] Yang Z., Hardy J.S., Walker M.S., Xia G., Simner S.P. and Stevenson J.W., "Structure and conductivity of thermally grown scales on ferritic Fe-Cr-Mn steel for SOFC interconnect applications," *Journal of the Electrochemical Society,* Vol.151(2004), pp.A1825-1831.

[4] Geng S. and Zhu J., "Promising alloys for intermediate-temperaturesolid oxide fuel cell interconnect application," *Journal of Power Sources,* Vol. 160(2006), pp.1009-1016.

[5] Matsuzaki Y. and Yasuda I., "Electrochemical properties of a SOFCcathode in contact with a chromium-containing alloyseparator," *Solid State Ionics* Vol. 132(2000), pp.271-278.

[6] Chen X., Zhen Y., Li J. and Jiang S., "Chromium deposition and poisoning in dry and humidified air at (La0.8Sr0.2)0.9MnO3td cathodes of solid oxide fuel cells," *International Journal of Hydrogen Energy,* Vol. 35(2010), pp.2477-2485.

[7] Petric A and Ling H., "Electrical conductivity and thermal expansion of spinels at elevated temperatures," *Journal of American Ceramic Society*, Vol.90 (2007), pp.1515-1520.

[8] Bateni M.R., Wei P., Deng X. and Petric A., "Spinel coatings for UNS 430 stainless steel interconnects," *Surface & Coatings Technology,* Vol.201(2007), pp.4677-4684.

[9] Wei P., Deng X., Bateni M.R. and Petric A., "Oxidation and electrical conductivity behavior of spinel coatings for metallic interconnects of solid oxide fuel cells," *Corrosion,* Vol.63(2007), pp.529-536.

[10] Geng S., Li Y., Ma Z., Wang L., Li L. and Wang F., "Evaluation of electrodeposited Fe-Ni alloy on ferritic stainless steel solid oxide fuel cell interconnect," *J. Power Sources,* Vol.195 (2010), pp.3256-3260.

[11] Geng S., Qi S., Zhao Q., Zhu S.and Wang F., "Electroplated Ni-Fe2O3 composite coating for solid oxide fuel cell interconnect application," *International Journal of Hydrogen Energy,* Vol.37 (2012), pp.10850-10856.

Nano RE coatings on ferritic steels in high steam content hydrogen atmospheres – A material study for SOFC and SOEC applications

P. Alnegren *, J. G. Grolig, J-E. Svensson , J. Froitzheim

The High Temperature Corrosion Center, Chalmers University of Technology, 412 96 Gothenburg, SWEDEN

e-mail: alnegren@chalmers.se

1. INTRODUCTION

High chromium ferritic steel is today the most commonly considered material as interconnects for solid oxide fuel (SOFC) and electrolysis cells (SOEC) due to many desirable properties, such as good machinability and lower cost compared to ceramic alternatives and matching TEC with other cell components. But there are still some issues to be addressed regarding long term stability of ferritic steel interconnect based fuel stacks. Interconnects are used to connect fuel cells in series into stacks in order to increase the power output and the role of the interconnect is to separate oxidizing and reducing gases and to conduct electricity between interlinked cells. A thin and dense oxide layer is desired not only for material preservation but also to minimize the electrical resistance of the interconnect. So far the major research focus for metallic interconnects has been on the air side (cathode in SOFCs, anode in SOECs). The current study instead focuses on the fuel side of a fuel or electrolysis cell.

A recent study performed in air atmosphere has shown that AISI 441 stainless steel with nanometer thick coatings could be a viable alternative to more expensive steels specifically developed for SOFC applications [1]. A similar approach is taken in the current study where AISI 441 and Sanergy HT are investigated under exposure in a low pO_2 environment which consists of Ar – 40 % H_2O – 3% H_2. This environment was chosen to simulate a high steam content fuel side corresponding to an SOEC inlet or SOFC outlet. The steels are tested both with and without a 10 nm coating of Ce and the corrosion performance is evaluated.

2. EXPERIMENTAL

The materials studied were Sanergy HT and AISI 441, both ferritic steels and their compositions can be found in Table 1. Coating of of both steels with a 10 nm PVD coating was performed by Sandvik Materials Technology. Steel sheets with 0.2 mm thickness were cut into 15x15 mm^2 specimen which were then cleaned by ultra-sonic agitation in acetone and ethanol for ten minutes respectively.

Table 1. Composition of the investigated steels in weight%. The compositions were given by the manufacturers for the received batches.

Material	Fe	Cr	C	Mn	Si	Mo	Nb	Ti	RE(Zr)
Sanergy HT	Bal	21.2	0.040	0.3	0.12	0.96	0.71	0.09	0.24
AISI 441	Bal	17.8	0.012	0.26	0.55	-	0.48	0.13	

Exposures of the materials were carried out in simulated fuel side conditions inside a horizontal tubular furnace (Al_2O_3 tube) with inner diameter of 46 mm. The gas composition was Ar - 40 % H_2O - 3 % H_2, which was achieved by bubbling dry Ar - 5 % H_2 through a humidifier and led through a condenser set at a temperature of 76.2 °C. The gas tube connecting condenser and reaction chamber was heated above 100 °C with a heating cord to ensure that no condensation occurred. The furnace temperature was 850 °C and the total gas flow rate was 250 smL/min in all experiments, which corresponds to a mean flow velocity of 1.0 cm/s inside the reaction chamber. Oxidation rates were measured by cooling down the furnace and weighing the samples, which were then placed back in the cold furnace which was flushed with dry Ar – 5 % H_2 for at least 20 min at 2000 smL/min before the experiments were resumed. Oxidation rates were measured for up to 500 h. Plan view and cross sectional images and EDX analyses of the samples after exposure were obtained by scanning electron microscopy. X-ray diffraction of the corrosion products was also performed.

3. RESULTS AND DISCUSSION

In Figure 1 the average mass gains of the tested samples after 24 h exposure are shown. The cerium coating is effectively reducing the oxidation of Sanergy HT from 0.22 to 0.10 mg/cm^2 and a slight reduction can be seen also in the case of 441

from 0.55 to 0.47 mg/cm^2. The scale compositions of the two steels are different. Sanergy HT forms a duplex scale of inner chromia and outer manganese-chromium spinel according to EDX and XRD analysis and the same is seen on the Ce coated version. EDX analysis of the 441 samples, both uncoated and coated, indicates an oxide scale with Fe as main constituent. Grazing incidence XRD analysis gave a diffraction pattern that matches to a spinel type oxide, thus it is concluded that an outer oxide of magnetite is formed. According to thermodynamics magnetite is the expected outermost ironoxide in the chosen exposure conditions. Reactive elements such as Ce are known to increase the selective oxidation of chromium, thus restricting the formation of iron oxides but the coating applied on 441 in this case is not sufficient for the formation of a more protective chromia scale [2]. The difference in oxide scale formation between the steels could be due to lower amount of alloyed Cr in and the lack of alloyed REs in 441, however, further analysis including cross-sections is needed to come to a conclusion on the observed differences.

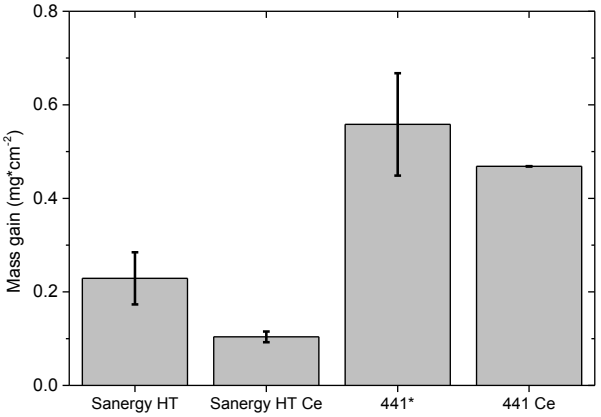

Figure 1. Average mass gain of Sanergy HT and 441 uncoated and coated after exposure for 24 h in Ar – 40 % H_2O and 3% H_2 at 850 °C. *Uncoated 441 and Ce coated 441 are different batches of the steel grade.

An interesting difference between the uncoated and coated samples is the formation of Si rich crystallites on both Sanergy HT and 441 substrates coated with Ce. This can be seen in Figure 2 where it is also apparent that the Si crystals formed on 441 are larger than those on Sanergy HT. The Si rich crystals were detected on both alloys already after 24 h and grew larger with time. These crystals are absent on the uncoated samples (same exposure run). According to EDX analysis the crystals on 441 are also more rich in Fe and on Sanergy HT more rich in Mn. Ce (10nm) coated Sanergy HT samples were exposed for 500 h and subsequently analyzed by XRD (Figure 3). Apart from the expected $(Cr,Mn)_3O_4$ phase a second phase with the composition $(Mn,Fe)_2SiO_4$, was found, so called tephroite. Thus, it is concluded that the Si rich crystals observed in Fig 2 are tephroite. The stability of such a compound also matches the exposure environment [3]. Since the exposure setup is designed in a way that no glassware is exposed to high temperature it is concluded that the most likely source of Si is the underlying steel. This is in line with the observation of less tephroite on Sanergy HT which has a lower Si content. Thus, it is postulated that Ce promotes the formation of an outer Si rich tephroite phase on Si containing steels. In order to test this hypothesis exposures with Si free steels are planned. Considering that it is critical for the interconnect of a fuel cell stack to form a conductive oxide scale, a continuous layer of tephroite could be detrimental since this compound is expected to be poorly conductive [3].

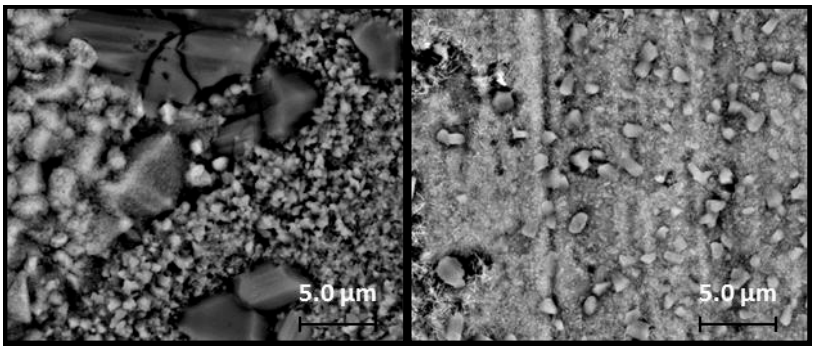

Figure 2. SEM backscattered micrographs of Ce coated 441 (Left) and Sanergy HT (Right) exposed for 24 h in Ar – 40 % H_2O and 3% H_2 at 850 °C. The larger crystals on both images are proposed to be $(Mn,Fe)_2SiO_4$.

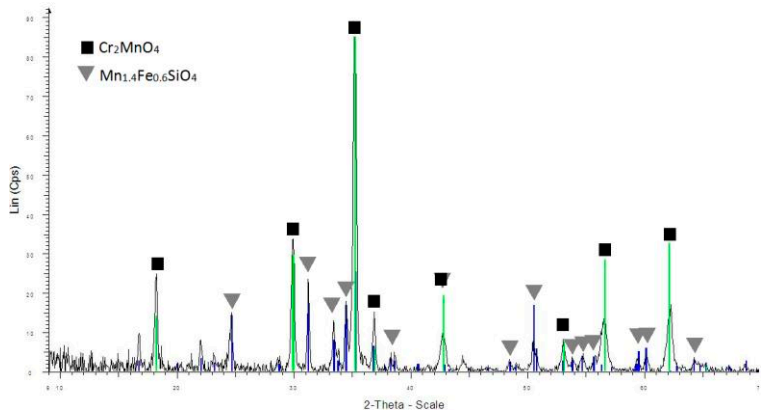

Figure 3. XRD pattern for a sample of Sanergy HT with 10 nm cerium coating exposed of Ar – 40 % H_2O – 3% H_2 for 500 h at 850 °C.

4. CONCLUSION

AISI 441 was compared to the higher alloyed ferritic steel Sanergy HT in a simulated solid oxide fuel or electrolysis cell environment representing the fuel side. The effect of a PVD deposited nano scale Ce layer was investigated. Ce decreased the oxidation rate for both steels, but more significantly for Sanergy HT. The oxidation rate for 441 was more than twice than that of Sanergy HT and the formed oxides were Fe_3O4 and Cr_2O_3-$(Cr,Mn)_3O_4$ respectively.
Formation of iron rich (441) and manganese rich (Sanergy HT) silicates seems to be promoted by the presence of Ce in the investigated environment. This poses a potential risk of decreased performance for Ce coated ferritic steel interconnects if a continuous layer is formed.

OUTLOOK

Area specific resistance measurements of the exposed samples are ongoing to validate the effect of a Ce coating on the electrical performance of a ferritic steel interconnect. Exposures with Si free steels are planned to test if tephroite formation is avoided. Cross sections of the samples will be prepared and analyzed in order to investigate the underlying mechanisms.

ACKNOWLEDGEMENTS

Sandvik Materials Technology is acknowledged for providing the test samples. This project was funded within Swedish High Temperature Corrosion Centre and the European Seventh Framework Programme for the Fuel Cells and Hydrogen Joint Technology Initiative (grant agreement no. 278257).

REFERENCES

[1] Grolig, J.G., J. Froitzheim, and J.E. Svensson, “Coated stainless steel 441 as interconnect material for solid oxide fuel cells: Oxidation performance and chromium evaporation”, *Journal of Power Sources*, Vol. 248(0) (2014), pp. 1007-1013.

[2] . Y. Hou, "The Reactive Element Effect - Past, Present and Future", *Materials Science Forum,* Vol. 696 (2011), pp. 39-44.

[3] Quan Bai, Z.-C. Wang, D.L. Kohlstedt, “Manganese Olivine I: Electrical Conductivity”, *Physics and Chemistry of Minerals,* Vol. 22 (1995), pp. 489-503.

Electrochemical corrosion behavior of Fe, Cr with a solid NaCl deposit in wet oxygen at medium temperature

Li Liu (*), Ying Li, and Fuhui Wang (*)

Sate Key Laboratory for Corrosion and Protection, Institute of Metal Research, Chinese Academy of Sciences, Shenyang 110016, China

e-mail: liliu@imr.ac.cn

1. INTRODUCTION

In late 1990's, people found that the corrosion of turbine blades in airplanes or ships in marine environments was much more seriously than those used at in inland areas. In analyzing this trend, the significantly different working environments immediately come to mind: the air is dry in inland area, while in marine areas the air is moist and with lots of salts, especially NaCl. The working blades, which operate at medium temperatures (around 400-700 ˚C), are covered by a layer of solid NaCl deposit. At the same time, the moist air with enough water vapor is assimilated in the machines. Therefore, the actual working environment is a combination of solid NaCl and water vapor [1-3].

From the results of a systematic investigation of this corrosion it has been suggested that there may be a ''dynamic water film" with H_2O molecules continuously being absorbed on, and evaporating from, the surface of the material and that electrochemical corrosion occurs in this water film, which accelerates the metal dissolution [2]. However, this hypothesis is very controversial and is not accepted by many scientists. It is therefore necessary to study the relevant electrochemical reactions.

The present work focuses on: (1) to determine whether electrochemical corrosion occurs on the surface of pure Fe with a solid NaCl deposit in water vapor at 600^{o}C; (2) if electrochemical reactions do occur, to clarify their role in the corrosion process. It is necessary to understand the corrosion mechanism of metals/alloys in this environment in order to develop effective protection techniques.

2. EXPERIMENTAL

Pure Fe , Cr (99.9%) specimens were used, the preparation of which has been reported elsewhere[4]. A special three-electrode system was built for the electrochemical measurements in this particular environment. The top and cross-section view of the electrode arrangement is shown in Fig. 1 [5]. A PAR2273 Electrochemical Measurement System manufactured by EG&G was used for electrochemical measurements. In chronopotentiometry measurements, a-0.5 mA cathodic current was applied to detect the transition times. In EIS measurements, the perturbation was 0.1 V because of the low conductivity of NaCl at 600^{o}C [4] and the frequency was swept from 10 kHz to 10 mHz.

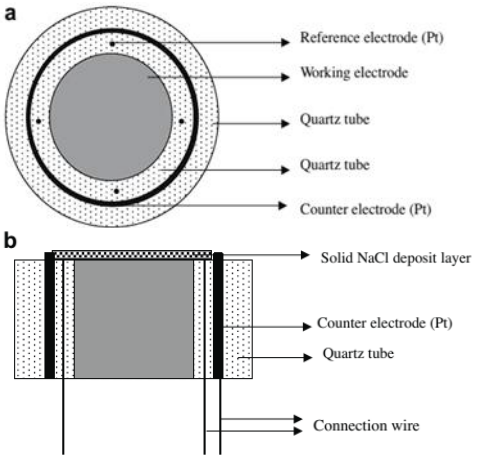

Fig. 1. Schematic diagram of three-electrode cell: the top view (a), the cross-section view (b).

3. RESULTS AND DISCUSSION,

In order to study the electrochemical reactions, the galvanic corrosion current (I_g) can be measured by the electrodes as pure Fe and pure Pt, under the synergistic effect of solid NaCl and water vapor at middle high temperature, as shown in Fig.2[5]. Compared to the I_g of the pure Pt –Pt couple (near to zero with some fluctuation), the I_g of the Fe-Pt couple was about 10^{-5} A/cm^2. It is believed that no corrosion reactions occurred on the inert Pt electrode [5] and its current should be a measure of the background current of the system. The current on the pure Fe-Pt electrode was higher, which suggested that electrochemical reactions occurred during corrosion in this environment.

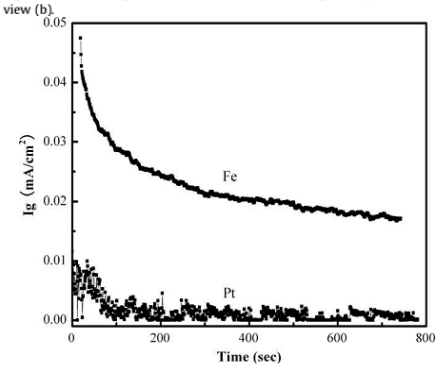

Fig. 2. The galvanic current of a pure Fe electrode and a pure Pt electrode with a soild NaCl deposit in water vapor at 600 ºC.

For pure Fe in this corrosion environment, the anodic reaction is simple (Fe = Fe^{2+}+ 2e), but the cathodic reactions are complicated. The chronopotentiogram of the cathodic reaction showed that there was only

one transition time for this cathodic reaction. Therefore, there is only one cathodic reaction on pure Fe. Authors think that the corrosion of pure Fe in this environment includes chemical and electrochemical corrosion reactions. After calculation, the percentage of electrochemical corrosion reaction to total whole corrosion reactions is about 8.0%. However, the corrosion rate was dramatically increased when electrochemical reaction occurred. The corrosion rate is controlled by the consuming of iron and the consuming of iron produced by electrochemical reaction is limited. Therefore, the cathodic electrochemical reaction accelerated the consuming of iron produced by chemical corrosion reaction, which lead to the increase of corrosion.

The methods for mechanistic diagnosis of the interaction between chemical and electrochemical processes have been studied by Smith [6]. According to this method, the interaction of chemical and electrochemical reactions for metals and alloys all follow a ce mechanism, which means that the electrochemical reaction is coupled with either a preceding chemical reaction [7]. During the corrosion, firstly the chemical reactions, i.e. oxidation reactions, take place and then electrochemical reactions follow. This reaction sequence has been found in the reaction of pure Fe, pure Cr and Fe-20Cr alloy. It is very interesting that the interaction between electrochemical reaction and chemical reaction also was found during the synergistic effect of Na_2SO_4 and water vapor at 600 ˚C [Y. Tang, et.al. 2010, personal communication]. The whole corrosion mechanism can thus be summarized as follows: The interaction of both reactions followed the ce mechanism, that is, chemical reactions first take place, and the electrochemical reactions then follow. Even though the contribution of the electrochemical reaction is not very pronounced, it still exerted a considerable influence on the overall process, which has been explained taking pure Cr as an example.

Cr reacts chemically with solid NaCl and water vapor to form Na_2CrO_4 and HCl [7]. This reaction is then followed by electrochemical reactions (reaction 1). The cathodic reaction involves HCl from the chemical reaction (2), while the anodic reaction is the oxidation of Cr (3). It is obvious that HCl produced in the chemical reaction (1) was consumed by the electrochemical reaction (2). As a consequence, the chemical reaction (1) will proceed faster in the forward direction. The electrochemical reaction thus promotes the progress of chemical reaction and accelerates the corrosion rate. Again, the NaCl produced by the electrochemical reaction (2) can chemically react with pure Cr, further promoting the chemical reaction (1). The Cr^{3+} formed by electrochemical corrosion reaction would exist as two compounds: one is Cr_2O_3, which is the combination of Cr^{3+} with O^{2-}; the other is volatile $CrCl_3$, which is the reaction of Cr^{3+} with Cl^-. The electrochemical reaction also promotes the formation of $CrCl_3$, which is highly volatile and adversely affects the morphologies of corrosion product by making it looser and more porous compared with reaction results without electrochemical reactions.

$$8NaCl + 8Cr + 9O_2 + 4H_2O \underset{K_2}{\overset{K_1}{\rightleftharpoons}} 4Na_2CrO4 + 2Cr_2O_3 + 4HCl \quad (1)$$

$$2HCl + Na^+ + 2e \rightarrow H_2 + NaCl + Cl^- \quad (2)$$

$$Cr - 3e \rightarrow Cr^{3+} \quad (3)$$

4. CONCLUSION,

The corrosion of metals or alloys under solid salts es-pecially NaCl and water vapor at medium temperature 400- 700 ˚C is very interesting. The synergistic effect of solid salt and water vapor accelerates the corrosion com-pared with only salt or pure water vapor. The chemical reactions and electrochemical reactions co-work during the whole corrosion. Based on the initial chemical reactions, electrochemical reactions happen. Although the chemical reactions (oxidation) are mainly responsible for the corrosion of metals or alloy under this corrosion environment studied, electrochemical reactions promote the corrosion further. Cr has special effect under the corrosion environment on the materials, which is poison and promote the corrosion.

Acknowledgements,

The investigation is supported by the National Key Basic Research and Development Plan of China under the Contract No.2014CB643303.

References.

[1] Shu Y., Wang F., Wu W., “Synergistic effect of NaCl and water vapor on the corrosion of 1Cr-11Ni-2W-2Mo-V steel at 500-700˚C.” *Oxid. Met.*, Vol. 51, (1999), pp. 97-110.

[2] Shu Y., Wang F. and Wu W., “Corrosion behavior of Ti60 alloy coated with a solid deposit in O_2 plus water vapor at 500-700˚C.” *Oxid. Met.*, Vol. 52, (1999), pp. 463-473.
[3] Shu Y., Wang F. and Wu W., “Corrosion behavior of pure Cr with a solid NaCl deposit in O_2 plus water vapor.” *Oxid. Met.*, Vol. 54, (2000), pp. 457-471.
[4] Liu L., Li Y., Zeng C. and Wang F., “Electrochemcial impedance spectroscopy (EIS) studies of the corrosion of pure Fe and Cr at 600 ˚C under solid NaCl deposit in water vapor.” *Electrochimica Acta*, Vol.51, (2006), pp.4736-4743.
[5] Tang Y., Liu L., Li Y. and Wang F., “Evidence for the occurrence of electrochemical reactsions and their interaction with chemical reactions during the corrosion of pure Fe with solid NaCl deposit in water vapor at 600˚C.” *Electrochemistry Communications*, Vol. 12, (2010), pp.191-193.
[6] Smith D. E., Alternating current polarography of electrode processes with coupled homogeneous chemical reactions I Theory for systems with first-order preceding, following, and catalytic chemical reactions. Anal. Chem. 1963, 35: 602-609D.
[7] Tang Y., Liu L., Li Y. and Wang F., “The electrochemical corrosion mechanisms of pure Cr with NaCl deposit in water vapor at 600 ˚C.” *Journal of the Electrochemcial Society*, Vol.158, (2011), pp. C237-C241.

O25

Vanadium Attack of Tube Materials in Boilers Firing Crude-Residues

Nobuo Otsuka

Technical Research & Development Bureau, Steel Research Laboratories, Nippon Steel & Sumitomo Metal Corporation,
1-8 Fusocho, Amagasaki, Hyogo 660-0891, JAPAN
e-mail: ohtsuka.8pp.nobuo@jp.nssmc.com

Abstract: Thermodynamic equilibrium calculation was conducted to identify the ash chemistry of boiler tubes firing crude residues. Laboratory corrosion test of ferritic 9-12%Cr and austenitic stainless steels and alloys was performed in 0.4% SO_2 -0.8%O_2 -10%H_2O -10%CO_2 -N_2 at 650° C for 72 h. Mixtures of 15wt.%Na_2SO_4 -$NaVO_3$ with and w/o magnesium addition were used as a corrosive. For the ash w/o magnesium addition, corrosion rate of 18-8 stainless steel was similar to 9-12%Cr steels, but 9wt.% addition of MgO or $Mg(OH)_2$ to the ash reduced the corrosion rate of 18-8 stainless steel significantly, while its effect was minor for 9-12%Cr steels.

1. INTRODUCTION

Recently, crude residues coming from oil refineries have attracted concern as potential fuel for power generation in some OPEC countries where abundant crude oil is available in their territory. Since crude residues generally contain considerable amount of vanadium, sodium, and sulfur, fireside corrosion of boiler tubes in recent high-efficiency steam generators can become a major materials damage of this system [1]. According to the literature, corrosion caused by impure element of vanadium in fuel, named the vanadium attack or oil ash corrosion, has been investigated intensively in the late 50's and 60's [2,3]. The corrosion was attributed to the formation of molten phases in the oil ash deposits, which react with protective oxide scale on tube surface to dissolve them into the melt. The type of corrosion is categorized as hot corrosion, where dissolution and precipitation of protective oxide scale in molten ashes are important [4]. The corrosive constituents are reported to be mixtures of Na_2SO_4 and Na-V-O compounds, in which Na_2O -V_2O_4 -5V_2O_5 (1-1-5), 5Na_2O -V_2O_4 -11V_2O_5 (5-1-11), $NaVO_3$ (meta-vanadate), and Na_3VO_4 (ortho-vanadate) were identified so far as the Na-V-O species [5,6]. The lowest melting point temperature of the binary Na_2SO_4 -V_2O_5 system was reported at around 600° C [2], and addition of "Na_2O" to the salt system can vary its melting point temperature [7]. The onset metal temperature to initiate corrosion of superehater and reheater tubes decreases when the flue gas temperature becomes high, suggesting that vapor-condensation of corrosive gas species on tube surface may play an important role to the ash chemistry [8]. Since high capability to "absorb" oxygen of the ambient gas atmosphere was indicated for molten Na_2SO_4-V_2O_5 mixtures [2,3], the rate-limiting step of the corrosion was proposed to be diffusion of oxygen through the molten film to metal surfaces [2]. Surprisingly, 18-8 stainless steels are reported not to have better corrosion resistance than the ferritic 9Cr and 12Cr steels [9], and inhibitors and fuel additives of MgO-based compounds have been widely used to alleviate the corrosion [1,5]. Addition of MgO is reported to result in raising the melting point temperatures of the tube deposits. Recently, increasing steam temperature of oil-fired boilers is favored, and information on the corrosion resistance of tube materials to boilers firing crude residues with fuel additives is needed. The purpose of the present study was to flash back the oil ash corrosion created by vanadium and fuel additives, and to evaluate the corrosion resistance of commercial boiler tube materials in this particular environment.

2. EXPERIMENTAL,

Thermodynamic calculation was conducted to obtain equilibrium composition of flue gas (gaseous and condensed species) at 1000° C upon "firing" heavy oil of 83.3%C, 12%H, 4%S, 0.2%N, and 0.5%H_2O (% in weight) [10], with addition of 130ppm V (232ppm as V_2O_5) and 100ppm Na. The amount of air (21 vol.%O_2 -N_2) needed for complete oxidation of carbon, hydrogen, sulfur, and nitrogen in 100g fuel was calculated about 47.6 mol. This air-fuel (AF) ratio was set to one. The computer program used was MALT II software package offered by Yokogawa [11]. Six steels and alloys were tested. Three ferritic steels of T91, T92, and HCM12A (T122), two stainless steels of SUPER304H (S30432, ASME Code Case 2328) and HR3C (S31042, A213 TP310HCbN) are commercial boiler tube materials. Alloy HR6W (VdTÜV WB559/2) [12], its nickel content is around 44.5% and is categorized as Ni-base alloys, was prepared in the laboratory. Detailed conditions of preparing these alloy specimens are given in the literature [13]. Coupon specimens of 15 mm x 15 mm x 3 mm were ground on emery paper of 320 grit, cleaned in acetone, and weighed by microbalance. Synthetic ash mixture of 15wt.% Na_2SO_4 -$NaVO_3$ was used as a corrosive. Ash mixtures with 9wt.% addition of MgO or $Mg(OH)_2$ were tested as well. The ash mixtures were coated on the entire specimen surface by using acetone. The amount of synthetic ash was 30 mg per unit specimen surface area of 1 cm^2. Coupon specimens were separately placed on a high-purity alumina crucible, and were set on a reaction chamber made of quartz. After purging the chamber with Ar at RT, the chamber was heated at 250°C for 1 h, and the gas atmosphere was changed from Ar to 0.4vol.%SO_2 -0.8%O_2 -

10%H_2O -10%CO_2 -N_2. In order to obtain equilibrium between SO_2, SO_3, and O_2, the gas mixture was reacted with agglomerates of Pt wire at 600° C before introducing it into the chamber. The equilibrium SO_3 concentration of this gas mixture at 600° C was calculated 1.83 x 10^{-3} (i.e. log p_{SO3}~-2.74). Test specimens were heated at 650°C and were reacted with the gas mixture for 72 h. Flow rate of the gas mixture was 300cc/min. Corroded specimens were alternately immersed in a boiling 18%NaOH -3% $KMnO_4$ solution and a boiling 10% ammonium citrate solution for descaling. After descaling, specimens were weighed again to obtain the corrosion weight loss.

3. RESULTS AND DISCUSSION,

1. Thermodynamic calculation

Thermodynamic calculation showed that the equilibrium gas composition at 1000° C upon reaction of 100g crude residues with air at an air-fuel ratio of 1.05 was 0.23%SO_2 -0.78%O_2 -11.3%H_2O -13.1%CO_2 -N_2. The maximum partial pressure of gaseous vanadium compounds at 1000° C was 4.6x10^{-12} for VO_2 and 9.5x10^{-13} for V_4O_{10} (V_2O_5), which were far below the expectation. These results indicate that vapor condensation of gaseous VO_2 and V_2O_5 from flue gas onto "cold" metal surface is not necessarily favored, at least at thermal equilibrium. Thus, vanadium compounds present in tube deposits are expected to form possibly via impaction of "fused" ash particles (containing vanadium compounds) in flue gas on tube surfaces. Condensed phases existing in the 1000° C flue gas of firing 100g crude residues were 3.51x10^{-5} mol of fused Na_2SO_4 and 2.55x10^{-4} mol of fused $NaVO_3$. Composition of this molten salt mixture was approximately 15wt.%Na_2SO_4 -$NaVO_3$. Residues with high vanadium content generated fuel ash of high $NaVO_3$ -low Na_2SO_4 contents, while high sulfur residues resulted in the formation of fuel ash of high Na_2SO_4 low-$NaVO_3$ contents. For high-sulfur residues, SO_2 concentration of the flue gas was high. Addition of MgO or $Mg(OH)_2$ to crude residues changed the oil ash chemistry drastically. Magnesium reacted to form solid $3MgO \cdot V_2O_5$ ($Mg_3V_2O_8$, m.p. of 1159° C) at 1000° C, with higher Na_2SO_4 and lower $NaVO_3$ contents. Excess addition of Mg of more than one point five Mg/V (atomic ratio in fuel) to crude residues resulted in the formation of solid MgO with $3MgO \cdot V_2O_5$ and Na_2SO_4. For this ash, liquid phase of $NaVO_3$ no-longer existed. Therefore, addition of magnesium compounds as inhibitors would enhance formation of solid phases of $3MgO \cdot V_2O_5$ and MgO, and could reduce the formation of liquid $NaVO_3$, raising the melting point temperature of the oil ash. Thus, the corrosion is expected to become slight.

2. Laboratory corrosion test

Test results of representative boiler tube materials reacted with 15wt.%Na_2SO_4 -$NaVO_3$ in 0.4%SO_2 -0.8%O_2 -10%CO_2 -10%H_2O -N_2 at 650° C for 72h is presented in Fig.1.

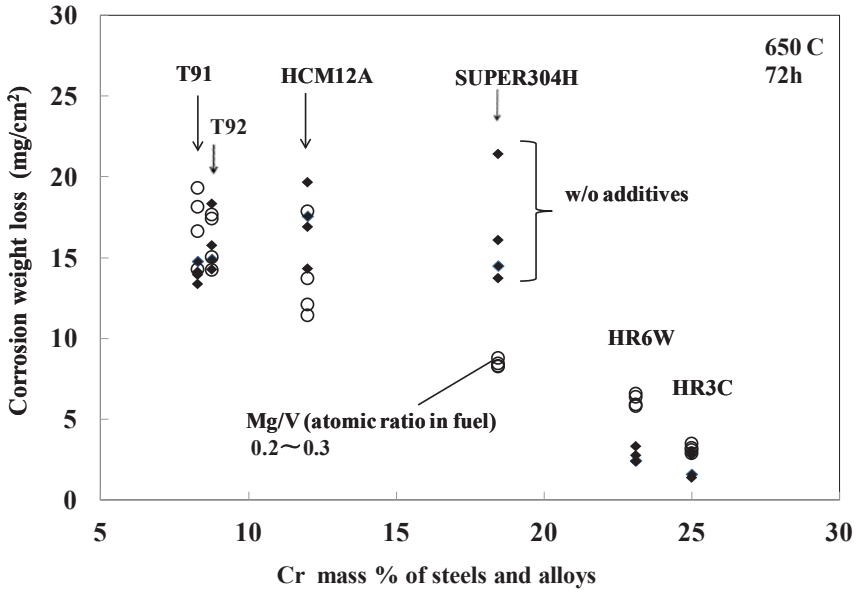

Fig. 1 Corrosion test results of steels and alloys reacted with 15wt.%Na_2SO_4 –$NaVO_3$ mixture w/o and with addition of 9wt.% MgO or $Mg(OH)_2$ at 650° C in 0.4%SO_2 -0.8%O_2 -10%H_2O -10%CO_2 -N_2 for 72 h.
◆: w/o additives, ○: Mg addition at an atomic ratio of 0.2～0.3 Mg/V (V in fuel)

For the synthetic ash w/o fuel additives, corrosion weight loss of ferritic 9-12%Cr steels was similar to the 18-8 stainless steel, and difference in their corrosion resistance was small. High-Cr stainless steel of HR3C and high-Cr high-

Ni alloy of HR6W had much better resistance than these steels. It should be pointed out that the present test results were consistent with the corrosion observed for boilers firing crude residues w/o inhibitors, since the corrosion resistance of 9-12%Cr steels was reported not quite different from the 18-8 stainless steels [9]. The reason for this is not clear. Demo compared the corrosion rates of iron-based alloys from boilers and furnace/reformer tubes with those of nickel-based alloys from turbine blades in vanadium-attack environments, and showed that nickel-based alloys had generally greater corrosion rates than the iron-base alloys [14]. This suggests that nickel oxide might dissolve into the melt greater than the iron oxide, and Cr steels containing nickel can lose its protection more easily than the Cr steels w/o nickel addition. For high-Cr steels and alloys such as HR3C and HR6W, protection by the Cr_2O_3 scale is dominating, thanks to high concentration of chromium in the alloy, and the corrosion becomes slight even though these alloys contain considerable amount of nickel. Further studies are needed to clarify this point.

For crude residues with magnesium inhibitors, i.e. 9wt.% addition of either MgO or $Mg(OH)_2$ to 15wt.%Na_2SO_4-$NaVO_3$, corrosion rates of T91 and T92 steels did not differ from the ash w/o magnesium inhibitors. However, corrosion weight loss of 18-8 stainless steel decreased significantly compared to the ash w/o magnesium inhibitors, suggesting that 18-8 stainless steel can have much better resistance to the ash when magnesium inhibitors are used with crude residues correctly. Unfortunately in this study, corrosion rate of 9-12%Cr steels was not influenced by magnesium inhibitors. The amount of magnesium addition might be insufficient to suppress the corrosion of 9-12%Cr steels. The reduced corrosion rate of 18-8 stainless steel is considered to be attributed to a decrease in molten phases at 650° C, which caused reduction of corrosion for the 18-8 stainless steel. For 9-12%Cr steels, addition of 9% MgO (or $Mg(OH)_2$) seems to be insufficient.

4. CONCLUSION,

Thermodynamic equilibrium calculation showed that firing crude residues would deposit Na_2SO_4-$NaVO_3$ mixture on tube surfaces. Magnesium inhibitors decreased $NaVO_3$ in oil ash, but increased $Mg_3V_2O_8$ and Na_2SO_4 instead. Sufficient addition of magnesium inhibitors will generate MgO in oil ash. Laboratory corrosion test of ferritic 9-12%Cr and austenitic 18-8 stainless steel at 650° C demonstrated that for crude residues w/o magnesium inhibitors, corrosion rate of 18-8 stainless steel was similar to the 9-12%Cr steels. Slight addition of magnesium inhibitors did not change the corrosion rate of ferritic 9-12%Cr steels, but it reduced the corrosion of 18-8 stainless steel significantly. For crude residues with and w/o fuel additives, high-Cr steel and high-Cr high-Ni alloy performed well.

References

[1] L.D.Paul, R.R.Seeley, “Oil ash corrosion -a review of utility boiler experience-”, *CORROSION/90* paper no.267, NACE, Houston TX, 1990

[2] G.W.Cunningham, A.deS.Brasunas, “The Effects of Contamination by Vanadium and Sodium Compounds on the Air-Corrosion of Stainless Steel”, *Corrosion*, Vol.12, August 1956, pp.389-405

[3] W.J.Greenert, “High Temperature Slag Corrosion of Metallic Materials”, *Corrosion*, Vol.18, February 1962, pp.57-102

[4] R.A.Rapp, Y.S.Zhang, “Hot Corrosion of Materials: Fundamental Studies”, *JOM*, Vol.46(1994), pp.47-55

[5] Y.Harada, M.Nakamori,”Low Molten Compounds in Oil Ahs and Prevention of High Temperature Corrosion with $Mg(OH)_2$ Additive”, *Boshokugijutsu*, Vol.29 No.12(1980), pp.615-621, in Japanese

[6] I.Kajigaya, J.Shigeta, F.Kojima, “Study of Ash Deposition and High Temperature Corrosion in Oil Firing Boiler”, *Fossil and Nuclear Power*, Vol.51 No.2(2000), pp.220-230.

[7] R.S.Roth, J.R.Dennis, H.F.McMurdie, Phase Diagrams for Ceramists Vol.VI, The American Ceramic Society, 1987, p.98.

[8] W.A.Hansen, G.W.Kessler, “Fuel Ash Corrosion and its Effect on Boiler Design”, *Trans.ASME*, Vol.87(1965), pp.210-214.

[9] P.A.Alexander, R.A.Marsden, J.M.Nelson-allen, W.A.Stewart, “”Operational Trials of Superheater Steels in a C.E.G.B. Oil-fired Boiler at Bromborough Power Station”, *J.Inst. Fuel*, Vol.37, February 1964, pp.59-69

[10] B.Cottis, M.Graham et al., Shreir`s Corrosion, Volume I, Elsevier(2010), p.459

[11] Thermodynamic data base MALT2, the Japanese Society of Thermo-Heat Measurement, supplied by Kagakugijutsusha Co., October 1992.

[12] A.Iseda, H.Okada, H.Semba, M.Igarashi, Y.Sawaragi, “HR6W High Strength Thick Wall Pipe for Advanced USC Boilers”, *Proc.Symposium on Heat Resistant Steels and Alloys for Advanced USC Power Plants 2007*, July 3-6 2007, Korea Institute of Science and Technology, Seoul, Korea.

[13] N.Otsuka, H.Matsuo, “Laboratory corrosion test results simulating fireside corrosion of austenitic superheater and reheater tube materials in advanced USC boilers”, *EUROCORR 2009*. paper no.7767, 6-10 September, Nice France.

[14] J.J.Demo, “Hot Ash Corrosion of High Temperature Equipment”, *J.Mater.Perform.* Vol.19(1980), pp.9-15

Hot Corrosion Modeling of Gas Turbine Materials in Novel Combusted Syngas Environments

Joy Sumner [(1,*)], Andrew Potter [(1)], Nigel J. Simms [(1)], John E. Oakey [(1)] and John R. Nicholls [(1)]

[(1)] Cranfield University, Cranfield, Bedfordshire, MK43 0FD, UK

*e-mail: j.sumner@cranfield.ac.uk

1. INTRODUCTION

The European Union is committed to a 20% reduction in CO_2 emissions by 2020 [1]. As such, power generating companies are facing ever greater pressure to increase their efficiencies and explore technologies capable reducing these emissions, including carbon capture and storage (CCS) technologies. One possible option is to use industrial gas turbines in a new generation of advanced, integrated gasification combined cycles (IGCC) which include pre-combustion CO_2 removal systems. The gas turbines in these new IGCC systems will be fired on H_2-rich syngases (resulting in far higher H_2O concentrations in the combusted gas stream than currently experienced), and/or less cleaned syngas (which typically contains higher trace contaminant levels than natural gas, e.g. increased levels of sulphur).

In the H_2-rich IGCC configuration, water-gas shift reactors would be required (converting H_2O to H_2, and CO to CO_2).

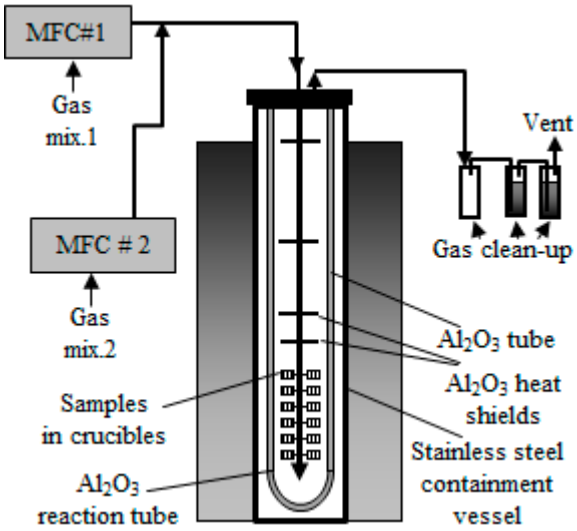

Fig. 1. Hot corrosion furnace set-up. (MFC: mass flow controller.)

Table 1. State-of-the-art materials exposed in the furnace tests.

Substrate	Bond coat	Thermal barrier coatings
GTD 111	Sicoat 2464	Yttrium stabilized zirconia
Rene 80	Sicoat 2231	
PWA 1483	RT22LT	
Hastelloy X	Amdry 997	
MarM 509		

Table 2. Simplified combusted gas compositions for furnace tests. Balance N_2. (vpm: volumes per million.)

Combusted gas simulated	CO_2	O_2	SO_2	H_2O
H_2-rich syngas	1%	8%	3.6 vpm	20%
Natural gas	6%	8%	3.6 vpm	10%
Partially cleaned syngas	10%	8%	86.4 vpm	5%

Table 3. 3 deposit/flux combinations were used at each temperature. These combinations changed over the 3 exposure temperatures.

Temp.	Deposit on surface	Deposit flux
700 ° C	80:20 Na_2SO_4:K_2SO_4	0, 1.5 & 5 µg/cm^2/h
900 ° C	80:20 Na_2SO_4:K_2SO_4	0 & 1.5 µg/cm^2/h
	100% Na_2SO_4	1.5 µg/cm^2/h
1050 ° C	CMAS	0 &1.5 µg/cm^2/h
	CMAF	1.5 µg/cm^2/h

These systems require additional gas clean up, especially H_2S and COS removal, but facilitate the removal of CO_2 from the syngases. Operation on less cleaned syngases would be a back-up option. Furthermore, in the event of a shut-down of the gasification system, such plants are intended to have the flexibility to operate on natural gas.

To study the potential for future H_2-rich ICGG, a 24-partner, 4 year EU project has been assembled to study the effects of these three different operating options. This paper addresses the response of materials used to fabricate gas turbine hot gas path components (e.g. blades, vanes, combustor cans) to hot corrosion laboratory tests. Damage levels have been quantified using dimensional metrology to form the basis of a hot corrosion model capable of predicting materials lifetimes in these novel syngas environments. This paper reports the results of a subset of the exposures carried out.

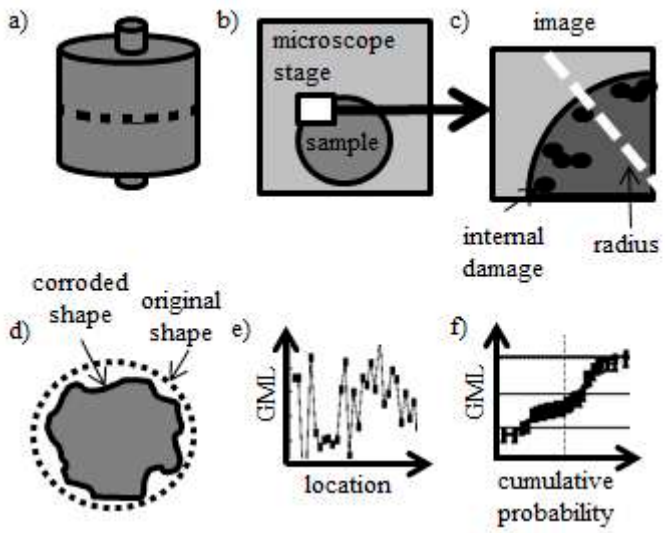

Fig. 2. Dimensional metrology technique. Samples must be measured before exposure. Then, following exposure in the corrosion test samples are (a) cross-sectioned carefully, and (b) set on a calibrated microscope stage which collects images at ≥ 24 evenly spaced locations from which (c) the locations of any oxide/coating interfaces or internal damage can be selected along a computer-generated radius. (d) pre- and post-exposure dimensions can be compared. Good metal loss (GML) data (e) is often random with respect to location, thus the data is reordered from least to most damage (f) enabling comparison of GML between different samples.

2. EXPERIMENTAL

Combinations of 5 base alloys, 4 bond coatings and a thermal barrier coating (see Table 1) were exposed to conditions intended to mimic those anticipated in IGCC operation. Three simplified gases (see Table 2) were chosen to mimic the anticipated combustion environments of the possible operational modes. Corrections were made to the sulfur trace contaminant levels to compensate for the pressure difference between the laboratory furnace (Fig. 1; 1 bar) and the gas turbine (ca.15 bar).

In addition to the three different gases, the test matrix included three temperatures: 1050 °C (principally oxidation damage mechanisms); 900 °C (a typical type I hot corrosion temperature, often resulting in internal damage); and 700 °C (a typical type II, or pitting, hot corrosion temperature). Deposition modeling, including the use of MTData, a thermodynamic stability software suit from the National Physics Laboratory, was used to select suitable deposits for these conditions (Table 3). Exposures were conducted for up to 500 hours, with samples being removed for the recording of weight measurements and deposit re-coating every 100 hours.

Post-exposure, samples were imaged by scanning electron microscopy and energy dispersive X-ray spectroscopy to study the microstructural evolution. The extent of metal loss has been compared between systems and environments via statistically significant dimensional metrology datasets collected by optical microscopy/image analysis (details in Fig. 2, [2]).

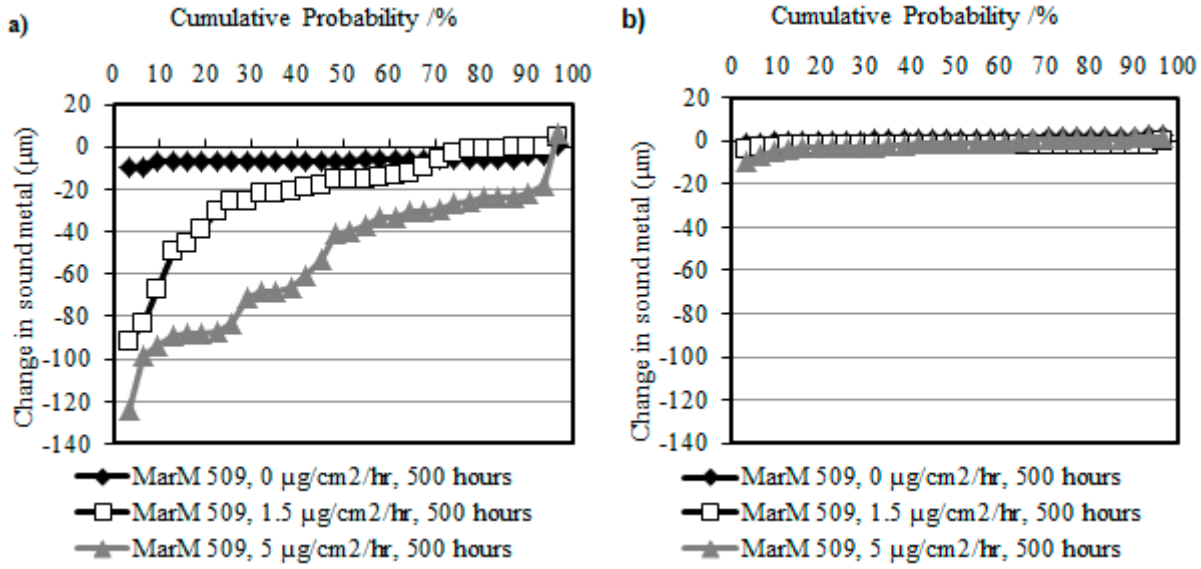

Fig. 3. Dimensional analysis data showing the loss in sound metal for uncoated MarM 509 samples exposed for 500 hours at 700 °C in (a) simulated combusted syngas and (b) simulated combusted natural gas.

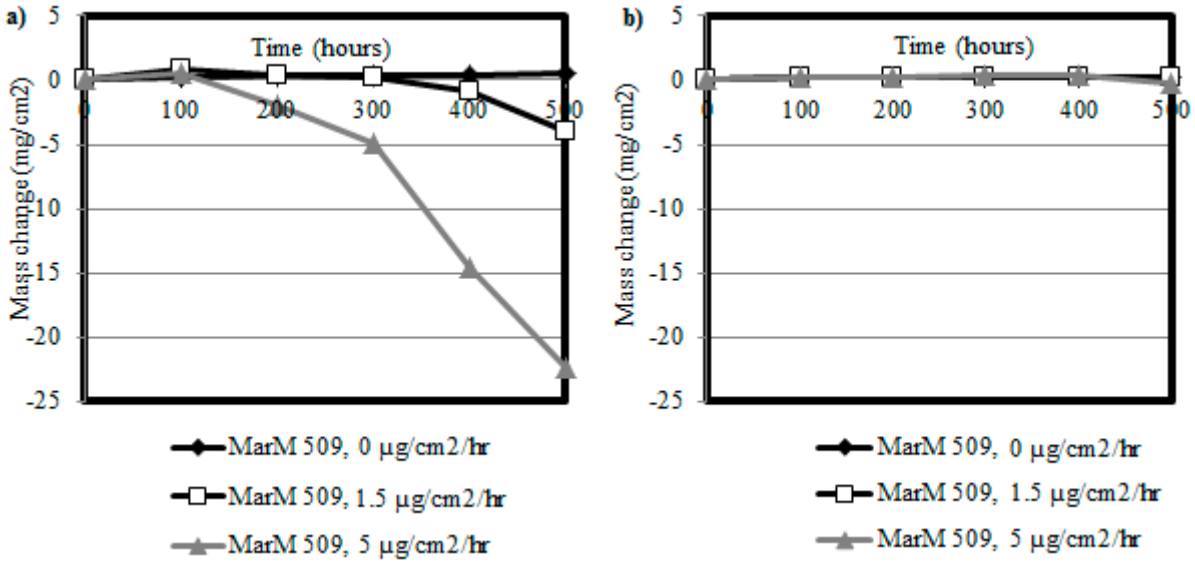

Fig. 4. Weight change data showing the oxidation and spallation of uncoated MarM 509 samples exposed for 500 hours at 700 °C in (a) simulated combusted syngas and (b) simulated combusted natural gas.

3. RESULTS AND DISCUSSION

Initial test data has been collected from the samples exposed to the simulated combusted partially cleaned syngas and combusted natural gas environments at 700 °C. Both dimensional metrology and weight change data concur that more damage occurs in the exposures under partially cleaned syngas environments than natural gas and this may be linked to the higher SO_2 concentration in the syngas, which will stabilize the formation of liquid deposits dependent on the existence of $NiSO_4$. Examples of the data collected are shown for a bare substrate alloy, MarM 509, in Fig. 3 and Fig. 4 for dimensional metrological and weight change data respectively.

However, when determining between the type II hot corrosion resistances of various alloys and coatings, weight change & dimensional metrology data may show different trends in protection. For example, in Fig. 5, while

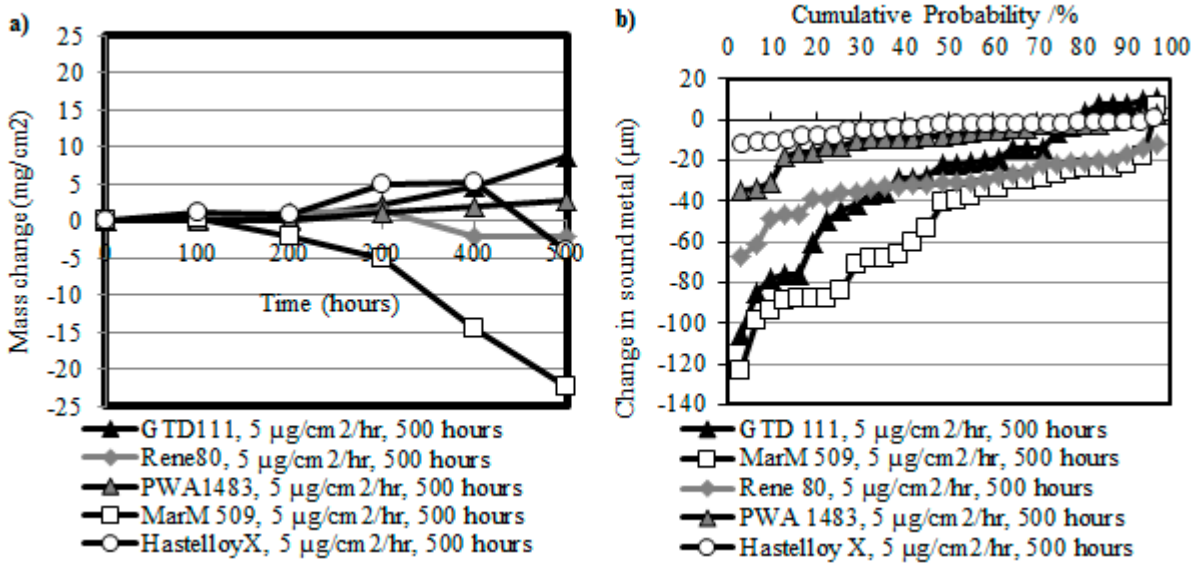

Fig. 5. A comparison of (a) weight change and (b) dimensional metrology data for 5 alloys exposed for 500 hours at 700 °C to a simulated combusted syngas environment and a 5 µg/cm$_2$/h 80:20 Na_2SO_4:K_2SO_4 deposit.

PWA 1483 appears to show relatively good responses and MarM 509 poorer responses, alloys such as Hastelloy X show variable behavior: weight change data shows the presence of oxide growth and spallation, while dimensional metrology only shows small losses in metal. This apparent discrepancy may be explained by scanning electron micrographs, which show the even development of damage across the entire of the Hastelloy X surface in contrast to the other alloys where localized pitting type damage seems more prevalent (Fig. 6).

The relatively low metal losses of Hastelloy X, indicated by dimensional metrology and scanning electron micrographs, can be linked to the high chromium fraction in the alloy (22 wt.%); needed to produce a protective oxide at such low temperatures. By contrast, GTD 111, Rene 80 and PWA 1483 (13.5, 14 & 12.2 wt.% Cr respectively) all show regions (to greater or lesser extents) where pitting has occurred, resulting in relatively high metal losses either locally or across the sample as a whole. One apparent exception is MarM 509, with 23.5 wt.% Cr which shows significant degrees of metal loss. Two factors may have a bearing on this: that the alloy is cobalt rather than nickel-based; and that there are a large number of precipitates within the alloy which may interrupt the formation of a protective oxide layer, providing potential sites for nucleation of type II hot corrosion.

4. CONCLUSION

At 700 °C, higher damage levels were found under simulated combusted partially cleaned syngas environments than for natural gas as a result of the higher contaminant levels (i.e. sulfur) in such gases. Alloys with higher chromium contents resisted the resultant type II hot corrosion more effectively, with the exception of MarM 509. Future work will cover the impact of H_2-rich syngas (determining whether the higher water content produced will also have a detrimental impact), higher exposure temperatures (900 and 1050 °C; where different corrosion mechanisms are anticipated), and coating systems.

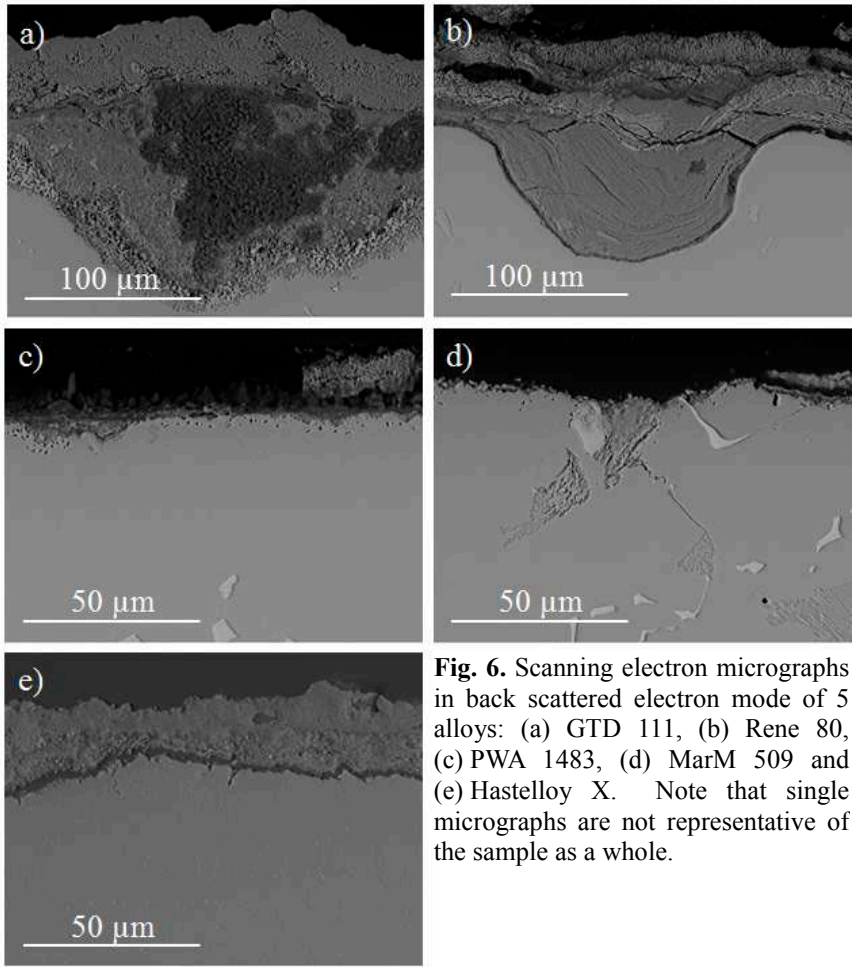

Fig. 6. Scanning electron micrographs in back scattered electron mode of 5 alloys: (a) GTD 111, (b) Rene 80, (c) PWA 1483, (d) MarM 509 and (e) Hastelloy X. Note that single micrographs are not representative of the sample as a whole.

Acknowledgements

The authors would like to acknowledge the financial support of the European Union's Framework 7 project, H2-IGCC. The authors would also like to thank K. Petra for assistance with sample preparation.

References

[1] "Renewable Energy Technology Roadmap: 20% by 2020", European Renewable Energy Council (Brussels, 2008).

[2] Sumner, J., *et al*, "High Temperature Oxidation and Corrosion of Gas Turbine Component Materials in Burner Rig Exposures" *Materials at High Temperature,* Vol. 28, No. 4 (2011), pp.369-376.

Electrochemical Characterization of the Behavior of Chromia and Alumina Passivation Layers on Nickel Base Superalloys in Contact with Molten Silicate Glass

Tuti Katrina Abdullah [1,2], Carine Petitjean [1], Pierre-Jean Panteix [1,*], Christophe Rapin [1], Michel Vilasi [1], Zuhailawati Hussein [2], Afidah Abdul Rahim [3]

[1] IJL-UMR 7198, Département CP2S, Equipe 206 (Surface et Interface: Réactivité Chimique des Matériaux), B.P. 70239 – 54506 Vandoeuvre les Nancy Cedex, FRANCE

[2] School of Materials and Minerals Resources Engineering, Engineering Campus, Universiti Sains Malaysia, Seri Ampangan, 14300 Nibong Tebal, Seberang Perai Selatan, Pulau Pinang, MALAYSIA

[3] School of Chemical Sciences, Universiti Sains Malaysia, 11800 Minden, Pulau Pinang, MALAYSIA

e-mail: pierre-jean.panteix@univ-lorraine.fr

1. INTRODUCTION

In high temperature industries, most of the metallic parts normally consist of nickel based alloys with high chromium and aluminum contents, which can lead to the formation of chromia Cr_2O_3 and alumina Al_2O_3 when having contact with air atmosphere at high temperature [1]. In molten glass, Ni-based superalloys with high chromium content (25-30 wt.%) are the best candidates for high temperature applications (*e.g.* glass industry, vitrification of nuclear wastes, *etc.*). It has been proved that this behavior is also observed when they are immersed in molten glasses [2-4]. Aluminium is also currently used as an alloying element in high temperature applications, as it can also lead to the development of a thermodynamically stable and protective oxide layer (*i.e.* Al_2O_3). However, the comparison of the respective performances of Cr and Cr-Al containing alloys in molten glass is not widely documented [5]. This work is a study of the behavior of chromia forming and alumina forming simplified model alloys (Ni-30Cr and Ni-8Al-28Cr (wt.%) respectively) immersed in a soda lime silicate glass (Na_2O-CaO-3SiO_2, noted as NC3S). Since the molten glass behaves as an electrolyte, an electrochemical technique has been used to explain the mechanisms of the reactions occurring at the alloys/melt interfaces. As the durability of the protection provided by the oxide layers first depends on the solubility of the oxides in the molten glass, it has been thoroughly studied by using a specific device allowing to control independently the temperature, glass composition, and oxygen fugacity. The solubility limits induced by the different oxidation states of a multivalent element as chromium could be directly correlated to the corrosion behavior characterized by anodic polarization of the chromia forming alloy.

2. EXPERIMENTAL

The experimental apparatus used for the electrochemical characterization of corrosion by molten glass at high temperature has already been described by Di Martino *et al.* [2-3]. 1 to 1.5 kg of glass contained in a Pt or in a fused-cast Al_2O_3-ZrO_2-SiO_2 crucible is placed in a high temperature furnace. The three electrodes are immersed in the molten glass through the top of the furnace and linked to an acquisition system. The electrodes are home made by using specific materials as mullite tubes, platinum wires, and refractory cements. The working electrode consists in a metal rod (diameter = 5.5 mm, polished to 1200 grid SiC paper). The counter electrode is a platinum plate (surface ~ 1cm²) for the current collection. The reference consist in yttria stabilized zirconia (YSZ) stick (diameter = 5mm), as this material is good conductor of oxide ions O^{2-}. The electrode is flushed with air through a syringe needle. So the reference used for the electrochemical potentials is the O_2/O^{2-} couple.

The determination of the solubility of oxides as a function of different parameters such as glass composition, oxygen fugacity and temperature has been described by Mathieu *et al.* [6]. The sample consists in a glass ball (diameter = 2 mm) added with an excess of oxide powder and placed in a closed system (silica tube) sealed under secondary vacuum. A glass reservoir allows the limitation of sodium volatilization. The oxygen fugacity is controlled by using solid redox couples M/M_xO_y buffers and determined from Ellingham diagram. The total chromium dissolved in the melts is then determined by Electron Probe Micro Analysis [7-8].

3. RESULTS AND DISCUSSION

3.1. CORROSION TESTS

The influence of the surface state on the corrosion behavior of the Ni-30Cr alloy in NC3S at 1100°C is presented on Fig. 1. Right after immersion, the Ni-30Cr sample exhibits a very low potential (E_{corr} < -1300 mV). Such a low potential can be explained by the oxidation of Cr^0 to Cr^{II} by the silica SiO_2 network, and by the O_2 dissolved in the glass: this is the active state. Then, an anodic peak is followed by a wide passivation plateau with a very low current density (I ~ 0.4 mA/cm²). In this potential range, chromium can be oxidized to Cr^{III} and thus give rise to the creation of Cr_2O_3 on the surface of the alloy, thus leading to the lower current density measured on the passivation plateau. Lastly, for the highest potentials, the current density increases again, due to the oxidation of chromium to Cr^{VI}: this is the transpassivation domain. This can be correlated to the SEM picture of the same sample after 24 hours of raw immersion in NC3S. The surface of the alloy is characteristic of the active state with corrosion by the molten NC3S: glass penetration is observed on more than 20 µm from the surface.

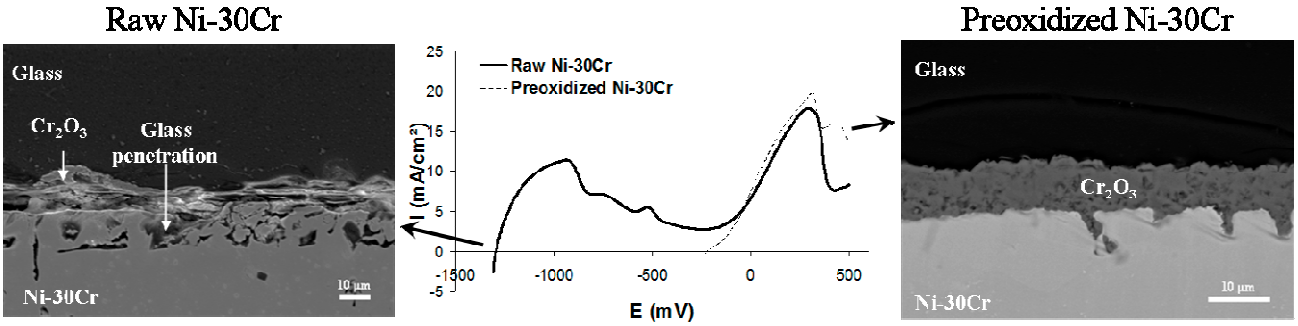

Fig. 1. SEM pictures after 24 hours of immersion in NC3S melt at 1100°C and anodic polarization (same glass, same temperature) of raw Ni-30Cr and of the same alloy after 2 hours of preoxidation in air at 1100°C.

As the existence of a passivation domain with a lower current density is due to the presence of chromia Cr_2O_3, a preoxidation treatment at 1100°C for 2 hours has been performed on Ni30-Cr just before immersion in NC3S. According to previous thermogravimetric analysis, a 5 µm thick chromia layer must be formed. On the anodic polarization plotted after 24 hours of immersion in soda-lime glass (Fig. 1), the corrosion potential is quite high (~ -200 mV), and exactly in the passivation domain defined above. The SEM picture of the same sample exhibits a compact, adherent and homogeneous Cr_2O_3 layer, avoiding contacts between the surface of the alloy and the molten glass. The alloy is perfectly protected against corrosion after 24 hours of immersion. It must be noticed here that in all cases of corrosion studies concerning contact between chromia and molten glass, some chromium dissolved in the melt has been detected and could be measured by Electron Probe Micro Analysis (0.3 at.%). Chromia is known to be an oxide with the lowest solubility in molten silicates [9]. Considering that the chromia layer has grown up to around 10 µm thick during the immersion in molten glass, this proves that there is a perpetual competition between the growth of the protective chromia layer and its dissolution in the corrosive media, *i.e.* molten glass.

The case of the corrosion of the alumina forming alloy Ni-8Al-28Cr by NC3S has been investigated in the same way. The anodic polarization of this alloy presents the same trend as Ni-30Cr, with three domains as defined above. However, as featured on Fig. 2 which reports the evolution of the potential of the raw and preoxidized alloy with time, the corrosion potential of raw Ni-8Al-28Cr is quite lower (E_{corr} ~ -1400 mV). In this case, the active state might be due to the preferential oxidation of Al^0 from the alloy to Al^{III} by the silica SiO_2 network, which is simultaneously reduced to Si^0 (which has been observed by SEM). As the alloy is alumina forming, a preoxidation treatment

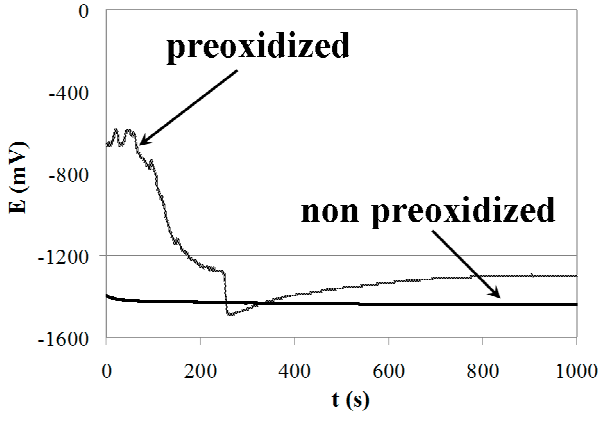

Fig. 2. Evolution with time of the corrosion potential of raw and preoxidized Ni-8Al-28Cr alloy immersed in NC3S.

has also been performed at 1100°C for 24 hours. It is supposed to lead to the formation of a 2 µm thick alumina layer, according to previous thermogravimetric analysis. The corrosion potential is then measured for 1000 seconds. As it starts from a quite higher value (E_{corr} ~ -600 mV), one can assume that the alloy is in passive state right after immersion. However, after less than 5 minutes, the corrosion potential has decreased and is back to values characteristic of the active state. During this short time, the alumina layer is completely dissolved in the melt, leading to the active state with direct contact between the alloy and the melt. This result is in coherence with the alumina solubility in molten soda lime silicates proposed in the literature [9-10], which is about 20 times higher than for chromia.

3.2. SOLUBILITY OF OXIDES IN MOLTEN GLASS

As seen above, there is possibility to provide protection against glass corrosion to superalloys containing enough chromium to give rise to a chromia layer. As the durability of the protection, *i.e.* the chromia layer, depends on the competition between the growth of the oxide and its solubility, it is of primary importance to study the physico-chemistry of Cr_2O_3 in molten silicates. Many studies report general aspects about the kinetic and mechanisms of dissolution of chromia in silicate melts with various compositions [7-8; 11-12], emphasizing the influence of several parameters as temperature, and composition (*i.e.* basicity) of the melt. In the case of a multivalent element as chromium, the influence of oxygen fugacity is of great interest. In the case of N3CS glass used in this corrosion study, the evolution of the Cr solubility with log fO_2 is typical, as presented for several temperatures on Fig. 3. At equilibrium, the total dissolved Cr in the glass (Cr(tot) is considered as the sum of all Cr species: $Cr(tot) = Cr^{II} + Cr^{III} + Cr^{VI}$. As chromia dissolution into Cr^{III} species is an acid base reaction only depending on the basicity of the melt, the Cr^{III} content is assumed to remain constant with fO_2 for a given temperature. Therefore, the minimum of solubility of each plot presented in Fig. 3 is considered as the sole contribution of the Cr^{III} specie. Under the reducing and oxidizing conditions, an increase of the solubility is observed. This increase is attributed to the reduction of Cr^{III} to Cr^{II} in reducing conditions (Cr^{VI} is neglected) and to the oxidation of Cr^{III} to Cr^{VI} in oxidizing conditions (Cr^{II} is neglected).

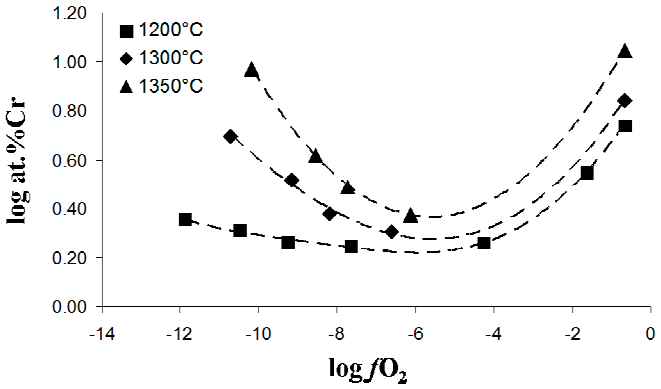

Fig. 3. Cr solubility in NC3S versus oxygen fugacity fO_2 at 1200°C, 1300°C and 1350°C

It is possible to correlate the thermodynamic solubility data obtained here to the kinetic data collected during the corrosion study through electrochemical characterization. The oxygen fugacity imposed for the solubility measurements can be translated to a potential value according to the Nernst's law: $E = RT/4F \cdot \ln(fO_2) + K$, where E is a potential, R the ideal gas constant, T the absolute temperature, F the Faraday's constant, fO_2 the oxygen fugacity and K a constant. Considering this, it is interesting to correlate the high solubility domains, corresponding to the highest and the lowest oxygen fugacities, to the potential domain exhibiting high current densities on Fig. 1. These ones correspond to the active and transpassive states for the lowest and highest potentials respectively. High solubility and high current density domains correspond to the stability domains of Cr^{II} and Cr^{VI}. In the same way, the slowest solubility values, measured for intermediate oxygen fugacities, correspond to the Cr^{III} specie and can be correlated to the large passivation plateau with low current densities. The relative stability of the chromia layer in molten glass is thus emphasized by the coherence between the low current density and the low solubility domains.

4. CONCLUSION

Molten glass media have been proved to be corrosive against metallic and ceramic materials. Specific devices have been developed to characterize (i) the corrosion by electrochemical methods and (ii) the physico-chemistry of oxides in contact with molten silicates. The comparison between chromia forming and alumina forming alloys gives advantage to chromia forming alloys. Alumina possesses a very high solubility in molten glass media, thus making it impossible to be used as a protection layer in this kind of media. Chromia forming alloys are the most promising as chromia solubility in molten silicates is one of the lowest amongst many oxides. It has been underlined here that the solubility limit is the main parameter governing the ability of chromia to give protection to the alloy in this very specific kind of media.

The measurement of the solubility limit of Cr_2O_3 in different oxygen fugacity conditions could be correlated to the ability of the oxide to provide protection to the chromia forming alloy. On one hand, the minimum solubility attributed to the Cr^{III} specie corresponds to the passivation domain due to the growth of the protective chromia layer. On the other hand, the higher solubility values due to the speciation of Cr^{III} to Cr^{II} or Cr^{VI} species correspond to the active and transpassive domains.

References

[1] Hindam, H., Whittle, D. P., "Microstructure, Adhesion and Growth Kinetics Of Protective Scales On Metals And Alloys," *Oxid. Met.*, Vol. 18 (1982), pp. 245-284.

[2] Di-Martino, J., Rapin, C., Berthod, P., Podor, R., Steinmetz, P., "Corrosion of Metals and Alloys in Molten Glasses. Part 1 : Glass Electrochemical Properties and Pure Metals (Fe, Co, Ni, Cr) behaviors," *Corros. Sci.*, Vol. 46 (2004), pp. 1849-1864.

[3] Di-Martino, J., Rapin, C., Berthod, P., Podor, R., Steinmetz, P., "Corrosion of Metals and Alloys in Molten Glasses. Part 2 : Nickel and Cobalt High Chromium Superalloys Behavior and Protection," *Corros. Sci.*, Vol. 46 (2004), pp. 1865-1881.

[4] Carton, A., Rapin, C., Podor, R., Berthod, P., "Corrosion of Chromium in Glass Melts," *J. Electrochem. Soc.*, Vol. 153, No. 3 (2006), pp. B121-B127.

[5] Dutta, R. S., Yusufali, C., Paul, B., Majumdar, S., Sengupta, P., Mishra, R. K., Kaushik, C. P., Kshirsagar, R. J., Kulkarni, U. D. & Dey, G. K., "Formation of diffusion barrier coating on superalloy 690 substrate and its stability in borosilicate melt at elevated temperature," *J. Nucl. Mater.*, Vol. 432 (2013), pp. 72–77.

[6] Mathieu, R., Khedim, H., Libourel, G., Podor, R., Tissandier, L., Deloule, E., Faure, F., Rapin, C., Vilasi, M., "Control of Alkali-Metal Oxide Activity in Molten Silicates," *J. Non-Cryst. Solids*, Vol. 354 (2008), pp. 5079-5083.

[7] Khedim, H., Podor, R., Rapin, C., Vilasi, M., "Redox Control Solubility of Chromium in Soda-Silicate Melts," *J. Am. Ceram. Soc.*, Vol. 91, No. 11 (2008), pp. 3571-3579.

[8] Khedim, H., Katrina, T., Podor, R., Panteix, P. J., Rapin, C., Vilasi, M., "Solubility of Chromium Oxide in Soda Lime Silicate Melts," *J. Am. Ceram. Soc.*, Vol. 93, No. 5 (2010), pp. 1347–1354.

[9] Manfredo, L. J., McNally, R.N., "Solubility of Refractory Oxides in Soda-Lime Glass," *J. Am. Ceram. Soc.*, Vol. 67, No. 8 (1984), pp. C–155–C–158.

[10] Monteiro, A., "Étude des mécanismes de réactivité chimique des précurseurs lors de l'élaboration d'un verre de confinement de déchet de haute activité : de l'expérimentation à la modélisation," PhD Thesis (2012), Université de Toulouse 3.

[11] Abdullah, T. K., Petitjean, C., Panteix, P. J., Rapin, C., Vilasi, M., "Stability of Protective Oxide Layer Against Corrosion: Solubility Measurement of Chromia in Soda Lime Silicate Melts," *Oxid. Met.*, Vol. 80 (2013), pp. 611–622.

[12] Abdullah, T. K., Petitjean, C., Panteix, P. J., Rapin, C., Vilasi, M., Hussain, Z., Rahim, A. A., "Dissolution Equilibrium of Chromium Oxide in a Soda Lime Silicate Melt Exposed to Oxidizing and Reducing Atmospheres," *Mat. Chem. Phys.*, Vol. 142 (2013), pp. 572-579.

High Temperature Oxidation from a Viewpoint of Solid State Chemistry

Toshio Maruyama
Executive Vice-President for Education and International Affairs, Tokyo Institute of Technology
2-12-1, O-okayama, Meguro-ku, Tokyo 152-8550 JAPAN
E-mail: maruyama@mtl.titech.ac.jp

1. INTRODUCTION

In high temperature oxidation of metals, transport of ions in oxide sales is driven by electrochemical potential gradients. The two major issues are growth rate of scales and adherence of scales with alloys. The adherence of the scales strongly depends on microstructure of scales itself and the alloy/scale interface. The microstructure is affected by mass transport of ions. This fact suggests that electrochemical potential distribution is the key issue to understand the processes in oxidation. This fact indicates that the view point of solid state chemistry may give the clear sight on high temperature oxidation.

2. POTENTIAL DISTRIBUTION

2.1 Chemical potential distribution of oxygen

Figure 1 shows schematically distribution of chemical potential of oxygen from the atmosphere to the metal/scale interface. Driven by the potential gradients, oxygen molecules are transported through the gaseous boundary layer and adsorbed on the surface of oxide. The adsorbed molecule dissociates to adsorbed atoms which ionized to oxide ion and contribute the scale growth. The diffusion of ions in the scale is driven by the electrochemical potentials.

2.2 Measurement of chemical potential of oxygen at the scale surface and in the gaseous boundary layer [1]

Quantitative determination of chemical potential of oxygen is inevitable to evaluate the oxidation process. Potentiometric oxygen sensor of stabilized zirconia is frequently used to monitor chemical potential of oxygen in a gaseous atmosphere. Figure 2 shows schematic illustration of oxygen sensor for measuring the chemical potential of oxygen. A needle sensor of stabilized zirconia can be applied to measure the chemical potential of oxygen at the scale surface. A needle of zirconia is connected with a zirconia tube. The cathode in a zirconia tube is exposed to air as the reference electrode and the needle that touches on the scale surface acts as the anode. The triple-phase boundary consists of the zirconia needle (electrolyte), the oxide scale of electronic conductor (electrode) and adsorbed atoms of oxygen.

2.3 Electrochemical potential distribution in the scale [2]

Transport of ions and electron (hole) determines the scale growth. These species have electric charges so that the transport is driven by the electrochemical potential gradients. Flux of species, i, is expressed as follows.

$$J_i = -(D_i/RT)(\mathrm{d}\,\eta_i/\mathrm{d}x) \quad (1)$$

where D is the self-diffusion coefficient, R the gas constant, T temperature, η electrochemical potential and x the coordination. The electro-neutrality is maintained through the transport process.

$$\Sigma\, z_i J_i = 0 \quad (2)$$

where z is the electric charge. Based on these two equations, one can evaluate the chemical and electrochemical potential gradients and electrostatic potential gradient, if the diffusion coefficient of species is given as a function of chemical potential.

3. VOID FORMATION IN OXIDE SCALES [2, 3]

The diffusion coefficient is basically proportional to the concentration of defects which is dependent on chemical potential. In this situation, the fluxes may have the non-zero divergences as seen in the following equation.

$$\Sigma\, z_i\, (\mathrm{d}J_i/\mathrm{d}x) = 0 \quad (3)$$

The excess or shortage of mass (n) per unit time (t) is expressed as

$$\mathrm{d}n_i/\mathrm{d}t = -(\mathrm{d}J_i/\mathrm{d}x) \quad (4)$$

The negative $\mathrm{d}n_i/\mathrm{d}t$ gives voids and the positive one leads the formation of excess oxide in the oxide scale. One more constraint is the conservation of the ratio of sublattices. In the case of the metal oxide to be $M^{z+}{}_a O^{2-}{}_b$ ($z = 2b/a$), the following relation shall be maintained.

$$(dn_M/dt)/a=(dn_O/dt)/b \quad (5)$$

These relations give distributions of the chemical potential, electrochemical potential, flux and its divergence. This enables to elucidate the void formation. Figure 3 shows the cross-section of CoO scale formed on Co after the oxidation in Ar-21%O_2 gas mixture at 1373 K for 86.4 ks [3]. (Void formation at the metal/scale interface)

Acknowledgement

The author appreciate Prof. Mitsutoshi Ueda for collaboration in construction of the concept of the void formation and Prof. Kenichi Kawamura for his help in measurement of chemical potential at the surface of oxide scale.

References

[1] K. Fujita, M. Ueda, K. Kawamura and T. Maruyama, *Proceedings of the 57th Japan Conference on Materials and Environments,* 506-507 (2010). (in Japanese)
[2] T. Maruyama, M. Ueda and K. Kawamura, *Defect and Diffusion Forum*, **289-292**, 1-13(2009).
[3] K. Akiba, M. Ueda, K. Kawamura and T. Maruyama, *Materials Transactions*, **48**(11), 2997-3006(2007).

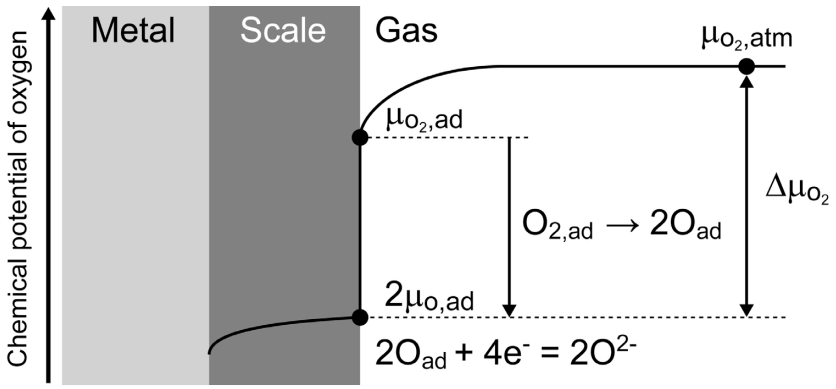

Figure 1 Distribution of oxygen chemical potential from gas phase to the metal/scale interface.

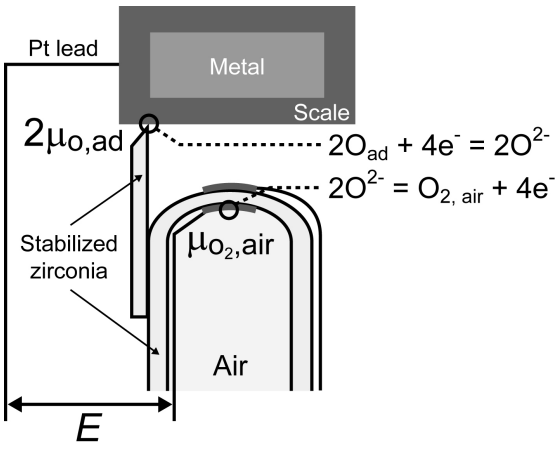

Figure 2 Schematic illustration of the oxygen sensor.

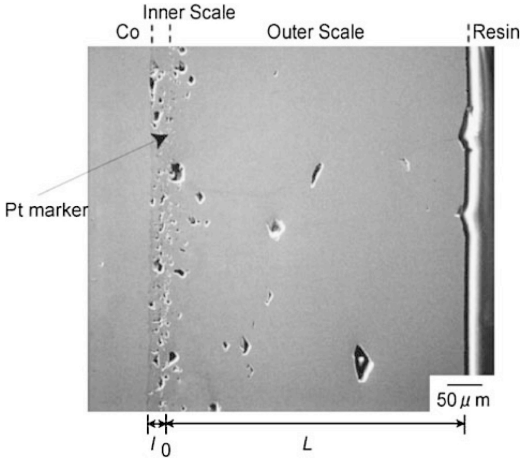

Figure 3 Cross-section of CoO scale formed on Co after the oxidation in Ar-21%O_2 gas mixture at 1373 K for 86.4 ks. (with Pt marker) [3]

Nucleation and Growth of ZnO Particles by Internal Oxidation in Pd

Norihito Sakaguchi [1,*], and Kei Watanabe [1]

[1] Graduate School of Engineering, Hokkaido University, Kita13 Nishi8, Sapporo 060-8628, JAPAN

e-mail: sakaguchi@eng.hokudai.ac.jp

1. INTRODUCTION

Oxidation of dilute alloys provides finely dispersed oxide particles in the matrix of solvent metal under suitable conditions. This phenomenon is called “internal oxidation”, which sometimes leads a degradation of mechanical and chemical properties in steels and alloys. A lot of studies have been conducted on internally oxidized metal/ZnO systems, for e.g., Ag/ZnO and Pd/ZnO [1–4]. However, these studies focus on the orientation relationships and atomic structures of metal/ZnO interfaces. The mechanism of nucleation and growth processes has not yet been clarified in these systems. In the present study, we show an electron microscopy study of the morphology and crystallography of ZnO precipitates formed by internal oxidation in a palladium (Pd) matrix. High-resolution transmission electron microscopy (HRTEM) was used to investigate the crystalline structure of the precipitates. The effect of oxidation temperature on their crystalline structure and morphology was also discussed. The mechanism of nucleation and growth of ZnO during internal oxidation is proposed.

2. EXPERIMENTAL

A 99.99% purity palladium rod was cold rolled down to a thickness of 0.1 mm. The palladium sheet was heated at 1273 K for 100 hours together with a zinc wire of 99.95% purity in an evacuated quartz tube to obtain the Pd–Zn alloy. The concentration of zinc in the alloy was 7 at.%. The Pd–Zn sheet was punched out into 3mm ϕ disks, and the disks were electrolytically polished in a solution of 80% acetic acid and 20% perchloric acid at 285 K by using a twin-jet technique. These thin-foil samples were then internally oxidized for 100 h at 973 to 1173 K in air. The samples were finally etched by ion milling for several minutes in order to remove the surface contaminant layer. A high-voltage transmission electron microscope (JEM-ARM-1300) was used for HRTEM observations.

3. RESULTS AND DISCUSSION

Fig. 1 shows the microstructures of the Pd–Zn alloy after internal oxidation at several temperatures. A lot of fine ZnO precipitates are found in all conditions. The average size of the precipitates increases with the oxidation temperature, whereas their number density decreases. The ZnO in the sample oxidized at 973 K are triangular in shape while plate-like ZnO are observed in the sample oxidized at 1173 K. At1073 K, both the triangular and the plate-like ZnO precipitates exist together. The average size of the plate-like precipitates is more than 100 nm in long axis direction. All of fine ZnO precipitates less than 10 nm are triangular in shape and larger than 100 nm are plate-like. It was clarified by the electron diffraction pattern of fine precipitates that the triangular precipitates are metastable sphalerite ZnO (s-ZnO) phase. It is also evident that both the face-centered cubic (FCC) Pd matrix and the s-ZnO precipitate have equivalent crystallographic orientations. The three-dimensional shape of the s-ZnO precipitate is expected to be a regular tetrahedron with four equivalent $\{111\}_{Pd}//\{111\}_{s\text{-}ZnO}$ polar interfaces as shown in Fig. 2. On the other hand, the plate-like ZnO precipitate is identified as a stable wurtzite ZnO (w-ZnO) phase with orientation relationships of $[110]_{Pd}//[11\text{-}20]_{w\text{-}ZnO}$ and $(111)_{Pd}//\{0002\}_{w\text{-}ZnO}$. It has also been found that ZnO precipitates in internally oxidized Ag–Zn and Pd–Zn alloys have the same crystalline structure and orientation relationship [1–4]. Fig. 3 shows a schematic illustration of a plate-like precipitate with large $(111)_{Pd}//\{0001\}_{w\text{-}ZnO}$ polar interfaces. It is evident that the interfaces consisting of $(111)_{Pd}//\{0001\}_{w\text{-}ZnO}$ planes are energetically favored in the Pd/w-ZnO system.

The triangular s-ZnO and the plate-like w-ZnO precipitate simultaneously at 1073 K. A unique change in the shape of triangular s-ZnO is observed. The shape of the precipitates appears trapezoidal rather than triangular. An HRTEM image of typical trapezoidal ZnO is shown in Fig. 4. It is observed that structures different from s-ZnO are periodically introduced parallel to the $(111)_{s\text{-}ZnO}$ lattice planes in the ZnO precipitate. It is found that regions different from s-ZnO corresponded to the w-ZnO phase. Thus, the trapezoidal ZnO precipitate contains a layered structure of s-ZnO/w-ZnO. The presence of layered structures of s-ZnO/w-ZnO implies that there was a correlation between the triangular s-ZnO and

platelike w-ZnO precipitates. The mechanism of the nucleation and growth of the ZnO precipitates during the internal oxidation process are discussed.

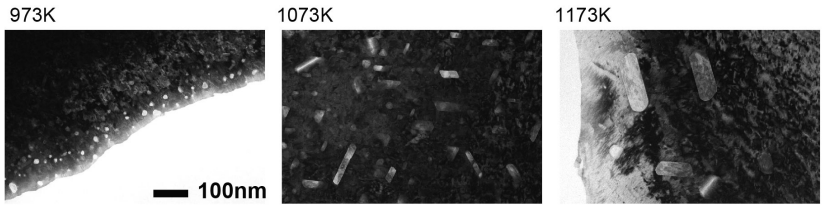

Fig.1 TEM image of ZnO precipitates in Pd-ZnO alloy after internal oxidation to 100 hours at several temperatures [5].

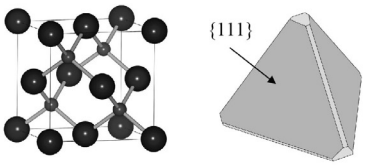

Fig.2 Atomic structure model and morphology of sphalerite ZnO precipitate [5].

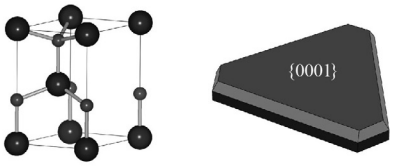

Fig.3 Atomic structure model and morphology of wurtzite ZnO precipitate [5].

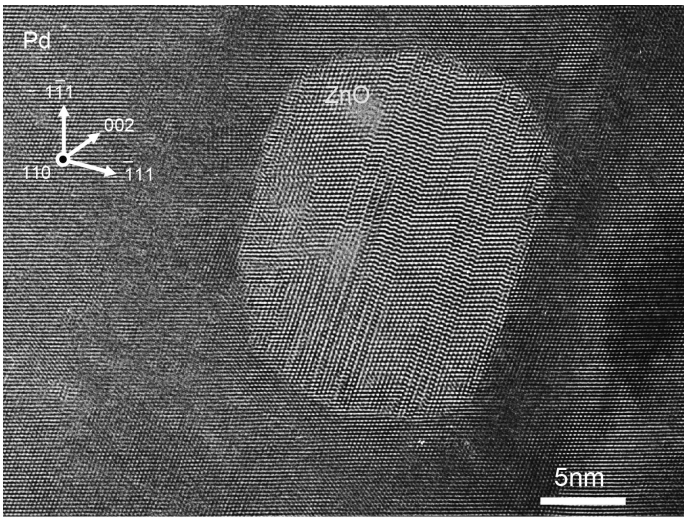

Fig.4 An HRTEM image of typical trapezoidal ZnO precipitate [5].

4. CONCLUSION

The crystalline structures of ZnO precipitates formed by the internal oxidation of a Pd–Zn alloy were examined at several temperatures. A metastable sphalerite ZnO with a tetrahedral shape preferentially nucleates in the Pd matrix at 973 K, while the plate-like precipitates consisting of a wurtzite ZnO phase preferentially grows at a high temperature. Tetrahedral s-ZnO and plate-like w-ZnO precipitates were simultaneously found at 1073 K. The trapezoidal ZnO precipitates having layered structures of s-ZnO/w-ZnO were examined by HRTEM.

References

[1] Vellinga, W. P. and De Hosson, J. TH. M., "Atomic Structure and Orientation Relations of Interfaces between Ag and ZnO", *Acta Mater.*, Vol. 45, No. 3 (1997), pp. 933-950.
[2] Groen, H. B. and De Hosson, J. TH. M., "Different Pd-ZnO interfaces Studied with High-Resolution Transmission Electron Microscopy", *Scripta Mater.*, Vol. 38, No. 5 (1998), pp. 769-773.
[3] Murakami, K., Saito, M., Takuma, E. and Ichinose, H., "ARHVTEM of the Pd/ZnO Heterointerface Chemical Structure", *J. Electron Microsc.*, Vol. 52, No. 1 (2003), pp. 27-32.
[4] Sakaguchi, N., Suzuki, Y., Watanabe, K., Iwama, S., Watanabe, S. and Ichinose, H., "A HRTEM and EELS Study of Pd/ZnO Polar Interfaces", *Phil. Mag.*, Vol. 88, No. 10 (2008), pp. 1493-1509.
[5] Watanabe, K., Sakaguchi, N. and Watanabe, S., "Formation of Sphalerite and Wurtzite ZnO in Pd–Zn Alloy after Internal Oxidation at Elevated Temperatures", *J. Mat. Sci.*, Vol. 46 (2011), pp. 4568-4573.

Experimental study and numerical simulations of high temperature (1100 – 1250°C) oxidation of pre-oxidized zirconium alloy

C. Desgranges [(1,*)], B. Mazères[(1,2)], C. Toffolon[(1)], D. Monceau[(2)]

[(1)] CEA, DEN, F-91191 Gif-sur-Yvette, France.
[(2)] CIRIMAT, Université de Toulouse, ENSIACET, 4 Allée Emile Monso, BP 44362, F-31030, Toulouse, France

e-mail: clara.desgranges@cea.fr

1. INTRODUCTION

Zirconium alloys (such as Zircaloy-4) are widely used as fuel cladding tubes in nuclear Pressurized-light-Water-Reactors (PWR). In service conditions, cladding tubes are in contact with the water of the primary circuit of PWR at a temperature around 320°C under 155 bar of pressure. This leads to the formation of a layer of zirconium oxide on the external surface of the cladding tube. After an irradiation cycle in a PWR, the maximum thickness of this zirconia layer, on Zircaloy-4 alloys, is about 100µm thick. This oxide layer has to be also considered in safety studies, especially for the hypothetical scenario of the Loss-Of-Coolant-Accident (LOCA). In this scenario, cladding tubes can undergo a high-temperature (HT) oxidation (T≈1200°C) in water steam environment for a maximum duration of a few minutes. The residual mechanical proprieties after the accidental transient temperature are directly linked to the oxygen profile inside the fuel cladding wall of 570µm thick. The behavior of fuel cladding tube during this high temperature oxidation can be influenced by the presence of the pre-oxide layer. Hence in literature, autoclave pre-oxidized samples were chosen in order to simulate the oxide layer formed in-service. During the first seconds of the HT treatment, the authors have noticed a reduction of the pre-oxide layer, in case of thick pre-oxide, before re-growth of a new additional zirconia layer at the metal/oxide interface [1]. This initial stage with reduction the pre-oxide layer can be explained by the oxygen flux balance at the metal/oxide interface. Indeed, this is a consequence of the formation of O-rich $\alpha_{Zr}(O)$ phase at high temperature at the β_{Zr} /zirconia interface. At the beginning of the HT treatment, because of the very high solubility of oxygen in the $\alpha_{Zr}(O)$ phase at HT, the oxygen gradient in the $\alpha_{Zr}(O)$ layer is high whereas the oxygen gradient is rather low in the thick pre-oxide layers (Fig.1a). Consequently, the inward flux of oxygen in oxide is lower than the inward flux in the $\alpha_{Zr}(O)$ phase. Hence, the balance of the fluxes at the metal/oxide interface leads to oxide reduction despite the oxidizing atmosphere. This also leads to a growth of the $\alpha_{Zr}(O)$ phase partly at the metal/oxide interface. With the establishment of oxygen diffusion profile in the metal, the flux of oxygen in the $\alpha_{Zr}(O)$ decreases with time, whereas inward flux in the oxide increases with the reduction of oxide thickness. Hence, for longer times, the flux balance at the metal/oxide interface reverses and the oxide starts growing (Fig.1b). In a previous work [2], EKINOX-Zr model calculations, which are based on 1D numerical resolution of diffusion-reaction equations describing the oxygen diffusion in the $ZrO_2/\alpha_{Zr}(O)/\beta_{Zr}$ system, has been used to reproduce this particular diffusion path. It was shown that the experimental data cannot be reproduced by simulations done with an assumption of a unique and constant diffusion coefficient of oxygen in each of the three phases. This result suggested that the LT oxide layer may have different diffusion properties than the HT oxide layer.

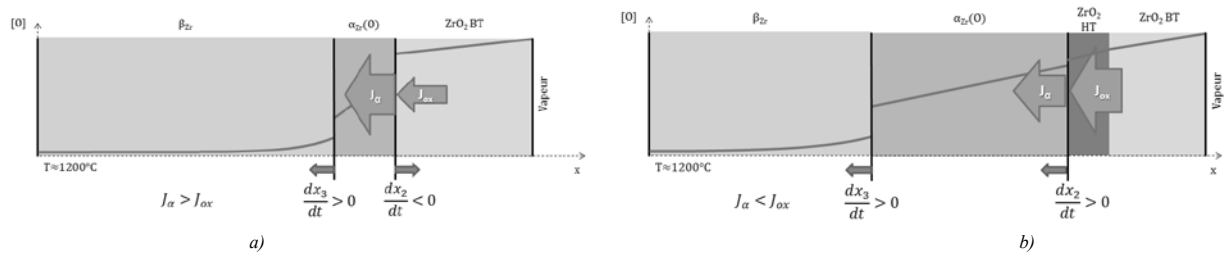

Fig 1: Schematic oxygen profile evolution in the $ZrO_2/\alpha_{Zr}(O)/\beta_{Zr}$ system in case of thick pre-oxide scale (a) first stage : oxide scale reduction b) second stage growth of HT oxide

Hence, the aim of the present work is to better understand the influence of a pre-oxide layer on the oxygen diffusion in the metallic matrix during HT oxidation. To do so, HT experiments have been performed on 30µm thick pre-oxidized Ziracloy and several hypotheses have been tested with EKINOX-Zr model. In particular, a set of new simulations considering the two different zirconia layers (LT and HT oxide layers) has been performed.

.

2. EXPERIMENTAL

In order to obtain 30µm of pre-oxide or Low Temperature (LT) oxide, samples stayed 1328 days in autoclave autoclave at 360°C under 190 bar of pressure with typical water chemistry of PWR. Notice that after this treatment the samples contain 700 wt. ppm of hydrogen as the samples used in a previous study [1]. Therefore, the effect of hydrogen on the oxygen diffusion during HT oxidation - effect has been put in obvious in [3,4] - is similar between this work and Le Saux *et al.* study [1]. In this work, to mimic the LOCA conditions, the thermal treatments consisted in oxidizing the samples at four different temperatures: 1100, 1150, 1200, 1250°C in O_2. The oxidation times (Table 1) have been previously evaluated using the EKINOX-Zr code to follow the reduction of the LT oxide layer.

Table 1– Temperature and duration of HT oxidations performed on pre-oxidized (30µm) Zircaloy-4 samples.

Samples	Pre-oxide (µm)	Oxidation T (°C)	Oxidation duration (s)
T1	30	1100	450
T2	30	1150	280
T3	30	1200	200
T4	30	1250	131

In parallel, the numerical EKINOX model has been modified in order to take into account a specific HT diffusion coefficient for the LT pre-oxide formed. Furthermore two different hypotheses have been tested concerning the LT oxide, porous or dense layer, once growth of the HT scale begins. Then, by successive adjustment of the unkown diffusion coefficients, two value of specific diffusion coefficient have been evaluated from the set of experimental HT treatments, one for the LT oxide scale, one for the part of the $\alpha_{Zr}(O)$ phase that is formed by reduction of the LT oxide.

3. RESULTS AND DISCUSSION

Results of the present study for oxidations performed at 1200°C on 30µm thick pre-oxidized Ziracloy-4 are in good accordance with previous results from Le Saux *et al.* [1] (Fig 2) for samples with 25µm and 35µm thick pre-oxide. Simulations with EKINOX-Zr model are also presented in Figure 2. Simulation with EKINOX are based on 1D numerical resolution of O diffusion and moving boundaries equations [4,5]; The equilibrium concentration at moving interfaces are obtained from the thermodynamics Zircobase database [6]. Calculations with EKINOX model enabled to calculate the oxygen diffusion profile evolution in the $ZrO_2/\alpha_{Zr}(O)/\beta_{Zr}$ system. The kinetics of the reduction/re-growth phenomenon can be well reproduced by calculations considering a different diffusion coefficient for the pre-oxide layer in respect to zirconia formed at high temperature and specific diffusion properties for the $\alpha_{Zr}(O)$ phase formed by reduction of the pre-oxide layer (Table 2). While, the experimental data cannot be reproduced by simulations done with an assumption of a unique and constant diffusion coefficient for zirconia phase no matter that it has been formed at LT or HT. The two hypotheses tested, porous LT oxide (dashed line) and dense LT oxide (continous line) once the HT oxide growth begins, enabled to reproduce experimental data. Forthcoming ^{18}O tracers experiment should bring some helpful information on the diffusion proprieties at high temperature of the LT zirconia pre-oxide layer.

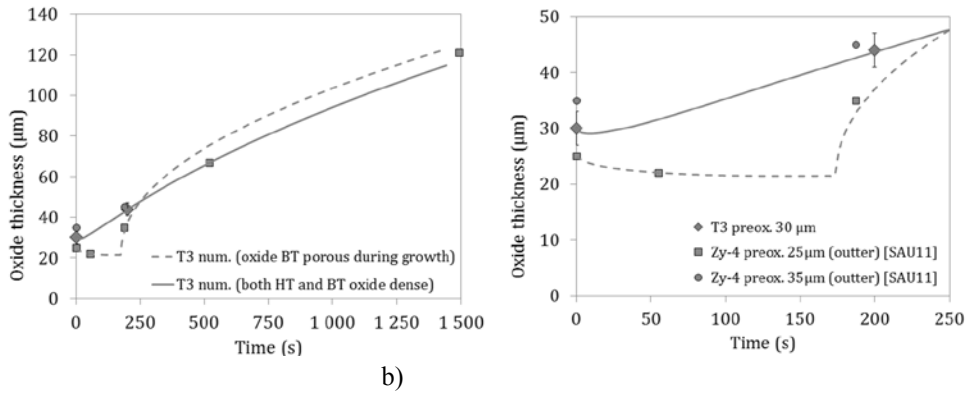

a) b)

Figure 2 – Comparison between oxide growth kinetics calculated with EKINOX-Zr and experimental data (from this work and from [1]). (a) Complete oxide growth kinetics. (b) Zoom of oxide growth kinetics between 0 and 250s. Diamonds: sample T3 (this work) oxidized at 1200°C during 200s. Squares: Zircaloy-4 samples with 25 µm oxidized 1200°C during 1492s from [1]. Circles: Zircaloy-4 samples with 35 µm oxidized 1200°C during 187s from [1]. Solid line: oxide growth kinetics calculated with EKINOX-Zr considering the hypothesis of dense LT oxide. Dashed line: oxide growth kinetics calculated with EKINOX-Zr considering porous LT oxide once HT oxide growth begins.

Table 2 – Input parameters for EKINOX calculations (HT and LT dense oxide layers and two different $\alpha_{Zr}(O)$ layers): kinetic data from [7] (except D_{LTox} and $D_{\alpha\ red.}$) in (cm^2/s), oxygen equilibrium concentrations calculated with ThermoCalc and the thermodynamic database Zircobase [6] in (%at).

D_{LTox}	D_{HTox}	$D_{\alpha\ red.}$	D_{α}	D_{β}	$[V_O]_{ox/\alpha}$	$C_{\alpha/ox}$	$C_{\alpha/\beta}$	$C_{\beta/\alpha}$
$5.29.10^{-7}$	$9.36.10^{-7}$	$3.87.10^{-8}$	$1.10.10^{-7}$	$1.55.10^{-6}$	6.92	30.5	10.5	2.76

Hence, first, the diffusion coefficient, D_{LTox}, for LT oxide at high temperature have been determined by successive adjustment of the unkown diffusion coefficient (Table 2).
Second, for the presented simulations a specific diffusion coefficient, $D_{\alpha\ red}$ (Table 2)., is also attributed for the part of the $\alpha_{Zr}(O)$ phase that grows at the oxide/metal interface from reduction of LT oxide, considering that this phase has particular diffusion proprieties with respect to the $\alpha_{Zr}(O)$ phase that grows at the $\alpha_{Zr}(O)/\beta_{Zr}$ interface from a metallic parent phase. Calculations show however that, because of the re-growth kinetics of the HT oxide at the metal/oxide interface, the part of $\alpha_{Zr}(O)$ phase that grows from LT oxide reduction disappears after short time stage. Nevertheless experiments should be done in order to evaluate the evolution of the diffusion coefficient of oxygen with its own concentration in $\alpha_{Zr}(O)$ the phase in order to have a more accurate simulation of diffusion of oxygen in this phase.

Simulations have been performed to evaluate the variation of the remaining thickness of ductile ex-βZr after the HT oxidation as a function of the temperature and of the pre-oxide thickness. The remaining thickness of ductile ex-βZr phase is evaluated as the thickness of the ex-βZr where the oxygen concentration is lower than 0.4 %wt. following Brachet *et al.* [8]. The objective of those last simulations is to clarify the role of the pre-oxidation on the residual ductility of the cladding after LOCA. As shown Fig 3b, considering this point, the pre-oxide is shown to have a detrimental effect, despite considering the weight mass gain of pre-oxide sample in respect to sample with no pre-oxide, the pre-oxide may appears as favorable (Fig3a).

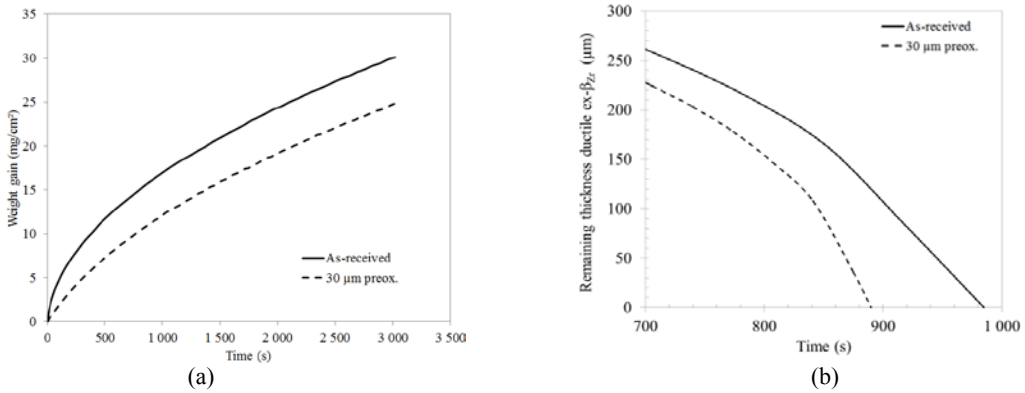

(a) (b)

Figure 3 – Comparison of (a) the variation of the weight gains (b) remaining thickness of ductile ex-β_{Zr} phase calculated for an as-received Zircaloy-4 samples oxidized at 1200°C and a pre-oxidized Zircaloy-4 samples with 30µm of pre-oxide oxidized at 1200°C as a function of time.

4. CONCLUSION,

The behavior of Zr-alloy fuel cladding tube during high temperature oxidation in water steam environment can be influenced by the presence of a pre-oxide layer. Experimental studies on Zy4 alloy have shown that in case of thick pre-oxide layer, the pre-oxide is reduced during the first seconds of the high-temperature treatment before the growth of a high temperature oxide layer. Results of the present study on oxidations performed at 1200°C on 30µm thick pre-oxidized Ziracloy-4 are in good accordance with previous results. Simulations with EKINOX-Zr model based on 1D numerical resolution of diffusion-reaction equations are also presented. They enabled to calculate the oxygen diffusion profile evolution in the $ZrO_2/\alpha_{Zr}(O)/\beta_{Zr}$ system. The kinetics of the reduction/re-growth phenomenon can be well reproduced by calculations considering a different diffusion coefficient for the pre-oxide layer in respect to zirconia formed at high temperature and specific diffusion properties for the $\alpha_{Zr}(O)$ phase formed by reduction of the pre-oxide layer. Last, it is shown that quantitative evaluation of the influence of the presence of a pre-oxide layer on the evolution of the quantity of ductile ex-β_{Zr} phase can be deduced from the calculated oxygen diffusion profiles.

Acknowledgements

The authors want to thank Laurent FAYETTE and Joël GODLEWSKI who performed the oxidation of Zircaloy-4 samples in autoclave at CEA center of Cadarache. They also want to thank Jean-Christophe BRACHET and Matthieu LE SAUX for their helpful advices. Finally, they want to thank AREVA NP and EDF for their financial and material supporting in this study.

References

[1] Le Saux M., Brachet J.-C., Vandenberghe V., Gilbon D., Mardon J.-P., Sebbari B. "Influence of a Pre-Transient Oxide on LOCA high temperature steam oxidation and post-quench mechanical properties of Zircaloy-4 an M5™ cladding" *Proc. of 2011 Water Reactor Fuel Performance Meeting* , Chengdu, China.

[2] Toffolon-Masclet C., Desgranges C., Corválan-Moya C., Brachet J.-C. "Simulation of the β Zr → α Zr(O) phase transformation due to oxygen diffusion during high temperature oxidation of zirconium alloys", *Solid State Phenomena*, Vol. 172-174, (2011), pp.652-657.

[3] Brachet J.-C., Vandenberghe V., Portier L., Gilbon D., Lesbros A., Mardon J.-P. "Hydrogen content, pre-oxidation and cooling scenario effects on post-quench microstructure and mechanical properties of Zircaloy-4 an M5™ alloys in LOCA conditions". *Journal ASTM International*, Vol.5, (2008). Paper ID: JAI101116.

[4] Mazères B., Desgranges C., Toffolon-Masclet C., Monceau D. "Contribution to Modeling of Hydrogen Effect on Oxygen Diffusion in Zy-4 Alloy During High Temperature Steam Oxidation". *Oxidation of Metals*, Vol.79, (2013), pp.121-133.

[5] Corválan-Moya C., Desgranges C., Toffolon-Masclet C., Servant, J.-C. Brachet C., "Numerical modeling of oxygen diffusion in the wall thickness of low-tin Zircaloy-4 fuel cladding tube during high temperature (1100-1250°C) steam oxidation. *Journal of Nuclear Materials*, Vol. 400, (2010), pp.196-204

[6] Dupin N., Ansara I., Servant C., Toffolon C., Lemaignan C., Brachet J.-C. "A thermodynamic database for zirconium alloy*"Journal of Nuclear Material*, Vol. 275 (1999), pp. 287-295.

[7] Ma X., Toffolon-Masclet C., Guilbert T., Hamon D., Brachet J.-C. "Oxidation kinetics and oxygen diffusion in low-tin Zircaloy-4 up to 1523 K", *Journal of Nuclear Materials*, Vol. 377, (2008), pp.359-369.

[8] Brachet J.-C., Pelchat J., Hamon D., Maury R., Jacques P., Mardon J.-P. "Mechanical behavior at room temperature and metallurgical study of low-tin Zircaloy-4 and M5™ after oxidation at 1100°C and quenching", *Proc. of the Technical Committee Meeting: "Fuel behavior under transient and LOCA conditions"*, Halden, Norway (2001)

The Development of Tensile Test to Asses the Adhesion of Thermal Oxide Scales Grown on Low Carbon Steels Oxidised in Water Vapour

Somrerk Chandra-ambhorn* and Nattapol Klubvihok

Department of Materials and Production Technology Engineering, Faculty of Engineering,
King Mongkut's University of Technology North Bangkok,
1518, Pracharat Sai 1 Road, Bangsue, Bangkok, 10800, Thailand

E-mail: sca@kmutnb.ac.th

1. INTRODUCTION

In a hot tolling process, the scale adhesion to steel substrate is one of the important properties for the hot-rolled product. The better adhesion is required when the hot-rolled coil is delivered for application in this form. In contrast, the poor scale adhesion is preferred if the hot-rolled coil is further sent to the cold rolling. This is because in that case the scale must be completely removed, by mechanical and chemical means, from the hot-rolled steel substrate before cold rolling. The scale adhesion to steel substrate is significantly influenced by steel chemistry. For instance, Si in low carbon steel can promote scale adhesion by formation of the Si-rich oxide at the scale-steel interface [1]. However, some elements such as Mo in AISI 444 stainless steel can deteriorate the scale adhesion by precipitation of the intermetallic compound at the scale-steel interface [2]. The scale adhesion to steel substrate is influenced not only by the steel chemistry, but also by the oxidising atmosphere particularly the water vapour which is significantly existed in the hot rolling process. It has been extensively reported that water vapour enhanced oxidation rate of the Si-containing steel [3, 4]. The scale adhesion was reported to be improved [5]. However, the systematic measurement of scale adhesion has been limited.

For the evaluation of scale adhesion, various methods have been proposed, e.g., the indentation test, the inverted-blister test and the tensile test. For the last one, the micro-tensile test has been developed to investigate the scale adhesion to steel substrate by straining the oxidised sample under a scanning electron microscope [1]. This technique is very useful for investigating scale on the cold-rolled steel. However its application is limited for the case of hot-rolled steel. This is because the hot-rolled steel sheet is relatively thick, for instance with the thickness of 3 mm or higher. Thus the conventional macro-tensile test has been used to investigate the scale adhesion to the hot-rolled steel [1, 5]. Recently, we have applied the macro-tensile test to investigate the scale adhesion to the commercial hot-rolled steel. The present work applied this technique to study the adhesion of scale grown on low carbon steels different in Si and C under the controlled atmosphere.

2. EXPERIMENTAL

The studied samples were the hot-rolled low carbon steels, called steels A and B in the following. Chemical compositions of the studied steels are listed in Table 1. It should be noted Si and C contents in steel B are higher than those in steel A. The sample was prepared to have a shape for the tensile testing according to ASTM E8M with the total length of 200 mm. The sample was oxidised in Ar-10%H_2O at 850 °C for the period up to 120 s. After cooled down in Ar to room temperature, the sample was taken for the adhesion test.

Table I. Chemical compositions of the studied steels (wt %).

Steel	C	Si	Mn	S	P	Cu	Ni	Cr	Fe
A	0.073	0.015	0.431	0.009	0.011	0.036	0.029	0.011	bal.
B	0.166	0.168	0.670	0.005	0.006	0.078	0.026	0.019	bal.

For the adhesion test, the sample was placed in the tensile testing machine with the maximum load of 600 kN. The extensometer with the gauge length of 50 mm was used for measuring the strain. The strain rate of 0.83 s^{-1} was applied. During straining, evolution of scale failure was monitored by the optical lens with the magnification of 5×. For characterisation, a scanning electron microscope equipped with an energy-dispersive spectroscopy (EDS) was performed to observe cross section of the oxidised sample as well as the metal surface on the spalled area after the tensile test. An X-ray diffusion diffraction (XRD) technique using Cu Kα line (k = 1.5406 Å) was performed for phase identification.

3. RESULTS AND DISCUSSION

For the scale adhesion assessment using the tensile testing machine, the critical strain initiating the first spallation was used to evaluate scale adhesion. This is because, for the scale with a given thickness, the higher value of this parameter implies the higher energy accumulated in the oxide scale and therefore the higher interfacial adhesion energy, indicating the superior scale adhesion [3,4]. It was found that the strain initiating the first spallation was 13.9 % for the steel A, while it was 0.59 % for the steel B. The lower critical strain of the sample B indicates the lower adhesion of scale to that steel. Cross sections of the oxide scale on steels A and B after oxidation for 120 s are depicted in Fig. 1. The oxide scale on steel B was ca. three times thinner than that of steel A. For these two scales, the XRD patterns presented the peaks of hematite, magnetite and wustite, while the EDS results implied the existence of the Si-rich oxide at the scale-steel interface.

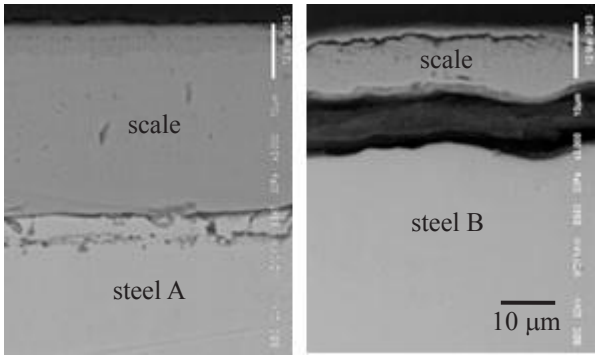

Fig. 1. Cross section of the oxide scale on steels A (left) and B (right) after oxidation at 850 °C in Ar-10%H_2O for 120 s.

In our previous work, thinner scale tended to exhibit the higher critical strain at the first spallation [2]. However in the present case, even though thickness of scale on steel B was less than that on steel A, the former steel had lower critical stain. This even implies the worse scale adhesion to steel B than to steel A. After the tensile test, the metal surface at the scale-steel interface was revealed on the spalled area. Carbon particles were found to disperse on that area because of the higher C content of the steel B. The existence of these particles deteriorated scale adhesion to steel substrate. In this study, the beneficial role of Si-rich oxide at scale-steel interface on improving scale adhesion [1] seemed to be less important than the deteriorating role of the carbon formation at that interface.

4. CONCLUSION

Low carbon steels different in Si and C were oxidised at 850 ºC in Ar-10%H_2O for 120 s. The macro-tensile testing machine equipped with the optical microscope has been developed to monitor scale failure during straining the sample. The strain initiating the first spallation was 0.59 % for the sample with higher Si (0.168 wt%) and C (0.166 wt%). It was 1.39 % for the sample with lower Si (0.015 wt%) and C (0.073 wt%). This result indicated the worse adhesion of scale grown on the former steel. Formation of carbon particles dispersed at the scale-steel interface was observed. This causes the deterioration of scale adhesion.

Acknowledgements

The authors acknowledge the 2012 Thailand Toray Science Foundation (TTSF) Science and Technology Research Grant, and the faculty of engineering of KMUTNB for the financial support.

References

[1] T. Nilsonthi, S. Chandra-ambhorn, Y. Wouters, A. Galerie, “Adhesion of Thermal Oxide Scales on Hot-rolled Conventional and Recycled Steels”, Oxidation of Metals Vol. 79, Issue 3-4 (2013), pp. 325-335.

[2] S. Chandra-ambhorn, Y. Wouters, L. Antoni, F. Toscan, A. Galerie, “Adhesion of Oxide Scales Grown on Ferritic Stainless Steels in Solid Oxide Fuel Cell Temperature and Atmosphere Conditions”, Journal of Power Sources, Vol. 171, Issue 2 (2007), pp. 688-695.

[3] M. Fugumoto, S. Maeda, S. Hayashi, T. Narita, “Effect of Water Vapor on the Oxidation Behavior of Fe-1.5Si in Air at 1073 and 1273 K”, Oxidation of Metals Vol. 55, Issue 5-6 (2001), pp. 401-422.

[4] H. Nakata, A. Yamauchi, S. Taniguchi, I.R. Shon, J.W. Choi, K. Kurokawa, “Failure Characteristics of Steels Formed on Si-containing Low Carbon Steels During Cooling – Influences of Cooling Rate and Water Vapor”, Materials Science Forum Vol. 696 (2011), pp. 101-106.

[5] S.R.J. Suanders, M. Monteriro, F. Rizzo, “The Oxidation Behaviour of Metals and Alloys at High Temperatures in Atmospheres Containing Water Vapour: a Review”, Progress in Materials Science Vol. 53, Issue 5 (2008), pp. 775-837.

[6] Krzyzanowski, M *et al.*, Oxide Scale Behavior in High Temperature Metal Processing, Wiley-VCH Verlag (Weimheim, 2010).

Solid state reaction of Fe and Cr_2O_3 in the H_2/H_2O gas mixture at 1073 K

K. Watanabe [(1,*)], M. Ueda [(1)], T. Maruyama [(1)], and M. Takeyama [(1)]

(1) Department of Metallurgy and Ceramics Science, Graduate School of Science and Engineering, Tokyo Institute of Technology
2-12-1-S8-11, Ookayama, Meguro-ku, Tokyo 152-8552 JAPAN

e-mail: watanabe.k.bp@m.titech.ac.jp

1. INTRODUCTION

Heat resistant steels for piping materials in fossil fuel power plants are required to have a good steam oxidation resistance. This property could be obtained by formation of continuous Cr_2O_3 layer on the surface of the steels. However, it is well known that the formation of Cr_2O_3 layer is retarded in humid condition and more Cr is needed to form continuous Cr_2O_3 layer in this condition. Ani *et al*. [1] investigated the effect of water vapor on the transition from internal to external oxidation of Fe-Cr ferritic alloys at 1073 K. They concluded that critical Cr concentration in the alloy increased in the presence of water vapor. Oxygen permeability in the alloy was enhanced by dissolved hydrogen, resulting in the increase of the critical Cr concentration. Ueda *et al.* [2] observed similar oxidation behavior of the Fe-Cr-Ni austenitic steels at 1073 K. Moreover, they examined oxidation test of the Fe-5Cr-30Ni (at.%) steel under the equilibrium oxygen partial pressure for coexistence of Fe and FeO and revealed that dispersion of $FeCr_2O_4$ spinel in the internal oxidation zone was also influenced by water vapor. Solid state reaction between Fe matrix and Cr_2O_3 particles might be affected by dissolved hydrogen. In this study, a diffusion couple of Fe and Cr_2O_3 is prepared to simulate solid state reaction in the internal oxidation zone and solid state reaction of $FeCr_2O_4$ formation is carried out at 1073 K in the H_2/H_2O gas mixture.

2. EXPERIMENTAL

A diffusion couple was prepared by sputtering Fe (99.99 %) on single crystal of Cr_2O_3 (5 mm × 5 mm × 1 mm) to simulate solid state reaction between Fe matrix and Cr_2O_3 particles in the internal oxidation zone. Table 1 shows sputtering condition. Fe was deposited on both sides of Cr_2O_3 substrate by radio frequency sputtering.

Table 1 Sputtering condition

Parameters	Conditions
Suptter Source	Radio Frequency (13.56 MHz)
Purging Method	Ar (10 sccm)
Working Pressure	10 Pa
rf Power	30 W
Sputtering time	1.8 ks × 8 (14.4 ks)
Substrate temperature	873 K

Solid state reaction of diffusion couple was conducted in the stream of Ar-2 %H_2-0.6 %H_2O gas mixture at 1073 K. The oxygen partial pressure was controlled to be 3.9×10^{-15} Pa, which is in the stable region of $FeCr_2O_4$. The diffusion couple was kept in the isothermal zone of the electric furnace and solid state reaction was conducted for 86.4 ks.

After solid state reaction, phase identification was examined by X-ray Diffraction (XRD). Cross-section of the sample was observed by a Field Emission-Scanning Electron Microscope (FE-SEM). The cross-section of the sample was fabricated by focused ion beam method (FIB). The thicknesses of Fe and $FeCr_2O_4$ layers of the sample, which was polished by a Cross-Section Polisher (CP), were measured by BE images obtained from FE-SEM.

3. RESULTS AND DISCUSSION

Figure 1 shows XRD pattern of the samples before and after solid state reaction. The peak of α-Fe was detected on the sample before solid state reaction. On the other hands, the peaks of $FeCr_2O_4$ and α-Fe were detected on the sample after solid state reaction. Figure 2 shows BE images of the cross-section of the samples before and after solid state reaction. Continuous layer of Fe was observed on the Cr_2O_3 substrate before solid state reaction and there is no void at the interface. $FeCr_2O_4$ layer as a reaction product was formed after solid state reaction. Figure 3 shows thicknesses of Fe and $FeCr_2O_4$ as a function of reaction time. Under the assumption that solid state reaction obeys parabolic rate law, parabolic rate constant (k_p) is estimated to be 2.5×10^{-17} m^2s^{-1}.

Solid state reaction between Fe and Cr_2O_3 occurs by the following reaction.

$$Fe + Cr_2O_3 + \underline{O} = FeCr_2O_4$$

The amount of consumed Fe by solid state reaction is estimated by mass balance of this reaction. The molar amount of the consumed Fe was calculated by using thickness change of Fe layer to be 1.6×10^{-6} mol. This is almost the same value, which is estimated from the thickness of $FeCr_2O_4$.

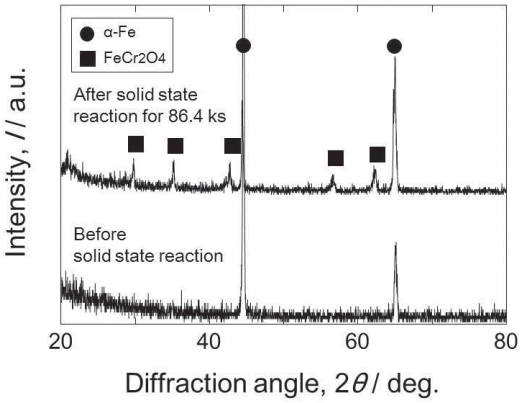

Fig. 1 XRD pattern of the samples before and after solid state reaction

4. CONCLUSION

Solid state reaction between Fe and Cr_2O_3 was investigated in humid condition at 1073 K under the oxygen partial pressure of 3.9×10^{-15} Pa for 86.4 ks. Uniform layer of $FeCr_2O_4$ was formed between Fe and Cr_2O_3 and parabolic rate constant for $FeCr_2O_4$ formation was estimated to be 2.5×10^{-17} m^2s^{-1}.

Acknowledgements

This study financially supported in part by the project of "Design principle of super heat-resistant steels applicable to innovative 800 ℃ class A-USC power plants" in Advanced Low Carbon Technology Research and Development Program, Japan Science and Technology Agency.

References

[1] M. Hanafi, T. Kodama, M. Ueda, K. Kawamura and T. Maruyama, *Mater. Trans.*, **50**(11) (2009), pp. 2656-2663.

[2] M. Ueda, Y. Inoue, H. Ochiai, M. Takeyama, T. Maruyama, *Oxid. Met.*, **79** (2013), pp. 485-494.

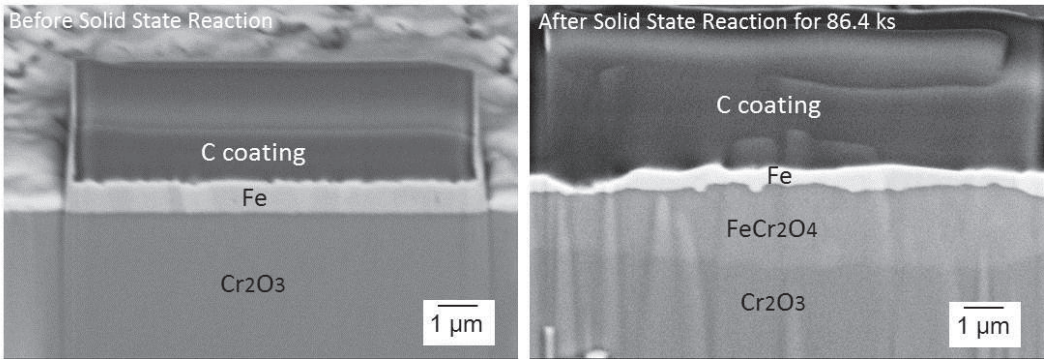

Fig. 2 BE images of the cross-section of the samples before and after solid state reaction.

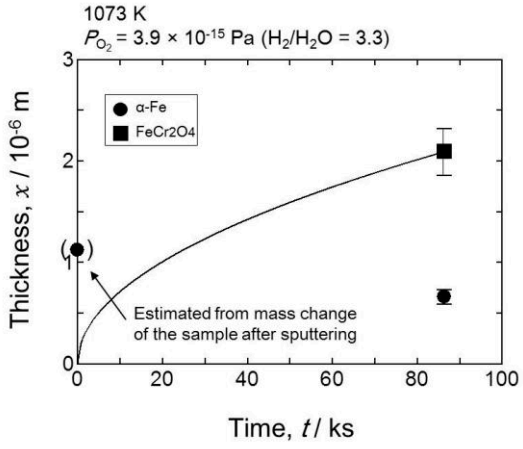

Fig. 3 Thicknesses of Fe and $FeCr_2O_4$ layer as a function reaction time.

Influences of the Base Element, the Oxide Scale Thickness and the Cooling Start Temperature on the Oxide Spallation of Cast Alloys during the Post-Isothermal Oxidation Cooling

Elodie Conrath [(1,*)] and Patrice Berthod [(1)]

[(1)] Institut Jean Lamour, University of Lorraine, Vandoeuvre-lès-Nancy 54506, FRANCE

e-mail: elodie.conrath@univ-lorraine.fr, patrice.berthod@univ-lorraine.fr

1. INTRODUCTION

Refractory alloys and superalloys present extraordinary properties at high temperature, in the mechanical field thanks to different metallurgical means of hardening [1] as well as in the hot corrosion resistance one [2]. In the second case chromium, aluminum or silicon are elements which are added in sufficient proportions to allow the development of very protective oxide scales over the alloys which play a barrier role for limiting the diffusion of anionic and/or cationic species and then the oxide scale thickening rate at constant temperature. After the isothermal oxidation rate, one of the most important properties characterizing the high temperature oxidation resistance of refractory metallic alloys is the resistance of the formed protective oxide scale against spallation during thermal variations. Indeed, repeated oxide spallation during thermal cycling accelerates the impoverishment of the alloy's sub-surface in aluminum or chromium. The well-known parameters influencing this phenomenon are the ratio between the average thermal expansion coefficients of the oxide and of the alloy, the cooling rate and the chemical composition of the alloy (notably the presence in small quantities of active elements or compounds as hafnium or yttria). Other parameters are maybe to be also taken into consideration, as the thickness of the oxide just before cooling and the level of temperature range in the first part of the cooling. To study the effect of these two other parameters, numerous model cast alloys based on cobalt, nickel or iron, rich in chromium (25 to 30wt.%) and containing carbides of different natures (chromium carbides, TaC, HfC…) and in various fractions (carbon contents varying between 0 to 2wt.%), were subjected to oxidation in dry synthetic air at different temperatures and for different durations, using a thermo-balance. For a same cooling rate, the mass variation curves recorded during the cooling were, after correction from the air buoyancy variations, plotted versus temperature instead time. Several parameters characterizing the oxide spallation were noted (temperature of spallation start, average rate of mass loss and final mass loss) and the noticed differences interpreted.

2. EXPERIMENTAL

All the alloys used for this study were elaborated by foundry way, from pure elements (Co, Ni, Fe, Cr and Hf: Alfa Aesar, purity > 99.9 wt.%, carbon: pure graphite). Fusion and solidification were realized in the water–cooled copper crucible of a CELES high frequency induction furnace, under an inert atmosphere of 300mbars of pure argon. The obtained compact–shaped ingots, all weighing about 40g, were cut using a Buelher Isomet 5000 precision saw, in order to obtain parallelepipeds (dimensions: about 10 × 10 × 3 mm^3) for the thermogravimetry oxidation tests. These latter samples were ground with SiC papers from 240 to 1200-grit, with smoothing of edges and corners.

The thermogravimetry runs were performed at 1000, 1100 or 1200°C, during about 50 hours (and also for much longer durations in the case of some of the alloys, e.g. 100, 200 hours) in a SETARAM TG92 thermo-balance, in dry industrial air (80%N_2 – 20%O_2). The heating and cooling rates were respectively of +20K min^{-1} and -5K min^{-1} for all the tests (since the influence of the cooling rate was not the subject of this study).

The obtained mass variations files were plotted not versus time but versus temperature. A correction from the mass changes only due to the air buoyancy variations (Archimede's pressure), extensively described in an earlier work [3] was systematically applied. The exploitation of the curves was realized as previously done in earlier studies [4-6] and briefly reminded in Figure 1.

In parallel, the oxidized samples were subjected to X-Ray Diffraction to specify the nature of the obtained external oxide scales, which must be taken into account in the analysis of the results. To complete the information about the external scales, the oxidized samples were coated by pulverized gold and electrolytic nickel (to prevent oxide loss during cutting), and cut in two parts before cross-sections preparation. They were embedded in a cold resin mixture (ESCIL), ground with SiC papers from 240 to 1200-grit, and polished with textile enriched with 1µm hard particles, to be finally examined

using a JEOL JSM 2010-LA Scanning Electrons Microscope (SEM) in Back Scattered Electrons mode (BSE). The chemical compositions of the scales observed in cross-section were controlled using the Energy Dispersion Spectrometry (EDS) apparatus equipping the SEM.

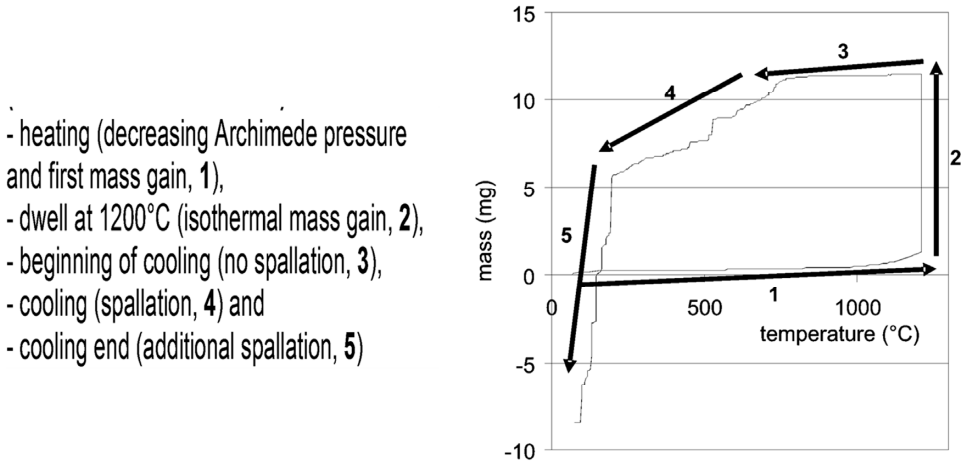

Fig. 1. Plot versus temperature of one of the thermogravimetry curves acquired in this work (Ni-30Cr-0.8C alloy oxidized 50 hours at 1200°C); description of the different parts and evidencing of the spallation start temperature (temperature of transition 3 → 4); average mass loss "rate" (mass per surface unit area per Celsius degree): here two successive parts: 4 and 5

3. RESULTS AND DISCUSSION

The isothermal oxidation rates of Co-based, Ni-based and Fe-based alloys at a given temperature were generally different since the Co-based alloys oxidized often faster than the Fe-based alloys, the all faster than the Ni-based ones. This led to different mass gains per surface unit area before cooling. Figure 2 presents, as illustration, selected thermogravimetry curves of the {mass gain versus temperature}- type obtained in the case of three M30Cr binary alloys (M=Co, Ni or Fe). Various mass gains before cooling were also obtained with greater differences form one to another by varying the temperature of the isothermal oxidation stage and the duration of the stages. Thus first correlations between oxide spallation easiness and mass of oxide by surface unit area were done.

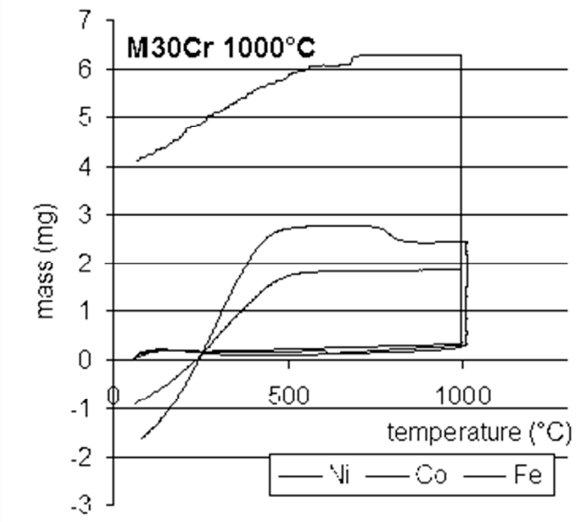

Fig. 2. Some examples illustrating the various thermogravimetry {mass variation versus temperature} curves obtained (here binary Co-30Cr, Ni-30Cr and Fe-30Cr binary alloys after 50 hours of oxidation at 1000°C)

However, as revealed by post-mortem characterization (XRD on surface before metallographic preparation, SEM observation in cross-section…), the natures of the obtained external oxides were often different from one another (e.g. chromia on nickel-based alloys, $(Fe,Cr)_2O_3$ with Fe/Cr varying between 0 and 1 and spinel $FeCr_2O_4$ on iron-based alloys, presence of CoO and spinel $CoCr_2O_4$ on Co-based alloys), with furthermore various orders from the alloy/scale interface to the oxide/air one. It generally appeared that the more complex oxide scale the greater loss by spallation at cooling.

To simplify interpretations and to study directly the effect of the mass of oxide per surface unit area on the parameters characterizing the oxide spallation at cooling, various temperatures and durations were tested only on clearly chromia-forming alloys (essentially based on nickel). This showed that generally the higher the mass of oxide per surface unit area the more severe mass loss by spallation during cooling, with frequently a final sample weigh lower than the initial one (i.e. negative mass gains after return to room temperature.

When the alloys are reinforced by interdendritic eutectic MC carbides (kind of carbides obtained by introducing new elements such as Ta or Hf) the behavior of the alloys in oxide scale spallation at cooling can be significantly modified. The most noticeable effect in the case of tantalum is a worsening of spallation. As revealed by SEM observation in sub-surface tantalum carbides dissolves over a depth increasing with time from the alloy/scale interface, with tantalum atoms diffusing towards the oxidation front. These ones tend to develop an intermediate complex oxide scale separating the external chromia scale and the metallic substrate, which has a very detrimental effect for the adherence of chromia on the alloy: spallation occurs very early during the cooling and the final mass loss is especially severe (e.g. total loss of the external oxide scale in the case of nickel-based alloys rich in tantalum, whatever the isothermal stage temperature). In contrast, in the cases of hafnium is the used MC-forming element, there is no such diffusion (HfC carbides much more stable, no diffusion of Hf towards the oxidation front) and no such scale adherence weakening is noted. Furthermore the well-known beneficial effect of Hf on oxide adherence may be partly observed.

4. CONCLUSION

In this work, the effects of several parameters concerning, either the alloys themselves (base element, presence of additional alloying elements and their contents…), or the process of oxidation before cooling (temperature, duration…), were revealed or confirmed. In future work this study may be extended to other cooling rates to examine whether there is or not correlation between these effects and the kinetic of cooling, and also to other oxidant atmospheres such as air containing water vapor (which is known to have an effect on the oxide scale spallation in thermal cycling, often considered as beneficial).

References

[1] Donachie, M. J., Donachie, S. J., Superalloys: A Technical Guide (2nd Edition), ASM International (Materials Park, 2002).

[2] Young, D., High Temperature Oxidation and Corrosion of Metals, Elsevier Corrosion Series (Amsterdam, 2008).

[3] Berthod, P., "Thermogravimetric study of oxide spallation for binary and ternary cobalt-based and iron-based alloys oxidized at high temperature", *The Open Corrosion Journal*, Vol. 2, (2009), pp. 61-70.

[4] Berthod, P., Aranda, L., Lemoine, P., "Oxide spallation during cooling from high temperatures affecting carbides-containing nickel-based alloys. Part I: Case of ternary Ni-Cr-C alloys with various carbides fractions", *Materials Science: An Indian Journal*, Vol. 5, No. 1 (2009), pp. 42-48.

[5] Berthod, P., Aranda, L., Vébert, C., "Oxide spallation during cooling from high temperatures affecting carbides-containing nickel-based alloys. Part II: Case of Ni–Cr–C alloys with addition of tantalum", Vol. 5, No. 1 (2009), pp. 49-54.

[6] Berthod, P., Chiaravalle, A., Raude, S., "Influence of the microstructure fineness on the high temperature oxidation during heating and on the oxide spallation during cooling for carbides-strengthened cast superalloys ", *Materials Science: An Indian Journal*, Vol. 5, No. 2 (2009), pp.94-100.

High Temperature Corrosion due to Biomass Firing: A Study on the Reactivity between Potassium Chloride and Oxides

Saeed Kiamehr *, Kristian V. Dahl, Trine N. Lomholt, Thomas L. Christiansen, Marcel A.J. Somers

Technical University of Denmark (DTU), Department of Mechanical Engineering, Produktionstorvet, Building 425, 2800 Kgs. Lyngby, Denmark

sabag@mek.dtu.dk

1. INTRODUCTION

During the past decades biomass has become a point of focus as a substitute source of energy to replace the fossil fuels. This is mainly because it has the potential to be a CO_2-neutral fuel. However, efficient utilization of biomass has shown to be a challenging task. In this regard the most important difficulty is the high temperature corrosion of heat exchangers due to the formation of deposits rich in potassium chloride (KCl). This, in turn, limits the output steam temperature of the current power plants to a maximum of 540°C [1]. There is still no general agreement in the literature about the exact mechanism of high temperature corrosion by KCl. Classic theory of corrosion under biomass firing environment considers $O_2(g)$ and $Cl_2(g)$ to be the prime species responsible for accelerated attack and considers $SO_2(g)$ as an intermediate species [2]. According to this mechanism $Cl_2(g)$ mainly evolves due to the sulfation of KCl (eq. 1) and then $O_2(g)$ and $Cl_2(g)$ compose the aggressive mixture that subsequently degrades the alloy according to the "active oxidation" model. Details of this mechanism can be found elsewhere [3–5].

$$2KCl + SO_2(g) + O_2(g) = K_2SO_4 + Cl_2(g) \qquad (1)$$

A second theory suggests potassium as the major degrading species, at least in the early stage of corrosion [6]. This is based on a reaction between KCl and Cr_2O_3 in the protective oxide layer (eq. 2).

$$4KCl + Cr_2O_3 + (5/2)O_2(g) = 2K_2CrO_4 + 2Cl_2(g) \qquad (2)$$

When Cr_2O_3 reacts with KCl the oxide layer loses its protective property and instead of a slow-growing Cr_2O_3-rich oxide a fast-growing double layer oxide is formed. In case of austenitic stainless steels such oxide is composed of an outward growing Fe_2O_3 and an inward growing $(Fe,Cr,Ni)_3O_4$ layer [6]. Corrosion beneath a porous KCl-containing deposit under a gaseous atmosphere containing multiple corrosive species is a complex phenomenon and there is still no general agreement in the literature on whether potassium or chlorine is more detrimental for the overall lifetime. Therefore a safe alloy design strategy requires simultaneous consideration of the reactivity of oxides with KCl as well as relative affinities of the alloying elements to both oxygen and chlorine.

2. THERMODYNAMIC CONSIDERATIONS

In the current study, as the first step, predominance diagrams for a large number of metallic elements of the periodic Table were calculated applying Thermocalc (database SSUB3) [7] and HSC Chemistry [8]. These diagrams show the stable phases at a constant temperature under different oxygen and chlorine partial pressures. Calculations show that Al, Si, Cr, Ti, Y, Ce, Ta, Hf and Zr possess large oxide stability areas making them candidates for an oxide forming element under a $O_2(g)$+$Cl_2(g)$ containing gas. Choice of employing pure elements is limited in many engineering applications due to insufficient mechanical properties and therefore alloys need to be utilized. For an alloy a suitable matrix element under oxidizing-chlorinating conditions is an element with low affinity to chlorine under low $P_{O2(g)}$ conditions i.e. beneath an oxide layer [9]. Referring to the predominance diagrams Mo, Ni and Co were found to have this characteristic. However, in this study Mo was not considered further as Mo(VI) oxide is volatile at 650°C [7]. At the end Fe and Mn were also included in the experimental plan. Choice of these was due to their abundance as well as

the fact that although these elements (in pure form) do not offer protection in oxidizing-chlorinating atmospheres, they might be a good choice of the matrix element if an oxide layer is able to establish quickly.

As mentioned earlier, in addition to oxygen and chlorine, potassium also plays a significant role in the degradation of materials during biomass combustion. This imposes an additional requirement for the alloying elements: low reactivity of the corresponding oxide with KCl. In this study, as a first step, affinities of the oxides were evaluated by calculating the standard Gibbs energy change for the corresponding reactions. Unfortunately, for some of the considered oxides the thermochemical data for possible reaction products are not available. Results of the calculations are given in Table 1. Based on these values it is expected that the reactivity increases in the order of Fe_2O_3<Al_2O_3<SiO_2<Ta_2O_5<Cr_2O_3<TiO_2. It has to be mentioned that the choice of reaction products is based on the available species in the databases of the employed softwares. In reality the reaction product and therefore the stoichiometry might be different from what has been considered here.

Table 1: Affinity of a number of oxides to KCl at 600°C. ΔG^o values are calculated by Thermocalc (database SSUB3) unless cited otherwise. Choice of temperature is based on a target temperature of 600°C for new generation of superheater materials. Due to the endothermicty of the reactions a similar trend (higher reactivity) is expected at higher temperatures. $P_{O2(g)}$=0.05 and $P_{H2O(g)}$=0.15 atm were used to calculate the equilibrium partial pressure of HCl(g). These values approximately correspond to the oxidizing potential of the off-gas due to the biomass combustion.

oxide	Reaction equation	ΔG^o (KJ)	P_{HCl}^{eq} *10^6
Al_2O_3	$(1/2)Al_2O_3 + KCl + (1/2)H_2O(g) = (1/2)K_2O.Al_2O_3 + HCl(g)$	+112.3	0.07
Cr_2O_3	$(1/2)Cr_2O_3 + KCl + (1/2)H_2O(g) = (1/2)K_2O.Cr_2O_3 + HCl(g)$	+95.4	0.76
	$(1/4)Cr_2O_3 + KCl + (1/2)H_2O(g) + (3/8)O_2(g) = (1/2)K_2O.CrO_3 + HCl(g)$	+37.8	690
	$(1/2)Cr_2O_3 + KCl + (1/2)H_2O(g) + (3/4)O_2(g) = (1/2)K_2O.2CrO_3(l) + HCl(g)$	+29.9 [8]	666
Fe_2O_3	$(1/2)Fe_2O_3 + KCl + (1/2)H_2O(g) = (1/2)K_2O.Fe_2O_3 + HCl(g)$	+131.0	0.005
SiO_2	$(1/2)SiO_2 + KCl + (1/2)H_2O(g) = (1/2)K_2O.SiO_2 + HCl(g)$	+96.2	0.68
	$SiO_2 + KCl + (1/2)H_2O(g) = (1/2)K_2O.2SiO_2 + HCl(g)$	+68.7	30
	$2SiO_2 + KCl + (1/2)H_2O(g) = (1/2)K_2O.4SiO_2 + HCl(g)$	+73.3	16
TiO_2	$(1/2)TiO_2 + KCl + (1/2)H_2O(g) = (1/2)K_2O.TiO_2 + HCl(g)$	-56.2 [8]	891*10^6
Ta_2O_5	$(1/2)Ta_2O_5 + KCl + (1/2)H_2O(g) = (1/2)K_2O.Ta_2O_5 + HCl(g)$	+58.5 [8]	122

3. EXPERIMENTAL PROCEDURE

Oxides considered in this study consist of ZrO_2, TiO_2 (both rutile and anatase), Y_2O_3, SiO_2, Ta_2O_5, Fe_2O_3, Cr_2O_3, HfO_2, CeO_2, Al_2O_3, NiO, Co_3O_4 and Mn_3O_4. Except Ta_2O_5, Mn_3O_4 and TiO_2(rutile), which had unspecified particle size, the rest of the oxides had particle sizes ranging from 20 to 200nm. In addition, KCl had a particle size of 63-90µm. Assuming that the condensed reaction product consists of 1 mole of K_2O and 1 mole of oxide (i.e. with the general formula $K_2O.M_2O_x$) the reaction equations were balanced and subsequently each oxide was mixed with KCl according to this anticipated stoichiometry. Mixing was done using an agate mortar. Thereafter, part of the mixture was transferred to a mold and pressed manually to produce cylindrical tablets of 17mm diameter. The thermal cycle consisted of heating to 650°C at a rate of ~5°C/min, holding at this temperature for 15 hours and then cooling to room temperature under furnace cooling. The Atmosphere was $N_2(g)$+5%$O_2(g)$+15%$H_2O(g)$ flowing at a rate of 0.5 cm/s at the inlet temperature. Heating and cooling was performed under the mentioned atmosphere when the temperature was above 500°C. Below this temperature the water bath was switched off to avoid condensation of water vapor on cold parts of the furnace tube. Flow rates of $O_2(g)$ and $N_2(g)$ were controlled by means of thermal mass flow controllers (GF40/80 series, Brooks Instrument). $P_{H2O(g)}$ was fixed at 0.15atm by keeping the temperature of the water bath at 54°C. To avoid cross contamination, exposures were performed separately for each sample. Before heating, samples were placed on a gold coated alumina plate and then loaded into the furnace lying close to the thermocouple tip. Prior to and after the exposures samples were studied by X-Ray Diffraction (XRD) using a Bruker D8 Discover diffractometer. Measurements were done in parallel beam condition using CrK_α (λ=2.2897 Å) radiation. In addition, morphology of the exposed samples were examined by a JEOL JSM-5900 Scanning Electron Microscope (SEM) equipped with an Energy Dispersive X-Ray Spectroscopy (EDS) detector.

4. RESULTS AND DISCUSION

For Fe_2O_3, TiO_2 (both anatase and rutile), NiO, Co_3O_4, CeO_2, Ta_2O_5, HfO_2, ZrO_2 and Y_2O_3 no new peaks emerged on the diffractograms after the exposure. No compound which is composed of K, M and O (where M is the corresponding metal) or hydrated form of that was found in the diffractograms. This suggests lack of reactivity between these oxides and KCl under the experimental conditions of this study. It is noted that XRD is not able to detect a phase if its amount is below ~3wt%. Therefore, these results only show that there is no *major* reactivity between the abovementioned oxides and KCl. Lack of reaction between TiO_2 and KCl is opposite to the thermodynamic calculations (Table 1). This indicates that the activation energy for this reaction is large in a way that higher temperatures are needed for the reaction to start. For Al_2O_3 there is an infinitesimal single peak appearing at 105.48°. However, this peak does not correspond to any compound containing K, Al and O (or hydrated form of that). This indicates lack of a major reaction between KCl and Al_2O_3. In case of Cr_2O_3 presence of K_2CrO_4 is clearly visible (figure 1a). This means that Cr_2O_3 is reactive and this oxide may not offer protection against KCl. In addition, this result shows that the reaction follows the stoichiometry of the second equation (among the reactions for Cr_2O_3) in Table 1. For Mn_3O_4 it was found that the compound $K_{2-x}Mn_8O_{16}$, where x denotes the non-stoichiometry, has major peaks that overlap with those of $Mn_{0.98}O_2$ and Mn_3O_4. Therefore, the result based on XRD is not conclusive for the reactivity of Mn_3O_4 and KCl. In case of SiO_2 new peaks emerge on the diffractogram after the exposure (figure 1b). These peaks correspond to either trydimite or cristobalite. As the SiO_2 was originally amorphous this means that crystallization has taken place to some extent. Calculation by Thermocalc shows that at 650°C quartz is the stable crystalline form of SiO_2. Tridymite should not form up to 870°C and cristobalite up to 1471°C. Therefore an explanation for the formation of these two phases can be due to KCl affecting the crystallography of phase transformation. This is supported by the observation that a pure SiO_2 sample (without KCl) exposed under similar conditions did not show a major crystallization. Co-existence of trydimite and cristobalite is likely due to small molar Gibbs energy difference between quartz, tridymite and cristobalite over a wide temperature range.

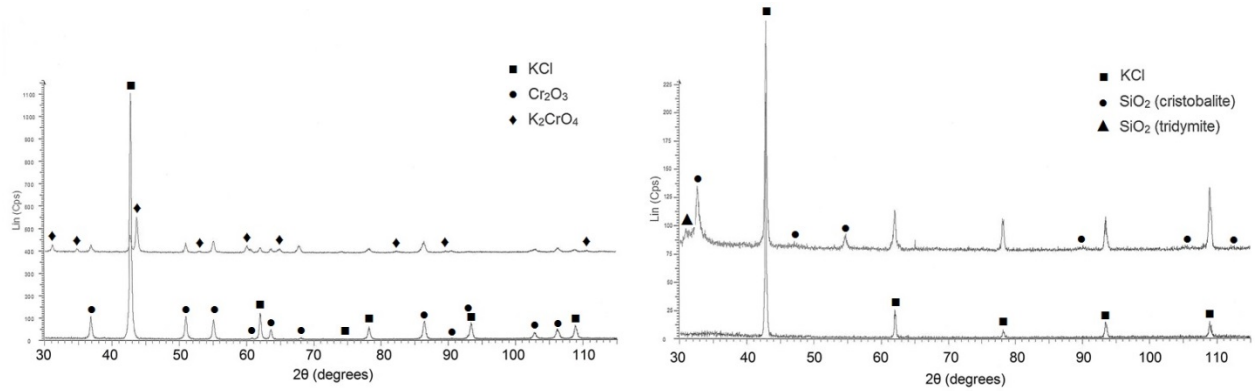

(a) (b)

Figure 1: X-Ray diffractograms corresponding to (a) Cr_2O_3+KCl and (b) SiO_2+KCl samples. The diffractogram at the bottom of each figure corresponds to the sample before the exposure and the one at the top to the sample after the exposure.

As the original SiO_2 was amorphous, due to concerns about the formation of amorphous reaction products, the SiO_2+KCl pellet was examined by SEM/EDS. The microstructure consisted of cubic KCl crystals partially covered by a Si-rich compound. This compound had a solidified appearance and at some points it only consisted of K, Si and O without any Cl. This indicates that SiO_2 has reacted and potassium silicate(s) has formed. Combining this information with XRD analysis of this compound shows that this is composed of amorphous potassium silicate(s) along with pure silica that has (at least partly) crystalline structures of tridymite and cristobalite. Comparing the obtained result with the data in Table 1, it is expected that when SiO_2 turns out to be reactive, then Ta_2O_5 should be reactive too. Lack of any reactivity for Ta_2O_5 indicates that, similar to TiO_2, the activation energy for the reaction is too high. Apart from the SiO_2 all the other oxides were crystalline in the as-received state. Therefore it is expected that the reaction product after KCl exposure is crystalline too. On this basis it seems that only Cr_2O_3 is reactive among the rest of the oxides. To

support this, all the samples were studied by SEM. The result showed a clear difference between Cr_2O_3/SiO_2 and the rest of the oxides. Only on these two samples a convoluted morphology had formed. Rounded edges of the reaction product in case of Cr_2O_3 and SiO_2 suggest formation of a molten phase. For the former oxide this can be attributed to the KCl-K_2CrO_4 system with a eutectic temperature of 650°C [10] and for the latter to the K_2O-SiO_2 system with a eutectic temperature of 649°C [11]. For the rest of the oxides, a granular structure of the oxide and a clear distinction between the oxide and KCl particles could be seen. These observations along with the results of XRD suggest that except for Cr_2O_3 and SiO_2 the oxides studied do not significantly react with KCl.

5. CONCLUSIONS

Reactivity of a number of oxides with KCl was studied at 650°C under flowing N_2(g)+5%O_2(g)+15%H_2O(g) gas atmosphere. It was observed that Cr_2O_3 and SiO_2 are reactive with KCl. This implies that care must be taken employing Cr and Si as alloying elements in KCl-containing high temperature environments. For Cr_2O_3 the reaction product is K_2CrO_4. For SiO_2 the exact stoichiometry of the product cannot be determined with XRD due to the amorphous nature of the silicate formed. For Mn_3O_4, XRD cannot give an indication whether this oxide is reactive with KCl due to peak overlap. However observation of the sample under SEM suggests lack of a major reactivity. For ZrO_2, TiO_2, Y_2O_3, Ta_2O_5, Fe_2O_3, HfO_2, CeO_2, Al_2O_3, NiO and Co_3O_4 results from XRD as well as observation under SEM suggest lack of a major reaction between theses oxides and the salt. Lack of reactivity between TiO_2 and KCl as well as Ta_2O_5 and KCl indicates that the activation energies for these reactions are too high.

Acknowledgement

This work is part of the project GREEN financed by the center DSF GREEN. Help and support from John C. Troelsen, Peter J.S. Westermann and Chamathkara Palangasinghe is greatly acknowledged.

References

[1] M. Montgomery, S. A. Jensen, U. Borg, O. Biede, and T. Vilhelmsen: *Mater. Corros.*, 2011, vol. 62, pp. 593–605.

[2] Hanne Philbert Nielsen, Flemming J. Frandsen, and Kim Dam-Johansen: *Energy & Fuels*, 1999, vol. 13, pp. 1114–1121.

[3] M.J. McNallan, W.W. Liang, S.H. Kim, and C.T. Kang: in *High Temp. Corros. NACE*, NACE, 1983, pp. 316–321.

[4] YY Lee and MJ McNallan: *Metall. Trans. A*, 1987, vol. 18, pp. 1099–1107.

[5] HJ Grabke, E Reese, and M. Spiegel: *Corros. Sci.*, 1995, vol. 37, pp. 1023–1043.

[6] J. Pettersson, H. Asteman, J. -E. Svensson, and L. -G. Johansson: *Oxid. Met.*, 2005, vol. 64, pp. 23–41.

[7] JO Andersson, T Helander, and L Höglund: *Calphad*, 2002, vol. 26, pp. 273–312.

[8] HSC Chemistry 7.00, www.hsc-chemistry.com

[9] R. Bender and M Schutze: *Mater. Corros.*, 2003, vol. 54, pp. 567–586.

[10] J. Lehmusto, D. Lindberg, P. Yrjas, B.-J. Skrifvars, and M. Hupa: *Oxid. Met.*, 2011.

[11] Mark D Allendorf and Karl E Spear: *J. Electrochem. Soc.*, 2001, vol. 148, pp. 59–67.

Oxide growth characterization of four commercially available high temperature alloys (RA 602CA; Inconel 693; Manaurite 40XO; Sumitomo 696) in air and Ar-H_2O at 950°C

Lionel Aranda[(1)], Léo Portebois[(1)], Stéphane Mathieu[(1)], Younès Bouizi[(1)], Pierre-Jean Panteix[(1,*)], Sandrine Mathieu[(2)], Michel Vilasi[(1)]

[(1)] Université de Lorraine, Institut Jean Lamour - UMR7198, Boulevard des Aiguillettes, BP70239, 54506 Vandoeuvre-lès-Nancy Cedex, FRANCE

[(2)] Université de Lorraine, Service Commun de Microscopie et Microanalyse, Boulevard des Aiguillettes, BP70239, 54506 Vandoeuvre-lès-Nancy Cedex, FRANCE

e-mail: pierre-jean.panteix@univ-lorraine.fr

1. INTRODUCTION

Most commercially available alloys used in high temperature applications differ in composition to a low extend. They generally contain between 25 and 30 wt.%Cr which confers to these alloys a chromia forming behavior [1-4]. Alloys also contain minor additions of elements (aluminum, manganese, silicon, yttrium, etc.) strongly influencing on the oxidation resistance. According to the type and amount of these minor additions, the oxidation behavior can differ to a large extend so that the specific behavior of such multi-elementary industrial alloys is generally difficult to anticipate and thus, justifies a specific study.

The study concerns the oxidation behavior of RA 602CA, Inconel 693, Manaurite 40XO and Sumitomo 696. These alloys are well known for their high temperature mechanical properties and also for their resistance in hydrocarbon processing or corrosive atmosphere. The goal of the present work was to evaluate their oxidation resistance both in high and in low PO_2 environments. Water being generally present in reducing atmosphere (low PO_2) of industrial plant where these alloys are employed, oxidation tests were conducted in an Ar-H_2O mixture (10 % Absolute Humidity) and also in industrial air for comparison. Water is known to enhance chromia growth rate in chromia forming alloys by changing the transport processes or properties of the oxide scale and also to increase internal oxidation of chromium in FeCr alloys [5]. Few studies are made for NiCr alloys [6,7] and even fewer on Al containing NiCr alloys which are among the most used in industry.

In the present work, the oxidation behavior was studied by thermogravimetry in air and Ar-H_2O at 950°C. The oxidation products were fully characterized using X-Ray Diffraction (XRD) and FEG-SEM observations. A special attention was paid in cross section preparation of samples. To avoid preparation artifact, they were polished using ion beam cross polisher.

2. EXPERIMENTAL

RA 602CA, Inconel 693, Manaurite 40XO and Sumitomo 696 are commercially available alloys that contain 25-30 wt.% Cr. Their main alloying elements from the oxidation point of view are Al, Si and Mn. The three former alloys contain 1.6 to 3.2 wt.%Al whereas SMI696 has no aluminum. Their nominal compositions are given in **TABLE 1** (except for C and N, which form carbides or nitrides, these values have been checked using quantitative EDS analysis with standards).

TABLE 1. Composition of the alloys (in bracket: values not quantified by EDS)

[wt. %]	C	Ni	Co	Fe	Cu	Cr	Mo	Nb	Ta	Ti	Zr	Y	Al	Si	Mn
602CA	(0.2)	64	-	9	-	**24**	-	-	-	0.13	0.19	(0.1)	**2.3**	(0.1)	(0.1)
693	(0.01)	61		5.8	-	**29**	-	0.6	-	0.5	-	-	**3.2**	(0.1)	**0.4**
40XO	(0.45)	44	-	26	-	**28**	(0.5)	(1)	(2)	0.2	-	-	**1.6**	**1.6**	**1.7**
696	(0.08)	64	0.7	2.8	2	**28**	1	-	-	0.2	-	-	-	**1.5**	-

Before oxidation test, alloy's surface was ground and the corners were rounded on SiC paper down to grit 800. Then, the samples were cleaned ultrasonically in ethanol. Thermogravimetry was performed at 950°C in dry air flow (1.2 L h^{-1}) and in Ar-H_2O (10 % HA; 1.2 L h^{-1}) using a SETSYS thermobalance (Setaram Instrumentation).

The oxidation products were identified by X-ray diffraction, using Kα (0.154056 nm) copper radiation, on a Philips

X'PERT pro diffractometer. The identification of the crystalline phases was made using 'Pearson's Crystal' Data [8] and/or the PDF data base. Surface and cross sections of the samples were observed using a Field Emission Gun Scanning Electron Microscope (FEG-SEM) equipped with an Energy Dispersion spectrometer of X-Ray (EDX) to perform elemental analysis. Polishing was performed using an ion beam cross section polisher (JEOL - IB9010 CP) to avoid mechanical modification of the substrate-oxide layer interface.

3. RESULTS AND DISCUSSION

The isothermal oxidation behaviour of the four samples was studied by thermogravimetry at 950°C for 48 h both in air and in Ar-H_2O. All curves followed a parabolic-like kinetic versus time in both atmospheres. The plot of normalised weight changes versus the square root of time gave straight lines, confirming that the weight gains are all governed by diffusion in the solid state at this temperature. This representation allowed the determination of the parabolic oxidation constants (k_p) given in **TABLE 2** for each composition. These values are systematically higher in Ar-H_2O atmosphere except for SMI696 for which k_p remains roughly unchanged. It has to be noticed that oxide spallation was not observed for all alloys during cooling.

TABLE 2. Parabolic constant (k_p, in $g^2.cm^{-4}.s^{-1}$) deduced from thermogravimetric measurements

	602CA	693	40XO	SMI696
Air	5.8×10^{-13}	3.45×10^{-13}	7.95×10^{-13}	1.3×10^{-12}
Ar-H_2O	1.8×10^{-12}	4.1×10^{-12}	3.7×10^{-12}	2.05×10^{-12}

X-ray diffraction was performed for each sample. As expected from Gibbs energy values, the nature of thermal oxides differs in both atmospheres. Chromia and spinels containing Fe, Cr, Ni were identified on XRD patterns in air whereas Cr_2O_3 and Cr_2TiO_5 are the main oxides in Ar-H_2O. It has also to be mentioned that diffraction peaks from substrate are strongly reduced in the case of alloys oxidized in Ar-H_2O. Alumina was not identified on XRD patterns whatever the composition of the alloy.

SEM observations of the surface were more surprising. Indeed, oxidation in air mainly led to the formation of alumina on Al containing alloys whereas only few areas are covered by oxides containing chromium. The ratio of surface covered by alumina was strongly affected in Ar-H_2O for these alloys as can be observed in **FIG.2a** and **2b** which represent the surfaces of 602CA alloy after 48h exposure at 950°C in air and Ar-H_2O respectively. At the opposite the surface of SMI696 did not differ in Ar-H_2O of those observed in air.

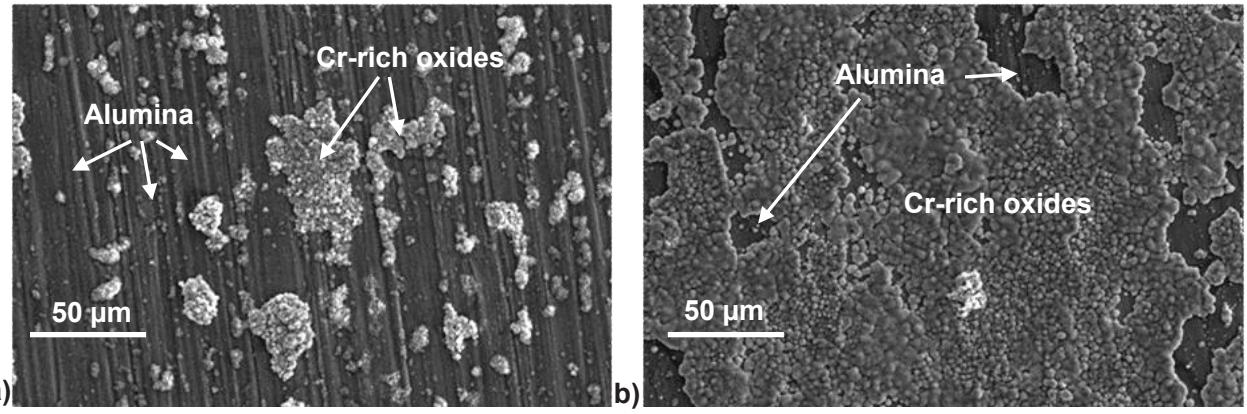

FIG.2. Surface observations of alloy 602CA after 48h of exposure at 950°C : a) in air and b) in Ar-H_2O

Cross section observations allowed the accurate location of each oxide through the oxide layer. **FIG.3** displays the typical cross section for each alloy in both atmospheres. The purpose of this paper is not to discuss point by point the obtained cross sections but to give the general results obtained. It is clear that all alloys containing Al develop protective and external alumina scales in air at 950°C. In Ar-H_2O, all these alloys exhibit internal alumina formation. Internal oxidation systematically takes place below a thick chromia layer. This increase of Cr_2O_3 thickness evidences the previously reported effect of water vapor on chromia growth [7,9]. Surprisingly, cross sections for SMI696 were identical in both

atmospheres. The oxide layer formed in air was just slightly thinner than the one formed in Ar-H_2O atmosphere confirming the surface observations. For this alloy, large dots of SiO_2 pegged the chromia layer to the substrate. Moreover, chromia was particularly dense contrarily to the rapidly formed chromia in all other cases.

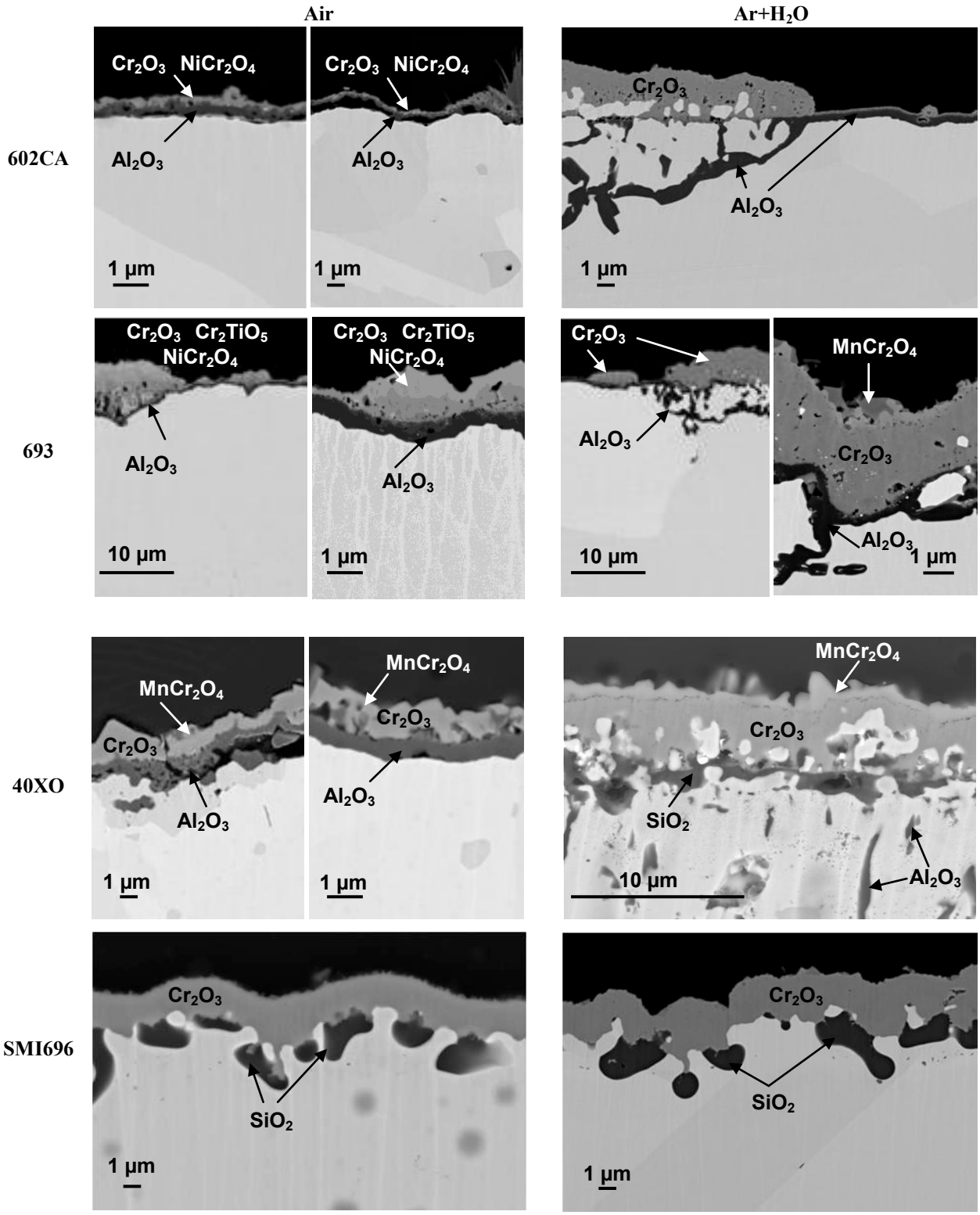

FIG.3. Cross section observations of alloy 602CA after 48h of exposure at 950°C : a) in air and b) in Ar-H_2O

From these experimental results on four commercial alloys, it clearly appears that water vapor has a strong effect on the oxidation behavior of Al rich chromia forming alloys. The effect of water vapor on chromia growth appears moderate on the SMI696 which develops dense chromia and silica dots. It is suggested that this behavior would be attributed to silicon.

Consequently the oxidation behavior of 40XO which contains both Si and Al shall be considered as an intermediate case between 602CA-693 and SMI696. Indeed its cross section in Ar-H_2O revealed the formation of a thick but dense chromia layer at the top of silica dots; internal alumina also formed.

4. CONCLUSIONS

The oxidation behavior of 602CA, 693, 40XO and SMI 696 was studied both in air and in Ar-H_2O at 950°C. Their oxidation rate (k_p) at 950°C was higher in water vapor containing atmosphere than in air. The effect was peculiarly clear for Al containing alloys (602CA, 696 and 40XO). For these alloys, internal oxidation of aluminum associated with thick chromia layer development was systematically observed. Consequently water vapor significantly enhanced oxygen diffusivity and chromia growth in Al containing chromia forming alloys. At the opposite silicon contributed to limit porosity development at the substrate-oxide scale interface as well as in the bulk of the chromia scale. Regarding these first results, SMI696 can be considered as the commercial alloy the most capable among the four tested alloys to withstand both oxidative, reductive and/or water containing atmosphere around 900-1000°C.

References

[1] C. Wood, I.G. Wright, T. Hodgkiess, D.P. Whittle, Werkstoffe und Korrosion 21 (1970) 900
[2] A. de S. Brasunas, J.T. Gow, O.E.Harder, 30th Annual Convention of the *American Society* for Metals, Proceeding 46 (1946) 870
[3] J.E. Croll, GR. Wallwork, Oxid.Met. 4 (1972) 121
[4] P. Kofstad, High temperature corrosion, Elsevier applied science publishers ltd (1988)
[5] E. Essuman, G.H. Meier, J. Zurek, M. Hänsel, W.J. Quaddakers, Oxid.Met. 69 (3/4) (2008) 143
[6] E. Essuman, G.H. Meier, J. Zurek, M. Hänsel, T. Norby, L. Singheiser, W.J. Quaddakers, Corros.Sci. 50 (2008) 1753
[7] J. Zurek, D.J. Young, E. Essuman, M. Hänsel, H.J. Penkalla, L. Niewolak, W.J. Quaddakers, Mat.Sci.Eng.A 477 (2008) 259
[8] P. Villars, K. Cenzual, Pearson'Crystal Data-Crystal Structure Database for Inorganic Compounds (on CD-ROM), Release 2010/11, ASM International, Materials Park, Ohio, USA.
[9] P. Berthod, L. Aranda, S. Mathieu, M. Vilasi, Oxid.Met. 79 (5/6) (2013) 517

Applicability of Thermodynamic Simulation in the Environmental Predication of the High-Efficiency Waste-to-Energy Plant Boiler

Yuta Sudo[(1,*)], Kazumasa Takemura[(1)], Masayuki Yoshiba[(1)], Toshiro Anraku[(2)], and Shigeru Tokura[(2)]

[(1)]Graduate School of Science and Engineering, Tokyo Metropolitan University, Minami-Osawa, Hachioji, Tokyo 192-0397, JAPAN

[(2)]Material Engineering Department, Nippon Steel & Sumikin Technology, Fuso-Cho, Amagasaki, Hyogo Prefecture 660-0891, JAPAN

E-mail: sudou-yuuta@ed.tmu.ac.jp

1. INTRODUCTION

From the viewpoint of energy and environment problems including global warming, introduction and dissemination of renewable energy alternative to fossil fuel is strongly required. Namely, Waste-to-Energy (WTE) is so much attractive as a base-load power plant, since it is staple and sustainable in resource as compared to the other solar and wind power generation. In addition, the activity also can be expected in terms of the disaster-prevention facility and infrastructure because they are dispersive across the country. However, WTE technology has to be further promoted for higher efficiency since their performance remains still up to 15% in average efficiency [1].

High increasing in the temperature and pressure of boiler is most effective for high efficiency of WTE. However, the complicated hot corrosive environment is formed in the superheater (SH) tube by the deposited ash in combination of gas and molten salt corrosion. These technical issues, such as mechanisms and main factors of corrosion reaction, must be clarified for solving the hot corrosion problem. In the previous study, the compound for causing the corrosion was hardly clarified in spite of various environmental analyses applied. Therefore, this study aims to identify the compounds by using thermodynamic simulation. In the present study, thermodynamic prediction was attempted for the high-efficiency WTE boiler environment, and its applicability and/or limitation was discussed in relation to different manners of the environmental analysis methodologies.

2. EXPERIMENTAL

In this study, the boiler environment was assumed by archiving the national NEDO project on WTE pilot plant at Tsukui [2]. Table 1 shows the design specifications of this plant. In order to identify the existence form and the constituent of compounds in the boiler environment, analysis by thermodynamic equilibrium calculation was carried out by using the software "MALT" (MALT for Windows). In this study, namely, mainly three cases of the environmental conditions were adopted; Case 1 to 3. These conditions are summarized in Table 2. As a common condition, the mass of input material was 100g, and their composition and the combustion gas components were determined on the basis of the database in the previous analytical study and NEDO project report [2].

Table 1 Specification of NEDO WTE plant at Tsukui

Disposal Capacity	50 t/day
Generating Capacity	800 kW
Thermal Efficiency	30 % (Large Icinerator Equivalent)
Combution System	Stoker Mass Burn
Temperture(Gas/Steam)	630 ℃/450 ℃
Duration of SH Tube Used	ca. 37,000 h (ca. 5 years)

In Case 1, an influence of controlling the ratio of combustion gas and input materials was mainly investigated. The amount of combustion gas/input materials ratio was adopted the following four, 1.0, 1.3, 1.6 and 1.9, based on the paper of N. Otsuka [3]. Temperature was uniquely fixed at 500℃. In Case 2, the effect of HCl concentraton as investigated. Calculations were carried out for totally four conditions: HCl was from 300 to 1500ppm, together with temperature of 600 and 650℃. It was assumed that the amount of gas is sufficient for input material. In Case 3, the calculation was made in order to clarify the constitution of the combustion gas phase. The amount of gas was similar to Case 2. There is the totally four temperature conditions of 450, 500, 550 and 600℃. The input of O_2 was 1/10, and dual Cl contents was applied to attempt the extreme conditions at 450℃ that is the typical SH tube wall temperature.

Table 2 Calculation condition of Case 1 to 3

	Case 1		Case 2		Case 3		
Temperature(℃)	500		600, 650		450※1, 500, 550, 600		
Composition of Conbustion Gas	O_2(%)	CO_2(%)	H_2O(%)	SO_2(ppm)	HCl(ppm)	N_2(%)	
	10	10	20	20	1000※2	bal.	
Composition of Input Material (wt%)	Na	K	Ca	Pb	Zn	S	Cl
	6	11	19	0.14	2	18	9
Combustion Gas / Input Material	1.0, 1.3, 1.6, 1.9		∞		∞		

※1 The input of O_2 is 1/10, and dual Cl contents.
※2 In Case 2, HCl is calculated for 300ppm to 1500ppm.

3. RESULTS AND DISCUSSION

3.1 Thermodynamic Calculation

Table 3 shows the major compounds obtained by the MALT calculation. This table is indicative that there is no pronounced difference between Case 2 and 3. The results of Case 1 to 3 are generally summarized as below.

In Case 1, it was predicted that most of the input materials formed the condensed phases. In particular, almost of all Cl was reacted to form condensed KCl and NaCl. In the gas phase, H_2S was reacted to form the chloride. A difference of the amount of combustion gas/input materials ratio was found to be little influence on the result. It was also predicted that input materials formed mainly the gas phase. In addition, sulfate compounds were predicted primarily in the condensed phase. There was no difference in the condition at 450℃ in Case 3.

Table 3 Primary compounds obtained by thermodynamic simulation in Case 1 to 3

	Primary Compound		
Elem.	Case 1	Case 2	Case 3
Cl	*Chloride of K, Na(C)*	Cl_2(V), Chloride of Pb, Zn, Na, K(V)	
S	H_2S(V), *Sulfate of Na, Ca(C), Sulfide of Ca, Zn, Pb(C)*	SO_x(V), *Sulfate of Na, Ca(C)*	SO_x(V), *Sulfate of Ca, K, Na(C)*
Pb	*PbS(C)*	$PbCl_2$(V)	
Zn	*ZnS(C)*	$ZnCl_2$(V)	
Ca	*CaS(C), $CaSO_4$(C)*	*$CaSO_4$(C)*	
Na	*Na_2SO_4(C), NaCl(C)*	*Na_2SO_4(C),* NaCl(V)	
K	*KCl(C)*	KCl(V)	*K_2SO_4(C)*, KCl(V)

(V) represents Vapor Phase. *(C) represents Condensed Phase.*

3.2 Comparison between Thermodynamic Prediction and Various Analytical Results

Figure 1 shows the fluorescent X-ray analysis results which were carried out for both the environment side and the alloy side of the deposited ash, for which was obtained in the previous study [1]. Thus, major elements of the deposited ash were identified, and its composition was found to vary significantly depending on the local site. Furthermore, heavy metals such as Zn and Pb tend to concentrate at the alloy/scale interfacial side to form mainly chlorides.

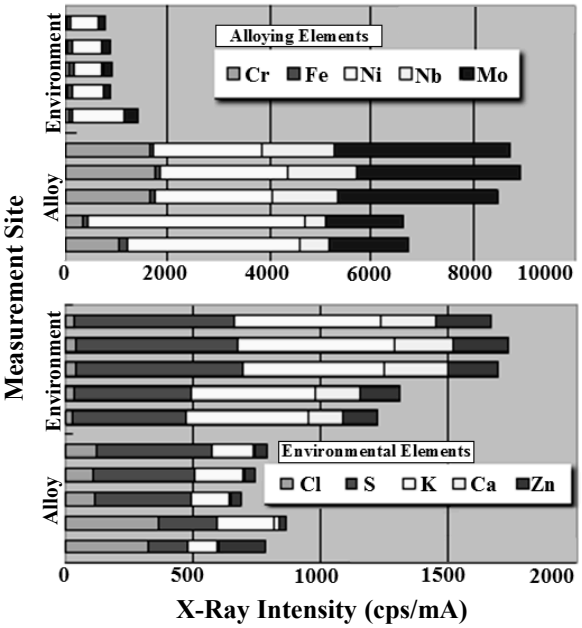

Fig. 1 Fluorescent X-ray analysis results

From the MALT prediction described above, the condensed phase in Case 1 and the gas atmosphere in Case 2 and 3 are consistent with the analytical results mentioned above. Consequently, it should be valid to predict the basic constituents of deposited ash and combustion gas. Moreover, it can be expected to helpful for the identification of compounds involved in the early stages of corrosion in SH tube in the macroscale. MALT calculation is suitable to predict the estimation of the environmental composition, since the extreme condition in Case 2 and 3 resulted in little difference. However, MALT simulation has the critical limitation for predicting detailed the environmental conditions because of the inability to apply to non-equilibrium materials such as the low-melting eutectic compounds, in spite of an advantage for predicting the macroscale environmental constituents.

4. CONCLUSION

Thermodynamic equilibrium calculation by MALT was applied to assume an actual environment of the deposited ash and combustion gas atmosphere. MALT simulation is applicable with respect to macroscale environmental constituents such as an identification of compounds associated in the initiation of corrosion in SH tube. However, MALT calculation has the limitations on predicting the microscale constituents of deposited ash, since this environment made from non-equilibrium constituents and their spatiotemporal fluctuation in the WTE boilers.

References

[1] K. Takemura, M. Yoshiba, H. Morita and M. Takakura, JSPS 123 Committee Research Report, Vol. 54 No.3, (2013), 303.

[2] NEDO, Development of High Efficiency Waste Power Generation Technology 1991 Report, 1st Volume (2000), 309.

[3] N. Otsuka, *Cor. Sci.*, Vol. 50 (2008), 1627.

Near Ambient Pressure XPS studies on the oxide formation on Fe-2Mn during thermal treatment

S. Borodin[(1,2)], D. Vogel[(1,*)], S. Merzlikin[(1)], P. Keil[(1)] and M. Rohwerder[(1,2)],

[(1)] Max-Planck-Institut für Eisenforschung GmbH, Max-Planck-Str. 1, 40237 Duesseldorf, GERMANY
[(2)] Christian Doppler Laboratory for Diffusion and Segregation during Production of High Strength Steel Sheet

e-mail: vogel@mpie.de

1. INTRODUCTION

The equilibrium between oxygen and the non-oxidized metal is of great importance in many industrial processes e.g. for steel finishing where selective oxidation during recrystallization annealing is a problem, or for catalysis at high temperatures where oxides such as iron-manganese oxides in Fischer-Tropsch synthesis often play an active role. For both cases, the activity of oxygen at the surface is of crucial importance. While it is easy to predict thermodynamic expectations, the effective kinetics of the involved reactions may lead to considerable deviations from this.

For instance, during the recrystallization-annealing step in steel production, the material is heated in a dedicated heating ramp, which mainly serves to control the final crystal structure and thereby the final mechanical properties. This process is performed under reducing atmosphere of forming gas (mixture of hydrogen and nitrogen) wherein the iron oxides at the surface are reduced. Small amounts of water vapor result in an increase of the thermodynamic oxygen activity, which often leads to the presence of manganese-rich oxides in the final product.

2. EXPERIMENTAL

We have found indications that in the Fe-Mn system, the presence of manganese lowers the activity of oxygen on the surface of the alloy. This is based on our preliminary work on Fe-Mn model alloys where we observed that hydrogen uptake from a forming gas atmosphere (95% nitrogen, 5% hydrogen) at 800°C was not affected by the dew point (i.e. the water partial pressure) while on iron without any manganese, a distinct decrease in hydrogen uptake was observed above a dew point (DP) of +6°C (fig.1).

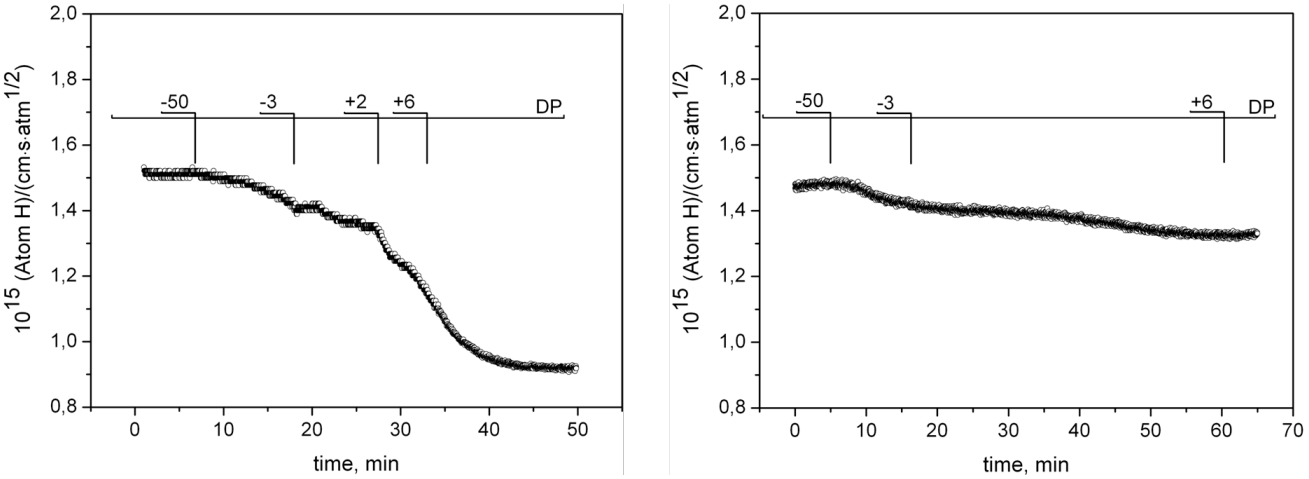

Fig. 1. Hydrogen permeation through iron and Fe-2%Mn membrane at different dew points in N_2-5%H_2 atmosphere at 800°C.

Assuming thermodynamic equilibrium, the dew point should define the partial pressure of oxygen. At DP +6°C, the oxygen activity is well below the critical activity for oxidizing iron. However, oxygen adsorption will already occur. Our assumption is that the sudden decrease in hydrogen uptake is due to the coverage of adsorbed oxygen, exceeding a critical coverage on the iron surface. But why is this not observed for the Fe-Mn alloy, where under these conditions the surface is still mainly iron with a few manganese oxide islands?

In order to look into this in more detail synchrotron-based in-situ XPS studies were carried out at the BESSY II facility in Berlin. The heart of the instrument is a differentially pumped electrostatic lens system that refocuses the photoelectrons that are emitted from the sample (which is in a gaseous atmosphere of up to several torr) into the focal plane of a standard electron energy analyser situated downstream, in the ultra high vacuum region.

The samples were heated from the reverse side with a laser and simultaneously analysed. After a heating phase up to 820°C within 10 minutes, the temperature was kept constant until the XPS signal became almost stable. Subsequently the sample was cooled down to 140°C within 10 minutes and afterwards down to room temperature exponentially.

A portable gas conditioning unit was used to supply a moistened forming gas N_2 / 5% H_2 / 7.1 mbar H_2O, which has an oxygen activity just below the onset of wustite for a temperature of 820°C. The total flow rate was set to approx. 35 l/h.

As a function of temperature and the partial pressure of water and hydrogen the oxygen partial pressure is not depending on the total pressure inside the reaction chamber:

$$p(O_2) = k(T) \cdot p^2(H_2O) / p^2(H_2),$$

where k(T) is the temperature dependent water dissociation equilibrium constant

3. RESULTS AND DISCUSSION

In figure 2 the obtained XPS spectra of the Fe-2Mn surface during the exposure at different pressure levels are displayed. According to thermodynamics the oxygen partial pressure ($<10^{-17}$ bar) is high enough to oxidize the manganese for the whole applied temperature range, but the oxidation of the iron is only possible in the low temperature range.

In case of the experiment performed at 0.5mbar the Fe^{2+} iron peak appears at 420°C and the metallic iron peak at 605°C. The oxygen peak declines while the iron oxide is getting reduced. As soon as the surface is becoming free of the iron oxide the manganese signal increases. For 0.2 mbar a similar sequencing is observed, but the effects are not that pronounced. Again the manganese oxide signal has the opposite tendency than the pure iron signal.

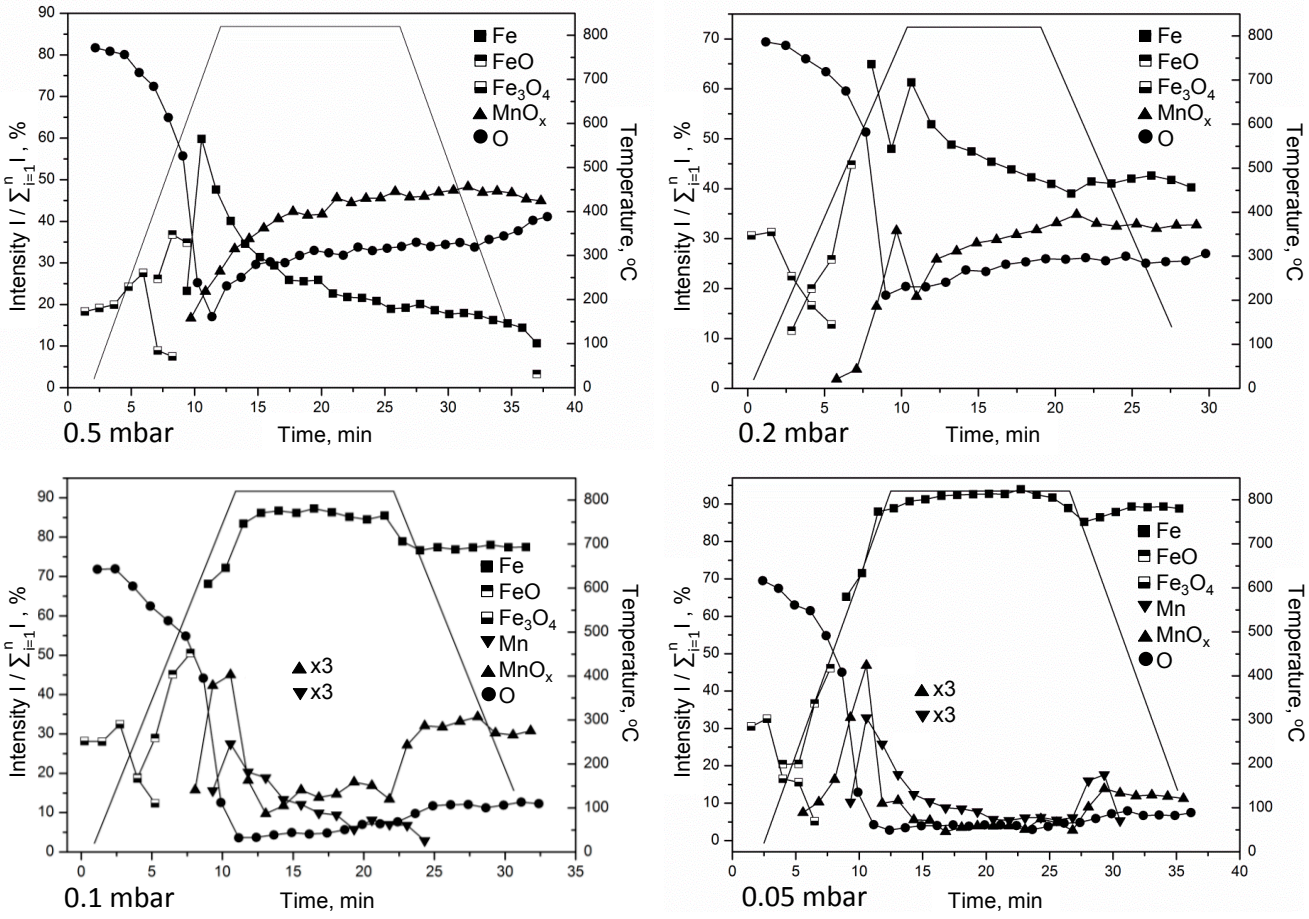

Fig. 2. XPS- characterization of the Fe-2%Mn surface during the temperature heating- holding-cooling processes under different total pressures in N_2 / 2.5% H_2 / H_2O atmosphere of DP +2°C

At 0.1 mbar and 0.05 mbar the signal for pure iron also increases after the reduction of the iron oxides. But here the manganese oxide signal collapses after a initial increase and the iron signal reaches a high maximum of 85% at 820°C.
At lower pressures the reduction of the iron oxides is shifted to lower temperatures.
Contrary to thermodynamics the effective oxygen activity seems to differ for the varied pressure values. It is even more striking that the manganese oxide does not remain stable during the exposure, it vanishes at higher temperatures. This also proves, that the effective oxygen effectivity is lower than the thermodynamic expected (fig.4)

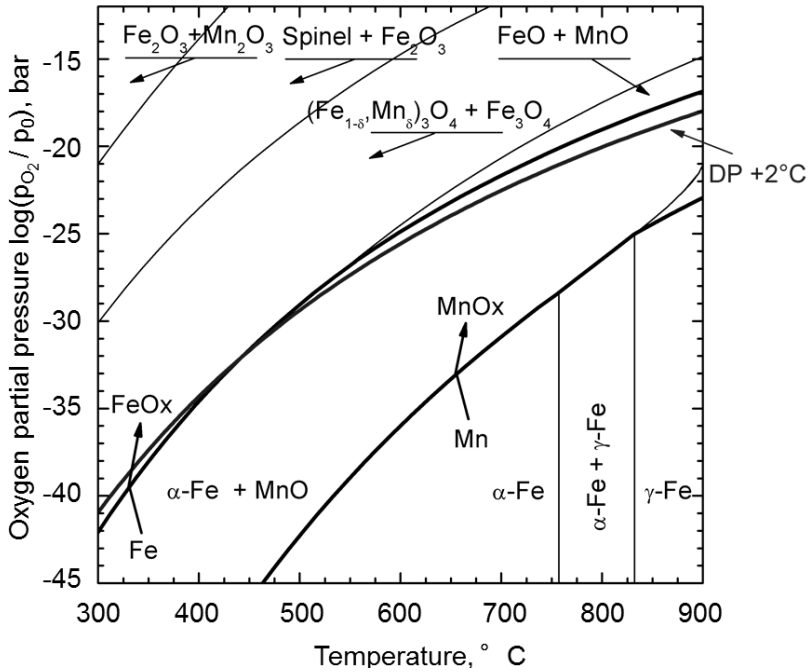

Fig. 3. Oxygen pressure-temperature phase diagram for the given settings for Fe-2Mn (FactSage)

4. CONCLUSION

Intense efforts have been taken to study the stability of oxide formation in a well-defined mixture of N_2 / 2.5 % H_2 / H_2O (DP+2 °C, 7100 ppm), which has an oxygen activity just below the onset of wustite formation during a typical annealing temperature of 820°C. Clear evidence for the formation of manganese-rich oxides could be verified under these conditions which are in full agreement with thermodynamic expectations.
Surprisingly already formed manganese oxides were reduced as soon as the total pressure of this gas mixture has been decreased but the nominal oxygen partial pressure remained unchanged.
It is assumed that kinetically controlled reactions at the surface begin to dominate the oxygen supply. Consequently the effective oxygen activity at the sample surface will be lowered by several orders of magnitude. Furthermore, hydrogen permeation experiments indicate that on pure iron, under same conditions, the oxygen partial pressure is higher than on Fe-Mn alloys.

Adhesion of scales on carbon steels containing boron or phosphorus

E. Ahtoy[1,2,3], G. Leprince[1], M. Picard [1], Y Wouters [2], A. Galerie [2,*], X. Wang [3], A. Atkinson [3]

[1]Arcelor Mittal Research, Voie Romaine, 52280 Maizières les Metz, FRANCE
[2]Simap Laboratory, Université de Grenoble, BP 75, 38402 Saint Martin d'Hères cedex, FRANCE
[3]Department of Materials, Imperial College, London, Exhibition road, London SW7 2AZ, UK

e-mail: alain.galerie@laposte.net

1. INTRODUCTION

Due to the increasing use of recycled materials, today-produced carbon steels may exhibit increasing contents of residual elements as silicon, copper, nickel, phosphorus and/or boron. It is of great importance for the producers to observe and understand the influence of these elements on the quality of the final products. Particularly sensitive to the metal chemistry are the high temperature processes as reheating and hot rolling. During these steps, the oxide scale which grows on the metal containing such impurities may suffer variations in composition, morphology and adhesion. This last property is directly linked to the descaling process taking place at the end of the hot line. In this paper, attention is focused on the determination of scale adhesion, in the presence of high amounts of boron and phosphorus in steel.

2. EXPERIMENTAL

A special device, designed and operated in Arcelor Mittal Resarch laboratory, allows preparing low amounts of well-defined B- and P-steels. It is based on the addition of elementary boron or phosphorus to 1 kg of molten iron and extraction of solid metal rods by suction. The operation is conducted under secondary vacuum. The size of the rods is several 10 cm with a diameter of 5 mm. For the present study, the composition of the prepared steels was Fe + 0.1% B and Fe + 0.15% P; the complete analysis of the steels is given in the full paper. Circular slices were cut, polished and oxidized in natural air at 800 and 1000°C, for short duration (2, 5 and 10 minutes). After cooling, the samples were submitted to normal Vickers indentation in order to force scale delamination. Various loads between 10 gf and 1 kgf were used and the area of the square imprint and of the circular delamination zone were both measured under the optical microscope. According to the formalism proposed by Drory and Hutchinson [1] and using the results of a simulation by Vasinontha and Beuth [2], the scale-metal delamination energy release rate was calculated and was shown to be independent of the load used. This confirms the validity of the model used. Surface and cross-sections of samples not submitted to Vickers indentation were analyzed using SEM, EDS, AES and Raman spectroscopy.

3. RESULTS AND DISCUSSION

All scales grown on unalloyed iron up to 15 min at 800 and 1000°C spontaneously spalled at cooling, showing their very low adhesion. On the contrary, all scales (except for 2 min oxidation at 1000°C) grown on 0.1%B- or 0.15%P-containing steels remained adherent and could therefore be submitted to Vickers indentation. This observation demonstrated that high levels of residual boron or phosphorus markedly increased the adhesion of the scales.

As shown on Figs 1 and 2, scale adhesion energy is much higher for scales grown at the highest temperature (1000°C) compared to scales grown at the lowest temperature (800°C). This shows that adhesion is not driven by the thickening of the oxide scale, through vacancy injection, for example, but by a chemical process involving the B or P addition element. The obtained values are rather high, but comparable to what was measured by tensile testing on scales produced in the hot rolling mill on low purity recycled steels [3]. Phosphorus has the strongest effect, inducing adhesion several times higher than boron.

When increasing oxidation time, adhesion increases, except for the B-containing steel which shows decreasing adhesion. In order to understand these features, the nature, location and morphology of the impurity-containing oxide(s) was carefully studied. It appeared that the B- or P-containing oxide(s) were located at the steel-wüstite interface, mostly in form of iron borate or phosphate. The full paper will present the different situations for various times and temperatures. The increase in adhesion is always the result of second-phase precipitation near the steel-wüstite interface, hindering crack propagation leading to scale delamination. This phenomenon belongs to the well-known "anchoring effect". The physical state of the precipitates at the oxidation temperature (solid or liquid) was shown to be of importance.

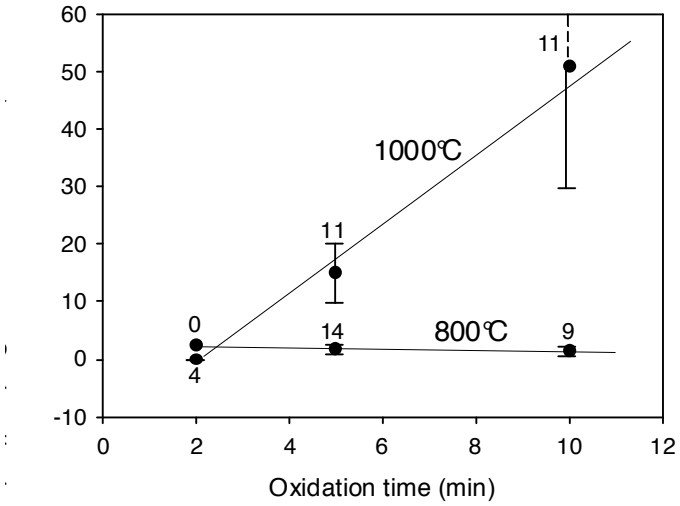

Fig.1. Adhesion energy of scales grown on the boron-containing steel at 800 and 1000°C as a function of oxidation time. The number of measurements is presented close to each point.

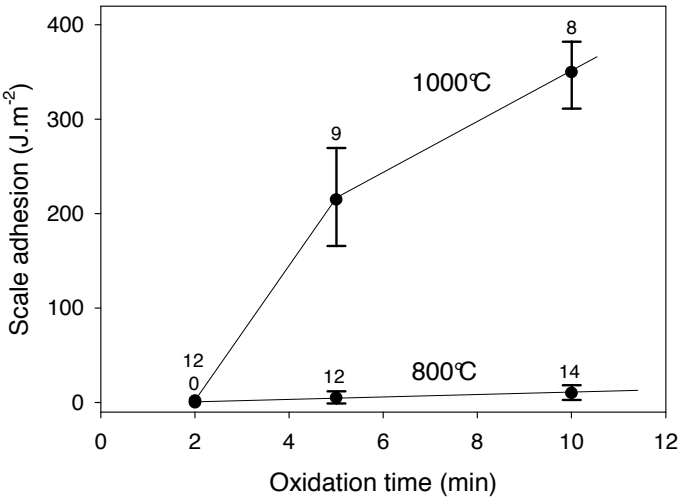

Fig.2. Adhesion energy of scales grown on the phosphorus-containing steel at 800 and 1000°C as a function of oxidation time. The number of measurements is presented above each point.

CONLUSIONS

Boron and phosphorus present in carbon steel in minor – but non negligible – amounts make the adhesion of oxide scales grown at high temperatures larger than observed on the bare steel. The increase is more pronounced when oxidized at 1000°C, a temperature where the oxide phase(s) containing the impurity is liquid. The results suggest right conditions to be followed by the process engineers where a good descaling ability is maintained.

Acknowledgements,

This work was performed under the CIFRE contract Nr. 216/2007 between ANRT and Arcelor Research, also under the collaboration protocol between Arcelor Research and Grenoble INP/IESA/CNRS. Imperial College London, Department of Materials is thanked for providing research facilities to E. A.

References.

[1] Drory M. D., Hutchinson J. W., “Measurement of the adhesion of a brittle film on a ductile substrate by indentation”, *Proc. R. Soc. Lond. A*, Vol. 452, (1996), pp. 2319-2341,

[2] Vasinonta A., Beuth J. L., “Measurement of interfacial toughness in thermal barrier coating systems by indentation”, *Engineering Fracture Mechanisms*, Vol. 68, (2001), pp. 843-860.

[3] Nilsonthi T. Chandra-ambhorn S., Wouters Y., Galerie A., “Adhesion of thermal oxide scales on hot-rolled conventional and recycled steels” *Oxid. Met.,* Vol. 79, (2013), pp. 325-335.

Effect of Scale layer Structure on Blister Generation during High Temperature Oxidation of Steel

Yasumitsu Kondo [1,*], Hiroshi Tanei [1], Kohsaku Ushioda [2]and Muneyuki Maeda [3]

[1] Process Research Laboratories, Technical Development Bureau, Nippon Steel & Sumitomo Metal Corporation, 20-1 Shintomi Futtsu-city, Chiba, 293-8511, JAPAN
[2] Technical Development Bureau, Nippon Steel & Sumitomo Metal Corporation, 20-1 Shintomi Futtsu-city, Chiba, 293-8511, JAPAN
[3] Oita works, Nippon Steel & Sumitomo Metal Corporation, 1 Oaza-Nishinosu, Oita-city, Oita, 870-0992, JAPAN

e-mail: kondo.x77.yasumitsu@jp.nssmc.com

1. INTRODUCTION

Surface defects are an important issue in the process of steel production. The steel surface is oxidized, and oxide scale is formed on the steel surface during the hot rolling process. The oxide scale happens to swell when the steel is oxidized at high temperature, and this phenomenon is called blistering. When scale is blistered during finishing rolling, the blistered scale causes surface defects. Two main mechanisms have been previously proposed for blistering. In one case, blistering is believed to be caused by stress generated during scale formation [1-4]. In the other case, gas generation at the scale/steel interface is thought to lead to the formation of blisters [1,2,5]. It was suggested that not only CO and CO_2, but also N_2, play a role in the blistering phenomenon [6,7]. No previous research has been reported on the role of scale structure on for blistering. Therefore, the present research is focused on the effects of the oxygen content in the atmosphere and scale layer structure on the blistering phenomenon. Furthermore, a stress evaluation test during oxidation was conducted in order to clarify the blistering mechanism.

2. EXPERIMENTAL

Steel containing 0.16mass%C was used for the oxidation experiments. Specimens were cut into a 30 mm×30 mm×4 mm rectangular shape. Oxidation was performed in an infrared furnace. The samples were heated up to the oxidation temperature in a N_2 atmosphere and held for 1 hour at that temperature. This treatment gives surface nitridation before the oxidation [7]. The oxidation was initiated by changing the flowing gas from N_2 to the oxidizing gas. The oxidizing conditions (temperature and atmosphere) are shown in Table 1. The purpose of the conditions A to D is to observe blistering behavior in various oxygen concentration conditions. The conditions E and F are conducted in order to clarify the effect of scale layer structure especially hematite layer formation. In these conditions the samples were firstly oxidized in low oxygen concentration atmosphere where hematite layer is not formed. The consecutive oxidations were performed in high oxygen concentration atmosphere where hematite layer is formed by changing to high oxygen concentration atmosphere.

Table 1 Experimental conditions.

No.	Temp.	Oxidation conditons/ Atmosphere and time
A	1000°C	(0.5% O_2+99.5% N_2)×300s
B	1000°C	(5% O_2+95% N_2)×180s
C	1000°C	Air×60s
D	1000°C	(5% O_2+95% N_2)×30s
E	1000°C	(1% O_2 +31% H_2O+68% N_2)×180s → Air×120s
F	1000°C	(1% O_2+31% H_2O+68% N_2)×600s → Air×120s

3. RESULTS AND DISCUSSION

The results of the oxidation tests for conditions A to C are shown in Fig. 1. There are no blisters on the sample oxidized in a low oxygen concentration (condition A). However, blisters form on the samples oxidized in a relatively high oxygen concentration (conditions B and C). The scale thicknesses for conditions A, B, and C are 150μm, 80μm, and 60μm, respectively, as calculated from the mass changes during the oxidations. The sample in condition A has the thickest oxide scale and no blister formation. These results suggest that the oxygen concentration has an effect on blister formation, but the scale thickness does not.

The surface appearance of the sample treated under condition D is shown in Fig. 2. Only the bottom side of the surface of the sample has blisters, while the other areas have no blisters. The bottom part of the sample is oxidized to a greater degree because the oxidant gases pass from the bottom side to the upper side in the experimental device. X-ray diffraction measurements were performed on Area 1 and Area 2 of the sample as indicated in Fig. 2. Area 1 contained wustite (FeO) and iron (α-Fe), suggesting that the scale in Area 1 is composed of a wustite mono-layer. Meanwhile, hematite (Fe_2O_3), magnetite (Fe_3O_4), and wustite (FeO) are present in Area 2, indicating that the scale in this region was a three-layered scale comprised of hematite, magnetite, and wustite. These results suggest that the scale layer structure has an effect on blister formation. Similar blister formation behavior was reported by Chen et al.[8].

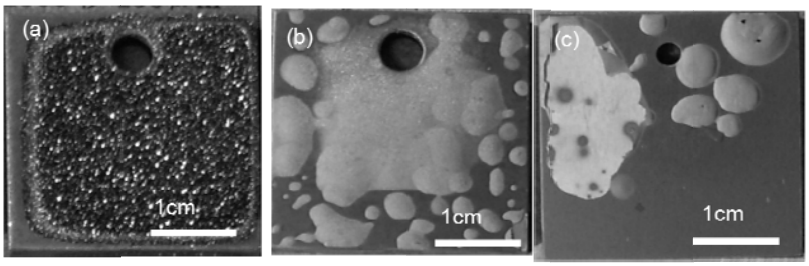

Fig. 1. Surface appearance after oxidation in various oxygen concentration atmospheres. (a) Oxidized in a 0.5% O_2 atmosphere (condition A). (b) Oxidized in a 5% O_2 atmosphere (condition B). (c) Oxidized in air (condition C).

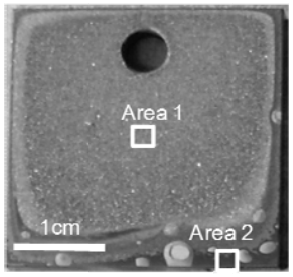

Fig. 2. Surface appearance after oxidation in a 5% O_2 atmosphere for 30s (Condition D). The areas where XRD analysis was conducted are shown.

Next, the results of the experiment in order to clarify the hematite layer formation are described. The change in the surface appearance during oxidation in the furnace under condition E is shown in Figs. 3 (a) to (f). The sample was first oxidized in an atmosphere with 1% O_2 +31% H_2O for 180 seconds. No blisters are formed at this stage (Fig. 3 (a)). In order to verify the scale layer structure an X-ray diffraction measurement was carried out on a sample at this stage. The result indicates wustite mono-layer scale is formed. Scale with a thickness of approximately 25μm is formed, as calculated from the mass gain during the oxidation at that stage. Blisters begin to form after the atmosphere was changed to air (Fig.3 (b) to (f)). The three-layered scale is believed to be formed in this high oxygen concentration atmosphere. It is observed that blisters are formed over the entire surface after the oxidation (Fig.3 (g)).

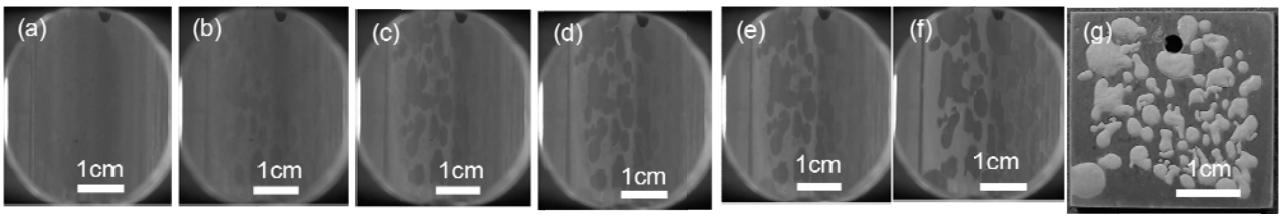

Fig. 3. Surface appearance during oxidation in air after oxidation in a 1% O_2+31% H_2O atmosphere for 180s (Condition E).
(a) Oxidized in 1% O_2+31% H_2O for 180s. (b) Oxidized in air for 10 s after the atmosphere change.
(c) Oxidized in air for 15 s after the atmosphere change. (d) Oxidized in air for 20 s after the atmosphere change.
(e) Oxidized in air for 25 s after the atmosphere change. (f) Oxidized in air for 120 s after the atmosphere change.
(g) After completion of the oxidation.

Similar experiment was conducted under condition F. The sample was first oxidized in an atmosphere with 1% O_2 + 31% H_2O for 600 seconds, which is about three times longer than that for condition E. Blisters are not formed at this stage. Scale with a thickness of approximately 80μm is formed as calculated from the mass gain during the oxidation. An X-ray diffraction measurement was carried out on a sample oxidized in the same low oxygen concentration condition. The result shows that two-layer scale comprised of magnetite and wustite are formed at this stage. A blister begins to form and grow after the atmosphere is changed from the low oxygen concentration atmosphere to air. The results of the oxidations carried out under conditions E and F show that blisters are only generated on the surface of the three-layered scale structure in high oxygen concentration conditions, and are formed on neither the wustite mono-layer scale nor two-layered scale comprised of magnetite and wustite in a low oxygen concentration atmosphere.

Firstly, we discuss scale grow stress during oxide formation. Blisters start to form when scale structure is changed from

wustite mono-layer to three-layer structure. So we focus on the scale grow stress at the situation that scale structure is changing not that at steady state oxidations. The stress generation in the scale was evaluated when the scale layer structure is changed from wustite mono-layer to three layer comprised of hematite, magnetite, and wustite. The side views during oxidation are shown in Fig. 4. The sample was first oxidized in a low oxygen concentration atmosphere of 1% O_2 + 31% H_2O for 300 seconds. The sample is slightly bent toward the side of the non-oxidizable surface (Fig. 4 (b)). Compressive stress is applied in the wustite mono-layer scale. However, the curvature of the sample decreased after the atmosphere was changed to air (Fig. 4 (c)). This result indicates that the compressive stress in the scale is mostly released during the change of the scale structure from a wustite mono-layer to a three-layered scale. Therefore, these results indicate that the compressive stress when blister formation is initiated is very low, and is not a major factor in blister formation. After further oxidation in air, the sample is gradually bent (Fig. 4 (d)) toward the side of the non-oxidized surface, indicating that a compressive stress is once again building within the scale. Thus, it is difficult to explain blister initiation by the grow stress mechanism.

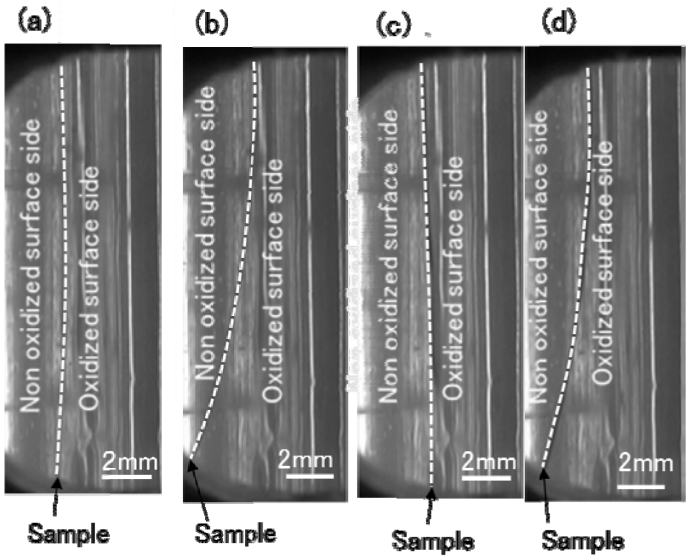

Fig. 4. Side views of thin specimens during the stress evaluation test. (a) Before oxidation. (b) Oxidized in a low O_2 concentration atmosphere for 300s. (c) Oxidized in air for 11 s after changing from the low O_2 concentration atmosphere. (d) Oxidized in air for 120s after changing from the low O_2 concentration atmosphere.

The decrease in the compressive stress as the scale structure changes from wustite mono-layer scale to three-layered scale is explained by the composition change of the wustite. Wustite has a wide range of non-stoichiometric composition, and the lattice constant of wustite depends on the non-stoichiometry [9]. The x value when the composition of wustite is expressed as $Fe_{1-x}O$ is relatively small and the size of the wustite lattice is larger when the scale is a wustite mono-layer, because the wustite scale forms in a lower oxygen potential situation. On the other hand, the x value becomes larger and the lattice size of the wustite becomes smaller when the scale is a three-layered structure, because the wustite is in a higher oxygen potential situation. Thus, the compressive stress applied in the scale decreases when the scale layer structure changes from a wustite mono-layer to a three-layered scale.

Next, we discuss gas generated at the scale/steel interface. Our previous research indicates that CO, CO_2, and N_2 gases are main gaseous composition in a blister at the initiation stage and the gas pressure generated there is possible to detach the scale from the steel [6]. At the growth stage of blister, N_2 alone was also found to have an effect on blister growth [7]. These results suggest that the pressure of the CO, CO_2, and N_2 gases generated at the scale/steel interface has a significant influence on blister initiation. We assume that spaces are already formed at the scale/steel interface before blister initiation.

Gas permeability through oxide scale is discussed. Two steel sheets were oxidized. Scale samples were prepared by mechanical and electro-chemical methods from the oxidized samples. One scale sample had three layers of hematite, magnetite, and wustite. The other had two layers of magnetite and wustite. Both sample had same thicknesses of 360 μ m. Gas permeabilities were measured. The results shown in Table 2 indicate two layer scale has 10 times higher gas permeability. This suggests that hematite layer has quite low gas permeability.

Table 2 Gas permeability through oxide scale

Scale compositions	Gas permeability $mol \cdot m^{-2} \cdot s^{-1} \cdot Pa^{-1}$
Fe_3O_4, FeO	2.48×10^{-8}
Fe_2O_3, Fe_3O_4, FeO	2.82×10^{-9}

Blister initiating behavior observed in this study is schematically summarized in Fig. 5. Blisters are not formed at the initial stage of oxidation, where oxidation rate is followed by liner rate low and only wustite mono-layer scale is formed

(Fig. 5 (a)). In this stage gases of CO, CO_2 and N_2 generated beneath the scale go out along the paths such as micro pores through the scale and no blisters are formed. During the transient from the region of the linear rate law to that of the parabolic rate law, two-layer scale comprised of magnetite and wustite is formed. The gases of CO, CO_2 and N_2 also can migrate through the scale and blisters are not formed at this stage (Fig. 5 (b)). This situation is observed in Fig.4 (a). However, this stage lasts only for short period. The oxidation is soon followed by the parabolic rate law and three-layer scale comprised of hematite, magnetite, and wustite is formed. The hematite layer has low gas permeability and the gas pressure beneath the scale increases. At this moment blisters start to be formed (Fig. 12 (c)). The main factor to blister inflation is supposed to be by gas pressure generated at the scale/steel interface.

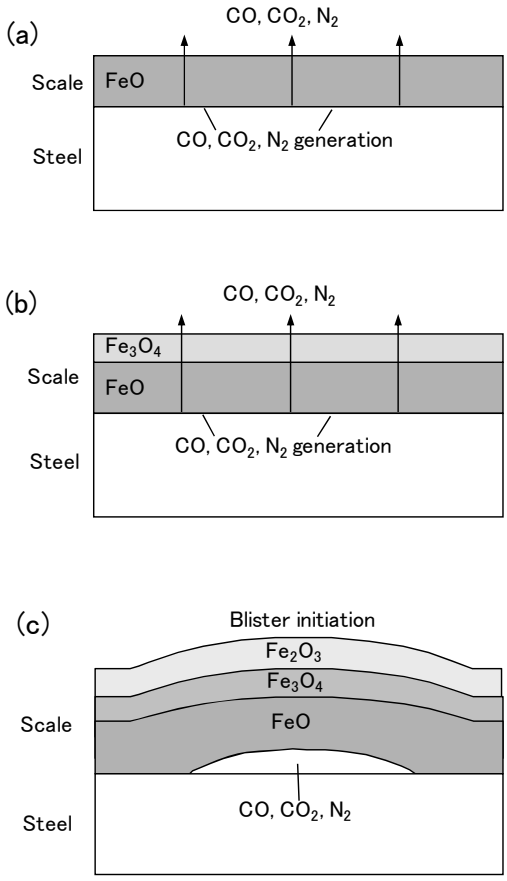

Fig. 5. Schematic image of the blister initiation mechanism. The arrows show the gas flow of CO, CO_2, and N_2. They are generated at the scale/steel interface.
(a) Initial stage of oxidation. The scale is the wustite mono-layer type. (b) A two-layered scale comprised of magnetite, and wustite is formed. (c) A three-layered scale comprised of hematite, magnetite, and wustite is formed. The blister is initiated.

4. CONCLUSION

The effects of oxygen concentration and scale structure on blister initiation behavior during oxidation of steel at high temperatures were investigated. The following conclusions are drawn:

1) Blisters do not form when the scale has a wustite mono-layer structure.

2) Blisters start to nucleate when the scale layer structure changes from a wustite mono-layer to a three-layered scale consisting of hematite, magnetite, and wustite.

3) Compressive stress applied in the oxide scale is mostly released when the scale layer structure changes from a wustite mono-layer to a three-layered scale consisting of hematite, magnetite, and wustite. This result suggests that compressive stress is not a main factor for blister initiation.

4) It is deduced that the pressure of the CO, CO_2, and N_2 generated at the scale/steel interface is a main factor in blister nucleation and growth, and that the hematite on the top surface of scale presumably acts as a barrier against gas permeation.

References

[1] Griffith, R., “The Blistering and Formation, ” Heat Treating and Forging, Vol. 20, No. 9 (1934), pp447-450.
[2] Rolls, R., “Scale Blisters on Ferrous Alloys, ” Metallurgie, Vol. 7, No. 2 (1967), pp53-60.
[3] Matsuno, F., “Blistering and Hydraulic removal of Scale Films of Rimmed Steel at High Temperature,” Transactions of ISIJ, Vol. 20 (1980), pp413-421.
[4] Kizu, T., Nagataki, Y., Inazumi, T., and Hosoya, Y., “Effects of Chemical Composition and Oxidation Temperature on the Adhesion of Scale in Plain Carbon Steels,” ISIJ International, Vol. 41, No. 12 (2001), pp1494-1501.
[5] Modin, S. and Tholander, E. “Observations concerning the structure of scale, and the mechanism of formation during the heating of steel,” Metal Treatment, Vol. 28 (1961), pp261-270.
[6] Kondo, Y., Tanei, H., Suzuki, N., Ushioda, K., and Maeda, M., “Blistering Behavior during Oxide Scale Formation on Steel Surface,” ISIJ International, Vol. 51, No. 10 (2011), pp1696-1702.
[7] Kondo, Y., Tanei, H., Ushioda, K., Maeda, M., and Abe, Y., “Effect of Nitrogen on Blister Growth Process during High Temperature Oxidation of Steel,” ISIJ International, Vol. 52, No. 9 (2012), pp1644-1648.
[8] Chen, R. Y. and Yuen, W. Y. D. “Short-time Oxidation Behavior of Low-carbon, Low-silicon steel in Air at 850-1,180° C- I : Oxidation Kinetics,” Oxidation of Metals, Vol. 70 (2008), 39-68.
[9] Foster, P. K. and Welch, A. J., “Metal-Oxide Solid Solustion Part 1. Lattice-Constant and Phase Relationships in Ferrous Oxide (Wustite) and in Solid Solutions of Ferrous Oxide and Manganous Oxide,” Trans. Faraday Soc., Vol. 52 (1956), pp1926-1635.

Adhesive Strength Measurement of Oxide Scale Formed on Low-Carbon Steel

Hiroshi TANEI [1,*] and Yasumitsu KONDO [1]

[1] Process Research Laboratories, Technical Development Bureau, Nippon Steel & Sumitomo Metal Corporation,
20-1 Shintomi Futtsu-city, Chiba, 293-8511, JAPAN
e-mail: tanei.sx7.hiroshi@jp.nssmc.com

1. INTRODUCTION

In steel production, the surface of steel is oxidized and scale forms on it at high temperature; this oxide scale may cause surface defects. Typically, scale is removed by high pressure water before hot rolling because the roll may push a thick scale into the steel surface. Surface defects may be caused by the spontaneous detachment of blistered scale; blistering occurs when oxide scale swells during oxidation. Thus, the adhesion property of scale at high temperature is an important characteristic, and understanding and controlling scale adhesion properties would contribute to the quality of steel produced.

Some methods of measuring scale adhesive strength qualitatively have been reported. These methods can evaluate the amount of detached scale or the detaching behavior when compressive [1] or tensile [2], [3] force applies on the sample material. A method of measuring such force when scale has been mechanically detached after a bolt is buried in scale has been reported. [4] However, it is difficult to use the method to evaluate adhesion quantitatively in the case of a thin oxide scale (tens of micrometers in thickness). A method of obtaining adhesive energy by in situ observation when a tensile test is conducted on an oxidized steel sample has been reported. [5] It is possible to apply this method at high temperature. Kushida et al. [6] proposed a method of estimating scale exfoliation stress. After generating scale on two pillar specimens at high temperature, the scales formed on the two samples were joined by pressurizing at high temperature. Next, by the tensile test of the joined specimen, the force and stroke curve was obtained. The scale exfoliation stress is estimated from the curve. The exfoliation stress between a scale and a material was affected by the joining stress. [6]

The authors improved the method of Kushida et al. [6] Scale merging is performed by oxidation with small compression stress rather than with high compression stress. Scale adhesive strength was measured with low compressive stress at high temperature quantitatively. Here, a detailed study of the effect of external axial strength on the scale adhesion is conducted.

2. EXPERIMENTAL

Steel materials with the chemical components shown in Table 1 were used for the experiment. Cylindrical samples with a diameter of 10 mm were used. An additional cylindrical specimen made of electrolytic iron was used for the sample with which the scaled sample is merged. This is why the iron has higher scale adhesive strength than the steel used for the experiment. Tensile test equipment with a furnace was used for the experiments. The atmosphere in the furnace could be controlled. The experimental method used to measure scale adhesive strength is shown in Fig. 1. Two cylindrical samples were placed 10 mm apart at room temperature. The electrolytic iron sample was placed on the top and the sample used to measure scale adhesive strength was placed at the bottom. The samples were heated up to 950 °C and oxidized for 360 s. Oxide scales formed on both samples. Then, the electrolytic iron sample was moved downward and positioned on the lower sample with constant compressive stress in the axial direction. The scale formed on the electrolytic iron sample merged with the scale formed on the lower sample. The

Table 1 Chemical compositions of the samples. (mass%)

	C	Si	Mn	P	S	Al
A	0.094	0.028	0.45	0.004	0.003	0.016
B	0.092	0.014	0.43	0.004	0.003	0.014

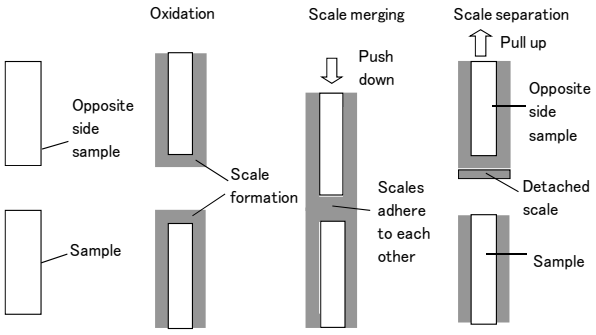

Fig. 1 Method of measuring scale adhesive strength.

axial compressive stress was varied from 6.4 kPa to 12.7 MPa during the scale merging. After the scales merged, the atmosphere was changed from oxidizing nitrogen to non-oxidizing nitrogen. Then, the electrolytic iron sample was pulled up and the load was recorded during scale detachment from the lower sample. The scale merging and separation processes were conducted at the oxidation temperature (950 °C). The maximum stress was considered to be the scale adhesive strength when the scale on the lower sample was completely detached.

3. RESULTS AND DISCUSSION

A photograph of typical samples after the separation for adhesive strength measurement is shown in Fig. 2. The scale of the lower sample is completely detached and the metal surface appears [Fig. 2 (b)]. Fig. 3 shows an example of the cross section of the detached scale. The scale formed on the lower sample is well merged with the scale formed on the electrolytic iron sample.

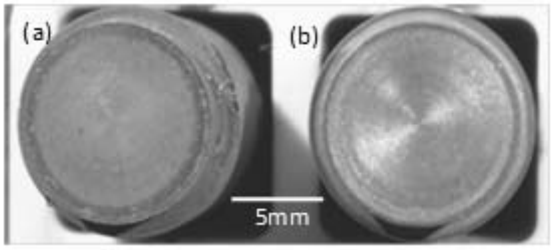

Fig. 2 Surface appearance after tests. (a) Opposite (upper) side sample. (b) Lower sample. Scale is completely detached.

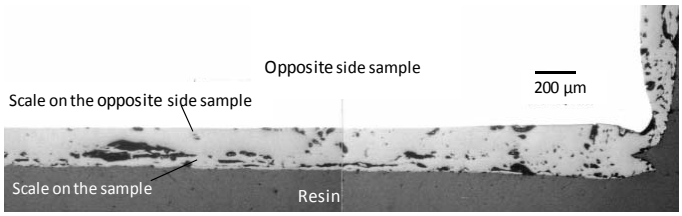

Fig. 3 Optical microscopy image of a cross section of the scale after adhesive strength measurement. Surface appearance after tests.

The axial compressive stress applied on the scale during scale merging changes from 6.4 kPa to 1.27 MPa using material A, as shown in Table 1. The measured scale adhesive strengths are shown in Fig. 4. Although scale adhesive strength has a certain range when the axial compressive stress is small, above approximately 0.1 MPa, the adhesive strength becomes higher in proportion to the axial compressive stress. When the compressive stress was 12.7 MPa, the measured stress became very high and reached 12.8 MPa and the attached part of the specimen was damaged. It is assured that under these conditions the scale adhesive strength is more than 12.8 MPa. The above results indicate that scale adhesive strength is proportional to compressive stress above a certain value and that it can be measured below that value. The scale adhesive strength of material A is on the order of 1 MPa.

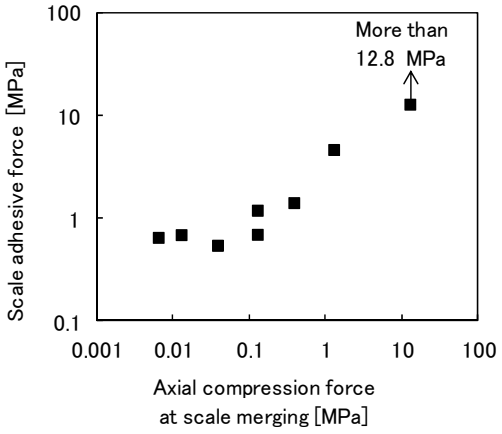

Fig. 4 Effect of axial compressive stress during scale merging on scale adhesive strength

The method used to measure scale adhesive strength in this study is similar to that used by Kushida et al. [6] The scale exfoliation stress obtained by Kushida et al. ranges from 15 to 50 MPa and is much higher than the adhesive strength we obtained, which may be attributed to the high compressive stress applied on during scale joining. The result shown in Fig. 5 indicates that measured scale adhesive strength is affected by compression stress during scale merging above 0.04 MPa. A sufficiently low compressive stress during scale merging is required to measure scale adhesive strength.

We should realize that the scale adhesive strength measured in this method may differ from the adhesive strength of the scale formed on an actual steel surface. The scale on the actual steel surface has three layers: hematite, magnetite, and wustite. In this method, the scale structure changes from a three-layer structure to a wustite mono layer structure during merging. The scale structure affects growth stress in oxide scale. Growth stress may be a factor for scale adhesion.
Using material B shown in Table 1, two experiments were conducted to examine the effect of outer force on scale adhesive strength. In the first experiment, the axial compressive stress was 25 kPa. After scale merging, the samples were

cooled down and the axial compressive stress was maintained at 25 kPa. After cooling, a cross section of the sample was obtained using the focused ion beam (FIB) technique to avoid damaging the structure of the scale/steel interface. Fig. 5 shows a scanning electron microscopy (SEM) image of the cross section of the scale/steel interface. Voids between the scale and the steel are observed. It is suggested that the scale makes partial contact with the steel. The void formation at the scale/steel interface is associated with the outward diffusion of iron ions in the oxide via ion vacancies, which condense and form voids near the scale/steel interface.

In the second experiment, quite a high axial compressive stress (12.7 MPa) was applied on. As in the first experiment, the axial compressive stress was held at 12.7 MPa while the samples were being cooled. A cross section of the sample was made by the FIB technique; the SEM image obtained at the cross sections is shown in Fig. 6. There are few voids between the scale and the steel. It appears that both the scale and the steel intruded on each other by plastic deformation at the interface, resulting in a rough interface. It is reported that the oxide of wustite deforms plastically above 700°C. [7] It is considered that the increased contact area and rough interface result in pronounced scale adhesion.

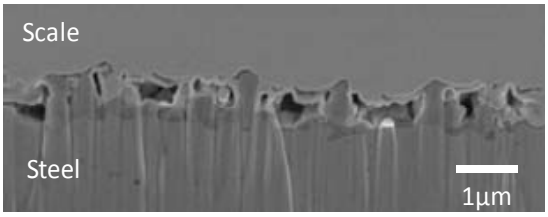

Fig. 5 SEM image of scale/steel interface when axial compression of 25 kPa is applied on during scalemerging.

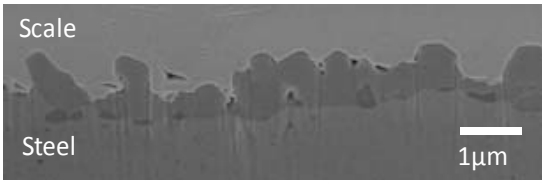

Fig. 6 SEM image of scale/steel interface when axial compression of 12.7 MPa is applied on during scale merging.

It is considered that the improvement of scale adhesion by external force is due to the increase in the contact area and roughness at the scale/steel interface. It is supposed that, during hot rolling, scale is compressed under high pressure in roll bites and has very high adhesive strength. In this study, we suggest that external force applied on oxide scale causes the scale/steel interface to deform plastically, thereby increasing the contact area between the scale and the steel; both the deformation and the increased contact area affect scale adhesive strength. However, the mechanism of scale adhesion on steel is not yet understood. Further research is necessary.

4. CONCLUSION

A method of measuring scale adhesive strength by oxidizing, scale-merging and separating two samples has been proposed. The application of this method revealed that the scale adhesive strength is on the order of 1 MPa and is increased by the application of compressive stress. The scale/steel interface is deformed by external force, thereby increasing the contact area between the scale and the steel. It is suggested that the contact area and rough interface between an actual scale and steel greatly affects scale adhesive strength.

References

[1] Takeda, M., Onishi, T., and Mukai, "Influence of Silicon Content on the Structure and Adhesion of Primary Scales on Si containing Steel," Y.: Kobe Steel Engineering Reports, Vol. 55, No. 1 (2005), pp. 31-36.
[2] Okada, H., "Scale Behavior during Hot-Rolling Process," J. JSPT, Vol.44, No. 505 (2003), pp. 94-99.
[3] Krzyzanowski, M. & Beynon, J. H., "Modelling the Behaviour of Oxide Scale in Hot Rolling," ISIJ Int., Vol. 46, No. 11 (2006), pp. 1533-1547.
[4] Morita, M., Nishida, M., and Tanaka, T., "Relationship between Scale Adhesive Force at High Temperature and Descaling Performance," Tetsu-to-Hagane, Vol. 68, No. 5 (1982), pp. 114.
[5] Chandra-Ambhorn, S., Roussel-Dherbey, F., Toscan, F., Wouters, Y., Galerie, A., and Dupeux, M., "Determination of mechanical adhesion energy of thermal oxide scales on AISI 430Ti alloy using tensile test," Materials Science and Technology, Vol. 23, No. 4 (2007), pp. 497-501.
[6] Kushida, H., Maeda, Y., and Ishikawa, T., "Experimental Analysis of Exfoliating Stress Between Metal and Scale at Hith Temperature," Tetsu-to-Hagane, Vol. 98, No. 11 (2012), pp. 593-600.
[7] Hidaka, Y., Anraku, T., and Otsuka, N., "Deformation of Iron Oxides upon Tensile Tests at 600-1250 °C," Oxidation of Metals, Vol. 59, No. 1/2 (2003), pp. 97-113.

Oxidation behavior of silicon containing steel due to heating processes

Shohei Nakakubo [1,*], Amane Kitahara [2], Reika Kamata [2], and Mikako Takeda [1]

[1] Material Research Lab., Kobe Steel Ltd., 1-5-5 Takatsukadai, Nishi-ku, Kobe, 651-2271, JAPAN
[2] Electronics Division, Kobelco Research Institute, inc., 1-5-5 Takatsukadai, Nishi-ku, Kobe, 651-2271, JAPAN

e-mail: nakakubo.shohei@kobelco.com

1. INTRODUCTION

Si containing steel is widely used for strengthening steel sheet. As a result, Si oxide formed in the manufacturing process influences the growth behavior of the scale and can cause the surface quality of the steel to be defective, so understanding the generation behavior of Si oxide is extremely important.**[1-4]** In this study, changes in the composition of scale due to heating were analyzed by in-situ X-ray diffraction (XRD) in SPring-8. In addition, the scale structure was examined with SEM-EDX, and the structure was found to correspond with the composition of the scale.

2. EXPERIMENTAL

In-situ XRD analysis of the composition of scale formed on the surface of steel was carried out in SPring-8 BL16XU. The X-ray energy was tuned to be 20 keV by a double-crystal monochromator of Si (111). The exposure was set to be one second every ten seconds for the measurement interval. The alloy, the composition of which was Fe-0.1%C-1.0%Si, was formed in a vacuum induction melting furnace by dissolving the trace metals in the melt for 10hour at 1100 ºC This produced a cylindrical sample, which was then machined into a steel sheet after hot rolling, de-scaling and cold rolling. 10mm×10mm×0.5mm square sheets were cut from the large sheet and the surfaces of these were polished to mirror finishes. The samples were heated to 500-900 ºC from room temperature at a ramp rate of 5ºC /sec. in dry air (N_2-20%O_2). The samples were then cooled with Ar gas immediately after reaching the target temperature. The heat-treatment patterns are shown in figure 1. Polished cross sections of the samples were prepared after cooling, and cross sections through the scale were observed with SEM. The amounts of Si in the lower levels of the scale were quantitatively analyzed by EDX.

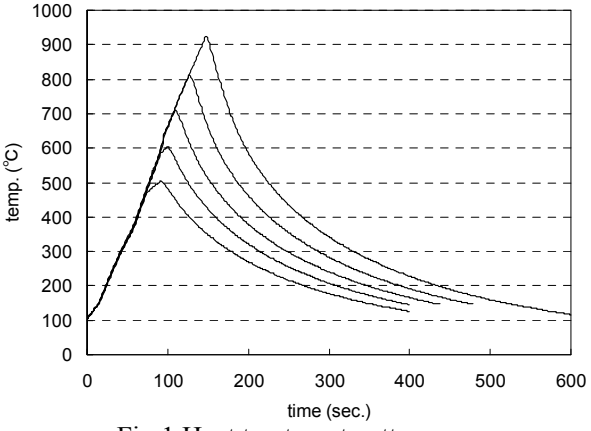

Fig.1 Heat treatment patterns

3. RESULTS AND DISCUSSION

The X-ray diffraction pattern for the sample heated to 900 ºC is shown in figure 2. Only the peaks for Fe_2O_3 and Fe_3O_4 were observed below 790 ºC. FeO began forming above 790 ºC, and Fe_2SiO_4 at 880 ºC. A quantitative analysis of the composition of the scale calculated from the peak strengths in the XRD pattern is shown in figure 3. The composition at 400℃ consisted of only Fe_3O_4, but between 500-800ºC it was mostly Fe_2O_3. The composition of the scale at 900 ºC is as follows: Fe_2O_3=18%, Fe_3O_4 =78%, FeO=3%, Fe_2SiO_4=1%. SEM images of cross sections through the scale heated to 500-900 ºC are shown in figure 4. In addition, the scale thickness is shown in figure 5. The thickness of the scale increases with oxidation temperature. In particular, there is a sudden increase in thickness between 800

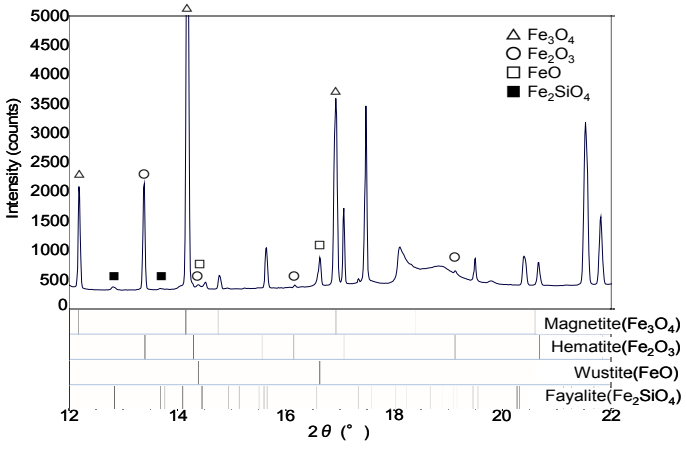

Fig.2 X-ray diffraction spectrum for sample heated to 900ºC

ºC to 900 ºC. The amount of Si in the lower level of the scale was measured by EDX and the results are shown in figure 6. Si oxide is present in the scale at 600 ºC and above, and the concentration increases with temperature. It is assumed that, up to 880 ºC, the Si in the scale is in the form of amorphous Si oxide. In addition, it is presumed that Fe_2SiO_4 is formed by the reaction of amorphous Si oxide with FeO.**[5]** On the other hand, the amount of Fe_2O_3 rose in the temperature range, in which the amorphous Si oxide was formed, 600-800 ºC. At temperatures above 570 ºC, the oxide in the scale on pure iron increases in the order Fe_2O_3, Fe_3O_4, and FeO, due to the different diffusion coefficients of Fe in each oxide.**[6-9]** On the other hand, for the Si containing steel studied here, it is assumed that the amorphous Si oxide has obstructed the generation of FeO, so that a large amount of Fe_2O_3 was formed in the 600-800 ºC temperature range. It is assumed that, above 800 ºC, the diffusion of Fe was accelerated by the generation of FeO, thereby suddenly increasing the scale thickness.

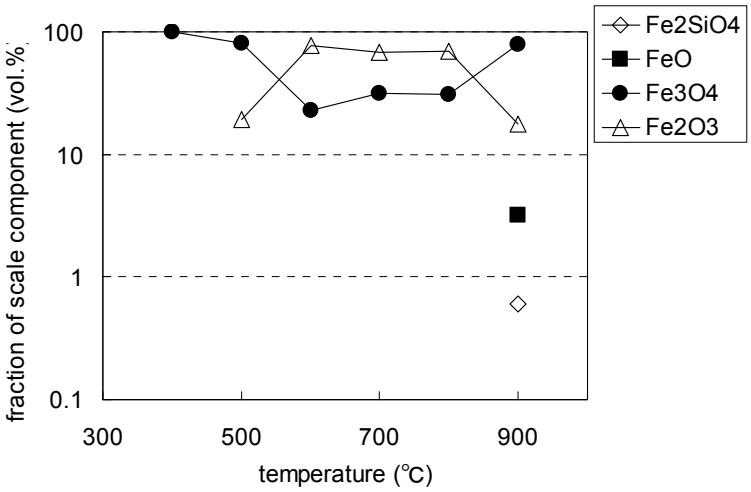

Fig.3 Quantitative analysis of the composition of the scale calculated from the peak strengths in the XRD spectra

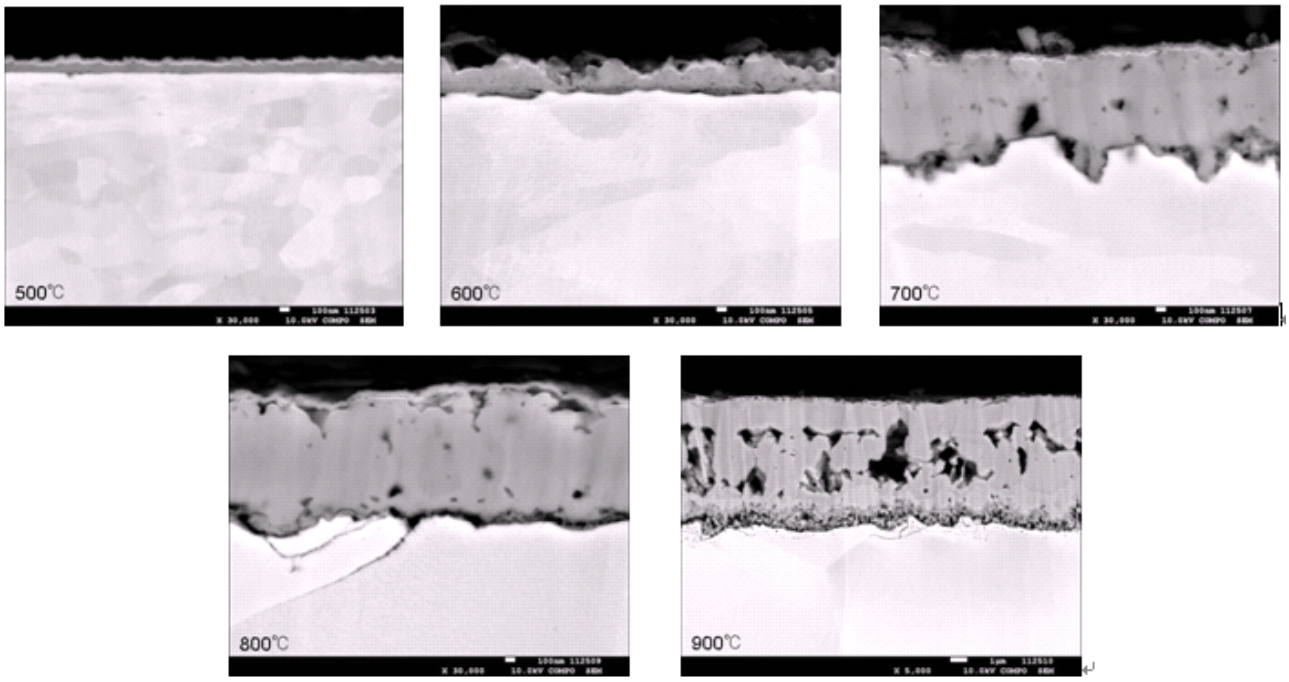

Fig.4 SEM images of cross sections through the scale formed at temperatures ranging from 500-900ºC

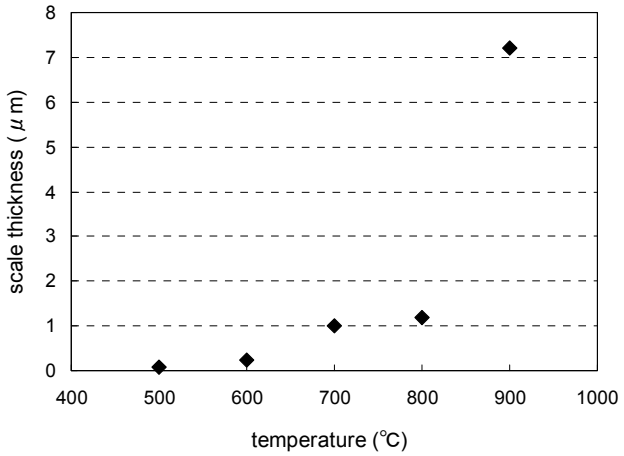

Fig.5 Scale thickness as a function of process temperature

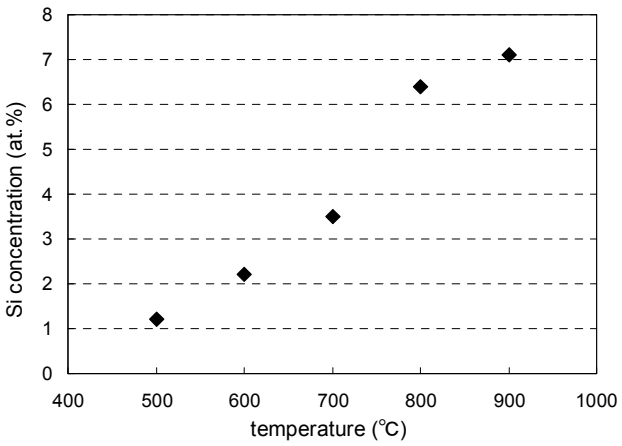

Fig.6 Amount of Si in the lower level of the scale measured by EDX as a function of temperature

4. CONCLUSION

In-situ XRD analysis at SPring-8 to analyze the composition of the scale formed on Si containing steel during heating processes and SEM observations of the structure of the scale were carried out. The following results were found. The scale formed at 400 ºC consisted only of Fe_3O_4, but at 500-800 ºC a large amount of Fe_2O_3 was formed. It was confirmed that FeO began to form from 790℃ and above, and Fe_2SiO_4 at 880 ºC. Si oxide started to form in the scale at 600 ºC, with the concentration increasing with temperature. It is assumed that the Si in the scale was present in the form of amorphous Si oxide below 880 ºC. In addition, it is assumed that Fe_2SiO_4 was formed by the reaction of amorphous Si oxide with FeO, and that the amorphous Si oxide obstructed the generation of FeO, with a large amount of Fe_2O_3 being formed in the temperature range from 600 to 800 ºC.

Acknowledgements

The authors wish to express their thanks to Professor T. Maruyama and Assistant Professor M. Ueda at Tokyo Institute of Technology for their useful advice on this work.

The synchrotron radiation experiments were performed at the SPring-8 with the approval of the Japan Synchrotron Radiation Research Institute (JASRI) (Proposal No. 2013B5020, 2013B5020).

References

[1] N. Birks, *et al,* Introduction to High Temperature Oxidation of Metals, Edward Arnold (London, 1983)
[2] T. Amano, *et al, Camp-ISIJ*, 16 (2003), pp. 1349
[3] C. W. Tuck, *et al, Corros. Sci.*, 5 (1965), pp. 631
[4] M. Fukumoto, *et al, Tetsu-to-Hagane,* 85 (1999), pp. 878
[5] K. Nishida, *et al,* Kinzoku-no-kouonsanka-nyumon, Maruzen (Japan, 1988), pp. 119
[6] J. Paidassi, *Rev. Met.*, 54, 569 (1957)
[7] L. Himmel, *et al, Trans. AIME*, 197, 827 (1953)
[8] S. M. Klotsman, *et al, Phys. Met. Metall.*, 10, 93 (1960)
[9] R. Lundner, *Ark. Kemi.*, 4, 381 (1952)

Study of the High Temperature Oxidation in Vapor-rich Air of Cast Chromia-forming Nickel-based and Cobalt-based Alloys

Patrice Berthod [(1,*)], Lionel Aranda[(1)], Thierry Schweitzer[(1)], Alexandre Navet[(2)] and Albert Leroy [(2)]

[(1)] Institut Jean Lamour, University of Lorraine, Vandoeuvre-lès-Nancy 54506, FRANCE
[(2)] Lycée Henri Loritz, 29 rue des Jardiniers, Nancy 54000, FRANCE

e-mail: patrice.berthod@univ-lorraine.fr

1. INTRODUCTION

Water vapor plays a particularly important role in the oxidation of the hottest pieces of jet engine and steam turbines for energy production. It may influence the high temperature oxidation which occurs for blades, as already observed in the cases of pure metals [1,2], intermetallic compounds [3,4], metallic coatings [5], alloys based on heavy refractory metals [6] and ceramic materials [7]. Water vapor is effectively known to modify the structural characteristics of the externally growing oxide scales (with consequences on the rates of mass gain or of mass loss [8]) and acts on the adherence of the external scale during isothermal oxidation [9] as well as when temperature varies [10,11]. The Cr-rich superalloys which resist high temperature oxidation by developing an external continuous chromia scale are especially sensitive to the presence of water vapor. Indeed their protective Cr_2O_3 scale can be affected by a re-oxidation described by the following equation: $\frac{1}{2}\ Cr_2O_3\ (s) + H_2O(g) + \frac{3}{4}\ O_2(g) \rightarrow CrO_2(OH)_2(g)$. The oxy-hydroxides are volatile for temperatures high enough. For example, several works showed that volatilization into gaseous $CrO_2(OH)_2$ may start to be significant at temperatures as low as 600°C for binary [12] or commercial [13] Fe-based chromia-forming alloys. Such volatilization phenomenon induces, when the oxidation progress is followed by thermogravimetry, an underestimation of the mass gain rate and then of the oxidation kinetic.

The high temperature oxidation behaviors of a Ni-25Cr alloy and of a Co-10Ni-30Cr alloy (contents in wt.%), respectively bases of many nickel-based and cobalt-based superalloys, were studied between 1000 and 1300°C in {water vapor}-enriched air: mass gain kinetics (thermogravimetry runs) and post-mortem characterization (XRD, SEM and EPMA). The results were compared to the ones obtained in parallel for the same alloys oxidized in dry air, allowing evidencing the effect of water vapor for several aspects of high temperature oxidation. In this extended abstract only the case of the Ni-25Cr will be shortly presented while the case of the cobalt alloy will be only briefly evocated.

2. EXPERIMENTAL

Compact 40g-weighing ingots were synthesized by high frequency induction melting of pure Ni, pure Co, and pure Cr (Alfa Aesar, purity > 99.9 %) under inert atmosphere (300 millibars of pure Argon), using a CELES high frequency induction furnace. For each alloy − Ni-25Cr (wt.%) and Co-10Ni-30Cr (wt.%) − and each test temperature, two parallelepiped samples (dimensions: about 10 × 10 × 3 mm^3) were prepared: one for the test in {water vapor}-rich air, and one for the test in dry air performed in parallel for comparison. They were cut in each ingot by using a precision saw. The samples were grinded all around with SiC papers from 240-grit to 1200-grit. Careful smoothing of their edges and corners was realized in order to avoid any risk of local catastrophic oxidation and to favor the adherence of the scales.

All thermogravimetry tests were carried out with a SETARAM Setsys thermo-balance coupled with a WETSYS vapor generator. Per alloy and per temperature a sample was oxidized in dry air (industrial 80%N_2-20%O_2) and another one was oxidized in wet air (industrial 80%N_2-20%O_2 with addition of water). Water was introduced in air by targeting a partial pressure of 180 millibars (corresponding to 90% of relative humidity at 60 °C) before introduction in the thermo-balance. Heating was realized at +20 °C min^{-1}; it was followed by a {48 hours}-long isothermal stage at 1000, 1100, 1200 or 1300 °C; cooling was achieved at -5 °C min^{-1}.

The obtained thermogravimetry files were first visualized to verify if the kinetic is globally parabolic, and second they were analyzed by plotting the mass gain according to the {m x dm/dt = Kp – Kv} method [14] for valuing the two kinetic constants Kp and Kv. Plotting m × (dm / dt) versus -m leads − after transient oxidation − to a straight line, the ordinate at origin of which is Kp and the slope of which is Kv.

The oxide scale adherence on the metallic samples was first observed, in term of fraction of denuded alloy. X-Ray Diffraction (Philips X'Pert Pro diffractometer; Cu K_α: λ = 1.5406 Angströms) was performed on the surface of the

oxidized samples before cutting, to identify the nature of the external oxide scales. These external scales were thereafter subjected to carbon deposition to allow the observation of their general morphology. This was realized at high magnification, using Scanning Electron Microscopes (SEM: Hitachi S4800 or FEG-SEM: JEOL JSM-7600F).
The oxidized samples were coated with pulverized gold, then with electrolytically deposited nickel layer, to protect the oxide scale against possible degradation during cutting. After coating the oxidized samples were cut in two parts, embedded in cold resin (ESCIL), ground with SiC papers from 120-grit to 1200-grit, ultrasonically cleaned and polished with a textile enriched with 1µm hard particles to obtain a mirror-like surface state.
The oxide scales were observed in cross-section with a SEM, and their thicknesses were measured. The natures of the scales were confirmed by Energy Dispersion Spectrometry (EDS) using the EDS device equipping the SEM. Wavelength Dispersion Spectrometry (WDS) profiles were performed across the alloy sub-surface to characterize the chromium-depleted zones.

3. RESULTS AND DISCUSSION

Only the mass gain curves obtained for the Ni-25Cr alloy at 1000, 1100, 1200 and 1300°C in wet air are given in Figure 1 as examples. They are all globally parabolic. The kinetics are all typical of a chromia-forming behavior although their shape is not totally parabolic: the 1000°C-curve is not quite regular (some small jumps) and the end of the 1300°C-curve is almost horizontal (typical of an intense volatilization of chromia). The mass gain data were also plotted as m × (dm / dt) versus –m. All the curves presented a linear part, the equation of which gave the values of the parabolic constant Kp (ordinate at the origin) and of the chromia volatilization constant Kv (slope). The Kv constant increases from about 50 × 10^{-10} g cm^{-2} s^{-1} at 1000°C up to 640 × 10^{-10} g cm^{-2} s^{-1} at 1300 °C. The real (not underestimated) parabolic constant Kp also increases with temperature, from 3 × 10^{-12} g^2 cm^{-4} s^{-1} at 1000°C to 230 × 10^{-12} g^2 cm^{-4} s^{-1} at 1300 °C.

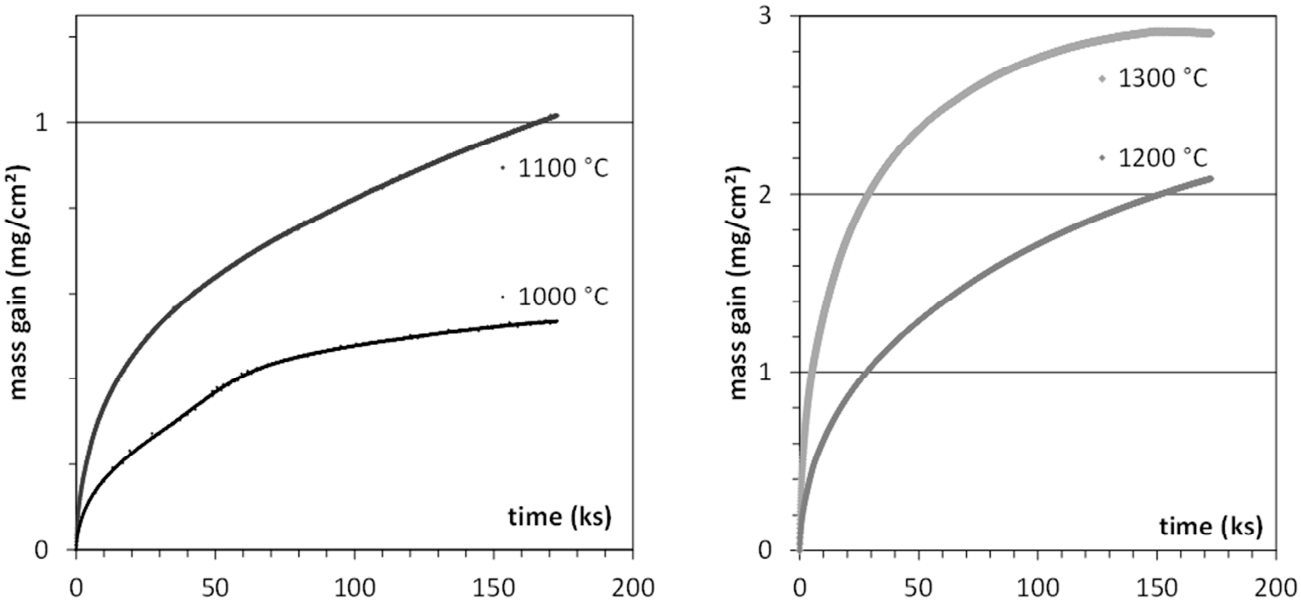

Fig. 1. The four thermogravimetry curves obtained in wet air for the binary Ni-25Cr alloy at the four temperatures in {water vapor}-enriched air

Preliminary observation of the oxidized samples allows seeing that spallation occurred during the cooling, and that the surface fraction of denuded alloy increased with the temperature stage. The samples oxidized at 1000°C were both still entirely covered by the oxide scale while the samples oxidized at 1300 °C were significantly denuded. The humidity of air seemingly influenced the scale spallation during cooling. Indeed, for a given stage temperature, the sample oxidized in wet air was, after cooling down to room temperature, more covered by the external scale than the one oxidized in dry air.
According to the SEM examinations of the oxidized surfaces (before cutting and cross-section preparation), the grain size of the scale tends to increase with the oxidation temperature. The X-ray diffraction runs all showed that chromia is the single oxide present on the sample surface, this confirming what was suggested by the mass gain rates and parabolic constants which were both typical of a chromia-forming behavior.

After cross section preparation, the SEM examinations of oxide scales were realized through their thickness. The oxide scale is effectively exclusively made of chromia as verified by several EDS pinpoint measurements. The thickness of this chromia scale logically increases with the isothermal stage temperature. As revealed by WDS concentration profiles acquired in the subsurface perpendicularly to the alloy/oxide interface, it appears that the chromium content in the sub-surface close to the alloy/scale interface does not vary systematically versus the stage temperature. The same WDS profiles show that the Cr-depleted zone is deeper for a higher temperature.

The Ni-25Cr alloy also presents a very good behavior in dry air for the same temperatures and durations. But its behavior in wet air is obviously of the same quality, this demonstrating that the presence of a significant content in water vapor did not threaten this basis good behavior. The oxidation rates are seemingly not significantly changed by comparison with oxidation in dry air and the presence of water vapor seemed improving the resistance against oxide scale spallation during cooling.

However some small differences may exist and it appeared interesting to directly compare the present kinetic and metallographic data to the corresponding ones obtained in dry air. This is done graphically thereafter.

The Kp and Kv values obtained in the “wet” air and the ones obtained in “dry” air are plotted together in Figure 2.

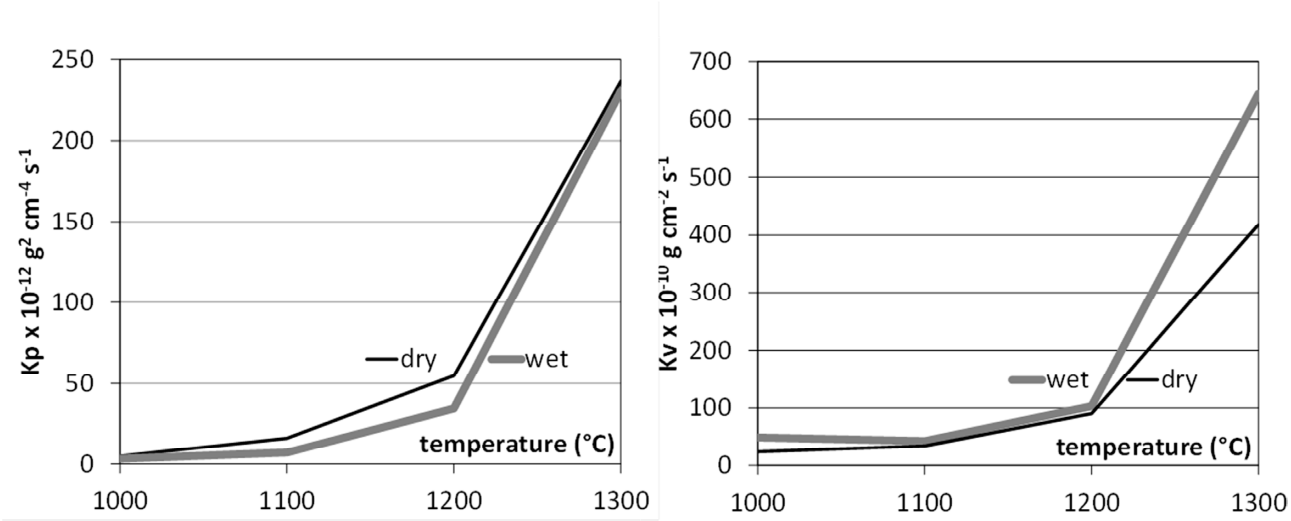

Fig. 2. Values of the parabolic constant Kp (left) and of the chromia volatilization constant Kv (right) plotted versus temperature (fine and black curves: values obtained in dry air, thick and gray curves: values obtained in humidified air)

The parabolic constants issued from the {m × (dm / dt) = f(–m)} plots tend to be lower for oxidation in wet air than in dry air. The volatilization constants are rather close to one another for the lowest stage temperatures (1000°C to 1200°C) but the Kv value obtained for 1300 °C is obviously higher in wet air than in dry air. This very high value of volatilization constant obtained at 1300 °C in wet air explains the apparent horizontalness of the end of the mass gain curve (Figure 1).

The presence of water vapor also influenced the nature of the oxide scales since the ones present over the four samples oxidized in wet air are of pure chromia, according to the XRD results. NiO and $NiCr_2O_4$ are additionally detected over the samples oxidized in dry air at the same temperatures. In contrast there are no real differences between the morphologies of the outer parts of the oxide scales formed in wet air and the ones formed in dry air at the same temperature. This is in good agreement with previous results concerning the chromia scales formed in dry and wet atmospheres over another binary Ni-25Cr alloys [15].

Other difference between wet air and dry air concerns the oxide scale thickness: this one is significantly lower when formed in wet air than in dry air, and the Cr-depleted depth in the alloy subsurface is lower for wet air than for dry air. Inversely, no systematic difference was noticed about the chromium content in the sub-surface close to the alloy / scale interface.

The presence of water vapor with a partial pressure of about 180 millibars did not significantly modify the good high temperature oxidation behavior of the Ni-25Cr alloy in dry air, notably at the three lowest temperatures tested here. In contrast some differences were seen about the parabolic rate which is a little slower at all temperatures in wet air than in

dry air and about the chromia volatilization which is slightly accelerated at 1000°C by water vapor air. The effect of water vapor on chromia volatilization is much more evident at 1300°C (clear acceleration of the volatilization of chromia). The effects of water vapor on Kp (lower in wet air than in dry air at 1100 and 1200 °C) and on Kv (higher in wet air than in dry air at 1000 °C and at 1300 °C) led to observe lower oxide scale thickness observed for oxidation in wet air than for oxidation in dry air.

To finish one can briefly say that the results exposed above and obtained for the Ni-25Cr alloy were globally also found in the case of the Co-10Ni-30Cr for the same temperatures and duration, despite the mass gains were slightly faster for the cobalt alloy at all temperatures than for the nickel one.

4. CONCLUSION

Thus, the presence of rather high water vapor in hot air did not significantly change the high temperature oxidation behaviors of these chromia-forming alloys. These behaviors were not really deteriorated in humidified air in term of oxidation kinetic (except an enhanced chromia volatilization at very high temperature). On the contrary a better adherence of the oxide scales on the alloys' surfaces was observed during the post-isothermal stage cooling, which lets think that water vapor may be favorable to a better behavior in thermal cycling.

References

[1] Jonsson, T., Pujilaksono, B., Hallström, S., Agren, J., Svensson, J.E., Johansson, L.G., Halvarsson, M., "An ESEM in situ investigation of the influence of H_2O on iron oxidation at 500 °C", *Corrosion Science*, Vol. 51 (2009) pp. 1914-1924.

[2] Pérez, P., "On the influence of water vapour on the oxidation behaviour of pure Ti", *Corrosion Science*, Vol. 49 (2007) pp. 1172-1185.

[3] Chevalier, S., Juzon, P., Przybylski, K., Larpin, J.P., "Water vapor effect on high-temperature oxidation behavior of Fe_3Al intermetallics", *Science and Technology of Advanced Materials*, Vol. 10 (2009), art. n°045006.

[4] Lin, Z.J., Li, M.S., Wang, J.Y., Zhou, Y.C., "Influence of water vapor on the oxidation behavior of Ti_3AlC_2 and Ti_2AlC", *Scripta Materialia*, Vol. 58 (2008) pp. 29-32.

[5] Kaplin, C., Brochu, M., "Effects of water vapor on high temperature oxidation of cryomilled NiCoCrAlY coatings in air and low-SO_2 environments", *Surface and Coatings Technology*, Vol. 205 (2011) pp. 4221-4227.

[6] Hellström, K., Tang, J.E., Jonsson, T., Halvarsson, M., Pompe, R., Sundberg, M., Svensson, J.E., "Oxidation behavior of a (Mo, W)Si_2-based composite in dry and wet oxygen atmospheres in the temperature range 350-950°C", *Journal of the European Ceramic Society*, Vol. 29 (2009) pp. 2105-2118.

[7] Yamauchi, A., Yi, X.M., Akiyama, T., Kurokawa, K., "Oxidation Behavior of β-SiAlON in H_2O-Containing Atmosphere", *Materials Science Forum*, Vol. 696 (2011) pp. 395-399.

[8] Saunders, S.R.J., Monteiro, M., Rizzo, F., "The oxidation behaviour of metals and alloys at high temperatures in atmospheres containing water vapor: A review", *Progress in Materials Science,* Vol. 53 (2008) pp. 775-837.

[9] Othman, N.K., Othman, N., Zhang, J., Young, D. J., "Effects of water vapor on isothermal oxidation of chromia-forming alloys in Ar/O_2 and Ar/H_2 atmospheres", *Corrosion Science,* Vol. 51 (2009) pp. 3039-3049.

[10] Zurek, J., Young, D.J., Essuman, E., Hänsel, M., Penkalla, H.J., Niewolak, L., Quadakkers, W.J., "Growth and adherence of chromia based surface scales on Ni-base alloys in high- and low-pO_2 gases", *Materials Science and Engineering*, A 477 (2008) pp. 259-278.

[11] Michalik, M., Hansel, M., Zurek, J., Singheiser, L., Quadakkers, W.J., "Effect of water vapor on growth and adherence of chromia scales formed on Cr in high and low pO_2-environments at 1000 and 1050°C", *Materials at High Temperature*, Vol. 22 (2005) pp. 213-221.

[12] Jonsson, T., Pujilaksono, B., Heidari, H., Liu, F., Svensson, J.-E., Halvarsson, M., Johansson, L.-G., "Oxidation of Fe-10Cr in O_2 and in O_2+H_2O environment at 600°C: A microstructural investigation", *Corrosion Science*, Vol. 75 (2013) pp. 326-336.

[13] Halvarsson, M., Tang, J.E., Asterman, H., Svensson, J.-E., Johansson, L.-G., "Microstructural investigation of the breakdown of the protective oxide scale on a 304 steel in the presence of oxygen and water vapor at 600°C", *Corrosion Science*, Vol. 48 (2006) pp. 2014-2035.

[14] Berthod, P., "Kinetics of high temperature oxidation and chromia volatilization for a binary Ni–Cr alloy", *Oxidation of Metals*, Vol. 64, No. 3/4 (2005) pp. 235-252.

[15] Essuman, E., Meier, G.H., Zurek, J., Hänsel, M., Norby, T., Singheiser, L., Quadakkers, W.J., "Protective and non-protective scale formation of NiCr alloys in water vapor containing high- and low-pO_2 gases", *Corrosion Science*, Vol. 50 (2008) pp. 1753-1760.

Fracture and Erosion Characteristics of Self-Fluxing Alloy Coatings in High Temperature Environment

Yoshinori Isomoto Oka[(1,*)], Yuuzou Kawahara[(2)] and Michiko Yoshihara[(3)]

[(1)] Graduate School of Engineering, Hiroshima University, Higashi-Hiroshima 739-8527, Japan
[(2)] Dai-ichi High Frequency Co., Ltd., Surface Treatment Dev., Kawasaki 210-0866, Japan
[(3)] Yokohama National University RI Center 240-8501, Japan

e-mail: iyoshi@hiroshima-u.ac.jp

1. INTRODUCTION

Self-fluxing alloy coatings are useful for components of industrial equipments, such as incinerators and boilers etc. in sand erosion or wear environments as well as high temperature corrosive and oxidation environments [1, 2]. However, the mechanical properties of the self-fluxing alloy coatings in high temperature environments have not been precisely investigated. It is very important to investigate the mechanical properties of the alloy coatings at high temperatures, in order to develop highly durable coating alloys and apply to practical erosive services. We have attempted to obtain dynamic mechanical properties of the alloy coatings by impact methods [3, 4]. Further investigations were conducted by using three point bending tests at temperatures from 773 to 1073 K, to obtain quasi-static fracture toughness K_{IC} and fracture energy U for the three types of self-fluxing alloys in this study. Also fracture surfaces and cross-sectional microstructures of the specimens after the bending tests were evaluated to discuss fracture mechanisms and to consider erosion behavior at high temperatures.

2. EXPERIMENTAL PROCEDURE

A Schematic illustration of the three point bending apparatus at high temperatures is shown in Fig. 1. Bending tests were carried out based on JIS R 1607 (Japan Industrial Standard). The three types of self-fluxing alloys were prepared from those coating layers, and elastic modulus and Brinell hardness were shown in Table 1. The specimen with approximate size of 2.5x4x20 mm^3, were heated at an arbitrary temperature in a universal testing machine. The test specimen were located in jig plate with distance of 16 mm on the two ceramic rods. The load to fracture F (N) and displacement were measured with an AD converter connected to a computer. Both scanning electron microscopy (SEM) and BEI observations were performed for tested specimens after the bending tests.

Table 1 Chemical Composition, elastic modulus and hardness of three types of self-fluxing alloys.

Material	E (GPa)	H_B(GPa)
A-1(15Cr-3B-4.5Si)	231	6.9
A-2(15Cr-2B-4Si) *	191	2.3
A-3(37Cr-4B-3Si)	136	1.7

*Mark: Low Hardness

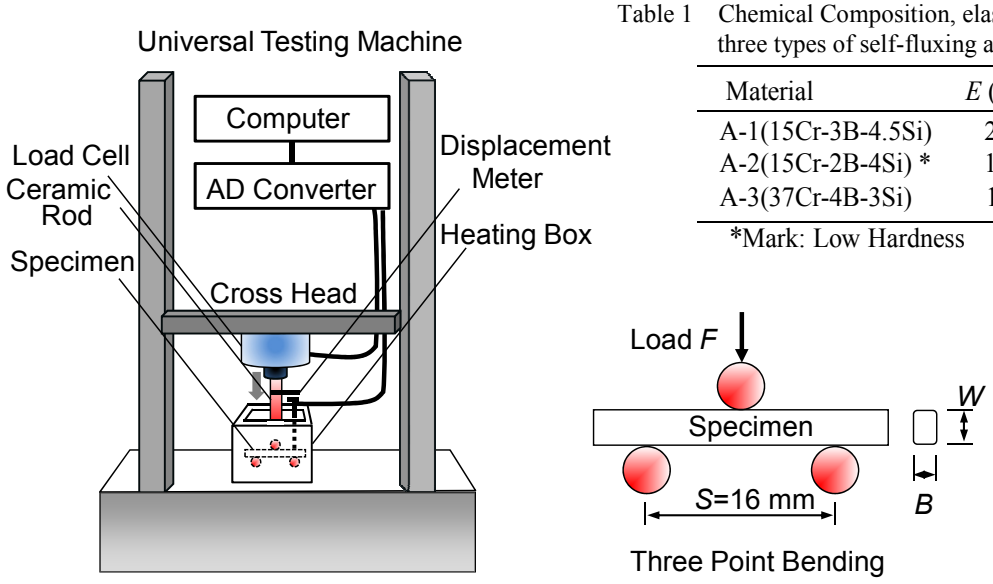

Fig. 1 Three point bending test apparatus and a specimen.

3. RESULTS AND DISCUSSION

3.1 FRACTURE TOUGHNESS K_{IC} AND FRACTURE ENERGY U

Fracture toughness, K_{IC} and fracture energy, U in three point bending tests were calculated by the equations (1) and (2).

$$K_{IC}=FS/(BW^{1.5}) \quad (1)$$

$$U=Ss/(2BW) \quad (2)$$

where F is load, S is the support span, B is the width of test beam, W is the depth of test beam, Ss is the area blow a load-displacement curve. The values of K_{IC} at various temperatures from room temperature (RT. 298 K) to 1073 K are shown in Fig. 2. The K_{IC} of A-2 alloy was the highest among the three self-fluxing alloys at room temperature, but greatly decreased at 1073 K. On the contrary, A-3 alloy had the lowest value of K_{IC} at tested temperatures and the K_{IC} values gradually decreased. A-1 alloy had same decreasing manners with the increase in temperature. These behaviors are associated with difference in microstructures and matrix softening by the increase in temperature.

The behaviors of U defined by Eq. (2) are shown in Fig. 3. A-2 alloy is a specified material both with high K_{IC} and with high U which suggests ability of plastic deformation. A-3 alloy had the lowest U values and was suggested by brittle matrix grains and existence of many pores. The high fracture energy of A-2 alloy at 1073 K was depending on matrix softening and on increased deformation. The fracture energy of three self-fluxing alloys also depends on characteristics at high temperatures.

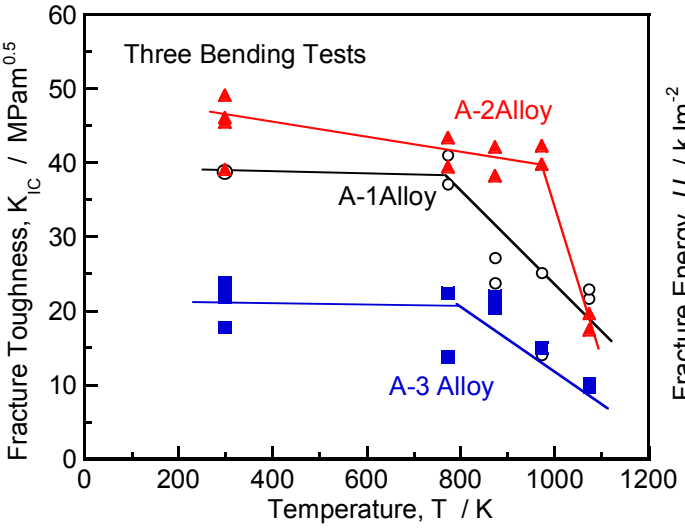

Fig. 2 Effect of temperature on fracture toughness.

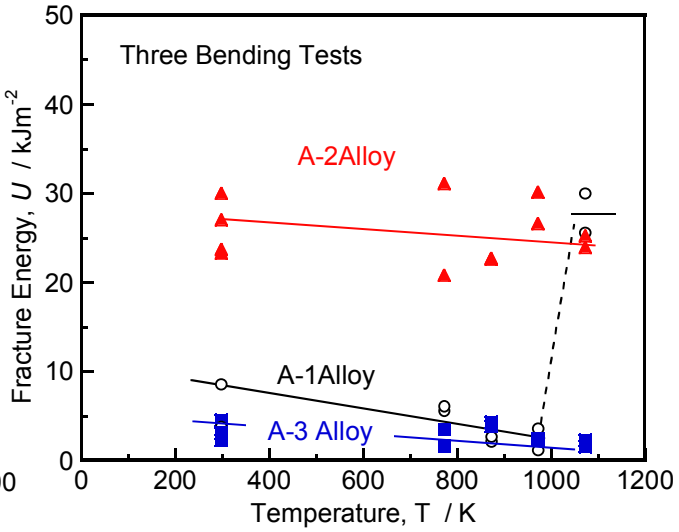

Fig. 3 Effect of temperature on fracture energy.

The dynamic fracture toughness of the three self-fluxing alloy coatings coated on carbon steel obtained by dynamic impact tests showed not too much difference at temperatures of RT and up to 873 K, and a little decrease at 1073 K [3].

3.2 OBSERVATIONS OF FRACTURE SURFACES AND MICROSTRUCTURES

Fig.4 shows fracture surfaces of three coating materials at RT and 973K. Fracture characteristics are recognized to change brittle manner at RT to slightly ductile manner at 973 K. While many micro-cracks penetrated Ni- and Cr-Borides grains were observed in cross-sectional microstructures of A-2 alloy near fractured surface area within approx. 220 μm at 873 K and 973 K. From these behavior of cracks shown in Fig.5, it is clear that micro-cracks are formed firstly on borides particles because of plastic deformation of matrix increased at high temperature of more than 973 K, and finally fracture propagates by connection of such micro-cracks. A-2 alloy, having relatively coarse grains of borides and toughness of matrix solid solution, keep higher toughness up to 973 K, but such K_{IC} greatly reduces more than 973 K. While in A-1 alloy, sub-cracks penetrated linearly in matrix solid solution were recognized at the range of approx..30 μ m near fracture surface. The tendency of brittle fracture is considered to be strong in A-1 alloy at high temperatures. Microstructures of A-3 alloy that have relatively porous microstructures were shown in Fig.6. Layer of increased porosity and fracture of bonding parts

with particles were recognized in the range of 1mm near fracture surface. This was formed by increased plastic deformation at high temperatures. Therefore fracture occur due to connection of microcracks formed on bonding parts of particles.

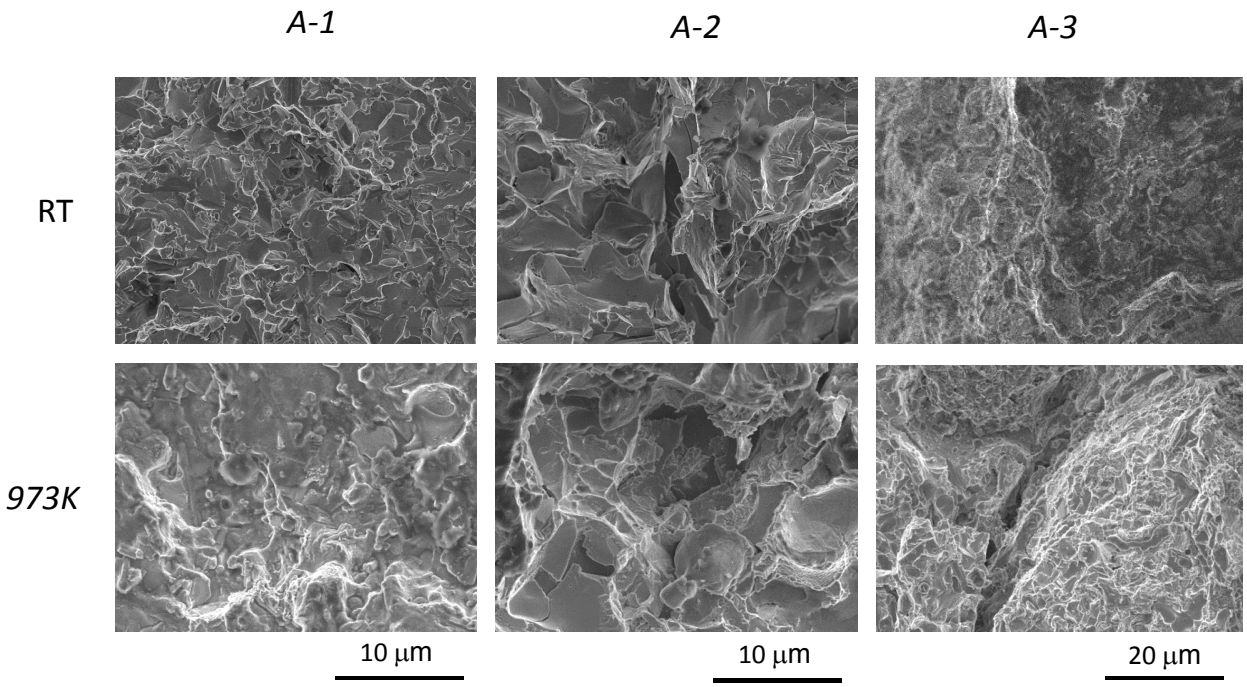

Fig. 4 Fracture surfaces of self-fluxing alloys at RT and 973 K.

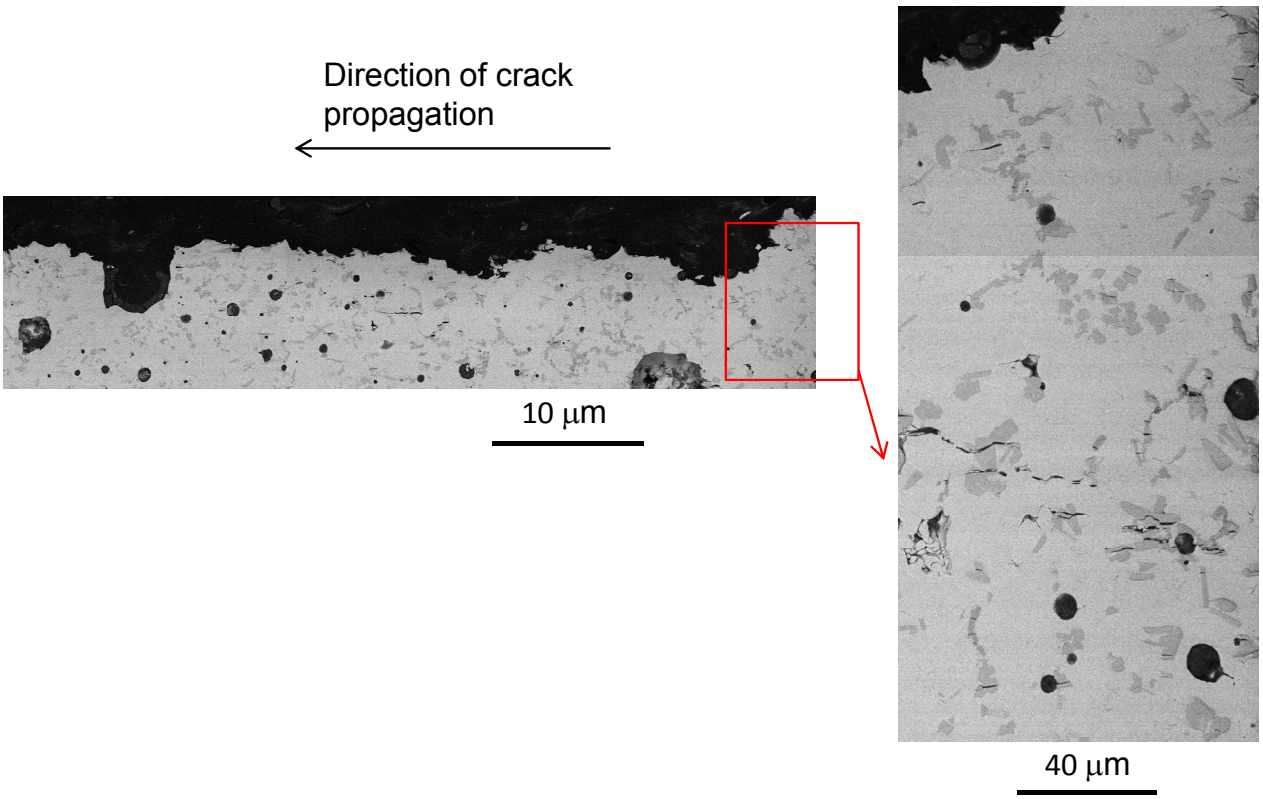

Fig. 5 Cross-sectional BEI images of sub-cracks formed in A-2 alloy near fracture surface at 973 K.

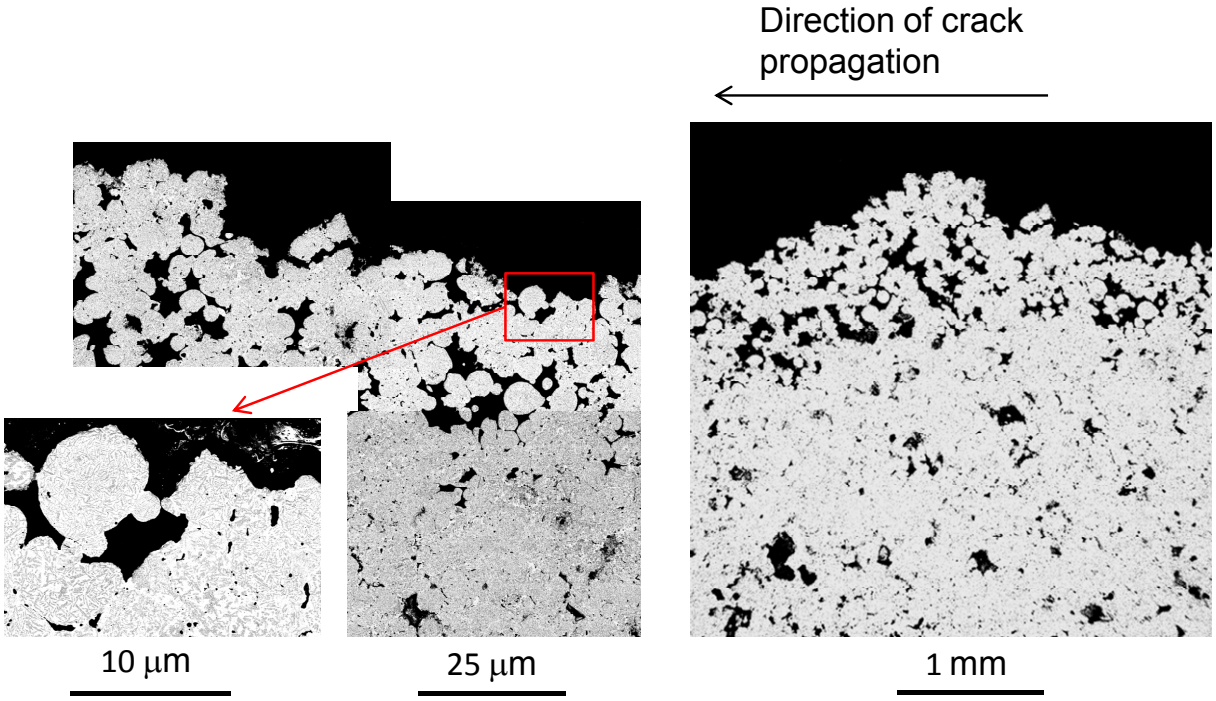

Fig. 6 Cross-sectional BEI images of sub-cracks formed in A-3 alloy near fracture surface at 973 K.

3.3 ESTIMATION OF EROSION BEHAVIOR OF ALLOYS AT HIGH TEMPERATURES

Erosion behavior by impact of solid particles should depend on quasi-static or dynamic hardness especially for metallic materials, and fracture toughness especially for ceramic (brittle) materials [5, 6]. The erosion behaviors of the self-fluxing alloy coatings definitely depend both on hardness and fracture toughness. The fracture energy is also associated with strength and deformation of material, and with material removal followed by repeated plastic deformation. The erosion mechanisms which involve two kinds of manner for material removal depend on the foregoing mechanical properties as well as high temperatures. Erosion damage to the self-fluxing alloy coatings in high temperature equipments and parts such as boiler tubes etc. can be estimated taking account of these mechanical properties at target high temperatures, even if the mechanical properties are quasi-static or dynamic. Erosion damages are considered to be possible to estimate practically if erosion data and these correlations with the mechanical properties at high temperatures are obtained. High temperature erosion tests and further investigations will be expected in the future.

4. CONCLUSIONS

It is clarified that a K_{IC} and U of the three self-fluxing alloys change with the increase in temperature with different manners depending on the type of three alloys. These mechanical behaviors were explained by fracture surfaces and cross-sectional observation results in this study. Further investigation results will be presented in the future.

References

[1] Y. Kawahara: J. of Thermal Spray Technology, ASM Vol. 16 (2007) pp. 202-213.
[2] Y. Matubara, Y. Sochi, M. Tanabe and A. Takeya: J. of Thermal Spray Technology, ASM Vol. 16 (2007) pp. 195-201.
[3] Y. Isomoto, T. Kawanishi and Y. Kawahara, J. Japan Inst. Met. Mater. Vol. 77 (2013) pp.225-230.
[4] Y. Isomoto, T. Kawanishi, Y. Kawahara and M. Yoshihara, J. Japan Inst. Met. Mater. Vol. 77 (2013 pp.231-236.
[5] Y. Isomoto Oka, K. Okamura and T. Yoshida, Wear Vol. 259 (2005) pp. 95-101.
[6] Y. Isomoto Oka, S. Mihara, T. Yoshida, Wear Vol. 267 (2009) pp. 129-135.

Origin of the ω-Zr Phase formed during High Temperature Oxidation of Zirconium Alloys

J. Favergeon [(1,*)], S. Chevalier [(2)], T. Montesin [(2)] and G. Bertrand [(2)]

[(1)] Laboratoire Roberval, UMR 7337, University of Technology of Compiegne, Rue Roger Couttolenc, CS 60319, 60203 Compiegne cedex, FRANCE
[(2)] Laboratoire Interdisciplinaire Carnot de Bourgogne, Université de Bourgogne, UMR 6303, 9 av. A. Savary, BP 47870, 21078 Dijon cedex, FRANCE

e-mail: jerome.favergeon@utc.fr

1. INTRODUCTION

In 1997, David Foord *et al* [1] observed the ω-Zr phase within oxidized zirconium alloys, under the oxide scale, within the Zr-O solid solution. Actually, little work was undertaken for the study of this phase in the context of zirconium alloy oxidation, in particular with regard to its origin and its role during oxide growth. However, it seems important to investigate this phase, since it is localized at the internal interface, place of the chemical reaction between zirconium and oxygen.

It is well-known that the ω-Zr phase is a high pressure phase. It can be formed starting from the α-Zr phase when stress reach values between –8 and –2 GPa at room temperature, or starting from the β-Zr phase, either by hardening or by application of very high pressures (30 to 60 GPa) [2]. With regard to its appearance during oxidation of zirconium alloys, it is rather the alpha/omega transition which must be brought into play, since all the authors who highlighted the presence of ω-Zr at the metal/oxide interface used oxidation temperatures below the alpha/beta transition temperature.

Consequently, one can think that the presence of ω-Zr is correlated with the presence of strong compressive stresses in the metal, near the internal interface. However, this possibility has been never considered. According to Foord [1], ω-Zr apparition is explained by the strong compressive stresses present in the oxide layer, near the metal/oxide interface. Ishii [3] disapproves this assumption mentioning that the compressive stresses in the oxide actually generate tensile stresses in metal which are particularly strong because of oxygen dissolution in the metal which causes dilatation of zirconium. Ishii then questions on the origin of the ω phase since these tensile stresses preclude its formation.

In the present paper, our aim is to clarify the reasons for apparition of the ω-Zr phase during high temperature oxidation of zirconium alloys in the scope of our work on stress/diffusion coupling..

2. MICROSCOPIC OBSERVATION OF THE Zr-ZrO_2 INTERFACE BY TEM

Metal coils of dimensions 2.3x15.0 mm are cut from rolling sheets of Zircaloy-4. They are chemically polished during 2 minutes in a HF/HNO_3 mixture, and then oxidized under dry oxygen (P_{O2} = 20 mbar) at 873 K during 5 minutes. The oxidized samples are cooled down slowly to avoid high damage of the scale. Oxide thickness is about 500 nm. Cross-sections for TEM observations are prepared from these oxidized samples.

The bright field image of figure 1 represents a general sight of the cross-section. The higher zone corresponds to the oxide scale which is characterized by the column-like morphology of monoclinic zirconia. In this layer, one also notices appearence of cracks parallel with the metal-oxide interface which have all the characteristics of the cracks developped during oxide growth which were observed by Bossis [4]. The diffraction pattern of the oxide scale (figure 1.b) revealed specific spots of diffraction in the selected area, whereas the bright field image shows that, in this zone, there exist many columns of oxide. This observation confirms that oxide orientation is very well-defined [5-7]. One metal grain is present under this oxide layer. Between metal and oxide, one notes the presence of a dark band (figure 1a). This zone was well-studied by Foord [1,8], Bossis [4] and Ishii [3]. They showed that it corresponds to the ω-Zr phase enriched by dissolved oxygen and that two types of distribution can coexist :

- the first one is the so-called "saw-toothed" microsctructure [8]. Such a microstructure is in relation with undulation of the metal-oxide interface. Defining this undulation as a succession of forward and backward zones of the oxidation front, Bossis showed that this ω-phase is localised around the backward zones.

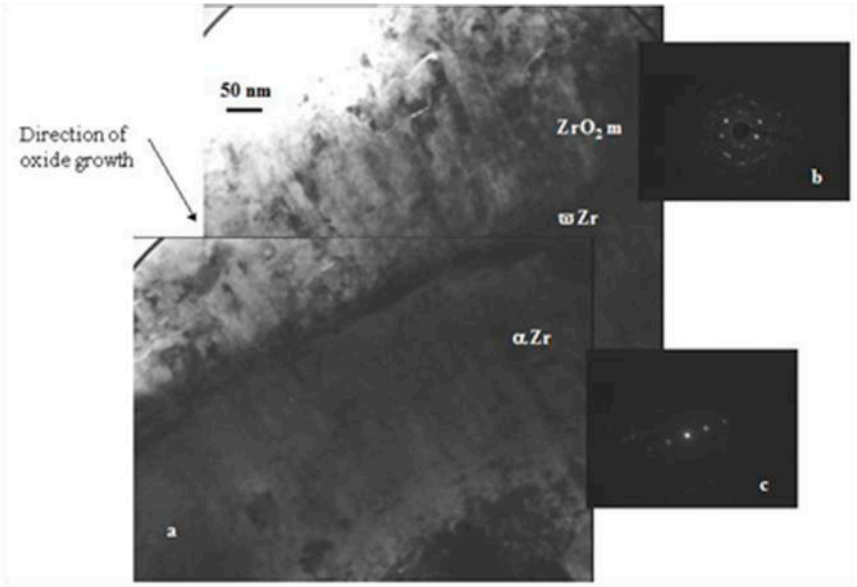

Fig. 1 TEM observation of a cross-section prepared from Zr oxidized at 873 K : a-bright field image; b-SAD from the oxide scale; c-SAD from the metal

- The second kind of microstructure reveals a stringcourse whith constant thickness along the metal-oxide interface [8]. Our observations are rather in conformity with this second type of localization.

These observations demonstrate the presence of the ω-Zr phase between the metal and the scale when oxide growth occurs at 873 K under dry oxygen. We don't observe undulations of the metal-oxide interface as Bossis did [4]. This is probably due to the short oxidation time we use.

3. MODELLING OF OXYGEN DIFFUSION IN ZIRCONIUM ALLOYS

We have developed a kinetic model to study high temperature oxidation of zirconium alloys [9]. In this model, we particularly take care of the oxygen transport in the metal, considering the coupling between oxygen diffusion and mechanical stress, based on the Larche and Cahn approach [10-11]. In the metal, we consider the strains developped by the variations of oxygen composition which are called the chemical strains ε_{ij}^{chem}, defined by:

$$\left(\frac{\partial \varepsilon_{ij}^{chem}}{\partial c}\right)_{\sigma_{kl},T} = \eta_{ij} \tag{1}$$

where c is the oxygen composition and η_{ij} are the chemical expansion coefficients.
Effect of stress on diffusion appears in the diffusion flux of oxygen, $\vec{J}$:

$$\vec{J} = -D\vec{\nabla}c_V + \frac{D\overline{M}_O}{RT} c_V \vec{\nabla}\left[\left(\frac{\partial S_{ijkl}}{\partial c_V}\right)_{\sigma_{kl},T} \sigma_{kl}\cdot\sigma_{ij} + \frac{\eta_{ij}}{\rho_0}\sigma_{ij}\right] \tag{2}$$

where D is the oxygen diffusion coefficient, c_V is the oxygen concentration (in kg.m^{-3}), $\overline{M}_O$ is the molar mass of the solid at zero stress (reference state), S_{ijkl} are the elasticity tensor components, ρ_0 is the density of the solid in the reference state and σ_{ij} are the stress components. More details on the constitutive equations of this model and on the numerical resolution are given in [9].
We consider a zirconium alloy sheet with infinite thickness compared to the oxygen diffusion distance, with the (014) rolling crystallographic texture. Simulation of oxygen diffusion at 873 K within this sample, without oxide growth, leads to the oxygen concentration and stress profiles given in figure 2. These results show that oxygen dissolution in the metal is reponsible for high compressive stress in the vicinity of the metal-oxide interface. When oxide growth is taken into account, we showed that stress repartition in the metal is modified, but still compressive stresses are present in the vicinity of the metal-oxide interface [12].

Then we can conclude that these results are in opposition with Ishii's point of view: as presented in the introduction, Ishii considered that oxygen dissolution in zirconium alloy leads to the metal expansion, which is reponsible for tensile stresses. In our model, we effectively takes into account metal expansion due to oxygen diffusion as the the chemical expansion coefficients η_{ij} are positive [11]. But this expansion actually generates compressive stress, in opposition with Ishii's assumptions, because stresses should be considered as the reaction of the metal against expansion induced by oxygen dissolution.

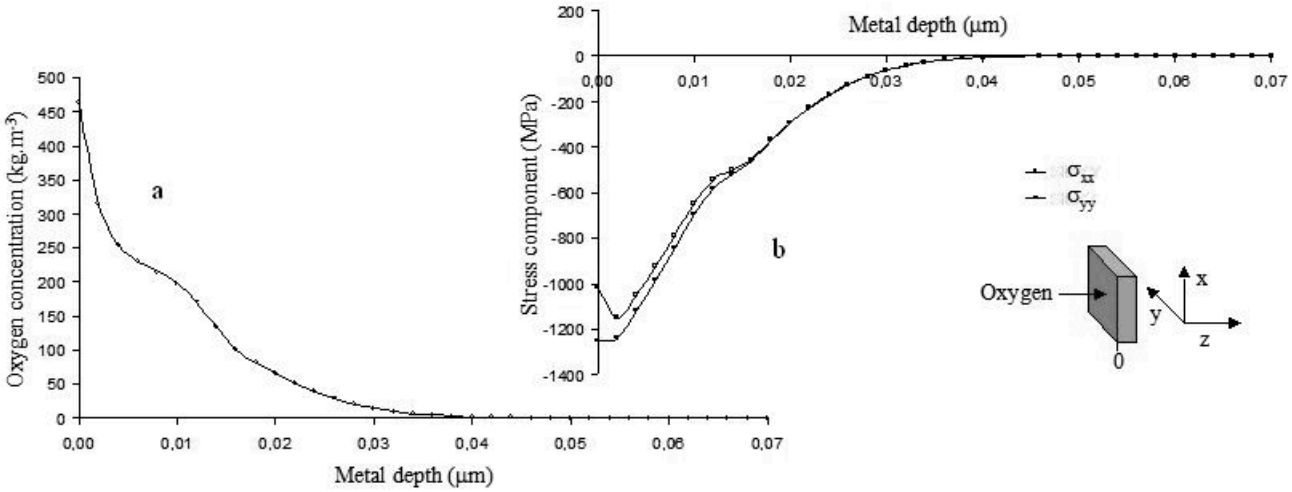

Fig. 2 Numerical simulation of the oxygen diffusion in zirconium at 873 K : a-oxygen profile; b-stress profile

Then presence of such compressive stress is in agreement with the presence and the localization of the ω-Zr phase and oxygen diffusion within the alloy appears as the fundamental reason for the α-Zr to ω-Zr phase transition.

All the simulations we performed consider that the metal-oxide interface remains flat during oxide growth, which is in agreement with our TEM obervations. But as explained in the previous section, for given oxidation conditions, this interface develops undulations and the ω-zr phase localization is then affected. So it seems important to consider undulated interface in our model in order to know how the undulations affect the stress repartition along the interface in the metal and, as a consequence, if this stress repartition can explain the "saw-toothed" microstructure.

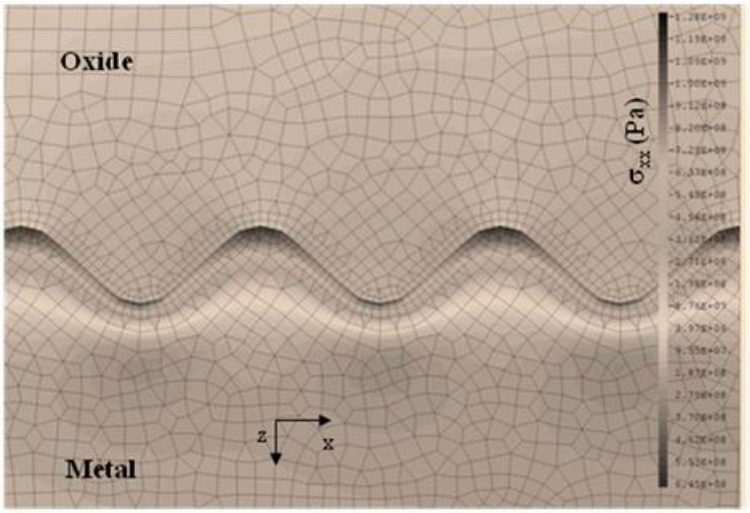

Fig. 3 2-D stress distribution in the Zr-ZrO_2 system at 873 K with an undulated metal/oxide interface

Two-dimensional simulations have been performed on the Zr-ZrO_2 system in the plane-strain approximation. For the purpose of this contribution we only need to calculate the stress repartition in the metal containing dissolved oxygen with an underlying scale of thermally grown oxide (so the oxide growth is not calculated). The simulation considers that the metal-oxide interface is undulated with a wave length equal to 1 µm., and the metal corresponds to a semi-infinite medium in the y-direction as the average thickness of the monoclinic zirconia scale is 2 µm.

Calculations are performed at 823 K. Map of the σ_{xx} stress component in the

metal-oxide sample is presented in figure 3. As shown experimentally [13-14], the oxide scale exhibits high compressive stresses. In the vicinity of the internal interface, the metal is still under compression as obtained in the previous section with the plane metal-oxide interface. But stress repartition is not uniform along the x-direction and one notes the presence of stronger compressive stress values in the vicinity of the backward zones of the oxidation front. These zones actually correspond to the places where the ω-Zr phase is formed when a saw-toothed microstructure is observed [4].
We show again that the localization of the high compressive stress in the metal, due to oxygen dissolution delimits the zone where the ω-Zr phase is formed during high temperature oxidation of zirconium alloys.

4. CONCLUSION

This contribution shows that the oxygen dissolution in zirconium during high temperature oxidation, can generate high compressive stress in the substrate. This high level of compressive stress could lead to the α-to-ω-Zr phase transition. The calculated repartition of the high compressive stress in the metal is compatible with the localization of the ω-Zr phase observed experimentally.

References

[1] Foord, D.T. and Newcomb, S.B., "Instabilities in the oxidation behaviour of Zircaloy-4" *2nd International Conference on the Microscopy of Oxidation, The Institute of Materials, London, UK*, 1993, pp. 374-386.

[2] Pichon, L. *et al*, "Evidence of omega-phase in ion beam sputtered zirconium thin films" *Thin Solid Films,* Vol. 342 (1999), pp. 93-99.

[3] Ishii, Y. and Sykes, J.M., "Microstructure of oxide layers formed on Zircaloy-2 in air at 450°C" *Materials at high temperatures,* Vol. 17, No 1 (2000), pp. 23-28.

[4] Bossis P., "Mécanismes de corrosion du Zircaloy-4 et de l'alliage Zr-1Nb en eau pressurisée hors et sous irradiation: rôle des interfaces", *PhD thesis*, Institut National Polytechnique de Grenoble (1999)

[5] Glavicic, M.G. *et al*, "Texture measurement of zirconium oxide thin films" *Eleventh International Conference on Texture of Materials, International Academic Publishers*, Beijing, China, 1996, pp. 1137-1142.

[6] Valot, C. *et al*, "Spatiotemporal dynamics in the oxidation of groups IV-V metals: study of zirconium" *Solid State Ionics,* Vol. 101-103 1997, pp. 769-774.

[7] Favergeon, J. *et al*, "Texture effects on Zircaloy oxidation: Experiment and simulation" *Material Science Forum,* Vol. 408-412 (2002), pp. 999-1006.

[8] Foord, D.T. and Newcomb, S.B., "The microstructural characterisation of factors which determine the degradation behavior of Zircaloy-4." *Third International Conference on the Microscopy of Oxidation., The Institute of Materials,* London, UK, 1997, pp. 488-499.

[9] Favergeon, J. *et al*, " Mechano-chemical aspects of high temperature oxidation: a mesoscopic model applied to zirconium alloys" *Oxidation of Metals* Vol. 64, No 3-4 (2005), pp. 253-279.

[10] Larché, F.C. and Cahn, J.W., "The effect of self-stress on diffusion in solids" *Acta Metallurgica,* Vol. 30 (1982), pp. 1835-1845.

[11] Favergeon, J. *et al*, "Stress-diffusion coupling applied to oxygen dissolution in metals: anisotropy, geometry and mechanical properties gradients effects" *Defect and Diffusion Forum*, Vol. 194-199 (2001), pp. 1017-1024.

[12] Favergeon, J. *et al*, "Theoretical and experimental studies of zirconium oxidation: stress and anisotropy effects" *Defect and Diffusion Forum,* Vol. 203-205 (2002), pp. 231-244.

[13] Jacquot, T. *et al*, "Residual stress of monoclinic zirconia obtained by X-ray diffraction in Zircaloy-4 oxidized cladding tubes" *4th European Powder Diffraction Conference*, *Materials Science Forum*, 1996, pp. 845-850.

[14] Godlewski, J. *et al*, "Stress distribution measured by Raman spectroscopy in zirconia films formed by oxidation of Zr-based alloys." *Zirconium in the Nuclear Industry, Twelfth International Symposium, American Society for Testing and Materials (ASTM) special technical publication*, 2000, pp. 877-900.

High temperature oxidation of austenitic stainless steels: effect of sulfur content on scale adhesion.

V. Parry[(1,*)], E. Fedorova[(2)], C. Pascal [(1)], M.Braccini[(1)], M. Mantel [(1,3)], D.Oquab[(4)], D. Monceau [(4)], Y. Wouters[(1)]
[(1)]SiMaP, University of Grenoble, FRANCE
[(2)] Polytechnic Institute of Siberian Federal University, RUSSIA
[(3)]UGITECH SA, Ugine, FRANCE
[(4)] CIRIMAT, University of Toulouse, FRANCE

e-mail: valerie.parry@simap.grenoble-inp.fr

Two austenitic stainless steels, AISI 304L and AISI 303, containing 0.025 and 0.249 wt%S were oxidized in thermobalance at 1000°C for 50h. The chemical composition and the crystallographic structure of the oxide scales were investigated by Raman spectroscopy. Adhesion of oxide scales was tested by SEM in situ tensile tests. A correlation between the specific mass change, the chemistry, the microstructure and the adhesion properties is made and results are discussed in relation with sulphur concentration in the alloy.

1. INTRODUCTION

The life time of metallic parts submitted to high temperature oxidation is often limited by scale spallation leading to rapid oxide loss or to initiation of breakaway oxidation by iron oxides formation on chromia-forming alloys. Scale spallation is the result of a complex process where two important parameters play a role: stresses and adhesion.
A majority of industrial stainless steels contain sulfur in order to improve their forgeability but sulfur is known to be a powerful weakener of iron and to strongly segregate to metal free surfaces and to metal/oxide interfaces. Interfacial segregation of sulfur impurities is believed to cause a weakening of the normally strong interfacial bond strength of alumina and chromia scales [1]. Deleterious effects of sulfur segregation on the adherence of oxide scale grown on alumina-forming alloys have been widely studied [2] and are known to be the major cause of alumina scale failure. However,for chromia scales interfacial morphology associated with growth stresses is a more important cause of scale failure and sulfur segregation is only a secondary effect [1].
In this paper, two austenitic stainless steels AISI 304L and AISI 303, containing 0.025 and 0.249 wt% S, were oxidized at 1000°C for 50h. Thermogravimetric analysis was performed. The chemical composition and the crystallographic structure of the oxide scales were investigated by Raman spectroscopy. Adhesion of oxide scales was tested by SEM in situ tensile test. A correlation between the specific mass change, the chemistry and the adhesion properties is made and results are discussed in relation with sulphur concentration.

2. EXPERIMENTAL

Oxidation tests were performed on specimens cut by electrical discharge machining from bars of AISI 304L and AISI 303 provided by Ugitech France. Their chemical composition, displayed in Table 1, is similar except the sulfur content which is 0.25wt%for AISI 304L and 0.249 wt% for AISI 303. Before oxidation tests, samples were polished with SiC paper up to 1200 grade, cleaned in ethanol and dried in air. Isothermal oxidations were performed under synthetic air at atmospheric pressure in dynamic condition (2 mm/s).

Table 1. *Chemical composition of austenitic stainless steels AISI 304L and AISI 303*

Steels	Ni	Cr	Mn	Mo	V	Cu	P	Sn	Co
304L	8.960	18.040	1.128	0.400	0.098	0.481	0.021	0.003	0.103
303	8.284	17.100	1.746	0.404	0.080	0.511	0.029	0.009	0.098
Steels	Si	Nb	C	S	N	O	Ca	Al	Ti
304L	0.458	0.012	0.021	0.025	0.048	0.010	0.005	0.003	<0.0001
303	0.443	0.011	0.055	0.295	0.035	0.015	0.013	<0.002	<0.002

Rectangular specimens with dimension of 17 mm × 9 mm × 2 mm were used for thermogravimetric tests at 1000°C. The thermobalance used is a SETARAM™ TAG 24S with a 1 µg sensitivity. The device makes use of a double symmetrical furnace designed to compensate all signal disturbances resulting from gas flow, buoyancy and convection.
Tensile specimens, characterized by a gauge section of 2 mm width x 1 mm thick and a gauge length of 3 mm long, were isothermally oxidized in a horizontal furnace at 900°C and 1000°C.
The chemical composition and the crystallographic structure of the oxide scales were investigated by Raman spectroscopy using a Renishaw RM1000 Raman microscope.
After oxidation, in situ tensile tests were performed in a horizontal tensile machine specially designed to be placed in the SEM chamber. JEOL JSM 6400 SEM was used. The procedure consists in regularly straining the sample by tensile loading while recording strength and elongation. A regular elongation rate of 50 µm.min^{-1} was applied. When oxide spallation is observed, SEM pictures are periodically taken and the series of pictures is treated by image analysis, leading to a characteristic curve: spalled fraction of surface area vs. strain.
Surface SEM views after tensile tests and EDS analysis were obtained with a LEO S440 Stereoscan instrument equipped with the EDAX Genesis software.

3. RESULTS AND DISCUSSION

Isothermal kinetics of the two austenitic stainless steels oxidized for 50h at 1000°C under synthetic air are displayed in Figure 1. Experiments performed on AISI 304L were reproduced three times. Despite some significant experimental variations the parabolic rate constant is around 3.5 10^{-6} mg^2.cm^{-4}h^{-1} for AISI 304L and one order of magnitude higher for AISI 303: 2.9 10^{-5} mg^2.cm^{-4}h^{-1}.
Assuming that the scale is only composed of chromina, the equivalent oxide thickness estimated from the weight gain after 50h of oxidation is about 6 µm for AISI 304L and 12 µm for AISI 303.

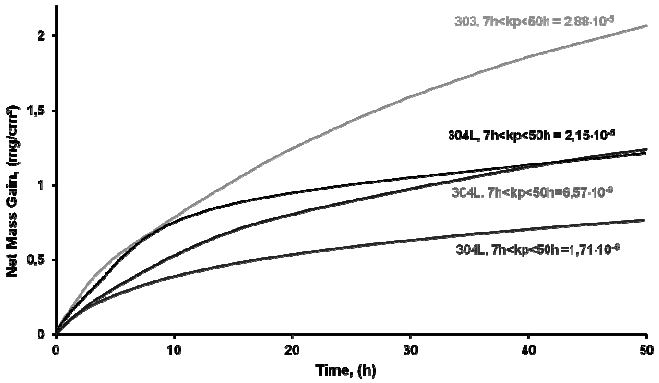

Fig. 1. Isothermal oxidation kinetics of AISI 304L and AISI 303 at 1000°C under synthetic air at atmospheric pressure in dynamic conditions (2 mm.s^{-1})

For AISI 304L, Raman spectroscopy results, displayed in Fig. 2. (a), have shown that chromia Cr_2O_3 and solid solution $(Fe,Cr)_3O_4$ are present in the scale [3].
Raman spectra of the oxide scale grown on AISI 303 are displayed in Fig. 2. (b). Two types of spectra are recorded, depending on the analyzed zone. The iron rich oxide scale is composed of hematite Cr_2O_3 and a solid solution of $(Fe,Cr)_2O_3$ and of spinel type oxide $(Fe,Cr)_3O_4$[3,4].

SEM observations in BSE mode of the surfaces of AISI 304L and AISI 303after oxidation for 50h at 1000°C are displayed in Fig. 3. (a). and Fig. 3. (b). respectively. Surface morphologies of the oxides scales grown on 304L and 303 are different. For AISI 303, the scale seems less homogeneous and more brittle. EDS surface analyses (not presented) indicate that the iron content in the oxide scale is higher for AISI 303 than for AISI 304L.

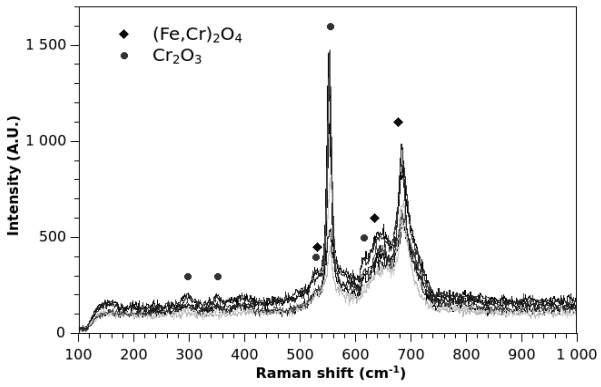

Fig. 2. (a) Raman spectra of oxide scale grown on AISI 304L after 50h at 1000°C under synthetic air.

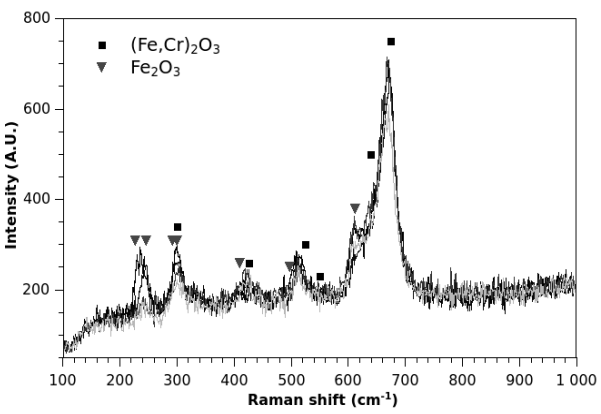

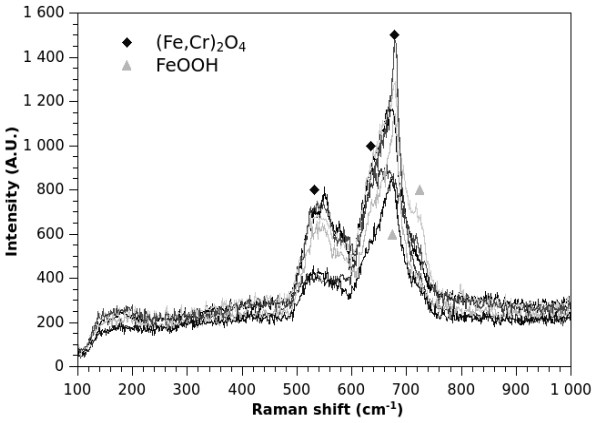

Fig. 2. (b) Raman spectra of oxide scale grown on AISI 303 after 50h at 1000°C under synthetic air

In situ tensile test were performed in SEM. During the test, the oxide scale is forced to spall, releasing the elastic energy stored. The behaviors of the oxide layers were quite different (see Fig. 3(c) and Fig. 3(d)). While in both steels we observed transverse crack initiation and growth in the oxide scale, the crack patterns were different. In both case the cracks grew perpendicular to the tension direction, but while straight cracks propagated in the oxide scale of the 303 steel, in the 304L steel cracks looked like waves. The critical strains at which first cracks were observed are quite different in the two steels: this strain is about 1.6% in the 303 steel and 3.4% in the 304L steel.

Finally, spallation occurs in the oxide scale in the 303 steel, but not in the 304L steel. In the 304L steel, instead of oxide scale buckling and spallation, the transverse cracks opened, following the ductile deformation of the underneath substrate. The metal appears for a strain of 7.8%. At the end of the test, this cracks opening was so wide that we could see the metal at the crack root.

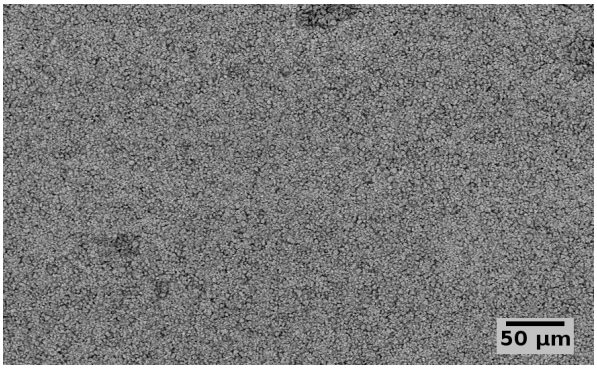

Fig. 3(a). Surface SEM view in BSE mode of the oxide scale on AISI 304L before tensile test.

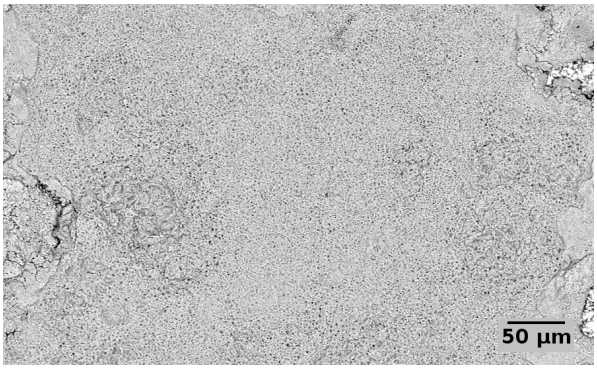

Fig. 3(b). Surface SEM view in BSE mode of the oxide scale on AISI 304L before tensile test.

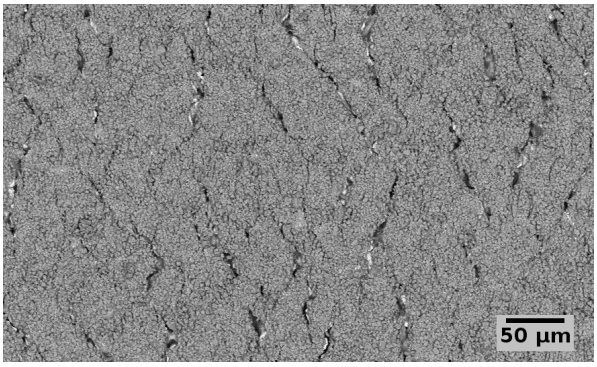

Fig. 3(c). Surface SEM view in BSE mode of the oxide scale on AISI 304L during tensile test (28% of strain)

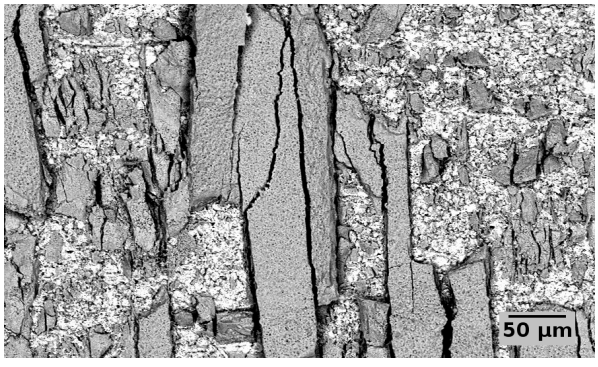

Fig. 3(c). Surface SEM view in BSE mode of the oxide scale on AISI 304L during tensile test (25% of strain)

These behaviors can be discussed in relation with sulphur concentration. Presence of impurities such as sulfur in the alloy may affect the scale microstructure. AISI 303 scale is iron rich. Iron oxides are known to be less protective [5] and their growth is ensured by cationic diffusion. The metal atoms are incorporated in the oxide at the metal/oxide interface and transferred across the interface. Since the oxide scale grows predominantly by an outward flux of cations, sulfur is believed to stay at the metal/oxide interface [1]. A relative enrichment of S occurs induced by the metal depletion leading to a lower adhesion of the oxide. On the contrary in the case of an oxide scales grown by oxygen inward diffusion, the interface moves inward and can incorporate sulfur from the alloy. The interface is the place of a chemical reaction, and sulfur is more likely to be integrated in the oxide rather than accumulated at the interface.

4. CONCLUSION

Two austenitic stainless steels, AISI 304L and AISI 303, containing 0.025 and 0.249 wt.% S were oxidized in thermobalance at 1000°C for 50h. For AISI 303, the parabolic rate constant is about one order of magnitude higher than AISI 304L. The oxide scale is thicker and brittle and richer in iron than the one obtained on AISI 304L. During tensile test, spallation occurs in the oxide scale of the AISI 303, but not in the 304L steel. In the 304L steel, instead of oxide scale buckling and spallation, the transverse cracks opened, following the ductile deformation of the underneath substrate.
These results are discussed in relation with sulphur concentration. The difference in scale chemistry and microstructure may be linked with sulfur content. Iron oxides growth is ensured by cationic diffusion. The metal atoms are incorporated in the oxide at the metal/oxide interface and transferred across the interface. Since the oxide scale grows predominantly by an outward flux of cations, sulfur is believed to stay at the metal/oxide interface. A relative enrichment of S occurs induced by the metal depletion leading to a lower adhesion of the oxide.

Acknowledgements

This work has been supported by National Center for Scientific Research (CNRS, France) through the Projet International de Coopération Scientifique (PICS) Adherons!2 and Russian Foundation for Basic Research (RFBR) Ref n° 13-08-91053-CNRS_a.

References.

[1] F. H. Stott, G. C. Wood and J. Stringer, “The influence of Alloying Elements on the Development and Maintenance of Protective Scales”, *Oxidation of Metals*, Vol. 44, Nos. 1/2 (1995), pp. 113-145.
[2] T. Gheno, D. Monceau, D. Oquab, Y. Cadoret, “Characterization of Sulfur Distribution in Ni-Based superalloy and Thermal Barrier Coating After High Temperature Oxidation: A SIMS Analysis”, *Oxidation of Metals*, Vol. 73 (2010), pp. 95-113.
[3] J.-P. Petit, M. Mermoux, Y. Wouters, A.Galerie and C. Chemarin, “Study of the Thermal Oxidation of Fe-15 Cr by Combined Raman and Photoelectrochemical Imaging”, *Materials Science Forum*, Vols. 461-464 (2004), pp. 681-688
[4] D. Oquab, D. Galy, C. Josse, A. Freulon, Y. Thebault, C. Charvillat, J. Esvan, O. Marsan; High temperature oxidation induced austenite to martensite phase transformation in austenitic 304L stainless steel at 1000°C(to be published).
[5] D. Young, High Temperature Oxidation and Corrosion of Metals, Elsevier Corrosion Series (2008)

Mechanisms of Localized Corrosion in Boiler Combustion Gas Environment

Yuuzou Kawahara[1,*)]

[1)] Dai-Ichi High Frequency Co., Ltd., Surface Treatment Dev., Kawasaki 210-0866, Japan
e-mail: y-kawahara@dhf.co.jp

1. INTRODUCTION

Many types of localized corrosion are observed according to environmental and material conditions in boilers burning biomass, waste and fossil fuels. These localized corrosions are actually difficult to predict and inspect on site. Therefore understanding for the cause of localized corrosion is considered to be important to maintain long life time with safety service in high temperature facilities. Localized corrosions are classified to two types, i.e. 1) Macroscopic localized corrosion such as pitting, wedge-like corrosion near welded parts, groove-like in fin welded parts etc. and 2)Microscopic localized corrosion such as intergranular corrosion, selective corrosion, internal corrosion etc.
This presentation shows the results of consideration for the form and cause of typical macroscopic localized corrosion in boilers exposed to many kinds of combustion gas environments.

2. EXPERIMENTAL

Localized corrosions have been experienced in the following boiler tubes.

1) Fossil fuel (heavy oil) burning boiler : Waterwall and Superheater
2) Biomass, Waste to energy boiler : Superheater

Corroded samples were investigated by microstructural observation and EPMA. Furthermore analyses of corrosion environments (deposits and gas composition) and operating conditions were carried out according to relating corrosion factors summarized in Fig.1. The cause of localized corrosion was determined considering mixed factors (material, chemical, mechanical), its morphologies and behavior of protective oxides layer in detail. In any cases, laboratory reproducing tests were done to clarify main factor of corrosion.

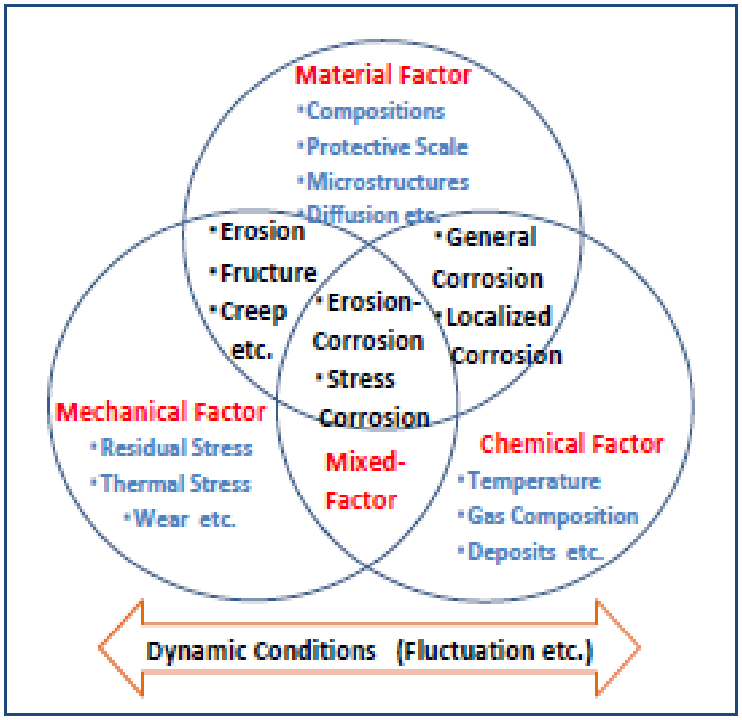

Fig.1 Schematic illustration of localized corrosion factors

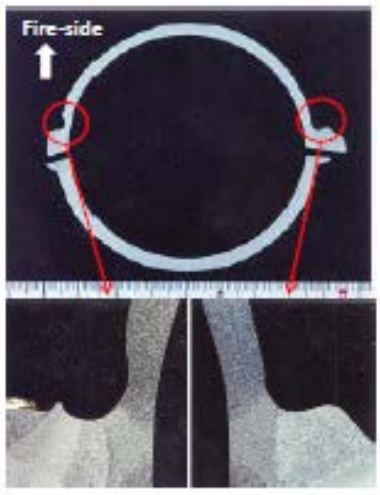

Fig.2 Groove-like corrosion in fin welded waterwalls of heavy oil fired boiler by formation of low melting point deposits

3. RESULTS AND DISCUSSION

3.1. Heavy Oil Boiler

1) CASE-1 : Groove-like corrosion along fin-welded line of membrane waterwall has been observed in heavy oil (including reforming oil) fired boiler and pulp recovery boiler etc. that are burning high sulfur fuels. An example of cross- sectional view is shown in Fig.2. Corrosion rate of groove is 0.15~0.34mm/year and approx. two times higher than that in top of tube [1]. Cause of corrosion was mainly due to chemical conditions, i.e. $O2/SO_3$-rich gas atmosphere without H_2S and formation of low melting point deposits that includes Sodium Hydrogen-sulfate ($NaHSO_4$,mp:186℃) and Sodium Pyro-sulfate ($Na_2S_2O_7$,mp:401℃). Light blue colored thick molten deposits and $FeSO_4$ as corrosion products were detected along with fin welding parts. Such deposites are formed in the limited gas condition of high-P_S and high-P_{O2} under thick ash deposition. Iron oxides of tube material was dissolved into deposits and not detected near fin weldings, otherwise protective oxides layer was formed near the top of tubes that don't corrode so large.

2)CASE-2 : Pock-marked surface was formed in superheaters of boiler burning bad heavy oil including much S,Ca,Si-rich ash contaminants as shown in Fig.3. In this position, local deposition of sticky ash and spalling-off of scale was found in a lower part of tubes exposed to combustion gas with reducing gas components. From EPMA results of damaged tube, local deposition of glass-like molten oxides with much Ca,Si oxide mixture that has relatively low melting point. Also many cracks of oxides layer on tube was observed. This type of corrosion was considered to occur by cyclic progress of accelerated sulfidation due to low P_{O2} /high P_S conditions under molten Si-rich oxides deposits and break down of protective oxide scales.

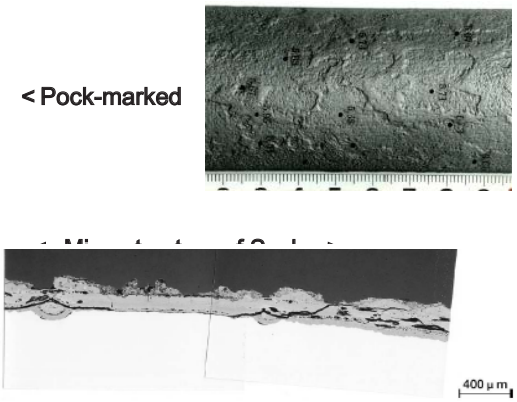

Fig.3 Pock-like surfaces formed on superheater tubes of feavy oil fired boiler by accelerlated sulfidation

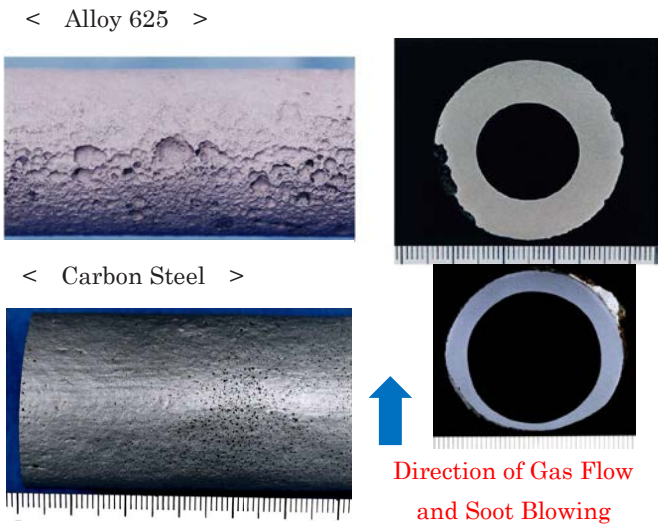

Fig.4 Pitting corrosion formed on Alloy 625 and carbon steel superheaters influenced by soot blowing in WTE boiler

3.2. Waste and Biomass Boiler

1) CASE-3 : Pitting corrosions are sometimes appeared in superheater of WTE and Biomass boilers. In severe corrosive environments, remarkable pittings were observed for highly alloyed corrosion resistant materials like Alloy 625. While for low alloy steels, pits are not so remarkable, but linear concaves appeared on descaled surface of carbon steels by crack formation for protective oxides layer as shown in Fig.4. The reasons why protective oxides layer break down are considered to be due to mechanical, thermal cyclic stresses in soot blower influenced area, chemical reaction with molten salts etc. Such factors are considered to be mixed each other and work for initiation of pitting [2]. Progress of these pits are controlled by mixed oxidants gas reactions such as chlorination, sulfidation and oxidation under condition formed by deposits etc. In the case of less corrosion-resistant materials that form of weak protective oxides layer, formation of large pits are difficult, and almost continuous scale spallation is connected to "erosion-corrosion " behavior .

2)CASE-4 : Wedge-like corrosion for welding parts is observed in welded joint of different materials such as Stainless steel/Carbon steel and Alloy 625/Cr-Mo steel etc. in WTE and Biomass boiler superheaters. Particularities of this corrosion are those 1) occur at metal temperature lower than melting point of deposits, 2) corrosion rate is larger in low corrosion

resistant material, but another material is corroded slightly in bonding part of weld joint and 3) corrosion progress along bonded line as shown in Fig.5. Corrosion factors are mainly due to break-down of protective oxides layer by thermal stress based on difference of thermal expansion between both materials and severe corrosion environment by large temperature fluctuation etc. in the bonding part. Same corrosion phenomena can be realized under temperature fluctuation conditions in laboratory temperature gradient test shown in Fig.5. This type of corrosion is difficult to occur under constant thermal condition [3].

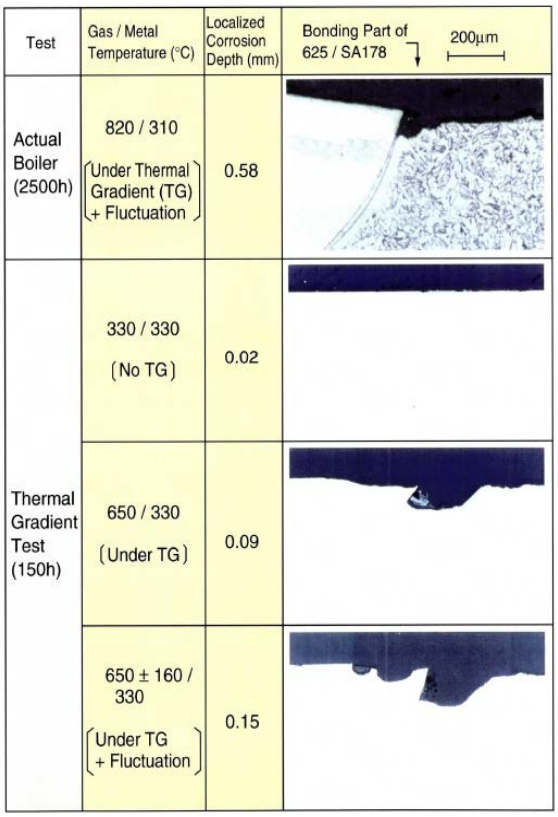

Fig.5 Edge-like corrosion formed in weld-joint of WTE superheater and in specimen after laboratory temperature gradient corrosion tests

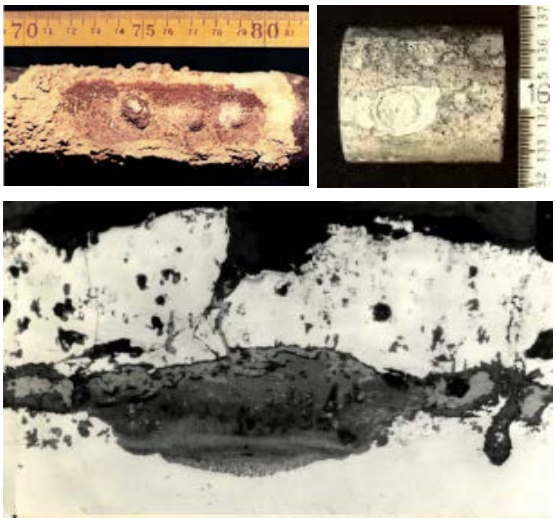

Fig.6 Localized corrosion formed on superheater specimen (carbon steel) exposed to WTE boiler

3.3. Localized corrosion in Coatings

Localized corrosion is the main deterioration pattern of corrosion resistant coatings in boiler. Coating materials are highly corrosion- resistant in almost cases, but if there are small initial defects, such as blow holes, inclusions of oxides formed by it's processing etc. and cracks, disbondings etc. formed by deterioration of coatings in operation, these become start points of localized corrosion. Fig.6 shows an example of localized corrosion in aluminized steel in WTE boiler environment. It is considered to be same phenomena that recognized in protective oxides layers, i.e. ceramics coating in these cases, mentioned above. Also same deterioration by sulfidation has been observed in 50Cr50Ni alloy spray coating layers etc. on waterwall tubes used for long years in heavy oil and coal fired boilers.

3.4. Mechanisms of localized corrosion

Flow diagram explaining mechanisms and factor of localized corrosion attack is shown in Fig.7. Localized corrosion is considered to be initiated by formation of defects on protective oxides layers and also on coating layers, and propagates by multi-oxidant gas reactions of chlorination/sulfidation/oxidation according to corrosive environment. In many cases, it is clarified that chemical, mechanical and material factors influence with individually or mixed conditions for break-down of protective oxides layer from results of scale analyses and simulated laboratory tests etc. mentioned above. Also corrosion scales show lamellar structures formed under the fluctuation condition of temperature and composition etc. in many cases,

also such dynamic condition acts as acceleration factor for localized corrosion. Therefore considerations of fluctuation are important to solve fire-side corrosion problems and estimation of durability in practical boiler.

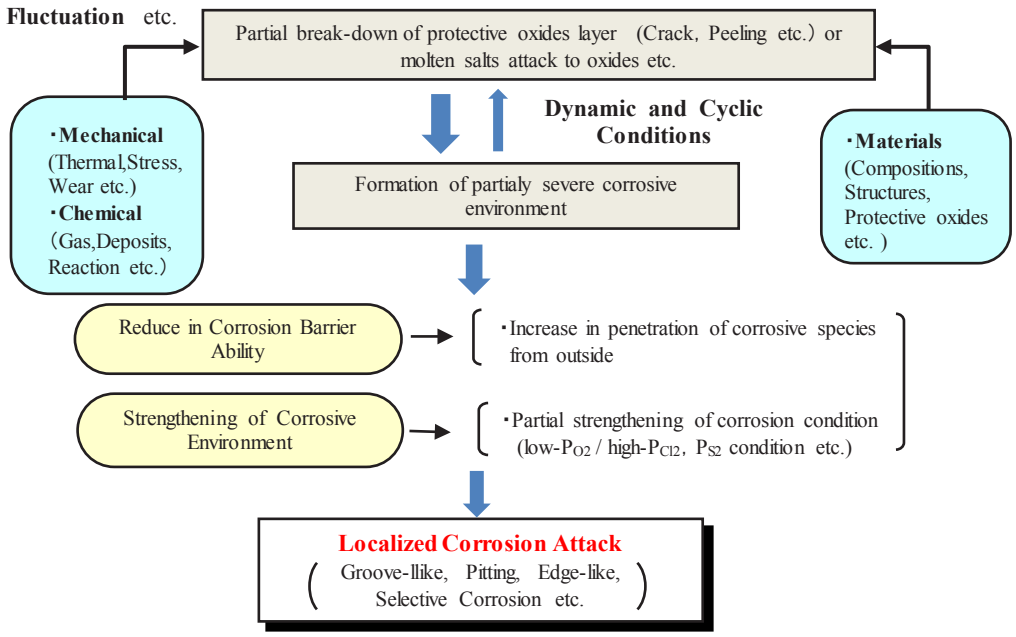

Fig.7 Flow diagram explaining mechanisms and factor of localized corrosion

4. CONCLUSION

Localized corrosion phenomena formed in many kinds of high temperature corrosive environments and those factors were considered in this study. Localized corrosion starts from partial differences of corrosive environment based on formation of molten deposits, break down of protective oxides or difference of microstructures in materials etc. Commonly high temperature corrosion conditions in actual boilers are not homogenous, and it's dynamic. Therefore considerations for these fluctuations are important to precisely evaluate the life time and corrosion protection methods. More quantitative studies to prediction methods are expected in the future.

References

[1] Kawahara Y., Journal of Japan Boiler Association, No.335, February, (2006), pp.15-26.
[2] Kawahara Y., Corrosion Science, 44, (2002), pp.223-245.
[3] Kawahara Y., Materials and Corrosion, 57, No.1 (2006), pp. 60-72.

How stress and temperature effect the high temperature corrosion mechanisms in Waspaloy in various gas/catalysts environments

Phillip Dowson[1,*], David Dowson[1], Hiroshi Yakuwa[2], Shigeru Sawada[3]

[1] Materials Engineering, Elliott Group Ebara Corporation, Jeannette, Pennsylvania, USA
[2] Materials Engineering Group, Ebara Corporation, Fujisawa, Japan
[3] Elliott Ebara Turbomachinery Corporation, Sodegaura, Japan

Email: pdowson@elliott-turbo.com, ddowson@elliott-tubo.com, yakuwa.hiroshi@ebara.com, sawada.shigeru@eetc.ebara.com

1. INTRODUCTION

FCC expanders operate in environments that can be both very erosive and corrosive. The source of erosion is spent catalyst from the FCC process that has not been recovered by separators and cyclones. In general, FCC catalyst, which is very abrasive, is comprised of a mixture of zeolite, active alumina, silica-alumina, clay, rare earth oxides, and other components. Under normal operating conditions, the catalyst concentration in the flue gas is on the order of 100 ppm. During upset conditions however, the catalyst content may exceed 1500 ppm. Although erosion in FCC expanders is an important concern, the current discussion will instead focus on how the corrosive environment in FCC expanders influences the mechanical properties and subsequent life of rotating components, i.e., turbine blades. A number of factors exist that make the FCC expander environment, relative to other Turbomachinery, very aggressive. These factors in part include the elevated temperatures under which expanders operate. At elevated temperatures creep and gaseous corrosion are important concerns. Therefore, the blades and rotor disks are fabricated from either iron or nickel-base superalloys. The nature of corrosive attack is primarily influenced by the type of crude oil stock, which in turn, has a bearing on the resulting flue gas composition and the nature, and quantity of additives injected into the FCC process.

Over the years, there have been a number of power recovery turbine blade failures that have occurred in units that operated under a partial combustion mode (for reasons unrelated to erosion, overheating, etc.). Typical flue gas inlet temperatures can range from 1202°F to 1400°F (650°C to 760°C). The fractures investigated have originated in the upper land of the blade root (Figure 1). Subsequent investigations have defined the factors that may give rise to failures in this location. Several important characteristics are noted. One such feature is that relatively thick corrosion products developed in the root section of the blade and disk. These corrosion products are primarily comprised of Cr_2O_3, CrS, and Ni_3S_2. In addition to being relatively thick, the corrosion products were found to be prone to cracking. As a result of this cracking, growth of the corrosion product into the metal substrate occurred. As described in detail later, the presence of such an oxide penetration acts as if it were a crack in the blade material. It was also observed that the fracture surfaces from the failed components were almost totally intergranular with sharp facet features. This suggests that the blade failed in a manner related to a stress/high temperature corrosion mechanism, i.e. some form of embrittlement effect. Both the blades and rotor disks are fabricated from nickel base alloys (Waspaloy). One important feature that was observed is that the gaps between the blade root and rotor disk were packed with regenerated catalyst residue. Initially it was thought that this catalyst was innocuous. However as will be shown in this tutorial, the regenerated catalyst has a detrimental effect on Waspaloy's fracture toughness.

2. EXPERIMENTAL

To better understand the relationship between temperature stress and corrosive environment a series of tests were performed to assess the role played by the catalyst, samples of regenerated catalyst taken from various expander locations were encapsulated in seamless Waspaloy tubes. One end of the Waspaloy tube was seal welded and the other end was crimped closed. The catalyst-filled Waspaloy tubes were placed in a furnace and heated at 1292°F (700°C) for 120 to 168 hours. A controlled Waspaloy tube with no catalyst present was also placed in a furnace and heated at 1292°F (700°C). A total of eight tubes were tested. After exposure, the tubes were sectioned and examined metallurgically. The results of the testing showed that with the catalyst present, significant amounts of corrosion (a layer ~ 40 μm thick) were observed. Analysis with x-ray indicated the corrosion product to be comprised primarily of Cr, Ni, O and lesser amounts of S.

Another feature observed was the cracking of the Waspaloy tubing (Figure 2), which was intergranular and exhibited brittle characteristics similar to actual blade failures. It also appeared that the cracking was related to stress, in that the cracks originated from the crimped tube ends and propagated to the tube center. In regions near the tube center where the stresses were low, crack growth was arrested. As a result of these observations, a set of experimental tests were undertaken in an effort to quantify a relationship between stress, temperature, and the onset of cracking in catalyst environment.

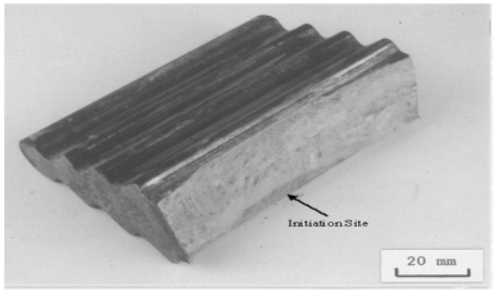

Figure 1. Illustration of a FCC Power Recovery Turbine Blade Failure and Showing Location of Initiation Site, (as Indicated by the Arrow).

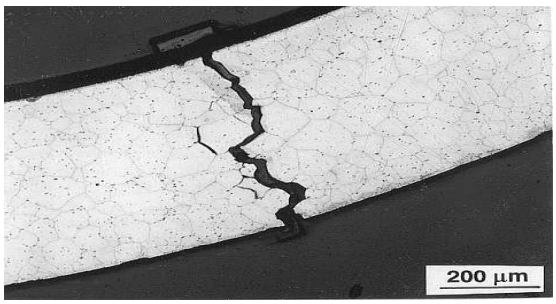

Figure 2. Crack Formation that Occurred in a Waspaloy Tube Filled with Regenerated FCC Catalyst

High Temperature Mechanical Testing

Stress rupture tests were conducted on notched combination Waspaloy bars under five different sets of "environmental conditions." The results of the tests are shown in Table 1. All tests were conducted from the same heat of AMS 5704, Waspaloy bar.

Table 1. Stress Rupture Test Results.

TEST #1			
Temperature F (C)	**Stress (MPa)**	**t_f(hr)**	**Location of Failure**
1292 (700)	482	663.3	Smooth Section
1202 (650)	654	931.3	Smooth Section
1112 (600)	757	2667+	Did Not Fail
TEST #2			
Temperature F (C)	**Stress (MPa)**	**t_f(hr)**	**Location of Failure**
1292 (700)	482	259	Smooth Section
1202 (650)	654	350	Smooth Section
1112 (600)	757	346	Smooth Section
TEST #3			
Temperature F (C)	**Stress (MPa)**	**t_f(hr)**	**Location of Failure**
1292 (700)	482	0.2	Notch
1292 (700)	482	2.3	Notch
1292 (700)	351	0.9	Notch
1292 (700)	234	334.9+	Did Not Fail
1292 (700)	234	333.6+	Did Not Fail
1202 (650)	654	3.3	Notch
1202 (650)	475	355.6+	Did Not Fail
1112 (600)	757	13	Notch
1112 (600)	757	12.2	Notch
*1022 (550)	137	50.7	Did Not Fail
*Cool down and unload; replenish with new catalyst			
**1022(550)	137	69.2	Did Not Fail
**Cool down and unload; replenish with new catalyst			
1292 (700)	70	0.3	Notch
TEST #4			
Temperature F (C)	**Stress (MPa)**	**t_f(hr)**	**Location of Failure**
1292 (700)	482	70+	Did Not Fail
1292 (700)	550	118+	Did Not Fail
TEST #5			
Temperature F (C)	**Stress (MPa)**	**t_f(hr)**	**Location of Failure**
1292 (700)	482	119+	Did Not Fail

For Test #1, notched combination creep rupture specimens were machined from the as-received Waspaloy bar in accordance with ASTM E292. These bars were directly tested in air atmospheres. For Test #2, the machined specimens were given a sulfur impregnation treatment. This treatment was performed using an evacuated quartz tube, backfilled with argon that contained the notched combination specimen and small amount of sulfur. The sealed quartz tube was then heat treated at 1472°F (800°C) for 100 hr. This treatment resulted in the formation of subsurface CrS precipitates (Figure 3).

For Test #3, a specifically modified creep rupture bar was utilized for insertion into a designed stainless steel chamber (Figure 4) that was filled with 33 gms of regenerated catalyst taken from a partial combustion FCC unit. The metallic species present were assumed to exist in the oxide form. A series of modified stress-rupture tests with this catalyst were performed under various load and temperature conditions.

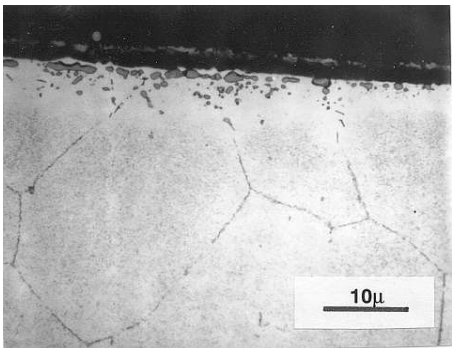

Figure 3. Illustration of Internal CrS Precipitates that Formed in a Waspaloy Coupon Heated in a Quartz Tube, Containing Sulfur at 1472°F (800 °C) for 100 h.

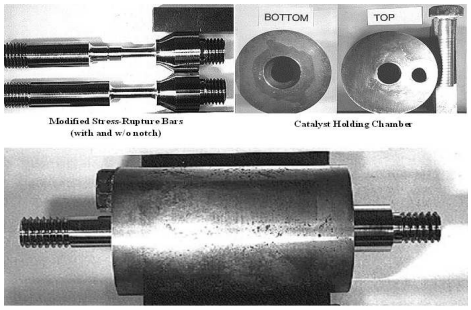

Figure 4. Illustration of the Modified Catalyst Stress-Rupture Test Arrangement with the Catalyst Holding Chamber and Modified Stress-Rupture Bar

For Test #4, similar tests to Test #3 were done except that the regenerated catalyst was taken from a complete combustion FCC unit.

For Test #5, the catalyst was the same as that used for Test #3, except that the catalyst was prebaked at 1292°F (700°C) for eight hours prior to testing. Two procedures were used to determine the gaseous species being evolved from the heated catalyst through two extraction methods. The first attempt was made by heating the catalyst to 1292°F (700°C) under a flow of nitrogen, passed through a charcoal filter, and the filter washed with solvent to collect any residue. For the second method, the evolved gas was passed through an impinger filled with 10% nitric acid in order to capture any metallic compounds. In both cases, the amount of species evolved was too small to detect.

3. RESULTS AND DISSCUSSION

The stress rupture tests conducted on the as-received and sulfur impregnated specimens found that the specimens failed due to creep. As listed in Table 1, the failure times were typically in the hundreds of hours. In addition, specimens exposed under these conditions did not exhibit notch sensitivity: i.e., all failed in the smooth section of the specimen. In the case of the modified catalyst stress-rupture tests, Test #3, significant and important differences were found. Under these conditions, rapid failure on the order of minutes occurred in the notched section of the specimen. As shown in Figure 5, failure occurred via intergranular crack propagation with sharp facet features.

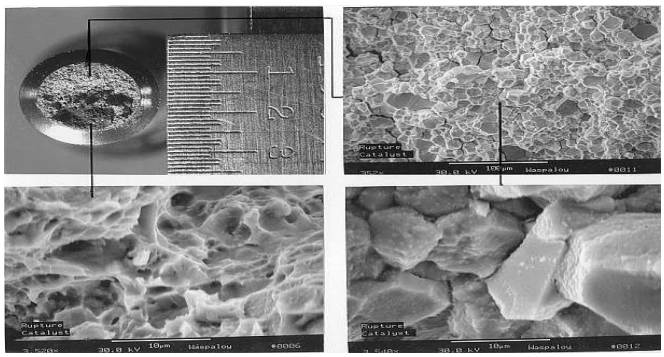

Figure 5. Fracture Surface of a Specimen Tested Under Modified Catalyst Stress-Rupture Test. Exposure Conditions: T = 1292°F (700°C), σ = 482 MPa, t_f = 20 minutes.

Regenerated catalyst taken from a fully combustion FCC unit did not exhibit rapid failure even at higher stress values (Test #4). Also, in the case of Test #5, the baked catalyst did not exhibit rapid failure.

The experimental tests performed clearly showed that stress played an important role in the time to fracture under highly corrosive conditions. To understand further the role of stress Waspaloy specimens (Figure 6) were subjected to static and dynamic stresses in a sulfidation environment. It was confirmed that the notch-shaped sulfidation/oxidation penetrations were grown like Figure 7.

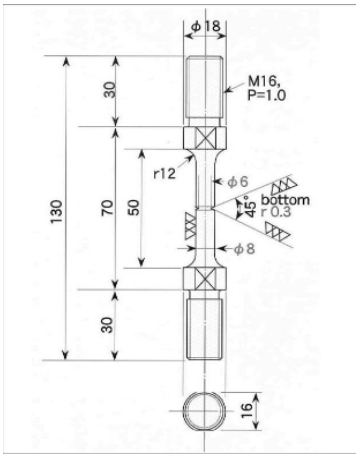

Figure 6. Size of test specimen

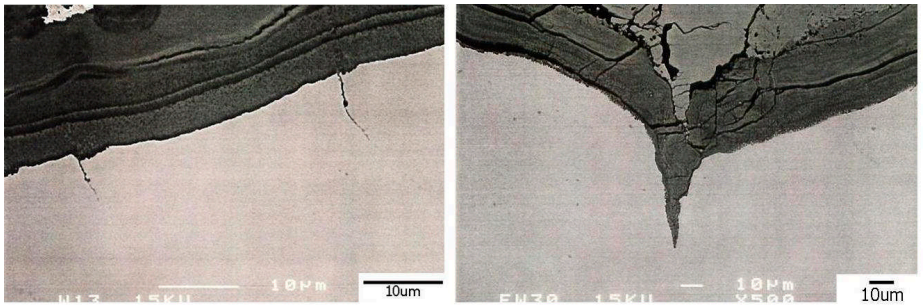

(a) under static stress of 60 kgf/mm² for 96 hours (b) under dynamic stress of 20±12 kgf/mm² for 192 hours

Figure 7. Oxide/sulfide wedges formed under static and dynamic stresses in an N_2-3%H_2-0.75%SO_2 gas mixture at 600°C.

A case study will be shown where the effect of stress whether cyclic or static in a sulfidation environment was observed on the cracking of hot gas expander blades during service (Figures 8 & 9).

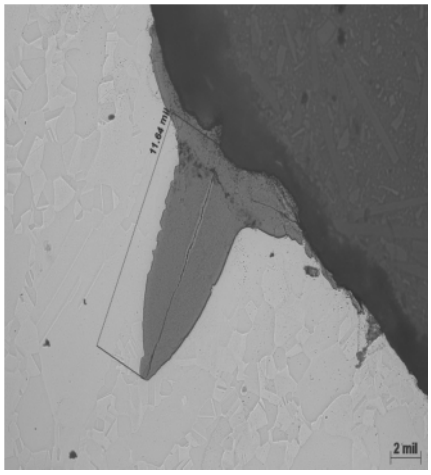

Figure 8. High magnification of the oxide wedge indicating its length to be approximately 11.64 mils.

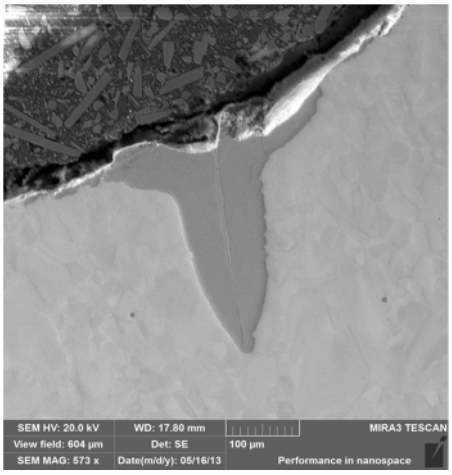

Figure 9. SEM micrograph of the oxide wedge on blade #33.

4. CONCLUSION

The paper clearly shows the effect of stress on the rapid embrittlement of Waspaloy in a partial combustion gas and catalyst state environments. A fracture mechanics model was developed to rationalize the observed blade failures. The model incorporates the influence of oxide wedges, Waspaloy reduced fracture toughness and the stress profile through the blade root. Laboratory testing shows that both static and cyclic stresses influenced the formation of oxide wedges and there depth of penetration in a corrosive environment

ACKNOWLEDGEMENT

The authors are grateful for the support from the Materials Engineering Department and Global Technical Services and recognize Elliott Group and Ebara Corporation for permission to publish the paper.

REFERENCES

[1] Dowson, P., Rishel, D. M., and Bornstein, N. S., 1995, "Factors and Preventive Measures Relative to the High Temperature Corrosion of Blade/Disk Components in FCC Power Recovery Turbines," Proceedings of the Twenty-Fourth Turbomachinery Symposium, Turbomachinery Laboratory, Texas A&M University, College Station, Texas, pp. 11-26.

[2] Sehitoglu, H., 1992, "Thermo-Mechanical Fatigue Life Prediction Methods," Advances in Fatigue Lifetime Predictive Techniques, ASTM STP 1122, Mitchell, M. R. and Landgraf, R. W., Eds., American Society for Testing and Materials, Philadelphia, pp. 47-76.

Structural Stability of Diffusion Barrier Coating at High Temperatures based on Experimental Phase Diagrams

Shigeru Saito [1,*], Toshiyuki Takashima [1], Katsumi Miyama [1], Kazuya Kurokawa [2], and Toshio Narita [3]

[1]Faculty of Engineering, Hokkaido University of Science, 7-15-4-1Maeda, Teine-ku, Sapporo, 006-8585, JAPAN
[2]Faculty of Engineering, Hokkaido University, Kita13 Nishi8, Kita-ku, Sapporo, 060-8628, JAPAN
[3]DBC System R&D Co., Ltd, 3-515-1 Zenibako, Otaru, 047-0261, JAPAN

e-mail: saito-sg@hit.ac.jp

1. INTRODUCTION

Thermal barrier coatings (TBC) are used to protect the Ni-based superalloy in the turbine blades from such extremely hot combustion gases and internal air or steam cooling is employed to reduce the temperature rise of the base material[1]. However, even when TBC and cooling systems are employed, Ni-based single-crystal superalloys with high-temperature strength still need to be developed because the temperature of the base material is expected to exceed 1000 °C. One problem is inward diffusion of Al, which is placed in the bond coat coating layer for the purpose of forming protective scales Al_2O_3. Such diffusion reduces the concentration of Al and lowers the oxidation resistance of the coating. It has also been reported that diffusion of alloying elements in the substrate could lead to decrease in the mechanical properties of the Ni-based superaolly.

To prevent diffusion of Al into the substrate, a number of diffusion barrier coatings have been proposed[2]; however, after a relatively short oxidation time the barrier layer loses its layer structure, resulting in rapid, catastrophic oxidation. Narita et al. proposed a diffusion barrier coating with a duplex layer structure, containing the σ-phase of Re-Cr-Ni as the diffusion barrier layer. In this coating, the σ-layer was sandwiched between a Ni-based superalloy and Ni-aluminides in the Al-reservoir layer[3].

To elucidate the properties of the Re-Cr-Ni alloy, information regarding its phase diagram and diffusivity is required. It is essential to determine the structural stability of the sandwiched Re-Cr-Ni alloy layer. Narita et al. proposed that the diffusion barrier layer should be formed at high-temperature such as 1300 °C. In the present study, the phase diagrams of the Re-Cr-Ni, Ni-Al-Re, and Ni-Al-Re-Cr systems at 1150 °C were investigated.

2. EXPERIMENTAL

The starting materials used to prepare these alloy samples were Re powder (purity: 99.9 wt%), Cr powder (purity: 99.99 wt%), Ni powder (purity: 99.95 wt%), and Al powder (purity: 99.99 wt%). After weighing them, metal foams were produced by pressurization (load: 502 MPa). The metal foams were obtained by dissolution and solidification using an argon-arc melting furnace with a titanium getter.

The arc-melted samples for the heat treatment experiment were enclosed in transparent quartz tubes (φ12 mm) with a reduced pressure of approximately 5×10^{-4} Pa. After maintaining them at 1150 °C for 2500 h, the tubes containing the samples were crushed underwater to quench the samples.

After being heat treatment at 1150 °C for 2500 h, the surface of the quenched samples were mirror-polished using polycrystalline diamond abrasives. Cross sectional microstructures were observed using a scanning electron microscope (SEM), and the concentration profiles of Ni, Al, Re, and Cr across each sample were measured quantitatively by an electron probe microanalyzer (EPMA).

3. RESULTS AND DISCUSSION

Fig.1 shows a phase diagram for the ternary Re-Cr-Ni system at 1150 °C obtained in the present investigation[4]. From comparison of these results, the three-phase γ, α, σ region was close to that of Huang et al.[5], and the δ-phase was close to that of Slyusarenko et al.[6]

Fig.2 show a phase diagram for the ternary Re-Cr-Ni system at 1300 °C[7]. Tie lines obtained in the present investigation plotted on the phase diagram of Re-Cr-Ni system at 1150 °C. The compositions of the σ phase tie line with the γ and δ phases are plotted on the phase boundary line of the σ phase. The phase boundary line of the σ phase at 1300 °C was found to be approximately equal to that at 1150 °C.These results imply that at 1300 °C, the γ-single phase region expands and the γ-σ two-phase coexistence region contracts.

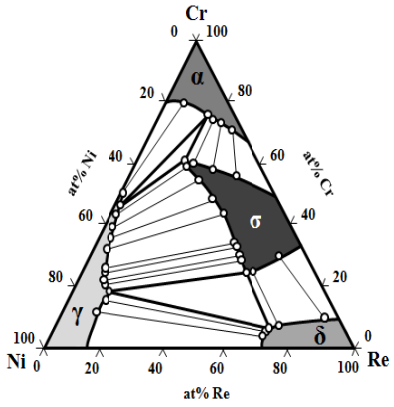

○Present investigation

Fig. 1 Isothermal section of ternary Re-Cr-Ni system at 1150 °C obtained from in thepresent investigation.

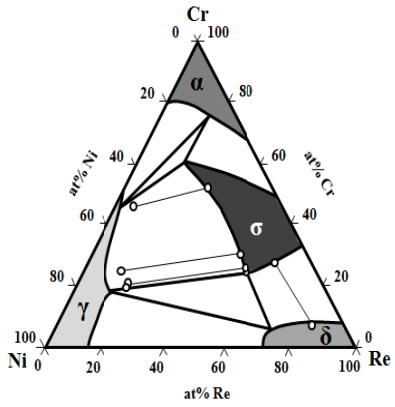

○Present investigation

Fig. 2 Tie lines obtained in the presentinvestigationplotted on the phase diagramof Re-Cr-Ni ternary system at 1150 °Creported bysaito et al.

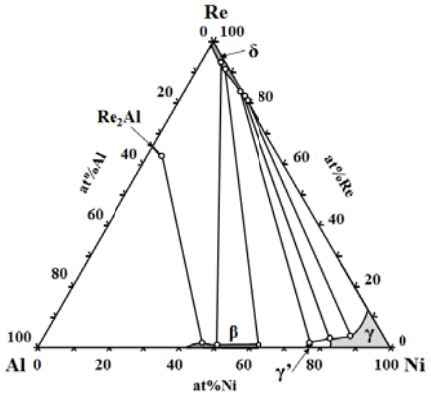

○Present investigation

Fig. 3 Isothermal section of ternary Ni-Al-Re system at 1150 °C obtained from in the present investigation.

Fig.3 shows isothermal sections of the Ni-Al-Re ternary system at 1150 °C reported by the authors[8]. There is no ternary intermetallic compound in the Ni-Al-Re system at 1150 °C. The δ-phase has tie-lines with γ-Ni, γ'-Ni_3Al, and β-NiAl for Al at less than 50 at%, while β-NiAl with more than 50 at% have tie-line with Re_2Al, respectively. Importantly, the solubility of Re in γ'-Ni_3Al and β-NiAl is very low, at less than 1.3 at% Re. In addition, the solubility of Al into the δ-phase is less than 1.8 at%.

Fig.4 shows the phase diagram for the 1150 °C experiments with Ni-Cr-Re system reported by the authors, as well as the phase diagram of the 1150 °C experiments with Ni-Al-Cr system reported by Kitajima et al.[9], where the cylindrical graphs represent the tie-line compositions of each phase. In addition, although the present experiment involves a quarternary Ni-Al-Re-Cr system, since we were unable to obtain a phase diagram for the quarternary system, Al and Re were plotted in the vertical direction in the phase diagrams for the Re-Cr-Ni and Ni-Al-Cr ternary systems, respectively.

In the Re-Cr-Ni system, as the Cr contents increased (i.e., Re contents decreased) in the γ phase, the solubility limits of Ni in the σ phase with tie-line to the γ phase increased from 19 at%Ni to 24 at%Ni. At the same time, it was clarified that the σ phase of the Ni-Al-Re-Cr system has a tie-line with the γ, γ', and β phases, which contain Re and Cr. The following tendencies were observed for these relations:

- When the solubility limits of Ni in the σ phase is in the range of 14.6~18.1 at%, the solubility limit of Al takes extremely low values in the range of 0.1~0.3 at%. On the other hand, when the solubility limit of Ni is reduced to 5.2 at%, the solubility limit of Al in the σ phase increases to 1.2 at%.
- When the concentration of Ni in the Ni-Al alloy is reduced, the solubility limit of Re in the γ, γ', and β phases decreases. In particular, the solubility limits of Re and Cr in β (48.7 at%Al) are extremely low, and the concentration of Ni in the σ phase, which has tie-lines with this β phase, decreases, while the Al concentration increases.
- As the concentration of Al in the β-phase increases from 48.7 at% to 56.0 at%, the tie-line relation changes from the σ phase to the Re_4Al_{11}-phase.

From the experimental results, in cases where the σ-phase is inserted as a diffusion barrier between a Ni-based superalloy and Al-reservoir, when an Al-rich β (56.0 at%Al) phase is introduced into the Al-reservoir, this will result in the breakdown of the σ-phase. On the other hand, it is suggested that when the concentration of Al in the Al-reservoir is within the range of γ (14.3 at%Al) to β (48.7 at%Al) phase, the phase stability of the σ phase can be maintained for extensive periods of time.

Fig.5 show the cross-sectional microstructure of the Ni-base single-crystal superalloy TMS-138 with the Rhenium-base diffusion barrier coating after heating at 1150 °C in air for 100 h[10]. The outer layer is apparently composed of two phases, as shown in Fig. 5. The dark phase contains (63-66) Ni, (30-32) Al, and (6-7) Cr, and the light phase contains (72-73) Ni, (20-22) Al, and (6-7) Cr. The dark and light phases were inferred from their chemical compositions to be β-NiAl and γ'-Ni_3Al, respectively. The intermediate layer of the σ (Re-Cr-Ni)-phase contains (42-52) Re, (25-30) Cr, and (15-25)

Ni, and the Al content in the σ-layer is small, less than 0.5 %.

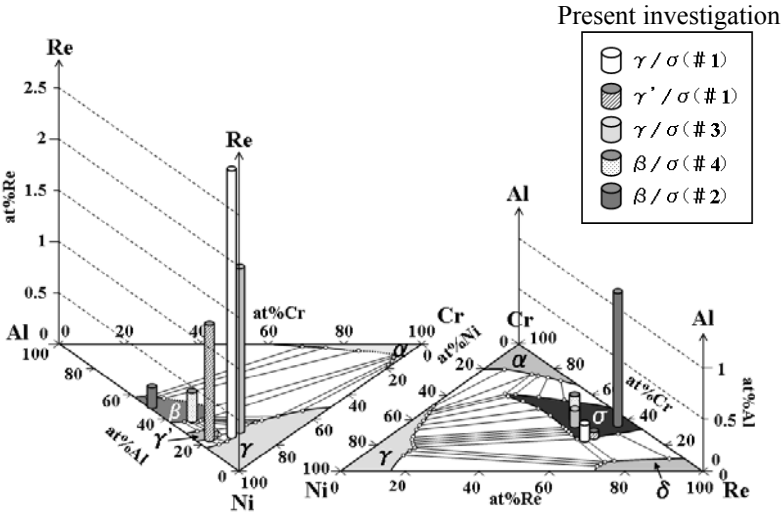

Fig. 4 Terminal composition of each phase in Ni-Al-Re-Cr system at1150 °C obtained in the present investigation.

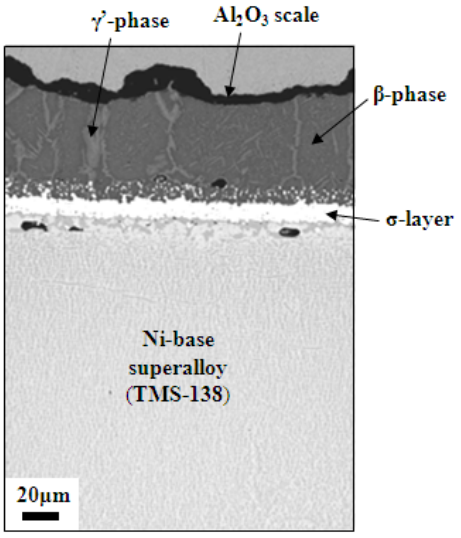

Fig. 5 Cross sectional microstructure of the Ni-base single-crystal superalloy with the Rhenium-base diffusion barrier coating after heating at 1150 °C.

4. CONCLUSION

Compositions with tie-lines between the σ and (γ, γ', β) phases in the quaternary Ni-Al-Re-Cr system were investigated by heat-treating various quaternary Ni-Al-Re-Cr alloys in vacuum at 1150 °C for times up to 2500 h. The results obtained may be summarized as follows.

(1) The concentration profiles of the γ phase became flat after short heat treatment, but longer times of up to 2500 h were required to achieve the same effect for the σ phase.

(2) The tie-line compositions (at%) of each phase at 1150 °C were experimentally determined.

(3) As the concentration of Al in the β phase increases from 48.7 at% to 56.0 at%, the tie-line relation shifts from the σ phase to the Re_4Al_{11} phase.

References

[1] Y. Matsunaga et al., "Thermal Barrier Coating System for Aircraft Jet Engine," *Ceramics Japan*, Vol. 39, No. 4 (2004), pp.286-290.

[2] H. Hosoda et al., "Design of Oxidation Resistant Coating Based on IrAl Alloy," *The Third Pacific Rim International Conference on Advanced Materials and Processing*, 1998, pp. 2379-2384.

[3] T. Narita, "Novel Coatings for Ultra-High Temperature Application," *Journal of High Temperature Society*, Vol. 28, No. 4 (2007), pp.135-143.

[4] S. Saito et al., "Experimental Determination of Isothermal Phase Diagram at 1150 °C in the Ternary Re-Cr-Ni System," *J.JAPAN Inst. METALS*, Vol. 72, No. 2 (2008), pp.132-137.

[5] E. M. Slyusarenko et al., "Ternary System of Nickel and Rhenium with Transition Metals," *Journal of Alloys and Compounds*, Vol. 264 (1998), pp.180-189.

[6] W. Huang and Y. A. Chang, "A Thermodynamic Description of the Ni-Al-Cr-Re System," *Materials Science and Engineering A*, Vol. A259 (1999), pp.110-119.

[7] S. Saito et al., "Tie-Lined Compositions of the σ and (γ, δ) Phases in the Re-Cr-Ni System at 1300 °C," *J.JAPAN Inst. METALS*, Vol. 75, No. 6 (2011), pp. 361-365.

[8] S. Saito et al., "Phase Equilibria and Tie-Lined Compositions in a Ternary Ni-Al-Re System at 1150 °C," *J.JAPAN Inst. METALS*, Vol. 71, No. 9 (2007), pp.793-800.

[9] Y. Kitajimaet al., "Phase Equilibria of the Nickel-Aluminum-Chromium System at 1150 °C," *Materials Science Forum*, Vols. 522-523 (2006), pp.103-110.

[10] D. Sumoyamaet al., "Formation of a Rhenium-base Diffusion-Barrier Coating System of Ni-base Single Crystal Superalloy and its Stability at 1423 K," *Oxidation of Metals*, Vol. 68 (2007), pp.313-329.

Effects of Cu Content on the Oxidation and Dissolution Behavior of Fe-Cu Alloys

T. Nishimoto [1,*], H. Tanei [2], Y. Kondo [2] and K. Uemura [1]

[1] Advanced Technology Research Laboratories, Nippon Steel & Smitomo Metal Corporation, 20-1 Shintomi, Futtsu, Chiba Prefecture 293-8511, Japan

[2] Integrated Process R & D Divisions, Nippon Steel & Smitomo Metal Corporation, 20-1 Shintomi, Futtsu, Chiba Prefecture 293-8511, Japan

e-mail: nishimoto.g9h.takumi@jp.nssmc.com

1. INTRODUCTION

Understanding the oxidation behavior of steels at high temperature is important for steel making processes. In these processes, steels are heated and hot-rolled, and oxide scales are formed on the steel surface. During or after these processes, oxide scales are usually descaled by mechanical and/or chemical methods. Descalability greatly depends on the structure and amount of defects in the oxide scale[1-5]. For example, Si-containing steels have poor descalability due to the formation of an Fe_2SiO_4 (fayalite) liquid phase at the FeO/steel interface above 1443K. Therefore, it is important to clarify the effect of alloy elements on the oxidation behavior of steels under several conditions. The purpose of this study was to characterize the structure and elemental distribution in oxide layers formed on Fe-Cu alloys in air at 1073K and to investigate the relationship between the scale structure and dissolution of oxide scale in HCl solution.

2. EXPERIMENTAL

Fe-0.01, 0.05, 0.3, 0.5, and 1.0wt.%Cu alloys were prepared from high-purity electrolytic metals by vacuum melting. The oxidation specimens were cut to a size of 30 x 30 x 3 mm. Prior to the oxidation tests, the specimens were cleaned with acetone. The oxidation specimens were oxidized in air at 1073K for different durations, in order to obtain an identical scale thickness of approximately 30μm. The mass gains during oxidation were measured gravimetrically as a function of time, and the scale structure, distribution of each element, and identity of oxide phases were determined using field-emission scanning electron microscopy (FE-SEM EDS), electron backscatter diffraction (EBSD), and X-ray diffraction analysis (XRD). Dissolution experiments were conducted at 358K in 9%HCl solution with Fe ions. After dissolution in HCl, mass changes were measured at room temperature with an electronic balance.

3. RESULTS AND DISCUSSION

Fig.1 shows the changes in mass gain with time for Fe-Cu alloys at 1073K in dry air atmospheres. The oxidation rate decreased with increasing Cu content. In the initial stage of oxidation (~15-50sec), the weight gain of Fe-alloys was similar; however, after that, the oxidation rate of Fe-Cu alloys with high Cu content decreased significantly. The results show that the oxidation kinetics described by the parabolic rate law of diffusion controlled the oxidation. The calculated parabolic rate constants (kp values) were 7.2×10^{-8} ($mg^2cm^{-4}sec^{-1}$) at the initial oxidation of Fe-Cu alloys and 1.7×10^{-7} after the initial stage of oxidation on Fe-0.3wt.%Cu and Fe-1.0wt.%Cu, respectively.

The oxide scale on Fe-Cu alloys with low Cu content consisted of two layers: an outer Fe_3O_4 and an inner FeO. No decomposition into α-Fe and Fe_3O_4 was observed. In Fe-0.3wt.%Cu and Fe-1.0wt.%Cu alloys, a pure Cu layer was formed at the scale/alloy interface and the thickness of the Fe_3O_4 layer increased compared with Fe-0.01wt.%Cu and Fe-0.05wt.%Cu alloys. Furthermore, Fe_3O_4 precipitated in the FeO grain boundaries and many voids were formed around Fe_3O_4 precipitation. From the results of the oxidation tests, oxidation rate and scale structure were changed according to the Cu content. This is due to the formation of a pure Cu layer at the scale/alloy interface, which suppresses the diffusion of iron ions from the alloy substrate to the scale. Thus, oxygen was significantly supplied compared with the supplement of iron ions from the alloy substrate.

The changes in mass loss with time for Fe-Cu alloys in the dissolution test are shown Fig.4. The slope of the mass loss curves shows that the process of scale dissolution on Fe-Cu alloys can be divided into three steps. From the cross-sectional microstructure of oxide scale on the Fe-Cu alloys, Fe_3O_4 mainly dissolved in the first step, FeO, which is more soluble than Fe_3O_4 in HCl, dissolved in the second step, and alloy substrate dissolved in the third step. Fig.5 shows the finishing time of scale dissolution, which means oxide scale had completely dissolved, in each alloy. The finishing time

of scale dissolution was shorter with Cu content in Fe-Cu alloys because transition from the first step to the second step was faster. This difference in transition time should be caused by voids in the scale on high-Cu-content alloys, which promoted the supply of HCl solution to the inner FeO layer.

4. CONCLUSION

The oxidation and dissolution behavior of Fe-Cu alloys was investigated. The oxidation rate of Fe-Cu alloys decreased with increasing Cu content. Observation of scale cross-sections indicates that the structure of oxide scale and elemental distribution in oxide scale depend on the Cu content. The finishing time of dissolution in HCl was shorter with Cu content in Fe-Cu alloys. The dissolution behavior of Fe-Cu alloys also changes according to the Cu content because the dissolution rate is influenced by the structure and amount of defects in oxide scale.

References

[1] K. Yanagihara, S. Suzuki, and S. Yamazaki, "Microscopic Features in the Transition from External to Internal Oxidation in an Fe-6 mol.% Si Alloy Annealed under Various H_2O-H_2 Atmospheres," *Oxid. Met.* Vol. 57 (2002), pp. 281-296.

[2] T. Fukagawa, H. Okada, and Y. Maehara, "Mechanism of Steel Sheets Red Scale Defect Formation in Si-added Hot-rolled steel sheets," *ISIJ International.* Vol. 34, No. 11 (1994), pp. 906-911.

[3] M. Diéz-Ercilla, T. Ros-Yáñez, R. Petrov, Y. Houbaert, and R. Colás, "Oxidation of Silicon Steels," *Corrosion Engineering, Science and Technology*, Vol. 39, No. 4 (2004), pp. 295-300.

[4] M. Fukumoto, S. Hayashi, S. Maeda, and T. Narita, "Effect of Water Vapor on the Oxidation Behavior of Fe-1.5Si in Air at 1073 and 1273 K," *Oxid. Met*. Vol. 55 (2001), pp. 401-422.

[5] S. Hayashi and T. Narita,"Competitive Effect of Water Vapor and Oxygen on the Oxidation of Fe-5 wt.% Al Alloy at 1073 K," *Oxid. Met.* Vol. 56 (2001), pp. 251-270.

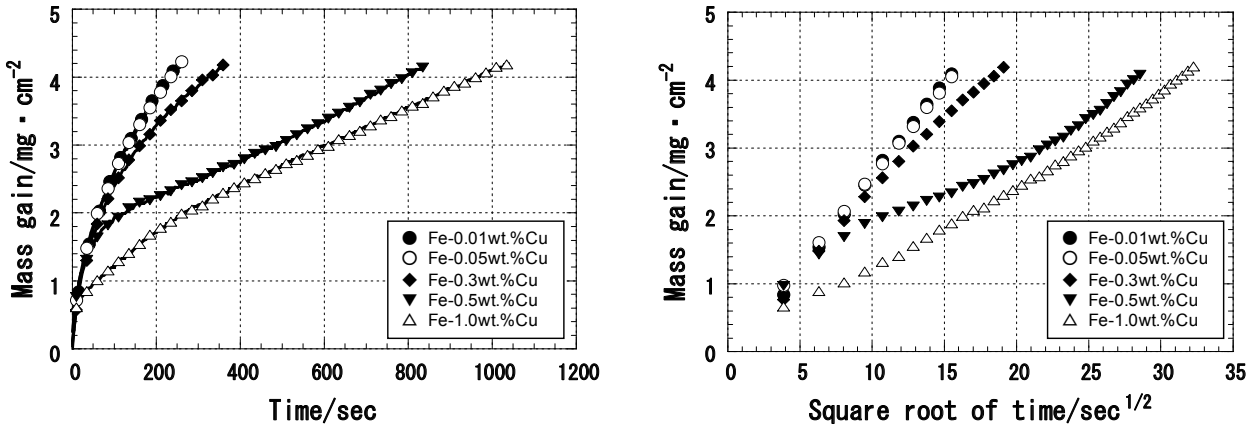

Fig. 1 Oxidation curve of Fe-Cu alloys at 1073K in dry air atmospheres.

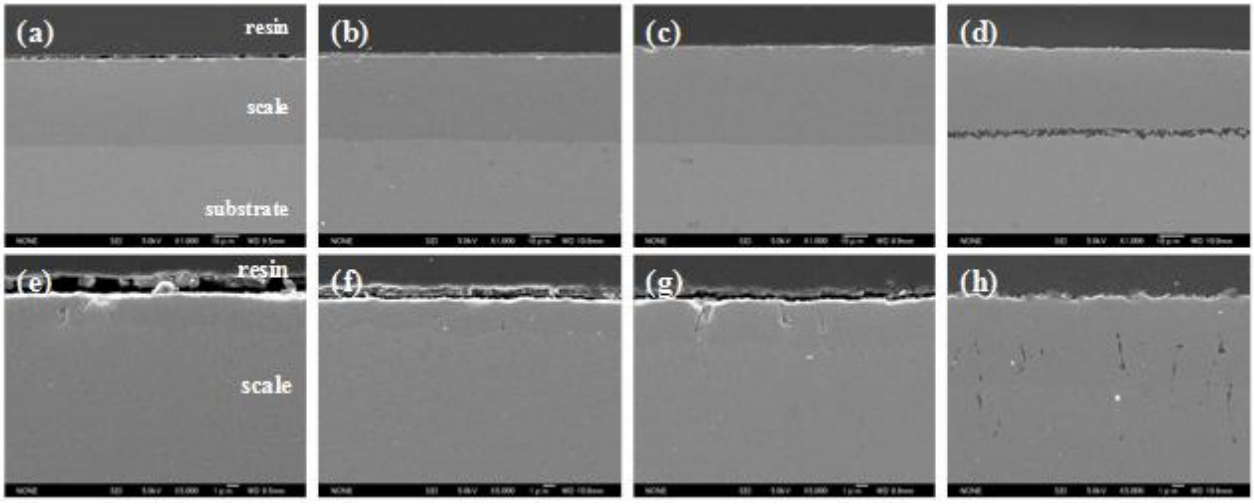

Fig.2 Cross-sectional microstructures of Fe-Cu alloys oxidized at 1073K in air.
(a)(e):Fe-0.01wt.%Cu (b)(f):Fe-0.05wt.%Cu (c)(g):Fe-0.3wt.%Cu (d)(h):Fe-1.0wt.%Cu
(e)-(h): high magnification of scale surface on Fe-Cu alloys

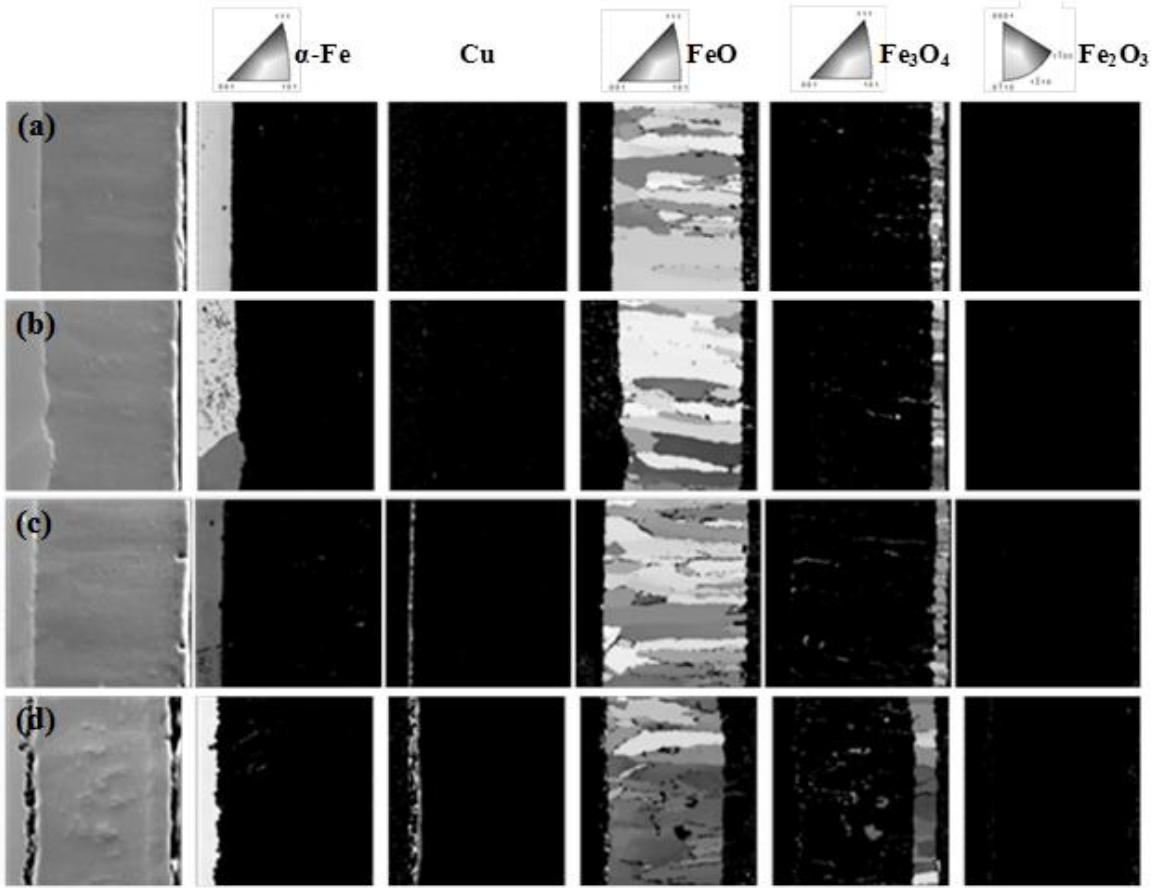

Fig.3 SEM images and phase maps of each iron oxide and α-Fe in the cross-sectional microstructures.
(a):Fe-0.01wt.%Cu (b):Fe-0.05wt.%Cu (c):Fe-0.3wt.%Cu (d):Fe-1.0wt.%Cu

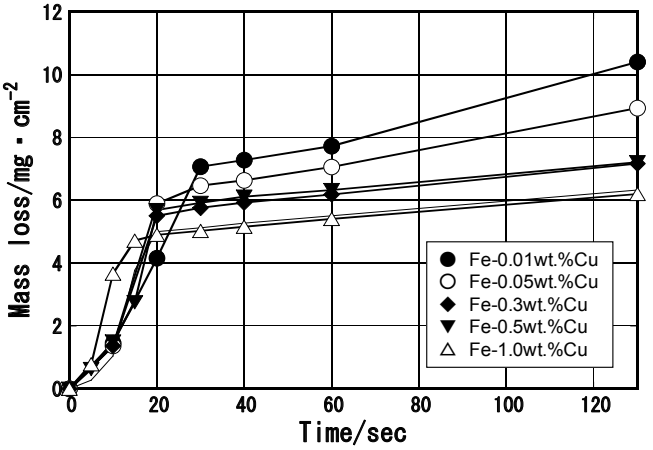

Fig. 4 Mass change of Fe-Cu alloys during dissolution in HCl solution.

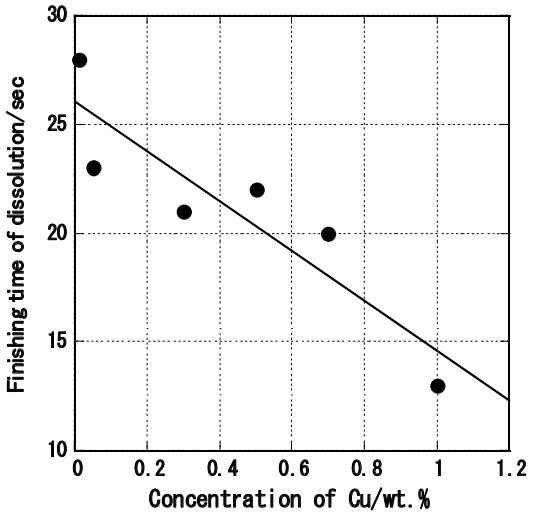

Fig. 5 Finishing time of scale dissolution in HCl solution on Fe-Cu alloys.

Inhibition of chromium volatilization on a 22 wt. % Cr austenitic alloy in wet environment containing traces of SO_2 and Na_2SO_4

Luciana Intiso[(1*)], N. Mortazavi [(2)], L-G. Johansson[(3)], M. Halvarsson[(2)]

[(1)] Centro Sviluppo Materiali S.p.A via di Castel Romano, 100 – 00128 Rome, Italy
[(2)] Department of Applied Physics, Chalmers University of Technology, SE-412 96 Göteborg, Sweden
[(3)] Department of Chemical and Biological Engineering, High Temperature Corrosion centre, Chalmers University of Technology, SE-412 96 Göteborg, Sweden

e-mail: l.intiso@c-s-m.it

1. INTRODUCTION

It is expected that coal-fired power plants will incorporate systems that enable the capture and sequestration of their CO_2 emissions. One of the promising technologies to reach this goal is oxy-combustion, where the fuel is burned in a mixture of oxygen and re-circulated flue gas. Due to the absence, or reduced volume, of nitrogen the re-circulated flue gas is enriched in CO_2, which makes the post-combustion extraction easier. The flue gas typically consists mainly of CO_2 (about 60 vol.%) and H_2O (about 30 vol.%) along with some N_2, O_2 and trace gases like SO_2 and NO_X. In addition, deposits can accumulate on the metal surfaces. In coal power plant a common deposit is Na_2SO_4 where the sodium and sulphur may exists as impurities in the fuel.

Both H_2O and CO_2 reduce the ability of alloys to form or maintain protective chromium-rich oxide scales, resulting in the formation of a less protective iron-rich oxide scales, influencing the materials corrosion resistance. It has been observed that the oxidation of most technical steels is faster in presence of water vapour [1,2] and carbon dioxide [3,4,5] than in air or dry oxygen. Indeed, when water vapour and carbon dioxide are also present, the oxidation rate can be one order of magnitude greater than in air or dry oxygen at certain temperatures.

Furthermore, the sulphurous corrosive components, such as SO_2 and sulphate-based salt components present in many commercial atmospheres, can contribute to severely degrade corrosion properties of alloys and accelerated corrosion can occur [6]. This process of deposit-induced accelerated oxidation is called hot corrosion. Most cases of sulphate-deposit induced accelerated attack occur when the deposit is liquid. In contrast, no catastrophic attack has been reported when the substance comprising the deposit exists as a gas [7] and when only SO_2 is present in the gas-phase [8,9,10,11], or when the Fe-Cr alloys can form solid sulphates at the scale/metal interface [12].

The aim of this work is to provide a detailed investigation of the effect of the salt-induced corrosion in presence of SO2 on 22 wt.Cr% (42Fe22Cr25NiWCuNbN) austenitic stainless steels. The 22 wt. Cr% (42Fe22Cr25NiWCuNbN) is a newly developed material with improved mechanical properties and high corrosion resistance due to the high Cr content. Due to its properties, the 22 wt.% Cr is an interesting material for the application in the new generation power plant at high temperature [13].

2. EXPERIMENTAL

Isothermal exposures were carried out up to 168 h at 700°C. Coupons of the alloy were exposed to a flow gas consisting of 30 vol.% H_2O, 60 vol.% CO_2, 4 vol.% O_2, 6000 ppm of SO_2 and N_2 (bal) with 1 mg/cm^2 of Na_2SO_4. The specimens were exposed for different times: 1, 24 and 168 h.

3. RESULTS AND DISCUSSION

The results show that the alloy exhibits protective behaviour at 700°C in wet-SO_2 + Na_2SO_4 environment. The material forms a slow growing thin and relatively smooth oxide scale (see Figure 1 and Figure 2). Similarly, earlier results [14] showed that the alloy exhibited a protective behaviour when exposed in dry-O_2 environment at 700°C, the material forming a slow-growing and relatively smooth Cr-rich oxide, no breakaway occurring. In contrast, breakaway oxidation has been observed on the alloy in wet environments (wet-O_2 and wet-CO_2) at 700°C [**Errore. Il segnalibro non è definito.**]. Thus, the slow oxidation kinetics and the formation of a thin oxide scale containing almost pure Cr_2O_3 in a wet environment at 700°C for this alloy, as observed in this study, are not expected.

The XRD analysis showed that the phases present are corundum-type and spinel oxide phases, metal and sodium sulphates (Cr and/or Fe sulphates). Metal sulphates stay at the scale/gas interface, no trace of Na (cation) was detected within the oxide scale or subjacent metal by cross-section STEM/EDX analysis. The observation that all Na_2SO_4 stays in a crystalline form it is also supported by the SEM overview (Figure 2), which does not show any diffuse morphology related to the presence of molten phases, which may have formed during the exposure. This observation suggests that Na_2SO_4 does not participate actively in the corrosion process, but stays on the surface for the whole exposure, see figure 2.

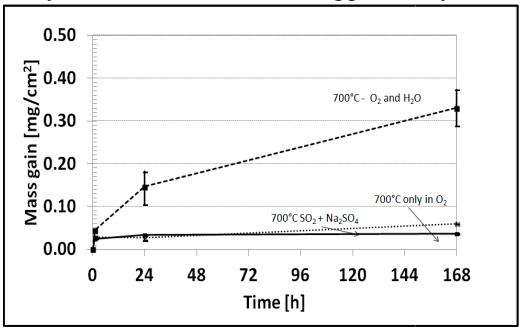

Figure 1. Mass gain vs time

Furthermore, the results show that the alloy accumulates sulphur also at the metal/scale interface. Quantitative STEM/EDX analysis showed that the S-accumulation consists of sulphides, (Cr,Mn)S and CrS. Sulphides of common metals (except Mn), including chromium sulphides, exhibit much greater non-stoichiometry and thereby higher defect concentration than the corresponding oxides [15]. This results in many orders of magnitude higher diffusion rates of cations in common metal sulphides than in the corresponding oxides [16]. Thus, it is expected that if chromium sulphidation (with no oxidation) occurs the corrosion rate is higher than that obtained through chromium oxidation. It has been found that in the present case also oxidation occurs, resulting in the formation of almost pure Cr_2O_3 at the metal/scale interface above the sulphides. Thus, it is suggested that the low oxidation rate is attributed to the presence of the almost pure chromia layer formed above the sulphides.

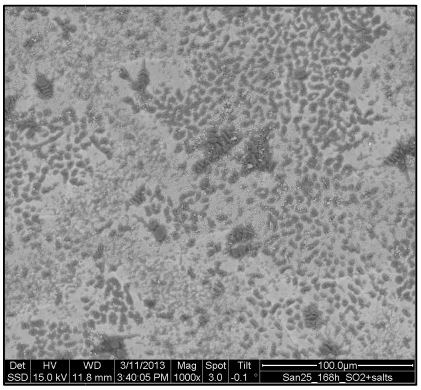

Figure 2. SEM/BSE micrograph of the 22 wt.% Cr in wet environment with SO2 + Na_2SO_4 at 700°C for 168h

To summarize, our results show that a thin, mainly outward growing oxide scale is formed on the alloy in the present conditions. The scale consists of almost pure chromia in the inner part and of Fe-rich oxide or Fe-Ni spinel in the outer part of the outward growing oxide scale. Also, a very thin Cr-rich (with patches of Fe and Ni) inward growing oxide scale has been revealed. In addition, CrS and (Cr,Mn)S (at the alloy grain boundaries) tend to accumulate at the scale/metal interface, while $M_2(SO_4)_3$ and Na_2SO_4 stay on the surface.

It is argued that the chromium volatilization is inhibited by the presence of sulphates on the surface, which stabilizes the chromia layer, making the alloy less liable to develop breakaway oxidation in a wet environment in presence of SO_2 and Na_2SO_4.

4. CONCLUSION

The present study shows that the alloy forms a thin, mainly outward growing oxide scale consisting of almost pure chromia in the inner part and of Fe-rich oxide in the outer part. In addition, CrS tends to accumulate at the scale/metal interface, while $M_2(SO_4)_3$ and Na_2SO_4 are present on the surface. The formation of a thin and smooth oxide scale in a wet environment (30% H_2O) at 700°C is not expected for this alloy. The reduced oxidation rate in a wet environment containing SO_2 and Na_2SO_4 is attributed to the inhibition of chromium volatilization, due to the presence of the sulphates on the surface. This limits the Cr-depletion of the oxide scale, stabilizing its protectiveness, inhibiting breakaway oxidation.

Acknowledgements

This work was carried out in collaboration with the Swedish High Temperature Corrosion (HTC) centre.

1 P. Kofstad, High Temperature Corrosion, Elsevier Applied Science Publishers Ltd, (London and New York, 1988)

2. J. Ehlers *et al;* "Enhanced oxidation of the 9%Cr steel P91 in water containing environments," *Corrosion Science,* Vol. 48, No 11 (2006), pp. 3428-3454

3 C.S. Giggins, F.S. Pettit; "Corrosion of metals and alloys in mixed gas environments at elevated temperatures," *Oxidation of Metals*, Vol. 14, No 5 (1980), 363-413.

4 G.H. Meier et al., Effect of alloy composition and exposure conditions on the selective oxidation behavior of ferritic Fe-Cr and Fe-Cr-X alloys, *Oxidation of Metals*, Vol. 74, No 5-6 (2010), 319-340.

5 T. Gheno, D.Monceau, D.J.Young, "Mechanism of breakaway oxidation of Fe-Cr and Fe-Cr-Ni aloys in dry and wet carbon dioxide", *Corrosion Science*, Vol. 64, (2012), pp 222-233.

6 F. Pettit, "Hot corrosion of Metals and Alloys", *Oxidation of Metals,* Vol. 76, No 1-2 (2011), pp 1-21

7 N.S.Bornstein and M.A. DeCrescente, Transaction of the Metallurgical Society of AIME **245**, (1969), 1947.

8 A.G. Andersen, P. Kofstad, "Reaction of chromium in SO2-containing atmospheres, *Oxidation of metals*, Vol. 43, No 3-4 (1995), pp 301-315.

9 A.G. Andersen, P. Kofstad, "The reaction of Ni-20Cr with SO2 at 600-900°C", *Corrosion Science,* Vol. 24, No 8 (1984), pp 731-743.

10 S. Mrowec, T.Werber, m. Zastawnik, "The mechanism of high temperature sulphur corrosion of nickel-chromium alloys", *Corrosion Science,* Vol. 6, No 2 (1966), pp 47-58.

11 A. Järdnäs, J.E. Svensson, L.G. Johansson, "Evidence for suppression of the oxidation of a Fe 2.25Cr 1 Mo Steel by traces of SO2, *Materials Science Forum,* Vol. 369-372, (2001), 173-180

12 A. Järdnäs, J.E. Svensson and L.-G. Johansson, "The inhibitive effect of traces of SO2 on the oxidation of iron", *Oxidation of metals*, Vol. 60, No (5/6), (2003), 427-445

13 R. Rautio, S. Bruce, Sanvik Sanicro 25, A new material for ultrasupercritical coal fired boilers - EPRI-Sanicro25 Sandvik

14 L. Intiso, J.E. Svensson, L.G. Johansson and M. Halvarsson; Oxidation of Sanicro 25 (42Fe22Cr25NiWCuNbN) in O_2 and O_2+H_2O environments at 600-750°C. In manuscript

15 S. Mrowec, "The problem of sulfur in high-temperature corrosion, *Oxidation of Metals*, Vol. 44, No (1/2), (1995), 177-209

16 S. Mrowec, T. Walec and T. Werber, "High temperature sulfur corrosion of iron-chromium alloys, *Oxidation of Metals*, Vol. **1**, No 1 (1969), 93-120

Initial Corrosion Behavior of Low Carbon Steel in Molten Lead-free Solder

Akira Yamauchi [1,*] and Kodai Uesugi [2]

[1] Department of Mechanical Engineering, Gunma National College of Technology, 580 Toriba-machi, Maebashi 371-8530, JAPAN
[2] Advanced Engineering Course, Gunma National College of Technology, 580 Toriba-machi, Maebashi 371-8530, JAPAN

e-mail: ayama@mech.gunma-ct.ac.jp

1. INTRODUCTION

The use of lead-free solder has been expanding widely in the world. Eutectic Sn-Ag-Cu solder has excellent mechanical properties and then is one of the promising candidates for replacing Sn-Pb solder [1, 2]. However, there are some problems for wave soldering and reflow process [3-5]. For example, Takemoto *et al*. showed the dissolution of stainless steel at the manufacturing apparatus [3]. These problems are attributed to the increased operation temperature and high reaction rate of metals.

In the previous study [6], a method for evaluating the thickness loss of pure iron, low carbon steel, and stainless steel by molten lead-free solder was investigated. It was found that the thickness losses of commercial steels with removing oxide film treatment are the same. However, the corrosion behavior of steels in the initial stage is not cleared. Therefore, the purpose of this study is to investigate the effect of carbon concentration on the initial corrosion behavior of pure iron and low carbon steels in molten lead-free solder.

2. EXPERIMENTAL

Table 1 shows the chemical compositions (mass %) of pure iron and low carbon steels used in this study. The corrosion test specimens were cut to 30×10×1mm in size. Their surfaces were polished with SiC paper up to # 1000 and then ultrasonically cleaned in ethanol.

In the corrosion test [6] the specimens were immersed vertically into molten Sn-3.0%Ag-0.5%Cu solder bath at 773 K for up to 300 minute. After corrosion test, the corrosion area and alloy substrate were characterized by optical microscopy (OM), scanning electron microscopy (SEM), X-ray diffractometry (XRD), and electron probe microanalysis (EPMA).

3. RESULTS AND DISCUSSION

Fig.1 shows the effect of carbon concentration on the corrosion behavior of pure iron and low carbon steel immersed in a molten Sn-3.0%Ag-0.5%Cu at 773 K for up to 300 minute. For all specimens, after an incubation period there was an increase in corrosion area thickness with increasing immersion time. The incubation time and the corrosion product growth rate increased with increasing carbon concentration. For example, the measurements of thickness of corrosion product results for 10 minutes at pure iron, for 20 minutes at S10C, and for 240 minutes at S45C confirmed the incubation period.

Fig.2 shows cross-sectional OM images of corrosion interfaces, after the corrosion test at 773 K for up to 300 minutes. As shown in figure 2, the corrosion product is formed at the metal substrate / molten solder interface, and the corrosion product consists of $FeSn_2$ from the results of XRD and EPMA. In the incubation time, there was no corrosion product at the metal / solder interface. This is caused by the dissolution of iron in molten lead-free solder. Thus, the area ratio of alpha iron have an important influence on the incubation time. And then the formation of corrosion products occur at the metal / solder interface after the dissolution of iron into molten lead-free solder bath.

Fig.3 shows the top view of the metal / solder interface of S10C specimens immersed at 773 K for up to 30minute. There are two phases (or morphology) in the microstructures, i.e., corrosion products (bright phase) and steel matrix (dark region). As seen in Fig. 3(a), the corrosion product formed in the initial corrosion stage is $FeSn_2$. However, relationship between corrosion point and metal microstructure is not clear. This phenomena will now be examined for evidence of site of incidence. Fig. 3(b) shows that the number of corrosion product ($FeSn_2$) increases and sizes of $FeSn_2$ grow. Fig. 3(c) shows that after a period of time has elapsed, the $FeSn_2$ layer grows and then metal

substrate covered with $FeSn_2$ layer wholly (Fig. 3(d)).

4. CONCLUSION

In this study, the effect of carbon concentration on the initial corrosion behavior of pure iron and low carbon steels in molten Sn-3.0%Ag-0.5%Cu solder were investigated. The results obtained are as follows.

(1) Corrosion incubation period of iron or low carbon steel with molten lead-free solder and the growth rate of corrosion layer after the formation of corrosion layer on specimen are dependent on the carbon concentration of steel. This is related to the dissolution rate of iron into the lead-free solder.

(2) The corrosion phase for iron or low carbon steel / molten lead-free solder at the interface was mainly $FeSn_2$.

Acknowledgements

This work is a cooperative program (Proposal No.14G0032) of the Cooperative Research and Development Center for Advanced Materials, Institute for materials Research, Tohoku University.

References

[1] L. Zhang, Z. G. Wang, J. K. Shang, "Current-induced Weakening of Sn3.5Ag0.7Cu Pb-free Solder Joints," Scripta Mater., Vol.56, Issue5 (2007), pp.381-384.

[2] J. Keller, D. Baither, U. Wilke, and G. Schmitz, "Mechanical properties of Pb-free SnAg solder joints," Acta Mater., Vol.59, Issue7 (2011), pp.2731-2741.

[3] T. Takemoto, T. Uetani and M. Yamazaki, "Dissolution Rates of Iron Plating on Soldering Iron Tips in Molten Lead-free Solders," Soldering & Surf. Mount Technol., Vol. 16, No.3 (2004), pp.9-15.

[4] T. Takemoto, H. Nishikawa, and F. Gao, "Erosion Protective Design for Lead-free Wave Soldering Bath," *Proc. EcoDesign 2006 Asia Pacific Symposium*, Tokyo, Dec. 2006, pp.77-80

[5] T. Takemoto and M. Takemoto, "Dissolution of stainless steels in molten lead-free solders," Soldering & Surf. Mount Technol., Vol. 18, No.3 (2006), pp.24-30.

[6] T. Kawamoto, A. Yamauchi, K. Kurokawa, and J. Tanaka, "Effect of Additional Elements on Corrosion Resistance of Carbon Steel in Molten Lead-free Solder," *Proc ICEP 2010 Conf*, Sapporo, May 2010, pp. 788-791.

Table1 Chemical composition of pure iron and low carbon steels (mass %)

	C	Mn	Si	Fe
pure iron	**0.004**	**-**	**-**	**bal.**
S10C	**0.09**	**0.45**	**-**	**bal.**
S45C	**0.44**	**0.75**	**0.25**	**bal.**

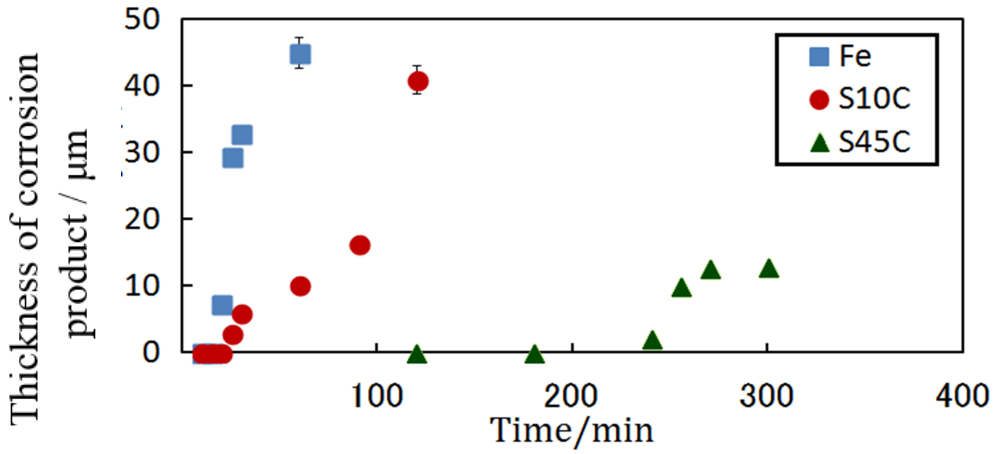

Fig.1 Corrosion behavior of pure iron, S10C, and S45C in molten lead-free solder.

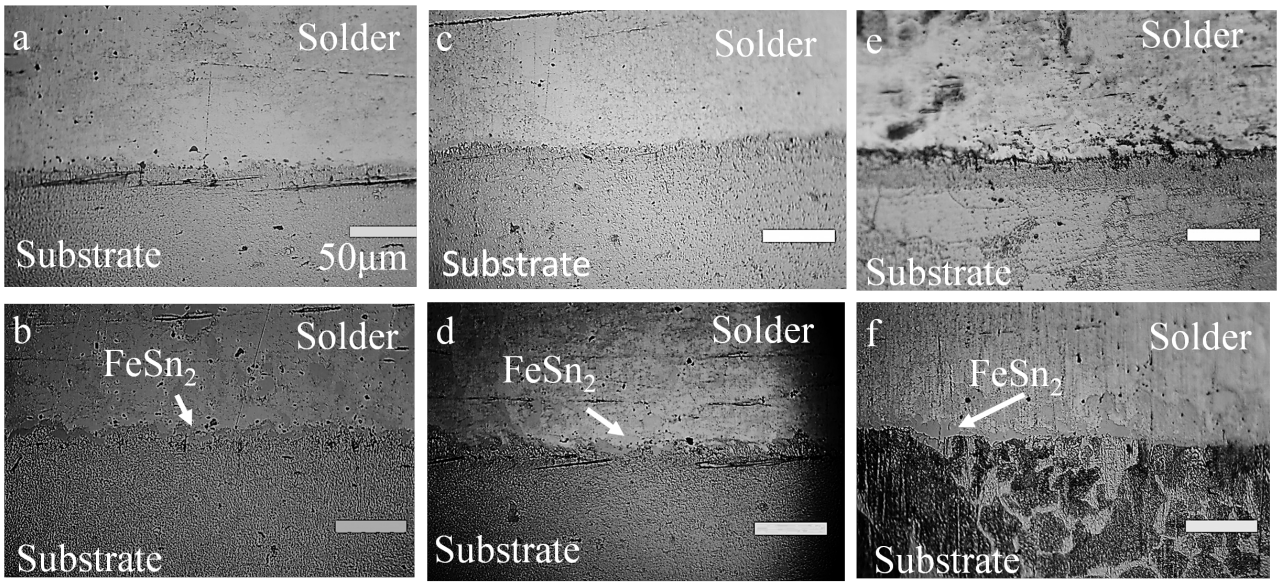

Fig.2 OM cross-sectional images of solder / pure iron ((a) and (b))or low carbon steels (S10C:(c) and (d), S45C:(e) and (f)) corroded at 773 K for 10 min.(a), 15 min.(b), 20 min.(c), 25 min.(d), 60 min.(e), and 300 min.(f).

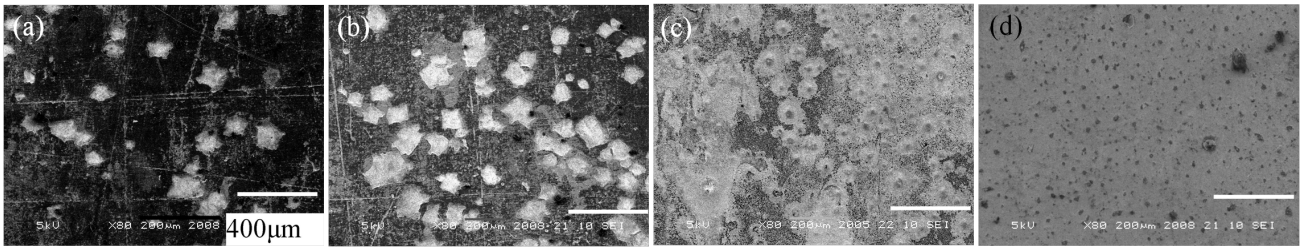

Fig.3 OM surface images of S10C corroded at 773 K for up to 30 minute.

High temperature oxidation behavior of CrMoV steel in carbon dioxide gas

Takehisa Hino [(1)], Kiyoshi Imai [(1)] , Daizo Saito [(1)] and Takeo Takahashi[(2)]

[(1)] Power and Industrial R&D center, Toshiba Corporation, 2-4 Suehiro-cho, Tsurumi, Yokohama 230-0045, JAPAN
[(2)] Thermal and Hydro Power Systems and Services div., Toshiba Corporation, 72-34 Horikawa-cho, Saiwai, Kawasaki 212-8585, JAPAN

E-mail: takehisa.hino@toshiba.co.jp

1. INTRODUCTION,

A turbine system based on a new concept, using carbon dioxide (CO_2) gas as a working fluid, has been developed by Toshiba[1)]. A Ni-based superalloy and a Co-based superalloy are planned to be used in high-temperature sections above 973 K, whereas low alloy steels, such as CrMoV, are planned to be used as components in sections below 773 K. However, it has been reported that Fe-based alloys such as 9Cr and 12Cr and mild steel suffer from breakaway oxidation and carburization[2)] when they are used in high-temperature CO_2 gas. Therefore, the oxidation and carburization behavior of CrMoV steel was evaluated in simulated exhaust gas at a gas pressure of 0.1 MPa and a temperature of 773 K.

2. EXPERIMENTAL,

Specimens of CrMoV steel (Fe-1.25Cr-1Mo-1V-0.15–0.75Si) were cut from a forged block. The oxidation test was conducted at 773 K for up to 1000 hours. Two gas conditions were used: simulated exhaust gas containing high amount of CO_2 and small amount of H_2O and O_2 (hereafter referred to as "CO_2 atmosphere") and air. The dimensions of the specimens were 15 mm × 10 mm × 2 mm. These specimens were polished to a mirror finish. After polishing, the specimens were cleaned with acetone in an ultrasonic cleaner. The oxidation test in the CO_2 atmosphere was conducted with a tube furnace, into which mixed gas was flowed at a rate of one liter per minute. The oxidation test in the air atmosphere was conducted with a muffle furnace in the static condition. Both oxidation tests were conducted at a gas pressure of 0.1 MPa. Mass changes of the specimens were measured at 100, 300, and 1000 hours. Oxide scales were analyzed with X-ray diffraction (XRD) and an electron probe micro analyzer (EPMA) to determine the oxide structure. Carburization was evaluated from the hardness and the cross-sectional microstructure. The hardness was measured from the gas/oxide interface by a micro Vickers tester. The load condition and time for the micro Vickers tester were set to 25 gf and 10 s, respectively.

3. RESULTS AND DISCUSSION

Fig. 1 shows the mass change of the specimens. The mass change of the specimen oxidized in the CO_2 atmosphere was larger than that of the specimen oxidized in the air atmosphere. The mass changes of the specimens oxidized in CO_2 and air both increased following a parabolic law. Breakaway oxidation was not observed.

Fig. 2 shows the XRD analysis results. Peaks attributed to Fe_2O_3 and Fe_3O_4 were observed in both specimens, and there was no significant difference between the two specimens.

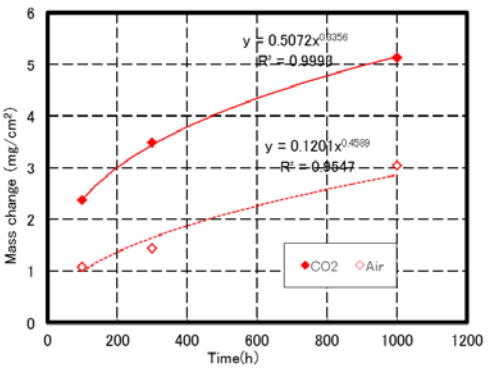

Fig. 1 Mass change of specimens.

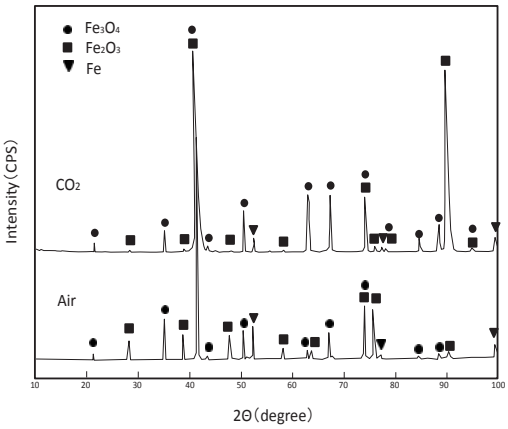

Fig. 2 XRD pattern of the specimens oxidized in CO_2 and air atmospheres.

Fig. 3 shows cross-sectional SEM images of the oxidized specimens. The oxide scale formed in the CO_2 atmosphere consisted of three layers. The outer and inner layers were thin and dense, whereas the middle layer was thick and porous. On the other hand, the oxide scale formed in the air atmosphere consisted of two layers. The outer layer was thicker than the inner layer and seemed to be easy to spall.

Fig. 4 shows the EPMA mapping. The oxide layer formed in the CO_2 atmosphere consisted of three layers. The outer layer and middle oxide layer were rich in Fe. The inner layer was rich in Cr, Mo and Si. The oxide scale formed in the air atmosphere consisted of two layers. The outer oxide layer was rich in Fe, and the inner oxide layer was rich in Cr, Si, Mo and V.

The morphologies of the samples oxidized in the CO_2 atmosphere and air were different; however, a Cr-rich continuous oxide layer was formed in both specimens after 1000 hours. The oxide scales seemed to be good barriers against additional oxidation.

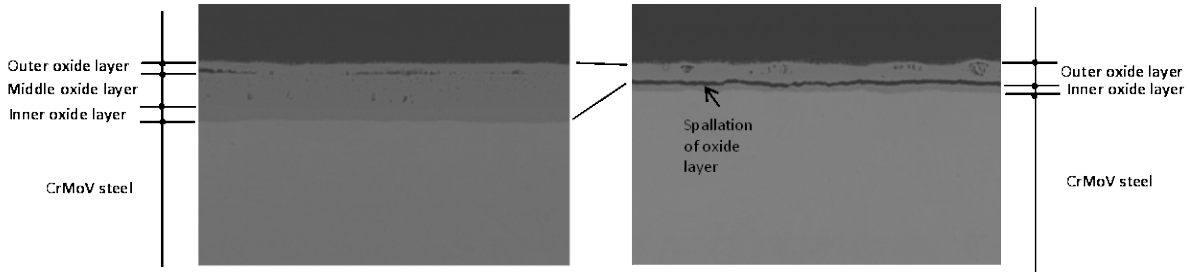

(a) CO_2 gas atmosphere (b) Air atmosphere

Fig. 3 Cross-sectional microstructure of oxidized specimens.

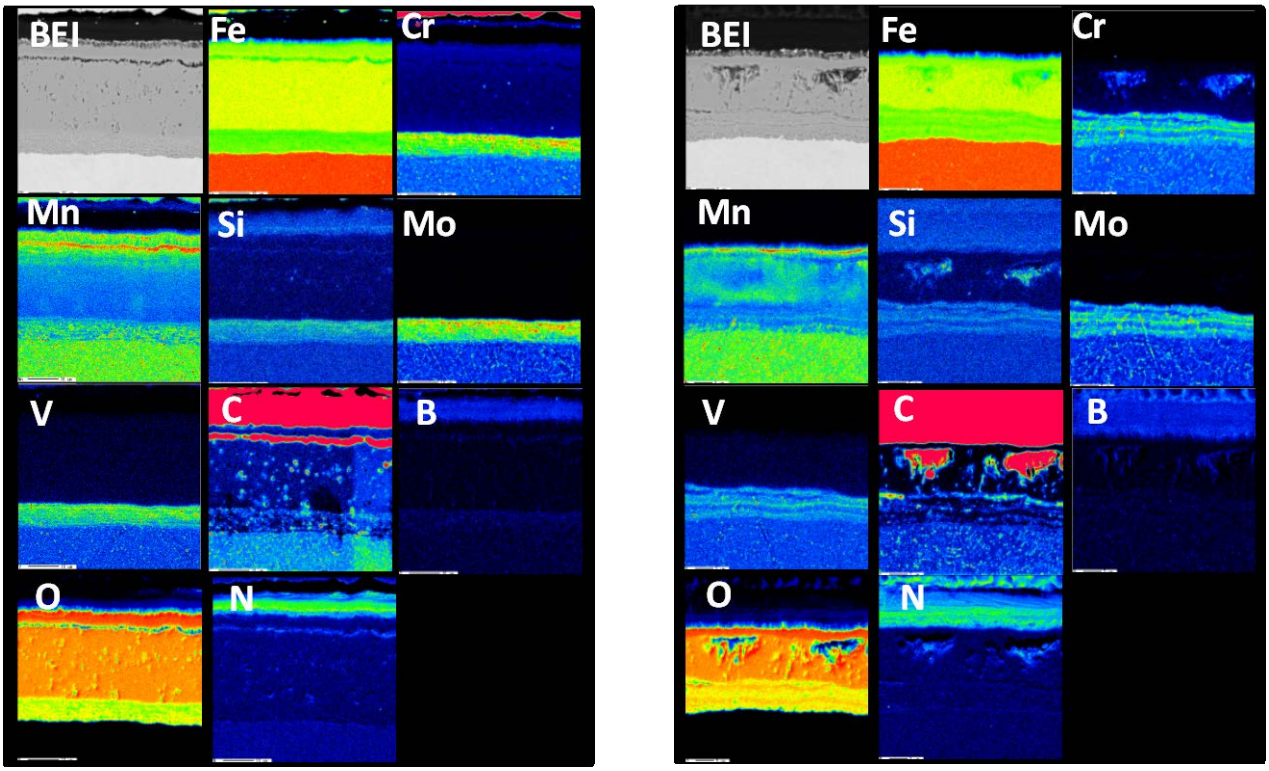

(a) CO_2 gas atmosphere (b) Air atmosphere

Fig. 4 EPMA results of specimens oxidized at 773 K after 1000 hours.

Fig. 5 shows the hardness of the specimens oxidized in the CO_2 and air atmospheres as a function of the distance from the oxide/metal interface. The hardness profile of the specimens oxidized in the CO_2 atmosphere was almost the same as that oxidized in the air atmosphere. Fig. 6 shows the cross-sectional microstructures of regions below the oxide scale and in the middle of the specimens. For both specimens, a microstructure in which fine particles precipitated in the matrix was observed. There was no significant difference between the two specimens. From the above hardness profile and microstructural observation results, it is concluded that carburization did not occur in the CO_2 atmosphere.

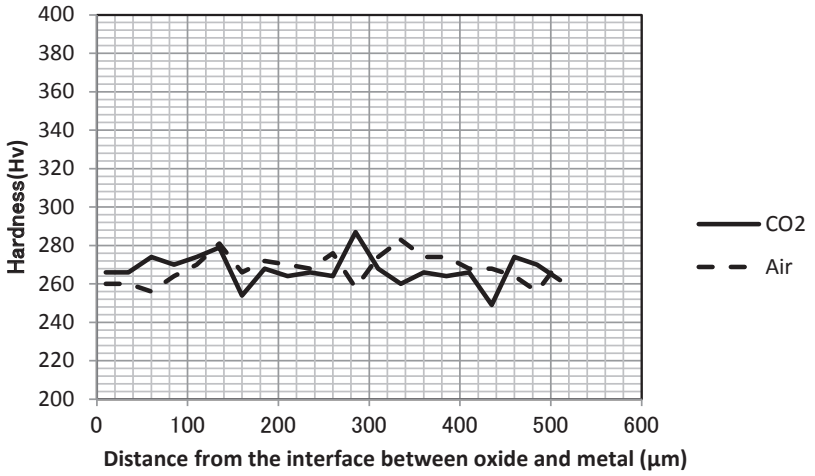

Fig. 5 Hardness profile of the specimens oxidized in the CO_2 and air atmosphere.

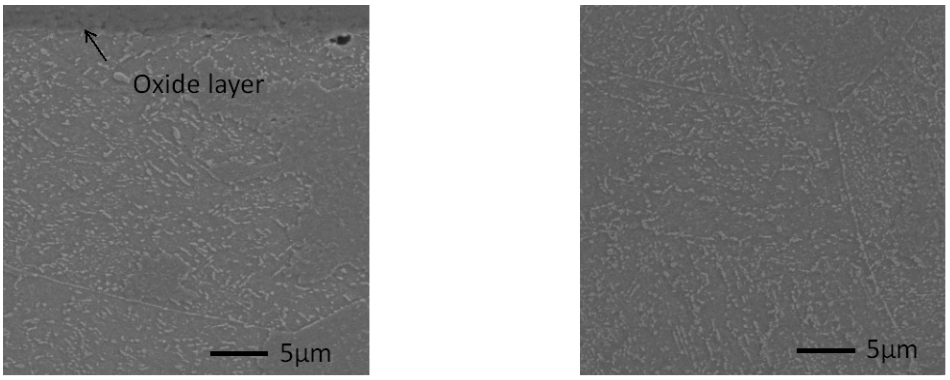

(a) Beneath the oxide scale (b) Middle of the oxidized specimen

Fig. 6 Cross-sectional microstructure of specimen oxidized in CO_2 gas atmosphere.

Ferrite/martensitic steel, such as mild steel[3] and 9Cr-1Mo,[4] have been reported to form double oxide layers in 100 % CO_2 gas. The oxide scale observed in the present study seemed to be the same as these previously reported structures.

Rouillard et al.[5] reported that a carburization layer is formed beneath an oxide layer oxidized in pure CO_2 at a temperature of 823 K and a gas pressure of 0.1 MPa. Furukawa et.al[6] also reported that carburization occurs at 773 K at 20 MPa. In contrast, a carburization layer was not observed in this work.

Fe_3O_4 is considered to be generated from Fe and CO_2 by the following reaction:

$$3Fe + 4CO_2(gas) \rightarrow Fe_3O_4 + 4CO(gas) \quad (1)$$

If the Boudouard reaction (2) occurs on the surface of the metal, a carburization layer is formed. Antill et al.[3] have demonstrated that the Boudouard reaction (2) is kinetically predominant.

$$2CO(gas) \rightarrow CO_2(gas) + C \quad (2)$$

Rouillard et al. proposed another carburization process with multiple steps.[5] First, CO_2(g) diffuses from the gas phase to the voids through nanochannels formed in the oxide scale:

$$CO_2^{out}(g) \rightarrow CO_2^{in}(g) \quad (3)$$

Then CO_2(g) reacts in the voids on a dissociative atomic site s (Fe for instance) to form atomic oxide O-s (which will then be part of a new Fe_3O_4 unit cell) and CO_{in}(g):

$$CO_2^{in}(g) + s \rightarrow O - s + CO^{in}(g) \quad (4)$$

Then, the formed CO reaches the oxide/metal interface, where it can react through the Boudouard reaction to deposit carbon on the oxidized surface, if allowed thermodynamically:

$$CO^{in}(g) \rightarrow 2CO_2^{in}(g) + C \quad (5)$$

In both of the above carburization mechanisms, C is deposited as a result of the Boudouard reaction.

The gas used in the experiments contained a small amount of H_2O. Depending on the amount of H_2O, the following reaction will occur:[7]

$$CO + H_2O \leftrightarrow CO_2(g) + H_2 \quad (6)$$

This seems to be the reason why carburization did not occur.

4. CONCLUSION,

As a result of oxidation tests at 773 K for up to 1000 h using two simulated exhaust gases, one whose composition CO_2 rich gas (CO_2 atmosphere) and the other air, the following findings were obtained.

1) The mass change of the specimen oxidized in the CO_2 atmosphere was larger than that of the specimen oxidized in air. However, breakaway oxidation was not observed in both conditions.
2) Carburization was not observed in the specimen oxidized in the CO_2 atmosphere. It seems that the H_2O gas was effective in suppressing carburization.

References.

[1] http://www.toshiba.co.jp/about/press/2012_06/pr_j1502.htm
[2] A. Uehara, JAEA Report. JNC-TN9400-2000-040
[3] J. E. Antill, K. A. Peakall, and J. Warburton, Corrosion Science 8, 689 (1968).
[4] F. Rouillard, G. Moine, M. Tabarant, J. C. Ruiz et.al., Oxid Met. vol 77(2012) 27‑55.
[5] F. Rouillard , G. Moine , M. Tabarant ,J. C. Ruiz et.al.; Oxid.Met vol.77 (2012), 57-70.
[6]T.Furukawa, Y Inagakiand M Aritomi J of Power and Energy Systems, vol.4,no.1 (2010),253-261
[7] H.Sudo et.al.; Tekkozairyo (Koza kinozokugaku zairyo-hen 4); Japan Institute of Metals (1985), 119. (in Japanese)

Effect of CaO addition on the Oxidation of Magnesium Alloys

Dong Bok Lee*, Soon Yong Park, Poonam Yadav, Muhammad Ali Abro, and Min Jung Kim

School of Advanced Materials Science and Engineering, Sungkyunkwan University, Suwon, 440-746, South Korea

e-mail: dlee@skku.ac.kr

1. INTRODUCTION

Magnesium alloys are used as light-weight structural components, because magnesium has the lowest density among metallic materials in practical use, high specific strength, good castability, good machinability, and a low elastic modulus. However, the widespread usage is limited due to poor oxidation resistance [1]. Previously, the addition of Ca was found to suppress the vigorous reaction of molten Mg with oxygen during casting, and increase the oxidation resistance of Mg alloys. The formation of a thin CaO-rich outer layer on the surface effectively retarded oxidation and ignition of Mg alloy [2]. Recently, Kim et al. has found that CaO also increases the oxidation resistance of Mg alloys, however the reason for this has not been adequately pursued [3]. The use of low-cost, stable CaO instead of Ca is strongly desirable for industrial applications. In this study, AZ31 alloys (Mg-3Al-0.8Zn in wt.%) with and without 0.3wt.% Ca or CaO were cast, oxidized between 450 and 650^{o}C in air. The effect of CaO on the oxidation of Mg alloys were discussed, and compared with that of Ca. The oxidation characteristics of CaO-added Mg alloys were investigated.

2. EXPERIMENTAL

The AZ31 alloy ingot was melted at 680^{o}C in a steel crucible using a furnace under a CO_2+1%SF_6 protective atmosphere. AZ31+Ca and AZ31+CaO alloys were cast at 680^{o}C in the mild steel crucible by adding 0.3 wt.% Ca chips and 0.3 wt.% CaO particles, respectively, into the AZ31 melt in atmospheric air. The prepared AZ31, AZ31+0.3 wt.%Ca and AZ31+0.3 wt.%CaO alloys were cut into small coupons, ground, degreased, and oxidized at 450-650^{o}C in air using a TGA. Ignition tests were performed by heating the sample at a rate of 5^{o}C/min using a furnace. The samples were inspected by SEM/EDS, XPS, AES, XRD, and TEM/EDS.

3. RESULTS AND DISCUSSION

Fig. 1 shows SEM image of the AZ31+0.3%CaO alloy cast in air. Secondary phases that consisted primarily of Al_2Ca and $Al_{12}Mg_{17}$ were aligned along grain boundaries of the α-Mg matrix. The use of CaO without CO_2+1%SF_6 gases is a cost-effective, and eco-friendly casting method.

Fig. 2 shows that the ignition temperatures were 578^{o}C (AZ31), 629^{o}C (AZ31+0.3% CaO), and 634^{o}C (AZ31+0.3% Ca). Both Ca and CaO were clearly beneficial to oxidation resistance. Despite this beneficial effect, all the alloys were subject to ignition, because the non-protective MgO was the main oxide. Although CaO is as good as Ca in improving the oxidation resistance of Mg alloys, the use of CaO is much better than that of Ca for economic, safety, and environmental reasons.

Fig. 3 shows TEM images of the oxidized AZ31+0.3% CaO alloy. At 500^{o}C, a small amount of Ca was incorporated in the MgO layer with a thickness of 120-300 nm. The Ca concentration in the Mg-Ca-O layer decreased from 5 at.% to 1 at.% while moving from the outer surface to the scale/matrix interface. At 600^{o}C, a distinct CaO-rich layer incorporated with Al and Mg formed at the outer surface of the oxide scale. The concentration of Ca in the outer Ca-Al-(Mg)-O layer was 20-50 at.%. Below the outer CaO-rich layer, a Mg-Ca-Al-O layer existed. At 600^{o}C, not only Ca but also Al diffused outward toward the surface according to the concentration gradient. The more oxidation progressed, the more Al, and moreover, Ca diffused outward to segregate at the outer oxide scale.

Fig. 4 shows the surface images of the oxide scales formed on the oxidized AZ31+0.3% CaO alloy. At 500^{o}C, grinding marks were seen, owing to the formation of a thin, compact, and uniform scale (Fig. 4a). As oxidation progressed further at 550 and 625^{o}C, loosely adherent or nonadherent oxide powders formed on the surface of the thickened scale (Figs. 4b and c). At 625^{o}C, oxide nodules having a cauliflower morphology formed by local ignition, and spread over the entire surface with further oxidation, resulting in disintegration into powders. The porous oxide layer allows oxygen to penetrate and acts as a channel for the outward transport of Mg vapor.

4. CONCLUSION,

The initially added CaO reacted with Al to become Al_2Ca along the grain boundaries of the AZ31 alloy during casting. The main reason for enhanced oxidation resistance of AZ31 with the initial addition of Ca or CaO is attributed to the formation of the CaO barrier layer with extremely low vapor pressures. Once the outer CaO-rich layer formed, the evaporation of the underlying Mg, the direct contact of Mg with oxygen to form MgO, and the inward transport of oxygen suppressed.

Acknowledgements

This work was supported by the Human Resource Development Program (No. 20114010203020) of KETEP grant funded by the Korea government Ministry of Trade, Industry and Energy.

References

[1] F. Czerwinski, "Factors affecting the oxidation nature of magnesium alloys," J. Met. 56(5) (2004) pp.29-31.

[2] B.S. You, W.W. Park, I.S. Chung, "The effect of calcium addition on the oxidation behavior in magnesium alloys," Scripta Mater. 42 (2000) pp.1089-1094.

[3] S.K. Kim, J.H. Seo, United States Patent Application No. 0236249 A1 (2011).

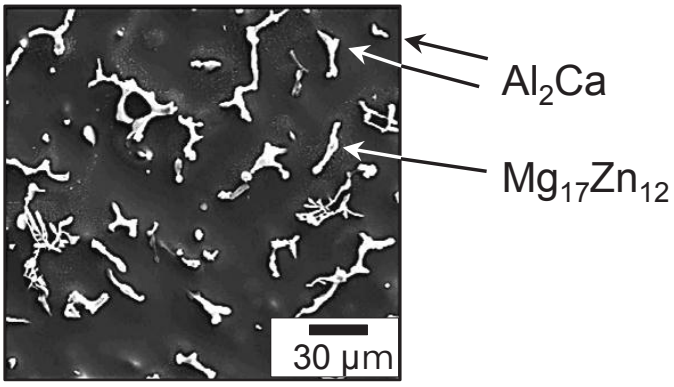

Fig. 1. SEM image of AZ31+0.3% CaO alloy (etched).

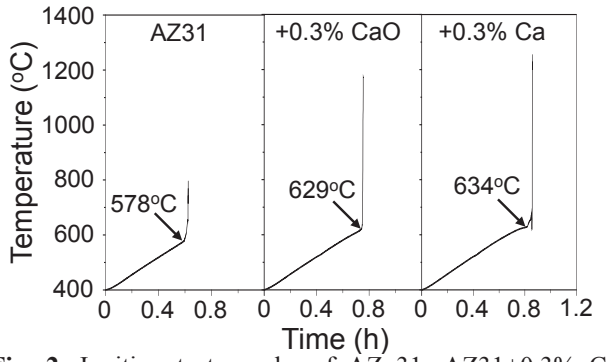

Fig. 2. Ignition test graphs of AZ 31, AZ31+0.3% Ca, and AZ31+0.3% CaO alloys.

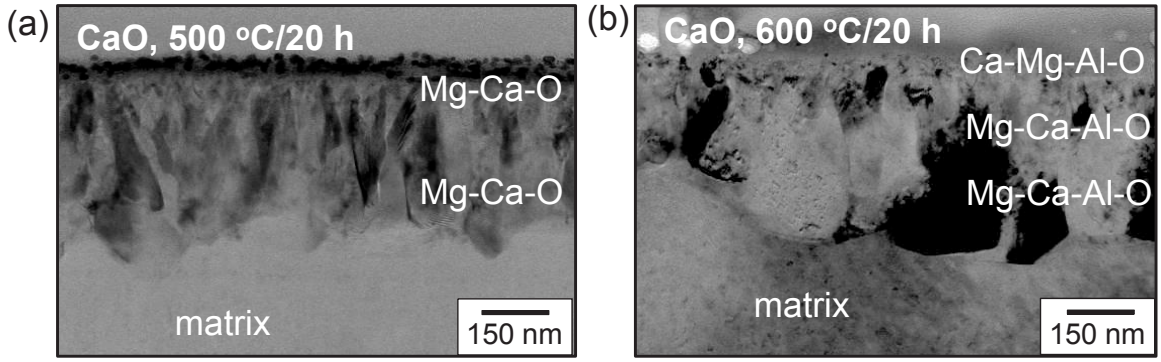

Fig. 3. Cross-sectional TEM images of AZ31+0.3% CaO after oxidation for 20 h at (a) 500°C, and (b) 600°C.

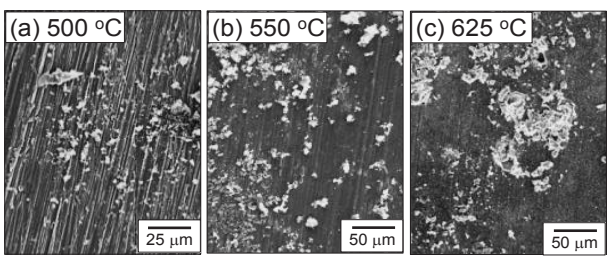

Fig. 4. SEM top view of the oxide scales formed on AZ31+0.3%CaO after oxidation for 20h at (a) 500°C, (b) 550°C, and (c) 625°C.

Effects of Si Addition on Fabrication of Ti-Al Intermetallic Coatings by Hot Pressing of Warm Sprayed Precursors

J. Sienkiewicz[(1,2,*)], S. Kuroda[(1)], K. Minagawa[(1)], H. Murakami[(1)], H. Araki[(1)], K.J. Kurzydłowski[(2)]

[(1)]National Institute for Materials Science, Tsukuba 305-0047, Ibaraki, Japan
[(2)]Warsaw University of Technology, Warsaw 00-661, Poland

e-mail: SIENKIEWICZ.Judyta@nims.co.jp

1. INTRODUCTION

In view of high specific strengths and excellent high-temperature properties, γ-TiAl intermetallic alloys are candidate materials for many high-temperature structural applications. These applications include airframe hot structures and thermal protection coatings for systems in aerospace vehicles operating under extreme temperature and environmental conditions.

Silicon is particularly effective in strengthening Ti alloys **[1]**. In solid solution it segregates to mobile dislocations, reducing their mobility and improving creep resistance at elevated temperatures **[2]**. Moreover, silicide compounds may promote useful dispersion strengthening and improved microstructural stability at elevated temperature **[3]**. The homogenously distributed fine silicides can also act as preferred nucleation sites during recrystallization in γ alloys **[4]**. Silicon improves also the oxidation and corrosion resistance of Ti-Al intermetallic phases **[5]**.

There are several ways to produce coatings based on TiAl intermetallic phase. One of them is warm spraying of feedstock consisting of titanium and aluminum powder mixtures **[6]**. Warm spray is an atmospheric coating process based on high-velocity impact bonding of powder particles, by which they can be accelerated to supersonic velocity, heated up to temperature under its melting point, and then impacted and bonded on a substrate in a solid state. By decreasing the temperature of combustion gas through mixing with the nitrogen, oxidation of feedstock powder can be significantly controlled compared with conventional thermal spraying e.g High Velocity Oxy-Fuel or Plasma Spray. This advantage is particularly important for Ti-based coating materials, which rapidly oxidize in elevated temperatures.

In this study, ternary Ti-Al-Si coatings was fabricated by warm spraying under different conditions followed by diffusion heat treatment. In order to convert deposits of Ti and Al-12Si particles into the TiAl intermetallic phases, two-stage heat treatment with pressure of 30 MPa were carried out. The effect of Si addition on the densification of hot pressed Ti-Al intermetallic coatings was examined.

2. EXPERIMENTAL

Three mixtures of elemental powders with different target compositions were prepared as the feedstock for the warm spray (WS) technique. Two commercially available powders were used for the experiment: Ti (TILOP-45 μm, Sumitomo, Tokyo, Japan) and Al-12Si alloy (Amdry 355, Sulzer Metco, Nagoya, Japan). Both powder particles had near-spherical morphology with the powder size range <45 μm (**Fig. 1**).

Three mixtures of various powder ratios were mixed mechanically for 3 hours. The characteristics of the mixtures A, B and C are shown in **Table I**. The obtained coating thickness and porosity values in the as-sprayed condition are also located in Table 1. The mixtures of Ti and Al-12Si alloy powders were deposited on stainless steel (SUS 316L) substrates with dimensions of 50 x 100 x 5 mm by WS with nitrogen flow rates of 1500 and 2000 dm^3/min. Grit blasting and degreasing were conducted just before the deposition. Alumina grit size was around 425–500 μm and

blasting pressure was 0.5 MPa. The time for ultrasonic degreasing in acetone was 10 min.

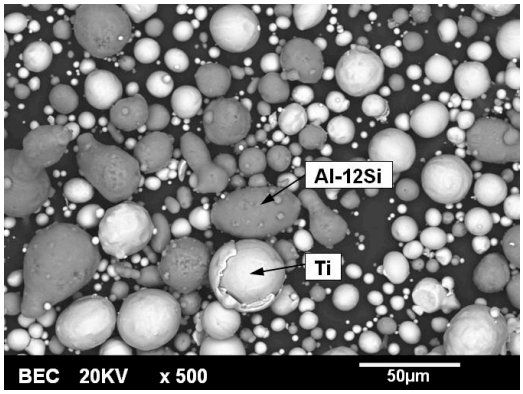

Fig. 1. SEM (back scattered electron mode) image showing structure of feedstock mixture A

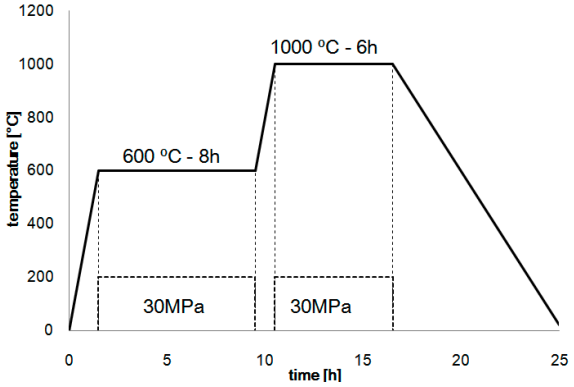

Fig. 2 The time-temperature/pressure schedule for hot pressing

Table I. Characteristic of warm spray deposits

	PM A		PM B		PM C	
Ti/Al ratio [at%]	50:50		45:55		40:60	
Chemical composition [at%]	47Ti-47Al-6Si		42Ti-51.4Al-6.6Si		37Ti-56Al-7Si	
Nitrogen Flow Rate [dm^3/min]	1500	2000	1500	2000	1500	2000
Coating thickness [µm]	192	197	193	186	176	188
Porosity [%]	5	6	8	6	10	6
Area of Ti [%]	35	43	36	42	23	23
Area of Al [%]	65	57	73	58	76	76
Theoretical area of Ti [%]	48		43		38	
Theoretical area of Al [%]	52		57		62	

Two-stage treatments as depicted schematically in **Fig. 2** were performed of the as-sprayed samples using a pressure of 30MPa. For hot pressing, the coated specimens were cut into 10 x 26 mm^2 pieces, put into a carbon die and hot pressed under vacuum atmosphere. Samples were heated at a heating rate of 10 °C/min and annealed at 600 ºC for 8 h during the first stage and at 1000 ºC for 6 h during the second stage. All the samples were furnace cooled at an average rate of 1 ºC/min.

3. RESULTS

Representative SEM images of the as-sprayed states of mixtures A, B and C obtained with nitrogen flow rate at 1500 and 2000 L/min are shown in **Fig. 3**. These coatings consist of relatively undeformed Ti particles embedded in highly deformed aluminum-silicon "matrix". The aluminum-silicon alloy eutectic undergoes much more deformation than titanium during spraying process by the fact of its lower yield strength and much lower melting point.

The analysis obtain from the SEM pictures show a loss of titanium particles during the spraying process (**Table I**). This effect is probably due to too relatively low temperature during spraying process. It is evident that nitrogen flow rate has significant effect on the heating and acceleration behavior by the propellant gas of Ti particles. It should be noted that gas velocity and temperature is less with higher nitrogen flow rate through the gun **[7, 8].** It creates a difference in deposition efficiency between Al-12Si alloy and Ti where Al-12Si is favored. Moreover, the melting point of eutectic alloy of Al-12Si is ~80 °C lower compared with pure Al. Due to the difference in the melting point and specific heat between Ti and Al-12Si, the chemical composition of the coating can be significantly different from that of the starting material.

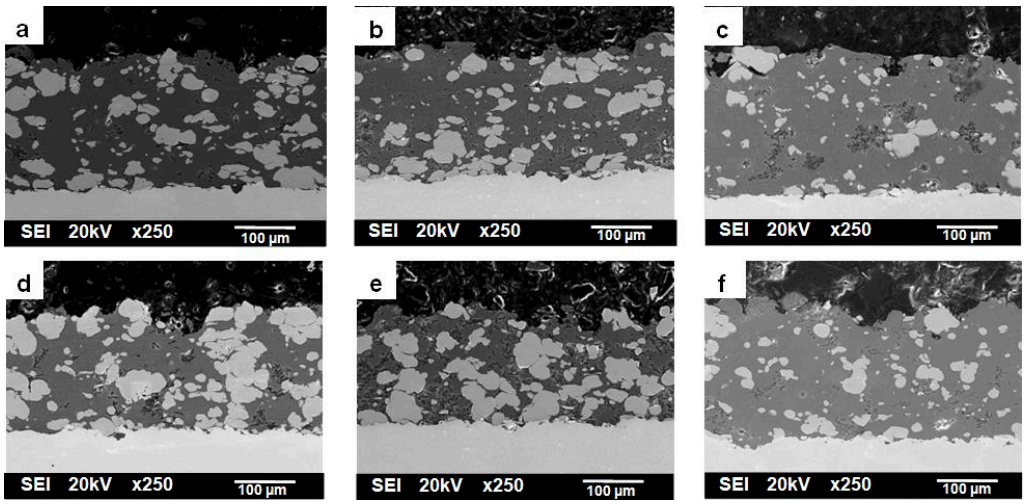

Fig. 3. SEM (secondary electron mode) images of cross sections of as-sprayed coating made from powder mixtures: a) PM A with NFR 1500 L/min, b) PM B with NFR 1500 L/min, c) PM C with NFR 1500 L/min, d) PM A with NFR 2000 L/min, e) PM B with NFR 2000 L/min, f) PM C with NFR 2000 L/min

Representative secondary electron SEM images of coatings after the hot pressing are shown in **Fig. 4**. They reveal homogenized microstructures with the fine irregular in shape and uniformly distributed silicides. The particles at grain boundaries are larger than those in the grain interiors (**Fig. 5.**). Besides, each element completely reacted to form quite homogenous intermetallic compounds. Voids were hardly remained in the hot pressed coatings. The measured porosity was less than 0.5 % for all three cases.

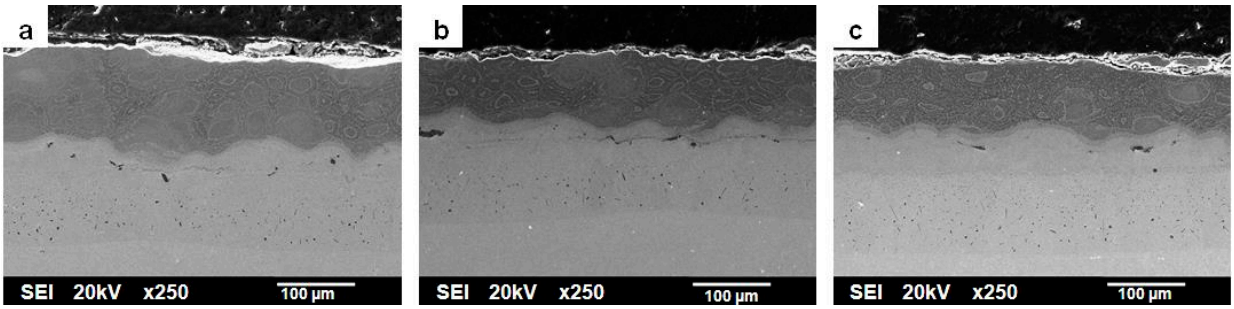

Fig. 5. SEM (secondary electron mode) images of cross sections of coating after hot pressing made under NFR at 1500 L/min from powder mixtures : a) PM A, b) PM B, c) PM C

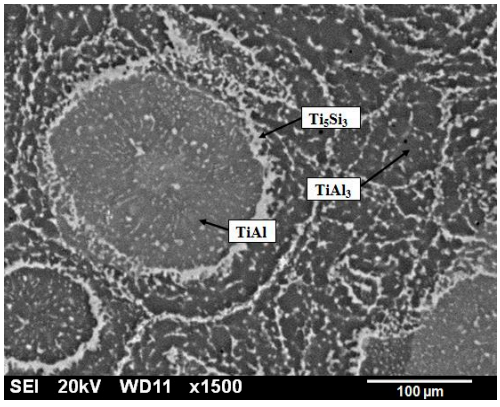

Fig. 4. SEM image of cross section of coating after hot pressing made under NFR at 1500 L/min from powder mixture A

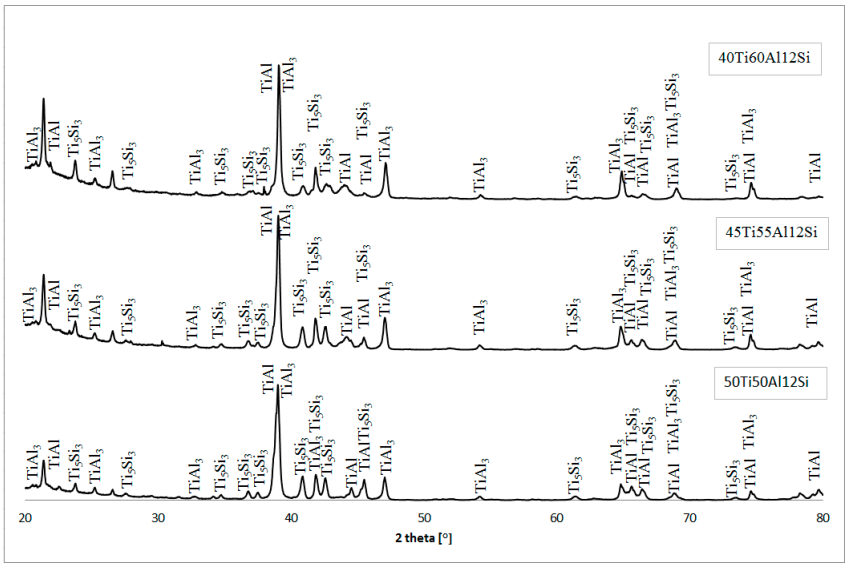

Fig. 6. XRD patterns of coatings after hot pressing

XRD measurements revealed that TiAl(Si) and $TiAl_3$(Si) intermetallic phases were the most dominant for all coatings after hot pressing (**Fig.6**). XRD analyses show that precipitations which appeared after hot pressing corresponds to Ti_5Si_3.

The cross section of coating made of Ti and Al powder mixture with Ti:Al ratio of 50:50 after hot pressing (with the same conditions as for coatings made from Ti and Al12Si powder mixtures) is presented for comparison in **Fig. 7**. The measured porosity for such prepared coating was 4.5%. Compared with pure Al, eutectic Al-12Si alloy has low melting point and higher fluidity. Therefore, Al-12Si liquid phase generated during first-stage hot pressing may enhance the densification of Ti-Al coatings. Besides, the eutectic Al-12Si, with lower eutectic temperature **[9]** can lower the temperature of reaction between Ti and Al. In case of pure Al, reaction between Ti and Al during first-stage of hot pressing occurred in solid state because melting point of Al was not reached.

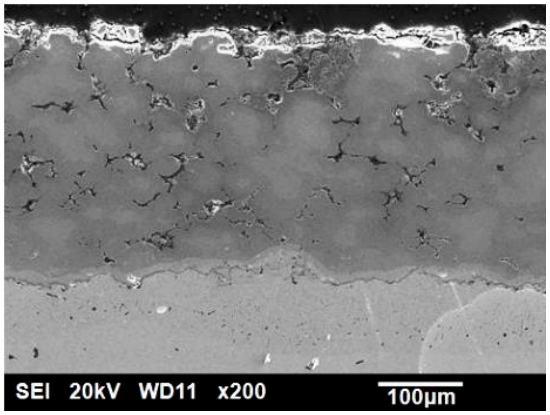

Fig. 8. SEM image of cross section of coating prepared from pure Ti and Al powder with Ti:Al ratio of 50:50 after hot pressing

4. CONCLUSION

Ti-Al-Si composite coatings were prepared by warm spraying of Ti and Al-12Si powder mixtures. No significant oxidation or diffusion between Ti and Al occurred during the spraying process. Two-stage heat treatment with pressure of 30 MPa of the warm sprayed coatings led to the formation of Ti-Al intermetallic phases, of which $TiAl_3$ and TiAl were the most dominant. Addition of silicon to the coating resulted in formation of the hard Ti_5Si_3 silicide particles. Void ratio of hot pressed coatings with addition of Si was reduced below 0.5% and densification was enhanced in comparison to coatings without Si added.

Acknowledgements

The authors would like to thank Mr. T. Hiraoka for operating the thermal spray equipment.

References

1. K. C. Antony: Trans. AIME, 1968, 242, 1454
2. N. E. Paton and M. W. Mahony: Metall. Trans., 1975, 74, 1685.
3. M. Es-Souni, P. A. Beaven, R. Wagner, D. Chen, A. Bartles, and F. Seeger: in Proc. 2nd European Conf. of Advanced Materials and Processes "Euromat „91", 226-229, 1992, London, The Institute of Materials
4. K. W. Liu, J. S. Zhang, J. G. Wang, and G. L. Chen, "Formation of intermetallic nanocomposites in the Ti-Al-Si system by mechanical alloying and subsequent heat treatment", Journal of Materials Research, vol. 13, No. 5, May 1998
5. K. Kasahara, K. Hashimoto, H. Doi, and T. Tsujimoto, "Collected abstracts of the 1987 autumn meeting of the Japan Institute of Metals", Sendai, Japan, 313, September 1987
6. J. Sienkiewicz, S. Kuroda, R. M. Molak, H. Murakami, H. Araki, S. Takamori, K. J. Kurzydłowski, "Fabrication of TiAl intermetallic phases by heat treatment of warm sprayed metal precursors", Intermetallics, In Press
7. S. Kuroda, M. Watanabe, K.H. Kim, H. Katanoda, "Current Status and Future Prospects of Warm Spray Technology", J. Therm. Spray Technol.20 (2011) 653-676
8. S. Kuroda, J. Kawakita, M. Watanabe, H. Katanoda, "Warm spraying-a novel coating process based on high-velocity impact of solid particles", Sci. Technol. Adv. Mater. 9 (2008) 1-17
9. W. Koster and A. Sampio: Z. Metallk. 48 (1957) p. 331

Oxidation of Type 430 Stainless Steel Covered with Aluminosilicate Thin Coating at Elevated Temperatures

Taiki Kimura [1,*], Takayoshi Yano[2], Etsushi Tsuji [1,3], Yoshitaka Aoki [1,3], and Hiroki Habazaki [1,3]

[1] Graduate School of Chemical Sciences and Engineering, Hokkaido University, Kita13 Nishi8, Sapporo 060-8628, JAPAN
[2] Steel Research Laboratory, JFE Steel Corporation, 1 Kawasaki-cho, Chuo-ku, Chiba 260-0835, JAPAN
[3] Division of Materials Chemistry & Frontier Chemistry Center, Faculty of Engineering, Hokkaido University, Kita13 Nishi8, Sapporo 060-8628, JAPAN

e-mail: coco-110@frontier.hokudai.ac.jp

1. INTRODUCTION

Stainless steels are important practical metallic materials with high corrosion resistance at ambient and elevated temperatures. Among various stainless steels, Type 430 stainless steel is cheap, but relatively low corrosion resistance in aqueous environments and at high temperatures. Thus, in some cases Type 430 stainless steel is coated for corrosion resistance and for functionality of surfaces. In this study, Type 430 stainless steel was coated with a very thin, ~65 nm thick, aluminosilicate sol-gel coating. The oxidation behavior of the stainless steel with and without the coating was examined by GDOES depth profile analysis and conductive AFM imaging as well as cross-sectional TEM observations.

2. EXPERIMENTAL

Amorphous aluminosilicate films were prepared from mixed precursor solutions of tetraethoxysilane (TEOS) and aluminum sec-butoxide ($Al(OsBu)_3$). The substrate for the deposition was Type 430 stainless steel sheets mirror-finished by electrochemical-mechanical polishing. The films were deposited by multiple spin coating cycles in a layer-by-layer fashion. The precursor sol solutions were prepared as follows: 0.833 g of TEOS and 0.145 mL of 1 M (mol dm^{-3}) HCl were added to 10 mL of 1-propanol (1-PrOH). After stirring for 1 h at room temperature, 0.246 g of $Al(OsBu)_3$ was added to the stirred solution and the mixture was further stirred at 80ºC for 40 min to obtain a precursor solution with the total 50 mM concentration of aluminum and silicon species and the atomic ratio of Al/Si = 20/80. The precursor sol solutions (0.2 mL) were spin-coated on to the stainless steel substrate at 3000 rpm for 20 s. The coated specimen was exposed to hot air for 120-240 s to promote further hydrolysis of the deposited gel layer. These cycles were repeated 10 times to get ~65 nm-thick coatings.

The coated specimens thus obtained as well as as-received specimens were oxidized in air at 400ºC for 1 h. Then, the surfaces of the specimens were observed by FE-SEM with EBSB facilities. Electron transparent cross-sections of the specimens were prepared by FIB and the sections were examined by TEM. Depth profile analysis was carried out using rf-GDOES. Furthermore, conductive AFM was used to characterize the coated specimens.

3. RESULTS AND DISCUSSION

Figure 1 shows the surface SEM image of the non-coated Type 430 stainless steel after oxidation at 400ºC. Obviously, the oxidation of the Type 430 stainless steel is dependent upon grain orientation. In Figure 1, grains at the bottom side appear to be more oxidized and island-like oxides are developed on the surface. In order to identify the grain orientation, EBSD analysis was carried out. The results indicated that the oxidation proceeded at the highest rate on the {111} plane while the slowest oxidation occurs on {100} plane. In bcc materials, the low surface density of the {111} plane may have some influence on the oxidation rate.

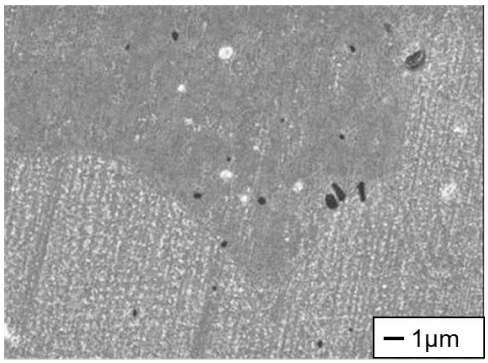

Fig. 1 Surface SEM image of Type 430 stainless steel after oxidation in air at 400ºC.

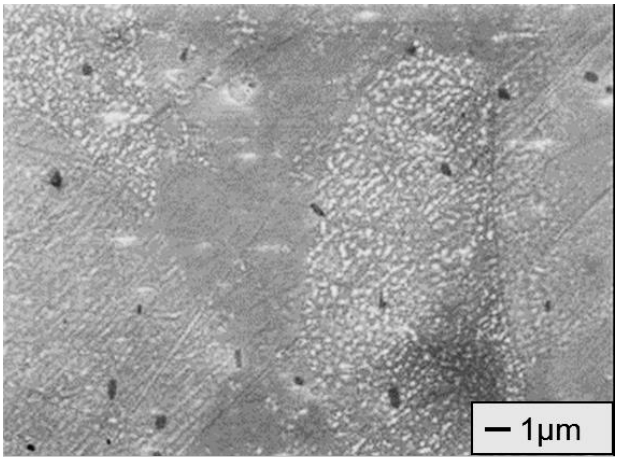

Fig. 2 Surface SEM image of the coated Type 430 stainless steel after oxidation in air at 400ºC.

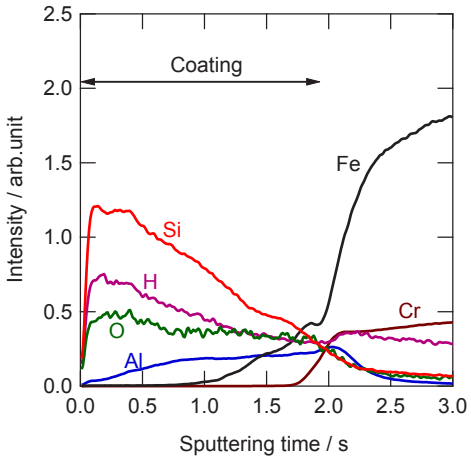

Fig. 3 GDOES depth profile of the coated Type 430 stainless steel after oxidation in air at 400ºC.

Figure 2 shows the surface SEM image of the coated Type 430 stainless steel after oxidation. Similar grain orientation-dependent surface image is obtained even after thin aluminosilicate coating. Figure 3 shows GDOES depth profile of the coated specimen after oxidation at 400ºC. Aluminum and silicon species are present in the coating throughout the thickness. It is obvious that iron diffuses into the coating and iron species are present in the approximately inner half of the coating. Such iron diffusion into the coating was not significant before oxidation at 400ºC. Thus, iron in the stainless steel substrate was oxidized at 400ºC and the oxidized iron should be diffused into the coating, probably through the micropores in the coating. Cross-sectional TEM observations disclosed that island-like oxide, probably composed mainly of iron oxide, was developed in the aluminosilicate coating. The island-like oxide formation is in agreement with the SEM observations shown in Figures 1 and 2.

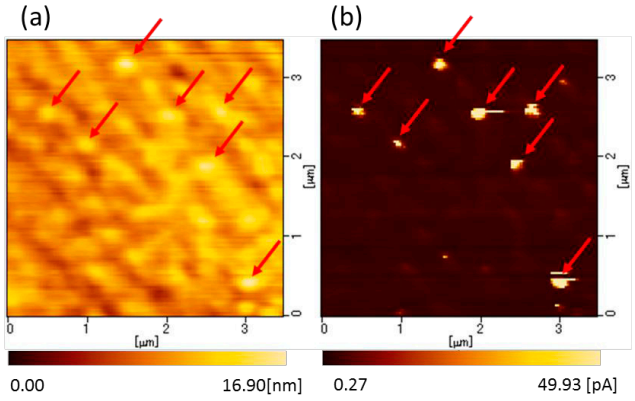

Fig. 4 (a) Height and (b) current AFM images of the coated Type 430 stainless steel after oxidation at 400ºC in air.

The coated specimens were further characterized by conductive AFM. Figure 4 shows the height and current images of the coated specimen after oxidation at 400ºC. Although the ~65 nm-thick aluminosilicate coating must be an insulator, high current flows at local regions when +10 V is applied to the metal substrate with respect to the conductive Rh-coated tip. From the comparison with the height image, the current flows at the ridge region of the coated specimen. The ridge may be developed by the formation of island-like iron oxide by oxidation of stainless steel substrate. The iron oxide formed is probably Fe_3O_4, and due to high electrical conductivity of this oxide, high current should flow at the ridge regions of the coated specimens. Thus, the oxidation of stainless steel strongly influences the properties of the thin oxide coating.

4. CONCLUSION

In summary, the oxidation of Type 430 stainless steel occurs at 400ºC even beneath the thin aluminosilicate sol-gel coating. The coating improved remarkably the corrosion resistance in NaCl aqueous solution, but the oxidation in air at elevated temperature is not effectively suppressed. Iron oxide is formed and diffuses into the coating, resulting in the introduction of electron-conducting channels in the coating.

Preparation and high temperature performance of a dual-phase PtAl coating on K38G superalloy

Yingfei Yang, Quan Liu, Zebin Bao*, Shenglong Zhu, and Fuhui Wang

Institute of Metal Research, Chinese Academy of Sciences, Wencui Rd. 62#, Shenyang 110016, CHINA

e-mail: zbbao@imr.ac.cn

1. INTRODUCTION

Pt modified aluminide coating has attracted much attention due to its integrated properties resisting both high temperature oxidation and hot corrosions [1-3]. Regardless the cost of platinum, PtAl coating still operates in some harsh applications which demand for higher reliability and longer service life. The major beneficial effect of PtAl coatings has been attributed to the enhanced oxide spallation resistance by the presence of Pt. In fact Pt is vitally essential for PtAl coating since it either gathers Al to support α-Al_2O_3 formation by uphill diffusion [4,5] or suppresses the detrimental effect of harmful elements like S [6-8]. A typical procedure to fabricate PtAl coating comprises pre-deposition of Pt, aluminization and several heat treatments [9].

Differed from phase constitution, there are four types of PtAl coating, including single phase $PtAl_2$, $PtAl_2$ + (Ni,Pt)Al dual phase, single phase (Ni,Pt)Al and γ/γ'-NiPtAl coatings. It is well known that $PtAl_2$ is not capable to satisfy practical services due to its notable brittleness, but $PtAl_2$ stores maximum amount of Al among the above-mentioned phases. The γ/γ'-NiPtAl coating has best high temperature mechanical property, but its Al content is much lower. Considering the oxidation resistance and mechanical property together, a dual phase $PtAl_2$ + (Ni,Pt)Al might be promising to provide relatively longer service life and proper mechanical property.

The goal of this study was to identify the property of a dual-phase PtAl coating prepared on a cast Ni-base superalloy. By evaluating the coated samples perform in cyclic oxidation and hot corrosion tests, the performance of the dual-phase PtAl coating will be understood.

2. EXPERIMENTAL

A K38G Ni-base superalloy (16.34Cr-8.38Co-4Al-2.66W-1.77Mo-1.75Ta-0.76Nb-0.16C-0.01B, balanced Ni, wt. %) was employed to cut samples with dimensions of 15×10×2 mm^3. After grinding down to 1000 mesh SiC sandpaper, the samples were grit blasted by 200 mesh Al_2O_3 dry beads and cleaned in acetone bath. Preceded by Ni-strike, the deposition of Pt was accomplished at 60 °C in an acid composite solution prepared from K_2PtCl_6 by electroplating using pulse current with duty ratio of 50 %. At last, a continuous thin film (3~5 μm) of Pt with good adhesion was acquired.

In order to mitigate the cracking trend induced by H_2 emission, the Pt-coated samples were step-by-step annealed at 200 °C for 0.5 h, 600 °C for 2 h and 1050 °C for 4 h, in vacuum. Then these specimens were buried in powder mixture of Fe-49Al (wt. %) and NH_4Cl, which the halide activator accounted for 2 wt. % of total. The pack-cementation process was conducted at 1000 °C for 2 h in a tube furnace made of steel. Prior to that, the furnace was pumped to 10 Pa and filled with Ar for 2 times, ensuring an inert environment during aluminization. Finally, a dual-phase $PtAl_2$ + (Ni,Pt)Al coating with thickness of 80 μm was obtained. As the pack aluminization is high aluminum activity process, a subsequent vacuum-annealing treatment was applied on the dual-phase PtAl coating samples at 1050 °C for 4h.

Oxidation behavior of specimens was performed cyclically in a vertical tube furnace at 1100 °C for 200 cycles, which one cycle consisted of 1 h in furnace and 10 min outside. The hot corrosion behavior was tested at 900 °C for 100 h, with painting salt mixture of 0.75Na_2SO_4 + 0.25NaCl (wt. %) for 1.5 $mg \cdot cm^{-2}$ at each interval. At intervals of oxidation and hot corrosion, the mass change of specimens was measured using a 10^{-5} g sensitive electronic balance. For preserving the oxide scale, an electroless plating of Ni was introduced for cross-sectional sample preparation.

3. RESULTS AND DISCUSSION

As shown in Fig.1, the Pt surface was beautifully dense and composed of numerous round-shaped platinum particles.

After careful inspection, some visible pinholes can be observed on the Pt surface. These pinholes were formed as a by-product from hydrogen evolution since the operating voltage for Pt deposition was quite high and an acid electroplating environment was involved. These pinholes could be extinguished after annealing treatment. The thickness of the Pt layer was about 3 μm and it bonded well to the pre-deposited Ni layer. After dehydrogenation and vacuum-annealing treatment, the Pt layer started to merge with K38G superalloy to form Ni-Pt solid solution. Actually this solid solution was quite Al-rich comparing with K38G superalloy and the phase constitution was still γ/γ′. As Pt possesses higher affinity to Al than Ni does [10], an uphill diffusion of Al must occur during the prior Pt diffusion. When a superalloy with higher Al-content is engaged, the γ/γ′ coating enriched with Al could behave well in resisting oxidation attack. Besides, the phase constitution of the coating is same to the substrate, thus their CTE values should get close to each other. As a result, the mechanical property at high temperature for the γ/γ′ coating would be guaranteed. Fig. 1d shows the microstructure of the dual-phase PtAl coating after aluminization and post-annealing treatment. It is clear $PtAl_2$ (white) and β-(Ni,Pt)Al (dark) evenly shares whole view of the dual-phase coating. Between the coating and K38G substrate, a 10 μm interdiffusion zone (IDZ) and Kirkendall holes were present. The contents of Pt and Al in the dual-phase coating are higher than 16 at. % and 50 at. %, respectively.

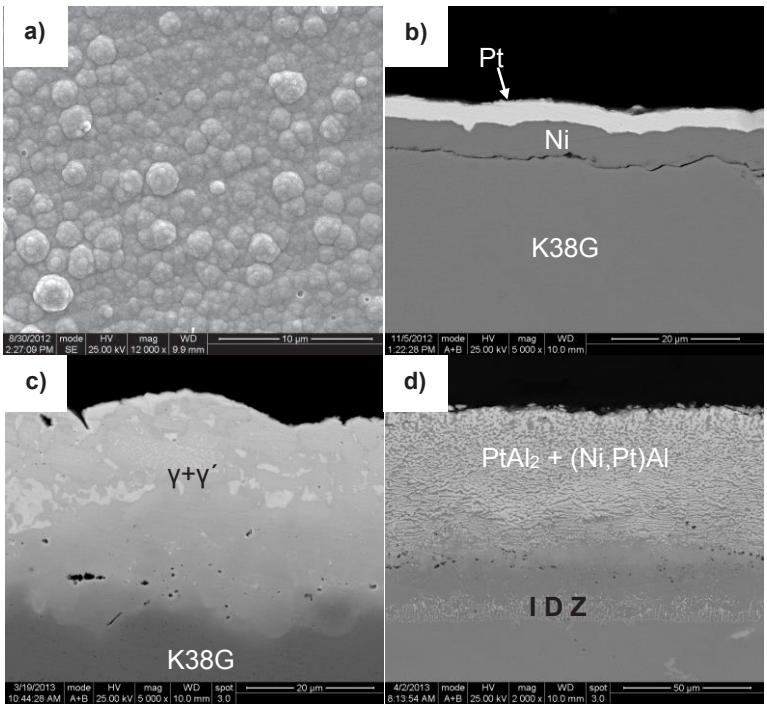

Fig. 1 Surface and cross-sectional morphologies of the PtAl coating (a: as-received surface; b: as-received cross-section; c: after prior Pt diffusion; d: pack aluminized + annealed)

As a matter of fact, Haynes et al have carried out a series of researches on γ/γ′-NiPtAl coatings, including Pt content effect [11], interdiffusion behavior [12], and comparison between NiAl, (Ni,Pt)Al and γ/γ′-NiPtAl [13]. Though γ/γ′-NiPtAl has shown much advantage for its improved mechanical properties while holding not-bad oxidation resistance, it did not surpass single phase β-NiPtAl coating. Also the γ/γ′ phase NiPtAl coating mainly fits Ni-base superalloys with comparatively higher Al content like Rene N5 and 142 (their Al content exceeds 14 at. %). To other superalloy with low Al content, the Al uphill diffusion induced by Pt would cause serious shortage of Al in the base alloy, which in further might lead to decomposition of coherent γ-γ′ structure. We examined the cyclic oxidation behavior at 1100 °C of γ/γ′ phase PtAl coating on K38G, and the result indicates depletion of Al occurred right after 40 cycles and a clear mass loss appeared by then.

Fig. 2 displays the phase identification results of the dual-phase PtAl coating during preparation. After prior Pt diffusion at 1050 °C for 4 h, simple Pt layer mainly changed to γ-(Ni,Pt) with various compositions. Based on the uphill diffusion of Al and Cr over-crowded from γ-phase, an intermetallic Al_8Cr_5 was formed too. The subsequent pack-cementation was a high activity process, leading to the formation of $PtAl_2$ and δ-Ni_2Al_3. With the further post annealing treatment, the phase

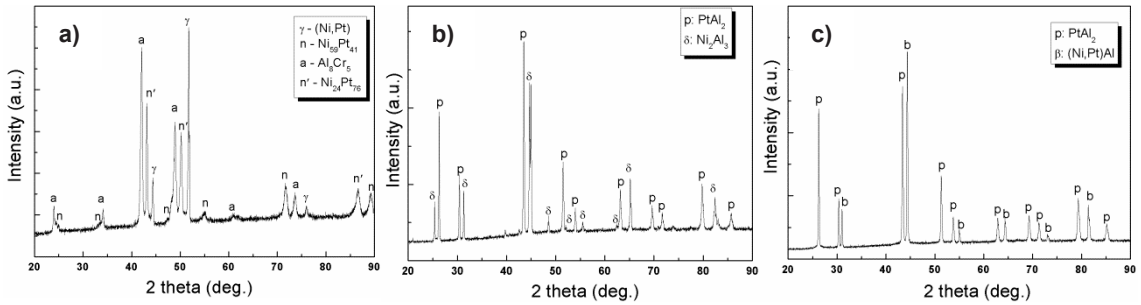

Fig. 2 XRD results for the PtAl dual-phase coating after prior Pt diffusion (a), pack-cementation (b) and post-annealing (c)

transformation from δ-Ni_2Al_3 to β-(Ni,Pt)Al was accomplished.

The mass change curves of the dual-phase PtAl coating in the cyclic oxidation and hot corrosion tests are shown as Fig. 3. The K38G substrate behaved poorly in both the cyclic oxidation and hot corrosion test by presenting obvious sustained mass losses throughout the tests. On the contrary, the dual-phase PtAl coating behaved perfectly in cyclic oxidation and exhibited an almost horizontal mass change till end. The total mass gain is merely 0.44 mg·cm^{-2} after 200 cycles. In the aggressive hot corrosion test involving NaCl salt, the dual phase coating exhibited a slow mass gain either. Both the mass change curves of oxidation and hot corrosion confirm an excellent protective capability for the dual-phase PtAl coating.

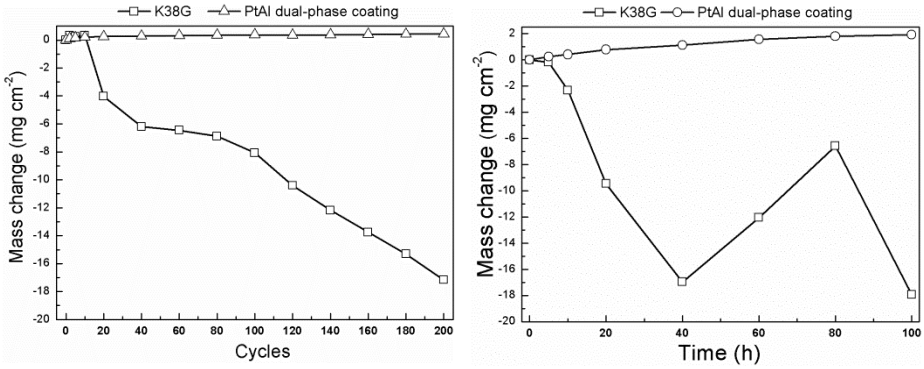

Fig. 3 Mass change curves of the PtAl dual-phase coating compared with K38G substrate (left: cyclic oxidation at 1100 °C, right: hot corrosion in 0.75Na_2SO_4 + 0.25NaCl at 900°C)

Fig. 4 displays the cross-sectional morphology of the dual-phase PtAl coating and K38G substrate after 200 cycles' oxidation and 100 h hot corrosion. After 200 cycles, an oxide scale of non-protective NiO and spinel was formed on K38G substrate. On some area, nodular oxides were formed either. Also internal oxidation (mainly relating to Cr) occurred in deeper region. Between the two nodules shown in Fig. 4a, a spallation of oxide scale can be inferred. This spallation of oxide has been reflected by the continuing mass loss shown in Fig. 3a. Being oxidized identically, the dual-phase PtAl coating developed a consecutive α-Al_2O_3 scale on the surface. The thickness of coating (~100 μm) and interdiffusion zone (50 μm) became larger than its as-received condition. In order to inspect the elemental composition of the dual-phase PtAl coating after oxidation, an energy dispersive X-ray analysis was carried out on the area marked with dash-line. The result indicates there were still 35 at. % of Al and 4 at. % of Pt remained, and this level of Al content could further support the exclusive formation of α-Al_2O_3 scale. Fig. 4c indicates a disastrous result of K38G substrate after hot corrosion. Although K38G possesses relatively higher amount of Cr and was designed on purpose to resist hot corrosion, once Cl^- was engaged this cast superalloy turned to be very fragile, leaving thick corrosion products, visible holes and internal oxidation behind. After same hot corrosion test, the dual-phase PtAl coating was undoubtedly superior by developing a thick oxide formation of α-Al_2O_3. The normalized EDAX analysis indicates there were 49 at. % of Al and 15 at. % of Pt left. It is believed the dual-phase coating could provide longer service life in future.

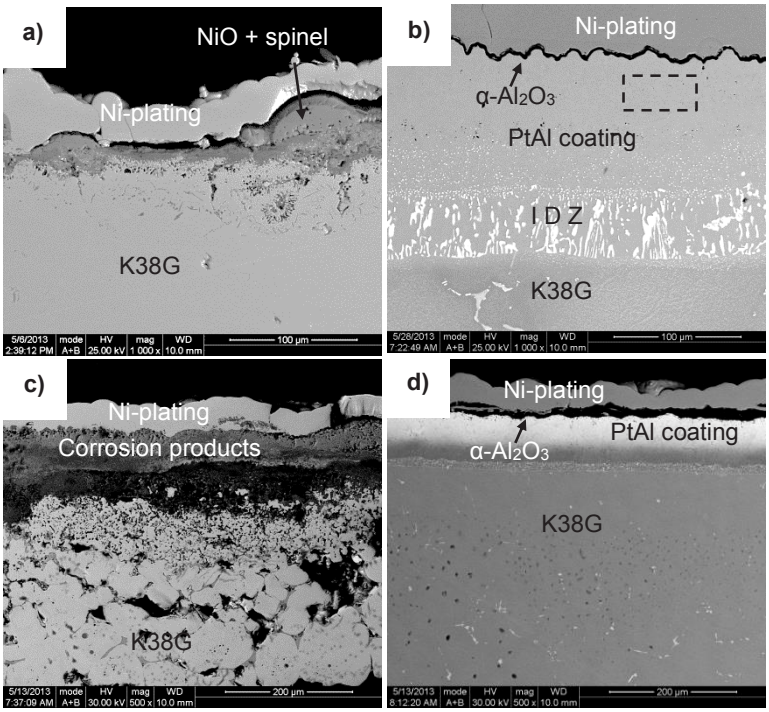

Fig. 4 Cross-sectional morphologies of K38G substrate (a, c) and PtAl dual-phase coating (b, d) after 200 cycles' oxidation at 1100 °C (a, b) and 100 h hot corrosion at 900 °C in 0.75Na_2SO_4 + 0.25NaCl mixed salt (c, d)

Based on the experimental result, it is clear the dual-phase PtAl coating is fully competent to offer excellent resistance against high temperature oxidation and hot corrosion. The superiority lies in its higher storage of Al by the presence of

dispersive $PtAl_2$ phase. After a certain time of oxidation or hot corrosion, the dual-phase PtAl coating would transfer to single phase β-(Ni,Pt)Al coating, still holding good oxidation and corrosion resistance. In the current design, $PtAl_2$ phase was homogeneously distributed within β-(Ni,Pt)Al coating, which could maximally alleviate the negative effect of $PtAl_2$. The experience of withstanding the cyclic oxidation test is a good example to explain its enhanced mechanical property than single $PtAl_2$ coating (the author also checked cyclic oxidation behavior of single $PtAl_2$ coating on K38G, and the $PtAl_2$ layer started to spall off after 5 cycles, indicating much brittleness). As the above results of cyclic oxidation and hot corrosion considered, the dual-phase PtAl coating might have the potential offering services in practical applications. The mechanical property like creep and stress-rupture resistance of the dual-phase PtAl coating needs to be investigated in the approaching future.

4. CONCLUSION

A dual-phase ($PtAl_2$ + β-(Ni,Pt)Al) PtAl coating was prepared through electroplating of Pt, prior Pt diffusion, pack-cementation and post annealing treatment. Inside the dual-phase PtAl coating, $PtAl_2$ and β-(Ni,Pt)Al were uniformly distributed with each other. The cyclic oxidation and hot corrosion tests confirmed a remarkably improved resistance for the PtAl dual-phase coating. From the aspect of oxidation and hot corrosion, the dual-phase coating could be competitive to the single $PtAl_2$, single β-(Ni,Pt)Al and γ/γ′-NiPtAl coating. Further investigation of mechanical property at high temperature is in need.

References:

[1] Wright, I.G. *et al*, "Bond Coating Issues in Thermal Barrier Coatings for Industrial Gas Turbines", *J. Power and Energy*, Vol. 219 (2005), pp. 101-107.

[2] Angenete, J. *et al*, "Oxidation of Simple and Pt-Modified Aluminide Diffusion Coatings on Ni-Base Superalloys— I. Oxide Scale Microstructure", *Oxid. Met.*, Vol. 60 (2003), pp. 47-82.

[3] Angenete, J. *et al*, "Oxidation of Simple and Pt-Modified Aluminide Diffusion Coatings on Ni-Base Superalloys— I. Oxide Scale Failure", *Oxid. Met.*, Vol. 60 (2003), pp. 83-101.

[4] Gleeson, B. *et al*, "Effects of Platinum on the Interdiffusion and Oxidation Behavior of Ni-Al-Based Alloys", *Mater. Sci. Forum*, Vol. 461-464 (2004), pp. 213-222.

[5] Hayashi, S. *et al*, "Interdiffusion Behavior of Pt-Modified γ-Ni +γ′-Ni3Al Alloys Coupled to Ni-Al-based Alloys", *Metall. Mater. Trans.*, Vol. 36(A) (2005), pp. 1769-1775.

[6] Warnes, B. M. *et al*, "Clean Diffusion Coatings by Chemical Vapor Deposition", *Surf. Coat. Technol.*, Vol. 94-95 (1997) pp. 1-6.

[7] Zhang, Y. *et al*, "Synthesis and Cyclic Oxidation Behavior of a (Ni, Pt) Al Coating on a Desulfurized Ni-Base Superalloy", *Metall. Mater. Trans.*, Vol. 30(A) (1999), pp. 2679-2687.

[8] Haynes, J. A. *et al*, "Comparison of the Cyclic Oxidation behavior of β-NiAl, β-NiPtAl and γ/γ′-NiPtAl Coatings on Various Superalloys", *Surf. Coat. Technol.*, Vol. 202 (2007), pp. 730-734.

[9] Benoist, J. *et al*, "Microstructure of Pt-modified Aluminide Coatings on Ni-Based Superalloys", *Surf. Coat. Technol.*, Vol. 182 (2004), pp. 14-23.

[10] Ouyang, Y. F. *et al*, "The Calculation of Enthalpies of Formation for Noble Metal-Aluminum Binary Alloys with EAM", *Acta Metall. Sin.*, Vol. 35 (1999), pp. 551-553.

[11] Haynes, J. A. *et al*, "The Effect of Pt Content on γ-γ′ NiPtAl coatings", *Surf. Coat. Technol.*, Vol. 203 (2008), pp. 413-416.

[12] Zhang, Y. *et al*, "Interdiffusion Behavior of Pt-diffused γ+γ′ Coatings on Ni-based Superalloys", *Surf. Coat. Technol.*, Vol. 203 (2008), pp. 417-421.

[13] Haynes, J. A. *et al*, "Comparison of the cyclic oxidation behavior of β-NiAl, β-NiPtAl and γ-γ′ NiPtAl coatings on various superalloys", *Surf. Coat. Technol.*, Vol. 202 (2007), pp. 730-734.

Development of Self-Mending Coating System on Nb and Nb-based Alloys

Motohiro Ohtsuka*1, Daisuke Hotta*1, Takayuki Yoshioka*1, Toshio Narita*1
Taiichi Nagata*2, Ideo Masuda*2, Tadashi Masuoka*2,

*1 DBC System R&D Co., Ltd. 1-515-3, Zenibako, Otaru-City Hokkaido 047-0261 Japan
*2 Japan Aerospace Exploration Agency 2-1-1 Sengen, Tsukuba-City Ibaraki, 305-8505 Japan

Corresponding e-mail address: T. Narita; dbc@dbcsystem.co.jp

Abstract

A self-mending coating system on Nb, Nb-Hf (C-103) and Nb-17at%Si alloys was proposed with a multi-layer structure, an outer $ReSi_{1.8}$ or $Re(Si,Al)_{1.8}$, an intermediate $(Re,W,Mo,Nb)Si_2$ and an inner $NbSi_2$, followed by a transient Nb_5Si_3. The coating formation process was developed, and changes in structures and compositions during high temperature oxidation were discussed, based on the phase diagrams for the Re-Nb-Si and Re-Nb-Si-Al systems. It was found that solubility of Nb in the $ReSi_{1.8}$ and $Re(Si,Al)_{1.8}$ is negligible. Both $ReSi_{1.8}$ and $Re(Si,Al)_{1.8}$ were self-mended by Si supplied from the decomposition reaction as $NbSi_2 \rightarrow Nb_5Si_3+Si$ during selective oxidation of Al and/or Si.

1. Introduction

Niobium-base alloys [1, 2] have the highest specific strength at elevated temperatures, while they suffer from severe degradation due to high temperature oxidation. A Nb-Hf based alloy (C103) has been used for LBF bipropellant engines [3, 4] . A number of investigations have been conducted to form protective SiO_2 and/or Al_2O_3 scales. Although the $NbSi_2$ coating [5] has much attention, there are several subjects. One of them is a formation of non-protective Nb_5Si_3 on the $NbSi_2$ layer due to selective Si oxidation and the other degradation of coating structure due to the inter-diffusion between the coating and alloy substrate. Narita et al [5-7] proposed the coating with Re-based diffusion barrier layer on Nb-Mo-W alloys. Meanwhile, suppression of the Nb_5Si_3 formation is still opened for discussion.

In this paper a concept of the self-mending coating system was proposed, based on the phase diagrams for the Re-Nb-Si and Re-Nb-Si-Al systems. The self-mending coating system on Nb, Nb-Hf and Nb-17at%Si alloys was developed with an outer $ReSi_{1.8}$ or $Re(Si,Al)_{1.8}$, an intermediate $(Re,W,Mo,Nb)Si_2$, and an inner $NbSi_2$, followed by a transient Nb_5Si_3. Changes in structures and compositions during high temperature oxidation were investigated and discussed.

2. Experimental

The 99.9at%purity Nb metal, Nb-Hf base alloy (Commercial alloy; C103), and Nb-17at%Si alloy were used. Coupon specimens were cut from the bar and/or ingot, and then a 1.5mm- diameter hole was drilled for electroplating lead-connection. Specimens were polished using 220~1200 grit waterproof SiC papers and then washed in an acetone solution under ultrasonic agitation.

Following processes were adopted to form the coating system.

(1) Electroplating of Re: A Re film containing more than 99at%purity was electroplated from the aqueous solution [8] using a Pt anode at a bath temperature 323K.
(2) Slurry coating: Slurries containing Re, and/or W, Mo powders were dip-coated and after drying at room temperature organic binders in the slurry were decomposed at elevated temperatures.
(3) Low Si activity pack cementation: The low activity Si-pack cementation was carried out in Ar at 1923K for 4~13hrs using a C or SiC crucible containing a specimen buried in a powder of $NbSi_2$-Nb_5Si_3 and SiC.
(4) High Si activity pack cementation: The high Si activity pack cementation was carried out in vacuum at 1623K for 10min~6 hrs using a carbon or SiC crucible containing a specimen buried in a powder of Si and SiC.
(5) Al pack cementation: The Al pack cementation was carried out in vacuum at 1573K for 4~13hrs using a carbon crucible containing a specimen buried in a powder of Al, Si, and SiC.

The coated specimens were oxidized at temperatures between 1373k and 1673K in air and at

1773K in various oxygen partial pressures as 10^{-4}Pa (D.P. vacuum) and 10^{-1} Pa (Ar). The coated and then oxidized specimens were examined using SEM-EDX to determine concentration of each element and their profiles. A phase diagram of ternary Re-Nb-Si system and a partial part of the Re-Nb-Si-Al system were determined using alloy ingots after heat treatment at 1773K for 24hr in vacuum.

3. Results

Figure 1 shows a structure and concentration profiles of Nb, Re, and Si across the Nb specimen coated using the processes (1), (3), and (4). The coating film is comprised of a two layer structure: an outer $ReSi_{1.8}$ layer (400) and an intermediate ternary Nb-Re-Si alloy layer (300), followed by a transient Nb_5Si_3 layer (110).

The Al pack cementation (5) was then carried out on the coated Nb specimen shown in Fig.1, and a coating structure and concentration profiles of Nb, Re, Si, and Al were shown in Fig.2. It was found after the Al pack cementation that the coating film is comprised of a three layer structure: an outer $Re(Si,Al)_{1.8}$ layer (400) and an intermediate ternary Nb-Re-Si-Al alloy layer (300), and an inner $NbSi_2$ layer (200), followed by a transient Nb_5Si_3 layer (110). As shown in Fig.2, concentration profiles of Re and Al in the coating are essentially coincident with each other, and it means that Al can replace Si in $ReSi_{1.8}$ to form $Re(Si,Al)_{1.8}$.

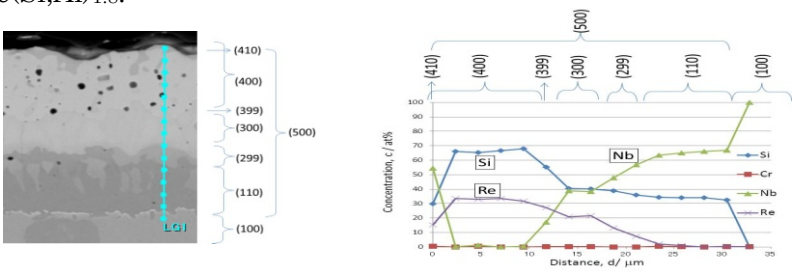

Fig.1 A cross-sectional microstructure and concentration profiles of each element across the coated Nb specimen with an outer $ReSi_{1.8}$ layer.

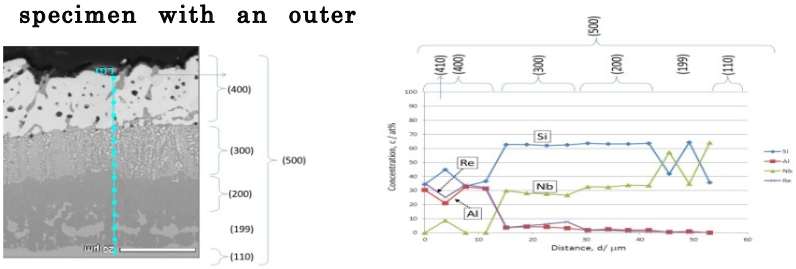

Fig.2 A cross-sectional microstructure and concentration profiles of each element across the coated Nb specimen with an outer $Re(Si,Al)_{1.8}$ layer.

Figures 3 and 4 show the cross-sectional microstructures and concentration profiles of each element across the Nb-Hf alloy (C103) and the Nb-17at%Si alloy with the coatings formed by using the processes (1)~(5). From these results the coating structures of these alloys are similar to that of the Nb specimen in Fig.2. Namely, both the coating films are comprised of three layer structures, an outer $Re(Si,Al)_{1.8}$ layer (400) and an intermediate $Re(Si,Al)_{1.8}$+ $(Mo,W,Nb)Si_2$ layer (300), and an inner $NbSi_2$ layer (200), followed by a transient Nb_5Si_3 layer (110).

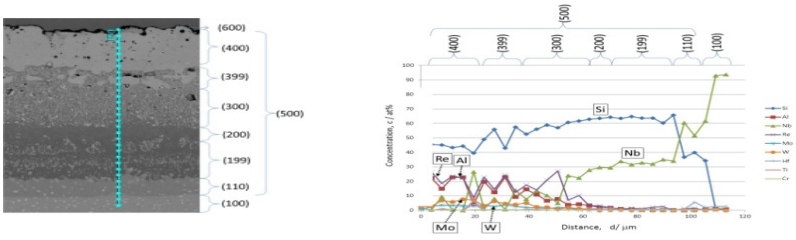

Fig.3 A cross-sectional microstructure and concentration profiles of each element across the coated Nb-Hf alloy specimen with an outer $Re(Si,Al)_{1.8}$ layer.

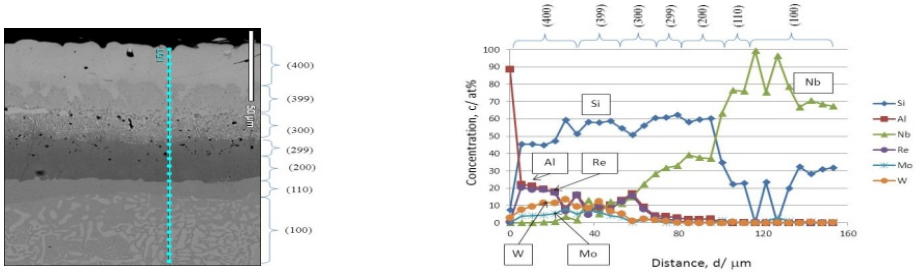

Fig.4 A cross-sectional microstructure and concentration profiles of each element across the coated Nb-17at%Si alloy specimen with an outer $Re(Si,Al)_{1.8}$ layer.

Figure 5 shows a cross-sectional microstructure and concentration profiles of Re, Si, Al, Nb, and O across the coated Nb specimen after oxidation at 1573K for 4 *1h*-cycles in air. It was found that the $Re(Si,Al)_{1.8}$ changed into $ReSi_{1.8}$ (400) due to selective oxidation of Al to form an external Al_2O_3 scale (600).

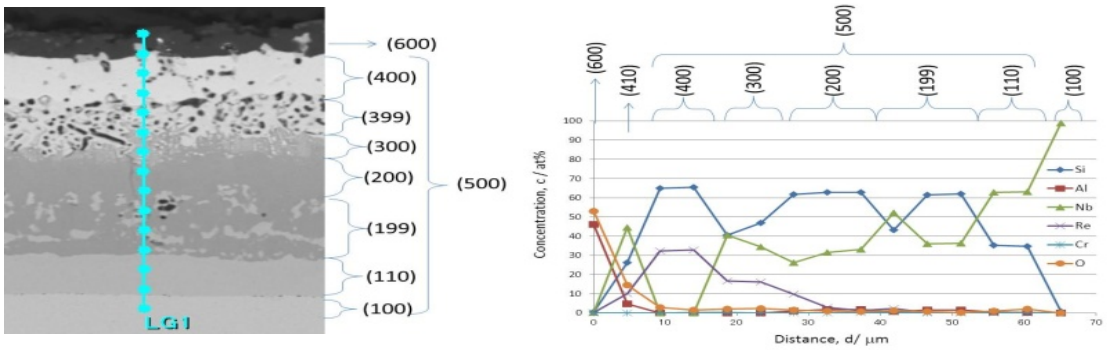

Fig.5 A cross-sectional microstructure and concentration profiles of each element across the coated Nb specimen after oxidation at 1573K for 4 *1h*-cycles in air.

Figure 6 shows the results obtained for the coated Nb-Hf alloy after oxidation at 1473K for 4 *1hr*-cycles in air. After the oxidation the $Re(Si,Al)_{1.8}$ is still existing, although Al content in the $Re(Si,Al)_{1.8}$ decreased, while Si content is increased. For both cases it was shown that a part of the inner $NbSi_2$ changed into Nb_5Si_3.

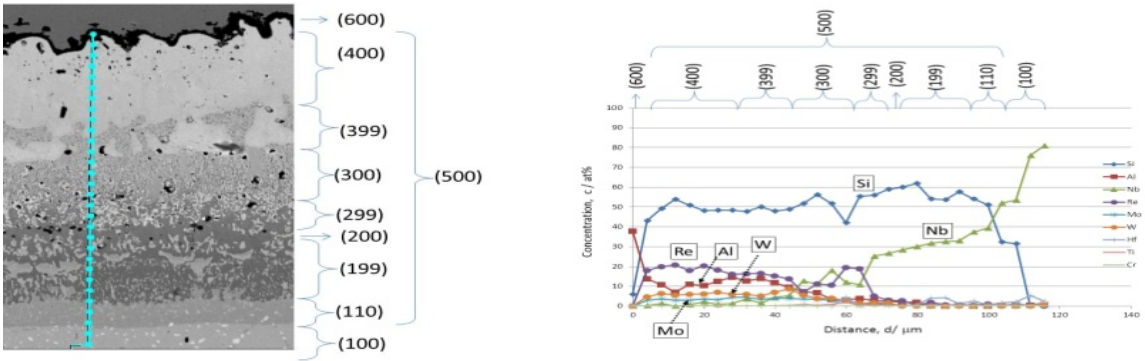

Fig.6 A cross-sectional microstructure and concentration profiles of each element across the coated Nb-Hf alloy specimen after oxidation at 1473K for 4 *1h*-cycles in air.

4. Discussion

The self-mending coating system on Nb and Nb based alloys proposed in this paper are characterized by two-items. One of them is an outer $ReSi_{1.8}$ or $Re(Si,Al)_{1.8}$ layer and the other is an inner $NbSi_2$ layer. Figure 7 shows a ternary Re-Nb-Si phase diagram [(7)], which was experimentally

determined, and a ternary Re-Nb-Si phase was confirmed, named as the Q phase. Further there are three-phases coexisting regions as $ReSi_{1.8}$-$NbSi_2$-Si (T1), $ReSi_{1.8}$- $NbSi_2$-Nb_5Si_3 (T2), and $ReSi_{1.8}$-Nb_5Si_3- Q (T3). Further solubility of Nb in the $ReSi_{1.8}$ and $Re(Si,Al)_{1.8}$ phases [9] was also experimentally determined, and it was found that solubility of Nb in both the phases is negligible.

It could be understand from the Re-Nb-Si phase diagram that Re can form $ReSi_{1.8}$ with both the processes (3) and (4). Meanwhile, the $NbSi_2$ seems to be stable exclusively in the process (4). Using the process (5) the $ReSi_{1.8}$ changed into the $Re(Si,Al)_{1.8}$ due to replacement of Si by Al.

During oxidation at elevated temperatures an external SiO_2 or Al_2O_3 scale forms on the outer $ReSi_{1.8}$ or $Re(Si,Al)_{1.8}$ layer by a selective Si or Al oxidation, lowering the Si or Al activity in the outer layer. At the low Si or Al activity in the $ReSi_{1.8}$ or $Re(Si,Al)_{1.8}$ the inner $NbSi_2$ (including NbSi2 in an intermediate layer) becomes unstable, decomposing into Nb_5Si_3 and Si. The Si released can move toward the outer $ReSi_{1.8}$ or $Re(Si,Al)_{1.8}$ layer. This explanation could be given to elucidate changes in structures and compositions of the coating system during high temperature oxidation. When the Al_2O_3 scale formation consumes completely Al in the outer $Re(Si,Al)_{1.8}$ layer, it changed into the $ReSi_{1.8}$ layer, as shown in Fig.5. This means that the coating proposed is self-mending. It could be emphasized that low Nb solubility in both the $ReSi_{1.8}$ and $Re(Si,Al)_{1.8}$ can avoid a non-protective Nb-oxide formation.

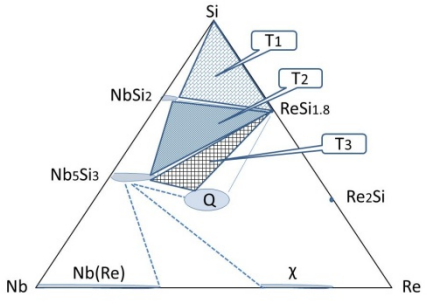

Fig.7 A ternary Re-Nb-Si phase diagram determined experimentally at 1773K

Acknowledgements

The author is indebted to JAXA (Japan Aerospace Exploration Agency) grant under contract number 13-0430001 supporting this investigation.

5. References

(1) Y. Yamabe-Mitarai, Y. Ro, S. Nakazawa, and H. Harada; J. Japan Inst. Metals, **64**(2000), pp.1068-1075.

(2) R. Tanaka; Materials at High Temperatures, **17**(2001), pp.457-464.

(3) M.L.Chazen; Long Life 5 LBF Bipropellant Engines ; AIAA'85 (1985) paper 1378

(4) US Patent : US 6,521,356 B2

(5) T. Narita, M. Fukumoto, Y. Matsumura, S. Hayashi, A. Kasama, I. Iwanaga, and R. Tanaka; Niobium for High Temperature Application, *Edited by Y-Won Kim and T. Carneiro*, TMS, 2004 ; Y. Matsumura, M. Fukumoto, S. Hayashi, A. Kasama, I. Iwanaga, R. Tanaka, and T. Narita; Oxidation of Metals, **61** Nos.1/2 (2004), pp. 105-124.

(6) Md. Zafir Alam, A. Sambasiva Rao, Dipak K. Das; Oxidation of Metals, **73**(2010), pp.513-530.

(7) Japanese Patent : #5295474

(8) Japanese Patents, #3904197, #4271399, #4323816

(9) M. Otsuka, D. Hotta, T. Yoshioka, T. Nagata, I. Masuda, T. Masuoka, and T. Narita; Unpublished data

The effect of co-firing of sewage sludge with waste wood on furnace wall corrosion

Yousef Alipour [1,*], and Pamela Henderson [1, 2]

[1] Surface and Corrosion Science Division, School of Chemical Science and Engineering, KTH Royal Institute of Technology, Drottning Kristinas väg 51, 10044, Stockholm, SWEDEN
[2] Vattenfall Research and Development AB, Stockholm, SWEDEN

e-mail: yousefa@kth.se

1. INTRODUCTION

The combustion of waste wood (recycled wood), which contains high amounts of chlorine, alkali and heavy metals [1-2], leads to severe corrosion problems in the furnace wall area of power plants [3-4]. Furnace walls are usually made of the low alloy carbon steel 16Mo3, with a coating of more corrosion resistant materials [5], for example nickel-base alloys, or high chromium-containing alloys.

It has been suggested that a fuel additive, such as sewage sludge, can change the flue gas chemistry and deposit composition, and consequently reduce high temperature corrosion problems [6-7]. Corrosion mechanisms are often studied in a simulated environment, where interpretation of the results is less complicated. However, in this study all the tests were made in a real environment. The samples were then studied under SEM/EDS, XRD and the thermodynamic stability of the corrosion product was also simulated.

2. EXPERIMENTAL

To study the effect of co-firing of sewage sludge, two air-cooled probes were exposed at the furnace wall in a bubbling fluidised bed boiler for 14.25 hours. Both probes contained low alloy steel 16Mo3 (the usual base of furnace walls), nickel-base alloy Alloy 625, iron-chromium-aluminium alloy APMT and stainless steel 310S. The Alloy 625 and APMT had previously been shown to have very good corrosion resistance to waste wood and together with 310S could be used for furnace wall coatings, [8]. The APMT sample was pre-oxidised by the supplier for 8 hours in air at 1050˚C to produce a protective 1 µm thick alumina layer on the sample surface. The temperature of the probes was controlled to 400˚C which is assumed to be the metal temperature of furnace walls. The power plant was operated on 100% waste wood during exposure of one probe, and then 8.4 wt% (1.7 vol%) of sewage sludge, as received, was added when testing the second probe. This corresponded to 3.5 dry wt% or 1.5% of the total energy. The chemical compositions of the samples are given in Table 1.

Table 1. Measuring Chemical compositions of coupons

Material	Wt%
Kanthal APMT	**Cr** 21.0, **Mo** 3.0, **Al** 5.0, **C** 0.08, **Si**0.7, **Mn** 0.4, **Fe** balance
16Mo3	**Mn** 0.55, **Si** 0.22, **Mo** 0.3, **Cu** 0.3, C **0.16**, **Fe** balance
310S	**Ni** 19.2, **Cr** 25.4, **Mo** 0.11, **Mn** 0.84, **Si** 0.55, **Ti** 0.001, **S** 0.001, **C** 0.046, **Cu** 0.08, **P** 0.015, **Ce** 0.004, **N** 0.04, **Fe** balance
Alloy 625	**Ni** 63, **Cr** 21, **Mo** 9.0, **Mn** 0.35, **Si** 0.2, **Ti** 0.25, **Al** 0.19, **Nb** 3.5, **Fe** balance

Deposits formed on the samples were chemically analysed under scanning electron microscopy (SEM)/energy dispersive spectroscopy (EDS) with 20 kV acceleration voltage. Fig. 1 shows the analysing protocol for all samples' deposits.

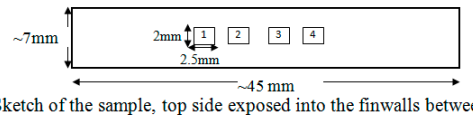

Fig. 1. Sketch of the sample, top side exposed into the finwalls between two tubes at furnace walls area. 4 different areas on the middle of each specimen were analysed under SEM/EDS.

The samples were dry polished by soft papers at the edge to facilitate the study of the interface between oxide layer and the substrate base metal, (see Fig. 2). Dry polishing avoided washing away the deposit, especially chlorine products which are soluble in water.

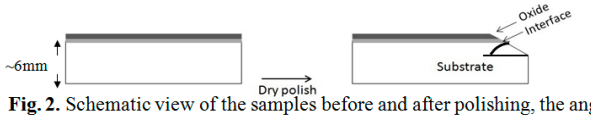

Fig. 2. Schematic view of the samples before and after polishing, the angle shown at the right figure was between 30˚ and 45˚.

X-ray diffraction (XRD) was performed on two nickel-base alloy samples. Specimens were first analysed on the deposit side. The deposit was then scraped off and the underneath layers were investigated separately.

3. RESULTS AND DISCUSSION

Average chemical compositions for 4 different areas on deposits are separately shown in Tables 2 and 3 for all the samples. The results show less chlorine, potassium and sodium in the deposits when burning sewage sludge along with waste wood, while deposits contain more aluminium, phosphorus and silicon.

Table 2. Average chemical composition results on waste wood samples

wt%	O	Na	Mg	Al	Si	P	S	Cl	K	Ca	Ti	Mn	Fe	Cu	Zn	Pb
APMT	40.4	6.4	1.3	1.5	1.5	0.5	11.3	5.0	7.5	8.9	2.6	0.2	1.6	0.3	2.5	8.1
16Mo3	31.8	8.9	1.1	1.7	1.6	0.4	6.0	15.4	8.4	6.7	2.0	0.8	5.5	0.1	4.9	4.4
310S	38.8	5.8	1.3	0.9	1.5	0.6	10.1	4.9	8.6	9.0	2.7	0.4	3.7	0.5	4.6	6.1
Alloy 625	40.8	4.5	1.5	1.0	1.9	0.7	10.6	4.0	8.5	10.7	3.2	0.2	1.1	0.2	4.2	6.6

Table 3. Average chemical composition results on waste wood + sewage sludge samples

wt%	O	Na	Mg	Al	Si	P	S	Cl	K	Ca	Ti	Mn	Fe	Cu	Zn	Pb
APMT	44.7	3.7	1.6	2.7	3.5	1.8	7.1	2.3	5.05	12.3	3.2	0.2	4.4	0.0	3.6	3.3
16Mo3	46.1	3.2	1.8	2.4	4.7	1.6	5.2	3.7	3.3	14.1	3.9	0.2	4.2	0.0	3.2	1.9
310S	43.7	4.2	1.4	3.4	3.6	1.7	6.6	2.7	4.4	11.2	3.0	0.2	4.8	0.2	3.6	4.7
Alloy 625	42.1	4.0	1.2	4.5	3.5	1.8	6.6	3.1	5.0	10.8	2.9	0.2	4.3	0.2	3.3	6.0

The sewage sludge contains aluminosilicates, phosphorus and sulphur. The interaction of alkali and aluminosilicates can probably reduce the deposition of potassium, sodium and chloride [9]. Sulphation was not expected because of reducing conditions in the furnace region.

The interface between oxide and metal base (initial corrosion front) was investigated by mapping under SEM/EDS. The 16Mo3 had corroded rapidly under both conditions so that it was difficult to say how much effect the sewage sludge had had. However it could be clearly seen that the chloride layer at the corrosion front was considerably reduced in thickness by use of the sludge, which implies a reduced corrosion rate. It could also be seen that the sludge lowers the initial corrosion in the other samples. The corrosion product in 16Mo3 samples was mainly iron chloride, Fig. 3.

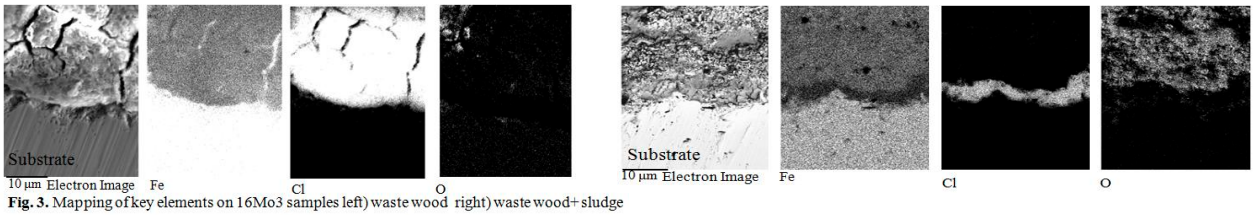

Fig. 3. Mapping of key elements on 16Mo3 samples left) waste wood right) waste wood+sludge

The result shows that oxygen and chlorine barely overlap at the corrosion front, which leaves an iron chloride at the corrosion front. Chlorine in hydrated form [10], or via the ionic transport of Fe and Cl [11], has been suggested to govern the chlorine-induced corrosion under an oxide layer of a steel, rather than by gaseous chlorine [12,13].

Co-firing of sewage sludge in 310S reduced the initial corrosion as can be seen in Fig. 4 which shows a reduced migration of nickel, chromium and iron into the deposit. It has been proposed that the protective chromia layer can be attacked by molten chloride-containing salts, e.g. KCl, to form a non-protective chromate [14]. The results (Fig. 4) imply that reducing the amount of potassium and chlorine in the deposit has helped to maintain the chromia layer.

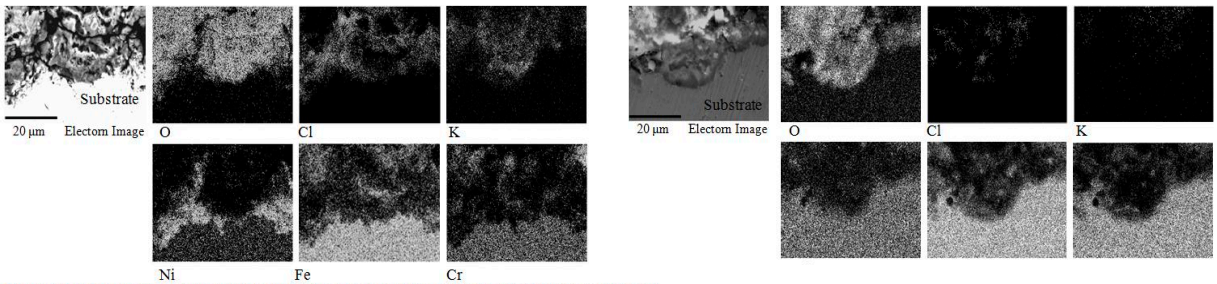

Fig. 4. Mapping of 310S stainless steel samples left) when firing waste wood right) when firing waste wood + sewage sludge

Co-firing sewage sludge had a positive effect on retaining the alumina layer in FeCrAl alloy APMT (see Fig. 5). Figure 5 shows that initial corrosion in APMT samples is less when burning sewage sludge along with waste wood and the alumina layer has not been destroyed.

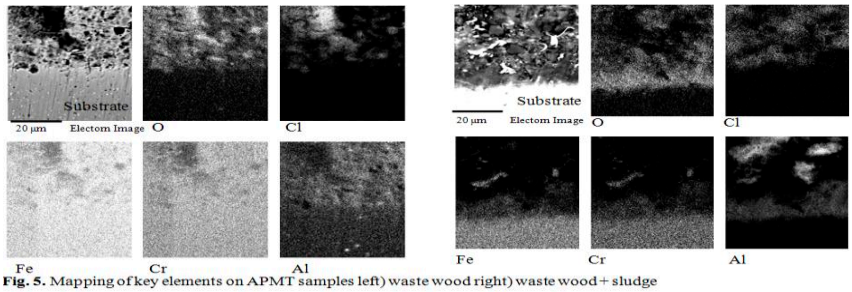

Fig. 5. Mapping of key elements on APMT samples left) waste wood right) waste wood + sludge

Alloy 625 overlay coating is reported to be acceptable in waste-burning power plants [15] and it can reduce the furnace wall corrosion attack [16]. The corrosion mechanism of Alloy 625 in biomass-fired boilers is a difficult issue and different corrosion mechanisms can occur simultaneously. It has been reported that lead oxide can attack protective chromia and reduce the corrosion resistance of nickel-based alloys by the formation of lead chromate [17], and it has been recently found that potassium can also attack the alloy by forming potassium chromate [14]. The XRD results, (Table 4) from this work are in agreement with those above and show the formation of $K_2Pb(CrO_4)_2$, even in this short 14.25 hours period, when burning waste wood This unprotective compound is also reported in some other works [18]. On the other hand the combination of potassium and lead doesn't seem to appear when burning 12% sewage sludge, leaving the protective chromia intact, Table 5.

Table 4. Compound found under XRD in Alloy 625, when burning waste wood

Strong intensity	Medium intensity	Weak intensity
NiO	(Na,K)2SO4	K2SO4, Pb, K2Pb(CrO4)2

Table 5. Compound found under XRD in Alloy 625, when burning waste wood + sewage sludge

Strong intensity	Medium intensity	Weak intensity
K2Ca2(SO4)3, Cr2O3	PbSiO3	Fe2O3, PCl3

Mapping of nickel-based Alloy 625, Fig. 6, shows that adding sewage sludge to the waste wood reduces the corrosion, as evidenced by the reduced spreading of nickel from the metal into the deposit.

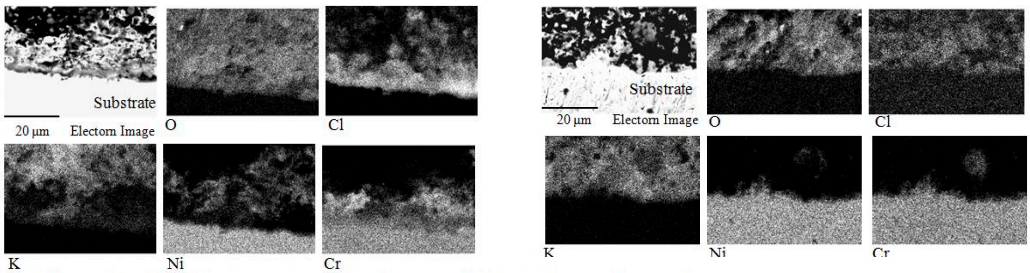

Fig. 6. Mapping of Alloy 625 nickel-based samples right) when firing waste wood left) when firing waste wood + sewage sludge

4. CONCLUSION

The results from this work showed that the co-firing of sewage sludge with recycled wood reduced the amounts of K, Na and Cl on the furnace wall deposits. This led to a reduction in the corrosion of Alloy 625 nickel-based alloy, 310S stainless steel, APMT FeCrAl alloy and the low alloy steel 16Mo3 during short-term tests. The dominant mechanism in the 16Mo3 was chlorine-induced corrosion. Attack by a potassium-lead combination appeared to be the main corrosion mechanism in the Alloy 625 during waste wood combustion. This resulted in the formation of a non-protective potassium-lead chromate. The addition of sewage sludge suppressed this attack and the protective chromia layer was maintained.

Acknowledgements

Financial support from Swedish Energy Agency and Vattenfall are gratefully thanked. The authors acknowledge Mattias Mattsson, and other colleagues at Vattenfall who have helped with the plant testing.

References

[1] Strömberg, B., Herstad, S.S., Bränslehandboken, Värmeforsk, (Stockholm, 2012).
[2] Krook, J., Mårtensson, A., Eklund, M., "Metal Contamination in Recovered Waste Wood Used as Energy Source in Sweden", *Resour. Conserv, Recycl.*, Vol. 41, No. 1, (2004), pp. 1-14.
[3] Andersson, C., Högberg, J. Fouling and Slagging Problems at Recovered Wood Fuel Combustion, Värmeforsk, (Stockholm, 2001), available at: www.varmeforsk.se/rapporter .
[4] Hohmann, U., Mohr, G., "High Temperature Corrosion in Biomass-Fired Boilers", *VGB PowerTech*, Volume 85/2005, No. 6, (2005), pp. 38-47.
[5] Kahawara, Y., "High Temperature Corrosion Mechanisms and Effect of Alloying Elements for Materials Used in Waste Incineration Environment", *Corros. Sci.,* Vol. 44, No. 2, (2002), pp. 223-245.
[6] Karlsson, S., Åmand, L., E., Pettersson, J., "Reducing High Temperature Corrosion when Burning Waste by Adding Digested Sewage Sludge", *Proc Swedish-Finish Flame Days*, Piteå, January,(2011), pp. 1-19.
[7] Davidsson, K.O., Åmand, L. E., Elled, A. L., Leckner, B., "Effect of Co-firing Coal and Biofuel with Sewage Sludge on Alkali Problems in a Circulating Fluidized Bed Boiler", *Energy Fuels*, Vol. 21, No. 4, (2007), pp. 3180-3188.
[8] Alipour Y., Henderson, P., "Corrosion of Furnace Wall Materials in a Waste-wood Fired Power Plant", **Submitted Paper**, KTH Royal Institute of Technology, Corrosion Science, Stockholm, Sweden.
[9] Yrjas, P., Aho, M., Zevenhoven, M., Taipale, R., Silvennoinen, J., Hupa, M., "Co-firing of Sewage Sludge with Bark in a Bench-scale Bubbling Fluidized Bed – a Study of Deposits and Emissions", *Proc of the 20th International Conference on Fluidized bed Combustion*, Xi'an, May, (2009), pp. 922-929.
[10] Szakalos, P., Henderson, P., Pettersson, R., "Mechanisms of chlorine induced corroson and effect of sulphur additive in superheater corrosion in biomass- and waste fired boilers", *Proc 16th International Corrosion Conference,* Beijing, September, (2005).
[11] Folkesson, N., Johansson, L. G., Svensson, J. E., "Initial Stages of the HCl-induced High Temperature Corrosion of Alloy 310", *J. Electrochem. Soc.*, Vol. 154, No. 9, (2007), pp. 515-521.
[12] Zahs, A., Spiegel, M., Grabke, H. J., "Chloridation and Oxidarion of Iron, Chromium, Nickel and Their Alloys in Chloridizing and Oxidizing Atmospheres at 400-700˚C", *Corros. Sci.*, Vol. 42, (2000), pp. 1093-1122.
[13] Reese, E., Grabke, H. J., "Einflu von Chloriden auf die Oxidation des 2¼ Cr-1 Mo-Stahls", *Werkst. Korros*, Vol. 43, (1992), pp. 547-557.
[14] Pettersson, J., Asteman, H., Svensson, J. E., Johansson, L. G., "KCl Induced Corrosion of a 304-type Austenitic Stainless Steel at 600˚C: The Role of Potassium", *Oxid. Met.*, Vol. 64, No. 112, (2005), pp. 23-41.
[15] Pettersson, R., Flyg, J., Viklund, P., "Materials Performance in Simulated Waste Combustion Environment", *Corros. Eng. Sci. Technol.*, Vol. 43, No.2, (2008), pp. 123-128.
[16] Viklund, P. PhD Thesis, Superheater Corrosion in Biomass and Waste Fired Boilers, KTH Royal Institute of Technology, (Stockholm, 2013).
[17] Chatterji, D., McKee, D.W., Romeo, G., Spacil, H.S., "The Effect of Lead on the Hot Corrosion of Nickel-base Alloys", *J. Electrochem, Soc.*, Vol. 122, (1975), pp. 941-952.
[18] Alipour, Y., Viklund, P., Henderson, P., "The Analysis of Furnace Wall Deposits in a Low-NOx Waste Wood- fired Bubbling Fluidised bed Boiler", *VGB PowerTech, Vol. 12, (2012), pp. 96-100.*

Behavior in Oxidation at 1200°C of Cast Co-based, Ni-based and Fe-based Alloys Containing HfC Carbides

Elodie Conrath [1,*] and Patrice Berthod [1]

[1] Institut Jean Lamour, University of Lorraine, Vandoeuvre-lès-Nancy 54506, FRANCE

e-mail: elodie.conrath@univ-lorraine.fr, patrice.berthod@univ-lorraine.fr

1. INTRODUCTION

Many cast superalloys working in hot conditions must be reinforced by interdendritic carbides. These ones must be extremely stable at high temperature when the alloys are considered for especially severe thermal applications. The volume fractions and morphologies of the most common carbides, as the chromium ones and even the TaC carbides, evolve too rapidly in such conditions [1] with consequently a loss in creep resistance. Fortunately, other interdendritic carbides – notably the HfC ones – are particularly resistant to such phenomena [2] and their script-like shape is globally maintained for longer times than for the TaC one. Hafnium, element known to significantly improve the high temperature oxidation behavior [3,4], is generally added to alloys in rather low quantities (e.g. in the 0.25 to 1.5 wt.% range) to commercial alloys. But this element is obviously rarely chosen for promoting MC carbides to resist creep.

In the present work, nine 25 wt.%Cr–containing cast alloys – three Co-based, three Ni-based and three Fe-based ones – containing various amounts in carbon (0.25 and 0.50 wt.%C) and hafnium with two levels of contents (from 4-5 to 7-9 wt.%Hf), were tested in oxidation at 1200°C in air. The aim was to study how these particularly high Hf contents, necessary to develop a sufficient network of reinforcing HfC carbides, may influence the high temperature oxidation behavior of the alloys.

2. EXPERIMENTAL

The nine alloys were elaborated by foundry way, from pure elements (Co, Ni, Fe, Cr and Hf: Alfa Aesar, purity > 99.9 wt.%). Fusion, the {5 minutes}–long stage in liquid state, cooling and solidification were realized in the water–cooled copper crucible of a CELES high frequency induction furnace, under an inert atmosphere of 300mbars of pure argon. The obtained compact–shaped ingots, weighing about 40g, were cut using a Buelher Isomet 5000 precision saw, in order to obtain parts for as-cast microstructure examinations and chemical composition control, as well as parallelepipeds (dimensions: about 10 × 10 × 3 mm^3) for the thermogravimetry oxidation tests. These latter samples were ground with SiC papers from 240 to 1200-grit, with smoothing of edges and corners.

The thermogravimetry runs were performed at 1200°C in a SETARAM TG92 thermo-balance, in dry industrial air (80%N_2 – 20%O_2). The heating rate, isothermal stage duration and cooling rate were respectively equal to +20K min^{-1}, 46h for the Ni-based and Fe-based alloys and 50h for the Co-based ones, and -5K min^{-1}. The oxidized samples were subjected to X-Ray Diffraction (nature of the external oxide scales), thereafter coated by pulverized gold and electrolytic nickel (to prevent oxide loss during cutting), and cut in two parts before cross-sections preparation.

The as-cast parts and the cut Ni-coated oxidized samples were embedded in a cold resin mixture (ESCIL). They were thereafter ground with SiC papers from 240 to 1200-grit, then polished with textile enriched with 1µm hard particles. The initial microstructures of the alloys were examined using a JEOL JSM 2010-LA Scanning Electrons Microscope (SEM) in Back Scattered Electrons mode (BSE). Their chemical compositions were controlled using the Energy Dispersion Spectrometry (EDS) apparatus equipping the SEM. The SEM was also used to characterize the external and internal oxides formed over the oxidized samples and in their sub-surface. Pinpoint EDS measurements were additionally performed to complete the identification of the oxides, as well as the local chemical compositions of the oxidized alloys close to the oxide scale/alloy interface.

The mass gain files were all classically analyzed for specifying the values of the Kp constant (in the case of really parabolic kinetic). However, since 1200°C is a temperature high enough to allow the re-oxidation of chromia into the gaseous CrO_3 specie, the mass loss due to this chromia volatilization must be taken into account to do not underestimate the oxidation kinetic. Thus, for the alloys finally found with an external oxide scale exclusively (or mainly) composed of chromia (Cr_2O_3), the files were analyzed using the {$m \times dm/dt = Kp - Kv \times m$}-method [5] (m being the mass gain per surface unit area) in order to specify the real Kp values as well as the linear chromia volatilization constant Kv.

3. RESULTS AND DISCUSSION

The chemical compositions of the initial alloys obtained by foundry are displayed in Table I. In each family (M=Co, Ni or Fe) there are one alloy with 0.25 wt.%C and two alloys with 0.50 wt.%C. The M1-1 alloy is a low carbon alloy and the M2-2 is a high carbon alloy, both with a Hf atomic content close to the C one. The M2-1 alloy is a high carbon alloy with a Hf atomic content lower than the C one.

Table I. Compositions of the nine alloys elaborated by casting and subjected to the high temperature oxidation tests (all contents in wt.%)

Alloy designation	M (bal.)	Cr	C	Hf
Co1-1	Co (bal.)	25.5	0.25	3.8
Co2-1	Co (bal.)	25.6	0.50	3.9
Co2-2	Co (bal.)	25.8	0.50	8.8
Ni1-1	Fe (bal.)	25.7	0.25	4.4
Ni2-1	Fe (bal.)	25.6	0.50	4.8
Ni2-2	Fe (bal.)	25.3	0.50	6.6
Fe1-1	Fe (bal.)	25.7	0.25	3.9
Fe2-1	Fe (bal.)	25.6	0.50	3.5
Fe2-2	Fe (bal.)	27.2	0.50	4.9

The microstructures of the nine alloys are composed of a dendritic matrix of Co, Ni or Fe solid solutions (also containing almost the whole Cr quantity, but no hafnium), script-like HfC carbides forming an interdendritic eutectic compound with the matrix, and in some alloys (notably the Hf-richest ones) additional blocky HfC carbides which are obviously pre-eutectic ones appeared in the first times of solidification.

The obtained mass gain curves are globally parabolic in the case of the Co-based alloys and the Ni-based ones, with however mass gains faster for the first ones than for the second ones. In contrast they are less regular for the Fe-based alloys. Examples of mass gain curves for the three families of alloys are presented together in Figure 1.

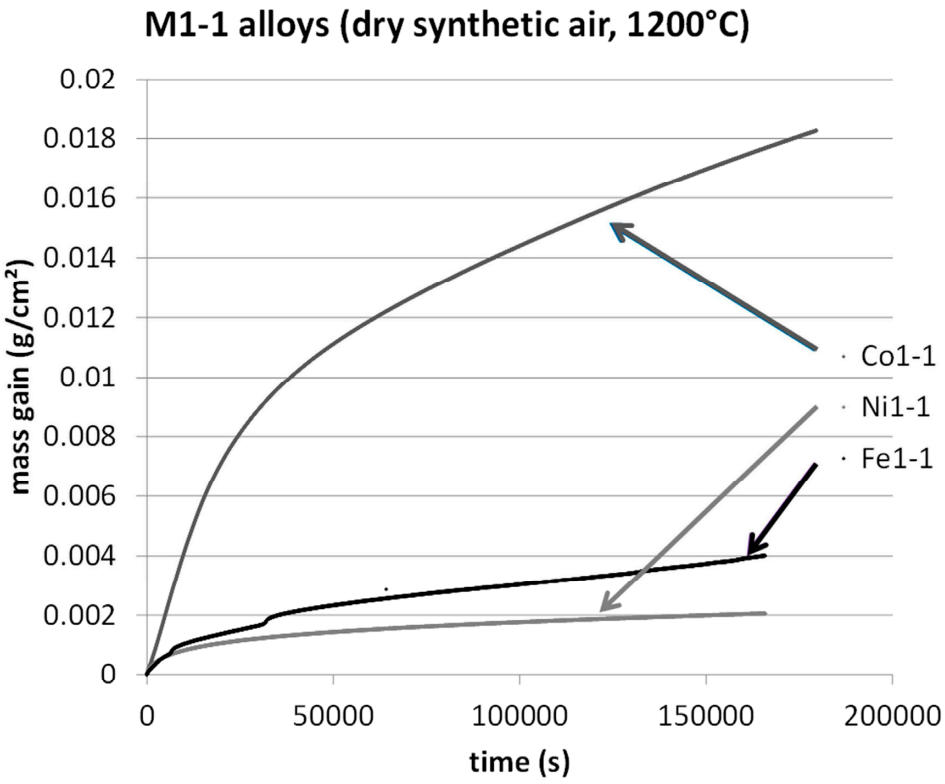

Fig. 1. Examples of obtained mass gain curves (here: the Co1-1, Ni1-1 and Fe1-1 alloys)

The nine mass gain curves were also plotted in the {mass gain versus square root of time}-type to specify the values of the parabolic constants. These classically determined Kp, presented in Table II (designed by *) confirm that the oxidation rate of the Co-based alloys were particularly fast, this suggesting that the oxidizing samples were covered by a continuous oxide scale (parabolic mass gains), oxides which were certainly not chromia (fast mass gains). The parabolic constants obtained for the three Ni-based alloys as well as for the two low Hf Fe-based alloys were significantly lower. In contrast, the Hf-richest Fe-based alloy oxidized as rapidly as the Co-based alloys.

Table II. Values of the Kp constants determined for all alloys by plotting the mass gain versus the square root of time (*); for the Ni-based alloys only: determination of the values of Kp and Kv by plotting {m × dm/dt} versus {- m} [5] (**)

Alloy designation	$Kp \times 10^{12}$ ($g^2\ cm^{-4}\ s^{-1}$)	$Kp \times 10^{12}$ ($g^2\ cm^{-4}\ s^{-1}$)	$Kv \times 10^{10}$ ($g\ cm^{-2}\ s^{-1}$)
Co1-1	830*	/	/
Co2-1	820*	/	/
Co2-2	590*	/	/
Ni1-1	12.3*	35.7**	126**
Ni2-1	20.0*	42.1**	95.6**
Ni2-2	32.0*	68.3**	137**
Fe1-1	45.2*	/	/
Fe2-1	60.5*	/	/
Fe2-2	990*	/	/

To allow interpreting these differences of oxidation rate seen among the nine alloys, the oxidized samples were subjected to post-mortem characterization. The XRD diffractograms performed on the oxidized samples before cutting and metallographic preparation, as well as the SEM observations and EDS pinpoint measurements in cross-sections, allowed specifying the natures of the oxides present on the surface of the oxidized samples, despite their partial loss by spallation during cooling. Three micrographs illustrating the surface states of the oxidized samples, one per alloy family (a Co-based alloy and a Fe-based one with high oxidation rate, and a Ni-based alloy with a low oxidation rate) are presented in Figure 2.

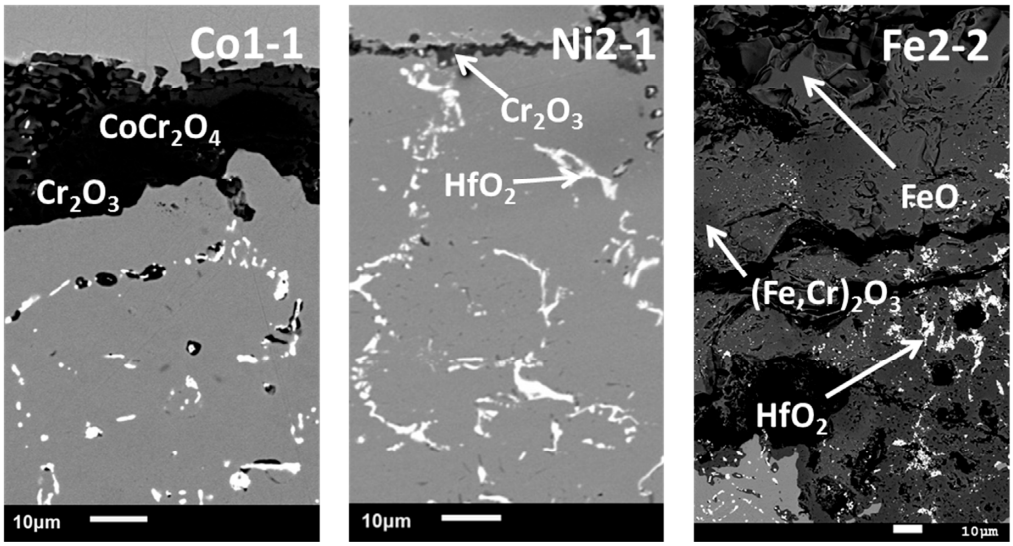

Fig. 2. Examples of surface states of the oxidized samples as observed using the SEM in BSE mode (here: the Co1-1, Ni2-1 and Fe2-2 alloys)

This characterization showed that the oxide scales formed over the Co-based samples were composed of $CoCr_2O_4$ and CoO essentially, with however the presence of a thin sub-layer of chromia Cr_2O_3. Hafnium was also oxidized as revealed

by the presence of small islands of HfO_2 in the external scale and also in the sub-surface as internal oxides. Over the Fe-based alloys the external scales were constituted of Fe_2O_3, Cr_2O_3, $(Fe,Cr)_2O_3$ mixed oxides with various Fe/Cr ratios, and sometimes the spinel $FeCr_2O_4$. In their cases too, the presence of HfO_2 oxides were noticed inside the external scales as well as in the sub-surface. The Ni-based alloys were covered by only chromia (Cr_2O_3), however with also the presence of some HfO_2 in the scale and as internal oxides in the sub-surface. In addition, their local chromium contents in the sub-surface close to the scale/alloy interface, analyzed by EDS, were still higher than 20 wt.%Cr.

Thus the three nickel-based alloys displayed a clear chromia-forming behavior which explains why the mass gain rates were much lower than the ones of the other alloys based on Co, and also lower than the ones based on Fe. Their parabolic constants were the lowest ones but they were probably underestimated because of the volatilization of a part of the formed external chromia layer which necessarily occurred at this so high temperature of 1200°C. This is the reason why the mass gain kinetics of these three chromia-forming alloys were analyzed according to the $\{m \times dm/dt = Kp - Kv \times m\}$ equation, to obtain the values of the volatilization constant Kv and not-underestimated values for the parabolic oxidation constant Kp. Indeed, plotting the $\{m \times dm/dt\}$ quantity versus $\{-m\}$ lead to a straight line the ordinate at the origin of which is Kp and the slope of which is Kv. These results, presented also in Table II (values designed by **), show that Kp tends to slightly increase with the contents in carbon and in hafnium. The values of Kv are typical of the rate of chromia loss by re-oxidation and volatilization usually found for this temperature (1200°C) in this atmosphere (dry air).

To complete the metallographic description of the oxidized samples, one must notice that no disappearance of carbides from the scale/alloy interface occurred, in contrast with other Co-based, Ni-based or Fe-based alloys containing chromium carbides or tantalum carbides for example, and therefore that no carbide-free zone developed in the subsurface. The HfC carbides stay where they appeared during solidification and some of them were simply oxidized in situ close to the oxidation front. The bulk HfC carbides, present deeper in the alloys, were not oxidized. They were also not morphologically modified, as least much less than the tantalum carbides in similar alloys exposed to high temperature in the same conditions of temperature and duration.

4. CONCLUSION

Hafnium carbides can be obtained in cast Co-based, Ni-based and Fe-based Cr-rich alloys with the same morphologie and repartition as the more common tantalum carbides. They are more stable than the latter ones during high temperature exposures but so high Hf contents obviously tend to weaken the resistance of the alloys to high temperature oxidation. The very fast mass gains observed for the Co-based alloys and for one of the Fe-based alloys (which are much higher than the ones that can be shown by the corresponding HfC-free M-Cr-C ternary alloys) as well as the complex natures of the oxides formed, clearly evidence these detrimental consequences. However one can think that their behaviors may be improved by increasing the chromium contents of these alloys − to 30wt.% for example − or by applying Cr-rich protective coatings.

Only the two low-Hf Fe-based alloys and the three Ni-based alloys showed an intrinsic good behavior in oxidation at 1200°C. These ones appear to be ready for applications at this high temperature for which they can be interesting candidates: thanks first to the creep-resistance allowed by their very stable reinforcing HfC carbides, and second to their good resistance against high temperature oxidation which is obviously not decreased by the presence of so high Hf contents and/or of so dense HfC carbides.

References

[1] Berthod, P., Michon, S., Aranda, L., Mathieu, S., Gachon, J.C., "Experimental and thermodynamic study of the microstructure evolution in cobalt-base superalloys at high temperature", C*alphad,* Vol. 27, No. 4 (2003), pp. 353-359.

[2] Berthod, P., "High temperature properties of several chromium-containing Co-based alloys reinforced by different types of MC carbides (M=Ta, Nb, Hf and/or Zr)", *Journal of Alloys and Compounds,* Vol. 481 (2009), pp. 746-754.

[3] Lee, S., Kim, G.M., "The effect of Hf, Y and Zr additions on the oxidation behaviour of Ni-based Inconel 601 at high temperature", *Han'guk Pusik Hakhoechi*, Vol. 24 (1995), pp. 124-133.

[4] Maragoudakis, N., Tsipas, D., Eggonopoulos-Papadopoulos, V., "The role of reactive elements on scale adherence in high-temperature oxidation behaviour of metals and alloys", Romanian Journal of Physics, Vol. 49 (2004), pp. 245-250.

[5] Berthod, P., "Kinetics of high temperature oxidation and chromia volatilization for a binary Ni-Cr alloy", *Oxidation of Metals*, Vol. 64, No. 3-4 (2005), pp. 235-252.

Corrosion behavior of Ti60 with a solid NaCl deposit in wet oxygen at 600°C

Lei Fan, Li Liu*, Ying Li, and Fuhui Wang

Sate Key Laboratory for Corrosion and Protection, Institute of Metal Research, Chinese Academy of Sciences, Shenyang 110016, China

e-mail: liliu@imr.ac.cn

1. INTRODUCTION

The corrosion of turbine blades in planes or ships is very serious in marine environments. The blades are covered with solid salt deposit, especially NaCl. And the air in marine environments contains water. The corrosion of working blades is accelerated due to the synergistic effect of solid NaCl and water vapor at medium temperatures (400-700˚C). Shu et al. [1-4] studied the corrosion behavior of pure Fe, Cr, 1Cr11NiW2MoV steel and K38G with solid NaCl deposit in water vapor at medium temperatures. According to their results, it has been suggested that the mechanism is a ‘‘dynamic water film” absorbed on the surface of the material and that electrochemical corrosion occurs in this water film, which accelerates the metal dissolution.

Titanium alloys have been considered as a candidate material for blades and other components to be used in the compressor section of aerospace engines due to their superior strength–weight ratio and corrosion resistance [5]. Shu et al.[2] found that the presence of solid NaCl deposit and water vapor accelerated the corrosion of Ti60 alloy, which is developed material used for high-temperature compressor blades of turbine engines. However, the micro-mechanism of solid NaCl and water vapor is not clearly. It is necessary to study the micro-mechanism of Ti60’corrosion with a solid NaCl deposit in wet oxygen at medium temperature.

The present work focuses on: (1) to clarify the roles of solid NaCl in the corrosion process Ti60 at 600°C; (2) to found a micro-mechanism of the corrosion process in marine environments at medium temperature.

2. EXPERIMENTAL

The material used in this study is Ti60 alloy. Its chemical composition (mass%) is Ti–5.62Al–3.85Sn–2.98Zr–0.9Mo–0.4Nb–1.05Ta–0.35Si. Samples are cut into pieces 15×10×2.0 mm and ground to 800 grit using silicon-carbide papers. Before the experiment, the specimens are degreased in ethanol and dried in air. The preheated specimen surface is coated with a NaCl deposit by repeated brushing and drying a saturated NaCl solution (distilled water). The amount of the NaCl deposit on the specimens is around 4 mg/cm^2.

The samples are tested in a thermo balance. The corrosion atmosphere(O_2+water vapor and NaCl+water vapor+O_2) is obtained by passing pure oxygen through distilled water by means of a glass bubbler, in which the distilled water is heated by the recycling water, which came from the water bath. The vapor pressure was controlled by adjusting the temperature of the water bath to about 60°C, producing a concentration of water vapor of about 19.9 vol.%. To prevent the water vapor from condensing inside the thermo balance, a counter flow of N_2 is passed through the experimental apparatus. The flow rate of N_2 is 400 ml/min and that of the carrying gas of O_2 is 140 ml/min. After the furnace reached the desired temperature and the gas flow is stabilized, the specimen is quickly lowered into the hot zone of the furnace tube. When the tests are carried out in air or NaCl+O_2, the glass bubbler is removed.

After exposure, the corrosion product on the surface is examined using X-ray diffraction (XRD), scanning-electron microscopy (SEM), and Electron Probe Microanalysis (EPMA).

3. RESULTS AND DISCUSSION

Kinetics curves for corrosion of Ti60 at 600°C are shown in Fig 1. The mass gain of samples in oxygen or in oxygen plus water vapor almost has no changes during the testing period, because of a compact TiO_2 scale forming on the surface when Ti60 is exposed to air or oxygen plus water vapor. A solid

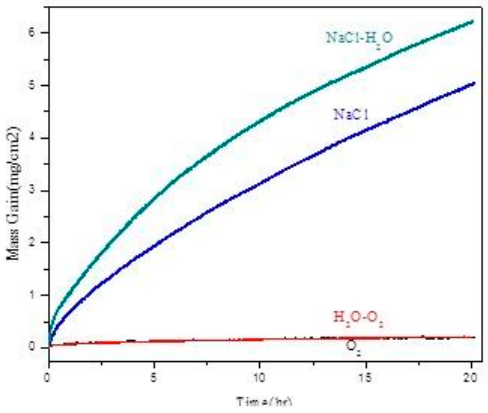

Fig.1. Corrosion kinetics of Ti60 at 600°C

NaCl deposit layer promotes the corrosion of Ti60 in oxygen or in oxygen plus water vapor. And the mass gain of Ti60 coated with NaCl deposit in oxygen plus water vapor is just a little greater than that only in oxygen after 20-hr corrosion. Therefore, solid NaCl deposit layer plays an important role in the corrosion process.

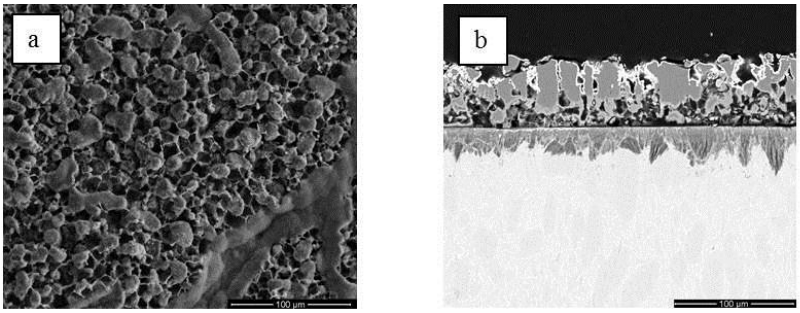

Fig.2. (a) Surface morphology and (b) cross section of the scale of Ti60 coated with NaCl after 20-hr corrosion in oxygen at 600℃

Fig.2. a and b show the surface morphology and cross section of a sample coated with a solid NaCl deposit layer after 20h corrosion in oxygen at 600°C. The scale is porous and a typical layered structure. The thickness of the oxides is about 80μm.

The cross sectional compositions of the Ti60 with solid NaCl in oxygen at 600°C are analyzed by EPMA, and the results are presented in Fig.3. As can be seen, the oxide scale is divided into outer layers, including two layers, and inner oxidation layer: a thick outer scale of TiO_2 and sodium compound, followed by a layer composes of Al and Zr rich oxides; and the inner oxidaion layer is an Cl and Sn-rich scale. The sodium compound is $Na_4Ti_5O_{12}$ by XRD,Fig.4. V.P.Yurkinskii et al.[6] found that $Na_4Ti_5O_{12}$ is the corrosion products of titanium in NaOH melt at 500°C. Seung Hee Woo et al.[7] also abserved bulk trigonal $Na_4Ti_5O_{12}$ via a solid state method by heating TiO_2(anatase) and Na_2CO_3 at 600°C. Therefore, $Na_4Ti_5O_{12}$ is the product of the reaction between TiO_2 and NaCl.

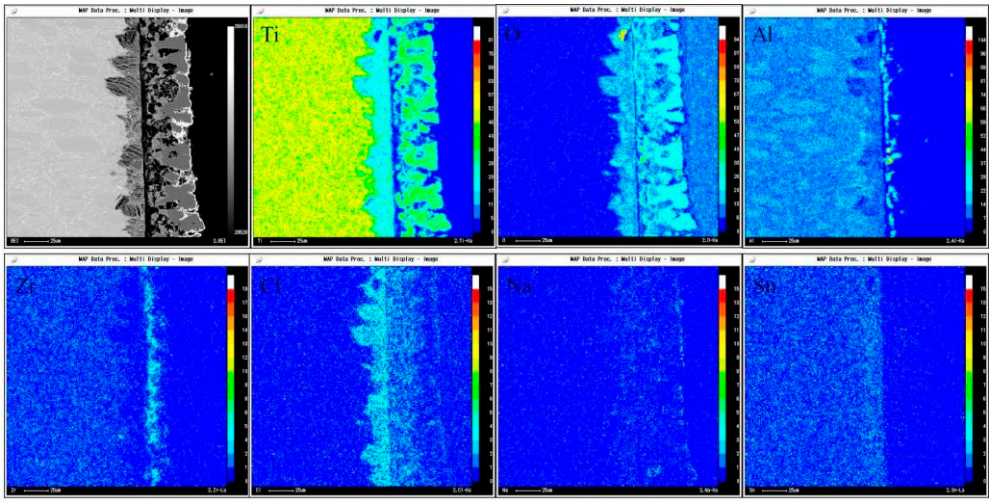

Fig.3. Cross sectional element analysis by EPMA of the Ti60 with solid NaCl in oxygen at 600℃

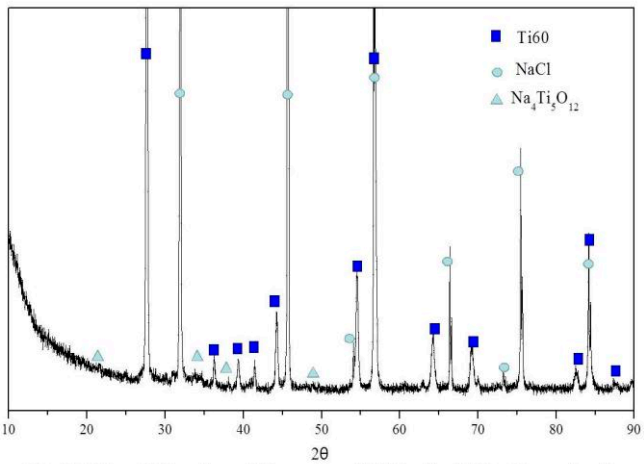

Fig.4. X-Ray Diffraction of the scale of Ti60 after 20-hr Corrosion in oxygen at 600℃

The surface morphology and cross section of Ti60 coated with an NaCl deposit after 20h corrosion in oxygen plus water vapor at 600°C is distinctly different, Fig.5. It shows that the scale of Ti60 is compact and the thickness is mutative between 50μm and 120μm.

The scale is a typical layered structure as same as Ti60 coated with an NaCl deposit after 20h corrosion in oxygen and divided into outer layers, including two layers, and inner oxidation layer from the result of EPMA, Fig.6: a thick and compact outer scale of TiO_2 and sodium compound; a Al, Zr-rich intermediate layer; and Cl, Sn-rich inner scale. The sodium compound also is $Na_4Ti_5O_{12}$ observed on the surface using XRD.

When specimens are coated with NaCl in oxygen, NaCl destroys the scale of TiO_2, a protective scale by the selective oxidation of Ti, producing an accelerated corrosion of Ti60. NaCl combined with the oxide scale to produce $Na_4Ti_5O_{12}$ by a reaction such as:

$$4\mathrm{NaCl} + 5TiO_2 + O_2 \rightarrow Na_4Ti_5O_{12} + 2Cl_2 \quad (1)$$

C_{l2} then diffusions into and reacts with the substrate metal, and forms the inner oxide layer, Cl-rich scale. There are enough oxygen because of the porous structure of the outer layers, thus the internal oxidation of Cl_2 reacts cyclically by

the following reactions:

$$Cl_2 + Ti \rightarrow TiCl_2 \quad (2)$$

$$TiCl_2 + O_2 \rightarrow TiO_2 + Cl_2 \quad (3)$$

At the same time, Al and Zr reacted with oxygen and form Al, Zr-rich oxide scale.

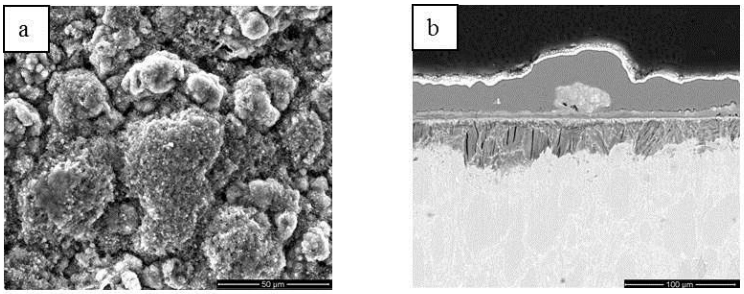

Fig.5. (a) Surface morphology and (b) cross section of the scale of Ti60 coated with NaCl after 20-hr corrosion in oxygen plus water vapor at 600℃

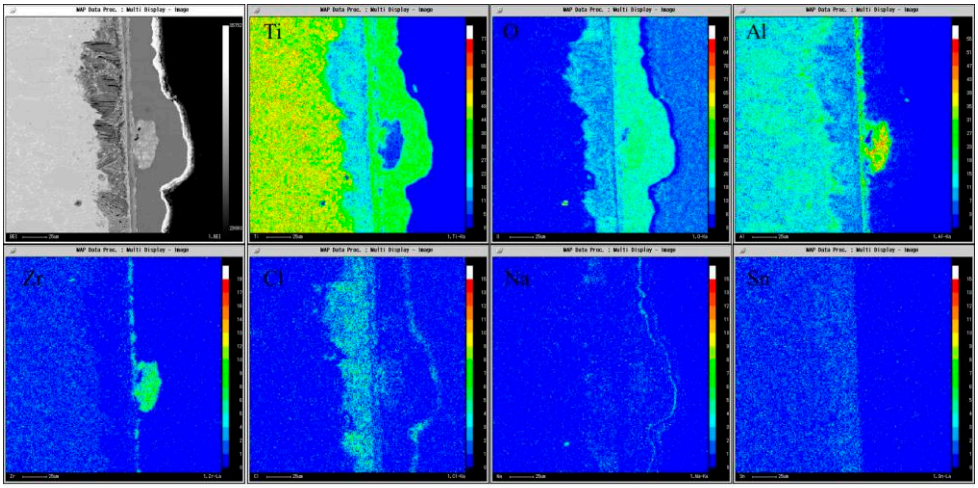

Fig.6. Cross sectional element analysis by EPMA of the Ti60 after 20 hr corrosion with solid NaCl in oxygen puls water vapor at 600℃

4. CONCLUSION

Solid NaCl promotes the corrosion of Ti60 in oxygen or in oxygen and water vapor at 600°C. The TiO_2 layer is broken by the reaction of NaCl, TiO_2 and O_2, and one of the products, chlorine, diffusions into and reacts cyclically with the substrate metal, which accelerates the corrosion rate of Ti60.

Acknowledgements

The investigation is supported by the National Key Basic Research and Development Plan of China under the Contract No.2014CB643303.

References

[1] Shu Y., Wang F., Wu W., "Synergistic effect of NaCl and water vapor on the corrosion of 1Cr-11Ni-2W-2Mo-V steel at 500-700˚C." *Oxid. Met.*, Vol. 51, (1999), pp. 97-110.

[2] Shu Y., Wang F. and Wu W., "Corrosion behavior of Ti60 alloy coated with a solid deposit in O_2 plus water vapor at 500-700˚C." *Oxid. Met.*, Vol. 52, (1999), pp. 463-473.

[3] Shu Y., Wang F. and Wu W., "Corrosion behavior of pure Cr with a solid NaCl deposit in O_2 plus water vapor." *Oxid. Met.*, Vol. 54, (2000), pp. 457-471.

[4] Liu L., Li Y., Zeng C. and Wang F., "Electrochemcial impedance spectroscopy (EIS) studies of the corrosion of pure Fe and Cr at 600 ˚C under solid NaCl deposit in water vapor." *Electrochimica Acta*, Vol.51, (2006), pp.4736-4743.

[5] Weiss I, Semiatin S L. "Thermomechanical processing of alpha titanium alloys." *Materials science and Engineering A*, Vol.263, (1999), pp.243-256.

[6] V. P. Yurkinskii, E. G. Firsova, and L. P. Baturova, "Specific features of the corrosion behavior of tantalum, titanium, and a number of nonmetallic materials in a NaOH melt." *Russian Journal of Applied Chemistry*, Vol. 84,(2011), pp. 811−814

[7] Seung Hee Woo, Yuwon Park, Woo Yeong Choi, Nam-Soon Choi, Seunghoon Nam, Byungwoo Park, and Kyu Tae Lee, “Trigonal $Na_4Ti_5O_{12}$ phase as an intercalation host for rechargeable batteries.” *Journal of The Electrochemical Society*, Vol. 159, (2012), pp. A2016-A2023.

Behavior in High Temperature Oxidation of Cast Chromium-rich Co-based, Ni-based and Fe-based Alloys containing Very High Fractions in Tantalum Carbides

Laura Corona[(1)], Thierry Schweitzer[(2)], Lionel Aranda[(2)], Patrice Berthod [(1,2)]

[(1)] Faculty of Science and Technologies, University of Lorraine, Vandoeuvre-lès-Nancy 54506, FRANCE
[(2)] Institut Jean Lamour, University of Lorraine, Vandoeuvre-lès-Nancy 54506, FRANCE

e-mail: patrice.berthod@univ-lorraine.fr

1. INTRODUCTION

Chromium-rich cobalt-based, nickel-based or iron-based alloys are used at cryogenic/ambient/body temperatures (as for prosthetic dentistry [1]) or at medium, high or very high temperatures (as in aero-engines [2] or industrial processes [3]). Their high Cr contents allow them resisting corrosion in corrosive aqueous milieus or high temperature corrosion by gases or by molten aggressive substances [4]. Many of these alloys also contain carbon which allows the development of carbides aiming to high mechanical resistance at high temperature [5]. Some versions very rich in carbon and in carbides-former elements are devoted to applications exploiting the intrinsically high ductility of the matrix and hardness of the carbides. An example is the cases of cobalt alloys for cutting tools [6] made of a Co-based matrix and hardened with high fractions in tungsten carbides or of Co-W_2C coatings [7], for which high wear resistance, and also resistance against high temperature oxidation, are required.

Besides Cr or W other elements can be chosen to obtain great quantities of hard carbides, with maybe a better efficiency in resistance against wear. Among them one can find the MC-formers ones: Ta, Hf, Zr... In this study it the case of tantalum which was selected, this for a cobalt base, a nickel base and an iron-base. To favor this single type of carbides, first helped by the fact that tantalum is a stronger carbide-former element than chromium (which was kept at a high level for high temperature oxidation resistance) , it was decided to take the same atomic content in Ta as the one in C to avoid the formation of chromium carbides. With this choice, to 1 wt.% of carbon corresponds 15 wt.% of tantalum, a very high content in such element. It was then chosen to limit the C content to 1 wt.% and then the Ta one to 15 wt.%. So, a Co(bal.)-30Cr-1C-15Ta, a Ni(bal.)-30Cr-1C-15Ta and a Fe(bal.)-30Cr-1C-15Ta were elaborated by foundry. Then, they were characterized in terms of microstructure, hardness and oxidation behavior at high temperature ($1000 < T < 1200°C$).

2. EXPERIMENTAL

The quaternary Co-30Cr-1C-15Ta, Ni-30Cr-1C-15Ta and Fe-30Cr-1C-15Ta alloys (targeted compositions, all contents in weight percents) were elaborated by foundry. This was done under inert atmosphere (pure Argon, 300mbars), by melting together pure elements (Co or Ni or Fe, Cr and Ta: Alfa Aesar, purity higher than 99.9 wt.%; C: graphite) using a CELES high frequency induction furnace. Melting and solidification were realized in the water–cooled copper crucible of the furnace to obtain an ingot of about 40 grams of each alloy. These ones were cut to obtain samples for the metallographic examination and the hardness characterization of the as-cast microstructure (Testwell Wolpert apparatus with Vickers indentor, load 30kg). Other samples also obtained by cutting are exposed to high temperature in dry synthetic air during 46h at temperatures belonging in the [1000, 1200°C] range. These oxidation tests were performed using a SETARAM thermo-balance.

The as-cast samples and the oxidized samples (for the later ones: after preliminary electrolytic Ni-coating for oxide scale protection and cutting) were embedded in a cold resin mixture and ground with SiC papers from 240 to 1200 grit. For the final polishing a textile disk enriched with 1µm alumina particles was used. The metallographic observations were carried out using a Scanning Electron Microscope (SEM JEOL JSM-6010LA). This was done in the Back Scattered Electrons mode (BSE) with an acceleration voltage of 20kV, with special attention to the bulk microstructure of the as-cast alloys and to the oxide scale and alloy sub-surface for the samples exposed to high temperature.

The mass gain files were all classically analyzed for specifying the values of the Kp constant (in the case of really parabolic kinetic). However, temperatures higher than 1050°C are high enough to allow the re-oxidation of chromia into the gaseous CrO_3 specie, a mass loss which risks to lead to underestimation for the oxidation kinetic. In such case the files were also analyzed using the $\{m \times dm/dt = Kp - Kv \times m\}$-method [8] (m being the mass gain per surface unit area) in order to specify the real Kp values as well as the linear chromia volatilization constant Kv.

3. RESULTS AND DISCUSSION

With high amounts in both carbon and tantalum, respectively 1 wt.% and 15 wt.%, great volume fractions in tantalum carbides were obtained in the cobalt-based alloy (Figure 1, left hand). Most of these carbides are script-like eutectic carbides and they are located in the interdendritic spaces. This microstructure type was earlier recognized to be favorable to good mechanical resistance at high temperature. Additionally other TaC carbides, of compact shape, are also present. They probably precipitated during the first step of solidification. The average hardness is of a good level (about 440 Hv_{30kg}).

The resistance to high temperature oxidation appeared to be good. The mass gain kinetics were globally parabolic and logically faster for higher temperature, but never significantly faster than similar cobalt alloys containing lower TaC fractions. The behavior of this alloy was obviously chromia-forming behaviour in all cases, as illustrated by Figure 1 (right hand). A carbide-free zone developed from the surface but it is less deep than in the case of cobalt-based superalloys reinforced by TaC carbides

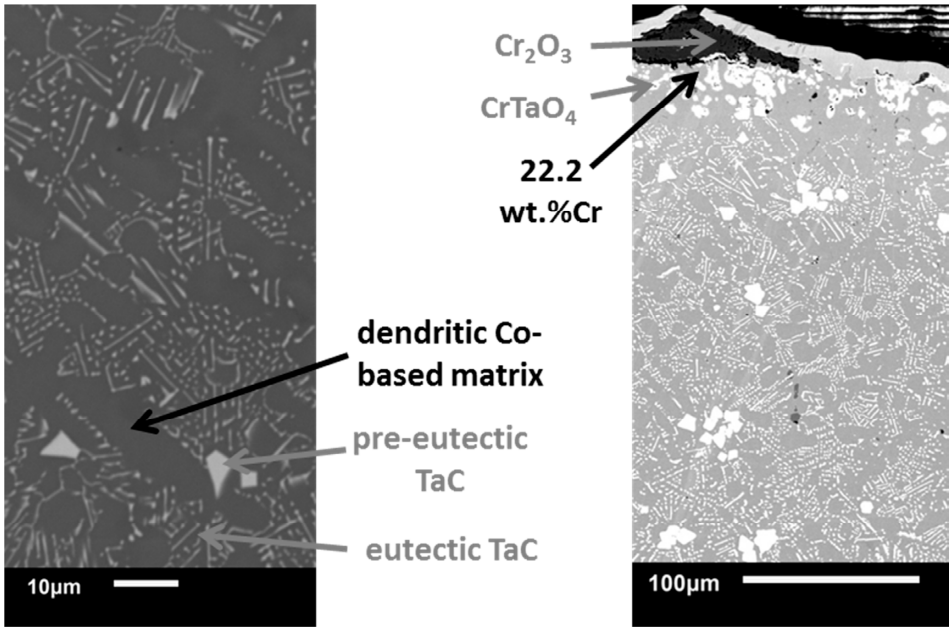

Fig. 1. As-cast microstructure (left hand) and oxidized surface state (right hand) of the TaC-rich cobalt alloy after oxidation at 1150°C for 46 hours

The Ni-30Cr-1C-15Ta alloy also contains eutectic script-like eutectic tantalum carbides and blocky pre-eutectic TaC. But, in contrast with the previous cobalt alloy with similar composition in Cr, C and Ta, some eutectic chromium carbides were also present (Figure 2, left hand). The hardness of the obtained nickel alloy is rather high but a little lower than for the cobalt alloy one. Its behavior in oxidation at high temperature was also good, as demonstrated by the parabolic-type slow kinetic, due to a chromia-forming behavior evidenced by metallographic characterization (Figure 2, right hand).

The solidification of the Fe-30Cr-1C-15Ta alloy was characterized by a great part of pre-eutectic crystallization of TaC carbides. These ones migrated towards the outer part of the ingot, which led to an alloy impoverished in tantalum by comparison with the targeted content, with consequently a microstructure different from the expected (Figure 3, left hand). The alloy obtained contains chromium and tantalum contents of 34 wt.% and 6 wt.% respectively. It presents a microstructure with a dendritic matrix and numerous eutectic chromium carbides and tantalum carbides, instead exclusively TaC as initially wished. Its hardness is thus not as high as required for wear application, but the obtained alloy presented a very good behavior in high temperature oxidation, as reveled by both the slow mass gain kinetic and the presence of the protective continuous chromia scale (Figure 3, right hand).

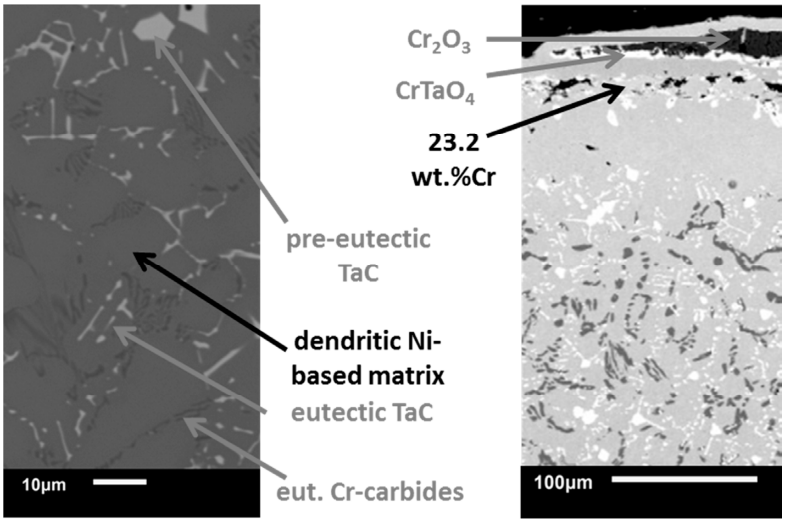

Fig. 2. As-cast microstructure (left hand) and oxidized surface state (right hand) of the TaC-rich nickel alloy after oxidation at 1150°C for 46 hours

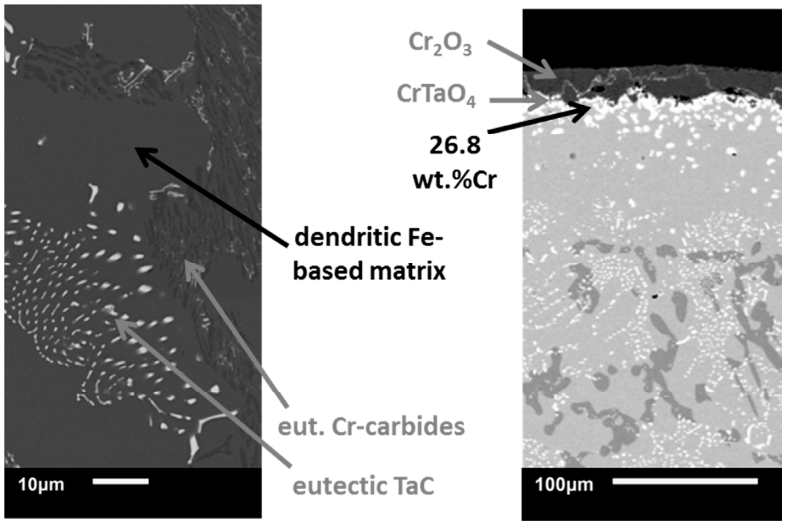

Fig. 3. As-cast microstructure (left hand) and oxidized surface state (right hand) of the TaC-rich ironl alloy after oxidation at 1150°C for 46 hours

4. CONCLUSION

The presence in very high contents in Ta and C in these alloys obviously led to microstructures different from what is commonly found in cast cobalt-based, nickel-based or iron-based alloys or superalloys with no so high carbon content and with equivalent atomic percentage in tantalum. The most noticeable difference, presence of pre-eutectic TaC carbides, caused problems during the elaboration of the iron-based alloy only, the hardness of which is too low, in contrast with the cobalt and the nickel alloys.

Concerning especially the behaviors in high temperature oxidation of these alloys, they all showed a very good resistance, as clearly shown by first slow parabolic mass gain rates, presence of a continuous external chromia scale (even spallation obviously occurred during cooling) and chromium contents in subsurface still high close to the alloy/oxide interface.

References

[1] Bridgeport, D.A., Brandtley, W.A., Herman, P.F., "Cobalt-chromium and nickel-chromium alloys for removable prosthodontics, Part 1: Mechanical properties", *Journal of Prosthodontics*, Vol. 2 (1993) pp. 144-150.

[2] Sims, C.T., Hagel, W..C., The superalloys, John Wiley & Sons (New York, 1972).

[3] Berthod, P., Bernard, J.L., Liébaut, C., Patent WO99/16919.
[4] Young, D., High Temperature Oxidation and Corrosion of Metals, Elsevier Corrosion Series (Amsterdam, 2008).
[5] Donachie, M. J., Donachie, S. J., Superalloys: A Technical Guide (2nd Edition), ASM International (Materials Park, 2002).
[6] Roebuck, B., Almond, E.A., "Deformation and fracture processes and the physical metallurgy of tungsten carbide-cobalt hardmetals", *International Materials Reviews*, Vol. 33 (1988) pp. 90-110.
[7] Klimpel, A., Dobrzanski, L.A., Lisiecki, A., Janicki, D.., "The study of properties of Ni-W_2C and Co-W_2C powders thermal sprayed deposits", *Journal of Materials Processing Technology*, Vol. 164-165 (2005) pp. 1068-1073.
[8] Berthod, P., "Kinetics of high temperature oxidation and chromia volatilization for a binary Ni-Cr alloy", *Oxidation of Metals*, Vol. 64, No. 3-4 (2005), pp. 235-252.

High Temperature Oxidation of Sintered β-$FeSi_2$ from Cast Iron Scrap Chips in Air

Assayidatul Laila [(1,*)], and Makoto Nanko [(2)]

[(1)] Graduate School of Engineering, Nagaoka University of Technology, 16-03-1 Kamitomioka, Nagaoka, Niigata, 940-2188, JAPAN

[(2)] Department of Mechanical, Nagaoka University of Technology, 16-03-1 Kamitomioka, Nagaoka, Niigata, 940-2188, JAPAN

e-mail: laila@stn.nagaokaut.ac.jp

1. INTRODUCTION

Semiconducting β-$FeSi_2$ is called the "environmental friendly semiconductor" because it is made from non-toxic materials without any rare-metals. In thermoelectric applications at high temperatures, oxidation resistance is very important criteria as well as thermoelectric properties [1]. High temperature oxidation on β-$FeSi_2$ was discussed on oxidation process in semiconductor devices [2]. In order to discuss the lifetime of thermoelectric devices at high temperatures, long-term oxidation should be examined. The previously authors reported amorphous SiO_2 was developed as an oxide scale at temperature 800 to 950°C in air [3]. Growth rate of oxide layer on doped β-$FeSi_2$ followed a parabolic law and its rates were similar to oxidation of undoped samples. In addition, they concluded that sintered β-$FeSi_2$ showed excellent oxidation resistance in high temperature thermoelectric materials. They also reported that there was no significant change in thermoelectric properties after high temperature oxidation on β-$FeSi_2$ sintered bodies [4]. On the other hand, cast-iron is one of the most popular alloys for mechanical components. Because cast-iron consists of mainly iron with carbon and silicon, scrap chips of cast-iron may be a good starting material for preparing β-$FeSi_2$. The authors have proposed "recycling of cast-iron scrap" toward β-$FeSi_2$ thermoelectric materials [5]. In this research, oxidation behavior of undoped and doped β-$FeSi_2$ prepared from cast iron scrap chips was reported.

2. EXPERIMENTAL

The undoped and n-type β-$FeSi_2$ powders were prepared by solid state reaction technique of cast-iron scarp chips, silicon grains (99.99%) and powders of dopant element Co (99%) for n-type. Numerical chemical compositions were cast-iron:Si = 1:1.86 for undoped ones and cast-iron:Co:Si = 0.98: 0.02:1.86 for n-type. The mixture was powdered by using a mortar and planetary ball milling for 1 d. Furthermore, the powder mixture was undergoing solid state reaction in vacuum at 1100°C for 3 d. The powder mixture was consolidated by using a pulsed electric current sintering technique at 950°C for 10 min in vacuum to under an uni-axial pressure of 80 MPa for undoped β-$FeSi_2$ and at 900°C for 10 min in vacuum to under an uni-axial pressure of 80 MPa for Co-doped one. Sintered samples were annealed at 900°C for 5 d in vacuum to obtain β-$FeSi_2$ phase. Sintered β-$FeSi_2$ samples were ground by using a #600 to #2000 abrasive paper. Isothermal oxidation tests were carried out at 800°C in air by using an electric furnace. After oxidation tests, phase identification by using X-ray diffraction (XRD) and scanning electron microscopy (SEM) with energy dispersion X-ray spectroscopy (EDXS) were performed.

3. RESULTS AND DISCUSSION

Fig. 1 shows XRD patterns of annealed β-$FeSi_2$ undoped and Co-doped from pure Fe and cast iron scrap chips. Dominant peaks in these samples could be identified as β-$FeSi_2$ for all samples. Almost fully β-$FeSi_2$ with a small amount of ε-FeSi was obtained after annealing treatment at temperature 900°C for 5 d in order to stabilize the desired volume fraction of β phase [6]. Fig. 2 shows XRD patterns of β-$FeSi_2$ for 14 d at 800°C. An oxidation product such as FeO, cristobalite and ferrosilite were not identified in oxidized β-$FeSi_2$. A peak of ε-FeSi phase increases slightly after oxidation experiment. Formation of ε-FeSi is caused by consumption of Si inβ-$FeSi_2$.

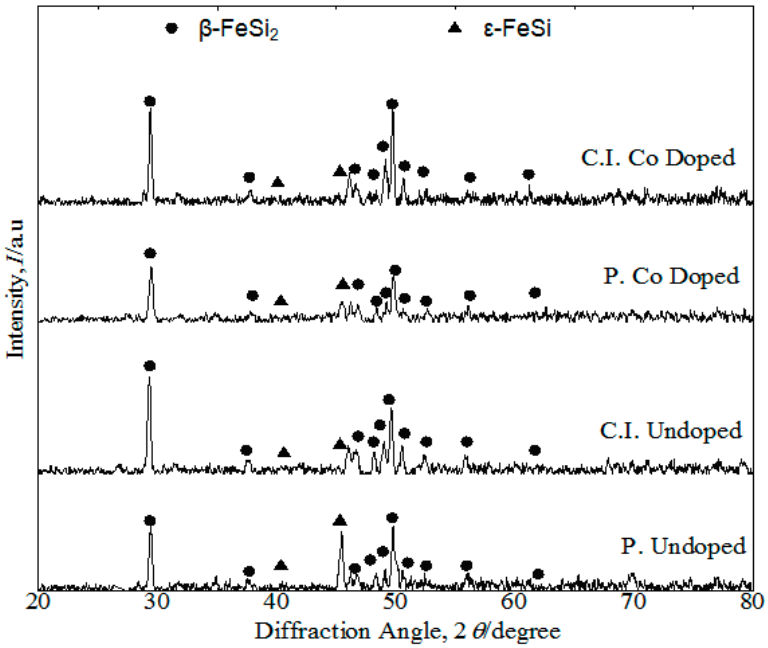

Fig. 1. XRD patterns of annealed β-$FeSi_2$ samples at 900°C for 5 d before oxidation.

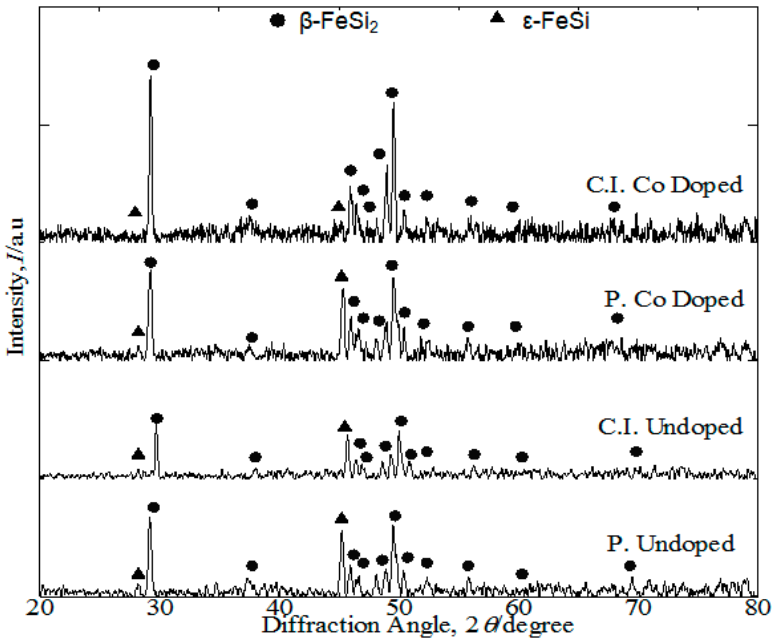

Fig. 2. XRD patterns of annealed β-$FeSi_2$ samples after oxidation at 800°C for 14 d.

Fig. 3 shows the SEM images on surface morphology of oxidized β-$FeSi_2$. Any cracks of oxidized β-$FeSi_2$ samples were not observed after high temperature oxidation. Furthermore, anomaly oxidation such as formation of large nodules was not observed on the surface morphology. Fig. 4 shows the cross sectional views of annealed sample (a) P. Co Doped and (b) C.I. Undoped after oxidation at 800°C for 14 d in air. An oxide scale is observed to be less than 2 μm in thickness. Taking account of the XRD results, the oxide scales is most likely amorphous SiO_2 as similar with Si and other silicide materials such as $NiSi_2$ [7] and $CoSi_2$ [8].

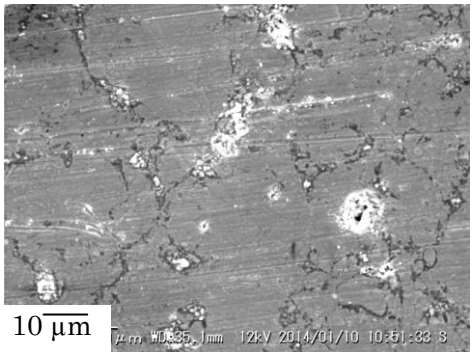

(a) P. Undoped

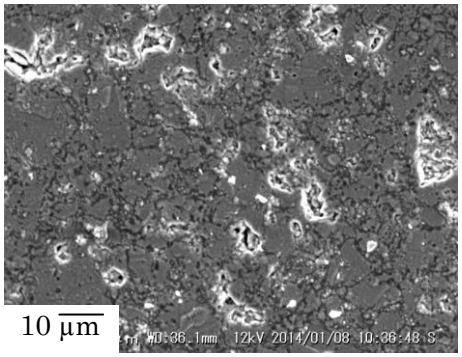

(b) C.I. Undoped

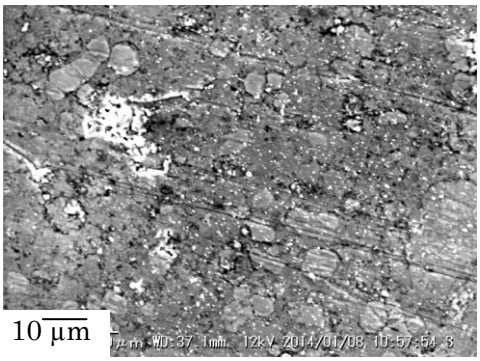

(c) P. Co Doped

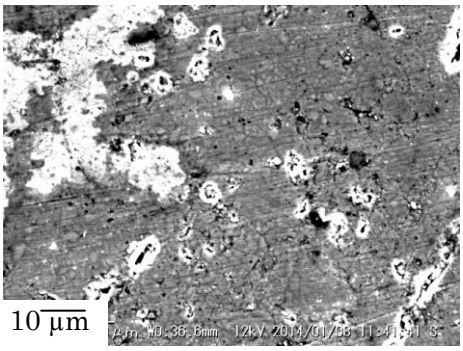

(d) C.I. Co Doped

Fig. 3. SEM images of annealed β-$FeSi_2$ samples after oxidation at 800°C for 14 d.

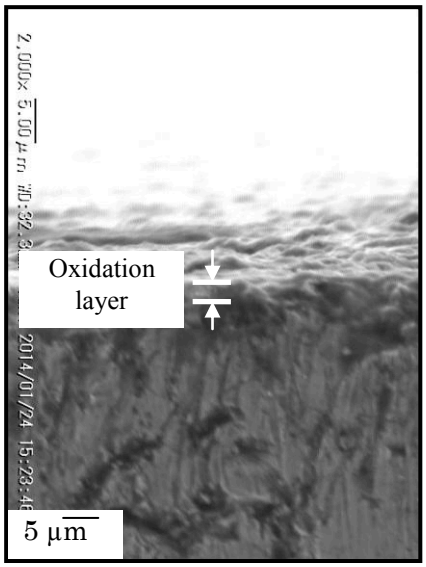

(a) P. Co Doped

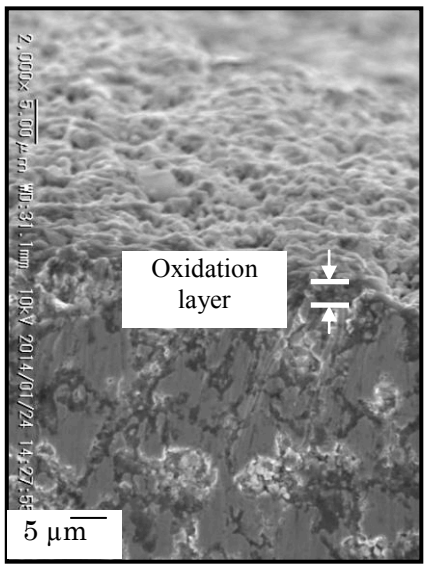

(b) C.I. Undoped

Fig. 4. Cross-sectional views of annealed β-$FeSi_2$ oxidized at 800°C for 14 d in air.

Fig. 5 shows the mass increase of the annealed β-$FeSi_2$ oxidized at 800°C for 14 d in air. The sample from cast iron indicated high value compared to pure Fe β-$FeSi_2$ sample. Thickness of oxide scale calculated from mass change assuming amorphous SiO_2 was approximately 2 μm in the present study. This value of the scale thickness agrees with the observation results shown in Fig. 3. This agreement is also evidence on formation of uniform amorphous SiO2 scale on β-$FeSi_2$ made from cast-iron.

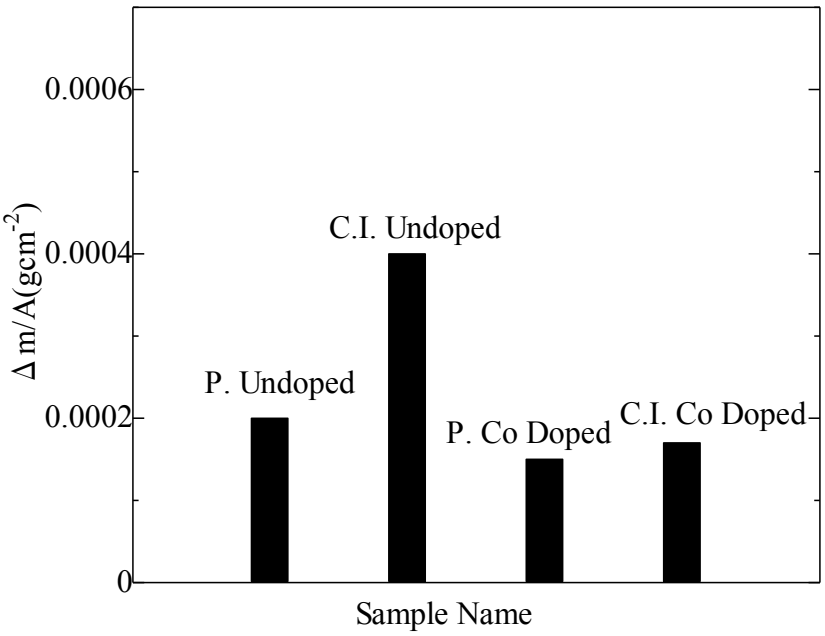

Fig. 5. Measurement of the mass increase of the annealed β-$FeSi_2$ oxidized at 800°C for 14 d in air.

4. CONCLUSION

High temperature oxidation of β-$FeSi_2$ made from cast iron scrap chips was investigated at 800°C for 14 d in air. A thin oxide scale with 2 μm, which was most likely made of an amorphous SiO_2 was developed as a protective oxide scale. Iron silicides β-$FeSi_2$, even made from cast iron scrap chips, has excellent potentials in high temperature stability in oxidizing atmosphere for high temperature thermoelectric materials.

Acknowledgements
The authors express the appreciation to the Ministry of Higher Education Malaysia for supporting partially the present study.

References

[1] Ware, M., "Iron disilicide as a thermoelectric generator material", *Proc. IEE.,* Vol. 111 (1964), pp. 178.
[2] Stolt, T. *et al*., "Oxidation of titanium, manganese, iron, and niobium silicides: Marker experiments", *J. Appl. Phys*., Vol. 68 (1990), pp. 5133.
[3] Chang, N. *et al*., "High temperature oxidation of sintered β-$FeSi_2$ bodies at elevated temperature", *Mat. Trans. J. Jpn. Inst. Met.,* Vol. 80 (2006), pp. 20.
[4] Chang, N. *et al*., "Isothermal oxidation of sintered β-$FeSi_2$ in air", *Mat. Sci. Forum*, Vol. 522 (2006), pp.641.
[5] Laila, A., and Nanko, M., "Characterization of Cast-Iron Scraps toward β-$FeSi_2$ Thermoelectric Materials", *Abst. ISEPD2014*, (2014), pp.112.
[6] Umemoto, M., "Preparation of Thermoelectric, β-$FeSi_2$ Doped with Al and Mn by Mechanical Alloying", *Mat. Trans., J. Jpn. Inst. Met.*, Vol. 36 (1995), pp.373.
[7] Bartur, M. et al., "Thermal oxidation of cobalt disilicide", *Appl. Phys. Lett*., Vol. 40 (1985), p.175.
[8] Strydom, W. J. *et al*., "Low temperature formation of insulating layers on silicides by anodic oxidation", *Thin Solid Films*, Vol. 131 (1985), p.215.

International Symposium on High-Temperature Oxidation and Corrosion 2014 in Hakodate

Effects of third elements on oxidation resistance of $NbSi_2$

Toshihiro KANAYA[(1,*)],Kenyu KIMURA[(2)], Misa UKEGAWA[(3)], Lihua ZHANG[(4)] and Kazuya KUROKAWA[(4)]

[(1)]Graduate School of Eng., Hokkaido University, Kita13 Nishi8, Sapporo 060-8628, JAPAN

[(2)]Ebara Elliott, 11-1 Haneda Asahi-cho, Ohta-ku, Tokyo 144-8510, Japan

[(3)]Mitsubishi Heavy Industry, 16-5 Konan 2-chome, Minato-ku, Tokyo, 108-8215, Japan

[(4)]Center for Advanced Research of Energy and Materials, Faculty of Eng., Hokkaido University

e-mail: t.kanaya@eng.hokudai.ac.jp

1. Introduction

The higher operating temperature of gas turbine is required for the problems of global warming and depletion of energy resource. However, the operating temperature is reaching the limit because of mechanical properties of high temperature materials such as Ni-based alloys. Therefore, development of new ultra-high temperature materials is required [(1)]. Nb-based alloys are one of the promising materials because of the high melting point, relatively low density, and excellent mechanical properties at high temperatures. However, the oxidation resistance is extremely poor [(2-4)]. For the improvement of oxidation resistance of Nb alloys, coating of $NbSi_2$ for the alloy is offered. However, oxidation resistance of $NbSi_2$ is not necessarily sufficient. Thus, in the present study, addition of B, Ge and Al was performed to improve oxidation resistance of $NbSi_2$.

2. Experimental Procedure

The compositions of main specimens used in the present study are shown in Table 1. To prepare the specimens, stating powders of $NbSi_2$(purity:99.9%, average grain size: 3.5μm), B(99%,45μm), Ge(99.999%,45μm) and Al(99.9%, 3.0μm) were used. The mixed powders were ball-milled, and then sintered by a spark plasma sintering (SPS) method. The sintering conditions are as follows: sintering temperature of 1673 K, compressive stress of 40 MPa, and vacuum of about 4 Pa.

The sintered compacts were cut into the size of about 10x5x2 mm^3 and polished up to 1 μm diamond finish before oxidation tests. The oxidation tests were carried out for up to 180 ks at 873, 1273, 1473, and 1673 K in air.

The oxidized specimens were characterized by XRD, FE-SEM, EDS, and TEM.

Table1 The compositions of main specimens / at.%

	Nb	Si	Third elements
$NbSi_2$	33.33	66.67	0.00
$NbSi_2$-3mass%B	23.36	46.73	29.90
$NbSi_2$-5mass%Ge	33.30	66.60	0.10
$NbSi_2$-5mass%Al	30.39	60.78	8.63

3. Results and Discussion

Fig. 1 shows the surfaces of sintered compacts. $NbSi_2$-B alloys had complex microstructure because of the formation of NbB_2, Si, etc. $NbSi_2$-B alloys and $NbSi_2$-Al alloys mainly consist of a $NbSi_2$ phase.

Using the sintered specimens, oxidation tests were carried out. Fig. 2 shows the mass gain of each samples. $NbSi_2$ with additives of B,Ge, and Al shows outstanding oxidation resistance, comparing with $NbSi_2$ that is not added them. From this result, it is recognized that B, Ge and Al addition into $NbSi_2$ leads to remarkable improvement of oxidation resistance.

Fig. 3 shows cross-sections of oxide scales formed on $NbSi_2$ alloys for each condition. In $NbSi_2$ without additives, a thick oxide scale consisting of Nb_2O_5 and SiO_2 is formed, while $NbSi_2$-3mass%B and $NbSi_2$-5mass%Ge alloys form thin oxide layer consisting of glass-like, dense SiO_2, and $NbSi_2$-5mass%Al alloys form a thin Al_2O_3 layer.

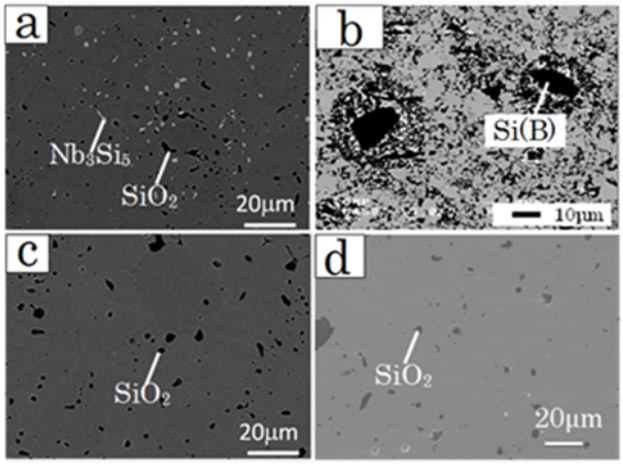

Fig.1 SEM photographs showing the surfaces of sintered compacts.
(a: $NbSi_2$, b: $NbSi_2$-3B, c: $NbSi_2$-5Ge, d: $NbSi_2$-5Al)

Ge and B are oxidized at high temperatures and formed glass-like GeO_2 and B_2O_3, which decreases viscosity of SiO_2 when dissolving [6)]. Therefore, spread of a protective SiO_2 scale become easily and fast. Once the substrate is

covered with the low viscosity SiO_2-GeO_2 or SiO_2-B_2O_3 solid solution, the oxygen potential at the scale/substrate interface is reduced extremely, resulting in stop of oxidation of Nb and selective oxidation of Si. Additionally, because of high equilibrium vapor pressure of GeO_2[7], Ge oxide is volatilized with oxidation time. And finally, purified SiO_2 scale remains and keeps high protection.

On the other hands, $NbSi_2$ added Al firstly forms crystalline SiO_2 on the surfaces. Gradually, Si and Nb are replaced by Al to form an Al_2O_3 layer on the surface because the oxygen affinity of Al is larger than that of Si and Nb at these temperatures.

From these results, addition of B or Ge is more effective solution for improvement of oxidation resistance. However, $NbSi_2$-B alloys have complex microstructure because of the formation of NbB_2, Si, etc. It may have a negative influence on mechanical properties. Moreover, addition of Al is very effective solution for pesting. Fig.4 shows the results of oxidation test at 873K. $NbSi_2$ became powder but $NbSi_2$ -3mass%Al alloys were almost unchanged. This means that we should judge the appropriate materials by taking a broad view of things.

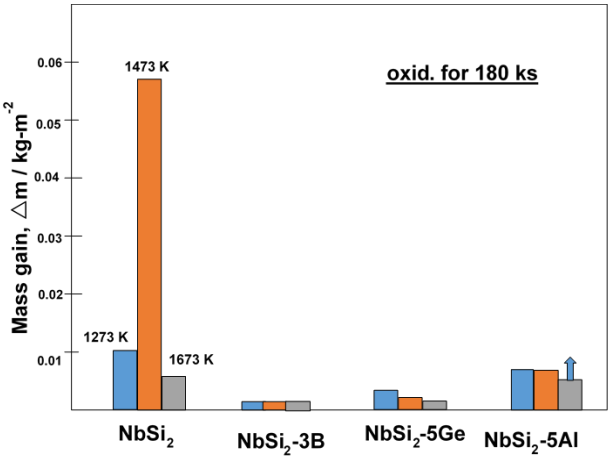

Fig.2 Mass gain of oxidized samples

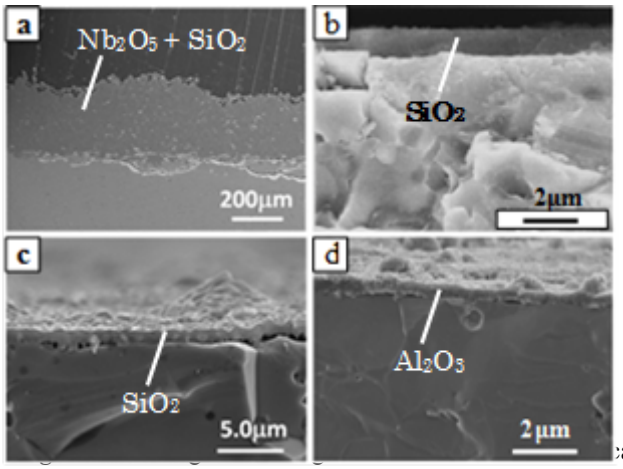

cales formed on $NbSi_2$ alloys for each condition.
(a: $NbSi_2$ [1473K 50hrs], b: $NbSi_2$-3B [1273K 100hrs], c: $NbSi_2$-5Ge [1473K 50hrs], d: $NbSi_2$-5Al [1473K 50hrs])

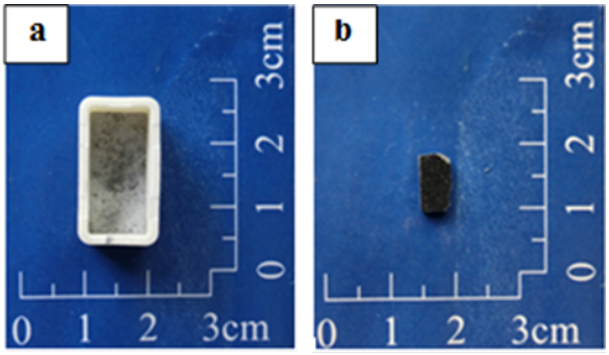

Fig.4 Samples oxidized at 873 K for 604ks.
(a:$NbSi_2$, b:$NbSi_2$-3mass%Al)

4. Conclusions

The conclusions obtained in this study are as follows.

(1) B addition leads to the formation of complex microstructure but Al or Ge addition doesn't lead to the formation of additional phases.
(2) Oxidation resistance of $NbSi_2$ is remarkably improved by B and Ge addition due to the formation of a low viscosity silica layer.
(3) Al addition also results in the improvement of oxidation resistance at high temperatures and prevents serious pesting due to the formation of an Al_2O_3 layer.

References

1)Tan Y, Ma CL, Kasama A, Tanaka R, Mishima Y, Hanada S, Yang JM, "Effect of alloy composition on microstructure and high temperature properties of Nb-Zr-C ternary alloys", Materials Science and Engineering A, V. 341[1-2], 2003, p. 282-288.

2)H. W. Lavendel ,R. A. Perkins, A. G. Elliot, J. Ong: *U.S. Air Force Rept.*AFML-TR-65-344 (1965).

3)R. E. Regan, W. A. Baginski, and C. A. Krier, "Oxidation Studies of Complex Silicides for Protective Coatings," *Ceram. Bull*, 46 [5]502–9 (1967),

4)T.P. Chow, K. Hamzeh and A.J. Steckl, "Thermal Oxidation of Niobium Silicide Thin Films," *J. Appl. Phys. Lett.* 42: 361 (1983)

5)K. Kurokawa, A. Yamauchi, S. Matsushita "Improvement of Oxidation Resistance of $NbSi_2$ by Addition of Boron": *Mater. Sci. Forum,* 502 (2005) 243-248

6)K. Tajima, M. Tateda, M. Ohashi, "Low Rayleigh-scattering loss P_2O_5-SiO_2-core single-mode fiber" *Journal of lightwave technology,* 12 (1994) 411-412

7)C. H. Lee, T. Tabata, T. Nishimura, K. Nagashio, K. Kita and A. Toriumi: "Ge/GeO_2 Interface Control with High-Pressure Oxidation for Improving Electrical Characteristics."*Applied Physics Express* 2 (2009) 071404 1-3

Corrosion of 316L steel in liquid Te at 550°C

L.Martinelli [1,*], K.Ginestar [1]

[1] CEA, DEN, DPC, SCCME, Laboratoire d'Etude de la Corrosion Non Aqueuse, F-91191 Gif-sur-Yvette, France.

e-mail: laure.martinelli@cea.fr

1. INTRODUCTION

Austenitic steels are considered as cladding material for Sodium Fast nuclear Reactor. Cladding is the first barrier, impeding the release of fission products. Cladding integrity is then necessary for safety reasons. Moreover, the time that fuel spends in reactor depends on the performance of this material. However, cladding is subjected to severe conditions of irradiation and corrosion. Indeed, among the fission products of plutonium-239 and uranium-235, two elements, tellurium and caesium are particularly corrosive. The corrosion mechanism of cladding in contact with these both elements, containing oxygen, is not yet completely understood. In order to better understand the effects of the two elements, it was decided, in a first step, to study austenitic steels corrosion in each element, Te and Cs, separately. In this context, this study deals with corrosion of 316L in pure liquid Te at 550°C.

2. EXPERIMENTAL

Tests were performed using 316L austenitic steel mechanically polished with SiC paper until 1200 grade before experiments. Samples are immersed one by one during 1, 5, 10 and 30 minutes into a quartz crucible contained into a quartz reactor heated at 550°C in a glove box in order to avoid oxygen pollution. During corrosion tests, Ar 4.5 was continuously sweeping above the pure liquid Te.

3. RESULTS AND DISCUSSION

Corrosion of 316L in pure Te leads to both phenomena: steel dissolution in liquid metal and formation of an intermetallic layer containing Fe-Cr-Ni-Te (Fig.1). Steel dissolution is the main corrosion phenomena as after 30 minutes, the dissolved steel thickness is around 100 µm and the intermetallic layer thickness is about 15 µm.

Inside the wetting Te which solidified during the samples removal, two phases of crystallites containing Fe-Cr-Ni-Te are found (Fig.1). Theirs sizes are close to several tens of microns (Fig.1). This study shows that these crystallites are formed during the samples cooling and correspond to precipitation of dissolved corrosion products (Fe, Cr, Ni) in liquid Te (Fig.1.).

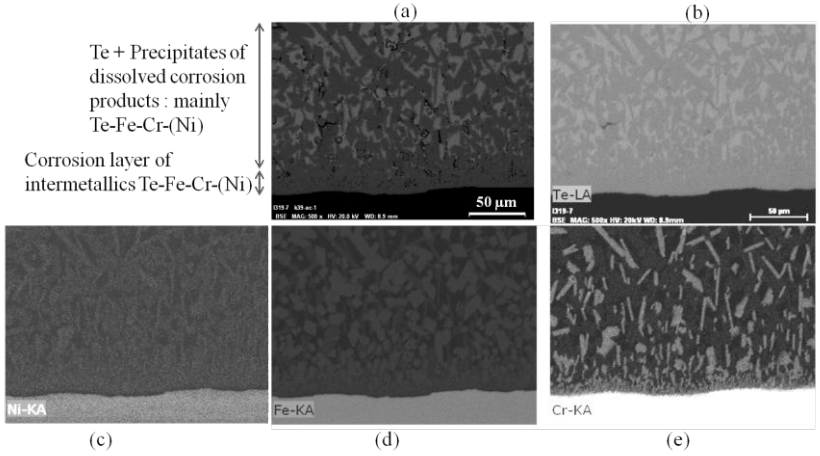

Fig.1. (a) SEM observation of the cross section of 316L and (b) (c) (d) (e) X ray images of Te, Ni, Fe and Cr after exposure to pure Te at 550°C after 30 minutes of testing.

Whatever the corrosion duration, corrosion facies and compositions, of the corrosion layer and of the precipitates in the solidified Te, are similar: (i) there is no concentration gradient in the sound 316L; (ii) precipitates stoichiometry are close to $(Fe,Cr,Ni)Te_2$, with Fe enriched precipitates (composition close to 20at%Fe-6at%Cr-3at%Ni) and less numbered Cr enriched precipitates (composition close to 15at%Fe-11at%Cr-3at%Ni); (iii) corrosion layer contains various compositions of Fe-Cr-(Ni)-Te grains with mainly Cr enriched grains at the 316/ interface and Fe enriched grains at the corrosion layer/Te interface. Concentration of Ni in the corrosion layer is roughly constant and equal to 3at%. Stoichiometry of the corrosion layer is not homogeneous and evolves with time.

Kinetics of the intermetallic corrosion layer follows a parabolic law (Fig.2a.) leading to assume that diffusion of species inside the layer controls its kinetics. The diffusing element (Te or Fe, Cr, Ni) responsible to the layer growth remains to be identified. Kinetics of the loss of sound 316L thickness is neither parabolic neither linear (Fig.2b.). Modelling of this total corrosion is performed taking into account diffusion of dissolved metal in liquid Te and dissolution reaction rate. Hypothesis, that the steel dissolution mechanism and the corrosion layer growth mechanism are separated, is considered.

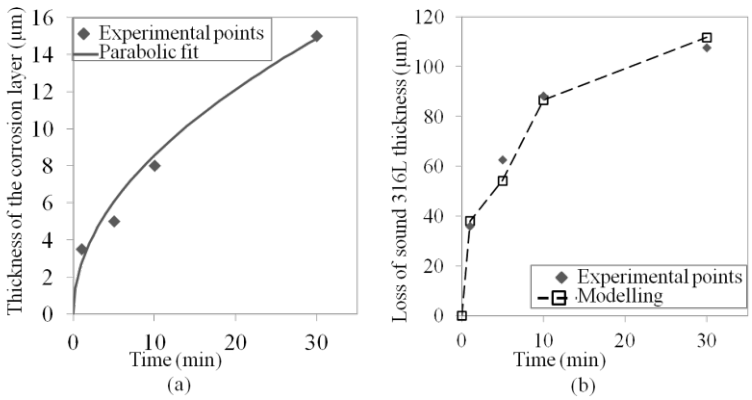

Fig.2. (a) kinetics of corrosion layer growth (b) total corrosion kinetics: kinetics of loss of sound 316L thickness. Experimental points and modelling considering control by pure diffusion of dissolved Fe in a closed system of liquid Te.

Two fluxes are involved in steel dissolution in Te (Fig.3.): (i) the first flux, $\vec{J}_{diss}$, is the dissolution flux linked to the dissolution rate of interfacial reaction:

$$M_{316L} \xleftrightarrow{k_d / k_p} M_{Te} \qquad (1)$$

with M_{316L}, the element in the solid 316L matrix, M_{Te} the dissolved steel element in liquid Te, k_d the reaction rate constant for M_{316L} dissolution and k_p the reaction rate constant for M_{Te} precipitation. (ii) The second flux, $\vec{J}_{diff}$, is the diffusion flux of the dissolved element M_{Te} in liquid Te, from the steel surface to the distance L equal to the half-height of Te in the crucible. These fluxes, represented on Fig.3., can be written according to equations (2) and (3):

$$J_{x,t}^{diff} = -D_M^{Te} \frac{\partial C_{x,t}^M}{\partial x} \qquad (2)$$

$$J_{x=0,t}^{diss} = k_d \left(a_M - \frac{C_{x=0,t}^M}{S_M} \right) \qquad (3)$$

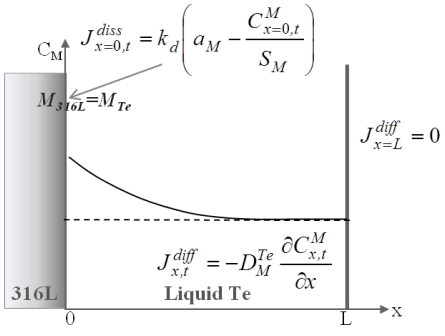

Fig.3. diagram representing the 2 fluxes involved in dissolution process and the concentration gradient of M in liquid Te.

With D_M^{Te}, the diffusion coefficient of dissolved element M in liquid Te, $C_{x,t}^M$, the concentration of dissolved element M in liquid Te as a function of time, t and the distance x from 316L/Te interface, a_M, the activity of solid M in 316L and S_M, the solubility limit of dissolved M in liquid Te at 550°C.

For simplicity, only the diffusion of Fe is considered. Values of L, a_{Fe}, S_{Fe}, $C_{x,t}^{Fe}$ are given by experiments characteristics and by literature. The best fit on experimental data, represented on Fig.2b., is obtained for $k_d L >> S_{Fe} D_{Fe}^{Te}$ and given by equation (4) representing the loss of sound 316L thickness as a function of time:

$$h_{n+1}(t) = h_n(t_n) + \frac{8 M_{Fe} L^2}{\rho_{Fe} \pi^2} \left(S_{Fe} - C_{n+1}^0 \right) \sum_{i=0}^{\infty} \frac{1}{(2i+1)^2} \left[1 - Exp\left(- \frac{(2i+1)^2 \pi^2 D_{Fe}^{Te} t}{4L^2} \right) \right] \qquad (4)$$

With $h_{n+1}(t)$, the thickness loss of sample n+1 after corrosion duration t; $h_n(t_n)$, the thickness loss of sample n after its corrosion test which lasted t_n; M_{Fe}, iron molar mass; ρ_{Fe}, Fe density; C_{n+1}^0, the iron concentration initially present in the liquid Te before immersion of sample n+1. The only unknown data in equation (4) is then the iron diffusion coefficient, D_{Fe}^{Te}.

Fig.2b. shows that good agreement between modelling and experimental data is obtained if $k_d L >> S_{Fe} D_{Fe}^{Te}$ and then if reaction rate is infinitely greater than diffusion rate. This modelling shows thus that the steel corrosion rate is purely controlled by diffusion of metallic species (Fe, Cr, Ni) in the liquid Te. Fitting modelling on experimental data permitted to determine an apparent diffusion coefficient of Fe in the liquid metal. This apparent diffusion coefficient is equal to 2×10^{-3} cm^2/s. It is roughly one to two orders of magnitude higher than usual diffusion coefficients in liquids. Then a part of convective transport of dissolved species should also occur.

Finally an overall corrosion mechanism is proposed, taking into account the presence of the steel dissolution phenomena, the corrosion layer and the crystallites observed in Te, on corroded samples.

4. CONCLUSION

To conclude, corrosion of 316L in liquid Te leads to the formation of an adherent layer, at the steel surface, containing Ni-

Fe-Cr-Te. The composition of this layer is complex and heterogeneous. The thickness of this layer is 15µm after 30 min of test. Otherwise the 316L steel dissolves very rapidly: more than 100µm of steel thickness is lost on each side of the sample after 30 min of immersion.

Then the overall corrosion kinetics is controlled by the steel dissolution rather than by the adherent layer growth. Modelling of steel dissolution reveals that it is controlled by diffusion of species (Fe, Cr, Ni) in liquid Te. Modelling fit on experimental data permits to determine an apparent diffusion coefficient. An overall corrosion mechanism taking into account all observations is performed.

P35

High-Temperature Oxidation of Zircaloy-4 in oxygen-nitrogen mixtures

Martin Steinbrück*, Steffi Schaffer

Karlsruhe Institute of Technology, Institute for Applied Materials, Hermann-von-Helmholtz-Platz 1,
76344 Eggenstein-Leopoldshafen, GERMANY

e-mail: martin.steinbrueck@kit.edu

1. INTRODUCTION

Air ingress and Zr oxidation in atmospheres containing nitrogen is of actual interest in many countries. So, the OECD SFP project [1] indicated a strong need for more experiments on this issue and two PhD thesis at EdF (France) and PSI (Switzerland) have just started in cooperation with KIT. From former experiments it is known that air oxidation of Zr alloys is very complex [2,3]. During air oxidation, the oxygen/nitrogen ratio changes due to preferred consumption of oxygen and the question arises which range of composition is affected by the mutual interaction of oxide and nitride formation.

2. EXPERIMENTAL

Isothermal oxidation tests with 2-cm cladding segments of Zircaloy-4 (Zr-1.5%Sn) in oxygen-nitrogen model mixtures have been performed at 800, 1000, and 1200°C for 6 hours, 1 hour, and 15 min, respectively. All experiments were conducted in a NETZSCH STA-409 thermal balance coupled with a mass spectrometer (MS) NETZSCH Aeolos for analyses of the off gas composition. The gas compositions were varied between 0 and 100 vol.% nitrogen including 1 and 99 vol.%. The gas flow rates were kept constant with 10 l/h (O_2+N_2) and 3 l/h argon as protective gas for the balance and reference for MS measurements. Post-test examinations were done mainly by optical microscopy after embedding, grinding and polishing the samples.

3. RESULTS AND DISCUSSION

A strong, accelerating effect of nitrogen on the oxidation kinetics was seen already with 1% nitrogen addition to oxygen. On the other hand, only 1% of oxygen in nitrogen also increases the reaction kinetics significantly compared to the ones in pure nitrogen and even in pure oxygen. At 800°C, all mixtures with between 1 and 99% nitrogen resulted in higher reaction rates than in the pure gases after transition from protective to non-protective oxide scales; see Fig.1. This so-called breakaway oxidation was observed much earlier compared to pure oxygen. At 1000 and 1200°C, only starvation of oxygen in mixtures with low oxygen content resulted in lower rates compared to pure oxygen.

The oxide/(nitride) scales formed in the mixtures were very porous due to the formation of zirconium nitride at the metal-oxide interface and its re-oxidation during continuing reaction; see Fig.2. The extent of the oxide-nitride zone increases with temperature. Nitrogen seems also to affect the pre-transition reaction kinetics. This effect should be connected with the with temperature rising solubility of nitrogen in the oxide.

4. CONCLUSION

The strong effect of nitrogen on the oxidation kinetics of zirconium alloys was confirmed in these tests in mixed oxygen-nitrogen atmospheres. Already very low concentrations of nitrogen (in oxygen) as well as of oxygen (in nitrogen) strongly affect reaction kinetics. Nitrogen strongly reduces transition time from protective to non-protective oxide scale (breakaway). The formation of zirconium nitride, ZrN, and its re-oxidation is the main reason for the strongly porous oxide scales after transition. Nitrogen seems to affect also the pre-transition reaction kinetics. This effect increases with temperature. The results of this study suggest the need of using well controlled gas atmospheres for experiments on oxidation of zirconium alloys.

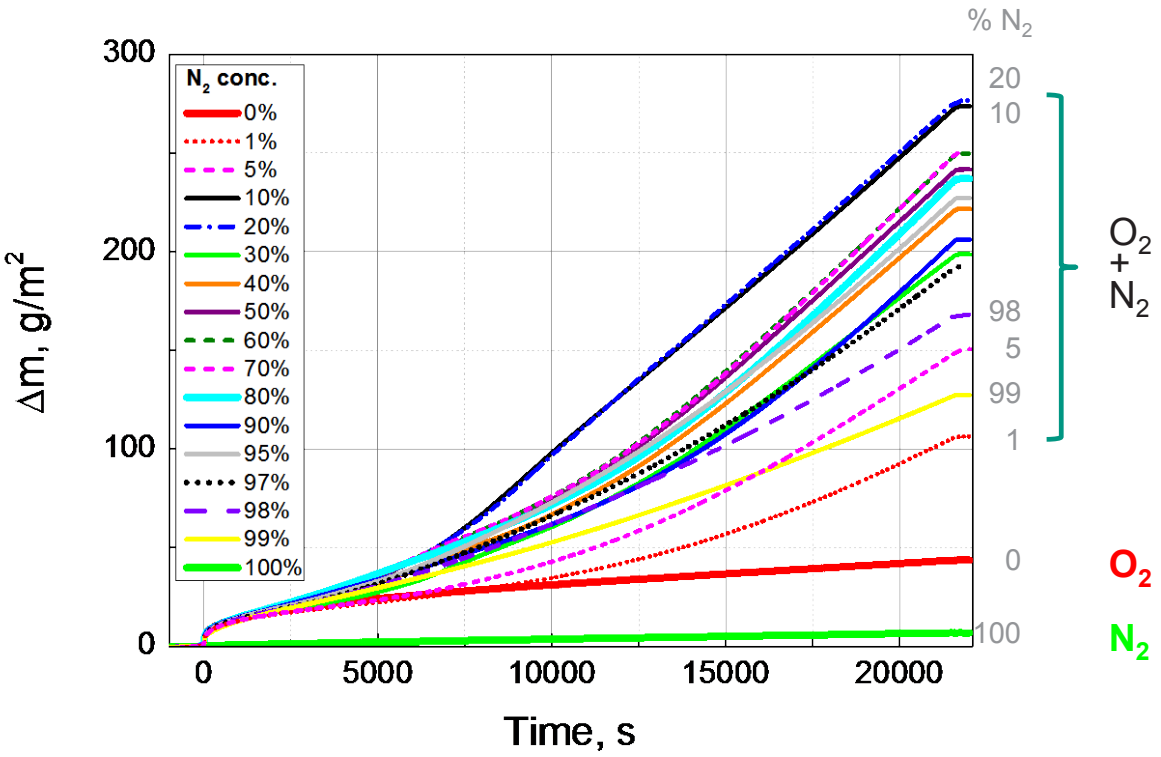

Fig.1. Mass gain during oxidation of Zircaloy-4 in mixtures of oxygen-nitrogen at 800°C.

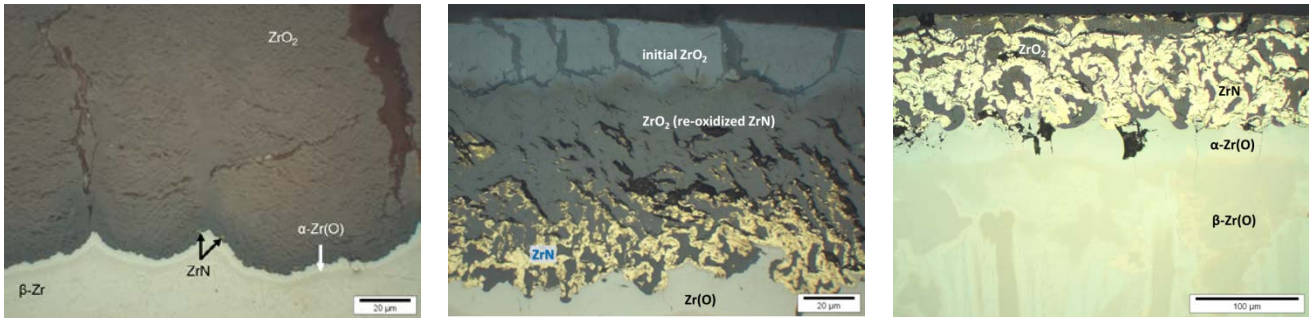

Fig.2. Typical micrographs after oxidation of Zircaloy-4 in oxygen-nitrogen. Left: 6 h at 800°C in 90% O_2 + 10% N_2; middle: 1 h at 1000°C in 5% O_2 + 95% N_2, right: 15 min at 1200°C in 2% O_2 + 98% N_2

References

[1] A. Zigh, A. Velazques-Lozoda, "Experiments on Ignition of Zirconium-Alloy in a Prototypical Pressurized-Water Reactor Single Fuel Assembly in a Spent Fuel Pool during a Complete Draindown," submitted to Nucl. Eng. Design (2013).

[2] M. Steinbrück, "Prototypical experiments relating to air oxidation of Zircaloy-4 at high temperatures," J. Nucl. Mater. 392, 531-544 (2009).

[3] M. Steinbrück, M. Böttcher, „Air oxidation of Zircaloy-4, M5® and ZIRLO™ cladding alloys at high temperatures," J. Nucl. Mater. 414, 276-285 (2011).

Process investigation of corrosion experiments at low oxygen activity environment containing H_2/H_2O

H. Hooshyar[(1,*)], J. Liske[(2)], J-E. Svensson [(3)]

[(1, 2, 3)]Environmental Inorganic Chemistry, Department of Chemical and Biological Engineering, Chalmers University of Technology, S-412 96, Göteborg, Sweden

e-mail: hamed.hooshyar@chalmers.se

1. INTRODUCTION

Gasification of biomass and waste is a key issue to reduce the usage of fossil fuels especially in transportation section (i. e. fuels for vehicles) and thus enabling a more sustainable society. However, the experience of corrosion issues in gasification plants is scarce. Compared to the combustion plants, gasifiers perform in a low oxygen activity environment which contains mostly H_2, H_2O, CO, CO_2 gases. At the High Temperature Corrosion (HTC) centre of Chalmers University both field and lab exposures directed towards corrosion issues in gasification environments are being deployed. The corrosion attack of metallic parts in the biomass gasification plant is characterized by a complex interplay between the above mentioned gases, HCl and H_2S, inorganic particles (e.g. KCl, NaCl) and the steel. In order to build generic knowledge about the corrosion mechanism in this complex environment, well-controlled (and thus simplified) laboratory exposures are needed. In the literature, laboratory studies of low oxygen activity environments have mostly been performed at high temperatures (900 °C and above) and long exposures times [1, 2]. The level of control of the parameters involved (e.g. temperature, gasmix and flow rate) is of great importance to be able to explain the cause of events leading to corrosion.
In this study, we have investigated the initial corrosion attack of 304L stainless steel at 600°C in H_2/H_2O mixtures, focusing on the transitional stages during start-up and end of the exposures. The transitional stages have been evaluated by means of an oxygen sensor and subsequent analysis with SEM/EDX and XRD.

2. EXPERIMENTAL

Coupons (15x15x2mm) of 304L stainless steel were grinded and polished with diamond paste down to 1µm. Exposures were performed in a alumina tube fitted furnace and the total gas flow was set to 200 ml/min. The samples were placed in an alumina sample holder standing parallel with the flow. A peristaltic pump or a humidifier was used in order to produce water vapour. Both calibrated by a humidity sensor (Optical Dew-Point Meter) with an accuracy of ±0.2°Cdp. Argon was used as carrier gas through the humidifier and the dew point of the water vapour was adjusted by a condenser controlled by a water bath thermostat. The peristaltic pump used a marprene tube connected to a container with distilled water in one end and a capillary alumina tube, placed in the hot part of the furnace, in the other end. The position of the capillary tube was optimized for a stable continuous water supply. In order to improve the mixing of the gases, a porous alumina flow restrictor was placed in front of the end tip of the capillary alumina tube.
In order to measure the oxygen partial pressure at various positions in the system, Rapidox 2100ZF Oxygen analyser was used. This analyser operates in the oxygen range between 10^{-20} ppm to 100% and the accuracy is ± 1% of the actual measured oxygen with a precision of ± 0.5% [3].

3. RESULTS AND DISCUSSION

The effect of oxygen impurities (even in ppm ranges) has a great influence on the gas phase chemistry, affecting the equilibrium in low oxygen activity exposures (e.g. H_2/H_2O mixtures). For example, in H_2O-Ar environment, the equilibrium partial pressure of oxygen is in the range of 10^{-9} to 10^{-6} bar at 500 °C to 900 °C and hence, impurities of as low as 1 ppm oxygen will change the $p(O_2)$ dramatically, especially at lower temperatures. In a H_2/H_2O mixture, hydrogen may react with the oxygen impurities decreasing the activity of oxygen [4, 5]. In addition to the effect of oxygen impurities during exposure, the risk of oxygen impurities and non-equilibrated gas during start-up and end of the exposure affecting the overall corrosion attack is especially pronounced.
In the present study, to highlight the importance of the oxygen impurity existence during start-up and end of exposure, relatively longer exposures (24 and 72 hour) were done at first. The exposures were started by placing the samples in a cold furnace. The samples inside the sealed alumina tube were flushed with Ar for 24 hours in order to remove any residual air. After this flushing period, the temperature in the furnace was set to 600°C. With a temperature ramp of about 15°C/min the desired exposure temperature was reached after approximately 40 minutes while flushing with pure Ar. Once the temperature was reached, the gas mix was switched to the intended gas mixture (as shown in table 1). After the intended exposure time (24 or 72 hours) the furnace is switched off with a continuous flow of pure Ar. The cooling down period lasts for about 9 hours in order to reach room temperature. Hence, the share of the total time allocated by the start-up and ending sequences is not negligible during a 24 or 72 hours exposure.
After exposure, all samples were investigated by means of XRD analysis, see figure 2. For all samples the corrosion products consisted of hematite (Fe2O3) and spinel type oxide. Diffraction peaks from the steel substrate was detected on the samples exposed in 10% H_2 + 2% H_2O + Ar, indicating a thin oxide covering the steel bulk. For the exposures with higher water vapor content (i.e. 20% and 50%) no diffraction peaks from the steel substrate was detected. It is important

to be noticed that for the H_2/H_2O exposures, the presence of hematite was rather unexpected. Based on Ellingham/Richardson diagram, the $a(O_2)$ needed to stabilize hematite at 600 °C is 10^{-16} bar. In the H_2/H_2O environments investigated the calculated oxygen levels are however much lower, thus making the hematite formation unfavourable.

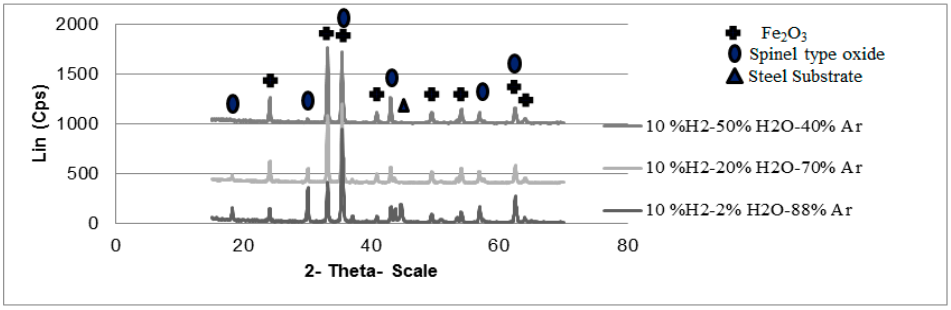

Figure 1. Crystalline phases detected by XRD on 304L samples exposed at 600 °C for 72 hours in 3 different environments.

In order to verify the system setup with respect oxygen activity an oxygen sensor was installed to the furnace outlet. For all H_2/H_2O mixtures, the measured oxygen level was however close to the calculated equilibrium value (see table 1). This implies that hematite did not form during the exposure, instead during the start-up or ending sequences. In order to investigate if the hematite formed during ramping up or down, the system was checked for a shorter exposure time (4 hour) using Ar, Ar + 10% H_2 and Ar+10 H_2 + 20 % H_2O as flushing gas during start-up and end of exposures.

Table 1. Exposure matrix using 100% Ar during ramping and ending sequences.

Gas Environment	**Calculated** $a(O_2)$*
10% H_2 + 2% H_2O + Ar	$5*10^{-26}$
10% H_2 + 20% H_2O + Ar	$2*10^{-24}$
10% H_2 + 50% H_2O + Ar	$3*10^{-23}$

***** **Oxygen** level **in Ar is** impurities, ***i.e.*** not calculated

Ar used as gas during start-up and ending sequences

As a reference, the oxygen activity was measured for the cold furnace with samples inside after one day of Ar flushing. The measured values are seen in table 2, row 1. The oxygen activity in the cold system varied between 35-85ppm, which is considerably higher compared to the oxygen impurities (5 ppm) from the Ar-flask. This indicates that there is some inward diffusion of air through joints and/or tubes. In order to verify the reproducibility of the results the same experiment was performed three times using the peristaltic pump. In addition, one experiment using a humidifier as water vapour generator was performed. There were however no observed differences with respect to oxygen content between using peristaltic pump or humidifier as water vapour generator. The second row in Table 2 shows the measured oxygen activity values after the furnace has reached 600 °C (still using 100% Ar as gas). The results showed that the $a(O_2)$ dropped dramatically to about 10^{-16} bar. Since there was no change in inlet gas composition the decrease in oxygen activity is suggested to be a result of oxide formation on the samples. This hypothesis was further strengthened when a corresponding exposure without any samples inside the furnace was performed. In the latter case, the oxygen activity remained high (i.e. in the ppm range) after heating up to 600 °C.

After the starting up sequence, using 100% Ar as gas and heating up the furnace to 600 °C, the gas mixture was changed to 10%H_2 + 20%H_2O + Ar. The exposure lasted for 4 hours. After this time, the oxygen content was around 10^{-24} bar, according to the oxygen sensor, see row 3 in table 2. This measured oxygen value is close to the calculated equilibrium value of oxygen, see table 1. The ending sequence started directly after the exposure time and 100% Ar was used as gas.

In all 4 exposures, the 304L samples had oxidized, forming hematite and spinel type oxide on the surface. According to the oxygen measurements the hematite formation is not thermodynamically favoured during H_2/H_2O exposures. Thus, it must have formed during start-up or ending sequences. In order to minimize this effect, 10% H_2 was added to the Ar during start-up and ending sequences.

	Exposure with pump			Exposure with humidifier
	#1	#2	#3	#4
Cold Furnace, Gas mix: Ar	35 ppm	85 ppm	55 ppm	41 ppm
Hot Furnace (600°C), Gas mix: Ar *Samples not present*	70 ppm			
Hot Furnace (600°C), Gas mix: Ar *Samples present*	$3*10^{-16}$	10^{-20}	$4*10^{-18}$	$3*10^{-19}$
Hot Furnace (600°C), Gas mix: 10% H_2 + 20% H_2O + Ar *Samples present*	$3*10^{-24}$	$2*10^{-24}$	$3*10^{-24}$	$3*10^{-24}$

Table 2. Oxygen activity measured at the furnace tube outlet during different stages of the exposure

10% H_2 + Ar used as gas during start-up and ending sequences

The exposures were repeated using 10% H_2 + Ar as gas during start-up and ending sequences. XRD analysis shows that the presence of H_2 during start-up and ending sequences effectively hinder the formation of hematite and only spinel type oxide is present see table 3. However, since the 10% H_2 + Ar is highly reducing, the spinel type oxide formed during the exposure may also be reduced during the ending sequence. Thus, in order to better control the oxygen activity a mixture of H2/H2O was used during start-up and ending sequences.

10% H_2 + 20% H_2O Ar used as gas during start-up and ending sequences

In similarity to the 10% H_2 + Ar test, no hematite formation was observed when 10% H_2 + 20% H_2O + Ar were used as gas mixture during start-up and ending sequences. However, the mass gain of the 304L samples used in the latter case was about two times higher, indicating that the spinel type oxide formed during exposure was reduced to metallic iron in the 10% H_2 + Ar test.

Table 3. Crystalline phases detected by XRD on 304L samples at 600 °C.

	Gas mixture during start-up and ending sequences.	Crystallin Phases	
		Spinel Type Oxide	Hematite
Exposure 1	Ar	X	X
Exposure 2	Ar	X	X
Exposure 3	Ar	X	X
Exposure 4	Ar	X	X
Exposure 5	10% H_2 + Ar	X	-
Exposure 6	10% H_2 + 20% H_2O + Ar	X	-

4. CONCLUSION

Running corrosion exposures at low oxygen activity environment are more difficult compared to high oxygen activity ones. To provide a low oxygen partial pressure environment and also avoid the formation of unexpected oxide layers by means of impurities entering to the system (e.g. via carrier gas bottles or small leakage in the system), a precise control from the start till the end of exposure is needed. It is important to know that not only during the exposure but also the start-up and end of exposure should be kept at environment containing low oxygen activity.

References**:**

1. Essuman, E., et al., Oxidation of Metals, 2008
2. Quaddakers, W.J., et al., JOM, 2009
3. *http://www.cambridgesensotec.co.uk/gallery/InstructionManualPDF/Rapidox_2100ZR_Instructio Manual_version_3.5.pdf.*
4. Tomlinson, L. and N.J. Cory, *Hydrogen emission during the steam oxidation of ferritic steels: Kinetics and mechanism.* Corrosion Science.
5. Zurek, J., et al., Oxidation of Metals,, June 2005.
6. Opila, E.J., Material Science.
7. Opila, E.J., et al., JOM.
8. Quadakkers, W.J. and J. Zurek, *Oxidation in Steam and Steam/Hydrogen Environment.* 2010.

Extra:
Thus it is important to investigate the environment at the start up and end of exposure (in addition to the main exposure time) to improve the whole process. It should be notice that the improvement of the process is based on the equipment used at the laboratories and one can use e.g. infrared furnace instead which needs a considerably lower time for ramping up and down. The problem of using infrared furnace is that to meet the requirement of the furnace application, a transparent tube like silica tube should be used. As can be seen in reaction 1 and 2, volatile Si- and Al- containing species, which may form in the system, are independent of oxygen partial pressure[6]. Opila[7] has shown that the rate of evaporation increases in the order of: $Al(OH)_3^{(g)} < Si(OH)_4^{(g)}$. In spite of showing excellent thermal shock resistance, quarts is not used as a construction material in low $p(O_2)$ environments and it is recommended to use materials made up of Alumina instead (to avoid the effect of volatile Si- containing species on oxide formation of the samples)[8].

$SiO_2 + 2H_2O^{(g)} = Si(OH)_4^{(g)}$ (1)

$1/2Al_2O_3 + 3/2H_2O^{(g)} = Al(OH)_3^{(g)}$ (2)

It has been also shown that H_2 impurities have substantial effect on equilibrium oxygen partial pressure and can act as for example hematite destabilizer in steels while oxygen traces would show opposite effects.[4, 5]

Characterization of Spark Plasma Sintered $FeSi_2$-Al Alloys Oxidized in Air at 1073 K

Toto Sudiro [(1,*)], Kemas Ahmad Zaini Thosin [(2)], and Kazuya Kurokawa [(3)]

[(1-2)]Research Center for Physics, Indonesian Institute of Sciences, Kawasan Puspiptek Serpong, Tangerang Selatan 15310, INDONESIA

[(3)]CAREM, Faculty of Engineering, Hokkaido University, Kita13 Nishi 8, Sapporo 060-8628, JAPAN

[*]e-mail: toto.sudiro@lipi.go.id

Abstract

Al added $FeSi_2$ alloys were fabricated by a spark plasma sintering technique. The specimens were oxidized in air at 1073 K for 200 h. The phase composition and surface morphology of alloy before and after the high temperature oxidation test were analyzed by XRD and SEM-EDX. The results show that depending on its concentration, Al affects the morphology and composition of the oxide scale.

1. INTRODUCTION

Transition metal dicilicides are promising material for high temperature applications because they have high melting point, relatively low density and high resistance against oxidation at high temperatures due to the formation of a SiO_2 scale by selective oxidation of silicon.[1-2)] The formation of oxide layer on the alloy surface plays a key role as a barrier from environmental degradation. Several studies were carried out to enhance the oxidation resistance and mechanical properties of $NbSi_2$ [2-3)] and $MoSi_2$ [4)] by adding an alloying element.

In this study, we fabricate $FeSi_2$ alloys with varying amount of Al content by a spark plasma sintering technique. The high temperature oxidation of alloy was studied in air at 1073 K for 200 h. The effect of Al concentration on the surface morphology and composition of oxide scale formed on the $FeSi_2$ alloy was discussed.

2. EXPERIMENTAL

Commercially, $FeSi_2$ and Al powders were used in this study. The nominal composition of elements is shown in Table 1.

Table I. Nominal Composition of Fe-Si-Al powders (mass%)

	Fe	Si	Al
$FeSi_2$	**49.86**	**50.14**	**0.00**
$FeSi_2$-1 mass% Al	**49.36**	**49.64**	**1.00**
$FeSi_2$-3 mass% Al	**48.36**	**48.64**	**3.00**
$FeSi_2$-5 mass% Al	**47.37**	**47.63**	**5.00**

$FeSi_2$-Al powders were prepared by mechanical alloying. The powder was then sintered by a spark plasma sintering technique. The fabrication of specimen was performed in an evacuated chamber of less than 4 Pa and under compressive pressure of 40 MPa. The sintered alloy was then machined into a rectangular shape and polished down for up to mirror finish. Hereafter, the polished alloys were oxidized at 1073 K in air for 200 h. The phase composition and morphology of alloy before and after the high temperature oxidation test were analyzed by XRD, SEM dan SEM-EDX.

3. RESULTS AND DISCUSSION

$FeSi_2$ alloys with varying Al content is mainly composed of $FeSi_2$ and FeSi phases with a small amount of Si-oxide. The fraction of each phase depends on the Al concentration.

The SEM images of surface morphology of $FeSi_2$ alloys with 0, 1, 3 and 5 mass% Al content oxidized for 200 h at 1073 K in air are shown in Fig. 1 (a), (b), (c) and (d), respectively. It can be seem that the surface morphology of the oxide scale varied with Al content in the alloy. Some amount of oxide particles are formed in the $FeSi_2$ and $FeSi_2$–Al alloys. However, there is a significant difference on the oxide morphology as shown in Fig. 1 (b) that the formation of oxide particle in the $FeSi_2$ alloy significantly decrease by the addition of 1 mass% Al.

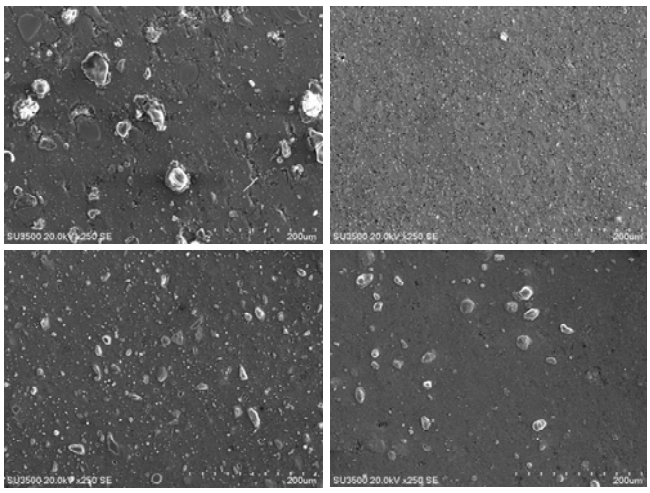

Fig. 1 SEM images of surface morphology of $FeSi_2$ alloys with (a) 0, (b) 1, (c) 3 and (d) 5 mass% Al content oxidized in air at 1073 K for 200 h

Figs. 2 (a) and (b) show the results of SEM-EDX elemental map of $FeSi_2$ alloys with 0 and 3 mass% Al content, respectively. The results indicate that the oxide scale formed on the alloy surface of $FeSi_2$ alloy is composed of the oxides of Si and Fe. On the contrary, $FeSi_2$ alloy with 3 mass% Al content forms mainly Al-oxide with some amount of Si-oxide.

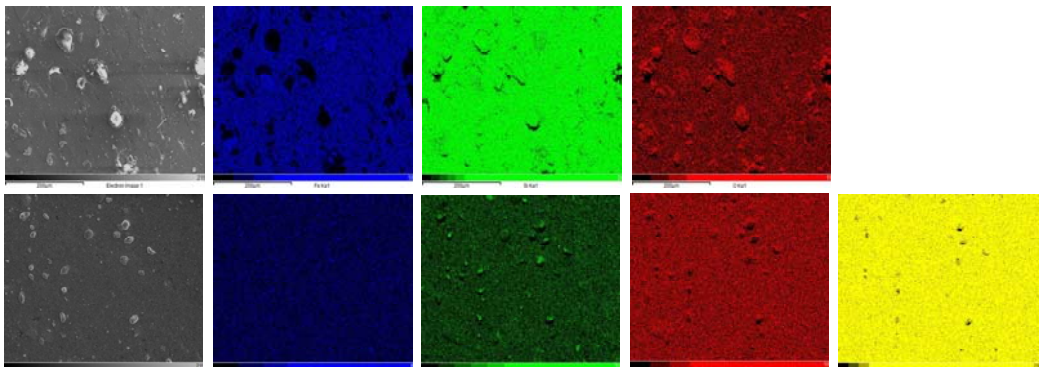

Fig. 2 SEM-EDX elemental map of $FeSi_2$ alloy with (a) 0 and (b) 3 mass% Al content oxidized at 1073 K for 200 h

The aforementioned results suggest that depending on the Al content in the alloy, the Al addition affects the morphology and composition of the oxide scale formed on the alloy surface. The addition of 1 mass% Al forms a homogenous oxide scale on the $FeSi_2$ alloy.

4. CONCLUSION

In summary, spark plasma sintered $FeSi_2$-Al alloys were oxidized in air at 1073 K for 200 h. The results as presented above reveal that the formation of oxide particles on the surface of $FeSi_2$ alloy is suppressed by the addition of Al. It depends on the content of Al.

Acknowledgements

T. Sudiro gratefully acknowledges the financial support from Indonesia Toray Science Foundation (ITSF).

References

[1] K. Kurokawa, A. Yamauchi: Solid State Phenomena **127** (2007), pp. 227-232.
[2] F. Zhang, L. T. Zhang, A. D. Shan, J. S. Wu: Journal of Alloys and Compounds **422** (2006), pp. 308-312.
[3] J. Cheng, S. Yi, J. S. Park: Int. Journal of Refractory Metals and Hard Materials 41 (2013), pp. 103-109.
[4] R. Mitra, V. V. Rama Rao, A. Venugopal Rao: Intermetallics **7** (1999), pp. 213-232.

High temperature cyclic oxidation with water cooling: The study of alumina-forming coatings

M. Brossard [(1,*)], F. Pedraza [(1)], M. Craig [(2)], J.R. Nicholls [(2)]

[(1)] Laboratoire des Sciences de l'Ingénieur pour l'Environnement LaSIE FRE-CNRS 3474, Université de La Rochelle, Avenue Michel Crépeau, 17042 La Rochelle Cedex 1, FRANCE

[(2)] Cranfield University, Cranfield, Bedfordshire MK43 0AL, UK

e-mail: mbrossar@univ-lr.fr

1. INTRODUCTION

The effect of water vapour on the high temperature oxidation of alumina-forming materials has been a subject of increased interest over the last decade [1]. This is a critical parameter to be considered for a better understanding of turbine parts durability in aero-gas engines. Indeed, turbine components are regularly exposed to water during their lifecycle, due to both the surrounding environment (relative humidity, water droplets from clouds) and the regime of the combustion engine (take-off, cruise and/or landing), with contents varying between 10-15%.vol. H_2O [2]. Therefore, the effect of water-containing environments on alumina-forming materials was first studied by the addition of water vapour in flowing air furnaces [3-5]. It is worth noting that water vapour affects spallation and the cracking mechanisms of the oxide scales especially under thermal cyclic conditions [3]. The influence of water vapour seems to be dependent of the interfacial metal/oxide toughness of the system studied and especially on the sulphur content segregated [5].

At ambient temperature, the exposure of thick alumina scales to humid laboratory conditions (relative humidity) showed an enhanced effect of the H_2O molecule on the onset of oxide spallation. This phenomenon, called "Moisture Induced Delayed Spallation" [6] provokes an early failure within a variety of different TBC systems, and is triggered by the addition of water drops [7-9]. The delamination at the bond-coat/TGO interface was observed when the alumina scale exhibited a critical number of cycles, and occurred for highly stressed (thickness, S segregation, rumpling) scales which proved more sensitive to water [10]. J.L. Smialek attributed this degradation to a mechanism that was similar to hydrogen embrittlement, associated with the dissociation of water and diffusion of protons to the metal/oxide interface [11].
The combination of cyclic oxidation and water drop tests at ambient temperature has already been reported. Indeed, drops were systematically added onto alumina-forming CeO_2 based coatings during the cold stage ($T < 80°C$) of cyclic oxidation at 1100°C [12]. This aims at simulating repeated condensation of water released by the kerosene combustion or relative humidity of air after engine operation. The results showed no spallation and a chemical inertness of the system to liquid water for the earliest stages of cyclic oxidation.
In this study, the influence of water during the cooling step (1100°C-T_{amb}) of cyclic oxidation will be investigated, as this step is already critical for oxide scales in dry conditions due to CTE mismatches [13]. In this sense, a new thermal cyclic rig with an automatic water projection onto hot samples has been developed. A cloud of water vapour is then generated all around the samples surface, followed by a liquid wetting of the surface when the specimen temperature is lower than 100°C. In this study, out-of-pack aluminide samples and similar samples overcoated with an EB-PVD YSZ thermal barrier are cyclically oxidized at 1100°C and cooled by water. The results are compared with a "dry" ambient air cooling.

2. EXPERIMENTAL

A CM247 directionally solidified (DS) Ni-based superalloy was employed in this study as a substrate material. An out-of pack aluminising (70 µm thick) was carried out at 1080°C for 6h from a 70Cr-30Al donor and NH_4F activator.
On top of this aluminide coating, a 7%wt yttria-stabilised tetragonal zirconia (7YSZ) was deposited by EB-PVD (215 ± 5 µm thick) on some of the samples after a grit blasting with a 220 mesh Al_2O_3.

The cyclic oxidation tests were performed at 1100°C for 1h-cycles in a custom designed cyclic rig with an automatic water cooling system (Fig. 1.a). The cooling chamber is contained in a closed area made of stainless steel, to avoid hot water projections and increased pressures due to the generation of steam. A tank containing deionised water is located underneath the cooling chamber and provides liquid water to cool down the samples. The samples are suspended in a FeCrAl carrousel thanks to FeCrAl wires. The cooling rate was measured by a type K thermocouple close to the samples surface (Fig. 1.b). Although the thermocouple indicates a fast cooling (15.9 s) from 1100°C to 100°C, additional IR thermometer measurements were used to take into account the global sample surface. A 5 min cooling was then chosen to get a specimen surface temperature of 40°C, saturated with liquid water.

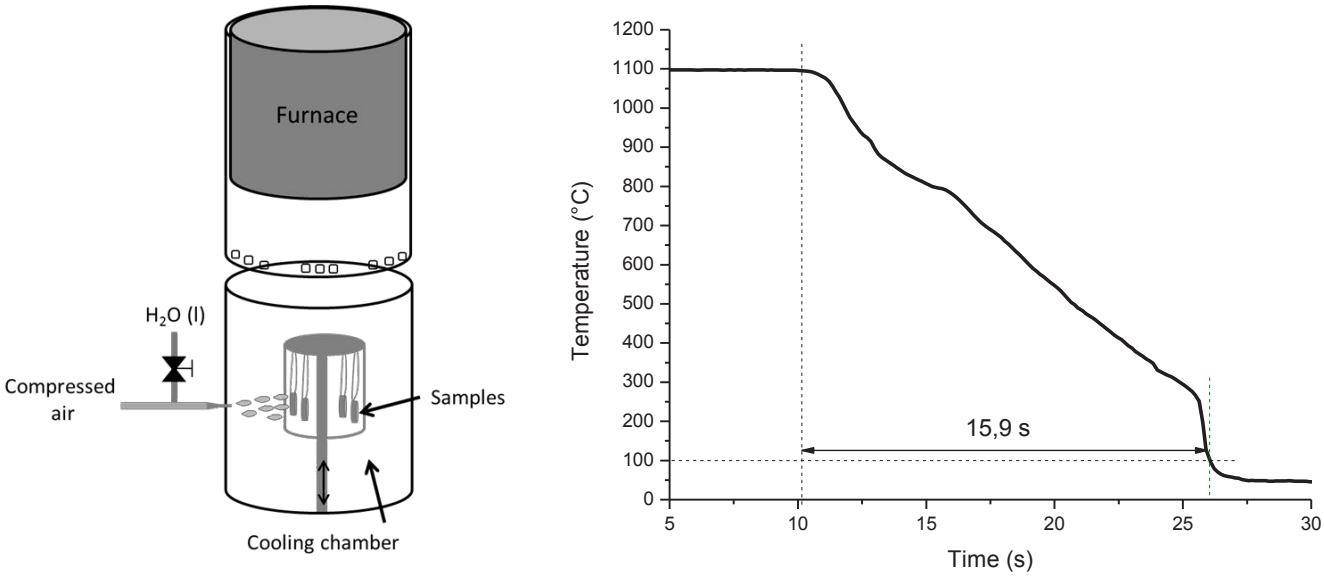

Fig. 1. a) Schematic of the cyclic oxidation rig with automatic water cooling; b) Measurement of cooling rate with a type K thermocouple.

Microstructural characterization of the coatings was performed by X-Ray Diffraction (Brüker D8 Advance, λ_{Cu}), and Scanning Electron Microscopy coupled to Energy-Dispersive Spectrometry (SEM/EDS, FEI Quanta 200F / EDAX). Local surface analyses were undertaken using non-destructive Raman spectrometry (Jobin Yvon Horibat LabRam HR, $\lambda_{He\text{-}Ne}$), as it allows to differentiate metastable alumina phases.

3. RESULTS AND DISCUSSION

The specific mass variations of the aluminide coated CM247 is presented in Fig. 2 for high cyclic oxidation with water cooling as well as under “dry” ambient air cooling. It can be seen that the wet cooling provoke a high mass gain until 370 cycles with a para-linear kinetic.

The formation of non-protective oxides is expected in comparison with the dry air cooling, where a sub-parabolic regime is obtained for similar oxidation times. The water cooling samples then exhibit a mass loss until 500 cycles, attributed to the spallation of the oxide scale, assisted by moisture. The mass curve increased again and reached a maximum around 825 cycles, followed by an important decrease until the end of the test (1000 cycles).

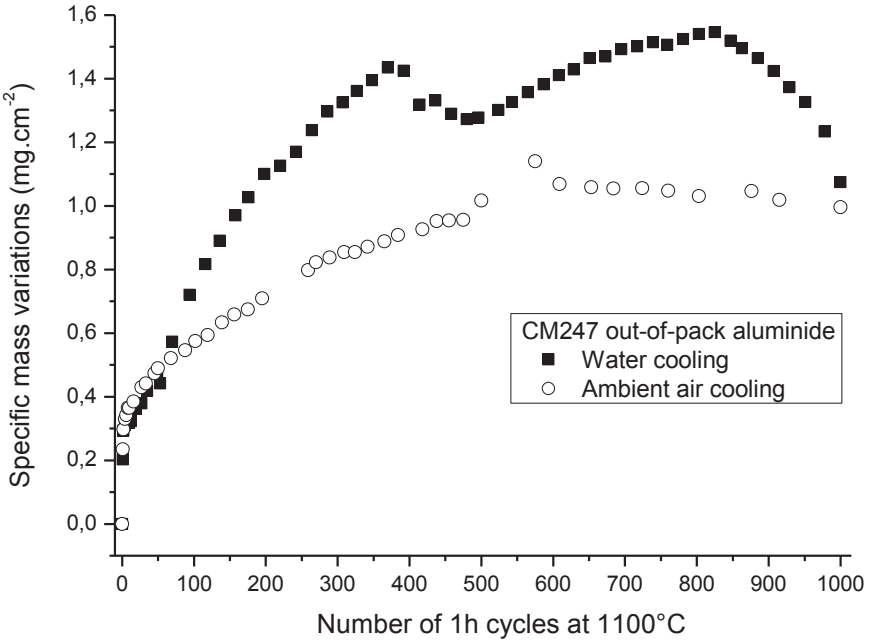

Fig. 2. Weight changes of an out-of-pack aluminide coated CM247 during high temperature cyclic oxidation: Water cooling compared to ambient air cooling.

XRD analysis revealed the detection of $(Ni,Co)Al_2O_4$ spinel phases together with α-Al_2O_3 and Cr_2O_3 at the surface of water cooled samples. SEM images also exposed a blade-like morphology (Fig. 3.a), attributed to the formation of the fast growing metastable θ-Al_2O_3. This presence was confirmed by fluorescence analysis. However, in the case of a dry ambient cooling, no such metastable alumina is observed in the SEM or through fluorescence. The transformation of transient alumina in stable alpha alumina is quick in dry air at 1100°C (28h for bulk NiAl) [14], and therefore theta phase is not expected for such oxidation times (500h). A hypothesis would be that the θ-Al_2O_3 is formed during the cooling step of the cyclic oxidation, where oxide scales are spalled off and re-formation can occur. The water vapour atmosphere generated at this time is thought to be responsible for the delay of $\theta \rightarrow \alpha$ transformation. A cross-section analysis (Fig. 3.b) revealed 100 µm deep internal oxidation at localised areas, as well as an advanced β-NiAl$\rightarrow\gamma$'-Ni_3Al transformation. Hydrogen embrittlement or an electrochemical mechanism may also be a cause of this rapid deterioration.

In what concerns the full TBC system made of an out-of-pack aluminide coated with a YSZ EB-PVD TBC, no delamination of the top-coat has occurred during the exposition of this system to both vapour and liquid water (1100°C$\rightarrow T_{amb}$). Longer oxidation times (higher than 1000 h) are needed to conclude about the TBC lifetime regarding this atmosphere.

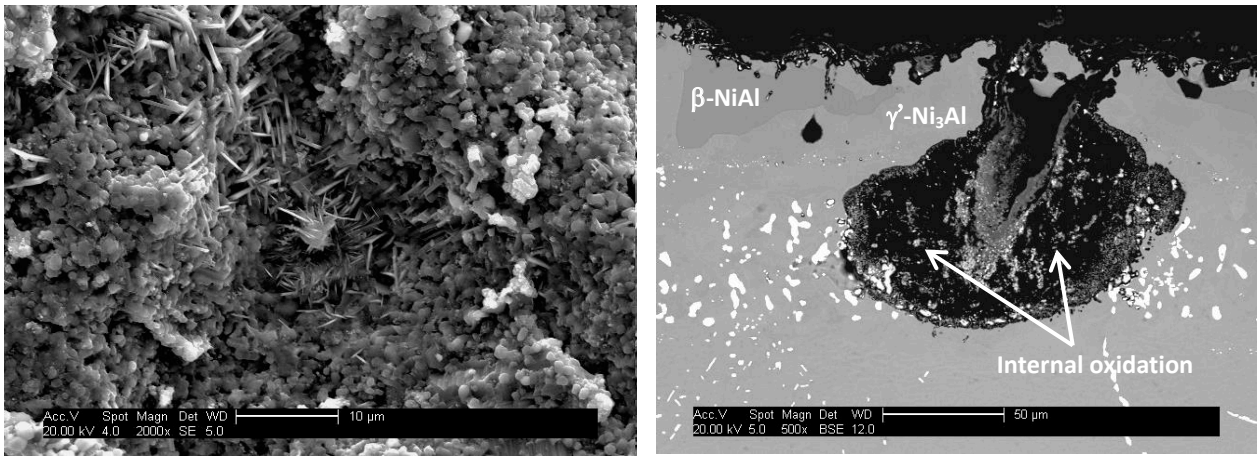

Fig. 3. SEM images of an out-of-pack aluminide coated CM247 oxidised for 500 1 h-cycles at 1100°C: a) Top-surface (secondary electrons); b) Cross-section (back-scattered electrons)

4. CONCLUSION

A new kind of cyclic oxidation with water cooling has been investigated in this study. The procedure consists of projecting liquid water onto hot samples during the cooling stage of 1h cyclic oxidation at 1100°C. The generation of water vapour occurs around the surface sample, followed by a full wetting of the surface when the temperature is lower than 100°C. Out-of-pack aluminide coatings were tested and exhibited higher mass gains than dry cooled samples, attributed to the formation of spinel $NiAl_2O_4$, metastable θ-Al_2O_3 and considerable internal oxidation zones. No moisture induced spallation took place for an YSZ EB-PVD TBC system oxidized during 1000h of water assisted cyclic oxidation.

Acknowledgements:

The University of La Rochelle is gratefully acknowledged for funding the exchange fellowship of *PhD student M. Brossard* as well as SR Technics Airfoil Services for aluminide coatings supply.

References:

[1] Saunders S.R.J., Monteiro M., Rizzo F., "The oxidation behaviour of metals and alloys at high temperatures in atmospheres containing water vapour: A review", *Progress in Materials Science* , Vol. 53, No. 5 (2008), pp. 775-837.
[2] Pint B.A. Garner W.G, Lowe T.M., Haynes J.A., Zhang Y., "The Effect of Water Vapor on the Oxidation Behavior of Ni-Pt-Al Coatings and Alloys",*Surface and Coatings Technology* , Vol. 201, No. 7, (2011), pp. 3852-3856.
[3] Janakiraman R., Meier G.H., Pettit F.S., "The Effect of Water Vapor on the Oxidation of Alloys that Develop Alumina Scales for Protection", *Metallurgical and Materials Transactions A* , Vol. 30, No. 11 (1999), pp. 2905-2913.
[4] Onal K., Maris-Sida M.C., Meier G.H., Pettit F.S., "Water Vapor Effects on the Cyclic Oxidation Resistance of Alumina Forming Alloys", *Materials at High Temperatures* , Vol. 20, No. 3 (2003), pp. 327-337.
[5] Maris-Sida M.C., Meier G.H., Pettit F.S., "Some Water Vapor Effects During the Oxidation of Alloys That are α-Al_2O_3 Formers", *Metallurgical and Materials Transactions A*, Vol.34, No. 11 (2003), pp. 2609-2619.
[6] Smialek J.L., Morscher G.N., "Delayed Alumina Scale Spallation On Rene'N5 + Y: Moisture Effects and Acoustic Emission" *Materials Science and Engineering A*, Vol. 332, No. 1-2 (2002), pp. 11-24.
[7] Smialek J.L., Zhu D., Cuy M.D., "Moisture-Induced Delamination Video of an Oxidized Thermal Barrier Coating", *Scripta Materialia* , Vol. 59, No. 1 (2008), pp. 67-70
[8] Déneux V., Cadoret Y., Hervier S., Monceau D., "Effect of Water Vapor on the Spallation of Thermal Barrier Coating Systems During Laboratory Cyclic Oxidation Testing", *Oxidation of Metals* , Vol. 73, No. 1-2 (2010), 83-93.
[9] Rudolphi M., Renusch D., Schütze M., "Verification of Moisture-Induced Delayed Failure of Thermal Barrier Coatings", *Scripta Materialia*, vol. 59, No. 2 (2008), pp. 255-257.
[10] Smialek J.L., "Moisture-Induced Delayed Alumina Scale Spallation on a Ni(Pt)Al Coating", *Oxidation of Metals,* Vol. 72, No. 5-6 (2009), pp. 259-278.
[11] Smialek J.L., "Moisture-Induced Delayed Spallation and Interfacial Hydrogen Embrittlement of Alumina Scales", *JOM,* Vol. 58, No. 1 (2006), pp. 29-35.
[12] Brossard M., Bouchaud B., Bonnet G., Rannou B., Pedraza F., "Early Stages of High Temperature Cyclic Oxidation of an Electrodeposited Ceria Coating on Nickel Superalloys Under Water-drop Tests", *Oxidation of Metals*, accepted.
[13] Tolpygo V.K., Clarke D.R., "Tensile Cracking During Thermal Cycling of Alumina Films Formed by High-Temperature Oxidation", *Acta Materialia*, Vol. 47, No. 13 (1999), pp. 3589-3605.
[14] Garriga-Majo D.P., Shollock B.A., McPhail D.S., Chater R.J., Walker J.F., "Novel strategies for evaluating the degradation of protective coatings on superalloys", *International Journal of Inorganic Materials*, Vol. 1, No. 5-6, pp. 325-336.

Effect of Pre-oxidation on Metal Dusting of Nano-crystalline Sputtering Coated Ni-Cr Alloys

Zheng Xiang[(1)], Jianqiang Zhang[(1,*)], Chunhua Kong[(2)], Xiao Peng[(3)], and David J. Young[(1)]

[(1)] School of Materials Science and Engineering, University of New South Wales, Sydney 2052 AUSTRALIA

[(2)] The Mark Wainwright Analytical Centre, University of New South Wales, Sydney 2052, AUSTRALIA

[(3)] State Key Lab for Corrosion and Protection, Institute of Metal Research, Shenyang, CHINA

e-mail: j.q.zhang@unsw.edu.au

1. INTRODUCTION

Metal dusting is a type of high temperature corrosion which occurs in highly carburising gas atmospheres ($a_C > 1$) in the temperature range of 400 to 800°C. Metal dusting leads to metal disintegration from bulk materials into a dust of metal or carbide particles in graphite. This metal loss reduces component lifetimes, ultimately leading to materials failure.

Metal dusting was first reported for ferritic iron-based alloys [1] and has been studied for decades [2-6]. The mechanism involves carbon adsorption, dissolution and further supersaturation of the metal surface, carbide formation, and decomposition and/or disintegration of metastable carbides which further catalyse carbon deposition. Unlike iron-based alloys, nickel and nickel-based alloys do not produce parent metal carbide during the dusting process. Direct graphite deposition, however, causes metal disintegration and then metal dusting.

It has been accepted that forming a dense layer of chromia or alumina can prevent carburisation and metal dusting. Refining the alloy grain structure can promote selective oxidation of chromium and aluminium [7,8]. This promotion effect becomes more significant, when alloy grain sizes are reduced to the nanometre range (less than~100nm). This grain structure not only promotes protective oxide formation, but also improves scale adhesion. It has also been reported [9] that pre-oxidation before metal dusting could improve oxide protective effect on metal dusting. On the other hand, however, fine grain structure potentially provides more graphite nucleation sites and carbon diffusion channels, which could accelerate metal dusting.

The aim of the present work is to investigate metal dusting behaviour of nanocrystalline Ni-Cr alloys with varied Cr contents and the effect of pre-oxidation on metal dusting of these alloys.

2. EXPERIMENTAL

Three NiCr alloys with Cr concentrations of 5, 10 and 20 wt% were prepared by vacuum melting, casting and annealing. Testing samples were cut from the ingots with the dimension 15mm×10mm×2mm, ground to a final 800 grit paper, and ultrasonically cleaned in acetone. The coatings were deposited on the surface of these samples with the same composition as the substrate of the alloy. This design avoids the effect of inter-diffusion due to different compositions between coating and the substrate at the reaction temperature and simplifies the process. A magnetron sputtering technique was used for coating to achieve about 30-40 μm thickness coating.

Metal dusting experiments were carried out in a controlled gas atmosphere with the composition of 47%CO-47%H_2-6%H_2O (vol%), with a calculated carbon activity of 5.49 (calculated based on $CO + H_2 = H_2O + C$) and $p_{O_2} = 1.1\times10^{-24}$ atm (based on $H_2 + 1/2O_2 = H_2O$) at the reaction temperature 650°C. The total gas flow rate was 400 mL/min. Weight gain kinetics during reaction were measured by thermogravimetric analysis (TGA).

For pre-oxidation & metal dusting experiments, samples were first pre-oxidised in 47%Ar-47%H_2-6%H_2O (vol%) gas atmosphere at 650°C for 24 h. After that, the gas was switched to above dusting gas directly without taking the sample out of the reactor.

After reaction, all samples were analysed using X-ray diffraction (XRD), scanning electron microscope (SEM) equipped with an X-ray energy dispersive spectroscopy (EDS), and some were further analysed using transmission electron microscope (TEM). All TEM samples were prepared using dual focus ion beam (FIB).

3. RESULTS AND DISCUSSION

All sputtering coated samples show typical columnar structures, as shown in Fig. 1a, and Fig. 1b shows that the average grain size of the coating is about 100 nm. It also reveals that the coating structure is not compact, with fine gaps decorated along the boundary of fine grain clusters. The size of these clusters corresponds well with that of the columnar domains, indicating possible discontinuous nano-gaps between columns. The optical microscopic analysis of substrate structure of the alloys reveals very large grain size, in a millimetre scale (not shown).

Figure 2 shows the TGA results of Ni5Cr, Ni10Cr and Ni20Cr samples carburised in 47%CO-47%H_2-6%H_2O gas mixture at 650°C for 50h. For Ni5Cr, the weight gain increased first, and then this increase became significant after 5 h. After about 14 h reaction, no clear weight gain was recorded and the weight change became fluctuated. After 20 h reaction, an abrupt weight loss was recorded, followed by fluctuated weight gain/loss. The weight gain kinetics of Ni10Cr and Ni20Cr are seen to be more or less linear and the rate of Ni20Cr is much less than that of Ni10Cr.

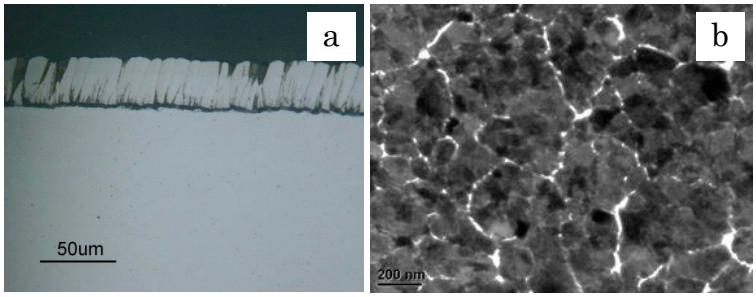

Fig. 1. NiCr sputtering coated Ni-5Cr sample: (a) cross-section, and (b) TEM bright field image, perpendicular to coating growth direction.

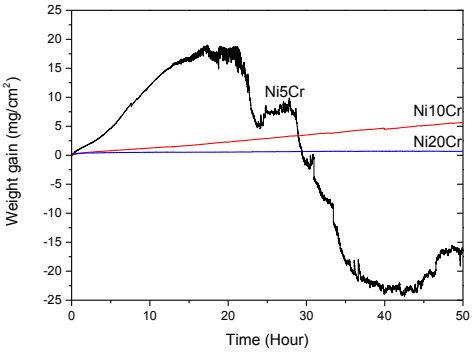

Fig. 2. TGA results of sputtering coated NiCr alloys during metal dusting.

SEM surface observation reveals that sample surface has fully been covered by graphite for Ni5Cr, partly covered by short fine carbon filaments for Ni10Cr, but almost no carbon deposition for Ni-20Cr. XRD analysis results of sputtering coated NiCr alloys after 50 h reaction show that graphite was detected on both Ni5Cr and 10Cr surfaces. Both Cr_2O_3 and Cr_7C_3 were detected on the Ni10Cr and Ni20Cr alloys but not Ni5Cr alloy.

Figure 3 shows the cross-sections of sputtering coated NiCr after metal dusting for 50 h using SEM. It can be seen that the Ni5Cr coated sample was covered with a coking layer mixed with graphite and particulate metals (Fig. 3a). The whole coating scale had disappeared. However, for higher Cr-containing coatings, the coating scales remained on the surface (Figs. 3b and c), but the morphologies were quite different. For Ni10Cr (Fig. 3b), there are many small carbon precipitates formed inside the coating layer, confirmed by TEM cross-section analysis. The coating also contains many grey strips, aligned more or less perpendicular to the surface (Fig. 3b). EDS analysis showed that they are Cr and oxygen rich phases. For Ni20Cr (Fig. 3c), many fine elongated-Cr carbide precipitates are formed, more or less uniformly in the whole coating layer. There are also some chromia formed penetrating deeply into the coating scale, at the coating surface and the interface between the coating and the substrate (not shown).

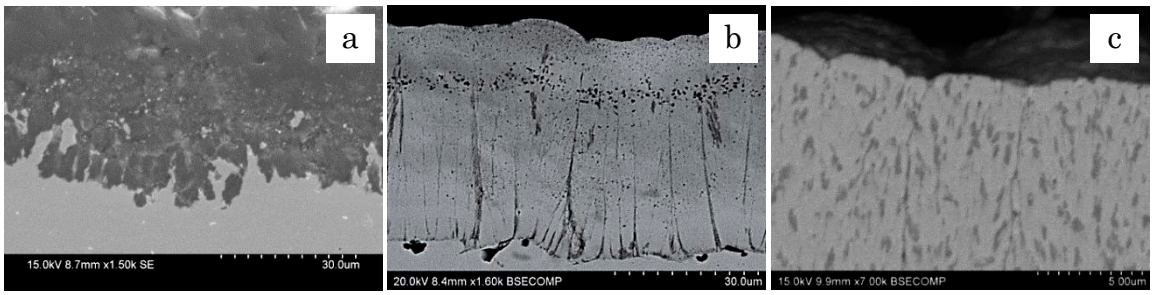

Fig. 3. SEM cross-sections of (a) Ni5Cr, (b) Ni10Cr and (c) Ni20Cr samples after 50h metal dusting.

Figure 4 shows the TGA results of Ni5Cr, Ni10Cr and Ni20Cr pre-oxidised in 47%Ar-47%H_2-6%H_2O gas at 650°C for 24 h and then carburised in 47%CO-47%H_2-6%H_2O gas mixture at 650° for 50 h. During pre-oxidation, the weight gain increased rapidly at the beginning of the reaction and then slowed down. Further carburisation resulted in an initial fast weight gain and then gradual weight increases. The rate of weight gain during carburisation decreased significantly with increasing in chromium contents. Total weight gain was very low. Even for Ni-5Cr, the weight gain was only 0.45 mg/cm^2 after 50h carburisation reaction.

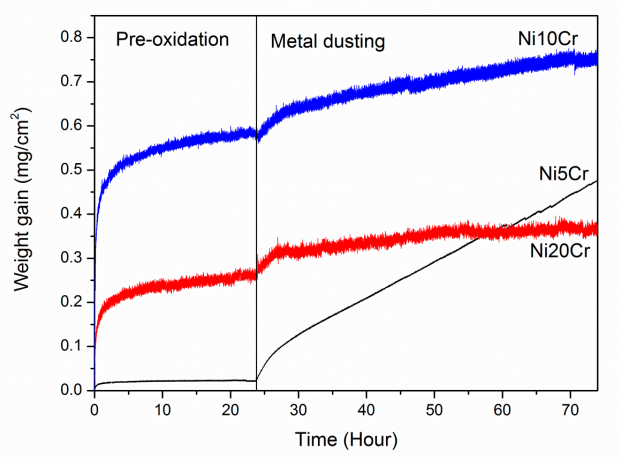

Fig. 4. TGA results of sputtering coated NiCr samples after pre-oxidation and then dusting

The surface morphologies of pre-oxidised sputtering coated NiCr alloys after dusting were analysed by SEM. The whole surface remained smooth with no apparent graphite deposition. The feature of coating surface can still be identified. Only few round pits were formed on the surface. SEM cross sections of NiCr alloys after pre-oxidation and metal dusting are shown in Fig. 5. Continuous, uniform, and compact nano-coating scale remained on the surfaces. For all alloys, a thin continuous layer of Cr_2O_3 scales formed on the surface. The inner Cr_2O_3 linked up and became a continuous layer along the grain boundaries and cracks.

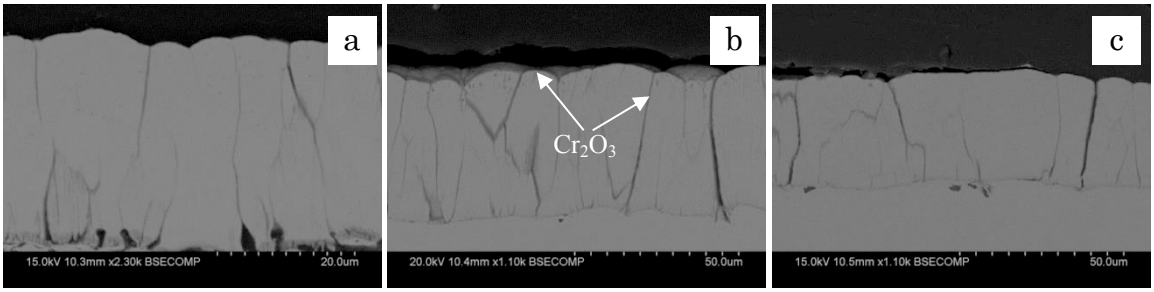

Fig. 5. SEM cross-section of (a) Ni5Cr, (b) Ni10Cr and (c) Ni20Cr after pre-oxidation and then metal dusting

The reaction condition used in this work is such that Cr is able to be oxidised, while Ni is not. The selective oxidation of chromium leads to the formation of Cr_2O_3. If a protective Cr_2O_3 scale is formed and maintained, carburisation and metal dusting will be retarded. The required chromium concentration for external chromia scale formation and maintenance can be estimated based on Wagner's analysis [10,11] to be 8.2 wt% Cr at 650°C. This result indicates that a stable chromia scale can be formed and maintained for both Ni-10Cr and Ni-20Cr, but not for Ni-5Cr. It is true for Ni-10Cr and 20Cr alloys as apparent Cr_2O_3 is detected by XRD. However, for low Cr content Ni-5Cr alloy, a significant weight gain was recorded, indicating a non-protective effect. Pre-oxidation before metal dusting stabilises the Cr_2O_3 formation which reduces significantly the weight gain kinetics from carbon attack in particular for Ni-5Cr. This observation clearly shows that there is a critical Cr content for protective Cr scale formation. The 5wt% of Cr should be the marginal value for protective Cr_2O_3 scale formation and maintenance.

Without pre-oxidation, a non-stable chromia scale of Ni-5Cr will soon be attacked by carbon in metal dusting condition. As a result, no protective effect is observed and dusting occurs. For high Cr-containing alloys, internal carbides were detected by XRD for both Ni-10Cr and 20Cr alloys. Significant amount of Cr_7C_3 was formed more or less uniformly in the whole coating layer of Ni-20Cr, showing fast C diffusion and necessary Cr content. The reaction between chromium in Ni-Cr alloy and carbon to produce carbides in these experiments can be expressed as:

$$m\underline{Cr} + n\underline{C} = Cr_mC_n\,(Ni) \quad (1)$$

The equilibrium condition for carbide precipitation is written

$$K_{sp}[Cr_mC_n] = [\underline{Cr}]^m[\underline{C}]^n = \exp\{\Delta G_f^0 / RT)/[\gamma_{\underline{Cr}}^m \gamma_{\underline{C}}^n] \quad (2)$$

where K_{sp} is the solubility product for Cr_mC_n in the equilibrium with the Ni-matrix; [Cr] and [C] are the concentrations of Cr and C in nickel, respectively; ΔG_f^0 is the Gibbs free energy change for the formation of Cr_mC_n from the Cr and C in their standard states; γ_{Cr} and γ_C are the activity coefficients of Cr and C in nickel. The solubility products [12] for $K_{SP}[Cr_7C_3]$ and $K_{SP}[Cr_{23}C_6]$ are calculated to be 1.76×10^{-17} and 1.61×10^{-31}, respectively. The solubility of carbon in nickel was measured [13] and is $N_C = 0.0017$ at 650°C. Then the minimum chromium concentration, N_{Cr}, for Cr_7C_3 and $Cr_{23}C_6$ formation are 0.06 and 0.24, equivalent to 5.5 and 22 wt%, respectively, which is in general in agreement with the experimental observation that there is no $Cr_{23}C_6$ in all tested alloys but Cr_7C_3 in both Ni-10Cr and 20Cr alloys. For Ni-20Cr alloy, relatively large Cr_7C_3 precipitates are formed uniformly in the whole coating layer and no free carbon is found. Therefore, no metal dusting occurs at this chromium level. For Ni-10Cr alloy, the amount of Cr_7C_3 can be detected by XRD, but cannot be identified clearly in microstructure, perhaps due to its fine size and limited amount. For this alloy, there are some graphite deposits distributed in the coating layer, showing the limitation of the external protective chromia scale.

All Ni-Cr alloys after pre-oxidation show a significant reduction in weight gain kinetics in following metal dusting, in particular for low chromium content alloys. Without pre-oxidation, no protective oxide scale is formed for Ni-5Cr alloy and metal dusting occurs rapidly in this alloy. Almost no metal dusting is detected for Ni-10Cr and 20Cr alloys in nano-crystallined grained structures. Without pre-oxidation, in metal dusting condition, chromia oxide formation and carburisation occur simultaneously. Although the same partial pressure of oxygen was applied in pre-oxidation and dusting, better protective oxide scale was formed after pre-oxidation, suggesting a deteriorated effect of carburisation on chromia scale formation.

4. CONCLUSION

Metal dusting of Ni-Cr nanocrystalline alloys prepared using magnetron sputtering deposition was investigated either directly in CO-H_2-H_2O dusting gas or pre-oxidation first and then carburisation in the dusting gas. Without pre-oxidation, nano-sized Ni-5Cr experienced a significant metal dusting. Higher Cr content, Ni-10Cr and 20Cr alloys, however, appeared little attack due to the formation of chromia scales on the surface and along the interfaces among the columns. Both alloys formed other reaction products inside of columnar coating scales, with fine graphite deposits for Ni-10Cr and relatively large Cr_7C_3 precipitates for Ni-20Cr. The effect of chromium content on protective chromia scale formation and chromium carbide formation is analysed using Wagner's analysis and product solubility calculation. The prediction is basically in agreement with the experimental observation.

Application of pre-oxidation before metal dusting significantly reduced metal dusting by forming more protective chromia scales. With the same p_{O2} used in both pre-oxidation and dusting, it is therefore concluded that

simultaneous carburisation deteriorates protective oxide scale formation. Pre-oxidation of nano-sized Ni-Cr alloys provided good dusting resistance as fine grain size accelerates chromium diffusion and therefore the protective oxide scale formation.

Acknowledgements

The authors would like to thank State Key Laboratory for Corrosion and Protection, Institute of Metal Research, Chinese Academy of Science, for providing testing alloys. Financial support by UNSW Science Faculty Research Fund is highly appreciated.

References

[1] J. Pattinson, *Journal of Iron & Steel Institute* **No. 1,** 85 (1876)
[2] R. F. Hochman: Theory of "metal dusting" in iron base alloys. *Proceedings of the Materials Engineering and Sciences Division Biennial Conference*, *AIChE 1970*, **Session No. 48**, 401 (1970)
[3] H. J. Grabke, R. Krajak, J. C. Nava Paz, *Corrosion Science* **35**, 1141 (1993)
[4] C. H. Toh, P. R. Munroe, D. J. Young, *Oxidation of Metals*, **58,** 1 (2002)
[5] J. Zhang, A. Schneider, G. Inden, *Corrosion Science* **45,** 1329 (2003)
[6] J. Zhang, P. Munroe, D.J. Young, *Acta Materialia* **56,** 68 (2008)
[7] C.S. Giggins, F.S. Pettit, *Transacttions TMS-AIME* **245**, 2509 (1969)
[8] X. Peng, F. Wang, *Oxidation – resistant nanocrystalline coatings, Development in high-temperature corrosion and protection of materials*, W. Gao, Z. Li (Eds.), CRC Press, 2008
[9] H. Liu, W. Chen, *Materials and Corrosion* **59,** 4 (2008)
[10] C. Wagner, *Journal of Electrochemical Society* **99**, 369 (1952)
[11] C. Wagner, *Zeitschrift Fur Elektrochemie* **63**, 772 (1959)
[12] A. T. Allen, D. L. Douglass, *Oxidation of Metals* **51**, 314 (1999)
[13] T. Wada, H. Wada, J.F. Elliott, J. Chipman, *Metallurgical Transaction* **2**, 2199 (1971)

Nano-Micro Structural Investigation of the Oxide Scale on Carbon Steel Substrate

Eni Sugiarti[(1,*)], Kemas A. Zaini[(1)], Yongming Wang[(2)], Naoyuki Hashimoto[(3)], Shigenari Hayashi[(3)] and Somei Ohnuki[(3)]

[(1)]Laboratory of High Temperature Coating, Research Center for Physics, Indonesian Institute of Sciences, Serpong 15314, INDONESIA

[(2)]Creative Research Institution, Hokkaido University, Kita 21 Nishi 10, Sapporo 001-0021, JAPAN

[(3)]Division of Material Science, Graduate School of Engineering, Hokkaido University, Kita13 Nishi 8, Sapporo 060-8628, JAPAN

e-mail: enis002@lipi.go.id

1. INTRODUCTION

Carbon steel has been one of the most useful materials for product manufacturing in the modern life because of its excellent mechanical properties, low cost and large recyclability [1, 2]. The low corrosion resistance especially in acid and alkali environments, however, limits its further application. Thus, the study for protecting carbon steel from corrosion is quite meaningful. Various surface techniques have been developed to enhance the life span of carbon steel products. One of the most useful methods is to coat the steel surface with protective coatings. Ni-based alloy coating has been widely used because of their workability at high temperature [3, 4]. Much related research has been done using different techniques such as thermal spray, HVOF, CVD and PVD methods [5, 6]. In the present study, NiCo-Cr-Al has been selected as a coating material and deposited by electroplating and pack cementation methods. However, the literature does not provide detailed data of metallic coating on carbon steel substrate.

Structure determination of crystallized material is a very useful way to understand material properties. Utilization of XRD and SEM which are commonly used in analyzing the phase formation and structure of the layer has been providing information for micro-scale. However, for gathering the nano-scale information, the use of TEM is getting more indispensible to determine the material properties in detail on a system layer. Nano- and micro-scale analysis also offer some detail information on the crystal structure and defects, topography, morphology and composition of the layers. Thus, the characterization of the coating system is crucially needed to understand the mechanism of coating formation and hence, the degradation of the layers can be prevented in the best way to extent the materials` life time.

In the present study, nano-micro scale characterization have been performed in order to provide detailed information on effect of oxidation exposure time when applied to the coating system and summarize the current understanding of the mechanism involved in a number of the scale formation and phase transformations.

2. EXPERIMENTAL

The coating process was carried out by deposition of NiCo using electroplating technique on carbon steel substrate followed by Cr and Al pack cementation. Details of the formation process of the coating were presented elsewhere [7]. The oxidation test of coating system was performed at temperature of 800°C in air for 100 hours. Further, the coating system will be analyzed in nano-micro scale. Nano scale characterization was performed by TEM (JEOL2010: 200keV) and the cross section TEM (XTEM) specimen should be prepared by ion beam milling (JEOL JIB-4600F) technique. In addition, micro scale characterization was performed by SEM (JEOL JSM 6380LA) equipped with an energy dispersive X-ray spectroscope (EDS) and FE-EPMA (JEOL JXA-8530F). Detailed characterization of as-coated and oxidized samples developed at different temperature process by using SEM and TEM has been described in Ref. 7. It noted that the coating sample developed at 800°C has better oxidation resistance than the coating sample developed at 900°C and 1000°C. By this result, coating sample developed at 800°C will be further investigated mainly in the transient oxidation stage from the initial exposure time below 50h and final stage at 100h.

3. RESULTS AND DISCUSSION

The cross-sectional structure of as-coated specimen is shown in Fig.1a. It was found from a SEM image in Fig.1a (top) and a EDS result in Fig.1a (bottom) that the coating sample developed at 800°C comprises two-layers: the first layer of Ni(Co) and the second layer of Ni(Al) with the total coating thickness of about 40 µm. Oxidation test has been carried out at temperature of 800°C for 100h and the cross-sectional structure is presented in Fig. 1b. Oxide scale is clearly shown in top layer indicated by dark area. Fig.1b (bottom) shows the concentration profile to describe the inter-diffusion of each element. After oxidation, Al diffused into layer (1) and influenced the thickness of NiCo and Ni(Al) layers. Oxygen interacts with the elements of Al, Ni, Co and Cr to form a protective oxide scale such as Al_2O_3, spinel and others.

Characterization of transient stage of oxidized sample is firstly carried out by SEM surface analysis as shown in Fig. 2. After 15h oxidation, the oxide products formed has fine particle size and the oxide were fully covered the surface of the specimen. After 31h oxidation, the oxide particle was being coarsened. It can be easy recognized from the increase of oxide particle grain size which was about 10µm to 30µm of 31h to 100h oxidation, respectively. Therefore, the oxide particles grain size increases with increasing the oxidation time and it can be obviously seen that oxide products have a porous structure.

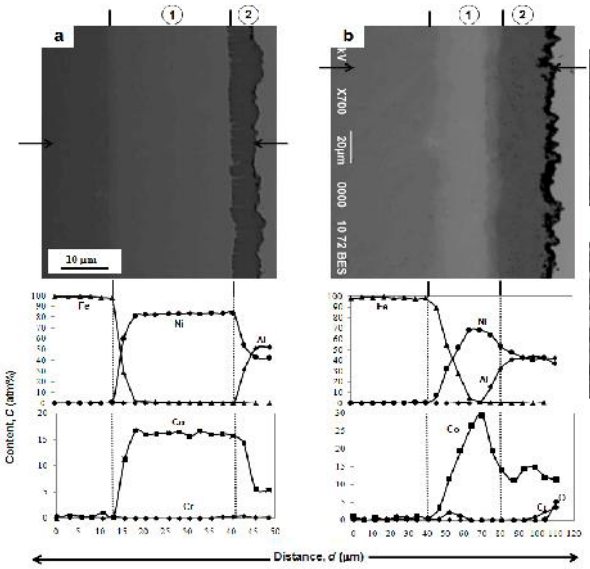

Figure 1. Cross-sectional microstructure and composition gradients: (a) as-coated and (b) oxidized sample.

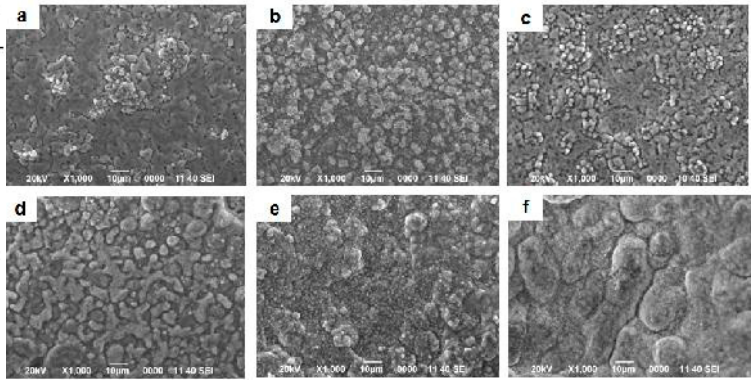

Figure 2. Surface morphologies of NiCoCrAl coating on carbon steel substrate with different periods of isothermal oxidation at 800° C: (a) 1h, (b) 5h, (c) 15h, (d) 31h, (e) 46h and (f) 100h.

Figure 3 shows a cross-sectional EPMA micrograph and elemental maps of the oxide scale formed on NiCo-Cr-Al coating layer with different periods of isothermal oxidation at 800°C in air. The image presented the thickness of oxide scale which decreases as the oxidation time increases. The outer layer of the scale consists of Al and O in all of specimens, while the inner layer consists of Cr, Ni, low concentration of Co and O in specimen below 15h exposure time. In other words, the scale mainly consists of Al_2O_3 on outer layer and may attribute to the formation of spinel structure in the initial oxidation stage.

In order to identify the crystal structure of the various phases in the NiCo-Cr-Al coating system, bright field cross-sectional image and selected area electron diffraction (SAED) patterns have been examined by using TEM as shown in Fig.4. Point analysis has been performed as indicated by circled mark and the result shows that the regions are correspond to the layer previously shown by SEM. Nano structural characterization results show that many voids and crystal defect such as dislocation are observed in the coating layer. Grain boundary of spinel is bigger than grain boundary of alumina structure.

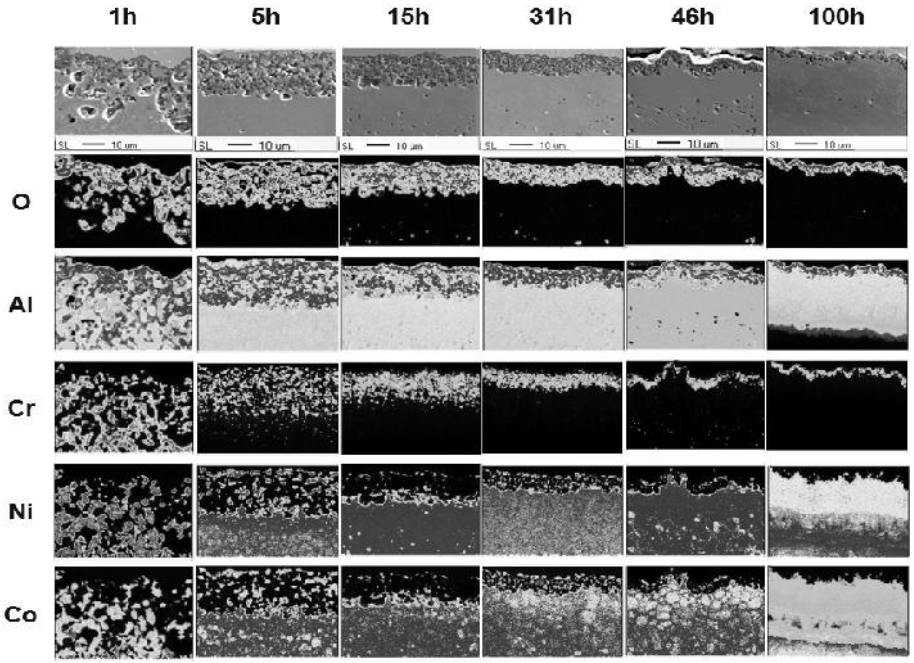

Figure 3. Cross-sectional micrograph and elemental distribution near the surface of oxidized sample.

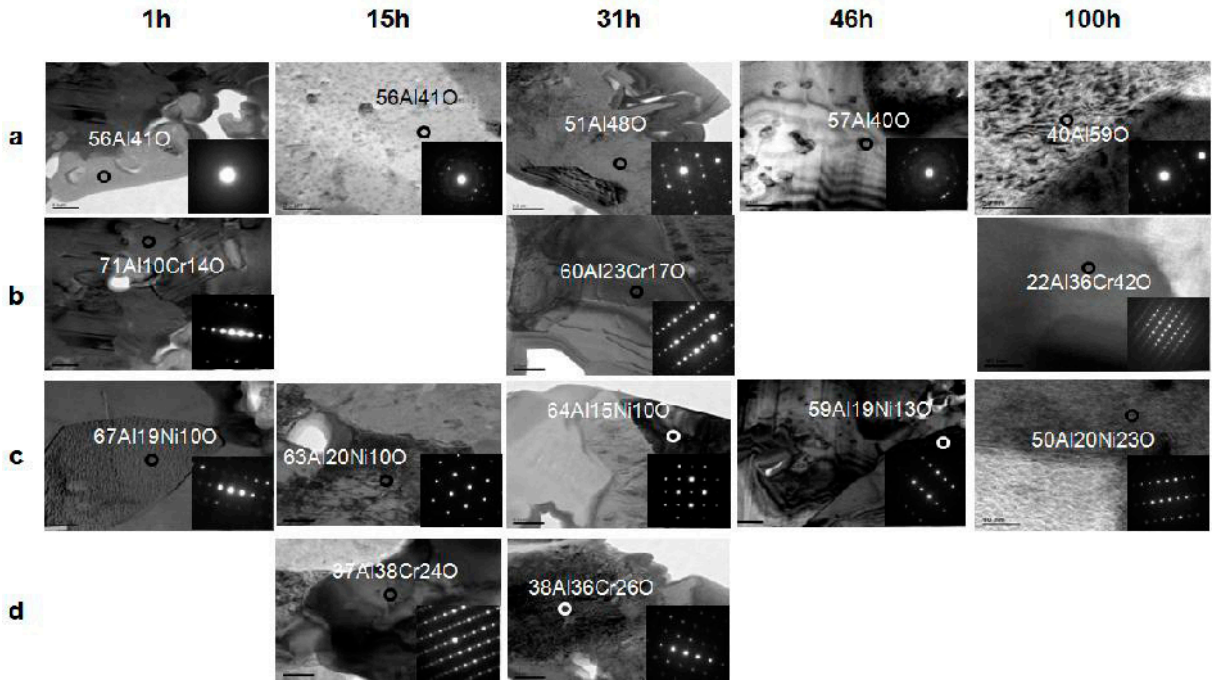

Figure 4. Bright field XTEM images of the NiCo-Cr-Al coating layer and SAED patterns showing crystal structure of circle area marked of each layer on carbon steel substrate: (a) α-Al_2O_3, (b) $\kappa \rightarrow \delta$ Al_2O_3 transformation, (c) $NiAl_2O_4$ and (d) $(Al,Cr)_2O_3$.

By using diffraction pattern, the crystal structure and lattice parameter can be determined as summarized in Fig.5a and Fig. 5b. The results show that the spinel $NiAl_2O_4$ and $(Al,Cr)_2O_3$ were formed from the beginning of oxidation test, while orthorhombic κ- Al_2O_3 and α-Al_2O_3 structure were distributed in the oxide scale. κ- Al_2O_3 transforms to δ- Al_2O_3 with tetragonal structure after 31h exposure time. In the oxide scale, α- Al_2O_3 were mainly formed with very small grain. On the basis of these results, an oxidation mechanism from transient stage to 100h exposure in air was proposed as shown in Fig.5c. As seen in Fig.5c, the oxide scale which was formed in the initial oxidation stage is a mixture of spinel $NiAl_2O_4$, $(Al,Cr)_2O_3$ and Al_2O_3. Cr_2O_3 was hardly formed because of low concentration of Cr in the coating layer. Ni diffuses outward through the spinel and its grain boundary preferentially. Therefore, the spinel $NiAl_2O_4$ and $(Al,Cr)_2O_3$ were observed in the oxide scale. Likewise, the inward oxygen diffusion occurs preferentially through the Al and form Al_2O_3 scale.

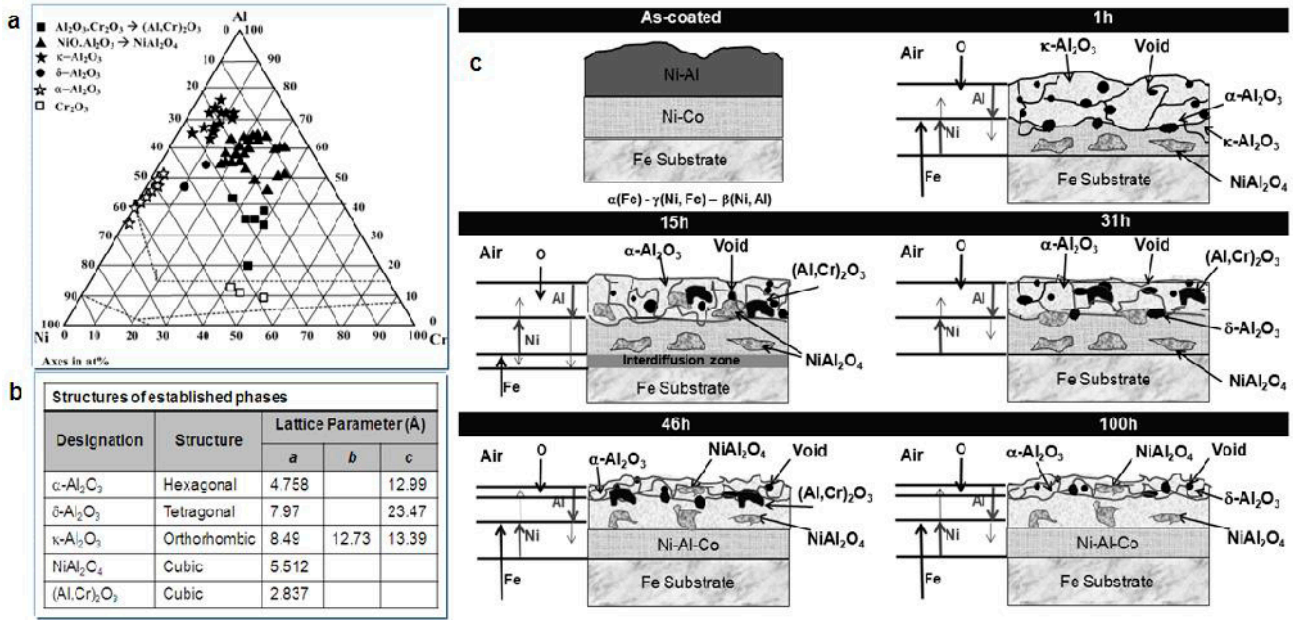

Figure 5. (a) Oxide morphology map of ternary Ni-Cr-Al at 800°C, (b) unit cell parameters determined from the coated layers and (c) schematic diagram showing the development of structure and identified phase of the oxide scales on the CoNi-Cr-Al coating layer during the oxidation in air.

4. CONCLUSION

The nano-and micro-scale structure of the oxide scale on carbon steel substrate has been observed by TEM and SEM. In addition phase identification was performed by SAED analysis. After oxidation, oxide scale formed consists of mainly α-Al_2O_3 and less distribution of spinel $NiAl_2O_4$ and $(Al,Cr)_2O_3$. The transition alumina grows by outward cation diffusion or coating elements as well as by inward diffusion of oxygen. Spinel forms with α-Al_2O_3 layer, due to the lack of aluminum to sustain the exclusive formation of alumina. Voids formation may also arise during the transformation of δ-Al_2O_3 to α-Al_2O_3.

Acknowledgements

A part of this work was conducted at Hokkaido University, supported by "Nanotechnology Platform" Program. This work was financially supported by JSPS Ronpaku PhD program, Japan and LIPI Competitive program, Indonesia.

References

[1] Praveen BM, Venkatesha TV, "Electrodeposition and properties of Zn-nanosized TiO_2 composite coatings,"Appl Surf Sci 254 (2008), pp 2418-2424.

[2] Prabhu RA, Shanbhag AV, Venkatesha TV, "Influence of tramadol [2-[(dimethylamino) methyl]-1-(3-methoxyphenylcyclohexanolhydrate] on corrosion inhibition of mild steel in acidic media," J Appl Electrochem Vol. 37 No. 4 (2007) pp. 491-497.

[3] D. Chaliampalias, G. Stergioudis, S. Skolianos, G. Vourlias, "The effect of the deposition temperature and activator concentration on the structure of NiCrBSi coatings deposited on low carbon steels by pack cementation process," Materials Letters 62 (2008) 4091–4093.

[4] D. Chaliampalias, G. Vourlias, E. Pavlidou, S. Skolianos, K. Chrissafis, G. Stergioudis, "Comparative examination of the microstructure and high temperature oxidation performance of NiCrBSi flame sprayed and pack cementation coatings," Applied Surface Science 255 (2009) 3605–3612.

[5] J.M. Miguel, J.M. Guilemany, S. Vizcaino, "Tribological study of NiCrBSi coating obtained by different process," Tribology International 36 (2003) 181–187.

[6] A. Fossati, M. D. Ferdinando, U. Bard, A. Scrivani and C. Giolli, "Influence of Surface Finishing on the Oxidation Behaviour of VPS MCrAlY Coatings," Coatings 1 (2011) 3-16.

[7] E.Sugiarti, K. A. Zaini, F.Destyorini, Y. Wang, N.Hashimoto, S. Hayashi and S. Ohnuki, "Characterization of Ni-based Coating on Carbon Steel by means of Electron Microscopy," (unpublished research).

Temperature Dependence of Oxidation Behaviors in Thermal Sprayed Bond Coatings by HVOF and Warm Spray

Takuma Ohnuki[(a,*)],Seiji Kuroda[(b)],Hideyuki Murakami[(b)],Hiroshi Araki[(b)],Yukihiro Sakamoto[(a)]

[(1)]Chiba Institute of Technology, Tsudanuma 2-17-1, Narashino 275-0016, JAPAN

[(2)]National Institute for Materials Science, Sengen 1-2-1, Tsukuba 305-0047, JAPAN

e-mail:OHNUKI.Takuma@nims.go.jp

1. INTRODUCTION

Jet engines are used as aircraft propulsion that is burned in compressed air. It is necessary to increase the combustion temperature in order to improve the thermal efficiency. By the way the energy resources imports from abroad in japan are most. Therefore, energy conservation has become an issue. It must improve the efficiency for resource saving. However, increasing the combustion temperature is required for efficiency. The combustion temperature is referred to as the turbine inlet temperature (TIT). At present, temperature of TIT is over 1500°C. This temperature is above the service temperature of the substrate in the turbine. So, it must suppress the degradation, Thermal Barrier Coating (TBC) is a suitable technique. It is composed of two layers of the bond coat and top coat. Ceramics are formed for heat shielding grant the top coat. Also, oxidation-resistant alloy is formed for the grant of corrosion and oxidation resistance in the bond coat. Physical Vapor Deposition (PVD) method or Thermal spraying method may be mentioned as a method for forming TBC. Presently, Low-Pressure Plasma Spraying (LPPS) can be mentioned as a bond coat deposition method by thermal spraying. However, since it is formed at high temperature, there is a problem that the bond coat film is thermally deteriorated. Therefore, High Velocity Oxygen-Fuel spraying (HVOF) capable of forming high-density film in the atmosphere has attracted attention recently. But although particle temperature is low in comparison with LPPS, in the formation of the atmosphere, oxidation in particle is a problem. Therefore, National Institute for Materials Science (NIMS) has developed a Warm Spray (WS) method that allows the oxidation control of film formation by introducing an inert gas into the flame, to control the speed and flame temperature. Predecessor had been considered for the process dependence of the bond coat oxidation properties in the acceleration test temperature higher than the actual temperature on the bond coat within the turbine as previous studies. [1] In addition to the test temperature, we examined the process dependence and oxidation properties at temperatures close to the actual operating temperature in this study.

2. EXPERIMENTAL

TMS82 + Ni-base single crystal super-alloy was used as substrate. The disk diameter was 25 mm with thickness of 2mm. The composition of the super-alloy is shown in **Table I.**

Table I. TMS82+ Composition

Element	Ni	Co	Cr	Mo	W	Al	Ti	Ta	Hf	Re
Composition [mass%]	62.4	7.8	4.9	1.9	8.7	5.3	0.5	6.0	0.1	2.4

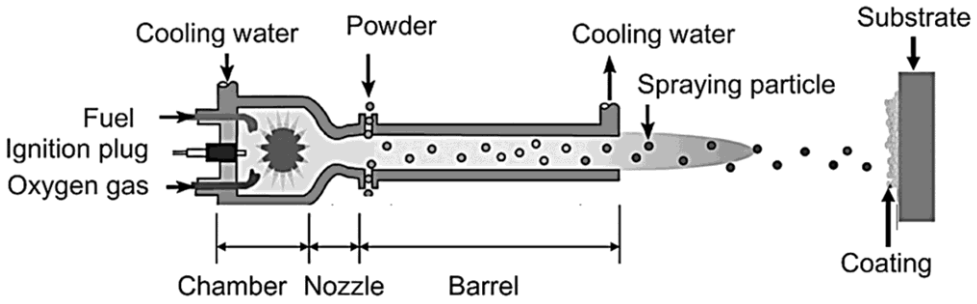

Fig. 1. Schematic drawing of HVOF apparatus

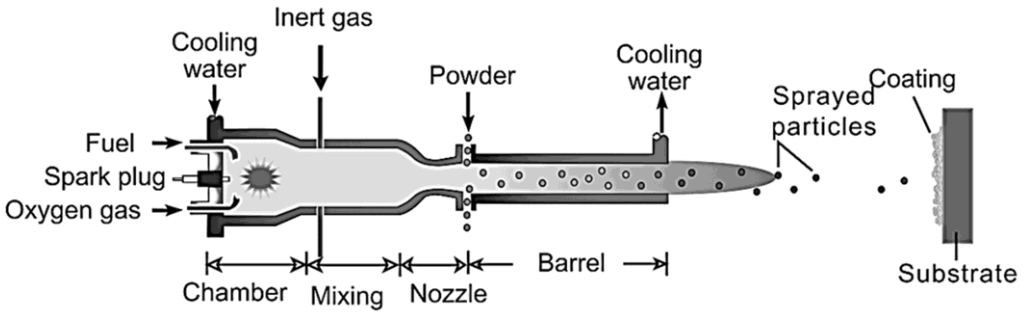

Fig. 2. Schematic drawing of WS apparatus

Grit blasting and degreasing were conducted just before spray deposition. Alumina grit size was around 425–500 μm, blasting pressure was 0.5 MPa and the time for ultrasonic degreasing in acetone was 10 min. The coating material for TMS82+ substrate was CoNiCrAlY alloy. CoNiCrAlY alloy was deposited on both sides of the substrate by WS and HVOF method. The thickness of the CoNiCrAlY alloy was 400 μm. Schematic drawings of WS and HVOF are shown in **Fig.1 and 2** [2]. For WS a mixing chamber with an inert gas feed port is attached to the HVOF device. Control of the combustion flame temperature and speed was made possible by introducing an inert gas into the combustion flame. The spraying conditions are shown in **Table II**. Properties of CoNiCrAlY(AMDRY9954) are shown in **Table III**. After the deposition, the sample was heat treated at 1100°C for 1hour in order to eliminate the residual stress by spraying. After the heat treatment, isothermal oxidation test was carried out at 950°C, 1050°C and 1150°C. The mass change at each temperature was measured by electric balance. In addition, the cross-section and surface after oxidation was analyzed by XRD and SEM.

Table II. Spraying conditions

		Warm Spray	HVOF
Kerosene flow rate	[l/min]	0.39	0.32
Oxygen flow rate	[l/min]	805	897
Nitrogen flow rate	[l/min]	500	—
Barrel length	[mm]	200	100
Spray distance	[mm]	200	350
Powder feed rate	[g/min]	60	60
Spray gun traversing velocity	[mm/s]	700	700

Table III. AMDRY9954 Properties

Properties		Values
Composition	[mass%]	Co-32Ni-21Cr-8Al-0.5Y
Density at 300K	[g/cm^3]	7.975
Specific heat at 298K	[J/(g·K)]	0.472
Latent heat of fusion	[J/g]	310.9
Thermal conductivity	[W/(m·K)]	4.0
Liquids temperature	[K]	1703
Solidus temperature	[K]	1635

3. RESULTS AND DISCUSSION

Change of the mass of each specimen is shown in **Fig.3,** where the spalled oxide scale in a crucible is included. When WS and HVOF are compared, WS coatings increased their mass by more than the mass of HVOF coatings at 1150°C. However, the trend of mass change is opposite at 950°C and 1050°C. From this result, the mass change of WS coatings depend more sensitively on the oxidation temperature. In addition, the total mass change is more affected by the mass change in the initial oxidation time. In the CoNiCrAlY bond coatings, there is a phase with Al-rich composition, which is called the β-phase. Maily from the β-phase, Al is diffused to the surface to form a protective layer of alumina at high temperature. Therefore β-phase disappears as Al is consumed. The depth of the region where β-phase disappeared is called the β-phase depletion distance. When the β-phase depletion distance is increased, mixed oxides other than alumina tend to be formed. The mixed oxides are generally more brittle and growth is faster the alumina. Therefore, they can be more easily peeled off, which can limit the lifetime of TBC. The β-phase depletion distance was measued on cross sections and compare for the WS and HVOF coatings. The results of cross-sectional orientation map by EBSD are shown in **Fig.4**. These orientation maps correspond to the longest oxidation periods at each temperature. The portions indicated by the solid and dashed white line in the figure are the thermally grown oxide (TGO) film surface and the β-phase depletion region. As compared to WS, the depletion distance always remained larger for HVOF. In addition, changes of the β-phase depletion distance in time are shown in **Fig.5.** The distance for HVOF is significantly larger than the WS at 1150°C, while HVOF remained slightly larger than the WS at 1050°C and 950°C. Based on these results, it can be said that from HVOF sprayed bond coatings, β-phase disappears more easily. For the WS coatings, even if the mass change upon oxidation is larger,

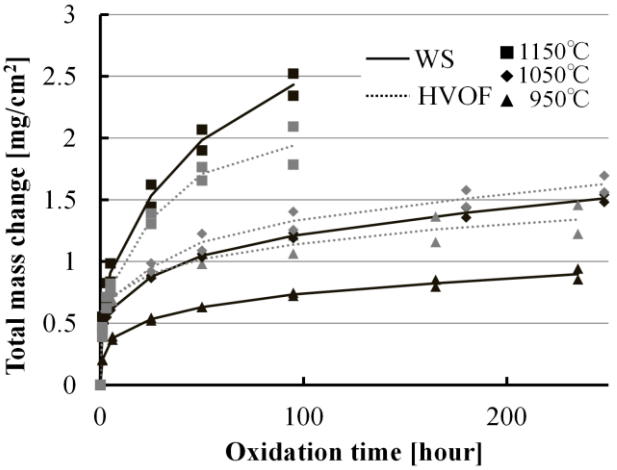

Fig.3. Change of the mass of each specimen

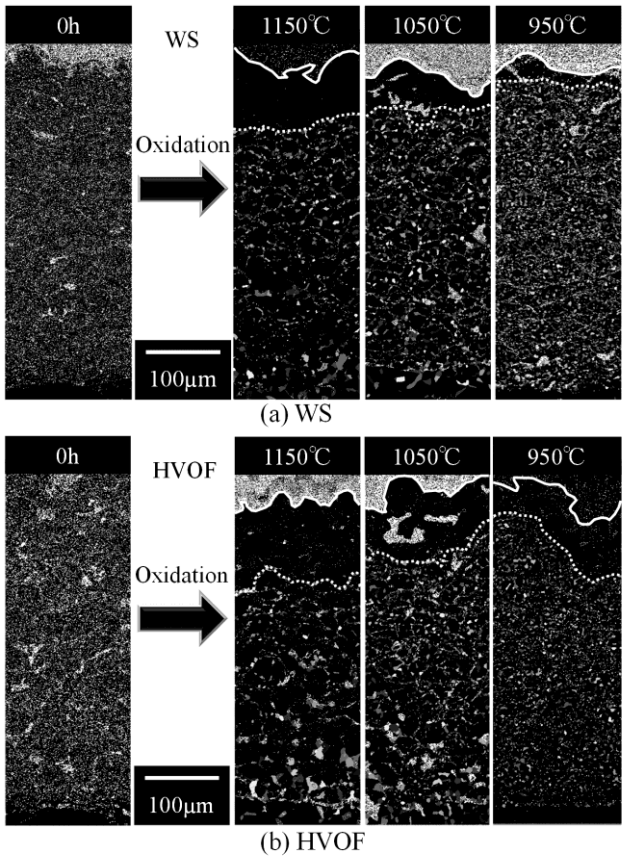

Fig.4. The results of cross-sectional orientation map by EBSD

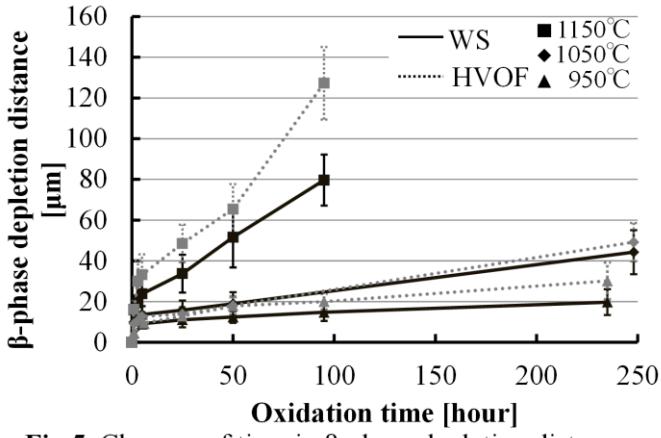

Fig.5. Changes of time in β-phase depletion distance

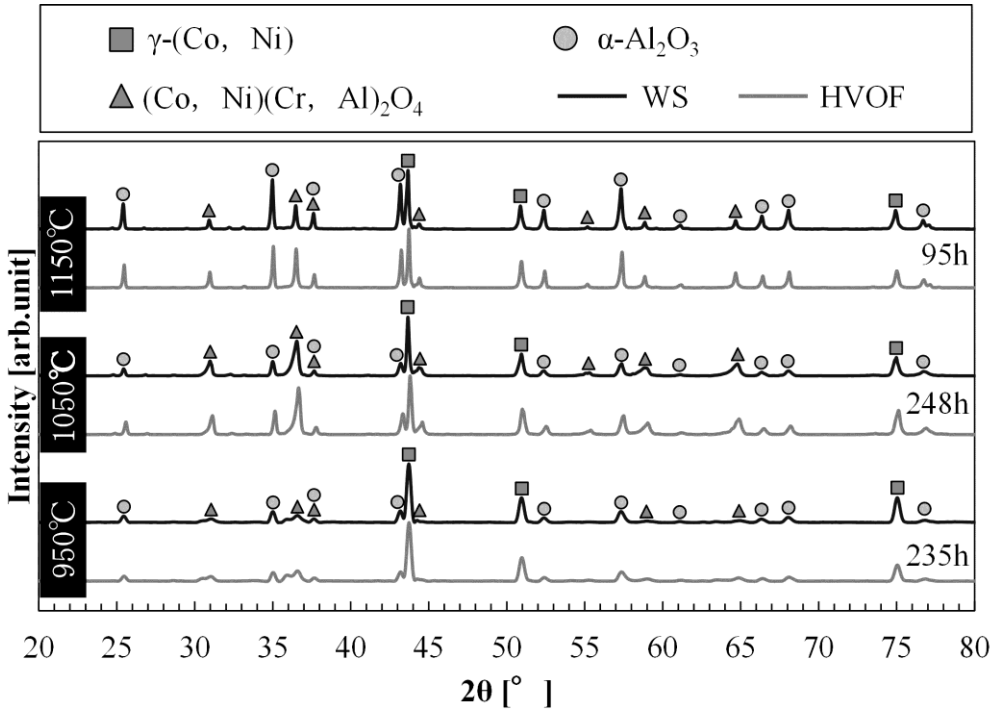

Fig.6. The results of analysis by XRD

it more slowly loses the β-phase than the HVOF sprayed coatings. Since the degree of oxidation during spraying is less with WS than HVOF, it has been suggested that the available Al content is higher in the WS coatings. Furthermore, the results of analysis by XRD are shown in Fig.6. Formation of mixed spinel oxides such as (Co, Ni)(Cr, $Al)_2O_4$ was observed at the all oxidation temperatures. Peak of the spinel oxide at 1050°C is higher than at 1150°C. This may be due to the spallation of the TGO scale from the bond coatings when they were taken out of the furnace. Since the spinel oxides on the substrate were exfoliated, their peaks in the XRD patterns were weaker at 1150°C than at 1050°C. Furthermore, formation of spinel oxides on the WS coatings was less than HVOF at 1050°C and 1150°C.

4. CONCLUSION

As a result of comparing the HVOF and WS coatings, even though the mass change of WS coatings were greater than HVOF at 1150°C, but its β-phase depletion distance was less. This is due to the fact that available Al content in the WS coatings was higher than HVOF due to less oxidation during spraying. In addition, WS coatings showed a tendency to form less spinel oxide on the surface as compared to the HVOF coatings.

References

[1]Mori, T., Kuroda, S., Murakami, H., Katanoda, H., Sakamoto, Y., Newman, S., "Effects of initial oxidation on β phase depletion and oxidation of CoNiCrAlY bond coatings fabricated by warm spray and HVOF processes," *Surface & Coatings Technology*, Vol.221, No.1 (2013), pp.59-69.

[2]Kuroda, S., Kawakita, J., Watanabe, M., Katanoda, H., "Warm Spraying—A Novel Coating Process Based on High-Velocity Impact of Solid Particles," *Science and technology of advanced materials*, Vol. 9, No.1 (2008)

Microstructure and Oxidation Resitance of Aluminized Ni-based superalloys

Kazuki Kasai [1,2], Hideyuki Murakami [1], and Yoshihiko Noda [2]

[1] Surface Kinetics Group, High Temperature Materials Unit, National Institute for Materials Science (NIMS), 1-2-1 Sengen, Tsukuba-Science-City, 305-0047, JAPAN
[2] Regional Environment Systems, Shibaura Institute of Technology, 3-7-5 Toyosu, Koto-ku 135-8548, JAPAN

e-mail: kasai.kazuki@nims.go. jp

1. INTRODUCTION

Aluminizing is one of the most cost-effective processes in enhancing the oxidation resistance of Ni-based superalloys, which are commercially used as turbine blades. By the aluminizing process the Ni-based superalloy substrates are covered with an Al-enriched surface layer which results in the formation of Al_2O_3-based thermally grown oxide (TGO), which protects them against accelerated oxidation damages. However, when the aluminized turbine blades are exposed to high temperatures, critical microstructure changes can take place in the vicinity of the interface between the coating layer and the substrate, owing to the interdiffusion of the alloying elements[1)]. One example is the formation of a secondary reaction zone (SRZ). The SRZ is defined as the region between the interdiffusion zone (IDZ) and the substrate that characteristically shows a high density of fine topologically close-packed (TCP) phase precipitates and high angle boundaries in the substrate and the SRZ formation significantly degrades the mechanical properties and the creep resistance of the substrate. Therefore, it is of significant importance to understand such microstructure changes as well as to evaluate the oxidation resistance. On the other hand, Ni-based superalloy substrates inherently have microstructural anisotropy by the directionally solidifying fabrication process, and it is expected that microstructural changes can be affected by such anisotropic features. Another factor should be the pre-surface treatment. Our recent study confirmed that there is a significant difference of microstructural changes between polished substrate surface and blasted ones [ref 2,3]. Different thermal history can also give rise to the difference in resulting microstructure. This study is aimed at systematically understanding such changes in microstructure and oxidation resistance caused by the crystal orientation of substrates, pre-surface treatments and thermal histories.

2. EXPERIMENTAL

Ni-based single crystal superalloy TMS-138 and UCSX 8 were used as the substrate material. Nominal composition of the alloys were listed in Table 1. The alloys were cut along either {100} direction or (110). Then various substrate surface finishes were conducted, e.g., electropolishing, mechanically polishing and grid blasting. The substrate materials were then subjected to the conventional aluminizing process, where they were embedded in a heat-resistant container with a powder mixture of 24.5 mass% Al, 24.5 mass% Cr, 49.0 mass% Al_2O_3 and 2.0 mass% NH_4Cl and the container was heated at 1273K in flowing Ar. Then a thermal cycling test (1373K for 1 h and cooling for 20 min in air as one cycle) and an isothermal heating tests (1373K kept for 100h in air) were performed to investigate the effect of the heating history on the microstructural changes occurring in the specimens. Specimens tested were analyzed using scanning electron microscopy (SEM), energy-dispersive X-ray spectroscopy (EDX), and electron backscatter diffraction (EBSD) analysis.

Table 1 Nominal composition of Superalloys. (mol%)

	Co	Cr	Mo	W	Al	Ta	Hf	Re	Ru	Ni
TMS-138	6.7	3.6	1.9	2.1	13.8	2.1	0.04	1.7	1.2	Bal.
UCSX8	6.7	1.9	2.4	2.1	11.4	2.9	0.0	2.1	1.9	Bal.

3. RESULTS AND DISCUSSIONS

As indicated in the introduction section, microstructure of substrates and oxidation resistance drastically changed depending on various conditions. In this section, we will introduce typical microstructural differences.

Effect of Pre-surface Treatment.

Fig. 1 shows cross-sectional BSE images of as-aluminized coatings conducted on (a) grit-blasted and (b) electropolished

TMS-138 surfaces. The rougher coating surface on the blasted one clearly indicated that surface roughness prior to the alumimizing process was followed by the coated surface roughness. More importantly, SRZ formation was already observed in the blasted specimen, while it was not observed in the electropolished one.

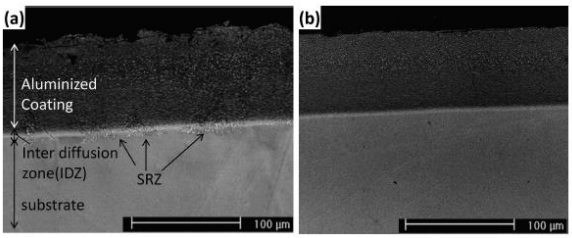

Fig. 1 Cross-sectional BSE images of as-aluminized TMS-138: (a) blasted and (b) electropolished

Effect of Thermal History

When these specimens are exposed at elevated tempareture, microstructure change takes place in the substrate, but in the different manner. For instance, when the thermal cycling exposure was conducted, the SRZ grows and develops in the blasted specimen while void formation was observed in the electropolished specimens, Fig. 2. However, while similar microstructure change was observed in the blasted specimen, even by the isothermal exposure was conducted, while dramatic difference in microstructure change was observed in the electropolished specimen, as shown in Fig. 3(b). In this case, there are no voids formed in the vicinity of substrate / coating interface, but so-called secondary diffusion zone (SDZ) was observed. The main difference between SRZ and SDZ can be explained by the occurrence of surface re-crystalzation of substrates. Further discussion can be seen in our previous papers[2,3].

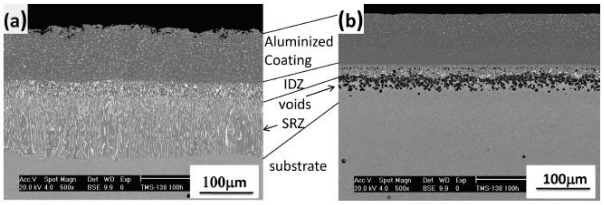

Fig. 2 Cross-sectional BSE images of TMS-138 specimens after 100 heat cycles: (a) blasted and (b) electropolished.

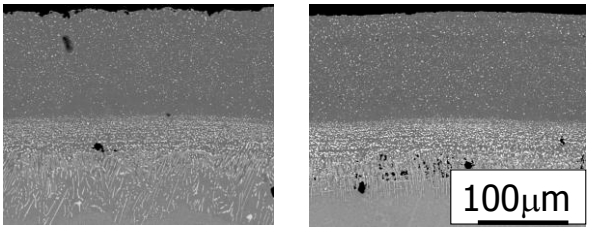

Fig. 3 Cross-sectional BSE images of TMS-138 specimens after 100 h heat exposure: (a) blasted and (b) electropolished.

Oxidation Resistance

To understand the relationship among surface crystal orientation, pre-surface treatment and oxidation resistance, the thermal cycling test was conducted for four kinds of specimens. Fig. 4 shows the surface morphologies of aluminized specimens UCSX8 after 75 thermal cycles, (a)mechanically polished (100), (b)blasted (100), (c)mechanically polished (110) and (c) blasted (110). While there is a difficulty in differentiating the surface morphology among the four samples, sample mass measurement revealed that blasted specimens demonstrated accelerated mass gain cmpaered to mechanically polished ones. However, effects of surface crystl orientation have not been clarified so far. Further investigation is required to understand the relationship between the microstructure changes and oxidation resistances.

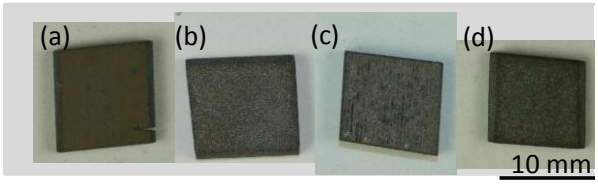

Fig. 4 Surface morphologies of aluminized UCSX8 specimens oxidized after 75 thermal cycles. (a)mechanically polished (100), (b)blasted (100), (c)mechanically polished (110) and (c) blasted (110)

4. CONCLUSION

There are several kinds of microstructural changes observed in the as-aluminized TMS-138 and UCSX8. For instance, in the case of a grit-blasted specimen, SRZ was formed in the vicinity of substrate/coating interfaces, by both thermal cycling and isothermal heating. On the otherhand, in the polished specimens, voids were formed by thermal cyclic heating, whereas SDZ was formed by isothermal heating. These differences in microstructural changes of the aluminized specimens can be explained by the diffusion kinetics between the coating layer and the substrate during heating/cooling processes. Relationship between microstructure changes of the specimens and oxidation resistance is still under investigation. Further study is now being conducted to elucidate it.

References

[1] S. Hayashi and T. Narita, Materia Japan 46 (2007) 225-228
[2] K. Kasai, H. Murakami, S. Kuroda and H. Imai: Mater. Trans. 52(2011) 1768-1772
[3] K.Kasai, H. Murakami, and K Noda, Mater. Trans. 54(2013) 2252-2257.

Selection Oxidation in Fe-Ga alloys Annealed under Low Partial Pressure of Oxygen

Shigeru Suzuki [1,*], Shun Fujieda [1], and Ryuji Ukai [1]

[1] Institute of Multidisciplinary Research for Advanced Materials, Tohoku University,
2-1-1 Katahira, Aoba-ku, Sendai 980-9577, JAPAN

e-mail: ssuzuki@tagen.tohoku.ac.jp

1. INTRODUCTION

Various alloying elements are added to iron based alloys, in order to improve their properties, such as the surface and mechanical properties. As the chemical characters of the alloying elements are different from those of iron, complicated oxidation phenomena are observed on the surfaces of the iron based alloys. For instance, when a reactive alloying element that is easily oxidized elements, such as silicon and manganese, is contained in an iron based alloy, it is known that complex morphology of oxides is formed in surface layers of the alloys depending on annealing conditions [1-4]. The formation of such complex morphology of oxides was particularly investigated in iron-silicon alloys, in which silicon is preferentially reacted with oxygen [2-4]. Although these reactive common elements are enriched to a surface layer so as to be oxidized, enrichment or oxidation of reactive rare elements to the alloy surface is still unclear. In this study, X-ray photoelectron spectroscopy (XPS) and secondary ion mass spectrometry (SIMS) were used to clarify the surface enrichment and oxidation of gallium on the surface of iron-gallium alloys. As the alloys is known to exhibit the magnetostrictive material [5,6], an influence of the surface oxide on the magnetostrictive properties is also discussed in this study.

2. EXPERIMENTAL

2.1 Sample Preparation

Buttons of several iron-gallium alloys were prepared by vacuum arc melting. The Fe-18mol%Ga alloys, which is referred to as Fe-18%Ga hereafter, was mainly used in this study. The button was cut to sheets of about 0.5 mm in thickness, and then its surface was mechanically polished. After the samples were washed in ultrasonic bath with acetone, they were annealed at different temperatures for 1800 s in 10%H_2-He gas. The partial pressure of oxygen was estimated to be approximately to 10^{-19} Pa at 1023 K, under which iron is not oxidized while gallium is oxidized. The samples were exposed to air at room temperature, when they were transfer from the furnace to surface analytical apparatus. Then, a thin native oxide layer with a few nanometers in thickness was formed on the sample surfaces.

2.2 Measurements

The chemical state and composition of the sample surfaces were analyzed by an XPS apparatus (PHI-5600). The incident X-ray was Al Kα and the analysis area was about 1 mm in diameter. The XPS spectra were usually measured at a take-off angle of 45 degree. The surface chemical composition was estimated from the XPS spectra coupled with the relative sensitivity factors. SIMS depth profiling for surface layers formed on the surfaces of iron-gallium alloys were performed using PHI-6600 equipped with a quadrupole-type mass spectrometer. An incident beam of 5.0 keV Cs^+ ions was used for obtaining positive secondary ions. The depth profiles are considered to correspond to the depth distribution of gallium, oxygen, and iron.

3. RESULTS AND DISCUSSION

Figure 1 shows a wide spectrum from the surface of as-polished Fe-18%Ga. The Fe and Ga 2p XPS spectra indicate that iron and gallium on the sample surface are oxidized and the composition of gallium is comparable to that of the bulk. The iron and gallium were oxidized on the surface of the as-polished Fe-18%Ga during exposure to air. Figure 2 shows a wide spectrum from the surface of Fe-18%Ga annealed at 873 K. The surface compositions were estimated from XPS data of the Fe-18%Ga samples annealed at different temperatures. The results revealed that the sample surface was covered with a gallium oxide layer during annealing at high temperatures. As the formation of an gallium oxide layer is considered to be influenced by the oxygen gas from the atmosphere and gallium outward diffusion, it is likely to be influenced by annealing conditions such as the partial pressure of oxygen in the annealing atmosphere.

In order to characterize the depth distribution of gallium in the surface layer of samples, SIMS depth profiling was

performed for the samples analyzed using XPS. SIMS depth profiles of Ga^+ for surface layers formed on the surfaces of Fe-18%Ga were measured. As Ga^+ ion counts may be saturated in the surface layers because of its high sensitivity, it is difficult to determine the quantitative thicknesses of each gallium oxide layers formed on Fe-18%Ga at high temperatures. Nevertheless, the oxide thickness was estimated to be approximately less than 100 nm. This result indicates that a tight gallium oxide layer was formed on the surface of a sample containing higher concentration of gallium because a sufficient amount of gallium is supplied from the substrate to form the oxide layer during annealing. It was shown that depth profiles of gallium are correlated with those of oxygen, although it is not shown here. As the properties of gallium oxides, such as elastic properties, are quite different from the iron based alloys, that the gallium oxide layer formed on the alloy surface is considered to significantly influence the magnetostrictive properties of the alloys. This is because the magnetostrictive properties are sensitively responded by external microscopic strain [6]. Thus, the present results suggest that a protective gallium oxide layer, which may influence the properties, is formed at an early stage of annealing at high temperatures.

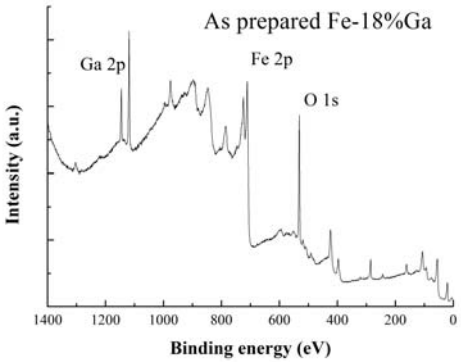

Fig.1 Wide XPS spectrum of as-prepared Fe-18%Ga alloy.

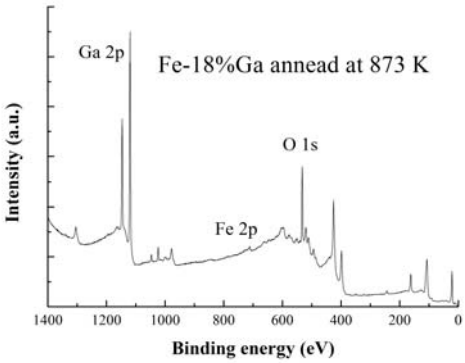

Fig.2 Wide XPS spectrum of Fe-18%Ga alloy annealed at 873 K.

4. CONCLUDING REMARKS

XPS and SIMS were used to analyze the surface layers formed on iron-gallium alloys annealed at high temperatures under a low partial pressure of oxygen. The results showed that a thin gallium oxide layer is formed on the surfaces of iron-gallium alloys annealed at high temperatures, and the thickness of the oxide layer is increased more than 673 K. The kinetics of the enrichment of gallium at the alloys surfaces seems to be dominated mainly by the outward diffusion of gallium in the alloy matrix. It was considered that the oxide layer formed on the surface layer is likely to influence the properties of the matrix, since the thermal expansion of oxides is different from that in the matrix.

Acknowledgements

This study was partially supported by Japan Science Technology Agency. The authors would like to express sincere to Mr. M.Itoh for their help and maintenance of XPS/SIMS apparatus.

References

[1] Kofstad, P., High Temperature Corrosion, Elsevier Applied Science, (London, 1988), pp. 324-341.

[2] Yanagihara, K., Suzuki, S. and Yamazaki, S., "Microscopic Features in the Transition from External to Internal Oxidation in an Fe–6 mol.% Si Alloy Annealed Under Various H_2O–H_2 Atmospheres", *Oxid.Metals,* Vol. 57, (2002) pp. 281-296.

[3] Suzuki, S., Yanagihara, K. and Yamazaki, S. and Waseda, S., "SIMS/XPS characterization of surface layers formed in 3 mass% Si-steel by annealing in oxygen at low partial pressure", *Surf. Interface Anal.,* Vol. 35, (2003) pp. 276-281.

[4] Suzuki, S., Yamamoto, T., Shinoda, K. and Sato, S., "Characterization of surface oxide layers formed on Fe-Al alloys by annealing under different atmospheres", *Surf. Interface Anal.*, Vol.40, (2008) pp. 311-314.

[5] Datta, S., Atulasimha, J., Flatau, A.B., "Figures of merit of magnetostrictive single crystal iron–gallium alloys for actuator and sensor applications", *J. Magnetism Magnetic Materials*, Vol. 321 (2009) pp. 4017–4031.

[6] Kellogg, R.A., Russell, A.M., Lograsso, T.A., Flatau, A.B., Clark, A.E. and Wun-Fogle, M., "Tensile properties of magnetostrictive iron–gallium alloys", *Acta Materialia* Vol. 52, (2004) pp. 5043–5050.

Formation of the NiAl containing Hf by the Simultaneous Electrodeposition of Al and Hf using a Molten-Salt and Cyclic Oxidation

Michihisa Fukumoto [(1,*)], Ai Yokobori [(1)], and Motoi Hara [(1)]

[(1)] Department of Materials Science and Engineering, Akita University, tegata-gakuen machi 1-1, Akita 010-8502, JAPAN

e-mail: fukumoto@ipc.akita-u.ac.jp

1. INTRODUCTION

Ni aluminide has become a promising material for the coating of high-temperature materials due to its high oxidation resistance. Its high oxidation resistance was maintained by the formation of an Al_2O_3 scale. However, for the Al_2O_3 scale on the Ni aluminide, spallation occurred during thermal cycling, and the oxidation resistance of the Ni aluminide was poor. It was reported that the addition of small amounts of a reactive element, such as Hf to the Ni aluminide was effective for decreasing the spallation of the Al_2O_3 scale on the Ni aluminide[1-3]. In this study, we tried to perform the simultaneous electrodeposition of Al-Hf on Ni when we prepared the Ni aluminide layer containing small amounts of Hf. The cyclic-oxidation resistance of these specimens was then evaluated.

2. EXPERIMENTAL

Ni was used as the cathode substrate. The electrolytic bath was an equimolar NaCl-KCl melt containing 3.5 mol%AlF_3 for the electrodeposition of Al. The electrolytic bath for the simultaneous electrodeposition of Al-Hf was equimolar NaCl-KCl melt containing 3.5 mol%AlF_3 and 0.05 mol%HfF_4, or 3.5 mol%AlF_3 and 0.1 mol%HfF_4. The potentiostatic polarization was performed at potentials from -1.25 to-1.8 V. The electrodeposition temperature was 1023 and 1173 K. The influence of the polarization potential and electrodeposition temperature on the surface layer morphology and cyclic-oxidation resistance was investigated. A cross section of the specimen after the electrodeposition treatment was observed by SEM and EPMA. The deposited materials were identified by XRD. In order to evaluate the cyclic-oxidation resistance of the Ni covered with the Ni aluminide layer containing Hf, the cyclic-oxidation test was carried out at 1423 K in air. For the experiment, each cycle consisted of heating for 3.6 ks.

3. RESULTS AND DISCUSSION

Fig.1 shows cross-sectional micrographs and concentration profiles of Ni, Al and Hf across the Ni specimens after the Al-Hf electrodeposition at 1173 K for 3.6 ks at －1.25 V in NaCl-KCl-3.5 mol%AlF_3-0.05 and 0.1 mol%HfF_4.The electrodeposition layer was formed on the Ni substrate in the order of Ni_3Al and NiAl in both of the molten bath. It was found from the EPMA analysis that the NiAl contained 0.9～1.0 at.%Hf. Particles of the precipitate that looked white in the Ni_3Al and NiAl layers were observed in the both of the molten baths. These particles were identified as Hf by the EPMA analysis.

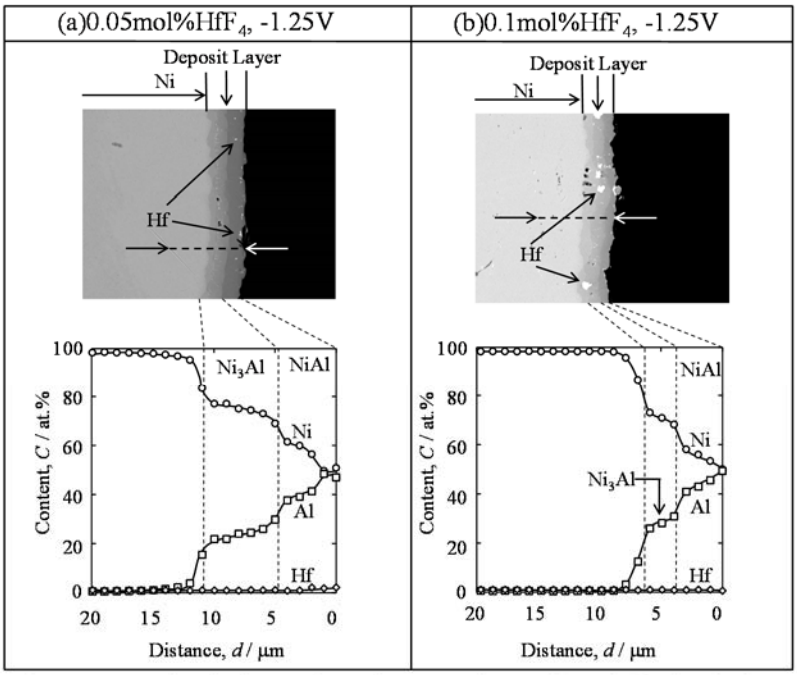

Fig. 1 Cross-sectional micrographs and concentration profiles of Ni, Al and Hf across Ni specimens after Al-Hf electrodeposition at 1173 K for 3.6 ks at －1.25 V in NaCl-KCl-3.5 mol%AlF_3-0.05 and 0.1 mol%HfF_4.

Fig.2 shows cross-sectional micrographs and concentration profiles of the Ni, Al and Hf across the Ni specimens after the Al-Hf electrodeposition at 1173 K for 3.6 ks at －1.35 V in NaCl-KCl-3.5 mol%AlF_3-0.05 and 0.1 mol%HfF_4. The NiAl was formed

as the outer layer in both of the molten baths. It is considered that the NiAl formed at －1.35 V was thicker than that formed at －1.25 V(Fig.3). No Al-Hf compounds were observed in the outer layer. It was found from the EPMA analysis that the NiAl contained 0.7～0.8 at.%Hf. Moreover, precipitate particles that looked white in the Ni_3Al and NiAl layers were observed. These particles were identified as Hf by the EPMA analysis.

Fig.3 shows cross-sectional micrographs and concentration profiles of Ni, Al and Hf across the Ni specimens after the Al-Hf electrodeposition at 1173 K for 3.6 ks at －1.5 V in NaCl-KCl-3.5 mol%AlF_3-0.1 mol%HfF_4.It was found that a thick NiAl layer was formed. Moreover, it was found from the high-magnification observation of the microstructure that the particles were uniformly distributed in the NiAl layer. It was presumed that these particles consisted of Hf. It was found from the EPMA analysis that the NiAl, except for the precipitate particles, contained 0.7～0.8 at.%Hf.

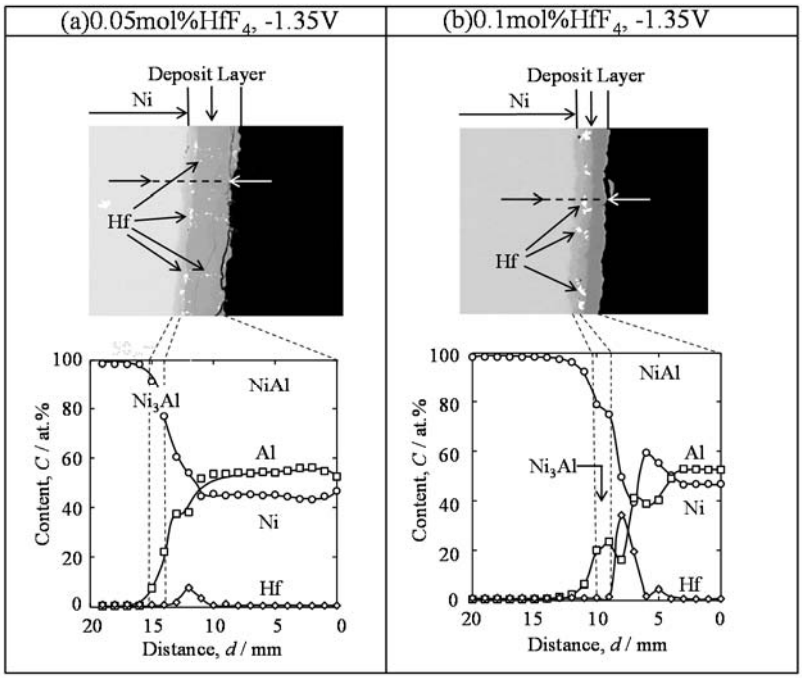

Fig. 2 Cross-sectional micrographs and concentration profiles of Ni, Al and Hf across Ni specimens after Al-Hf electrodeposition at 1173 K for 3.6 ks at －1.35 V in NaCl-KCl-3.5 mol%AlF_3-0.05 and 0.1 mol%HfF_4.

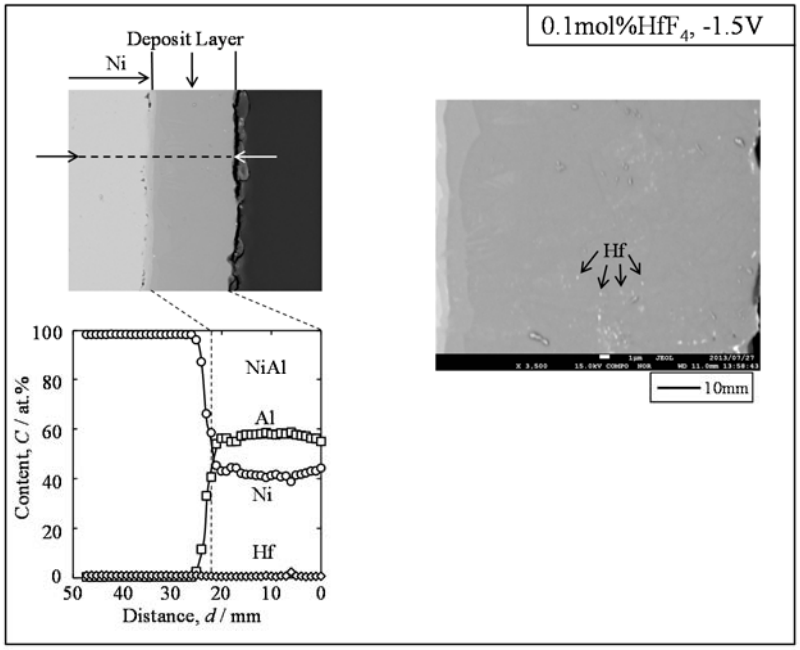

Fig. 3 Cross-sectional micrographs and concentration profiles of Ni, Al and Hf across Ni specimens after Al-Hf electrodeposition at 1173 K for 3.6 ks at －1.5 V in NaCl-KCl-3.5 mol%AlF_3-0.1 mol%HfF_4.

Fig.4 shows the results of the cyclic-oxidation test at 1423 K in air for the specimens coated with the NiAl layer by the Al-Hf deposits at 1173 K for －1.25～－1.5 V(Figs.1, 2 and 3). For comparison, this figure contains the results of the specimen treated by only the Al deposition(1173 K, －1.5 V) . For the specimen treated with the Al deposition, the deposition layer consisted of Ni_2Al_3. For this specimen, the mass gain was small during the initial stage, then the oxidation rate increased after 10 cycles. Its mass gain at 40 cycles was greater than that of the specimen undergoing the Al and Hf deposition at －1.35 V and －1.5 V. For the specimen treated in 0.05 mol%HfF_4 at －1.25 V, the mass gain increased with the number of cycles. This specimen shows the biggest increase compared to the other samples. For the specimen treated in 0.1 mol%HfF_4 at －1.25 V, the mass gain increased during the initial stage of oxidation, and the mass started to decrease due to the spallation of the scale after 10 cycles. The cyclic oxidation resistance of the specimen treated at －1.25 V in both molten baths(Fig.1) was poor. It is presumed that when the deposited layer was thin, the NiAl layer underwent mutual diffusion with the Ni substrate, and then NiAl was changed to a Ni_3Al and Ni solid solution. On the other hand, for the specimen treated at －1.35 V(Fig.2), no mass decreased was observed during 40 cycles. Especially, for the specimen treated in 0.1 mol%HfF_4 at －1.5 V (Fig.3), the mass gain was small even if the number of cycles increased. This suggests that this sample had a high cyclic-oxidation

resistance. It is considered that when the deposited layer of NiAl was thick and contained small amount of Hf, the spallation of Al_2O_3 was suppressed by the effect of Hf.

Fig.5 shows cross-sectional micrographs and the concentration profiles of Ni, Al, Hf and O across the Ni specimens with deposit layers formed at -1.25 V in the molten salt containing 0.05 mol%HfF_4 and at -1.5 V in the molten salt containing 0.1 mol%HfF_4 after the cyclic oxidation test of 40 cycles at 1423 K in air. For the specimen treated in 0.05 mol%HfF_4 at －1.25 V, a thick oxide scale was formed. It was confirmed from the EPMA analysis that this oxide scale consisted of NiO. On the other hand, for the specimen treated in 0.1 mol%HfF_4 at －1.5 V , a thin scale consisting mainly of Al was formed. This scale adhered to the coating. It was confirmed that the NiAl layer formed before the cyclic-oxidation test had disappeared. This resulted from the fact that Al diffused from the NiAl coating layer into the Ni substrate. It was reported that for a Ni-Al compound, when the Al concentration in the metal was less than 35 at.%, $NiAl_2O_4$ and NiO were formed on the metal, while Al_2O_3 was not formed[4]. In this study, though the Al concentration under the scale was less than 10 at.%, the formation of $NiAl_2O_4$ and NiO was not observed. These results showed that the cyclic oxidation resistance was not dependent on the Al concentration under the scale, when adhesion of the scale was good and the protective scale was formed.

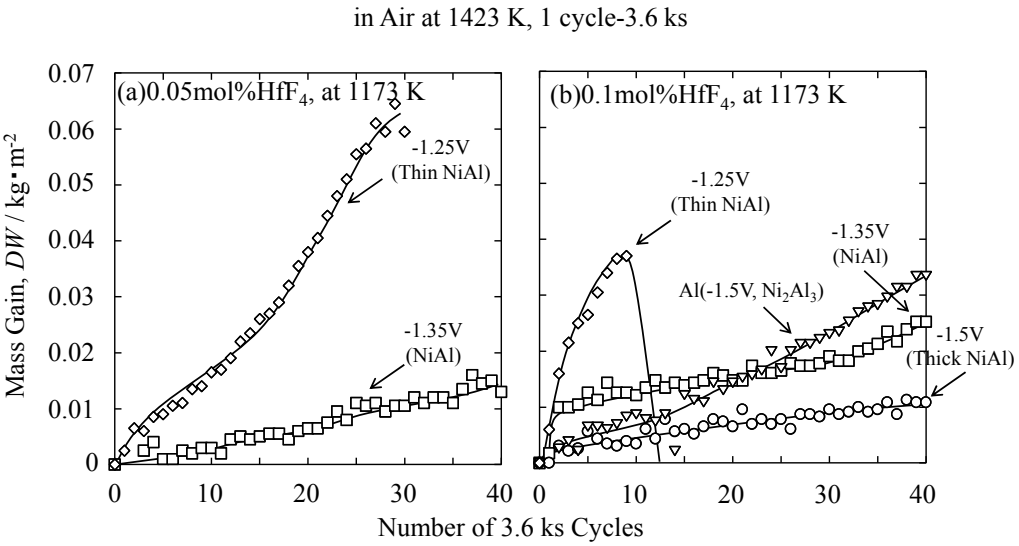

Fig. 4 Mass change-time curves of Ni specimens with and without Al-Hf deposits during cyclic oxidation at 1423 K in air. For comparison, this figure contains mass change-time curve of Ni specimen with Al.

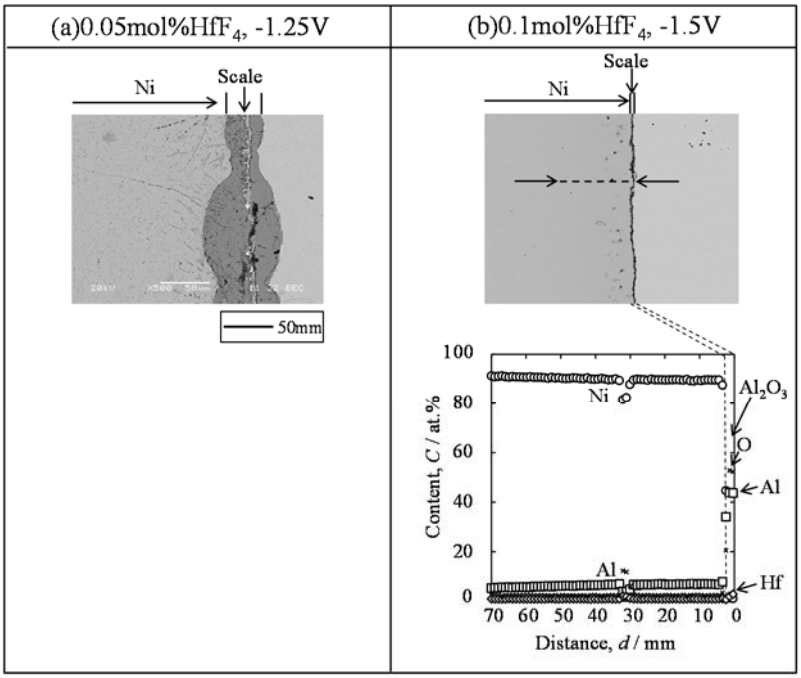

Fig. 5 Cross-sectional micrographs and concentration profiles of Ni, Al, Hf and O across Ni specimens with deposit layers formed at -1.25 V in the molten salt with 0.05 mol%HfF_4 and at -1.5 V in the molten salt with 0.1 mol%HfF_4 after cyclic oxidation test of 40 cycles at 1423 K in air.

4. CONCLUSION

A NiAl layer containing Hf was formed on a Ni specimen by the simultaneous electrodeposition of Al and Hf using a molten-salt bath. The cyclic-oxidation resistance of the Ni covered with the NiAl containing Hf was evaluated. The following conclusions were developed.

(1) When the simultaneous electrodeposition of Al and Hf was carried out in molten NaCl-KCl containing 3.5 mol%AlF_3 and 0.05 mol%HfF_4 at 1173 K, －1.35 V and －1.5 V for 3.6 ks, an electrodeposited layer consisting of NiAl containing Hf was formed. Especially, for the samples treated by the simultaneous electrodeposition of Al and Hf at -1.5 V in an NaCl-KCl-3.5 mol% AlF_3-0.1 mol% HfF_4 melt, a thick NiAl layer was formed.

(2) The specimen coated with thick NiAl containing a small amount of Hf showed a higher cyclic-oxidation resistance.

An adhesive scale having a spiked shape, which consisted of Al_2O_3 and HfO_2, was formed on the sample having a high cyclic-oxidation resistance.

References

[1] Pint, B. A., More, K. L. and Wright, I. G.: Oxid. MET Vol.**59** (2003), pp.257-283.
[2] Ning, B., Shamsuzzoha, M. and Weaver, M. L.: Surface & Coating Technology Vol.**200** (2005), pp. 1270-1275.
[3] Guo, H., Sun, L., Li, H. and Gong, S.: Thin Solid Films Vol.**516** (2008), pp.5732-5735.
[4] Hara, M.: Chemical Engineering Vol.57 (2012), pp.329-336.

Preparation of Ni Aluminide / Ni Bilayer Coating on Nb –W Alloys by Molten Salt Electrodeposition and Oxidation Resistance

Naka Sato[(1,*.a)], Masahiko Fuji[(1)], Naoya Kohiruimaki[(1)], Michihisa Fukumoto[(1)],and Motoi Hara[(1,b)]

[(1)] Department of Materials Science and Engineering, Graduate School of Engineering and Resource, Akita University, 1-1,Tegata-Gakuen-cho, Akita, 010-8502, Japan

e-mail:[(a)] satonaka@ipc.akita-u.ac.jp, [(b)] hara@ipc.akita-u.ac.jp

1. INTRODUCTION

Nb-base alloys are promising materials for high temperature equipment because of their high melting point and high specific strength at high temperature. However, they have a very poor oxidation resistance above 973 K due to the inability of the Nb-oxide scale that forms on the surface to provide any oxidation protection. As a result, the use of the Nb-base alloys at high temperature is severely restricted.

We have succeeded in the preparation of a coating consisting of Ni-aluminide on a Ni-base alloy[1], TiAl[2] and stainless steel[3] by Ni electrodeposition in an aqueous solution, followed by Al electrodeposition in a molten salt. We also have indicated that the oxidation resistance of the alloys was significantly improved by the coating consisting of Ni-aluminide.

In the present study, it was attempted to form a Ni-aluminide layer on Nb-W and Nb-W-Mo alloys, which are promising materials for high temperature equipment, by the electrodeposition of Ni and Al which can be electrodeposited using a molten salt as the electrolyte. When the formation of the Ni-aluminide was carried out by the Ni electrodeposition for a long time, followed by the Al electrodeposition, a Ni layer as the intermediate layer between the Ni-aluminide layer and the alloy substrate was formed. In the present study, we tried to prepare the Ni-aluminide/Ni bilayer coating by the Ni electrodeposition for a long time, followed by the Al electrodeposition. For the specimens with this coating, the oxidation resistance was evaluated.

2. EXPERIMENAL

Nb-10mass%W and Nb-10mass%W-5mass%Mo alloys were used as the cathode substrate. The alloy ingot was prepared by argon-arc melting. Coupons about 1.5-mm thick were cut from the ingot. The sample surface were polished with #800 SiC paper and ultrasonically washed in acetone.

The preparation of the Ni aluminide/Ni bilayer coatings were carried out in two electrodeposition steps. First, Ni was electrodeposited on the alloys using a Watt's solution. Second, Al was electrodeposited on the Ni film using an equimolor NaCl-KCl melt at 1023K containing 3.5 mol% AlF_3. The Ni-deposition time was changed in order to change the thickness of the Ni layer.The electrodeposition of Ni was carried out by galvanostatic electrolysis at 200 A m^{-2} for 3.6, 7.2, 10.8 and 12.6 ks. The electrodeposition of Al was carried out by potentiostatic electrolysis at -1.4 V for 3.6ks.

The high-temperature oxidation test of the samples treated with the Ni and Al depositions was carried out at 1273K in air for 259.2 ks using a thermobalance. In order to evaluate the change in the coating layer and the scale formed on the coating layer after the oxidation test, a cross-section of the specimen was observed by SEM and analyzed by EPMA.

3. RESULTS AND DISCUSSION

3. 1 Morphology of Ni-aluminide/Ni Bilayer Coating

Fig. 1 shows cross-sectional micrographs and the concentration profiles of the Al, Ni, Nb and W across the Nb-10mass%W alloys after the Ni electrodeposition for 3.6~12.6 ks, followed by the Al electrodeposition. For each specimen, the formation of a uniform coating layer was observed. It was found from the concentration profiles that the outer and inner layers consisted of Ni_2Al_3 and Ni, respectively. At the interface between the Ni layer and the alloy substrate, the formation of a thin layer consisting of a Nb-Ni-W alloy was observed. The thickness of the Ni layer increased with an increase in the Ni electrodeposition time. Such a Ni_2Al_3 / Ni bilayer was also observed for the Nb-10mass%W-5mass%Mo alloy after the same Ni electrodeposition, followed by the Al electrodeposition.

3. 2 Oxidation Behavior at High Temperature

Figs. 2 (a) and (b) show the oxidation curves of the Nb-10mass%Nb and Nb-10mass%W-5mass%Mo alloys, respectively, after the Ni electrodeposition for 3.6~12.6 ks, followed by the Al electrodeposition, during the oxidation test in air at 1273 K. This figure also contains the oxidation curve of a nontreated alloy in the same atmosphere. For both alloys

with the coating formed by the Ni electrodeposition for 3.6 ks, the mass gains largely increased during the initial period due to a vigorous oxidation. On the contrary, for both alloys with the coatings formed by the Ni electrodeposition for a time longer than 7.2 ks, the mass gains were scarcely observed, showing that these specimens had a high oxidation resistance.

3.3 Morphology of Coating and Scale after Oxidation Test

Fig. 3 shows a cross-sectional micrograph and the concentration profiles of Al, Ni, Nb, W and O across the Nb-10mass%W alloy after the Ni electrodeposition for 3.6 ks, followed by the Al electrodeposition, after the oxidation for 3.6 ks at 1273 K in air. For this specimen, vigorous oxidation occurred during the initial period (Fig. 2). This micrograph was taken for the area in which the coating adhered to the alloy substrate. The coating consisted of Ni_2Al_3 as same as the outer layer before the oxidation test. A scale consisting of Al_2O_3 was formed on the coating. At the interface between the coating and the alloy substrate, a thin layer consisting of the Ni-Nb-W alloy was formed. It was found that at the interface between the the Ni-Nb-W alloy layer and the Ni_2Al_3 layer, spallation of the Ni_2Al_3 layer partly occurred. In the Ni_2Al_3 layer, cracks lying perpendicular to the surface were observed. It was presumed that such a spallation and cracks took place due to the thermal stress generated by the rise and fall in temperature before and after the oxidation test caused by the difference in the expansion coefficient between the Ni_2Al_3 layer and the Ni-10mass%W alloy substrate. Consequently, the large oxidation mass gain observed for the alloy after the Ni electrodeposition for 3.6 ks seems to result from the spallation of the Ni_2Al_3 layer.

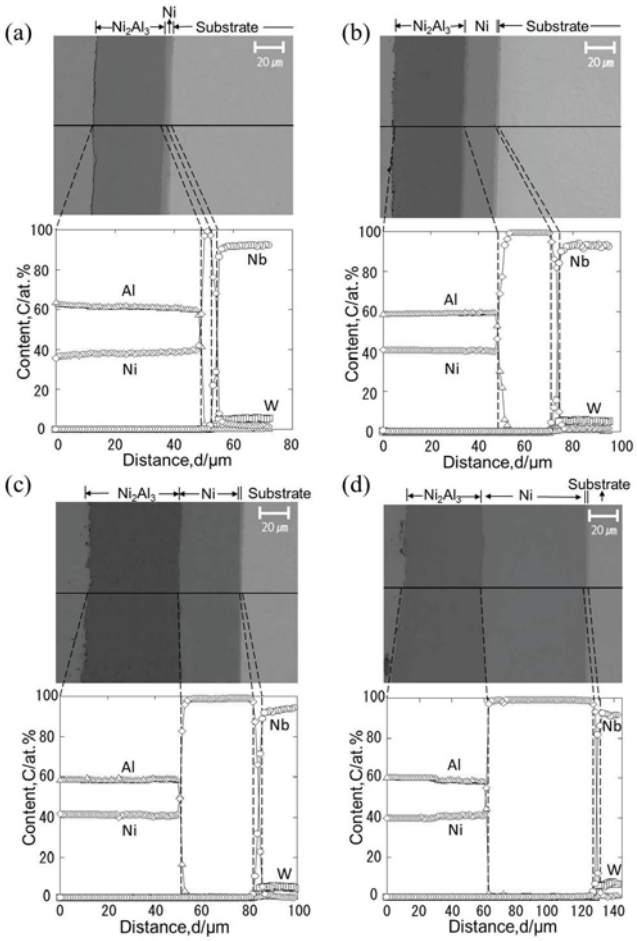

Fig.1 Cross-sectional micrographs and concentration profiles of Nb, W, Al and Ni across Nb-10mass%W alloy after Ni electrodeposition for (a) 3.6ks, (b)7.2ks, (c)10.8ks, (d)12.6ks, and Al electrodeposition.

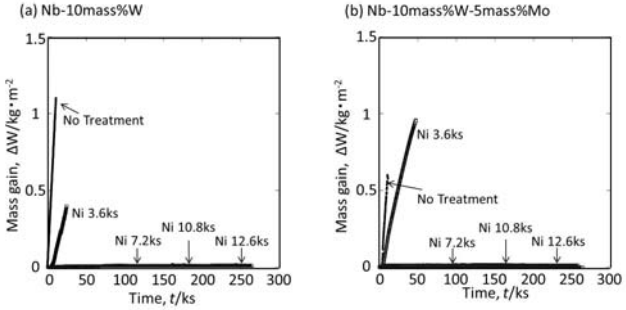

Fig.2 Mass gain-time curves of (a) Nb-10mass%W and (b) Nb-10mass%W-5mass%Mo alloy specimens, deposited with Al after Ni electrodeposition for 3.6 ~ 12.6 ks, during oxidation at 1273 K in air.

Figs. 4 (a) and (b) show cross-sectional micrographs and the concentration profiles of Al, Ni, Nb, W and O across the Nb-10mass%W alloys after the Ni electrodeposition for 7.2 and 12.6 ks, respectively, followed by the Al electrodeposition, after the oxidation for 259.2 ks at 1273 K in air. These specimens showed a high oxidation resistance (Fig. 2). For the alloy with the coating formed by the Ni electrodeposition for 7.2 ks (Fig. 4(a)), the outer layer changed from the Ni_2Al_3 phase to the NiAl phase after the oxidation due to a decrease in the Al concentration. It was presumed from the concentration profiles in the coating and the Ni-Al-Nb ternary diagram[4] that the inner Ni layer before the oxidation test reacted with the outer Ni_2Al_3 layer to form a NiAl layer and a layer consisting of NiAl and Ni_3Al, and that reacted with the alloy substrate to form a Nb_7Ni_6 layer and a layer consisting of Nb_7Ni_6 and a Nb-solid solution phase containing Ni. On the other hand, for the alloy with the coating formed by the Ni electrodeposition for 12.6 ks (Fig. 4(b)), it was presumed that the coating consisted of an outer NiAl layer and an inner Ni_3Al layer / a layer consisting of Ni_3Al and a Ni-solid solution phase containing Al / a layer consisting of a Ni-solid solution phase containing Nb / a layer consisting of $NbNi_3$ and Nb_7Ni_6 / a

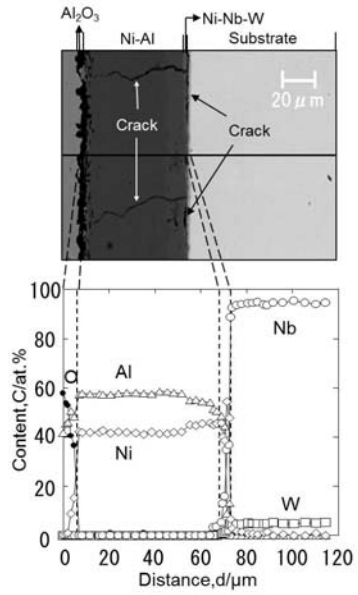

Fig.3 Cross-sectional micrographs and concentration profiles of Nb, W, Al and Ni across Nb-10mass%W alloy deposited with Al after Ni electrodeposition for 3.6ks, after oxidation for 3.6 ks at 1273K in air.

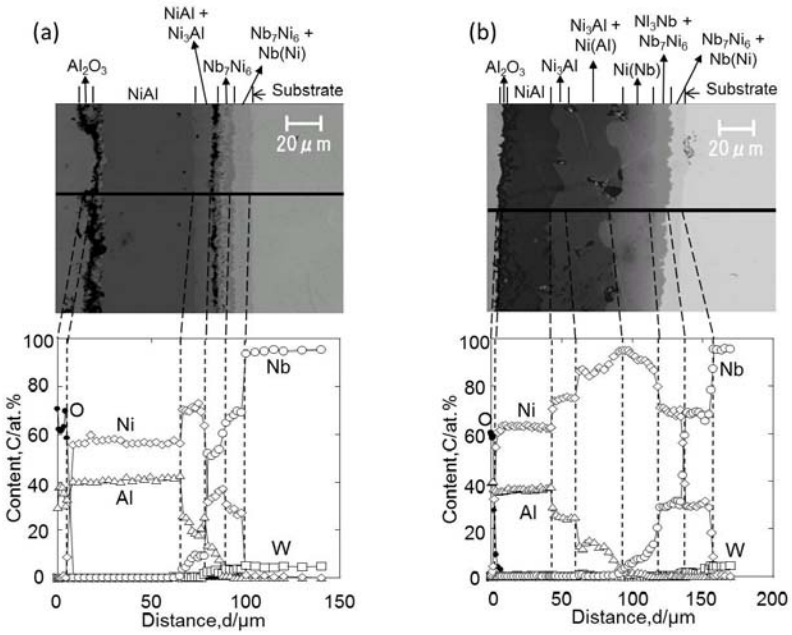

Fig.4 Cross-sectional micrographs and concentration profiles of Nb, W, Al and Ni across Nb-10mass%W alloy deposited with Al after Ni electrodeposition for (a) 7.2ks and (b) 12.6 ks , after oxidation for 259.2 ks at 1273K in air.

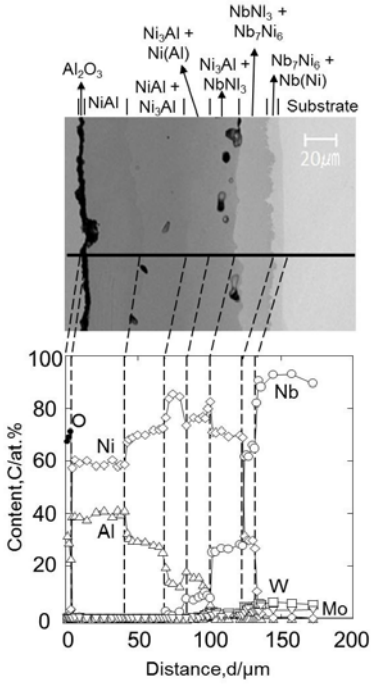

Fig.5 Cross-sectional micrographs and concentration profiles of Nb, W, Mo, Al and Ni across Nb-10mass%W -5mass%Mo alloy deposited with Al after Ni electrodeposition for 12.6 ks , after oxidation for 259.2 ks at 1273K in air.

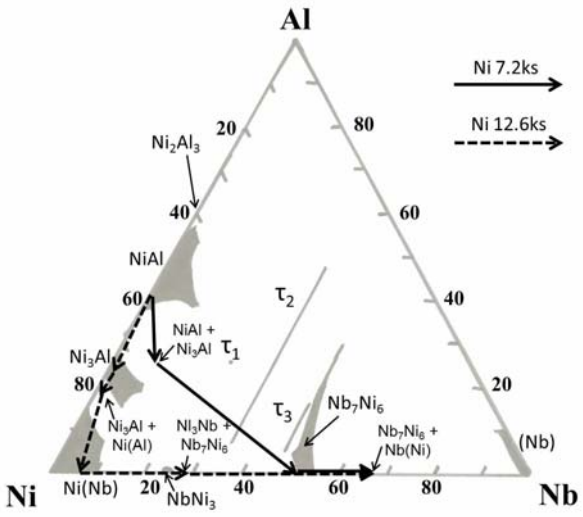

Fig.6 Composition path for the Nb-10mass%W alloys after Ni electrodeposition for 7.2 and 12.6ks, followed by the Al electrodeposition after the oxidation test in the Nb-Al-Ni system phase (isothermal section at 1300K).

layer consisting of Nb_7Ni_6 and a Nb-solid solution phase containing Ni. It was found that corresponding to such a gradual change in the phase, the concentration of Al gradually decreased with a change in place form the coating surface to the alloy substrate. For both specimens shown in Figs. 4 (a) and (b), scales consisting of Al_2O_3 were formed on the outer NiAl layers. It was also found for both specimens that the area inside the layer consisting of the Nb_7Ni_6 phase scarcely

contained Al, suggesting that this layer seems to act as a diffusion barrier layer of Al.

Fig. 5 shows cross-sectional micrographs and the concentration profiles of Al, Ni, Nb, W, Mo and O across the Nb-10mass%W-5mass%Mo alloy after the Ni electrodeposition for 12.6 ks, followed by the Al electrodeposition, after the oxidation for 259.2 ks at 1273 K in air. This specimen showed a high oxidation resistance (Fig. 2). It was presumed that the coating consisted of an outer NiAl layer and an inner layer consisting of NiAl and Ni_3Al / a layer of Ni_3Al and a Ni-solid solution phase containing Al / a layer consisting of Ni_3Al and $NbNi_3$ / a layer consisting of $NbNi_3$ and Nb_7Ni_6 / a layer consisting of Nb_7Ni_6 and a Nb-solid solution phase containing Ni. Such a tilting morphology of the coating was the same as that of the Nb-10mass%W alloys after the Ni electrodeposition for 12.6 ks, followed by the Al electrodeposition, after the oxidation test (Fig. 4(b)). It was also found that on the outer NiAl layer, a scale consisting of Al_2O_3 had formed.

3. 4 Effect of Ni Layer Thickness on Oxidation Behavior

Based on the results of this study that for Ni-10mass%W and Ni-10mass%W-5mass%Mo alloy substrates, the formation of the thick Ni layer as an intermediate layer led to the improvement of the oxidation resistance. This fact results from two factors. One factor is that the Al concentration in the outer layer was maintained at a high concentration due to the formation of the intermediate layer consisting of the Nb_7Ni_6 phase, which seems to act as the diffusion barrier layer of Al. The other factor is that the crack generation in the coating due to the thermal stress during the temperature increase was depressed when the inner Ni layer was thick. Fig. 6 shows the composition path for the coating formed on the Nb-10mass%W alloys after the Ni electrodeposition for 7.2 and 12.6 ks, followed by the Al electrodeposition, after the oxidation test (Fig. 4 (a), (b)), in the Nb-Al-Ni system phase diagram at 1300 K. For the coating formed on the Nb-10mass%W alloy after the Ni electrodeposition for 7.2 ks (Fig.4 (a)), the number of passing phases after starting from the outer NiAl layer is three. On the contrary, for the coating formed on the Nb-10mass%W alloy after the Ni electrodeposition for 12.6 ks (Fig.4 (b)), the number of the passing phases after starting from the outer NiAl layer is six. This indicated that the formation of the thick Ni layer led to the formation of the numerous layers having a variable chemical composition after the oxidation test. The fact seems to lead to a decrease in the thermal stress, which occurs on each layer constituting the coating during a change in temperature, thus suppressing spallation of the coating.

4. CONCLUSION

The preparation of a Ni-aluminide / Ni bilayer coating on the Nb-10mass%W and Nb-10mass%W-5mass%Mo alloys was attempted by Ni electrodeposition using an aqueous solution and Al electrodeposition using a molten salt. The oxidation resistance of the alloys with this coating was evaluated. The following conclusions can be drawn.

(1) For the alloys treated with Ni-deposition in a Watt's solution, followed by Al-deposition in the molten salt, a coating consisting of a Ni-aluminide/Ni bilayer was formed. An inner Ni layer became thick with an increase in the Ni-deposition time.

(2) The alloys with a coating consisting of a Ni-aluminide /thin Ni layer (Ni-deposition time; 3.6 ks) showed a vigorous oxidation during the initial period, while the alloys with a coating consisting of a Ni-aluminide /thick Ni layer (Ni-deposition time; longer than 7.2 ks) showed a high oxidation resistance.

(3) For the alloys with a coating consisting of a Ni-aluminide/thick Ni layer showing a high oxidation resistance, several intermediate layers consisting of Ni-Al and Ni-Nb alloys were formed between the outer NiAl layer and the substrate alloy.

References

[1] M. Hara, Y. Matsuda, M. Fukumoto and T. Narita, Oxidaiton of Metals, 77(2008), pp. 295-306
[2] T. Abe, N. Sato, M. Fukumoto and M. Hara, J. Japan. Trst. Met. Mater, 77(2013), pp. 245-252
[3] M. Fukumoto, M. Hara and T. Narita, Materials Science Forum, (2006), pp.522-523, 377-384
[4] V. Raghavam, J. Phase Equilibria and Diffusion, Vol. 27, No. 4(2006), pp.397-402

Study on oxidation behavior of pure Cr at high temperature in water vapor

Zhiwu Wang [1,*], Tao Song [2]

[1] School of Power and Mechanical Engineering, Wuhan University, Wuhan 430072, Hubei, China
[2] Rods Main Workshop Large Branch of WISCO, Wuhan 430083, Hubei, China

e-mail:wzw1618@163.com

1. INTRODUCTION

Because of its excellent ability at resistance to high temperature oxidation chromium are widely used in steel for power plant boiler tubes[1-2]. And with the content of chromium increase the temperature of this steel be on service significantly improve. Such as the T23 steel whose chromium content is 2.25%, its service temperature is 540℃, the T91 steel with a chromium content of 9.0%, its service temperature is 590℃, and the Super304 steel whose chromium content is 18.0%, its service temperature is 620℃[3-5]. Researches show that the reason for the excellent behavior of chromium on oxidation resistance is chromium will form a compact chromium rich protective film which can slow down the oxidation rate. On the other hand, some researches show that, the protective Cr_2O_3 film can't be exist steady for the hydrone at high temperature in water vapor, in this process, chromium will volatilize in the form of $CrO_2(OH)_2$[6-8].

This study focus on study the oxidation behavior of pure casted chromium at high temperature in water vapor individually, include oxidation kinetics, nucleation and grow up of oxidation particles, volatility of chromium.

2. EXPERIMENTAL

All of the materials in this study are casted pure chromium which are wire-electrode cut into diamonds with size of 19.5×12.3×7.2 mm. Specimens are divided into nine groups, each group have seven specimens among the seven specimens three of them for oxidation kinetics, two of them for SEM observation and two of them for XRD and XPS tests. Each specimens will be polished and oxidized in specific water vapor stove (Fig.1) at 650℃ for different time. The oxidation time from 1h to 100h, and tail gases be collected through the gas pipe from the stove to alcohol sulfate solution.

The weight change before and after oxidation are tested by analytical balance, and use QUANTA 400 scanning electron microscope to observe morphology of oxidation film, the EDS which is attached on the SEM to test the composition of oxidation film, the type of oxidation film is tested by DX-2500 x-ray diffraction and VGESCALAB MKII x-ray photoelectron spectroscopy, the HC-800 ion analyzer to analysis the ion of tail gases.

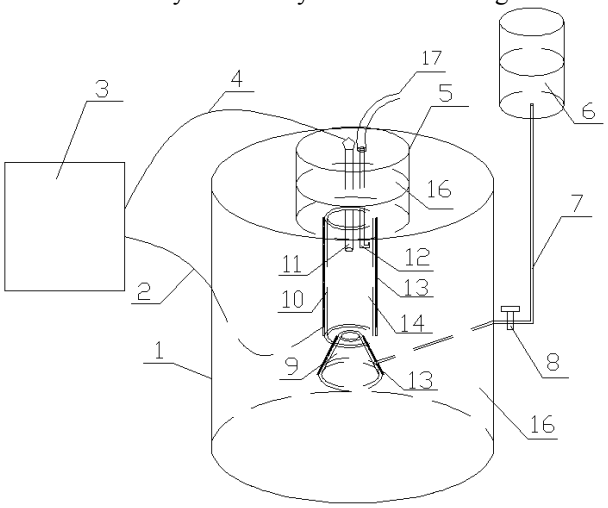

Fig. 1 High temperature oxidation water vapor stove
1- shell, 2- control circuit,3- temperature control, 4- temperature transmission circuit, 5- head cover, 6- water supply, 7- water transfer line, 8- flow control valve, 9- steam producer, 10- furnace wall, 11- thermo receptor, 12- pothook, 13- heating resistor, 14- oxidation stove, 15- head cover groove, 16- thermal insulation, 17- tail gas pipe

3. RESULTS AND DISCUSSION

3.1 Results of oxidation kinetic

Specimens groups are oxidized for 1h, 2h, 4h, 8h, 16h, 32h, 50h, 80h, 100h respectively at 650℃ in water vapor, the average value weight change showed in Fig. 2.

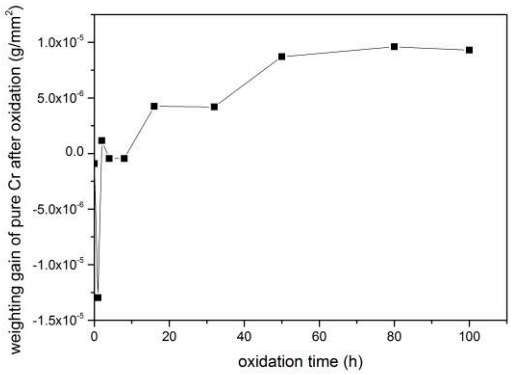

Fig. 2 Oxidation kinetic of pure Cr during oxidation at 650℃ in water vapor

The weight gain data is negative after oxidize for 1h while the data after oxidize for 2h is positive from Fig. 2. This means on the initial stage of oxidation the elements run off are more than weight gain during oxidation. For the specimens in the experiment is pure Cr, so the run off element must be chromium. After oxidize for 50h, the curve be steady around 1×10^{-5}g/mm^2, this means pure Cr can form a whole protective film in a short time. In order to explore the reason of weight loss, the tail gases in each procedure are collected. From the ion analyzer, Cr^{6+} are found in tail gas, and after oxidize for 1h, the content of Cr^{6+} is 190.5mg/L.

3.2 Results of oxidation film morphology

Morphology of pure Cr specimens oxidized for 1h, 2h, 4h, 8h, 16h, 32h, 50h, 80h, 100h are show in Fig.3.

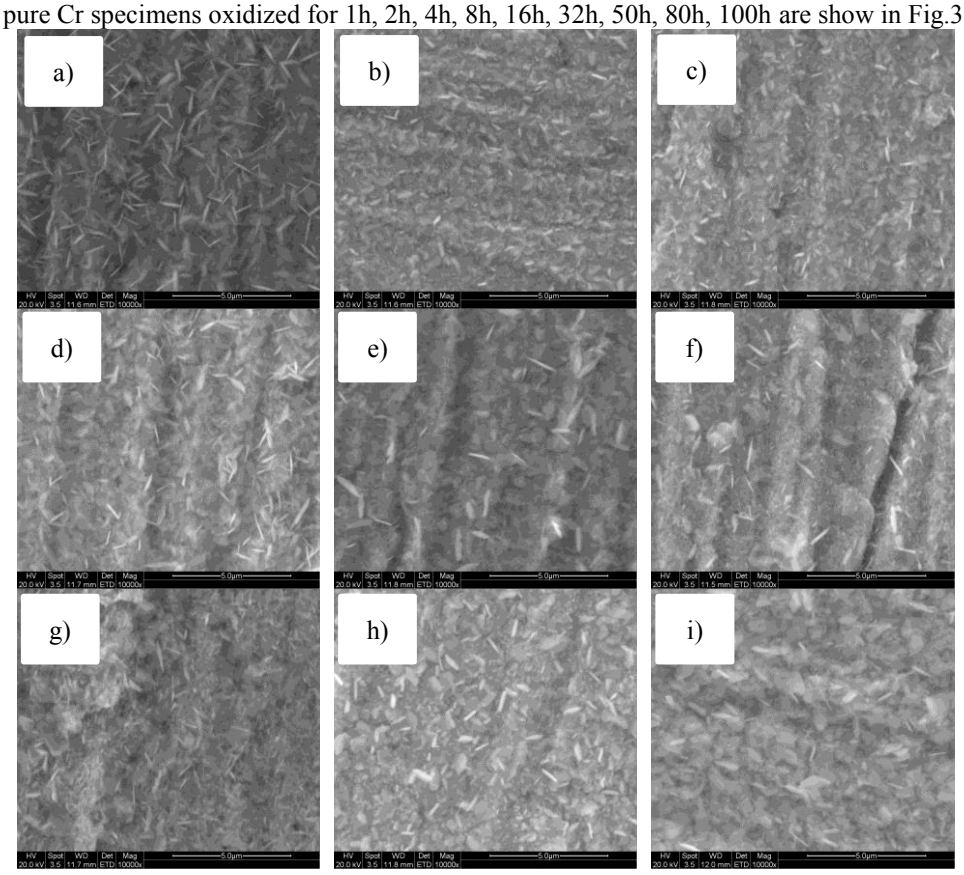

Fig. 3 Surface morphology of pure Cr oxidation film

a)1h, b)2h, c)4h, d)8h, e)16h, f)32h, g)50h, h)80h, i)100h

Fig. 3 show a constant process of oxidation film formation at high temperature. The oxidation begins with the appearance of needle like embryo in 3a) and with the extend of oxidation time the needle like embryo develop into lamellar oxidation in 3b) and 3c), in addition, in 3d) the needle like embryo decrease but there is a lamellar oxidation layer underneath, this means that the needle like embryo are new nucleation. In 3e) and 3f), the needle like embryo is quite a few, but the lamellar oxidation layer be more compact, that is to say, the layer underneath is growing up, and from 3h) it's the new oxidation particles grow up on the underneath oxidation film, and in 3i) the outer oxidation film formed. Even from oxidation kinetic the negative value of weight gain appear, the oxidation formation procedure is constant and intact. The second oxidation film is grow from the first oxidation film.

3.3 Results of EDS

The atom fraction of oxidation film during oxidize at 650℃ in water vapor by EDS are show in table 1.

Table 1 EDS results of pure Cr oxidize at 650℃ in water vapor

Oxidation time/h	O		Cr		Me：O (at%)
	wt%	at%	wt%	at%	
1	12.99	32.46	87.01	67.54	2.08:1
2	10.57	27.56	89.43	72.44	2.62:1
4	9.74	25.82	90.26	74.18	2.87:1
8	20.16	44.86	79.84	55.14	1.22:1
16	17.37	40.59	82.63	59.41	1.46:1
32	16.21	38.47	83.79	61.53	1.59:1
50	19.73	44.25	80.27	55.75	1.26:1
80	18.56	42.56	81.44	57.44	1.34:1
100	20.81	45.89	79.19	54.11	1.18:1

From table 1 the value Me/O is decrease to 1/1 with the extend of oxidation time. The oxides formed by Cr is Cr_2O_3 generally which the Me/O is 0.4, but from table the proportion is quite high than this value. This means the oxygen atom is poor in oxidation film.

3.4 Results of XPS

XPS is used to analysis the structure of oxidation film for XRD can't analysis such thin film, the results show in Fig. 4

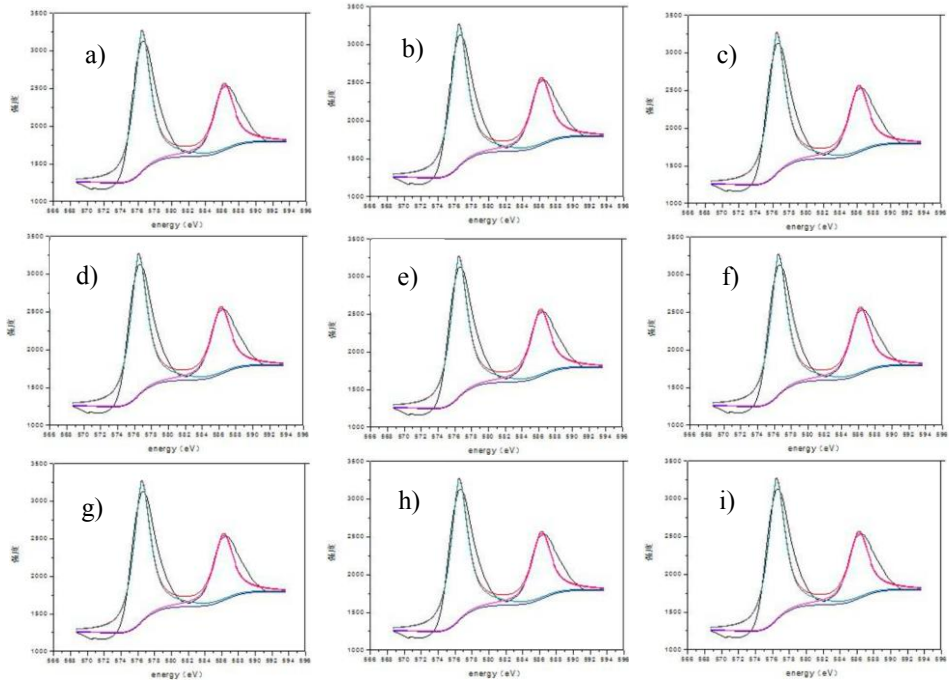

Fig. 4 XPS results of pure Cr oxidation film

a)1h, b)2h, c)4h, d)8h, e)16h, f)32h, g)50h, h)80h, i)100h

Although tiny difference exist in XPS graphs, the results stay the same overall which is correspond with Cr_2O_3. So during the oxidation process, the oxidation film formed are all constitute by Cr_2O_3.

4. CONCLUSION

1) During oxidize at 650℃ in water vapor the element chromium in pure Cr will volatilize in the form of Cr^{6+}.

2) The oxidation film procedure is needle like embryo formed first and then needle like embryo grow to form the lamellar oxide. The new oxidation layer formed in 4～8h and 32～50h during oxidation.

3) The thickness of oxidation film is in 5μm during oxidation at 650℃ in water vapor in 100h. Oxidation film is composed by Cr_2O_3, and external oxidation is dominated in oxidation procedure.

Acknowledgements

The financial support by the National Natural Science Foundation of China (51071113) is gratefully acknowledged.

References.

[1] Wagner C. Formation of composite scales consisting of oxides of different metals[J]. Journal of the Electrochemical Society, 1956, 103(11): 627-633.
[2] Halvarsson M, Tang J E, Asteman H, et al. Microstructural investigation of the breakdown of the protective oxide scale on a 304 steel in the presence of oxygen and water vapour at 600 C[J]. Corrosion Science, 2006, 48(8): 2014-2035.
[3] Helis L, Toda Y, Hara T, et al. Effect of cobalt on the microstructure of tempered martensitic 9Cr steel for ultra-supercritical power plants[J]. Materials Science and Engineering: A, 2009, 510: 88-94.
[4] Sawaragi Y, Ogawa K, Kato S, et al. Development of the Economical 18-8 Stainless Steel(SUPER 304 H) Having High Elevated Temperature Strength for Fossil Fired Boilers[J]. Sumitomo Search(Japan), 1992 (48): 50-58.
[5] Stringer J, Wilcox B A, Jaffee R I. The high-temperature oxidation of nickel-20 wt.% chromium alloys containing dispersed oxide phases[J]. Oxidation of Metals, 1972, 5(1): 11-47.
[6] Asteman H, Svensson J E, Norell M, et al. Influence of water vapor and flow rate on the high-temperature oxidation of 304L; effect of chromium oxide hydroxide evaporation[J]. Oxidation of Metals, 2000, 54(1-2): 11-26.
[7] Jianian S, Longjiang Z, Tiefan L. High-temperature oxidation of Fe-Cr alloys in wet oxygen[J]. Oxidation of Metals, 1997, 48(3-4): 347-356.
[8] Fujii C T, Meussner R A. Oxide Structures Produced on Iron‐Chromium Alloys by a Dissociative Mechanism[J]. Journal of the Electrochemical Society, 1963, 110(12): 1195-1204.

Influences of several coatings on oxidation behavior of single crystal superalloy DD98M

Long Shi [1,2], Li Xin[1,*], Xinyue Wang [1], Shenglong Zhu [1], Fuhui Wang [1], Hua Wei [1]

[1] State Key Laboratory for Corrosion and Protection, Institute of Metal Research, Chinese Academy of Sciences, 62 Wencui Road, Shenyang 110016, Liaoning, PR China
[2] School of Materials and Metallurgy, Northeastern University, 3-11 Wenhua Road, Shenyang 110819, Liaoning, PR China

e-mail: xli @imr.ac.cn

1. INTRODUCTION

Nickel-based superalloys have been widely used in industrial gas turbines, aircrafts, jet engines owing to their excellent mechanical strength at high temperature. DD98M alloy is a second generation single crystal nickel--based superalloy without Re addition, which is developed by Institute of Metal Research, Chinese Academy of Sciences. It is a combination of attractive strong points such as low cost and high strength. Conventional high-temperature protective coatings such as aluminized coating, MCrAlY overlay coating etc. are usually applied on the superalloys to protect them from oxidation and corrosion attack. But interdiffusion between substrate and coating may cause the formation of harmful brittle phases in the substrate after exposure at high temperature. It has been extensively reported due to the interdiffusion between the coating and single crystal nickel--based superalloy, secondary reaction zone (SRZ) and detrimental topologically close-packed (TCP) phase form in the superalloy, leading to significant reduction in mechanical properties of the superalloy. However, up to now the high temperature oxidation resistance of DD98M, the influences of conventional high-temperature protective coatings on the oxidation resistance of the DD98M alloy and their interdiffusion behaviors have not been investigated. “Nanocrystalline Coating” invented by Lou and Wang[1] has the same chemical composition as the substrate alloy it put on, so any possible harmful effects induced by the inter-diffusion between the coating and the substrate were avoided, and high temperature oxidation and corrosion resistance were improved [1]. Therefore it could be a kind of promising coatings suitable for single crystal superalloy. In this paper, the oxidation resistance of DD98M alloy and the influences of MCrAlY and sputtered nanocrystalline coating on the oxidation resistance of DD98M were investigated.

2. EXPERIMENTAL

The nominal chemical composition (wt.%) of DD98M is Cr 6, Co 5, Al 6.3, Ta 6, Ti 1,W 6, Mo 2. Two kinds of MCrAlY coatings with nominal composition (wt.%) Ni27Cr11Al0.5Y and Ni19Co27Cr11Al0.5Y0.2Hf0.1Si were deposited on DD98M specimen by arc ion plating. Nanocrystalline coating were sputtered on DD98M alloy using a target whose composition was the same as that of the DD98M superalloy. Quasi-isothermal oxidation tests were performed in box furnaces at 1000 and 1050 ^{o}C in air, where the oxidation was stopped every 20 h during the first 200 h and every 50 h during the following 300 h, and the specimens placed in alumina crucibles were weighed and visually inspected. During cooling the alumina crucibles were covered with alumina lids in order to collect any spalled oxide. The mass changes of the specimens were measured using an eletronic balance with sensitivity of 0.01mg. After oxidation, the specimens were examined using X-ray diffraction (XRD), scanning electron microscopy with energy-dispersive X-ray analysis (SEM/EDX) and electron-probe microanalysis (EPMA).

3. RESULTS AND DISCUSSION

The oxide scale formed on DD98M after oxidation at 1000 ^{o}C and 1050 ^{o}C in air stratified, cracked and spalled seriously (Fig.1 (a-b) and Fig. 2 (a-b)). The outer gray layer is mixed oxides of NiO, Cr_2O_3, $CoCr_2O_4$and $NiAl_2O_4$ and the inner dark layer is α-Al_2O_3. The bright white phase in the oxide scale is Ta-rich oxide ($Ta_{0.8}O_2$ and $CrTaO_4$ identified by XRD). Inner nitrides formed in the alloy, the black phases are AlN and the grey phases are TiN (Fig.3). The application of the NiCrAlY and NiCoCrAlYHfSi coatings improved the oxidation resistance of DD98M obviously at the both temperatures. After 500h oxidation, α-Al_2O_3 is still the dominate phase in the oxide scales formed on both coatings. At 1000 ^{o}C, the oxide scale formed on NiCoCrAlYHfSi is very adherent but that formed on NiCrAlY spalled slightly (Fig. 1 c-f). At 1050 ^{o}C, the oxide scale formed on the both coatings spalled and the spallation of the oxides is more serious for the NiCrAlY coating (Fig. 2 c-f). Interdiffusion occurred for the coated specimens. Interdiffusion zone (IDZ) and discontinuous secondary reaction zone (SRZ) formed between the coatings and the substrate. For the NiCoCrAlYHfSi coated specimen, EPMA results (Fig.4) show that after oxidation Mo, W, Ta and Ti in the substrate alloy has diffused outward and are detected in the coating. Co, Cr and Al in the coating diffused inward and Ni in the alloy diffused outward led to the formation of IDZ and SRZ. A thin layer of titanium oxide formed between the coating and substrate. Yttrium mainly exits in the coating and the content of hafnium and silicon in the coating was too low to be detected. The composition of the IDZ is similar to that of the coating after oxidation and the thickness of IDZ increased with increasing temperature. Needle-like phases rich in Mo and W precipitated in the SRZ at the both temperatures. With increasing temperature, the thickness of the SRZ increased but the amount of needle-like phases in SRZ decreased. For the NiCrAlY coated specimen

after oxidation, similarly, Mo, W, Ta and Ti were detected in the coating due to their outward diffusion and titanium oxides detected at the coating/substrate interface (Fig. 5). But it is interesting that unlike the NiCoCrAlYHfSi coated specimen, IDZ formed are composed of two phases. The composition of the darker phases is similar to that of the coating after oxidation and the brighter phases are with more Ta and Al and less Co and Cr (Fig. 5 and Table 1). In addition, SRZ formed at 1000 ^{o}C after oxidation but seldom form at 1050 ^{o}C, or at least needle-like TCP phases seldom form. Furthermore the amount of needle-like phases in SRZ is less than that of the NiCoCrAlYHfSi coated specimen after oxidation at 1000 ^{o}C. The formation of SRZ and IDZ is due to the interdiffusion of coating and substrate. The only difference in element diffusion flow of the two coated specimens is that Co diffuses outward for the NiCrAlY coated specimen and inward for the NiCoCrAlYHfSi coated specimen. The outward diffusion of cobalt led to the formation of bright phases in the IDZ, which is depleted in Co and Cr and rich in Al and Ta, provided a reservoir for the inward diffusing aluminium, so the SRZ formation was suppressed to some extent. The diffusion rate of coating and alloy elements increased with increasing temperature, so the bright phases formed quickly at 1050^{o}C, and SRZ formation was almost totally suppressed at this temperature. More detailed research work on the microstructure of needle-like TCP phases and bright phases, and diffusion behavior and precipitation mechanism will be conducted in the near future.

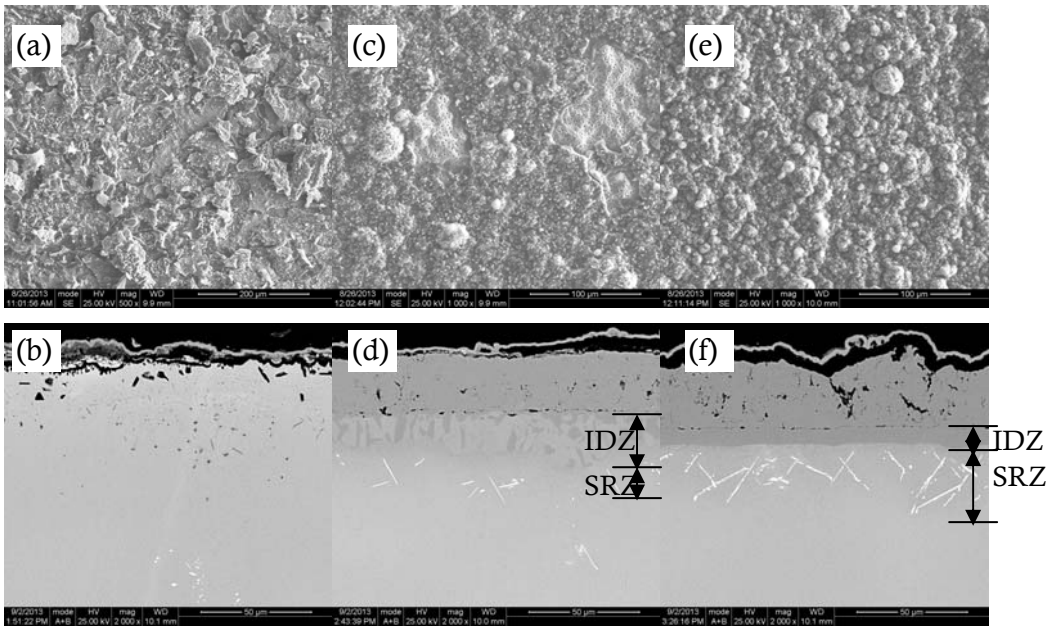

Fig. 1 Surface and cross-sectional morphologies of DD98M alloy (a)(b) and NiCrAlY coating (c)(d) and NiCoCrAlYHfSi coating (e)(f) after oxidation at 1000^{o}C for 500h

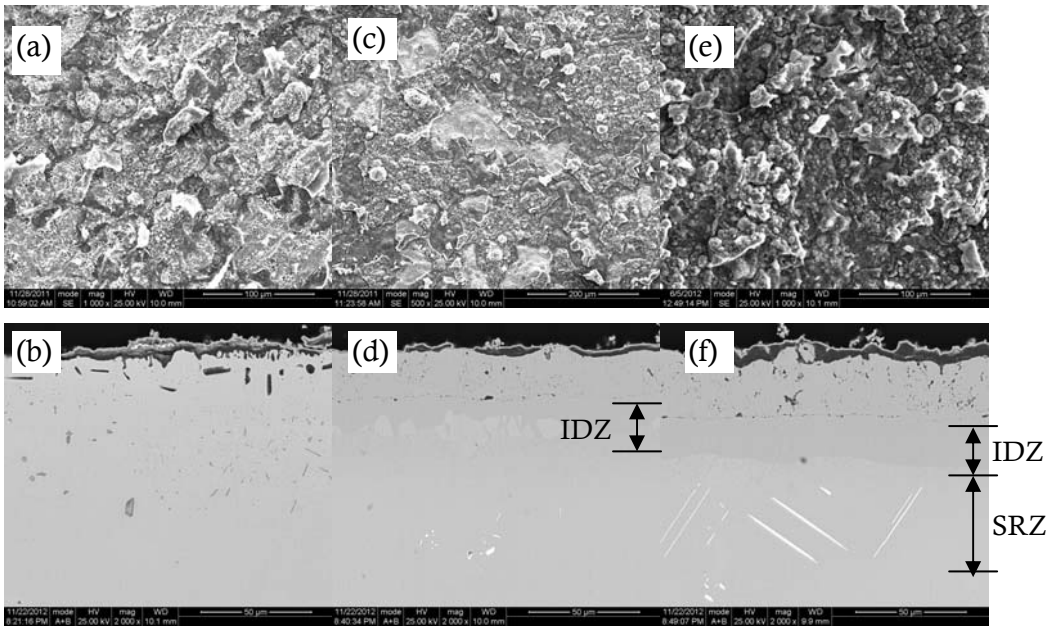

Fig. 2. Surface and cross-sectional morphologies of DD98M alloy (a)(b) and NiCrAlY coating (c)(d) and NiCoCrAlYHfSi coating (e)(f) after oxidation at 1050^{o}C for 500h

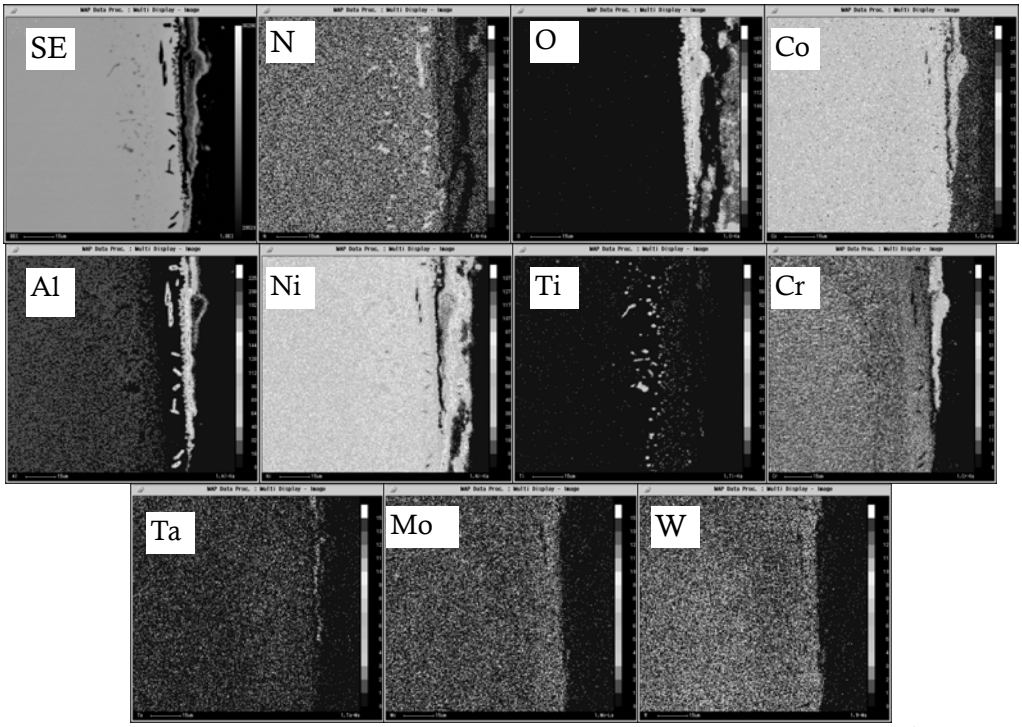

Fig. 3 EPMA element maps of a cross-section of DD98M alloy after oxidation at 1050°C for 100h

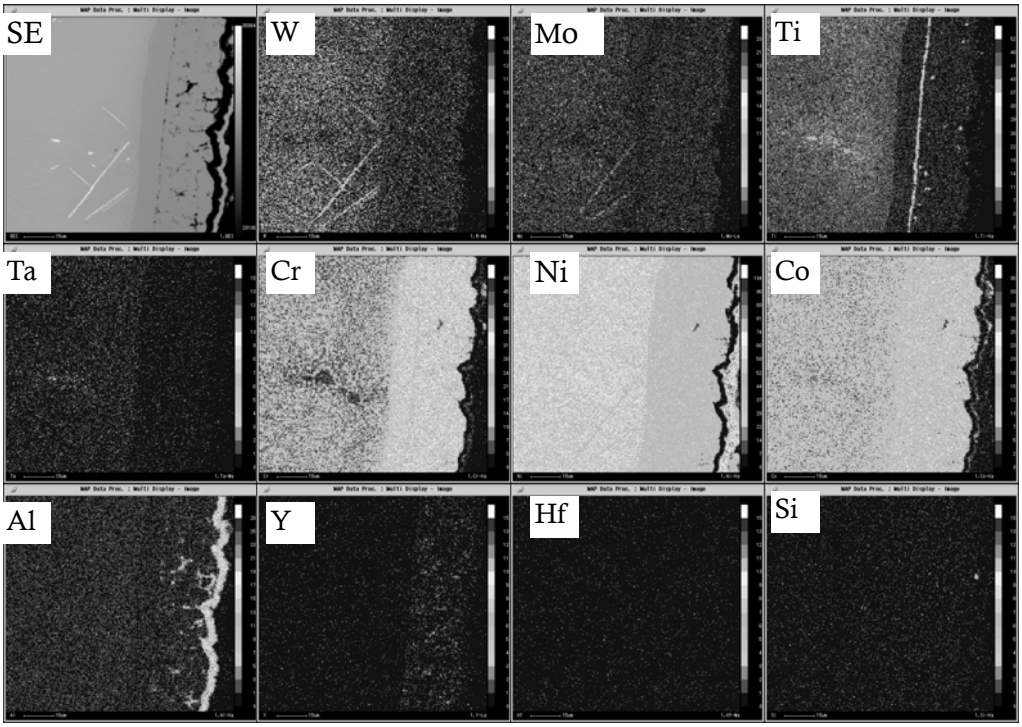

Fig. 4 EPMA element maps of a cross-section of NiCoCrAlYHfSi/DD98M specimen after oxidation at 1050°C for 100h

Table 1 The EPMA composition of the coating and the IDZ of the NiCrAlY coated specimen after 100h oxidation

	Co	Ni	Cr	Ti	Al	Mo	Ta	W	Y
Coating	5.05	61.44	22.69	0.13	4.45	1.32	1.13	3.46	0.33
Dark phase of IDZ	5.21	61.53	22.55	0.16	4.46	1.27	1.18	3.64	_
Bright phase of IDZ	2.54	72.17	5.34	0.47	8.68	0.32	7.45	3.00	0.04

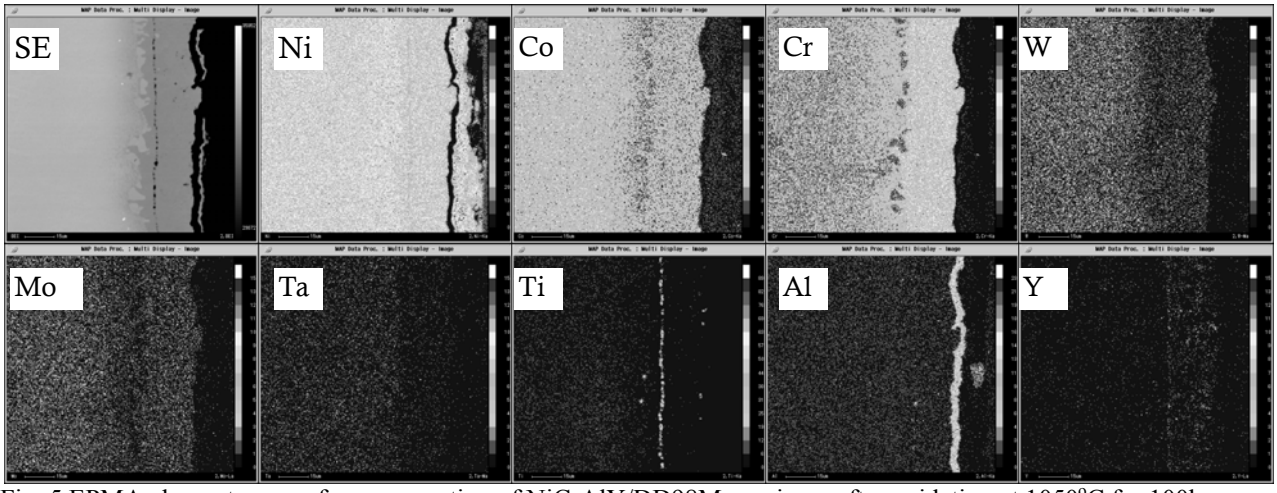

Fig. 5 EPMA element maps of a cross-section of NiCrAlY/DD98M specimen after oxidation at 1050°C for 100h

The mass gain of the DD98M alloy was decreased apparently by the application of nanocrystalline coating with the same composition when oxidized at 1000 °C for 500h (Fig. 6). The oxide scale is mainly composed of α-Al_2O_3, adherent to the substrate alloy for the first 300h and cracked and spalled slightly afterwards (Fig. 7). Interdiffusion between the coating and substrate did not occur for the nanocrystalline coating coated specimen. Nanocrystallization promoted rapid formation of Al_2O_3 scale and enhanced the adhesion of the oxide scale, thus improved the oxidation resistance of the substrate alloy. Meanwhile, the formation of harmful brittle phases in the substrate due to interdiffusion of coating and substrate was suppressed. Nanocrystalline coating with the same composition of the substrate is a promising protective coating for single-crystal superalloy.

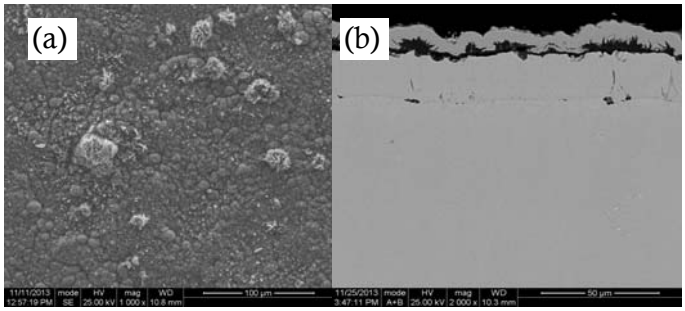

Fig. 7. (a)Surface and (b)cross-sectional morphologies of DD98M sputtered nanocrystalline coating after oxidation at 1000°C for 100h

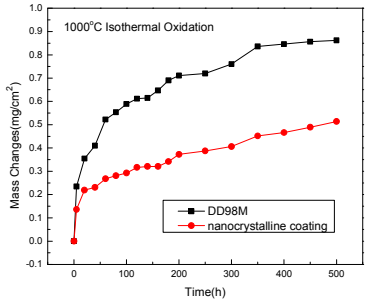

Fig.6. Quasi-isothermal oxidation kinetics of DD98M with and without nanocrystalline coating at 1000 °C in air.

4. CONCLUSION

(1) The application of the NiCrAlY and NiCoCrAlYHfSi coatings improved the oxidation resistance of DD98M obviously at 1000 °C and 1050 °C.

(2) Nanocrystalline coating with the same composition of DD98M alloy promoted rapid formation of Al_2O_3 scale and enhanced the adhesion of the oxide scale, thus improved the oxidation resistance of the DD98M alloy at 1000°C.

Acknowledgements

This work was financially supported by the National Key Basic Research and Development Program (973 Program) 2010CB631206 and 2012CB625100.

References.

[1] Lou H Y, Wang F H, Zhu S L, et al. 'Oxide formation of K38G super-alloy and its sputtered micro grained coating', *Surf. Coat. Technol.*, Vol. 63, No.2(1994), pp. 105-114.

Microstructure and Oxidation Resistance of Ti and Ir Based Alloys Aluminized with NiAl Alloy Powders

Hideyuki Murakami [(1*)], Daishi Ohtsubo[(1,2)], Ryo Zempo[(1,2)], Kazuki Kasai[(1,2)] and Yoshihiko Noda [(2)]

[(1)] Surface Kinetics Group, High Temperature Materials Unit, National Institute for Materials Science (NIMS), 1-2-1 Sengen, Tsukuba-Science-City, 305-0047, JAPAN
[(2)] Shibaura Institute of Technology, 3-7-5 Toyosu, Koto-ku 135-8548, JAPAN

e-mail: murakami.hideyuki@nims.go. jp

1. INTRODUCTION

Materials which are used in high temperature environments must possess not only mechanical strength in the used environment, but also the chemical stability to withstand oxidation and corrosion at elevated temperatures. Unfortunately, to find a base material which satisfies all the properties demanded is most difficult thus it is necessary to complement those properties by surface modification, in other words, oxidation resistant coating. An aluminizing treatment, by which a coated layer with a high Al concentration can be formed on the specimen surface, is one of the most cost-effective methods when the designed coating layer is developed. However, in order to form a desirable coating, optimization of the aluminizing process is also required. In this study, aluminizing on Ir and Ti alloys was attempted. Fabrication of alloyed powder for the aluminizing, and the relationship between microstructure of coated layer and oxidation resistance is discussed.

2. EXPERIMENTAL

In this study, pure Ir (5mm x 5mm x 1mm in size) and commercial near-α Ti alloy (Ti-834, 8mm x 5mm x 1mmin size, composition of which is listed in Table 1) were used as substrate materials. These materials were embedded in a powder mixture of Ni-Al alloy, Al_2O_3 and NH_4Cl and heated under Ar atmosphere. Detailed fabrication method for the Ni-Al alloy and Al_2O_3 powder mixture, and aluminizing conditions are explained in the next section. Powder mixture ratio of Ni-Al, Al_2O_3 and NH_4Cl was set to 49:49:2 (mass %) throughout this study. Mass changes by the aluminizing treatments, microstructure, and composition of coated layer of the as-aluminized specimens were investigated. After the aluminizing treatment, thermal isothermal heating tests (1273K kept for 100h in air for Ire and 1023K kept for 100h for Ti-834) and thermal cycling tests (1273K for 1 h and cooling for 20 min in air as one cycle for Ir and 1023 K for Ti-834) were performed to evaluate the oxidation resistance of the specimens. Specimens tested were analyzed using scanning electron microscopy (SEM), energy-dispersive X-ray spectroscopy (EDX), X-ray fluorescent Spectroscopy (XRF) and X-ray diffractometory (XRD).

Table 1 Nominal Composition of Ti-834

	Ti	Al	Sn	Zr	Nb	Mo	Si	C
at %	Bal.	10.3	1.6	1.8	0.36	0.25	0.6	0.24
Mass %	Bal.	5.8	4	3.5	0.7	0.5	0.35	0.06

3. RESULTS AND DISCUSSIONS

Fabrication of Ni-Al and Al_2O_3 mixed powder.

In the aluminizing process, an Al-source in the powder mixture reacts with NH_4Cl to form gaseous aluminum chlorides (AlClx). Thickness and Al-concentration of the coated layer can be determined by the partial pressure of AlClx. Therefore, to control the reactivity of Al in the aluminizing process is important for the fabrication of desirable coatings. In fact, our preliminary aluminizing treatment, in which 25 mass% of Al and 75 mass% of Al_2O_3 were used as an aluminizing agents, the sample surface was completely melted, as shown in Fig. 1. This is due to the high heat of reaction: ΔH=236kJ/mol for Ir+Al→IrAl,

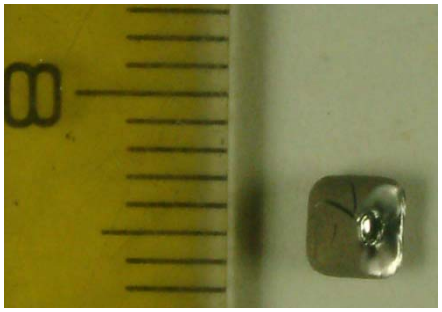

Fig. 1: Surface morphology of aluminized Ir conducted with Al+ Al_2O_3 powder mixture

suggesting that a combustion synthesis-type reaction took place. To avoid such a violent reaction, pure Ni, pure Al and Al_2O_3 were mixed, and they were heated up to 1273K for 1 h in Ar, followed by furnace cooling. Then the resulting agglomerated powder mixture was mechanically crashed into powder, as shown in Fig. 2. In this manner, several Ni-Al alloy powders with varying Al contents were fabricated. XRD phase identification confirmed that the Ni-Al powders are completely reacted to form intermetallic phases that were expected from the Ni-Al phase diagram, Table 2.

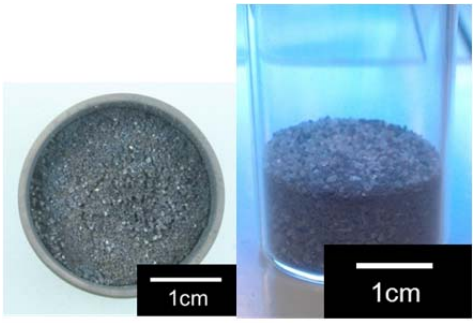

Fig. 2: Appearance of Ni-Al alloy and Al_2O_3 powder mixture, left: as-heat treated, right: as crashed.

Table 2 Identification of Ni-Al alloy

Ni (at%)	Al (at%)	Expected phase	XRD identification
75	25	Ni_3Al	Ni_3Al
65	35	NiAl	NiAl
50	50	NiAl	NiAl
40	60	Ni_2Al_3	Ni_2Al_3
25	75	$NiAl_3$	$NiAl_3$

Aluminizing on Ti-834

Since the β phase transformation temperature of Ti-834 is 1253K, aluminizing temperature was set from 1023K to 1223K. Figure 3 shows the relationship among Al content in the Ni-Al alloy powder, the surface Al concentration and the mass change of specimens by the aluminizing treatment, where aluminizing was conducted at 1173K for 5 h in Ar. It was confirmed that when the Al content in the Ni-Al alloy is not larger than 50 at%, Al concentration on the specimen surface was lower than that in the substrate. In addition, mass loss was observed by the aluminizing treatment. These results confirmed that in this condition, surface etching of the specimen took place, which led to the roughened and porous specimen surface, as shown in Fig. 4(a).

When the aluminum content in the Ni-Al alloy powder is between 55 and 60 at%, there is a very small mass change, while surface Al concentration reached 40 at%, indicating that surface etching and Al deposition were taking place simultaneously. This phenomenon is called displacement coating. The typical microstructure of such a case was shown in

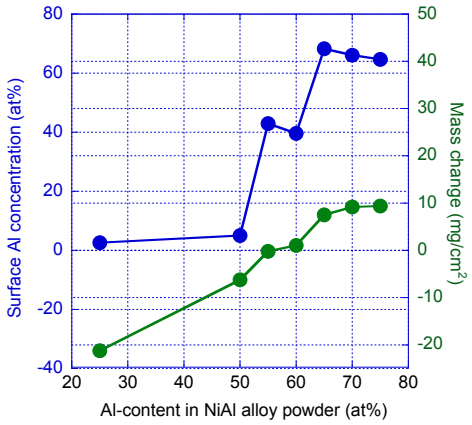

Fig. 3. The Effects of Al-content in NiAl alloy powder, on the mass change and surface Al concentration by aluminizing treatment.

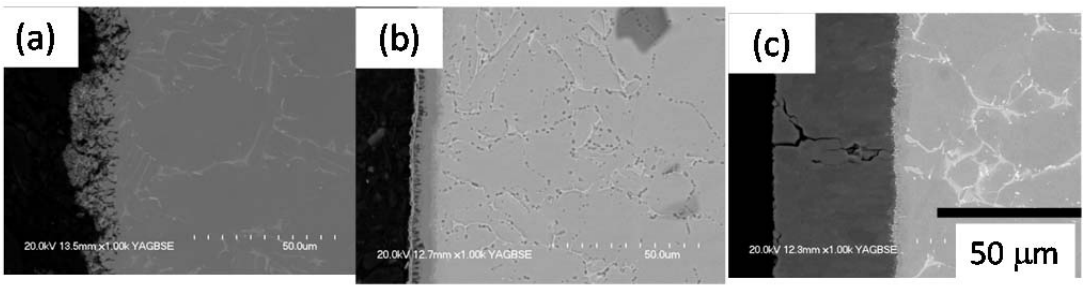

Fig. 4 Cross-sectional BSE images of as-aluminized Ti-834 conducted at 1173K for 5h. Al content in the aluminizing Ni-Al alloy powder is (a) 25at%, (b) 60 at% and (c) 75 at%, respectively

Fig. 4(b), where an Al-enriched surface is present but very small amount of mass change is observed. When the aluminum content in the Ni-Al alloy powder was higher than 60 at%, a typical aluminized layer was formed as shown in Fig. 4(c). However, in this case, surface Al concentration of the specimen reached above 60at%, indicating that brittle TiAlx (x=2 to 3) phase was formed and due to its brittleness, formation of cracks on the surface layer was observed.
An isothermal oxidation test and a cyclic oxidation test at 1023 K were conducted for these aluminized specimens. It is revealed that while TiAlx-coated specimens exhibited slower oxidation rate in the isothermal test, Displacement-coated specimens demonstrated better oxidation resistance in the thermal cycling test. The accelerated mass gain in the TiAlx-coated specimens in the cyclic oxidation test can be caused by the continuous formation of cracks in the brittle coated layer, which accordingly increased the oxidizing surface area.

Aluminizing on Ir

In the case of Ir substrates, aluminizing temperature of 1223K and 1323K, aluminizing time of 2h and 5h were employed. The effect of aluminizing conditions and Al content in the Ni-Al alloy powder on mass changes of specimens were summarized as shown in Fig. 5. Note that the vertical axis of this figure is plotted as a logarithmic scale. This figure showed the significant increase in mass gain when using the Al content in Ni-Al alloy powder was increased from 50 at% to 60 at%. Figure 6 is the cross sectional microstructure and corresponding element concentration depth profile of as aluminized specimens. When Ni-50at%Al (NiAl phase) powder was used, thickness of aluminized layer is less than 2 μm. On the other hand, when Ni-60at%Al (Ni_2Al_3 phase) powder was used, coating thickness was two-order of magnitude larger than that of the former one. The outer surface is Al-rich $IrAl_{2.75}$ phase with approximately 120 μm thick and the IrAl layer with 10 μm thick were formed. Similar to the aluminized Ti-alloy, many vertical cracks were observed in the Al-rich and thick layer, due to its brittleness. Cyclic oxidation tests at 1273K were also performed for the aluminized Ir specimens. Specimens having thick but brittle layer showed larger mass loss by the cyclic oxidation test. In the cyclic oxidation test, crack formation in the Al-rich brittle layer is accelerated due to the thermal shock and these cracks easily penetrate into substrate. Then evaporation of Ir from the substrate occurs, which results in the mass loss and poor oxidation resistance.

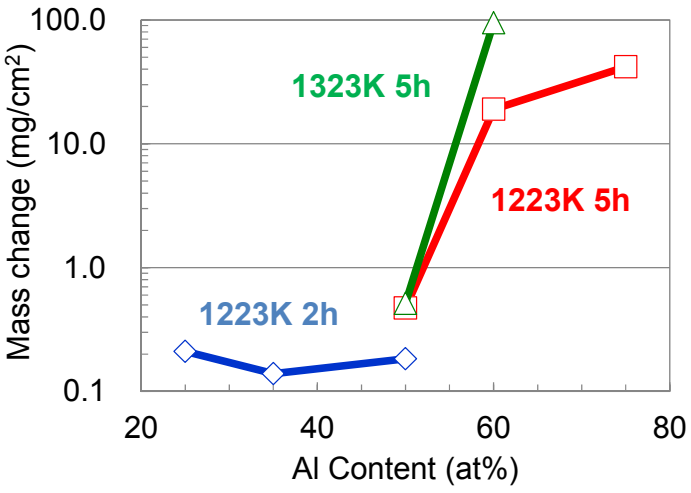

Fig. 5. The effects of Al-content in NiAl alloy powder, on the mass change and surface Al concentration by aluminizing treatment.

Since the crack formation in the brittle layer is accelerated under the thermal cycling condition, deterioration of oxidation resistance for both aluminized Ti-alloy and Ir was observed in the cyclic oxidation test. It is thus concluded that for the fabrication of coatings with good oxidation resistance, less brittle phases are preferable for the coating layer. In this sense, γ-TiAl coating for Ti-834 and β-IrAl coating for Ir with 10 to 50 μm could be desired. This study has not demonstrated such an ideal coating so far, nevertheless, controlling the partial pressure of AlClx can be done by precisely changing the Al content in the Ni-Al alloy powder. Further detailed investigation would enable us to form further better oxidation coatings on Ti and Ir alloys.

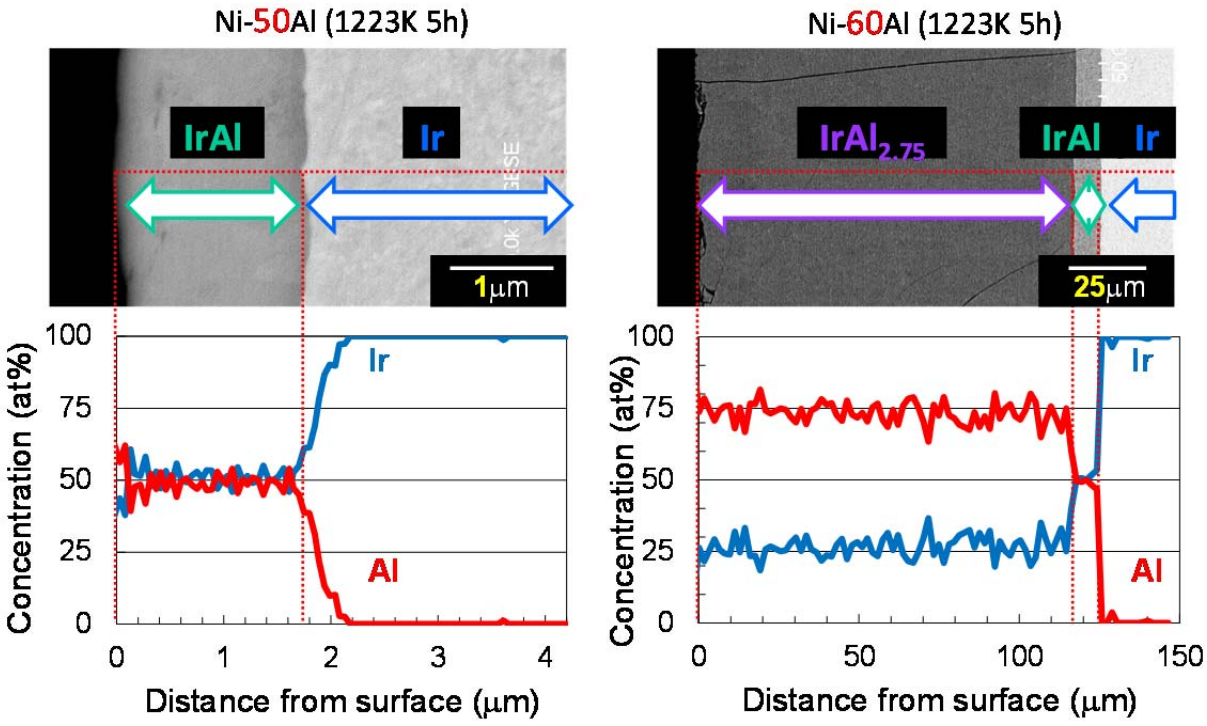

Fig. 6. Cross-sectional morphologies and corresponding concentration profiles of as-aluminized Ir, using (a) Ni-50at%Al and (b)Ni-60at% alloy powder

4. CONCLUSIONS

Pack aluminization of Ti-alloy and Ir was performed using powder mixture of Ni-xat%Al, Al_2O_3 and NH_4Cl, and following results were obtained.

i) Ni-Al alloy, with Al content ranging 25 to 75 at%, and Al_2O_3 mixed powder was successfully obtained by pre-heating powder mixture of pure Al, Ni and Al_2O_3. Phases obtained by this method were identical to those expected from the Ni-Al binary phase diagram.
ii) In the case of Ti-alloy, surface etching, displacement coating, and normal aluminized coating were observed, with increasing Al content in the Ni-Al alloy powder.
iii) In the case of Ir, drastic increase in mass was observed when the Al content in the Ni-Al alloy was 60 at % or more.
iv) For both cases, dramatic microstructure change was observed, from slow deposition with low Al content, to quick deposition with high Al content, which can be explained by Ti-Al and Ir-Al phase diagrams.
v) Controlling the Al content in Ni-Al alloy powder enables a controlled aluminizing process. Nevertheless, further study should be required to optimize the aluminizing process.

Acknowledgement
The authors would like to thank Prof. Makoto Nanko, Nagaoka University of Technology, Japan for advising the fabrication of Ni-Al alloy powder.

Mechanical and Physical Properties of Iron Oxides

Takuya Aiza[(1)], Yuki Kurashige[(2)] and Le Thung Dung [(1)] Makoto Nanko [(2,*)],

[(1)] Graduate School of Engineering, Nagaoka University of Technology, 1603-1, Kamitomioka, Nagaoka, Niigata 940-2188, JAPAN
[(2)] Department of Mechanical Engineering, Nagaoka University of Technology, 1603-1, Kamitomioka, Nagaoka, Niigata 940-2188, JAPAN

e-mail: nanko@mech.nagaokaut.ac.jp

1. INTRODUCTION

Oxidation resistance of heat-resistance alloys is given by external oxide scale formed on the alloys. Slow diffusivity of ions in oxide scales is very important for slow growth rate. As well, mechanical properties such as Young's modulus and fracture strength are also very important for stable growth of protective oxide scale. Cracking and spallation of oxide scale cause breakaway oxidation, which is defined as the acceleration of oxidation rate under certain conditions.
On the other hand, mechanical properties of oxide scale are important for understanding high-temperature deformation processing such as rolling and forging. In their deformation process, physical properties such as coefficient of thermal expansion and thermal conductivity are also necessary. Their processes are usually carried out at higher temperatures and shorter oxidation time than high-temperature oxidation for structural applications.
In order to simulate their deformation process numerically, mechanical and physical properties are required as a function of temperature. However, mechanical and physical properties of oxides that are formed on alloys as scales were poor, in particular, iron oxides at high temperatures. In this paper, some of mechanical and physical properties of iron oxides are evaluated by using sintered bodies.

2. EXPERIMENTAL,

A commercial Fe_2O_3 powder and Fe_3O_4 powders were used as starting materials. FeO was synthesized from powder mixture of Fe and Fe_3O_4 to form stoichiometric FeO. Powder compacts of Fe_2O_3 were prepared by cold isostatic pressing. Dense Fe_2O_3 bulks were sintered at 1000 and 1300°C for 3 h in air. Bulk Fe_3O_4 were prepared by using pulsed electric current sintering (PECS) at 1000°C for 5 min under 30 MPa in vacuum. Bulk FeO was sintered with PECS of the synthesized FeO powder compact mount in boron nitride powder with Fe_2O_3 compact as a buffer. The condition of PECS for FeO was 1000°C for 5 min under 30 MPa in vacuum.
High temperature hardness tests were conducted for FeO, Fe_3O_4 and Fe_2O_3. 3-point Bending tests were carried out for Fe_2O_3 in air. Thermal expansion of Fe_2O_3 was also investigated with the thermal mechanical analyzer.

3. RESULTS AND DISCUSSION

Fig. 1 shows Vickers hardness of sintered iron oxides as a function of temperature. Data on some steels were also plotted in Fig. 1. Fe_2O_3 is the hardest in the iron oxides. With increasing temperature, hardness of iron oxide decreases. Hardness of FeO is as small as hard steels.
Fig. 2 shows bending strength of sintered Fe_2O_3 as a function of temperature. The value of bending strength of bulk Fe_2O_3 with 5 μm in grain size is about 150 MPa and almost constant until 800°C. Sintered Fe_2O_3 with 500 μm in grain size, which sintered at 1300°C, has much lower in bending strength than that with 5 μm, which is sintered at 1000°C. Fracture strength of brittle materials is sensitive on surface defect. The largest defect leads to the largest stress concentration and results in the fracture strength. In the case of bulk Fe_2O_3 with 500 μm, the grain boundaries with loose bonding would be the defect to determine the bending strength. In oxide scales formed on alloys, the largest defect in scale is very important.
Fig. 3 shows CTE of bulk Fe_2O_3 as a function of temperature. The value of CTE on Fe_2O_3 has the peak around approximately 700°C. The value of CTE as a function of temperature is in good agreement with the data from lative parameter given by [1]. This peak of CTE on Fe_2O_3 agrees with Neel temperature of Fe_2O_3 (685°C).

4. CONCLUSION

Mechanical and physical properties of iron oxides were evaluated by bulk iron oxides prepared by sintering. Sintered Fe_2O_3 has the highest hardness even at high temperatures in the iron oxides. Sintered FeO shows the lowest hardness in the iron oxides and comparable with hard steels. With respect to high-temperature bending strength of sintered Fe_2O_3, the value is almost constant until 800°C. Coefficient of thermal expansion of Fe_2O_3 was measured at temperature ranging from room temperature to 1000°C in air. The value has a peak around approximately 700°C, which is the Neel temperature of Fe_2O_3 (680°C) [2].

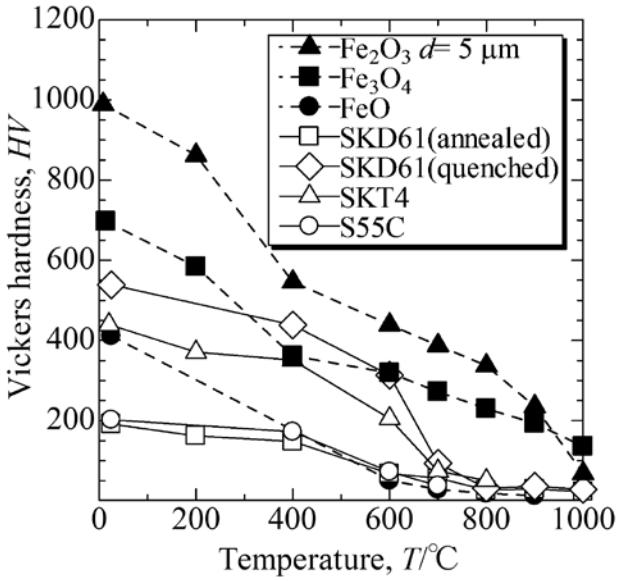

Fig. 1 High-temperature Vickers hardness of various iron oxides

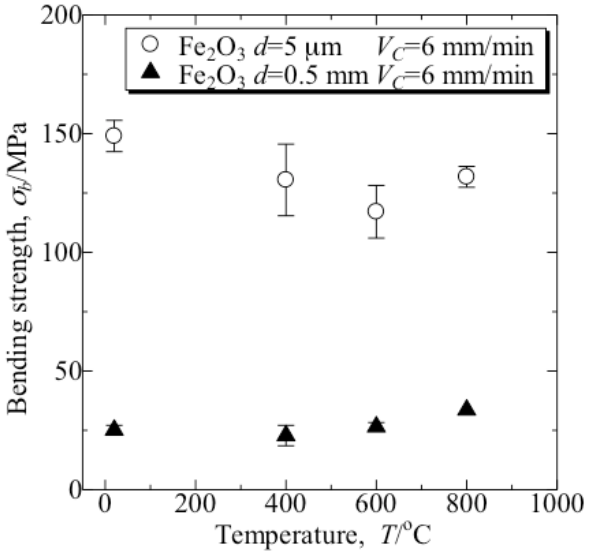

Fig. 2 High-temperature 3-point bending strength of Fe_2O_3

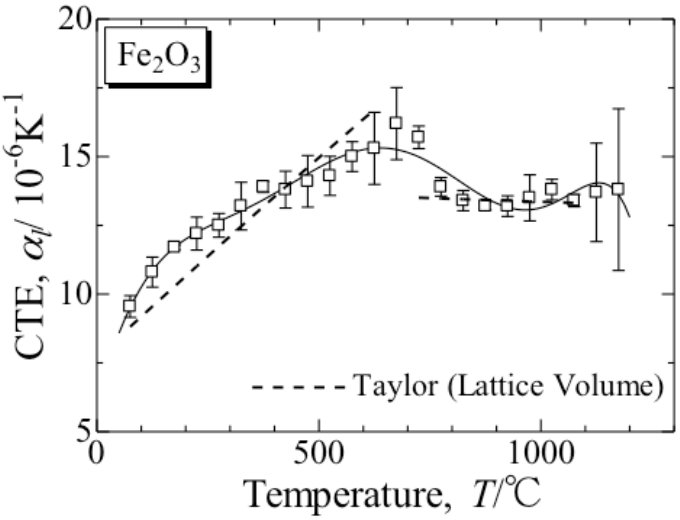

Fig. 3 Coefficient of thermal expansion of sintered Fe_2O_3 as a function of temperature.

Acknowledgements

The present study was supported partially by the Amada foundation.

References.

[1] Taylor, D., "Thermal expansion data: III Sesquioxides, M2O3, with the corundum and the A-, B- and C-M2O3 structures", *Trans. J. Br. Ceram.Soc.*, Vol. 83 (1984), pp. 92-98.

[2] Sun, Z., "A Highly Efficient Chemical Sensor Material for H_2S: α-Fe_2O_3 Nanotubes Fabricated Using Carbon Nanotube Templates", *Adv. Mater.*, Vol. 17, No. 24 (2005), pp. 2993-2997.

P51

Suppressing the selective oxidation during the recrystallization annealing of steel band for improved hot dip galvanizing: laboratory study

Sergiy V. Merzlikin [1*], A. Vogel [1], M. Auinger [1,2], D. Vogel [1] and M. Rohwerder [1,2]

[1] Max-Planck Institute for Iron Research, Max-Planck-Strasse 1, 40237 Dusseldorf, Germany
[2] Christian Doppler Laboratory for Diffusion and Segregation Mechanisms during Production of High Strength Steel Sheets

e-mail: s.merzlikin@mpie.de

1. INTRODUCTION

Modern advanced light high strength, high alloyed steel grades (AHSS) are widely used in automotive applications. One of the main demands for AHSS sheet steels for automotive applications is a good wettability with respect to zinc bath during hot dip galvanizing. Therefore, non-wettable inert oxides of the alloying elements on the surface of the steel formed during the recrystallization annealing could lead to a major problem.

One of the ways to avoid this is to create a thin iron oxide layer on the surface of the steel prior or during the recycling annealing, which will act as a barrier to selective oxidation and segregation of alloying element oxides at the surface. At the end of the recrystallization annealing step this iron oxide layer has to be further reduced to create an ideal surface for galvanizing. There are a number of approaches to form an iron oxide layer such as a sol-gel process or oxidation/reduction technique which uses a direct fired furnace for oxidation or a complete separation of heating and soaking steps inside a radial tube furnace. These techniques result in a rather thick (thicker than 0,2µm) iron oxide layers which are known to be brittle and therefore, affected to the so-called powdering, ruining the conditions for good zinc wettability.

The idea of the presented study is to create a iron oxide layer with a thickness of 0,05-0,1µm during the short time annealing in the whole heating / soaking section of the furnace using slightly oxidizing nitrogen-oxygen mixed atmospheres or atmospheres at controlled high dew points (DP=+17°C) and then finally, reduce iron oxide under reducing atmosphere between end of soaking and hot dip galvanizing. As the reactivity of oxygen with iron at 700°C – 800°C is very strong, it is easy to create and stabilize an oxide layer with a thickness ≤ 100 nm during the whole heating and soaking using oxygen injections. The strong reactivity of oxygen with iron could however result in inhomogeneous surface. Therefore, such high reactivity can be slowed down by utilizing N_2/H_2O gas composition which has a slight reducing component. Furthermore, the possibility to reduce the oxidation kinetic improving the control of the oxidation/reduction process by adding CO/CO_2 into the annealing atmosphere was tested. This is of interest especially for direct fired furnaces.

In order to do fulfil these tasks detailed studies on oxidation / reduction kinetics in oxygen and water containing atmospheres in dependence on temperature, time and steel composition have been made. To monitor the oxidation and reduction kinetics a high precision thermo-balance were used.

Reduction during soaking at high temperatures with high hydrogen (5 to 20%) concentrations was necessary for excellent zinc wetting results in sessile drop test.

2. EXPERIMENTAL

Thermogravimetric in-situ trials of the full oxidation/reduction cycle as well as isothermal annealing combined with the chemical analysis of the sample surface and subsurface region were carried out. This analysis was done with the help of FE-SEM using Zeiss Leo 1550 VP instrument; the thicknesses and composition of surface oxides were determined using Ar^+ depth profiling in XPS using PHI Quantum 2000 ESCA Scanning Microprobe with monochromated Al Kα as

primary X-ray source.

Thermogravimetry in different atmospheres was done using a novel set-up specially designed at MPIE [1]. Full control of gas flows during the thermogravimetric measurements inside a thermo-balance set-up and oxidation was made by precision mass flow controllers; the dew point temperatures of humid atmospheres were set up by purging the gas mixtures through the heatable (up to 100° C) lines into the water column and subsequently controlled by a cooled dew point mirror. As in-situ thermogravimetry inside an infrared furnace appeared to be strongly affected by the buoyancy effect (i.e. thermal drifts due to the heated gas regions in close vicinity of the sample's surface) in the region of high temperatures and at heating rates of more than 5 K s^{-1}, needed for emulation of the short-term annealing prior to hot-dip galvanizing), these measurements were carried out at normal and reduced pressure. The reaction chamber and the balance head were separated from the gas line with pressure reducing valves, enabling the adjustment (reducing) of the pressure inside the chamber using a membrane pump.

Zinc wetting measurements (the sessile drop method, determination of the zinc droplet's contact angle with the surface of the sample) were made on steel samples after oxidation in different atmospheres and following reduction step, using a modified zinc coater set-up described previously elsewhere [2]. As all wetting methods imperatively need a very dry atmosphere with dew point around –60°C and the oxygen concentrations less than 3 ppm, which is very different from the soaking atmosphere, the zinc coater set-up at MPIE has been modified to allow in-situ zinc wetting experiments inside one enclosed apparatus with precisely controlled atmosphere and heating regimes.

3. PRELIMINARY RESULTS AND DISCUSSION

Thermogravimetry and kinetics in humid atmospheres

In-situ thermogravimetric measurements inside an infrared furnace appeared to be strongly affected by the buoyancy effect (i.e. thermal drifts due to the heated gas regions in close vicinity of the sample's surface) in the region of high temperatures and at heating rates of more than 5 K s^{-1}, needed for emulation of the short-term annealing prior to hot-dip galvanizing). As a flow of inert gas typically makes up to 95% of the forming atmosphere inside the thermo-balance, it was possible to reduce nitrogen content by performing the thermogravimetry experiments at lower pressure (30 to 40 mbar), while keeping the same composition of the reacting species (oxygen and hydrogen). Dew point for humid oxidizing atmospheres (H_2/H_2O mixtures; DP=+17°C had to be set correspondingly to DP=+71.7°C for the lower pressure values. Experiments on pure iron and industrial steel samples showed a reduction of thermal buoyancy effect on the measurement by a factor of ten.

Experiments on industrial steel showed possible decarburization during the short term annealing, experiments in reducing and oxidizing atmospheres have been performed to differentiate between buoyancy and oxidation in the total mass signal.

Oxidation in CO/CO_2 containing atmospheres

In order to enable a direct comparison of the oxidation kinetics in humid atmospheres and carbon oxide mixtures, the CO / CO_2 ratio was chosen to realize the same oxygen partial pressure in the mixture as compared to the humid mixtures, which corresponds to the gas compositions 100 ppm CO_2 / 436 ppm CO and 100 ppm CO_2 / 272 ppm CO during the annealing step. After reaching a temperature of 800 °C, the flow of CO / CO_2 has been switched off to decrease the oxygen partial pressure and avoid oxidation during cooldown. All industrial samples were investigated by SEM and EDX to determine surface morphology and composition after selective oxidation. For the experiments at low oxygen partial pressures, a pure iron oxide surface could only be detected on low alloyed IF-steel samples, that resulted in a good zinc wetting behavior after the reduction step. Mainly iron oxide but mixed with some alloy contents on the surface after annealing and a very small amount of carbon (~3 at%) could be found on the interstitial free steels. All of these steels contain a very small amount of carbon, which seems to be beneficial for the formation of external iron oxides. Comparing this behavior to industrial samples, which contain a high amount of carbon (i.e. TRIP steels), high amounts of manganese, silicon and aluminum oxides were detected in the iron oxide layer. Under the given conditions, decarburization of the steel is thermodynamically possible, which may consume enough oxygen to allow the formation of more complex oxides at the surface, as alloying elements are more reactive than iron and forming oxides preferentially. The same temperature cycle performed at lower oxygen activities in gas mixture of 100 ppm CO_2 and 436 ppm of CO resulted in iron oxides and traces of manganese formed on the surface of IF-steel. No major changes of the surface oxide composition were

observed in this case for the high alloyed TRIP-steel concept. It has been shown by now that all used annealing atmospheres are basically capable for iron oxide formation according to the desired range of 100 nm.

Oxidation in O_2 containing atmospheres
Samples were oxidized in 100s up to 800 °C under nitrogen atmosphere with 250 ppm of oxygen and then reduced at 800°C in reducing atmosphere consisting of inert gas and 2,5% of hydrogen. Throughout all experiments, the thickness of the iron oxide layer tends to increase with increasing oxygen activity in the reaction gas. To deeper investigate the effect of the oxidation and reduction cycle of the temperature program, XPS-analyses have been made after the completed oxidation cycle and after finished reduction step as well. After the first cycle (oxidation), a thick iron oxide of up to more than 100 nm could be formed on the surface of the samples of the steel grades. Herein, high-alloyed steels (for example, TRIP) tend to oxidize preferentially and form mixed oxides on the surface. Especially manganese oxide forms, which easily forms stable mixtures with iron oxides under normal conditions. After the second cycle (reduction) it was possible to reduce the thickness of the surficial oxide layer successfully down to 10-20 nm. The remaining oxide comprises of iron and a high amount of alloying elements (mostly Mn but also Al and Si) which may diffuse towards the surface during the reduction step. Especially, a surficial segregation of Mn after annealing in Mn-rich steels at increasing partial pressure of oxygen could be clearly seen, it manifested itself also in a very poor wetting behavior.

Zinc wetting sessile drop experiments
Results of the wetting experiments for industrial samples after short term annealings in different atmospheres and after reduction indicated good wettability of IF steel grades, while high alloyed steels have a general problem in wetting behavior.

4. CONCLUSION

Kinetics of the processes taking place at the surface of the steel during the short time annealing could be seen with the help of the thermogravimetric measurements.

High alloyed steels (for example, TRIP) tend to form mixed oxides on the surface. Especially manganese oxide forms, which easily forms stable mixtures with iron oxides under normal conditions. Dual phase steels, Complex Phase steels and interstitial-free steels contain a significantly lower amount of alloying elements and hence show mostly iron oxide at the surface after reduction step. Nevertheless, manganese again seems to diffuse to the surface and forms stable mixed oxides with iron in these steel grades

Annealing time and oxygen partial pressure play the key role in oxide thickness evolution. An increasing dew point can additionally enhance oxide evolution and growth, whereas hydrogen serves as a reducing component and therefore hampers the oxide growth. The higher the amount of alloying elements the more oxygen partial pressure is needed to form iron oxides in a thickness of about 100 nm. In this context, the alloying elements have individual impacts: Aluminum and silicon hamper the iron oxide evolution rather strongly when compared to manganese and chromium. A deeper look on the surface chemistry after oxidation and reduction reveals that any incorporation of alloying elements, e.g. Mn, in the iron oxide layer could not be excluded completely. This leads to a remaining surface enrichment of stable oxides after the reduction step. Nevertheless, the amount of this remaining oxides seem to be rather small in some cases and planned in-situ galvanizing trials directly inside the annealing apparatus will give more sight into their impact on the coating quality.

Using high dew points during heating and soaking allow the formation of oxide layers in the desired thickness range. It could be further observed that hydrogen content in the atmosphere should be as low as possible to allow enough oxidation potential for an oxide growth in the desired thickness regime. It was found that high carbon contents, e.g. in dual phase or TRIP steels, hinder the growth of iron oxide. This could be explained by a parallel decarburization reaction which may act as a reducing side reaction to the oxide formation. When compared to the oxide formation in oxygen containing atmospheres, the thickness of iron oxide in water containing atmosphere seem to be lower at these levels of partial pressure. Beside the abovementioned decarburization reaction, water vapor needs additional step of dissociation before oxygen is available for the reaction of iron oxidation. Furthermore, during the dissociation of a water molecule hydrogen

is formed, which in turn could re-react with oxygen.

Acknowledgements:
The authors thank Research Programme of the Research Fund for Coal and Steel of European Commission for funding within the project RFCS-CT-2010-00012.
The authors would also like to thank Mr. Bernd Schönberger for his continuous efforts and support.

[1] Auinger M., Vogel A., Vogel D., Spiegel M and Rohwerder M., "A novel laboratory set-up for investigating surface and interface reactions during short term annealing cycles at high temperatures**"** Review of Scientific Instruments (2013) **84**, art. no. 085108
[2] Frenznick, S., Stratmann, M., Rohwerder, M., „A new advanced experimental setup for in-depth study of the interfacial reaction during reactive wetting" Review of Scientific Instruments, (2008) **79** (4), art. no. 043901

Reduction of iron oxide scale formed on steel surface by containing elements

Keita Ikeda [1,*] and Hikaru Okada [1]

[1] Technical Research & Development Bureau, Nippon Steel & Sumitomo Metal Corporation,
3 Hikari, Kashima, Ibaraki Prefecture, 314-0014 Japan

e-mail: ikeda.6p9.keita@jp.nssmc.com

1. INTRODUCTION,

In the continuous annealing process, iron oxide formed on the steel surface is reduced in the furnace during annealing in H_2 gas atmosphere. However, in silicon and manganese additional steel, the solute silicon and manganese in the steel may reduce iron oxide than H_2 gas atmosphere because these elements are baser than iron. In generally, it is known that silicon and manganese oxide on the surface of the steel causes some problems, such as wetting by molten zinc and deterioration of galvannealing reaction [1,2]. In order to solve these problems, it is necessary to clarify the behavior of oxidation and reduction in the annealing process. Thus, the effect of containing elements on reduction of iron oxide is investigated.

2. EXPERIMENTAL,

A pure iron sheet and a silicon and manganese additional steel sheet were used for the experiments. The analyzed compositions of the materials are shown in Table 1. Specimens were cut to square shapes with dimensions 20mm × 20mm. These specimens were heated in an infrared heating furnace at 673K for 30 sec. in the air and then they were heated up to 773-1073K for 60 sec. in N_2 gas atmosphere. After cooling, a degree of whiteness (L^* value) on the surfaces of the specimens were measured by a spectrophotometer. And element concentrations of the surface layer in the specimen were measured by GD-OES (Glow discharge optical emission spectrometry).

Table 1. Chemical compositions of material used. / wt%

	C	Si	Mn	P	S	Al	Fe
Pure iron	<0.01	-	-	-	-	-	99.99
Si-Mn steel	0.1	0.73	1.47	0.021	0.004	0.025	97.65

3. RESULTS AND DISCUSSION,

3-1 Changes of L^* value by heat treatment

The appearances of annealed specimens are shown in Fig. 1. While the appearance of pure iron does not change by any heat treatment condition, the appearance of the Si-Mn steel becomes white. After the oxidation of the Si-Mn steel at 673K in air, the surface of the specimen turned to black. This change suggests that oxide scale forms on the surface of the steel. After this specimen was heated successively at 1073K in N_2 gas atmosphere, the surface of the specimen becomes white. This result is assumed that iron oxide, which generated at the previous heat treatment, was reduced to iron.

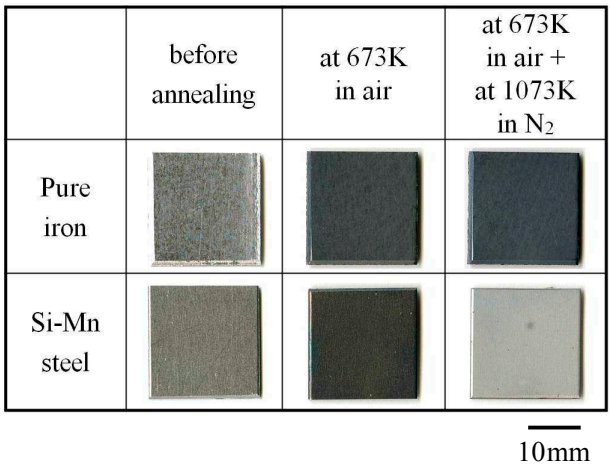

Fig. 1. Appearances of specimens.

These results are shown in Fig. 2. Figure 2 shows the relationship between heating temperature and whiteness (L^* value) on the surface of specimens. The L^* value is constant by any heating temperature in the case of pure iron. On the other hand, in the case of Si-Mn steel, the L^* value increases above around 800K. And this increase of the L^* value is saturated around 900K. This result is suggested that iron oxide was reduced in N_2 gas.

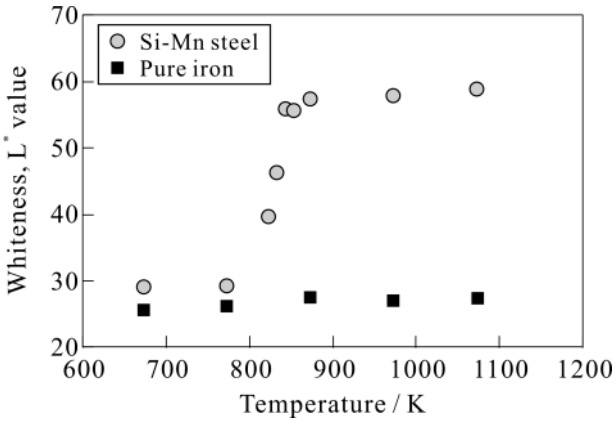

Fig. 2. The relationship between temperature and L^* value.

3-2 Reduction of iron oxide by solute Si, Mn,

In order to clarify the reduction of iron oxide in N_2 gas atmosphere, GD-OES was performed on the surfaces of heat treated specimens. The results of GD-OES in Si-Mn steel are shown in Fig. 3. After heat treated at 673K in air, there are oxygen sharp peak near the surface and Silicon peak inside from the surface of the steel (Fig. 3(a)). Therefore, it is thought that iron oxide scale formed on the surface by the heat treatment. Silicon oxide is also formed at the scale/steel interface. By contrast, the profile of the specimen heated at 1073K in N_2 gas after oxidation at 673K in air shows that silicon and manganese peaks at the surface layer appear and oxygen peak was decreased when compared with the result was heated at 673K in air (Fig. 3(b)). This result suggests that iron oxide formed at 673K oxidation was reduced by solute silicon and manganese in the steel.

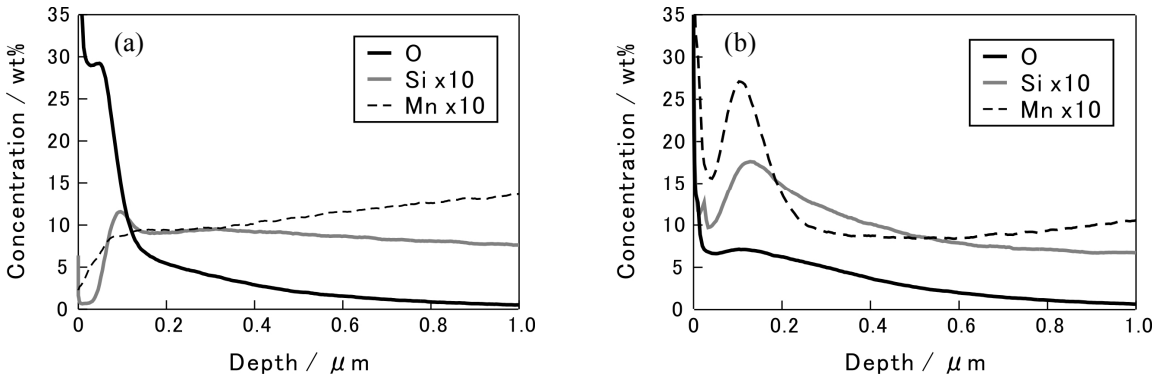

Fig. 3. Results of GD-OES in Si-Mn steel. (a) oxidized at 673K in air. (b) annealed at 1073K in N_2 after the oxidation at 673K.

4. CONCLUSION

In this study, the effect of containing alloying elements in the reduction of iron oxide is studied. It is suggested that in Si-Mn steel, iron oxide, which forms at lower temperature, was reduced at higher temperature under the inert atmosphere by solute elements of silicon and manganese.

References

[1] Y.Hirose, H.Togawa, and J.Sumitani: Tetsu-to-Hagane, 68(1982), 665.

[2] A.Nishimoto, J.Inagaki, and K.Nakaoka: Tetsu-to-Hagane, 68(1982), 1404.

Spallation behavior of oxide scale on stainless steels

Atsutaka Hayashi [1,*], Nobuhiko Hiraide [1], and Yoshiharu Inoue [2]

[1] Research & Development Center, Nippon Steel & Sumikin Stainless Steel Corporation,
Shimata 3434, Hikari, 743-8550, JAPAN
[2] Yawata Research & Development Laboratory Nippon Steel & Sumitomo Metal Corporation,
Tobihatacho 1-1, Tobata-ku, Kitakyushu, 804-8501, JAPAN

e-mail: hayashi.atsutaka@ns-sc.co.jp

1. INTRODUCTION

Stainless steels are used under heat cycle conditions as a heat resistant material. The resistance against high temperature oxidation is usually provided by the oxide scale of chromium or aluminum because they form by adhering compactly and grow slowly. The protective scale may be spalled during cooling under heat cycle conditions. If the scale is not protectively reproduced when it is spalled, iron oxide may grow rapidly and the protection is lost. When the scale of an upstream component is spalled, erosion may occur in a downstream component with flying scales and current may be blocked by deposited scales. Since it is necessary to control spallation practically, it is important to understand spallation behavior. Spallation behavior was often statically evaluated with the mass loss of the sample, the mass of spalled scale and the appearance of the sample after oxidation test. Spallation behavior was dynamically analyzed by the mass change of the sample measured by thermogravimetric analysis [1,2], elastic wave of spallation detected by acoustic emission analysis [3] and stress generated in the scale measured by Raman spectroscopic analysis during cooling [3]. However, there is no report on dynamic visual observation of spallation. In this study, we dynamically observed the spallation behavior of oxide scale on ferritic and austenitic stainless steel.

2. EXPERIMENTAL

In this study, 17Cr-Nb ferritic and 19Cr -14Ni-3Si (SUSXM15J1) austenitic stainless steel were used. Their chemical compositions are shown in Table.1. Cold-rolled and annealed ferritic stainless steel sheet of 1.5 mm thickness was produced in a laboratory. Austenitic stainless sheet of 0.8 mm thickness was produced commercially. The specimens of 40 mm length and 40 mm width were cut from the sheets. The surfaces of the specimens were prepared by wet polishing with emery paper up to #600.

Table 1. Chemical Compositions of Stainless Steel Samples Used in This Study (mass%)

	C	Si	Mn	Ni	Cr	Nb	N
Ferritic stainless steel	0.01	0.5	0.1	0.1	17	0.5	0.01
Austenitic stainless steel	0.05	3.3	0.8	14	19	0.0	0.01

A schematic view of the oxidation test furnace and video recording system during cooling is shown in Fig.1. A specimen was connected to the thermocouple by welding. It was placed horizontally in an alumina crucible and set at the oxidation position in the furnace and oxidized in air at 1273K for 100 hours. Then the crucible was withdrawn to the observation position and cooled to room temperature. The appearance of the specimen during cooling was recorded on video. The thermocouple was connected to the temperature recorder immediately after withdrawing the specimen.

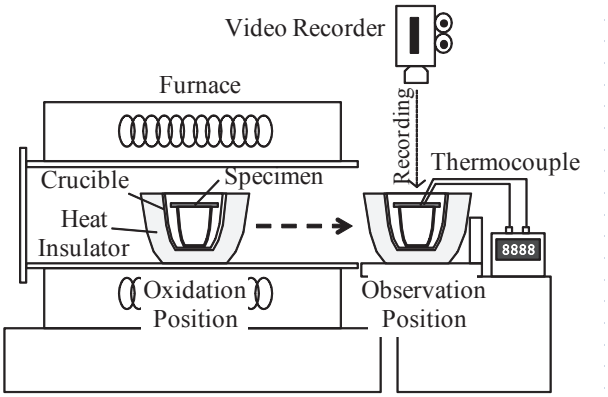

Fig. 1. Schematic view of oxidation test furnace and video recording system

Mass gain of the specimens and mass of the spalled scale were measured under different oxidation test from the observation. The specimens of 40 mm length and 20 mm width were cut from the sheets. The surfaces of the specimens were prepared by wet polishing with emery paper up to #600. The specimens were placed in alumina crucibles with 150 mm depth in order to co llect spalled scale. They were set in a muffle furnace and oxidized in air at 1273K for 100 hours.

Then the specimens were moved to other crucibles at 773K, 673K, 573K, 473K, 373K during cooling. The mass gains including spalled scale during cooling from 1273K to room temperature were measured. The mass of spalled scale during cooling from 1273K to each temperature at which the specimens moved to other crucibles and room temperature were measured.

3. RESULTS AND DISCUSSION

Temperature curves and appearances in every 100K of ferritic and austenitic stainless steel during cooling after oxidation in air at 1273K for 100 hours are shown in Fig.2. The white spots were spallation spots. Spallation spread according to cooling. Spallation did not spread combinatorially, but small spallation was generated in a scattered pattern. The reason for this is considered to be that the stress of the spallation part circumference was released by the dissipation of the next scale. The behavior of spallation spread for the ferritic stainless steel and that for the austenitic stainless steel was the same.

The start temperature of spallation was analyzed by detailed observation of the images that distinguish between spallation and contamination. Expanded images and the start temperature of the spallation are shown in Fig.3. The scale of the ferritic stainless steel began to spallation at 770K. The white spots of ferritic stainless steel above 770K were contamination since they appeared immediately after the start of cooling. The scale of the austenitic stainless steel began to spallation above 983K at which the temperature measurement was started. The energy required for spallation (γ_F) was estimated from the start temperature of spallation [1-3]. The growth stress during isothermal heating and the thermal stress during cooling was accumulated in the scale. In this study, the growth stress was disregarded since it was small. The thermal stress value (σ_{th}) was calculated by using Eq.(1) if it was accumulated equally to two axes.

$$\sigma_{th} = \frac{E_{ox}(-\Delta T)(\alpha_{me} - \alpha_{ox})}{(1 - \nu)(1 + 2(E_{ox} / E_{me})(\xi_{ox} / \xi_{me})} \qquad (1)$$

The symbols are defined as E : elastic modulus, ν: Poisson's ratio, α: thermal expansion coefficient,ξ: thickness, ΔT : amount of cooling temperature, and the subscript "*ox*" and "*me*" refer to oxide and metal, respectively. The strain energy in the scale (W^*) by this thermal stress was calculated by using Eq.(2).

$$W^* = \sigma_{th}^2 (1 - \nu) / Eox \qquad (2)$$

The strain energy (γ) in the interface of the scale and base

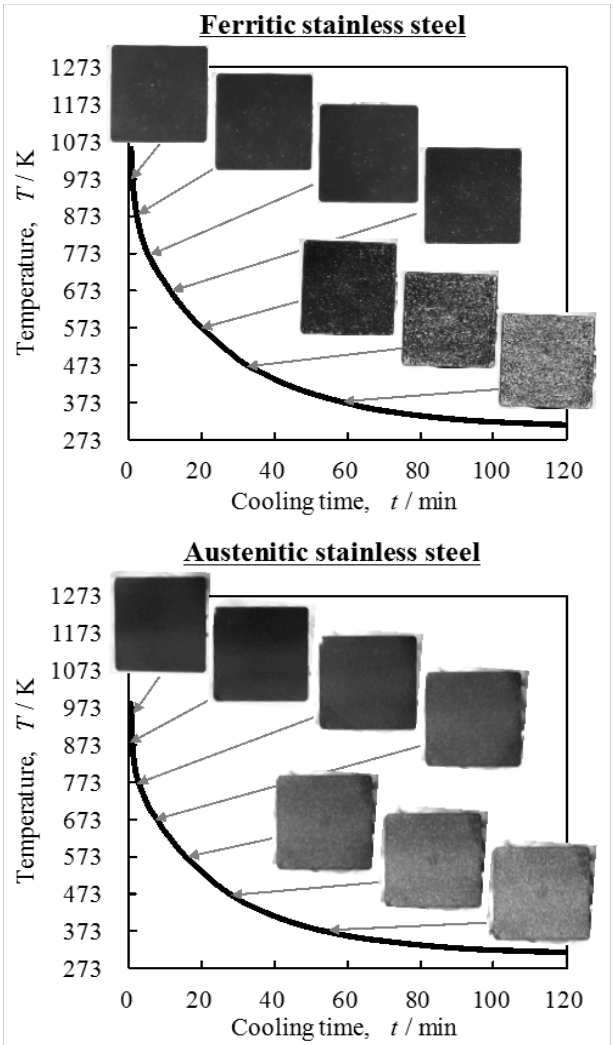

Fig. 2. Scale spallation behavior during cooling after oxidation in air at 1273K for 100 hours

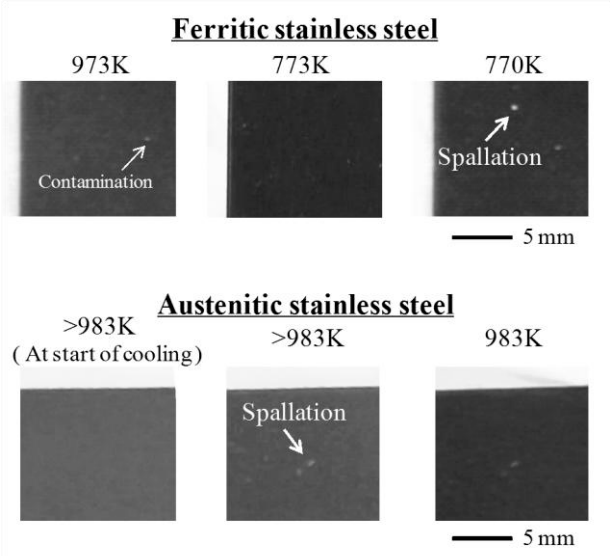

Fig. 3. Starting spallation during cooling after oxidation in air at 1273K for 100 hours

metal which was used for spallation was calculated by using Eq.(3).

$$\gamma \cdot \lambda^2 = f \cdot W^* \cdot \lambda^2 \cdot \xi_{ox} \qquad (3)$$

The symbols are defined as f : ratio of conversion to strain energy in the interface of the scale and base metal from it in scale, λ^2 : area of the interface of scale and base metal. γ_F is γ when ΔT is the amount to the temperature of starting spallation from the isothermal heating temperature. In this study, oxide scale was assumed to be Cr_2O_3 for ease of calculation because the oxide scale consisted of Cr_2O_3 inner layer and $(Mn,Cr)_3O_4$ outer layer and the inner layer was the main layer. The regression value from the literature elastic moduluses of Cr_2O_3 (196~321 GPa) [3-12] was used as E_{ox}. The elastic moduluses of 17Cr (91~214 GPa) and SUSXM15J1 (97~186 GPa) measured independently were used as E_{me}. The theoretical Poisson's ratio (0.3) was used as v. The thermal expansion coefficients of 17Cr (11.4~13.0×10-6) and SUSXM15J1 (19.1~22.5×10^{-6}) measured independently were used as α_{me}. The literature thermal expansion coefficient of Cr_2O_3 (8.5×10^{-6}) [4] was used as α_{ox}. The half of the specimen's thicknesses (0.75 mm, 0.4 mm) since scale is made at both sides of the surface of the specimen were used as ξ_{me}. The scale's thickness (8 μm, 8 μm) estimated from mass gains were used as ξ_{ox}. f was assumed 1. γ_F of this study and other studies [1-3] are shown in Table 2. γ_F of the ferritic stainless steel in this study was 10.3 J・m^{-2} and almost equivalent to the value in the other studies. The reason that the value was slightly larger might be that the detection of spallation in this study was macroscopic and the other studies could be detected microscopic spallation before macroscopic spallation. γ_F of the austenitic stainless steel in this study could not be estimated but it was less than 42 J・m^{-2}. If γ_F of the austenitic stainless steel was 4.1~10.3 J・m^{-2} , the start temperature of the spallation is 1177~1124K.

Table 2. Strain Energy Required for Spallation

	This study		Evans *et al.*	Nishiyama *et al.*
Scale	Cr_2O_3	Cr_2O_3	Cr_2O_3	Cr_2O_3
Base metal	17Cr-Nb	19Cr-14Ni-3Si	20Cr-25Ni-Nb	25Cr-20Ni
analysis	Visual Observation	Visual Observation	TG	AE, Raman
Scale thickness	8 μm	8 μm	0.6~4.8 μm	0.7 μm
γ_F	10.3 J・m^{-2}	<42 J・m^{-2}	5.0~6.0 J・m^{-2}	4.1 J・m^{-2}

※TG : Thermogravimetric Analysis, AE : Acoustic Emission Analysis, Raman : Raman Spectrometric Analysis

Spallation for the ferritic stainless steel spread dramatically at low temperature and the spallation unit for the ferritic stainless steel was larger than that for the austenitic stainless steel, as shown in Fig.2. The mass of spalled scale during cooling after oxidation in air at 1273K for 100 hours are shown in Fig.4. Spallation for the ferritic stainless steel increased dramatically below 473K and that for the austenitic stainless steel increased gently. The appearance of spalled scale during cooling after oxidation in air at 1273K for 100

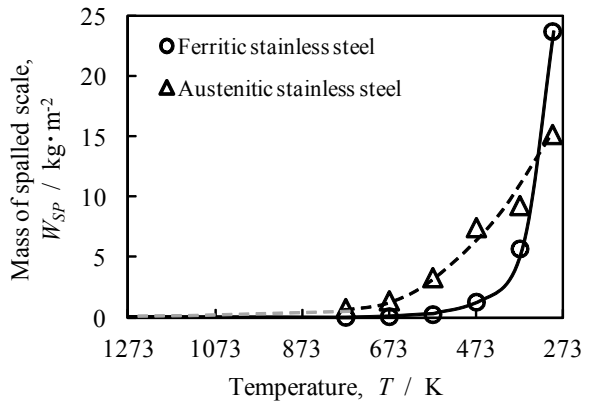

Fig. 4. Mass of spalled scale during cooling after oxidation in air at 1273K for 100 hours

Spalled scale of ferritic stainless steel during cooling from 1273K to room temperature

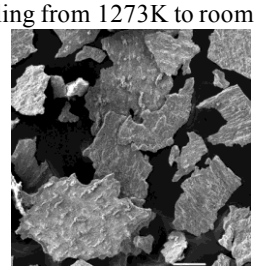

Spalled scale of austenitic stainless steel during cooling from 1273K to 673K

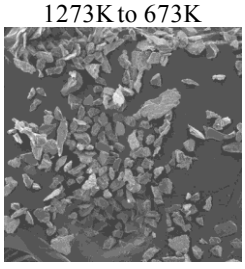

during cooling from 373K to room tempeatre

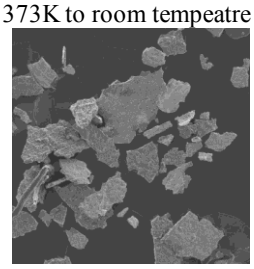

Fig. 5. Appearance of spalled scale during cooling after oxidation in air at 1273K for 100 hours

hours is shown in Fig.5. Many of spalled scales for the ferritic stainless steel during cooling from 1273K to room temperature were larger than 100 μm. Many of spalled scales for the austenitic stainless steel during cooling 1273K to 673K were smaller than 100 μm and several of those during cooling from 373K to room temperature were larger than 100μm. These reasons are considered as follows. Spallation increases dramatically and spalled scales becomes large, so that excess energy of γ becomes large when γ is accumulated more than γ_F until spallation. The accumulation behavior of γ during cooling in case there is no spallation is shown in Fig.6. The accumulation rate of γ for the ferritic stainless steel is later than that for the austenitic stainless steel. Therefore, γ for the ferritic stainless steel is easily accumulated more than γ_F. γ for the austenitic stainless steel is easily released by fine spallation with rapidly. Although γ decreases by previous spallation of the next scale, excess energy of γ for spallation at low temperature is larger than that for spallation at high temperature.

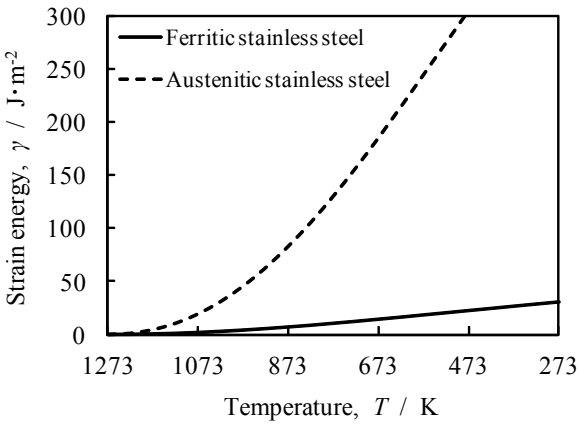

Fig. 6. Strain energy accumulated in the interface of the scale and base metal during cooling after oxidation in air at 1273K for 100 hours in case there is no spallaion

4. CONCLUSION

The spallation behavior of oxide scale on the ferritic stainless steel and the austenitic stainless steel during cooling after oxidation in air at 1273K for 100 hours were investigated by dynamic visual observation. The spallation spread as small spallation which was generated in a scattered pattern. The reason is considered that spallation releases the stress of the circumference. The spallation for the ferritic stainless steel started at 770K and that for the austenitic stainless steel started immediately after cooling. The energy required for spallation (γ_F) for the ferritic stainless steel was estimated to be 10.3 $J \cdot m^{-2}$ and that for the austenitic stainless steel was less than 42 $J \cdot m^{-2}$. The spallation unit size of the ferritic stainless steel was larger than that of the austenitic stainless steel. The reason for this is considered to be that excess energy of γ accumulated more than γ_F until spallation for the ferritic stainless steel is larger than that for the austenitic stainless steel since the ferritice stainless steel accumulates γ slowly. Dynamic visual observation is one of the effective methods that understand the spallation behavior of oxide scale on stainless steels.

References

[1] H.E.Evans and R.C.Lobb : Corros. Sci., Vol.24 (1984), pp.209-222.
[2] H.E.Evans : Mater. Sci. Technol., Vol.4 (1988), pp.415-420.
[3] Y.Nishiyama, K.Kitamura, T.Kudo, N.Otsuka : J.Japan Inst.Met.Mater., Vol.71 (2007), pp.55-60.
[4] J.Robertson and M.I.Manning : Mater. Sci. Technol., Vol.6 (1990), p.81.
[5] J.R.Nicholls, D.J.Hall and P.F.Tortorelli : Mechanical Properties of Protective Oxide Scales, Special Issue Mater. High Temp., Vol.12 (1994), p.141.
[6] S.Venkataraman, D.L.Kohlstedt and W.W.Gerberich : Thin Solid Films, Vol.223 (1993), p.269.
[7] P.E.Tortorelli : Proc. 3rd Int. Symp. High Temp. Corrosion and Protection of Materials, Vol.3, No.2 (1993), p.943.
[8] P.Hancock and R.C.Hurst : Adv. Corros. Sci. Technol., Vol.4 (1974), p.1.
[9] J.B.Johnson, J.R.Nicholls, R.C.Hurst and P.Hancock : Corros. Sci., Vol.18 (1978), p.527.
[10] R.C.Hurst and P.Hancock : Werkst. u. Korros., Vol.23 (1972), pp.773-776.
[11] P.Hancock : Proc. Materials. Science Symposium on Stress Effects and the oxidation of Metal, (1974).
[12] D.Zhu, J.H.Stout, J.C.Nelson, and D.A.Shores : Mater. Sci. Forum No.251-254 (1997), pp.437-444

Effect of Ni addition on the Formation of SiC-$ZrSiO_4$ Porous Composites and Thermal Cyclic Oxidation Behavior

Kaori KOBIYAMA [(1,*)], Takaya AKASHI[(2)]

[(1)] Graduate School of Science and Engineering, Hosei University, Tokyo, 184-8584, JAPAN
[(2)] Faculty of Bioscience and Applied Chemistry, Hosei University, Tokyo, 184-8584, JAPAN

e-mail: akashi@hosei.ac.jp

1. INTRODUCTION

Silicon Carbide (SiC) and SiC-based ceramic composites have been proposed for use as high-temperature structural materials such as diesel particulate filter (DRF) because of its excellent thermal shock resistance and high-temperature oxidation resistance [1]. The oxidation of SiC, however, is promoted at higher temperature than 1000 °C at oxidizing atmosphere by the following reaction [2],

$$SiC(s) + 3/2O_2(g) \rightarrow SiO_2(s) + CO(g) .$$

The protective SiO_2 layer formed by the oxidation transforms a cristobalite phase from a glass phase. Upon heating and cooling, the cristobalite phase of SiO_2 causes cracking due to transition between low and high-temperature phases, resulting in the degradation of SiC materials.

To prevent the cracking of protective layer on SiC materials, the formation of $ZrSiO_4$ layer at the boundary of SiC grains is promising because of the thermal stability of $ZrSiO_4$ without phase transition at temperatures less than 1676 °C. One of the obstacles to using this method is an extremely slow rate of the $ZrSiO_4$ formation by solid state reaction even at 1500 °C. The purposes of this study are to prepare the SiC-$ZrSiO_4$ porous composite from core/shell particle of SiC and $ZrSiO_4$ as shown Fig. 1, to investigate the effect of Ni addition on the formation of $ZrSiO_4$, and to evaluate therrmal cyclic oxidation resistance of the SiC-$ZrSiO_4$ porous composite in the atomosphere containing oxygen.

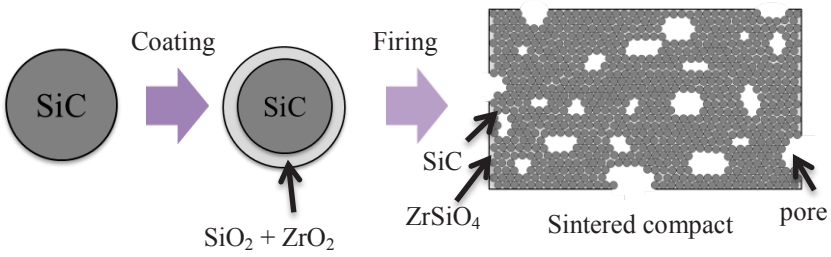

Fig. 1. Schematic illustration of procedure to prepare the SiC-$ZrSiO_4$ porous composite.

2. EXPERIMENTAL

Silicon tetraethoxide (TEOS) and Zirconium tetra-n-butoxide (n-butyl alcohol solution, assay: 28.8 % ZrO_2) were prepared as the sources of SiO_2 and ZrO_2, respectively. These reagents and 2-methoxyethanol with $Ni(NO_3)_2 \cdot 6H_2O$ were mixed in an equal molar ratio of Si and Zr in Ar, and stirred for 1 h. SiC powder (1 μm) was added in the solution, and dried by a rotary evaporator at 65 °C for 1 h. For comparison, the powder without $Ni(NO_3)_2 \cdot 6H_2O$ was also prepared in the same procedure. Two kinds of powder thus obtained and SiC powder were mixed with PEG (polyethylene glycol, particle diameter: 100 μm) and pressed with 36 MPa to form powder compacts. After sintering the compacts at 1500 °C for 3 h, the three sintered specimens were characterized by X-ray diffraction, scanning electron microscope, transmission electron microscope, X-ray photoelectron spectroscopy, Brinell hardness test, and thermogravimetry. Relative densities were determined by Archimedes method. The surface areas of

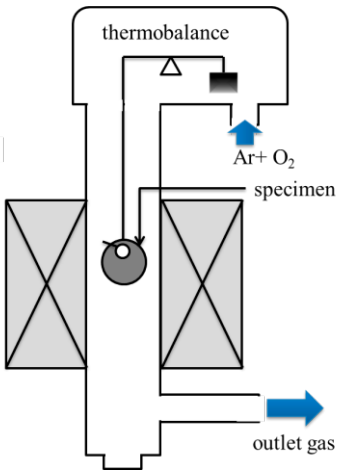

Fig. 2. Schematic of microbalance apparatus for thermal cyclic oxidation.

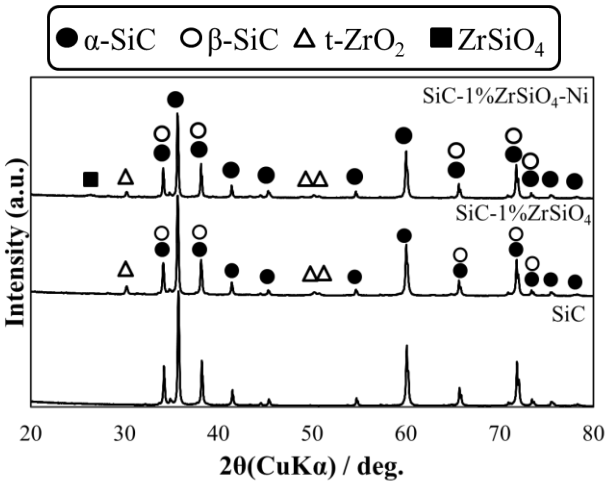

Fig. 3. X-ray diffraction patterns of sintered SiC composites at 1500 °C for 1h.

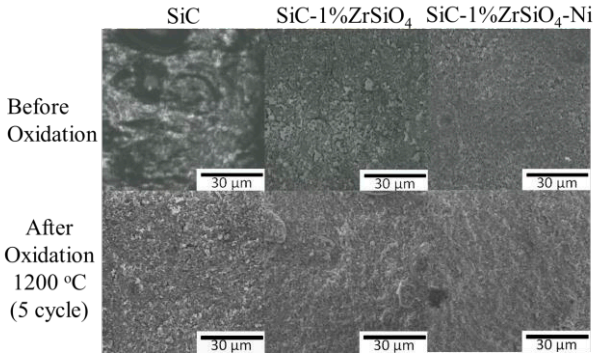

Fig. 4. SEM images of SiC composites before and after the 5 thermal cyclic oxidation at 1200 °C for 18 ks.

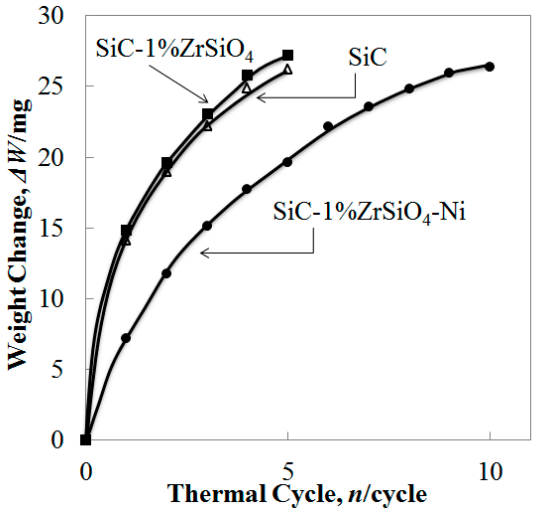

Fig. 5. The weight changes of SiC composites as a function of the thermal cycle of a maximum temperature of 1200 °C for 3.6 ks.

the sintered compacts were measured by BET (Brunauer, Emmet and Teller) analysis.

Fig. 2 shows a microbalance apparatus for therrmal cyclic oxidation studies. To investigate thermal cyclic oxidation resistance, the sintered SiC composites were oxidized at a maximum temperature of 1200 °C for 3.6 ks at a heating/cooling rate of 20 °C /s in Ar - 20 % O_2 with a flow rate of 50 sccm. The oxidized samples were characterized by X-ray diffraction and scanning electron microscope.

3. RESULTS AND DISCUSSION

Fig. 3 shows X-ray diffraction patterns of the three sintered specimens. It explains that $ZrSiO_4$ was formed only for SiC-1%$ZrSiO_4$-Ni, which implies that Ni promotes the formation of $ZrSiO_4$. The effect of Ni addition was verified by XPS analysis for the sintered SiC composites. The relative densities of three porous sintered composites were all approximately similar values, and the specific surface area of SiC, SiC-1%$ZrSiO_4$ and SiC-1%$ZrSiO_4$-Ni compacts were 4.56 m^2/g, 4.98 m^2/g and 4.07 m^2/g, respectively. The specific surface area of dense SiC was 7.42×10^{-4} m^2/g, which was 5490 times smaller than the porous SiC-1%$ZrSiO_4$-Ni composite. The Brinell hardness of SiC and SiC-1%$ZrSiO_4$-Ni porous compacts were 0.28 HBW 3/1 and 36 HBW 3/1. SiC-1%$ZrSiO_4$ porous composite was too brittle to measure. These results indicate that the sintering of SiC composite was promoted by Ni addition.

Fig. 4 presents SEM images of each sintered SiC composites before and after the 5 thermal cyclic oxidation at a maximum temperature of 1200 °C. As shown in the SEM images of the specimens after the 5 thermal cyclic oxidation, the porous structure was sustained on the surface of these composites even after the oxidation.

The weight change of the SiC composites oxidized during 10 thermal cyclic oxidation obeyed the parabolic rate kinetics, as shown in Fig. 5. The weight change of the SiC-1%$ZrSiO_4$-Ni composite was smallest of all, which manifested that the oxidation resistance of SiC was improved by the formation of $ZrSiO_4$ around the SiC grains.

4. CONCLUSION

Addition of Ni promotes the formation of $ZrSiO_4$ and sintering of SiC in preparation of SiC-$ZrSiO_4$ porous composites by pressureless-sintering. The SiC-$ZrSiO_4$-Ni porous composite had 5490 times greater specific surface area than that of dense SiC, and had greater thermal cyclic oxidation resistance than that of the sintered SiC porous sample at a maximum temperature of 1200 °C in the atmosphere containing oxygen.

References

[1] N.S.Jacobson : *J. Am. Ceram. Soc.*, **76**, 3 (1993)
[2] E. J. Opila: *J. Am. Ceram. Soc.*, **82**[3] (1999) 625-36.

Preparation of Carbon Composite Bricks and its Interfacial Reaction Behavior with Hot Metal and Slag

Jiao Ke-xin[1,2)], Zhang Jian-liang[1,2)], Liu Zheng-jian [1,2)] , Hou Xin-mei[1,2)], Liu Yan-xiang[1,2※)], Zhao Yong-an[3)]

(1.School of Metallurgical and Ecological Engineering, University of Science and Technology Beijing, Beijing 100083, China
2.State Key Laboratory of Advanced Metallurgy, University of Science and Technology Beijing, Beijing 100083, China.)
3 Henan Winna Industrial group Co. LId, Gongyi 451250, China)

e-mail: jiaokexin_ustb@126.com

1. INTRODUCTION

Hearth was an important part of blast furnace. Hearth security had become a limit key link of one generation blast furnace service life[1-3]. The traditional hearth refractory materials mainly included carbon brick and ceramic cup[4-5]. However, both of them had disadvantages. For example, the anti-hot metal erosion property of carbon was very pour, and the heat-conducting property of ceramic cup was very low. These would cause the damage of hearth structural and the service life of blast furnace[6-7].

The carbon composite bricks were developed by introducing the carbon composition to the oxide materials reasonably basing on the existing blast furnace materials and the production and use of carbon brick and ceramic cup experience. The behavior and interfaces between carbon composite bricks and iron slag were analyzed, which can provide guidance for the application of carbon composite bricks in hearth bottom.

2. EXPERIMENTAL,

2.1 The preparation of carbon composite bricks

A series of corundum based microporous refractories were prepared via high-temperature roasting with some materials such as aluminum oxide and fine calcined bauxite and natural flake graphite. Si power was added as additive. The grain and the binder were mixed and grinded with some water. Some powder additives were added. The mixed materials were not compression molded until the materials had better formability. Then the bricks were dried and roasted under the reducing atmosphere through high temperature. The main properties of raw materials for carbon composite brick production were shown in table 1.

Tab. 1 The main raw materials and chemical performances of carbon composite bricks

material	granularity	Al_2O_3 /%	Fe_2O_3 /%	density /g/cm^3
dense fused corundum	1-5mm	≥98.5	≤0.5	≥3.9
natural flake graphite	0.15mm	C ≥95%	H_2O ≤0.5%	≥1.9
carbon black	-1μm	C ≥98%		
phenolic resin		C≥78%; viscosity 40-60pa•s		

2.2 Experimental installation

The element composition, mineral composition and microstructure were analyzed using XRF (Shimadzu XRF - 1800, Japan), XRD (Shimadzu XRD - 1800, Japan) and SEM EDS (JEOL JMS - 5600 - lv, Japan) for the sampled bond. And the phase diagram of bond phase was analyzed by using Factsage (Thermochemical Database System) software.

3. RESULTS AND DISCUSSION,

3.1 Microscopic analysis and performance indicators of carbon composite bricks

The chemical component of the carbon composite bricks we shown in Table 1.

Tab.1 The chemical component of the carbon composite bricks

chemical component	Al_2O_3	C	SiO_2	TiO_2	Fe_2O_3	Na_2O	K_2O	SiC
content, %	73.05	10.2	8.18	1.2	0.9	0.29	0.11	6.0

The key properties of the carbon composite bricks were shown in Table 2.

Tab. 2 The property of the carbon composite bricks

Al_2O_3	Volume	Apparent	Molten iron	Slag erosion	<1μm	Thermal conductivity

	density	porosity	dissolution index	resistance	Pore volume	Room temperature	300℃	600℃	800℃
%	g/cm^3	%	%	%	%		W/(m·K)		
74.32	2.94	12.9	1.3	2.8	88.8	18.16	16.04	14.81	13.37

X-ray diffraction pattern of the carbon composite bricks was shown in Figure 1.

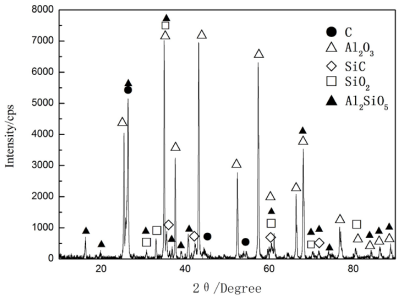

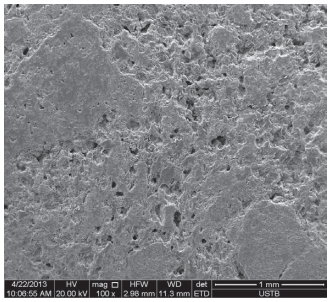

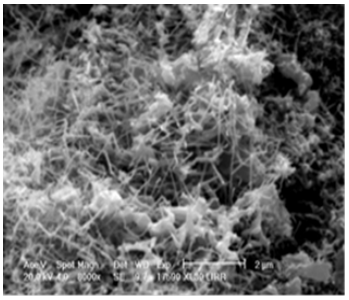

Fig.1 X-ray diffraction of carbon composite bricks **Fig.2 SEM of carbon composite bricks**

SEM of the carbon composite bricks was shown in Figure 2. It can be seen from the diagram that carbon composite bricks were sintered very well. The microporous degree was very high. The average pore size was small. The microporous evenly distributed in the matrix relatively. The fibrous silicon carbide was generated in situ and filled the gap, which made the carbon composite bricks much more dense microstructure.

3.2 Anti-slag erosion property of carbon composite bricks

The chemical composition of blast furnace slag used in the experiment was shown as below.

Tab.4 The chemical composition of blast furnace slag

SiO_2	CaO	MgO	FeO	Al_2O_3	TiO_2
32.66	36.89	11.17	0.32	15.02	0.75

Figure 3 was SEM-EDS of carbon composite bricks anti-slag erosion experiment. There was good wettability between the slag and carbon composite bricks. Slag reacted with alumina at the interaction of carbon composite bricks and penetrated gradually to the interior of the carbon composite bricks.

However, in the actual process, with the invasion of the molten slag and chemical reaction, the content of alumina in slag was increased. A part of them precipitated in the form of magnesium aluminate spinel. There still existed a lot of alumina particles in interfacial reaction layer. Therefore, the viscosity of alumina slag mixed with a large amount of solid particle phase increased significantly. Slag was difficult to further erode carbon composite bricks under the condition of hearth bottom cooling. A layer of viscous phase formed in the reaction interface layer, which isolated from the slag and carbon composite bricks and carbon composite bricks were effectively protected.

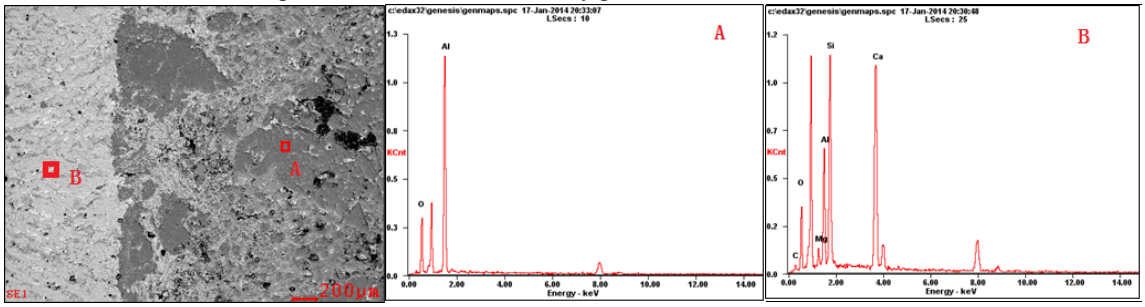

Fig.3 SEM-EDS of carbon composite bricks anti-slag erosion experiment

3.3 Anti-hot metal erosion property of carbon composite bricks

Figure 4 was SEM-EDS of carbon composite bricks anti-hot metal erosion experiment. There was no wetting between the carbon composite bricks and molten iron. There was an obvious phenomenon of carbon enrichment in contact with the molten iron and carbon composite bricks, where the alumina particles were small and diffused in the carbon matrix. The erosion degree of carbon composite bricks was small. That was for the following reasons. Carbon composite bricks consisted of high alumina content which was not wet by hot metal. When hot metal in contact with carbon composite bricks, the contact area that of carbon in carbon composite bricks and hot metal were small. Therefore, hot metal was difficult to erode carbon composite bricks. Carbon in carbon composite bricks contacted with hot metal continuous exchanged with carbon from hot metal. With the loss of carbon, the carbon

composite bricks formed a decarburization layer and naked alumina in the hot surface. Carbon composite bricks had high porosity. The average pore diameter was 0.238 microns. Some research showed that [8], the molten iron can be difficult to erode the brick lining when the refractory porosity was less than 1 microns.

In practical production, a transition layer can form in the interface between hot metal and carbon composite bricks because of the effect of cooling. The viscosity of the layer was big because of the existence of Al_2O_3 particles and solid graphite carbon. The layer isolated from the direct contact of hot metal and carbon composite bricks and effectively guaranteed the safety of carbon composite bricks.

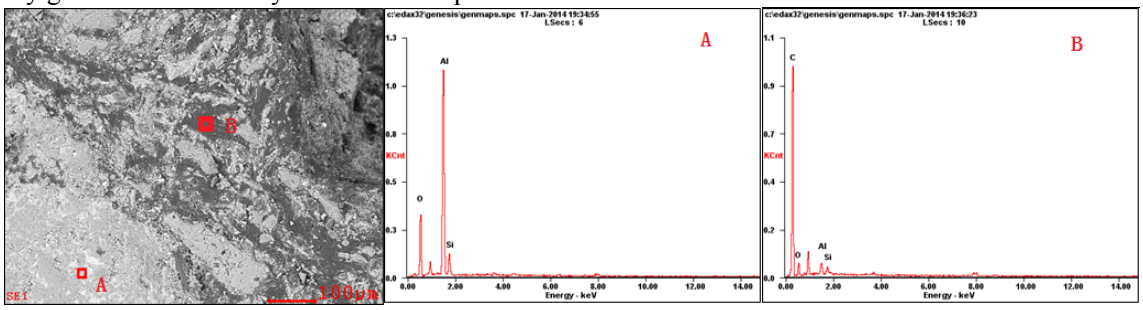

Fig.4 SEM-EDS of carbon composite bricks anti-hot metal erosion experiment

4. CONCLUSION,

(1) A series of corundum based microporous refractories were prepared via high-temperature roasting with some material such as aluminum oxide and fine calcined bauxite and natural flake graphite. Si power was added as additive. The product had excellent property.

(2) Slag and molten iron contact were with refractory and chemical reactions were occurred. However, the viscosity slag was formed on the surface of carbon composite bricks, due to the high melting point phase such as the carbon, magnesium aluminate spinel and alumina was formed. Then the material diffusion velocity was reduced, and refractory erosion rate decreased.

(3) The advantages of the traditional carbon brick and ceramic cup material were retained in the carbon composite bricks. It was suitable for the conditions of blast furnace hearth bottom for the high thermal conductivity and corrosion resistance to slag iron.

References.

[1] M.E.Barbes, Fernandez,E. Marinas.G. Design of Blast furnace crucibles by means of the Nodal Wear Model[J]. ISIJ Inter.2008,48(2),134-140.

[2] LIU Zheng-jian, ZHANG Jian-liang, YANG Tian-jun. Study on the formation mechanism of viscous layer in blast furnace hearth[J]. Asia Steel 2012.

[3] ZHANG Shou Rong. Some questions about the longevity of blast furnace[J]. The ironmaking production technology conference. Wuxi, 2012.

[4] Zheng-jian LIU, Jian-liang ZHANG, Hai-bin ZUO. Tian-jun YANG. Recent Progress on Long Service Life Design of Chinese Blast Furnace Hearth[J]. ISIJ International, 52 (10), 2012:1713–1723.

[5] TANG Qing Hua, WANG Xiao Liu. The blast furnace hearth bottom burn-out accident handling and strive to improve the life[J]. The ironmaking production technology conference. Wuxi, 2012.

[6] TANG Qing Hua. Efforts to improve the service life of blast furnace hearth bottom[J]. The national seminar of bf longevity and high blast temperature technology. Beijing, 2012.

[7] Song Musen,Yu Zhongjie, Xiong Yafei. Investigation on the lining erosion of No.5 BF in Wuhan Iron and Steel Corporation[J]. Ironmaking.2008,27(4):1-10.

[8] Xiang Zhongyong, Wang Xiaoliu. BF design-the theory and the practice of ironmaking process[M].Beijing: Metallurgical Industry Press，2007：330-393．

Contribution of high-temperature oxidation of self-healing agent for strength recovery behavior of self-healing ceramics

Shunsuke Yoshioka [1,*], Wataru Nakao [2]

[1] Graduate School of Engineering, Yokohama National University, 79-5 Tokiwadai, Hodogaya-ku, Yokohama, 240-8501, JAPAN

[2] Faculty of Engineering, Yokohama National University, 79-5 Tokiwadai, Hodogaya-ku, Yokohama, 240-8501, JAPAN

e-mail: yoshioka-shunsuke-tg@ynu.ac.jp

1. INTRODUCTION

Oxidation Induced Self-healing Ceramic (Oi-SHC) can improve brittleness due to self-healing and is expected apply to the high temperature use structural materials. Self-healing of Oi-SHC is induced by the oxidation of non-oxide self-healing agent as shown in Fig. 1, so that self-healing phenomena is strongly influenced by surrounding temperature. On the other hand, there is huge variety of high temperature structural material and each has own operation temperature. Therefore, it is critical issue that clarifying the relationship between oxidation behavior of self-healing agent and strength recovery behavior of self-healing ceramics as a function of temperature.

The present authors investigated the oxidation behavior of several self-healing agents by simple thermal analysis, TG-DTA. On the other hand, the strength recovery behavior of Oi-SHC which embedded the agents was investigated by the combination of heat treatment and three-point bending test. Compering those results, the relationship between oxidation behavior of self-healing agent and strength recovery behavior of self-healing ceramics was quantified.

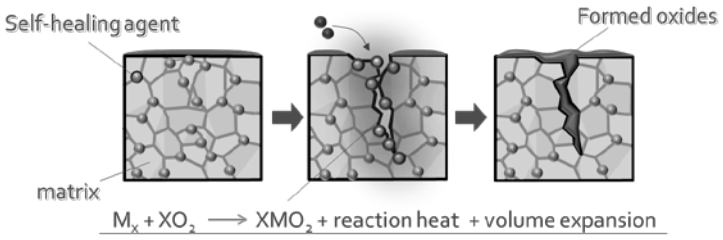

Fig.1 self-healing mechanism of Oi-SHC

2. MATERIAL SELECTION

Mullite was selected as a matrix for Oi-SHC in this study because mullite has suitable properties for high-temperature structural ceramics, such as high melting point, light weight, high creep resistance, low thermal expansion coefficient and low oxygen diffusion coefficient.

On the other hand, silicon based binary alloys were chosen as candidates because the alloys formed silica which is anticipated to bond strongly with mullite. Furthermore, as shown in Table 1, several silicon based binary alloys were chosen as eligible self-healing agent for mullite based Oi-SHC in the previous study [1].

In this study, oxidation behavior of the candidates was investigated by TG-DTA. Subsequently, the strength recovery behavior of Oi-SHC which embedded the agents was investigated.

Table 1 several silicon based binary alloys which chosen as eligible self-healing agent for mullite based Oi-SHC

Element	Clarke number	Oxidation stability	Phase	Melting point [°C]	Reaction enthalpy [kJ/mol-O_2]	Volume expansion [%]
Fe	4.7	○	$FeSi_2$	1410	705	279
Ti	0.46	○	Ti_5Si_3	1920	855	217
			TiSi	1570	858.6	232
			$TiSi_2$	1480	873.7	252
Mn	0.09	○	MnSi	1275	675.9	278
Cr	0.02	○	Cr_3Si	1770	758.3	233
			CrSi	1413	801.7	251
			$CrSi_2$	1490	827.7	276
V	0.015	○	V_5Si_3	2010	655.0	321
			VSi_2	1677	743.5	314

3. EXPERIMENTAL

A TG/DTA analyzer was used for investigating the oxidation behavior of self-healing agents in the present study. Each about 20mg of Si-based alloy powders and mullite powders were put into alumina cell and heated up to 1450 °C in dried air with 10 ml/min. The values of heating rate β were 5, 10, 20, 40 °C/min.

Mullite matrix composite containing 15 vol% Si-based alloys as a self-healing agent was prepared. Mullite and agent powders were mixed well at the volume ratio of 85 vol% and 15 vol%. After drying, the powders was formed to the rectangular plate (35×45×6 mm^3) by using an uniaxial pressing at 100N and cold isostatic pressing (CIP) at 200MPa. The formed powders were sintered at 1450 °C for 10h in Ar. Subsequently, the sintered plate was cut into $4\times3\times22$ mm^3 rectangular bar specimens. Moreover, the specimens were healed at temperatures from 400 °C to 1200 °C for 1 and 10 h after cracked at the center of the specimens by a Vickers indentation. Strength test was conducted on a three-point bending. By way of comparison, the strengths of non-cracked and cracked specimens were similarly measured.

4. RESULTS AND DISCUSSION

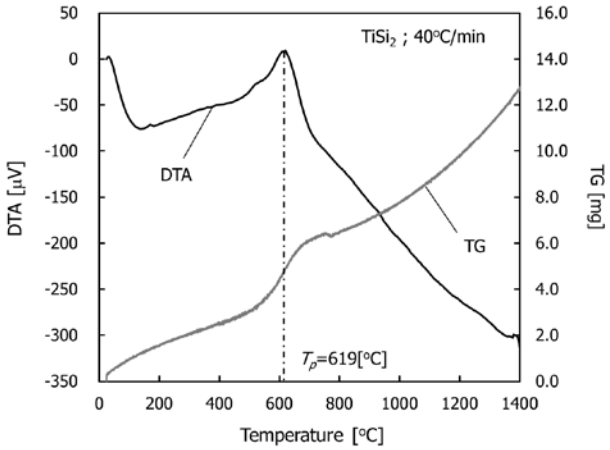

Fig. 2 Example of TG-DTA results

Fig. 2 shows TG and DTA curves of the oxidation of $TiSi_2$ particles which is one of encouraging self-healing agent at the constant heating rate of 5°C/min. At the temperature which DTA curve exhibits a maximum, the TG curve is found to increase significantly. This implies that at this temperature $TiSi_2$ oxidation exhibits a maximum rate. Thus, the oxidation peak temperature, T_p, was defined as the on-peak temperature of DTA curve in this paper, and evaluated to be 619 °C when β = 40 °C/min. Similar analyses were conducted for whole condition of β.

Fig. 3 shows the relationship between oxidation reaction rate of the agents and surrounding temperature. The value of ln (β/T_p^2) as the vertical axis corresponds to the reaction rate constant according to following equation, known as Kissinger-Sunose-Akahira equation [2];

$$\ln\left(\frac{\beta}{T_p{}^2}\right)+\frac{E_a}{RT_p}=constant$$

According to previous study [3], the oxidation rate constant ln (β/T_p^2) should be -13 in order to heal cracks in 1h. Therefore, by inserting the value of -13 to this figure, one can easily estimate the temperature at which Oi-SHC can heal cracks in 1h. For example, it can be estimated that Oi-SHC includes $TiSi_2$ can heal cracks from 577 °C for 1h.

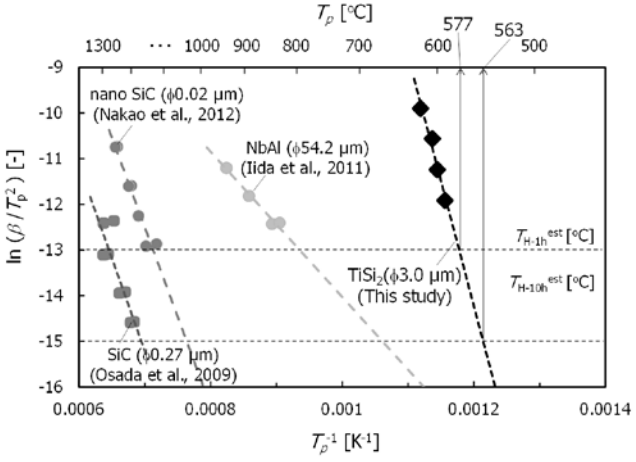

Fig. 3 the relationship between oxidation reaction rate of the agents and surrounding temperature

Fig. 4 shows the strength recovery behavior of the mullite/ $TiSi_2$ composites healed at several temperatures for 1 h as an example. The strength recovery of the composite was occurred from around 600 ^oC. This experimental value shows very good consistency with the estimated value which determined from TG/DTA analysis. Similarly, the strength recovery behavior of Oi-SHC which includes other Si-based alloy indicates a similar tendency.

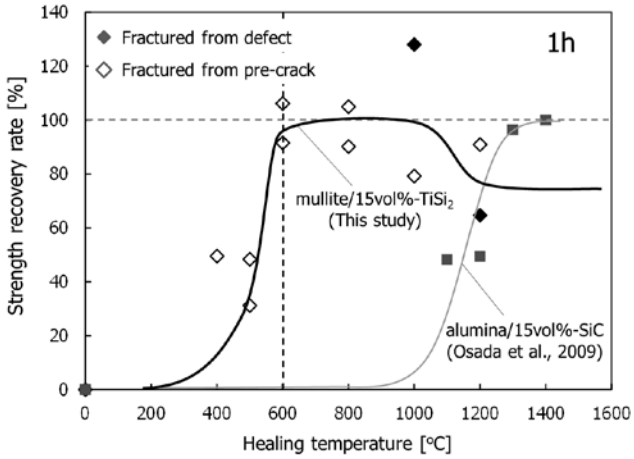

Fig.4 strength recovery behavior of the mullite/ $TiSi_2$ composites

5. CONCLUSION

The present authors aimed to investigate the relationship between oxidation behavior of self-healing agent and strength recovery behavior of self-healing ceramics. From simple thermal analysis, the oxidation behavior of several self-healing agents was investigated, and the estimated value of the lowest temperature at which Oi-SHC can heal crack was determined. On the other hand, the strength recovery behavior of Oi-SHC which embedded the agents was investigated by the combination of heat treatment and three-point bending test, and the experimental value of the lowest temperature at which Oi-SHC can heal crack was determined. The estimated value and experimental value show good consistency for several self-healing agent. From those results, it was revealed that the self-healing phenomena of Oi-SHC were strongly controlled by oxidation behavior of self-healing agent. Moreover, simple methodology to evaluate availability of self-healing agent has been established.

Acknowledgements

This investigation was financially supported by the Kumagai Foundation for Science and Technology. The authors thank Dr. Tatami for allowing to use equipment for uniaxial pressing and cold isostatic pressing, and Mr. Negishi for giving technical guidance of electron probe micro analyzer.

References

[1] S. Yoshioka., W. Nakao., "Advanced self-healing ceramics embedding silicon based alloy as self-healing agent," *18th the Japan society of Mechanical Engineers Kanto Branch Conf*, Tsudanuma, JP, May. 2012
[2] T. Akahira, T. Sunose, *1969 Research Report*, Chiba Institute of Technology, vol.16, (1971), pp. 246.
[3] T. Osada, W. Nakao, K. Takahashi, K. Ando, "Kinetics of Self-Crack-Healing of Alumina/Silicon Carbide Composite Including Oxygen Partial Pressure Effect," *Journal of the American Ceramic Society*, vol. 92, (2009) pp. 864-869.

Influence of Al_2O_3 matrix on crack-healing function and high temperature oxidation of nano-Ni/Al_2O_3 composites

Hai Vu Pham [(1,*)], Daisuke Maruoka [(2)], and Makoto Nanko [(3)]

[(1)] Nagaoka University of Technology, 1603-1, Kamitomioka, Nagaoka, 940-2188, JAPAN
[(2)] Faculty of Engineering, Yokohama National University, 79-5, Tokiwadai, Yokohama 240-8501, JAPAN
[(3)] Department of Mechanical Engineering, Nagaoka University of Technology, 1603-1, Kamitomioka, Nagaoka, 940-2188, JAPAN
E-mail: haipv@stn.nagaokaut.ac.jp

1. INTRODUCTION

Alumina (Al_2O_3) has been well-known as a high performance structural material and has been widely applied in industries because of its advantages such as excellent heat resistance, high mechanical strength and wear resistance. However, low fracture toughness of Al_2O_3 has been required to be improved to expand its applications. This issue could be mitigated by dispersing small amount of non-oxide dispersoids such as Ni, NiAl and SiC in Al_2O_3 [1,2].

Ando and his co-workers reported that crack-healing can be happened on ceramic-based composites such as SiC/mullite [3]. When non-oxide dispersoids in the matrix were oxidized at high temperatures, the oxidation product then filled up the cracks and involved reduction of stress concentration at crack tips. As a result, the mechanical strength was recovered up to the level of as-polished samples. Furthermore, this mechanism improves its performance and increases its lifetime and reliability of Al_2O_3 ceramic.

Recently, nano-Ni dispersed Al_2O_3 composites have been raised up as intelligent materials with self-healing function via thermal oxidation [4-6]. The cracks on the sample surface were filled up by oxidation product via diffusion of Ni^{2+} and Al^{3+} along grain boundaries. Maruoka et al. reported that the recovery of mechanical strength for nano-Ni/Al_2O_3 can be achieved when the fraction of surface crack disappearance is over 50% and crack disappearance effectiveness depended on the formation of $NiAl_2O_4$ that was mostly referred to diffusion of Ni^{2+} along grain boundaries of the Al_2O_3 matrix [7]. It indicates that finer grain size of the matrix could give positive effect to the crack-healing function.

Dispersion of 3 mol% yttria doped zirconia (YZ) in nano-Ni/Al_2O_3 composite could improve its mechanical properties due to transformation-toughening mechanism of YZ. This mechanism inhibits crack propagation and enhances fracture toughness. Recently, there has been a research that the fracture toughness of Ni/(YZ+Al_2O_3) composites is higher than the sum of fracture toughness of composites containing only YZ and only Ni dispersoid [8]. On the other hand, dispersion of YZ could enhance oxidation process because of its high oxygen ion conduction. Promotion of oxidation process means degradation of oxidation resistance.

In this study, the influence of different structure of Al_2O_3 matrix on crack-healing and high-temperature oxidation was estimated through remaining crack length on sample surface after heat treatment with various temperatures ranging from 1100 to 1300^{o}C. Investigation of growth rate of oxidation zone was carried out in order to evaluate the influence on the oxidation resistance.

2. EXPERIMENTAL PROCEDURE

In order to fabricate two types of 5 vol% Ni dispersed Al_2O_3 composites with different Al_2O_3 grain structure, two different types of Al_2O_3 powder (Sumitomo Chemical Co. Ltd, AA-04, d = 0.44 μm and Taimei Chemicals Co. Ltd, TM-DAR, d = 0.14 μm) were used as starting materials. Aqueous slurries containing Ni $(NO_3)_2 \cdot 6H_2O$ (Kojundo Chenmical Laboratory Co. Ltd, purity 99.9%) and the Al_2O_3 powders were prepared by using a magnetic stirrer. The materials that was prepared from Al_2O_3 with average particle size of 0.44 μm is referred to as Ni/Al_2O_3-044, hereafter. Similarly, Ni/Al_2O_3-014 is referred to the one that was prepared from the Al_2O_3 with average particle size of 0.14 μm. For nano-Ni/(YZ+Al_2O_3) preparation, YZ (Tosoh Corporation, TZ-3YB, d = 0.3 μm) was also added to be 10 vol% for Al_2O_3-014. After drying at 400^{o}C in a glass tube, the powder mixtures were milled by using an alumina mortar for 10 min. These

powder mixtures were reduced at 600°C for 12 h in a steam of Ar-1% H_2 gas mixture in order to achieve very fine and homogeneous nano-Ni dispersed Al_2O_3 matrix. The powder mixtures were consolidated in a graphite die by pulsed electric current sintering (PECS) at 1400°C for Ni/Al_2O_3-044, 1200°C for Ni/Al_2O_3-014 and 1300°C for Ni/(YZ+Al_2O_3) under 50 MPa uni-axial pressure in a vacuum for 5 min in holding time. Relative density of all the consolidated samples used in this study attained at least 99% of the theoretical density after sintering. Fig. 1 shows fractured surface of the as-sintered samples. Ni particles, could be seen as bright contrast dots, were homogeneously dispersed in the Al_2O_3 matrix. The average particle size of these Ni particles was approximately 300 nm, while the average Al_2O_3 grain size of Ni/Al_2O_3-044 was 1.1 μm, that of Ni/Al_2O_3-014 was 0.5 μm and in the term of Ni/(YZ+Al_2O_3) was 0.3 μm.

Oxidation test and investigation of crack-healing function were conducted at temperature ranging from 1100 to 1300°C for 1 up to 24 h in air with 400 K/h in heating rate. In order to evaluate the effectiveness of crack-healing function, each sample was introduced 3 Vickers indentations with 49 N for 10 s to generate cracks on polished sample surface. These samples with cracks were put on alumina balls (3 mm in diameter) in an alumina crucible and exposed in the air at the investigated conditions. Phase identification of the samples was carried out by X-ray diffraction (XRD). Microstructure and sample surface were observed by scanning electron microscope (SEM).

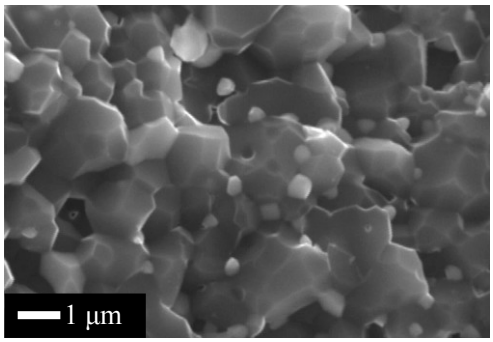

(a) nano-Ni/Al_2O_3-044

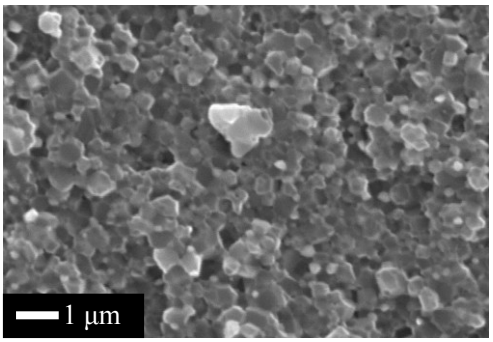

(b) nano-Ni/Al_2O_3-014

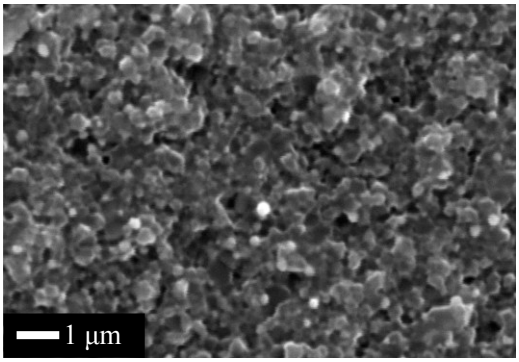

(c) nano-Ni/(YZ+Al_2O_3)

Fig. 1 SEM images of fractured surface of as-sintered samples: (a) Ni/Al_2O_3-044, (b) Ni/Al_2O_3-014, (c) Ni/(YZ+Al_2O_3)

3. RESULTS AND DISCUSSION

Fig. 2 shows SEM images of surfaces before and after heat-treatment in air. The cracks with average length of 55 μm were generated on polished surface by Vickers indentation which is outlined by dashed lines, as shown in Fig. 2(a). After heat-treatment at 1200°C for 1 h, the fraction of crack disappearance observed on surface of Ni/Al_2O_3-044 sample was 60% as shown in Fig. 2(b), while that of Ni/Al_2O_3-014 was 80%, Fig. 2(c). In addition, observation on Fig. 2(c) shows the surface of Ni/Al_2O_3-014 sample was mostly covered by oxidation product, whereas, uncovered dots could be seen as the circles describing on Fig. 2(b) of surface of Ni/Al_2O_3-044 sample. This different surface morphology indicates that diffusion of cations on Ni/Al_2O_3-014 was faster than that of Ni/Al_2O_3-044 due to difference of microstructure. In the case of Ni/(YZ+Al_2O_3), cracks totally disappeared on the surface of tested sample after heat treatment at 1200°C for 1 h, as shown in Fig. 2(d). Additionally, the fraction of crack disappearance was 82% for the Ni/Al_2O_3-044 sample after heat-treatment at 1100°C for 24 h while the completed crack-disappearance was observed on the sample surface of Ni/Al_2O_3-014 and Ni/(YZ+Al_2O_3) at this condition. It is clearly that the effectiveness of crack-

disappearance of Ni/Al_2O_3-014 and Ni/(YZ+Al_2O_3) was stronger than that of Ni/Al_2O_3-044. Effectiveness of crack-healing function depends on the formation of $NiAl_2O_4$ which was mostly referred to diffusion of Ni^{2+}. Dispersion of YZ in the matrix shows positive effect for crack-healing.

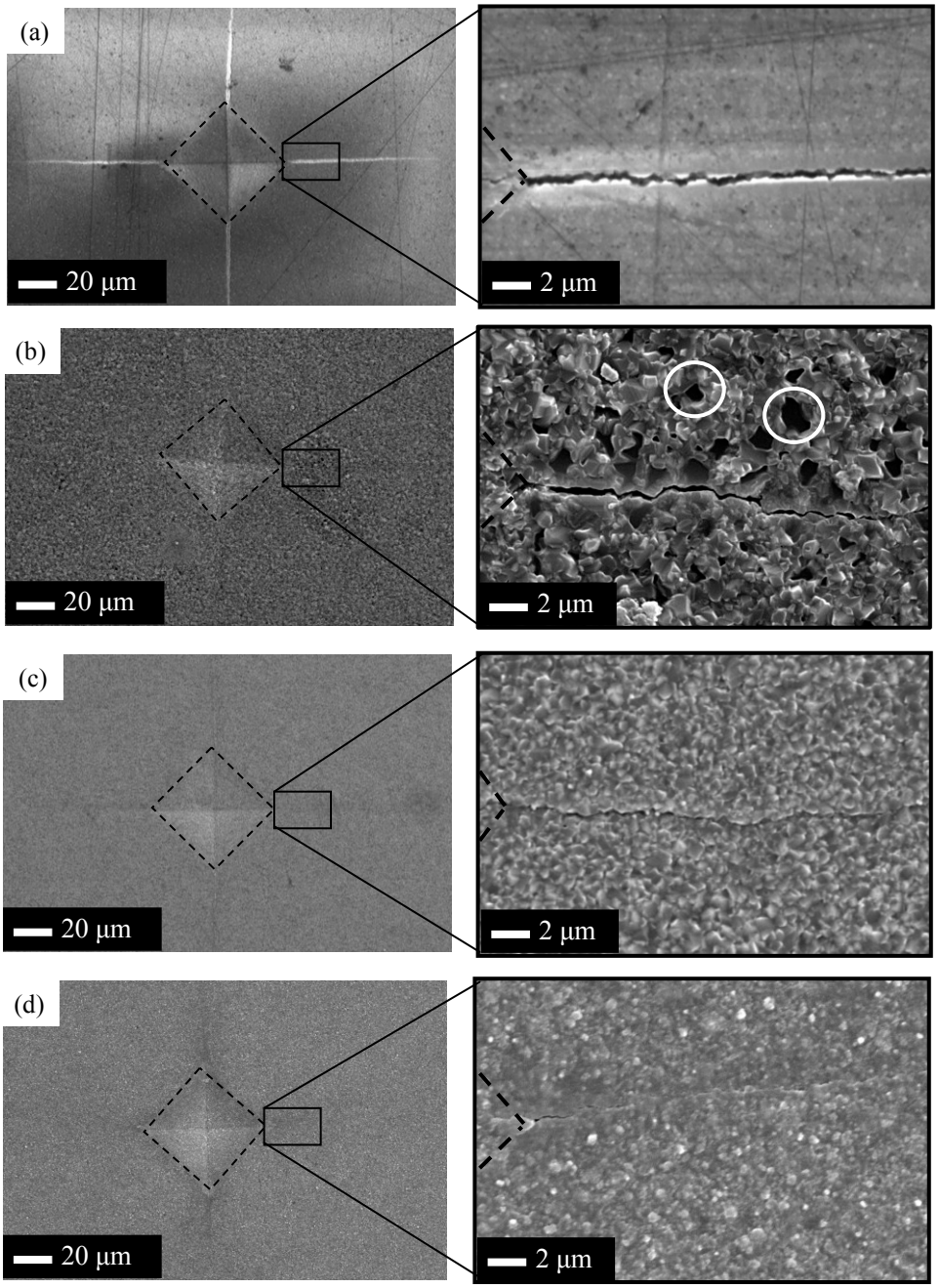

Fig. 2 SEM images of sample surface of (a) as-cracked Ni/(YZ+Al_2O_3) sample, the samples heat-treated at 1200°C for 1 h (b) Ni/Al_2O_3-044, (c) Ni/Al_2O_3-014, (d) Ni/(YZ+Al_2O_3) in the air.

Fig. 3 shows the SEM image of cross-section surface of Ni/Al_2O_3-014 sample heat-treated at 1200°C for 24 h. In the region from surface to the depth of 40 μm, the grains larger than Ni particles were oxidation product formed by heat-treatment. Nano-Ni particles only could be seen as the bright dots in the region deeper 40 μm from the surface. For the reasons above, the region consisting of the oxidation product was defined as the oxidized zone. With increasing heat-treatment temperature or holding time, the thickness of the oxidized zone increases. The growth of oxidized zone obeyed the parabolic law. Fig. 4 shows comparison of the parabolic rate constant, k_p, of high-temperature oxidation with the growth of oxidized zone. The value of k_p on Ni/Al_2O_3-014 is comparable with that of Ni/Al_2O_3-044. Dispersion of YZ degraded the oxidation resistance of Ni/Al_2O_3. It could be explained by characteristic structure of YZ, O^{2-} ions diffused not only along grain boundaries of Al_2O_3 matrix but also in YZ grains. However, this degradation by YZ

dispersion is decreased at lower temperatures.

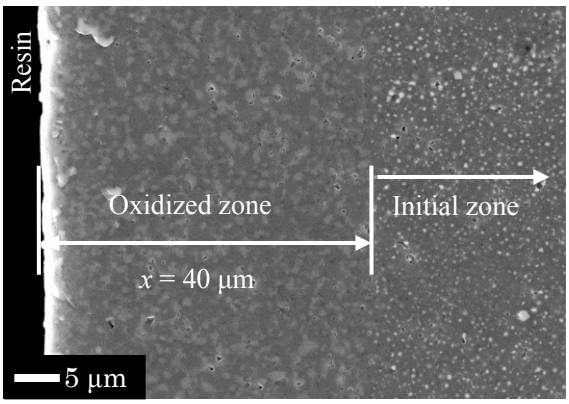

Fig. 3 SEM image showing cross-section surface of Ni/Al_2O_3-014 sample heat-treated at 1200°C for 24 h in air.

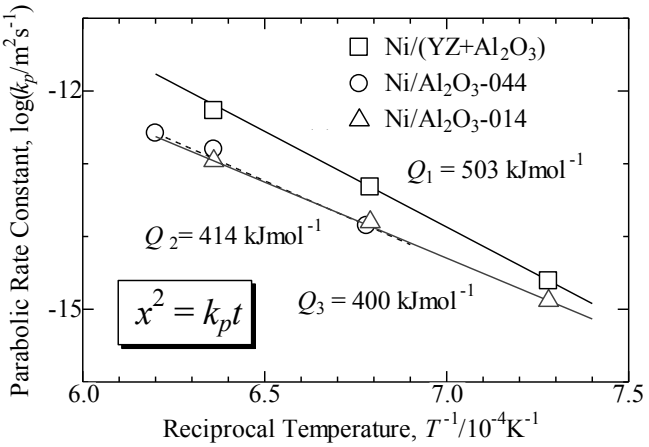

Fig. 4 Temperature dependence of parabolic rate constant on growth of oxidized zone of Ni/Al_2O_3 nano-composites.

4. CONCLUSION,

Influences of Al_2O_3 matrix on crack-healing function and oxidation behaviour at temperature at 1100~1300°C for 1~24 h were investigated in this study. As the result, crack-healing effectiveness was improved by improvement of fine microstructure of Al_2O_3. Dispersion of YZ in nano-Ni/Al_2O_3 shows positive effect on crack-healing function. Whereas, the difference in grain size of Al_2O_3 microstructure did not affect to the oxidation behaviour of nano-Ni/Al_2O_3. For nano-$Ni/(YZ+Al_2O_3)$, the growth of the oxidized zone also followed the parabolic law. Growth of oxidized zone of $Ni/(YZ+Al_2O_3)$ was slightly faster than that of nano-Ni/Al_2O_3.

Acknowledgements,

The authors wish to express their gratitude to the Japan Science and Technology Agency for supporting this study through the Advanced Low Carbon Technology Research and Development Program.

References

[1] Sekino, T., Nakajima, T., Ueda, T. and Niihara, K., "Reduction and sintering of a nickel-dispersed-alumina composites and its properties," *Journal of American Ceramic Society*, Vol. 80 (1997), pp. 1139-1148.

[2] Abe, O., Ohwa, Y. and Kuranobu, Y., "Possibility of enhanced strength and self-recovery of surface damages of ceramics composites under oxidative conditions," *Journal of European Ceramic Society*, Vol. 26, (2005), pp. 689-695.

[3] Chu, M. C., Sato, S., Kobayashi, Y. and Ando, K., "Damage healing and strengthening behaviour in intelligent mullite/SiC ceramics," *Fatigue and Fracture of Engineering Materials and Structures*, Vol. 18 (1995), pp. 1019-1029.

[4] Salas-Villasenor, A.L., Lemus-Ruiz, J., Nanko, M. and Maruoka, D., "Crack disappearance by high-temperature oxidation of alumina toughened by Ni nano-particles," *Advanced Materials Research*, Vol. 68 (2009), pp. 34-43.

[5] Maruoka, D., Sato, Y. and Nanko, M., "Crack-healing effectiveness of nano-Ni+SiC co-dispersed alumina hybrid materials," *Advanced Materials Research*, Vol. 89-91 (2010), pp. 365-370.

[6] Maruoka, D. and Nanko, M., "Crack healing of nano-Ni/Al_2O_3 hybrid materials via high-temperature oxidation," *Materials Science Forum*, Vol. 696 (2011), pp. 378-383.

[7] Maruoka, D. and Nanko, M., "Recovery of mechanical strength by surface crack disappearance via thermal oxidation for nano-Ni/Al_2O_3 hybrid materials," *Ceramics International*, Vol. 39 (2013), pp. 3221-3229.

[8] Chen, R. Z., Chiu, Y.T. and Tuan, W.H., "Toughening alumina with both nickel and zirconia inclusions," *Journal of the European Ceramic Society*, Vol. 20 (2000), pp. 1901-1906.

Evaporation of Gallium Suboxide from Mixture by Carbothermal Reduction and Deposition of Gallium Trioxide on Different Substrates by Oxidation

Yuto ANDO [1,*], Takaya AKASHI [2]

[1] Graduate School of Science and Engineering, Hosei University, Tokyo, 184-8584, JAPAN
[2] Faculty of Bioscience and Applied Chemistry, Hosei University, Tokyo, 184-8584, JAPAN

e-mail: akashi@hosei.ac.jp

1. INTRODUCTION

Gallium is becoming one of the most important chemical elements that are used for electrical and electronics industries, such as CIGS solar cells, LED devices, IGZO liquid crystal display, and so on. Therefore, the supply of gallium-containing raw materials must meet the increasing demand of the industry. However, the supply of gallium-containing raw materials is limited because of a lack of the natural resources. In our group, gallium trioxide was separated from a Japanese domestic natural ore which contains several tens ppm of gallium using a carbothermal reduction and oxidation process [1]. In this process, Ga_2O_3 that is contained in the natural ore is evaporated in the form of gallium monoxide, $Ga_2O(g)$, by the following reaction (1).

$$Ga_2O_3(\text{in ore}) + 2C(s) \rightarrow Ga_2O(g) + 2CO(g) \quad (1)$$

Then, the gaseous gallium monoxide is transferred to an oxidizing atmosphere and oxidized, forming gallium trioxide, $Ga_2O_3(s)$, by the following reaction (2).

$$Ga_2O(g) + O_2(g) \rightarrow Ga_2O_3(s) \quad (2)$$

In this study, the carbothermal reduction and oxidation process was applied to gallium-containing mixture using different substrates for deposition, and the influence of substrates on the concentration of gallium trioxide in the deposited substance was investigated. Sintered 8%Y_2O_3-stabilized ZrO_2 (YSZ) plate and sintered α-Al_2O_3 plate were used as the substrates for the deposition of gallium trioxide.

2. EXPERIMENTAL

Powders of Ga_2O_3, Al_2O_3, Fe_2O_3, $MgCO_3$ and $CaCO_3$ were mixed by a mortar and pestle. The ratio of each powders were 20 wt%, 32 wt%, 12 wt%, 8 wt%, 16 wt% and 12 wt%, respectively. The gallium-containing mixed powder was set in a Al_2O_3 crucible with the equal weight of activated carbon, and located in the middle section of three-zone tubular furnace, which can control the temperature independently (see Fig. 1). Both sintered YSZ and Al_2O_3 substrate for deposition of gallium trioxide were set in the lower section of tubular furnace as in Fig. 1. Upper and middle sections of the tubular furnace were heated at 1150 °C and lower section was heated at 1000 °C. After heating for 2 h, the concentration of the deposited substance on each substrate was analyzed by X-ray photoelectron spectroscopy (XPS).

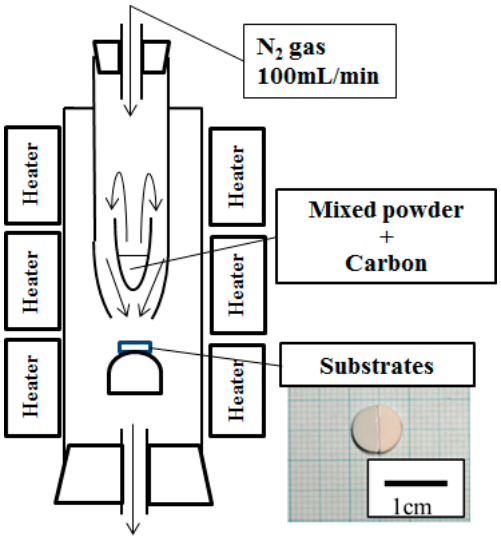

Fig. 1 three-zone tubular furnace for carbothermal reduction and oxidation.

3. RESULTS AND DISCUSSION

Fig. 2 shows XPS spectrums for the surfaces of sintered YSZ and Al_2O_3 substrates before and after the heat-treatment for carbothermal reduction and oxidation of gallium compound. Before the heat-treatment, only the peaks from the substrates can be detected; For the YSZ substrate, Y, Zr, and O can be seen (Fig. 2(a)), whereas, for Al_2O_3 substrate, Al and O as well as a small amount of Na and C can be seen (Fig. 2(c)). After the heat-treatment (Figs. 2(b) and 2(d)), peaks of gallium can be identified on the both substrates. From the peak intensity, the concentrations of gallium were determined to be 9.8 atm% and 3.4 atm % on the surface of YSZ and Al_2O_3, respectively. The amount of gallium on YSZ substrate was about three times greater than that of gallium on Al_2O_3 substrate. This tendency was verified by four experiments, although the concentration of gallium was varied with experiments from 7.3% to 14.3% for YSZ substrate, and from 3.0% to 3.4% for Al_2O_3 substrate. This result indicates that oxide ion conduction in YSZ substrate promotes oxidation of Ga_2O(g).

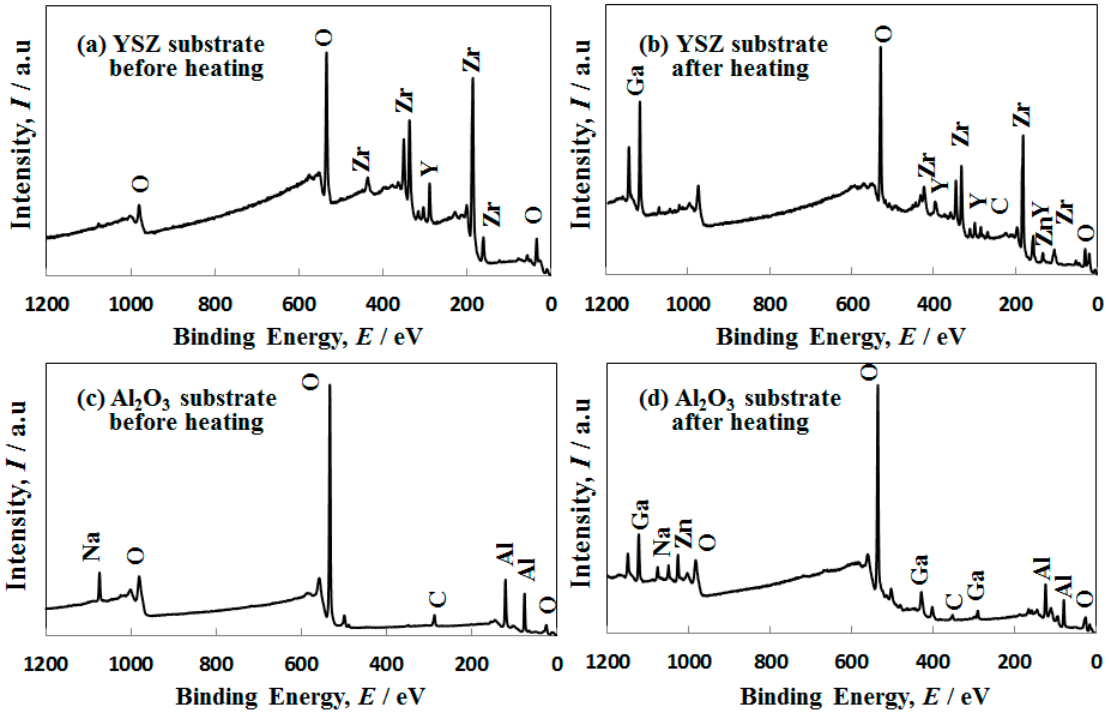

Fig. 2 XPS spectrums for the surfaces of sintered YSZ and Al_2O_3 substrates before and after the heat-treatment for carbothermal reduction and oxidation.

4. CONCLUSION

Gallium monoxide was evaporated from the mixed powder composed of Ga_2O_3, Al_2O_3, Fe_2O_3, $MgCO_3$ and $CaCO_3$ by carbothermal reduction, and gallium trioxide was deposited on the surface of Al_2O_3 substrate and YSZ substrate by oxidation. Greater amount of gallium was collected on the surface of YSZ substrate than that of Al_2O_3 substrate.

Reference

[1] PCT Patent No. 2012-191071.

Simulation of SiC Passive Oxidation and oxidation transitions

Toshinari Yoshinaka[(1*)]; Yuuki Kubota[(2)]; Hiroshi Hatta[(3)]

[(1)]Japan Aerospace Exploration Agency, Jindaiji-Higashi, Chofu, 182-8522, Japan
[(2)]The Graduate University for Advanced Studies, Yoshinodai, Sagamihara, 229-8510, ,Japan
[(3)]Institute of Space and Astronautical Science, Japan Aerospace Exploration Agency,Sagamihara, 229-8510, Japan

e-mail: yoshinaka.toshinari@jaxa.jp

1. INTRODUCTION

The carbon/carbon composite with Chemical Vapor deposition (CVD)-SiC coating is regarded as a promising candidate for re-usable space transportation systems. The investigations of SiC oxidation under the atmospheric re-entry conditions are important. SiC is oxidized by $SiC+O_2 \rightarrow SiO+CO$ and continuously evaporated. In the passive oxidation regime, i.e. high-pressure/low-temperature environments, SiC is oxidized by $SiC+3/2O_2 \rightarrow SiO_2+CO$ and stable SiO_2 coating is formed on the surface. Usage in the passive oxidation conditions is essential. Thus the investigations of the active-to-passive transition (A/P transition) and acquisition of the oxidation speeds are thought to be necessary. So far, a lot of investigations have been conducted. Several types of SiC have been prepared, the oxidation experiments performed under various kind of environmental conditions [1].The oxidation speeds and the A/P transitions are widely scattered. These data were arranged by the partial pressure of oxygen far upstream from a sample (P_F). The measured data may be different from those near the surface or near the sample surfaces or those of SiO_2/SiC interfaces, i.e. oxidation surface. We think the acquired data should be evaluated by the pressure at the oxidation surfaces (P_r). There are 2 kinds of A/P transition, i.e. active to passive and passive to active. The acquired data should be evaluated in this respect. Kubota [2] conducted the experiments and numerical calculations in the case of active oxidation. He indicated that the P_r are largely different for the experimental apparatus and this can be thought one of the reasons of the scattering. He also indicated the active to passive transition. In the next step, we conducted numerical calculations in the case of passive oxidation and evaluated the passive to active transition. In this paper, newly acquired outcomes discussed.

2. Numerical calculation

(1) Active -to-passive oxidation transition

The active-to-passive transition can be estimated by Volatility Diagram [3] in Si-C-O system and following reactions are taken into consideration.

$$SiC+1/2O_2 \rightarrow SiO + C \quad (1)$$

$$SiC+1/2O_2 \rightarrow SiO_2 + C \quad (2)$$

$$SiO_2 \rightarrow SiO+1/2O_2 \quad (3)$$

$$SiO_2 \rightarrow SiO_2(g) \quad (4)$$

The diagram indicates a vapor pressure of the most volatile species at a given oxygen pressure together with stable condensed phase. Fig.1 shows the Volatility Diagram in Si-C-O system at 1948K for example. The lines on the Figure can be calculated from the free energy changes of each reaction. The numbers on the figure corresponds to the above mentioned equations.

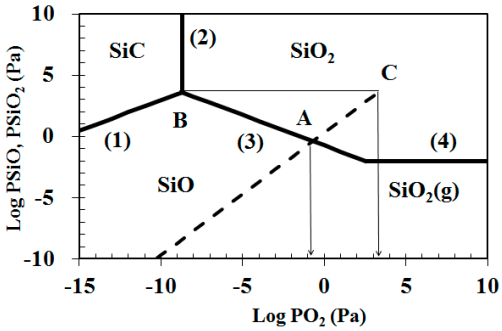

Fig. 1 Volatility Diagram of Si-C-O system at 1948K

The dotted line in the figure is called “isomolar line”, which means that $P_{SiO}=2P_{O2}$ is satisfied. In this case, from Equation (3), no SiO nor Oxygen molecules remain and passive oxidation can start at Point A. We defined this pressure/temperature condition as the beginning of passive oxidation and SiO_2 is produced in the higher Oxygen partial pressure region,. SiO partial pressure reaches its maximum at point B and point C is plotted on the “isomolar line”. The SiO partial pressure at Point C is equal to that at Point B. We define the Oxygen partial pressures at point A and C are P^L_{Ox}, P^U_{Ox} respectively. All the transitions investigated so far are located between point P^L_{Ox} and P^U_{Ox}.

(2) Outline of passive oxidation

The schematic diagram of SiO_2 generation and other phenomena are shown in Fig.2.Oxygen solve into SiO_2 at the Gas/SiO_2 interface and diffuse toward the SiO_2/SiC interface. When SiC is converted to SiO_2, the volume of the molecular is increased to approximately 2.2 times. To prevent distortion caused by volume change, Si and Carbon

atoms emit from the SiO_2/SiC interface [4], and the emitted atoms will diffuse toward the SiO_2/gas interface and are oxidized inside SiO_2 to generate SiO_2 and CO

(3) Equations of oxidation

Oxygen, Si and Carbon diffuse and cause oxidation inside SiO_2 film. These phenomena can be written as shown in equations (5)-(7). Concentration, diffusivity and reaction speeds are described as C, D, and R respectively. The subscript Ox,Si,C means Oxygen, Si and Carbon respectively.

$$\frac{\partial C_{Ox}}{\partial t} = \frac{\partial}{\partial x}\left(D_{Ox} \frac{\partial C_{Ox}}{\partial x} \right) - R_{Si} - R_C \qquad (5)$$

$$\frac{\partial C_{Si}}{\partial t} = \frac{\partial}{\partial x}\left(D_{Si} \frac{\partial C_{Si}}{\partial x} \right) - R_{Si} \qquad (6)$$

$$\frac{\partial C_C}{\partial t} = \frac{\partial}{\partial x}\left(D_C \frac{\partial C_C}{\partial x} \right) - R_C \qquad (7)$$

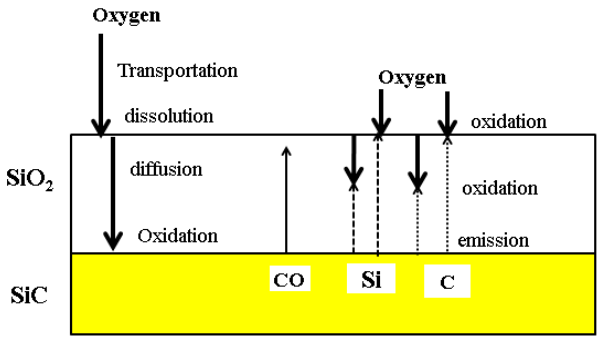

Fig.2 The schematic diagram of passive oxidation

At the SiO_2/SiC interface, Oxygen is consumed to produce SiO_2. The flux of Oxygen, its consumption and SiO_2 generation are balanced. This phenomenon is described as shown in equation (8). The flux, passive oxidation rate constant and SiO_2/SiC interface, density, and molecular weight are written as J_{Ox}, k, ρ, and M respectively.

$$J_{Ox} = -D_{Ox} \left. \frac{dC_{Ox}}{dx} \right|_I = \frac{3}{2} k C_{Ox}^I = \frac{\rho_{SiO_2}}{M_{SiO_2}} \frac{dx}{dt} \qquad (8)$$

The emission of Silicon and Carbon are described in Equations (9) and (10) respectively. ν means the emission rate.

$$J_{Si}^I = -\nu_{Si} J_{Ox}^I = -\nu_{Si} k C_{Ox}^I \qquad (9)$$

$$J_C^I = -\nu_C J_{Ox}^I = -\nu_C k C_{Ox}^I \qquad (10)$$

The emitted Silicon and Carbon atom decrease the reaction speeds and the effect it can be described in Equation (11).

$$k = k_0 \left(1 - \frac{C_{Si}^I}{C_{Si}^0} \right) \left(1 - \frac{C_C^I}{C_C^0} \right) \qquad (11)$$

The reaction speeds of emitted atoms can be described Equations (12) and (13) respectively. κ^1, κ^2 means reaction rate constant.

$$R_{Si} = k_{Si}^1 C_{Ox} + k_{Si}^2 C_{Ox}{}^2 C_{Si} \qquad (12)$$

$$R_C = k_C^1 C_{Ox} + k_C^2 C_{Ox}{}^2 C_C \qquad (13)$$

(3) Material properties

The material properties are quoted from literatures, but they were measured in lower under 1400℃. Thus we must extend them to up to approximately 1700℃. The diffusivity of Oxygen, Silicon and Carbon are shown in Fig.3 as a typical example.

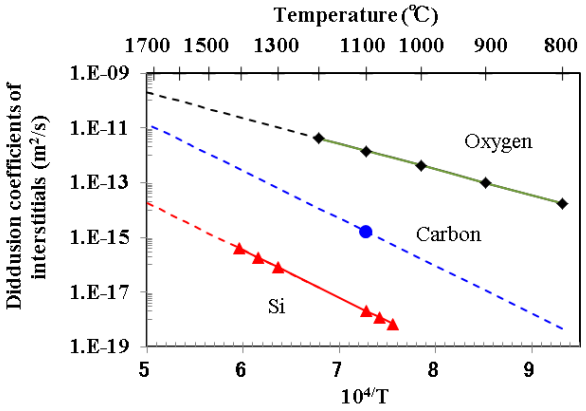

Fig.3Diffusivity of Oxygen, Si and Carbon

3 Results and Discussion

We calculated the growths of SiO_2 thickness under the temperatures from 1550℃ to 1675℃ and showed good agreements with those of Narushima/Goto's results [5]. Thus it can be thought that our simulation can be suitable for evaluation of SiC passive oxidation. Based on the outcomes, we also calculated the oxygen partial pressure at SiC/SiO_2 interface (P_{Ox}^I) . The calculated time history of P_{Ox}^I is shown in Fig.4. It decreases with time and will reach the lower transition and will reach to P^L_{Ox} in a long oxidation time. This can be thought the beginning of active oxidation.

Based on our calculation and the Volatility Diagram, the relation between the oxygen partial pressure and A/P transition (passive to active) can be estimated. Here in respect to experimental verification, we selected the case that P_{Ox}^I will reach P^L_{Ox} within 10000 sec and the newly acquired A/P transition (passive to active) is shown in Fig.5.It will differ for temperature/pressure conditions. If the pressure is lower, active oxidation will begin before 10000 sec. In addition, i

locates in lower pressure area compared with that of Kubota (active to passive). This needs further research.

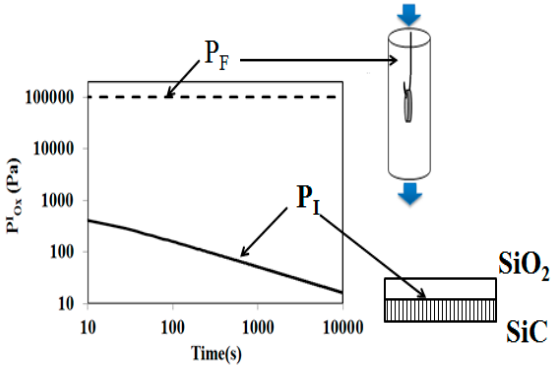

Fig,4 he oxygen partial pressure at SiC/SiO_2 interface

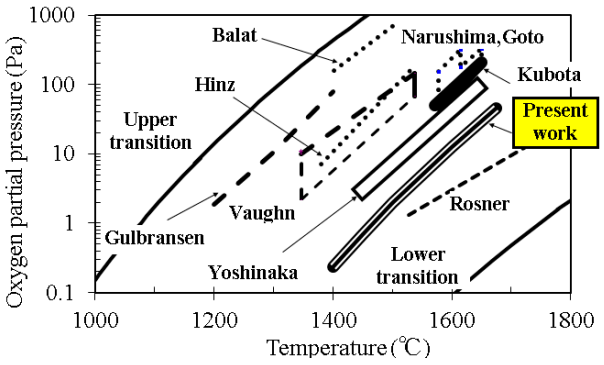

Fig 5 Estimated active-to-passive oxidation transition

4 CONCLUSION

It made clear that the active-to passive transitions must be evaluated in respect to the oxygen partial pressure also in the case of passive oxidation. In addition it was also made clear that the transitions will differ for oxidation time. In the future, our predicted transitions should be verified by static heating experiments.

Reference

[1] T.Narushima, T.Goto, and T.Hirai, Y. Iguchi, "High-Temperature Active Oxidation of Silicon Carbide and Silicon Nitride," Material Transactions, Japanese Institute of metals, 38, 10, 1997, pp821-835

[2] Y.Kubota, H.Hatta, T.Yoshinaka, T.Kogo, T.Goto, T.Rong, "Use of Volume Element Methods to understand Differences in Active/Passive Transitions and Active Oxidation Rates for SiC" Journal of American Ceramic Society, 2013. pp1-7

[3] Heuer, A.H., and. Lou, V.L.K., "Volatility diagram for Silica, Silicon Nitride, and Silicon Carbide and Their Application to High-Temperature Decomposition and Oxidation," Journal of American Ceramic Society, 73-10, 1990, pp2789-2803

[4] Y.Hijikata,H.Yamaguchi, and S.Yoshida, "A kinetic Model of Silicon Carbide Oxidation Based on the Interfacial Silicon and Carbon Emission Phenomenon", Applied Physics Express .2, 2009, p021203

[5] T.Narushima, T.Goto, and T.Hirai, "High-Temperature Passive Oxidation of Chemically Vapor Deposited Silicon Carbide," Journal of American Ceramic Society,72..1989, pp1386-1390

Interface Reaction Between Different Refractory and Hot Metal

Liu Zheng-jian [1,2*], *Zhang Jian-liang* [1,2], *Jiao Ke-xin*[1,2], *Hou Xin-mei*[1,2], *Liu Yan-xiang*[1,2]

(1.School of Metallurgical and Ecological Engineering, University of Science and Technology Beijing, Beijing 100083, China

2.State Key Laboratory of Advanced Metallurgy, University of Science and Technology Beijing, Beijing 100083, China.)

e-mail: liuzhengjian@126.com

Abstract: Research bf longevity and safety technology adapt to the change of the ironmaking new situation to ensure the safety of bf longevity has huge potential economic and environmental benefits. It is of far-reaching significance in practical application. In this paper, the experiment simulated the blast furnace hearth refractory with iron liquid interface behavior, analyzed and compared the carbon brick, carbon composite bricks, ceramic cup three kinds of refractory on the behavior with the liquid iron. The interfacial reaction between the hot metal and refractories were observed by scanning electron microscope with energy dispersive X-ray spectroscopy. The results show that the reaction layer generated by the carbon brick and ceramic cup with iron liquid interface has a weak effect on the performance of the liquid iron, and a layer of the decarburization layer generated after carbon composite bricks and iron liquid interface reaction, bare Al_2O_3 oxide obvious has a remarkable influence on the viscosity of molten iron. The formation of viscous layer reduced further erosion between the molten iron and the carbon composite bricks.

1. INTRODUCTION

With the requirement of high quality steel increased, continuous development of steel smelting process provided higher requirements on refractory material. To improve the service life of refractory materials had become the enormity of task for workers. In terms of saving resources, protect the environment, and satisfy the requirements of modern metallurgical industry, it was an inevitable trend for detailed researching on the damage mechanism of refractory and use the results to protect and prolong the service life of refractory materials. Hearth security had become a limit key link of one generation blast furnace service life. Systematic study of iron corrosion mechanism of refractory material and use the research results to improve the overall life of the refractory will become a new trend in the development of refractory materials.

2. EXPERIMENTAL

The iron powder and coke were put into refractory crucible (carbon brick, microporous corundum brick, carbon composite bricks). A panel in the upper portion of the crucible and was set up, which made the coke below the liquid surface. Then the crucible refractories were put in high temperature furnace with argon protection gas and heating up to 1500℃ for 4 h. Then the crucible refractories were removed in air and cooled to room temperature. Experimental apparatus was shown in figure 1.

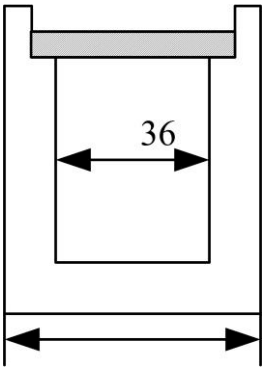

Fig.1 Experimental apparatus

3. RESULTS AND DISCUSSION

Figure 2 was the SEM of three kinds of refractories. It can be seen that the microporous of the three kinds of refractories were very high. The air gap was small and distributed in the matrix.

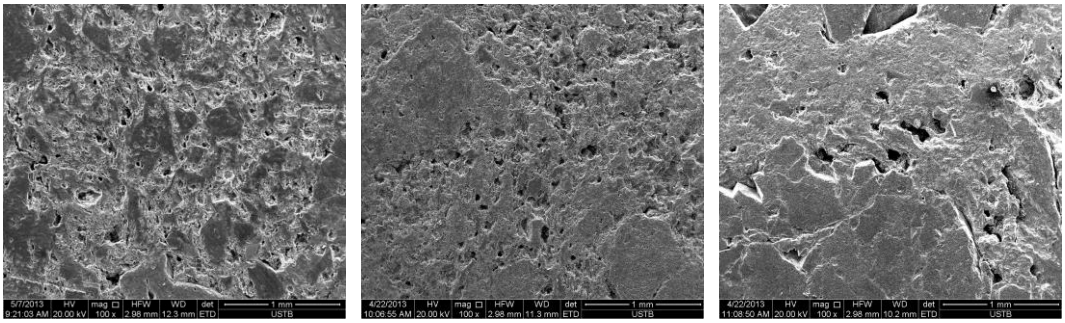

carbon brick microporous corundum brick carbon composite bricks

Fig.2 microstructure analysis of three kinds of refractories

Figure 3 was the erosion condition of the three kinds of refractories by hot metal. It can be seen from the diagram that carbon brick was erode for a certain amount. The wettability was good between the molten iron and carbon brick interface. There was no wetting between the hot metal and the microporous corundum brick. The molten iron had good liquidity, which sank at the bottom of the refractory. However, the molten iron was together with coke on carbon composite bricks, molten iron and carbon composite bricks were completely separate.

The reaction layer generated by the carbon brick and ceramic cup with iron liquid interface has a weak effect on the performance of the liquid iron, and a layer of the decarburization layer generated after carbon composite bricks and iron liquid interface reaction, bare Al2O3 oxide obvious has a remarkable influence on the viscosity of molten iron. The formation of viscous layer reduced further erosion between the molten iron and the carbon composite bricks.

carbon brick microporous corundum brick carbon composite bricks

Fig.3 the erosion condition of the three kinds of refractories by hot metal

4. CONCLUSION

Compared to the traditional hearth refractory material, carbon composite bricks had special performance of the interface between hot metal and hot face. a layer of the decarburization layer generated after carbon composite bricks and iron liquid interface reaction, bare Al2O3 oxide obvious has a remarkable influence on the viscosity of molten iron. The formation of viscous layer reduced further erosion between the molten iron and the carbon composite bricks.

References.

[1] Zheng-jian LIU, Jian-liang ZHANG, Hai-bin ZUO. Tian-jun YANG. Recent Progress on Long Service Life Design of Chinese Blast Furnace Hearth[J]. ISIJ International, 52 (10), 2012:1713–1723.

[2] LIU Zheng-jian, ZHANG Jian-liang, YANG Tian-jun. Study on the formation mechanism of viscous layer in blast furnace hearth. Asia Steel 2012.

[3] XUE Qun Hu, XU Wei Zhong. Refractory. Beijing, Metallurgical Industry Press.,2009.

[4] ZHANG Shou Rong, YU Zhong Jie. The blast furnace abnormal and accident treatment. Beijing, Metallurgical Industry Press.,2012.

[5] Xu Ruitu, He Rusheng, Cao Yongguo. The new brick lining and the applying of the Thermal insulation interlining. 2012 national meeting of high blast temperature and longevity of BF. 2012, 234-240.

[6] Sang-Jin NAM, Youn-Bae KANG, Sung-Mo JUNG. Feasibility of BF Hearth Protection Using Spinel Formation by Slag Composition Control. ISIJ International, 2013,53(10) :1779–1785.

Effect of SiC Addition on the Oxidation Behavior of ZrB_2 at 1273 K and 1473 K

Lihua ZHANG[(1,*)], and Kazuya KUROKAWA[(1)]

[(1)] Center for Advanced Research of Energy and Materials, Faculty of Engineering, Hokkaido University, Kita13 Nishi8, Sapporo 060-8628, JAPAN

e-mail: zhanglihua@eng.hokudai.ac.jp

1. INTRODUCTION

Ultra-high temperature ceramics (UHTCs) have been proposed as candidates for applications such as thermal protection systems for hypersonic aerospace vehicles[1]. Among the UHTCs, zirconium diboride has the lowest theoretical density (6.09 $g \cdot cm^{-3}$), and has good thermal shock resistance because of its high thermal conductivity (65-135 $W \cdot m^{-1} \cdot K^{-1}$)[2]. These attributes make it attractive for aerospace applications. However, the oxidation resistance of ZrB_2 is very poor at temperatures above 1673 K due to the volatilization of B_2O_3, which results in formation of a porous, non-protective ZrO_2 layer.[3,4] Numerous investigations to improve the oxidation resistance of ZrB_2 have been reported.[3,5-8] It was found that SiC addition provided outstanding oxidation resistance by promoting the formation of borosilicate glass. This borosilicate glass afforded more oxidation protection than B_2O_3 since it is more viscous, has high melting temperature and lower vapor pressure, and is more of a barrier to oxygen diffusion.

The oxidation behaviors of ZrB_2-SiC composites in air have been well-defined previously.[5,7,8] A. Rezaie *et al.*[9] also reported the oxidation behavior of ZrB_2 with 30 vol% SiC addition at low partial pressure of oxygen. However, the SiC content discussed in these studies is usually in the range of 20 vol% to 30 vol%, and the influence of different SiC contents on the oxidation behavior of ZrB_2 is rarely reported. Therefore, the oxidation of ZrB_2 with different SiC contents is researched in this study. Thermodynamically, both ZrB_2 and SiC should be oxidized when exposed to air. However, the oxidation rates of both species are negligible below about 1073 K.[7] Above 1373 K, the evaporation of B_2O_3 will affect the effectiveness of the diffusion barrier. Therefore, this study selected the oxidation temperature of 1273 K and 1473 K.

2. EXPERIMENTAL

Processing: Commercially available ZrB_2 and SiC powders were used as raw materials. The ZrB_2-SiC powders with different SiC content (0 wt%, 5 wt%, 10 wt%, 20 wt%, and 30 wt%) and 1 wt% B_4C were prepared and then pressureless sintered at 2523 K for 3 h in an Ar atmosphere after metal injection molding process.

Oxidation: The oxidation tests were performed using a horizontal tube furnace. Before the tests, specimens were prepared using conventional polishing with a diamond abrasive, down to a 0.5 μm finish. They were then placed on an alumina boat and inserted into the center of the furnace. The oxidation tests were conducted at 1273 K and 1473 K for 12 h under an air atmosphere.

Characterization: The densities of the sintered specimens were measured using the Archimedes method, and the theoretical densities of the composites were calculated using the rule of mixture. The microstructures of the cross-sections of the oxidized specimens were characterized using scanning electron microscopy (SEM). To analyze the microstructures of the vertical sections after the tests, the specimens were cross-sectioned and mounted in epoxy, carefully polished with a diamond abrasive down to a 0.5 μm finish, and cleaned in an ultrasonic bath. The thicknesses and element profile of the resulting reaction layers were measured and analyzed from the polished cross-sections by electron probe micro-analyzer (EPMA).

3. RESULTS AND DISCUSSION

The relative densities of the specimens before oxidation test is in the range of 97%-99%. Consequently, porosity was not considered to have a significant effect on the oxidation behavior.

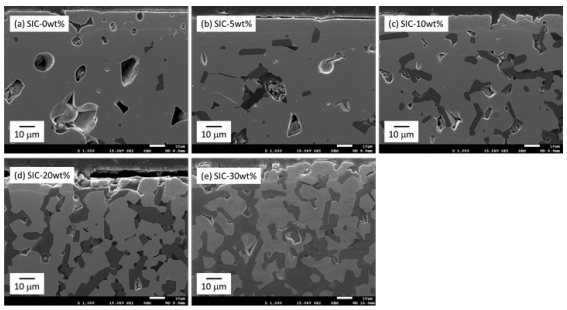

Fig. 1. SEM images of ZrB_2-SiC specimens after exposure to air for 12 h at 1273 K. (a) without SiC addition; (b) SiC: 5 wt%; (c) SiC: 10 wt%; (d) SiC: 20 wt%; (e) SiC: 30 wt%.

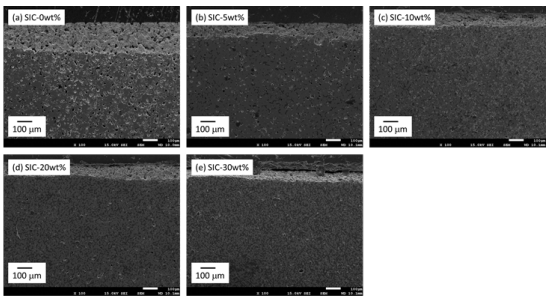

Fig. 2. SEM images of ZrB_2-SiC specimens after exposure to air for 12 h at 1473 K. (a) without SiC addition; (b) SiC: 5 wt%; (c) SiC: 10 wt%; (d) SiC: 20 wt%; (e) SiC: 30 wt%.

Figs. 1 and 2 show the SEM images of ZrB_2-SiC specimens with different SiC addition after exposure to air for 12 h at 1273 K and 1473 K, respectively. Combing with the data of EMPA, the thickness of the oxidation layer could be obtained. For the specimens oxidized at both 1273 K and 1473 K, with SiC content increasing, the thickness of oxide layer decreased. It has been reported that SiC additions do not affect the oxidation rate or the composition of the protective oxide layer below 1373 K. However, in this work at 1273 K the increase of SiC contents shows an increase oxidation resistance of ZrB_2. The reason was considered that the addition of SiC decreased the diffusion of oxygen in the specimen. While at 1473 K, with the increase of SiC content, the formation of SiO_2 on surface has effective protection of ZrB_2, which results in the decrease of oxide layer. Fig. 3 shows the schematic diagram of proposed reaction sequence during the oxidation of ZrB_2-SiC at 1273 K and 1473 K in air.

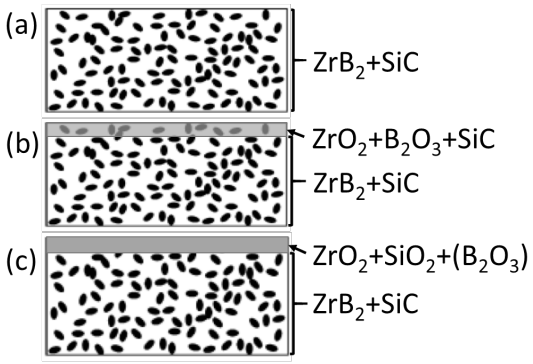

Fig. 3. Schematic diagram of proposed reaction sequence during the oxidation of ZrB_2-SiC at 1273 K and 1473 K in air. (a) unoxidized ZrB_2-SiC; (b) the structure when the specimen reaches 1273 K; (c) the structure when the specimen reaches 1473 K.

4. CONCLUSION

The oxidation behavior of ZrB_2-SiC composites with different SiC addition was investigated at 1273 K and 1473 K in air. The following conclusions could be obtained. At 1273 K in air, a B_2O_3 layer could be formed, which acts as an oxygen diffusion barrier; while at 1473 K, the evaporation of B_2O_3 results in the formation of the non-protective porous ZrO_2 layer on the surface. The addition of SiC offers effective protection of ZrB_2 at 1473 K because of the formation of SiO_2 on the surface. With the increase of SiC content at 1273 K and 1473 K, the thickness of the oxide layer decreased, indicating that the increasing addition of SiC shows effective improvement of oxidation resistance of ZrB_2. When SiC addition is 30 wt%, ZrB_2-SiC composites have the highest oxidation resistance.

References.

[1] Opeka, M. M., *et al.*, "Oxidation-Based Materials Selection for 2000°C+ Hypersonic Aerosurfaces: Theoretical Considerations and Historical Experience," *J. Mater. Sci.*, Vol. 39, No. 19 (2004), pp. 5887-5904.

[2] Tripp, W. C. *et al.*, "Thermogravimetric Study of the Oxidation of ZrB_2 in the Temperature Range of 800-1500°C," *J. Electrochem. Soc.*, Vol. 118, No. 7 (1971), pp.1195-1209.

[3] Fahrenholtz, W. G., "The ZrB_2 Volatility Diagram," *J. Am. Ceram. Soc.*, Vol. 88, No. 12 (2005), pp. 3509-3512.

[4] Levine, S. R. *et al.*, "Evaluation of Ultra-High Temperature Ceramics for Aeropropulsion Use," *J. Eur. Ceram. Soc.*, Vol. 22, No. 22 (2002), pp. 2757-2767.

[5] Kuriakose, A. K. *et al.*, "The Oxidation Kinetics of Zirconium Diboride and Zirconium Carbide at High Temperatures," *J. Electrochem. Soc.*, Vol. 111, No. 7 (1964), pp. 827-831.

[6] Opila, E. J., *et al.*, "Oxidation of ZrB_2-SiC," *Ceram. Eng. Sci. Proc.*, Vol. 22, No. 3 (2001), pp. 221-228.

[7] Chamberlain, A. L., *et al.*, "Oxidation of ZrB2-SiC Ceramics under Atmospheric and Reentry Conditions," *Refract. Appl. Trans.*, Vol. 1, No. 2 (2005), pp. 1-8.

[8] Monteverde, F., *et al.*, "Oxidation of ZrB_2-Based Ceramics in Dry Air," *J. Electrochem. Soc.*, Vol. 150, No. 11 (2003), pp. B552-B569.

[9] Rezaie, A., *et al.*, "Oxidation of Zirconium Diboride-Silicon Carbide at 1500°C at a Low Partial Pressure of Oxygen," *J. Am. Ceram. Soc.*, Vol. 89, No. 10 (2006), pp. 3240-3245.

$TiSi_2$ assisted SiC oxidation for self-healing function in fiber reinforced self-healing ceramics at high-temperature

*Daisuke Maruoka[(1)] , Hiroshi Yo[(1)] and Wataru Nakao[(1)]

[(1)] Department of Materials Science and Chemical Engineering, Yokohama National University, 79-5, Tokiwadai, Hodogaya, Yokohama, Kanagawa, 240-8501, JAPAN

e-mail: daisuke@ynu.ac.jp

1. INTRODUCTION

Fuel efficiency improvement of jet engine for air plane has subsequently been taking account of one of important issues to realize low-carbon society. One of the approaches to improve fuel efficiency is to attain weight saving and to adapt non-cooling system using ceramic materials for turbine blades. Ceramic materials are well-known to have high-temperature strength, light weight and chemical stability. However low damage tolerance of ceramic materials lead to catastrophic failure by large impact [1]. An innovative methodology to endow ceramic materials with high mechanical reliability is necessary to actualize ceramic turbine blade.

Self-healing function in ceramic-based composite has been investigated by Ando and his co-workers [2]. In these ceramic composites, non-oxide dispersoids are allows oxidizing with the surrounding atmosphere by surface cracking, thereby the oxidation product fills the cracks and re-bonds the crack surfaces. As a result, the mechanical strength is recovered up to the virgin strength. The self-healing function extends the life time of ceramic components and results in easy maintenance [3].

Sugiyama et al. [4] proposed the fiber reinforced self-healing ceramic composite (shFRC) as an advanced self-healing ceramics for turbine blade. The shFRC reported by Sugiyama et al. consists of alumina continuous fiber bundle, alumina matrix and SiC interlayer as healing agent, where SiC dispersoids are typical self-healing agent in ceramic-based composites [2, 4, 5]. When crack is initiated in the shFRC, the crack can be branched along SiC interlayer. Crack propagation is arrested due to friction of interface between crack surfaces. Subsequently the exposed SiC interlayer reacts with oxygen in surrounding atmosphere and then self-healing function appeared. The self-healing function in shFRC appeared 1200^{O}C for 1 h and 1000^{O}C for 50 h, respectively. The shFRC can realize autonomic self-healing if the shFRC is employed as turbine blade operated at temperatures from 1000^{o}C to 1200^{o}C. The available temperature region for self-healing in the shFRC corresponds to the operated temperature region of middle pressure turbine. However, 50 h healing at 1000^{o}C cannot be confirmed to ensure the mechanical reliability of ceramic composites.

Yoshioka et al. [6] reported that $TiSi_2$ is a candidate of the advanced self-healing agents which produces the self-healing function at lower temperature than that of SiC self-healing agent. According to the report, the self-healing function due to $TiSi_2$ oxidation appears above 400^{o}C. $TiSi_2$ interlayer is expected not to have crack branching function, because $TiSi_2$ is easily densified during sintering compared to the alumina. As the interlayer of shFRC should be designed as weakest region in the composite to introduce cracks, $TiSi_2$ interlayer is inadequate to use the interlayer of shFRC.

In this study, $TiSi_2$/SiC composite is proposed as interlayer of shFRC to realize advantages both of lower temperature self-healing function and branching cracks. For the first step, high-temperature oxidation behavior of $TiSi_2$/SiC composite was investigated and the enhancement of SiC oxidation by ectothermic heat provided from $TiSi_2$ oxidation was discussed.

2. EXPERIMENTAL

Starting materials used in this study were $TiSi_2$ powder (GfE, average particle diameter d = 324 μm) and SiC powder (Ultrafine, Ibiden Co. Ltd., Average particle diameter d = 0.35 μm). $TiSi_2$ powder was ball-milled for 24 h to be sieved under 75μm. Bead mill using ZrO_2 beads (d = 0.3 mm) was carried out the sieved $TiSi_2$ powder for 7 h with 2-propanol to be approximately 1 μm of $TiSi_2$ powder. These powders were mixed with distilled water into ball mill for 12 h. Mass composition of the powder mixture were $TiSi_2$: SiC =0: 100 (named as SiC), 10 : 90 (10$TiSi_2$), 30 : 70 (30$TiSi_2$) and 50 : 50 (50$TiSi_2$), respectively. After drying at 100^{o}C, powder mixture were uniformed to be green body using uniaxial pressure under 50 MPa for 1min then CIPed under 200 MPa for 1min. The green body was sintered at 1300^{o}C for 10 h in Ar. Figure 1 shows the morphology of samples after sintering.

After cutting and polishing to be rectangular sample (approximately 5×5×5 mm), heat-treatment was conducted. Samples were put into electric furnace after reaching holding temperature. Heat-treatment condition was 1000°C for 10-720 min in air. Sample masses were measured before/after heat-treatment. Microstructures were observed by optical microscopy.

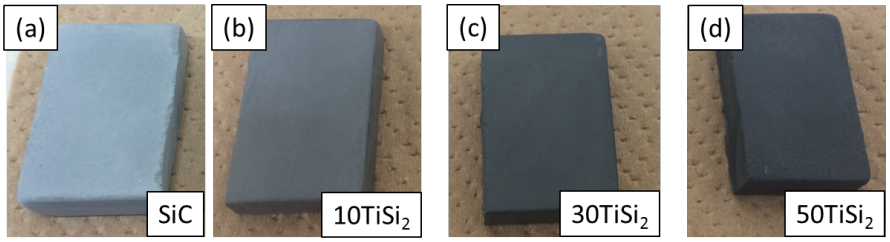

Fig.1. Morphology of $TiSi_2$/SiC Samples after sintering (a) SiC, (b) 10mass% $TiSi_2$/SiC, (c) 30mass% $TiSi_2$/SiC and (d) 50mass% $TiSi_2$/SiC

3. RESULTS AND DISCUSSION

Figure 2 shows time changes in mass gain of $TiSi_2$/SiC composites during oxidation at 1000°C. Mass gains of these samples increase with heat-treatment time as following parabolic manner. The values of the parabolic rate constant, k_p, were determined from the gradients of these lines. Figure 3 shows the obtained parabolic rate constant, k_p, as function of mass fraction of $TiSi_2$. The value of k_p at f_{mTiSi2}= 10 is almost same value as SiC, whereas the values of k_p at f_{mTiSi2}= 30 and 50 are higher than that of SiC. It is implied that more than 30$TiSi_2$ contributes to accelerate mass gain of $TiSi_2$/SiC at 1000°C. As the values of k_p at further high temperature might be same value in spite of different f_{mTiSi2}, the activation energies at $f_{mTiSi2} \geq 30$ can be estimated to be smaller than that of SiC. Therefore, the deference in activation energy is confirmed to be caused by the ectothermic heat of $TiSi_2$ oxidation.

Figure 4 shows optical images of sample surface before/after heat-treatment. After heat treatment for 10 min, black contrast regions were observed on 50$TiSi_2$. Since 10$TiSi_2$ were observed no black contrast region, those regions are considered as $TiSi_2$. Those $TiSi_2$ would provide heat of reaction to surrounding SiC for oxidation at 1000°C. Similar surface morphologies were observed on 10$TiSi_2$ and 50$TiSi_2$ for 720 min. It is implied that $TiSi_2$/SiC were oxidized as same mechanism among 10$TiSi_2$, 30$TiSi_2$ and 50$TiSi_2$.

The obtained oxidation behavior supports the strength recovery behavior of shFRC having $TiSi_2$/SiC composite interlayer. As an example, 30$TiSi_2$ interlayer can exhibit the self-healing at 1000°C for 1 h, however, SiC and 10$TiSi_2$ interlayers cannot do the self-healing.

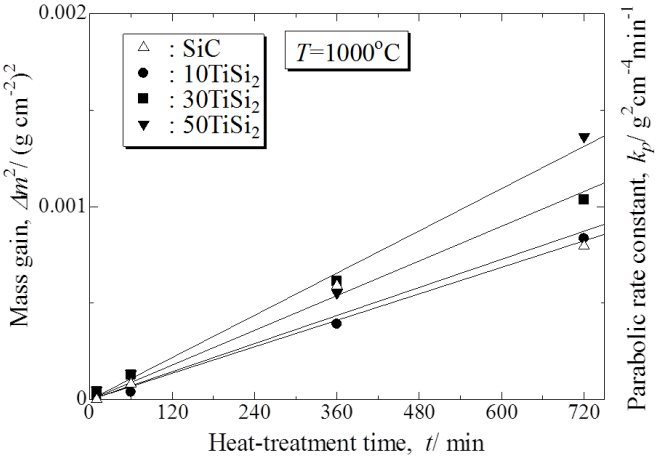

Fig.2. Mass gain of $TiSi_2$/SiC as function of heat treatment time

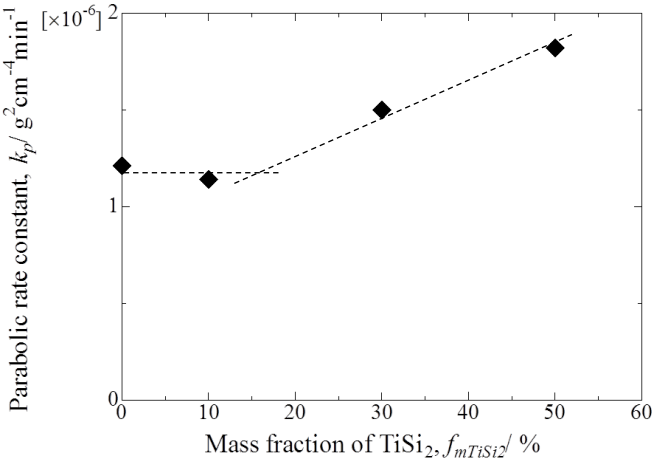

Fig.3. parabolic rate constant as function of mass fraction of $TiSi_2$

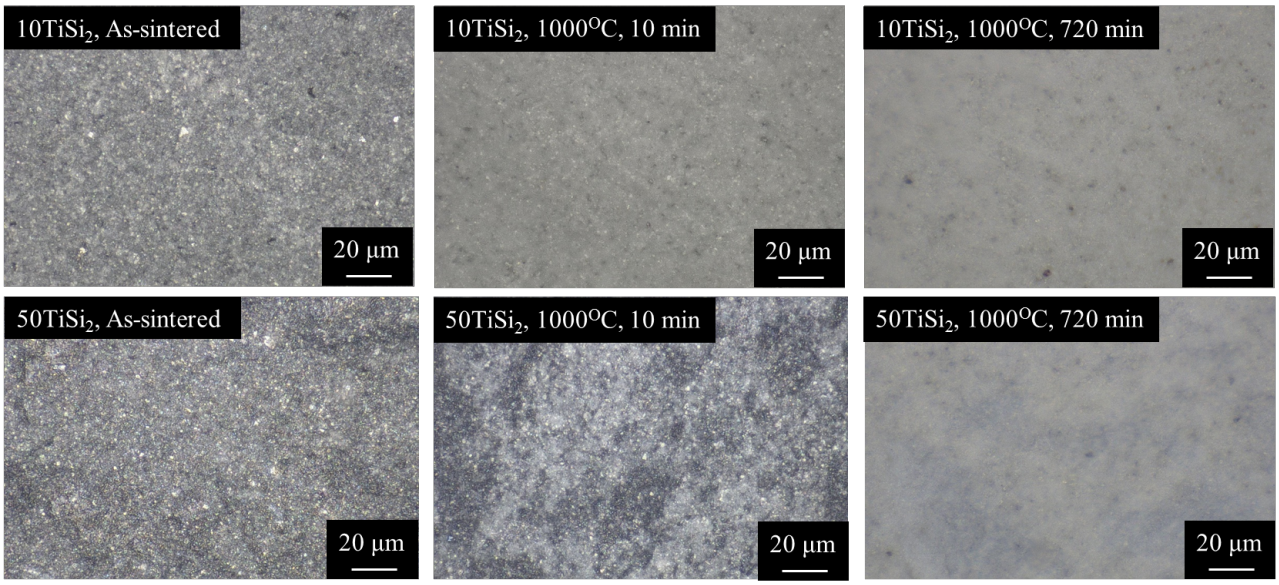

Fig.4. Surface views of sample before/after heat-treatment

4. CONCLUSION

In this study, oxidation behaviors of $TiSi_2$/SiC composites for self-healing agent of shFRC were investigated at high-temperature. Mass gains of $TiSi_2$/SiC composites at 1000°C were measured as function of heat treatment time and composition of $TiSi_2$. Mass gains of these composites were followed parabolic manner. The value of k_p at f_{mTiSi2}= 10 is almost same value as SiC, whereas the values of k_p at f_{mTiSi2} = 30 and 50 are higher than that of SiC. More than 30$TiSi_2$ contributes to accelerate mass gain of $TiSi_2$/SiC at 1000°C. Recovery of mechanical strength was obtained on shFRC sample using 30$TiSi_2$ self-healing agent as interlayer. The obtained oxidation behavior supports the strength recovery behavior of shFRC having $TiSi_2$/SiC composite interlayer. $TiSi_2$ assisted SiC oxidation was concluded to enhance self-healing ability in fiber reinforced self-healing ceramics at high-temperature.

Acknowledgements

This work has been funded through Advanced Low Carbon Technology and Development Program organized by Japan Science and Technology Agency (JST-ALCA).

References

[1] Guedou, J. Y., "Materials evolution in hot parts of aero-turbo-engines." *Proceedings of the 27th international congress of aeronautical science*, Nice, France, September. 2010, pp. 1-7.
[2] Chu, M. C., Sato, S., Kobayashi, Y., Ando, K., "Damage healing and strengthening behavior in intelligent mullite/SiC ceramics," *Fatigue Fract. Engng Mater. Struct,.* Vol 18, (1995), pp. 1019-1029.
[3] Maruoka, D., and Nanko, M., **"**Recovery of Mechanical Strength with Surface Crack Disappearance via Thermal Oxidation on Nano-Ni/Al_2O_3 Hybrid Materials," *Ceram. Intl.*, Vol68, (2013), pp.34-43.
[4] Sugiyama, S. and Nakao, W., "Self-Healing Behavior of Fiber-Reinforced Self-Healing Ceramics," *Proc. the Fourth International Conference on Self-Healing Materials ICSHM2013*, Ghent, Belgium, June. 2013, pp. 560-563.
[5] Nakao, N., Takahashi, K. and Ando K., Self-healing Materials, Fundamentals, Design Strategies, and Applications, WILEY-VCH (Weinheim, 2009), pp. 183-217
[6] Yoshioka, S. and Nakao, W., "Methodology to Evaluate Availability of Self-Healing Agent for Structural Ceramics," *Proc. the Fourth International Conference on Self-Healing Materials ICSHM2013*, Ghent, Belgium, June. 2013, pp. 274-277.

New approach for identifying areas of sulfidation on water wall tubes in coal-fired boilers

Shin Najima [(1)], Masahiko Morinaga [(2)] and Shigenari Hayashi [(3)]

[(1)]Materials Science Research Laboratory, [(2)] Energy Engineering Research Laboratory, Central Research Institute of Electric Power Industry, 2-6-1 Nagasaka, Yokosuka, Kanagawa 240-0196, Japan
[(3)]Graduate School of Engineering, Hokkaido University, Kita 13, Nishi 8, Sapporo, Hokkaido 060-8628, Japan

E-mail: najima@criepi.denken.or.jp

1. INTRODUCTION

Recently, the corrosion wastage of boiler water wall tubes has been observed in many pulverized coal-fired boilers in Japan. The corrosion is caused by sulfidation in reducing atmospheres created by low oxygen combustion. It is necessary to identify where sulfidation occurs in the boiler in order to deal with this issue. The wastage of the tubes has previously been investigated over a limited area because sulfidation is normally observed between the two-stage combustion air inlet port and burner in the side walls. However, sulfidation area tend to be transferred by recent changes in the combustion conditions and coal property, as a result, sulfidation was observed on the front and rear walls and above the two-stage combustion air inlet port. Therefore, low-cost methods for identifying sulfidation areas in a short maintenance period are required. The most common approach is to measure the remaining wall thickness of the tube by using ultrasonic measurement. However, this method is costly and requires a longer inspection time for large areas because scale on the tube surface must be removed for inspection, which may cause accelerating tube wastage. Although a method using an electromagnetic acoustic transducer (EMAT) that does not require removal of the corrosion product has been reported, it is still not suitable for practical use. Another approach is to measure the composition of the combustion gas to which the tube is exposed to during operation. Because the number of gas sampling ports in the boiler is limited, investigating the combustion gas composition of the entire boiler is difficult. In this study, we investigated the coal ash deposited on the tube surface, the scale structure formed on tube surface, and the composition of the combustion gas in several boilers in Japan. Based on our observations, we propose a fast, low-cost approach for identifying areas of sulfidation in boilers.

2. EXPERIMENTAL

Coal ash deposited on the tube surface and the corrosion products formed on the tube surface were sampled at 12 supercritical or ultra-supercritical pulverized coal-fired boilers in Japan during routine maintenance carried out every two years from 2004 to 2013. The samples were taken at 3 m intervals from below the burner level to above the two-stage combustion air inlet port level. The number of samples was 50-200 for each boiler. The time-dependent change in ash composition was determined from samples taken in different years from the same boiler. The composition of the ash samples was analyzed by X-ray fluorescence and X-ray diffraction. The corrosion products formed on the tube surface were sampled at 5 boilers. Corrosion products were sampled from areas where severe sulfidation and mild sulfidation occurred. The scale structure of the corrosion products was investigated by scanning electron microscopy and electron probe microanalysis.

3. RESULTS AND DISCUSSION

The composition of the coal ash sampled from the surface of the water wall tube varied by sampling position. The first type of ash was composed of mullite and SiO_2, which is typical coal ash. The second type was greenish brown and contain a large amount of Zn (>30 wt %). X-ray diffraction showed that Zn was present as ZnS. The corrosion products sampled from the surface of the water wall tube showed that the composition of the ash deposited on the top of the scale was different depending on the scale structure. Where severe sulfidation occurred, thick $Fe_{(1-x)}S$ was formed mainly, and ash containing ZnS was deposited on the scale surface. However, ash containing ZnS was not observed on the scale surface where sulfidation did not occur, because only a thin layer of Fe_3O_4 was formed mainly. Thus, ZnS is deposited on areas where severe sulfidation occurs.

In general, the Zn concentration in coal ash and coal is a few parts per million. We propose the following mechanism that explains why ZnS was enriched in the ash deposited on areas where severe sulfidation was observed. Zn in coal is converted into ZnO in the combustion gas in an oxidizing atmosphere where sulfidation is less likely to occur. Because

the melting point of ZnO is high, solid ZnO is mixed with other coal ash, such as SiO_2 and mullite, and flows downstream of the boiler. In contrast, ZnS is thermodynamically stable in a reducing atmosphere in which severe sulfidation occurs. ZnS sublimes at 1180 °C, and thus exist as gas phase in the combustion gas, which is at a temperature of about 1300 °C. However, ZnS condenses on the tube surface, which is cooled to about 500 °C by the steam in the tube. Therefore, ZnS can only be deposited during the combustion of coal containing Zn, in a reducing atmosphere, and where there is a sufficient temperature difference between tube surface and combustion gas. These environment are similar to those in which severe sulfidation of the water wall tube occurs, thus it is reasonable to assume that sulfidation occurs where ZnS is also condensed in the ash on the tube surface. Consequently, we investigated whether areas of sulfidation in the boiler could be identified by detecting Zn in the coal ash.

Figure 1 shows an example of a contour map of Zn concentration in ash deposited on the water wall tube surface of a pulverized coal-fired boiler in Japan. The Zn concentration was high at the burner level of the right and left walls, the corner of the right wall and the front wall below the two-stage combustion air inlet port level. In these areas, the water wall tube appeared to be corroded by sulfidation. In contrast, at the level between the two-stage combustion air inlet port and burner in the left and right walls where severe sulfidation has often been observed in the past, the absence of ZnS indicates that tube wastage caused by sulfidation did not occur in this boiler.

The entire boiler was measured with a hand-held X-ray fluorescence analyzer within a few hours. Moreover, because pre-treatments, such as removing corrosion products, are not required, our method can reduce the cost of this process and can maintain a protective scale. However, the temperature of tubes is not considered and there is insufficient data on the relationship between the wastage of the tube and the Zn concentration in the ash. Therefore, the recession in thickness of the water wall tube cannot be evaluated directly from the Zn concentration in the ash at the moment. However, we expect that the Zn concentration in the ash deposited on the tube surface is related to the combustion gas atmosphere. If the atmosphere to which the tube was exposed can be estimated everywhere in the boiler, the sulfidation area can be identified. Therefore, our technique can be used to check only areas where inspection the remaining tube thickness by ultrasonic measurements are required, and reveal unexpected areas of sulfidation.

4. CONCLUSION

We investigated the coal ash deposited on the tube surface, the scale structure formed on the tube surface, and the composition of combustion gas in several boilers in Japan. We found that ZnS was deposited on areas where severe sulfidation occurred. Detecting ZnS provides a fast method for identifying areas where sulfidation occurred in the boiler.

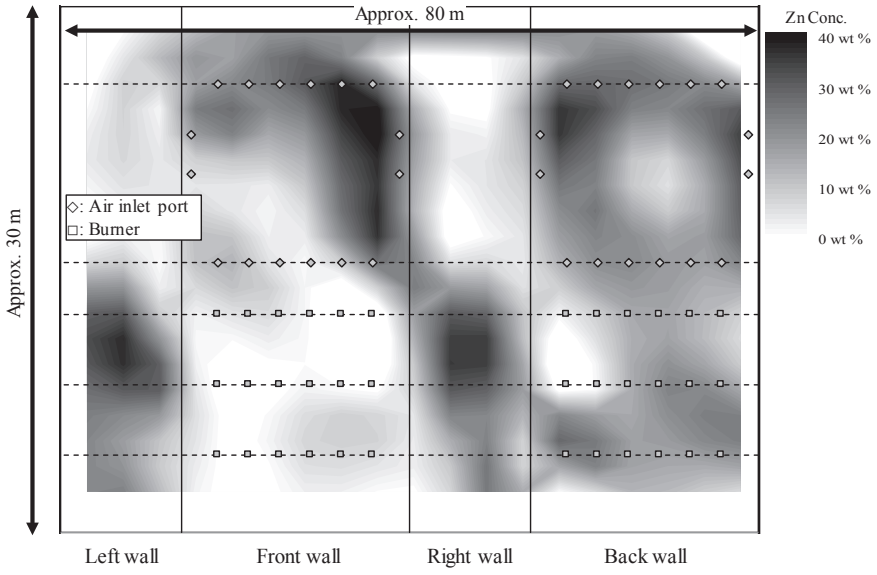

Fig. 1 Contour map of Zn concentration in ash deposited on the water wall tube surface of a 700 MW pulverized coal-fired boiler in Japan.

Oxidation Behavior of Cladding Tube-Shaped 15Cr-20Ni Austenitic Stainless Steels in Supercritical Water at 700°C

Ryuichi Suzuki *, Hiroshi Abe, Yutaka Watanabe

Graduate School of Engineering, Tohoku University, 6-6-01-2 Aoba, Aramaki, Aoba-Ku, Sendai, 980-8579, JAPAN

e-mail: ryuichi.suzuki@rbm.qse.tohoku.ac.jp

1. INTRODUCTION

Supercritical water-cooled reactor (SCWR) is one of the advanced reactor concepts for generation IV nuclear reactors. SCWR offers higher thermal efficiency over 40% compared to over 30% for current generation light water reactor and simpler plant systems due to the higher enthalpy content of the supercritical water coolant [1]. Material of fuel cladding for SCWR is required long term integrity and durability at metal temperature of 700°C. Zr alloys which are widely used for light water reactors can not be applied to SCWR , because of the luck of mechanical strength above 400℃. Then, 15Cr-20Ni austenitic stainless steel which has sufficient creep strength at 700°C was proposed for the candidate materials for fuel cladding of SCWR. Oxide layer growth of fuel cladding cause problems as follows: increase of channel flow resistance caused by reduction in the gap between fuel rods, decrease of the heat transfer coefficient and possible contamination of the whole system by exfoliation of oxide layers. In the previous work [2], oxidation behavior of candidate materials including three types of 15Cr-20Ni austenitic stainless steel in supercritical water at 700°C under 24MPa for 500h have been discussed. The previous work showed that the tube-shaped specimens had good oxidation resistance because protective Cr_2O_3 oxide layer formed on the outside surface. It has been estimated that Cr diffusion of outside surface of tubes was accelerated as a result of increase of dislocation density and/or grain refinement by a high degree of cold work. It has been considered that the tube-shaped 1520 SSs show good performance as fuel cladding in SCWR from oxidation kinetics point of view. In this study, further oxidation experiments of three types of 15Cr-20Ni austenitic stainless steel up to 1000h have been carried out. The main objective of this work is to discuss the protectiveness of Cr_2O_3 oxide layer formed on the tube surface after long-term exposure in supercritical water a temperature of 700 °C. Detailed structure of the outmost surface of the tube-shaped specimens and degradation behavior of the protective oxide layer have been investigated.

2. EXPERIMENTAL

Three types of 15Cr-20Ni austenitic stainless steel, standard type (1520S), Ti modified type (1520Ti), and Zr modified type (1520Zr) were prepared. The chemical compositions of these materials are shown in Table 1. Plate-shaped and tube-shaped specimens were prepared. The former were solution annealed and cold rolled with 20%, 30% and 40% reduction respectively, and the latter were cold drawn with 20% reduction. The specimens were exposed to supercritical water at 700°C under 24Mpa up to 1000h. DO level was adjusted less than 1ppb by purging nitrogen gas into the reservoir tank and by measuring the DO meter. Oxidation rate were calculated by measuring the weight changes of specimens at 30h, 100h, 250h 500h, and 1000h. A part of raising/decreasing the temperature process was performed under the nitrogen gas environment to prevent the weight change caused by dissolution/precipitation in the liquid phase. Microstructure and compositions of oxide layers were investigated by scanning electron microscope (SEM), energy dispersive X-ray spectrometry (EDX), transmission electron microscope (TEM), and X-ray diffraction (XRD).

Table 1. Chemical compositions of materials, wt%

	C	Si	Mn	P	Ni	Cr	Mo	Ti	Nb	B	Zr	Fe
1520S	0.063	0.87	1.75	0.028	19.88	15.11	2.51	0.23	0.10	0.0032	–	Bal.
1520Ti	0.060	0.87	1.75	0.028	19.85	15.19	2.50	0.42	0.09	0.0040	–	Bal.
1520Zr	0.061	0.79	1.68	0.026	19.98	15.26	2.45	0.24	0.10	0.0032	0.17	Bal.

3. RESULTS AND DISSCUSION

Figure 1 shows the weight gain vs time of 15Cr-20Ni austenitic stainless steels during oxidation test at 700°C. Weight gain of plate-shaped specimens decreased with increasing cold work degrees. However, weight change of tube-shaped specimens was lower than 40% cold work plate-shaped specimens. Though weight gain of 1520S tube-shaped specimen

was somewhat large compared with other tube-shaped specimens, there was small difference in the oxidation kinetics in the three investigated types of 15Cr-20Ni austenitic stainless steel in other case. Exfoliation of oxide layers occurred in only plate-shaped specimens. Oxidation rate was calculated by following equation (1) from the Figure 1.

$$\log(\Delta m) = C + n \cdot \log(t) \quad (1)$$

where, Δm : weight gain, t : time, n : slope and c: intercept. n value is important to predict the long-term oxidation behavior. In general, oxidation kinetics of metals often fit into parabolic rate law [3,4], in the case of n=0.5 by above-mentioned formula (1), however this test results was not applied to the parabolic rate low. n value decreased from 0.5 as increasing cold work degree of plate-shaped specimens and n value of tube-shaped specimen was lower than 40% cold work plate-shaped specimens.

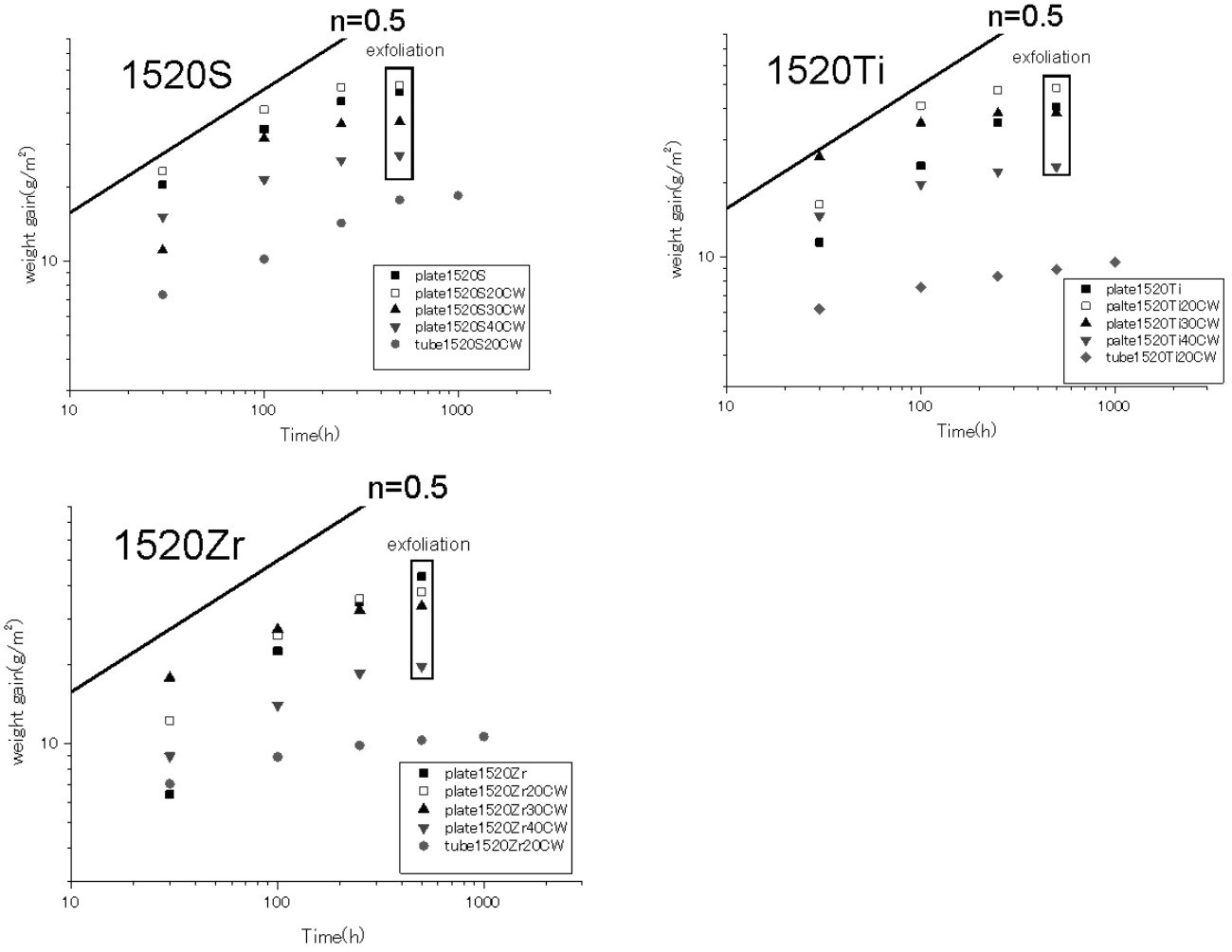

Figure 1 Weight gain vs time of 15Cr-20Ni austenitic stainless steels (log-log layer).

Figure 2 shows the SEM images of the surface of tube-shaped specimens after 1000h exposure. There were thick nodule oxides on the whole surface of the 1520S tube-shaped specimens. These nodules were also observed on a single part of other tube-shaped specimens, but the most surfaces were covered with the thin oxide layers since the polishing trace was observed clearly. This is the reason why the 1520S tube-shaped showed higher weight gain than others. Figure 3 shows the SEM cross sectional images of 1520S tube-shaped specimens after 100h and 1000h exposure. A uniform thin oxide layer was observed after 100h exposure (figure 3 (a)). On the other hand, thin oxide layer was not maintained and a non-uniform thick oxides (nodule oxides) formed on the surface after 1000h (figure 3 (b)). Similar nodule oxides were also observed on the plate-shaped specimens (figure 3 (c)). Results of XRD analysis of the oxide layers formed on the outside surface of tube-shaped specimens were shown in Figure 4. Protective Cr_2O_3 oxide layer was detected on the specimens except 1520S specimen after 1000h exposure. Cr_2O_3 oxide layer formed only outside surface of tube-shaped specimens because the Cr diffusion in the outside surface of the tubes was accelerated as a result of an increase of dislocation density and/or grain refinement by a high degree of cold working [2, 5]. However, after 1000h, protective oxide layer was not maintained and thick nodules formed on 1520S tube-shaped specimens. Figure 5 (a) shows cross-sectional TEM

image of the outer surface image of the as-received 1520S tube-shaped specimen. Fine-grained layer were observed on the outmost surface. The fine-grained layer which was formed by cold drawing process provided Cr short-circuit diffusion path and promoted the protective Cr_2O_3 oxide layer. However, this fine-grained layer disappeared shown after 100h exposure because of re-crystallization during oxidation test. Figure5 (c) shows the outer surface image of 1520S tube-shaped specimen after 1000h exposure. Internal oxidation advanced along with the grain boundary, and Cr_2O_3 oxide layer was not observed clearly. In the future work, it's necessary to find a correlation between oxidation morphology and oxidation rate, and to feed back to the prediction of the oxidation kinetics of the fuel cladding in the service exposure for up to 5 years.

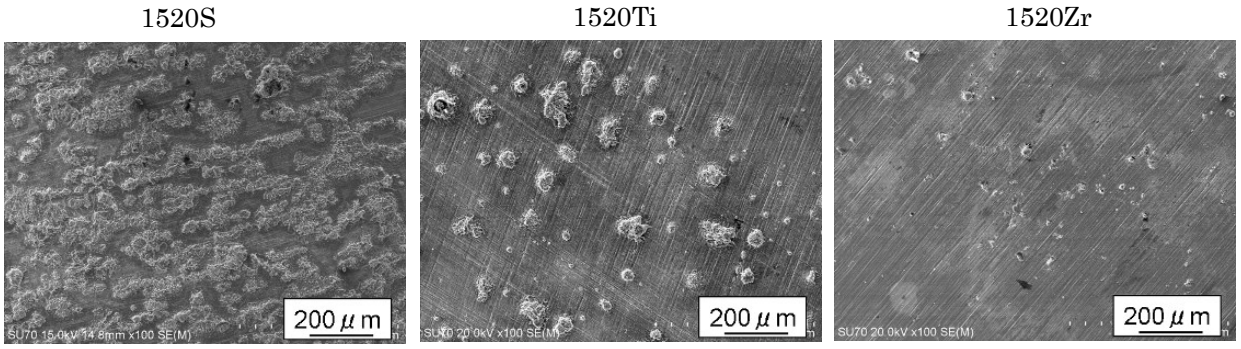

Figure 2 SEM images of the surface of tube-shaped specimens after 1000h exposure.

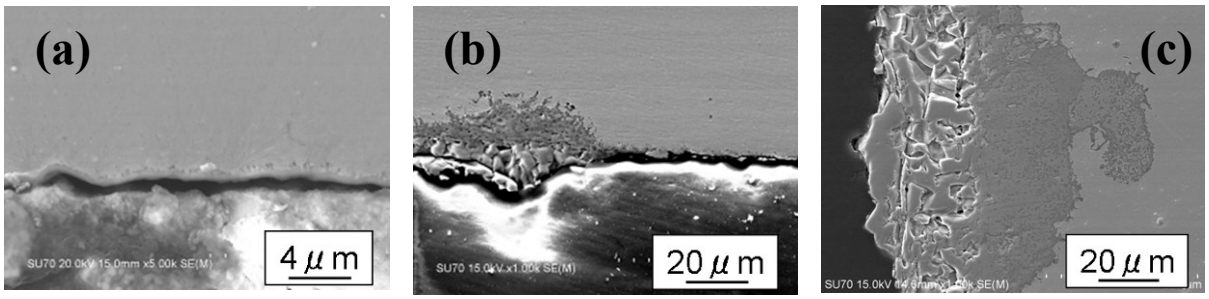

Figure 3 SEM images of the cross section of 1520S tube-shaped specimens: (a) 100h and (b) 1000h, and solution annealed plate-shaped 1520S specimen: (c) 500h.

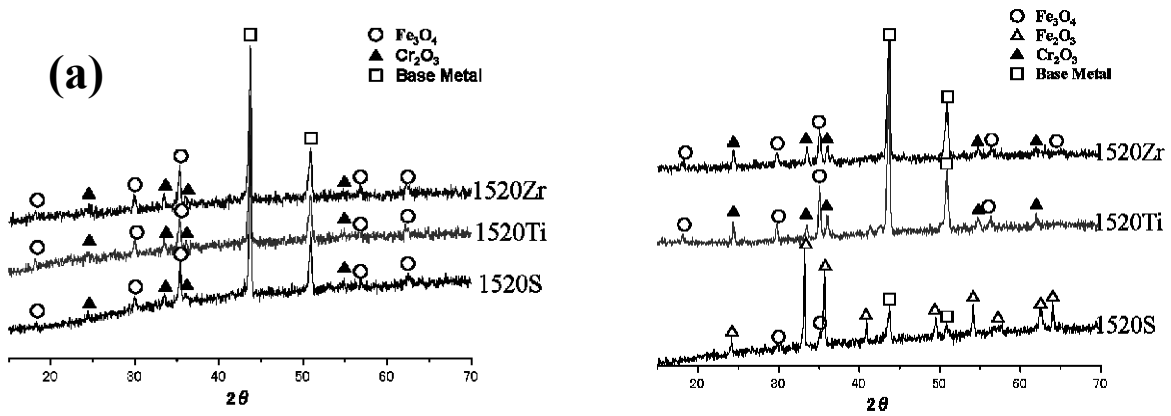

Figure 4 Results of XRD analysis of the outer surface of tube-shaped specimens: (a) 100h and (b) 1000h

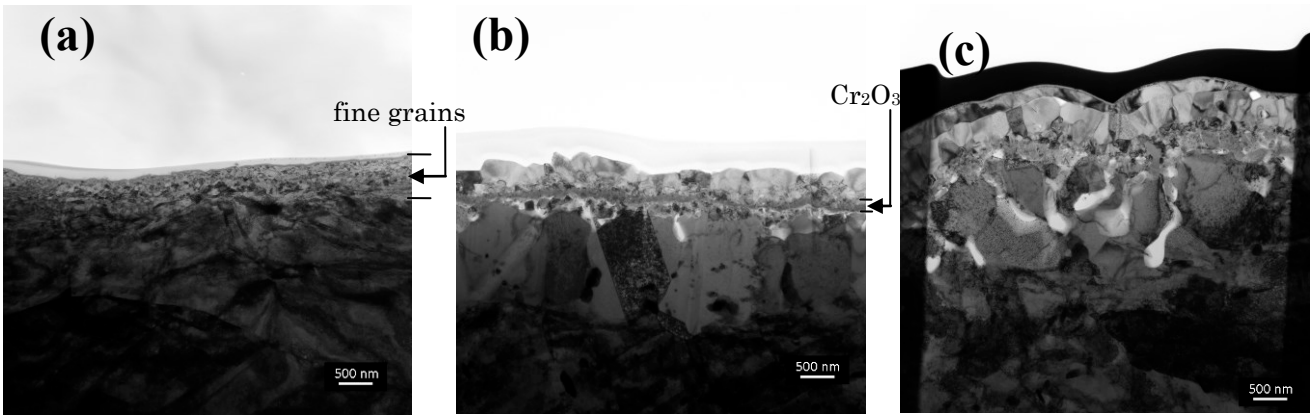

Figure5 TEM cross section images of tube-shaped 1520S: (a) as-prepared, (b) 100h and (c) 1000h

4. CONCLUSION

Oxidation behavior of three types of 15Cr-20Ni austenitic stainless steel in supercritical water at 700°C under 24MPa up to 1000h have been investigated. Detailed structure of the outmost surface of the tube-shaped specimens and degradation behavior of the protective oxide layer have been also investigated. Oxidation rate of 1520S tube-shaped specimen was higher compared with other tube-shaped specimens because Cr_2O_3 oxide layer was not maintained and Fe_2O_3 nodules formed on the surface of 1520S tube-shaped specimens after 1000h exposure. Although the fine-grained layer which was formed by cold drawing process provided Cr short-circuit diffusion path and promoted the protective Cr_2O_3 oxide layer, internal oxidation beneath the Cr_2O_3 layer and degradation of the Cr_2O_3 layer were observed after 1000h exposure. In the future work, it's necessary to find a correlation between oxidation morphology and oxidation rate, and to feed back to the prediction of the oxidation kinetics of the fuel cladding in the service exposure for up to 5 years.

Acknowledgements

Present study includes the result of "Research and Development of the Super Fast reactor" entrusted to the University of Waseda by the Ministry of Education, Culture, Sports, Science and Technology of Japan (MEXT).

Reference

[1] U.SDOE, A Technology Roadmap for Generation IV Nuclear Energy Systems, December(2002)

[2] H.Abe, R.Suzuki, S.M.Hong, Y.Watanaeb, Oxidation behavior of austenitic stainless steels in supercritical water. 16th Int. Conf. on Environmental Degradation of Materials in Nuclear Power Systems-Water Reactors. (2013)

[3] J.C.Langevoort, T.Fransen, and P.J.Gelling, "On the influence of cold work on the oxidation behavior of some austenitic stainless steels: High temperature oxidation" Oxid. Met. Vol.21, (1984), pp.271-284

[4] R.Naraparaju, H.-J.Christ, FU.Renner, A.Kostka, "Effect of Shot-peening on the Oxidation Behaviour of Boiler Steels", Oxid.Met. Vol.76, (2011), pp.233-245

[5] S.Penttila, A.Toivonen, J.Li, W.Zheng, R.Novotny, "Effect of surface modification on the corrosion resistance of austenitic stainless steel 316L in supercritical water conditions", J. of Supercritical Fluids, Vol.81, (2013), pp. 157-163

Failure Mechanism by Hot Corrosion of Alloy 625 Superheater Tube in High-Efficiency Waste-to-Power Plant Boiler

Naoki Kamiyama [1,*], Kazumasa Takemura [1], Hiroyuki Morita [1], Masayuki Yoshiba [1], and Masaru Takakura[2]

[1] Graduate School of Science and Engineering, Tokyo Metropolitan University, Minami-Osawa, Hachioji, Tokyo 192-0397, JAPAN
[2] JEOL Ltd., Musashino, Akishima, Tokyo 196-8558, JAPAN

e-mail: kamiyama-naoki@ed.tmu.ac.jp

1. INTRODUCTION

From the viewpoint of energy and environment issues including global warming problem, the introduction and dissemination of alternative renewable energy to fossil fuel is strongly required. Waste-to-Power (WTP) generation including biomass power generation are highly anticipated because of so much stable performance by their power generation. Because of the extremely severe corrosive environment, however, it is difficult to increase temperature and pressure of WTP plant boiler. Therefore, on the basis of the corrosive failure analysis, WTP plant boiler needs to solve the urgent problem on R&D for boiler material technology that can endure against high temperature and high pressure.

In the present study, corrosive failure analysis was conducted on the Ni-base Alloy 625 superheater (SH) tube. The candidate alloy is operated in the long period of time in Tsukui Clean Center which is the demonstration plant of the NEDO national project for high-temperature and high-efficiency WTP in Japan. From this analytical result, both the corrosive failure process and corrosion mechanism are discussed. The ultimate aim of the present study is for promoting the high-efficiency WTP generation technology through the development of boiler tube material with high performance to higher temperature and pressure in aggressive environment.

2. EXPERIMENTAL

2.1 WTP Plant Investigated

The corrosive failure analysis of the boiler SH tube Alloy 625 with 8mm thickness was conducted in Tsukui Clean Center. The principal specifications are summarized in Table 1. The thermal flow of the boiler zone is shown in Fig.1.

Table 1. Specification of the Tsukui WTP plant and boiler[1].

Disposal capacity	50 t/day
Generating capacity	800 kW
Thermal efficiency(%)	30 %(large incinerator equivalent)
Disposal method	Mass burn
Temperature (Gas/Steam)	630 ℃/450 ℃
Duration of SH tube used	ca. 37,000 h (5 years)

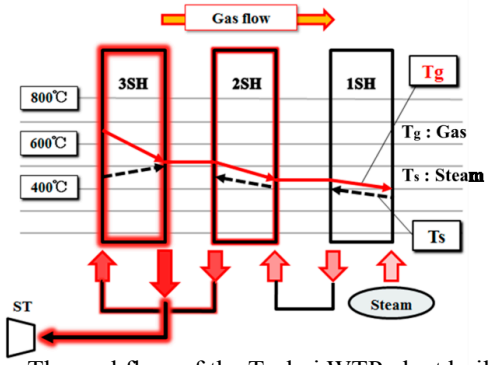

Fig. 1. Thermal flow of the Tsukui WTP plant boiler.

2.2 High-temperature Corrosive Failure Analysis

The corrosive failure analysis was carried out for the final (3rd) SH tube Alloy 625 with 8mm thickness, which was practically operated for about 37,000 h (ca. 5 years). The entrance of 3rd SH zone of the boiler is attainable for the steam temperature of 450℃, and at where combustion gas temperature is approximately 630 ℃. The surface appearance of this SH tube is shown in Fig. 2.

In order to investigate the corrosive environment at the vicinity of corrosion part, the constituent elements of bulky ash adhesive on SH tube and the scale were conducted by means of the fluorescent X-ray spectrometer (Element Analyzer). In this study, plural analyzed spot was set on both environment side of the ash and the metal/scale interface side for consideration of the non-uniformity of the distribution of environmental components. Furthermore, area and line analyses of both backscattered electron image (BEI) and element distribution of the cross-section surface zone were carried out by using the field emission electron probe micro-analyzer (FE-EPMA), together with the dry cross section taken by the cross-section polisher (CP) using Ar ion for corrosive failure analysis of Alloy 625.

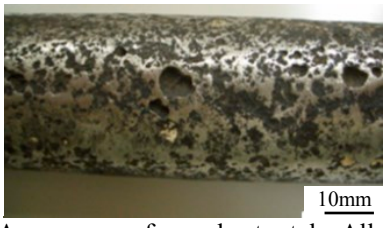

Fig. 2. Appearance of superheater tube Alloy 625 applied for 37,000 h in the Tsukui WTP plant boiler.

3. RESULTS AND DISCUSSION

From the previous research using the TG-DTA analysis of ash deposited onto the SH tube, it was found that the presence of the endothermic peak was observed to suggest the presence of the partly low-melting ash in the operating temperature regime. From the IC analysis of ash deposited, moreover, highly-concentrated Zn was detected. Furthermore, from spot X-ray analysis of multiple sites of ash deposition, the component distribution is inhomogeneous. Namely, it was found that Cl tends to concentrate near the metal scale side rather than the combustion gas side.

Figure 3 shows both backscattered electron image (BEI) and characteristic X-ray area analysis of the corrosion tip of the Alloy 625 SH tube. The main results obtained from there analytical studies are as follows:

a) In Area 1, the ash deposition onto the SH tube was so heavy as to induce the molten salt corrosion by the low-melting chlorides of Na, K, Zn, and so forth.

b) In Area 2, it is suggested that gaseous corrosion also occurred, since the tendency of internal corrosion was observed.

c) In both Area 1 and Area 2, Cl and S tend to be attainable to the corrosion tip. So these elements react preferentially with Cr and Ni. On the other hand, Mo and Nb are concentrated at the corrosion tip, so that they appear to resist against the complicated corrosion reaction associated with both the molten and gaseous corrosion.

d) From the analysis result at Area 2, when the dynamically stable chlorides composed mainly of Ca are formed in the molten salt, the molten salt corrosion tends to be suppressed.

On the basis of the various analytical result denoted above, the corrosive failure of SH tube surface is considered to proceed by the generation and propagation processes of hot corrosion like as follows:

1) Ash deposits onto the SH tube. It is highly possible that molten fly ash containing a large amount of the low-melting point component deposits selectively. Then, the ash deposited constitutes the molten salt corrosive environment.

2) Molten salt corrosion induces the protective oxide film degradation so as to enhance a rapid corrosion.

3) Gaseous corrosion induced by oxy-chlorination reaction also is likely to occur where the molten salt is solidified near alloy surface of the low-temperature region by virtue of alloy elements being incorporated in the molten salt. In some case, the gas such as Cl_2 which is more corrosive than HCl can be produced by Deacon reaction.

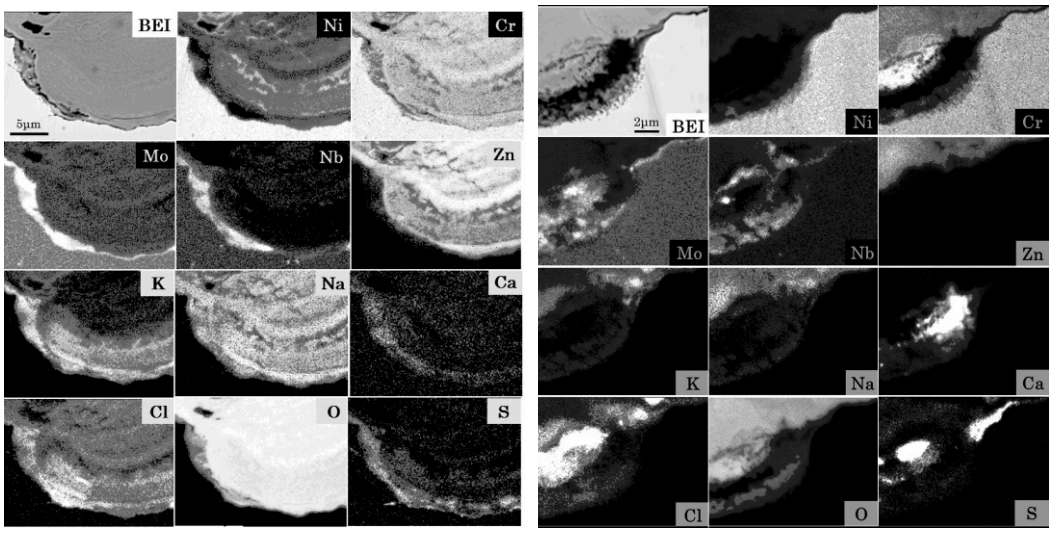

(a) Area 1 (b) Area 2

Fig. 3. Area analysis by FE-EPMA at the cross section of Alloy 625 SH tube applied for 37,000h in the Tsukui WTP plant boiler.

4. CONCLUSION

1) Depending on the characterization of ash deposition, the constituent elements of molten salt corrosive environment are likely to fluctuate spatiotemporally. In particular, molten salt corrosion appears to enhance the pitting corrosion.

2) Where the molten salt corrosion is suppressed, it is also possible that gaseous corrosion is alternatively induced.

Acknowledgements

Authors would like to acknowledge H. Onodera of JEOL Ltd, and T. Sakaki of Tosoh Co., Ltd., for their technical support.

References

[1] H.Morita, M.Yoshiba, Y.Suzuki and Y.Takakura: JSPS 123 Committee Research Report, Vol.52, No.3, (2011), 299.

Enhanced Formation of Chromia Scale on Fe-20Cr-30Ni Alloys by Addition of Nb, Mo and W in Steam Environments

Norifumi Kochi [1,*], Shigehiro Ishikawa [1], and Yoshitaka Nishiyama [1]

[1] Technical Research & Development Bureau, Nippon Steel & Sumitomo Metal Corporation, 1-8 Fuso-Cho Amagasaki, 660-0891, JAPAN

e-mail: kohchi.2yz.norifumi@jp.nssmc.com

1. INTRODUCTION

Operation of advanced thermal power plants with higher efficiency can reduce the CO_2 emission. Increase of steam temperature is one of the most effective ways to improve the efficiency of power plants. The target condition of A–USC has been set to be of 973K at pressures around 35MPa [1]. It has been already known that in austenitic stainless steels containing additional alloying elements, the creep strength at high temperatures can be increased by the precipitation of intermetallic compounds on grain boundaries [2]. However, the effect of the precipitation on the resistance of water vapor oxidation has been still unclear. In this study, we have investigated the effect of addition of precipitating elements, such as Nb, Mo, and W to an Fe–20Cr–30Ni (at.%) alloy on the formation behavior of continuous Cr_2O_3 (chromia) scale in steam atmosphere at elevated temperatures and the function of these elements is discussed.

2. EXPERIMENTAL

Sample alloys with alloying element X of Fe–20Cr–30Ni–X (at.%) were prepared by an arc melting. The amount of Nb was varied from 0 to 2.5%, and that of Mo and W was changed from 0 to 2%. Ingots were heat-treated at 1373 K for 3.6 ks in air, and then hot-rolled to 5 mm in thickness, followed by a solution heat treatment from 1333 to 1473 K for 600 s or 3600 s, resulting in the grain size of 68 to 101 μm. Coupons of 2 t × 10 w × 25 L (mm) were cut from the hot–rolled and solution–treated plates and were mechanically ground with 2000–grits emery paper and electrochemically polished, followed by ultrasonic cleaning in acetone. Water vapor oxidation tests were conducted in a horizontal reaction chamber with a heat resistant steel tube. Water vapor was prepared by heating water that contained dissolved oxygen of 100 ppb at 673K in a pre–heated vessel. The coupons were exposed to the reaction gas at 973K for up to 1000h under a pressure of 1atm. After the exposure, the cross sections of oxide scales were observed with an optical microscope. An electron probe microanalyser (EPMA) was used to determine the chemical composition of the oxide scale.

3. RESULTS AND DISCUSSION

Figure 1 shows the relationship between the amount of additional elements and thickness of the inner oxide scale in the test coupons after the exposure of 200 hours. Its thickness begins to decrease over about 1% of Nb or Mo. In the case of W, the thickness of the inner oxide scale decreases more rapidly from 0.5% of W addition, indicating stronger inhibition effect of W. Figure 2 shows the cross section of 0% Nb and 2.5% Nb alloy coupons after the exposure of 200 hours. Both alloys have two oxide layers on their surfaces; the outer layer consists of Fe_3O_4 and the inner one the spinel-oxide containing Fe and Cr. Growth of both outer and inner oxide scales for 2.5% Nb alloy was clearly inhibited compared to that for the base alloy without Nb. Furthermore, in the 2.5% Nb alloy a continuous Cr_2O_3 scale was found to be formed beneath the inner oxide scale.

From these results, we propose a hypothesis that the precipitation of intermetallic compounds containing the alloying element X and Fe would alter the chemical composition of the matrix of alloy, which leads to the change of activity gradient of Cr. The activity gradient would enhance the flux of Cr from the bulk to the subsurface regions, which enables the Cr_2O_3 scale to form continuously beneath the inner oxide layer, resulting in the retardation of the growth of the whole oxide scales.

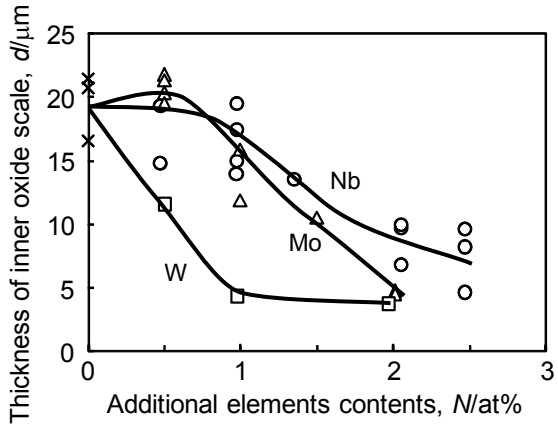

Fig. 1 Relationship between the amount of additional elements and thickness of inner oxide scale after the water vapor oxidation at 973K × 200h. (× : 0% additional elements alloy)

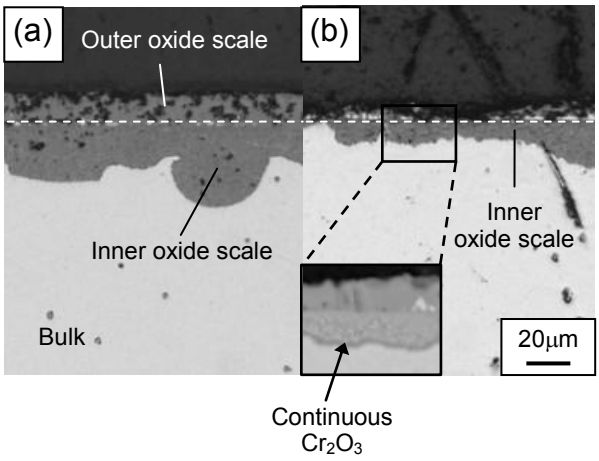

Fig. 2 Cross sections of (a) 0% Nb and (b) 2.5% Nb alloy coupons after the water vapor oxidation at 973K × 200h.

4. CONCLUSION

The effects of Nb, Mo, and W addition to Fe–20Cr–30Ni (at.%) alloy were investigated in terms of the formation behavior of the continuous Cr_2O_3 (chromia) scale in steam atmosphere at 973K. With increasing the amount of additional elements, the thickness of the inner oxide scale decreased and the continuous Cr_2O_3 scale was formed at the boundary between the inner oxide scale and the interior of the alloy. We have proposed one hypothesis that the precipitations of intermetallic compounds in the alloy would change the gradient of Cr activity, which enables the Cr_2O_3 scale to form continuously beneath the inner oxide layer by enhancing the outgoing flux of Cr from the bulk of the alloy.

References

[1] H. Okada, S. Ishikawa, H. Semba, and M. Yoshizawa, “Precipitation Behavior and Creep Properties of Ni-23Cr-7W Alloys,” *Report of the 123rd Committee on Heat Resisting Materials and Alloys*, Vol. 53 (2012), pp. 399-408.

[2] N. Hashizume, N. Takada, T. Matsuo, and M. Takeyama, “Creep Properties od Carbon Free Fe-20Cr-30Ni-2Nb Austenitic Heat Resistant Steel,” *Report of the 123rd Committee on Heat Resisting Materials and Alloys*, Vol. 49 (2008), pp. 151-161.

Water Vapor Oxidation Behavior of Precipitation-Strengthened 15Cr Ferritic Steels with Ni Addition

Mitsunari Auchi [1,*], Yoshiaki Toda [1], Kouta Sawada [1], Hideaki Kushima [1] and Kazuhiro Kimura [1]

[1] National Institute for Materials Science, 1-2-1 Sengen, Tsukuba 305-0047, JAPAN

e-mail: AUCHI.Mitsunari@nims.go.jp

1. INTRODUCTION

In order to reduce carbon pollutants, more efficient thermal power generation is needed. To achieve this, power turbines will need to operate at higher temperatures and pressures, which will in turn require steel components with improved high temperature creep strength and steam oxidation resistance. The authors have proposed using 15Cr steels, which have a higher chromium content than conventional 9Cr or 12Cr ferritic heat-resistant steels, with a tempered martensitic microstructure. It has also been discovered that by optimizing the alloy content and applying heat treatments to these new-concept precipitation-strengthened 15Cr ferritic steels [1], it is possible to produce higher long-term creep strength at a temperature range between 923 K and 1023 K, compared with that achieved by conventional ferritic heat-resistant steels . In this study, water vapor oxidation resistance of the 15Cr ferritic steels was investigated in order to discuss the possibility of using the steels for high-temperature structural components in high-effective thermal power plants.

2. THE EXPERIMENTS

The oxidation experiments were carried out using a high frequency vacuum furnace. The chemical composition of the steels that were tested is shown in Table 1. The steels were hot forged and hot rolled before being solution heat treated at 1473K for 30 minutes and then water quenched. The steels were then cut into coupons measuring 10mm×20mm×2mm, abraded with 600 grit SiC paper and then ultrasonically cleaned in ethanol prior to oxidation. The water vapor was generated from pure water with electric conductivity of less than 0.1μS/cm and dissolved oxygen of less than 0.005mg/l, and the water vapor flow was controlled by the water supply to a steam generator. Oxidation tests were performed at 923K, 973K, and 1023K for up to 3000 hours. Samples were taken from the furnaces at certain times in order to measure mass change. Furthermore, the same experiments were carried out to the conventional Mod.9Cr-1Mo steel for the comparison.

Steel	Fe	C	Si	Mn	P	S	Co	Cr	Ni	Mo	V	Nb	Al	N	B	W
0Ni	Bal.	0.049	0.21	0.50	<0.001	0.001	3.00	14.99	<0.01	1.01	0.20	0.050	0.001	0.051	0.0029	6.00
0.8Ni	Bal.	0.044	0.22	0.49	<0.001	0.001	2.98	14.98	0.79	1.00	0.20	0.048	0.001	0.045	0.0026	6.01
2.0Ni	Bal.	0.047	0.22	0.50	<0.001	0.001	2.99	15.10	1.99	1.01	0.20	0.048	0.001	0.046	0.0030	6.04

Table 1. Chemical composition of steels (mass %)

3. RESULTS AND DISCUSSION

Figure 1 shows the mass change of the 15Cr ferritic steels and the 9Cr steel containing detached oxide scale at the three temperatures. The weight gain of 15Cr steels are smaller than that of existing 9Cr steel, and it becomes more remarkable at the higher temperature. The weight gain decreased with Ni addition at 923K. The results show a tendency to decrease

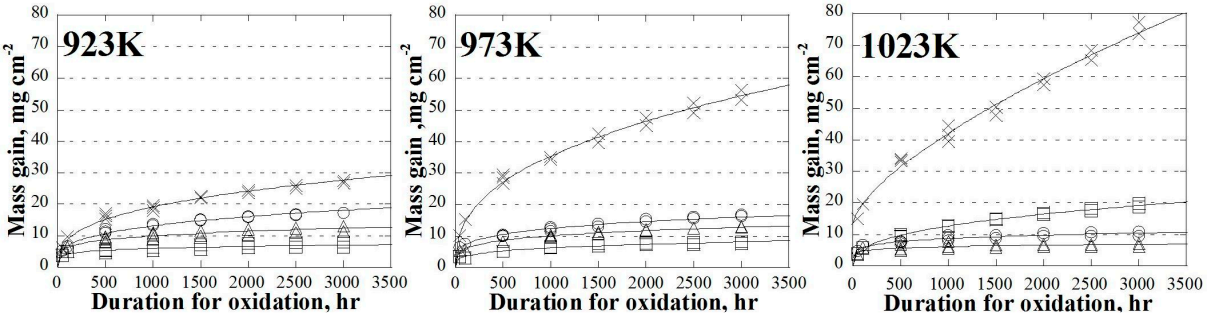

Figure 1. Mass gain of the ferritic steels and the 9Cr steel at each temperature. ○:0Ni, △:0.8Ni, □:2.0Ni, ×:9Cr

weight gain at 973K, so Ni addition is effective to improve resistance to water vapor oxidation under 973K. On the other hand, the results of the oxidation at 1023K show the highest weight gain for the 2.0Ni steel and the lowest weight gain for the 0.8Ni steel, therefore Ni addition isn't necessarily going to increase oxidation resistance. The quantity of oxide that detaches cannot be determined because of individual differences, but the results show a general tendency for oxide scale detachment to decrease as Ni addition or the oxidation temperature increases.

Figure 2 shows SEM images of cross-sections of the oxide layers that formed on samples exposed for 1000 hours at various temperatures. The oxide scale can be classified into two distinct layers: a Fe-rich outer oxide layer and an inner Cr-Fe-rich oxide layer. The tendency is for scale thickness to correspond to weight gain. The chemical analysis obtained by EDS-mapping on cross sectional view revealed a small amount of Ni concentration in the inner Cr-Fe-rich oxide layer. Where Ni addition affects the defect structure and lowers diffusivities, then oxidation resistance is improved. On the other hand, the oxidation resistance of 2.0Ni steel is aggravated at 1023K. It is thought that a large increase of diffusion coefficient in ferritic steel resulting from a rise in temperature [2] will accelerate rather than reduce the oxidation rate, due to changes in the defect structure.

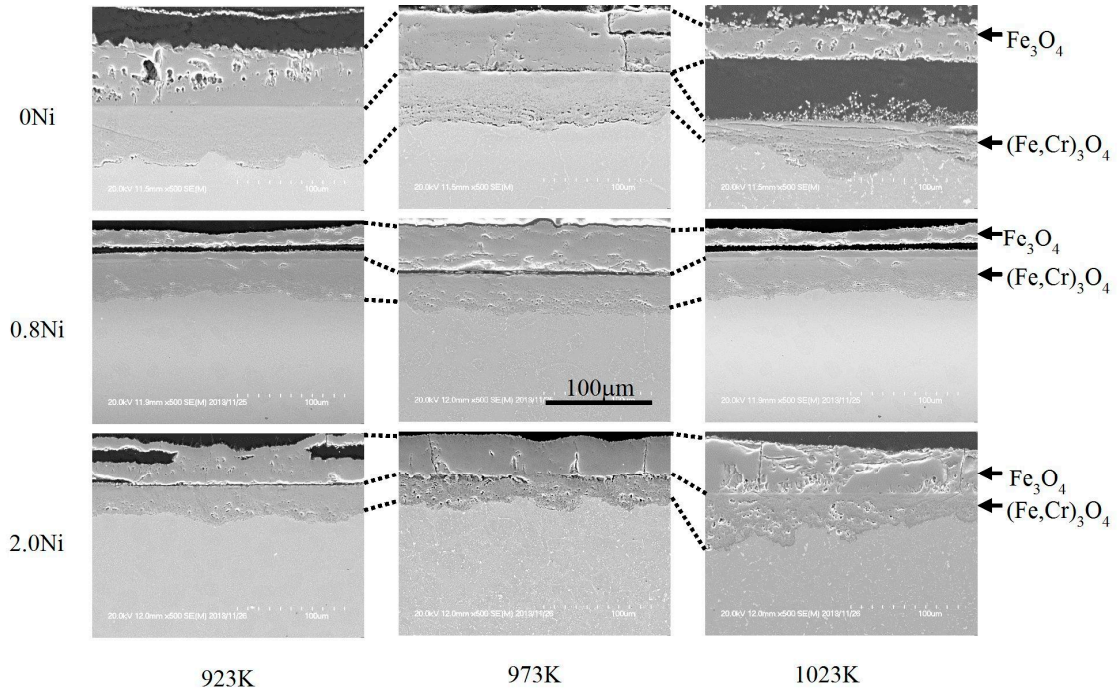

Figure 2. Cross sections of the oxide layers formed on the surface of steels by exposing them to steam atmosphere at 923–1023K for 3.6Ms.

4. CONCLUSION

The water vapor oxidation behavior of precipitation-strengthened 15Cr ferritic steels at 923K, 973K, and 1023K for 3000 hours was investigated. The oxidation rate was decreased with Ni addition under 973K. The oxide scale formed on the steels consisted of an outer Fe-rich oxide layer and an inner Cr-Fe-rich oxide layer. Ni dissolution to the inner layer declined the scale growth, but increase of diffusivity in ferritic steel with temperature rise became one of the factors of oxidation resistance deterioration.

References

[1] Y. Toda, *et al*, Collected Abstracts of the 2013 Autumn Meeting of the Japan Inst. Metals and Materials 2013 No. 405 (DVD)

[2] Zs. Tökei, K. Hennesen, H. Viefhaus, and H. J. Grabke, Materials Science Technology 16, 1129–1138 (2000).

Microstructure development of oxide scales in the early stage of steam oxidation of the Fe-20Cr-30Ni-2Nb (at.%) steel at 1073 K

M. Ueda [1,*], A. Okubo[1], M. Takeyama [1], and T. Maruyama [1]

(1) Department of Metallurgy and Ceramics Science, Graduate School of Science and Engineering, Tokyo Institute of Technology, 2-12-1-S8-11, Ookayama, Meguro-ku, Tokyo 152-8552 JAPAN

e-mail: mueda@mtl.titech.ac.jp

1. INTRODUCTION

Fossil fuel-fired power plants are required to be operated at higher temperatures to achieve higher thermal efficiency. Target temperature of the boiler in advanced ultra super critical (A-USC) power plants is 973 K (700 ℃). In order to achieve target temperature of A-USC power plants, piping materials must have both high creep rupture strength and good steam oxidation resistance. Nickel based alloys are one of the candidates for A-USC power plants. However, the manufacturing cost is more expensive compared to commercial austenitic steels. Thus, Takeyama [1,2] proposed a newly developed austenitic steel, which composition is Fe-20Cr-30Ni-2Nb (at.%). This steel is strengthened by intermetallic compounds and has creep rupture strength of 80 MPa at 973 K for 10^5 h. The authors are now challenging to develop novel austenitic steel in order to meet the requirement of 1073 K (800 ℃) class power plants. Further investigations are needed to improve both creep rupture strength and steam oxidation resistance of the steel for application at 1073 K. Lyta *et al*. [3] conducted steam oxidation tests of the pre-aged Fe-20Cr-30Ni-2Nb (at.%) austenitic steel at 1073 K. In the early stage of steam oxidation, oxide scale formed on the steel mainly consisted of magnetite as the outer scale and the mixture of internal oxidation zone and discontinuous layer of Cr_2O_3. In this steel, the transition from internal to external oxidation finished within about 20 ks and continuous Cr_2O_3 layer was formed at the scale/steel interface. After the formation of continuous Cr_2O_3 layer, internal oxidation zone became inner scale and the growth rate of the oxide scale was suppressed by the Cr_2O_3 layer. Microstructure development of the oxide scale in the early stage of steam oxidation is very important to understand the mechanism of Cr_2O_3 formation. In this study, short-term steam oxidation of the Fe-20Cr-30Ni-2Nb (at.%) steel is carried out at 1073 K to clarify the mechanism of the scale formation in the early stage.

2. EXPERIMETAL

The specimens were prepared from a rod of the Fe-20Cr-30Ni-2Nb (at.%) steel. The steel was solution treated at 1523 K for 3.6 ks before water quench. Grain size after the solution treatment is about 150 μm. The pre-aged steel was made by annealing the solution treated steel at 1173 K in air for 864 ks before water quench. Fe_2Nb Laves phase was precipitated in the matrix of the steel after the aging treatment. The pre-aged steel was cut into $2.5 \times 2.5 \times 1.5$ mm^3, ground and polished to mirror finish. Electrolytic polishing was performed prior to oxidation tests. Short-term steam oxidation was carried out by using hot stage as shown in Figure 1 [4]. The sample was heated on the hot stage up to 1073 K in the stream of Ar-15%H_2O gas mixture for up to 1800 s. The oxygen partial pressure was controlled to be 10^{-6} Pa, which is in the stable region of Fe_3O_4. Figure 2 shows a schematic representation of heat pattern of the sample during the experiment. After each oxidation test, the sample was taken out from the hot stage and microstructure observation was performed by a field emission scanning electron microscope (FE-SEM) equipped with an energy dispersive spectrometer (EDS). Subsequently, the sample was put into the crucible again and next oxidation test was conducted. Oxidation time was defined as the sum of heating time at 1073 K.

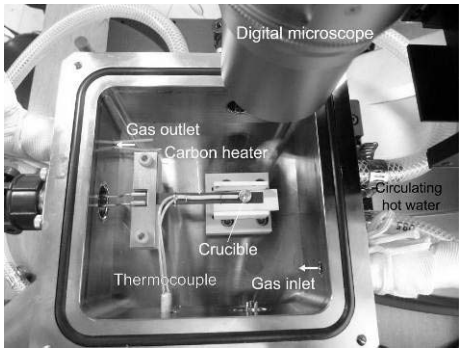

Figure 1 View of the hot stage.[4]

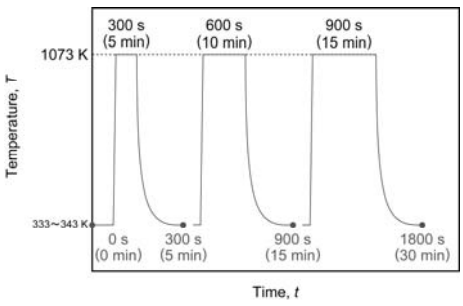

Figure 2 Heat pattern of the sample during the experiment.

3. RESULTS AND DISCUSSION

Figure 3 shows BE image of the cross-section of the oxide scale after short-term steam oxidation at 1073 K for up to 1800 s. The cross-section of the oxide scale was made by focused ion beam method (FIB). Before oxidation, the surface of the sample is slightly etched already due to electrolytic polishing and several Fe_2Nb Laves phase could be located on the surface. Thin duplex scale, which mainly consists of outer scale and initial inner scale, forms on the surface and metallic particles are located at the initial surface after the oxidation for up to 900 s. Internal oxidation locally occurs under the thin duplex scale and discontinuous layer is also observed beneath the thin duplex layer. Duplex scale which consists of outer iron oxide and the mixture of internal oxidation zone and discontinuous layer is observed on the sample oxidized for 1800 s. This morphology is almost the same as that observed in our previous study [3]. In the early stage of steam oxidation, Fe is preferentially oxidized to form outer iron oxide and continuous layer of the initial inner scale is formed beneath the outer scale. Elemental mapping of the sample reveals that sight enrichment of Ni is observed beneath the thin duplex scale. Local change of the chemical composition in the substrate may give the mixture of both internal oxidation zone and discontinuous layer under the thin duplex scale. The mechanism of scale formation in the early stage will be discussed based on the microstructure observation.

Acknowledgements

This study financially supported by the project of "Design principle of super heat-resistant steels applicable to innovative 800 ℃ class A-USC power plants" in Advanced Low Carbon Technology Research and Development Program, Japan Science and Technology Agency.

References

[1] M. Takeyama, *Mater. Sci. Forum*, **539-543** (2007), pp. 3012-3017.
[2] M. Takeyama, *NMS-ISIJ*, **194・195** (2008), pp. 1-23. (in Japanese)
[3] Lyta, M. Ueda, K. Kawamura, M. Takeyama and T. Maruyama, *Mater. Trans.*, **54**(12) (2013), pp. 2276-2284.
[4] A. Okubo, M. Ueda, K. Kawamura, M. Takeyama and T. Maruyama, EFC Workshop, Book of Abstracts, (2012), p. 39.

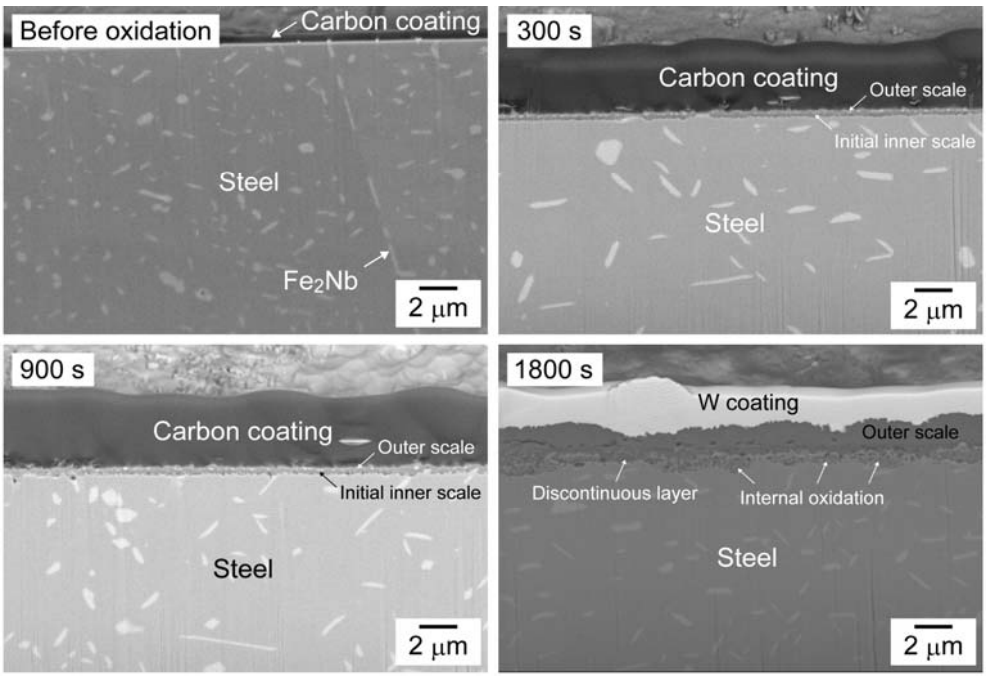

Figure 3 BE images of the cross-section of the oxide scale after short-term steam oxidation at 1073 K for up to 1800 s.

The Long Term Coal Ash Corrosion Behavior of the Superheater Tube Materials in Oxy-fuel Gas Conditions

Yasuo Matsunaga [1,*], Kiyokazu Nakagawa [1], and Takahiro Goto [2] , Toshihiko Yamada[2] , Naoki Fujiwara[2] , Takashi Kiga[2] , Kazuya Kurokawa[3]

[1] Materials Department, Research Laboratory, IHI Corporation, 1 Shin-Nakaharacho, Isogo-ku, Yokohama
[2] Research and Development Dept.,Energy Operations, IHI Corporation, Toyosu IHI Building, 1-1, Toyosu 3-chome, Koto-ku, Tokyo 135-8710, Japan
[3] Center for Advanced Research of Energy and Materials, Faculty of Engineering, Hokkaido University, Kita 13 Nishi 8, Kita-ku, Sapporo 060-8628, Japan

e-mail: yasuo_matsunaga@ihi.co.jp

1. INTRODUCTION

Coal ash corrosion is known as accelerated corrosion caused by formation of molten alkali iron tri-sulfate such as $(Na,K)_3Fe(SO_4)_3$ which melts at 833K[1,2]. Therefore many reports performed coal ash corrosion tests of materials applying the synthetic coal ash (mixture of Na_2SO_4, K_2SO_4 and Fe_2O_3) on the specimens and heating them in O_2 and SO_2 containing gas atmosphere to form alkali iron tri-sulfate on the specimens by reaction of Fe_2O_3 in the ash and SO_3 formed in the gas[1,2].

Oxyfuel combustion of boilers causes the increase of CO_2 content in combustion gas than conventional air firing combustion does. CO_2 content increase is reported as the cause of carburization of steels[3]. However, other report showed that the CO_2 increase did not cause carburization[4].

The 100 hrs. laboratory coal ash corrosion tests revealed that the effect of CO_2 increase on the corrosion behavior were negligible[5]. However, in the 100hrs tests under low SO_2 (under 0.08 vol.%) conditions in which the synthetic coal ash does not melt , corrosion rate of materials were very small irrespectively of the CO_2content in the gas. To investigate the effect of CO_2 content in gas on the long term coal ash corrosion behavior at low SO_2 conditions, This study performed 1000 hrs. laboratory coal ash corrosion test in synthetic combustion gas atmospheres with different CO_2 content.

2. EXPERIMENTAL

Two austenitic stainless steels , alloy A (18Cr- 11Ni- 1Nb- bal. Fe in mass %) and alloy B (25Cr- 20Ni- 0.5Nb- 0.3N- bal. Fe in mass %) and a Ni-based alloy, alloy C (22Cr- 9Mo- 12Co- 1Al- bal. Ni in mass %) were employed for the test materials. The test coupons of each materials were covered with the synthetic coal ash (34 wt.% Na_2SO_4- 41 wt.% K_2SO_4- 25 wt.% Fe_2O_3 mixture) and heated in electric furnace at 973K under synthetic combustion gas atmosphere. Tests were performed under two different compositions gas mixture, one contained 15 vol.% CO_2 which correspond to conventional air- firing combustion gas, and the other contained 66 vol.% CO_2 which correspond to oxyfuel combustion gas. Both gas contained 13vol. % of H_2O, 4vol. % of O_2 , 0.08 vol.% of SO_2 and residual part of the gases were N_2. In these gas composition with 0.08 vol.% SO_2, the synthetic coal ash does not melt after exposure at 973K for 100 hrs.

The heating time of the tests were 100hrs, 240hrs, 480hrs. (alloy A) and 1000hrs, and during the tests longer than 240 hrs., specimens were pulled out from the furnace after each. 240hrs, and the synthetic coal ash were re-applied on the specimens. The final exposure duration of 1000 hrs. test were 280hrs. After the exposure, each specimens were subjected to the corrosion weight loss measurement and cross section observation.

3. RESULTS AND DISCUSSION

The change of corrosion weight losses of the specimens with time were shown in Figure.1. For all alloys, the effect of CO_2 content on the corrosion rates were not significant. Cross section observation did not showed difference also, and no significant carburization were observed even in higher CO_2 content condition.

The 25% Cr stainless steel (alloy B) showed low corrosion rate during totally 1000 hrs. exposure. The corrosion weight loss of 18 %Cr stainless steel (alloy A) was also small until 240 hrs. exposure, however after then , the corrosion rate increased, and after 1000 hrs. exposure, severe corrosion losses were observed.

The synthetic coal ash placed in alumina crucible without specimens were also exposed under the synthetic combustion

gas atmospheres at 973K. In the both gas mixture, the synthetic coal ash did not melt after exposure. This fact means that under 0.08 vol.% SO_2 atmosphere at 973K, in which iron sulfate was not stable thermodynamically, Fe_2O_3 in the ash cannot be converted to sulfate. It can be considered that the corrosion rate increase after 240 hrs. exposure is not caused by formation of alkali iron tri-sulfate, but by other molten salt mixture, which is consist of Na_2SO_4, K_2SO_4 in the ash and other metal sulfate formed as corrosion product of alloys. The metal sulfate should be much stable than $Fe_2(SO_4)_3$ under relatively low SO_2 atmosphere, such like $NiSO_4$. And since it takes certain time duration to form enough amount of the metal sulfate as corrosion product, the accelerated corrosion began after 240 hrs. exposure.

In the case of Ni-based alloy (alloy C) , higher corrosion losses than Alloy A after 100 hrs. exposure were observed. Since alloy C contains 9 mass% of Mo, it is considered that formation of MoO_3 lowered melting point of synthetic ash and formed molten salt in early stage of the exposure[4]. After 1000 hrs. exposure, the corrosion losses of alloy C became comparable to that of alloy A.

4. CONCLUSION

The 1000 hrs. coal ash corrosion test at 973K showed that the effect of CO_2 content increase in the gas on the coal ash corrosion behavior of alloys were not significant. In 0.08vol% SO_2 containing atmosphere in which the Na_2SO_4 - K_2SO_4 -Fe_2O_3 synthetic ash does not melt, the corrosion weight loss of 18% Cr stainless steel was small until 240hrs, but then increased by formation of molten salt of corrosion product.

Acknowledgements

The main part of this study was performed with the support of New Energy and Industrial Technology Development Organization (NEDO).

References

[1] Nelson *et.al*, Transactions of the ASME,(1960) pp.194-204

[2] Cain *et.al*, Transactions of the ASME,(1961) pp.468-474

[3] Tuurna *et.al*,: "*9th Liege Conference; Materials for Power Engineering "* (2010) , pp.1052-1060.

[4] Abellan *et. al*, International. Journal of materials Research, (2010) pp.287-299

[5] Matsunaga. *et al*, "*Report of the 123rd Committee on Heat-resisting Metals and Alloys, Japan Society for the Promotion of Science*"(2011),pp.223-229

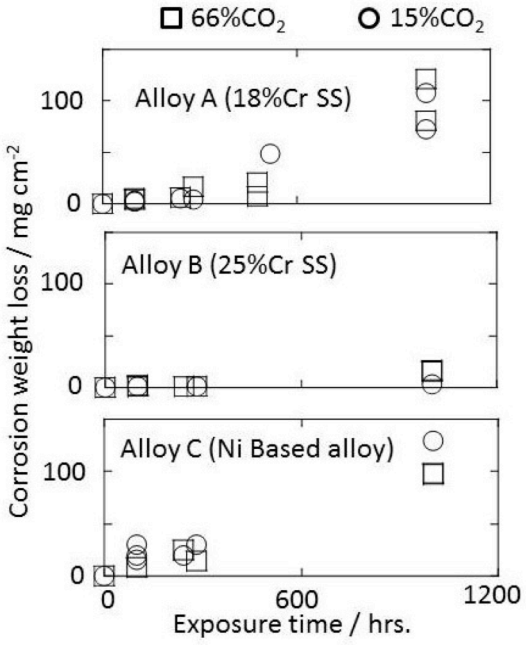

Figure.1 The change of corrosion weight losses of materials with exposure time at 973K.

Effect of Electrical Current on Growth of Oxide Scale in Interface between Electrode and Fe-22mass% Cr SOFC Interconnect at 1073 K

M. Febry [1,*], M. Ueda [1], K. Kawamura [1], and T. Maruyama [1]

[1] Department of Metallurgy and Ceramic Science, Graduate School of Science and Engineering, Tokyo Institute of Technology, 2-12-1 Ookayama, Meguro-ku, Tokyo 152-8550, JAPAN

e-mail: febry.m.aa@m.titech.ac.jp

1. INTRODUCTION

The solid oxide fuel cell (SOFC) is a promising candidate for future energy conversion system, not only because its high efficiency in generating electricity from variety of fuel such as hydrogen, methane, and even natural gas but also it generates very low pollutant to the environment during the operation.

One of the challenges in development of SOFC is developing low cost materials for the components. Metallic alloy is one of the options for reasonable-cost interconnect material. Among the metallic alloy, chromia (Cr_2O_3)-forming alloy is favored due to its good balance between growth rate and conductivity of protective Cr_2O_3 scale under oxidizing atmosphere at high temperature.

However in the operation of SOFC, the interconnect material is not only exposed to oxidizing atmosphere but also current flow due to the electrochemical reaction of the cell, Under the current flow, the growth of Cr_2O_3 scale is enhanced on low potential side [1]. This resulted in formation of thick Cr_2O_3 scale, which increases the stack resistance. As the stack resistance increasing, there is a possibility that the current could not spread throughout the entire interconnect and concentrate in some areas. Current concentration may lead to cell deficiency. Thus, the issue of current concentration needs to be investigated.

In order to clarify the issue of current concentration, the current spread and area which influenced by the current are important to be known. Based on previous result [1], the thickness of Cr_2O_3 scale could be used as indicator for the amount of current flows. Thus in this study, the current spread on the interface between the interconnect and electrode is clarified by comparing the thickness of Cr_2O_3 scale.

2. EXPERIMENTAL

The sheet of Fe-22mass% Cr ferritic steel (JFE Techno Research Corporation) was cut into 10 x 10 x 1 mm. The chemical composition of the alloy is shown in Table I. The sample was polished with SiC paper(#320 to #2000), cleaned by ultrasonic cleaning with ethanol, and pre-oxidized in Ar-19%H_2-0.6%0_2 at 1073 K for 3.6 ks prior to oxidation experiment.

Table I. Chemical Composition of the sample

Fe-22mass% Cr	Fe	Cr	Mn	Ni	Si	Sol. Al
Mass %	Bal.	21.92	0.01	0.01	0.02	0.008

Fe-22mass% Cr	C	S	P	N	O
Mass %	0.024	0.002	0.003	0.0049	0.0079

The porous Ni-YSZ electrode was made by mixing NiO:8YSZ (volume ratio 6:4) and carbon powder 12% from the total mass. Mixed powder was put into 10mm-diameter die, pressed (50 MPa) for 60 s, and sintered in ambient air at 1573 K for 10.8 ks. In order to reduce NiO to Ni, the sintered electrode was exposed to Ar-20% H_2 at 1223 K for 3.6 ks.

The sample was sandwiched by Ni-YSZ electrodes (d= 8mm, t= 2mm) and oxidized in Ar-19%H_2-0.6%H_2O gas mixture (log (P_{O2}/Pa) = -16.4) with 0.5 Acm^{-2} electrical current flows at 1073 K for up to 864 ks. This condition is corresponding to the real anode atmosphere of SOFC.

The oxide scale was identified by XRD. The distribution of elements in the oxide scales was analyzed by EPMA, and the thickness of oxide scales was measured from cross sectional images.

3. RESULTS AND DISCUSSION

Figure 2 shows cross-sectional image of the sample after oxidation for up to 864 ks. The area could be distinguished by low potential side contact and non-contact area and high potential side contact and non-contact area. Figure 3 shows the thickness of the oxide scale and the average on each area. On the low potential side, the contact area has a higher thickness average compared to non-contact area. On the high potential side, the contact area has a smaller thickness average compared to non-contact area.

Figure 4 shows the square thickness of the oxide scale and k_p value of the samples after the oxidation test. Different thickness in each area indicates different amount of current passed through each area. The contact area of low potential side has a higher thickness and k_p value, while high potential side has a smaller thickness and k_p value, compared to the non-contact area for both 604.8 and 864 ks oxidation time. These results indicate that current did not spread throughout the entire scale and interconnect but more concentrated on the contact area between the electrode and sample compared to the non-contact area. Figure 5 shows the elemental mapping of the sample after oxidation for up to 864 ks. It shows that the oxide scale of the sample was only composed of Cr_2O_3 scale.

4. CONCLUSION

Under the current supply, growth of Cr_2O_3 scale is most accelerated at the contact area of low potential side. It indicates that current did not spread throughout the entire scale and interconnect but more concentrated on the contact area between the electrode and interconnect.

Figure 2. Cross-sectional OM images of the sample after oxidation test for 864 ks

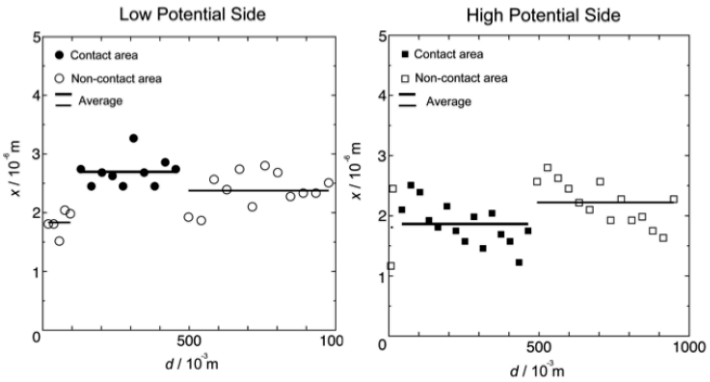

Figure 3. Average thickness of the sample after oxidation test for 864 ks

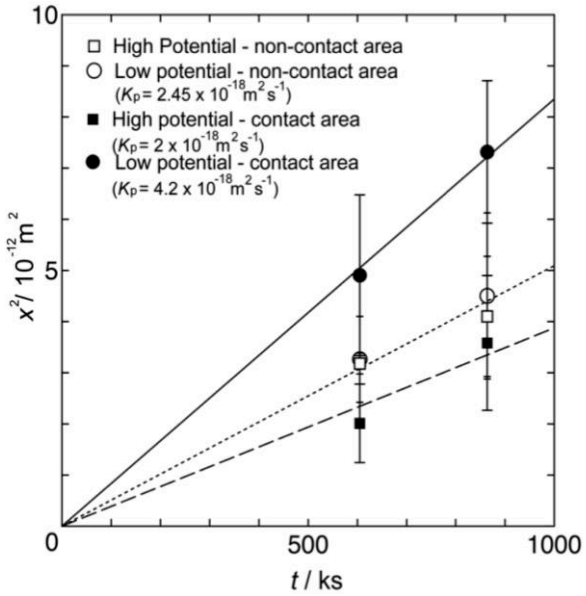

Figure 4. Square thickness of the sample after oxidation test for up to 864 ks

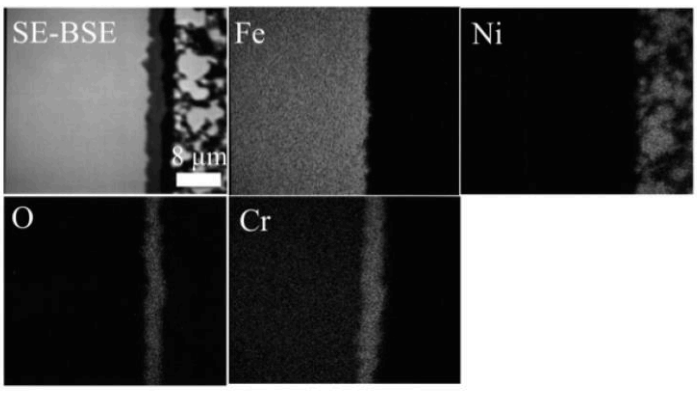

Figure 5. Elemental mapping of the sample after oxidation test for 864 ks

Reference:

[1] K. Kawamura *et al.*, "Effect of Electrical Current on Growth of Oxide Scale on Fe-25Cr Alloy for SOFC Interconnect at 1073 K," *Journal of The Electrochemical Society*, Vol. 159 No.3(2012), pp. B259-B264.

The influence of La_2O_3 nanoparticles on the oxidation resistance of Crofer 22 APU steel

A. Gil [(1,*)], J. Wyrwa, [(1)] and T. Brylewski [(1)]

(1) Department of Materials Science and Ceramics, AGH-University of Science and Technology, Al. Mickiewicza 30, 30-59 Kraków, POLAND

e-mail: gil@agh.edu.pl

1. INTRODUCTION

The high chromium ferritic steel Crofer 22 APU is specially manufactured for the production of interconnectors for SOFC fuel cells. This steel contains an addition of lanthanum, which acts as the active element and is responsible for reducing of the oxidation rate and improving of the adhesion of Cr_2O_3 scale to the metallic phase. Lanthanum has a greater solubility in α-Fe phase than other active elements (Y, Ce, Zr, …) and does not form intermetallic phases with iron. For these reasons lanthanum acts more effective as an active element [1]. The improving of the corrosion resistance of high-chromium ferritic steels is possible by deposition of the nano-particles of reactive element oxides. The deposition of oxide nano-particles is low price process, possible of applying for the ready-made elements. Ma et al. [2] demonstrated that deposited Y_2O_3 film on the surface of the steel 18Cr-9Ni-Ti promotes the selective oxidation of chromium, as well as causes change of growth mechanism of the scale, reduces the rate of oxidation and improves scale adherence to the metallic substrate.
The aim of this study was to investigate whether lanthanum oxide film deposited on the surface of the steel Crofer 22 APU improves its oxidation resistance. For this purpose, has been studied cyclic oxidation at 900˚C in air of unmodified material and coated with lanthanum oxide.

2. EXPERIMENTAL

The samples were cut from the sheet with a thickness of 0.5 mm to size 20x10 mm^2 and the next were polished to smoothness as mirror. Lanthanum was deposited on the surface of samples in the electrolytic process in ethanol solution of lanthanum nitrate (0.01M). The current density was 0.25 mA/cm^2 and deposition time of 30 sec. Lanthanum reacted with a residual water to form a hydroxide. Oxide layer was obtained by thermal decomposition of hydroxide (400˚C, 30min.). The structure of the film of lanthanum oxide was examined by AFM. Oxide layer was formed by thermal decomposition of lanthanum nitrate film deposited on the glass by dipping. Cyclic oxidation test was carried out in a horizontal furnace at 900˚C in laboratory air. One cycle composed of oxidation for 1 hour and 15 minutes of cooling. The morphology, chemical and phase composition of the scales was studies with SEM, EDS and XRD.

3. RESULTS AND DISCUSSION

Fig. 1 presents the AFM image of the morphology of the surface of La_2O_3 film. As can be seen, the film is composed of nanoparticles having a size no larger than 50 nm.

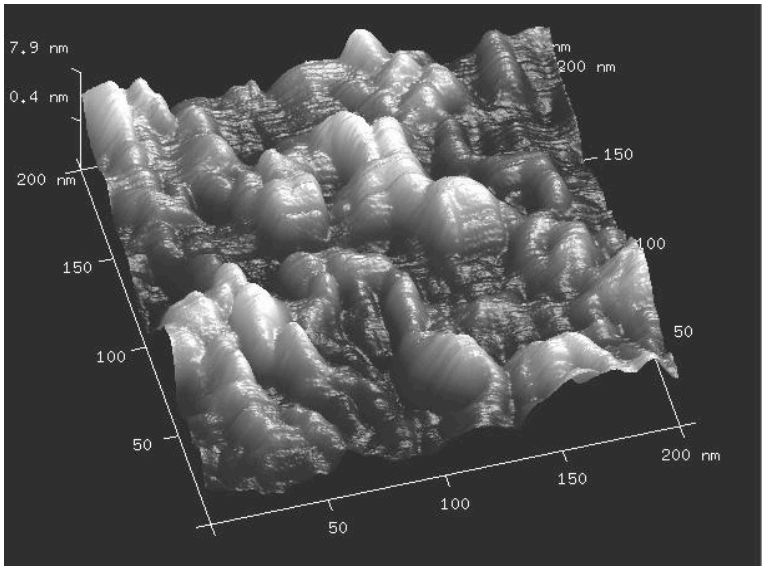

Fig.1 AFM image of La_2O_3 film deposited on the surface of glass

The results of the thermal cycling oxidation (900˚C, 750x1h, air) are shown on Fig.2. Effect of long-term improvement of the oxidation resistance was found. The decreasing of the mass gain of modified steel was less that the half of the mass gain of non-treated one. The metallographic cross-sections observations show that the scale formed on Crofer 22 APU was two-layered. The inner sub-layer composed of Cr_2O_3 and the outer one - $MnCr_2O_4$ spinel. The structure of the scales formed on the samples modified with oxides nano-particles was similar as non-treated steel but their thicknesses was smaller. The oxide scale formed on modified steels had perfect adherence to metallic core.

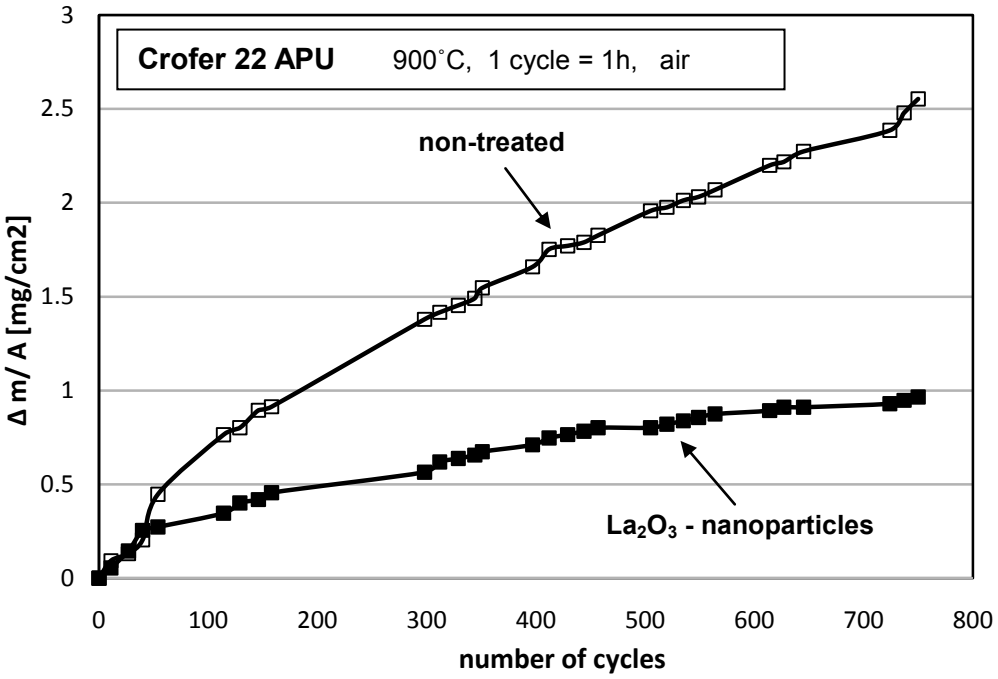

Fig. 2 The cyclic oxidation of non-treated and modified with La_2O_3 nanoparticles Crofer 22 APU steel

4. CONCLUSION

1. La_2O_3 nanoparticles deposited on the surface of Crofer 22 APU gives effect of long-term improvement of the oxidation resistance.
2. The mass gain of Crofer 22APU steel modified with lanthanum oxide was less than the half of the mass gain of non-treated one.
3. Lanthanum oxide nanoparticles do not change the phase composition of the scale formed on the steel Crofer 22 APU.

Acknowledgements

The author kindly acknowledges a support from the European Institute of Innovation and Technology (EIT). The study has been performed within the EIT KIC InnoEnergy project on “New Materials for Energy Systems”.

References

[1] W.J. Quadakkers, “Practical Aspects of the Reactive Element Effect” Mater. Sci. Forum, Vol. 77 (2001) pp. 369-372.
[2] Ma, J., He, Y., Wang, D., Gao W., „The effects of pre-oxidation and thin Y_2O_3 coating on the selective oxidation of Cr18-Ni9-Ti steel”, Matter. Let., Vol. 58, (2004), pp. 807-812.

Fabrication of Cobalt Oxide Coating by Electrodeposition followed by Thermal Conversion for SOFC Interconnector

Isao Saeki (*), Taiki Yoshida, and Yusuke Watanabe

Department of Materials Science and Engineering, Muroran Institute of Technology,
Mizumoto 27-1, Muroran 052-0035, JAPAN

e-mail: isaos@mmm.muroran-it.ac.jp

1. INTRODUCTION

Ferritic stainless steel is a candidate material for interconnector of SOFC as it shows slow oxidation kinetics, high electron conductivity, and constant of thermal expansion is similar to that of other components. Chromium oxide formed on stainless steel, however, vaporizes and reacts with cathode to degrade of catalytic activity of the cathode. To overcome this problem, high manganese stainless steels were investigated. The steels form an outer manganese chromite layer which slows down the vaporization of hexavalent chromium species. However, the vaporization could not reach zero in this case. Cobalt oxide coating by PVD was examined and it was found that the coating effectively prevented the vaporization at 800 C. However, high production cost is a major problem of this method if the PVD coating is applied to stainless sheet strips with wide area. In this study, we examined the effectiveness of Co and Co-La electroplating.

2. EXPERIMENTAL

A commercial type 430 stainless steel was used. After degreasing a 20 x 30 x 0.5 mm^3 strip, thin Ni layer was electroplated to improve adhesion between Co plating and the steel. Co or Co-La electroplating was carried out with baths shown in table 1 to 5 micrometer. Co plating is simply a reduction of Co ion. For Co-La codeposition, precipitation of La hydroxide formed by chemical reaction was used. If the cathodic current efficiency of Co deposition is less than 1, H_2 gas evolves in acidic media according to the reaction (1).

$$2H^+ + 2e^- \rightarrow H_2(g) \qquad (1)$$

In this case, solution pH in the vicinity of cathode surface rises and $La(OH)_3$ precipitates, then it is incorporated into Co plating layer to form a Co-La codeposition film. The High-temperature oxidation test was carried out at 800 ˚C in Air-3 vol.% H_2O gas flow up to 2000 hrs. Cr evaporation is assessed by collecting sublimated Cr species in inside of the quartz tube kept at 5 ˚C (Fig. 1). The quartz tube was washed with aqua regia, then dissolved Cr was measured by ICP-AES. An SEM/EDS was used for observation and cross section distribution of elements. Electro-conductivity of the oxide formed on type 430 stainless steel was measured with a 4-terminal method together with a frequency response analyzer. A DC conductivity was evaluated by extrapolating AC resistance to zero frequency.

Table 1 chemical composition of electroplating baths

plating	component	concentration
strike Ni plating	$NiCl_2$	1 M
	HCl	125 cm^3/L
Co-La plating	$CoCl_2$	0.1 M
	$LaCl_3$	0.01 M
	glycine	0.1-1 M
	NaOH	to adjust pH

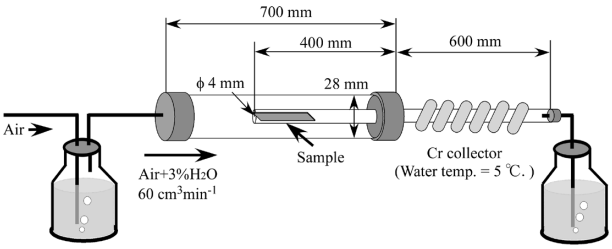

Fig. 1 Test tube for Cr sublimation measurement

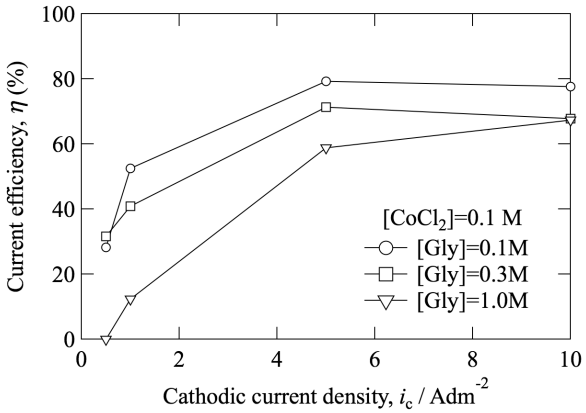

Fig. 2 Effect of cathodic current density on current efficiency.

3. RESULTS AND DISCUSSION

3.1 Co and Co-La electroplating

For Co-La deposition reaction, partial H_2 evolution reaction must proceed on the cathode. Figure 2 shows the effect of

glycine concentration in electroplating bath and cathodic current density on cathodic current efficiency for Co deposition at pH 6.5. At low current densities, current efficiencies were lower than 50% and H_2 gas evolution was evident. The efficiency increased with increasing cathodic current density and decreasing glycine concentration. Figure 3 shows the effect of solution pH on La content in the film. La content tends to increase with increasing the pH. La hydroxide precipitation occurs at pH 10. High solution pH tend to increase the pH at the vicinity of the cathode. The effect of concentration of glycine is not clear from this result. However, because cobalt ion forms soluble glycine complex at mol ratio of 1:1, we decided glycine concentration to 0.3 M. Cathodic current density was adjusted to1 and 3 A dm^{-2} at pH=6.5 to obtain 1 and 3 mol% La containing Co-La deposits.

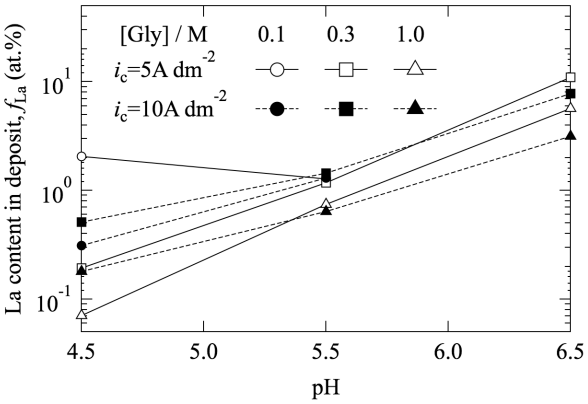

Fig. 3 Effect of bath pH on the La content in deposit.

Prior to Co and Co-La electroplating, thin Ni layer was deposited using the solution in table 1 at room temperature. Figure 4 shows surface appearance of Co, Co-1%La, Co-3%La plating with cross scratches. Independent of the time of Ni strike plating, there was no spallation of Co and Co-La electroplating layers. From this result, time of Ni strike plating was determined to 180 s.

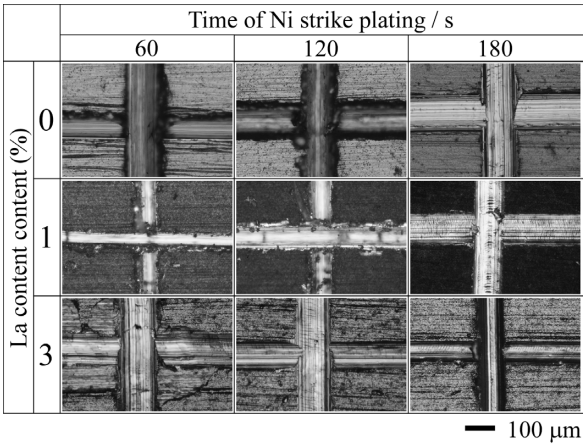

Fig. 4 Surface appearance after scratch test of Co-La plating after Ni strike plating

3.2 Structure of oxide after the oxidation tests

Figure 5 shows cross section and results of EDS analysis of oxidized Co and Co-La coated stainless steels after oxidation for 10 hrs. It was found that Co and Co-La electroplating layers were converted to oxides within 10hrs. The oxide was composed of Co_3O_4 with a few percent of La for Co-La codeposition. Cr oxide was detected at the bottom of Co_3O_4 layer. Estimated thickness of Cr oxide to outer Co_3O_4 oxide was indicated by vertical broken lines. It was less than a few micrometers for all specimens. Result after 2000 hrs of oxidation test was shown in Fig. 6. For longer oxidation time, the structure of oxides was similar to that for 10 hrs oxidation. Cr oxide under Co_3O_4 layer became thick in these cases. However, penetration of Cr oxide to the oxide surface was not observed. Cr penetration depth estimated as shown in Figs. 5 and 6 was plotted against oxidation time in Fig. 7. Although the data scattered, the penetration depth tended to increase with increasing oxidation time. If the lifetime of SOFC is assumed to 20,000 hrs. Maximum depth may be 10 micron meters. To obtain this Co_3O_4 layer, at least 5 micrometer of Co electroplating is needed.

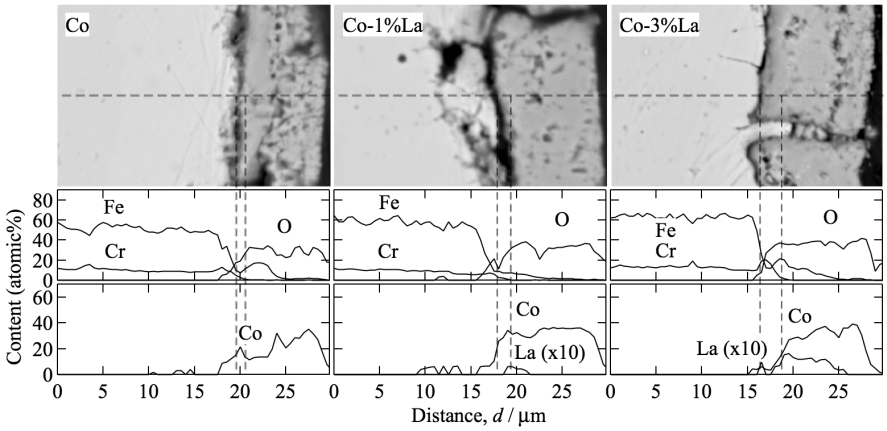

Fig. 5 Cross section and EDS analysis of Co and Co-La plated type 430 stainless steels oxidized at 800 ˚C for 10 hrs in Air-3 vol.% H_2O.

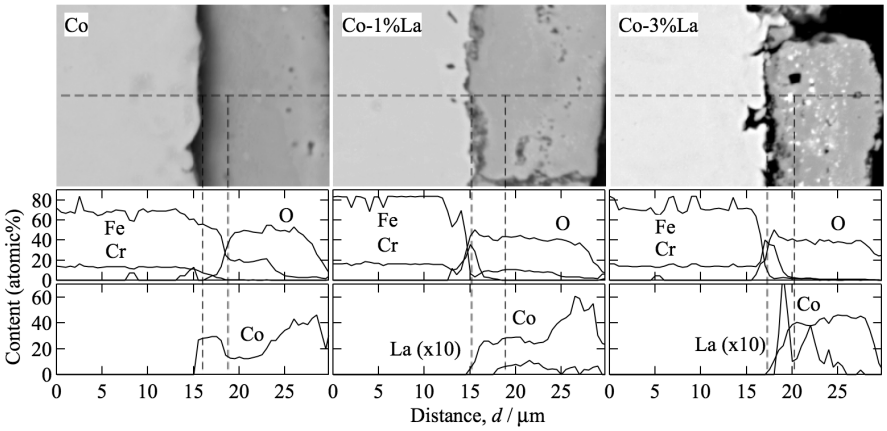

Fig. 6 Cross section and EDS analysis of Co and Co-La plated type 430 stainless steels oxidized at 800 ˚C for 2000 hrs in Air-3 vol.% H_2O.

3.3 Cr evaporation test

ICP spectra of Cr after the test is shown in Fig. 8. From type 430 stainless steel without the electroplating showed Cr evaporation for 2000 hrs of oxidation at 800 ˚C. However, the amount of Cr is less than the limit of quantification. Co and Co-1.5% plating sample showed no Cr evaporation. This means that there were no cracks through Co_3O_4 layers formed by the oxidation of Co and Co-La electroplating.

3.4 Electric conductivity

Figure 9 summarizes electric conductivity of samples oxidized up to 2000 hrs. For all specimen oxidized for 10 hrs, electric conductivities were similar to that of Co oxide in literatures [1-3]. The conductivity increased with increasing oxidation time. This may be related to the dissolution of Fe in Co_3O_4 layer and the formation of Cr_2O_3. However the conductivity values obtained in this experiment were higher that those of pure Cr_2O_3 and $CoFe_2O_4$ for more than a few orders of magnitude [4, 5]

4. CONCLUSION

Co-La oxide coating was carried out by electroplating and high-temperature oxidation. Formed oxide layer was mainly composed of Co_3O_4 that dissolves La. With increasing oxidation time, Fe dissolved in the layer and Cr oxide formed under the layer. Cr evaporation was not detected up to 2000hr, and 5 micrometer of Co electroplating is needed to prevent Cr evaporation up to 20,000 hrs.

References

1. V. R. Shinde, S. B. Mahadik, Gujar, C. D. Lokhande, *Appl. Surf. Sci.,* 252 p. 7491 (2006).
2. V. Patil, P. Joshi, M. Chougule, S. Sen, *Soft Nanoscience Lett*., 2, pp. 1-7 (2012).
3. H. Duan, D. Xu, W. Li, H. Xu, *Catalysis Lett*., 124, p. 320 (2008).
4. D. M. Shakhtin (1984).
5. M. Soliman Selim, G. Turky, M. A. Shouman, G. A. El-Shobaky, *Solid State Ionics*., 120, p. 177 (1999).

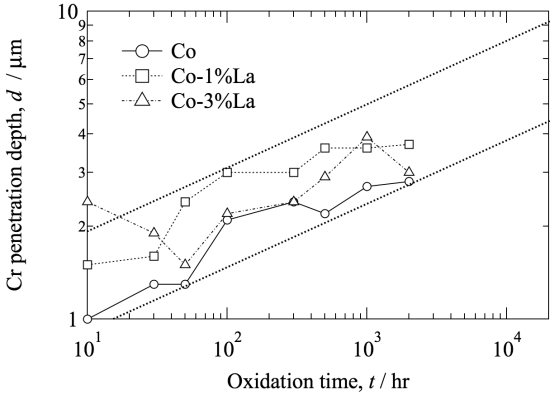

Fig. 7 Estimation of Cr penetration depth up to 20,000 hrs.

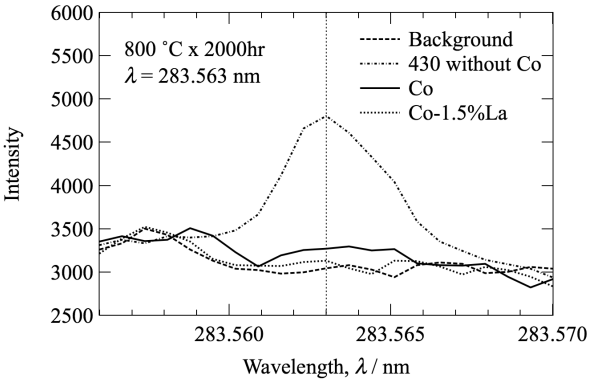

Fig. 8 ICP spectra of Cr collected from quartz tube after 2000 hr of evaporation test at 800 ˚C.

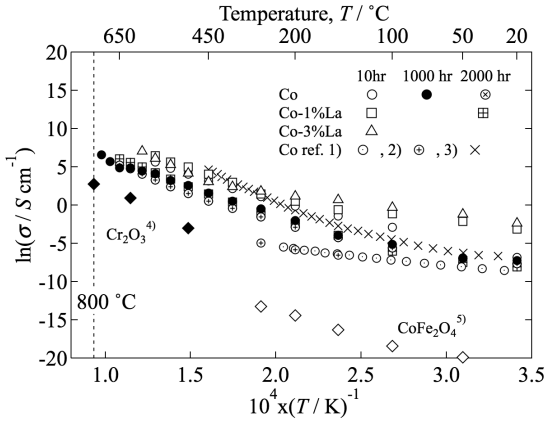

Fig. 9 Temperature variation of electric conductivity of Co plated type 430 stainless steel after oxidation test up to 2000 hrs.

Effect of Nano Metal Coatings on Growth Kinetics of α-Al_2O_3 Formed on Ni-50Al Alloy

Ali Shaaban [1, 2], Kazuhisa Azumi [3], and Shigenari Hayashi [3]
[1] Graduate School of Chemical Sciences and Engineering, Hokkaido University, Kita13 Nishi8, Sapporo 060-8628, JAPAN
[2] Surface Protection and Corrosion Control Lab., Central Metallurgical Research and Development Institute (CMRDI), Egypt
[3] Graduate School of Engineering, Hokkaido University, Kita13 Nishi8, Sapporo 060-8628, JAPAN
e-mail: ali@eng.hokudai.ac.jp

1. INTRODUCTION

The oxidation resistance of Al_2O_3 forming alloys depends on the formation of slow growing protective Al_2O_3 scales. Therefore, rapid formation of stable α-Al_2O_3 is strongly required in order to improve the reliability and the life-time of alumina-forming alloys and coatings. From our previous study, it was found that meta-stable Al_2O_3 formation at 900 °C by oxidation in air was completely suppressed by very thin, about 50 nm, coating of Fe, or Cr, which was deposited directly on the Fe-50Al alloy [1], but Ni was found to delay the transformation. The aim of this study is to evaluate the effect of introducing these metal coatings and different transformation behaviors of α-Al_2O_3 on long term growth kinetics of the oxide scale at 1000 °C formed on Ni-50Al alloy in air.

2. EXPERIMENTAL

50 nm of pure metallic coating of Ni, Fe or Cr was deposited onto the samples of Ni-50Al alloy. Ni-50Al samples with/without Ni, Fe and Cr-coating were firstly oxidized at 900 °C in air and kept for 4 h then furnace-cooled in order to pre-form meta-stable or stable alumina scale. The pre-oxidized samples were then oxidized again at 1000 °C in air and kept for different time intervals in order to evaluate the effect of metallic coatings on the α-Al_2O_3 scale growth rate at 1000 °C. FE-SEM was used for the observation of the surfaces of the oxidized samples after each oxidation step. XRD was used to characterize the structure of the oxidation products formed on the oxidized samples.

3. RESULTS AND DISCUSSION

3.1. OXIDATION KINETICS AND PRODUCTS IN PRE-OXIDATION STAGE

The oxidation mass gain of the blank sample and Ni-coated sample were greater than those of Cr-coated and Fe-coated samples. The surface of the pre-oxidized blank sample was covered by oxide scale of blade-like morphology. This oxide scale was identified by XRD to be a mixture of predominant θ-Al_2O_3 phase and α-Al_2O_3 phase. Ni-coated sample was covered by oxide scale of faceted morphology. This oxide scale was identified to contain NiO, $NiAl_2O_4$, θ-Al_2O_3 and α-Al_2O_3 phases. On the other hand, fine nodular oxide scale was developed on Cr-coated sample. This oxide was identified to be α-Al_2O_3. Tetrahedral shaped oxide was developed on Fe-coated sample. This oxide was also identified to be mainly α-Al_2O_3 and Fe_2O_3.

3.2. OXIDATION KINETICS AND PRODUCTS OF THE PRE-OXIDIZED SAMPLES AT 1000 °C

The oxide scales formed on the pre-oxidized samples were confirmed to be predominantly θ-Al_2O_3 on the blank sample and NiO and θ-Al_2O_3 on Ni-coated sample, α-Al_2O_3 on both of Cr- and Fe- coated samples. The samples with those oxide scales were then oxidized isothermally at 1000 °C for different time intervals up to 100 h in air. The oxidation kinetics of Ni-50Al with/without Ni, Cr or Fe-coating for up to 100 h at 1000 °C was shown in **Fig. 1.** The oxidation behavior of the oxidized samples could be categorized into three different groups, the bare NiAl alloy sample, the Ni-coated sample and the Cr- and Fe-coated samples. During the main oxidation stage, at 1000 °C the oxidation mass gain of the pre-oxidized blank sample was greater than those on the coated samples, but the k_p value of the blank sample rapidly decreased, due to θ → α-Al_2O_3 phase transformation. The Ni-coated sample has the lowest oxidation mass gain from the beginning of oxidation and the lowest k_p value. The k_p values of the samples with Cr- or Fe- coating, on which α-Al_2O_3 scale has been already developed before the main oxidation stage at 1000 °C were the same, and greater than those of blank and Ni-coated samples.

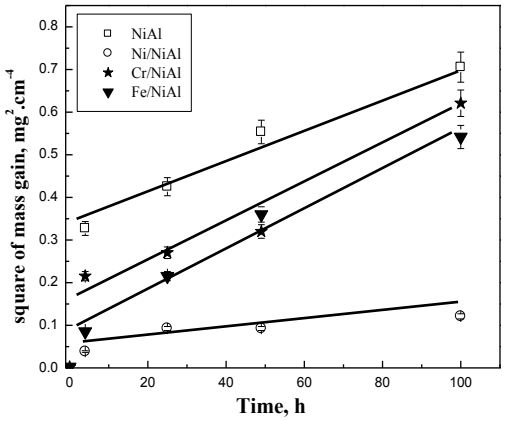

Fig.1 The oxidation kinetics of NiAl with/without Ni, Cr or Fe-coating at 1000 °C in air

Table.1 The parabolic rate constants of the oxide scale growth, k_p and the grain size of α-Al_2O_3 , r_G at 1000℃

Sample	k_p	r_G
	× 10^{-6} ($mg^2.cm^{-4}.s^{-1}$)	μm
Bare alloy	1.1	0.7
Ni coating	0.2	1.8
Cr coating	1.4	0.2
Fe coating	1.4	0.3

The XRD patterns showed that the α-Al_2O_3 phase is completely developed on all samples including blank and Ni-coated samples after 100 h of oxidation at 1000 °C. The thickness of the Al_2O_3 scale formed on bare alloy was the thickest and the thickness decreased in the order of Cr-coated > Fe-coated > Ni-coated samples. This order of thickness of Al_2O_3 scale was in agreement with that of oxidation mass gain after 100 h as shown in **Fig. 1**. Moreover, the size of α-Al_2O_3 grains was found to be significantly different depending on the coating element. **Table 1** summarizes the obtained parabolic rate constants of the alumina scale growth, k_p and the columnar grains size, r_G, of α-Al_2O_3 that measured from the cross sectional observations of the oxide scale.

As shown in **Fig. 1 and Table 1,** the grain size of α-Al_2O_3 was smaller on the alloys with Cr or Fe coating, on which θ-Al_2O_3 to α-Al_2O_3 transformation occurs rapidly. Such fast formation of α-Al_2O_3 is attributed to the formation of coated metal oxides, Cr_2O_3 and Fe_2O_3, which have an isomorphous corundum structure with α-Al_2O_3 [1, 2]. These metal oxides may provide higher density of the sites for α-Al_2O_3 nucleation, resulting in smaller grain size. Similar effect was observed on Ni-50Al with Cr- addition by Brumm et al. [3]. They suggested that the introducing of Cr as an alloying element could increase the oxide mass gain due to the smaller size of the grains.

On the alloy with the Ni-coating, the transformation to α-Al_2O_3 was further delayed; however, the oxidation mass gain was the smallest among the coated samples. The reason for the slower growth rate of θ-Al_2O_3 formed on the Ni-coated sample is not clear at the moment. Probably the formation of NiO and/or $NiAl_2O_4$ layer(s) above the θ-Al_2O_3, at the early stage of oxidation, decreases the oxygen potential gradient across the θ-Al_2O_3 scale because of the reduced oxygen potential at the $NiAl_2O_4$/ θ-Al_2O_3 interface [4] and decreased the growth rate of θ-Al_2O_3. Moreover, the delayed the transformation to α-Al_2O_3 by Ni- coating apparently resulted in the largest grain size of α-Al_2O_3.The grain size of α-Al_2O_3 formed on bare alloy was not the smallest among the oxidized samples; however the oxidation mass gain after 100 h of oxidation was the greatest. This is because of the fast growing θ-Al_2O_3 that continuously grew thicker for longer time of oxidation due to the delayed transformation to α-Al_2O_3.

4. CONCLUSION

The effect of metal coatings on the growth kinetics of α-Al_2O_3 formed on β-Ni-50Al at 1000 °C in air was investigated. The parabolic rate constant of α-Al_2O_3 scale formed on the different coated samples was significantly affected by the size of α-Al_2O_3 grains. This effect was in a relation with the time for the θ-Al_2O_3 to α-Al_2O_3 phase transformation. The α-Al_2O_3 scale that transformed earlier always consists of smaller size of grains; on the other hand the size of grains became greater with the delay of the θ-Al_2O_3 to α-Al_2O_3 transformation. Different metal coatings affect the long-term oxidation kinetics at 1000 °C in air because they affect the θ-Al_2O_3 to α-Al_2O_3 phase transformation and, therefore, the size of the grains of the α-Al_2O_3 scale.

5. References

1. Y. Kitajima, S. Hayashi, T. Nishimoto, T. Narita, S. Ukai, Oxid Met., 73, 375–388 (2010)
2. Y. Kitajima, S. Hayashi, T. Nishimoto, T. Narita, S. Ukai, Oxid Met., 75, 41–56 (2011)
3. M.W. Brumm and H.J. Grabke, Corr. Sci., 33, 11, 1677-1690(1992)
4. Birks N, Meier G, Frederick S. Petit, Introduction to high temperature oxidation of metals, 2nd. Ed., Cambridge, London (2004)

Factors Affecting the Development Mechanism of the Protective Oxide Scale on Alumina-Forming High Temperature Materials: A Brief Survey

Jerzy Jedliński

Surface Engineering & Analysis Lab and Department of Physical Chemistry & Modeling of Processes, Faculty of Materials Science and Ceramics, AGH University of Science and Technology, al. Mickiewicza 30, 30-059 Kraków, Poland, e-mail: jedlinsk@agh.edu.pl, phone: +48 126172816; fax: +48 126172493

Short Abstract

Current state of the art concerning development mechanism of protective α-Al_2O_3 scale on *alumina formers* during their exposures under various service conditions is briefly summarized. It is emphasized that the evolution of the oxide scale occurring prior to formation of the α-Al_2O_3 layer should be carefully followed in order to determine the consecutive stages of this process. Application of such approach to own results and reported by other authors ones led to the factors affecting the early oxidation stages of scale development on *alumina formers* as well as determination of how they affect this process. Moreover, they enabled to differentiating between their influence on the scale growth mechanism ('mechanistic effect') and on the rate of the scale evolution ('kinetic effect'). The factors leading to accelerated and retarded development of α-Al_2O_3 scale are discussed based on detailed elucidation of the phase transformation of transient aluminium oxides into α-Al_2O_3.

Keywords: high temperature oxidation, protective alumina scale, scale growth mechanisms

Statement of the Problem

Alumina Formers

Although referred to as the group, *alumina formers* are largely different materials. Fig. 1 illustrates main differences between the materials classified in this group. Obviously, there are several links between various factors, properties and features shown in Fig. 1.

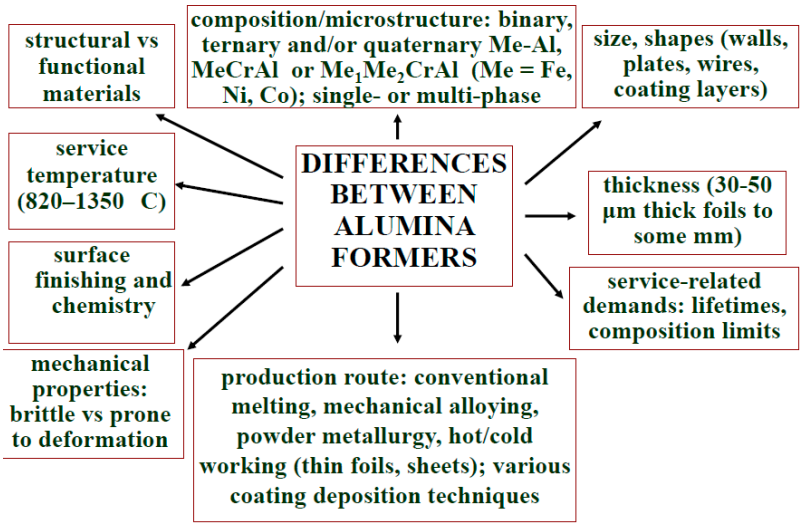

Fig. 1 Differences between *alumina formers*: schematic representation

However, despite of the differences, there are following important similarities of *alumina formers*: (1) the Al content exceeding the critical concentration necessary to form the stable and continuous layer of protective α-Al_2O_3; (2) superior to other metallic materials oxidation resistance at high temperatures (> 850°C) associated also with the additions of small amounts of reactive elements and/or of noble metals, essentially Pt, which reduce significantly the scale spallation; (3) formation of transient aluminium oxides (γ-, δ- and/or θ) later transformation of which into α-Al_2O_3 being accompanied by ca. 10% volume contraction; (4) 'sensitivity' of the oxidation behaviour and resistance to the presence of contaminations and impurities.

Oxidation-Induced Degradation of *Alumina Formers*

For a given *alumina former* the crucial parameter related to its oxidation-induced degradation rate is the rate of the depletion of aluminium at the surface layer of component or sample. Two following processes affect this rate: (i) consumption rate of Al via formation of the oxide scale; and (ii) the rate of supply of Al from the interior of substrate to its surface. Obviously, the capability of the formation of α-Al_2O_3 is affected by the initial content of Al in the substrate.

Consumption of Al may be accelerated by scale cracking and/or spallation which result from generation and relief of stresses (growth, structural and/or thermal) in the whole scale-substrate system ([2]).

Development of the Protective α-Al_2O_3 Scale

Formation of protective α-Al_2O_3 layer or sub-layer in the scale occurs during the final part of the early oxidation stages of *alumina formers*. Detailed understanding of these stages is important not only as fundamental issue but also has its practical significance for three following reasons: (i) development of transient aluminas corresponding to fast consumption of Al from the substrate; (ii) stress-generating phase transformation of transient aluminas into α-Al_2O_3 due to mentioned above volume contraction; and (iii) service and testing exposure conditions frequently involve relatively short heating-cooling cycles, 1 hour or less, during which the reacting scale-substrate system is subjected to high thermal stresses.

The systematic study of the development mechanisms of α-Al_2O_3 scale on representative *alumina formers* led to four 'Scale Growth Routes' ([1]) based on the evolution of three following observables: (i) scale morphology, (ii) scale phase composition, and (iii) growth mechanism of the scale. It should be explained that the latter is described in terms of the region were 'new' scale is formed.

The next step is the elucidation of the factors which affect the scale development process and to assess their effects. In particular, it is important to differentiate between their influence on the scale growth mechanism ('mechanistic effect') and on the rate of the scale evolution ('kinetic effect').

Description of the Approach

Because the approach applied to define the mentioned above 'Scale Growth Routes' was rather mechanistic than kinetic it is necessary to complete it with data which describe the rate of the scale evolution, obviously taking into account also the effect of the oxidation temperature. The first step towards this goal is to find the major factors which affect the evolution rate of the scale.

This paper is focused on such a goal. However, discussing the factors should be preceded by short description of the phase transformation of transient aluminium oxides into α-Al_2O_3, the crucial process which occurs during early oxidation.

Phase Transformation of the Transient Aluminium Oxides into α-Al_2O_3: what we know (in brief)

It is accepted that the phase transformation of transient aluminium oxides (γ-, δ- and/or θ-Al_2O_3) into α-Al_2O_3 occurs via nucleation-growth mechanism. It can be affected in three following ways ([3,4]): (i) chemical; (ii) microstructural; and (iii) mechanical. The first one is related to concentration of defects required for transformation to occur (anion vacancies), the second one to either heterogeneous nucleation or crystallographic relationships between the oxides initially formed (i.e. chromia) and α-Al_2O_3, while the third one to the strain energy brought about by large (or small) ions.

Experimental Findings

Fig. 2 illustrates the surface morphology and phase composition of the scale on two single-phase *alumina formers* β-NiAl and Fe20Cr5Al alloy. It follows from this results that: (i) α-Al_2O_3 develops much faster on Fe20Cr5Al alloy than on β-NiAl intermetallic compound; and (ii) the phase transformation exhibits local nature.

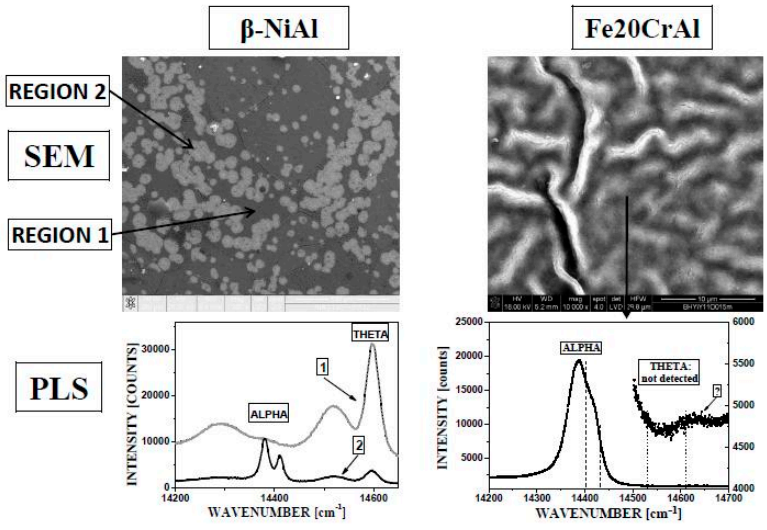

Fig. 2 Surface morphology (SEM) and phase composition (PLS) of the scale on β-NiAl and Fe20Cr5Al *alumina formers* oxidized at 1100°C for 15 min. in air (Fe20Cr5Al after [5]

Fig. 3 indicates that chromium even present at the impurity level (100 wt. ppms) in β-NiAl may agglomerate and offer preferential regions for the phase transformation of aluminium oxides ([6]).

In Fig. 4 it is shown the surface of the scale on different grains of β-NiAl ([7]). Taking into account that round regions (patches) indicate regions of the phase transformation of alumina oxides, it appears that this process occurs with different rates on various substrate grains, i.e. its rate depends on the surface substrate grain orientation.

Other findings can be summarized as follows:

(i) on FeCrAl alloys initially the multilayered scale is formed, the outermost being Fe-rich, the intermediate Cr-rich (presumably Cr_2O_3) and the innermost Al_2O_3 ([8]);

(ii) it is possible to accelerate substantially development of α-Al_2O_3 on FeCrAl alloy by their pre-oxidation in vacuum, i.e. by lowering oxygen partial pressure in reacting atmosphere ([9]);

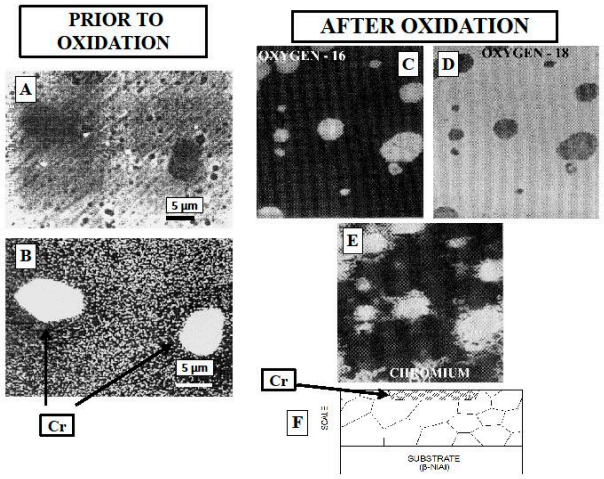

Fig. 3 Distribution of chromium impurity (90 ppm) at the surface of β-NiAl prior to oxidation (Prior to Oxidation: SEM/BEI and corresponding EDX map of Cr distribution; After Oxidation: Distributions of oxygen isotopes and chromium at the surface of the scale formed during oxidation (SIMS-images) (after [6])

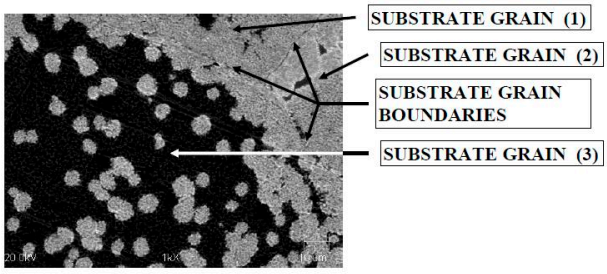

Fig. 4 Different surface fraction of patches indicating different progress of phase transformation in alumina scale on various substrate grains of β-NiAl oxidized at 1373 K for 15 min. in oxygen ([7])

(iii) the phase transformation may result in radial cracks, which occurs on β-NiAl ([1,10,11]) and/or in convoluted scales on FeCrAl alloys ([1,1,13]). Cracked regions where α-Al_2O_3 is preferentially formed, referred to as patches, grow laterally and successively dominate in scale, as is illustrated in Fig. 5. Simultaneous growth of the oxide in cracks leads to ridges (Fig. 6).

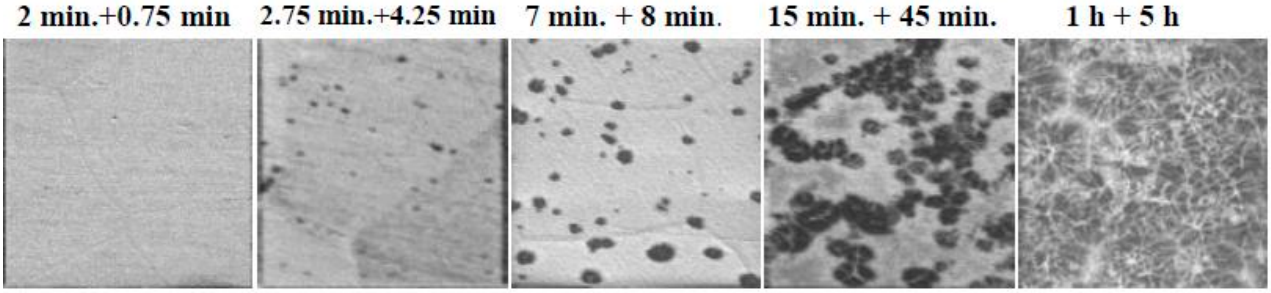

Fig. 5 SIMS image of ^{18}O ions from external scale surface on β-NiAl oxidized using two-stage oxidation exposure procedure at 1100°C for periods shown above images (the first period corresponds to exposure in $^{16}O_2$ and the second to exposure in $^{18}O_2$): darker regions indicate the predominant inward growth mechanism typical for α-Al_2O_3, while brighter predominant outward growth typical for transient aluminium oxides and growth of ridges in cracks ([14])

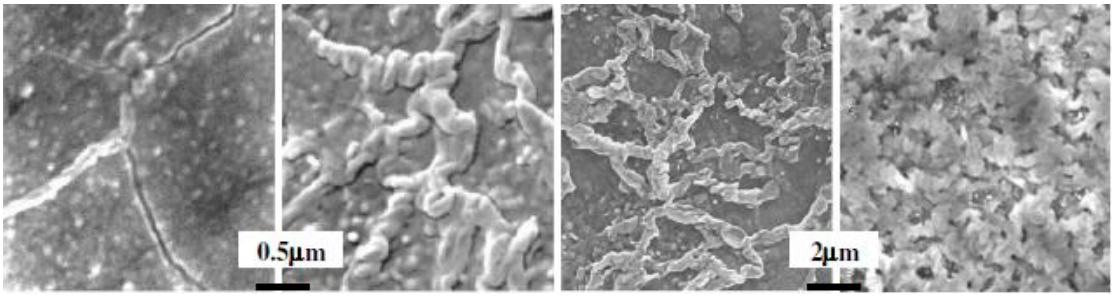

Fig. 6 Oxide growth in cracks and formation of ridges in scale on β-NiAl at 1100°C (15 min., 1 hr, 6 hrs, 24 hrs) ([15])

(iv) the influence of reactive elements on the early oxidation stages depends on their amount, form and solubility in the substrate and in the aluminium oxides ([5]). They may affect both: the scale growth mechanism and kinetics of the scale evolution. This issue need more detailed discussion which is offered in this paper;
(v) the mature α-Al_2O_3 scale in most cases is duplex and consists of an inner, compact layer formed by typical thickening due to progress of the oxidation reaction and an outer layer formed via growth of ridges and/or dislocation climbing mechanism proposed elsewhere ([16]).

Concluding Remarks

The early oxidation stages of *alumina formers* involve many processes and should be described by the scale evolution and the effect of various factors on it. For instance, chromium found as the phase transformation accelerator can provide this effect by virtue of formation of the outer sub-layer of the scale and, thereby, lowering the oxygen partial pressure or by crystallographic effect related to its isomorphic structure to α-Al_2O_3: it may serve as the template for formation of this oxide.
The effect of reactive elements, on the other hand, is not such unambiguous: under some conditions they may accelerate the development of α-Al_2O_3, while under other ones, retard it.
It follows from the above that for each material it should be constructed a diagram in which the scale evolution described by its morphology, phase composition and growth mechanism will constitute one of the axis and time and temperature constitute two other ones. Such diagrams will be shown. The discussed above findings and other reported in the literature will be discussed aiming at integrated description of the development of the protective α-Al_2O_3 scale on *alumina formers*.
It should be noted that very interesting and surprising results were reported concerning the very initial stages of the scale development on FeCrAl-type foils ([17]): the formation of α-Al_2O_3 was found at the very beginning of the oxidation process which for unclear reasons disappears and re-appears later as a result of phase transformation of transient oxides. This finding needs further discussion and investigation.

Acknowledgements

The National Science Centre (Grant No. UMO-2011/01/B/ST5/06432) is gratefully acknowledged for its financial support.

References

1. J. Jedliński, *High Temperature Oxidation and Oxidation-Induced Degradation of Alumina Formers,* Mater. Sci. Forum, **595-598**, 995-1003 (2008)
2. J.R. Nicholls, H.E. Evans, S.R.J. Saunders, *Fracture and spallation of oxides*, Mater. High Temp., **14**, 5-13 (1997)
3. J. Jedliński, *Comments on the effect of yttrium on the early stages of oxidation of alumina formers*, Oxid.Met. **39**, 55-59 (1993)
4. S. Hayashi, B. Gleeson, *Phase Transformation Behavior of Al2O3 Scale Formed on Pt-Modified c0-Ni3Al-Based Alloys With and Without Hf Addition*, Oxid.Met., **77**, 237–251 (2012)
5. J. Jedliński*, Development of Oxide Scale at 1,100°C on Fe20Cr5Al Alloy Non-Implanted and Yttrium-Implanted*, Oxid.Met., **79**, 41–51 (2013)
6. J. Jedliński, M.J. Graham, G.I. Sproule, D.F. Mitchell, G. Borchardt, A. Bernasik, A *Combined Approach : Isotopic Exposure / SIMS Analysis / SEM to Study the Early Stages of Oxidation of β-NiAl at 1473 K*, Mater.Corros., **46**, 297 - 305 (1995)
7. J. Jedlinski, *Local and Microstructure-related Effects Affecting the High Temperature Oxidation of Alumina Formers: A Brief Survey*, Mater. High Temp., **12**,485-496 (2005)
8. J. Jedliński, A. Glazkov, M. Konopka, G. Borchardt, E. Tscherkasova, M. Bronfin, M. Nocun, *An XPS/SEM/EDX study of the early oxidation stages of Fe19Cr5Al (+Y) alumina-forming alloys at 1173 K*, Applied Surface Science, **103**, 205 - 216 (1996)
9. M. Göbel, A. Glazkov, M. Konopka, J. Jedliński, G. Borchardt, J. Le Coze, *Influence of start-up oxidation procedure on the composition of oxide scales of high temperature alloys during the initial oxidation*, 'Microscopy of Oxidation 3', Eds. S.B. Newcomb, J.A. Little, The Institute of Materials, London, 1997, p. 12-18
10. J.K. Doychak, *Ph.D. Thesis,* Case Western Reserve University, Cleveland, USA, 1986
11. G.C. Rybicki, J.L. Smialek, *Effect of the θ-α-$A1_20_3$ Transformation on the Oxidation Behavior of β-NiAI+Zr*, Oxid.Met., **31**, 275-304 (1989)
12. P.Y. Hou, A.P. Paulikas, B.W. Veal, Growth Strains and Stress Relaxation in Alumina Scales during High Temperature Oxidation, Mat.Sci.Forum, **461-464**, 671-680 (2004)
13. Ch. Rallan, A. Akah, P. Hill, A. Garforth, Growth of Hierarchically Structured High-Surface Area Alumina on FeCrAl Alloy Wires, Indian Journal of Materials Science, vol. 2013, Article ID 251495, 7 pages, 2013. doi:10.1155/2013/251495
14. J. Jedliński, M. Konopka, K. Kowalski, A. Bernasik, G. Smoła, J. Dąbek, Z. Żurek, J. Camra, Scale Development During Early Oxidation Stages of Polycrystalline β-NiAl at 1100°C and the Effect of Implanted Yttrium: II. Growth Mechanism and Distribution of Elements in the Scale, Microscopy of Oxidation'9 Conference and Mater. High. Temp., submitted
15. J. Jedliński, Defect-Diffusion-Stress Relationships in Modeling the Oxidation and Degradation Processes of Alumina Formers : A Brief Survey", Defect and Diffusion Forum, **237-240**,911-92 (2005)
16. D.R. Clarke, *The lateral growth strain accompanying the formation of a thermally grown oxide*, Acta Mater., **51**, 1393–1407 (2003)
17. R. Chegroune, E. d Salhi, A. Crisci, Y. Wouters, A. Galerie, On the Competitive Growth of Alpha and Transient Aluminas During the First Stages of Thermal Oxidation,of FeCrAl Alloys at Intermediate Temperatures, Oxid. Met., **70**, 331-337 (2008)

Reducing effect of a slight amount of NaCl vapor to pest oxidation of Ta-75at%Al at high temperature

Yoshiyuki SATO [(1,*)], and Motoi HARA[(1)]

[(1)] Department of Materials Science and Engineering, Graduate School of Engineering and Resource Science, Akita University, 1-1 Tegata Gakuen-machi, Akita 010-8502, JAPAN

e-mail: satoyosi@ipc.akita-u.ac.jp

1. INTRODUCTION

"Pest oxidation" is a destructive corrosion which occurs on intermetallic compounds such as Ti-Al system, Nb-Al system, Ni-Al system, and many other aluminides at temperature range around 800 - 1000°C. Metallic materials are to oxidize into some oxide particle and hard to remain its original shape any more. This phenomenon is explained as preferential oxidation of grain boundary and internal crack originated from volume change of alloy grains according to oxidation process [1]. The way how to avoid the pest oxidation is rather difficult that only the way of them is explained either to change alloy system or pass through the temperature range as fast as possible.

NaCl vapor is usually thought to be a harmful component to high temperature oxidation of metals, since it induces chlorination of metals and accelerated hot corrosion. However, some studies report an opposite effect of NaCl vapor, i.e. a reduction effect of high temperature corrosion. Kumagai et al [2] reported that oxidation rate of Ti-Al alloy made by powder metallurgy was reduced by a trace amount of NaCl mixed into pores of the alloy. In this case, NaCl was produced from Cl which was used when Ti had been refined. One of the authors [3] reported that oxidation resistance of TiAl alloy is improved by a slight amount of NaCl vapor at high temperatures.

And the authors have already reported the similar effect of NaCl vapor on oxidation of $NbAl_3$ intermetallic compound [4]. In this study, oxidation behavior of another intermetallic compound, $TaAl_3$ was investigated in oxygen with a trace amount of NaCl vapor at 800°C and 900°C (1073 K and 1173 K) .

2. EXPERIMENTAL

Ta aluminide of Ta-75at%Al sample was prepared from commercial pure Ta and pure Al by arc melting method. Because the melting points of Ta and Al differ much, it is not easy to melt and make a liquid mixture of a molten alloy. Therefore, Ta ingot was melt separately, and then added a small shot of Al into Ta melt within a chamber. Continuing this procedure, almost homogenious button with about 20 mm diameter and 10 mm hight was obtained. This button was sliced vertically to make about 1.2 mm-thick experimental specimen. The surface area was measured by a photo scanner and a personal computer.

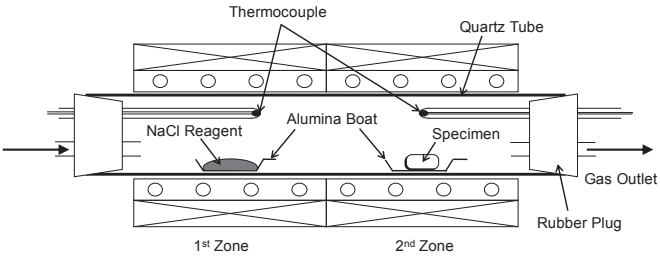

Fig. 1. Schematic illustration of the apparatus for oxidation experiment.

Oxidation test of Ta-75at%Al was accomplished by a two-zoned electric furnace. Fig. 1 shows a schematic illustration of the apparatus. Oxygen gas was introduced into the 1st zone, which was regulated at a fixed temperature, at a constant flow rate of 40 cm^3 min^{-1}. This flow rate is slow enough for the atmosphere to reach an equilibrium state. Table 1 shows the concentration of NaCl vapor at 3 kinds of fixed temperatures. These values were calculated by the equilibrium partial pressure

Table 1. Concentrations of NaCl vapor for various temperatures of the 1st zone of the furnace.

Temperature [K]	p NaCl /Pa	Vol. fraction of NaCl at 1.01×10^5Pa [ppm]
923	7.30×10^{-1}	7.2
973	3.26×10^{0}	32.1
1023	1.25×10^{1}	123

of NaCl, *p*NaCl from the reference data book [5].

Oxidation test was done to fix the temperature of the 2nd zone to 1073 K or 1173 K. Since these temperatures are always higher than that of the 1st zone, NaCl vapor will not deposit in the reaction tube. Mass gain per unit area was obtained by measuring the mass of a specimen precisely before and after a certain period of oxidation.

3. RESULTS AND DISCUSSION

Fig. 2 shows outlooks of corroded samples. Fig. 2(a) is a sample on which pest oxidation has been taken place. Ta-75at%Al was completely crushed into white particles and a little of black ones. In this way, pest oxidation brings catastrophic nature to metallic materials. On the contrary, with a slight amount of NaCl vapor in atmospheres including oxygen, the pest oxidation was suppressed as Fig. 2(b). The sample maintains its shape with a black film on the surface. It seems to be a "normal" oxidation behavior of metals and alloys.

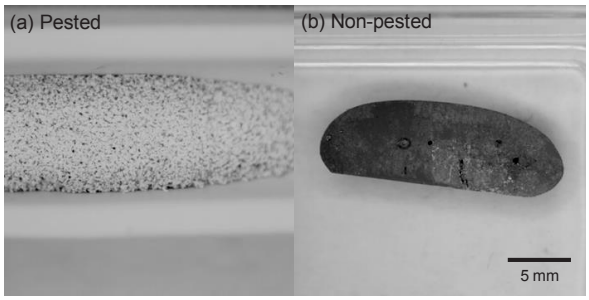

Fig. 2. Photographic images of oxidized Ta-75at%Al at 1073 K after 72 h. (a)Pested in 100%O_2, (b)non-pested in O_2 with 32.1 ppm NaCl.

Fig. 3 shows mass gain curves of Ta-75at%Al alloys in atmospheres of O_2 with a small amount of NaCl vapor at 1073 K and 1173 K. For all the oxidation conditions, mass gain has a tendency to grow with time. Oxidation kinetics is hardly determined by these figures because some of the plots include much error. In case of NaCl including conditions, pest oxidation did not occur at both the two temperatures. However, making attention on the concentration of NaCl vapor, values of mass gain are not in the order of the concentration of NaCl. Namely, neither in smaller concentration of 7.2 ppm nor in larger of 123 ppm, mass gains are relatively smaller than in the middle concentration of 32.1 ppm. This tendency is almost the same in 1073 K and in 1173 K.

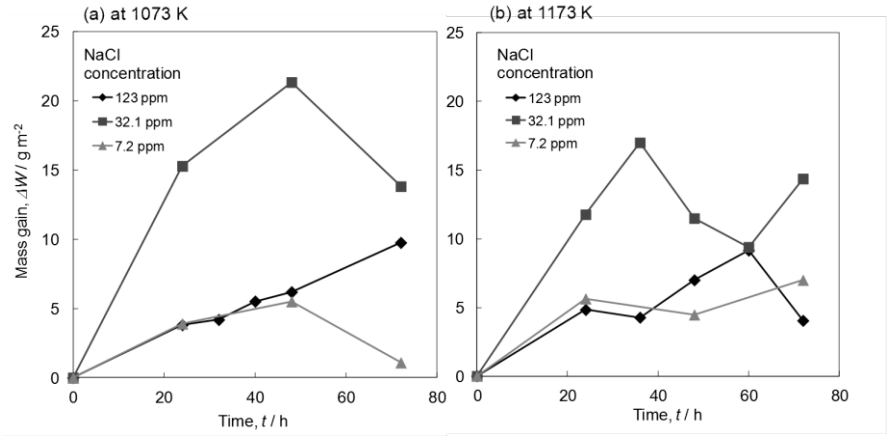

Fig. 3. Mass gain curves of Ta-75at%Al in O_2 containing various concentration of NaCl vapors (a)at 1073 K, (b)at 1173 K.

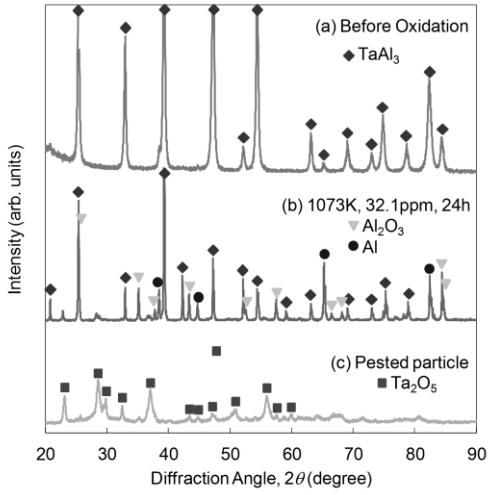

Fig. 4. X-ray diffraction patterns of the surfaces of Ta-75at%Al samples of (a) as casted, (b) oxidized at 1073 K in O_2 with 32.1 ppm NaCl after 24 h and (c) oxidized in NaCl free O_2 at 1073 K after 72 h.

Fig. 4 shows X-ray diffraction patterns for sample as cased, oxidized in NaCl containing vapor and in NaCl free atmosphere. Form Fig. 4(a), it was confirmed that Ta-75at%Al mainly contained intermetallic compound of $TaAl_3$. After the pest oxidation took place in NaCl free oxygen atmosphere at 1073 K, formed oxides were able to identify as Ta_2O_5 in Fig. 4(c). While in Fig. 4(b), on conditions in which the pest oxidation did not occur, oxidation product mainly consisted of Al_2O_3 in addition to $TaAl_3$ in the substrate under a thin oxide layer. In other conditions of non-pesting oxidation, identified compounds are the same.

Cross-sectional investigation was done to the non-pested sample

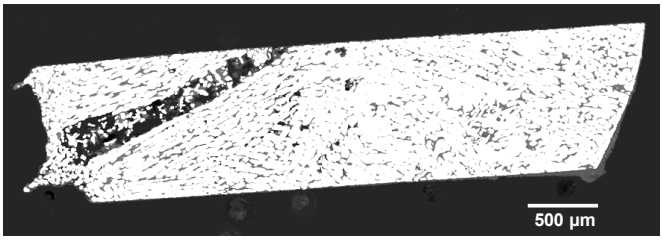

Fig. 5. Cross-sectional back scattered electron image of Ta-75at%Al oxidized in O_2 with 7.2 ppm NaCl at 1073 K after 48 h.

oxidized in 7.2 ppm NaCl at 1073 K for 48 h. Fig. 5 shows a back scattered electron image of a cross-section. From this figure, although the pest oxidation did not take place, it is obvious that grain boundary corrosion was proceeding silently. It seems that the sample barley maintained its form but destruction of the body is about to begin. Aside from that, a thin scale of several tens of micrometers is observed on the top surface of the sample. It suggests that the scale layer has a possibility to be a protective layer of oxidation or corrosion in NaCl containing atmosphere.

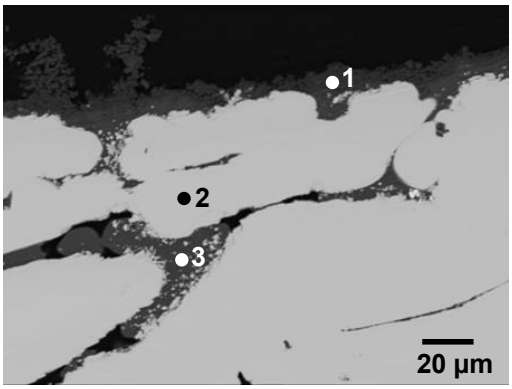

Pos.	Ta	Al
1	0.1	99.9
2	32.0	68.0
3	0.5	99.5

Fig. 6. Enlarged cross-sectional images of Fig. 5 and EDS spot analysis in atomic percent of Ta and Al elements corresponding to numbered positions.

Fig. 6 shows an enlarged image at around alloy/scale interface of Fig. 5 and results of EDS spot analysis of corresponding locations. Because of the difficulty of light elements detection, the EDS analysis was done only over metallic elements. The very outer layer (position 1) and region resembles like grain boundary (position 3) were constructed from almost Al element itself, not from Ta. This indicates that these parts consisted of only Al_2O_3. Considering about the mechanism of pest oxidation, formation Al_2O_3 at grain boundaries is natural. However, formation of Al_2O_3 layer at the outer surface is unexpected, because on $TaAl_3$, protective Al_2O_3 film won't form due to a slow diffusion rate of Al within the intermetallic compound just like the case in $NbAl_3$ [1]. This suggests another different mechanism of forming Al_2O_3 at the outer surface. As for position 2 in Fig. 6, atomic ratio of Ta and Al was out of 1:3 but was about 1:2. This indicates Al spilling out from the $TaAl_3$ grains to form Al_2O_3 around them. And further, Ta did not form Ta oxides at all in this stage of oxidation.

Pest oxidation of Ta aluminides will proceed consuming oxygen provided by grain boundary diffusion from the surface of the alloy. Oxidation of Ta-75at%Al proceeds step by step as eq. (1) ~ eq. (3).

$$TaAl_3 + 3/4O_2 \rightarrow TaAl_2 + 1/2Al_2O_3 \quad (1)$$

$$TaAl_2 + 3/4O_2 \rightarrow TaAl + 1/2Al_2O_3 \quad (2)$$

$$TaAl + 3/4O_2 \rightarrow Ta + 1/2Al_2O_3 \quad (3)$$

Along with these reactions, corrosion product of Al_2O_3 will stay at the grain boundaries and then oxidation of Ta will follow later on. Finally, by some cracks originated from volume shrinkage , spallation of grain would take place and Ta-75at%Al reaches particles of Ta_2O_5.

Reduction mechanism of oxidation for Ta-75at%Al by NaCl vapor is proposed as follows. First, NaCl vapor reacts with O_2 at high temperature to produce Cl_2 gas by eq. (4).

$$2NaCl(g) + 1/2O_2(g) \rightarrow Cl_2(g) + Na_2O(s) \quad (4)$$

At an equilibrium state, partial pressures of O_2, NaCl and Cl_2 gases were calculated as Table 2 [5]. Concerning about Gibbs free energy change at 1073 K and 1173 K, Cl_2 gas reacts with Al not with Ta, nor O_2 gas with Al and Ta. This results in formation of volatile $AlCl_3$ at the surface of Ta-75at%Al.

Table 2. Equilibrium partial pressures of O_2, NaCl and Cl_2 calculated at 1173 K for O_2 with 32.1 and 123 ppm NaCl atmospheres.

NaCl concentration [vol ppm]	$p\,O_2$ /Pa	p NaCl /Pa	$p\,Cl_2$ /Pa
32.1	1.01×10^{-5}	3.23×10^{0}	6.27×10^{-15}
123	1.01×10^{-5}	1.24×10^{1}	9.25×10^{-14}

$Al(s) + 3/2Cl_2(g) \rightarrow AlCl_3(g)$ (5)

$AlCl_3(g)$ will vaporize into atmosphere, where the oxygen partial pressure is high enough to oxidize $AlCl_3$.

$2AlCl_3(g) + 3/2O_2(g) \rightarrow Al_2O_3(s) + 3Cl_2(g)$ (6)

Al_2O_3 film formed on the surface of Ta-75at%Al has a protective nature against oxidation, being a diffusion barrier against O_2. This film also prevents plenty supply of O_2 along the grain boundary. Therefore, pest oxidation of Ta-75at%Al was reduced in NaCl vapor containing atmospheres. However, it is still not clear that in which concentration of NaCl vapor is most suitable. And it is noteworthy that pest oxidation is about to take place even if in NaCl vapor containing atmospheres referring to an observation of cross-section shown in Fig. 5.

4. CONCLUSION

High temperature oxidation behavior of Ta-75at%Al was investigated in O_2 with a slight amount of NaCl vapor at 1073 K and 1173 K. Pest oxidation did not take place in atmospheres containing NaCl vapor. Mass gain of Ta-75at%Al was effectively reduced from pest oxidation in NaCl free O_2, and the values of them were increased with oxidation time. The mass gains were largest in 32.1 ppm NaCl atmosphere. In NaCl containing atmospheres, Al_2O_3 film was formed at the surface of Ta-75at%Al and also Al_2O_3 was detected on grain boundaries inside the alloy. Intermetallic compound of $TaAl_3$ no longer maintained its aluminum content of original. The mechanism of reducing effect of pest oxidation by NaCl vapor was discussed thermodynamically, and protective Al_2O_3 formation mechanism via $AlCl_3$ production by Cl_2 induced from NaCl was proposed.

References

[1] Taniguchi, S. and Kurokawa, K, Kouon Sankano Kiso To Ouyou (in Japanese), Uchida Rokakuho (Tokyo, 2006), p. 37.

[2] Kumagai, M *et al*, "Influence of Minor Elements on Oxidation Behavior of TiAl Intermetallic Compound", *J. Japan Inst. Metals* (in Japanese), Vol. 57, No. 6 (1993), pp. 721-725.

[3] Hara, M. and Kitagawa, Y., "Effect of Trace Amounts of NaCl Vapor in High-Temperature Oxidation of TiAl", *Oxidation of Metals*, Vol. 52, Nos.1/2 (1999), pp. 77-94.

[4] Sato, Y. *et al*, "Effect of a Trace NaCl Vapor to Depression of Pesting Oxidation on Intermetallic Compound of $NbAl_3$", *Zairyo-to-Kankyo* (in Japanese), Vol. 60 (2011), pp.81-86.

[5] Barin, I., "Thermochemical Data of Pure Substances", VCH (Weinheim, 1989).

Oxidation Behavior of Cu-modified Alumina Forming Austenitic Fe-Ni-Cr-Al Alloys

Shigenari Hayashi [(1)], Taiki Kudo [(2)], Suzue Yoneda [(2)], and Shigeharu Ukai [(1)]

(1) Division of Materials Science and Engineering, Faculty of Engineering,
Hokkaido University, Kita13 Nishi8, Sapporo 060-8628, JAPAN
(2) Division of Materials Science and Engineering, Graduate School of Engineering,
Hokkaido University, Kita13 Nishi8, Sapporo, 060-8628, JAPAN

e-mail: hayashi@eng.hokudai.ac.jp

1. INTRODUCTION

Heat-resistant Cr_2O_3 forming austenitic stainless steels, which have good weldability, manufacturability, and excellent high-temperature mechanical properties are widely used in various industries. However, high-temperature capability, particularly its oxidation and corrosion resistance of Cr_2O_3 scale forming austenitic stainless steels is approaching its temperature limit due to recent demands for increasing the operation temperature of plants in order to improve the thermal efficiency. Al_2O_3 scale forming alloys have higher capability against high temperature oxidation and corrosion at higher temperatures than Cr_2O_3 scale forming alloys, since Al_2O_3 is much more stable in various oxidizing and corrosive atmospheres and has much lower growth rate than Cr_2O_3 scale[1]. Therefore much effort has been paid to develop Al_2O_3 forming austenitic stainless steels in the steel making industries, however, Al_2O_3 forming austenitic steels has not been well developed yet. The reason of difficulty for producing Al_2O_3 forming austenitic steels is that higher alloy Al content is required to form the protective Al_2O_3 scale in austenitic alloys and higher additions of Al results in decrease various properties of alloys, such as weldabilty and ductility by formation of brittle intermetallic compounds of β-NiAl, γ'-Ni3Al, and α-Cr. In order to develop Al_2O_3 forming austenitic stainless steels, decrease the critical Al content for a protective Al_2O_3 scale formation on austenitic matrix is strongly requested.

Our recent investigation of high-temperature oxidation of Al_2O_3 forming austenitic alloys found that Cu is favor to high temperature oxidation resistance and small additions of Cu (~5at.%) is very effective to decrease the critical Al content for Al_2O_3 scale formation on austenitic Fe-Ni-Cr-Al alloys. In this study, we investigated the oxidation behavior of Cu modified Fe-Ni-Cr-Al alloys at 1000°C in air and discussed the effect of Cu on decrease in the critical Al content for a protective Al_2O_3 scale formation.

2. EXPERIMENTAL,

Cu-modified Fe-Ni-Cr-Al austenitic alloys of nominal composition (in at.%) Fe-17Ni-16Cr-5Al-0.06Zr and with 3.5, 5, 7Cu were prepared by argon-arc melting the pure consistent metals (~99.99% pure). In order to confirm the effect of Cu, Fe-20.5, 22, or 24Ni-16Cr-5Al-0.06Zr alloys without Cu addition were also prepared in this study. The alloy ingots were homogenized in a vacuum at 1200˚C for 24 h. Approximately 1 mm thick oxidation samples were cut from the homogenized ingots. The samples were polished up to 3μm diamond paste, followed by ultrasonic cleaning in acetone.

Oxidation experiments were performed using a box furnace in air at 1000˚C for different time intervals up to 100h. Samples were hanged in Al_2O_3 crucible in order to collect spalled oxide scale during oxidation including heating and cooling, and placed in the furnace hot zone. Surface morphology and cross-sectional microstructure was examined by conventional technique such as scanning electron microscope (SEM) and electron probe micro analyzer (EPMA). Element distributions of samples oxidized for shorter time were measured as a function of depth from the sample surface using glow discharge optical emission spectroscopy (GD-OES).

3. RESULTS AND DISCUSSION,

<Oxidation kinetics>

Figure 1 shows the oxidation kinetics of Fe-17Ni-16Cr-5Al alloys with and without different Cu content in air at 1000˚C. In Figure 1, short-term oxidation kinetics up to 4h of Fe-20.5, 22, or 24Ni-16Cr-5Al-0.06Zr alloys was also plotted for comparison. Oxidation rate for Fe-17Ni-16Cr-5Al alloy without Cu was rapid during an initial 20h of oxidation, and decreased for longer oxidation. The oxidation mass gain of an initial oxidation stage, up to around 20h, decreased with increasing alloy Cu content, but the alloy with 3.5%Cu still oxidized with relatively faster rate. The oxidation mass gain

of 5%Cu alloy at the initial oxidation stage significantly decreased, and this alloy oxidized continuously with a very slow rate up to 100h. The oxidation rate of alloys in a slow oxidation stage after around 20h was also found to decrease with Cu addition. Higher Ni addition, which corresponds to Cu content in Cu-modified alloy, to the alloys decreased the oxidation mass gain at a short-term oxidation stage, however the oxidation mass gains of those alloys without Cu addition were still higher than that of alloys with sufficient Cu content 5%~. This result strongly indicates that the Cu addition to Al_2O_3 forming Fe-base austenitic alloys improves oxidation resistance.

<Cross-sectional microstructures>

Figure 2 shows the cross-sections of Fe-17Ni-16Cr-5Al-Zr with and without different Cu contents after 100h of oxidation in air. Thick duplex with an outer Fe and Ni rich and inner Cr-rich oxide layers was formed on the alloy without Cu addition. Below the thick duplex oxide scale internal Al_2O_3 and AlN precipitates were formed. With increasing Cu content, the thickness of an external duplex oxide scale became thinner, and the number of internal precipitates decreased due to a formation of the thin Al_2O_3 layer at the top of rod-like internal Al_2O_3 precipitates. However, this internal Al_2O_3 layer could not prevent formation of internal Al_2O_3 and AlN precipitates. Continuous and thin exclusive Al2O3 scale was developed on the alloy with 5%Cu addition. Only a few internal precipitates were formed below the Al2O3 scale, and those precipitates were identified to be Zr-rich oxide. Those results apparently suggested that Cu promotes formation of exclusive Al_2O_3 scale, and decreases critical Al content to form a protective Al_2O_3 scale on austenitic Fe-base alloys.

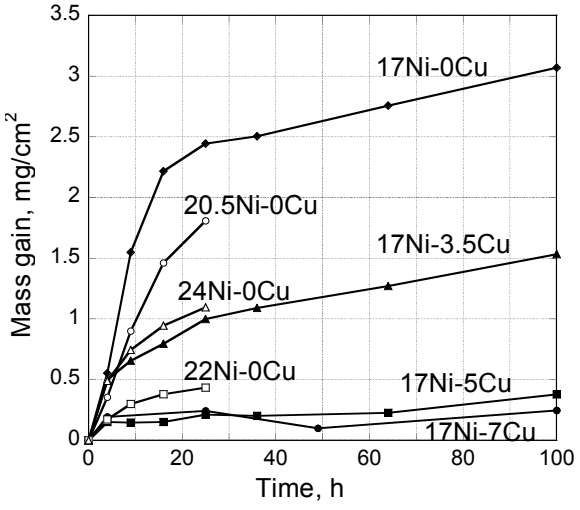

Fig. 1 Oxidation kinetics of Cu-modified Fe-Ni-Cr-Al-Zr alloys at 1000˚C in air.

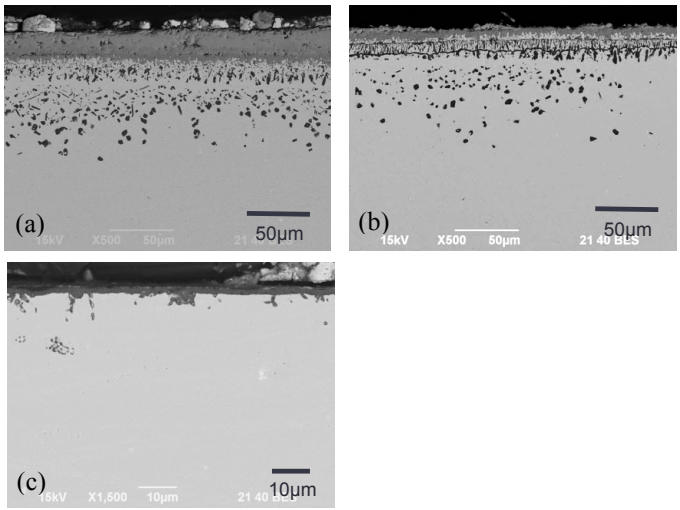

Fig. 2 Cross-sectional microstructures of Fe-Ni-Cr-Al-Zr alloys with/without Cu addition oxidized for 100h, (a) 0Cu, (b) 3.5Cu, and (c) 5Cu.

4. CONCLUSION,

Oxidation behavior of Cu-modified austenitic Fe-Ni-Cr-Al-Zr alloys was investigated. Cu promoted the exclusive Al_2O_3 scale formation and was found to decrease critical Al content down to at least 5at.% to form a external Al_2O_3 scale on austenitic Fe-base alloys without any detrimental intermetallic compounds formation. This alloy system is expected to alternative materials for conventional Cr_2O_3 scale forming austenitic stainless steels.

Acknowledgements,

This work was supported by JKA and its promotion funds from AUTO RACE.

References.

[1] Hindam, H. and Whittle, D.P., Microstructure, “Adhesion and Growth Kinetics of Protective Scales on Metals and Alloys”, Oxid. Met., Vol. 18, Nos. 5/6 (1982), pp.245-284.

Influence of Mo on High Temperature Oxidation Behavior of La added 20 mass%Cr-6 mass%Al Ferritic Stainless Steel

Akito Mizutani [1,*], Mitsuyuki Fujisawa [1], Chikara Kami, [1] and Shigenari Hayashi [2]

[1] Steel Research Laboratory, JFE Steel Corporation, Kawasaki-cho1, Chuo-ku, Chiba 260-0835, JAPAN
[2] Faculty of Engineering, Hokkaido University, Kita13 Nishi8, Sapporo 060-8628, JAPAN

e-mail: a-mizutani@jfe-steel.co.jp

1. INTRODUCTION,

Ferritic stainless steel containing Al has excellent high temperature oxidation resistance because of the formation of a protective Al_2O_3 scale on the surface. It is well known that the addition of reactive elements, such as La, Zr, Y, and Hf to that steel improves their oxidation resistance. Mo addition to a stainless steel is known to improve its corrosion resistance at room temperature. However, there were few studies about the influence of Mo on the high temperature oxidation behavior of Fe-Cr-Al alloy. In this study, the influence of Mo on the high temperature oxidation behavior of La-added 20Cr-6Al ferritic stainless steel was investigated.

2. EXPERIMENTAL,

Chemical compositions of the steels are shown in Table 1. 50kg ingots were prepared with the vacuum induction melting method. These ingots were rolled into 1mm thickness sheet with hot rolling and cold rolling, followed by solution treatment at 1000℃ for 1min. Specimens of 20 mm width and 30 mm length were cut down from the sheets and abraded to 320-grid finish by SiC-paper. The specimens were oxidized at 1100℃ in air. The weight change of specimens after the oxidation was measured periodically until total oxidation time became 200h. Fracture sections of Al_2O_3 scale were observed by SEM using snapping samples after they had been immersed for several minutes in liquid nitrogen.

Table 1. Chemical compositions of steels (mass%)

Steel	Al	Cr	Mo	La
La free steel	5.6	20.1	-	-
	5.6	20.1	5.0	-
La-added steel	5.6	20.1	-	0.06
	5.5	19.8	4.9	0.08

3. RESULTS AND DISCUSSION,

Fig. 1 shows the influence of Mo on the weight change of La-free steel and La-added steel at 1100℃ in air. The weight changes of all the steels obeyed a parabolic law after 25h of oxidation. The comparison of the weight change of Mo-free steel with and without La addition indicate that the weight change after 200h of oxidation was reduced by La-addition. The influence of Mo on the oxidation behavior varies depending on La-free steel or La-added steel. For La-free steel, growth of the Al_2O_3 scale was slightly accelerated by Mo addition before 50h of oxidation, whereas the growth rate of the scale was reduced by 5Mo addition after 100h of oxidation. After the 200h of oxidation, the weight change of 5Mo steel was smaller than that of Mo-free steel. On the other hand, the growth rate of the scale on La-added steel was obviously increased by 5Mo addition. The effect that La addition decreases the oxidation rate of 20Cr-6Al steel was weakened by Mo addition.

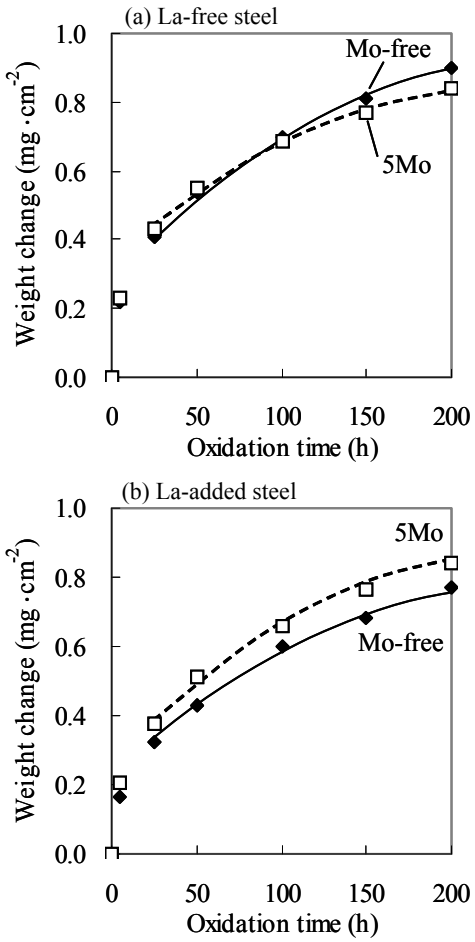

Fig.1. Influence of Mo on weight change of (a) La-free steel and (b) La-added steel at 1100℃ in air.

Fig. 2 indicates the fracture sections of Al_2O_3 scale of La-free steel and La-added steel without Mo addition after 200h of oxidation. Al_2O_3 scales consist of two grain layers i.e. outer equiaxed grain and

inner columnar grain. For Mo-free steel, thickness of equiaxed grain of La-added steel was thinner than that of La-added steel. Fig. 3 shows change in the thickness of columnar grain and equiaxed grain in Al_2O_3 scale formed on La-free steel and La-added steel as a function of square root of oxidation time. The both thickness of columnar grain and equiaxed grain increased obeying a parabolic law on all the steels. For Mo-free steel, La addition considerably suppressed the growth rate of equiaxed grain in Al_2O_3 scale. The growth rates of equiaxed grain were almost unchanged by Mo addition on the both La-free steel and La-added steel. However, the growth rate of the columnar grain was influenced by Mo addition. 5Mo addition to La-free steel reduced the growth rate of columnar grain in the Al_2O_3 scale. In contrast, 5Mo addition to La-added steel obviously increased the growth rate of the columnar grain on that steel.

According to Isii et al. [1], it was observed that segregation of La to grain boundary in Al_2O_3 scale formed on La-added 20Cr-5Al steel. They inferred the segregation suppressed the diffusion of Al and O via grain boundaries and reduced the growth rate of the Al_2O_3 scale. In this study, it is considered that increase in the growth rate of the Al_2O_3 scale by Mo addition was caused by decrease in the segregation of La at the grain boundary due to Mo addition.

4. CONCLUSION,

Influence of Mo on high temperature oxidation behavior of La-added 20Cr-6Al stainless steels at 1100℃ was investigated. When 5Mo added to La-free steel, oxidation rate of this steel slightly decreased. Contrastingly, the oxidation rate of La-added steel was increased by the 5Mo addition. Beneficial effect that La addition decreases the oxidation rate of 20Cr-6Al steel was weakened by the Mo addition.

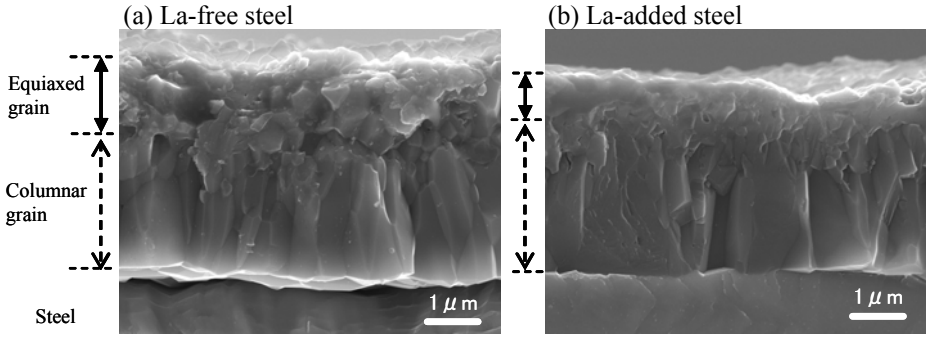

Fig.2. SEM cross sectional images of Al_2O_3 scale of Mo-free (a) La-free steel and (b) La-added steel after 200h of oxidation at 1100℃.

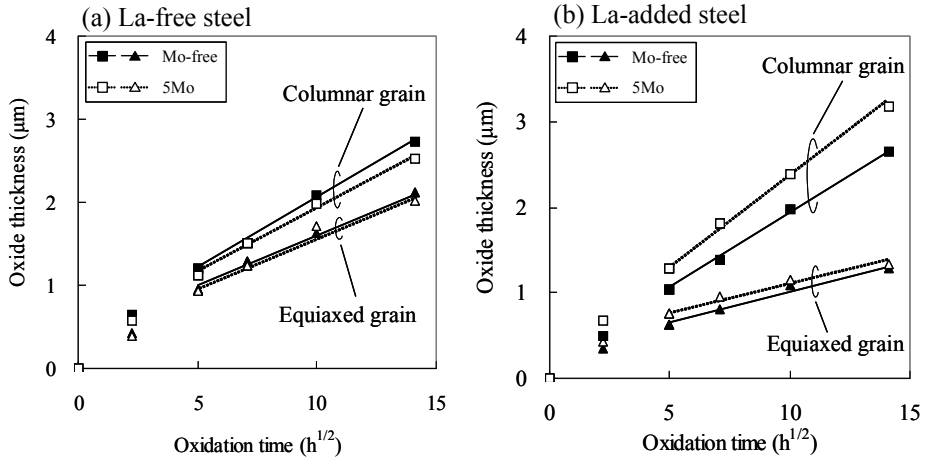

Fig.3. Change in thickness of columnar grain and equiaxed grain in Al_2O_3 scale formed on (a) la-free steel and (b) La-added steel at 1100℃.

References

[1] K. Ishii, M. Kohno, S. Ishikawa and S. Satoh : Mater. Trans., **38**(1997), 787

Case study for boiler tube failure of welded austenitic stainless steel

Han-sang Lee*, Se-hee Na, Jine-sung Jung, Doo-soo Kim and Keun-bong Yoo

Power Generation Lab., Research Institute of Korea Electric Power Corporation,
Munji-Ro 105, Yuseong-Gu, Daejeon, KOREA
e-mail: hs1213@kepco.co.kr

1. INTRODUCTION

Increasing operating temperatures in fossil power plants require better oxidation and corrosion resistances as well as higher creep strength. Especially, the welded joints in steam boiler tube can be a weak point for long operating hours. The failed welded joints of austenitic stainless steel, TP347H were prepared from the operating facilities. A microstructural investigation for the welded joints analysis was carried out to find the root causes in the present study.

2. EXPERIMENTAL

The welded joint of a boiler tube, TP347H were exposed to the steam temperature of 550 ~ 620°C for 8,400hrs (Fig. 1(a)). The crack was detected at boundary between fusion and heat affected zone by non-destructive test (Fig. 1(b)). The chemical compositions of TP347H tube are shown at Table 1 and microhardness was measured along boundaries between fusion and heat affected zone using a vickers hardness tester under 200 g load. For the microsturctural observation, we used scanning electron microscope (JSM6360, JEOL) at 15kV.

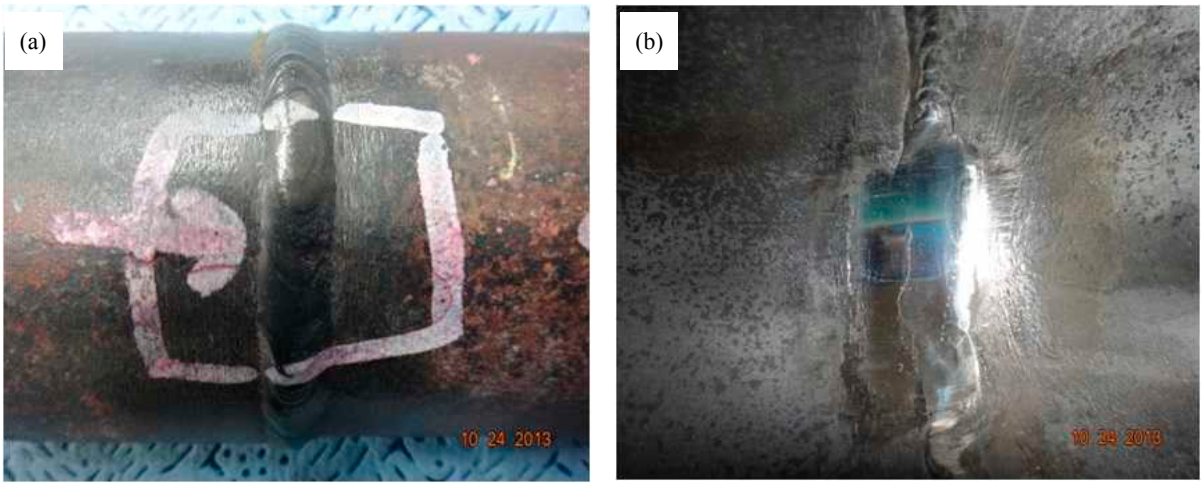

Figure 1. Failed welded joint of boiler tube exposed to 550 ~ 620°C for 8,400hrs

Table 1. Chemical compositions of boiler tube, TP347H

C	Si	Mn	P	S	Ni	Cr	Nb	Fe
0.072	0.32	1.99	0.03	0.012	10.1	18.02	0.97	Bal.

3. RESULTS AND DISCUSSION

Figure 1(a) and (b) are optical micrographs of failed welded joint. Crack initiated and propagated along grain boundaries next to interface of fusion and heat affected zone. Oxidized layer was found around crack and its thickness decrease from 50um at steam-side to 20um at fire-side (Fig. 1(b)). Therefore, it can be thought that crack initiated steam-side and propagated to fire-side.

At the opposite heat affected zone and substrate of crack occurred region, narrow bands were found especially at fire-side. These bands are determined as a b.c.t phase by EBSD (Electron Back-Scattered Diffraction) analysis. Heat affected zone next to fusion zone can be deformed during welding process and strain-induced martensite can be formed [1]. It can be assumed that narrow bands were formed in the accommodation process of plastic deformation during welding process [2].

Cr-rich carbides are seen along grain-boundaries of heat affected zone and its density was higher than grain-boundaries

of substrate. On the other hand, Nb-rich carbides are not seen at grain interior of heat affected zone. Nb-rich carbides next to fusion zone for stabilizing can be disappeared by the input-heat of welding process. These findings and grain-boundary oxidation are known as 'knife line attack' [3].

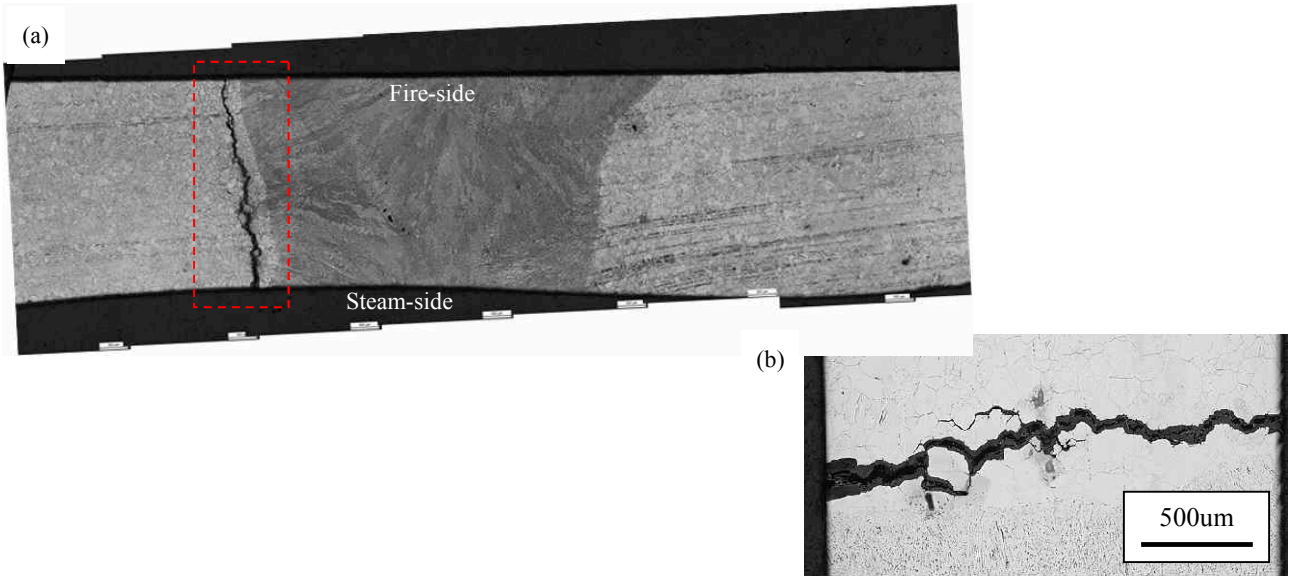

Figure 2. Optical microscope images of (a) welded joint, (b) is higher-magnification micrograph of marked rectangular region(a)

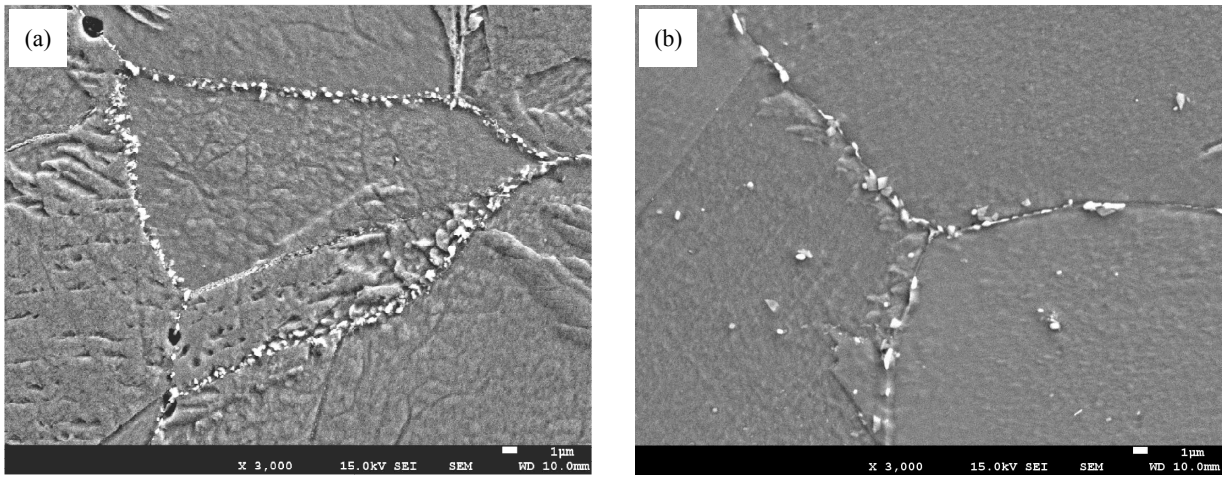

Figure 3. SEM micrographs of the grain-boundaries of (a) heat affected zone and (b) substrate

4. CONCLUSION,

The welded joint of a boiler tube, TP347H was failed by intergrannular cracking at heat affected zone. The intergrannular crack surrounded oxidation layer was initiated at steam-side and propagated to fire-side. Cr-rich carbides were formed along grain-boundaries and its density was higher than substrate. It can be assumed that Nb-rich carbides were disappeared by heat input of welding process and Cr-rich carbides were formed during operation instead of Nb-rich carbides.

References

[1] H. Lee et al, "Influence of peening on the corrosion properties of AISI 304 stainless steel", Corrosion science, vol.51 (2009), pp. 2826-2830.
[2] Mitsuhiro Okayasu et al, "Strain-induced martensite formation in austenitic stainless steel", J. Mater. Sci, vol. 48 (2013), pp. 6157-6166.
[3] S.A. Jenabali Jahromi et al, "Failure analysis of welded joints in a power plant exhaust flue", Eng. Failure analysis, vol. 13 (2006), pp. 527-536.

Early stage oxidation behaviour of single-crystal nickel-base superalloy during heating in various environments

Jine-sung Jung[*1], B. A. Shollock[2] and Keun-bong Yoo[1]

[1]Power Generation Lab., Research Institute of Korea Electric Power Corporation,
Munji-Ro 105, Yuseong-Gu, Daejeon, KOREA
e-mail: 96105436@kepco.co.kr
[2]WMG, International Manufacturing Centre, University of Warwick, Coventry, U.K.
e-mail: b.shollock@warwick.ac.uk

1. INTRODUCTION

Single-crystal nickel-base superalloys are extensively used for turbine blades with thermal barrier coating (TBC) systems in gas turbine engines. In the event of the coating failure in service, the substrate is directly exposed to a corrosive gas environment and is damaged by oxidation. Understanding the oxidation behaviour of the bare metal is crucial to improve the performance of single-crystal nickel-base superalloys.

Traditionally, researchers have assumed that all oxidation occurs at an isothermal temperature and any initial oxidation may be disregarded. In order to fully understand oxide evolution, the initial oxidation stages during heating must be investigated. Furthermore, there have been no controlled studies comparing changes at and near the alloy surface as a function of oxygen partial pressure [1-3]. The present chapter evaluated the oxide formed during heating and the effect of partial oxygen pressure on both oxide formation and near-surface microstructural changes for single crystal CMSX-4.

2. EXPERIMENTAL

The used alloy is the second generation single-crystal nickel-base superalloy CMSX-4. Prior to oxidation test samples were ground and polished ant then were cleaned using acetone and methyl alcohol in ultrasonic cleaner. In order to investigate the early stages of oxidation during heating to temperature, samples were heated to a temperature of 1135℃ in various environments, under pure oxygen, argon, and vacuum. As temperature reached 1135℃ rapid cooling was carried out by pulling the furnace. The surface roughness of samples was measured using a white light interference microscope (ZYGO) before and after heating. After heating experiments, field emission gun SEMs equipped with EDX were used to investigate the surface morphology and chemical composition. Subsequently, SIMS analysis was conducted on the tapered surfaces of thin scale and adjacent regions to obtain distributions of positive ions. For the TEM examination, TEM/STEM was done suing a JEOL 2010.

Table 1. Heating conditions for the superalloy

Alloy	Temperature (℃)	Environment	Partial Pressure (atm)	Notation
CMSX-4	1135	Oxygen	0.2	H
		Argon	2×10^{-9}	M
		Vacuum	2×10^{-11}	L

3. RESULTS AND DISCUSSION

Spallation on the surfaces of all the samples was not observed after rapid cooling from the heating temperature. The surface morphologies obtained from the tested samples are shown in Figure 1. In Fig. 1 (a), an as-polished sample shows a rectangular array of square gamma-prime precipitates. In the condition H (Fig.1 (b)) reaction products were exhibited on the surface. The surface from condition M (Fig. 1(c)) exhibited discrete particles of surface reactants in the form of irregular blades. On the other hand, in the case of condition L (Fig. 1 (d)), there were no evident particles of surface products.

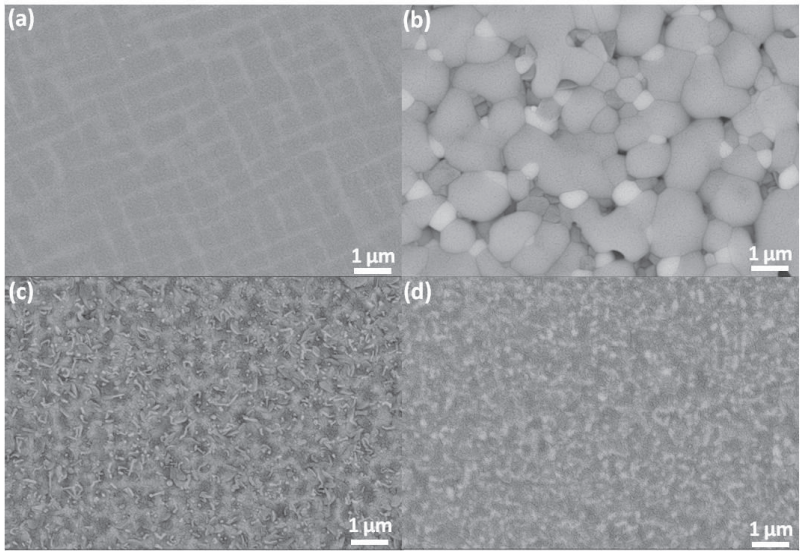

Figure 1 Back-scattered electron micrographs showing surface morphologies of samples before and after heating to 1135℃: (a) as-polished, (b) condition H, (c) condition M, and (d) condition L.

Figure 2 shows the cross-sectional microstructure together with the as-polished sample for comparison. For the as polished sample, the typical microstructure of nickel-base superalloys showing gamma-prime precipitates was shown in the crater (Fig. 2 (a)). For condition H, some oxide layers on the surface were formed during heating as seen in Fig.2 (b). The oxide layer was roughly divided into three layers; the upper layer had a thickness of 1.33 μm with some pores observed in the layer. The thickness of the middle layer was about 1.2 μm. Lastly, the black contrast bottom layer was present with a thickness of 0.73 μm and showed protrusions into the substrate metal. Also, a gamma-prime depletion area was observed beneath the bottom layer.

For the condition M, a continuous and dark contrast layer was observed on the top surface with a thickness of about 100 nm (Fig.2 (c)). A narrow gamma-prime depletion area existed beneath this oxide layer. As compared to the H condition, the width of the gamma-prime depletion area was less. For the condition L, a very thin continuous dark contrast layer was observed (Fig.2 (d)). A depleted area of gamma-prime precipitates did not clearly exist such as that observed in conditions H and M.

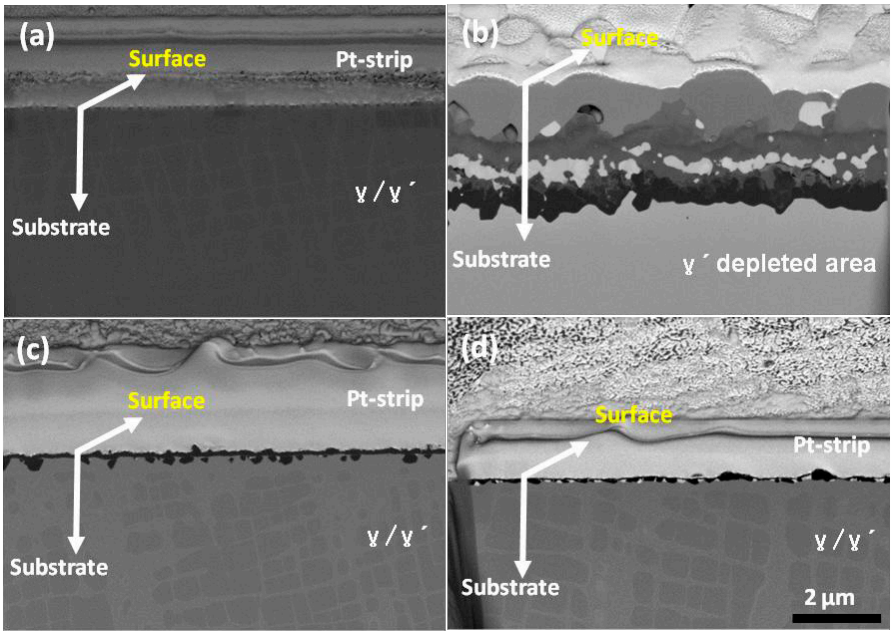

Figure 2 Cross-sectional microstructures of samples obtained in BSE mode: (a) as-polished, (b) condition H, (c) condition M, and (d) condition L.

Transmission electron microscopy was used to complement the cross-sectional microstructure and compositional information. The surface oxide of condition H was largely composed of three layers, which were classified based on the contrast observed (Fig. 3 (a)), an upper layer having a thickness of about 1.1 μm, a complex middle layer (~ 1.3 μm), and then finally a continuous lower layer (~ 0.8 μm) adjacent to the metal surface. For the condition M, the microstructure of the surface oxide consisted of a very thin continuous layer on the external surface. The thickness of the oxide formed in an argon atmosphere of condition M during heating was about 60 nm. Concurrently, some discontinuous crystallites were identified beneath the continuous dense oxide layer. The surface oxide layer was formed through the outward migration of aluminium from the bulk.

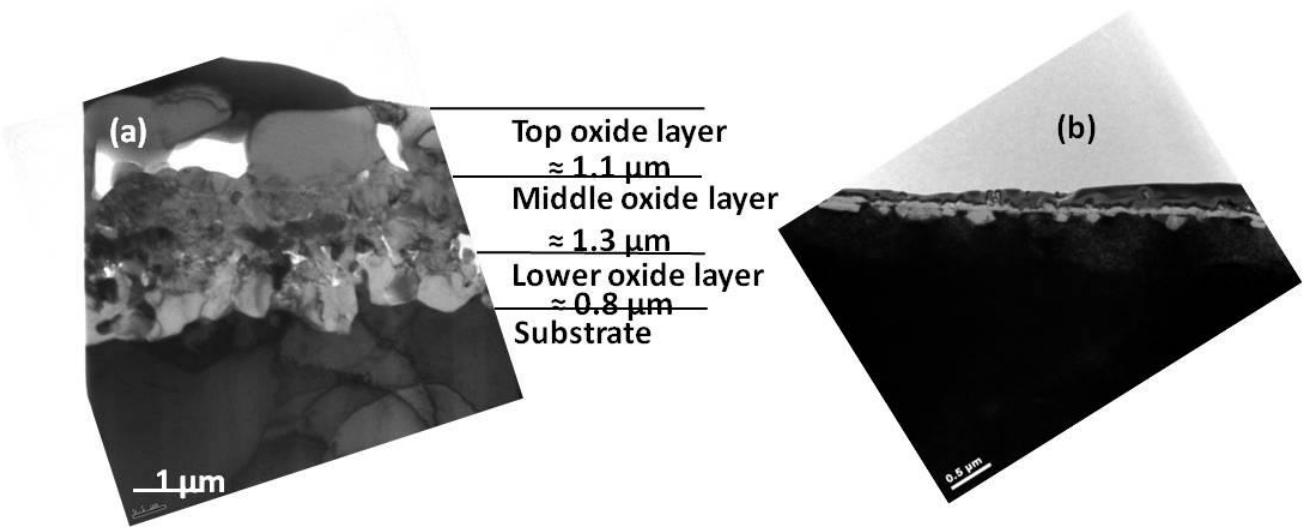

Figure 3 Bright field TEM micrographs of samples after heating to a temperature of 1135℃: (a) the H condition and (b) the M condition.

4. CONCLUSION,

A dense and continuous protective aluminium oxide layer is formed during very short exposure to high temperature in a range of oxygen partial pressure during heating up to 1135°C.

At the high oxygen partial pressure, a triple-layered oxide microstructure is formed on the alloy surface through the initial fast diffusion of nickel for the outer layer, followed by an aluminium - and chromium - enriched middle layer, and an inner alumina layer formed by outward diffusion of aluminium from the alloy combined with inward oxygen diffusion, with new oxide formed at the alloy/oxide interface.

At the lower oxygen partial pressures, the oxide microstructure consists of an exclusive aluminium oxide layer. Aluminium is the only element involved in the oxidation due to the lower oxygen activity. The source of the aluminium for the oxide layer is the decomposed aluminium from the gamma-prime precipitates present in the alloy.

A precipitate free area beneath the oxide layer evolves by the decomposition of the gamma-prime phase to form the oxide. The final oxide microstructure, or oxidation behaviour of the alloy, is significantly affected by the oxygen partial pressure through the control of the main elements involved in the oxidation.

References

[1] T.J. Nidam et al, “Effect of partial oxygen pressure on the initial stages of high-temperature oxidation of gamma-NiCrAl alloys”, Materials at High Temperatures, **20**(3) (2003), pp. 311-318.

[2] T. Jo et al, “Thermal degradation behavior of Inconel 617 alloy”, Metals and Materials International, **14**(6) (2008), pp. 739-743.

[3] A. Duval et al, “Influence of the oxygen partial pressure on the oxidation of Inconel 617 alloy at high temperature”, Oxidation of Metals, **74**(5-6) (2010), pp.215-238.

FTT Scientific Ltd

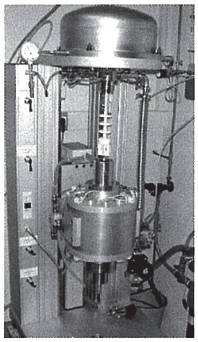

Automated Multi-Sample Thermogravimetric Analyser (CTGA-5) featuring high speed thermal cycling and continuous measurement

Unique Advantages of CTGA-5:

- **Simultaneous test and comparison of up to 5 samples**
- **Significant time savings from testing multiple samples simultaneously and fast heating and cooling rates**
- **High precision analysis of the degradation kinetics**
- **No manual intervention between thermal cycles and no contamination of samples**
- **Measurements under vacuum or chosen gas flow is possible**

Address: Unit 19 Charlwoods Road, East Grinstead, West Sussex, RH19 2HL, UK
Tel: +44 (0) 1342 323600 Fax: +44 (0) 1342 323608
Website: www.fttscientific.com Email: sales@fttscientific.com

KOUKAGIKENKOUGYOU CO.,Ltd.

～We produce the various testing machine,
we meet the demands of the researcher.～

●Products

- Tensile testing machine (simple tension、cyclic fatigue etc.)
- Creep testing machine (in high temperature etc.)
- Corrosion testing machine (acid or alkaline solution)

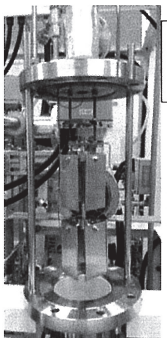

Corrosion testing machine in High Temp.Steam

1-30-6 Hayabuchi, Tsuzuki-ku,
Yokohama 224-0025, Japan
TEL/FAX:+81-45-591-9044 / 9045
E-mail:somu@koukagiken.co.jp
URL:http://www.koukagiken.co.jp

スモールパンチクリープ試験装置

本装置は、高温・ガス雰囲気中にて、微小試験片に小型のパンチャーで一定荷重を負荷し、クリープ破断強度を評価可能な試験装置です。

仕　様

スモールパンチクリープ試験装置

型式	SPC-SERT
負荷容量	1kN, 2kN, 3kN
駆動方式	デジタルプログラムサーボ方式□
試験速度	0.001～0.1mm/min
加熱装置	電気炉（300℃～1000℃）
試験容器	円筒型透明石英 （真空、Arガス、大気）
試験片	□10mm φ 3mm
データロガー	荷重、変位、温度

東伸工業株式会社

TOSHIN KOGYO CO., LTD.

〒206-0025　東京都多摩市永山6丁目20番地
TEL: 042-357-0781（営業部）　FAX: 042-357-0788
E-mail : tsk@toshinkogyo.com
URL : http://www.toshinkogyo.com

M E M O

M E M O

ISHOC 2014

Hakodate, Hokkaido Japan 2014